INTERPRAEVENT
2018 – Toyama, Japan

INTERPRAEVENT 2018
in the Pacific Rim

October 1-4, 2018 in Toyama, Japan
Symposium proceedings

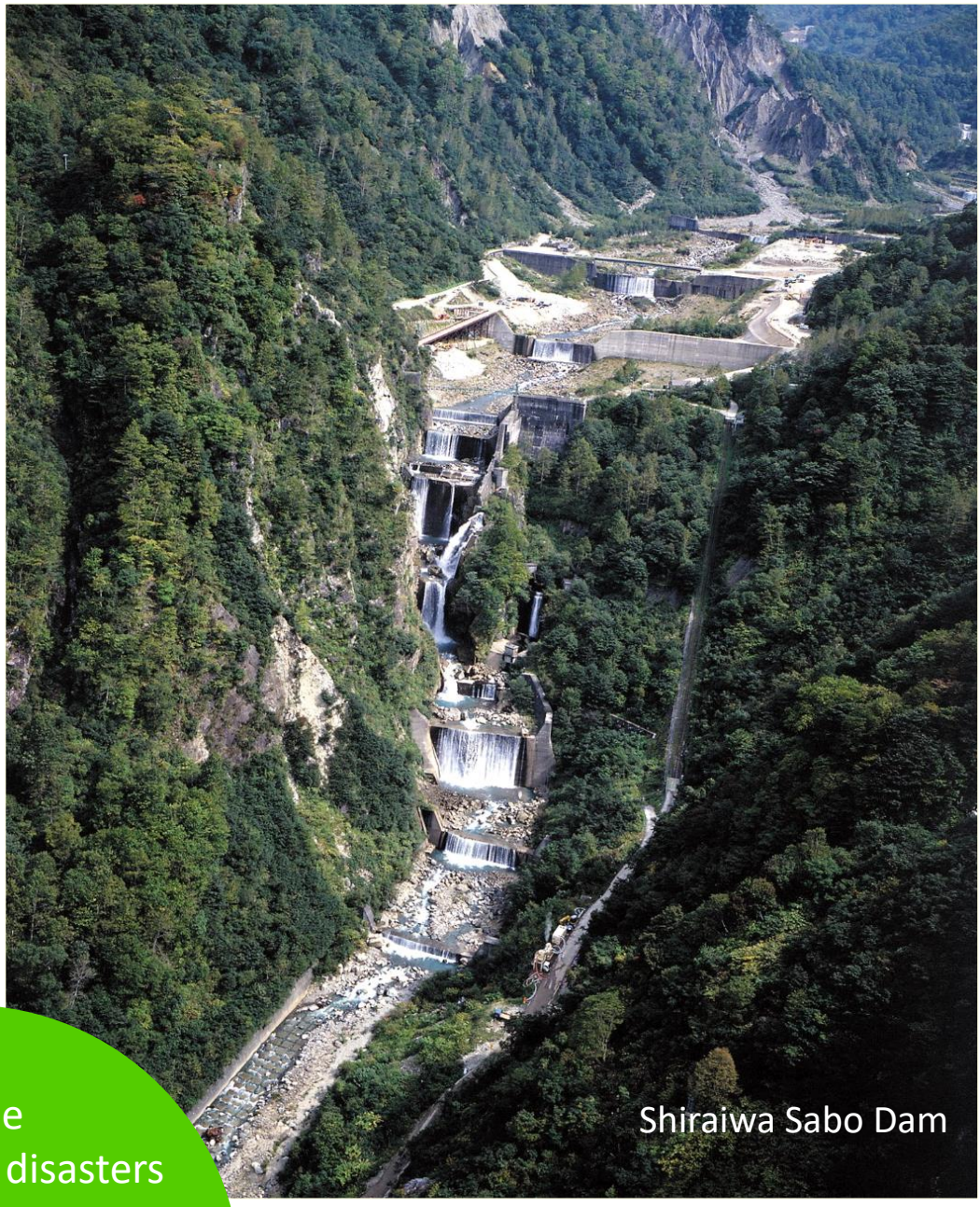
Shiraiwa Sabo Dam

Large scale
sediment disasters
in orogenic zones
and countermeasures

Edited by YAMADA T. et al.

INTERPRAEVENT2018

in the Pacific Rim

Large scale sediment disasters
in orogenic zones and countermeasures

October 1-4, 2018 in Toyama, Japan

Symposium Proceedings

Contents

Topic 1: Monitoring and modelling for debris flow, landslide, slope failure and rock fall

Evaluation of Different Methods for Debris Flow Velocity Measurements at the Lattenbach Creek
Johannes HÜBL, Andreas SCHIMMEL and Richard KOSCHUCH · 2

Recognition of the Susceptibility of Hydrogeomorphic Processes in Mountainous Watersheds through Morphometric Indicators and Field Reconnaissance
Hsienter CHOU, Chingfang LEE, Chengyi LIN, Ciyin HUANG, Tingchi TSAO, Chihhsuan HUANG and Weikai HUANG · 9

Assessment of Landslide Recurrence by Onsite Monitoring - Incidence of Hung-yeh Landslide -
Chia-Chun WU, Pei-Hsi WANG, Chih-Hui WANG, Ching-Yen CHANG and Te-Ling WU · · · · · · · · · · · · 15

Landslide Monitoring and Potential Assessment from Differential Interferometric Radar Analysis and Ground Instrumentations
Kuo-Lung WANG, Jun-Ting LIN, Yi-Hsuan LEE, Li-Wen CHEN, Jheng-Ru LAI, Tsung-Wen CHEN, Yo-Ming HSIEH, Meei-Ling LIN, Ray-Tang LIAO, Chao-Wei CHEN and Ching-Weei LIN · 24

Estimating Landslide Volumes Using LS-rapid Model - The 2000 Stože Landslide in NW Slovenia
Jošt SODNIK, Matej MAČEK and Matjaž MIKOŠ · 32

Rainfall Characteristics and the Related Geological Hazards of Slag Disposal Pit in Shanghang Region, China
Hua-li PAN, Zhi-shan ZHENG, Ming-jian HU and Guo-qiang OU · 42

Effect of Bent Flexible Vegetation on Fluvial-bed Change Under Flood Conditions
Jin-Fu LI and Su-Chin CHEN · 53

Considering the Quantitative Effect of Antecedent Rainfall on Slope Stability to Predicting Rainfall-induced Shallow Landslides at the Basin Scale
Yu LUO and Si-ming HE · 61

A Study on Setting Half-life of Effective Rainfall as a Standard of Debris Flow Occurrence by Considering Geology
Naomasa HONDA · 69

Property of Sediment Movement in Azusa River (Kamikochi)
Akihiko IKEDA, Yuki IGARASHI, Osamu FUSHIKI, Hiroki UEMORI, Shoji IGARASHI, Masahide HASEGAWA and Hidenori SAKO · 78

Analysis and Reconstructed Modeling of the Debris Flow Events on the 29th of August and the 4th of September 2016 of Afritz (Carinthia, Austria)
Claudia SAUERMOSER, Markus MOSER and Susanne MEHLHORN · 85

Critical Rainfall Analysis of Large-scale Landslide Occurrence
Tsai-Tsung TSAI, Yuan-Jung TSAI and Chjeng-Lun SHIEH ・・・・・・・・・・・・・・・・・・・・・・・・・・・・・91

Estimation of Temporal Change of River Bed Elevation Upstream of a Check Dam During Debris Flow
Naoki FUJIMURA, Yuya TAKAHASHI and Hideaki MIZUNO ・・・・・・・・・・・・・・・・・・・・・・・・・・・・97

Critical Rainfall Thresholds for Hydrological Processes Leading to Debris Flow due to Torrent Bed Material Scouring
Yasushi SANO, Takashi YAMADA, Tsuyoshi IKESHIMA and Sadakazu MATSUMOTO ・・・・・・・・・・・・・・104

Study on Correlation of Electrical Conductivity and Potential Large-scale Landslide in Taiwan
Chieh-Hsuan WENG, Yuan-Jung TSAI, Chjeng-Lun SHIEH and Tomohiro EGUSA ・・・・・・・・・・・・・・・110

Geologic and Topographic Features of Slope Failure Sites in the Aso Caldera Wall Inducted by the 2016 Kumamoto Earthquake
Haruka SAITOU, Shin'ya KATSURA, Ryota UMETANI, Mio KASAI and Tomomi MARUTANI ・・・・・・・・・・・117

Topic 2: Large scale sediment disasters: Phenomena and countermeasures

Characteristics of a Landslide Occurred in May 2015 in Mt. Hakusan and its Influence on Downstream System
Seiji YANAI ・・・124

Small Flume Experiment on Deep-seated Landslide Collapsed Material Movement
Hefryan S. KHARISMALATRI, Yoshiharu ISHIKAWA, Takashi GOMI and Katsushige SHIRAKI ・・・・・・・・・・132

A Method for Predicting and Taking Measures Against Soil Slips Generating Debris Flows in a Case Study of the 2014 Hiroshima Sediment Disasters
Yoshiharu ISHIKAWA, Hiroyuki UMEZAWA, Risa TANABE, Aya TAMEIKE and Quoc Dung DANG ・・・・・・・・・139

Safety Verification of Sabo Dams Against Large Scale Debris Flow
Nobutaka ISHIKAWA, Joji SHIMA, Ryo MATSUZAWA and Takahisa MIZUYAMA ・・・・・・・・・・・・・・・145

Emergency Responses to Debris Flow Disaster at Serizawa District, Nikko City Triggered by the 2015 Torrential Rains in the Kanto and Tohoku Region
Kenji MIWA and Kenji TAKETOSHI ・・・・・・・・・・・・・・・・・・・・・・・・・・・・・・・・・・・・・・153

Grain Size Distribution of the 1926 Volcanic Mudflow at Mt. Tokachi, Japan
Tomoyuki NANRI, Takashi YAMADA, Mio KASAI, Tomomi MARUTANI, Shigenori TAKASHIMA and Takayuki YAMAHIRO ・・・163

Extreme Torrential Flooding at Simbach on June 1st, 2016 - Key Finding of a Detailed Event Analysis -
Andreas RIMBÖCK, Johannes HÜBL and Rainer HÖHNE ・・・・・・・・・・・・・・・・・・・・・・・・・・170

Experimental Study of the Use of Stakes to Prevent Driftwood and Natural Debris from Blocking Bridges
Norio HARADA, Kana NAKATANI, Yoshifumi SATOFUKA and Takahisa MIZUYAMA ・・・・・・・・・・・・177

Study on Risk Analysis of Large-scale Landslide
Teng-Chieh HSU, Yuan-Jung TSAI, Chjeng-Lun SHIEH and Jen-Yuen CHENG ・・・・・・・・・・・・・・・・183

Topic 3: Structural countermeasures：New technology and strategy

Ten Years' Experience in Flexible Debris Flow Barriers
Corinna WENDELER, Nobuhito NISHIMURA and Matthias DENK ・・・・・・・・・・・・・・・・・・・・・192

Assessing Torrential Endangered Areas in Bavaria - Consideration of Log Jams at Culverts and Bridges -
Peter DRESSEL, Peter WAGNER and Andreas RIMBOECK ・・・・・・・・・・・・・・・・・・・・・・・199

Literature-based Expedient Criterion for Assessing the Impact Strength of Switzerland’s Rockfall Protection Embankment Inventry
Stéphane LAMBERT, Bernd KISTER and Bernard LOUP ・・・・・・・・・・・・・・・・・・・・・・・208

Experimental Study on Sediment Deposition Using Bandal Like Structure with Different Ratio of Permeable and Impermeable Part
Yuji HASEGAWA, Shuichi TAI, SHAMPA, Kenji KAWAIKE and Hajime NAKAGAWA ・・・・・・・・・・215

New Strategy for Landslide Mitigation Considering Cost Sustainability
Giulia BOSSI and Gianluca MARCATO ・・・・・・・・・・・・・・・・・・・・・・・・・・・・・・222

Load Evaluation of Debris Flow Against Steel Open Sabo Dam Using DEM
Toshiyuki HORIGUCHI, Yoshiharu KOMATSU, Satoshi KATSUKI and Nobutaka ISHIKAWA ・・・・・・・・228

Debris Capture Example by Flexible Barrier and Its Performance Verification
Hiroyuki UMEZAWA, Risa TANABE and Peihong ZHU ・・・・・・・・・・・・・・・・・・・・・・・・236

Effect of Emergency Measures to Minimize Debris Flow Disaster after the Pyroclastic Material Deposition in Gendol River due to the 2010 Eruption of Mt. Merapi, Indonesia
Naryo Widodo, ST., MT, Suyanto, ST., M.Tech, Ir. Tri Bayu Adji, MA and Masaharu MIZOGUCHI ・・・・・・243

A Novel Approach to Assess the Ability of a Protection Barrier to Mitigate Rockfall Hazard
David TOE, Alessio MENTANI, Stéphane LAMBERT, Laura GOVONI, Guido GOTTARDI and Franck BOURRIER ・・・249

Sabo Works in Wakayama Prefecture - Evolution Through Learning a Lesson from 2011 Disasters -
Keio CHITO, Yasuyoshi MIKI, Shigenori IMADA, Satoru MORIKAWA, Takehiro SAKAGUCHI and Tsuneshi NISHIOKA ・・・258

Small Fish-pond Design for Debris Flow Disaster Measure with Kanako-2D
Masato KOBIYAMA, Rossano D.L. MICHEL, Maurício A. PAIXÃO and Gean P. MICHEL ・・・・・・・・・・264

The Effects of Hydraulic Structures on Streams Prone to Bank Erosion in an Intense Flood Event: A Case Study from Eastern Hokkaido
Daisuke AOKI, Mio KASAI and Mari IGURA ・・・・・・・・・・・・・・・・・・・・・・・・・・・・・270

Topic 4: Integrated basin-scale sediment management for sustainable development

Maintenance and Utilization of a Sabo Facility Designated as an Important Cultural Property - The Shiraiwa Sabo Dam -
Takeshi OSAKA and Hisashi WATANABE · 277

Engineering Assessment of Aging Degradation for Small Sediment Control Structures
Sangjun IM, Won CHOI and Song EU · 287

Effects of Landslide and Forest Fire on Rainfall Threshold to Induce Bedload Discharge in Watershed in Republic of Korea
Junpyo SEO, Kihwan LEE, Changwoo LEE, Dongyeob KIM, Choongshik WOO, Heonho LEE, Taro UCHIDA and Wataru SAKURAI · 294

Maintenance of Historical Sabo Facilities by the Tateyama Mountain Area Sabo Office - An Evaluation of the Soundness and Utility of Sabo Facilities -
Hisashi WATANABE · 301

The History of Sediment Disasters and Sabo Projects in the Yomase River Basin, Nagano Prefecture, Japan
Makoto KITAHARA, Masashi TASHITA, Masaru NISHIZAWA, Masaaki KINOSHITA, Takao YAMAZAKI, Kunihiro HASEGAWA, Junichi KANBARA, Kimio INOUE, Kouji OYA and Kazuhiko NAKANE · · · · · · · · · · · 311

Topic 5: Non-structural countermeasures：Early warning and hazard mapping

A Pilot Construction of a Real-Time Monitoring System for Slow-Moving Landslide, Republic of Korea
Dongyeob KIM, Changwoo LEE, Choongshik WOO, Junpyo SEO, Minjeng KANG, Kidae KIM, Man-Il KIM and Jaehyeon PARK · 321

Advanced Hazard Information and Methods for Appropriate Evacuation During Sediment Disasters
Kana NAKATANI, Kazuki YAMANOI, Yuji HASEGAWA, Seiya HAYASHI, Shusuke MIYATA and Masaharu FUJITA · 327

Towards an Auto-nowcasting System for Landslide Hazards
Cheng-Chien LIU, Hsiao-Yuan YIN, Hsiao-Wei CHUNG, Wei LUO and Ke-Wei YAN · · · · · · · · · · · · 336

The Educational Methods Immediately after the Sediment-related Disasters on a Basis of Local Historical Experience - The Case Study of Environmental Educational Programs in Kumamoto Earthquake 2016 -
Reiko MACHIDA, Mito ICHIKAWA, Miu KITAZATO, Junya MACHIDA, Hijiri SHIMOJIMA, Teruaki IRIE, Tadakazu KANEKO and Naomasa HONDA · 341

Comparison of Debris Flow Hazard Mapping between Empirical Function and Numerical Simulation - a Case Study in Taiwan -
Ting-Chi TSAO, Chuan-Yi HUANG, Jung-Hsing CHIEN, Hsiao-Yuan YIN and Chen-Yu CHEN · · · · · · · 349

Debris Flow Detection Using LVP Sensors in Japan
Hitoshi KATO, Nobuyuki NODA, Kazuhiko HASHI, Satoshi TAGATA, Takahiro ITOH and Takahisa MIZUYAMA

・・ 355

Monitoring System of a Large Rockslide in Heisei-Shinzan Lava Dome, Mt. Unzen, Japan
Yasuyuki HIRAKAWA, Nobuhiro USUKI, Kouji FUJITA, Toshiaki TANAKA, Masafumi KANEKO, Toshiyasu UENO, Hidenori EGUCHI and Kazuhiro SHIMOKUBO ・・・・・・・・・・・・・・・・・・・・・・・・・・・・ 363

Subsurface Investigation and Landslide Monitoring as a Basis for Planning Protection Measures - Case Study Doren Landslide -
Thomas FRANDL and Margarete WÖHRER-ALGE ・・・・・・・・・・・・・・・・・・・・・・・・・・ 373

Relationship Between the Process of Large-scale Sediment Movement and Ground Vibration
Hiroshi ASAHARA, Atsuhiko KINOSHITA, Yasutaka TANAKA, Hiroaki SUGAWARA, Gengo YOSHIMURA, Wataru SAKURAI, Teruyoshi TAKAHARA and Soichi KAIHARA ・・・・・・・・・・・・・・・・・・・・・・・・ 380

A Study on Criteria of Warning and Evacuation for Large-scale Sediment Disasters Considering the Relationships with Sediment Movement and Damage
Yuna SUZUKI, Shin-ichiro HAYASHI, Shin'ya KATSURA, Mio KASAI, Nobutomo OSANAI and Tomomi MARUTANI ・・ 387

New Prediction of Sediment-related Disaster Critical Rainfall Using Meteorological Model WRF
Toshihide SUGIMOTO, Toshiyuki SAKAI and Hiroshi MAKINO ・・・・・・・・・・・・・・・・・・・・・ 394

A Method for Estimating Maximum Damage Caused by Sediment Disaster by Surveying with Artificial Satellite SAR Imagery
Shin-ichiro HAYASHI, Shin'ya KATSURA, Mio KASAI, Nobutomo OSANAI, Takashi YAMADA, Tomomi MARUTANI, Tomoyuki NORO and Joko KAMIYAMA ・・・・・・・・・・・・・・・・・・・・・・・・・・ 401

Sediment Disaster Notification System Established for the Reservoirs in Southern Taiwan
Tsai-Tsung TSAI, Kuang-Jung TSAI, Chjeng-Lun SHIEH and Yie-Ruey CHEN ・・・・・・・・・・・・・・・ 408

Detection of Landslide Candidate Interference Fringes in DInSAR Imagery using Deep Learning
Jyoko KAMIYAMA, Tomoyuki NORO, Masayuki SAKAGAMI, Yamato SUZUKI, Kazuo YOSHIKAWA, Shuhei HIKOSAKA and Ikushi HIRATA ・・・・・・・・・・・・・・・・・・・・・・・・・・・・・・・・・ 416

Topic 6: Management for sustainable land use

A Quantitative Approach for Classifying Governance Unit of Watershed Management and Flood Mitigation Based on a Long-term Landslide Inventory
Cheng-Chien LIU, Ming-Hsun KO, Huei-Lin Wen, Kuei-Lin FU and Shu-Ting CHANG ・・・・・・・・・・・ 427

Topic 1: Monitoring and modelling for debris flow, landslide, slope failure and rock fall

Evaluation of Different Methods for Debris Flow Velocity Measurements at the Lattenbach Creek

Johannes HÜBL[1*], Andreas SCHIMMEL[1] and Richard KOSCHUCH[2]

[1] Inst. of Mountain Risk Engineering, BOKU University (Vienna, Austria)
[2] IBTP Koschuch e.U., (Styria, Austria)
*Corresponding author. E-mail: Johannes.huebl@boku.ac.at

The Lattenbach creek, District of Landeck, Tyrol, is a very active torrent located in a geologic fault zone in the western part of Austria. The channel separates the Northern Limestone Alps in the North from the Crystalline Alps in the South. Aside from the regular flood events with bedload transport, the torrent produced seven debris flows and three debris floods within recent years. Due to the frequent debris flow and debris flood events the torrent is monitored by the Institute of Mountain Risk Engineering since several years. The parameters that are currently measured during an event include meteorological data in the upper part of the catchment and run-off data from the middle and lower reach of the torrent at the villages Grins and Pians. In the last years the monitoring equipment has been constantly improved. Additional to the standard sensors like radar for water level measurements, seismic sensors for ground motion detection and infrasound sensors for acoustic wave identification, a high frequency Pulse Doppler Radar has been installed, which provides the opportunity to measure the instantaneous surface velocity of a debris flow in different range gates. Together with a recently installed 2D-Laser scanner this setup provides the possibility to determine a very precise approximation of the discharge with a high temporal resolution. On this basis different methods to determine the velocity of debris flows were applied and compared. The results show, that the applied concept to record data of debris flows in a high temporal resolution seems to be promising.

Key words: Debris flow, monitoring, surface velocity, surge velocity, Lattenbach

1. INTRODUCTION

The Lattenbach creek, District of Landeck, Tyrol is a very active torrent located in a geologic fault zone in the western part of Austria. Due to the frequent debris flow and debris flood events the torrent is monitored by the Institute of Mountain Risk Engineering for several years. The parameters that are currently measured during an event include meteorological data in the upper part of the catchment (station Dawinalpe) and flow depth, flow surface topography, ground movement and velocities in the middle reach of the torrent.

To get a debris flow hydrograph typically data of channel geometry, flow depth and velocity, derived by time-distance method or particle image velocimetry, are used. To facilitate the calculation of an instantaneous debris flow hydrograph, velocity data collected by a High Frequency Radar utilizising the Doppler effect [*Hübl et al.*, 2017], are applied.

For the September, 16th 2016 debris flow at Lattenbach, these velocities are than compared with velocity estimates by the time-distance method, using either flow height or seismic signals as input.

2. LATTENBACH CATCHMENT

The watershed of the Lattenbach torrent has a catchment area of 5.3 km² and is located westwards the city of Landeck, Austria. The Lattenbach feeds the river Sanna, which is a tributary to the river Inn. The upper limits of the watershed is at around 2900 m above sea level (asl.), the outlet at 840 m asl. Both, the village Grins in the middle reach of the channel and the village Pians at the fan of the catchment, are affected by debris floods and debris flows [*Arai et al.*, 2013].

Geologically the catchment is divided into a northern part, Northern Limestone Alps, and a southern part, Crystalline Alps. The tectonic transition between these geologic units is marked by the incised channel of the Lattenbach. Due to intense mechanical loading of the rock and often unfavorable bedding of the strata parallel to the

hillslope numerous mass movements have led to an unlimited debris potential for mass wasting processes. Hence sediment transport processes are supposed to be limited by the availability of a transporting media rather than by the availability of erodible debris.

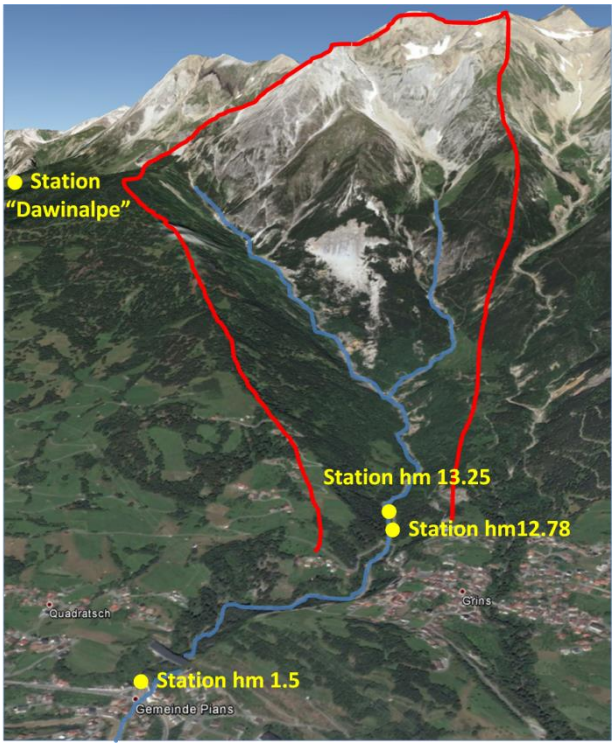

Fig. 1 Catchment Lattenbach and location of the monitoring sites (modified from Google earth, Image©2018DigitalGlobe).

Severe events of debris flows and debris floods are reported in the years 1911, 1912, 1925, 1944, 1949, 1965, 1966, 1973 and 1998, 2005, 2007, 2010, 2015, 2016 and 2017. Analyzing the chronicle, the most probable triggers resulted from short-duration thunderstorms.

Following these major events, structural mitigation measures were continuously constructed along the channel. Since 1908, approximately twenty check dams were built to stabilize the channel bed and to consolidate the slopes. However, until today a considerable number of them had already been destroyed, in particular those situated in the middle reaches of the catchment.

3. MONITORING CONCEPT

The recent monitoring concept is the result of about 10 years of experience. It consists of two sites, one at the apex of the fan at hm 1.5 and one in the middle reach of the torrent (**Fig. 1**) with two stations at hectometer (hm) 12.78 and 13.25. Additionally a meteorological station was set up in the headwater (Dawinalpe).

The discharge in the middle reach is calculated by the measurement of cross-section area and flow velocity with a frequency of 1 Hz. Therefore, three radar sensors for continuous level measurement, a 2D-laser scanner and a High Frequency Radar were chosen to collect the data (**Fig. 2**).

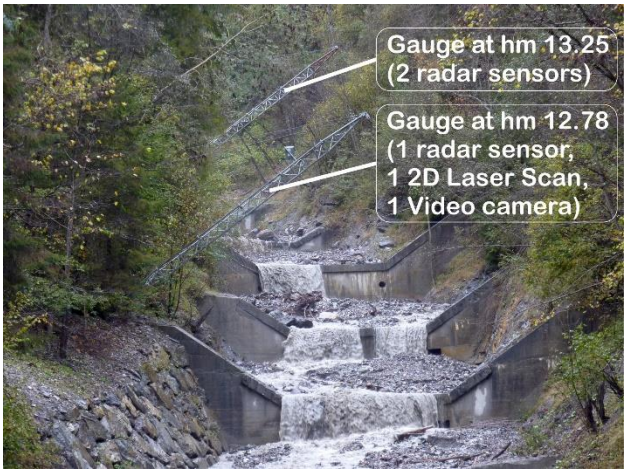

Fig. 2 Monitoring site "Grins" in the middle reach of Lattenbach, consisting of two single steel supports made of Garaventa elements with mounted sensors.

4. VELOCITY ESTIMATION

To demonstrate the velocity calculation by different methods the debris flow on September 10th, 2016 is used. This debris flow with a duration of one hour consisted of about 50 surges, most of them lasting only a few seconds. Obviously the velocities varied according to the surges and the times in-between.

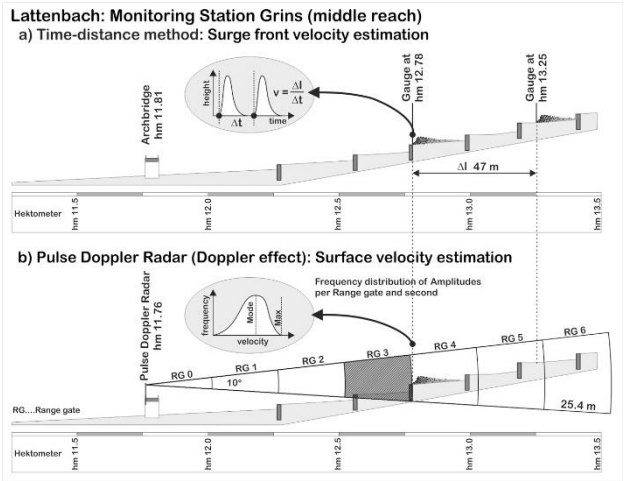

Fig. 3 Velocity estimation concepts for debris flows

4.1 Instantaneous velocity estimation by Radar signal

All radar technologies have in common to get information about distant objects by using electromagnetic waves. The behavior of electromagnetic waves between the transmitter, target and receiver is determined by the laws of wave propagation and strongly depends on the frequency. The used frequency range is from 1 MHz to 100 GHz. Roughly speaking, a low frequency means large wavelength (long antenna needed), has a long range, because of the low atmospheric attenuation and has a poor resolution. High frequency means the opposite. The choice of suitable frequency is determined by these properties on the one hand and on the other hand by the available technology for active and passive components. Additional to that, a frequency range for the operation of the radar must be requested from the public administration office.

The basis for all applications is the radar equation, which establishes a relationship between the specifications of a system and its detection range. To monitor torrential hazards, landslides, rock fall and snow avalanches the detection range should be up to 2 km with a distance resolution of some tens of meters, the temporal resolution should cover the expected speed range from 1 to 100 m/s and the minimal target size to be detected should be about one square meter. The radar should work in any weather conditions at any time continuously with a low power consumption to ensure autonomous energy supply.

A high-frequency signal in the X-band (10.425 GHz) is pulse-modulated in a high-frequency switch, amplified to an output power of about 1 W and radiated from a parabolic antenna to the detection area. The reflected beam from the observed area returns to the antenna and is recorded by the receiver. If an object is moving within the detection area with the velocity v, the reflected signal will experience a frequency shift (Doppler effect). The frequency shift of the reflected radar signal is proportional to the velocity of the moving object. It is positive for approaching objects and negative for objects veering away. The velocity of the moving object can thus be determined via frequency analyses of the reflected radar beam. The resulting velocity spectrum has well defined peaks for compact objects with a single speed and becomes broad banded for avalanches or debris flows where many objects are moving at different speeds. The detection area is devided in so called range gates. For each of these the radar cross section the intensity is measured.

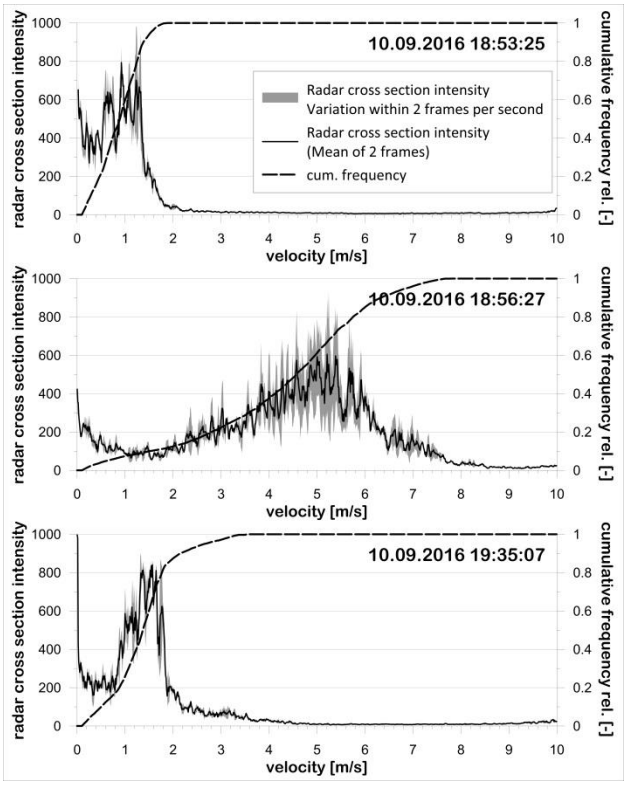

Fig. 4 Typical velocity spectrums of a debris flow surge at different times

The best type of Radar to meet all the above criteria is the Doppler Pulse Compression Radar. The selected radar system was developed by "H&S Hochfrequenztechnik" and already successfully tested for snow avalanches in Sedrun/Switzerland [*Lussi et al.*, 2012] and in Ischgl/Austria [*Kogelnig et al.*, 2012]. The maximum range for detecting moving objects with a cross-section of 1 m² in heavy weather condition (rain/snow) is about 2 km. The range gate length is adjustable between 15 m and 250 m and the detectible velocity ranges from 1 to 300 km/h. The adaption to debris flows was made within the Austrian Research Promotion Agency project (2012-2014) "Automatische Detektion alpiner Massenbewegungen mittels Hochfrequenz Radartechnik: Naturgefahren-Radar" [*Hübl et al.*, 2012].

The aperture of the antenna is 10° with the beam orientation almost parallel to the channel gradient in order to illuminate the maximum range of the slope and to get as many range gates as possible. The space-resolution is equal to the range gate length and therefore a linear function of the duration time of the pulses. The duration time itself influences the signal to noise ratio of the data in such a degree, that the longer the duration time is, the better the signal to noise ratio will be. The pulse repetition frequency of the radar device is up to 90 kHz, resulting in 90,000 pulses per second, giving about 2 frames per second for the analysis.

Within the monitoring area between hm 11.76 and 13.5 seven range gates with a range gate length of 25.4 m give a maximum range of about 175 m. The first two range gates (0, 1) are “blind” gates in air. The radar beam hits the channel in the 3rd range gate, in a distance between 75 and 100 m from the radar (**Fig. 3**). A total of 5 range gates (3-6) provide information of the flow velocity spectrum with a sampling rate of 2 Hz. The radar cross section intensities correspond to the moving objects in each of the velocity classes of 0.01 m/s width. The assumption of this method is, that during a surge the reflectivity of all moving objects does not change and corresponds to the reflectivity of water. This assumption is valid as long as the moving objects are larger with respect to the wavelength of 3 cm. The two spectrums per second are averaged and stored as one spectrum per second (**Fig.4**).

From this averaged velocity spectrum the most frequent value of the radar intensity is considered as average flow surface velocity (v.mod) in the cross-section per second. The maximum velocity of the spectrum is identified as the velocity value, when the radar cross-section intensity falls below 50 (v.max). **Fig. 4** shows the velocity distribution in range gate 3 just before, during and in the recession time of a debris flow surge.

With this method the temporal evolution of surface velocities in the different range gates can be calculated. The relative frequency of the velocities (v.mode and v.max) show a different pattern in the range gates 3 to 4 (**Fig. 5, right**). This may be due to the longitudinal profile of the monitoring sections, because the channel gradient is modified by a series of checkdams, causing a variation of the debris flow velocity inside the range gate.

4.2 Time distance method – flow height

The velocity of a debris flow surge front can be calculated with the elapsed time of the steep increase of the flow height of a surge between two nearby gauging stations. The distance between these sites divided by this timespan yields the velocity of the surge (**Fig. 3**). The recording interval for the flow height was two Hertz. This means, the flow height is recorded each 5 meter if the surge velocity is 10 m/s or each 2.5 meter if the surge velocity is 5 m/s. The onset of clearly identified surges was digitized for the gauging stations at hm 13.25 and 12.78 respectively. The estimated front velocities with this method range from 4 to 11 m/s.

4.3 Time distance method – seismic signal

This method of estimation of the front velocity uses the signals of two installed stations along the channel, recording infrasound and seismic data, whereby one station is located at hm 12.78, and the second station is installed around 90 m upstream

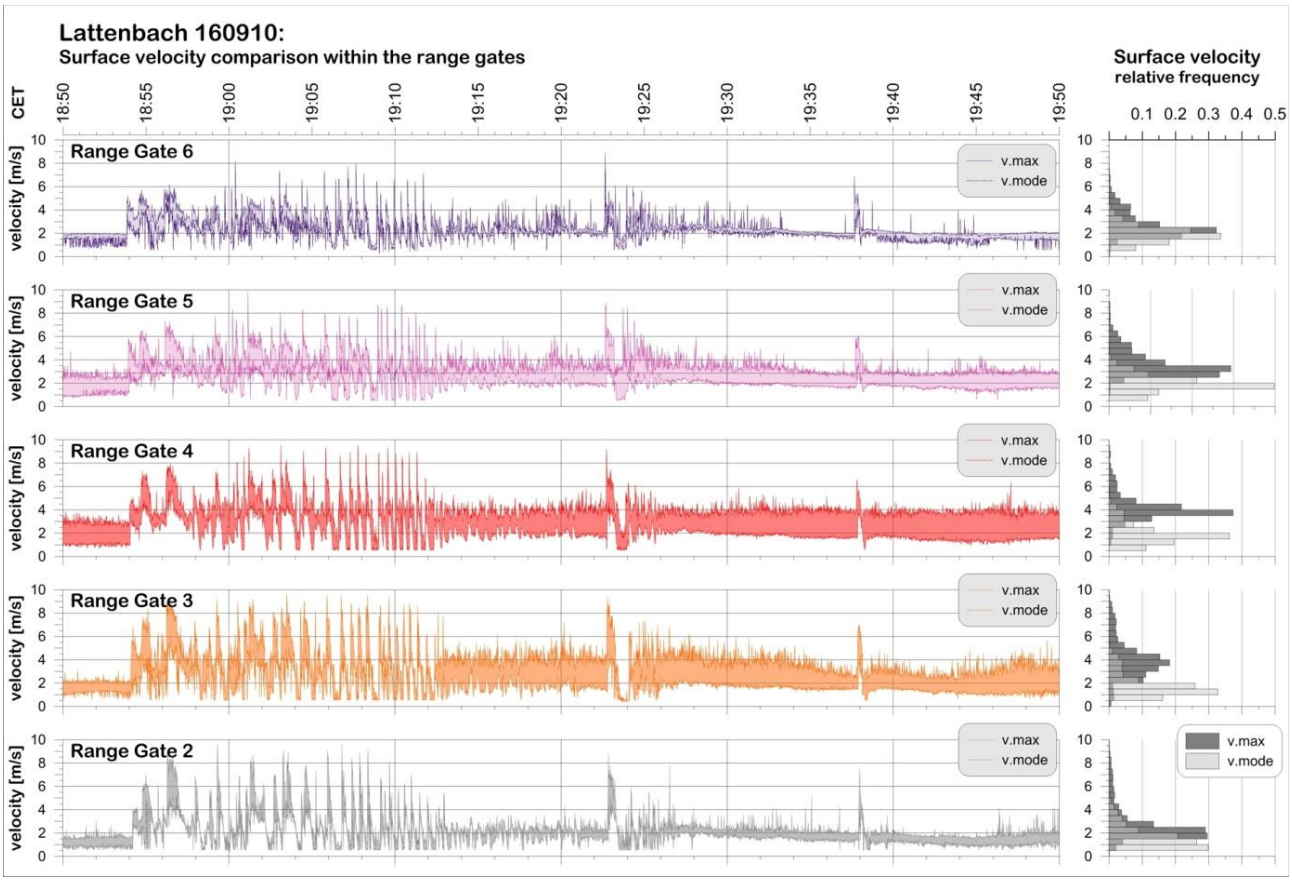

Fig. 5 Surface velocity distribution in the observed range gates (v.max means maximal velocity, v.mode stands for the most frequent velocity in the range gate)

[*Schimmel et al.*, 2016]. For the velocity estimation only the seismic signals are used, since they have a smoother signal sequence than the infrasound signal. The signal progression of the average amplitudes in a 10 to 30 Hz band (which is calculated by fast Fourier transform for every second) has been used to identify the different surges and calculate the time difference between the upper and the lower station. The estimated front velocities derived from seismic signals range from 4 to 11 m/s.

illumination the recorded video sequences of the event could not be used for this kind of analysis.

5. RESULTS

The whole debris flow consists of about 50 surges. Each debris flow surge starts with a rapid increase of flow height followed by a recession of several seconds. The largest peaks can be found at the frontal part of the event and again after half an hour. The surface velocities go in phase with flow

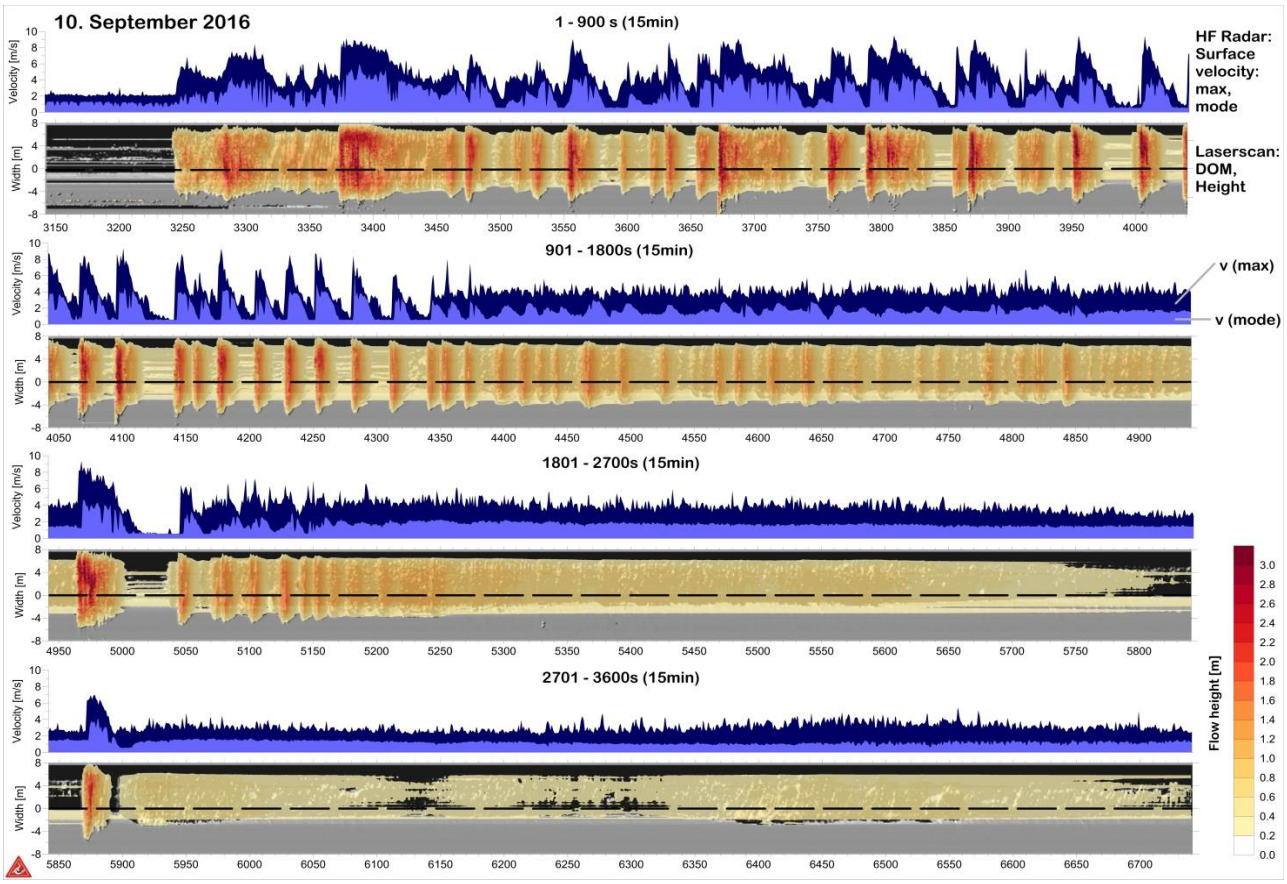

Fig. 6 Surface velocity distribution for the 10.09.2016 debris flow (v.max means maximal velocity, v.mode stands for the most frequent velocity in the range gate) in addition to the recorded flow heights by the 2D Laserscanner; sampling rate: 1 Hz

4.4 Particle image velocimetry

Large-scale particle image velocimetry (LSPIV) is a video imagery technique often used in rivers to measure two dimensional velocities from high-resolution images at high frame rates [e.g. *Fujita et al.*, 1998; *Hauet et al.*, 2008; *Le Coz et al.*, 2010; *Muste et al.*, 2014]. Therefore bubbles, ice, debris, and artificial seeding are tracked and cross-correlations are made between time-step imagery within a given search window.

This method can also be used to determine the surface velocity of debris flows [*Theule et al.*, 2018], by tracking specific features of these processes (e.g. fast stage variations or boulders on the flow surface). Because of the poor conditions of

height (**Fig. 6**). The instantaneous maximum velocity characterizes the surge front velocity. Therefore these measured values can be compared with the velocities derived by the time-distance method (**Fig. 7, 8**).

The peak velocities of the time-distance methods are in the range of 9 to 11 m/s, whereas the surge velocities of smaller ones range from 5 to 7 m/s, independent of the used variable flow height or seismic signal. Although the maximum surge front velocities derived from the radar signal is below 9 m/s, the comparison shows a maximum difference either to the flow height or seismic signal based surge front velocities of less than 1 m/s.

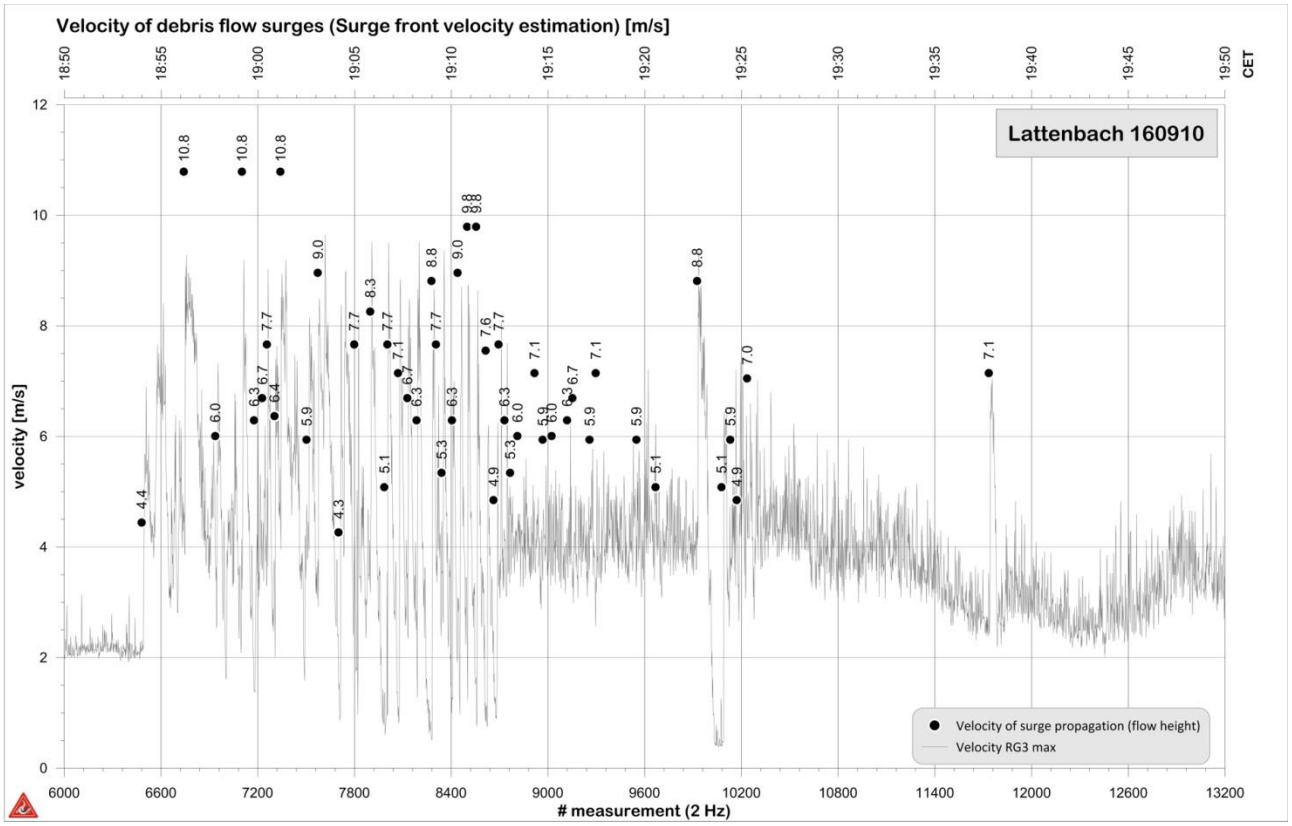

Fig. 7 Surge front velocities calculated by the time-distance method using the flow height as variable in comparison to instantaneous velocity measurement at hm 12.78 applying the maximum velocity

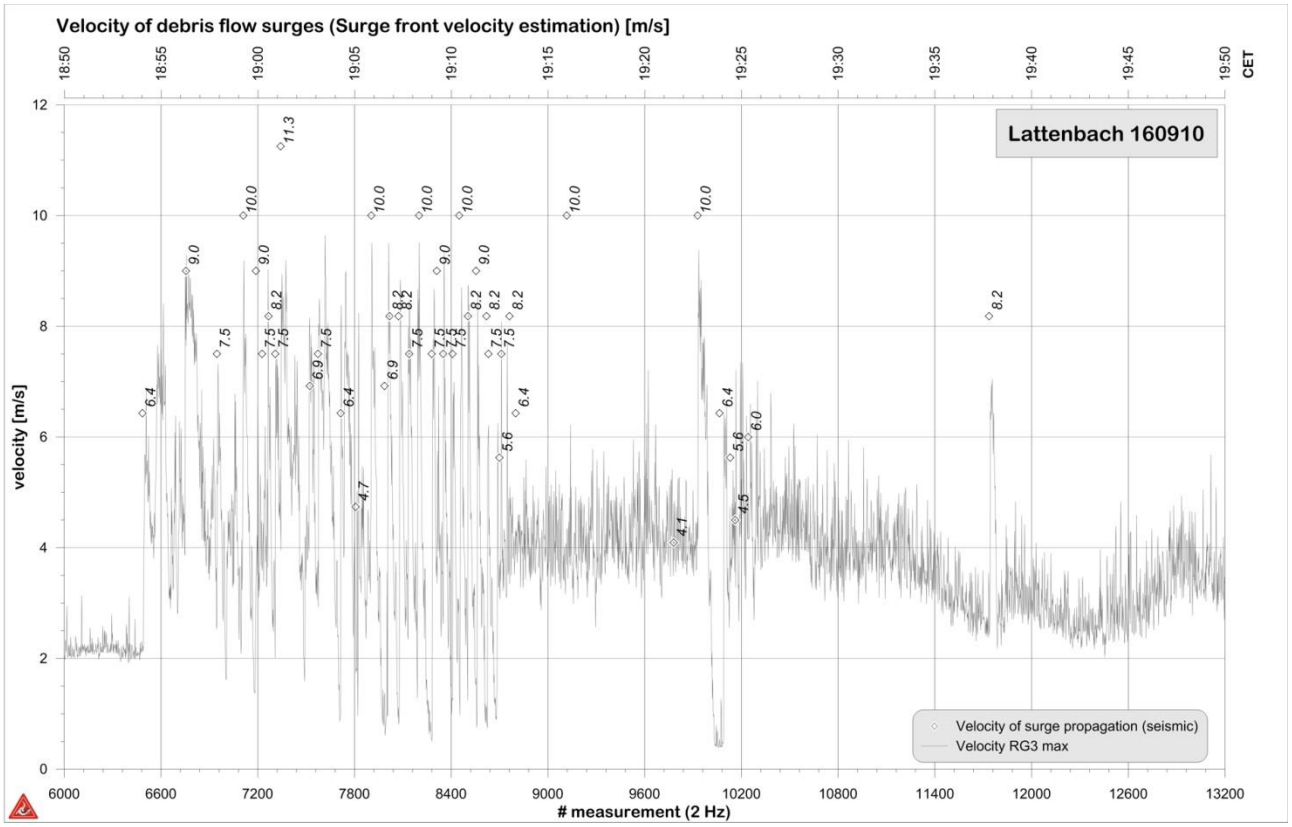

Fig. 8 Surge front velocities calculated by the time-distance method using the seismic signal as variable in comparison to instantaneous velocity measurement at hm 12.78 applying the maximum velocity

6. CONCLUSION

The debris flow velocity estimation using high-frequency radar seems to be a practical way to directly estimate velocities and discharges, but there is still some effort needed to define the proper statistical parameters of the surface velocity distribution. The measured maximum velocity may produce the best result for the surge front velocity and may therefore be used for impact calculations, whereas the most frequent velocity of the measured velocity spectrum may contribute to the instantaneous discharge estimation of a debris flow.

ACKNOWLEDGMENT: We want to thank the Austrian Forest Service for Torrent and Avalanche Control for the support during installation of the monitoring setup and our technician Friedrich Zott for his ongoing efforts to improve the monitoring system.

REFERENCES

Arai, M., Hübl, J., Kaitna, R. (2013): Occurrence conditions of roll waves for three grain–fluid models and comparison with results from experiments and field observation, Geophysical Journal International, Volume 195, Issue 3, pp. 1464–1480.

Fujita, I., M. Muste, and A. Kruger (1998): Large-scale particle image velocimetry for flow analysis in hydraulic engineering applications, J. Hydraul. Res., 36, pp. 397–414.

Hauet, A., Creutin, J.-D., Belleudy, P. (2008): Sensitivity study of large-scale particle image velocimetry measurement of river discharge using numerical simulation, J. Hydrol., 349, pp. 178–190.

Hübl J., Koschuch R., Pichler J. (2012): Automatische Detektion alpiner Massenbewegungen mittels Hochfrequenz Radartechnik: Naturgefahren-Radar; IAN-Report 149; Institut für Alpine Naturgefahren, Universität für Bodenkultur Wien (in German, unpublished).

Hübl, J; Schimmel, A; Koschuch, R (2017): Monitoring of Debris Flows with an Improved System Setup at Lattenbach Catchment, Austria, In: Mikos, M; Casagli, N; Yin, Y; Sassa, K (Eds.), Advancing Culture of Living with Landslides - Diversity of Landslide Forms 4, 707; Springer Nature, Cham, Switzerland; ISBN 978-3-319-53484-8

Kogelnig, A., Wyssen, S., Pichler, J. (2012): Artificial release and detection of avalanches: Managing avalanche risk on traffic infrastructures, a case study from Austria, Congress contribution ISSW 2012.

Le Coz, J., Hauet, A., Pierrefeu, G., Dramais, G., and Camenen, B. (2010): Performance of image-based velocimetry (LSPIV) applied to flashflood discharge measurements in Mediterranean rivers, J. Hydrol., 394, pp. 42–52.

Lussi, D., Schoch, M., Meier, L., Rüsch M. (2012): Projekt Lawinendetektion Schlussbericht, WSL-Institut für Schnee- und Lawinenforschung SLF.

Muste, M., Hauet, A., Fujita, I., Legout, C., Ho, H.-C. (2014): Capabilities of large-scale particle image velocimetry to characterize shallow free-surface flows, Adv. Water Resour., 70, pp. 160–171.

Schimmel, A., Hübl, J. (2016): Automatic detection of debris flows and debris floods based on a combination of infrasound and seismic signals. Landslides Vol. 13(5), pp. 1181—1196.

Theule, J. I., Crema, S., Marchi, L., Cavalli, M., Comiti, F. (2018): Exploiting LSPIV to assess debris-flow velocities in the field; Nat. Hazards Earth Syst. Sci., 18, pp. 1–13.

Recognition of the Susceptibility of Hydrogeomorphic Processes in Mountainous Watersheds through Morphometric Indicators and Field Reconnaissance

Hsienter CHOU [1*], Chingfang LEE[2], Chengyi LIN[1], Ciyin HUANG[1], Tingchi TSAO[2], Chihhsuan HUANG[1] and Weikai HUANG [2]

[1] Department of Civil Engineering, National Central University, 32001, Taiwan
[2] Disaster Prevention Technology Research Center, Sinotech Engineering Consultants, INC.11494, Taiwan
[*]Corresponding author. E-mail: profhtchou@gmail.com

The morphometric parameters associated with hydrogeomorphic disasters such as debris flows, debris floods and floods in western Taiwan and Sichuan, China are analyzed in this study by employing the 5-m resolution digital terrain map and field studies. The drainage areas for debris-flow prone basins are within a wide range of 0.01-100 km^2. The morphometric parameters such as Melton Ratio (*MR*) and watershed length (*L*) are applicable to the identification of the debris-flow prone ravines. Through field reconnaissance, *MR*=0.3 can be regarded as the morphometric threshold for debris-flow basins in different regions, and their fan slopes are greater than 3 degrees. The debris-flow fan slope also increases with increasing *MR* values.

Key words: hydrogeomorphic processes, debris flows, fans, micro drainage, Melton Ratio

1. INTRODUCTION

Tremendous hydrogeomorphic disasters, including floods, debris floods, debris flows and landslides, often occur in Taiwan during the attack of severe typhoons or rainstorms. For the purpose of disaster prevention and response drills, there were 485 potential debris-flow torrents mapped island-widely by Soil and Water Conservation Bureau of Agriculture Council, Taiwan in 1990. The delineation criteria are based on both the risk of downstream protected targets and the topographic characteristics of the upstream catchments such as the drainage area exceeding 3 hectares at the channel slope of 10^o. In 2017, the total number of designated debris-flow torrents reached 1705, while only 986 torrents (58%) among them with debris-flow records. On the other hand, in Taiwan debris flows also occurred in non-designated torrents without protected targets. Thus, there is a need of an identification scheme of specific hazards associated with the hydrogeomorphic processes, which is beneficial not only for the proper design of countermeasures but also for land development and evacuation operation of the affected areas.

The drainage areas of debris flows cover a wide range of a few hectares to hundreds of kilometers [*Mizuyama*, 1982]. The dimensionless Melton ratio (*MR*, watershed relief (*H*, i.e., the difference between the highest and lowest elevations above the fan apex of a watershed) divided by the square root of watershed area (*A*)) is an indicator for watershed ruggedness, and it has been adopted to categorize debris-flow watersheds [*Melton*, 1965; *Jackson et al*., 1987; *Wilford et al*., 2004].

In this study, we evaluate the topographic information of debris-flow torrents in different watersheds of western Taiwan. The catchment geomorphic parameters such as Melton ratio and watershed length are used to categorize their hydrogeomorphic processes, and the identification scheme was verified by field reconnaissance and available debris-flow events in China.

2. STUDY AREAS

The study areas in this paper include three drainage basins in western Taiwan, i.e., the watersheds of Pingguang Creek, Chenyoulan River, and Chishan River. They are located in New Taipei City (northern Taiwan), Nantou County (central Taiwan), and Kaohsiung City (southern Taiwan), respectively (**Fig.1**). The detailed geomorphologic characteristics of the corresponding basins are

shown in **Table 1**.

Typhoon and rainstorm events are the primary triggering factors to induce regional landslides, floods and debris flows. The annual mean precipitations in Pingguang Creek, Chenyoulan River, and Chishan River are 2,210 mm, 3,504 mm, and 2,645 mm, respectively. According to the historical record, Typhoon Morakot was the most critical event triggering the sediment-related disasters in both Chenyoulan River, and Chishan River watersheds in 2009. Furthermore, a severe Typhoon Soudelor brought heavy rainfall in northern Taiwan on 8th, August in 2015. The short-term rainfall intensity exceeded 80 mm/hr, and the accumulated precipitation had reached 769 mm in 24 hours and many landslides, debris flows, and debris floods occurred in Pingguang Creek basin (**Fig.2**).

Table 1 The geomorphologic characteristics of the study areas

Watershed	Pingguang Creek (PG)	Chenyoulan River (CYL)	Chishan River (CS)
Length	7.5 km	42.2 km	118 km
Area	19.4 km^2	447.3 km^2	736.2 km^2
Mean slope	9.85^o	6.75 ^{o}	8.37^o
Max. EL.	970 m	3,926 m	3,500 m
Min. EL.	45 m	301 m	43 m

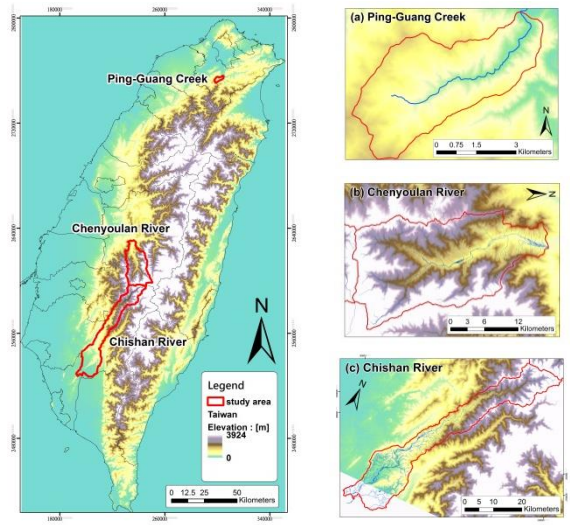

Fig. 1 Study areas in western Taiwan

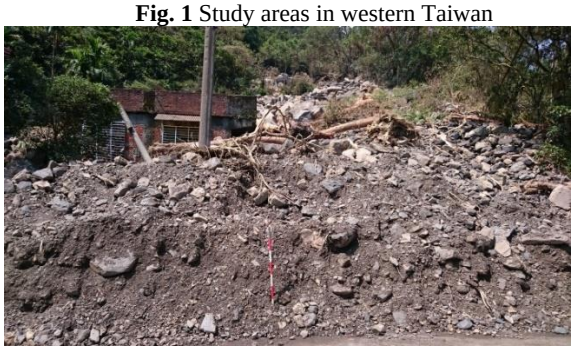

Fig. 2 Debris flow deposition in downstream reach in Ping-Guang Creek watershed (2015/08/13)

3. MATERIAL AND METHODOLOGY

3.1 High-resolution DEMs and micro-drainage classification

For the extraction of the geomorphologic feature, digital elevation models (DEMs) with two different resolutions are adopted in the study; one is 5m x 5m, and the other is 1m x 1m. The dataset was provided by Soil and Water Conservation Bureau, Taiwan. We utilized 5-m DEMs (2004 version) to divide micro-drainage basins and to construct streamlines through Geographic Information Systems (GIS) software. The airborne LiDAR (2009) can remove the surface vegetation and provides the 1-m high-resolution DEM, which is useful to enhance particular landscape features. After pre-processing, this data were transformed into visualization shading relief and applied to map old landslides, debris-flow and fluvial fans by their geomorphic features.

3.2 Micro-topography interpretation

The occurrence of landslides at the upper stream reaches usually contributes loose colluvium and material to trigger the subsequent debris flows. The topographic lineaments, scarps, landslide mass and debris-flow fans in three watersheds were characterized by visualization enhancement approach [*Lee et al*., 2017; *Lo et al*., 2017]. A powerful visualization technique, being referred to as sky-view factor (SVF) relief, is utilized in this study instead of traditional analytical hill shading from multiple directions. In brief, SVF can be regarded as a geophysical parameter that demonstrates the space of the sky visible from the given point on the ground surface [*Zakšek et al*., 2011]. SVF represents the largest range that can be encompassed over the observer or a certain point (the projected area of the hemisphere over the observer in a unit of space; [*Lo et al*., 2017]:

$$\Omega = \int_0^{2\pi} \int_0^{\pi/2} cos\varphi d\varphi d\lambda = 2\pi \qquad (1)$$

where, Ω, φ and λ denote the solid angle, latitude and longitude within the hemisphere, respectively. One can normalize the solid angle in Eq. (1) by using 2π, which gives the SVF:

$$\text{SVF} = 1 - (\sum_{i=1}^{n} sin\gamma_i)/n \qquad (2)$$

where γ_i and n represents the elevation angle from the horizontal surface and the selected number of azimuth directions, respectively. SVF=1 means that the entire hemisphere of sky is visible (such as on a plain or from a peak); SVF=0 means that virtually no sky can be seen from the observation point (canyon). **Table 2**

lists the morphological features for manual mapping criteria in SVF relief maps. It is noted that some landscapes of landslides and debris-flow fans are affected by man-made countermeasures or training works. Once the micro-topography interpretation was performed, one can analyze the geometric parameters such as slope gradient (along with the centerline from the apex to the end of the broader fan) and area of debris-flow fans. Furthermore, the relationship between fan slope gradient and the drainage basin will be examined in the following section.

3.3 Melton's number(MR) assessment

The watershed boundaries, watershed lengths and stream orders were established by using DEM and GIS. The DEM has a cell size of 5 x 5 m and the lowest point of the feeding channel in a watershed was the apex of the fan. The Melton ratio (*MR*) and watershed length (*L*) is a suitable scheme for the differentiation of the hydrogeomorphic processes in mountainous watersheds [*Melton*, 1965; *Wilford et al*., 2004; *Chou et al*., 2017]. The watersheds in Pingguang Creek, Chenyulang River, and Chi-Shan River were derived based on DEM and GIS. The dominant hydrogeomorphic processes, including debris flows, debris floods, and floods, for each sub-basin are determined by their geomorphic parameters, *MR* and *L*, and verified by the depositional patterns in the fan areas through field reconnaissance.

Table 2 Micro-topography interpretation for recent landslides and debris-flow fans (summarized by *Lee et al*., 2016)

Feature	SVF relief map	Description
Landslide scarp		Most of the cliffs formed by slope slumps are scarps of slope top failure. The flanks are the result of the steep slumps and can be used to gauge the strain rate of the slope failure process
Landslide body		The original sliding body presents a dustpan-shaped depression with the upper section displaying subsidence, the middle section showing a gentle slope, and the lower section exhibiting hummocky relief
Debris-flow fan	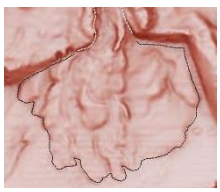	It usually is formed at the gentle slope and broad downstream reach (deposition section: 3-6°). The shape of the fan is dominated by magnitude of debris flow, material, and geometrical condition of the channel. It could be symmetrical fan-shaped or lobe-shaped deposition.

4. RESULTS AND DISCUSSIONS

4.1 The geomorphologic characteristics of debris-flow fans

The formation process of an alluvial fan is dominated by the ratio between the power of the water discharge and the sediment supply from the upslope catchment [*Harvey et al*., 1999]. As shown in **Table 3**, this study identified and mapped 97 debris-flow fans over the watersheds of Ping-Guang Creek, Chenyoulan River, and Chishan River (**Fig. 3**). The area of debris-flow fans ranges from 0.05 to 25.47 ha depending on the scale of stream discharge

Table 3 The debris-flow/alluvial fans mapped in the study areas

Watershed	Pingguang Creek (PG)	Chenyoulan River (CYL)	Chishan River (CS)
Num. of fans	7	37	53
Area [ha.]	0.50- 2.76	0.05-25.47	0.57-21.58
Slope [deg.]	5.5-13.7	1.8-20.7	2.9-27.6

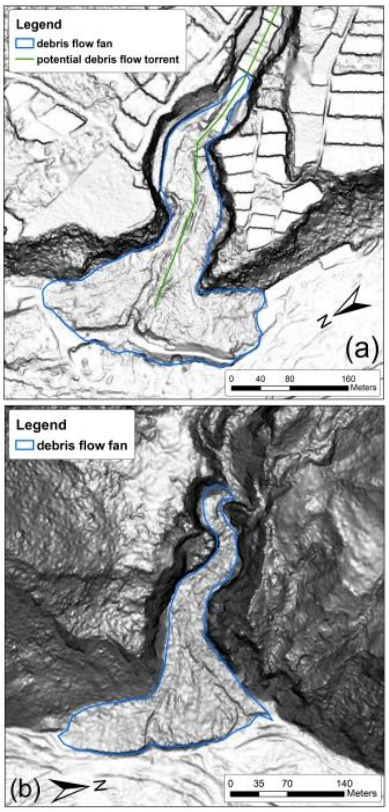

Fig. 3 Recent debris-flow fans mapped in (a) Chenyoulan River watershed and (b) Chishan River watershed.

and sediment yield via the feeding channel. Several geomorphologic characteristics in the study areas are summarized as follows. (1) The thickness and the area of deposition of the debris-flow fan increases in proportion to the number of the historical landslides in the upstream region (source area). The amount of in-channel sediment transportation may become more evident during the occurrence of a deep-seated landslide in the past. (2) The fan area at the upstream tributary is usually small, but the slope gradient is comparatively high. On the other hand, the slope gradient of debris-flow fan is gentle while it is located on the river terrace or adjacent to the main stream. (3) The landform of watershed predominates the slope gradient of debris-flow fan. Once the topography of upstream reach belongs to concave-typed depression, it will contribute rainfall transferring into surface runoff quickly. The classic fan-shaped deposition may be eroded and incised, and form a serval meandering channel at the distal end.

The Melton ratio ($\mathrm{MR} = \frac{H}{\sqrt{A}}$) is a critical morphometric variable related to the basin dynamics, and fan surface slope S_{fd} (in degrees) in general is a function of MR as follows [*Melton*, 1965].

$$S_{fd} = a(MR)^b \qquad (3)$$

where a and b are site-specific coefficients.

The variations in coefficients a and b reflect the differences in climatic settings, sediment availability, tectonics and geological characteristics in the drainage basins. Greater values of a and b depict more active fans currently. The fan slopes in the study areas are closely related to the Melton ratio MR with a = 8.57 and b = 0.89) as shown in **Fig. 4**. The surface slopes of the alluvial fans are close to Melton's Group 1 for active tectonic regions or the regression with a = 8.51 and b = 1.065, which was proposed by *Kovanen and Slaymaker* [2008]. The Melton ratio is thus a morphometric variable reflecting the tectonics and the ratio of flood power to the sediment transport capacity. The Melton ratios for debris-flow dominated fans in the study areas have a value greater than 0.4 and the fan slopes are greater than 3 degrees.

4.2 The watershed hydrogeomorphic processes

The distributions of watershed areas for debris-flow basins in Japan [*Mizuyama*, 1982] and in the study areas are shown in **Fig. 5**. The drainage areas are within a wide range of 0.01-100 km^2, while most of them are small basins of less than a few square kilometers.

The debris-flow basins of Chenyoulan River (middle western Taiwan) are generally larger than those of Pingguan Creek (northwestern Taiwan), while those of Chishan River are in between. The Melton ratio (MR) and watershed length (L) form a suitable scheme for the differentiation of the hydrogeomorphic processes in Pingguan Creek with lower bound of MR of 0.5 and the upper bound of L of 2.2 km for debris-flow torrents (see **Fig. 6(a)**).

While the scatterplot of Melton ratio and watershed lengths for torrents in Chenyoulan River and Chishan River are shown in **Fig. 6(b)**, which depicts a lower bound of 0.43 for MR and an upper bound of 7 km for watershed length for debris-flow prone torrents. There is a buffer zone for the co-existence of debris flows and debris floods under the condition of $MR > 0.43$ with $7 < L < 12$ km, and $0.3 < MR < 0.43$ in watersheds of Chenyoulan River (CYL) and Chishan River (CS) through field

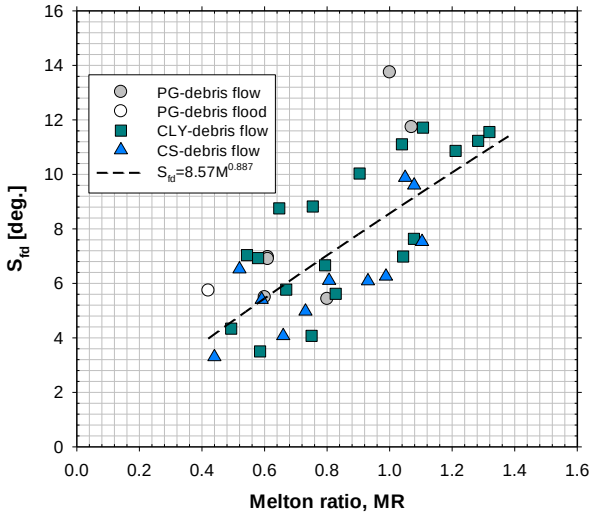

Fig. 4 Fan slopes as a function of the Melton ratios in the study areas as shown in Table 3.

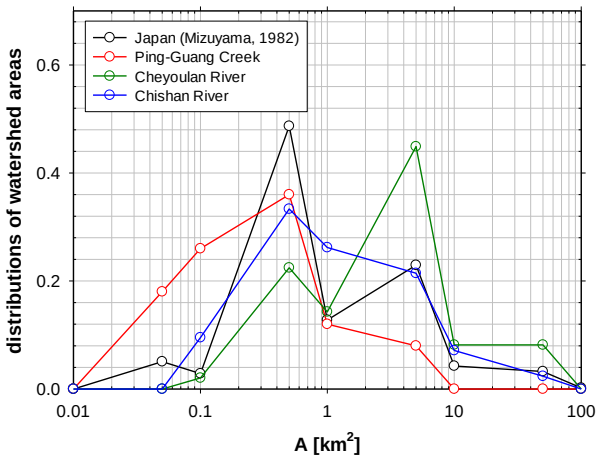

Fig. 5 The distributions of watershed areas for debris-flow basins in Japan and in western Taiwan

Table 4 Classification of sediment-related hazards in the study areas

Watershed	Pinggung Creek (PG)	Chenyoulan River (CYL)	Chishan River (CS)
Debris flows	50	47	50
Debris floods	3	3	4
Floods	0	0	1

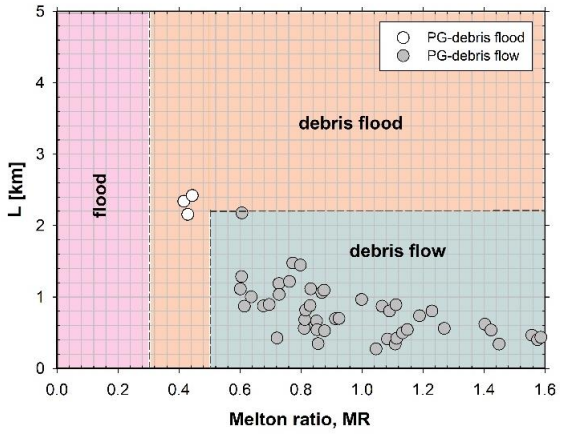

(a) Pinggung Creek (PG) in Northwestern Taiwan

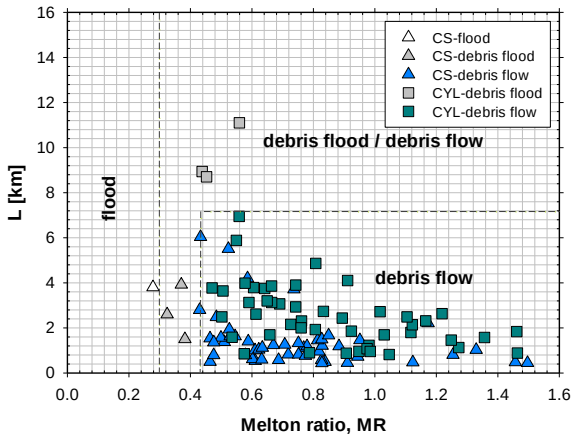

(b) Chenyoulan River (CYL)and Chishan River(CS)

Fig. 6 The relationship between watershed length (L) and Melton ratio (MR) for hydrogeomorphic hazards in western Taiwan

investigations. In accordance with analysis result and overlay by potential debris flow torrents, one may identify the sediment-related hazards occurred in three study areas (**Table 4**). For small Pingguang Creek watershed, fifty debris flows and three debris floods are clarified by integrating geomorphic factor and field investigation.

To verify the applicability of aforementioned morphometric parameters for hydrogeomorphic hazards in different regions, a data set of 147 debris-flow torrents in 5 counties (Ching-ping, Bai-chuan, Yin-shou, Long-tse and Der-chan) of

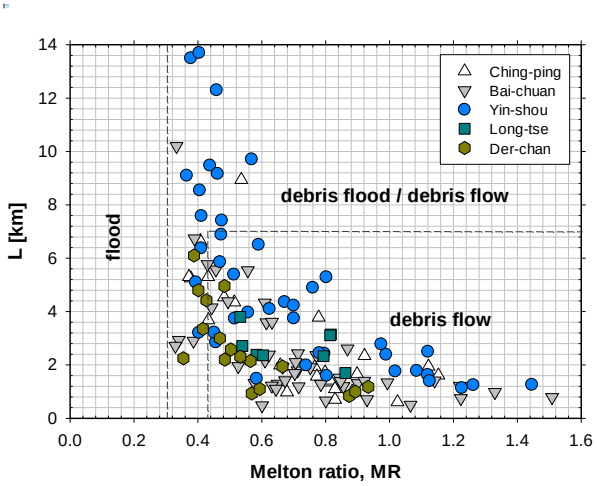

Fig. 7 The relationship between watershed length (L) and Melton ratio (MR) for hydrogeomorphic disasters in Sichuan, China.

Sichuan province, China was adopted for comparison (Dr. Bin Yu, personal communication). The results are shown in **Fig. 7**, which indicates a lower MR limit of 0.3 and a higher watershed length limit of 14 km for debris-flow prone torrents; so the scatting of debris-flow torrents in China covers both regimes of debris flow (DF) and debris flood (DFL) delineated in the study areas (**Fig. 6b**). As shown in **Fig. 7**, the maximum watershed length for debris-flow basins in Sichuan is about 13.7 km in Yin-shou region, and the corresponding drainage area is 48.7 km^2, which is within the range of 0.01-100 km^2 as shown in **Fig. 5**. Thus *MR*>0.3 and *L*<14 km should be the morphometric parameters for debris-flow basins in Sichuan, China.

The differences in their threshold values of *MR* and *L* for debris-flow prone watersheds among western Taiwan and China are mainly due to the differences of lithology, sediment supply, geological settings and climate. The zonation between debris flow and debris flood deserves further investigation. Above all, MR = 0.3 seems to be the lower bound for debris-flow basin as proposed by *Jackson et al.* [1987], and itself also serves as the upper bound for flood-related disasters.

5. CONCLUSION

The morphometric parameters, i.e., Melton Ratio and drainage length, are applicable to an identification scheme of hydrogeomorphic processes such as debris flows, debris floods and floods. Regarding the debris-flow torrents in the study areas, the lower bound of *MR* is about 0.3-0.5, while the upper bound of *L* is about 2.2 -14 km in different regions in western Taiwan and China due to their

different lithology, sediment availability, geological and climate settings. *MR*=0.3 seems to be the lower bound for debris-flow basins as proposed by *Jackson et al*. [1987], and itself also serves as the upper bound for flood-related disasters. A buffer zone for the co-existence of debris flows and debris floods under the condition of $0.3 < MR < 0.43$, or $MR > 0.43$ with $7 < L < 12$ km deserves further research. The fan slope for debris-flow fans in this study areas generally exceed 3 degrees, and the fan slopes versus Melton Ratio are close to Melton's type Group 1 for active tectonic regions.

ACKNOWLEDGMENT

This study was financially supported by the Ministry of Science and Technology of the Republic of China, Taiwan under Contract No. MOST-106-2625-M-008-007.

REFERENCES

Chou, H.T., Lee, C.F. and Lo, C.M. (2017): The evolution of a coastal alluvial fan caused by rainfall-induced landslides in eastern Taiwan. Landslides, Vol.14(1), pp.109-122.

Harvey, A.M. Silva, P.G. Mather A.E. Goy. J.L. Stokes, M. and Zazo, C. (1999): The impact of Quaternary sea-level and climatic change on coastal alluvial fans in the Cabo de Gata ranges, southeast Spain. Geomorphology, Vol. 28, pp.1-22.

Jackson, L.E. Kostaschuk, R.A. and MacDonald G.M. (1987): Identification of debris-flow hazard on alluvial fans in the Canadian Rocky Mountains. Rev. Eng. Geol., Vol. 7, pp.115–124.

Kovanen, D.J. and Slaymaker, O. (2008): The morphometric and stratigraphic framework for estimates of debris flow incidence in the North Cascades foothills Washington State USA. Geomorphology, Vol.99, pp.224-245.

Lee, C.F., Lo, C.M., Chou, H.T. and Chi, S.Y. (2016): Landscape evolution analysis of large scale landslides at Don-Ao Peak, Taiwan. Environ. Earth Sci., Vol.75:29.

Lee, C.F., Huang, W.K. Huang, C.M. and Chi, C.C. (2017): Deep-seated landslide mapping and geomorphic characteristic using high resolution DTM in northern Taiwan. In: Mikos M., Tiwari B., Yin Y., Sassa K. (eds) Advancing Culture of Living with Landslides. 4th World landslide Forum, Ljubljana, Slovenia, Vol. 2, pp.767-777.

Lo, C.M., Lee, C.F. and Keck, J. (2017): Application of sky view factor technique to the interpretation and reactivation assessment of landslide activity. Environ. Earth Sci., Vol. 76:375.

Melton M.A. (1965): The geomorphic and paleoclimatic significance of alluvial deposits in southern Arizona. The Journal of Geology, Vol. 73(1), pp.1-38.

Mizuyama, T. (1982): Analysis of sediment yield and transport data for erosion control works. Recent Development in the Explanation and Prediction of Erosion and Sediment Yield (Proceedings of the Exeter Symposium). IAHS Publ. No. 137.

Wilford, D.J. Sakals, M.E. Innes, J.L. Sidle, R.C. and Bergerud, W.A. (2004): Recognition of debris flow, debris flood and flood hazard through watershed morphometrics. Landslides, Vol. 1, pp.61-66.

Zakšek, K. Oštir, K. and Kokalj, Ž. (2011): Sky-view factor as a relief visualization technique. Remote Sens., Vol. 3, pp. 398-415.

Assessment of Landslide Recurrence by Onsite Monitoring - Incidence of Hong-yeh Landslide -

Chia-Chun WU[1,*], Pei-Hsi WANG[2], Chih-Hui WANG[3], Ching-Yen CHANG[3] and Te-Ling WU[3]

[1] Dept. of Soil and Water Conservation, National Pingtung University of Science and Technology (Neipu, Pingtung 92101, Taiwan)

[2] Lipang Engineering Consultant Co. Ltd. (Kaohsiung 80755, Taiwan)

[3] Taitung Branch, Soil and Water Conservation Bureau, Council of Agriculture, Executive Yuan (Taitung 95055, Taiwan)

*Corresponding author. E-mail: ccwu@mail.npust.edu.tw

Typhoon Meranti invaded Taiwan from Sept. 12 through 16 in 2016 and brought 633 mm of rain in 48 hours. A large-scale landslide behind Hong-Yeh Village of Taitung County consequently occurred on Sept. 15, which produced 40,000 m^3 of debris. Debris that affecting local settlement and blocking the bridge clearance was dredged. Countermeasure structures were immediately designed and implemented. Locations for permanent resettlement were evaluated. Nevertheless, uncertainty of landslide recurrence and feasibility of the countermeasures in coping with future disaster either caused by landslide or debris flow has troubled the government agencies. Hence, field geological survey, outcrop assessment, micro-terrain interpretation, core samples from core drills, Electrical Resistivity Image Profiling, and inclination as well as water stage readings from five boreholes were used to assess the likelihood of landslide recurrence. All evidence gathered onsite suggested the recurrence of landslide is highly possible. The unstable mass situated on upper landslide site displaced another 6.5 m eastward along the slope after a 5-day 924-mm torrential storm with peak one-day rainfall of 407 mm. Numerical simulations at different storm return periods with countermeasure designs scenarios were conducted to ensure the safety of Hong-Yeh Village and the functionality of countermeasure structures from debris-flow disaster. Adjustments on structure design were made accordingly and were implemented onsite, which helped reduce the areas of risk scope by 40.1%.

Key words: landslide, recurrence assessment, onsite monitoring, numerical simulation

1. INTRODUCTION

Typhoon Meranti invaded Taiwan from Sept. 12 through Sept. 16, 2016 and brought 633 mm of rain in 48 hours. A large-scale landslide occurred behind Hong-Yeh Village in Taitung County on Sept. 15, with an extent covering 7.8 ha from which 40,000 m^3 of debris were yielded. The front lobe of debris rushing downstream damaged 39 housings, three public buildings as well as local traffic system that situated at the foothill of the mountain range (**Fig. 1**).

A magnitude 5 earthquake trembled the entire Taitung County on Oct. 6, 2016 followed by Typhoon Aere that brought 1,010 mm of rain within a week. Earthquake and intensive rainfall further deteriorated the landslide and resulted a 1.8-ha expansion on landside scarp. Residents of Hong-Yeh Village were immediately evacuated.

Emergency relief task forces were immediately dispatched to help restore public facilities. Research team was also called up by government officials to conduct borehole drilling, to install monitoring system with the aim of assessing the recurrence of succeeding landslide, and to observe the possible movement of landslide scarp as well as changes of groundwater levels respectively.

Check dam and gully control structures were immediately designed and commissioned for construction. Debris that affecting local settlement was removed, and that blocking the clearance of bridge and torrent was dredged. Locations for permanent resettlement were evaluated.

Fig. 1 Disaster caused by September 15, 2016 landslide

Prior to landslide disaster, the torrent coded as DF-166 running through the Village has been announced as a debris-flow torrent with high recurrence potential. Eocene or earlier Hong-Yeh Stratum consisting of black slate with occasional inclusions of metamorphic sandstone covers most of the upper watershed; whereas gravel - sand - silt - clay terraced deposits from Late Pleistocene - Holocene period forms the geologic formation at the mid-lower watershed where Hong-Yeh Village was located. Fragile geology has brought about tension cracks as well as nonuniform slumps except large-scale landslide on hill slope for more than half a century.

To ensure the safety of Hong-Yeh Village and the functionality of countermeasures, results from this study were used to assess the likelihood of landslide recurrence and the feasibility of control structures. Modifications on countermeasure structures were made accordingly and promptly based upon data analysis from inclinometer readings, water-level readings as well as numerical simulations under several storm return period scenarios.

2. METHODS

2.1 Field geological survey

The purpose of field geological survey was to log the locations of outcrop, cleavage, stratification, joint, and the corresponding attitude. Geological phenomena such as existence of shear zone and tension cracks as well as signs of slope instability; such as unusual seepage, road slump, and cracks in structures that helped identify the possible causes or bearings of sliding were also documented.

2.2 Core drills and rock mechanical analyses

Total of five boreholes along the landslide scarp and right-side ridge was drilled on Apr. 12, 2017. Depths of drill varied from 20 m to 59 m.

Core samples from each borehole were taken for mechanical property analysis, which included Uniaxial Compression and Direct Shear Strength Tests on rock samples, Direct Shear Strength, Triaxial Consolidated Drained cohesion, Hydraulic Conductivity Tests on remolded soil samples.

2.3 Electrical Resistivity Image Profiling

Electrical Resistivity Image Profiling (RIP) was conducted by deploying two routes perpendicular to strikes of slate. Route 1 (RS1) ran between borehole #1 (B1) and borehole #2 (B2) with the stretch of 385 m; whereas, Route 2 (RS2) ran across borehole #4 (B4) with the stretch of 275 m.

2.4 In situ monitoring

Dual-axis inclinometer was used to take monthly displacement readings from ground level to the bottom of each borehole. Rain gauge was installed in the vicinity of the landslide site with a data logger attached to record rainfall events automatically. Water-level sensor was placed in each borehole casting to log groundwater levels continuously at 10-minute interval. It was then retrieved for data readout every month or shorter duration when needed.

2.5 Construction of digital elevation models

Digital elevation models (DEMs) were created using land survey resources gathered by different government agencies from different periods, which included Taitung County 1:1000 DEM taken in 2010, high-resolution Light Detection And Ranging (LiDAR) scan taken in 2012, 1-m DEM generated from aerial photos taken in 2014 by Forestry Bureau Aerial Survey Office, and 1-m DEMs generated from Unmanned Aerial Systems (UAS) images taken on Feb. 18, 2017 after emergency relief and June 19, 2017 during the construction of gully controls.

2.6 Numerical simulation of debris-flow affecting areas

FLO-2D model [*O'Brien et al*, 1993; *O'Brien*, 2003] was used to simulate the possible extent of debris-flow affecting areas under 50- and 200-yr storm recurrence intervals. Log-Pearson Type III Distribution was used for hydrologic frequency analyses to get one-day maximum rainfall, and Digital Elevation Models as previously described were used as terrain baseline maps respectively for periods prior to the disaster and during gully control constructions.

DEM with design elevations reflecting the final elevations at the completion of gully controls were also used to predict the likely debris-flow affecting areas as well as to identify the locations of overflow. Simulation results thus generated were used during gully control constructions for design adjustment or improvement. Standards for Debris-flow hazard zoning proposed by Rickenmann [2001], which considered flow velocity and maximum flow depth of the debris-flow, was used in this study to delineate levels of risk induced by debris-flow.

3. RESULTS AND DISCUSSION

3.1 Geology and micro-terrain interpretation

Results from field geological survey indicated that attitude of cleavage at landslide site was N12°W~N16°E, dip angle was 21°SE~30°NE, and the representative apparent dip was about 26°; whereas, attitude of cleavage and dip angle at the landslide scarp was N24°~36°E and 22°~34° SE respectively.

Field survey also found the representative weak planes formed by J1 and J2 joint (**Fig. 2**) respectively that affecting hillslope stability. J1 joint is less apparent and discontinuous; whereas, J2 joint forms the major joint with good ductility that fractures the rock stratum for more than 1 m and quartz veins [*Yang*, 2010] was found along tension joint fissures. Evidence collected onsite suggested that J2 joint was the weak plane that mainly affected the hillslope stability and caused landslide to occur.

Micro-terrain interpretation was conducted by analyzing satellite images and orthophotos taken from various periods. Interpretation results suggested that hillslope behind Hong-Yeh Village not only possesses avalanche features but also experienced large-scale landslide during modern geological history. **Fig. 3** is the results obtained from micro-terrain interpretation, in which boundaries of suspected potential slump mass and that of landslide scarps were marked.

By comparing the satellite images taken in 2016 and orthophotos taken on Feb. 18, 2017, a 240-m long scarp was also detected. Second field survey was carried out and the distribution of black-gray slate and highly weathered yellow sandstone was found at the detected scarp. Location of massive slump that matched the location where small-scale slump took place in 2012 was also discovered.

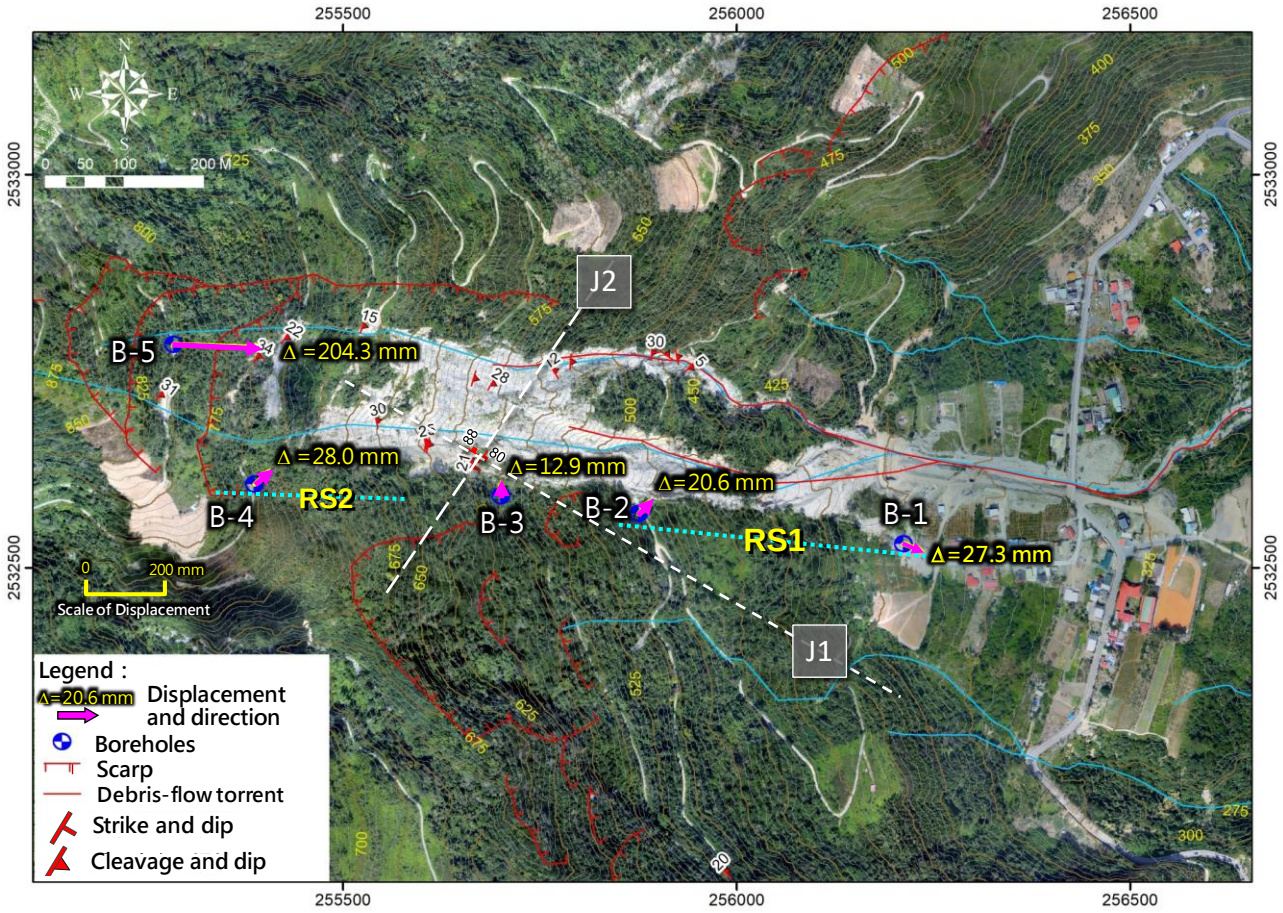

Fig. 2 Results of field geological survey and total displacement readings from each borehole

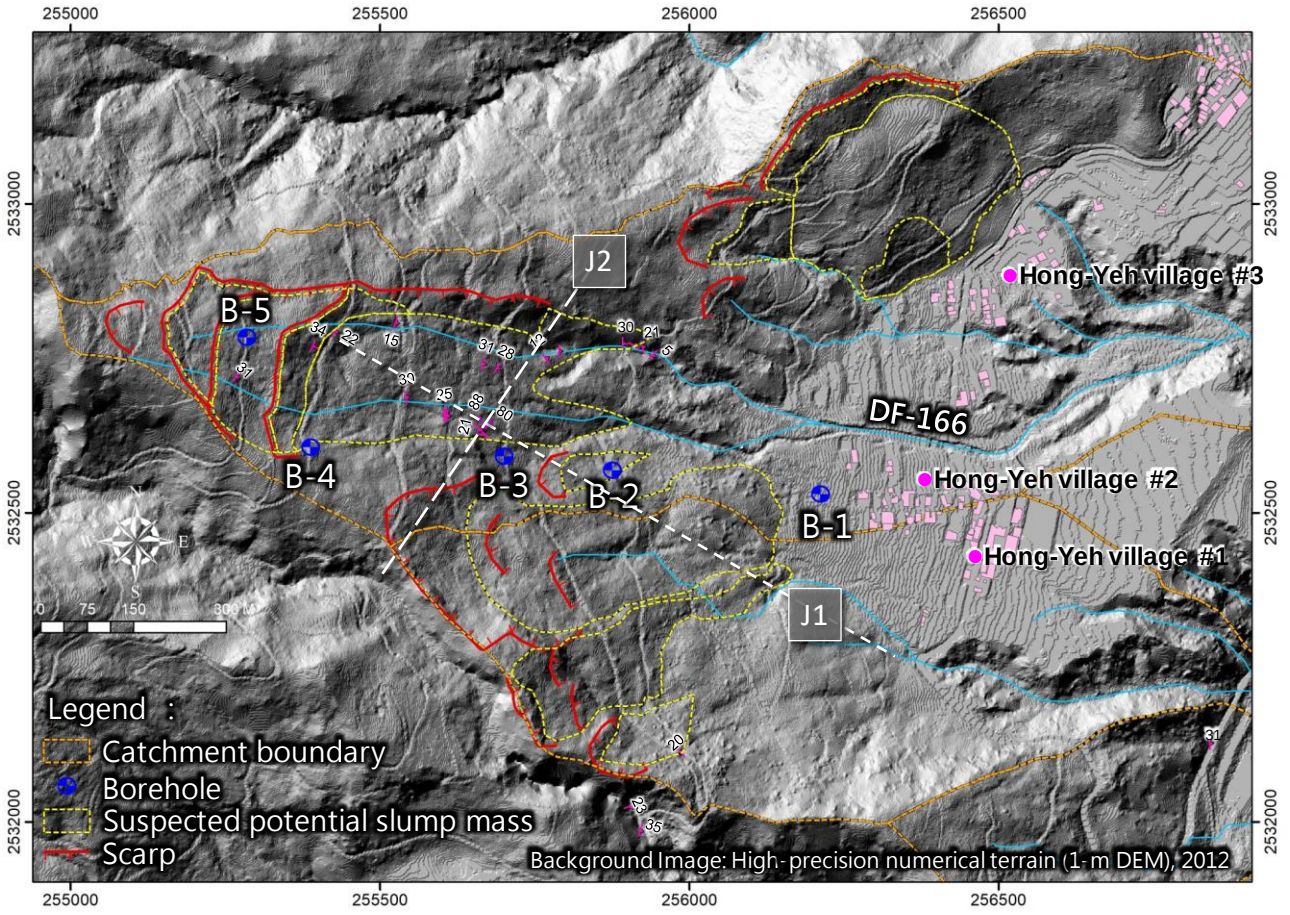

Fig. 3 Results of micro-terrain interpretation

3.2 Borehole samples interpretations and Electrical Resistivity Image Profiling results

By examining the depths of colluvial deposits from five boreholes′ core samples and the field findings from fresh outcrop survey, we were able to estimate the thickness of colluvial deposits as that shown in **Fig. 4**.

Estimation of colluvial deposits especially the extent of unstable mass as that shown in **Fig. 4** helped corresponding government agencies as well as residents of Hong-Yeh Village prepare for the worst scenario to come. It also helped emergency relief task forces to seek all control practices options and landslide recovery actions.

Electrical resistivity distribution readings taken along Route 1 (RS1) and Route 2 (RS2) suggested that rock stratum at the landslide site consists of three main layers. They are colluvial deposits, fracture zone, slate, and/or slate and sandstone interbed, where are denoted as ①, ②, and ③ respectively in **Fig. 5**.

Colluvial deposits covers from ground level to 50 m below, which were resulted from mass movements occurred at different periods. Core samples taken from borehole B-1 also confirmed the existence of colluvial deposits.

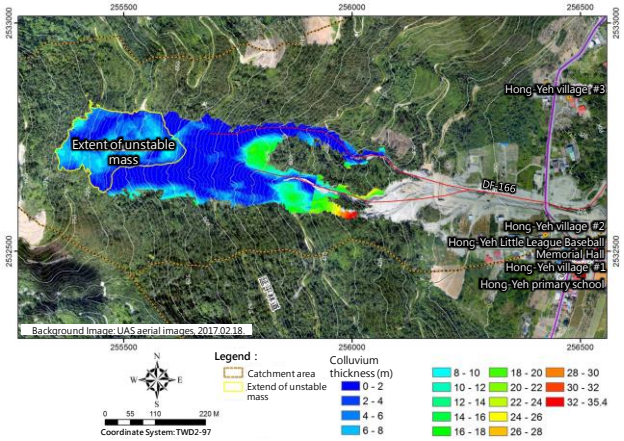

Fig. 4 Estimated thickness of colluvial deposits

Joints are abundant in the fracture zone so that surface water can easily seep into and form water pockets that were clearly registered in electrical resistivity readings as that shown in **Fig. 5**. This fracture zone may affect the stability of hillslope and the maximum affecting depth may reach 50 m.

3.3 Inclination and water-level monitoring

Total displacement (Δ) with respect to borehole bottom within 5-month period (from 2017/04/22 to 2017/09/27) was marked for each borehole along

with the displacement vector as that shown in **Fig. 2**.

The monthly average displacement rate taken from borehole B-1 to B-4 was 5.5, 4.1, 2.6, and 5.6 mm/mo. respectively; whereas the monthly average displacement rate from B-5 reached 40.9 mm/mo., which met the confirmed mass movement criterion proposed by Japan Association for Slope Disaster Management [2007].

The active moving zone in B-5 that estimated from inclination readings in the A-axis direction (pointing downslope) was about 21.0 ~ 21.5 m underneath the ground surface as that shown in **Fig. 6**. Inclination readings from B-5 also indicated that landslide is continuously moving in a rapid speed. All these evidences clearly verify the existence of dip slope.

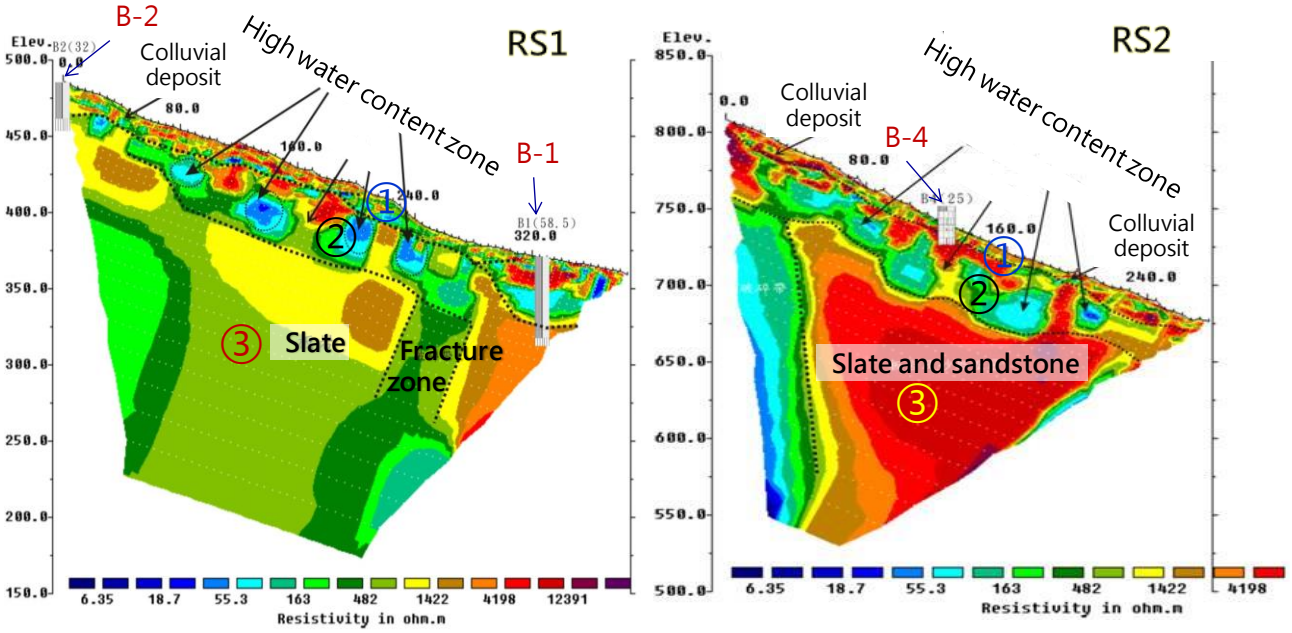

Fig. 5 Electric resistivity readings from Route 1 (RS1) and Route 2 (RS2)

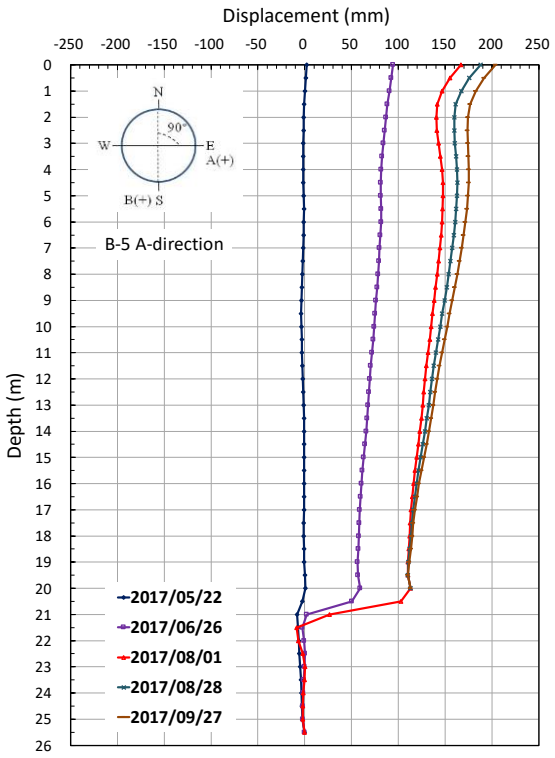

Fig. 6 Inclination readings from borehole B-5

Monitoring water levels in boreholes began in April 2017. **Figs. 7**, **8**, and **9** showed the records of water level elevations obtained from B-2, B-3, and B-5 respectively. 'Colluvial Deposits', 'Slate', and 'Fracture Slate / Sandstone' that marked in **Figs. 7**, **8**, and **9** was based on the readings from corresponding borehole core samples. Because of continuous sliding of the active moving stratum where B-5 was located, water-level sensor deployed in B-5 was unable to retrieve for data download after Oct. 8, 2017 9:50 a.m. Therefore, B-5 water level monitoring was forced to terminate.

In general, water levels in borehole were found synchronized with rainfall for B-2, B-3, and B-5 that situated along the landslide scarp. In contrast, there were almost no apparent changes in water levels for B-1 and B-4.

Three rainfall events occurred on June 3, July 4, and July 30 which brought 117.5, 91.5, and 204.5 mm of rain with the maximum hourly intensity of 16.5, 71.0, and 29.0 mm/hr to the site respectively. The water level in B-5 rose on June 3 and July 30 events to the elevation where suspected active moving stratum was located, but not on July 4 event as that

shown in **Fig. 9**. One of the possible reasons that causing no response of water level in B-5 on July 4 event was the sliding of active moving stratum (**Fig. 6**) that rearranged the stratum structure, porosity, and permeability. The entire hillslope at the vicinity of B-5 moved 50 ~ 100 mm between May 22 and June 26 and continued its movement with approximately the same speed that led to a total displacement of 204.3 mm at B-5 as that shown in **Fig. 2**.

In addition, a 5-day 924-mm torrential storm (10/11 Storm) from Oct.12 till Oct. 16 with peak one-day rainfall of 407 mm on Oct. 15 caused significant rise of water level at all boreholes except B-4. The maximum rise of water level was 0.8, 19.7, and 8.7 m for B-1, B-2, and B-3 respectively. The amount of rainfall brought by 10/11 Storm already exceeded 24-hour rainfall / 15-day cumulative rainfall prior to landslide occurrence criterion of triggering disastrous slope failure [*Lump*, 1962, 1975; *Brand*, 1982, 1989]. DEMs generated from UAS survey after 10/11 Storm confirmed the unstable mass situated in upper landslide site as that marked in **Fig. 4** moved 6.5 m eastward but slightly southward.

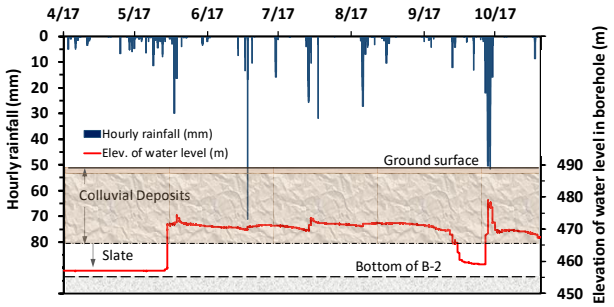

Fig. 7 Records of elevation of water level from borehole B-2

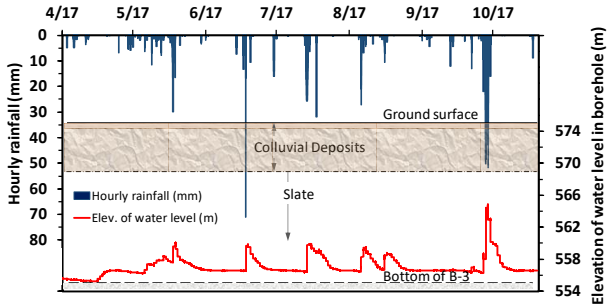

Fig. 8 Records of elevation of water level from borehole B-3

3.4 Landslide recurrence assessment

Judged by results from field geological survey, landslide scarp, micro-terrain interpretation, stratum distributions from core samples as well as inclinations and water level readings in boreholes, we reached the conclusion that recurrence of landslide is very likely. We speculate future landslide will probably occur in four levels as illustrated in **Fig. 10**. The total unstable mass counting all four levels was estimated to reach 920,000 m^3.

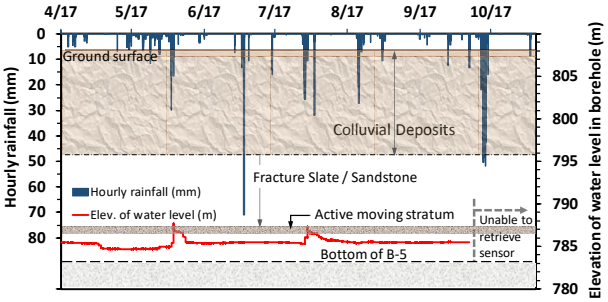

Fig. 9 Records of elevation of water level from borehole B-5

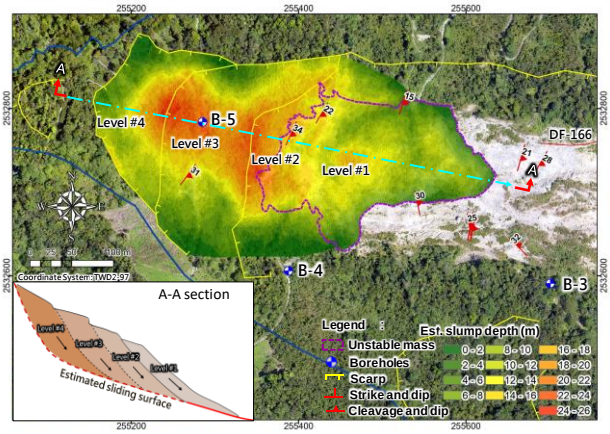

Fig. 10 Recurrence of possible sliding in levels

3.5 Debris-flow simulation

FLO-2D was used to estimate the extent of flooding and level of risk induced by debris flow. **Table 1** summarizes the results of numerical simulations at three event scenarios. All scenarios were conducted to simulate sediment-laden flow. The rheological parameters including fluid viscosity and yield stress as well as sediment concentration was carefully selected based upon the best judgement learned from debris flow residuals that observed from field survey performed on Sept. 16, 2016 immediately after the debris-flow disaster and recommendations proposed by FLO-2D.

Table 1 Levels of risk induced by debris flow

Scenario		Risk Classification			Total
		High	Med.	Low	
I	Area (m^2)	7,204	197	30,062	37,463
II	Area (m^2)	16,184	754	27,140	44,078
	% diff.	124.7	282.7	-9.7	17.7
III	Area (m^2)	3,286	145	19,014	22,445
	% diff.	-54.4	-26.4	-36.8	-40.1

Scenario I used the high-precision DEM map generated from the orthophotos taken on Aug. 15, 2014, which provided good topographic presentation of the landslide site prior to the landslide disaster. Runoff from 50-yr return period was used as inflow.

Scenario II used the high-precision DEM map generated by UAS taken on Feb. 18, 2017, which characterized the topography during the early stage of gully control constructions. Runoff from 50-yr return period was also used as inflow.

To cope with extreme event, sediment-laden runoff from 200-yr return period was used as inflow; whereas LiDAR survey when 50% of the control measures reaching to its completion was conducted to generate an updated DEM topographic base map for FLO-2D simulations. The extent of debris-flow risk caused by 200-yr return period is shown in **Fig. 11**.

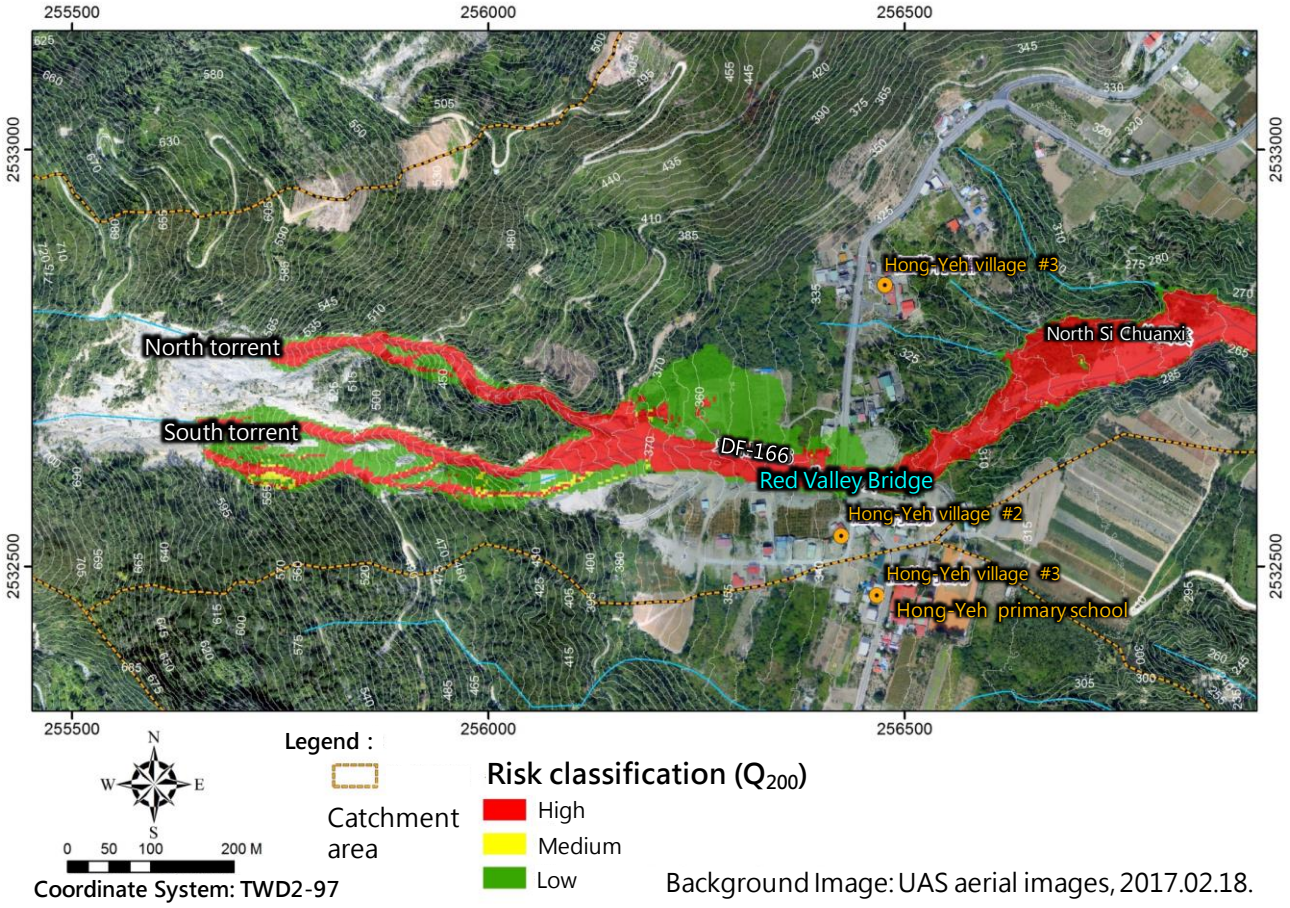

Fig. 11 Extent of debris-flow risk from 200-yr return period event if occurred during the construction of countermeasures

Simulation results shown in **Fig. 11** indicated that there was a weak spot along the left embankment after the confluence where North and South torrents met, at which 200-yr return period debris flow may overflow. Another possible overflow spot was likely to occur before Red-Valley Bridge because the clearance under Red-Valley Bridge was insufficient to convey the flood.

Scenario III simulation was carried out by altering the elevations at left embankment, clearance under Red-Valley Bridge, and channel cross section after Red-Valley Bridge. Runoff from 200-yr return period was also used as inflow.

Fig. 12 illustrated the simulation results using the topographic map obtained from field topographic survey conducted on June 19, 2017, which represented the completion of gully controls with necessary adjustments at spots where overflow or debris clogging may likely occur. Adjustment involved in gully control designs included increasing left embankment height by 2.5 ~ 3.0 m, increasing Red-Valley Bridge clearance to 7.0 m, and expanding channel width to 22.0 m. Results summarized in **Table 1** showed that 40.1% reduction in risk extent from 37,463 m^2 of Scenario I to 22,445 m^2 of Scenario III.

4. CONCLUSIONS

Heavy rainfall produced large amount of surface runoff that rushed into DF-166 high potential debris-

flow torrent and caused severe scour at the torrent bed. The sever scour at the torrent bed induced slope slump at both banks of the torrent. Early colluvial deposits with high permeability constitute most parts of the stratum so that rainwater could easily infiltrate into the deposits and cause reductions in shear resistance. The chain reaction consequently began. Continuous rainfall brought by Typhoon Aere, development of tension cracks along landslide scarp, and movement of unstable mass at the upper reach of landslide scarp further deteriorated the status of landslide.

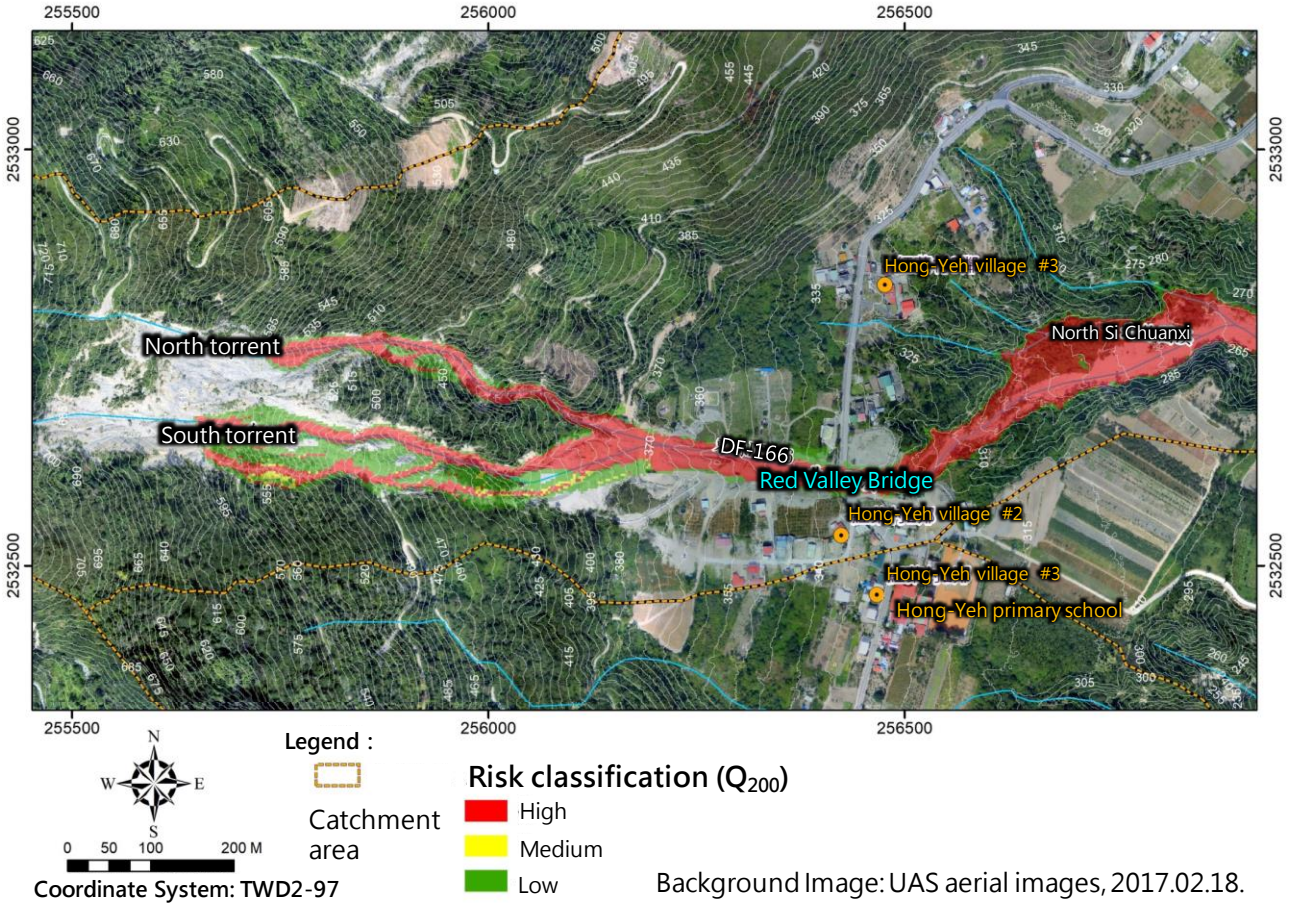

Fig. 12 Extent of debris-flow risk from 200-yr return period event if occurred after the construction of countermeasures

Construction of check dam and gully control structures reached completion in November 2017, which marked the end of the first phase of reconstruction project. Numerical simulations with three storm scenarios helped foresee the weak spots in control structure design.

Field geological survey, outcrop assessment, micro-terrain interpretation, core samples from borehole drill as well as inclination and water stage readings from five boreholes all suggests the cause of Sept. 15 landslide was mainly due to continuous, heavy rainfall and existing rock fractures. Hence, the likelihood of landslide recurrence is expected.

Recurrence of Hong-Yeh landslide is certain. However, there are still many issues that are uncertain including the scale, volume, and frequency of recurrent landslide, which require further investigations and onsite detail monitoring.

The second phase of reconstruction project is current on its way to detail design mainly on slope stabilization as well as continuous onsite monitoring the inclination, ground surface displacement along the landslide scarp and water-level changes in boreholes. An automatic monitoring system is scheduled for online operation at the site in mid-2018 so that rainfall amount, ground surface displacement, and water level stages can be monitored at remote office instantaneously.

ACKNOWLEDGMENT: Outcomes of this study were the join efforts from Lipang Engineering Consultant Co. Ltd., National Pingtung University of Science and Technology, Dept. of Soil and Water Conservation, Soil Erosion Research Unit, and Soil and Water Conservation Bureau Taitung Branch Office. The assessment project was funded under FY2017 SWCB-106-157 contract.

REFERENCES

Brand, E. W. (1982): Analysis and design in residual soils, Proceedings of the ASCE Geotechnical Engineering Division Speciality Conference on Engineering and Construction in tropical and residual soils, Honolulu, Hawaii, January 11-15.

Brand, E. W. (1989): Correlation between rainfall and landslides, Proceedings of the 12th International Conference on Soil Mechanics and Foundation Engineering, Vol. 5.

Japan Association for Slope Disaster Management (2007): Landslide Countermeasure Technical Design Implementation Manual (in Japanese).

Lumb, P. (1962): Effect of rainstorms on slope stability, Proceedings of the Symposium on Hong Kong soils, Hong Kong, pp. 73-87.

Lumb, P. (1975): Slope failures in Hong Kong, Quarterly Journal of Engineering Geology, Vol. 8, pp. 31-65.

O′Brien, J. S. (2003): FLO-2D User Manual, FLO-2D Software, Inc.

O′Brien, J.S., Julien, P.Y., and Fullerton, W. T. (1993): Two-dimensional water flood and mudflow simulation. Journal of Hydraulic Engineering, ASCE, Vol. 119, No. 2, pp. 245-261.

Rickenmann, D. (2001): Methoden zur Gefahrenbeurteilung von Murgangen. In: Projet CADANAV, Etablissement d'une methodologie de mise en oeuvre des cartes de dangers naturels du canton de Vaud; 2eme rapport intermediaire, Ecole Polytechnique Federal de Lausanne, Switzerland.

Yang, C.N. (2010): A case study on age relationship between obliquely intersected quartz veins in metasandstone, Taiwan Mining Industry, Vol. 62, No. 4, pp. 16-26 (in Chinese with English abstract).

Landslide Monitoring and Potential Assessment from Differential Interferometric Radar Analysis and Ground Instrumentations

Kuo-Lung WANG[1*], Jun-Ting LIN[1], Yi-Hsuan LEE[1], Li-Wen CHEN[1], Jheng-Ru LAI[1], Tsung-Wen CHEN[1], Yo-Ming HSIEH[2], Meei-Ling LIN[3], Ray-Tang LIAO[4], Chao-Wei CHEN[4] and Ching-Weei LIN[5]

[1] Dept. of Civil Engineering, National Chi Nan University (Puli, Nantou, Taiwan)
[2] Dept. of Construction Engineering, National Taiwan University of Science and Technology (Taipei, Taiwan)
[3] Dept. of Civil Engineering, National Taiwan University (Taipei, Taiwan)
[4] Safe Consultant Co. (Taipei, Taiwan)
[5] Dept. of Earth Sciences, National Cheng Kung University (Taipei, Taiwan)
*Corresponding author. E-mail: klwang@ncnu.edu.tw

Typhoons and earthquakes attack Taiwan every year even by month. Landslide hazard mitigation is very important in hazard prevention chain. Synthetic aperture radar images acquired by JAXA (Japan) are used in this research to monitor landslide displacement in large area. The study is trying to propose a method to produce landslide potential map from differential interferometric synthetic aperture radar (DInSAR). Small baseline subset (SBAS) is adopted for higher accuracy. This method searches points with the same radar signal strength through observing years and keep tracking locations in each scene. The RMS error directly from radar shows 10mm with 95% confidence. MEMs accelerometer with tilt and dynamic signal are also collected for ground motions. However, locale tilt or acceleration cannot reflect overall deformation. Thus a single/dual frequency GPS system is also installed in study area. The result of one monitoring landslide during a heavy rainfall event in June, 2017. The results also proved that SBAS method derived displacement map.

Key words: Landslide, SAR, MEMS, GPS

1. INTRODUCTION

Taiwan locates in the collision zone of sea plate and continental plate, which inducing earthquake and orogeny. Moreover, this island is surrounded with warm and cool sea water. Typhoons and heavy rainfall attacked this island frequently, especially after year 2000. Several typhoons and heavy rainfall with unexpected large rainfall attacked Taiwan in past 10 years. Typhoon Morakot in 2009 brings maximum 3,000 mm accumulated rainfall and the rainfall is 3/4 of average annual precipitation.

Landslide potential map is the first work for landslide hazard mitigation. There are several methods to produce landslide potential map. The logistic regression method combines potential factors with landslides and give landslide potential prediction. Two major categories including bivariate analysis and multivariate analysis are used in logistic regression analysis. Gupta and Joshi (1990) used Landslide Nominal Risk Factor (LNRF) to derive dimensionless factors and calculate the potential risk. Jade and Sarkar (1993) adopted Information Theory and classified the potential risk into three classes. Keefer (2000) proposed a landslide concentration (LC) factor to establish the relationship between landslide and earthquake. The landslide susceptibility mapping using bivariate analysis without seismic condition was conducted by different researchers. [Çevik et al., 2003; Chau et al., 2004; Lee, 2004; Lee et al., 2004; Lee, 2005; Ohlmacher and Davis, 2003]. However, the bivariate analysis does not take into account the independency of factors. Therefore, multivariate analysis has been developed for that purpose. The independency of factors must be checked and the matrix of factors is thus established.

Two classification algorithms – logistic regression and discriminating analysis are the most well-known methods to identify the susceptibility of landslide. Lin and Tung (2004) used structural equation model to establish a measuring matrix for landslide evaluation for the cases of Chi-Chi earthquake. Süzen and Doyuran (2004) compared the landslide susceptibilities using bivariate and multivariate analysis (logistic regression) based on northwest Turkey study area.

The neural network analysis uses factors related to landslides to perform training and evaluation of landslide susceptibility. The accuracy can be as high as 90% in the same area and using same event (Lee et al., 2003). However, the training process needs to restart when encountering different condition.

Semi-logistic regression methods which combined factor of safety to produce probability of landslide can be used to establish the susceptibility map. Pack et al. (1998, 1998a, 2001) used the stability index derived from factor of safety to classify susceptibility into several groups: stable, moderately stable, quasi-stable, lower threshold, upper threshold, and defended. Lan et al. (2004) used the module to analyze the landslide hazard in Yunnan, China. Another semi-logistic method adopts displacement as the index of landslide susceptibility. Wang et al. (2010) proposed a semi-mechanical and semi-regression method to produce landslide potential map.

The study is trying to propose a method to produce landslide potential map from differential interferometric synthetic aperture radar (DInSAR). Potential landslide zones are mapped after fringes and displacements are generated from ALOS/PALSAR radar image processing. Meanwhile, a deep-seated landslide site has been selected for instrumentation. Monitoring data more than 5 years has been collected and analyzed to find relationship between landslide displacement and rainfall, and groundwater. Mems accelerometer is designed for active or quick displacement area. The design is considered tilt and dynamic data collection.

2. METHODOLODY

2.1 Study area and geological condition

The study area is located at central Taiwan and the elevation ranges from 1000m to 2500m. A landslide potential map was mapped by expert from LiDAR data, which means the scars were generated by some events with unknown years and unknown active status. Most aspects of scars are facing north or south-north owing to geological condition. The geological condition in this area is quite unique, which is slate of Lushan Formation, Miocene. Lushan Formation is slate interlayered with thin metamorphosed sandstone and slate. The dip angles of slate in this area ranges from 20-70 degrees owing to gravity and tectonic forces.

2.2 Leveling verification

In order to discover landslide displacement without monitoring data, leveling data from government is a better solution to discover. However, Chi-Chi earthquake attacked Taiwan in 1999 and resulted large displacement in central Taiwan. Previous leveling data is too difficult to compare with recent result. There are only two leveling data, which are 2002 and 2009, can be found from government. Leveling was executed from Taiwan's originated point – Hutzushan to the mountain area with 1mm±1ppm accuracy. The differences between 2002 to 2009 in elevation is as shown in **Fig. 1** The differences are almost increasing except some benchmarks. The increasing of elevation is undoubtedly the effect orogeny. If rank the elevation difference and select a threshold for stable zone, the others can be eliminated the average value of stable zone. Thus benchmark C032, C034, C035 and C036 located at the river side and assumed as the elevation change to zero. The other benchmark elevations are modified from that. The benchmarks locate in landslide scars can be identified and the true landslide displacement can be calculated based on this assumption as shown in **Fig. 2**. There are four benchmarks show elevation decreasing, which means locate in landslide scars and moving between 2002~2009. The displacement has been calculated as shown in **Table 1**. The values have been transferred to annual velocity for DInSAR comparison.

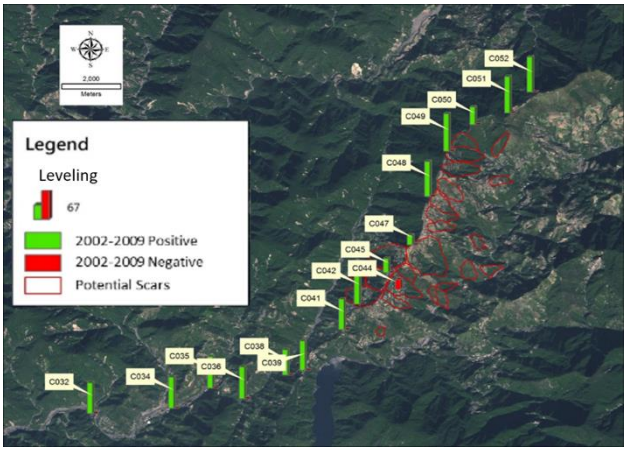

Fig. 1 The elevation change from benchmark survey in 8 years (2002-2009)

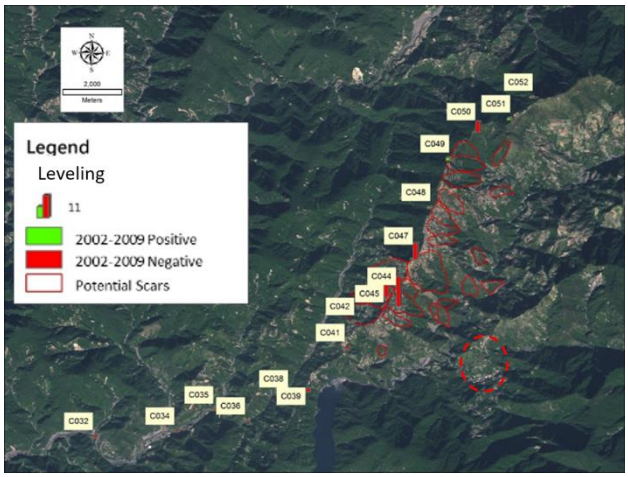

Fig. 2 Elevation differences adjusted for landslide displacement

Table 1 Elevation differences derived for landslide velocity

Benchmark Number	Relative decreasing velocity (mm/year)
C050	8.02
C047	12.03
C045	9.90
C044	22.06

2.3 Past monitoring condition

Soil and Water Conservation Bureau initiated a monitoring project in study area from 2005 to 2006. Central Geological Survey followed the monitoring system and started a long-term monitoring project from 2007. We collected data from these projects and carefully check abnormal conditions. **Fig. 3** illustrates how the monitoring works were aligned in the slope locations. The slope located in the circle area of **Fig. 2**. The prefix E denotes in-hole extensometer, A denotes ground water observation well with slope indicator, and SAA denotes shape acceleration array. Relationship between rainfall and groundwater is as shown **Fig. 4**. The figure shows that groundwater is highly related to rainfall but varies with their location within the slope. Also **Fig. 5** shows rainfall condition with groundwater level variance at site A-20. The result shows that regression has better result once lower rainfall events were removed from database. The same condition also revealed in **Fig. 6**, which is Shape Acceleration Array (SAA) displacement monitoring results comparing with accumulated rainfall events.

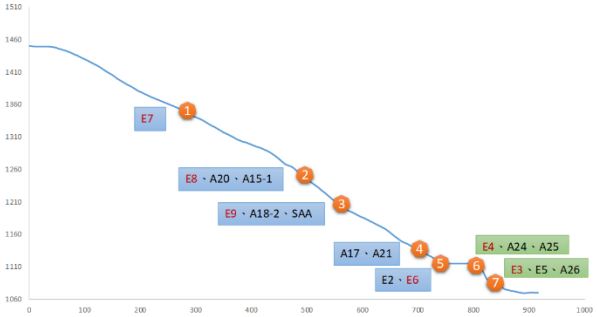

Fig. 3 The location of monitoring system on slope

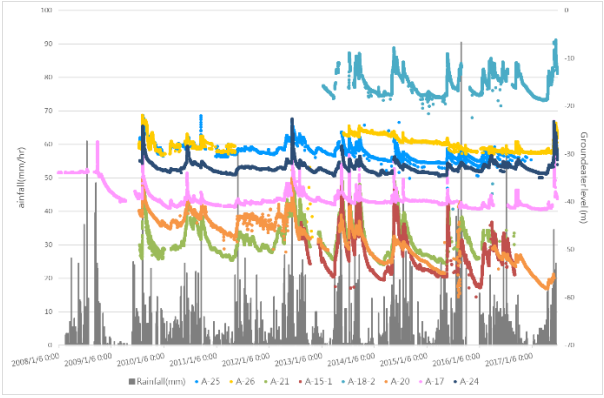

Fig. 4 The relationship of rainfall versus groundwater level

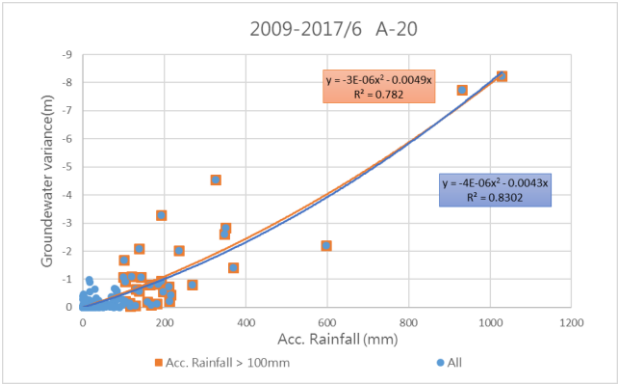

Fig. 5 Typical rainfall versus groundwater variance

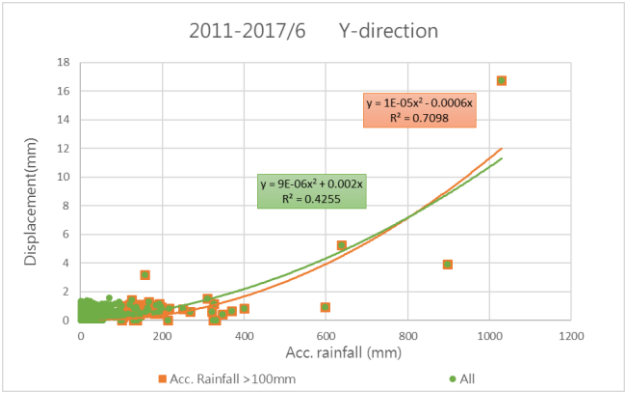

Fig. 6 Demonstration of displacement versus rainfall in study area

2.4 Potential landslide mapping with DInSAR

SAR measures the distance between satellite and ground surface by sending and receiving radar signals. Measurement of ground topography using SAR represents two locations of antenna that sensing the surface and are separated by a baseline. If the viewing geometry is controllable or known with sufficient accuracy, then the topography can be derived from the phase measurement of the two sensing radar waves. The topography can be obtained by geometry of satellite and observation point. Two important conditions that need to be understood for detecting and measuring surface change with SAR are:

(1) The changes between two successive images must not be too large.

(2) The radar-scattering characteristics within each pixel must remain similar.

The deformation of ground surface derived from DInSAR could be less than centimeter with high accuracy digital elevation model. When doing interferometry analysis by temporal SAR data, the phase information generated is including topography, change of ground characteristics, ground movement and atmosphere effect, etc. Phase difference of topography can be removed by high accuracy digital elevation model and short base line. Atmosphere effect can be reduced by long term analysis. The deformation can be trusted to high precision and after removed previous described errors and simply left ground deformation and noise.

DInSAR, PS, and SBAS has been well developed in recent years thus the monitoring of landslide displacement is becoming more possible. [Pieraccini et al. 2003, Tarchi et al. 2003, Guzzetti et al. 2009, Cal al. 2013, Liu et al. 2013, Lowry et al. 2013, Jebur et al. 2015, Tang et al. 2015, Casagli et al. 2016, Uhlemann et al. 2016].

The SAR images used in this research is Advanced Land Observing Satellite (ALOS) Phased Array type L-band Synthetic Aperture Radar (PALSAR) and ALOS-2 L band image. The polarization of radar electromagnetic wave is Horizontal - Horizontal (HH) mode and incident angle is 34.3 degree. The range resolution from this area is approximately 10 meter. There are several SAR images can be used for differential interferometric SAR. However, ALOS PALSAR/ALOS2 with L band has longer wave length, which is 23cm and possible could be eliminated the effect of vegetation.

DInSAR method is fine to observe landslide scar at two images with close dates. However, the displacement data shows too much noise to identify accuracy and comparison with benchmark data. An example of DInSAR event is as shown in **Fig. 7**, the even is typhoon Morakot with about 1000mm rainfall in study area. The result shows some displacement signal within landslide but not obvious.

Thus another approach small baseline subset (SBAS) is adopted for higher accuracy. This method searches points with the same radar signal strength through observing years and keep tracking locations in each scene. SBAS analysis is performed with only 13 ALOS images owing to lack of small baseline dataset. The RMS vertical displacement error directly from radar shows 10mm with 95% confidence. The ALOS satellite was not in function after 2011 until ALOS2 was back to track in 2014. The ALOS data with previous analysis combining with 6 ALOS2 images are adopted for analysis in study area. SBAS analysis result combining ALOS with ALOS2 is as shown in **Fig. 7**. The RMS vertical displacement error directly from radar shows 7.6mm with 95% confidence. The result combing ALOS/ALOS2 images not only reveals more displacement data points but also show more fit with mapped scars previous described. Two fastest landslide masses are found in study area within landslide scars as shown in **Fig. 8.** GPS monitoring were initiated to verify SBAS analysis result.

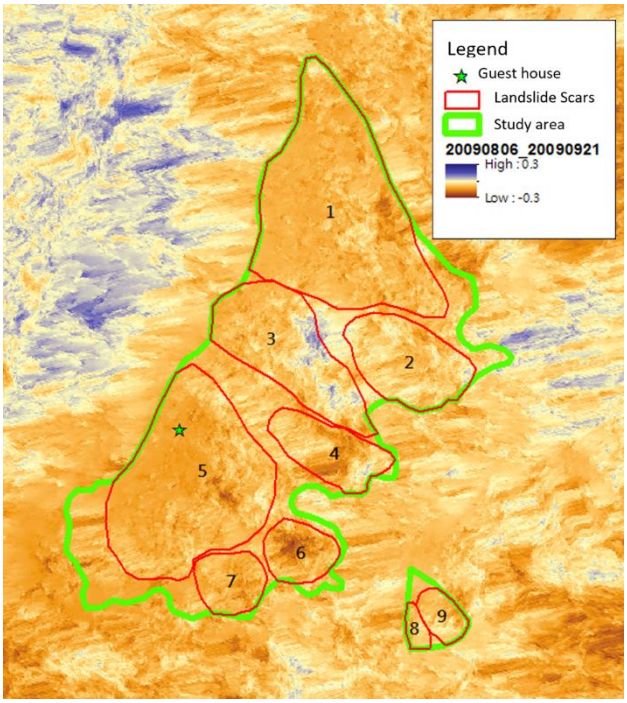

Fig. 7 Displacement map derived from DInSAR between tyhoon Morakot event in 2009 (unit: m)

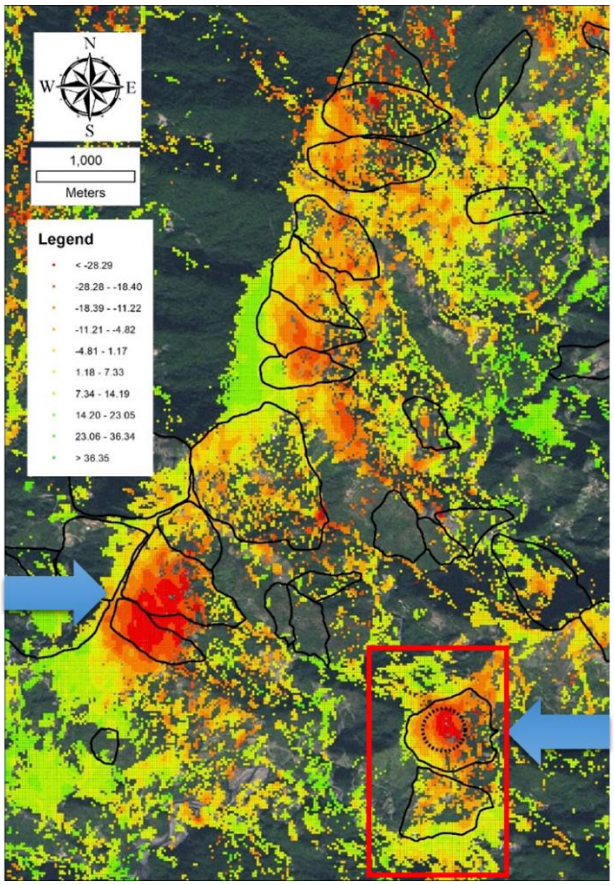

Fig. 8 Vertical displacement velocity map produced with SBAS (2007-2017/07) (unit: mm/year)

2.5 Low-cost mems accelerometer monitoring

Owing to landslide instrumentation is too expensive and unnecessary. In this work, we present a low-cost slope-monitoring device. The device is constructed using components purchased online at reasonable costs. The device is capable of recording triaxial accelerations at 200Hz onto standard SD (secure digital) memory cards. In addition, the sensed triaxial accelerations can be converted to tilt, which can then be sent via onboard GPRS module to a cloud server. Thus, the constructed device can be used for both static measurements of the slope surface and dynamic measurements of ground-surface acceleration. This information can assist assess slope condition regularly and dynamic force experienced by the slope after earthquake. **Fig. 9** illustrates distribution of dual frequency GPS and MEMs installed in to selected landsides, which are as shown rectangular in **Fig. 8**. The recorded data has been calculated to tilt as shown in **Fig. 10**. The results shows the tilt direction s toward landside direction at toe.

Fig. 9 Locations of dual frequency GPS and MEMs

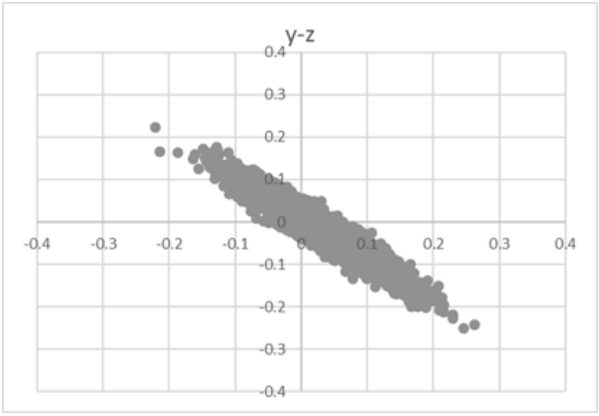

Fig. 10 Tilt derived from MEMS accelerometer of Y-Z plane

2.6 GPS monitoring

GPS monitoring system were initiated for monitoring landslide activity after DInSAR results show that the study are is highly active. Five dual frequency GPS stations were set up for monitoring and verification of DInSAR result. Owing to lack f funding, GPS stations were set up in April, 2017 without funng. Two GPS solution methods are adopted in this study, which are node to node and network calculation. Open source code RTKLib was adopted as node to node solution and network solution uses commercial software MAGNET from TOPCON for comparison. **Fig. 11** shows the result at the same location of MEMS station, which shows obvious displacement and tilt direction in June, 2017 event.

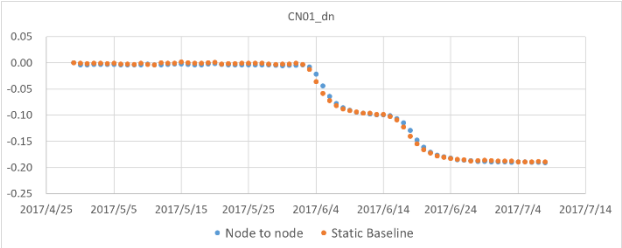

(a) Displacement of north direction

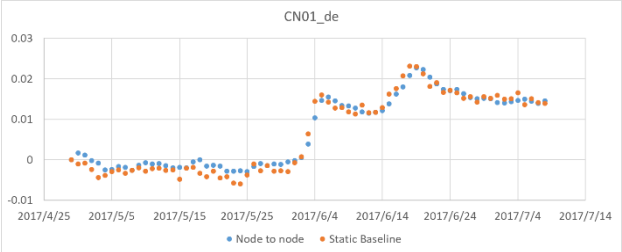

(b) Displacement of east direction

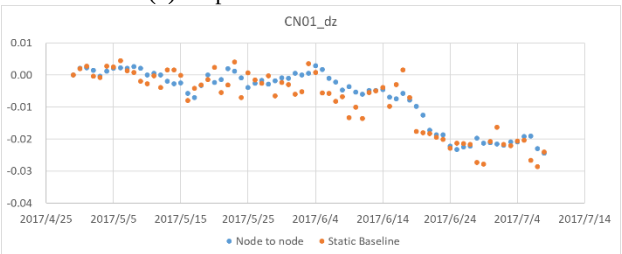

(C) Displacement of vertical direction

Fig. 11 GPS1 monitoring results at MEMS location

The other special GPS monitoring result locates at the dashed circle in **Fig. 8**. The GPS solution is as shown in **Fig. 12**. The results show -3 cm in north, 12 cm in east and -6 cm in June, 2017 rainfall event.

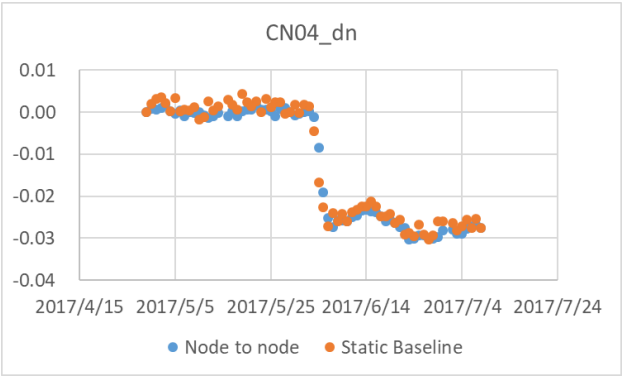

(a) Displacement of north direction

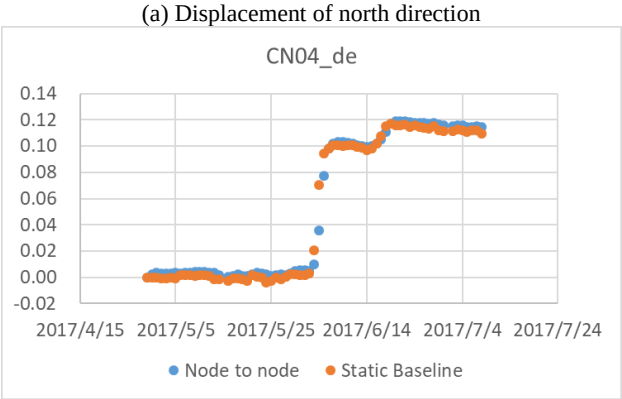

(b) Displacement of east direction

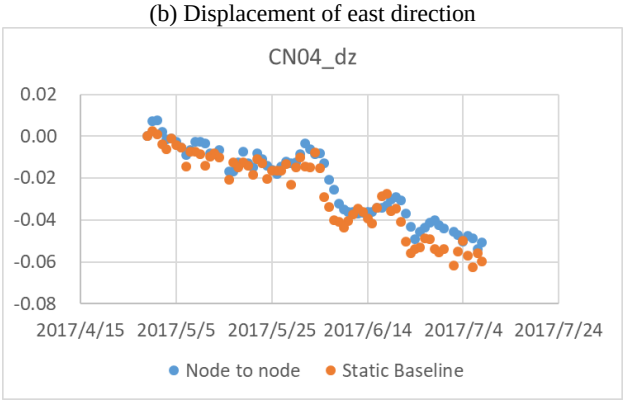

(C) Displacement of vertical direction

Fig. 12 GPS4 monitoring results at MEMS location

3. DISCUSSION

As previous described about leveling data in 8 years (2002-2009). Benchmark number C044 shows 22mm/year gradually sliding down. The SBAS analysis result at the same point from 2007 to 2017 is as shown in **Fig. 13**. According to benchmark survey data, the elevation lowering velocity is about 22mm/year, which means approximately 220mm from 2007 to 2017. The results shows a slightly difference from SBAS result in **Fig. 13** but still have the same trend. Also the elevation has a significant difference during heavy rainfall event in 2017.

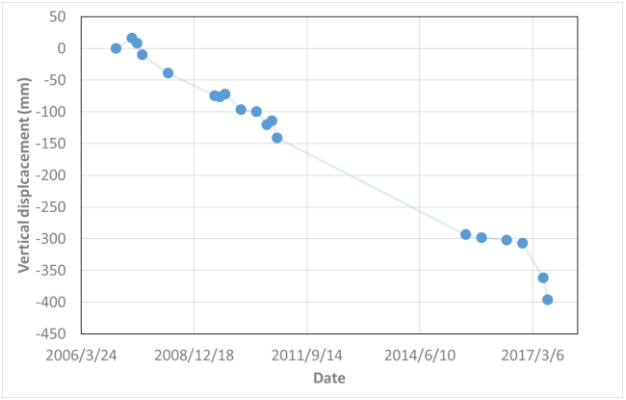

Fig. 13 Vertical displacement of benchmark number C044 point from SBAS

In order to verify the accuracy of SBAS analysis result, a dual frequency GPS was installed for analysis at the center of dashed line circle in **Fig. 8**. Vertical displacement at the same point of SBAS analysis result was extracted and as shown in **Fig. 14**. The figure shows vertical displacement is continuously sliding down and has a jump in 2017 owing to a heavy rainfall event in June. The event resulted in 1500mm rainfall in two weeks. According to SBAS result from Dec., 2016 to July, 2017, vertical displacement calculated is about 8cm at this

point. A dual frequency GPS was installed in April, 2017 to verify SBAS result. A refer GPS station located at stable location 1.1km away from this point is adopted for node to node displacement calculation. Three dimensional GPS displacement of June event was calculated as shown in **Fig. 12**. The displacement toward east about 11cm, south about 3cm and down about 6cm from April to August. The monitoring period difference is from January to April in 2017. However, the results of two differential methods reveal high accuracy result. However, SBAS results are not easy to compare with GPS data owing to GPS monitoring initiated from 2017. The only way to verify long term landslide deformation is from leveling data. The displacement shows good coincidence when treat leveling data from displacement magnitude to velocity. Moreover, the GPS installed from April, 2017 monitored an event in June, 2017, which displacements measured are the same with SBAS results.

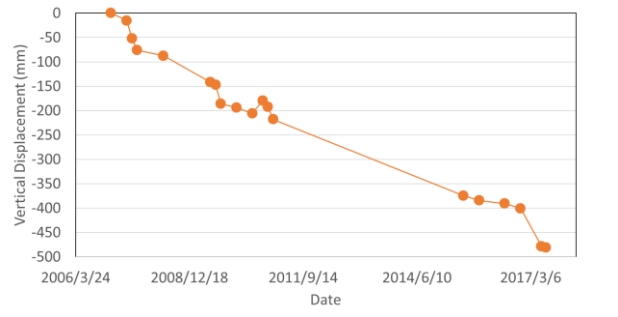

Fig 14 Vertical displacement derive from ALOS/ALOS 2 SBAS analysis

4. CONCLUSIONS

Landslide potential map is typically generated by factors by statistic method or mechanic equilibrium approach. In this work we propose a monitoring methodology from DInSAR and SBAS data processing. This method can identify active landslide scars in the same rainfall condition area, which means should pay more attention to monitoring. DInSAR can map landside scars from fringe and displacement map roughly. SBAS has more precise displacement monitoring and landslide boundary can be thus defined. Two deep seated landslides were selected for instrumentation to compare with DInSAR and SBAS method. SBAS results show more appropriate for active landslide mapping. The verification from GPS shows that SBAS can derive high accuracy result for landslide monitoring. Therefore large area landslide monitoring can be performed with such method and expensive monitoring instrumentation can be selected to install at fast displacement locations. Moreover, SBAS method can detect un-stable landslide and provide early warning for engineering treatment or monitoring works.

The underground instrumentations show that landslide displacement has good coincidence with accumulative rainfall. However, landslide instrumentation is too expensive when there are many potential scars in study area. Thus a low-cost mems monitoring sensor was developed in this work. In this work, we share our experience on building a low-cost slope-monitoring device that senses temperature and dynamic accelerations at 200Hz, provides 6-month long-term storage with a 16GB micro SD card, and sends calculated tilt to cloud servers via GPRS module. The low-cost system works well and provides more quick response to landslide warning much earlier than DInSAR and SBAS methods.

ACKNOWLEDGMENT: The authors would like to present their grateful thanks for the research grant from Ministry of Science and Technology and research possibilities from Central Geological Survey, Taiwan.

REFERENCES

Cal, F., F. Ardizzone, R. Castaldo, P. Lollino, P. Tizzani, F. Guzzetti, R. Lanari and M. Manunta (2013) Landslide analysis through the multi-sensor SBAS-DInSAR approach: The case study of Assisi, Central Italy. 2013 IEEE International Geoscience and Remote Sensing Symposium - IGARSS. 2916-2919.

Casagli, N., F. Cigna, S. Bianchini, D. Hölbling, P. Füreder, G. Righini, S. Del Conte, B. Friedl, S. Schneiderbauer, C. Iasio, J. Vlcko, V. Greif, H. Proske, K. Granica, S. Falco, S. Lozzi, O. Mora, A. Arnaud, F. Novali and M. Bianchi (2016) Landslide mapping and monitoring by using radar and optical remote sensing: Examples from the EC-FP7 project SAFER. Remote Sensing Applications: Society and Environment 4: 92-108.

Chau, K.T., Y.L. Sze, M.K. Fung, W.Y. Wong, E.L. Fong and L.C.P. Chan (2004) Landslide hazard analysis for Hong Kong using landslide inventory and GIS. Computers and Geosciences. 30:429-443.

Gupta, R.P and B.C. Joshi (1990) Landslide Hazard Zoning Using the GIS Approach – A Case Study from the Ramganga Catchment, Himalayas. Engineering Geology. 28:119-131.

Guzzetti, F., M. Manunta, F. Ardizzone, A. Pepe, M. Cardinali, G. Zeni, P. Reichenbach and R. Lanari (2009). Analysis of Ground Deformation Detected Using the SBAS-DInSAR Technique in Umbria, Central Italy. Pure and Applied Geophysics. 166(8): 1425-1459.

Jade S. and S. Sarkar (1993) Statistical models for slope instability classification. Engineering Geology., 36:91-98.

Jebur, M. N., B. Pradhan and M. S. Tehrany (2015) Using ALOS

PALSAR derived high-resolution DInSAR to detect slow-moving landslides in tropical forest: Cameron Highlands, Malaysia. Geomatics, Natural Hazards and Risk 6(8): 741-759.

Keefer D.K. (2000) Statistical analysis of an earthquake-induced landslide distribution – the 1989 Loma Prieta, California event. Engineering Geology. 58:231-249.

Lan H.X., C.H. Zhou, L.J. Wang, H.Y. Zhang and R.H. Li (2004) Landslide hazard spatial analysis and prediction using GIS in the Xiaojiang watershed, Yunan, China. Engineering Geology. 76:109-128.

Lee, C. N. (2001) Preliminary study on the Tsao-Ling landslide area under earthquake. Master's Thesis. National Taiwan University.

Lee S. (2004) Application of likelihood ratio and logistic regression models to landslide susceptibility mapping using GIS. Environmental Management. 34(2):223-232.

Lee S. (2005) Application of logistic regression model and its validation for landslide susceptibility mapping using GIS and remote sensing data. International Journal of Remote Sensing. 26(7):1477-1491.

Lin, M. L. and C.C. Tung (2004), A GIS-based potential analysis of the landslides induced by the Chi-Chi earthquake. Engineering Geology. 71:63-77.

Liu, G., R. Wang, Y. K. Deng, R. Chen, Y. Shao, W. Xu and D. Xiao (2013). Monitoring of ground deformation in Beijing using SBAS-DInSAR technique. 2013 Asia-Pacific Conference on Synthetic Aperture Radar (APSAR). 300-303.

Lowry, B., F. Gomez, W. Zhou, M. A. Mooney, B. Held and J. Grasmick (2013) High resolution displacement monitoring of a slow velocity landslide using ground based radar interferometry. Engineering Geology. 166: 160-169.

Ohlmacher G. C. and J.C. Davis (2003) Using multiple logistic regression and GIS technology to predict landslide hazard in northeast Kansas, USA. Engineering Geology. 69:331-343.

Pack, R. T., D.G. Tarboton and C. N. Goodwin (1998) The SINMAP approach to terrain stability mapping. The 8th Congress of the International Association of Engineering Geology, Vancouver, Canada.

Pack, R. T., D.G. Tarboton and C.N. Goodwin (1998a) Terrain stability mapping with SINMAP, technical description and user guide for version 1.00. Report Number 4114-0, Terratech Consulting Ltd., Salmon Arm, B.C., Canada.

Pack, R. T., D.G. Tarboton and C.N. Goodwin (2001) Assessing terrain stability in a GIS using SINMAP. The 15th annual GIS conference, Vancouver, Canada.

Pieraccini, M., N. Casagli, G. Luzi, D. Tarchi, D. Mecatti, L. Noferini and C. Atzeni (2003) Landslide monitoring by ground-based radar interferometry: A field test in Valdarno (Italy). International Journal of Remote Sensing. 24(6): 1385-1391.

Süzen, M.L. and V. Doyuran (2004) A comparison of the GIS based landslide susceptibility assessment methods: multivariate versus bivariate. Environmental Geology. 45:665-679.

Tang, P., F. Chen, H. Guo, B. Tian, X. Wang and N. Ishwaran (2015) Large-Area Landslides Monitoring Using Advanced Multi-Temporal InSAR Technique over the Giant Panda Habitat, Sichuan, China. Remote Sensing. 7(7): 8925.

Tarchi, D., N. Casagli, S. Moretti, D. Leva and A. J. Sieber (2003) Monitoring landslide displacements by using ground-based synthetic aperture radar interferometry: Application to the Ruinon landslide in the Italian Alps. Journal of Geophysical Research: Solid Earth. 108(B8): n/a-n/a.

Uhlemann, S., A. Smith, J. Chambers, N. Dixon, T. Dijkstra, E. Haslam, P. Meldrum, A. Merritt, D. Gunn and J. Mackay (2016) Assessment of ground-based monitoring techniques applied to landslide investigations. Geomorphology. 253: 438-451.

Wang, K.-L. and M.-L. Lin (2010) Development of Shallow Seismic Landslide Potential Map Based on Newmark's Displacement: The Case Study of Chi-Chi Earthquake, Taiwan. Environmental Earth Sciences. 60(4), 775-785.

Estimating Landslide Volumes Using LS-rapid Model -The 2000 Stože Landslide in NW Slovenia

Jošt SODNIK[1,2*], Matej MAČEK[1] and Matjaž MIKOŠ[1]

[1] Faculty of Civil and Geodetic Engineering, University of Ljubljana (Jamova c. 2, 1000 Ljubljana, Slovenia)
[2] TEMPOS Environmental Civil Engineering Ltd. (Tehnološki park 21, 1000 Ljubljana, Slovenia)
*Corresponding author. E-mail: jost.sodnik@gmail.com

Potential landslides may after activation present a debris-flow source, and hence reliable potential landslide volume estimation is a significant factor when assessing regional debris-flow hazard. A 3D landslide simulation model LS-Rapid was applied to analyze the triggering phase of the rainfall-induced 2000 Stože Landslide in NW Slovenia, Europe. It was triggered on a steep Stože slope in November 2000. The destabilized mass moved and fluidized, and flowed as a dry debris flow to a torrent channel; due to inflow of rainfall and flow from the Mangartski potok torrent, after 35h it turned into a wet debris flow that reached the village of Log pod Mangartom, several kilometers away from the landslide source area. The known volume of the 2000 Stože Landslide was estimated using LS-Rapid simulation results. In addition, other parameters of the 2000 Stože Landslide (e.g. triggering factors, landslide source area, landslide contour, volume and depth, super elevation on its path, deposition area) were used to validate the LS-Rapid modeling results. Based on this case study, limiting boundaries for key soil parameters in the LS-Rapid model were proposed to help with the LS-Rapid model data preparation, when the model is applied for potential landslides where no model validation and calibration is possible, and when no ring-shear apparatus is at hand to estimate soil parameters.

Key words: debris flow, event magnitude, hazard assessment, landslide simulations

1. INTRODUCTION

Landslides and variety of their forms are focus of worldwide landslide research efforts for decades. An important part of the on-going research is how to assess landslide hazard, i.e. connecting their triggering (initation), transport (motion) and deposition (reach-out) phases. As a result, many landslide models have been developed worldwide; for a recent review on landslide models see *Yavari-Ramshe and Ataie-Ashtiani* [2016], p. 1335, **Table 3**).

One of the 3D landslide simulation models is the LS-Rapid model developed to assess the initiation and motion of landslides triggered by earthquakes, rainfalls or the combined effect. This model has been originally developed in 1988 by *Sassa* [1988] and improved upon in 2004 [*Sassa et al*., 2004]; it is based on the measured landslide mass dynamic properties determined by applying a ring-shear apparatus [*Sassa et al*., 2014a]. Its theoretical background is described in detail in *Sassa et al*. [2010].

The LS-Rapid model has found many applications all over the world:

a) for the earthquake-induced landslide cases such as the 2006 landslide in the Leyte Island, Philippines [*Sassa et al*., 2010], the 1792 Unzen-Mayuyama megaslide in Shimibara, Japan [*Sassa et al*., 2014a], the Daguangbao Landslide triggered by the 2008 Wenchuan Earthquake [*Tsuchiya et al*., 2013], hypothetical Senoumi submarine megaslide in the Suruga Bay, Japan [*Sassa et al*., 2012], the 2016 Kumamoto earthquake-induced Takanodai and Aso-ohashi landslides on Kyushu Island, Japan [*Dang et al*., 2016], the deep large-scale 2008 Arotazawa Landslide, Japan with a combined effects of seismic loading and pore pressure increase including volume increase during its motion [*Setiawan et al*., 2016; 2017] etc.;
b) for rainfall-induced landslide cases such as for the Kostanjek Landslide, Croatia [*Gradiški et al*., 2013], landslides at Iwa Valley area of Enugu State, Nigeria [*Igwe et al.*, 2014], the 2009 Marappalam landslide in Tamil Nadu state, India [*Senthilkumar et al*., 2017], the 2015 rapid landslide at Ha Long City, Vietnam [*Loi et al*., 2017], the multi-stage Montaguto Earthflow, Italy [*Cuomo et al*., 2017], the formation of the

2011 Akatani Landslide dam in Kii Peninsula, Japan [*Tien et al*., 2017], the 2014 Hiroshima landslide disasters [*Sassa et al*., 2014b], the reactivated Grohovo Landslide, Croatia [*Arbanas et al*., 2017] and the Valići Landslide, Croatia [*Vivoda Prodan and Arbanas*, 2017] etc.;

c) for regional landslide susceptibility analyses such as for the Istrian Peninsula, Croatia [*Dugonjić Jovančević et al*., 2013; *Dugonjić Jovančević and Arbanas*, 2017], and the Koroška Bela landslides, Slovenia [*Sodnik et al*., 2017], as well as for the precursor stage of the Haivan Station Landslide, Vietnam [*Quang et al*., 2017].

The purpose of this study was to evaluate the 3D landslide simulation model LS-Rapid as a tool to estimate potential landslides volumes that once triggered can be debris-flow sources, and the estimated landslide volume can be used as the estimation of the maximum debris-flow magnitude. All this has a sense, if there is not enough field data available to perform a statistical (empirical) analysis of debris-flow magnitudes, as is the case in a small country such as Slovenia (20,273 km^2), where debris flow hazard is increasing in last two decades [*Mikoš and Majes*, 2012]. We used the well-investigated 2000 Stože Landslide case study as the validation case for the model LS-Rapid, with a goal to be able to use it in future for regional landslide susceptibility analyses, as well as for estimation of maximum debris-flow magnitudes triggered on slopes as landslides.

2. THE 2000 STOŽE LANDSLIDE

The Stože Landslide was triggered after intensive rainfall in November 2000 [*Mikoš et al*., 2004] (for location see **Fig. 1**).

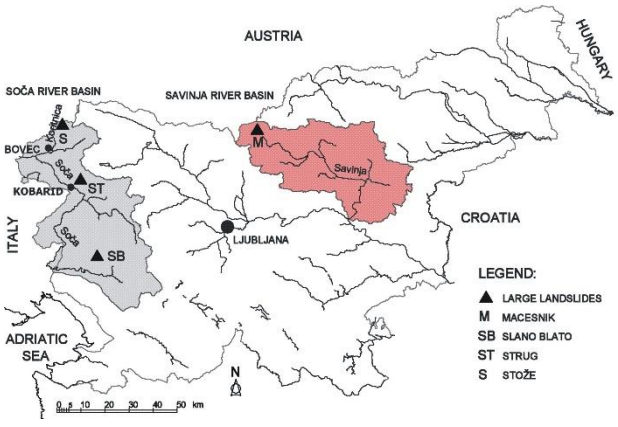

Fig. 1 The 2000 Stože Landslide and other recent large landslides in Slovenia (volume > 1 mio m^3) [*Mikoš et al*., 2004].

On November 15, 2000 in the first phase, landslide was triggered and stopped in the Mangartski potok torrent. The landslide was triggered on the altitude between 1200m and 1600m a.s.l. In the second phase on November 17, 2000, after additional 36h of rain and inflow of the Mangartski potok discharge, the deposited landslide mass turned into a wet debris flow and destroyed part of the village Log pod Mangartom and caused 7 casualties [*Mikoš*, 2011]. This was one of the most devastating landslides in the last century in Slovenia [*Mikoš and Majes*, 2012].

The second phase of the wet debris flow was investigated by applying debris-flow numerical modelling in order to assess debris-flow hazard in the area under assumption that potential debris flows can be triggered on the Stože slope [*Četina et al*., 2006].

The triggering phase was not investigated in details and results of such a study with a landslide triggering simulation would be useful for investigating potential landslides as debris flow sources. In this study, the LS-Rapid model was used to simulate triggering of the Stože landslide (the first phase of the 2000 event), and to compare simulation results with the field observations during the two-stage event and the post-event field investigations.

On November 15th 2000, the Stože landslide was triggered as a relatively dry debris slide (1st phase), and then, on November 17th 2000, turned into a wet debris flow (2nd phase). The main cause of the Stože landslide was prolonged heavy rainfall. The measured rainfall at Log pod Mangartom village was 1638 mm in the previous 48 days, which presents a recurrence interval of more than 100 years. In the first phase, a "dry" slide was triggered on the slope and the landslide mass stopped in the Mangartski potok torrent channel with a slope of 16%. During the next 36 h, the landslide mass was additionally wetted by heavy rainfall and a direct water inflow from the Mangartski potok. Early on 17 November 2000, a second event happened. The previously deposited landslide mass turned into a wet debris flow that travelled for approximately 5 km with approx. 500 height difference. In the village of Log pod Mangartom, the debris flow on its way destroyed 6 houses and severely damaged 23 houses, and caused 7 casualties. The simulated debris-flow velocities in the steepest part of the Mangartski potok channel of 45° were up to 60 km/h. [*Četina et al*., 2006].

3. LS-RAPID SIMULATION MODEL

For the topographic data of the Stože debris-flow numerical model a new LiDAR-based DTM with the resolution of 1 m was used. At the location of the

landslide, the DTM was manually using CAD tools corrected to the original state before the 2000 event based on topographic maps in scale 1:5000. With a combination of both data in CAD tools, a pre-event topography of the triggering area was made to be used in the simulation model (**Fig. 2**). For the determination of geological units and soil parameters for the LS-Rapid model, the Basic Geological map of Slovenia in scale 1:100,000 was used (**Fig. 3**).

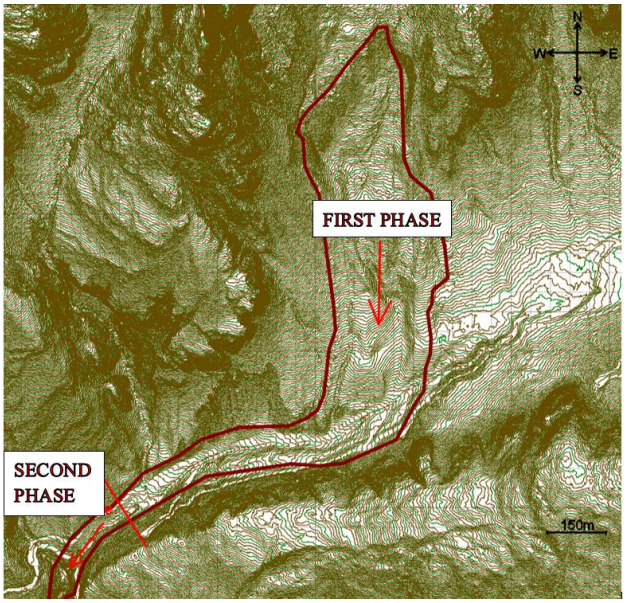

Fig. 2 Pre-event topography of the case study area with the contour of the Stože landslide.

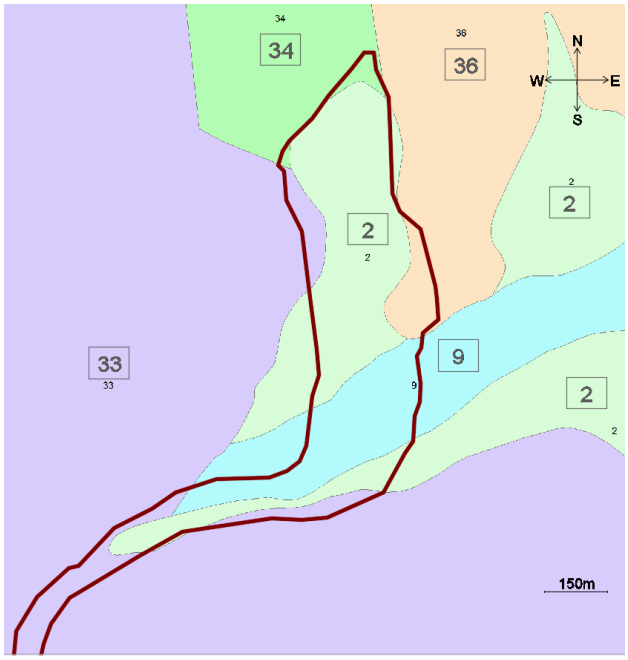

Fig. 3 Geological map of the area: 33 – bedded dolomite; 34 – limestone, marlstone, dolomite; 36 – massive or bedded dolomite; 2 – Scree; 9 – moraine**.**

Soil parameters and the depth of unstable mass for each geological unit on the Stože slope were assessed based on the geotechnical laboratory test results, expert experience and judgement.

With additional topographical analysis, we determined geological units where terrain slope exceeds the angle of internal friction of the soil. In reality, these areas are steep bare weathered rocks with no or sporadic soil cover and are more prone to rock falling then sliding.

After this analysis, the two "potentially unstable" geological units were "scree material" and "moraine". For these two units soil parameters were assessed, and detail conditions are described in chapter 5. To determine τ_{ss} (steady state shear resistance at the sliding surface) authors of the model suggested to use an undrained ring-shear apparatus of this type, such as ICL-1 to ICL-3 [e.g. *Oštrić et al.*, 2012].

No tests were performed in a ring shear apparatus, since it was not available at the time of the laboratory testing and has limitations in terms of the maximum grains size of the mixture (2mm). More than 60% of the landslide mass has grain sizes over 2mm that makes ring-shear apparatus less useful when modelling landslides in the European Alpine environment. [*Maček et al.*, 2017].

Due to these limitations, a following relationship was proposed Eq. (1) between τ_{ss} and τ_p (peak/maximum shear resistance before failure).

$$\tau_{SS} \approx 0.45\tau_p \xrightarrow{up\ to} 0.65\tau_p \qquad (1)$$

Other soil parameters were proposed based on experiences with laboratory testing and professional judgement: Scree material: K_0=0.5; ϕ_i=40°; ϕ_m=40°; τ_{ss}=190kPa; B_{ss}=1.0; ϕ_p=42°; c_p=5.0kPa; γ=22KN/m^3; and Moraine: K_0=0.5; ϕ_i=36°; ϕ_m=36°; τ_{ss}=190kPa; B_{ss}=1.0; ϕ_p=37°; c_p=25kPa; γ=23KN/m^3, where K_0 is lateral pressure ratio, ϕ_i friction coefficient inside landslide mass, ϕ_m friction coefficient during motion at sliding surface, τ_{ss} steady state shear resistance at sliding surface, B_{ss} rate of excess pore-pressure generation, ϕ_p peak friction coefficient at sliding surface, c_p peak cohesion at sliding surface, and γ unit weight of mass).

Based on the available borehole data, a soil depth (potentially unstable mass) of 30m was used in the model for both geological units. For better presentation of the real conditions, a "smoothing" function was applied to ensure smooth increase at the landslide edges from 0 to 30m in the middle of the debris slide area.

The LS-Rapid model includes two triggering

factors: earthquakes and pore pressure. In case of the Stože landslide, the increase of pore pressures triggered the landslide. The LS-Rapid model uses pore pressure ratio (r_u) for determination of pore pressures in the landslide body.

$$r_u = \frac{h_w \gamma_w}{h_m \gamma_m} \quad (2)$$

Therefore, r_u=0.3, based on Eq. (2) presents approx. water table at 67%-layer height and r_u=0.45 represents water table at ground surface. In our simulations, r_u=0.3 was used, as one of possible realistic scenarios. On the other hand, r_u=0.45 represents full saturation and so called "worst case scenario".

4. SIMULATIONS OF THE 2000 STOŽE LANDSLIDE

4.1 Triggering simulation

Fig. 4 shows model topography with unstable mass (scree and moraine). Other parameters of the model were set as: simulation time of 100 s with time step 0.005s, shear displacement at the point of failure *DL*=1 mm, and at the end of shear strength reduction *DU*=1000 mm.

The simulation purpose was to analyse the triggering phase of the Stože landslide and to compare the modelling results with the surveyed landslide contour, traveling distance of the first phase e.g. "dry" slide and the landslide volume.

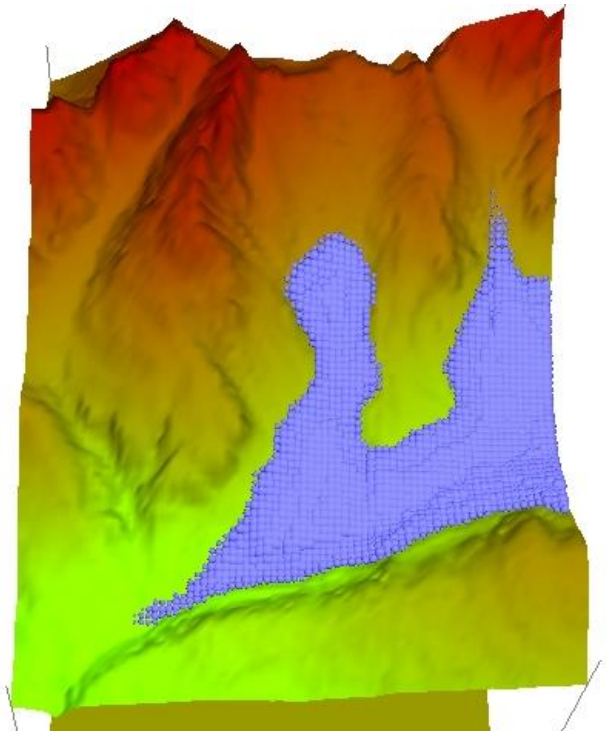

Fig. 4 Model topography and unstable mass.

Table 1 LS-RAPID model topography and results legend

Color	Moving mass thickness (m)
	stable mass
	0-6
	6-12
	12-18
	18-24
	24-30
	>30

In **Table 1** colors of the simulation topography and modeling results are shown. Different colors represent the thickness of the moving mass.

Unstable and moving mass is presented as balls, which is one of the options in the model. Larger radius of the ball means thicker unstable or moving mass. Size of the largest ball is defined with maximum thickness of the unstable mass at the start of the simulation. During simulation size of the balls does not change, therefore this kind of modelling presentation is more suitable for graphical presentation. For exact measurements and calculations of the moving mass thickness, one has to use txt (matrix) output files where exact thickness is given for each simulation step of the modelling process.

4.2 Sensitivity analysis of the model

A sensitivity analysis of τ_{ss} and r_u parameters was carried out to determine the influence of each parameter on the simulation results and to determine the soil parameters of the model that is closest to real landslide behaviour.

4.2.1. Influence of r_u

For analysis of influence of pore pressure ratio, we chose fixed value τ_{ss}=150kPa and changed values of r_u in the following steps: r_u=0.0 (no pore pressure); r_u=0.1; 0.2; 0.3; 0.4 and 0.45 (ground water table at slope surface).

For r_u value estimations we used relationship proposed with Eq. (2). We used different values of r_u and compared the simulation results in the initial and final state of simulation. On **Fig. 5** we can see that with no pore pressure there is no unstable areas and no landslides are triggered. But on **Fig. 6** we can see that with high pore pressure ratio numerous areas become unstable, even outside of the surveyed 2000 Stože Landslide contour. This result shows that higher pore pressures could lead to even larger magnitudes of the 2000 event. With enlarging r_u values more unstable areas are simulated, therefore the movement of the landslides depends more on the τ_{ss} value which will be presented in the following chapter.

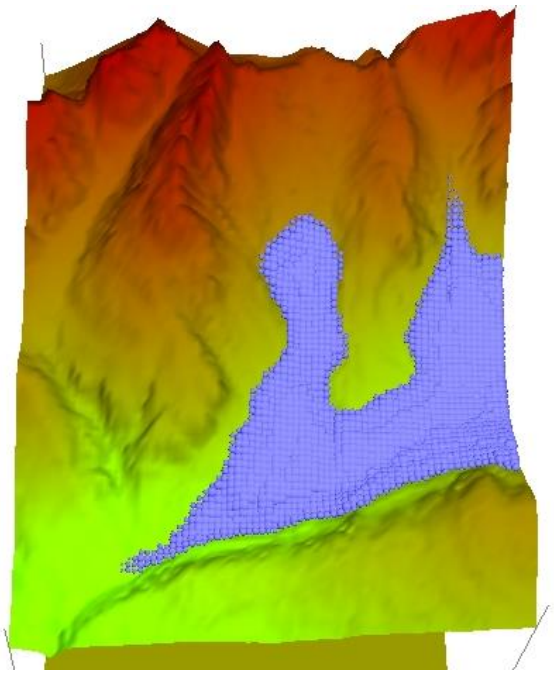

Fig. 5 Final simulation result with r_u=0.0.

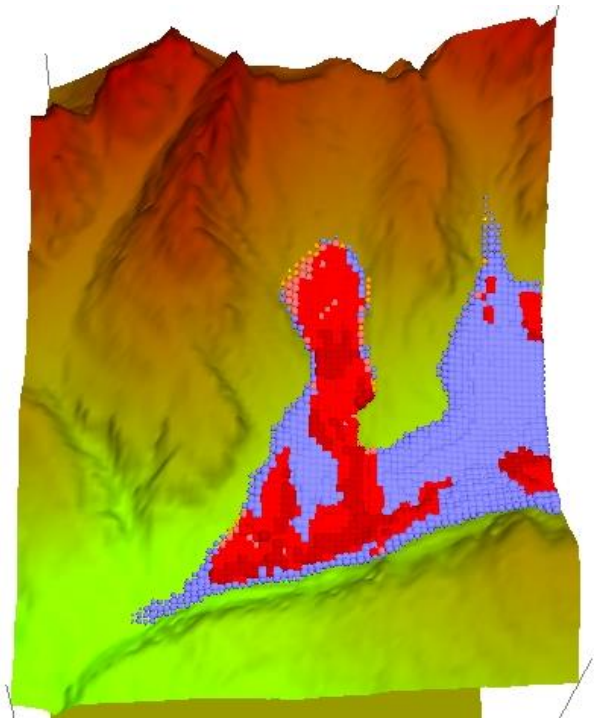

Fig. 6 Final simulation result with r_u=0.4.

On **Fig. 7** we can see that value r_u=0.2 causes unstable areas inside Stože landslide area, but in much smaller amount then surveyed on the field (**Fig. 2)**. These results show that r_u value defines unstable areas in the model, but the spreading of unstable areas and landslide movement depend on τ_{ss} value. Also based on these results we concluded that r_u value of Stože landslide event was approx. 0.3.

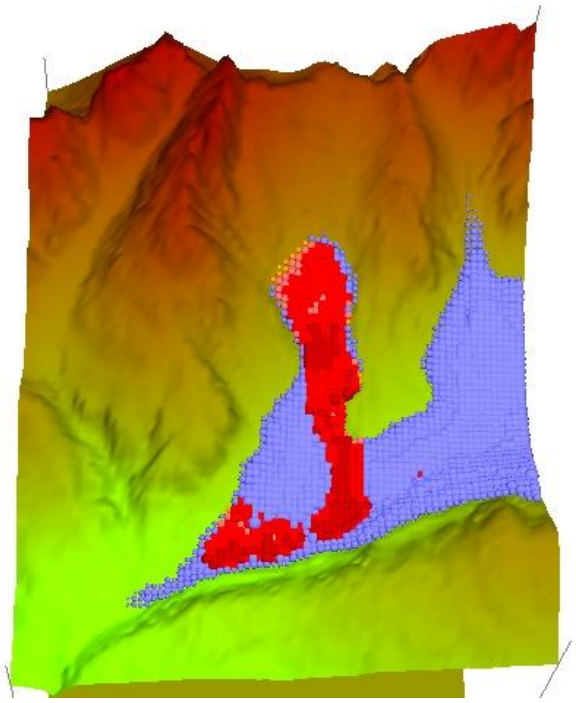

Fig. 7 Final simulation result with r_u=0.2.

4.2.2. Influence of τ_{ss}

After testing the influence of r_u parameter and conclusions about approx. value of November 2000 Stože landslide event, we tested influence of τ_{ss} parameter. We choose r_u=0.3 for all the models and changed τ_{ss} values with following steps: τ_{ss}=2 kPa (measured value after *Lenart and Fifer Bizjak*, 2010); 50 kPa (lower boundary after *Sassa et al*., 2010); 100 kPa; 150 kPa; 200 kPa, and 250 kPa. Models with low τ_{ss} values (**Fig. 8**) show that already in the initial phase all unstable areas start to spread and move. On the other hand, we can see (**Fig. 9**) that higher values of τ_{ss} prevent all the simulated area to collapse and move. Small spots of unstable areas can be found, but no spreading of instability or mass movement is simulated.

With low τ_{ss} values model simulates also very unrealistic scenarios. With τ_{ss}=2kPa after 10s practically all the modelling area is mobilized (**Fig. 10**), or even more unrealistic scenario with landslide mass splashing over the reef (**Fig. 11**) (approx. 200m height difference between Mangartski potok channel and reef height). In the calculation no viscosity effect on shear strength or non-frictional dissipation of energy was used. In case it would be used the spreading should be smaller. These results show realistic and correct values of τ_{ss} parameter are crucial for getting realistic and reliable simulation results.

With such differences in the simulation results, depending of τ_{ss} values, some first estimations before the simulation are necessary. Therefore, our proposal for τ_{ss} estimation in Eq. (1).

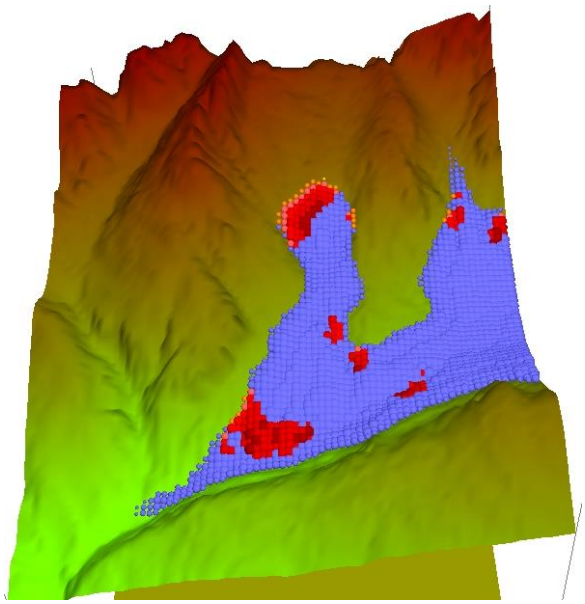

Fig. 8 Simulation result after 1s with τ_{ss}=2kPa.

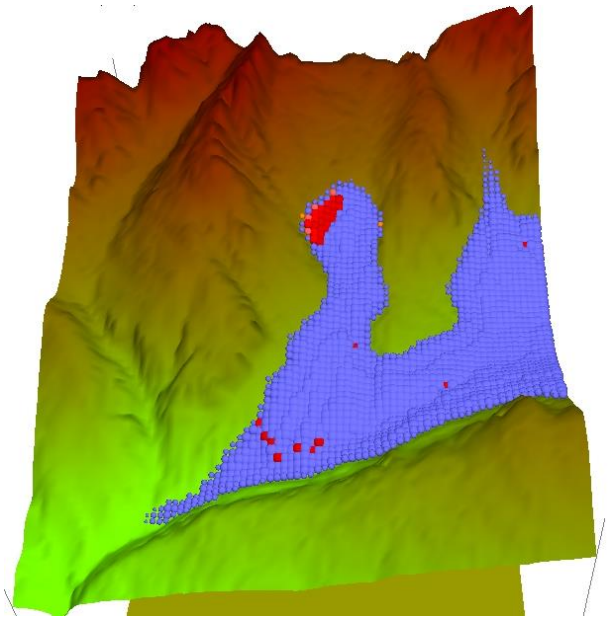

Fig. 9 Final simulation result with τ_{ss}=250kPa.

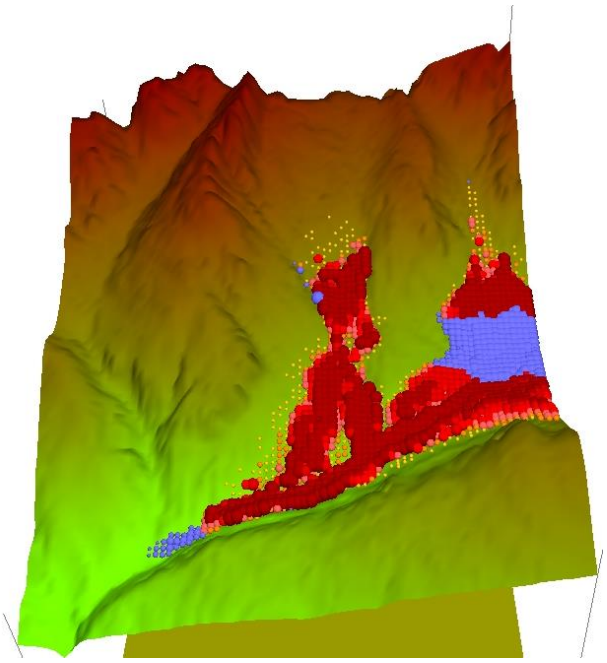

Fig. 10 Simulation after 10s at τ_{ss}=2kPa.

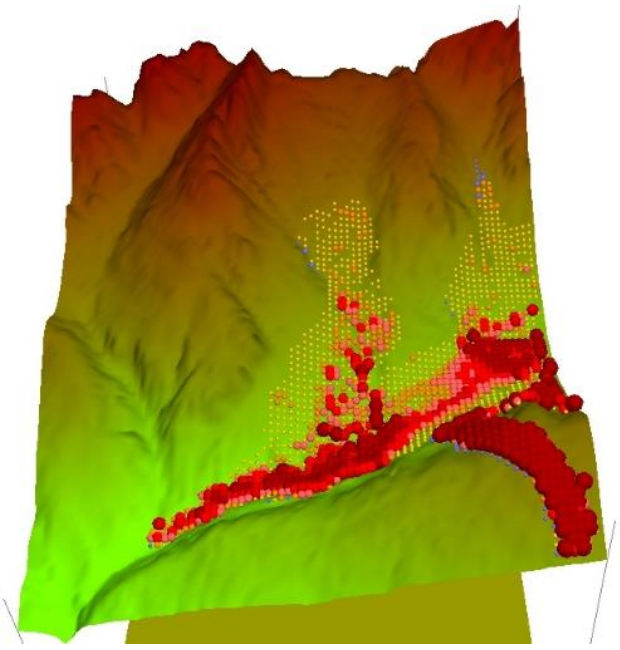

Fig. 11 Simulation after 27s at τ_{ss}=50kPa.

5. RESULTS

5.1 Contour of the 2000 Stože landslide

The comparison of the final simulated landslide area and the surveyed landslide contour after the 2000 event is presented in **Fig. 12**. A good agreement of the results and the surveyed contour is achieved.

In the upper part of the Stože landslide, the simulated area is narrower than the real contour, most likely due to inaccuracy of the basic geological map and therefore lower accuracy of the position and surface of each geological unit in the model. In the lower part of the Stože landslide, the simulated area is wider than the observed contour. The reason for this difference can be found in differences of the geological situation between the model and field situation or also in the fact that some of the areas are very prone to sliding, but in the November 2000 event, they did not move. Some unstable areas outside of the landslide (the upper right part in **Fig. 12**) could be found, but can also be related to the fact that this small unstable area lies at the model border where simulation conditions are not fully regular.

5.2 Traveling distance of the Stože landslide

In the phase 1 the Stože debris slide travelled to the small bridge over the Mangartski potok (Mlinč).

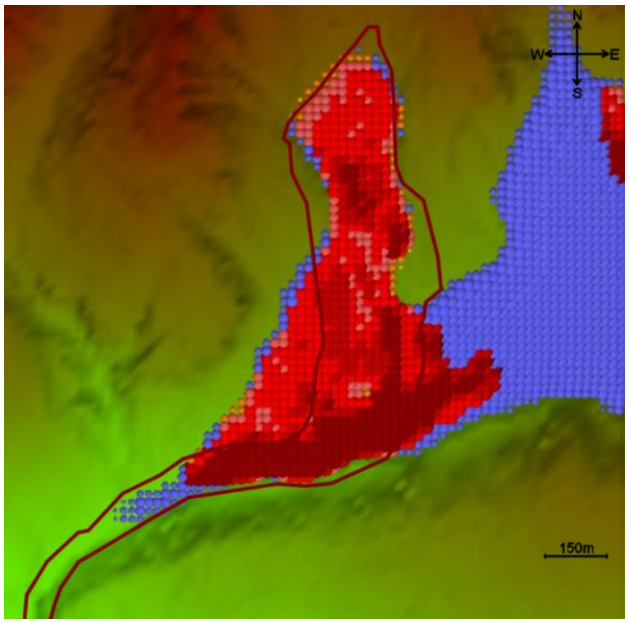

Fig. 12 LS-Rapid model results compared with surveyed landslide contour.

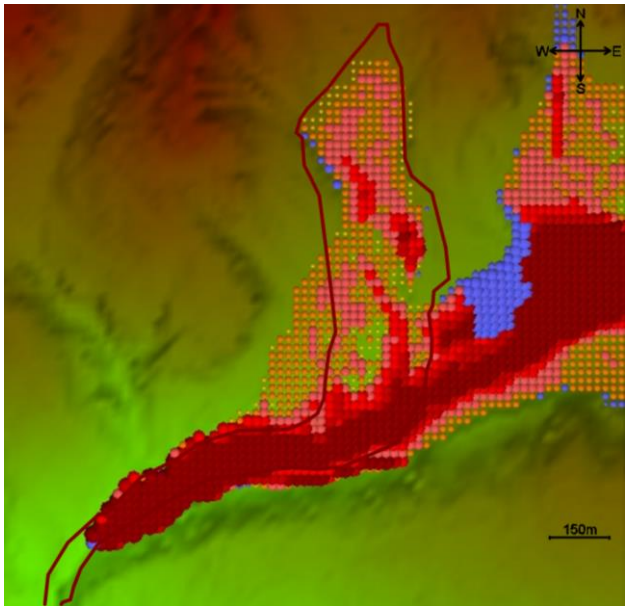

Fig. 13 Model with the correct traveling distance of the Stože landslide.

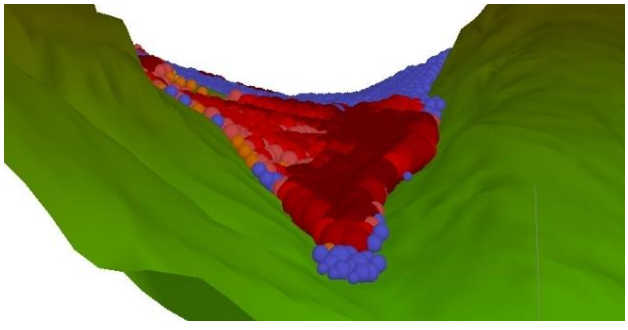

Fig. 14 Mangartski potok left bank final simulation conditions.

The final model results (**Fig. 12**) show stopping of the landslide mass upstream of the bridge, but the model with lower τ_{ss}=125kPa shows good agreement from that point of view (**Fig. 13**). The model with τ_{ss}=125kPa is however unsatisfactory in other comparisons (area, volume). It is possible that lower τ_{ss} values that are needed to stop the debris slide at the bridge and not upstream as in the modelling result, are caused by additional water inflow from the Mangartski potok, which lowers the τ_{ss} values on the field and cannot be modelled in one simulation.

Another specific characteristic of the first phase of the 2000 Stože Landslide were the conditions on the left bank of the Mangartski potok where the landslide travelled across the Mangartski potok channel and damaged the local road to the Mangart Mountain. **Fig. 14** shows the final simulation conditions/result on the Mangartski potok left bank where the flow super elevation is clearly seen. Red balls represent thickness of the material. Dark red is the thickest area and light red is the thinnest. Exact thickness of the material can be found in the matrix output data of the model. Blue color represents potentially unstable mass which did not move during simulation. Computational grid was selected at 20m x 20m.

5.3 The Stože landslide volume

A reliable estimation of the landslide volume is very important in the process of debris-flow hazard assessment since the landslide mass presents an important sediment source for the following debris flows. In the process of volume estimation, values of τ_{ss} and r_u were varied and the landslide volume for each combination was calculated (**Table 2**). All other parameters of the model remained the same as given in chapter 3.

Table 2 τ_{ss} and r_u combinations with landslide volume calculations.

τ_{ss} (kPa)	r_u	Volume (m^3)
150	0.2	2,480,00
200	0.2	735,000
250	0.2	51,000
150	0.3	2,460,000
180	0.3	1,547,000
190	0.3	1,195,000
195	0.3	990,000
200	0.3	775,000
250	0.3	72,000
200	0.35	800,000
150	0.4	2,470,000
200	0.4	825,00
250	0.4	105,000

The landslide volume was calculated using matrices of the input topography and the final simulated topography, respectively. The estimated volumes of the Stože landslide after the event were according to *Rajar et al*. [2001]: mobilized volume: 1,580,000m^3; material deficit volume: 1,200,000m^3; material stopped inside debris slide triggering area: 380,000m^3, and according to *Četina et al*. [2006]: 1,200,000m^3.

A comparison of the estimated volumes and the simulation results show that the best agreement is found with τ_{ss}=190kPa and r_u=0.3 with the simulated volume of 1,195,000m^3. With τ_{ss}=190kPa we confirmed our proposed τ_{ss}=0.45 x τ_p and τ_{ss}=0.45 x 421kPa=189kPa (Eq. (1)). The best agreement with the real landslide volume is obtained with the lowest boundary of τ_{ss} proposed by Eq. (1), while the upper limit gives unrealistically low landslide volumes.

6. THE SIMULATION AND MODEL ISSUES

First issue about the LS-Rapid model is matrix-based system with the matrix-based "user unfriendly" data input. That problem becomes important with geologically heterogeneous areas where each geological unit has different parameters and the manual data input becomes very time consuming and inaccurate. To solve this problem, we developed a MS Excel based application for the data matrix preparation. Additional functions were implemented in the matrix preparation as previously mentioned "smoothing" function for ensuring linear transition between two soil materials with a different depth of the unstable mass.

Second important issue of the model is that only one pore pressure ratio value as the triggering factor can be used for the whole area in the model. Again, with geologically heterogeneous areas this becomes an important issue since according to Eq. (2) not all units have the same specific weight (for instance scree and fine grain material) and therefore r_u factor is not comparable. To overcome this model issue, we propose that the angle of internal friction of the fine-grained geological units should be reduced in a model as given in Eq. (3).

$$\tan \varphi_{model} H\gamma\left(1 - r_{u,model}\right) \approx \tan \varphi \, H\gamma(1 - r_u) \quad (3)$$

where: φ is friction angle, φ_{model} is the angle of internal friction used in the model, γ is the unit weight of landslide mass, H is the depth of slip surface, r_u is the pore pressure ratio, and $r_{u,model}$ is the pore pressure ratio used in the model.

The determination of τ_{ss} should be carried out using LS-Rapid linked ICL-1 to ICL-3 ring shear apparatus. The maximum grain-size limitation of this apparatus (D_{max}=2mm) is an important issue when modelling landslides in the Alpine areas with prevailing gravel materials. This limitations of determining exact material parameters will bring some uncertainty in the performed calculations, especially when modelling potential events where model validation is not possible.

7. DISCUSSION

Debris flows present serious hazard in Alpine regions, including Slovenia, and debris-flow hazard assessment should be well implemented in the process of spatial planning and land use management. Since landslides often present a debris-flow source and the landslide volume is the main factor for debris-flow magnitude estimation, landslide-triggering simulation presents an important part in the process of debris-flow hazard assessment. Due to complexity of the landslide triggering phenomena this research topic is challenging with a goal of developing reliable methodology for potential landslide volume estimations. The results of our study present that a good estimation of key parameters and input data can result with good agreement of simulation results and field observations. LS-Rapid model has been recognized as a useful tool for landslide triggering simulations. However, the large differences in the modelled and observed landslide volumes were observed for different soil parameters. With this knowledge and experience, such an approach could be also used for potential landslide simulation and potential debris-flow magnitude estimation, taking into account possible range of volumes.

Besides soil parameters of the potential landslide, soil cover depth (depth of potentially unstable mass) is very important when simulating landslide triggering. This data should be available in the updated geological maps, which should be prepared in smaller scale (e.g. 1:10,000/1:25,000). Other more expensive option is to carry out detailed geological mapping of each potential debris-flow hazard area.

On the other hand, the proposed approach to landslide-triggering simulation, where only pore pressure is considered as the triggering factor, we see an opportunity for further model development and a link of the triggering model with a hydrological model. In this case, triggering pore pressures could be linked with hydrological process of precipitation, infiltration, direct runoff, and evapotranspiration and

in the final phase determination of critical precipitation or precipitation triggering threshold.

ACKNOWLEDGMENT: The authors acknowledge the financial support from the Slovenian Research Agency (research core funding No. P2-0180).

REFERENCES

Arbanas, Ž., Mihalić Arbanas, S., Vivoda Prodan, M., Peranić, J., Sečanj, M., Bernat Gazibara, S., and Krkač, M. (2017): Preliminary Investigations and Numerical Simulations of a Landslide Reactivation, In: Mikoš, M., Tiwari, B., Yin, Y., Sassa, K. (eds.): Advancing Culture of Living with Landslides, Vol. 2 - Advances in Landslide Science, pp. 649-657.

Cuomo, S., De Chiara, V., Dugonjić Jovančević, S., Vivoda Prodan, M. and Arbanas, Ž. (2017): Insights from LS-Rapid Modeling of Montaguto Earthflow (Italy). In: Mikoš, M., Tiwari, B., Yin, Y., Sassa, K. (eds.): Advancing Culture of Living with Landslides, Vol. 2 - Advances in Landslide Science, pp. 611-619.

Četina, M., Rajar, R., Hojnik, T., Zakrajšek, M., Krzyk, M. and Mikoš, M. (2006): Case Study: Numerical Simulations of Debris Flow below Stože, Slovenia, Journal of Hydraulic Engineering, Vol. 132, No. 2, pp. 121-130.

Dang, K., Sassa, K., Fukuoka, H., Sakai, N., Sato, Y., Takara, T., Quang, L.H., Loi, D.H., Tien, P.V. and Ha, N.D. (2016): Mechanism of two rapid and long-runout landslides in the 16 April 2016 Kumamoto earthquake using a ring-shear apparatus and computer simulation (LS-RAPID), Landslides, Vol. 13, No. 6, pp. 1525-1534.

Dugonjić Jovančević, S., Nagai, O., Sassa, K. and Arbanas, Ž. (2013): Deterministic Landslide Susceptibility Analyses Using LS-Rapid Software. Proceedings of the 1st Regional Symposium on Landslides in the Adriatic-Balkan Region, Zagreb, pp. 73-77.

Dugonjić Jovančević, S. and Arbanas, Ž. (2017): Influence of the runout potential on landslide-susceptible areas along the flysch–karst contact in Istria, Croatia, Natural Hazards, Vol. 85, No. 3, pp. 1347-1362.

Gradiški, K., Sassa, K., He, B., Arbanas, Ž., Mihalič Arbanas, S., Krkač, M., Kvasnička, P. and Oštrič, M. (2013): Application of Integrated Landslide Simulation Model LS-Rapid to the Kostanjek Landslide, Zagreb, Croatia. Proceedings of the 1st Regional Symposium on Landslides in the Adriatic-Balkan Region, Zagreb.

Igwe, O., Mode, W., Nnebedum, O., Okonkwo, I. and Oha, I (2014): The analysis of rainfall-induced slope failures at Iva Valley area in Enugu State, Nigeria, Environmental Earth Sciences, Vol. 71, pp. 2465-2480.

Lenart, S. and Fifer Bizjak, K. (2010): Particularities of Stože and Lokavec landslides – special laboratory tests for landslides modeling, WSEAS Transactions on Environment and Development, Vol. 7, No. 5, pp. 355-364.

Loi, D.H., Quang, L.H., Sassa, K., Takara, K., Dang, K., Thanh, N.K. and Tien, P.V. (2017): The 28 July 2015 rapid landslide at Ha Long City, Quang Ninh, Vietnam, Landslides, Vol. 14, No. 3, pp. 1207-1215.

Maček, M., Smolar, J. and Petkovšek, A. (2017): Influences of rheometer size and the grain size on rheological parameters of debris flow. In: Mikoš, M., Tiwari, B., Yin, Y., Sassa, K. (eds.): Advancing Culture of Living with Landslides, Vol. 2 - Advances in Landslide Science, pp. 399-406.

Mikoš, M. (2011): Public Perception and Stakeholder Involvement in the Crisis Management of Sediment-Related Disasters and their Mitigation: the Case of the Stože Debris Flow in NW Slovenia, Integrated Environmental Assessment and Management, Vol. 7, No. 2, pp. 216-227.

Mikoš, M., Četina, M. and Brilly, M. (2004): Hydrologic conditions responsible for triggering the Stože landslide, Slovenia, Engineering geology, Vol. 73, No. 3/4, pp. 193-213.

Mikoš, M. and Majes, B. (2010): Mitigation of large landslides and debris flows in Slovenia, Europe, In: Landslides: Causes, Types and Effects, Nova Science Publishers, New York, pp. 105-131.

Oštrić, M., Ljutić, K., Krkač, M., Setiawan, H., He, B. and Sassa, K. (2012): Undrained ring shear tests performed on samples from Kostanjek and Grohovo landslide. In: Sassa, K., Takara, K. and He B. (eds.) Proceedings of the 10th Anniversary of ICL, January 2012, Kyoto, Japan, pp. 47–52.

Quang, L.H., Loi, D.H., Sassa, K., Takara, K., Ochiai, H., Dang, K., Abe, S., Asano, S. and Ha, D.N. (2017): Susceptibility assessment of the precursor stage of a landslide threatening Haivan Railway Station, Vietnam, Landslides, https://doi.org/10.1007/s10346-017-0870-3.

Rajar, R., Hojnik, T., Četina, M., Zakrajšek, M. and Krzyk, M. (2001): A one-dimensional model of a debris flow in the area of Log pod Mangartom, Proceedings 12. Mišičev vodarski dan, pp. 92-101 (in Slovene).

Sassa, K. (1988): Geotechnical model for the motion of landslides, Proceedings 5th International symposium on Landslides, "Landslides", Vol. 1, Balkema, Rotterdam, pp. 37-56.

Sassa, K., Wang, G., Fukuoka, H., Wang, F., Ochiai, T, Sugiyama, M and Seguchi, T (2004): Landslide risk evaluation and hazard zoning for rapid and long-travel landslides in urban development areas, Landslides, Vol. 1, No. 3, pp. 221-235.

Sassa, K., Nagai, O., Solidum, R., Yamazaki, Y. and Ohta, H. (2010): An integrated model simulating the initiation and motion of earthquake and rain induced rapid landslides and its application to the 2006 Leyte landslide, Landslides, Vol. 7, No. 3, pp. 219-236.

Sassa, K., He, B., Miyagi, T., Strasser, M., Konagai, K., Ostric, M., Setiawan, H., Takara, K., Nagai, O., Yamashiki, Y. and Tutumi, S. (2012): A hypothesis of the Senoumi submarine megaslide in Suruga Bay in Japan—based on the undrained dynamic-loading ring shear tests and computer simulation, Landslides, Vol. 9, No. 4, pp. 439–455.

Sassa, K., Dang, K., He, B., Takara, K., Inoue, K. and Nagai, O. (2014a): A new high-stress undrained ring-shear apparatus and its application to the 1792 Unzen-Mayuyama megaslide in Japan, Landslides, Vol. 11, No. 5, pp. 827-842.

Sassa, K., Fukuoka, H., Sato, Y., Takara, K., Huy, L., Setiawan, H., Pham, T. and Dang, K. (2014b): Initiation mechanism of rapid and long runout landslides and simulation of Hiroshima landslide disasters using the integrated simulation model (LS-RAPID). Proc. of the International Forum "Urbanization and Landslide Disaster, 85-112 (in Japanese).

Senthilkumar, V., Chandrasekaran, S.S. and Maji, V.B. (2017): Geotechnical characterization and analysis of rainfall—induced 2009 landslide at Marappalam area of Nilgiris district, Tamil Nadu state, India, Landslides, Vol. 14, No. 5, pp. 1803-1814.

Setiawan, H., Sassa, K., Takara, K., Miyagi, T. and Fukuoka, H. (2016): Initial pore Pressure Ratio in the Earthquake Triggered Large-scale Landslide near Arotazawa Dam in Miyagi Prefecture, Japan, Procedia Earth and Planetary Science, Vol. 16, pp. 61-70.

Setiawan, H., Sassa, K., Takara, K., Miyagi, T. and Fukuoka, H. (2017): Detail Study of the Aratozawa Large-Scale Landslide in Miyagi Prefecture, Japan. In: Mikoš, M., Vilimek, V., Yin, Y., Sassa, K. (eds.): Advancing Culture of Living with Landslides. Vol. 5 - Landslides in Different Environments: 473-480.

Sodnik, J., Kumelj, Š., Peternel. T., Jež, J. and Maček, M. (2017): Identification of Landslides as Debris Flow Sources Using a Multi-model Approach Based on a Field Survey - Koroška Bela, Slovenia, In: Mikoš, M., Tiwari, B., Yin, Y., Sassa, K. (eds.): Advancing Culture of Living with Landslides, Vol. 2 - Advances in Landslide Science, pp. 1119-1126.

Tien, P.V., Sassa, K., Takara, K., Dang, K., Luong, L.H. and Ha, N.D. (2017): Simulating the Formation Process of the Akatani Landslide Dam Induced by Rainfall in Kii Peninsula, Japan, In: Mikoš, M., Vilimek, V., Yin, Y., Sassa, K. (eds.): Advancing Culture of Living with Landslides. Vol. 5 - Landslides in Different Environments, pp. 497-506.

Tsuchiya, S., Kyoji, S. and Nagai, O. (2013): Simulation of the Largest Landslide Caused by the 2008 Wenchuan Earthquake by Rapid-Landslide-Movement Simulation, In: Ugai, K., Yagi, H., and Wakai, A. (eds.): Earthquake-Induced Landslides, Springer Verlag, Berlin, Heidelberg, pp. 575-582.

Vidoda Prodan, M. and Arbanas, Ž. (2017): Parametric Analysis of Weathering Effect on Possible Reactivation of the Valići Landslide, Croatia, In: Mikoš, M., Tiwari, B., Yin, Y., Sassa, K. (eds.): Advancing Culture of Living with Landslides, Vol. 2 - Advances in Landslide Science, pp. 621-631.

Yavari-Ramshe, S. and Ataie-Ashtiani, B. (2016): Numerical modeling of subaerial and submarine landslide-generated tsunami waves - recent advances and future challenges, Landslides, Vol. 13, No. 6, pp. 1325-1368.

Rainfall Characteristics and the Related Geological Hazards of Slag Disposal Pit in Shanghang Region, China

Hua-li PAN[1,2]*, Zhi-shan ZHENG[3], Ming-jian HU[4] and Guo-qiang OU[1,2]

[1] Key Laboratory of Mountain Surface Process and Hazards, Chinese Academy of Sciences, Chengdu, P.R China,
[2] Institute of Mountain Hazards and Environment, Chinese Academy of Sciences, Chengdu, P.R China,
[3] University of Chinese Academy of Sciences, Beijing, P.R.China,
[4] Institute of Rock and Soil Mechanics, Chinese Academy of Sciences, Wuhan, P.R.China,
*Corresponding Author, E-mail: hlpan@imde.ac.cn

There were lots of geological hazards in kinds of slag disposal pit these years. The rainfall, in particular the heavy rain, was direct dynamic factor for geological hazards, but the occurrence probability of geological hazards was different because of the sensitivity of the geological environment though of the same rainfall intensity. This study took a Gold-Copper deposit in Shanghang region, China, as an example, mainly analyzed the relationships between geological hazards and critical rainfall. According to the nearly 80 heavy rainfall data and related hazard events from 2002 to 2010, the rainfall characteristics in the region were studied, and the regional rainfall threshold for debris flow was obtained.

Key words: rainfall characteristics, rainfall threshold, debris flow, geological hazards, slag disposal pit

1. INTRODUCTION

To obtain the characteristics of soil erosion under the rainfall condition, the rainfall characteristics and its related hazards of slag disposal pit of a certain Gold-Copper Deposit in Fujian province was analyzed by the meteorological and rainfall data. The regional rainfall threshold was obtained which was provided reference for the rainfall value design of artificial rainfall test model in laboratory for the soil erosion of slag disposal pit and also used for the analysis of numerical simulation of debris flow of slag disposal pit.

2. THE ANALYSIS OF RELATIONSHIP BETWEEN RAINFALL AND GEOLOGICAL HAZARDS

2.1 The relationship between regional rainfall and geological hazards

The adequate water was the most important condition for the debris flow's formation, which was also the power source for the debris flow in slag disposal pit. The source of water was mainly from the rainfall, then the melting snow ice. The water, on the one hand, was the component of debris flow, which was the multi-phase flow of solid, liquid and gas, on the other hand, it was the dynamic condition for the debris flow starting, because once more and more rainfall formed into the powerful stream flow, it brought a huge of soil and debris into the debris flow.

The rainfall-type debris flow was the most one and distributed all over the China, but the rainfall condition in which results the debris flow was complicated. According to the rainfall ranges, there were two different types, the one was the local torrential rain with small rainfall range and short duration, the other was the regional rainstorm with large rainfall range and long duration, for example, the rainstorm of Longmenshan in northwest China on July 13th, 1981 and the Dongte rainstorm on July 26th, 1982. These two extreme rainstorms resulted in extreme debris flow disasters. For example ,there were 51 ditches happen triggered by the heavy rain in Pingwu-Songpan area of Sichuan Province On August 19, 1981(Lu, 1986). Every year there was about no less than one billion Yuan loss in China, therefore, there were many the long-term observation study for the rainfall triggered debris flow by a large number of researchers.

After the rainfall was on the ground, when the composition effect surpassed the threshold, which was composed of various factors from the air and

the ground, then the rainfall triggered debris flow happen (Kang, 1987; Tan et al., 1992). The discriminative model to forecast the rainstorm debris flow, in which the main parameters included the 10 minutes rainfall intensity with short duration rainstorm, the 60 minutes rainfall intensity and the 24 hours rainfall, was set up based on the monitoring data from 64 debris flow hazards in Ganluo forecast testing zone of Chengdu-Kunming railway from 1989 to 1990. Then the model was testified by 75 debris flow hazards happened along the railways distributed in southwest, northwest, and northeast of China since 1960, the results indicated that the discriminative model is with a certain degree of representation and accuracy.

Tan et al. (2000) discussed the four basic principles of the forecast of rainstorm debris flow, the phenomenon predictability principle, the genetic classification principle, the discriminant factor simplification principle and the forecast decision respective principle. Then the forecast model was classified. The long-term trend prediction model and the state predicting model of frequency were set up based on the superposition of periods of activity and precipitation and the combination of frequency of yearly activity and precipitation gradation respectively.

The debris flow could be forecasted by the rainfall, which was not only the theoretical issue but also the methodological issue. The study of the monitoring data (Chen, 1985, 1990; Jing, 1986; Wu et al., 1990; Tan et al., 1992; Yin, 1992; Tan et al., 1994) showed that it still followed some rules to predict and forecast the debris flow through the natural phenomenon. Such as debris flow have the following characteristics: the significant regional and geographical differences for its development regional distribution, the significant periodicity and stage activity in time series, the popular collective and regional hazard severity in the process of hazard evolution. The main factors of rainstorm triggered debris flow were the characteristics and rainfall during the raining including rainfall type, quantum and intensity. The rainfall threshold of rainstorm triggered debris flow was obtained by study the long-term observation or the influenced factors in region including the historical hazard, geomorphology, geology, vegetation, etc., then the simplified discriminant model between the debris flow and rainfall, which was helpful to operation and forecast analysis. The forecast of debris flow was based on the regional average forecast information of rainfall in a year, quarter, month, day or hour. At present for the meteorological department, it just provided the rainfall ranges or levels in some region with a certain period. For example, it forecast the rainfall level was R_L-R_H (mm) in some region with 24 hours, the rainfall level was R_L'- R_H'(mm) in local region, which meant the low limit value for the rainfall was R_L (mm) and its upper limit was R_H'(mm). It supposed that the region discount coefficient of some certain region with the rainfall level of R_L-R_H and R_L'- R_H' was K_1 and K_2 respectively, and they were satisfied with the following equations (1):

$$\begin{gathered} R_L < R_H \le R_L' < R_H' \\ 0 < K_1(K_2) < 1 \\ K_1 > K_2 \end{gathered} \tag{1}$$

Then the average rainfall in this region was deduced by the rainfall forecast registration (2):

$$R_m = (R_L + R_H) \times K_1 + (R_L' + R_H') \times K_2 \tag{2}$$

It supposed that the rainfall threshold of debris flow in the forecast region was R_a.

When R_m was less than R_a, the debris flow was less likely to happen,

When R_m was no less than R_a, the debris flow was likely to happen,

When R_H' was no more than R_a, the debris flow wasn't likely to happen,

When R_L was no less than R_a, the debris flow was inevitable to happen.

Therefore, the debris flow prediction was deduced by the rainfall forecast. Its timelines and reliability was the core for the debris flow forecast decision basis. To make the accurate forecast, it was important for the successful forecast to obtain the threshold rainfall R_a which triggered the debris flow by the long-term observation. The rainfall thresholds in different regions are showing in **Table.1**. It showed that the rainfall threshold to trigger the debris flow was 70.0mm in Fujian province with the rainfall more than 1200.0mm per year. But there was not strictly relationship between the debris flow scale and the rainstorm level, because it happened frequently that there was the heavy rainfall but the debris flow was small, there was the small rainfall but the debris flow was large. In a word, the rainfall threshold was just the preliminary value for the discriminant of debris flows happen in some region, it should be considered other factors such as geomorphology and terrain, soil, deposit state, et al.

Table.1 Rainfall threshold in different regions (Tan, 1994)

Annual rainfall	$H_{24(D)}$	$H_{1(D)}$	$H_{1/6(D)}$	$H_{o(D)}$	Different regions
>1200	100	40	12	70	Zhejiang, Fujian, Taiwan, Guangdong, Guangxi, Jiangxi, Hunan, Hubei, Anhui, Henan, Beijing suburb, east of Liaoning, west of Yunnan, southeast of Tibet, etc..
1200-800	60	20	10	35	Sichuan, Guizhou, east of Yunnan, south of Shaanxi, Henan, east of Shandong, west of Hebei, Jilin, Heilongjiang, west of Liaoning, etc..
800-400	30	15	6	20	North of Shaanxi, part of Xinjiang, Inner Mongolia, Ningxia, Shanxi, Gansu, northwest of Sichuan, Tibet, etc..
<400	25	15	5	15	Tibet, Xinjiang, Qinghai, west of Yellow River in Gansu and Ningxia

$H_{24(D)}$——rainfall threshold in 24 hours to trigger the debris flow possibly
$H_{1(D)}$ ——rainfall threshold in an hour to trigger the debris flow possibly
$H_{1/6(D)}$——rainfall threshold in 10 minutes to trigger the debris flow possibly
$H_{o\,(D)}$——rainfall threshold to trigger debris flow in region

2.2 The relationship analysis between landslide and debris flow triggered by rainfall in heap leaching field

The risk assessment of debris flow in the slag disposal pit was a complicated system engineering, which depended on the following factors: geomorphology and terrain factor, provenance factor, meteorological and hydrological vegetation factor, geological condition factor, human activity factor, effect factor, etc. After quantization, it was analyzed comprehensively by using multi factors. During the quantization, the three basic conditions of debris flow was the direct evaluation factors including the natural environmental condition, development situation and forming factor of debris flow, then the evaluation index system of debris flow was set up.

For the geomorphology and terrain factor, it includes:

(1) The basin relative height difference. It was the difference between the highest elevation in basin and the lowest elevation in gully, which was measured from the topographic map,

(2) The hill slope of gully banks. It was the average gradient both sides of gully that was reflected from the rainfall collecting capacity of slope and measured from the topographic map,

(3) The longitudinal gradient of groove bed. It was the average gradient of main gully above gully mouth, which was calculated by the weighted average in the segmented statistics; it thought that it was dangerous very much when the longitudinal gradient of groove bed was no less than 50%,

(4) The length of gully, which was from the gully mouth to the watershed.

For the provenance factor, it includes:

(1) The gully blocking level. There were three levels with mild, moderate and severe, which was obtained by in situ investigation. It had the obvious flowing phenomenon when the debris flow happened in the severe blocking level of gully that increased the risk of debris flow,

(2) The soil reserve of mining disposal or slag disposal pit. It was the reserve of mixture with disposal soil, stone and sands from the underground mine and open quarry in the gully region, obtained by in situ investigation.

(3) The loose natural material reserve. It included the total reserve of loose debris, slope sediments and riverbed alluvial deposits in the gully region, obtained by in situ investigation and estimation.

(4) The landslide volume. It included the whole landslide volume in the gully region, obtained by in situ investigation and estimation.

(5) The collapse volume. It included the whole collapse volume in the gully region, obtained by in situ investigation and estimation.

(6) The reserve of loose solid material in unit area. It was the ratio between the whole volume of loose solid material and the collecting water area in the gully, which reflected the seriousness degree of loose landslide deposits.

For the meteorological and hydrological vegetation factor, it included the rainfall data and vegetation coverage ratio of fixed point meteorology and rainfall observation station in detail. The more the rainfall, the more possibility and the larger scale the debris flow. The vegetation coverage ratio was the coverage ratio of Trees, Shrub, Grasses, etc.

The rainstorm was the direct dynamic factor for

the debris flow and also the trigger factor for the rainstorm triggered debris flow and collapse. During the raining, the rain was permeated into the soil of slag disposal pit, hence its strength was changed to poor, as a result, there was the chain disaster process such as the landslide and the debris flow both triggered by the rainfall. During the process of debris flow triggered by the rainfall, there was the rainfall threshold, once it was to the rainfall threshold; the stable state of loose deposit was broken. Therefore, the rainfall statistics was the main method for qualitative prediction of debris flow. By statistical analysis of the rainfall and debris flow, the rainfall forecast value was suggested for the loose deposit in Shanghang, Fujian province when the debris flow happened.

The monitoring data (Tan et al., 1981; Cui et al., 1997) showed that there was at least one rainfall center or more for every rainstorm in every region, in which there was one main rainfall center and several non-main rainfall centers. Because of the more rainfall and intensive strength of the rainfall center, it was the center for the occurrence of debris flow and landslide. For example, in the debris flow happening center of Ya'an and Wanxian county of Sichuan province, the day rainfall threshold was between 100.0mm and 200.0mm. In the debris flow occurrence center of Miyun county of Beijing, it had the same the day rainfall threshold. In the debris flow happening center of Helanshan mountain region of Ningxia, Dongshenxian county of Inner Mongolia, the day rainfall threshold was about 100.0mm. In the debris flow happening center of Panxi region of Sichuan province, the day rainfall threshold was between 50.0mm and 70.0mm, which was smaller than that of the above region. From the above examples, there was the triggered rainfall threshold in different regions when the debris flow happened. But the value of triggered rainfall threshold in different regions was different due to the difference of geography, geology, climate, etc. That was to say, during the rainstorm in some region, once the rainfall and strength of rainstorm was over the triggered rainfall threshold, the most of debris flow gullies and many landslide was unstable that indicated the concentrated happen of the landslide and debris flow

Study showed that if the regional rainstorm in the rainbelt was larger, the region of debris flow and landslide was wider and the number of hazards was larger, the lower limit of minimum rainfall was lower. On the other hand, if the entire regional rainstorm in the rainbelt, the region of debris flow and landslide and the number of hazards was small, the lower limit of minimum rainfall was higher. For the large regional rainstorm, it was influenced by the whole weather system, and then there was the regional rainfall process with long duration, the rainfall in early or late period was more, the water content of soil was higher, therefore the lower limit of triggered rainfall threshold was lower, vice versa. The relationship between the daily rainfall and debris flow on July 8th, 1985 was shown in **Fig.1**.

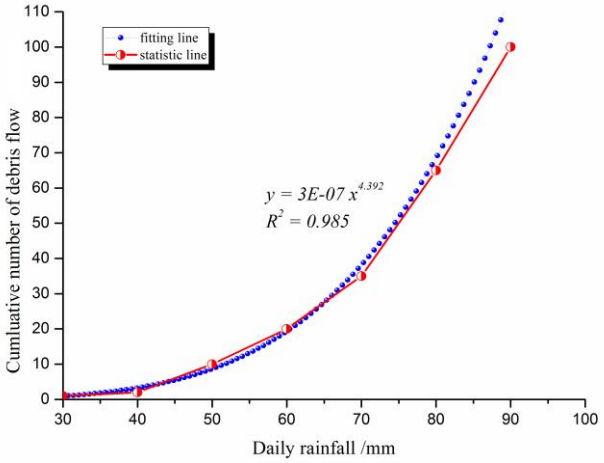

Fig.1 Relationship between cumulative number of debris flow and daily rainfall in Panxi on July 8th, 1985

Fig.1 showed that the cumulative density of debris flow increased exponentially with the increasing of rainstorm, once the daily rainstorm was larger than the 75.0mm ~80.0mm, the curve had the linear increasing tendency, but when the daily rainstorm was lower than 70.0mm, the curve had the slow change tendency. The fitting relations between daily rainfall and debris flow was $y=3E\text{-}07x^{4.392}$. From the fitting relations, it showed that there was the rainfall threshold between the rainstorms triggered debris flow gullies and the rainstorm. When the rainfall was larger than the rainfall threshold, the quantity and density of debris flow increased rapidly with the increasing of rainstorm level, but when it was lower than 30.0mm, there was no debris flow to happen.

It was the rainfall that increased the water content of soil in the loose deposits and decreased its strength and the stability of slope, particularly the soil strength couldn't keep the stability of slope, which was the rainfall threshold. When the rainfall was lower than that, the debris flow or rainstorm landslide was less likely to happen, when the rainfall was more than it, the debris flow or rainstorm landslide was likely to happen. The value of minimum rainfall was related to the antecedent precipitation and different with the difference of regions. Then the regional minimum rainfall

threshold was suggested. The regional minimum rainfall threshold was the rainfall threshold that resulted in the occurrence of debris flow in the most of debris flow gullies in this region or the occurrence of most landslides in this region, which was obtained by a lot of statistic information. For example, there were the daily rainfall and the total effective rainfall information of 272 cases of debris flow and 46 cases of landslides monitored in Panxi region, the rainfall in the early 14 days was calculated by following equation(3):

$$R_t = \sum_{i=1}^{14} a_t P_t \qquad (3)$$

In equation,

Pt---- rainfall in t days (mm),

$a_t = (0.5)^{t/T}$ ----rainfall attenuation coefficient

t---- Days, (day)

T---- days of half life

The total effective rainfall was the above calculated value with the rainfall on the day. The relationships among the debris flow or landslide and the daily rainfall, the total effective rainfall in Panxi region are as show in **Fig.2**. It showed that all of the points distributed below the line with 45° at coordinates, which indicated that there was some rainfall in early before the day of debris flow and landslide's occurrence. It also showed that most of the points distributed below and close to the line with 45° at coordinates, which indicated that the antecedent precipitation account for a substantial proportion before the day of debris flow and landslide's occurrence.

$$R_t = T_t + R_{day} \qquad (4)$$

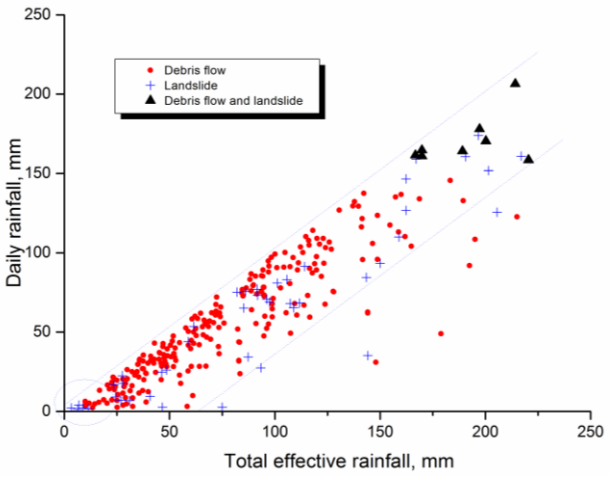

Fig.2 Relationship between debris flow & landslide and the daily rainfall, the total effective rainfall

In **Fig.2**, there were a few points distributing at the total effective rainfall with 10.0mm or 20.0mm, it was probable because the local rainstorm in mountain triggered the debris flow & landslide. But in the meteorological station, it was the regional average rainfall not the local rainstorm that was monitored; furthermore the local rainstorm happened far away from the meteorological station, which had the poor representation as the condition of rainfall threshold on the day of occurrence of debris flow & landslide. Therefore, the regional minimum rainfall threshold in Panxi region, which triggered the debris flow & landslide to happen, was about 25.0mm ~30.0mm.

There was the important relationship between the occurrence of debris flow and the antecedent precipitation, the rainfall on the day and the triggered rainfall threshold, therefore, the antecedent precipitation, the rainfall on the day and the triggered rainfall threshold were the basis for the prediction and forecast of rainstorm triggered debris flow. The antecedent precipitation and the rainfall on the day was measured by the self-recording rain gauge and the remote recording rain gauge, the antecedent precipitation dissipated gradually with the increasing of days and it was calculated by the following equation:

$$P_{a0} = P_1K + P_2K^2 + P_3K^3 + P_4K^4 + \cdots\cdots + P_nK^n \qquad (5)$$

Where,

P_{a0} is the antecedent precipitation of the debris flow occurrence,

P_1, P_2, P_3…P_n is the rainfall before the day before the outbreak of debris flow, the first two day of debris flow, the first three day of debris flow, the first n day of debris flow

K is reduction coefficient. It was obtained by latitude, sunshine, potential evaporation and infiltration capacity of the solid substance, generally it was 0.8. For one rainfall, it dissipated at about 20 days; therefore the maximum n was 20.

The rainfall threshold as show in **Table.2** when the debris flow was triggered by the hazard-inducing rainfall in mountain region of China, was statistical analyzed comprehensively (Cui et al., 2000). When it was lower than the rainfall threshold, the debris flow was less likely to happen, but once it was more than the rainfall threshold, the debris flow was likely to happen. At present, the prediction of debris flow to happen in advance had been achieved by taking full advantages of the triggered rainfall threshold

Table.2 The rainfall threshold of the debris flow triggered by the hazard-inducing rainfall in mountain region of China (Cui et al., 2000)

Region	Tianshan mountains	Xiqin area of Qilianshan mountain	Gangdisi mountains	Shaluli area Nien-ch'ing-t'ang-ku-la Mountains	Minshan mountains	Ailao area of Gaoligong mountain	Quhaoshan mountains
Daily rainfall /mm	25～50	25～200	25～50	30～100	35～300	50～200	50～200
hourly rainfall /mm	20	20	20	25	30	30	30
Region	**Helanshan mountains**	**Liupanshan mountains**	**Lvliangmountains & Huoyanshan mountains**	**Daba mountains & Qinling mountains**	**Daxing'anling mountains**	**Xiaoxing'anling mountains**	**Longgan mountains & Taihang**
Daily rainfall /mm	100～300	100～300	100～300	100～300	100～200	200～300	200～300
Hourly rainfall /mm	30	30	40	40	40	40	50
Region	**Qainshan area of Beilaotu**	**Zhongtiao-shan area of Wutaishan**	**Daloushan mountains**	**Wudangshan area of Dabieshan mountains**	**Mu'ao area of Xufengshan mountains**	**Wuyishan mountains, Alishan mountains,Mounta**	**Laoshan area of Qinshan**
Daily rainfall /mm	100～300	100～300	100～300	100～300	150～300	200～300	200～300
Hourly rainfall /mm	50	50	50	50	50	60	60

3. CHARACTERISTICS OF HAZARDS AND RAINFALL IN STUDY AREA

3.1 The rainfall characteristics of slag disposal pit

The study area was located at Shanghang County, Longyan City, Fujian Province, China, as was shown in **Fig.3**. According to the distribution of monitoring stations of hydrological and rainfall in Longyan city of Fujian province and the location of gold-copper deposit, the Shanghang monitoring station of hydrological and rainfall was chosen, which is the nearest one to the gold-copper deposit. The annual rainfall statistics both of Shanghang monitoring station and gold-copper deposit was analyzed. The rainfall bar chart of Shanghang County for 70 years from 1939 to 2008 was shown in **Fig.4**, the annual rainfall bar chart of Zijinshan monitoring station from 1988 to 2010 was shown in **Fig.5**, the monthly rainfall statistics in different years was shown in **Fig.6**.

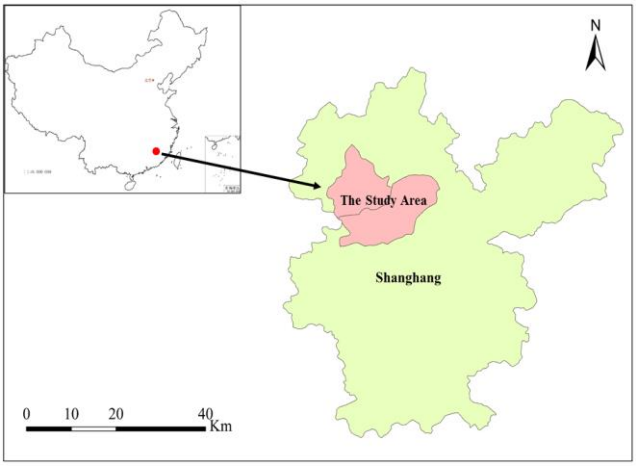

Fig.3 Location of the study area (Shanghang County, Longyan City, Fujian Province, China)

Fig.4 showed that the minimum rainfall was 860.5mm in 1943, which belonged to the extreme lowest flow year, the maximum rainfall was 2437.3mm in 1959, belonged to the high flow year, and the average rainfall was 1581.2mm for 70 years. **Fig.5** showed that the minimum rainfall was 1048.5mm in 1991, which belonged to the low flow year, the maximum rainfall was 2118.6mm in 1997, belonged to the high flow year, and the average

rainfall was 1841.8mm from 1988 to 2010. **Fig.6** showed that they were abundant rainfall months including May, June and August, in which there was the frequency of debris flow hazards triggered by heavy rainfall.

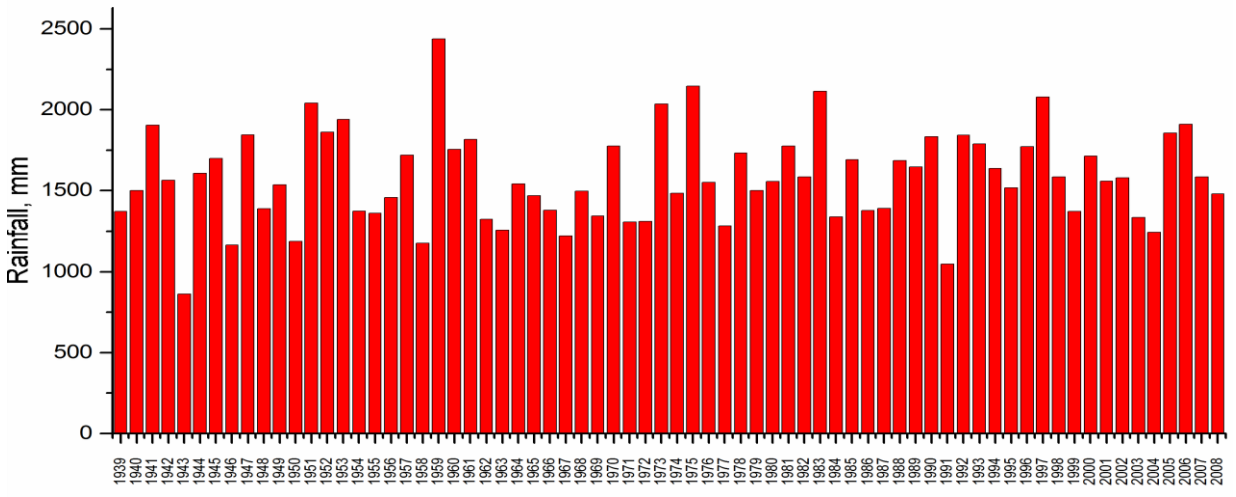

Fig.4 Rainfall bar chart of Shanghang county for 70 years from 1939 to 2008

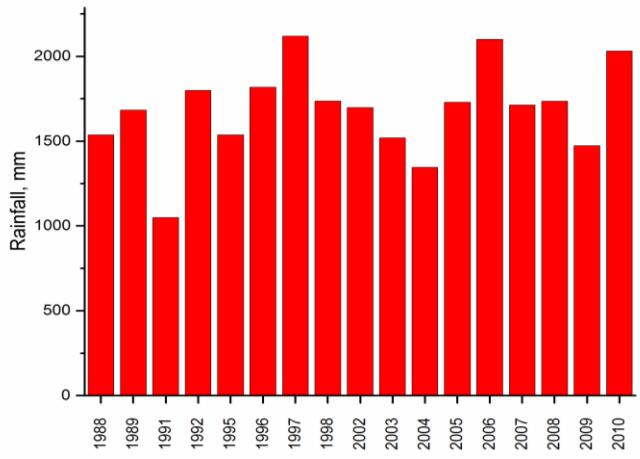

Fig.5 Rainfall bar chart of Zhijinshan monitoring station from 1988 to 2010

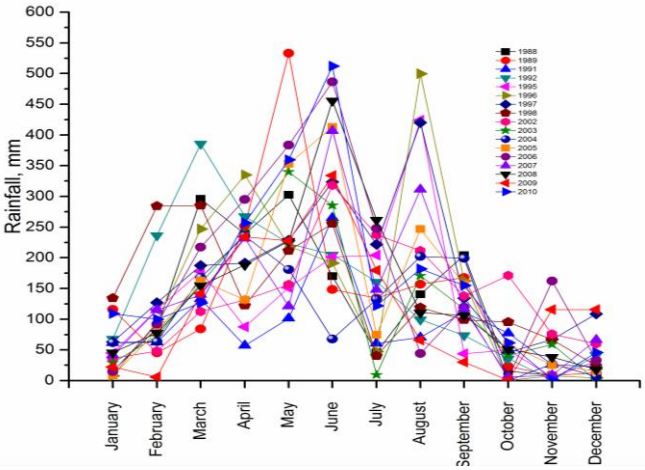

Fig.6 Rainfall statistics of Zijinshan monitoring station in different years from 1988 to 2010

According to records(Gao et al., 2010), from August 25th to 28th, 2000 it was the rainfall with 342.0mm, on April 3rd, 2003 it was the rainfall with 107.0mm, from May 16th to 17th, 2003 it was the rainfall with 170.0mm, the above rainfall resulted in the serious collapse of slope. On May 22th, 2010, from 10:10 p.m to 11:30 p.m, the rainfall was 75.3mm, which meant the rainfall was 56.5mm/h and the rainfall intensity was 0.94mm/min. The rain continued to the 1:00 a.m on 23rd with the rainfall of 32.1mm and the maximum rainfall was 62.0mm. This heavy rainfall resulted in the serious collapse because the water eroded the road surface due to (1) the small temporary pipe of drainage ditches beside the roads of Dalongli and (2) the broken drainage pipe of Yanzigou. The total economic loss was about ¥700,000 yuan. The above rainfall statistics showed that they were the rich rainfall regions for Shanghang & Zijinshan, particularly it was the heavy rainfall from March to June and August in every year, which indicated that it had the condition for the debris flow triggered by rainfall. It found that the debris flow in Fujian province was controlled by the heavy rainfall (Gao et al., 2008), the amount of valley shaped debris flow hazards was about 82.0% of total debris flow hazards, the amount of slope shaped debris flow hazard was about 18.0% of total debris flow hazards (Liu et al.,2008, Gao et al., 2010).

3.2 The characteristics of geological hazards in study area

According to the geological investigation in Fujian province, during 2002-2010, the total

number of geological hazards was 9513, in which the number of landslide, collapse, unstable slope and surface collapse was 5816, 1888, 1591, 103 and 115 respectively. The main geological hazard was the landslide with 61.1% of total geological hazards, the collapse was 19.9%, the unstable slope was 16.7%, the surface collapse was 1.2% and the debris flow was 1.0%. Among all these geological hazards, only 6.0% was relative stable, 17.0% was basic stable, and nearly 76.0% was unstable. The slope disaster was the main geological hazard, if the unstable slope was the potential landslide or collapse; the slope collapse was 98.0% of all geological hazards.

3.3 The relationship of rainfall and geological hazards in study area

The rainfall was the main cause of geological hazards, but the occurrence probability of geological hazards was different because of the sensitivity of the geological environment though of the same intensity rainfall. The relationship between geological disaster and rainfall was analyzed based on the division of environmental sensitive region in Fujian province (Huang et al., 2003, 2005, 2011). The division showed that the occurrence probability of geological hazards was 50.0%, 55.0% and 70.0% in the low sensitive, moderate sensitive and high sensitive region under the same condition of 200.0 mm rainfall respectively. The prediction model of geological hazards was set up based on the relationship between the geological hazards and the rainfall, geological environment, which was the main basis of weather forecast of geological hazards. From the above discuss, the debris flow with landslide collapse had the characteristic with chain hazard process, particularly in the mountains. Therefore, there was the comprehensive analysis with consideration of the rainfall on the day, the antecedent precipitation when the landslide collapsed, based on the hazard analysis between the debris flow with landslide collapse and the daily rainfall from 2002 to 2010. The antecedent precipitation was calculated by the following equation (6) when the debris flow happened. The hazard analysis between the debris flow with landslide collapse and the daily rainfall from 2002 to 2010 was shown in **Table.3.**

$$P_{a0} = P_1K + P_2K^2 + P_3K^3 + P_4K^4 + \cdots\cdots + P_nK^n \quad (6)$$

In equation (6), all indices were the same as the equation (5).

And the relationships between geological hazards and the rainfall characteristics were shown in **Fig. 7**.

Table.3 Statistics of rainfall index when debris flow with landslide collapse

Rainstorm date	The antecedent precipitation P_{a0}		Rainfall on the day (P_t) /mm	Total rainfall /mm	Whether hazard happened
	Count day	P_{a0} /mm			
2002.3.16	11	1.9	48.6	50.5	no
2002.3.24	11	10.5	30.6	41.1	no
2002.4.10	5	28.3	50.2	78.5	no
2002.5.15	7	19.4	45.0	64.4	no
2002.5.23	13	19.4	39.6	59.0	no
2002.6.11	3	4.0	51.3	55.3	no
2002.6.12	4	44.2	67.2	111.4	no
2002.6.14	6	85.1	45.8	130.9	no
2002.6.18	9	77.6	62.1	139.7	no
2002.7.22	13	28.5	48.7	77.2	no
2002.7.30	15	43.4	27.0	70.4	no
2002.8.9	6	29.7	42.3	72.0	no
2002.8.10	12	13.0	30.1	43.1	no
2003.3.3	3	7.7	30.1	37.8	no
2003.4.12	6	42.5	72.4	114.9	no
2003.5.7	5	8.4	58.1	66.5	no
2003.5.17	14	61.1	150.0	211.1	yes
2003.6.6	1	4.4	71.1	75.5	no
2003.6.27	20	22.3	37.5	59.8	no
2003.9.21	20	11.5	46.7	58.2	no
2003.10.22	0	0.0	41.3	41.3	no
2003.11.8	1	7.2	42.5	49.7	no
2004.3.8	17	1.8	61.3	63.1	no
2004.5.13	12	12.7	50.1	62.8	no
2004.7.8	3	18.0	74.8	92.8	no
2004.8.20	19	9.8	91.0	100.8	no
2005.3.29	20	11.2	49.2	60.4	no
2005.5.9	6	22.3	59.0	81.3	no
2005.6.2	10	19.8	59.2	79.0	no
2005.6.12	4	4.4	52.0	56.4	no
2005.6.23	13	100.0	45.5	145.5	no
2005.8.14	8	27.7	138.6	166.3	yes
2005.9.3	1	11.6	81.1	92.7	no
2006.4.6	6	4.1	40.8	44.9	no
2006.4.27	21	38.5	86.8	125.3	no
2006.5.17	15	12.9	45.6	58.5	no
2006.6.8	18	72.7	138.0	210.7	yes
2006.6.17	8	40.0	80.3	120.3	no
2006.7.15	11	33.1	74.6	107.7	no
2006.11.26	10	24.4	52.7	77.1	no
2007.4.24	9	45.6	47.6	93.2	no
2007.5.29	13	17.9	44.7	62.6	no
2007.6.8	7	61.0	44.4	105.4	no
2007.6.13	12	72.4	61.3	133.7	no

2007.7.13	12	1.9	63.6	65.5	no
2007.8.14	5	21.7	48.0	69.7	no
2007.8.15	6	55.8	45.1	100.9	no
2007.9.3	15	37.3	44.7	82.0	no
2007.9.4	16	65.6	42.4	108.0	no
2008.2.1	7	17.1	35.0	52.1	no
2008.4.20	10	10.2	80.0	90.2	no
2008.5.28	10	31.0	39.4	70.4	no
2007.8.15	6	55.8	45.1	100.9	no
2007.9.3	15	37.3	44.7	82.0	no
2007.9.4	16	65.6	42.4	108.0	no
2008.2.1	7	17.1	35.0	52.1	no
2008.4.20	10	10.2	80.0	90.2	no
2008.5.28	10	31.0	39.4	70.4	no
2008.5.30	12	121.1	39.1	160.2	no
2008.6.12	19	51.0	102.5	153.5	yes
2008.6.18	5	28.8	44.2	73.0	no
2008.6.27	2	2.8	75.1	77.9	no
2008.6.30	5	45.7	74.2	119.9	no
2008.7.29	1	0.5	80.6	81.1	no
2008.7.30	1	64.8	50.1	114.9	no
2009.4.25	13	28.1	66.8	94.9	no
2009.5.20	7	29.4	48.5	77.9	no
2009.6.11	1	8.8	56.1	64.9	no
2009.6.14	4	45.3	41.4	86.7	no
2009.6.24	14	63.7	48.1	111.8	no
2009.7.3	1	0.6	42.2	42.8	no
2009.7.4	2	34.1	38.4	72.5	no
2009.11.13	5	23.2	44.3	67.5	no
2010.4.8	6	35.9	40.9	76.8	no
2010.4.13	11	31.5	38.7	70.2	no
2010.5.6	1	11.5	52.5	64.0	no
2010.5.23	18	32.3	107.4	139.7	yes
2010.6.15	6	57.9	136.2	194.1	yes
2010.7.26	5	29.9	47.8	77.7	no
2010.8.10	0	0.0	78.3	78.3	no
2010.8.10	6	9.9	78.3	88.2	no
2010.8.25	3	5.1	38.6	43.7	no
2010.6.25	16	83.3	53.5	136.8	yes
2007.6.14	13	107.0	60.6	167.6	yes

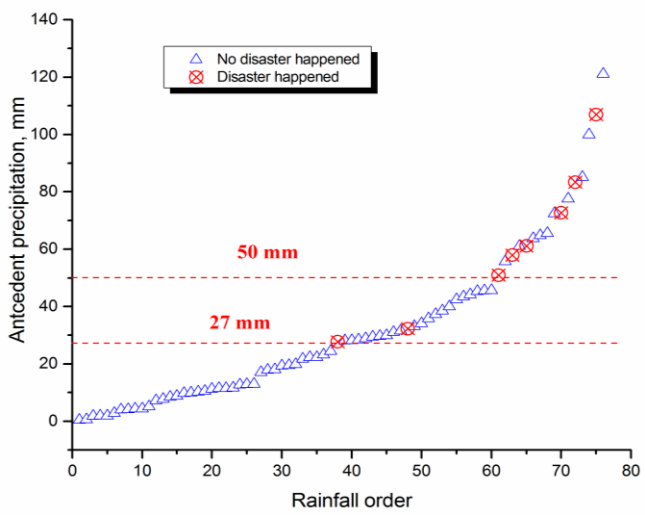

(a)

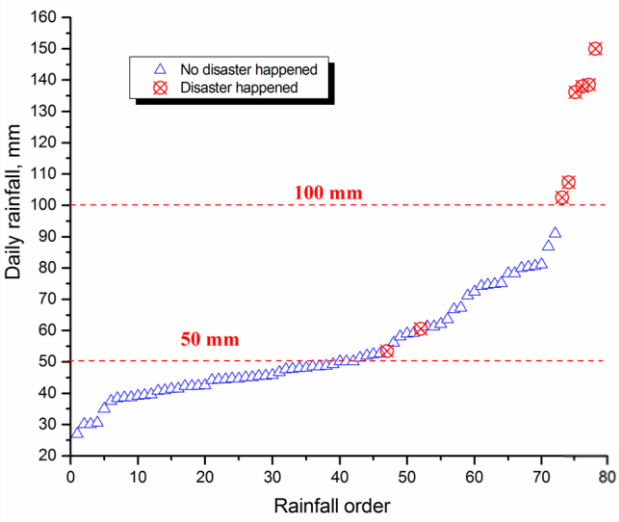

(b)

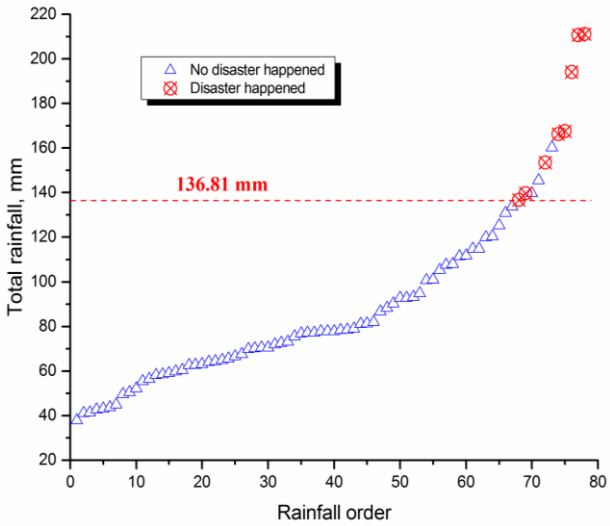

(c)

Fig. 7 Relationship between geological hazards and critical rainfall from 2002 to 2010: (a) antecedent precipitation; (b) daily rainfall; (c) total rainfall

4. RESULTS

According to the **Table.3**, the relationship between the debris flow with landslide collapse and the antecedent precipitation, the rainfall on the day, the total rainfall respectively was shown from **Fig.7 (a)** to **Fig.7 (c)**. From **Fig.7 (a)** to **Fig.7 (c)**, there were four hazards on the condition that (1) the antecedent precipitation was lower 50.0mm, (2) the rainfall on the day was lower 100.0mm. The antecedent precipitation of 27.7 mm, 32.3mm, 60.6mm and 53.5mm was on August 14th, 2005, on May 23rd, 2010, on June 14th, 2007, on June 25th, 2010 respectively. If it was satisfied with the one of the following conditions, the risk of debris flow with landslide collapse was higher, when the antecedent precipitation was more than 50.0mm, the rainfall on the day was more than 100.0mm or the total rainfall was more than 137.0mm. When the antecedent precipitation was more than 50.0mm, the risk probability of debris flow with landslide collapse was 37.5%. When the rainfall on the day was more than 100.0mm, the risk probability of debris flow with landslide collapse was nearly 100.0%. When the total rainfall was 136.0mm, the risk probability of debris flow with landslide collapse was 72.7%. There were two hazards when the antecedent precipitation was less than 50.0mm, but the rainfall on the day was 138.6mm and 107.4mm, the total rainfall was 166.3mm and 139.7mm. There were two hazards when the rainfall on the day was less than 100.0mm, but the antecedent was 107.0mm and 83.3mm, the total rainfall was 167.6mm and 136.8mm.

The results indicated that there was high risk for the debris flow with landslide collapse when either the daily rainfall was more than 100.0 mm, or the total rainfall was more than 136.0mm in the gold-copper deposit and the Shanghang region. At the same time, although there was few risk for the debris flow when the daily rainfall was between 50.0~100.0mm, if the soil was saturated or nearly saturated because of the continuous antecedent precipitation, debris flow hazards would occur even the daily rainfall was only 50.0mm. In addition, it was prone to trigger debris flow hazards when the daily heavy rainfall was more than 100.0mm or the torrential rainfall in 3 days was between 250.0~300.0mm. At last, once the continuous heavy rainfall reached to 300.0mm, it was the frequent period of debris flow and usually generated to large scale and clusters of debris flow.

5. CONCLUSION

The analysis of the nearly 80 heavy rainfalls and related hazards from 2002 to 2010 indicated that there was high risk for the debris flow with landslide collapse when the daily rainfall was more than 100.0mm; or the total rainfall was more than 136.0mm in the gold-copper deposit and the Shanghang region.

ACKNOWLEDGMENTS: This work was funded by National Key R&D Program of China (2017YFC1502502, 2017YFC1502506), the National Natural Science Foundation of China (41672318, 41372331, and 51679229), also supported by Youth Innovation Promotion Association of the Chinese Academy of Sciences (2018405).

REFERENCES

Chen,J.W. (1985): Analysis of relationship between debris flow and rainstorm in Jianjiagou of Dongchuan in Yunnan province, Science Press, Beijing, pp.85-95(in Chinese).

Chen,J.W. (1990): Analysis of debris flow triggered by rainstorm in Jiangjiagou, Analysis of debris flow of Jiangjiagou in Yunnan province, Science Press, Beijing, pp.197-212 (in Chinese).

Cui, P.D., Liu, S.J., Tan, W.P. (2000): Progress of debris flow forecast in China, JOURNAL OF NATURAL DISATERS, Vol. 9(2), pp.10-15.

Cui, P.D., Zhong, L., Li, Y. (1997): Landslide and Debris Flow in Zezu, Meigu County in Sichuan Province, MOUNTAIN RESEARCH, Vol.15(4), pp.282-287.

Gao, S., Liu, A.M., Huang, Z.G. (2010): The character analysis on heavy rainfall inducing geological hazards in Fujian province, Geology of Fujian, Vol.SUPP1, pp.64-71.

Gao,S., Liu,A.M., Huang,Z.G.(2008): Analysis on Characterlstics of Geological Hazard Induced by Heavy Rainfall In Fujian Province, JOURNAL 0F FUJIAN METEOROLOGY, Vol.6, pp.1-7.

Huang, Z.G. (2010): Because of ArcGis the evaluation model for geo-hazard susceptibility of rainfall in Fujian Sheng, Geology of Fujian, Vol.29(SUPP), pp.72-76.

Huang, Z.G., Lin, X.H., Gao, S. (2003): Preliminary Study on meteorological conditions of geological disasters in Fujian, JOURNAL OF FUJIAN METEOROLOGY, Vol.5, pp.8-10(in Chinese).

Huang, Z.G., Liu, A.M., Lin., X.H.(2005): Analysis of Meteorological features of mountain torrent disaster in Fujian Province, JOUTURNAL OF GUANGXI METEOROLOGY, Vol.26(SUPP), pp.10-12 (in Chinese).

Jing, S.H.(1986) : Analysis of rainfall threshold and triggering rainfall of debris flow, Journal of Railway Engineering Society, Vol.12(4) , pp.91-95

Kang, Z.C. (1987): THE MECHANICAL ANALYSES OF

DEBRIS OF THE GENERATION FLOW, MOUNTAIN RESEARCH, Vol.5(4), pp.225-229.

Liu,A.M., Gao,S., Huang,Z.G. (2008): Analysis on Characteristics of Geological Hazard Induced by Tropical Cyclone Rainfall in Fujian, JOURNAL OF CATASTROPHOLOGY, Vol.23(4), pp.45-4

Lu, R. (1986): Active characteristics, formative conditions and control of debris flow in hengduan mountainous region. Journal of Mountain Research.

Tan, W.P., Li, D.J., Jin, Y.T. (1981): Analysis of rainstorm triggered debris flow in south region of Liangshan county in Sichuan province, Chongqing Branch, SCIENTIFIC AND TECHNICAL DOCUMENTATION PRESS, Chongqing, pp.21-26 (in Chinese).

Tan, W.P., Luo, X.M., Wang, C.H. (2000): Forecast models of rainstorm debris flows, JOURNALOF NATURAL HAZARDS, Vol. 9(3), pp.106-111.

Tan, W.P., Wang, C.H., Yao, L.K. (1994): The prediction and forecast for debris flow landslide triggered by rainstorm, Institute of Mountain Hazards and Environment, CAS, Science Press, Beijing(in Chinese).

Tan, B.Y.(1994): Results of Study on the Prediction of Rain storm Debris Flow Along Montane Railways, China Railway Science, Vol.1994 (4) , pp.67-78.

Tan, B.Y., Yang, D.W., Shi, S.G. (1992): THE STUDY OF PREDICTION FOR DEBRIS FLOW CAUSED BY RAINSTORM, JOURNAL OF THE CHIAN RAILWAY SOCIETY, Vol.14(3), pp. 92-101.

Wu, J.S., Kang, Z.C., Chen, X.Q. (1990): Monitoring study of debris flow in Jiangjiagou of Yunnan province, Science Press, Beijing, pp.197-212 (in Chinese).

Yin, Y.K. (1992): REVIEWS ON THE PREDICTION OF LANDSLIDE HAZARD, Geological Science and Technology Information, Vol.11(4), pp.59-62.

Effect of Bent Flexible Vegetation on Fluvial-bed Change Under Flood Conditions

Jin-Fu LI* and Su-Chin CHEN

Department of Soil and Water Conservation, National Chung Hsing University, Taiwan
*Corresponding author. E-mail: dennis4607@hotmail.com

To understand the effects of vegetation on sand-bed, we designed three different densities and nine random distributions of bent flexible vegetation in flume experiments. Current velocity was controlled to be larger than the critical velocity and sediments were supplied upstream during the experiment to simulate the real river condition under flood conditions. Ultrasound Velocity Profiler (UVP) was used to measure the flow field and a high-precision laser scanner (F5, Mantis Vision) was used to measure the final topography of sand-bed in each experiment. The results showed that the evolutionary process of sand-bed can be divided into four stages; scouring stage, growth stage, supplement stage, and deposition stage, forming a dynamic cycle. The deposition was dominant in front of the vegetation area, while scour dominated the area behind the vegetation. However, in the vegetation area, sand-bed was mainly affected by the concentration and blockage effects of vegetation, so it changed from depositional to erosive as vegetation density increases. The findings from this study will provide crucial information towards river management through understanding the links between channel bed, flow and vegetation.

Key words: river vegetation, sediment transport, flood condition

1. INTRODUCTION

The frequency of heavy rains and typhoons caused by climate fluctuation has increased in recent years. Rains and typhoons cause a lot of sediments to move from mountains, hills, and plains into rivers and often result in serious sediment disasters. Therefore, understanding how sediments are transported in rivers is crucial. Generally, the existence of vegetation can change the flow conditions and the sediment transport characteristics of a river. When a current encounters single vegetation, the current would produce downward jet-flow and horseshoe vortex by the shape resistance of the vegetation. They would cause the riverbed be scoured around the vegetation. The scouring model is similar to that of a pier scour [*Raudkivi and Ettema*, 1983; *Melville*, 1997; *Melville and Chiew*, 1999]. Additionally, vegetation also reduces the critical velocity of incipient motion for sediments by increasing the drag force and lift force in the flow [*Tang et al.*, 2013; *Wang et al.*, 2015]. Consequently, the riverbed becomes unstable. On the contrary, vegetation can decrease the current velocity by supplying the drag coefficient to induce sediment deposition thereby stabilizing the riverbed [*Sand-Jensen*, 2003; *Wilson* et al., 2008]. Moreover, roots and underground stems also can provide additional tensile strength for ground-holding to adsorb some insoluble colloids and organic debris [*Pollen-Bankhead et al*., 2009][]. It can effectively inhibit the re-suspension of the sediment and slow down the riverbank retreat which was scoured by the current [*Horppila and Nurminen*, 2001; *Horppila and Nurminen*, 2003].

In some extreme weather events, when a flood caused by rainfall or typhoon event sweeps past the riparian vegetation communities on the sandbank, stream-side, and floodplains, its high-sediment-concentration current will cause a series of complicated interactions with the vegetation communities. These interactions can be simply categorized into three different groups by their location. First, in the upstream of vegetation communities, the high-sediment-concentration current is blocked by the vegetation communities, so the water surface rises and the sediments are deposited in front of the vegetation communities. Secondly, in the downstream of vegetation communities, the current which crosses the top of the vegetation will deflect downward to scour the riverbed behind the vegetation communities. Finally, in central vegetation community, several counteractive forces influence each other, so the net

effects on the current and riverbed are uncertain. For example, the vegetation can reduce the cross-sectional area of the flow channel, thus increase the current velocity, but the vegetation also can provide drag force to consume the kinetic energy of the current, thus decrease the current velocity [*Gurnell and Petts*, 2006; *Gurnell*, 2014]. Therefore, the different vegetation characters have different influences on the current and riverbed.

In previous research work, researchers changed the vegetation characters such as densities (single or multiple), arrangements (staggered, columnar, or aligned), and rigidities (rigid, flexible, or mixed) to observe the interactions among the vegetation, current, and sediments by a series of flume experiments [*Nepf and Vivoni*, 2000; *Wilson*, 2000; *Okamoto and Nezu*, 2010; *Sanjou and Nezu*, 2010; *Chen et al.*, 2011; *Luhar and Nepf*, 2011; *Ghisalberti and Nepf*, 2002]. In different density experiments, the current could flow straight through the low-density vegetation and deposit sediment on both sides of the downstream wake to develop an open-bed formation. But, in the high-density vegetation condition, the Von-K´arm´an vortex would appear in the downstream wake and make sediment deposit again to develop a closed-bed formation [*Follett and Nepf*, 2012]. Additionally, the vegetation density also could affect the type of maximum scour hole and the deposition dune. Even if the density remained consistent, the different arrangement types of the vegetation could have different results of the erosion and the deposition. Particularly, the influence of the longitudinal change of the spacing length was found to be more significant than the latitudinal change of the spacing length [*Chen et al.*, 2012]. In different rigidity experiments, the flexible vegetation has the smaller shape resistance than the rigid vegetation, so it is easily bent by a current. The bending leaves of the flexible vegetation have a function of protecting the riverbed and slowing down erosion [*Chen et al.*, 2012].

Moreover, the above researches focused on the normal flow conditions (i.e. experimental velocity was less than the critical velocity and there was no sediment input during the experiment). Flood conditions were rarely discussed. Therefore, we designed a series flume experiments to observe the situation of vegetation under flood conditions. In order to simulate the situation of sediments moving from mountains, hills, and plains into rivers, the experimental velocity was designed to be greater than the critical velocity and continually supplied sands in the upstream during the experiments. In addition, we also changed the density and arrangement of vegetation in the flume experiments to observe the effects on a channel.

2. METHOD

The experiments were conducted in a 15m length, 0.6m width, glass-sided recirculation flume system. The structure of the flume system is shown in Fig. 1(A). The head tank was located upstream of the main channel to keep a constant water head. At the entrance of the main channel, a honeycomb flow straightener was installed to steady the current. A right-angle wedge, 0.4m length, 0.6m width, and 0.1m height, was set 1.8 m after the flow straightener. Then, an acrylic block, 3m length, 0.6m width, and 0.1m height with quartz sand (SiO2, D50 = 1.22 mm) glued to its top surface to keep the same surface roughness as the sand area that followed. The sand area of 4.8m length by 0.6m width was filled with quartz sands to a height of 0.1m. Behind the sand area, a sand-trap was laid to collect sand transported by the current. At the exit of the main channel, a tail-water gate was installed to control the water depth to 0.1 m. Finally, an underground water tank was used to collect water, and a recirculation pump was used to raise the water back to the head tank to form a closed loop. Each experiment had continuously running water for 10 hours then turned off the recirculation pump to stop the current. A water discharge rate of 0.03 m^3/s was set to give an initial velocity of 0.5 m/s under no vegetation. This velocity was greater than the critical velocity, as a result quartz sand was slightly eroded to simulate flood conditions. Concurrently, the quartz sand was supplied at a rate of 0.35 kg/min from a sand-supplying device located at the beginning channel bed area.

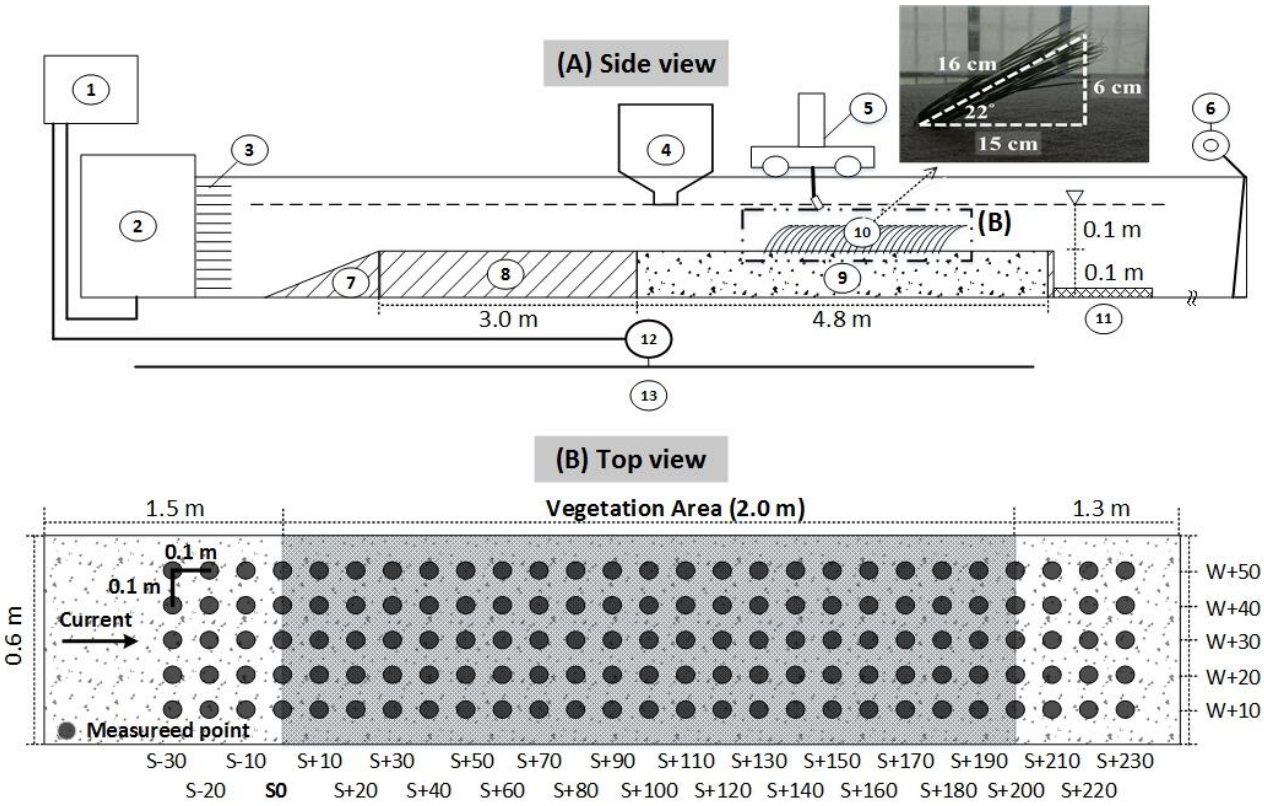

Fig. 1 The flume system used for the experiments. (A) Side view of the flume system where; 1. Head tank. 2. Water storage tank. 3. Flow straightener. 4. Sand-supply device. 5. UVP. 6. Tail-water gate. 7. Right-angle wedge. 8. Acrylic block. 9. Quartz sand area. 10. Vegetation area. 11. Sand trap. 12. Recirculation pump. 13. Underground water tank. (B) Top view of the measured area. Dots represent measuring points. Vegetation models were randomly placed in area between S+0 and S+200.

Before the experiment, we arranged the vegetation models, which were made of flexible plastic material, in the sand-bed area at 2m long by 0.6m wide. Individual vegetation model was arranged on grid points randomly determined by their X and Y coordinates on a 1cm x 1cm grid system drawn in this area. The vegetation was inserted into the bed at an angle of about 22°.

Three different vegetation densities were designed: 33.33 (test 1~3), 66.67 (test 4~6), and 100 (test 7~9) stems/m^2. Each density was triplicated, although each replicate was with a different random distribution pattern as described earlier. Five hours after the start of an experiment, we started measuring velocities and turbulence intensity of the flow field using an Ultrasound Velocity Profiler (UVP) [*Met-Flow*, 2006]. Turbulence intensity was represented by the root mean square (RMS) of velocity. The entire channel totally contained 135 measuring points, shown in **Fig. 1(B)**. At each point, measurements were made at thirteen depths, at intervals of 0.5 cm, ranging from 2 to 8 cm under the water surface. Each velocity and turbulence was the result of average measurement 2000 times. The measuring frequency was 20 Hz. After turning off the pump, we measured the final topography of the entire sand-bed, which totally had 45000 point cloud data from S-150 to S+330, using a high-precision laser scanner (F5, Mantis Vision). The precision of the scanner was 0.5 mm.

3. RESULTS AND DISCUSSION

3.1 The influence of single vegetation on the sand-bed

We observed the process of sand-bed evolution around the single vegetation during the experiments. The mainly evolutionary process could be divided into four stages, as follows: (A) scouring stage; (B) growth stage; (C) supplement stage; and (D) deposition stage. The flowchart are shown in **Fig.2**.

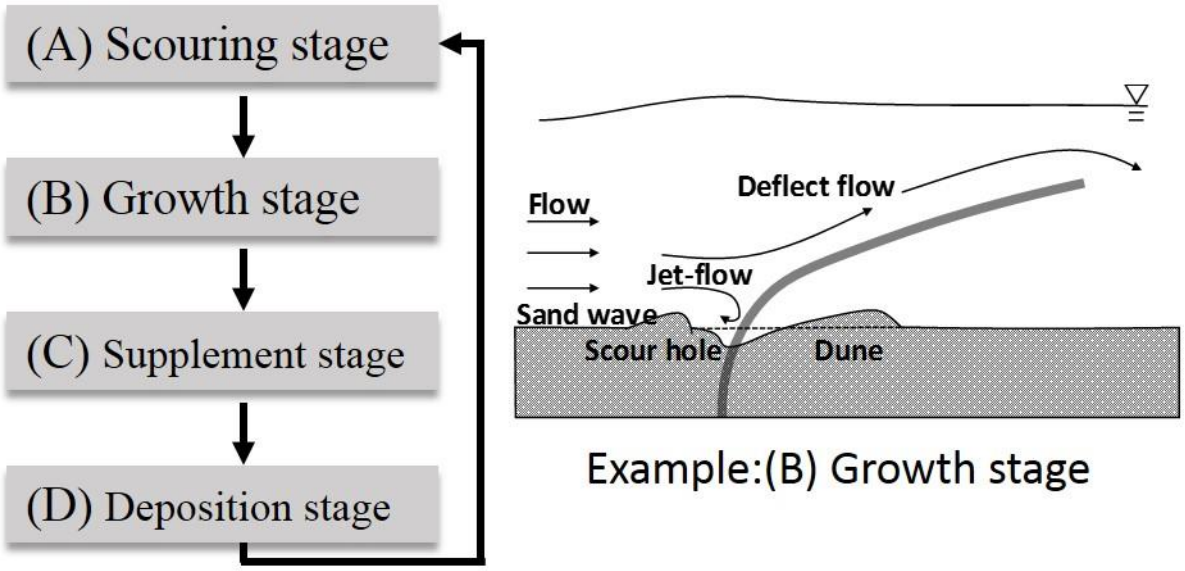

Fig. 2 Flowchart of the dynamic process of the sand-bed evolution.

In the first stage, scouring stage, the sand-bed was affected by the downward jet-flow in front of the vegetation and the horseshoe vortex in the both sides of vegetation. This effect made a small scour hole appear around the vegetation. Then, the sands, which were transferred from the scour hole by the current, deposited to form a small dune behind the vegetation. At the same time, a lot of sands converged to form a sand wave in the upstream and gradually moved to the downstream.

In the second stage, growth stage, the scour hole, which was affected by the downward jet-flow, grew toward the upstream and the dune, which was affected by the flowing current, grew toward the downstream. The volume of both was gradually increased. At the same time, the sand wave was close to the front end of the scour hole.

In the third stage, supplement stage, the sand wave entered the scour hole. It filled the scour hole to make the scour hole disappear. Then, the residual sands moved to supply the dune. That made the slope of the upstream surface of the dune become gentle.

In the fourth stage, deposition stage, the sand of dune was transferred continuously to further downstream by the flowing current. That made the slope of the downstream surface of the dune become gentle. Then, the depositional sand made the dune to have the bulge at the center and low at both ends. Finally, the process of sand-bed evolution would recover to the first stage and the new scour hole and sand wave appeared again.

From the above results it is observed that the sand wave was the most important factor in the entire evolutionary process, as it had a recovery function. It made the sand-bed reach a dynamic cycle in the evolutionary process. Therefore, the process of sand-bed evolution was different between the normal condition and flood condition, because the sand-bed did not reach the final equilibrium stage, which was proposed by Chen, et al., 2012 in their normal condition experiments, under flood condition.

3.2 The influence of vegetation communities on the sand-bed

We observed the final sand-bed topographies of three different vegetation densities, 33.33, 66.67, and 100 stems per square meter, in the vegetation area (S0 ~ S+200). The topographies of 33.33 stems/m^2 experiments are shown in **Fig. 3**. In these minimum density experiments, most of the sand invaded the entire vegetation area to form a depositional sand-bed. The cross-sectional area for water passage was not significantly reduced, so the rate of velocity increase was inconspicuous. In addition, because the distance of each vegetation was wide, we found some evolutionary processes of sediment, which were caused by the single vegetation, on the sand-bed. **Fig. 3(a)** represents the type of scouring stage; **Fig. 3(b)** the type of growth stage; **Fig. 3(c)** the type of supplement stage; **Fig. 3(d)** the type of deposition stage.

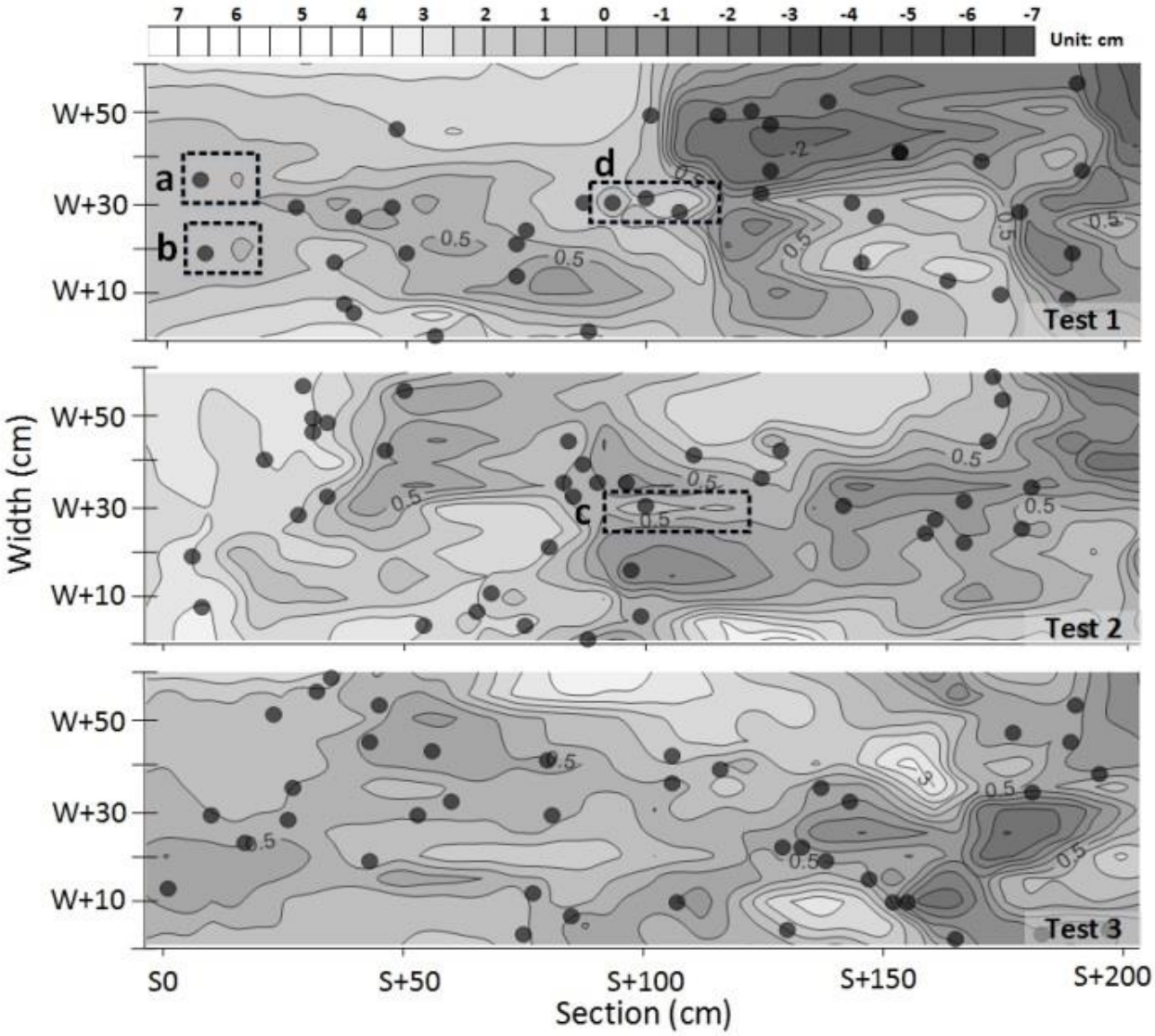

Fig. 3 The final sand-bed topographies after the 33.33 stems/m^2 experiments. (a) The dune type of the scouring stage. (b) The dune type of the growth stage. (c) The dune type of the supplement stage. (d) The dune type of the deposition stage. Black dots represent vegetation. Color-bar on top shows topographic height.

Then, in the 66.67 stems/m^2 experiments, the topography of erosion and deposition was half and half. The current was easily impeded by the vegetation to produce a backwater when current came from the sparse vegetation area into the dense vegetation area. The backwater was a low velocity and opposite direction current, so it easily caused the sediment deposited toward the upstream and formed a new sandbar.

Finally, in the 100 stems/m^2 experiments (**Fig. 4**), most sand-bed was erosive. The vegetation and other vegetation were very close to affect each other, so the flow field was very complicated in this area. Therefore, we are difficult to observe the phenomenon described above. Only in few area with dense vegetation like **Fig. 4 (a) ~ (c)**, the dense vegetation could provide a lot of resistance to deposit many sediments behind the denser vegetation. These sediments formed a large dune, which was like an island in the river, and gradually extend to downstream.

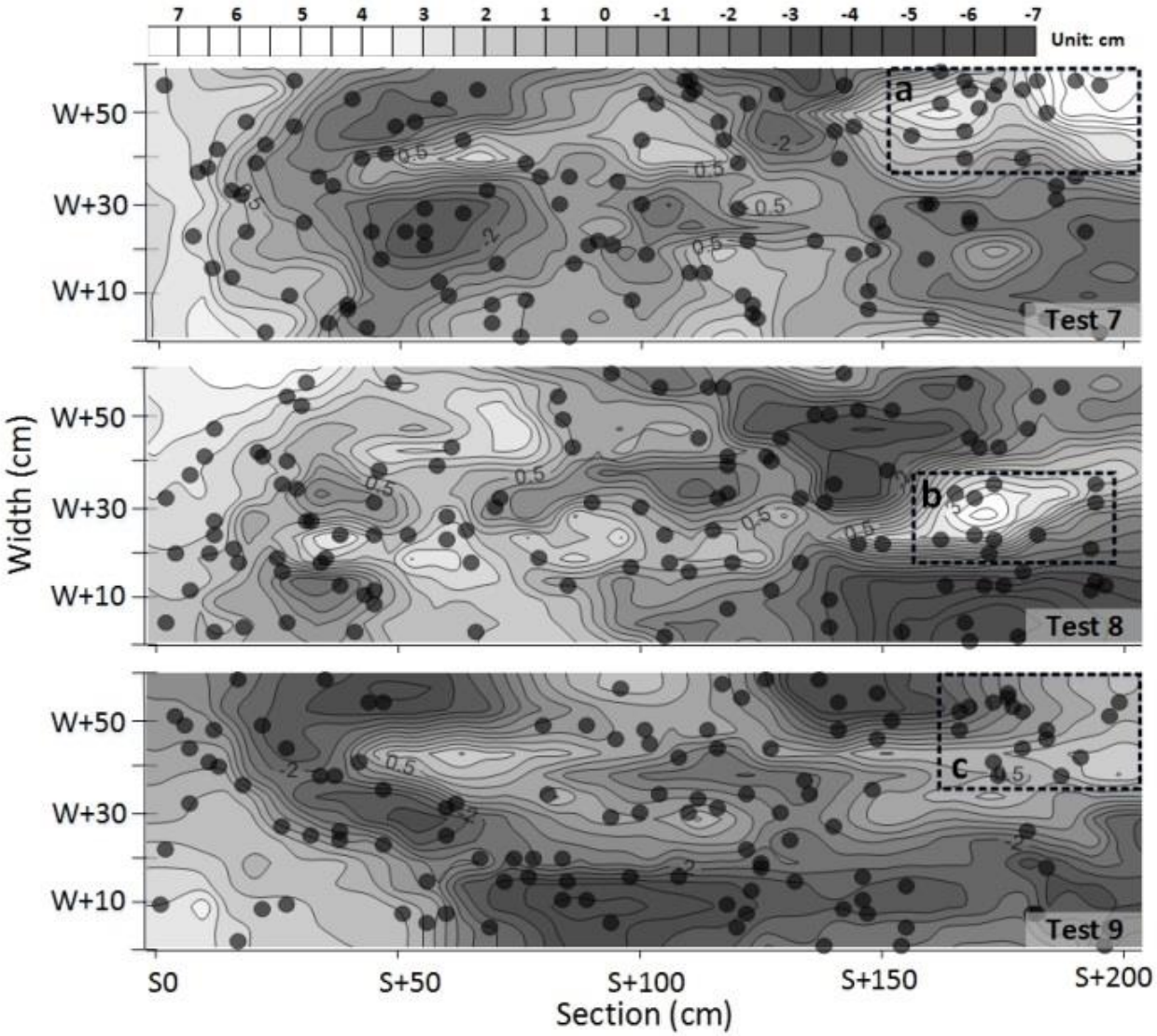

Fig. 4 The final sand-bed topographies after the 100 stems/m^2 experiments. Black dots represent vegetation. Color-bar on top shows topographic height. The Rectangular area was island location of developing toward the downstream.

From the above results, we find that the sand-bed was affected by two main influences in the vegetation area. One was that the vegetation could increase current intensity by decreasing the cross-sectional area for water passage. The large current intensity easily scoured the sand-bed to form an erosive sand-bed. In addition, the vegetation decreased the current intensity by supplying shape resistance. The small current intensity promoted sediments to deposit and form the depositional sand-bed. Therefore, the form of sand-bed depended on the current intensity and vegetation resistances in the vegetation area. If the vegetation resistance was greater than the current intensity, the sand-bed was depositional such as **Fig. 3**. Conversely, if the current intensity was greater than the vegetation resistance, the sand-bed was erosive such as **Fig. 4**.

3.3 The influence of vegetation on sediment transportation

We compare the amount of sand-bed sediment change before and after each experiment. The results were shown in Table 1.

Tab. 1 Average amount of sand-bed sediment change per m^2

Density (stems/m^2)	Upstream area (kg/m^2)	Vegetation area (kg/m^2)	Downstream area (kg/m^2)
33.33	+5.57	+22.93	-38.28
66.67	+17.22	+1.19	-35.63
100	+31.31	-24.38	-20.81

Note : + means deposition; - means erosion

The amount of sediment increased in the upstream area, mainly due to the blockage effect of vegetation. If the current was blocked by obstructions, part of the kinetic energy would be converted to potential energy and cause the phenomena of flow velocity decrease and water level increase. These phenomena could promote the sediment to deposit in this area and to form the depositional bed. As the vegetation density increased, the sediment which was blocked by vegetation also increased. In the vegetation area, the amount of sediment was increased in the 33.33 stems/m^2 and 66.67 stems/m^2 experiments. However, the amount of sediment was reduced in the 100 stems/m^2 experiments. This change was caused by the vegetation's effects of concentration and blockage. As the vegetation density increased, the influence of concentration effect would be greater than the blockage effect. Therefore, the sand-bed changed from depositional to erosive in the vegetation area. Finally, the amount of sediment was always decreased in the downstream area. The reason was that the current above the vegetation could deflect to downward when leaving the vegetation area. This deflective current scoured the sand-bed, so the amount of sediment was decreased in the downstream area. A special feature was that the erosive amounts, 38.28 kg/m^2 and 35.63 kg/m^2, were not obviously different between the 33.33 stems/m^2 and 66.67 stems/m^2 experiments, respectively. Moreover, it reduced to 20.81 kg/m^2 in the 100 stems/m^2 experiments. The reason for this difference was that the sand-beds of vegetation area were depositional in the 33.33 stems/m^2 and 66.67 stems/m^2 tests, so the downstream sand-beds were only affected by the deflective flow to scour. Nevertheless, the sand-bed of vegetation area was erosive in the 100 stems/m^2 tests, such that the downstream sand-bed was not only scoured by the deflective flow but also got a supplement of sediments from the erosive vegetation area to slow down the scouring.

4. CONCLUSIONS

From the results, we can conclude that: 1. The existence of sand wave made the sand-bed to be divided into four stages, scouring stage, growth stage, supplement stage, and deposition stage, in the evolutionary process and follow these stages to form a dynamic cycle. 2. The topography of sand-bed was mainly affected by the concentration and blockage effects of vegetation. In addition, the backwater caused that the sediments deposit to form a sandbar and develop toward upstream, and the dense vegetation caused a lot of sediments deposit to form an island and develop toward downstream. 3. The sand-bed was always depositional in front of the vegetation area and erosive behind the vegetation area. However, the sand-bed in the vegetation area changed from depositional to erosive as vegetation density increases. The findings from this study will provide crucial information towards river management through understanding the links between channel bed, flow and vegetation.

REFERENCES

Chen, S.C., Kuo, Y.M. and Li, Y.H. (2011): Flow characteristics within different configurations of submerged flexible vegetation, Journal of Hydrology, Vol. 398, pp. 124-134.

Chen, S.C., Chan, H.C. and Li, Y.H. (2012): Observations on flow and local scour around submerged flexible vegetation, Advances in Water Resources, Vol. 43, pp. 28-37.

Chen, S.C., Kuo, Y.M. and Yen, H.C. (2012): Effects of submerged flexible vegetation and solid structure bars on channel bed scour, International Journal of Sediment Research, Vol. 27, No. 3, pp. 323-336.

Follett, E.M. and Nepf, H.M. (2012): Sediment patterns near a model patch of reedy emergent vegetation, Geomorphology, Vol. 179, pp. 141-151.

Ghisalberti, M. and Nepf, H.M. (2002): Mixing layers and coherent structures in vegetated aquatic flows, Journal of Geophysical Research, Vol. 107, No. C2, pp. 3-1--3-11.

Gurnell, A. and Petts, G. (2006): Trees as riparian engineers : the Tagliamento river, Italy, Earth Surface Processes and Landforms, Vol. 31, No. 12, pp. 1558-1574.

Gurnell, A. (2014): Plants as river system engineers, Earth Surface Processes and Landforms, Vol. 39, No. 1, pp. 4-25.

Horppila, J. and Nurminen, L. (2001): The effect of an emergent macrophyte (Typha angustifolia) on sediment resuspension in a shallow north temperate lake, Freshwater Biology, Vol. 46, pp. 1447-1455.

Horppila, J. and Nurminen, L. (2003): Effects of submerged macrophytes on sediment resuspension and internal phosphorus loading in Lake Hiidenvesi, Water Research, Vol. 37, pp. 4468-4474.

Luhar, M. and Nepf, H.M. (2011): Flow-induced reconfiguration of buoyant and flexible aquatic vegetation, Limnology and Oceanography, Vol. 56, No. 6, pp. 2003-2017.

Melville, B. W. (1997): Pier and Abutment Scour: Integrated Approach. Journal of Hydraulic Engineering, Vol.123, No. 2, pp. 125-136.

Melville, B.W. and Chiew, Y.M. (1999): Time Scale for Local Scour at Bridge Piers. Journal of Hydraulic Engineering, Vol. 125, No. 1, pp. 59-65.

Met-Flow. (2006): UVP-DUO user 's guide.

Nepf, H.M. and Vivoni, E.R. (2000): Flow structure in depth-limited, vegetated flow, Journal of Geophysical Research: Oceans, Vol. 105, No. C12, pp. 28547-28557.

Okamoto, T.-a. and Nezu, I. (2010): Large eddy simulation of 3-D flow structure and mass transport in open-channel flows with submerged vegetations, Journal of Hydro-environment Research,Vol. 4, No. 3 pp. 185-197.

Pollen-Bankhead, N., Simon, A., Jaeger, K., Wohl, E., (2009): Destabilization of streambanks by removal of invasive species in Canyon de Chelly National Monument, Arizona, Geomorphology, Vol. 103, pp. 363-374.

Raudkivi, A.J. and Ettema,R. (1983): Clear-water scour at cylindrical piers. Journal of Hydraulic Engineering, Vol. 109, No. 3, pp. 338-350.

Sand-Jensen, K., (2003): Drag and reconfiguration of freshwater macrophytes, Freshwater Biology, Vol. 48, pp. 271-283.

Sanjou, M. and Nezu, I. (2010): Large eddy simulation of compound open-channel flows with emergent vegetation near the floodplain edge, Journal of Hydrodynamics, Vol. 22, No. 5, pp. 582-586.

Tang, H.W., Wang, H., Liang, D.F., Lv, S.Q., Yan, J. (2013): Incipient motion of sediment in the presence of emergent rigid vegetation, Journal of Hydro-environment Research, Vol. 7, pp. 202-208.

Wang, H., Tang, H.W., Zhao, H.Q., Zhao, X.Y., Lu, S.Q. (2015): Incipient motion of sediment in the presence of submerged flexible vegetation, Water Science and Engineering, Vol. 8, No. 1, pp. 63-67.

Wilson, C.A.M.E., Hoyt, J. and Schnauder, I. (2008): Impact of Foliage on the Drag Force of Vegetation in Aquatic Flows, Journal of Hydraulic Engineering, Vol. 134, No. 7, pp. 885-891.

Wilson, C.A.M.E., et al., *Open Channel Flow through Different Forms of Submerged Flexible Vegetation.* journal of Hydraulic Engineering, 2003. **129**(11): p. 847-853.

Considering the Quantitative Effect of Antecedent Rainfall on Slope Stability to Predicting Rainfall-induced Shallow Landslides at the Basin Scale

Yu LUO[1]* and Si-ming HE[1,2]

[1] Institute of Mountain Hazards and Environment, Chinese Academy of Sciences, Chengdu 610041, China

[2] Center for excellence in Tibetan plateau earth sciences, China academy of sciences, Beijing 100101, China

*Corresponding author. E-mail: ly@imde.ac.cn

In this study, a new predicting models that can considering the quantitative effect of antecedent rainfall on shallow landslide for shallow landslides prone area predicting at the basin scale. The hillslope hydrology model is used to construct the relationship of antecedent rainfall to the height of ground water, the infinite slope stability theory is used to construct the relationship of antecedent rainfall to slope stability. At last, the model was applied at a basin area. Comparisons are made between considered and unconsidered antecedent rainfall. The results show that in the basin area, the shallow landslides prone area for considered the antecedent rainfall is larger than that unconsidered the antecedent rainfall. It is can be concluded that the antecedent rainfall is quite important and should not be ignored in shallow landslide hazard assessment.

Key words: shallow landslide, antecedent rainfall, slope stability, hillslope hydrology, infinite slope stability theory

1. INTRODUCTION

In mountainous areas, landslides are a common geological phenomenon and often result in a major financial losses, and even to a major human life losses. Landslides are triggered by many external environmental factors among which rainfall is the most significant one. Much data indicate that in the rainy season of China, the main and common type of rainfall-induced landslide are shallow landslides (*Wei et al*., 2006; *Guo et al*., 2005; *Li et al*., 1999; *Liu*, 1996). Generally, this phenomenon is main caused by extreme intense rainfall or intermittent rainfalls of medium intensity rainfall events. In previous studies of landslide-rainfall relationship, many researches focused on the intensities and durations of rainfalls and get the proper understanding. Caine (1980) is the first one using the empirical approaches to constructing the limiting threshold of rainfall intensity and duration for shallow landslide. Meanwhile, other researches (*Ono et al*., 2014; *Jemec*, 2013; *Guzzetti et al*., 2007; *Tsai*, 2006; *Chen et al*., 2006; *Aleotti*, 2004; *Brand et al*., 1984) also using the same method to explored the relationship of rainfall intensity and duration between shallow landslide. Another researchers using the physically-based model approaches which considering the physical features of slopes including local topographic, geologic and soil parameters as well as rainfall intensity and duration using to analysis the stability of shallow landslide (*Luo*, 2015; 2014; *Chang and Chiang*, 2009; *Rosso et al*., 2006; *Casadei et al*., 2003; *Borga et al*., 2002, 1998; *Wu and Sidle*, 1995; *Montgomery and Dietrich*, 1994). Here, Rosso et al. (2006) developed a physically-based model which considered some key characteristics of the soil mantle and both rainfall intensity and duration into the physical-based model to predict rainfall-induced shallow landslides. But, those researches seldom considered the antecedent rainfall.

Of course, some researchers have been aware of the significance of antecedent rainfall on rainfall-induced landslide. Glade (2000) using an empirical "Antecedent Daily Rainfall Model" which is a combination of rainfall occurring in a period before the event (antecedent rainfall) and rainfall on the day of the event to calculate the regional landslide-triggering rainfall thresholds for three and slide-prone regions in the North Island of New Zealand. Khan (2012) using the historical rainfall-landslide data of Chittagong City, Bangladesh to analyse the critical rainfall condition of the landslide events by Gumbel's extreme value distribution. And then using the antecedent rainfalls to do the Gumbel's distribution of the critical rainfall intensity–durations of each historical

landslide. Guo (2013) take 23 debris flow events in Jiangjia Ravine as the study objects, found an I-D (Intensity-Duration) threshold of rain for debris flow by considering the antecedent rainfall. But, From these existing references, we found that almost all the studies are based on the empirical approach. This method have the advantage of simplicity using, but it considered the physics feature of hillside slopes as a 'black box' and overlooks the actually physical processes of landslide triggered by rainfall.

In this paper, according to the physical mechanics of rainfall-induced shallow landslide, a physically based model considered the antecedent rainfall is presented. This model using the Rosso's model of rainfall versus ground water table as the base, considered antecedent rainfall to construct the hillslope hydrology, and then combined with the infinite slope stability theory to explore the quantitative effects of antecedent rainfall on shallow landslide occurrence. At last, the model is apply in the Baisha river basin of Chengdu, Sichuan, China and the comparisons are made with the results from unconsidered the antecedent rainfalls.

2. HILLSLOPE HYDROLOGY MODEL AND SLOPE STABILITY MODEL

2.1 Hillslope hydrology model

This study is aim to explore quantitative effects of antecedent rainfall on shallow landslide. So we should construct the hillslope hydrology model first. The hillslope hydrology is consists of two mathematical parts (equations), one is used to describe the rainfall induce the ground water raising, and the other is used to describe the ground water recession after the rainfall stop. In this study, the expressions for ground water raising using the one's presented by Rosso et al. (2006). And the expressions for ground water recession is derived in this study.

2.1.1The expressions for ground water raising

In Rosso's model (2006), the expressions to describe rainfall induce the ground water raising is used widely (*Luo et al*., 2015; 2014). The expressions for ground water raising presented by Rosso et al (2006) is derived by coupling the conservation of mass of soil water with the Darcy's law and some assumptions:(1) overland water flow is generated by saturation excess; (2) the impermeable layer is shallow. And then, using the intersection of contour and flow tube boundaries orthogonal to the contours to define the topographic elements and a hillslope will be consisted by those topographic elements; (3) null soil volumetric strain and above the ground water table soil saturation degree of constant average; (4) rainfall is constant between time. So, Rosso et al (2016) obtained the equations for rainfall induce the ground water raising and which is shown as follows.

$$h=\frac{apz}{Tb\sin\theta}[1-\exp(-\frac{1+e}{e-es_r}\frac{Tb\sin\theta}{az}t)] + h_0\exp(-\frac{1+e}{e-es_r}\frac{Tb\sin\theta}{az}t), \quad for\frac{ap}{Tb\sin\theta}>1 \tag{1}$$

where, p is the net rainfall, a is the upslope contributing area, b is the width of the topographic elements, h is the height of the ground water table, θ is the slope angle to the horizontal, s_r is the average degree of saturation, e is the average void ratio above the groundwater table, K is the saturated conductivity of the soil, t is the rainfall duration time, T is the hydraulic transmissivity, with $T = Kz$, z is the thickness of the landslide, h_0 is the initial height of ground water table before it rains.

2.1.2 The expressions for ground water recession

Rosso et al (2006) presented the expressions for ground water raising in exp. (1). From the expression (1), we can see that there has an initial condition should be given. The initial condition is the height of ground water table before it rains. So, in this study, the initial height of ground water table h_0 is using to considering the quantitative effects of antecedent rainfall on groundwater. That is to say, if we know how high does the ground water table generated by antecedent rainfall when it is rain, the quantitative effects of antecedent rainfall can be solve out.

As we all know, after rain stop, the ground water table will be lowered by seepage flow, evaporation and other ways. Thus, the expressions for ground water recession should be derived to determine there has how much ground water generated by antecedent rainfall was left before this rains happen.

In order to building the expressions of ground water recession, some additional assumptions had been made as follow:

(1) The ground water table lowered only by seepage flow.

(2) After the groundwater table lowered the soil water content should be return to the initial water content.

Then, based on the assumptions and the principle of water balance (seepage flow discharge equate to the reduced groundwater), we can establish the following expression.

$$q=\frac{ds}{dt}=-a\frac{e}{1+e}(1-S_r)\frac{dh}{dt} \tag{2}$$

where q is the seepage flow discharge, and the other parameters are as before.

Here, using the Darcy's law provides the seepage flow in the groundwater table. We can obtained,

$$q = bhK\sin\theta \tag{3}$$

And then, substituting the expression (3) into expression (2) yields

$$bhK\sin\theta = -a\frac{e}{1+e}(1-S_r)\frac{dh}{dt} \tag{4}$$

By solve the equation (4), we can obtained

$$h = h_a \exp(-\frac{1+e}{e-es_r}\frac{Tb\sin\theta}{az}t) \tag{5}$$

where h_a is the height of groundwater table at the time of the antecedent rainfall stop, and the other parameters are as before. Here, h_a can be obtained by using expression (1) for set h_0 =0. It should be note that before the antecedent rainfall happen, we can considering the simple case of no groundwater in a hillslope .

By solve expression (5), the height of groundwater table varies with the time can be obtained. And a simple case is using here to illustrate the process of ground water recession after rainfall stop. And the results obtained by using the expression (5) is shown is **Fig. 2**. All the parameters using here are also shown in **Fig. 2**. From the **Fig. 1**, we can see that the groundwater table become lower and lower after rain stop. At the twelfth day after rain stop, the height of groundwater table is about $0.001h_a$. For this example the landslide thickness assume as 1m, that is means at this time the height of ground water is less than 1mm ($h_a \leq z$) which almost could be ignored. That is to say if the interval between rainfalls is larger than twelve days, the effect of the antecedent rainfall could not be take into account.

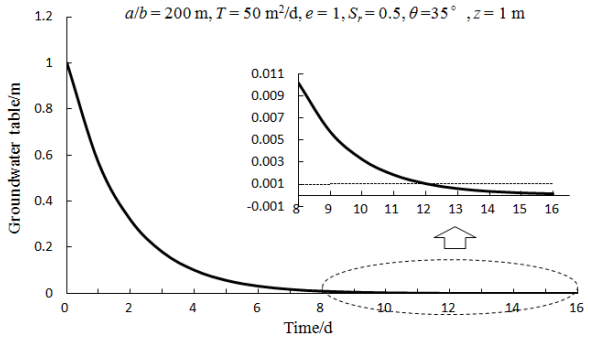

Fig. 1 Height of the groundwater table versus time after rain stop

Thus, Equation (1) and (5) compose the hillslope hydrology model. By the hillslope hydrology model presented in this study, the quantitative effect of antecedent rainfall on groundwater table can be take into account and calculated. Here, we take a simple case to illustrate this process. We assume that the antecedent rainfall is stop 3 days before this rain, and lasted 4 day (**Fig. 2**). Before the antecedent rainfall, there is no rain occurred. By using the hillslope hydrology model presented in this study, we can calculate the variation of groundwater table in this process and the results shows as follow.

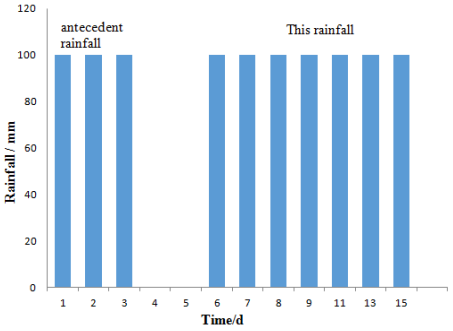

Fig. 2. The distribution of antecedent rainfall and this rain

Fig. 3 shows the height of the groundwater table versus rainfall duration considered and unconsidered the antecedent rainfall. It shows that before the antecedent rainfall occurring, the height of groundwater table is 0. When the antecedent rainfall happen the groundwater table begin to rising, and then reducing by rain stop till the second rainfall come. Here, at the beginning of the second rainfall, there has an initial height of groundwater table which is generated by the antecedent rainfall. This is the quantitative effects caused by the antecedent rainfall. By comparison to the results that unconsidered the antecedent rainfall, we can see the initial height of groundwater table is assumed as 0, and the height of groundwater table is lower than results that obtained by considered the antecedent rainfall. The antecedent rainfall has the strong effect on the groundwater table.

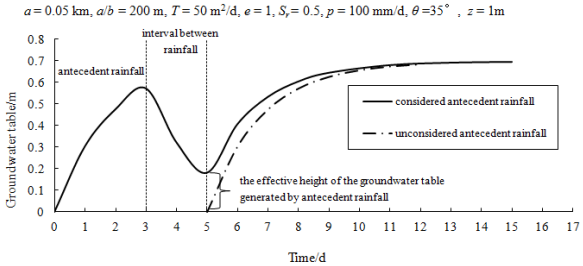

Fig. 3. Comparison of height of the groundwater table versus rainfall duration considered and unconsidered antecedent rainfall

In the simple case, only once antecedent rainfall is taken into account in our hillslope hydrology model. It should be note that no matter how many times antecedent rainfall occurred, we

can using the model in this study by put the effective height of groundwater table generated by the previous rainfall as the initial height of the groundwater table for the latter rainfall, and so on. The effect of all the antecedent rainfall on the groundwater table can be taken into account.

2.2 Slope stability model

Many data indicated that rainfall-induced shallow landslides are often sliding along the interface between soil and rock. In mountainous, the surface of the slope is often parallel to the interface between soil and rock. So, for a hilly area the depth of rainfall-induced shallow landslide is small if compared with the length of the shallow landslide. As we all know, if the thickness of a sliding mass on a slope is much smaller than the slope's length, the infinite slope assumption can be used to calculate the safety factor of the slope by analysis of a rigid wedge or rigid slice of material of unit width and unit thickness.

A rigid slice with unit width and unit thickness is chosen to calculate the safety factor for a slope as shown in **Fig. 4**.

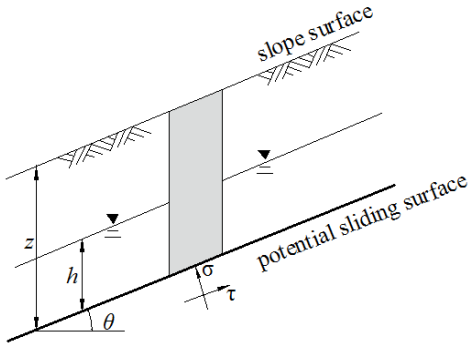

Fig. 4. Computed model for slope stability analysis

Based on the Mohr-Coulomb theory, the shear stress of the soil along the potential failure plane τ_f can be expressed as follow

$$\tau_f = c + (\sigma - u)\tan\varphi \tag{6}$$

where, c is the cohesion of the soil, σ is the normal total stress, u is the pore water pressure, and φ is the internal friction angle of the soil.

If we use the τ_s to denote the shear stress, the safety factor can be written as follows.

$$F_s = \frac{\tau_f}{\tau_s} \tag{7}$$

Here, the expressions for total stress σ, u, and τ_s are

$$\sigma = [(z-h)\gamma + hr_{sat}]\cos^2\theta \tag{8}$$

$$u = hr_w\cos^2\theta \tag{9}$$

$$\tau_s = [(z-h)\gamma + h\gamma_{sat}]\cos\theta\sin\theta \tag{10}$$

where γ is the average unit weight of the soil, γ_{sat} is the saturated unit weight of the soil, and γ_w is the unit weight of water, z is the depth of the shallow landslide.

Then, with the assumption that the slice is rigid and by substituting expressions (8)-(10) and (6) into Equation (7), the expression for the safety factor of a slope can be obtained as the following.

$$F_s = \frac{c + [(z-h)\gamma + h\gamma']\cos^2\theta\tan\varphi}{[(z-h)\gamma + h\gamma_{sat}]\sin\theta\cos\theta} \tag{11}$$

Based on the results as shown in **Fig. 3**, the results of the safety factor versus rainfall duration considered and unconsidered the antecedent rainfall as shown in **Fig. 5**. From **Fig.5** we can see that the safety factor varies with the height of groundwater table. *Fs*=1 is the limiting equilibrium condition of slope stability (*Chang*, 2009; *Rosso*, 2006; *Tasi*, 2006; *Montgomery*, 1994). At the time of the antecedent rainfall stop, the safety factor is larger than 1. That is to say the slope is stable at that time. And then subsequent rainfall caused the slope failure. By comparisons between considered and unconsidered the antecedent rainfall, we can see that the slope failure may occur at the eighth day which is the rainfall lasted 3 days by considered the antecedent rainfall. And if unconsidered the antecedent rainfall, the slope failure may happen at the ninth day which is the rainfall last 4 days. That is to say for the rainfall lasted 3 days, the slope will become unstable by considered the antecedent rainfall, and remain stable by unconsidered the antecedent rainfall. It is demonstrate that the antecedent rainfall effect on the shallow landslide should not be ignored.

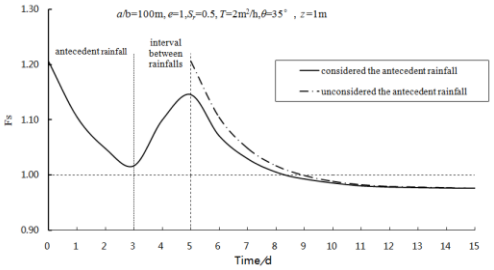

Fig. 5. Comparison of safety factor versus rainfall duration considered and unconsidered the antecedent rainfall

3. APPLICATION AND DISCUSSION

3.1Study area

Baisha river basin of Dujiangya city is chosen as the study area to mapping prone areas of rainfall-induced shallow landslides from the application of the model presented in this study. Meanwhile, comparisons are made with the results unconsidered the antecedent rainfall. Baisha river

basin is located in Dujiangyan. Dujiangyan is on the west side of Chengdu city in Sichuan Province, China. Baisha river basin is high in north-west, and low in south-east. Based on the geological data of Dujiangyan, the Lithological formations in Bashahe river basin can be divide as three major groups. They are pyrolith and metamorphic rock, carbonate and clastics in carbonate rock, carbargillite in sand and mud interbeded rock. Rainfall is abundant in Baisha river basin, the mean annual average precipitation is 1134.8mm. And the rainfall occur main in May to September every year. Thus, many landslide occur in Baisha river basin at those months. From the rainfall-induced landslide data of the Chengdu Land Resources Bureau, we found that rainfall-induced landslide in Baisha river basin are main in shallow landslide, and the depth of the shallow landslide is generally about 1m. Thus, the soil depth is assumed to 1m in our application.

In order to mapping the prone areas of rainfall-induced shallow landslides from the model and make comparisons to unconsidered the antecedent rainfall, the precipitation is assumed to 100mm/d in Baisha river basin, and antecedent rainfall is assumed to happen before 4 day and lasted 3 days with the precipitation is 100mm/d too. That is to say, the interval between rainfalls is 1 day. Before the antecedent rainfall there is no rain happen. Digital elevation data with 25×25m grid resolution were used. The soil parameters of the three major lithological formations used in this study is given in **Table 1**. The soil parameters is obtained by soil sample tests and consulting geological survey data and a handbook of engineering geology.

Table 1. Input soil parameters

Lithological unit	γ (kN/m^3)	T (m^2/d)	c' (kPa)	φ'(°)
Pyrolith and metamorphic rock	21	55	3.5	40
Carbonate and clastic in carbonate rock	19.6	80	3.0	38
Carbargillite in sand and mud interbeded rock	17.6	60	2.6	33

3.2 Results

Based on the hillslope hydrology model presented in this study, distribution of the effective height of groundwater table generated by the antecedent rainfall in Baisha river basin is obtained, as shown in **Fig.6**. From the **Fig.6**, the effective height of groundwater table generated by the antecedent rainfall in Baisha river basin is main in 0-0.1m, only a few areas has the effective groundwater table height in the range of 0.1-0.409m. The maximum height of groundwater table generated by the antecedent rainfall in Baisha river basin is 0.409m. And then, the distribution of groundwater table height which is considered the antecedent rainfall in Baisha river basin at rainfall duration t=1d is shown in **Fig. 7**. From **Fig. 7**, we can see that the maximum height of groundwater table is 0.994m. By comparison to the results of unconsidered antecedent rainfall, at the same area the height of the groundwater table of considered antecedent rainfall is larger than the one's unconsidered antecedent rainfall. And the maximum height of groundwater table in Baisha river basin for unconsidered antecedent rainfall is 0.924m. Therefore, the effect of antecedent rainfall on groundwater table is obviously. It is thus the antecedent rainfall should be take part in the hillslope hydrology analysis.

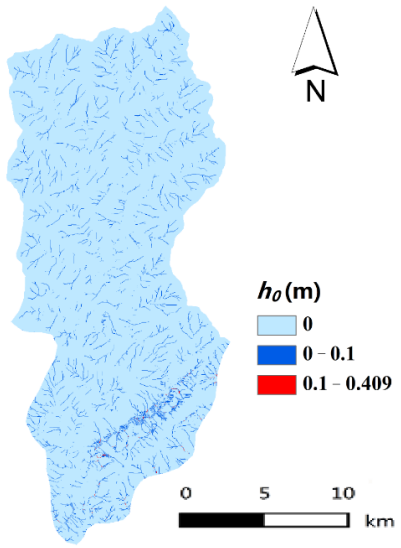

Fig. 6 Distribution of the effective height of groundwater generated by the antecedent rainfall in Baisha river basin

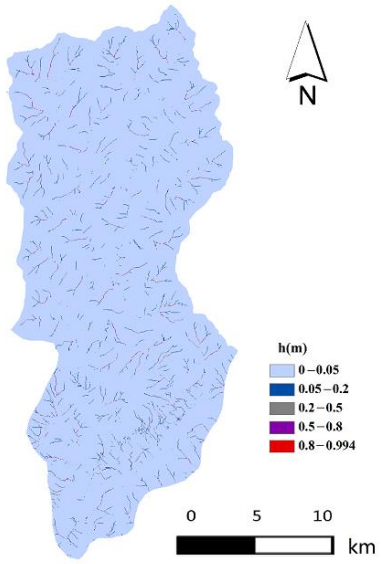

Fig. 7 Distribution of the height of groundwater table considered antecedent rainfall in Baisha river basin at rainfall duration *t*=1d

Based on the distribution of the groundwater table height *h* obtained by considered the antecedent rainfall, using the slope stability model, the results of unstable shallow landslide regions in Baisha river basin at the rainfall durations *t*=1d can be obtained and which is shown in **Fig. 8**. Furthermore, in order to show the difference of shallow landsliding prone areas in Baisha river basin between considered antecedent rainfall and unconsidered antecedent rainfall, a table of unstable topographic cells percentage for rainfall durations *t*=1d obtained by considered and unconsidered antecedent rainfall is worked out, and shown in table 2.

Fig. 8 is a map of Baisha river basin showing unstable shallow landslide region by overlap the unstable shallow landslide area distribution between considered and unconsidered antecedent rainfall at the rainfall duration of 1d. It shows that unstable rainfall-induced shallow landslide are widely distributed in Baisha river basin. The shallow

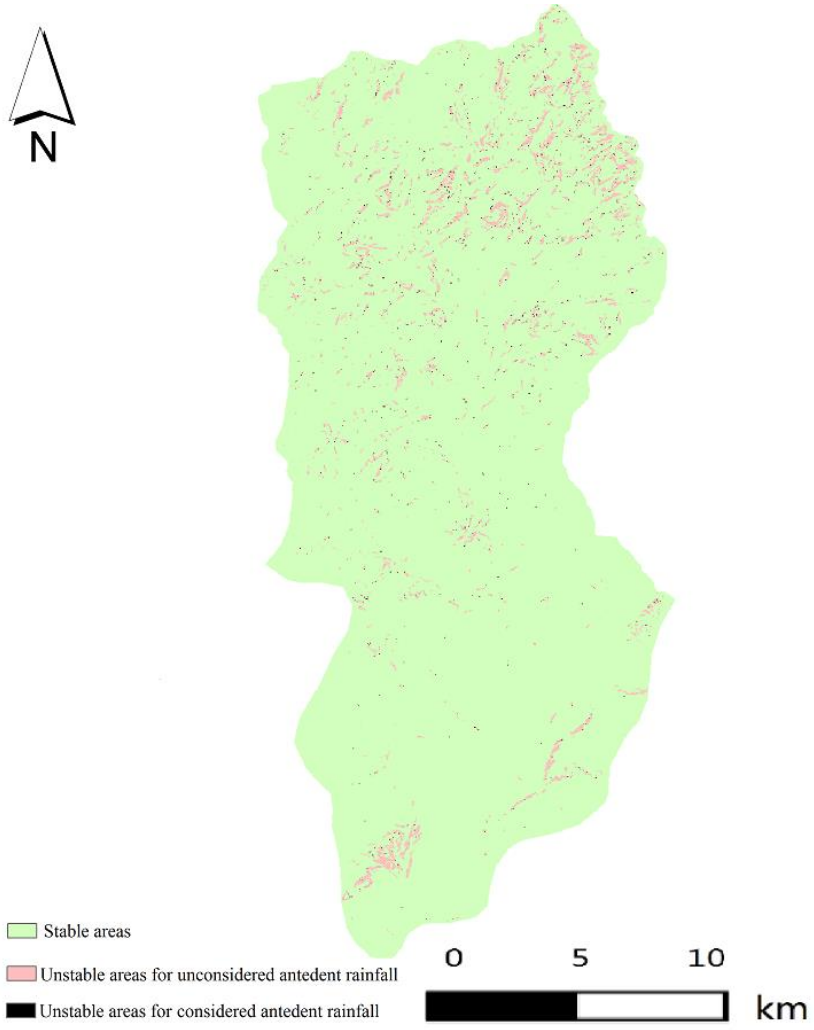

Fig. 8. Comparison of the unstable shallow landslide areas in Baisha river between considered and unconsidered antecedent rainfall

landslide prone areas of considered the antecedent. rainfall is more than the one's unconsidered the

antecedent rainfall.

Table 2 shows the percentage of unstable topographic elements for the different rainfall durations obtained by the two different conditions. It shows that the percentages of unstable topographic elements obtained by considered and unconsidered the antecedent rainfall are 4.08% and 3.88% respectively. that is to say the unstable topographic elements by considered the antecedent rainfall in Baisha river basin are more than unconsidered the antecedent rainfall. Although, the difference are only 0.2%, but we known the area of Baisha river basin is 363km^2.This means that the 0.2% difference represents a different unstable topographic cells area of 726000m^2. Therefore, we have demonstrated that the antecedent rainfall has an obvious effect on shallow landslides. It is quite important to consider the effect of antecedent rainfall in mapping the hydrologic controlled shallow landslide prone area predicting.

Table 2. Percentage of unstable topographic cells for rainfall durations t=1d obtained by considered and unconsidered antecedent rainfall.

Conditions	Considered antecedent rainfall	Unconsidered antecedent rainfall
Total area of unstable cells	4.08%	3.88%

4. CONCLUSIONS

A physically-based model considered the antecedent rainfall, which is an improvement from the pioneering model presented by Rosso et al. (2006), was developed in this study and is used to mapping the rainfall-induced shallow landslide prone area in Baisha river basin. The model combined hydrologic and topographic control on shallow landslides, adding the effect of antecedent rainfall on shallow landslide by an additional expression to describe the ground water recession to improve the hillslope hydrology model and considered the quantitative effect of antecedent rainfall on the slope stability to improve the shallow landslide stability analysis. This paper used simple examples and applied in study area to illustrate the method. Lastly, comparisons are made between considered and unconsidered the antecedent rainfall to demonstrate the rationality of the model of this study.

The main conclusions of the study follow.

(1) The quantitative effect of antecedent rainfall on groundwater table can be take into account by an additional initial height of groundwater table. By comparisons, the height of groundwater table of unconsidered the antecedent rainfall is lower than results of considered. The antecedent rainfall has the strong effect on the groundwater table.

(2) For a same slope, the results of the stability analysis may be different for considered or unconsidered the antecedent rainfall. That is to say, the slope may be stable by unconsidered the antecedent rainfall and unstable by considered the antecedent rainfall. It is demonstrated that the antecedent rainfall effect on the shallow landslide should not be ignored.

(3) Application is made in Baisha river basin, the results showed that antecedent rainfall has an obvious effect on shallow landslides. The percentage of unstable topographic cells obtained by considered the antecedent rainfall is larger than that unconsidered. That is, some parts of stable elements become unstable by considered the effect of antecedent rainfall. Antecedent rainfall has strongly effect on rainfall-induced shallow landslide predicting.

(4) The study show that considered the antecedent rainfall in mapping the hydrologic controlled shallow landslide prone area predicting and landslide hazard assessment are quite important. The model presented in this study provided a new approach to solve the problem of the quantitative effects of antecedent rainfall on shallow landslide in rainfall-induced landslide predicting and hazard assessment. It is hope to improve the accuracy of results of rainfall-induced landslide hazard assessment and found useful for regional landslide forecast.

Acknowledgements. This work was Supported by Major Program of National Natural Science Foundation of China(41790433), the Key research and development projects of Sichuan province (2017SZ0041), NSFC-ICIMOD (Grant No. 41661144041),The authors thank the two anonymous reviewers.

REFERENCES

Aleotti, P., 2004. A warning system for rainfall-induced shallow failures. Engineering Geology, 73(s3-4):247-265.

Borga, M., Fontana, G. D., Deros, D., Marchi, L., 1998. Shallow landslide hazard assessment using a physically based model and digital elevation data. Environmental Geology, 35(2-3):81-88

Borga, M., Fontana, G. D,, Gregoretti, C., et al., 2002. Assessment of shallow landsliding by using a physically based model of hillslope stability. Hydrological Processes 16(14):2833-2851.

Brand, E. W., Premchitt, J., Phillipson, H. B., 1984. Relationship between rainfall and landslides in Hong Kong. In: Proceedings of the IV international symposium on landslides, Toronto 1:377-384

Caine, N., 1980. The rainfall intensity duration control of shallow landslides and debris flow. Geografiska Annaler**,** 62(1):23-27

Casadei, M., Dietrich, W. E., Miller, N. L., 2003. Testing a model for predicting the timing and location of shallow landslide initiation in soil-mantled landscapes. Earth Surface Processes and Landforms 28(9): 925-950.

Chang, K. T., Chiang, S.H., 2009. An integrated model for predicting rainfall-induced landslides. Geomorphology 105(s3-4)：366-373.

Chen, H., 2006. Controlling factors of hazardous debris flow in Taiwan. Quaternary International, 147(1):3-15

Guo, X., Cui, P., Li, Y., 2013.Debris Flow Warning Threshold Based on Antecedent Rainfall：a Case Study in Jiangjia Ravine, Yunnan, China, Journal of Mountain Sciences, 10(2)"305-314.

Guo, X., Zhao, C., Yu, W., 2005. Stability analysis of unsaturated soil slope and its progress. China Safety Science Journal, 15(1): 14-18.

Guzzetti, F., Peruccacci, S., Rossi, M., Stark, C. P., 2007. Rainfall thresholds for the initiation of landslides in central and southern Europe. Meteorology and Atmospere physics 98(3-4):239-267.

Glade, T., Crozier, M., Smith, P., 2000. Applying Probability Determination to Refine Landslide-triggering Rainfall Thresholds Using an Empirical "Antecedent Daily Rainfall Model", Pure & applied geophysics 157(6-8):1059-1079.

Jemec, M., Komac, M., 2013. Rainfall patterns for shallow landsliding in perialpine Slovenia. Nature hazards 67(3):1011-1023.

Khan, Y. A., Lateh, H., Baten, M. A., Kamil A. A., 2012. Critical antecedent rainfall conditions for shallow landslides in Chittagong City of Bangladesh. Environmental earth sciences 67(1):97-106.

Li, T., Chen, M., Wang, L., 1999. Real-time tracing prediction of landslides. Chengdu technology university Press, Chengdu.

Liu, H., 1996. theory and method of forecasting occurrence of slope failure. Yellow River Hydraulic press, Zhenzhou.

Luo, Y., He, S., He, J., 2014. Effect of rainfall patterns on stability of shallow landslide. Earth science-journal of china university of geosciences 39(9):1357-1363.

Luo, Y., He, S., Chen F., Li X., He J., 2015. A physical model considered the effect of overland water flow on rainfall-induced shallow landslides. Geoenvironmental Disasters 2:8.

Montgomery, D., Dietrich, W., 1994. A physically based model for topographic control on shallow landsliding. Water Resources Research 30(4):1153-1171

Ono, K., Kazama, S., Ekkawatpanit, C., 2014. Assessment of rainfall-induced shallow landslides in Phetchabun and Krabi provinces, Thailand. Nature hazards 74(3):2089-2107.

Rosso, R., Rulli, M. C., Vannucchi, G., 2006. A physically based model for the hydrologic control on shallow landsliding. Water resources 42(6): 1-16.

Tsai, T. L., Yang, J. C., 2006. Modeling of rainfall-triggered shallow landslide. Environmental Geology. 50(4):525-534.

Wei, N., Qian, P. Y., Fu, X. D., 2006. Effects of rainfall infiltration and evaporation on soil slope stability. Rock and Soil Mechanics 27(5): 778-786.

Wu, W., Slide, R. C., 1995. A distributed slope stability model for steep forested basins. Water resource Research 31(8):2097-2110.

A Study on Setting Half-life of Effective Rainfall as a Standard of Debris Flow Occurrence by Considering Geology

Naomasa HONDA[1*]

[1] Faculty of Regional Environment Science, Tokyo University of Agriculture
(1-1-1 Sakuragaoka, Setagaya-ku, Tokyo 1568512, Japan)
*Corresponding author. E-mail: nh205379@nodai.ac.jp

This study discusses how to set the half-life of effective rainfall as a standard of debris flow occurrence while also giving consideration to geological conditions. We investigated debris flow disasters at three different Japanese locations (the Osumi district, Nagiso town, and Hiroshima city) and calculated rainfall index *R'*, which expresses the rainfall history with a single value that combines long-term and short-term effective rainfalls. Our results suggest that around 20% of *R'* increases or decreases based on the differences in setting the half-life value by considering geology. However, we need to focus our attention on when the long-term half-life is less than 12 hours (e.g., with such volcanic ash as shirasu), since *R'* considerably decreases when it is calculated under those conditions. Geology greatly influences effective rainfall and *R'* as viewed through half-life. Consequently, precise prediction of debris flow occurrences is expected by incorporating geological feature information in calculating rain indexes.

Key words: effective rainfall, half-life, rainfall index *R'*, geology, debris flow occurrence

1. INTRODUCTION

Generally, both previous prolonged rainfall and the most recent episodic but strong rainfall affect debris flow occurrence [*Yano*, 1990; *Ushiyama et al.*, 2001]. When they act on the ground, which has such inherent factors as weak geological features and topography, and when resistance to sediment-related disasters exhausted, mass movements of material and sediment runoff begins [*Takahashi*, 1977; *Egashira et al.*, 1997]. Studies have been conducted on the relationships among geology, rainfall runoff characteristics, and sediment-related disasters, as well as on establishing rain indexes as warnings of sediment- related disasters [*Suzuki et al.*, 1978; *Kato et al*., 2000; *Kurihara and Yamakoshi*, 2005; *Onda et al*., 2006; *Nakai et al.*, 2007; *Honda et al.*, 2014; *Honda*, 2016].

Kurihara and Yamakoshi concentrated on the relationship between soil storage characteristics and debris flow occurrence, and they performed a runoff analysis using a tank model to determine the half-life of effective rainfall based on geological features [*Kurihara and Yamakoshi*, 2005]. Nakai et al. proposed rainfall index *R'*, which expresses rainfall history with a single value that combines long-term effective rainfall (R_w) and short-term effective rainfall (r_w) [*Nakai et al.*, 2007]. Honda et al. showed that both slope failure occurrence time and *R'* at that time were different for slopes in spite of studying adjacent slopes, and they assumed that this difference originated in the differences in geological features, topography, and covering vegetation [*Honda et al.*, 2014]. In addition, Honda showed that the precision of risk judgment of sediment-related disaster occurrences by *R'* might improve by considering geologic differences, based on previous results of examining debris flow [*Honda*, 2016].

In this study, our purpose is to develop a guideline of the setting half-lives of effective rainfall and rainfall index *R'* as a standard of debris flow occurrence, giving consideration to geology. We investigated debris flow disasters at three different Japanese locations: the Osumi district, Nagiso town, and Hiroshima city, all of which have specific rainfall conditions and geological features.

2. METHOD

2.1 Effective rainfall

Effective rainfall R_t is a standard value used to investigate debris flow occurrences that applies the impact of past rainfall. It is calculated as follows [*Yano*, 1990]:

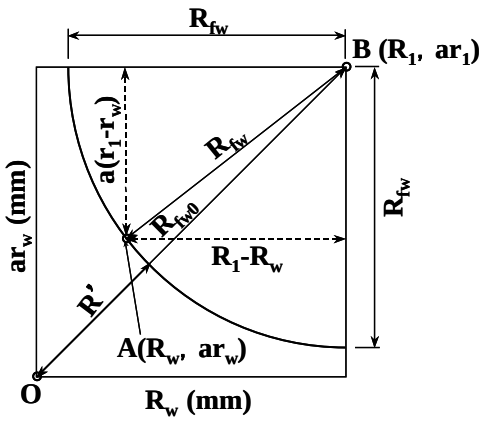

Fig. 1 Rainfall index *R*'

$$R_t = r_t + \sum_{n=1}^{x} a_n r_{t-x} = r_t + a_1 r_{t-1} + \cdots + a_x r_{t-x} \quad (1)$$

$$a_n = 0.5^{n/T} \quad (2)$$

where t is time, r_t is precipitation, a_n is the decrease coefficient, and T is half-life. Generally, for T, the value of 1.5 hours and 72 hours used for short-term and long-term effective rainfall, respectively. In this study, short-term effective rainfall is denoted by r_w, while long-term effective rainfall is denoted by R_w.

2.2 Rainfall index *R'*

Rainfall index *R'* is calculated as follows [*Nakai et al.*, 2007]:

$$R_{fw} = \sqrt{(R_1 - R_w)^2 + a^2 (r_1 - r_w)^2} \quad (3)$$

$$R' = R_{fw0} - R_{fw} \quad (4)$$

where R_{fw} is the long diameter of an oval, R_1 and r_1 are its central coordinates ($R_1 = ar_1$), R_{fw0} is a value for $R_w = r_w = 0$, and a is a coefficient to replace the oval with a circle (**Fig. 1**).

3. COMPUTATIONAL CONDITIONS

3.1 Outline of debris flows

In the Osumi district in Kagoshima Prefecture (**Fig. 2**), several debris flows were caused by the devastating typhoon No. 4 of July 2007. **Table 1** shows the debris flow occurrence time, the surface geology, and the gradient. **Figure 3** shows the observed rainfall data and the debris flow occurrence time at the nearest rainfall gauging station.

Fig. 2 Locations of three actual basins

Table 1 Debris flow occurrence in Osumi district

No.	Occurrence Time	Rainfall gauging	Surface geology	Gradient (degrees)
[1]	7/14 12:00	Kihoku	Shirasu	25～30
[2]	7/11 7:00	Tashiro	Granite	25～35
[3]	7/14 11:00	Tashiro	Shirasu	20～25
[4a]※	7/4 0:00	Sata	Shirasu	20～30
[4b]※	7/11 2:00	Sata	Shirasu	20～30
[5]	7/11 7:00	Sata	Sandstone	15～20
[6]	7/11 9:00	Sata	Shale	25～35

※ [4a] and [4b] are different debris flows on the same slope.

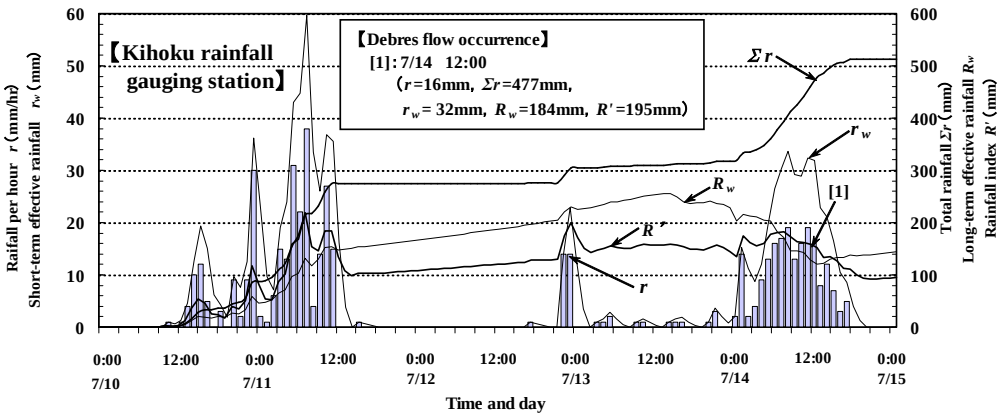

(a) Case of [1]

Fig. 3 Relationship between observed rainfall and debris flow occurrence in the Osumi district
(a = 3, R_1 = 600 mm, and r_1 = 200 mm, which are necessary for calculating R', as shown in section **3.2**)

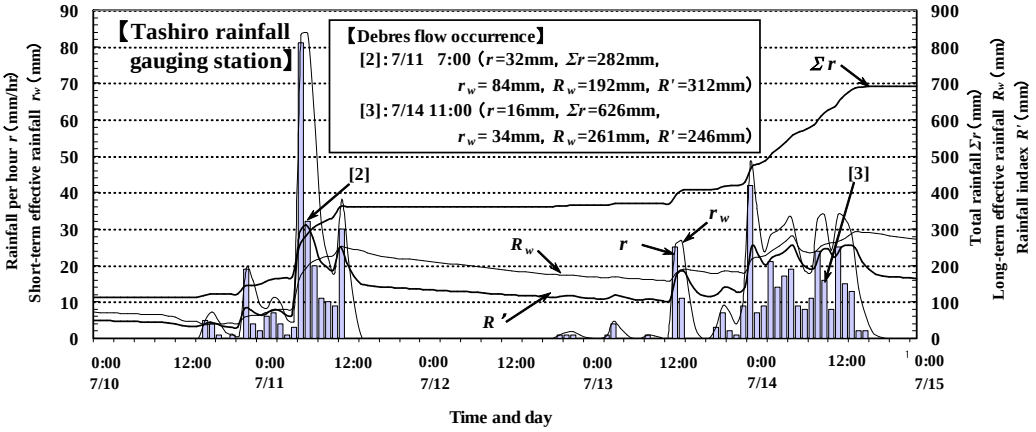

(b) Cases of [2] and [3]

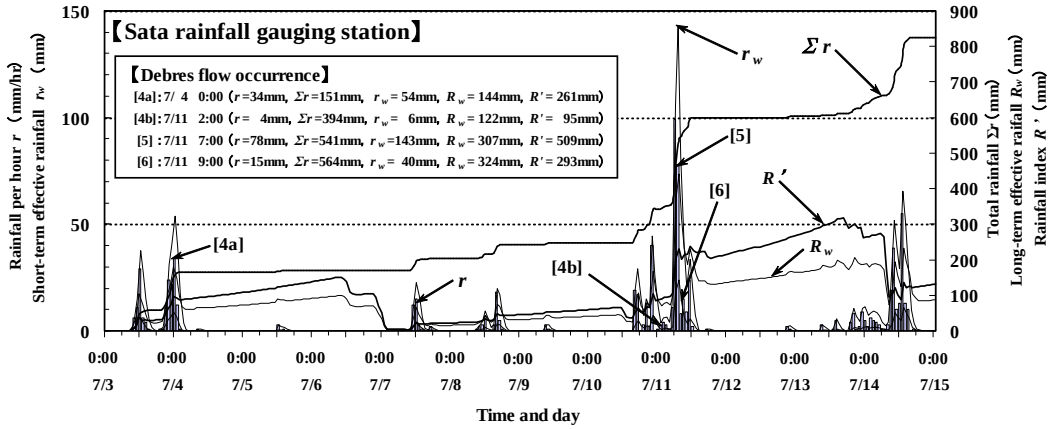

(c) Cases of [4a], [4b], [5], and [6]

Fig.3 (continued) Relationship between observed rainfall and debris flow occurrence in the Osumi district (a = 3, R_1 = 600 mm, and r_1 = 200 mm, which are necessary for calculating R', as shown in section **3.2**)

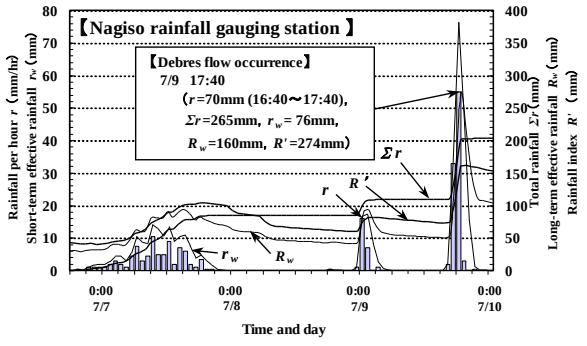

Fig.4 Relationship between observed rainfall and debris flow occurrence in Nagiso town (a = 3, R_1 = 600 mm, and r_1 =200 mm, as shown in section **3.2**)

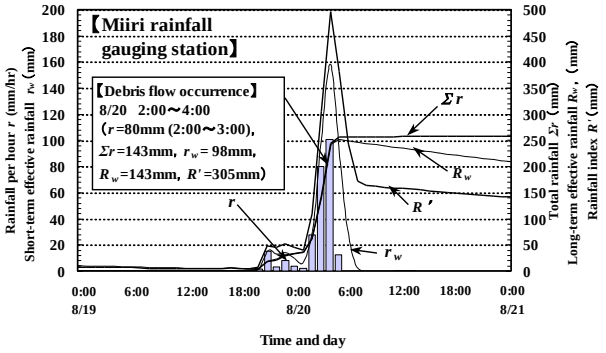

Fig.5 Relationship between observed rainfall and debris flow occurrence in Hiroshima city (a= 3, R_1 = 600 mm, and r_1 = 200 mm, as shown in section **3.2**)

In Nagiso town in Nagano Prefecture (**Fig. 2**), a debris flow was caused by heavy rainfall in July 2014. The surface geology of the debris flow occurrence zone was granite, and the gradient exceeded 30 degrees. **Figure 4** shows the observed rainfall data and the debris flow occurrence time at the nearest rainfall gauging station.

In Hiroshima city in Hiroshima Prefecture (**Fig. 2**), several debris flows were caused by heavy rainfall in August 2014. The surface geology of the debris flow occurrence zone was granite, and the gradient was about 20 degrees. **Figure 5** shows the observed rainfall data and the debris flow occurrence time at the nearest rainfall gauging station.

3.2 Computational conditions

r_w and R_w are calculated based on the observed rainfall data (**Figs. 3**, **4**, and **5**). Here, in reference to previous research (**Table 2**) [*Kurihara and Yamakoshi*, 2005], the condition of the short-term effective rainfall's half-life changed from 30 minutes to 2.0 hours, and the long-term effective rainfall's half-life changed from 3 to 72 hours.

R_1, r_1, and a ($R_1 = ar_1$), are necessary for calculating R', and we can select them in any combination. As a condition of the present study, R_1 should be decided by the value of R_w (cross axis of the graph), which can express all of the calculation results on the same graph for comparison. According to the calculation results, we judged that 600 mm was an appropriate value for R_1.

a is determined by the test calculations that produced R_1 while assuming a. In this study, R_1 is given with 600 mm and a is assumed to be 3, 4 and 5. As a result, a = 3 most closely matches all of the examples on the same graph. The preceding study also used a = 3 [*Nakai et al.*, 2007]. Therefore, we adopted these values: R_1 = 600 mm, a = 3, and $r_1 = R_1/a$ = 200 mm.

Table 2 Half-life of effective rainfall for predicting debris flow occurrence according to geological features [*Kurihara and Yamakoshi*, 2005]

Geology	Half-life (hr)	
	Short-term	Long-term
Granite	1～2	24～48
Sedimentary rock	1～2	12～72
Volcanic ashes	1 or less	12 or less

4. RESULTS AND DISCUSSION

Table 3 shows the calculation results of r_w, R_w, and R' for long-term T=12 hr, 24 hr, 48 hr, and 72 hr. **Figure 6** shows the relationships among r_w, R_w, R', and T by geological features.

In **Fig. 6**, the subscripts of each sign, for example, $R'_{72,\ 1.5}$, are the half-lives used for the calculation. In the vertical axis of **Fig. 6**, no dimensions by values were calculated using general-purpose half-lives (short-term T = 1.5 hours and long-term T = 72 hours), i.e., $r_{w1.5}$, R_{w72}, and $R'_{72,\ 1.5}$.

4.1 Relationships among T, r_w, and R_w

4.1.1 Relationship between T and r_w

As shown in **Table 3**, **Figs. 6(a)(1)**, **(b)(1)**, and **(c)(1)**, when short-term T ranges from 1.0 to 2.0 hours, $r_{wT}/r_{w1.5}$ ranges from 0.72 to 1.17, except for $r_{w1.0}/r_{w1.5}$ and $r_{w2.0}/r_{w1.5}$ of Sata [6] (**Table 3,** $r_{w1.0}/r_{w1.5}$ = 0.48 and $r_{w2.0}/r_{w1.5}$ = 1.50).

In Sata [6] (**Fig. 3(c)**), a brief but strong rainfall of 78 mm per hour fell 2.0 hours before a debris flow. These rainfall data did not influence $r_{w1.0}$, while on the other hand they strongly affected $r_{w.2.0}$.

According to **Table 2**, short-term T of the volcanic ash is less than 1.0 hour. As shown in **Table 3** and **Fig. 6(a)(1)** (for volcanic ash), when short-term T equals 30 minutes, $r_{w0.5}/r_{w1.5}$ ranges from 0.65 to 0.83. Furthermore, when short-term T equals 1.0 hour, $r_{w1.0}/r_{w1.5}$ ranges from 0.72 to 0.83, except for Sata [4b] (**Table 3**, $r_{w1.0}/r_{w1.5}$ = 1.00). These values are considerably smaller than 1.00 (for general- purpose short-term T = 1.5 hours).

Sata [4a] and [4b] have different debris flows on the same slope (identical inherent factors). Since Sata [4b] occurred several days after Sata [4a] (**Table 1** and **Fig. 3(c)**), Sata [4b] might have an occurrence mechanism unlike the others.

4.1.2 Relationship between T and R_w

As shown in **Table 3**, **Figs. 6(a)(1)**, **(b)(1)**, and **(c)(1)**, when long-term T ranges from 24 to 72 hours, R_{wT}/R_{w72} ranges from 0.70 to 1.00, except for Nagiso town (**Table 3**, R_{w24}/R_{w72} = 0.65 and R_{w48}/R_{w72} = 0.69). In Nagiso town, even though a large amount of rain fell three days before the debris flow occurrence (**Fig. 4**), these rainfall data did not influence Nagiso's R_{w24} and R_{w48}.

According to **Table 2**, long-term T of the volcanic ash is less than 12 hours. As shown in **Table 3** and **Fig. 6(a)(1)** (for volcanic ash), when long-term T equals 12 hours, R_{w12}/R_{w72} ranges from 0.56 to 0.74, which is considerably smaller than 1.00 (for general-purpose long-term T = 72 hours).

According to **Table 2**, long-term T of the accretionary complexes ranges from 12 hours to 72 hours. As shown in **Table 3** and **Fig. 6(a)(1)** (for accretionary complexes), when long-term T equals 12 hours, R_{w12}/R_{w72} ranges from 0.66 to 0.73. These results are considerably smaller than 1.00 (for general-purpose long-term T = 72 hours).

4.1.3 Considerations

According to our results, when r_w and R_w are calculated using T in consideration of geology, an increase or decrease of about 20% to 30% occurs in comparison with the results by the general-purpose values of T, except for volcanic ash.

In general, areas with volcanic ash deposits have a low tendency to be penetrated, and both the long-term and short-term half-lives are very small [*Kurihara and Yamakoshi*, 2005]. Moreover, when R' is calculated by these short half-lives rather than by the generally used value of T, it drops by more than 30%. Similarly, for accretionary complexes, R' considerably also decreases when the long-term half-life is less than 12 hours. We must carefully set the half-lives for such geology as volcanic ash and accretionary complexes, and our

Table 3 Examples of calculation results

Long-term T (hr)	Rainfall (mm)	Volcanic ashes (Shirasu)															
		Kihoku [1]				Tashiro [3]				Sata [4a]				Sata [4b]			
		Short-term T (hr)				Short-term T (hr)				Short-term T (hr)				Short-term T (hr)			
		0.5	1.0	**1.5**	2.0	0.5	1.0	**1.5**	2.0	0.5	1.0	**1.5**	2.0	0.5	1.0	**1.5**	2.0
	r_w	21	23	**32**	37	22	28	**34**	38	40	45	**54**	62	5	6	**6**	7
	$r_w/r_{w\,1.5}$	0.66	0.72	**1.00**	1.16	0.65	0.82	**1.00**	1.12	0.74	0.83	**1.00**	1.15	0.83	1.00	**1.00**	1.17
12	R_w	125				147				107				73			
	$R_w/R_{w\,72}$	0.68				0.56				0.74				0.60			
	R'	130	141	156	167	148	162	175	185	160	171	189	204	61	62	64	65
	$R'/R'_{72,\,1.5}$	0.67	0.72	0.80	0.86	0.60	0.66	0.71	0.75	0.74	0.79	0.88	0.94	0.64	0.65	0.67	0.68
24	R_w	145				201				131				86			
	$R_w/R_{w\,72}$	0.79				0.77				0.91				0.70			
	R'	144	155	169	181	182	196	210	221	176	188	206	222	69	71	72	73
	$R'/R'_{72,\,1.5}$	0.74	0.79	0.87	0.93	0.74	0.80	0.85	0.90	0.81	0.87	0.95	1.03	0.73	0.75	0.76	0.77
48	R_w	176				231				140				96			
	$R_w/R_{w\,72}$	0.96				0.89				0.97				0.79			
	R'	164	175	190	202	199	214	228	239	183	195	213	229	77	77	79	80
	$R'/R'_{72,\,1.5}$	0.84	0.90	0.97	1.04	0.81	0.87	0.93	0.97	0.85	0.90	0.99	1.06	0.81	0.81	0.83	0.84
72	$\boldsymbol{R_w}$	**184**				**261**				**144**				**122**			
	$R_w/R_{w\,72}$	**1.00**				**1.00**				**1.00**				**1.00**			
	$\boldsymbol{R'}$	169	180	**195**	208	216	231	**246**	257	185	197	**216**	231	92	94	**95**	97
	$R'/R'_{72,\,1.5}$	0.87	0.92	**1.00**	1.07	0.88	0.94	**1.00**	1.04	0.86	0.91	**1.00**	1.07	0.97	0.99	**1.00**	1.02

Long-term T (hr)	Rainfall (mm)	Accretionary complexes								Granite											
		Sata [5]				Sata [6]				Tashiro [2]				Nagiso				Hiroshima			
		Short-term T (hr)				Short-term T (hr)				Short-term T (hr)				Short-term T (hr)				Short-term T (hr)			
		0.5	1.0	**1.5**	2.0	0.5	1.0	**1.5**	2.0	0.5	1.0	**1.5**	2.0	0.5	1.0	**1.5**	2.0	0.5	1.0	**1.5**	2.0
	r_w	103	128	**143**	154	17	19	**40**	60	52	73	**84**	91	63	72	**76**	79	87	94	**98**	101
	$r_w/r_{w\,1.5}$	0.72	0.90	**1.00**	1.08	0.43	0.48	**1.00**	1.50	0.62	0.87	**1.00**	1.08	0.83	0.95	**1.00**	1.04	0.89	0.96	**1.00**	1.03
12	R_w	224				214				140				88				133			
	$R_w/R_{w\,72}$	0.73				0.66				0.73				0.55				0.93			
	R'	372	414	435	447	178	182	232	277	210	251	272	284	195	211	221	227	267	289	297	303
	$R'/R'_{72,\,1.5}$	0.73	0.81	0.85	0.88	0.61	0.62	0.79	0.95	0.67	0.80	0.87	0.91	0.71	0.77	0.81	0.83	0.88	0.95	0.97	0.99
24	R_w	263				271				156				104				138			
	$R_w/R_{w\,72}$	0.86				0.84				0.81				0.65				0.97			
	R'	402	447	470	483	208	213	265	314	221	262	284	297	207	223	233	239	279	293	301	306
	$R'/R'_{72,\,1.5}$	0.79	0.88	0.92	0.95	0.71	0.73	0.90	1.07	0.71	0.84	0.91	0.95	0.76	0.81	0.85	0.87	0.91	0.96	0.99	1.00
48	R_w	279				294				165				111				140			
	$R_w/R_{w\,72}$	0.91				0.91				0.86				0.69				0.98			
	R'	415	461	485	499	220	225	278	328	228	269	291	304	212	229	238	244	281	295	303	308
	$R'/R'_{72,\,1.5}$	0.82	0.91	0.95	0.98	0.75	0.77	0.95	1.12	0.73	0.86	0.93	0.97	0.77	0.84	0.87	0.89	0.92	0.97	0.99	1.01
72	$\boldsymbol{R_w}$	**307**				**324**				**192**				**160**				**143**			
	$R_w/R_{w\,72}$	**1.00**				**1.00**				**1.00**				**1.00**				**1.00**			
	$\boldsymbol{R'}$	435	483	**509**	524	234	239	**293**	344	246	290	**312**	326	247	264	**274**	280	283	297	**305**	310
	$R'/R'_{72,\,1.5}$	0.85	0.95	**1.00**	1.03	0.80	0.82	**1.00**	1.17	0.79	0.93	**1.00**	1.04	0.90	0.96	**1.00**	1.02	0.93	0.97	**1.00**	1.02

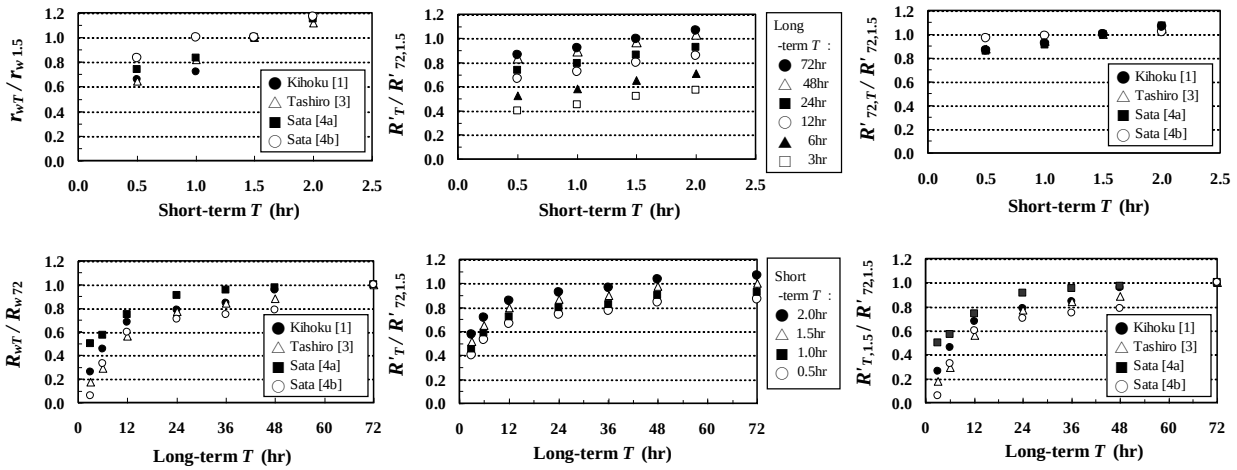

(1) Relationships among T, r_w and R_w (2) Examples of relationship between T and R' (Kihoku [1]) (3) Relationship between $R'_{72,\,1.5}$ and $R'_{T,\,1.5}$ (T : long-term half-life)

(a) Case of volcanic ash (Shirasu)

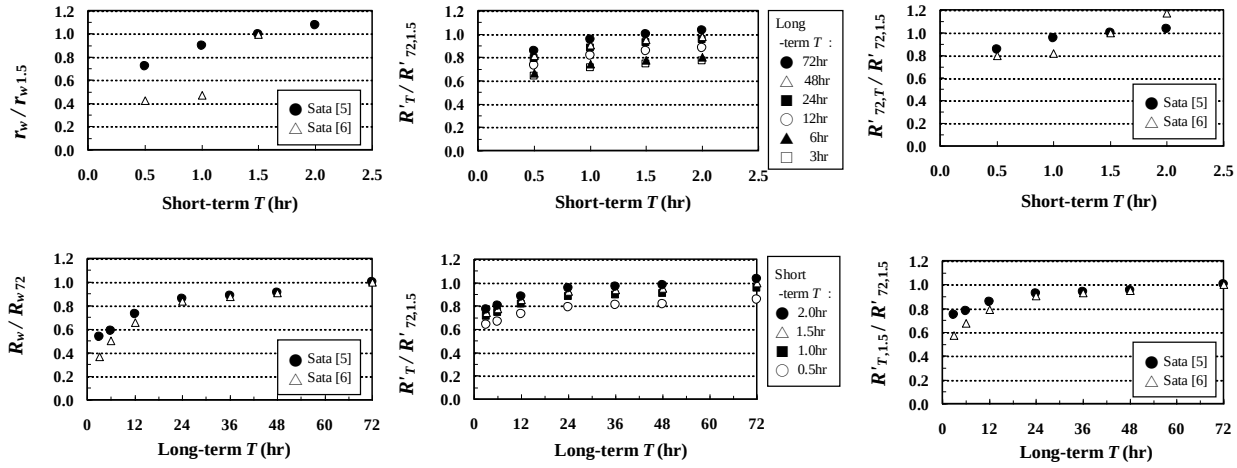

(1) Relationships among T, r_w and R_w (2) Examples of relationship between T and R' (Sata [5]) (3) Relationship between $R'_{72,\,1.5}$ and $R'_{T,\,1.5}$ (T: long-term half-life)

(b) Case of accretionary complexes (sandstone and shale)

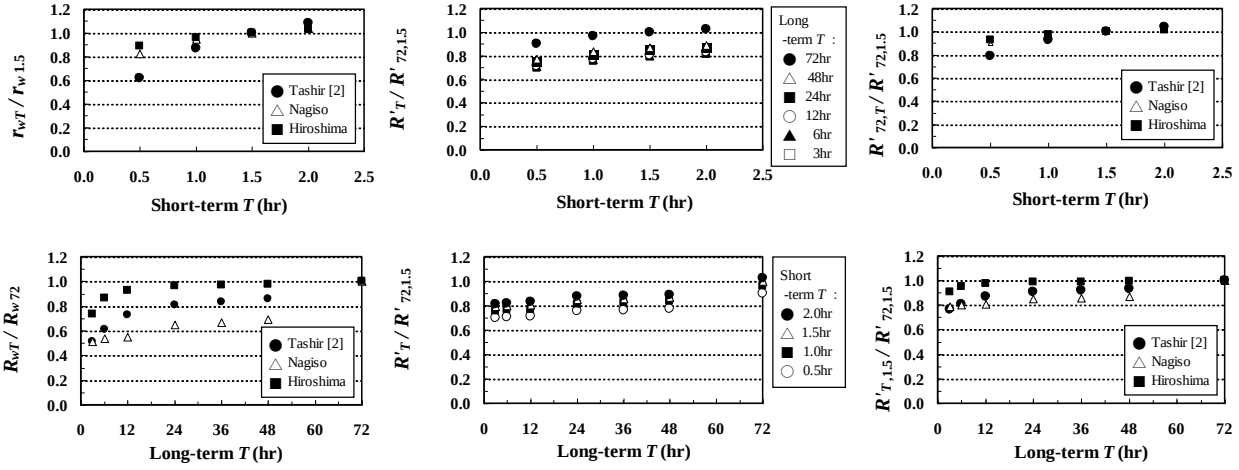

(1) Relationships among T, r_w and R_w (2) Examples of relationship between T and R' (Nagiso) (3) Relationship between $R'_{72,\,1.5}$ and $R'_{T,\,1.5}$ (T: long-term half-life)

(c) Case of granite

Fig.6 Relationships among R_w, r_w, R', and T corresponding to geology

purpose is to develop a guideline of the setting half-lives of effective rainfall while considering geology, although attention must also be given to rainfall conditions before a debris flow occurrence, i.e., episodic but strong rainfall as well as total amount of rainfall.

4.2 Relationships among *T*, *R'*, and geology

4.2.1 Relationship between *T* and *R'*

As shown in **Figs. 6(a)(2)**, **(b)(2)**, and **(c)(2)**, when long-term *T* is constant and short-term *T* ranges from 30 minutes to 2.0 hours, the fluctuation range of $R'_T / R'_{72,\ 1.5}$ with a change in short-term *T* is almost always less than 20%. Similarly, when short-term *T* is constant and long-term *T* ranges from 12 hours to 72 hours, the fluctuation range of $R'_T / R'_{72,\ 1.5}$ with a change in long-term *T* almost always reaches below 20%. These results are slightly smaller than the fluctuation ranges of r_w and R_w with the change in *T* (increase or decrease from about 20% to 30%, Section **4.1.3**), since *R'* expresses the rainfall history by a single value that combines r_w and R_w.

4.2.2 Relationships among *T*, *R'*, and geology

When we focus our attention on the fluctuation range of $R'_T / R'_{72,\ 1.5}$ with a change in long-term *T*, the increase rate of $R'_T / R'_{72,\ 1.5}$ becomes small where *T* = 12 hours is a boundary in **Figs. 6(a)(2)** and **(b)(2)**, i.e., for volcanic ash and accretionary complexes. On the other hand, it is nearly constant in **Fig. 6(c)(2)**, i.e., for granite. Even though volcanic ash and accretionary complexes are not uniform for the rainfall runoff characteristics and the half-life, granite has uniformity [*Kurihara and Yamakoshi*, 2005]. Thus, we assume that the non-homogeneity of the half-life due to geological characteristics influences effective rainfalls and *R'*.

Figures 6(a)(3), **(b)(3)**, and **(c)(3)** show examples of $R'_{72,\ T} / R'_{72,\ 1.5}$ with a change in short- term *T* for long-term *T* = 72 hours and $R'_{T,\ 1.5} / R'_{72,\ 1.5}$ with a change in long-term *T* for short-term *T* = 1.5 hours.

When long-term *T* equals 72 hours, the fluctuation range of $R'_{72,\ T} / R'_{72,\ 1.5}$ with a change in short-term *T* is almost always less than 20%. When short-term *T* equals 1.5 hours, the fluctuation range of $R'_{T,\ 1.5} / R'_{72,\ 1.5}$ with a change in long-term *T* in the range from 12 to 72 hours almost always reaches below 20%, except for **Fig. 6(a)(3)**, i.e., for volcanic ash. In addition, when long-term *T* ranges from 24 to 72 hours, the fluctuation range of $R'_{T,\ 1.5} / R'_{72,\ 1.5}$ with a change in long-term *T* is almost always less than 20%, except for Sata [4b] in **Fig. 6(a)(3)** (**Table 3,** $R'_{24,\ 1.5} / R'_{72,\ 1.5} = 0.76$). The uniqueness of Sata [4b] was mentioned above (section **4.1.1**).

When we focus our attention on the fluctuation range of $R'_{T,\ 1.5} / R'_{72,\ 1.5}$ with a change in long-term *T*, the increase rate of $R'_{T,\ 1.5} / R'_{72,\ 1.5}$ becomes small where *T*=12 is a boundary in **Figs. 6(a)(3)** and **(b)(3)**, i.e., for volcanic ash and accretionary complexes. On the other hand, the fluctuation range is nearly constant in **Fig. 6(c)(3)**, i.e., for granite. They have the same tendency in the case of $R'_T / R'_{72,\ 1.5}$ (**Figs. 6(a)(2)**, **(b)(2)**, and **(c)(2)**). Even though volcanic ash and accretionary complexes are not uniform for the rainfall runoff characteristics and the half-life, granite has uniformity [*Kurihara and Yamakoshi*, 2005]. Thus, we assume that the non-homogeneity of the half-life due to geological characteristics influences effective rainfalls and *R'*.

4.2.3 Considerations

According to the results, when *R'* is calculated using *T* in consideration of geology, an increase or decrease of less than 20% occurs in comparison with the results by the general-purpose values of *T*. However, we excluded the cases where the geological features are comprised of volcanic ash or accretionary complexes and long-term *T* is 12 hours or less. This is our intention when we consider the geological elements of *R'*.

4.3 Example of *R'* for investigating the application range of *T*

Judging from the previous work's results [**4.1**, **4.2**], we assume that short-term *T* in practice ranges from 1.0 to 2.0 hours and long-term *T* ranges from 24 to 72 hours. **Figure 7** shows the relationship between the effective rainfalls of the debris flow occurrence and *R'* curves. The combinations of *T* used for calculation are short-term *T* = 1.0 hour and long-term *T* = 24 hours (none " ' " plots in **Fig. 7**), and short-term *T* = 2.0 hours and long-term *T* = 72 hours (available " ' " plots in **Fig. 7**).

In **Table 3**, the combinations of none " ' " and available " ' " plots in **Fig. 7** range from 0.77 to 1.17 (the increase or decrease is mostly less than 20%) except for Sata [6] ($R' / R'_{72,\ 1.5} = 0.73$) and Sata [4b] ($R' / R'_{72,\ 1.5} = 0.75$). The uniqueness of Sata [6] and Sata[4b] was mentioned above (section **4.1.1**).

In the Osumi district, much of the debris flow occurred in the distribution of such volcanic sediment as shirasu (**Table 1,** Kihoku[1], Tashiro[3], Sata[4a], and Sata[4b]), which is generally not too hard and poor against water. Each *R'* value at the time of a debris flow occurrence was small (**Fig. 7**). Such flow occurrences also occurred in an incline area that ranged from 20 to 30 degrees (**Table 1**).

Spots also exist where each *R'* value at the time of debris flow occurrences was large (**Fig. 7**).

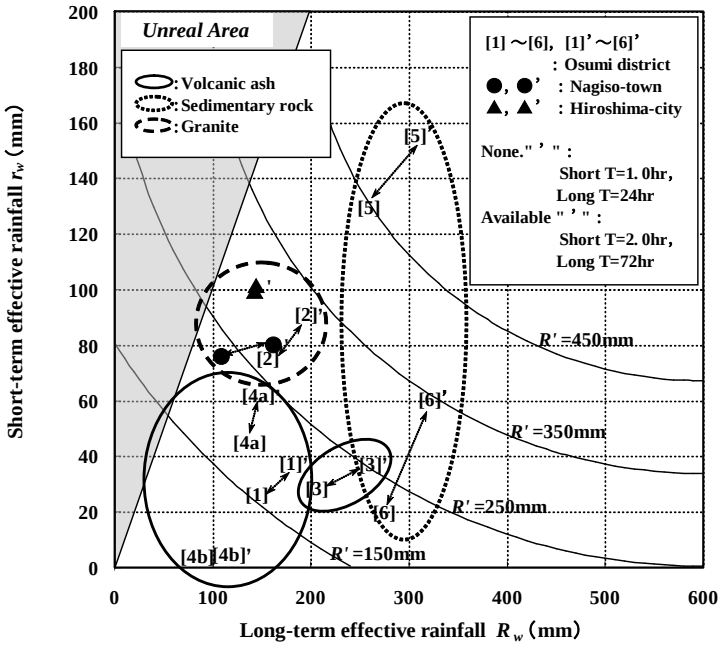

Fig. 7 Relationship between effective rainfalls of debris flow occurrence and curves of *R'*

Their geological features are granite (**Table 1**, Tashiro [2] in the Osumi district, Nagiso town, and Hiroshima city) and sedimentary rock of such accretionary complexes as sandstone and shale (**Table 1**, Sata [5] and Sata [6]). They are harder than volcanic sediment.

For such similar geological features as Sata [5] and Sata [6], *R'* of the latter at the time of debris flow occurrences is smaller than that of the former, and this difference in *R'* is large. This is because the incline of Sata [6] is steep, and it is a weak point for sediment-related disasters.

Figure 7, which considers the application range of *T*, shows a very useful guideline as a standard of debris flow occurrence by *R'*.

5. CONCLUSIONS

This study discussed an approach to establishing the half-life of effective rainfall as a standard of debris flow occurrence. Although we focused our attention on only nine spots, we derived the following conclusions:

(1) When r_w and R_w are calculated using *T* based on geological features, an increase or decrease of about 20% to 30% occurs in comparison with the results obtained by the general-purpose values of *T* (short-term T = 1.5 hours and long-term T = 72 hours), except for such volcanic ash as shirasu.

(2) When *R'* is calculated using *T* based on geological features, an increase or decrease of less than 20% occurs in comparison with the results by the general-purpose values of *T*; however, we excluded the results when the geological features are volcanic ash or accretionary complexes and long-term *T* is 12 hours or less.

(3) (1) and (2) allow us to derive a useful guideline when we investigate the geological composition in relation to *R'*, although we must also give attention to the rain conditions before debris flow occurrences, i.e., episodic but strong rainfall and total amount of rainfall. Furthermore, care is required when the long-term half-life is less than 12 hours.

(4) When the calculation result of *R'*, which considers the application range of *T*, is shown with the *R'* curves, it is a very useful guideline as a standard of debris flow occurrence.

(5) Geology greatly influences effective rainfall and *R'* through half-lives. We expect to precisely predict debris flow occurrences by adding geological feature information to rain indexes.

ACKNOWLEDGMENT: Part of this study was supported by the Strategic Research Project of Tokyo University of Agriculture.

REFERENCES

Egashira, S., Miyamoto, K. and Itoh, T. (1997): Bed-lopd Rate in View of Two Phase Flow Dynamics. Annuals of Hydraulic Engineers, Japan Society of Civil Engineering, Vol.41, pp.789-797 (in Japanese with English abstract).

Honda, N., Kato, N. and Kasai, M. (2014): Relationship between surface failure due to rainfall and geology - Experience of sediment-related disasters in Miyazaki Prefecture due to typhoon No. 4 and No.5 in July 2007 as example -. Journal of the Japan Society of Erosion Control Engineering, Vol. 66(6), pp. 25-30 (in Japanese with English abstract).

Honda, N. (2016): A Study on Relationship among Rainfall, Geology Characteristics and Debris Flow Occurrence. Annuals of Hydraulic Engineers, Japan Society of Civil Engineering, Vol.60, pp.241-246 (in Japanese with English abstract).

Kato, Y., Onda, Y., Mizuyama, T., Kosugi, K., Yoshikawa, I., Tsujimura, M., Hata, K. and Okamoto, M. (2000): The Difference of Runoff Peak Response Time in Upstream of Ibi River Underlain of Different Geology. Journal of the Japan Society of Erosion Control Engineering, Vol. 53(4), pp. 38–43 (in Japanese with English abstract).

Kurihara, J. and Yamakoshi, T. (2005): Study on Effective Rainfall for Prediction of Debris Flow Occurrence Base on Rainfall Runoff Characteristics. Outline of Priority Research Projects Report, Public Works Research Institute, pp.629-634 (in Japanese).

Nakai, S., Kaibori, M., Sasaki, Y. and Moriwaki, T. (2007): Applicability of a New Rainfall Index R' for Recent Cases and Proposal of the Method for Warning against Sediment-related Disaster. Journal of the Japan Society of Erosion Control Engineering, Vol. 60(1), pp. 37–42 (in Japanese with English abstract).

Onda, Y., Tsujimura, M., Tanaka, T., Sasaki, K., Mizuyama, T., Uchida, T., Tainaka, O. and Tanaka, H. (2006): Determining the Criteria Rainfall for Debris Flow Warning and Evacuation by Rainfall-Runoff response. Journal of the Japan Society of Erosion Control Engineering, Vol. 58(5), pp. 13–17 (in Japanese).

Suzuki, M., Fukushima, Y., Takei, A. and Kobashi, S. (1978): The Critical Rainfall for the Disasters Caused by Debris Movement. Journal of the Japan Society of Erosion Control Engineering, Vol. 31(3), pp. 1–7 (in Japanese with English abstract).

Takahashi, T. (1977): A Mechanism of Occurrence of Mud-Debris Flow and their Characteristics in Motion. Annuals of Disaster Prevention Research Institute, Kyoto University, Vol. 20B-2, pp. 405–435 (in Japanese with English abstract).

Ushiyama, M., Ohido, S. and Takara, K (2001): The Critical Line for Sediment Disaster Warning Based on Precipitation Data in Hiroshima Prefecture in June 1999. Advances in River Engineering, Japan Society of Civil Engineering, Vol.7, pp.167-170 (in Japanese with English abstract).

Yano, K. (1990): Study of the Method for Setting Standard Rainfall of Debris Flow by the Reform of Antecedent Rain. Journal of the Japan Society of Erosion Control Engineering, Vol. 43(4), pp. 3-13 (in Japanese with English abstract).

Property of Sediment Movement in Azusa River (Kamikochi)

Akihiko IKEDA[1*], Yuki IGARASHI[1], Osamu FUSHIKI[1], Hiroki UEMORI[1], Shoji IGARASHI[2], Masahide HASEGAWA[3] and Hidenori SAKO[4]

[1] Sabo and Landslide Technical Center, Japan (4-8-21 Kudan-minami, Chiyoa-ku, Tokyo 1020074, Japan)
[2] Kagoshima Prefectural Office
(10-1 Kamoike-Shinmachi, Kagoshima City, Kagoshima 8908577, Japan: Former in Matsumoto Sabo Office, MLIT)
[3] Matsumoto Sabo Office, Hokuriku Regional Development Bureau, Ministry of Land, Infrastructure, Transport and Tourism, Japan
(1-8-28 Motomachi, Matsumoto City, Nagano 3900803, Japan)
[4] Hokuriku Regional Development Bureau, Ministry of Land, Infrastructure, Transport and Tourism, Japan
(1-1-1 Misakicho, Chuo-ku, Niigata City, Niigata 9508801, Japan: Former in Matsumoto Sabo Office, MLIT)
*Corresponding author. E-mail: ikeda@stc.or.jp

Upstream region of Azusa River is widely known as Kamikochi, renowned for its beautiful mountainous scenery. Heavy rain causes sediment discharge including debris flow and significant riverbed aggradation in main stream of the Azusa River that sightseeing facilities were damaged and tourists were isolated due to severed roads and footpaths in the past. The Ministry of Land, Infrastructure, Transport and Tourism (MLIT) has installed rainfall and water level gauges in the entire watershed and observed the actual condition of sediment movement to predict the future river bed changes and sediment discharge. In this paper, we will present the property of sediment movement and rainfall-runoff processes in the upstream region of Azusa River (Kamikochi) based on actual condition of sediment movement and results of monitoring data. The active sediment production and discharge source are identified, and one reason of the riverbed changes (aggradation and degradation) estimated that the riverbed width and meandering with the quantity of the sediment discharge. The sediment movement that causes the riverbed change tends to occur during the flood time.

Key words: Kamikochi, property of sediment movement, monitoring, rainfall-runoff processes

1. INTRODUCTION

The upstream region of the Azusa River in the Shinano River System which runs through the western part of Nagano Prefecture is widely known as Kamikochi, renowned for its beautiful mountainous scenery. Kamikochi is designated not only as the Chubu Sangaku National Park but also as a special place of scenic beauty and a special natural monument in Japan. With Taisho-ike pond located at the foot of Mt. Yakedake (2,455m), an active volcano, as the downstream end, Kamikochi is a grand valley at the elevation of 1,500m that is surrounded by high mountains as much as 3,000m high in the Northern Japan Alps including the Yari-Hotaka range. The watershed area is 112.4 km^2, channel length of the main stream is 17.0km and an average riverbed gradient is 1/55 (the section of Taisho-ike pond to Yokoo is 1/150). The main stream of the Azusa River is braided, while the average riverbed width is approximately 100m, the minimum and maximum riverbed width is approximately 50m and 200m. Significant changes of the riverbed width forms the contraction and expansion section repeatedly.

In the upstream region and the tributary, sediment production and discharge are active due to the steep terrain and fragile geology such as volcanic rocks and granite, as well as severe weather conditions. A massive amount of sediment discharge from these areas and erosion along the main stream cause a significant riverbed aggradation of the main stream. The riverbed has been increased 0.27m on average in the entire main stream between 2003 and 2010 based on LiDAR analysis. Thus, during the flood it is feared that there will be flooding into the important district of Kamikochi consisting of sightseeing and lodging facilities located along the main stream. Furthermore, heavy rain may causes debris flows and sediment discharge from the tributaries and significant riverbed aggradation in main stream that sightseeing

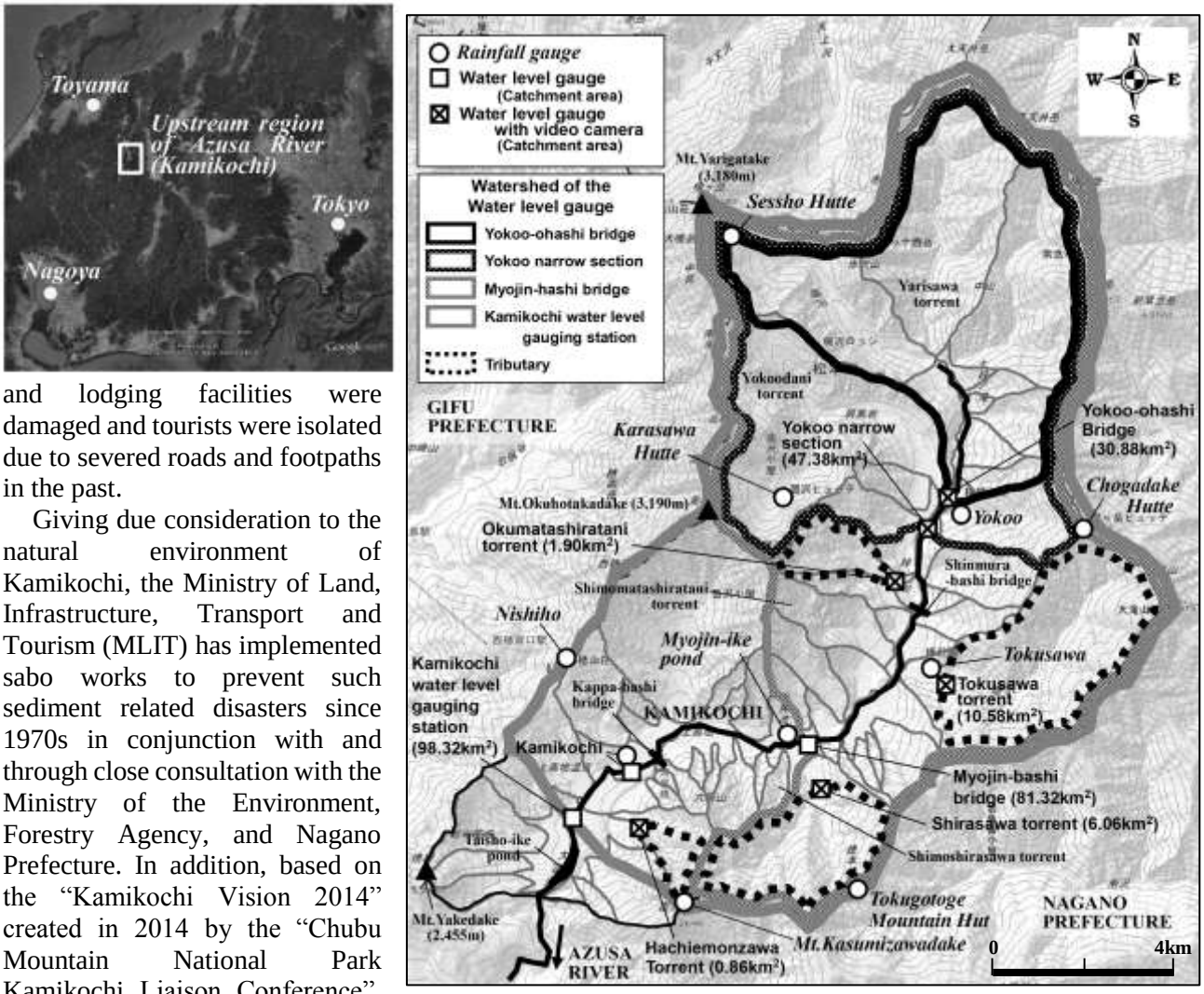

Fig.1 Location of the monitoring sites

and lodging facilities were damaged and tourists were isolated due to severed roads and footpaths in the past.

Giving due consideration to the natural environment of Kamikochi, the Ministry of Land, Infrastructure, Transport and Tourism (MLIT) has implemented sabo works to prevent such sediment related disasters since 1970s in conjunction with and through close consultation with the Ministry of the Environment, Forestry Agency, and Nagano Prefecture. In addition, based on the "Kamikochi Vision 2014" created in 2014 by the "Chubu Mountain National Park Kamikochi Liaison Conference", related organizations including the MLIT have been addressing disaster prevention projects while giving due consideration to the ideal state of Kamikochi. Thus, it is necessary to clarify the actual condition and property of sediment movement in the upstream region of the Azusa River, and predict the future riverbed changes and sediment discharge. In the past study of the Azusa River, the factor of sediment movement such as geology, grain size of riverbed material, structure of riparian forest and its formation, geomorphological dynamics of riverbed including channel shifts were clarified that based on aerial photograph interpretation and field investigation [e.g., *Rees*, 1967; *Shin et.al.*, 1999; *Shimazu*, 2013]. Incidentally, MLIT in cooperation with universities have undertaken field observations of debris flow in Japan at locations where the debris flow occurs frequently, and clarified the flow property of debris flow [e.g., *Takahashi*, 1977; *Suwa et.al.*, 1990; *Ikeda et.al.*, 2003]. However, the rainfall-runoff process and discharge including debris flow that dominates the sediment movement in the entire watershed of the Azusa River are not clarified. To this end, the MLIT observes the rainfall of the entire watershed including ridge lines and the discharge of the main stream and tributary that causes the sediment movement. Based on actual sediment movement and these monitoring results, this study introduces the property of sediment movement and rainfall-runoff processes in the upstream region of the Azusa River (Kamikochi) that has been clarified.

2. OUTLINE OF MONITORING METHOD

In the upstream region of the Azusa River, sediment movements are being monitored to grasp 1) actual condition of sediment movement, 2) conditions dominate the sediment movement, and 3) the effect of sediment movement in the Kamikochi.

The actual condition of sediment movement are observed by aerial photograph interpretation, topography analysis based on LiDAR (1m mesh) in the entire watershed, and riverbed cross-sectional surveying, and field investigations along the main

stream and tributaries since 1975.

The rainfall and discharge, which dominates the sediment movement, are observed by installing rainfall gauges and water level gauges since 1981. Rainfall gauges are installed at 6 locations in the mountain huts and ridge lines (elevation around 2,000m; Sessho Hutte, Karasawa Hutte, Chogadake Hutte, Nishiho, Tokugotoge Mountain Hut and Mt.Kasumizawadake), and 4 locations along the main stream in the grand valley (elevation around 1,500m; Yokoo, Tokusawa, Myojin-ike pond and Kamikochi). Rainfall gauges in the ridge line are used for observation only when the mountain huts are open (for 5 months of the non-snow season). Water level gauges are installed at 4 locations in tributaries where sediment discharge flow into the main stream is significant (Okumatashiratani torrent, Tokusawa torrent, Shirasawa torrent and Hachiemonzawa torrent), and 5 locations in the main stream from upstream to downstream (Yokoo-ohashi bridge, Yokoo narrow section, Myojin-bashi bridge, Kamikochi and Kamikochi water level gauging station). At Okumatashiratani torrent, Tokusawa torrent, Shirasawa torrent, Hachiemonzawa torrent, Yokoo-ohashi bridge and Yokoo narrow section, the video camera has also installed for observing the flow condition. The discharge of main stream is calculated according to the relationship between the water level and discharge (H-Q formula) and the discharge of tributaries according to Manning's formula.

Herewith, spatial distribution of rainfall and discharge from the upstream (sediment production source) to downstream (sediment deposition area) in the entire watershed of upstream region of Azusa River became clear. The location of monitoring equipment is shown in **Figure 1**.

3.ACTUAL CONDITION AND PROPERTY OF SEDIMENT MOVEMENT

Based on observed and investigation results since 1975, sediment discharge that flow into the main stream frequently were confirmed such as Yokoodani torrent, Okumatashiratani torrent, Shimomatashiratani torrent, Tokusawa torrent, Shirasawa torrent, Shimoshirasawa torrent and Hachiemonzawa torrent. Especially, in Yokoodani torrent, Okumatashiratani torrent and Hachiemonzawa torrent are characterized by huge amount of sediment discharge flow into the main stream as debris flow.

Figure 2 shows the average riverbed variation from 1975 to 2017 of the main stream. In this period, 4 large-scale flood occurred in 1979, 1983, 1993 and 2006 that caused inundation damage and also eroded mountain trail and road along the riverbank in the upstream. In the section of Yokoodani torrent to Yokoo narrow section that is the upstream end of the main stream, significant riverbed degradation caused by 1993 flood but no major riverbed change causes since then. At the junction of Okumatashiratani torrent, huge amount of sediment discharge flows out forming a wide debris fan that causes the expansion in the main stream. Furthermore, this fan blocks the main stream and causes a riverbed aggradation in the upstream toward Yokoo narrow section. Along with this, downstream section of this fan toward Shinmura-bashi bridge that is the contraction point, significant riverbed degradation has caused. In the section of Shinmura-bashi bridge to Tokusawa torrent that little change in the riverbed width, 1993 flood flushed out the riverbed deposit and causes significant riverbed degradation, no major riverbed

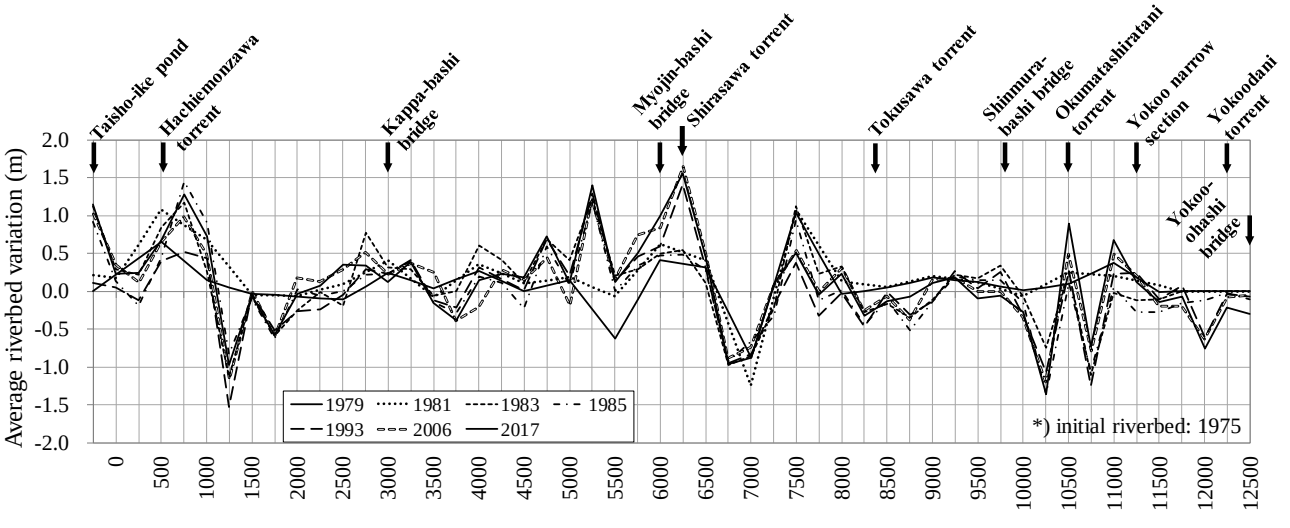

Fig.2 Average riverbed variation from 1975 to 2017

Table 1 Flood event at Kamikochi in recent years

Date of flood event	Rainfall condition							Discharge condition		
	Maximum hourly rainfall (mm/hr)			Continuous rainfall (mm)			Duration of rainfall (hr)	Peak Discharge (m^3/s) [Specific discharge ($m^3/s/km^2$)]		
	Kamikochi	Yokoo	Ridge line	Kamikochi	Yokoo	Ridge line		Yokoo-ohashi bridge	Yokoo narrow section	Kamikochi
July 1st, 2015	7.0	12.5	8.0	52.0	111.0	71.0	18	51.27 [1.66]	41.45 [0.87]	100.68 [1.24]
October 2nd, 2015	20.0	8.5	26.0 (Karasawa Hutte)	56.0	27.0	167.5 (Karasawa Hutte)	21	46.71 [1.51]	34.68 [0.73]	69.29 [0.85]
May 11th, 2016	9.0	10.0	–	64.0	100.5	–	18	48.01 [1.55]	–	114.71 [1.41]
June 25th, 2016	16.5	13.5	29.0 (Karasawa Hutte)	83.5	139.0	158.0 (Karasawa Hutte)	17	61.55 [1.99]	–	127.67 [1.57]
September 18th, 2016	13.0	14.0	32.0 (Karasawa Hutte)	175.0	231.0	418.5 (Sessho Hutte)	33	32.40 [1.05]	–	81.21 [1.00]
July 1st, 2017	19.0	21.0	16.0	362.0	583.5	381.0 (Nishiho)	127	96.54 [3.13]	92.12 [1.94]	206.91 [2.49]
September 7th, 2017	8.5	13.0	25.0 (Sessho Hutte)	112.0	164.0	325.5 (Sessho Hutte)	52	52.23 [1.69]	23.81 [0.50]	85.90 [1.06]

Fig.3 Installation of rainfall and water level gauges

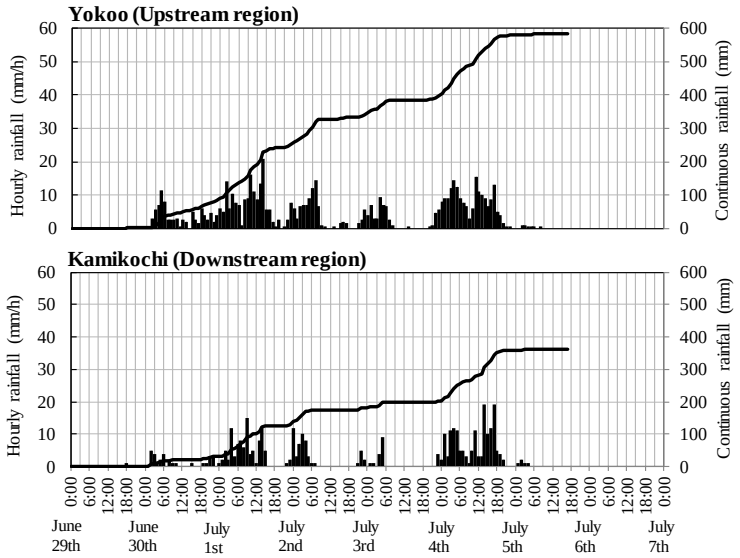

Fig.4 Rainfall condition during the flood on July 1st to 4th in 2017

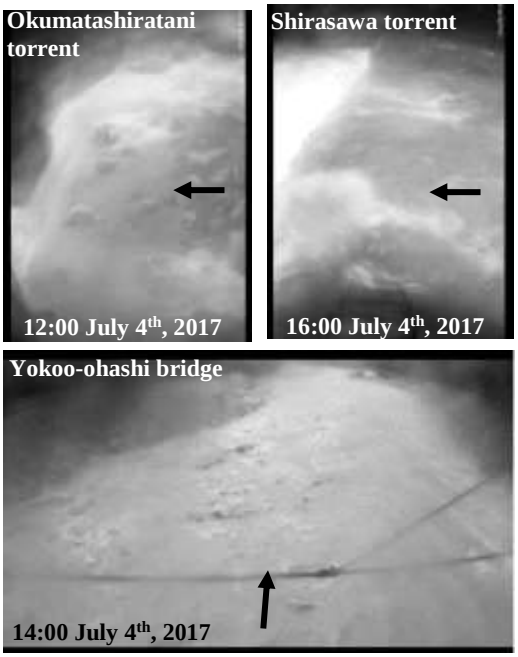

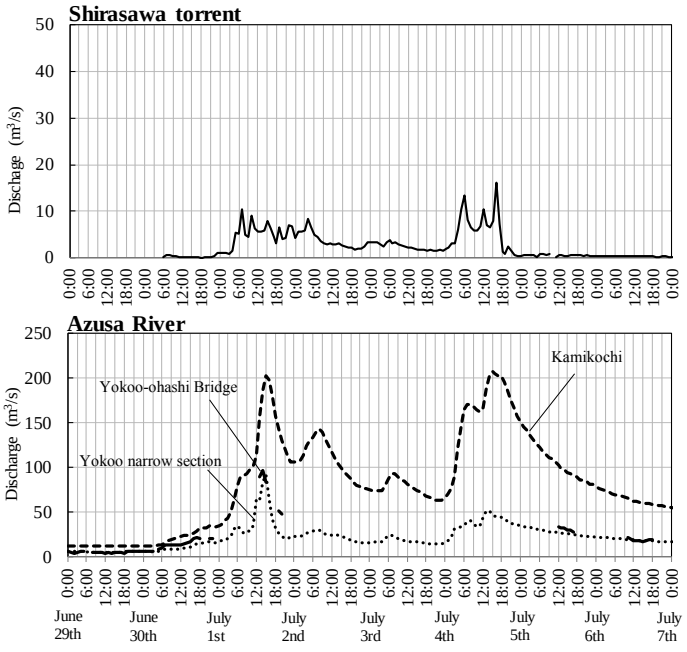

Fig.5 Time changes of discharge and flow condition during the flood on July 1st to 4th in 2017

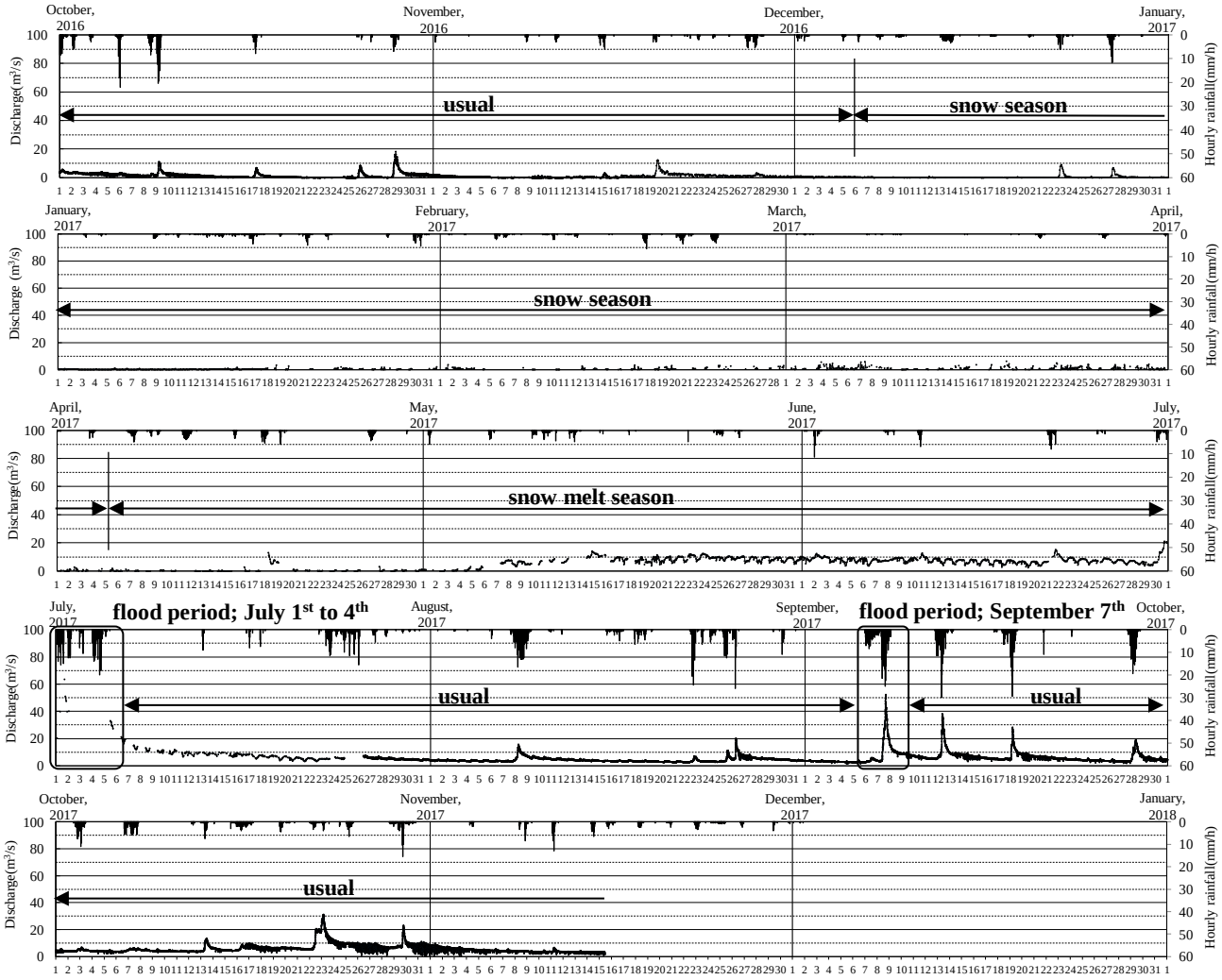

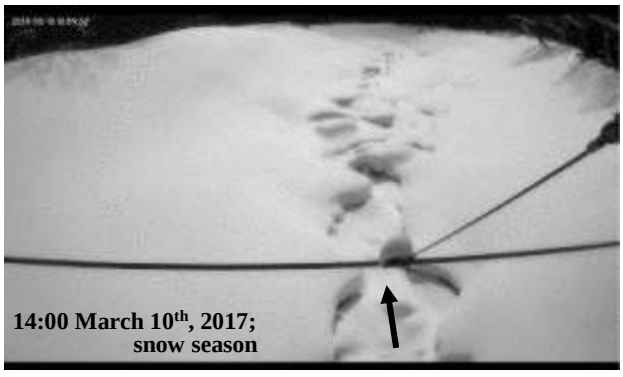

Fig.6 Time changes of discharge and flow condition during October, 2016 to November, 2017 at Yokoo-ohashi bridge

change causes since then. In the section of Tokusawa torrent to Shirasawa torrent that is the contraction section, 1979 flood flushed out the riverbed deposit that has been stored gradually since 1975 flood, and no major change causes since then. In the section of Shirasawa torrent to Kappa-bashi bridge riverbed aggradation causes gradually until 2006 while no major change causes in the next decade.

4. PROPERTY OF RAINFALL-RUNOFF PROCESS

4.1 Property of rainfall-runoff process during flood

Table 1 shows the outline of flood events that occurred in 2015 to 2017, after the installation of the rainfall gauges at the ridge line and water level gauges in the tributary (**Figure 3**). The flood is defined that more than 20mm of hourly rainfall, 80mm of continuous rainfall, 50m^3/s of discharge at Yokoo-ohashi bridge and 100m^3/s of discharge at Kamikochi water level gauging station. In Kamikochi, the movement of heavy rain area during the flood tends to move west to east or southwest to northeast in the past floods influence of the movement of the seasonal rain front or typhoon. We focused on the flood occurred on July 1st, 2017 (hereinafter called 2017 flood) that the largest peak discharge in the past and significant sediment movement has been confirmed.

Figure 4 shows the rainfall condition during the 2017 flood at Yokoo and Kamikochi rainfall gauge that locates in the upstream and downstream along the main stream because of that rainfall gauges of the ridge line has not been installed because of the snow cover during the flood. Both of the maximum hourly rainfall precipitation is approximately 20mm/hr and rainfall waveform is similar, while continuous rainfall precipitation of Yokoo (583mm) is 1.6 times that of Kamikochi (362mm). Incidentally, hourly and continuous rainfall precipitation of the ridge line is almost 2 or 3 times that of the main stream in the grand valley is confirmed at the past flood events.

Figure 5 shows the time changes of discharge at main stream of Azusa River from upstream to downstream and Shirasawa torrent, with the images of flow condition in Okumatashiratani torrent, Shirasawa torrent and Yokoo-ohashi bridge. It was not clear by the waveform of rainfall, but two clear peaks of discharge were confirmed on July 1st (first peak) and July 4th (second peak). As for the first peak, the discharge and turbidity started to increase simultaneously and rapidly 3 hours later after beginning of rainfall, that the waveform shape is similar to rainfall with good responsiveness at Shirasawa torrent. On the other hand, the discharge started to increase gradually 2 hours later after beginning of rainfall at Yokoo-ohashi bridge and Yokoo narrow section, while 4 hours later at Kamikochi water level gauging station. After that the discharge stared to increase rapidly with the rainfall, while the waveform shape differs after the peak from the rainfall that influence of the subsurface runoff. The peak discharge of Yokoo-ohashi bridge, Yokoo narrow section and Kamikochi water level gauging station that locates upstream to downstream of the main stream is 96m^3/s, 92m^3/s and 202m^3/s, and the specific discharge is 3.13m^3/s/km^2, 1.94m^3/s/km^2 and 2.49m^3/s/km^2 (**Table 1**). Kamikochi water level gauging station has a discharge almost twice that of Yokoo-ohashi bridge, and that of the peak appearance time delayed for 2 hours. In spite of Yokoo narrow section locates downstream and watershed area is larger than Yokoo-ohashi bridge, the peak discharge and specific discharge is smaller than Yokoo-ohashi bridge.

4.2 Property of annual runoff process

In Kamikochi it begins to snow from around December and covered with snow until May, while that start to melt around April, so that it is covered by snow through the half of year. **Figure 6** shows the time changes of discharge and flow condition during October, 2016 to November, 2017 at Yokoo-ohashi bridge. The time changes of discharge roughly divided into 4 periods according to the season, such as usual, flood period, snow season (December to April) and snow melt season (April to June). The average discharge at Yokoo-ohashi bridge is approximately 2-5m^3/s as usual, less than 3m^3/s in the snow season, and 2-3m^3/s during the early snow melt season with 10m^3/s in late period. During the snow melt season, as the temperature changes, the discharge is changing in the day. Such a trend is confirmed at Kamikochi water level gauging station, Tokusawa torrent and Shirasawa torrent. At Kamikochi water level gauging station downstream end of the main stream, the average discharge is approximately 5-10m^3/s as usual, 3-4m^3/s in the snow season, and approximately 5m^3/s during the early snow melt season with 10-25m^3/s in late period.

5. CONCLUSIONS

The upstream region of the Azusa River (Kamikochi) is an aggrading braided river that is characterized by the significant changes of the riverbed width that forms the contraction and expansion section, and the meandering. Based on the actual condition of the long-term sediment movement

including the flood event and results of monitoring data, property of the sediment movement, rainfall-runoff process during flood and annual runoff process became clear as follows:

(1) Main active sediment production and discharge source in upstream region of the Azusa River is the riverbed deposit in the main stream, and tributaryies such as Yokoodani torrent, Okumatashiratani torrent, Shimomatashiratani torrent, Tokusawa torrent, Shirasawa torrent, Shimoshirasawa torrent and Hachiemonzawa torrent.

(2) Yokoodani torrent, Okumatashiratani torrent and Hachiemonzawa torrent are characterized by huge amount of sediment discharge flow into the main stream as debris flow forming a wide debris fan that causes the expansion or blockage.

(3) Significant riverbed changes (aggradation and degradation) has confirmed at the contraction and expansion that the riverbed width changes and the meandering, especially at the junction of the tributary. It is estimated that one of the reason of riverbed changes due to the riverbed width and meandering because of almost no changes in the riverbed gradient in the main stream.

(4) Rainfall precipitation is different between upstream and downstream, and also in the grand valley and ridge line. It tends to be larger at the ridge line that depends on the elevation.

(5) Along the main stream, peak discharge tends to be large at the downstream, while the specific discharge is small. It is estimate that one reason of the loss of discharge is the influence of the infiltration to the riverbed deposit.

(6) Based on the monitoring data during April 2015 to November 2017, sediment movement that causes the riverbed change tends to occur during the flood time, and the sediment movement increases significantly according to the discharge.

On the other hand, because of the monitoring period is short and the scale of observed floods was relatively small, there are challenges to be addressed that to monitoring continually, examining the H-Q formula and the property of the sediment movement during large-scale flood as the design scale of sabo works. In addition, we are now preparing the numerical simulation model that can predict the future riverbed changes and sediment discharge, and also evaluate the effect of sediment movement, so that it is necessary to calculate the quantity of sediment yield and production in the tributaries throughout the year including flood period.

ACKNOWLEDGEMENT: Authors should be thankful for the kind advices provided by Prof. Masaharu FUJITA, Prof. Shinya HIRAMATSU, Prof. Keisuke SUZUKI and Dr. Hikaru KITAHARA as the member of study committee for discussing the mechanism of sediment movement in the upstream region of the Azusa River (Kamikochi).

REFERENCES

Rees, D.G.T. (1967): A Study of the Movements of Bed-sediment along Azusa River, Japan, Geographical Reports of Tokyo Metropolitan University, 2, pp.29-40.

Shin, N., Ishikawa, S. and Iwata, S. (1999): The mosaic structure of riparian forest and its formation pattern along the Azusa River, Kamikochi, Central Japan, Japanese Journal of Ecology, 49, pp.71-81 (in Japanese with English Abstract).

Shimazu, H. (2013): Interannual Landform Changes and Formation of Environmental Diversity in the Riverbed at the Upper Reaches of the Azusa River, Central Japan, Journal of Geography, Vol.122, No.4, pp.709-722 (in Japanese with English Abstract).

Takahashi, T. (1977): A Mechanism of Occurrence of Mud-Debris Flows and their Characteristics in Motion, Annuals of Disaster Prevention Research Institute, Kyoto University, 20B-2, pp.405-435 (in Japanese).

Suwa, H. and Okunishi, K. (1990): Motion, Debris Size and Scale of Debris Flows in a valley on Mount Yakedake Japan, Annuals of Disaster Prevention Research Institute, Kyoto University, 33B-1, pp.191-203 (in Japanese with English Abstract).

Ikeda, A. and Hara, Y. (2003): Flow properties of debris flows on the Kitamata Valley of the Name River, Japan, Debris-Flow Hazards and Mitigation: Mechanics, Prediction and Assessment, Rickenmann & Chen (eds), pp.101-112.

Analysis and Reconstructed Modeling of the Debris Flow Events on the 29th of August and the 4th of September 2016 of Afritz (Carinthia, Austria)

Claudia SAUERMOSER[1*], Markus MOSER[2] and Susanne MEHLHORN[2]

[1] Regional Headquarters Carinthia Northeast, Austrian Service for Torrent and Avalanche Control, Austria
[2] Department of Torrent Processes, Austrian Service for Torrent and Avalanche Control, Austria
*Corresponding author. E-mail: claudia.sauermoser@die-wildbach.at

Afritz, a small village located on the debris cone of the Tronitzer Torrent, was hit two times by subsequent debris flows on the 29th of August and on the 4th of September 2016. These events caused damages to residential buildings and other infrastructural facilities. A detailed event documentation and analysis was carried out to understand the extreme processes and to reconstruct and simulate two-dimensionally the debris flows itself with FLO-2D and RAMMS. Beside surveys in the field after both events, an airborne laser scan (ALS-Data) was used to determine the amount and depth of erosion during the events. The protection measures for the village of Afritz were planned immediately after the events on the basis of the analysis results. They are currently under construction.

Key words: debris flow, event documentation, event analysis, FLO-2D, RAMMS, DEM of Difference (DoD)

1. INTRODUCTION

On the 29th of August and on the 4th of September 2016 Afritz, a small village located on the debris cone of the Tronitzer Torrent was hit two times by subsequent debris flows, this caused damages to residential buildings and other infrastructural facilities. The aim of the detailed event documentation and analysis was to understand the extreme process sequence. The purpose of the two-dimensionally simulations with FLO-2D and RAMMS of the debris flow itself was to calibrate input parameters for further simulations in similar torrents. Also the comparison of the two models should give more information which model fits better for this kind of process type. The protection measures for the village of Afritz were planned on the basis of the collected data for the event analysis. They are currently under construction whereby the sediment control dam and the control measures in the lower reach were nearly finished at the end of 2017.

2. STUDY SITE

The catchment area of the Tronitzer Torrent, with a size of 1.99 km², is located in the Nock Mountains,

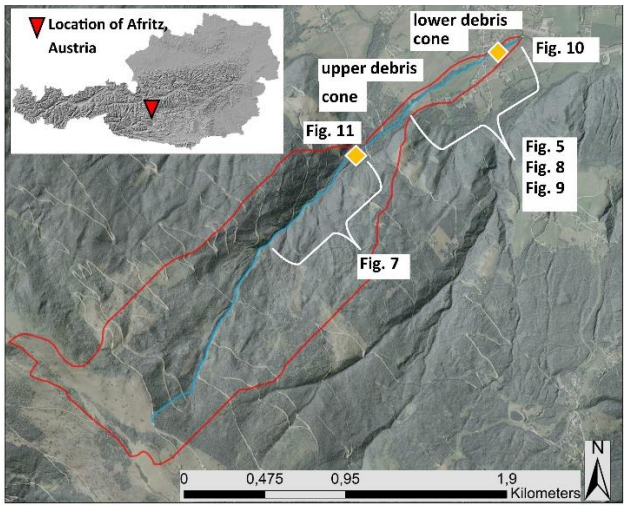

Fig. 1 Catchment area of the Tronitzer Torrent including the location of figures, upper and lower debris cone

the westernmost part of the Gurktal Alps in Carinthia, Austria **(Fig. 1)**. The catchment area extends from 720 m to 1,844 m above Adriatic Sea level and is exposed towards Northeast. Paragneiss and mica schist dominate in the upper and middle catchment and the bedrock is covered by moraines in the middle part of the catchment. The average slope is about 35 % in the upper reach, between 35 % and 50 % in the middle reach, between 15 % and 20 % in the upper debris cone and between 10 % and 15 % in the

lower debris cone.

The annual precipitation rate at the weather station in Afritz (715 m above Adriatic Sea level) is 1,005 mm and the maximum one-day-precipitation is 127.7 mm (29/08/2003) since 1970. 75 % of the total catchment area is covered by forest, mainly by spruce. At the time of the debris flow events no protection measures were implemented at the Tronitzer Torrent.

3. METHODS

3.1 Data Collection

To analyze the triggering precipitation events on the 29th of August and the 4th of September INCA (Integrated Nowcasting through Comprehensive Analysis) data were used.

After both events, comprehensive documentation works were performed from the head along the channel and down to the fan. At the fan sediment deposition was mapped, grain-size distribution was measured and the damages on residential buildings were documented. To determine the discharge, cross-sections were measured along the channel accessible areas after the events. In addition, several helicopter flights were carried out.

After the second event, an airborne laser scan was carried out over the entire catchment area in order to determine how much debris was eroded. The generated DEM was then compared with the existing DEM (DEM of Difference (DoD)) with a 1-m-resolution created in 2014.

3.2 Model description

In addition to the event documentation in the field, an attempt was performed to reconstruct the first debris flow with FLO-2D and RAMMS::DEBRIS FLOW.

Numeric models of debris flows have uncertainties because of the complexity of the processes. The results show a range of possible flow directions, depths and velocities. The advantage of well-known events, such as the one from August 29th at the Tronitzer Torrent, is that the input parameters are based on measured data in the field. The second debris flow was not reconstructed because the data basis was too strongly influenced by the traces of the first debris flow.

3.3. Model parameters

The ALS-Data (1x1 m), the surface areas of the buildings on the debris cone, the bed roughness and a reconstructed sedigraph served as input data.

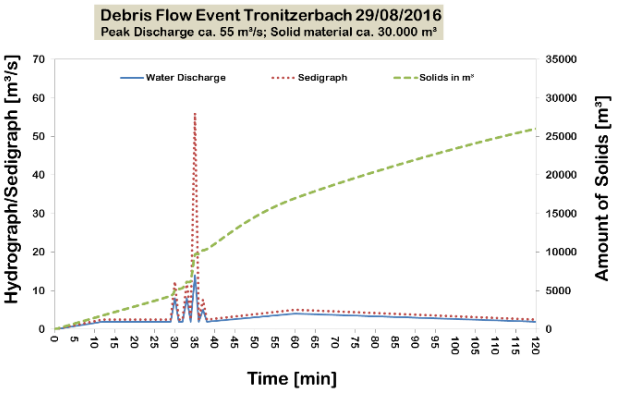

Fig. 2 Hydrograph as input parameter for FLO-2D and RAMMS with a peak discharge of 55 m³/s and a max. bed load of 30,000 m³

For both models a grid size of 1.5x1.5 m was used. The Manning coefficients for FLO-2D were determined on the basis of the field survey. As a basis for the estimation of the sedigraph **(Fig. 2)**, the documented outcomes from the event analysis (reconstructed impact boundaries based on the silent witness, debris flow peak discharge, analyzed event time for event-duration, debris flow mass) were used.

Out of several parameter combinations the BEST-FIT variations was defined. It was obtained by recommended parameters and optimized by several trials.

The main rheological parameters for the FLO-2D model based on the Bingham model are shear stress and Bingham viscosity. Parameter were selected depending on the sediment concentration [*Kaitna et al. 2015]*. Shear stress τ_y *(1a)* and Bingham viscosity *(1*b) are defined by the following equations with α_1 = 0.0005, β_1 = 27.4, α_2 = 0.0336, β_2 = 16 and c_v(%) between 0.2 and 0.75.

$$\tau_y = \alpha_1 e^{\beta_1 c_v} \qquad (1a)$$

$$\mu = \alpha_2 e^{\beta_2 c_v} \qquad (1b)$$

For RAMMS friction parameters *[Schraml K. et al. 2015*] variations were used for μ between 0.05 and 0.15 and for friction parameter ξ between 200 and 300. The Best-Fit-Combination for RAMMS was with μ = 0.10, ξ = 200, stopping criteria of 15 % and a velocity of 6 m/s.

For both models a debris flow density of 1,700 kg/m³ was assumed. Using the Austrian Standards ONR 24801 the debris flow type may be categorized as a muddy debris flow with low sediment concentration.

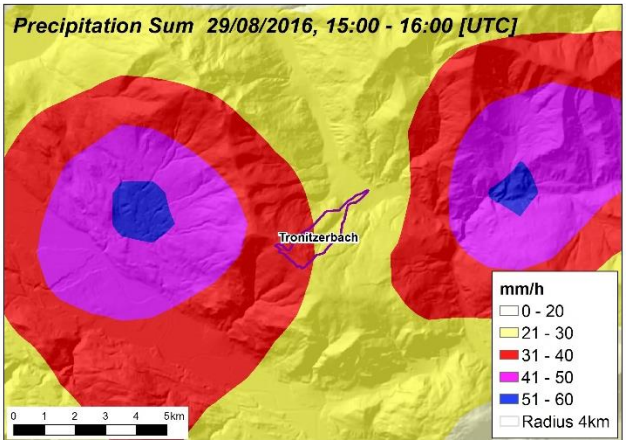

Fig. 3 INCA data: precipitation sum on the 29th of August 2016 [15:00 – 16:30 UTC, yellow ~ 20mm, dark blue ~ 55mm]

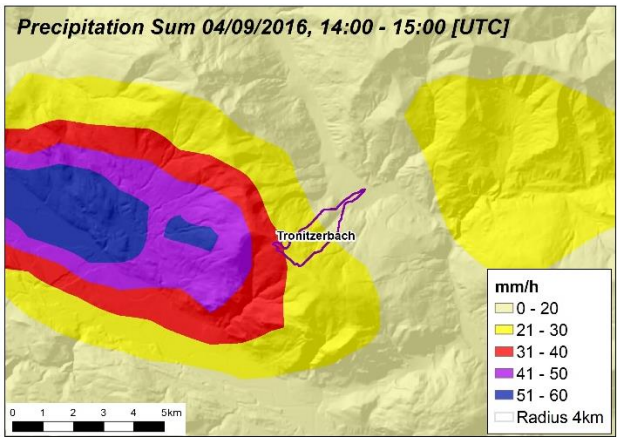

Fig. 4 INCA data: precipitation sum on the 4th of September 2016, [14:00 – 15:00 UTC, yellow ~ 20mm, dark blue ~ 55mm]

4. HYDROLOGY AND METEOROLOGY

In order to analyze the triggering event, INCA data, based on radar data calibrated by observation stations, were used [*Moser and Mehlhorn*, 2016]. Due to frequent convective rainfall during summertime, the soil was almost saturated.

Heavy precipitation on the 29th of August started at 15:00 [UTC]. The INCA data show two thunderstorm cells, which encircled the catchment area and led to the first debris flow. The main direction of the thunderstorm cells was from Northwest to Southeast. The highest intensity inside the catchment was about 11 mm/15 min, increasing to the western border of the catchment to 19 mm/15min. This led to a precipitation between 27-35 mm in the middle and in the western part up to 55 mm **(Fig. 2)**. After one hour the precipitation decreased.

The precipitation for the second event was slightly higher, with 13 to 33 mm, and again for the middle and the western part up to 58 mm. The highest measured intensity was 20 mm/15 min **(Fig. 3)**.

Similar to the first event two thunderstorm cells circled around the catchment area.

Additional to the high precipitation, hail was reported in the upper part of the catchment during the second event. A massive surface runoff was observed during both events. Even a few days after the debris flow events, signs of surface runoff were visible.

5. EVENT DESCRIPTION AND PROCESS SEQUENCE

On August 29th, at around 15:00 [UTC] the first debris flow hit the village of Afritz. After that several much smaller debris flows were observed until midnight. A helicopter flight was carried out on the next day, which showed a superficial landslide triggered by a drainage pipe of a forest road. Above this forest road there is mostly alpine pasture. Signs of an extreme surface runoff were observed in this part of the catchment even a few days after the event.

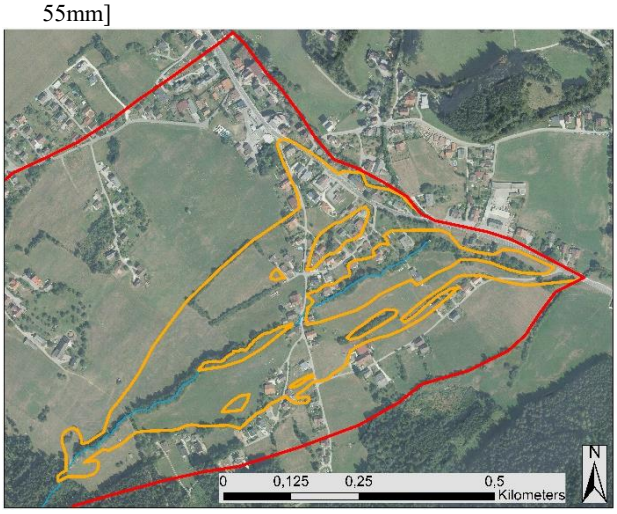

Fig. 5 Deposition area [orange] of the first debris flow on the 29th of August 2016 at the debris cone [red]

Starting in the very upper part of the catchment a massive lateral and vertical erosion happened that initiated a debris flow in the middle reach of the Tronitzer Torrent and spread out at the fan. One reason might be wood close to and in the torrent bed which probably formed blockages, ultimately leading to an outburst from the torrent bed.

At the fan, the maximum deposition depth of debris was about 1.10 m with grain sizes up to 1.0 m in the upper part. In total, an area of about 0.15 km² was covered by debris **(Fig. 5)**. For the first event approximately 25,000 – 30,000 m³ material was deposited at the cone.

Within one week, precisely on the 4th of September 2016, the second debris flow occurred at about 14:00 [UTC]. Due to the open banks caused by the first debris flow, around the same amount of

Fig. 6 Damaged buildings after the 2nd debris flow on 4th of September 2016

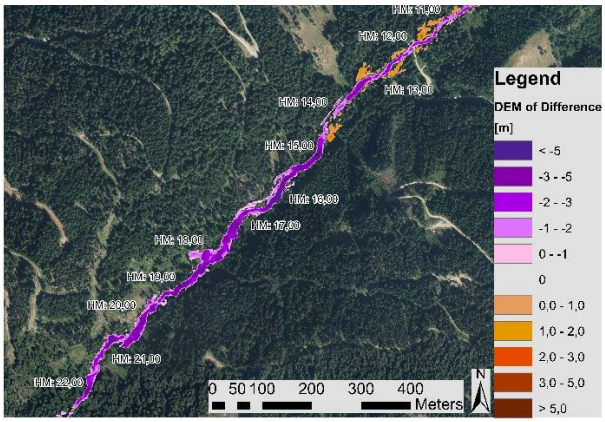

Fig. 7 Result of the DoD with a deepening of more than 5 m in the middle reach [purple = erosion > 5m, dark red = deposition > 5m]

debris was mobilized and transported down to the debris cone. The maximum grain size was up to 1.50 m and an area of 0.13 km² was affected by the debris flow. The dominant process type of the second mass movement event was a more fine-grained flow than by the first one. Again about 30,000 – 35,000 m³ debris were eroded over the main channel.

However, because of early warning, the affected settlement area was already evacuated. Therefore no persons were hurt or killed.

In total, 45 buildings and infrastructure were damaged along the Tronitzer Torrent **(Fig. 6)**. However no people were hurt or killed by the debris flows.

5.1 DEM of Difference

After the second debris flow an airborne laser scan was carried out to determine more precise how much debris was eroded by the two debris flow events.

With the use of ArcGIS the channel was separated in several erosion and deposition polygons and a DEM of Difference (DoD) was used to calculate the total erosion and deposition.

The erosion areas were separated into two parts: the upper and middle reach. For the deposition areas also the temporarily formed protection dams, which were built out of the sediment, were regarded for the DoD. At the time of the airborne laser scan the debris was already removed from the houses, therefore the settlement area was not observed.

According to the DoD debris was only mobilized through vertical and lateral erosion. Larger landslides were not observed near the channel. The superficial landslide underneath the forest road was probably the initialization of the process but regarding the total amount of debris at the cone, this landslide is negligible. The DoD shows a deepening of the stream bed with more than 5 m in the middle reach **(Fig. 7)**. At hectometer 12.0 from the mouth the deposition started because of a change in the slope gradient.

In total, about 56,000 m³ of debris was eroded in the upper and middle reach of the Tronitzer Torrent. As the ALS-flight was carried out after both debris flow events, it's not possible to differentiate between the respective debris flows.

As an emergency measure after the first event, in total 25,500 m³ sediment (without large boulders) was packed to build protection dams for the Tronitzer Torrent and another torrent nearby (Kraagraben). Another 28,000 m³ debris was detected by the DoD at the deposal site. **Table 1** shows the results of the DoD in detail.

Table 1 results of DEM of Difference of both debris flows

TOTAL EROSION	**-**	**56,000 m³**
hm 23.00 – hm 7.00	-	52,000 m³
upper reach	-	4,000 m³
TOTAL DEPOSITION	**+**	**52,500 m³**
hm 12.00 – hm 7.00	+	6,000 m³
emergency dams Tronitzer Torrent	+	18,500 m³
emergency dams Kraagraben	+	7,000 m³
deposal site	+	21,000 m³

The difference of 3,500 m³ between the erosion and deposition might be because debris was removed immediately after the events and some debris might be carried along by the receiving stream, the Afritzer River. Together with the estimated deposition of debris immediately after the events the results of the DoD fits well.

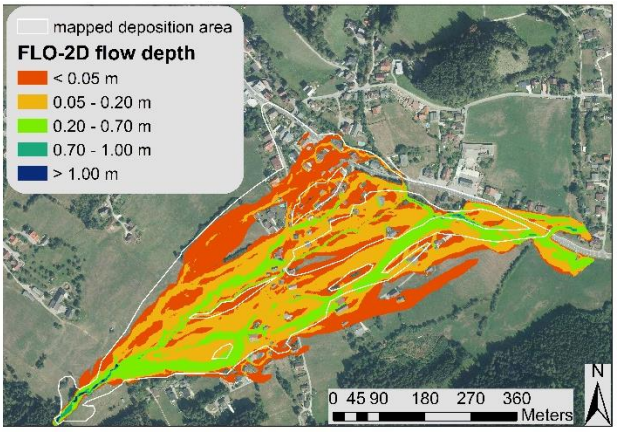

Fig. 8 Modeled flow depth with FLO-2D; the white line shows the documented deposition area of the event on the 29th August 2016

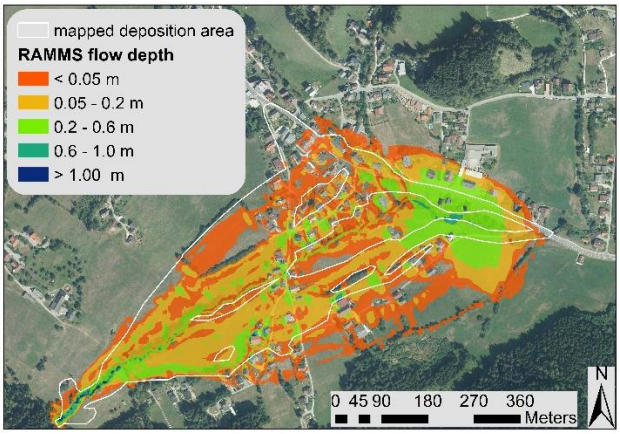

Fig. 9 Modeled flow depth with RAMMS; the white line shows the documented deposition area of the event on the 29th August 2016

5.2 FLO-2D

The results with FLO-2D show good agreement with the documented flow paths but flow depth and the heights of the debris flow depositions are overestimated. **Fig. 8** shows the modeled flow depth and the documented sediment deposition area. The outbreak on the left side to the settlement area is underestimated.

5.3 RAMMS

The flow depths modeled with RAMMS::DEBRIS FLOW vary strongly. The BEST-FIT combination is shown in **Fig. 9**. In comparison with the documented deposition area after the first event, the outbreak to the right is strongly overestimated. In the settlement area the outbreak on the left is however underestimated, too. Regarding the flow depth, the model shows a fundamental overestimation in the estuary area.

Fig. 10 Bedded rockfill and concrete sills along the lower reach

PROTECTION MEASURES

Immediately after the first debris flow event protection measures were implemented by the Austrian Service for Torrent and Avalanche Control. The first measures were the reconstruction of the bed of the torrent and a number of temporary protection dams above the settlement area. With the help of the Austrian Federal Armed Forces wood was removed from the middle reach and the settlement areas were cleared up.

In addition to the protection measures structural measures were planned consisting of:

- a water retention basin in the upper catchment to reduce the impact of the surface runoff
- a chain of check dams to stabilize the bed and the banks in the middle reach
- a debris flow breaker to transform the process, filtering of coarser fraction of the debris and to retain 6,000 m³ of solids
- a bedload sorting dam with a length of 250 m and a height up to 14 m to retain 37000 m³
- a bedded rockfill and concrete sills along the lower reach in the settlement area **(Fig. 10)**.

In total, the structural measures to protect the village of Afritz amounts 11.4 million Euros.

The control measures in the lower reach of the Tronitzer Torrent were finished in 2017. After finishing the sediment control dam in 2018 **(Fig. 11)** the water retention basin in the upper catchment and the debris flow barrier will be built.

6. CONCLUSIONS

The two debris flows at the Tronitzer Torrent were a result of several circumstances e.g. intensive

Fig. 11 Bedload sorting dam with a retention capacity of 37,000 m³ with a length of 250 m and a height up to 14 m

precipitation with hail in short time, the extreme surface runoff and the water concentration at the drainage of the forest road. The back-calculation of such debris flow events is seriously hampered by the extent and quality of the data basis. Phenomena registered in the course of event documentation were collected and input parameters defined for the calculations. For nearly all of the necessary input parameters, only ranges of values can reliably be given, due to the great complexity of the underlying processes. The rheological parameters might be used for modelling debris flows in similar torrents as well. On the basis of the collected data such as grain-size distribution or peak discharge, protection measures were planned and are currently under construction. These measures comprise a debris flow breaker and a bedload sorting dam with a capacity of 43,000 m³ in total at the debris cone head, bedded rockfill and concrete sills to stabilize the bed in the middle reach and a water retention basin in the upper catchment.

ACKNOWLEDGMENT: Thanks to the Regional Headquarters and the Department of Torrent Processes for supporting the event documentation and -analyse of the two debris flow events.

REFERENCES

Kaitna, R., Schraml, K., Delago, L., Kamper, S. (2015): Evaluierung von rheologischen Parametern verschiedener Einzugsgebiete für das numerische Simulationsprogramm Flo2d (EZG-Rheo), IAN Report 159, Institut für Alpine Naturgefahren, Universität für Bodenkultur – Wien

Moser, M., Mehlhorn, S. (2016): INCA- Auswertung Niederschlagsereignisse August und 09. September 2016 Tronitzerbach, Gemeinde Afritz; Bundesministerium für land- und Forstwirtschaft, Umwelt und Wasserwirtschaft, Abteilung III/5 Wildbach- und Lawinenverbauung (Hrsg.). (unveröffentlicht).

ONR 24801: Schutzbauwerke der Wildbach- und Lawinenverbauung – Statische und dynamische Einwirkungen. Österreichisches Normungsinstitut, Ausgabedatum: 2013-08-15

Schraml K., Thomschitz B., McArdell, B. W., Graf, C., Kaitna, R. (2015): Modeling debris-flow runout patterns on two alpine fans with different dynamic simulation models, Nat. Hazards Earth Syst. Sci., 15, 1483–1492, 2015 www.nat-hazards-earth-syst-sci.net/15/1483/2015/doi:10.5194/nhess-15-1483-2015

Critical Rainfall Analysis of Large-scale Landslide Occurrence

Tsai-Tsung TSAI,[1,3*] Yuan-Jung TSAI [2] and Chjeng-Lun SHIEH [1,2,3]

[1] Disaster Prevention Education Center, National Cheng Kung University
(No.1, University Road, Tainan City 701, Taiwan R.O.C.)
[2] Disaster Prevention Research Center, National Cheng Kung University
(3F., No.500, Sec. 3, Anming Rd., Annan Dist., Tainan City 709, Taiwan R.O.C.)
[3] Department of Hydraulic and Ocean Engineering, National Cheng Kung University
(No.1, University Road, Tainan City 701, Taiwan R.O.C.)
*Corresponding author. E-mail: victor@dprc.ncku.edu.tw

The disaster event in Xiaolin village awakens the public awareness of large-scale landslide. The pre-warning procedure of large-scale landslide is one of the most important issues in Taiwan recently. In this study, 36 cases from Xiaolin village disaster event were used to estimate possible occurrence rainfall thresholds of large-scale landslide. The methods of rainfall time-series analysis and dimensionless rainfall analysis were taken in this study, the information including area, volume, location, occurrence time, and hydrography data of each landslide sites were considered in those analysis. Some trends of occurrence rainfall in Taiwan could be found in this study.

Key words: large-scale landslide, critical rainfall, pre-warning system

1. ORIGIN

The topography and geological conditions of Taiwan are very special, the mountainous terrain is steep, the valleys are high, many faults and folds, geological environment conditions are complex. Typhoons, heavy rainfalls and earthquakes also made the occurrence of landslides and debris flows frequently in Taiwan. In addition, due to the influence of extreme weather in recent years, there have been even 7 to 8 typhoon attacks every year, the risks of sediment disasters are increasing for each heavy rainfall.

Typhoon Morakot, during 8th to 10th Aug. 2009, is the most serious disaster case. The typhoon and the subsequent southwesterly flow have characteristics with long duration, high intensity, high accumulation, and wide affected area. In the southern-central part of Taiwan, there are 3000mm of rainfall been observed in four consecutive days. Meanwhile, various types of disasters such as deep and shallow landslides, debris flows, landslide dams, and flooding were induced.

These disasters hit the same area at the same time or one after another and cause serious disasters in the region. Xiaolin village case(**Fig.1**) is the most famous one. Due to the large-scale landslide disaster, there are 474 people died, and the property loss is more difficult to be estimated.

This event awakens the public awareness of large-scale landslide disaster. As a preparation for future large-scale landslide prevention, this study was focus on the characteristics of rainfall that triggers large-scale landslide.

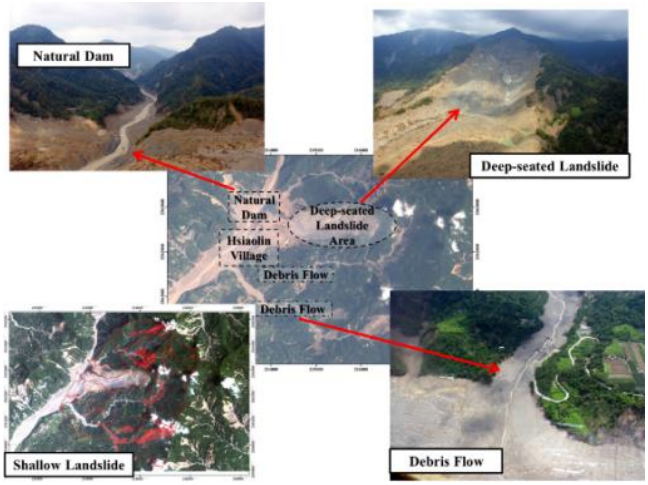

Fig. 1 Large-scale landslide in Xiaolin village during Typhoon Morakot

2. RESEARCH METHODS

As **Fig. 2** shown, to find out the trend of critical rainfall in Taiwan, this study is based on the following procedures. The details are described as follows.

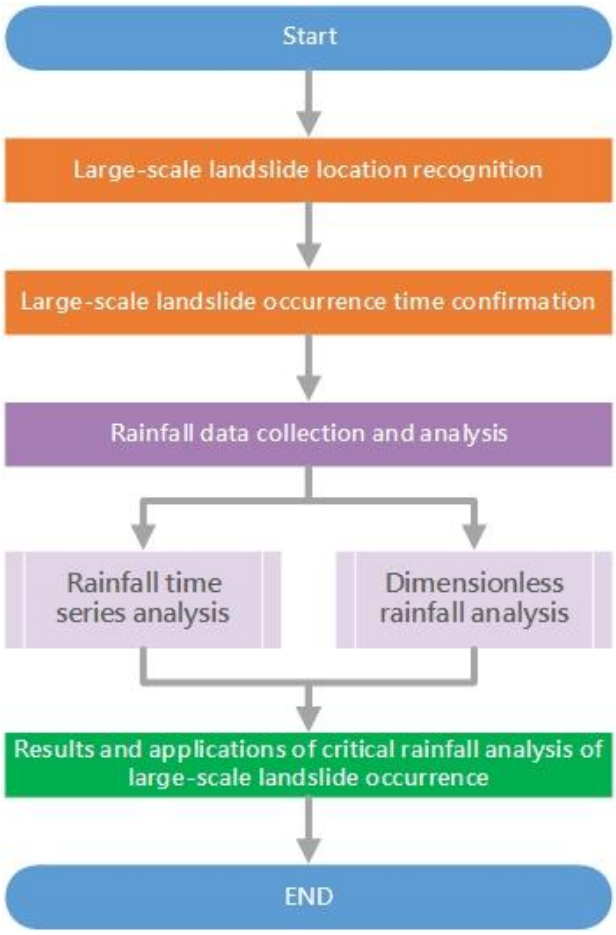

Fig. 2 Research process of critical rainfall analysis of large-scale landslide occurrence

2.1 Large-scale landslide location recognition

In this step, the multi-spectral imagery with original 8m ground resolution of FORMOSAT-II was used to find out the accurate locations and types of landslides.

Follow the procedure from NCKU Research and Development Foundation (2010), using imagery after Typhoon Sinlaku as pre-event imagery and imagery after Typhoon Morakot as post-event imagery, respectively produced catalogues of landslides and then do the comparison.

Fig. 3 shown the workflow of large-scale landslide location recognition. The workflow can be divided into two parts, one is semi-automatic extraction prat, and the other one is manual inspection.

Imagery from different phases may contain some bias cause by shooting, orthorectification, algorithm, and some random issues. In the beginning of semi-automatic extraction is to reduce the spatial bias between images by multi-phase imagery registration.

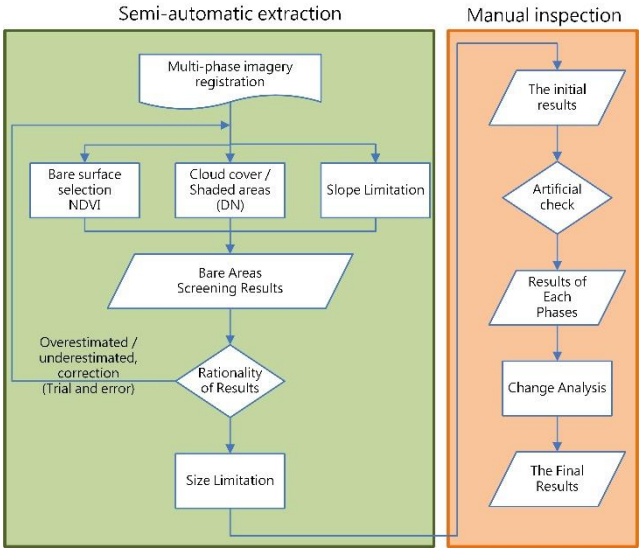

Fig. 3 Workflow of large-scale landslide location recognition

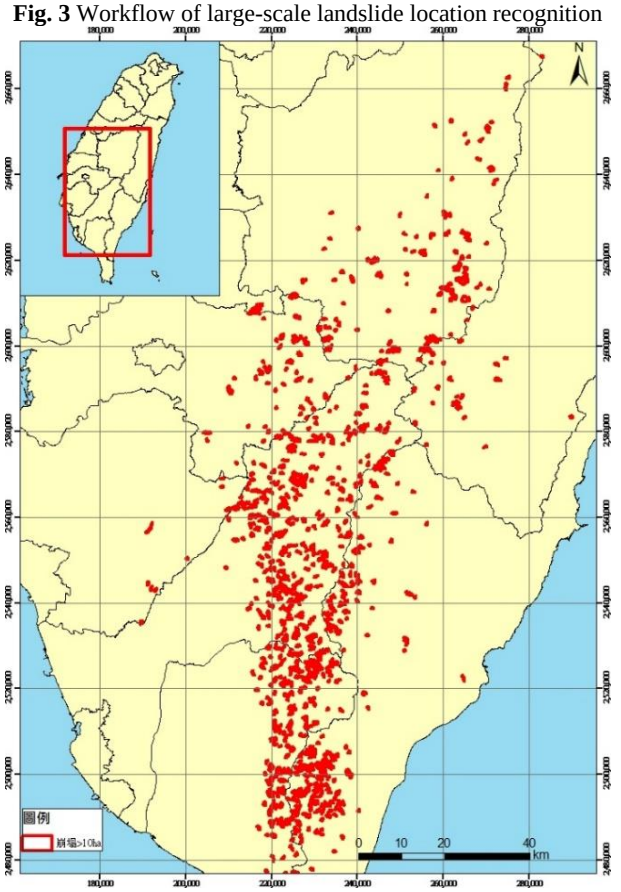

Fig.4 The distribution of variants larger than 10 ha

After multi-phases imagery registration, some indexes such as NDVI, brightness, and slope were used to quickly filtering the bare areas. The results of this part need to confirm whether the overestimation or underestimation is through rational analysis and use the trial and error method to correct the parameters until the results are

reasonable. Finally, through the size parameters remove those under reasonable recognizable size objects, the semi-automatic extraction part is finished, the catalogues of landslides were made. Each result from the semi-automatic extraction should pass the artificial check, to make sure the result of each phase is correct. Then compare results from different phases, the variant regions will be found.

In this study, 10 ha condition was used to filter large-scale landslide form variant regions. There are total 764 landslides met the qualify, of which there were 308 new landslides (**Fig. 5**) and 456 expanded ones (**Fig. 6**). These large-scale landslides are the targets of this study. GIS software was used to collect the need data from landslide such as area size and average slope.

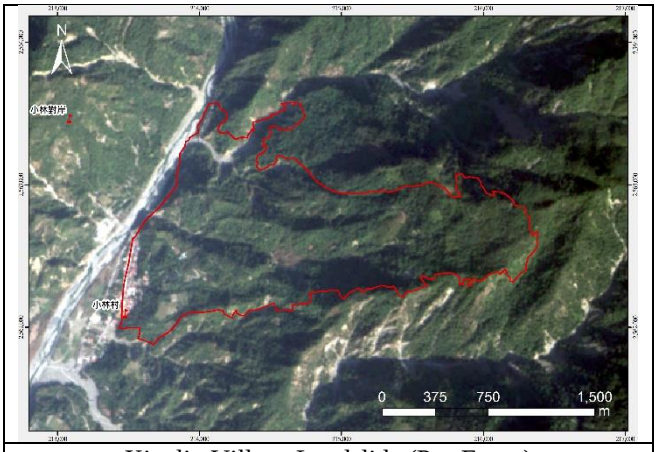

Xiaolin Village Landslide (Pre-Event)

Xiaolin Village Landslide (Post-Event)

Fig. 5 The demonstration of new landslides

In this step, the results shown some more type of landslides, include multiple landslides merged cases. Therefore, there two types of landslides were defined for following discussion, one type is newborn type, only single new landslide included, the other one is mixed type, include single expanded landslide, multiple new/expand landslides merged cases, and new and expand landslides merged cases.

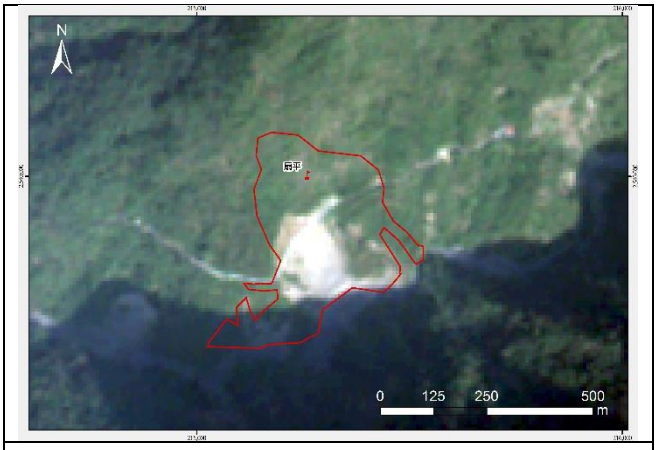

Shanping Landslide (Pre-Event)

Shanping Landslide (Post-Event)

Fig. 6 The demonstration of expanded landslides

2.2 Large-scale landslide occurrence time confirmation

This step is trying to link the records from formal government reports or seismic data with landslides found in foregoing step to confirm the occurrence time of landslides. The time data used in this study mainly comes from the research report of the Sinotech Engineering Consultants, Inc. (2013) and Chinese Geoscience Union (2010), NCKU Research and Development Foundation (2015, 2016) and the investigation and interview records of the National Cheng Kung University Disaster Prevention Research Center.

Those time data from Sinotech Engineering Consultants, Inc. (2013) which referred to the major landslide disaster report of SWCB are also investigation and interview records of filed works.

Those time data from Chinese Geoscience Union (2010), used the records of Broadband Array in Taiwan for Seismology, built by the Institute of Earth Sciences of the Academia Sinica and the Central Meteorological Bureau, and was analyzed with the HYPO 71 software.

Those time data from NCKU Research and Development Foundation (2015, 2016), also used the records of Broadband Array in Taiwan for Seismology and follow the locating method from Wech & Creager (2008) to confirm every landslide event.

After the comparison, the link between location and time of large-scale landslide were founded in 36 cases, the distribution of these cases shown as **Fig. 7**. Half of these cases are newborn type, and the other half are mixed type.

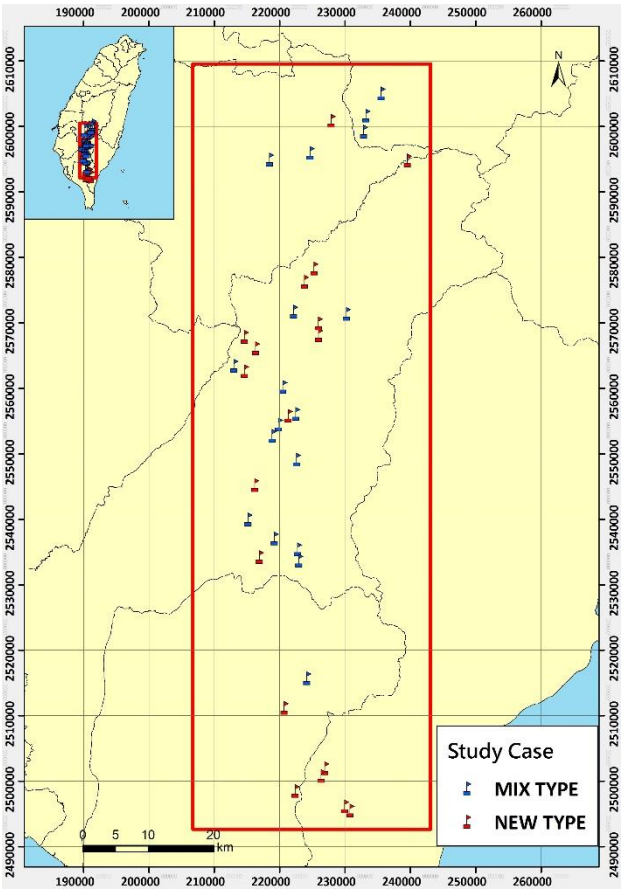

Fig. 7 Study cases distribution

2.3 Rainfall data collection and analysis

In terms of rainfall data, the precipitation data assurance by the Central Weather Bureau was used in this study. The rainfall period has been defined from 0 o'clock on August 6, 2009 to 23 o'clock on August 10, 2009. After removing the stations with missing data, the final amount of station used was 354 stations. Base on the data of those stations, each rainfall value at landslide site were calculated with inverse distance weight method, and the result is shown in Figure 8.

After data preparing stage, two analysis Rainfall time series analysis and Dimensionless rainfall analysis were executed.

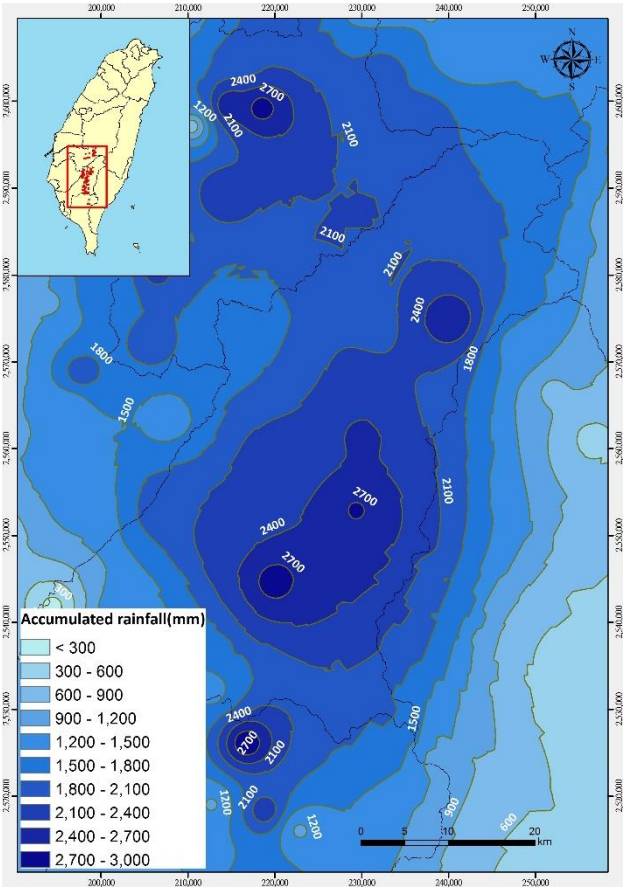

Fig. 8 Rainfall distribution of the study area

2.3.1 Rainfall time series analysis

Draw two kinds of hydrograph, rainfall intensity-duration diagram and rainfall accumulation-duration diagram then mark the landslide occurrence point on them. Then try to find out the trend and zoning for large-scale landslide.

2.3.2 Dimensionless rainfall analysis

Two dimensionless factors, the ratio accumulate rainfall (R) to landslide depth (D) and the ratio of equivalent friction angle (ψ) to average slope (θ) of landslide, were used to draw a regression relationship.

(a) Accumulate rainfall, R:

The hourly precipitation data of each landslide case was calculated with inverse distance weight method, the total amount of rainfall was accumulated from 0:00 on August 6, 2009 to the time of occurrence of landslides, as cumulative rainfall R (unit: m).

(b) Landslide depth, D:

The projected area of landslide was calculated with ArcGIS software in this study. The empirical formula from National Cheng Kung University (2013) was used, volume V (m^3), was calculated from Eq. (1), and landslide depth D (m) was calculated from Eq. (2).

$$V = 0.075A^{1.45} \quad (1)$$

$$D = \frac{V}{A} \quad (2)$$

(c) Average slope, θ:

Due to the nature terrain was not uniformed, the slope of landslide site maybe changes in gradient. Therefore, the slope here was defined as the average slope within the landslide range. The average slope was calculated with the spatial statistics function of the spatial analysis module of the ArcGIS software.

(d) Equivalent friction angle, φ:

The relation between the equivalent friction coefficient f and the landslide volume V was described in Scheidegger (1973) shown as Eq. (3). The relationship between the equivalent friction coefficient f and the equivalent friction angle φ was existed as Eq. (4). From Eq. (1), the relationship between the projected area A and the volume of the landslide surface V can be deduced from the equivalent friction angleψ.

$$\log_{10} f = -0.1466 \log_{10} V + 0.62419 \quad (3)$$

$$f = \tan \phi \quad (4)$$

2.4 Results and applications of critical rainfall analysis of large-scale landslide occurrence

Base on the foregoing results, the threshold for pre-warning system of large-scale landslide could be setup, and the volume of soil production will be estimated easily.

3. RESULTS

In this study, the following results were found.

3.1 The distribution of study case

Base on **Fig. 7** and **Fig. 8**, the distribution of study cases and rainfall distribution of the study area where are drawn as **Fig. 9**. According to the distribution of known cases, mix type cases and new type cases are occurred as randomly distributed, meanwhile all the cases are occurred nearby the rainfall hotspot.

3.2 The rainfall threshold of triggering large-scale landslide

As **Fig. 10** shown, those study cases could be divided into two groups; the red colored group were composed with new born type landslides, the large-scale landslides were occurred after the peak rainfall, the relative accumulated rainfall value exceeded 800 mm and the occurrence time was close to the turn point of hydrograph curve. In the other group, the blue colored group were composed with mix type landslides, the large-scale landslides were occurred before or close to the peak rainfall, the relative accumulated rainfall value was around 600 mm and the occurrence time was fall into the rise part of hydrograph curve.

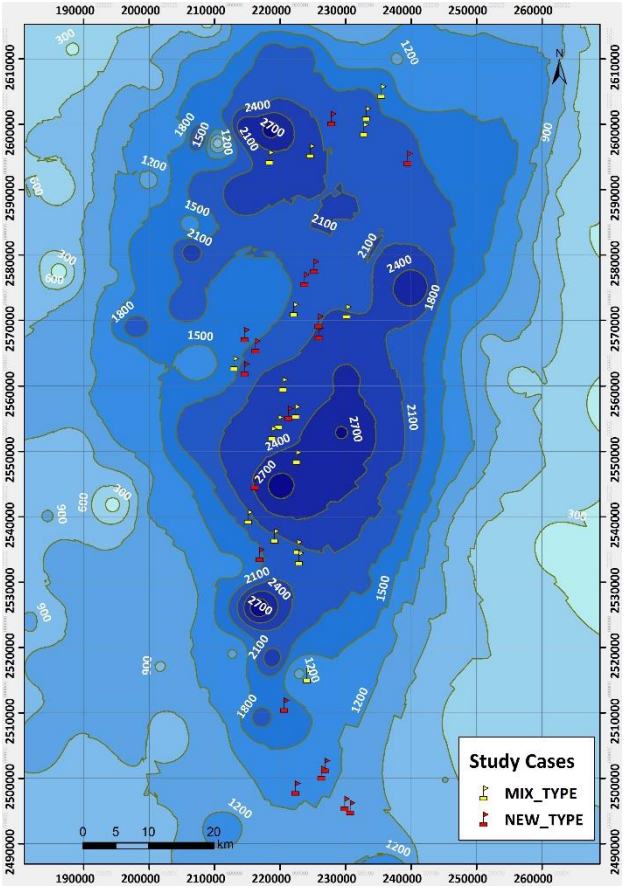

Fig. 9 Hydrograph of study cases

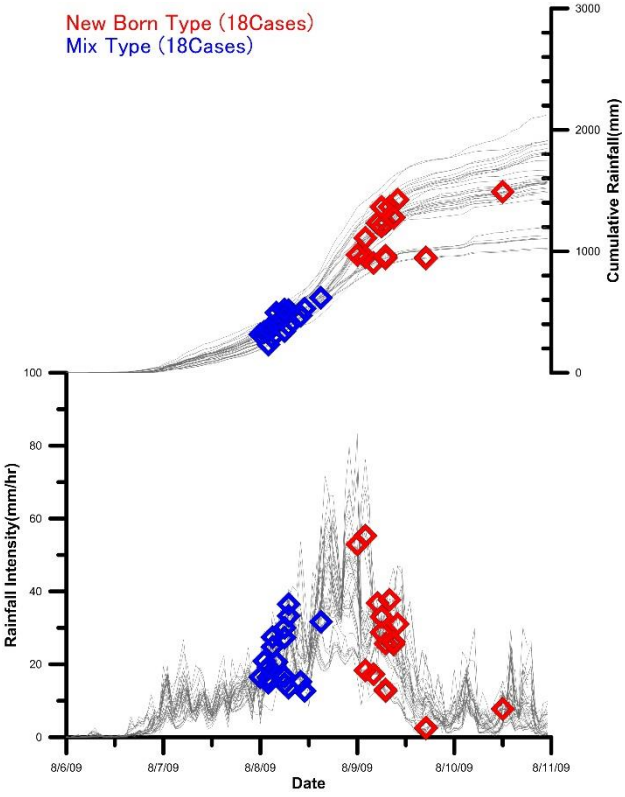

Fig. 10 Hydrograph of study cases

As 2.1 mentioned, mix type landslides include single expanded landslide, multiple new/expanded landslides merged cases. For expanded landslide case, the surface of landslide is not covered or poorly covered by plants, it's reasonable that expanded landslides would be triggered in lower accumulated rainfall value than new born ones. Base on this condition, study cases in Fig 10 shown as two groups were quite reasonable.

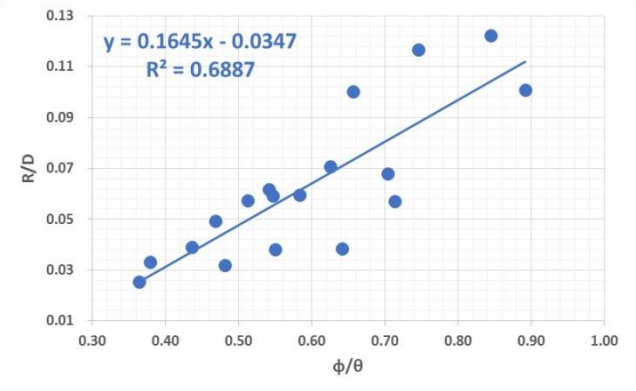

Fig. 11 Dimensionless rainfall analysis results

3.2 The result of Dimensionless rainfall analysis

As **Fig. 11** shown, through linear regression the relationship of the ratio of equivalent friction angle (ψ) to average slope (θ) of landslide and the ratio accumulate rainfall (R) to landslide depth (D) was found as the Eq. (5), and it's R2 value is about 0.6887.

$$\frac{R}{D} = 1.645 \times \frac{\phi}{\theta} - 0.0347 \qquad (5)$$

As Eq. (5) shown, R toψand D to θ both shown the positive relationship, these means the more rainfall would cause the more soil mass been moved and the steeper slope would cause the deeper landslide.

4. CONCLUSIONS

Purely single new large-scale landslide will occur after the peak rainfall, the relative accumulated rainfall value exceeded 800 mm and the occurrence time was close to the turn point of hydrograph curve; although there are obvious groups in the hydrograph, there was still need more cases to support. Since it is not easy to obtain the exact time of occurrence, the number of valid samples is still insufficient. Therefore, this research needs to include other analytical methods in the future to obtain more reliable research results. The study is still ongoing.

ACKNOWLEDGMENT:

Thank you for the financial funding supported by the Ministry of Science and Technology of the Executive Yuan and the Soil and Water Conservation Bureau of the Agricultural Committee of the Executive Yuan.

REFERENCES

Adrian E. Scheidegger (1973), On the Prediction of Reach and Velocity Catastrophic Landslides, Rock Mechanics 5, 231-236, Springer-Verlag.

Chinese Geoscience Union (2010), Applications of Seismic Network on Sediment Disaster Monitoring of Slopeland, Report of the Soil and Water Conservation Bureau of the Agricultural Committee of the Executive Yuan.

NCKU Research and Development Foundation (2010), Analysis of Slopeland Disasters with the Formosat-II Imagery, Report of the Central Geological Survey of the Ministry of Economic Affairs.

NCKU (2013), Geological Survey and Database Construction of Upper Catchments of High Flooding Risk Area - Investigation and Evaluation of Erosion and Sedimentation in the Watershed Area (3/3), Report of the Central Geological Survey of the Ministry of Economic Affairs.

Sinotech Engineering Consultants, Inc. (2013), Intensified Real-Time Dynamic Assessment of Potential Landslide Caused by Heavy Rainfall and Development of Alert Model(3/4), Report of the Central Geological Survey of the Ministry of Economic Affairs.

NCKU Research and Development Foundation (2015), Detecting large scale landslides by Taiwan broadband seismic network and the study of triggering rainfall for landsliding, Report of the Soil and Water Conservation Bureau of the Agricultural Committee of the Executive Yuan.

NCKU Research and Development Foundation (2016), The application study of Taiwan seismic network on alert information of landslide hazard, Report of the Soil and Water Conservation Bureau of the Agricultural Committee of the Executive Yuan.

Wech, A.G. & Creager, K.C. (2008),Automated detection and location of Cascadia tremor, Geophys. Res. Lett., 35, L20302, doi:10.1029/ 2008GL035458.

Estimation of Temporal Change of River Bed Elevation Upstream of a Check Dam During Debris Flow

Naoki FUJIMURA[1*], Yuya TAKAHASHI[1] and Hideaki MIZUNO[2]

[1] Erosion and Sediment Control Research Group, Public works Research Institute
(1-6 Minamihara, Tsukuba, Ibaraki, 3058516, Japan)
[2] Faculty of Agriculture, Kyusyu University (6-10-1 Hakozaki, Higashi-ku, Fukuoka, Fukuoka, 8128581, Japan)
*Corresponding author. E-mail: n-fujimura@pwri.go.jp

A check dam has various functions, which includes sediment control. In the past, the effects of the sediment control function were assessed either by obtaining measurements upstream of a check dam or by performing numerical simulations based on information after flooding. Therefore, the purpose of this study is to clarify the temporal change of the river bed elevation upstream of a check dam during flooding along with sediment transportation. The authors estimated the river bed elevation based on data continuously measured by a laser profile scanner (LPS). Similarly, the sediment concentration was altogether estimated. The longitudinal profile measurement of the check dam's sedimentation area, which was obtained using the LPS, made it possible to estimate the temporal change of the river bed elevation, as well as the erosion and deposition processes. Sediment accumulation in the decay phase was confirmed in either case of all the debris flows that were observed under the decay phase conditions, such as the lower flow velocity and higher sediment concentration during the peak flow.

Key words: sediment control function, debris flow, laser profile scanner

1. INTRODUCTION

A check dam has various functions, particularly in sediment-related disaster prevention. Sediment control is one of those functions. Through this function, the upstream runoff sediment during a large flood is temporarily stored. Thereafter, this sediment is carried downstream through a transport medium, or when small floods occur after several years or even decades after the large flood [*Nishimoto*, 2011].

In the past, the effects of the sediment control function were assessed by measuring the longitudinal gradient upstream of a check dam or by numerical simulations.

For example, a study on the sediment gradient included a case where the longitudinal profile of the sedimentary layer was evaluated through the survey of check dams filled with sediments after flooding through sediment transportation [*Murano*, 1962]. The longitudinal profiles of the sediments were approximately represented by a quadratic curve, although it varied according the amount of sediments and flow rate.

In the case of measuring the sediment gradient through a hydraulic experiment [*Yoshida et al.*, 1964], it was found that water and sediments are continuously supplied to the flume. Moreover, when the temporal change of the sediment profile of the dam is tracked, it gradually approached the straight line from the quadratic curve. This shows that the coefficient of the curve equation varies according to the supplied amounts of sediments and water.

Similarly, succeeding studies were conducted to evaluate sediment control effects and functions of check dams through observations, which focused on the type of check dams [*Mizuyama et al.*, 1990; *Satou* et al., 2000 etc.], and through numerical simulations [*Fujita et al.*, 2001; *Honda* and *Okumura*, 2005].

The effect of the sediment control function is determined by the amount of sediments and water supplied to the check dam, and not where the installed check dam is located. The amount of upstream sediment supply and flow rate of sediment-carrying water can fluctuate during actual events. However, past studies were analyzed based exclusively on the information after flooding either by performing a survey or numerical simulation. Thus, the actual fluctuation of the river bed as the process of the appearance of the sediment control function during flooding is not clarified.

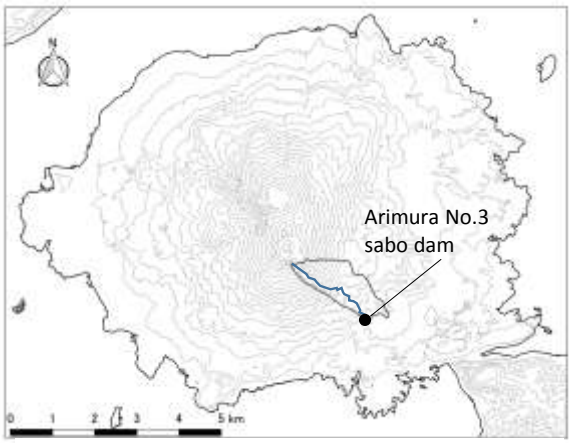

Fig. 1 Observation site

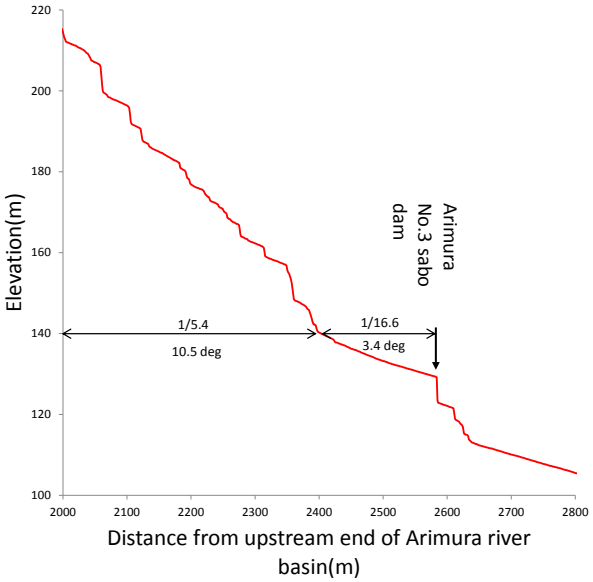

Fig. 2 Gradient of Arimura river

In this regard, the purpose of this study is to clarify the temporal change of the river bed elevation upstream of a check dam during flooding with sediment transportation. The authors estimated the river bed elevation with data that are continuously measured by the laser profile scanner (LPS). The sediment concentration was estimated altogether. The events that indicate when the sediment control function appears cannot be expected only in a few years. Thus, in this paper, we will report the result of the conducted observation of the debris flow in the river, where several sediment transportations are expected.

2. METHOD

2.1 Observation site

The study site is the Arimura River located in the southeastern area in Sakurajima, Japan (**Fig. 1**). It is a debris-flow prone river where several check dams are installed. Through an observation system, the

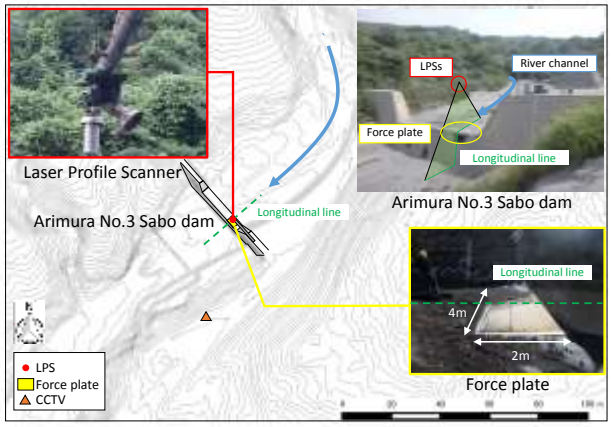

Fig. 3 Image of installed LSP and force plate

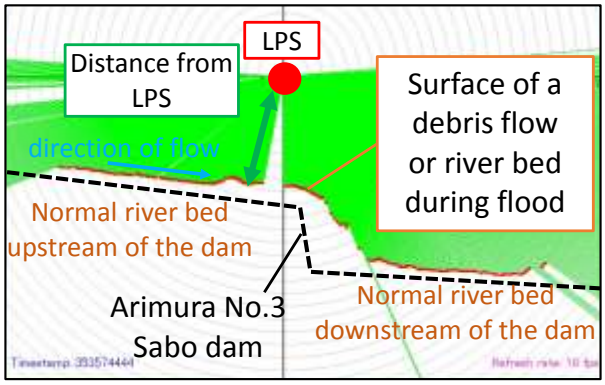

Fig. 4 Longitudinal elevation measured by LPS

authors and the MLIT Osumi Office of River and National Highway observed the debris flow system on the spillway of the Arimura No. 3 Sabo dam. The catchment in the upstream area of the dam is 1.55 km^2 and the slope gradient above the dam is 3.4° (**Fig. 2**).

2.2 Observation devices

The observation system is mainly composed of LPSs, a force plate, and closed-circuit television (CCTV), etc. (**Fig. 3**).

A force plate installed by MLIT measures unit weight of debris flow. It is located on the spillway of the dam to the left bank because flow tends to biased to the side due to river curvature.

The Public Works Research Institute installed two LPSs (UXM-30LX-EW, Hokuyo Co., Ltd.) approximately 9 m above the dam, which continuously measure the profiles of the river bed within a 30-m radius. Thus, the LPSs longitudinally measure 15 m of the upstream area and 15 m of the downstream area of the dam. Measurements are performed 20 times per second, and the average values per second are used as profiles. One LPS measures the temporal change of the longitudinal elevation of the river bed surface or the debris flow (**Fig. 4**), whereas the other LPS makes measurement in the transverse direction.

The force plate installed by MLIT measures the

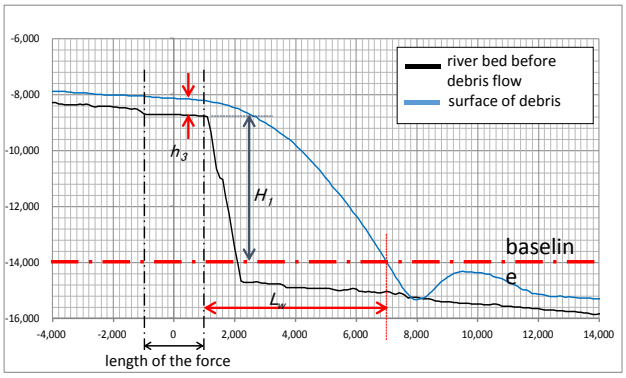

Fig. 5 Measured values for semi - theoretical equation

unit weight of the debris flow. It is located at the spillway of the dam, on the left bank. The flow tends to be biased to that side because of the river curvature.

The CCTV records a video of the debris flow. It was installed by MLIT on the left side and at approximately 30 m downstream from the check dam.

2.3 Calculation of hydraulic quantity of debris flow

2.3.1 Flow velocity of debris flow

Ultrasonic velocity sensors are often used to measure the debris flow velocity. Ultrasonic velocity sensors installed by MLIT at the observation site measure the flow velocity per minute. Consequently, the flow velocity per minute data cannot be compared with the flow velocity per second data. In order to obtain the flow velocity per second data, the velocity was calculated with a semi-theoretical equation using the nappe distance [*Yoshinaga*, 2017] obtained from the longitudinal profile of the flow surface, which is measured every second downstream of the dam.

The velocity is calculated with Eq. (1) shown below [*River bureau, Ministry of Construction*, 1997].

$$V = L_w \times \left\{\frac{2\times(H_1+0.5\times h_3)}{g}\right\}^{-0.5} \quad (1)$$

Where V is the debris flow velocity on the spillway of the check dam (m/s); L_w is the nappe distance (m); H_1 is the vertical distance from the crown of the check dam (m); h_3 is the overflow water depth on the spillway of the check dam; g is the gravitational acceleration (m/s^2).

The baseline for H_1 was set vertically downward at 14 m from the sensor to avoid the influence of bounding water and splash (**Fig. 5**). The values of h_3 are calculated as average depths between 2 m from the downstream edge of the dam, so as to eliminate the influence of the error caused by a splash or huge boulder.

Table 1 Measured data of debris flows

Date	Data of LPS	Data of Force plate
2015/12/10	✓	✓
2016/5/9	✓	
2016/6/19	✓	✓
2016/9/20	✓	

2.3.2 Sediment concentration of debris flow

The sediment concentration of the debris flow is estimated using Eqs. (2) and (3) [*Osaka*, 2013]:

$$\gamma_d = PA_{FP}/AL \quad (2)$$

$$C_v = (\gamma_d - \gamma_\sigma)/(\gamma_\sigma - \gamma_\rho) \quad (3)$$

where γ_d is the unit weight of the debris flow (kN/m^3); P is the basal normal stress (kPa); A_{FP} is the plane area of the force plate (m^2); A is the cross-sectional area of the debris flow (m^2); L is the longitudinal length of the force plate (m); C_v is the sediment concentration; γ_σ is the unit weight of grains (kN/m^3); and γ_ρ is the unit weight of water (kN/m^3).

3. RESULT

The list of measured data since December 2015 when the LPS started to measure the longitudinal profiles of the river bed on the check dam are summarized in **Table 1**. Similarly, **Fig. 6** shows the temporal change of the debris flow depth with rainfall intensity observed at Kagoshima rainfall observatory near the Arimura river and the river bed elevation expressed by the distance from the LPS. The situations of the river bed elevation are focused on the start, peak, decay, and end phases. To be precise, the elevation of the peak and decay phases did not show an accurate state of the river bed, since LPS scanned one part of the flow surface during these phase. The debris flow that occurred on (a) December 10, 2015, (b) May 9, 2016, (c) June 19, 2016, and (d) September 26, 2016 are presented in **Fig. 6**.

The depths of each event, including the debris flow, are shown within 2 h. The start phase is the situation before the debris flow. The peak phase is the first peak of the depth of the debris flow. The decay phase is the time immediately before the depth increased after the first peak. Concerning (c) June 19, although second peak appeared right after the first peak depth tended to decrease. Thus, in this case the

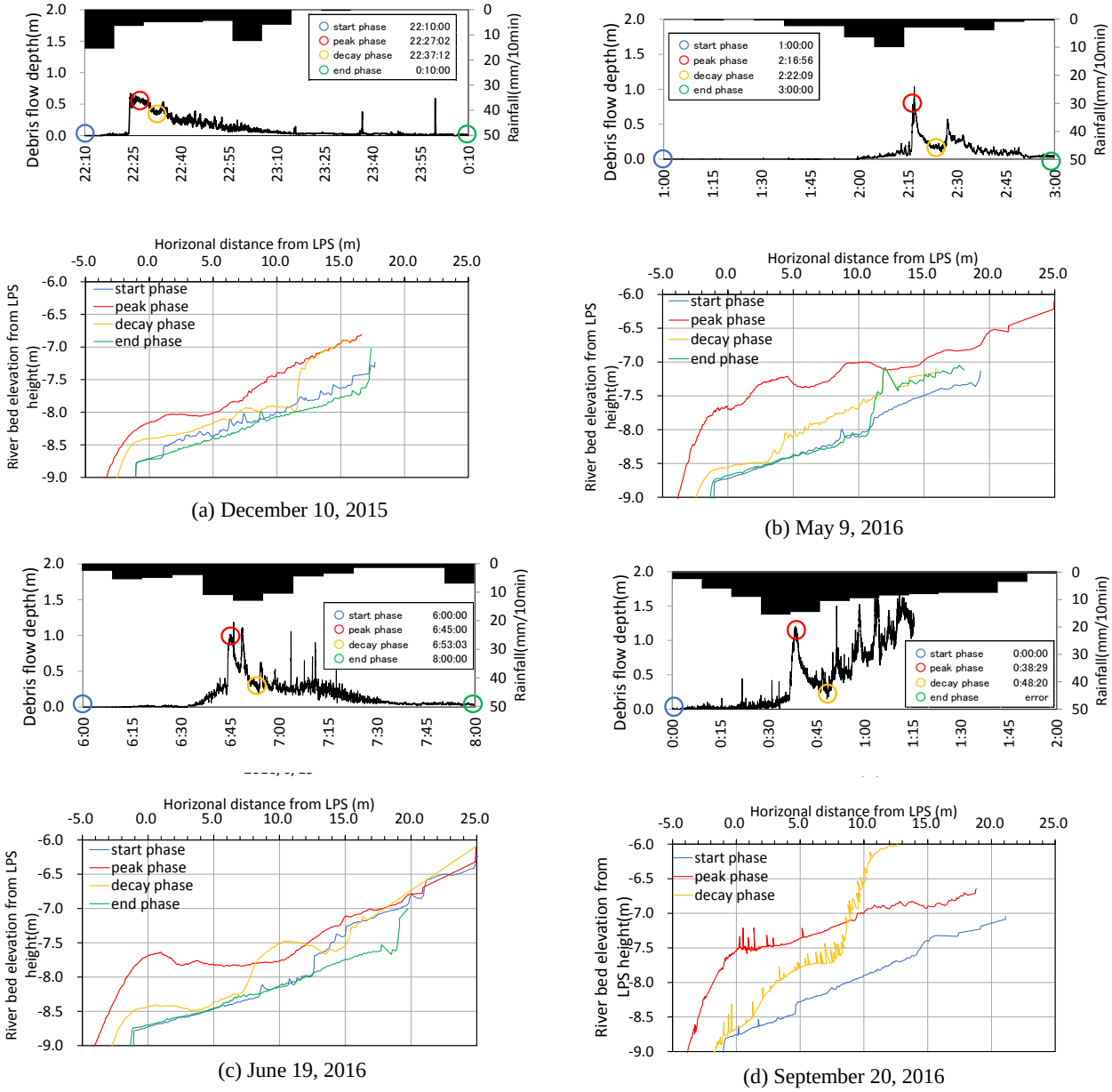

Fig. 6 Depth of debris flow and river bed elevation

moment after the second peak was regarded as decay phase. Concerning (d) September 26, decay phase was not clear since depth increased after the first peak continuously. Thus, in this case the moment after the first peak was regarded as decay phase even though depth tended to increase.

3.1 Elevation of river bed surface or debris flow

3.1.1 Debris flow at December 10, 2015

The debris flow occurred at approximately 22:23 and peaked 4 min later, at 22:27. Thereafter, the depth gradually lowered at approximately 23:15. The accuracy of that change, which occurred at 00:00, is difficult to confirm. In the longitudinal direction of the decay phase, although most of the profiles were lower than those during the peak phase, the elevation above upstream, 12 m from the LPS was almost the same as that of the peak. In the end phase, the high elevation range, which was confirmed in the decay phase, disappeared. Additionally, the elevation of the entirety of the river bed generally decreased compared to that during the start phase. In this case, it is seen that sediment was temporarily deposited upstream of the check dam during debris flow even though it was finally eroded.

3.1.2 Debris flow at May 9, 2016

The depth of the debris flow started to rise at approximately 2:00 and rapidly peaked at approximately 2:16. Thereafter, the depth decreased for 5 min, then increased again starting at 2:22. At 2:27, the depth attained the second peak, which is lower than the first peak. The change in elevation at 3:00 is difficult to confirm.

In the measured range during the decay phase,

the elevation was lower than the peak. On the other hand, the elevation above upstream, 12 m from the LPS, was almost the same as that in the end phase.

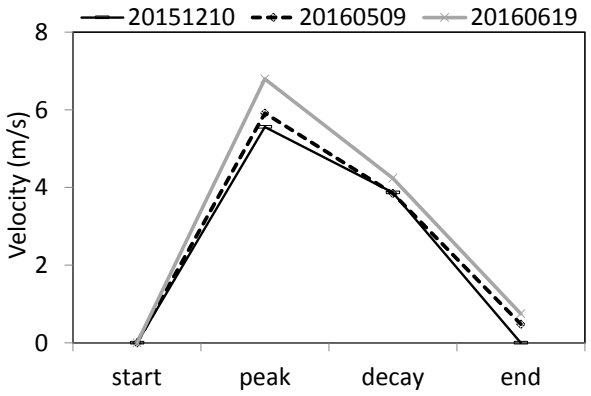

Fig. 7 Flow velocity on each phase

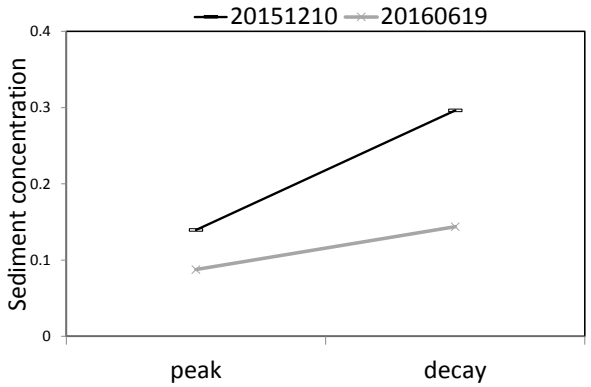

Fig. 8 Sediment concentration on each phase

As a result, the elevation above upstream, 11 m from the dam, at the end phase was higher than that in the start phase. The sediment is approximately 30 cm deep and accumulated at a maximum of approximately 80 cm after the debris flow, which was higher compared with that of the previous. In this case, it is seen that sediment was temporarily deposited upstream of the check dam and one part of it was stored after debris flow.

3.1.3 Debris flow at June 19, 2016

The depth of the debris flow started to rise at approximately 6:30, and then peaked at 6:45 to a height of 1 m. The depth decreased for 8 min until 6:53, across the second peak. The sedimentation, confirmed at this time, was at a point above upstream 7 m from the LPS. The sediment accumulated at a maximum of approximately 80 cm at a point above upstream 10 m from the LPS.

Ultimately, the elevation in the end phase, compared with that in the start phase, was approximately of the same height up to a section 12 m upstream in the longitudinal direction from the LPS. However, it decreased from 18 to 12 m. In this case, it is seen that sediment was temporarily deposited upstream of the check dam during debris flow even though it was finally eroded.

3.1.4 Debris flow at September 20, 2016

Approximately, the depth of the debris flow started to rise gradually at 00:00 and peaked at 00:35. After that, the depth decreased for over 10 min. In the range above upstream, 10 to 14 m from the LPS, the depth was higher than that in the start phase at approximately 2 m. In this case, it is seen that sediment was temporarily deposited upstream of the check dam after the peak of debris flow.

3.2 Calculated hydraulic quantity of debris flow

The flow velocity and sediment concentration shown in **Fig. 7** and **8** are based on Eqs. (1) and (2), respectively. The flow velocities are shown in three cases, from which all the phase data were obtained. Two of the three cases had basal normal stress data.

The velocity during the peak phase was the fastest in all cases, with values of approximately 5–7 m/s, whereas the velocity in the decay phase in all cases was approximately 4 m/s. On the other hand, the sediment concentration in the decay phase was higher than that in the peak phase.

4. DISCUSSION

4.1 Accuracy of the temporal change of river bed elevation measured by LPS

The status of the river bed, which was indicated by the measured data, was confirmed through the CCTV recording of debris flow at June 19 which was clear enough to observe since the flow occurred in the daytime and was not influenced by the noise caused by heavy rains. As shown in **Fig. 9,** the change in the sedimentary condition from the start to the end phase was able to be seen clearly.

The yellow line represents the longitudinal line, which was measured by the LPS, whereas the white line is the range where the sediments were deposited during the decay phase.

At 6:00, a boulder was confirmed to be at the legs of the sediment, which was deposited at the center of the river channel of the area surrounded by a white rectangle. At the peak of the debris flow at 6:45, the boulder was almost invisible. At 6:52, it was confirmed that there was a flow towards the bank in a direction perpendicular to the debris flow. Thereby, the progress of the sediment deposition was confirmed by the intermittent occurrence of sediment-containing flow at the legs of the sediments deposited at the center of the river channel. As a result, the sediments were accumulated upstream where the boulder was located. At approximately 6:53, the depth of the debris flow decreased near the

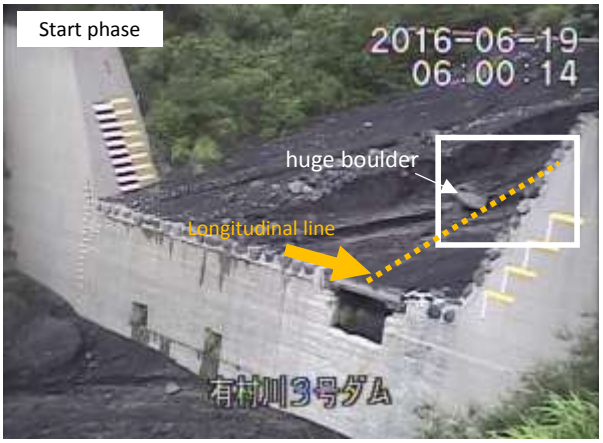

(1) Start phase at 6:00

(2) Peak phase at 6:45

(3) Decay phase at 6:52

(4) Decay phase at 6:53

(5) Decay phase at 6:54

(6) End phase at 8:00

Fig. 9 Temporal change of condition of river bed during debris flow, June 19, 2016

spillway of the dam. At 6:54, the accumulated sediments started to erode. At approximately 8:00, the sediment that accumulated at the right side of the upstream of the boulder disappeared.

Based on **Fig. 9**, it was confirmed that the sedimentary condition in the debris flow shown by CCTV images and the transformation of the longitudinal course measured by the LPS are substantially the same.

4.2 Sedimentation when debris flow occurred

Comparing debris flow elevations in the start phase with those in the end phase of the three cases, which were measured over the entire event, the river bed elevation fell after the debris flow two of the cases. On the other hand, temporal sedimentation was confirmed after the peak in all cases. This was particularly true in the May 9 case, during which the sediments deposited in the decay phase were

retained. Consequently, the sediments had already accumulated before the debris flow.

4.3 Condition that sedimentation appeared

As shown in **Fig. 7**, the flow velocity in the decay phase is lower than that in the peak. Moreover, **Fig. 9** shows that in the decay phase, where the sedimentation occurred, the flow caused not only a downward flow direction, but also one in a direction perpendicular to the main flow. As shown in Fig. 8, the debris flow in the decay phase has a high sediment concentration. Accordingly, when the flow velocity is low and flow with high sediment concentration occurs, the sedimentation in the check dam is assumed to progress.

In two of the three cases that were observed until the end phase, the sediments, which accumulated in the decay phase, disappeared. However, after the peak, the debris flow is assumed to have a low-velocity condition with high sediment concentration. Thus, sedimentation, although temporary, is expected during the debris flow.

5. CONCLUSION

The measurement of the longitudinal profile of the check dam's sedimentation area, which was obtained through the LPS, made it possible to estimate the temporal change in the river bed elevation, as well as the sediment erosion and deposition processes. Sediment accumulation in the decay phase was confirmed in either case of all the debris flow observed. This indicated that sediments had accumulated upstream of the check dam for a brief period during the debris flows. During that time, the flow velocity was lower than the velocity in the peak phase. Moreover, the sediment concentration was higher. This implied that sedimentation occurs when the debris flow rate with high sediment concentration decreases. From these results, it is assumed that the sediment amount deposited may be larger than the measurements given in this report, if the debris flow rate with high sediment concentration decreases and if the subsequent flow does not continue for an extended time.

In the future, it is necessary to gather cases that will consider other observation sites and study the conditions when the sediment control function is expected to occur.

ACKNOWLEDGMENT: The authors thank the Osumi Office of Rivers and Highways for cooperating with us in performing our observation and for providing the data of the debris flow unit weight at the Arimura River.

REFERENCES

Fujita, M, Mizuyama, T and Musashi, Y (2001): Sediment runoff control by a series of sabo dams, Annual Journal of Hydraulic Engineering Vol. 45.

Honda, N and Okumura, T (2005): Estimation of debris flow control with sabo facilities based on numerical simulation, Annual Journal of Hydraulic Engineering Vol. 49.

Mizuyama, T, Irasawa, M, Fukumoto, A and Kobayashi, M (1990): Sediment Control Effect of a Sabo Dam with Large Drainage Condits, Journal of Japan Society of Erosion Control, Vol. 43, No. 2, pp. 29–34.

Murano, Y (1962): On the Longitudinal Profile of Sabo Dam Accumulation, Journal of Japan Society of Erosion Control, No. 47, pp. 21–28.

Nishimoto, H (2011): Discussion on the transition of idea about sediment control effect functioned by check dam, Journal of Japan Society of Erosion Control, Vol. 64, No. 4, pp. 46–51.

Osaka,T, Takahashi, E, Kunitomo, M, Yamakoshi, T, Nowa, Y, Kisa, H, Ishizuka, T, Utsunomiya, R, Yokoyama, K and Mizuyama, T (2013): Field observation of unit weight of flowing debris flows by force plate in Sakurajima, Japan", Journal of Japan Society of Erosion Control, Vol. 65, No. 6, pp. 46–50.

River bureau, Ministry of Construction (1997): Ministry of Construction Technical criteria for river works for research

Satou, K, Hongou, K, Uehara, S and Mizuyama, T (2000): Case study on sediment control by a slit sabo dam, Journal of Japan Society of Erosion Control, Vol. 53, No. 2, pp. 43–47.

Yoshida, Y, Matsuyama, K, Murano and Y, Izumi, I (1964): On the Longitudinal Profile of Sabo Dam Accumulation, Journal of Japan Society of Erosion Control, No. 55, pp. 23–29.

Yoshinaga, S, Shimizu, T, Mizutani, T, Takahashi, Y, Fujimura, N, Izumiyama, H and Ishizuka, T (2017): A method for measuring nappe distance and depth of debris flow using laser range finder and application to estimate debris flow velocity, Journal of the Japan Society of Erosion Control Engineering, Vol. 70, No. 1, pp. 46–53.

Critical Rainfall Thresholds for Hydrological Processes Leading to Debris Flow due to Torrent Bed Material Scouring

Yasushi SANO[1], Takashi YAMADA[2], Tsuyoshi IKESHIMA[3] and Sadakazu MATSUMOTO[3]

[1] Nippon Koei CO.,LTD,Japan (former Graduate School of Bioresources,Mie University,Japan)

[2]Graduate School of Agriculture,Hokkaido University,Japan(former Graduate School of Bioresources,Mie University,Japan)

[3]Nippon Koei CO.,LTD,Japan

*Corresponding author. E-mail: a8359@n-koei.co.jp

In this study, we employ the 10-minute rainfall intensity and the effective rainfall with a half-life period most similar to the characteristics of torrent bed material water storage in the storage type model to calculate and evaluate the critical rainfall thresholds for hydrological processes leading to the generation of debris flow due to torrent bed material scouring. Critical rainfall thresholds for hydrological processes leading to debris flow since 2008 were effective rainfall of 41.2 mm and 10-minute rainfall of 6 mm for pipe flow without generating a debris flow, effective rainfall of 129.1 mm and 10-minute rainfall of 8 mm for a clogged pipe exit without generating debris flow, and effective rainfall of 126.8 mm and 10-minute rainfall of 19 mm for debris flow generation. These results suggest that a pipe flow has a small possibility of debris flow generation. For a clogged pipe exit, the amount of water stored in the torrent bed material meets the quantitative conditions required to generate a debris flow, indicating that a 10-minute rainfall of 19 mm or more may increase the possibility of a debris flow occurrence.

Key words: debris flow, hydrological process, rainfall indices, critical rainfall threshold

1. INTRODUCTION

Generation and development process of debris flow has not been revealed as yet. As a study on debris flows due to torrent bed material scouring, it suggested that torrent bedmaterial saturated due to rising groundwater level and debris flow occurred using hydraulic model experiments [*Takahashi*, 1977]. Field observations have been conducted in Japan and overseas in recent years [*Suwa et al.*, 1989 ; *Imaizumi et al.*, 2002 ; *M.Berti et al.*, 2005 ; *Jeffrey A.Coe et al.*, 2008 ; *C.Gregoretti et al.*, 2008 ; *Mizutanii et al.*, 2008 ; *Hayami et al.*, 2013 ; *Imaizumi et al.*, 2016].

In these previous studies, it suggests that debris flow occurs even if torrent bed material is not saturated or sediments are scoured due to surface flow. But there are still many unclear points on the process of generation of debris flow.11 Debris flows due to torrent bed material scouring occurred at the Nishinokaito River of Mount Fujiwara in Inabe City of the Mie Prefecture, Japan between 1999 and 2012. Our hydrological observations including runoff of subsurface flows from the torrent bed material, aim to reveal the mechanism of hydrological processes (pipe flow, clogged pipe exit, and debris flow) leading to debris flow and to propose a method to predict the timing and magnitude of debris flow. Due to high-intensity rainfall, hydrological processes including pipe flow and clogged pipe exits induce debris flow at the Nishinokaito River. The authors studied affected and non-affected areas by the occurrence of hydrological phenomenon using the RBFN (Radial Basis Function Network) method [*Yamada et al.*, 2017]. However, the relationship between the occurrence of hydrological phenomenon and the values of soil moisture index or

effective rainfall using the storage type model based on actual discharge data are not elucidated. We employ the 10-minute rainfall intensity and the effective rainfall with a half-life period most similar to the characteristics of torrent

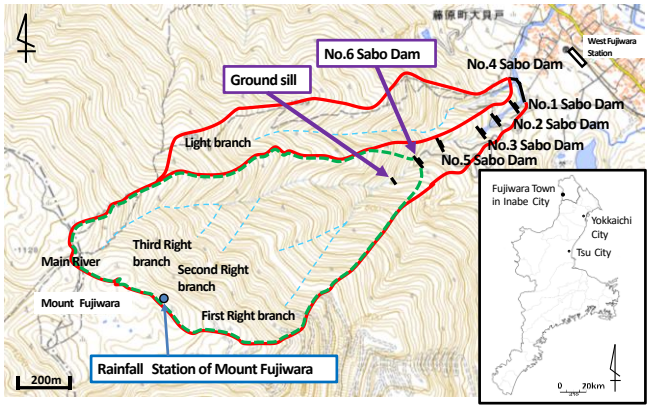

Fig.1 Location of the Nisinokaito river
(Dotted areas show study area.)

bed material water storage in the storage type model to calculate and evaluate the critical rainfall thresholds for hydrological processes leading to the generation of debris flow due to torrent bed material scouring.

2. METHODS

2.1 Study area

The basin upstream of the No. 6 Sabo Dam (**Fig. 1**) has an area of 0.75 km^2, a flow path length (horizontal distance from the No. 6 Sabo Dam to the summit) of approximately 1.8 km, and a mean gradient of 24.3°. The geological setting is mainly composed of Paleozoic and Mesozoic lime rocks. Outcrops of calcareous breccia, which are mixed in the top layer of riverbed, are re-consolidated by rainfall. In 2010, the Kuwana Construction Office of Mie Prefecture conducted a boring investigation at the middle reach of the Nishinokaito River (an upstream area 250 m from the No. 6 Sabo Dam). The results revealed that a debris flow with a thickness between 5 m to 20 m is deposited at the riverbed. The main component of the sediment is sand and sub-granular gravel, which is a few centimeters in size. Some parts also contain silt and clay .

Although construction of the No. 6 Sabo Dam was completed in 2010, it became fully sediment-filled due to the 2012 debris flow and the river has not been dredged. Upstream of the No. 6 Sabo Dam has a thick layer of debris sediment between 5 m to 20 m. Thus, surface water is not permitted

Fig 2 Observation of subsurface flow discharge at drainage holes of the No.6 Sabo dam

except for heavy rainfall. Rainfall runs as a subsurface flow inside the riverbed sediment prior to discharging from drainage holes in the No. 6 Sabo Dam.

Observations of the subsurface water flow from right above the basin of the No. 6 Sabo Dam were conducted using the drainage holes of the dam. Between 2009 and 2011, an interval camera (KADEC21-EYEII) was installed at the lower of the No.6 Sabo Dam to record the subsurface flow conditions from the drainage holes such as water levels. In 2012 two ultrasonic water level gauges (SE-QT50U) were installed to monitor the water levels. One monitors two of the five drainage holes on the right and the other monitors the lowest left one (**Fig. 2**). It was difficult to install and maintain an ultrasonic water level gauge for the drainages located at the middle and upper levels;

hence, an interval camera (KADEC21-EYEII) was installed at the right wing of sub dam of the No.6 Sabo Dam.

The subsurface water levels at the middle and upper drainage holes were obtained by the imagery analysis of the flow from each drainage hole. Assuming a circular cross-section of drainage hloe, the water surface width of the subsurface water was read from the imagery. Then the water level was calculated using a geometrical relationship, which was subsequently converted into the discharge using the h–Q curve obtained by the authors previous study.

The hydrological phenomena related to the processes leading up to the debris flow such as pipe flow and the occurrence timing of pipe exit clogging were based on the authors' past observations (using imagery data obtained from the multiple interval cameras installed at approximately 150 m upstream from the No. 6 Sabo Dam) [*Yamada et al.*, 2017].

In August 2015, we also set an interval camera at the lower of the dam to observe of the night-time subsurface flow discharge from drainage holes of the dam.

2.2 The hydrological processes leading to debris flow in this study

A debris flow occurred at Nishinokaito river on September 2 to 3, 2008. A photo analysis of the hydrological process leading up to the generation of the debris flow showed an increase in discharge and turbidity of the subsurface flows from the cross-section of the torrent bed material (In this paper, this is defined as water spouting from pipe exits.) Due to clogged pipe exits, subsurface flows spouted from several places, and a cross-section of torrent bed material collapsed (excavation cross-section area for the Sabo Dam construction). These observations indicate that when subsurface flows spout, pipe flows occur within the torrent bed material. Therefore, these hydrological phenomena should be studied to elucidate the process for generating torrent bed scouring-induced debris flow at the Nishinokaito river [*Yamada et al.*, 2009].

In this study, the hydrological processes leading to debris flow were defined as pipe flow, clogged pipe exits, and debris flow, obtained by photo -analysis of our observation s conducted since 2008. By following the convention used in the previous study [*Yamada et al.*, 2009], "pipe flow occurrence" means a subsurface water spurt from the large pores (pipe holes) formed by gravel in the surface of riverbed sediment,

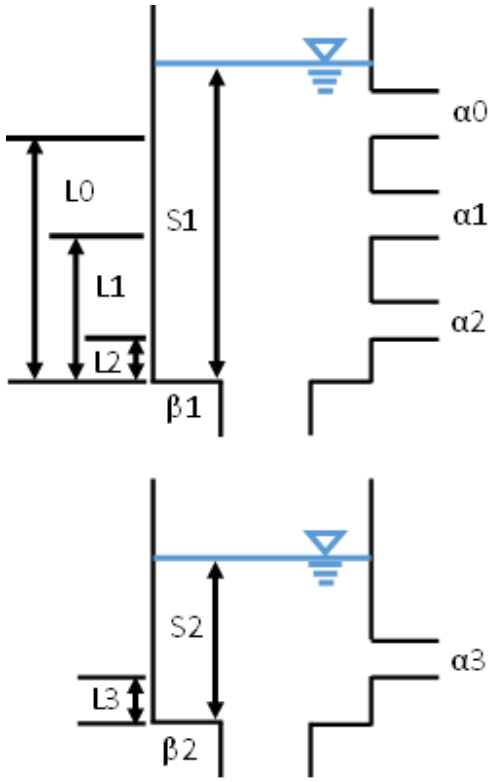

Fig 3 storage type model
(first tank and second tank)

Table 1 Parameters of the storage type model

$\alpha 0$ (1/hours)	0.062	$\beta 1$ (1/hours)	0.110	$L0$ (mm)	160
$\alpha 1$ (1/hours)	0.024			$L1$ (mm)	60
$\alpha 2$ (1/hours)	0.007			$L2$ (mm)	28
$\alpha 3$ (1/hours)	0.003	$\beta 2$ (1/hours)	0.087	$L3$ (mm)	5

and "pipe exit clogging" indicates that a drainage exit clogs or subsurface water flow suddenly stops during torrential rainfall(pipe exit clogging would be induced by collapse of pipe walls during increasing subsurface flow in torrential rainfall[*Yamada et al.*, 2017].

2.3 Rainfall index

In this study, rainfall of the occurrence of each hydrological process was regarded as "rainfall of occurrence".
Both the 10-minute rainfall and the effective rainfall were employed as rainfall indices.

Storage type model (first tank and second tank) proposed by previous study [*Sano et.al.*,2015] was employed (**Fig.3**). This storage type model assumes the first tank is the surface flow layer and the subsurface flow layer, as indicated by a boring investigation of the local riverbed sediment [*Kuwana Construction Office of Mie Prefecture*, 2010] and the flow characteristics of subsurface water during torrential rainfall. Table 1 shows each parameter. The parameters were determined based on repeated trial and error to recreate the water flow amount of the effective rainfall events between 2012 and 2014 with a clear flow peak. (This is a total of 26 rainfall events.) Since the storage type model uses timescale parameters, each parameter for the flow coefficient (αn) and the permeability coefficient (βn) is 1/6 of its value to fit on a 10-minute scale.

We employ the 10-minute rainfall intensity and the effective rainfall and evaluate the critical rainfall thresholds for hydrological processes.

The effective rainfall was calculated by using Equation 1.

$$R_w = \sum a_{1i} \times R_{1i} \cdots\cdots\cdots\cdots (1)$$

where R_w : effective rainfall, R_{1i} : 10 minute rainfall before i minute (i=10,20,30…), a_{1i} : Reduction coefficient before i minute, $a_{1i} = 0.5^{i/T}$, T : half-life period(minute)

To observe the changes in water storage of the first tank and to find similarities to the half-life period, we arbitrarily set 240, 300, 360, and 420 minutes for the half-life periods. To observe the changes in the water storage of the sum of the first and second tanks and to find similarities to the half-life period, we arbitrarily set 540, 600, 660, and 720 minutes for the half-life periods.

The half-life period of effective rainfall, which is equivalent to the changes in a tank's water storage in the storage type model (first tank and second tank) on a 10-minute scale was determined using the similarities between the water storage of each tank and the effective rainfall or the mean value of their absolute difference.

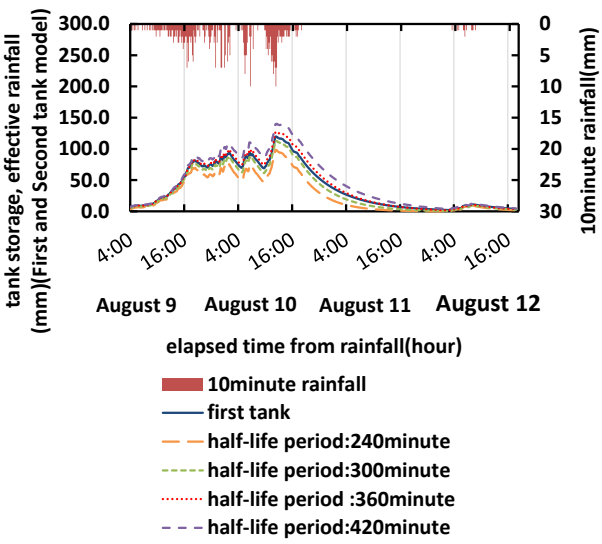

Fig.4 Half-life period of the effective rainfall equivalent to the first tank (Case on August 9, 2014)

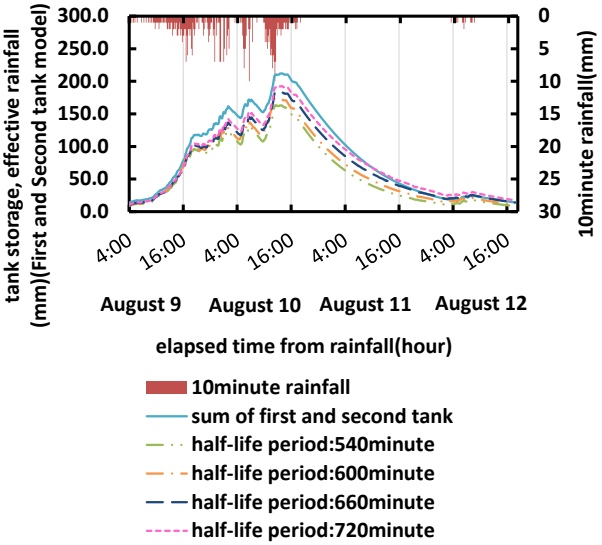

Fig.5 Half-life period of the effective rainfall equivalent to the sum of first and second tank (Case on August 9, 2014)

3 RESULTS

3.1 The correspondence of effective rainfall to the water storage of each tank in a storage type model

Figure 4 shows the correspondence of the effective rainfall to the water storage in the first tank and changes in half-life periods. A half-life period of 360 minutes for the effective rainfall was the closest to the changes observed in the first tank's water storage and its mean value of the absolute difference was also the smallest.

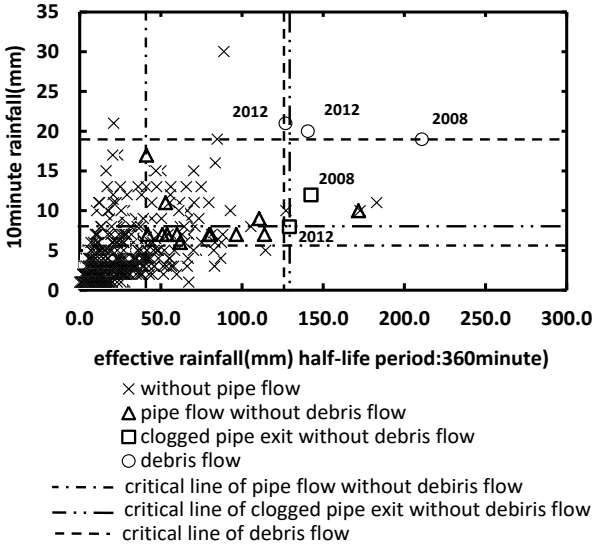

Fig6 Critical rainfall thresholds(effective rainfall with a half-life period of 360minutes) to generate a hydrological processes

Figure 5 shows the sum of the water storage of the first and second tanks as well as half-life periods of the effective rainfall. A half-life period of 720 minutes of the effective rainfall was the closest to the sum and its absolute difference was also the smallest.

It is assumed that first tank storage is closely related to hydrological processes leading to debris flow. Therefore, effective rainfall with a half-life of 360 minutes corresponding to the storage height of the first tank was employed.

3.2 The critical rainfall thresholds for hydrological processes leading to the generation of debris flow

Critical rainfall thresholds (effective rainfall with a half-life period of 360 minutes) for hydrological processes leading to debris flow since 2008 were effective rainfall of 41.2 mm and 10-minute rainfall of 6 mm for pipe flow without generating a debris flow, effective rainfall of 129.1 mm and 10-minute rainfall of 8 mm for a clogged pipe exit without generating debris flow, and effective rainfall of 126.8 mm and 10-minute rainfall of 19 mm for debris flow generation (**Fig. 6**). These results suggest that a pipe flow has a small possibility of debris flow generation. For a clogged pipe exit, the amount of water stored in the torrent bed material meets the quantitative conditions required to generate a debris flow, indicating that a 10-minute rainfall of 19 mm or more may increase the possibility of a debris flow occurrence.

4 CONCLUSIONS

1) Half-life period of the effective rainfall equivalent to the first tank and the sum of first and second tank were 360 minutes and 720 minutes, respectively.

2) Critical rainfall thresholds (effective rainfall with a half-life period of 360 minutes) for hydrological processes leading to debris flow since 2008 were revealed.

3) Possibility of debris flow generation during pipe flow is small, but a clogged pipe exit increases the possibility of debris flow generation with a 10-minute rainfall of 19 mm or more at the Nishinokaito River.

REFERENCES:

C. Gregoretti, G. Dalla Fontana (2008) : The triggering of debris flow due to channel-bed failure in some alpine headwater basins of the Dolomites: analyses of critical runoff, Hydrological Processes, No.22, p.2248-2263.

Fumitoshi Imaizumi, Satoshi Tsuchiya, Okihiro Ohsaka (2002) : Observation of the formation and dynamic process of debris flows in a mountainous debris torrent, Journal of the Japan Society of Erosion Control Engineering, Vol.55, No.3, p.50-55. (in Japanese with English abstract)

Hiroshi Suwa, Tomohisa Manaka, Atsushi Inaniwa (1989) : Occurrence of debris flows and their scales in the Kamikamihori Valley of Mount Yakedake, Disaster Prevention Research Institute Annuals, No.32, B-1, p.229-247. (in Japanese with English abstract)

Imaizumi Fumitoshi, Tsuchiya Satoshi and Ohsaka Okihiro (2016) : Behavior of Boulders within a Debris Flow Initiation, International Journal of Erosion Control Engineering, Vol.9, No.3, p.91-p.100.

Jeffrey A. Coe, David A. Kinner, Jonathan W. Godt (2008) : Initiation conditions for debris flows generated by runoff at Chalk Cliffs, central Colorado, Geomorphology, No.96, p.270-297.

M. Berti, A. Simoni (2005) : Experimental evidences and numerical modelling of debris flow initiated by channel runoff, Landslides, No.2, p.171-182.

Satoshi Hayami, Yoshifumi Satofuka (2013) : Observation of moisuture changes in the deposit on riverbed and sediment movement in the mountainious watershed, Journal of Japan Society of Civil Engineers, Ser. B1 (Hydraulic Engineering) , Vol.69 , No.4 , I_943-I_948. (in Japanese with English abstract)

Takashi Yamada, Hirofumi Sato, Shingo Yamada, Hideaki Kikuchi (2017): Hydrological Observation of Subsurface Flows Spouting from Pipe Exits in Torrent Bed Material and its Triggering Rainfall Conditions of the Nishinokaito River in Mount Fujiwara, Mie Prefecture, Japan. International Journal of Erosion Control Engineering. Vol. 10, No. 1.

Tamotsu Takahashi (1977) : A mechanism of occurrence of mud-debris flows and their characteristics in motion, Disaster Prevention Research Institute Annuals, No 20, B-2, p.405-435. (in Japanese with English abstract)

Taro Mizutani, Yoshifumi Satofuka, Daizo Tsutsumi, Takahisa Mizuyama (2008) : Moisture changes in deposits on a steep stream, Journal of the Japan Society of Erosion Control Engineering, Vol.61, No.3, p.27-30. (in Japanese with English abstract)

Yasushi Sano, Ryutaro Kobayashi, Takashi Yamada (2015): Characteristics of subsurface flow in torrent bed materials and it's storage model during torrential rainfall in case of Nishinokaito River of Mount Fujiwara, Inabe city ,Mie Prefecture, Abstract of Annual Meeting of Erosion Control Engineering,B-252-253. (In Japanese)

Study on Correlation of Electrical Conductivity and Potential Large-scale Landslide in Taiwan

Chieh-Hsuan WENG[1], Yuan-Jung TSAI[2*], Chjeng-Lun SHIEH[3] and Tomohiro EGUSA[4]

[1] Master, International Master Program on Natural Hazards Mitigation and Management, National Cheng Kung University, Taiwan (No.1, University Road, Tainan City 701, Taiwan)

[2] Researcher, Disaster Prevention Research Center, National Cheng Kung University, Taiwan (3F., No.500, Sec. 3, Anming Rd., Annan Dist., Tainan City 709, Taiwan)

[3] Director, Disaster Prevention Research Center, National Cheng Kung University, Taiwan (3F., No.500, Sec. 3, Anming Rd., Annan Dist., Tainan City 709, Taiwan)

[3] Researcher, Agricultural and Life Sciences, the University of Tokyo (7 Chome-3-1 Hongo, Bunkyō, Tokyo 113-8654, Japan)

*Corresponding author. E-mail: rongtsai@dprc.ncku.edu.tw

In this study, a total of 415 water samples were taken in southern and eastern Taiwan. The concentration of inorganic ions is detected using ion chromatography with an electricity conductivity meter to detect the electricity conductivity in water samples. In terms of time difference, the electricity conductivity of dry season is larger than wet season, the electricity conductivity value is about 300 μS/m, as electricity conductivity is affected by rainfall. For spatial difference, out of four study zones, the Kaoping watershed has highest value and coastal area in Taitung has lowest value. In Kaoping watershed, the difference of electricity conductivity value is about 200 μS/m. For the relationship between landslide rate and electricity conductivity, the potential landslide rate is calculated by dividing the sub-watershed area into large-scale potential landslide area, using the measurement points at downstream of the sub-watershed to represent the sub-watershed. It can regress a straight line, which R^2=0.59. If the landslide rate is high, the electricity conductivity will be high. For analysis of electricity conductivity of stream, the electricity conductivity of stream is affected by inrush water from the potential landslide. When the measurement points are close to the inrush water, electricity conductivity will raise, on the contrary, when the measurement point is further from inrush water, the electricity conductivity will decrease. Above all, it can handle the relationship between landslide and electricity conductivity and hope to establish the warning system of the large-scale landslide, to fight for more time to respond to large-scale landslides.

Key words: large-scale landslide, water quality, electricity conductivity

1. INTRODUCTION

Large-scale landslide (depth>10 meter, area> 10 hectare, or volume > 100,000 cube meter) disasters have become an important issue after Typhoon Morakot in 2009, which caused more than 400 deaths in Hsiaolin Village [*Shieh et al.*, 2010]. To avoid reoccurrence of disasters, Taiwanese government has proposed a series of disaster prevention and mitigation projects to establish a risk-based framework for large-scale landslide disasters [*Soil and Water Conservation Bureau*, 2015].

The first step of the framework, high resolution digital elevation models, was used to identify potential large-scale landslide areas (PLA). With microtopography, the location and boundary of potential large-scale landslide could be better identified [*Lin et al*, 2012]. There are more than 2,000 sites of potential large-scale landslides identified by the Forestry Bureau, Council of Agriculture, Executive Yuan and Central Geological Survey, Ministry of Economic Affairs [*Forestry Bureau*, 2012*; Central Geological Survey*, 2011].

After the investigation of potential large-scale landslides, it is necessary to predict the occurrence of the large-scale landslide. Rainfall, infiltration and groundwater variation play important roles in the triggering of large-scale landslides [*Shieh et al*, 2013; *Lee et al*., 2015]. It is important to clarify the volume or ratio variation of groundwater as it is the key for early warning systems of large-scale landslides.

The monitoring of volume or ratio variation of groundwater is not easy in mountainous areas, Jitousono et al tried to use electrical conductivity

(EC) as a factor to respond to groundwater condition changes during rainfall events. [*Jitousono et al.*, 2006]

For potential large-scale landslides, the slip surface was under development; when infiltration occurs, groundwater would path the cracks as the flow path. With the development of slip surface, the flow path would increase. With longer flow duration, the EC of the groundwater will increase with more soluble material [*Jitousono*, 2014]. This concept shows the possibility of the early warning system to detect the occurrence of large-scale landslide through EC.

The main purpose of this research is to reproduce the relationship between EC and PLA in Taiwan. Furthermore, to find the possibility of early-warning through monitoring EC of stream water in mountain area.

2. RESEARCH METHOD

2.1 Study area

To reproduce the relationship between EC and PLA in Taiwan, this research attempts to use wide range survey for EC at investigated PLA in south and east Taiwan. In **Fig.1**, PLA, with microtopography of landslide and area is larger than 10ha, were identified from 2010 to 2012 by Forestry Bureau and Central Geological Survey.

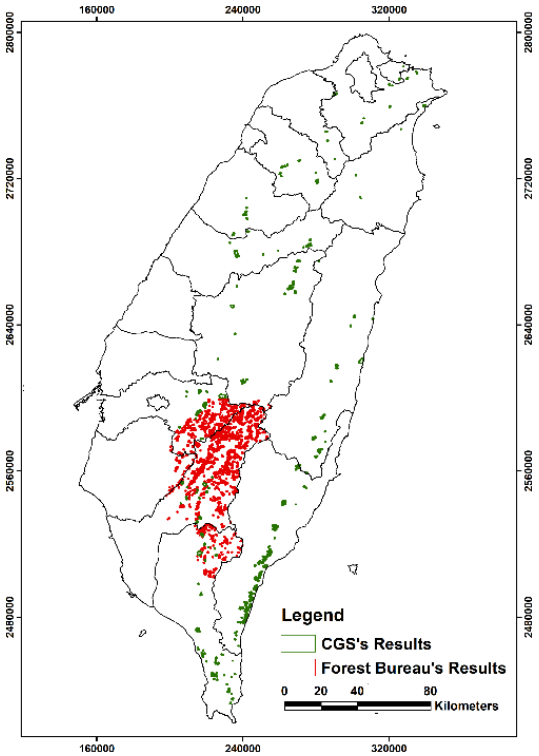

Fig. 1 Investigation of PLA in Taiwan

2.2 Water sampling

To set the relationship between EC and PLA, different geology, seasons, and locations were considered.

For different geology, water sampling work was taken in 8 different watersheds, such as Tsengwen, Kaoping, Linbian watersheds, from western Taiwan, and Zhiben, Dazhu, Beinan and Daniao watersheds, from eastern Taiwan. In consideration of the effect of different seasons, sampling was taken in dry and wet seasons at the same locations. In consideration of spatial difference, the sampling work was taken at three locations in the same watershed (**Fig.2**) such as spring on the slope, start of the stream, and outlet of the stream.

Water samples were collected in a 200 ml pre-washed plastic bottles filled with source water and ensuring there was no air in the bottle for more reliable samples.

	i. Sample at spring on the slope To analyze the water from subsurface water of groundwater.
	ii. Sample at the initial of the stream To clarify the basic condition without groundwater.
	iii. Sample at the outlet of the stream To clarify the mixture condition of stream water and groundwater.

Fig. 2 Location of water sampling

2.3 Source analysis

To avoid polluted water samples, Piper diagram were applied. Piper diagram was used to separate groundwater into four catalogues (**Fig.3**) by anions and cations in the groundwater [*Chiang*, 1994].

Zone I, called Carbonate hardness, was focused on Ca-HCO_3 and identified as unconfined groundwater, rainfall or stream water. Zone II, called Carbonate alkali, was focused on Na-HCO3 and identified as deep confined groundwater. Zone III was called Non-carbonate hardness, focused on Ca-SO4 and Ca-Cl, usually found in volcanic areas. Zone IV, called Non-carbonate alkali, focused on Na-SO4 and Na-Cl, usually identified as saltation by sea water. In this research, only water samples belong to Zone I and Zone II were used for further analysis.

2.4 Water sample analysis

To classify the water sample with Piper diagram, the concentration ions of water samples need to be valued. All water samples were send to

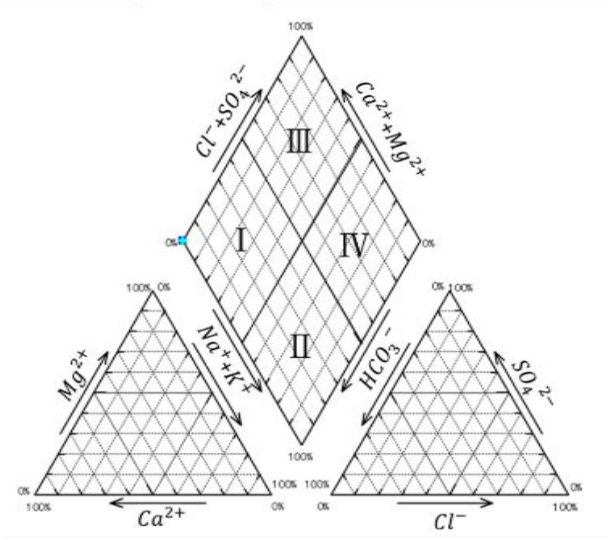

Fig. 3 Piper diagram

the University of Tokyo for ion chromatography (with Shimadzu LC10-A). EC was measured with EC meter such as HORIBA B-713.

Box-and-Whisker Plot was selected to confirm the basic value of EC. This method can show not only maximum, minimum and median, but also first quartile, third quartile and Interquartile range (IQR). The IQR is the 1st quartile subtracted from the 3rd quartile; these quartiles can be clearly seen on a box plot and the interquartile range is a measure of variability, based on dividing a data set into quartiles. The quartile won't be affected by extremum.

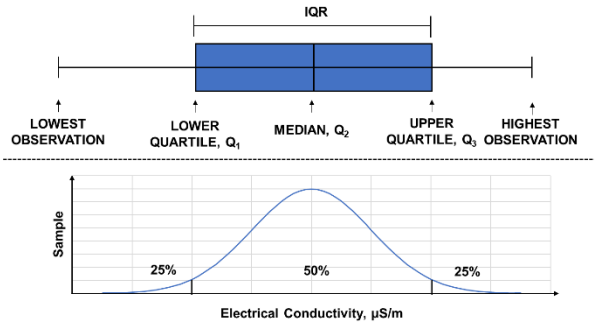

Fig. 4 Box-and-Whisker Plot

3. RESULT

3.1 Result of source analysis

There were 415 water samples collected from PLA in southern Taiwan and coastal areas in Taitung (**Fig.5**). After source analysis (**Fig.6**), 6 samples were removed to reduce the effect of human activities or saltation by sea water, all reliable water samples are as listed in **Tab.1**.

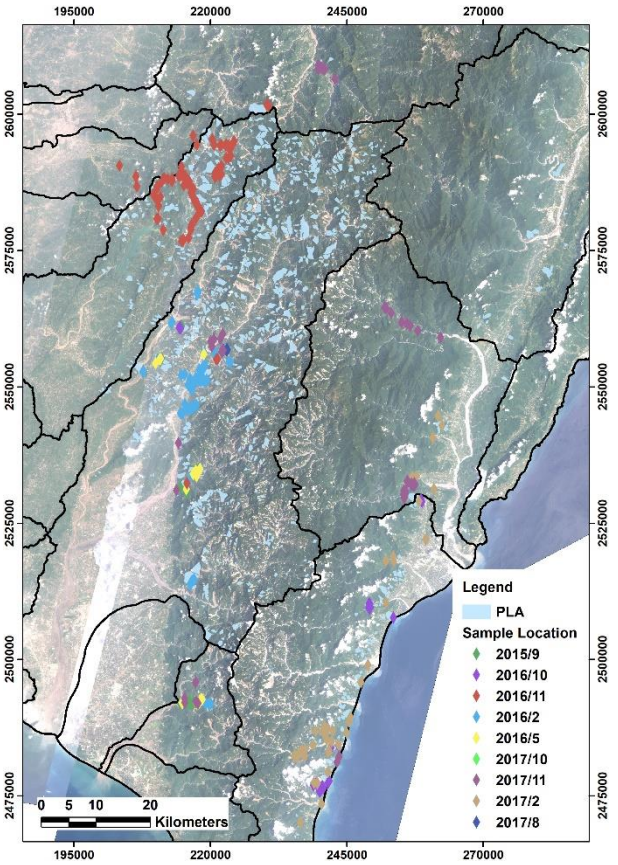

Fig. 5 Location of water sampling

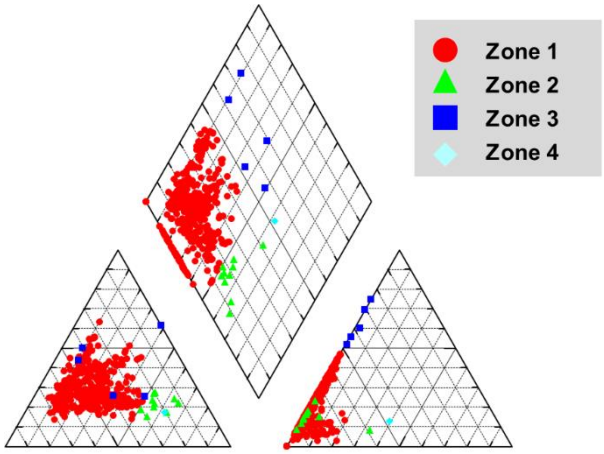

Fig. 6 Source analysis with Piper diagram

Table 1. List of water samples in different basin

Name of basin	Number
Tsengwen	101
Kaoping	207
Linbian	51
Coastal areas in Taitung	48
Total	409

3.2 Time difference of water sample

The time difference was considered dry and wet season. It is obvious that dry season is larger than wet season that electricity conductivity is affected by rainfall. Hence, the electricity conductivity in dry season is higher. It means EC in dry season could be more discernible.

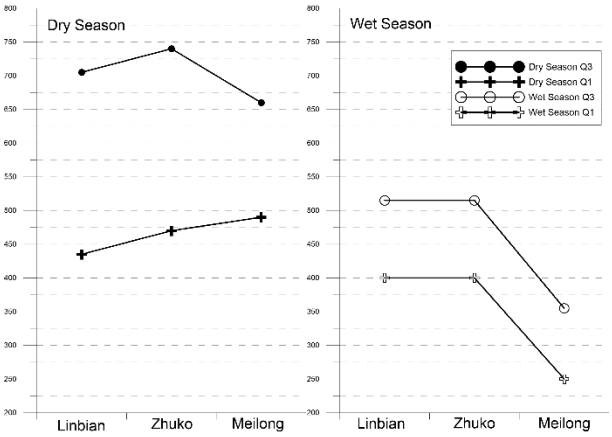

Fig. 7 Time difference of water samples

3.3 Spatial difference of water sample

The spatial difference was compared with dry season water sample from four different watersheds. Kaoping watershed has highest EC, following with Linbian watershed, Tsengwen watershed and coastal area in Taitung (**Fig.8**). This indicates each watershed had different background values of EC.

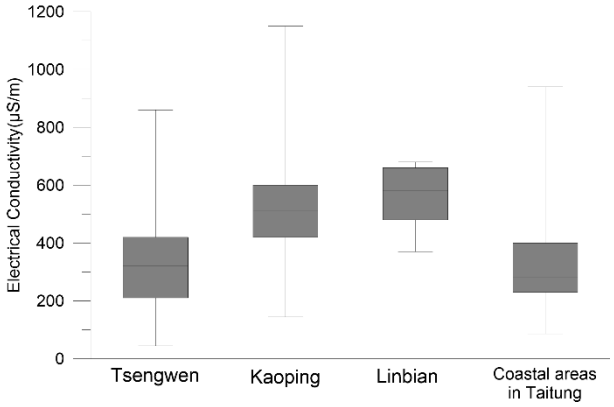

Fig. 8 The variation of EC in different watershed

3.4 Relationship between Potential landslide and conductivity

From results of time difference and spatial difference, EC could be used to clarify for different watersheds or seasons. It would be possible to set EC as a pre-warning factor for PLA. To verify the idea, EC should have some relationship with PLA.

The potential landslide rate of the watershed was evaluated by the area of PLA and watershed by Eq. (1). **Fig.9** shows the concept of analysis. EC of the watershed was measured at the outlet of the watershed plotted as red points. The boundary of PLA was shown in red lines and the boundary of the watershed was shown in yellow lines. Landslide potential rate was counted as follows:

$$\alpha=(A_{PLA}/A_w)\ X\ 100\% \quad (1)$$

where α is potential landslide rate, A_{PLA} is total area of PLA in the watershed, A_w is area of the watershed.

There are 24 watersheds (**Table2.**) from 4 different basins were selected to clarify the relationship between EC and PLA. Based on the results of the experiment, geology differences didn't alter EC value.

The relationship between EC and potential landslide rate was plotted as **Fig.10**. It could regress as a straight line, which R^2=0.59. It shows EC getting higher with increased potential landslide rate in the watershed. The relationship between EC and PLA could be confirmed.

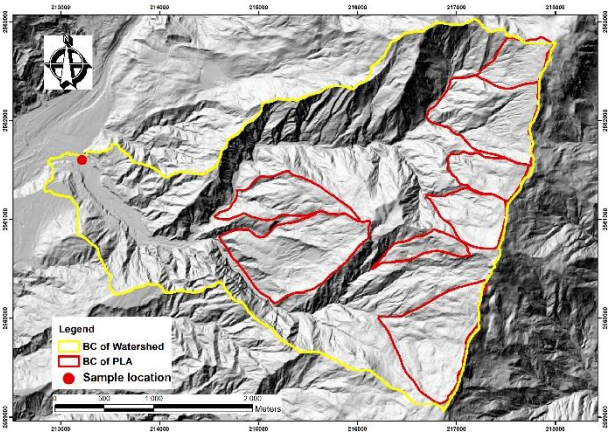

Fig. 9 Illustration of potential landslide rate

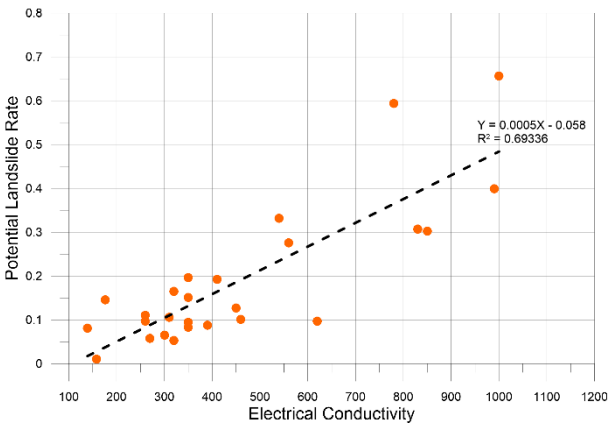

Fig. 10 Relationship between potential landslide rate and EC

Table 2. List of water sample in different watershed

Name of watershed	Area of watershed (ha)	Basin	Geology	Area of PLA (ha)	Potential landslide rate (%)	EC (μS/m)
Zhiben	15,578	Taitung	Alluvium	164	1.05	158
Daxi	3,990	Taitung	Alluvium	440	11.02	260
Daniao	4,346	Taitung	Sandstone Lentils	422	9.71	260
Nanpingpu	1,249	Kaoping	Massive Sandstone	66	5.30	320
Youkuang	1,308	Kaoping	Massive Sandstone	216	16.50	320
Huaguoshan	5,093	Kaoping	Massive Sandstone	421	8.26	350
Putou	3,042	Kaoping	Massive Sandstone	267	8.77	390
Zhipu river	879	Kaoping	Massive Sandstone	111	12.66	450
Wuziliaobei	1,042	Kaoping	Massive Sandstone	345	33.15	540
Huaguoshan	448	Kaoping	Massive Sandstone	43	9.70	620
Putou	98	Kaoping	Massive Sandstone	39	39.92	990
Zhenwoshan	10,710	Kaoping	Sandstone and Shale	614	5.74	270
Zhuowushan North	1,957	Kaoping	Sandstone and Shale	184	9.42	350
Meilunshan	525	Kaoping	Sandstone and Shale	161	30.70	830
Dongtengzhi	2,869	Kaoping	Argillite or Slate	289	10.06	460
Ailiaobei	2,407	Kaoping	Argillite or Slate	663	27.53	560
Zhipu	98	Kaoping	Argillite or Slate	58	59.36	780
Shanhuangma	2,697	Tsengwen	Limestone lentils	530	19.64	350
Shanmeiqiao	551	Tsengwen	Massive Sandstone	58	10.55	310
Caoshan	915	Tsengwen	Sandstone and Shale	74	8.07	139
Hudiqiao	890	Tsengwen	Sandstone and Shale	130	14.57	176
Dabang	1,097	Tsengwen	Sandstone and Shale	71	6.51	300
Huanggoukeng	695	Tsengwen	Sandstone and Shale	105	15.11	350
Longmei	647	Tsengwen	Sandstone and Shale	125	19.24	410

4. EFFECT BETWEEN PLA AND EC

After the relationship between EC and PLA was established, two watersheds were selected in Kaoping watershed to discuss the effect of PLA to EC along the stream flow.

4.1 Watershed I

4.1.1 Basic characteristics

Watershed I was located at midstream of Kaoping watershed (**Fig.11**). The watershed was listed as a potential debris flow torrent by the Soil and Water Conservation Bureau due to historical events, such as Typhoon Morakot. Lots of PLA were identified upstream of the watershed. The area of watershed is 478 ha, and area of total PLA is 166ha. The area of PLA at downstream is 28 ha. The main geology is argillite or slate

4.1.2 Investigation results

EC collected in the dry season were used in Watershed I. Sampling locations were shown in **Fig.12** with green cross. Main stream was shown with blue line and red line means the boundary of PLA. There are total five PLA in the watershed.

EC along Watershed I from downstream to upstream was showed in **Fig.13**. From upstream to downstream, EC got higher while got close to the PLA (point 6 to 8). After passing through the PLA, EC decreased (Point 8 to 10). The EC value changed little once passed the PLA. Numbers of PLA in the upstream didn't affect the EC value.

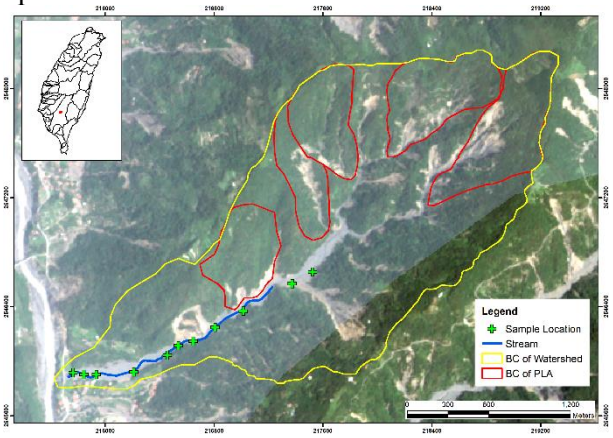

Fig. 11 Location of watershed I

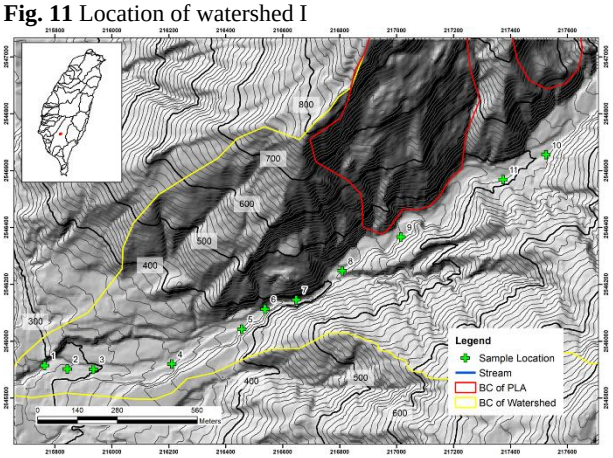

Fig. 12 Sampling locations in Watershed I

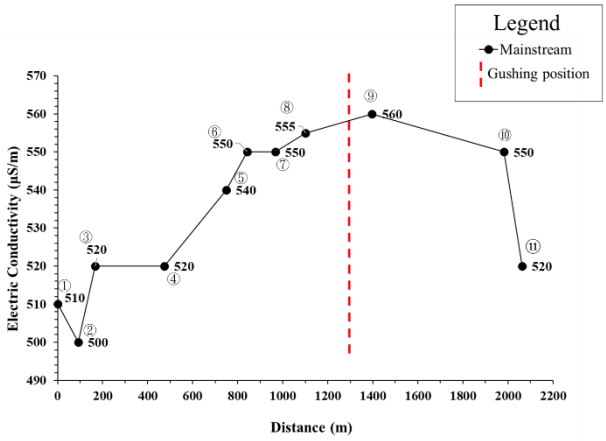

Fig. 13 EC distribution in Watershed I

4.2 Watershed II

4.2.1 Basic Characteristics

Watershed II was also the sub-watershed of Kaoping watershed. The watershed area is 561 hectares, as shown in **Fig.14**. There is only one PLA (39 ha) at the upper boundary of the watershed and many existing landslides in the watershed.

4.2.2 Investigation results

EC was investigated in watersheds during the dry season. Water samples were collected from downstream to the end of the streams where no water flowed. In **Fig.15**, green cross means sampling locations of the main stream shown by blue line from downstream to upstream. Red lines are the boundaries of PLA.

Based on the samples, there were three peaks along the stream. For first peak, EC value increased from point 2 to 5 because of the existing landslide in the brunch. After point 6, leaving the landslide area, EC decreased. EC increased significantly as it passed through PLA (point 6 to 8). The results showed that the idea from Jitousono could be reproduced in Taiwan. From point 10, EC increased again with another existing landslide area.

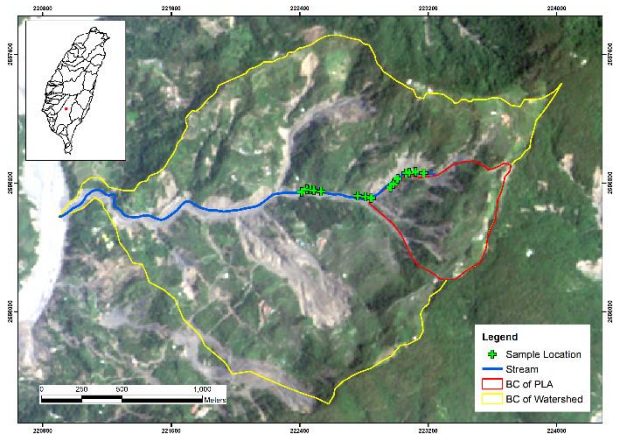

Fig. 14 Location of Watershed II

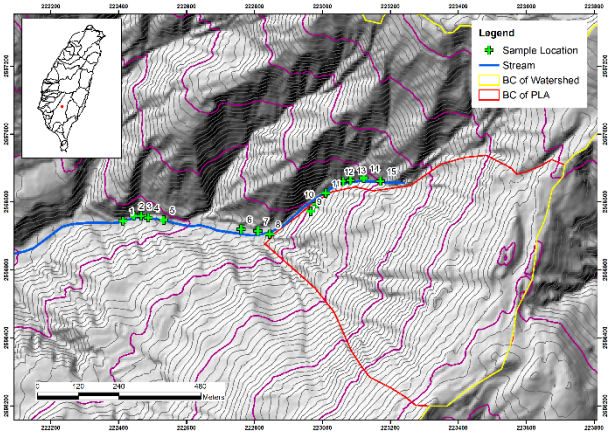

Fig. 15 Distribution of sampling locations in Watershed II

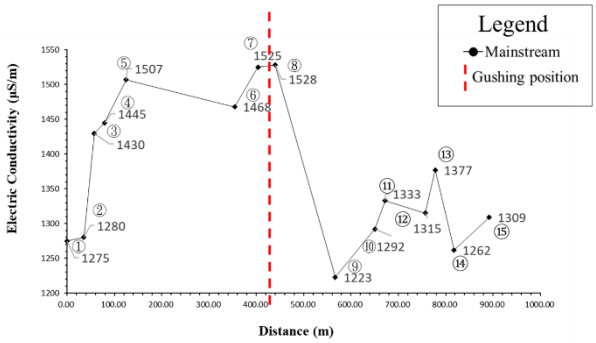

Fig. 16 EC distribution in Watershed II

According to the experimental results from two watersheds, there are some significant relationship between PLA and EC. Firstly, EC is higher with existing landslide area compare to those with no landslides. Secondly, EC rises rapidly before entering PLA and slowly decreases within PLA.

5. CONCLUSIONS

This study tried to clarify the relationship between EC and PLA in Taiwan. EC of stream is affected by inrush water from the potential landslides or existing landslides. When the sample collection points get close to inrush water, the electricity conductivity raises. On the contrary, when the sample collection points get away from the inrush water, the electricity conductivity decreases.

In short, this study proved the relationship between landslide and EC and intends to establish the warning system of the large-scale landslide using EC as an indicator for more emergency response time.

ACKNOWLEDGMENT

We thank the Soil and Water Conservation Bureau of the Council of Agriculture under the Executive Yuan for providing information regarding Large-Scale Landslides project. We also thank the Ministry of Science and Technology for support.

REFERENCES

Central Geological Survey, Ministry of Economic Affairs (2010) Project of Investigation and Analysis for Geologically Sensitive Areas under the Program of National Land Preservation (in Chinese)

Chiang H.C. (1994): Principal Chemical Constituents in Groundwater of Lan-Yang Plain. Journal of Agricultural Engineering Vol.40, No. 4, December. (in Chinese with English abstract)

Jitousono T., Shimokawa E., Teramoto Y. (2006): Potnetial site prediction of deep-seated landslide on the western flank of Mt. Yahazu-dake, Izumi City, Kagoshima Prefecture, Japan. Journal of the Japan Society of Erosion Control Engineering, Vol. 59, NO. 2, pp 5-12(in Japanese with English abstract)

Jitousono T. (2014): Site prediction of potential deep-seated landslides by using electric conductivity of mountain stream water, Journal of the Japan Society of Erosion Control Engineering, Vol. 6, No. 6, pp 56-59. (in Japanese with English abstract)

Lee W.L., Lin Y.F., Shieh C.L., Miyamoto K., Tai Y.C., (2015): The study on seepage hummer in the process of vertical seepage, The 16th Conference on Current Researches in Geotechnical Engineering in Taiwan. (in Chinese with English abstract)

Lin C.W., Yi D.C., Huang M.L. (2012) Digital terrain from airborne LiDAR - an effective tool for seeking potential large-scale landslides. Geo Topic 31(2):44–48

Shieh C.L., Lee W.L., Tai Y.C. and Lin Y.F. (2014): Occurrence Mechanism of Rainfall-induced Catastrophic Landslide. 2014 International Debris-Flow Workshop, Tainan, Taiwan

Shieh C.L., Wang C.M., Chen Y.S., Tsai Y.J. and Tseng W.H. (2010): An overview of disasters resulted from typhoon Morakot in Taiwan. Journal of Disaster Research. Vol 5, No3, pp. 236–244

Soil and Water Conservation Bureau, Council of Agriculture, Executive Yuan (2015): Development and application of disaster prevention and mitigation technologies for large-scale landslides. Nantou Taiwan (in Chinese)

Forestry Bureau, Council of Agriculture, Executive Yuan (2012) Investigation and Assessment of Deep-Seated Landslide Risk of National Forest – Key Watersheds in Southern Taiwan (in Chinese).

Geologic and Topographic Features of Slope Failure Sites in the Aso Caldera Wall Induced by the 2016 Kumamoto Earthquake

Haruka SAITOU[1,*], Shin'ya KATSURA[2], Ryota UMETANI[1], Mio KASAI[2] and Tomomi MARUTANI[2]

[1] Graduate school of Agriculture, Hokkaido University (Kita 8, Nishi 5, Kita-ku, Sapporo, Hokkaido 060-0808, Japan)
[2] Research Faculty of Agriculture, Hokkaido University (Kita 8, Nishi 5, Kita-ku, Sapporo, Hokkaido 060-0808, Japan)
*Corresponding author. E-mail: saitoudaifuku@eis.hokudai.ac.jp

Large-scale earthquakes can trigger slope failures. To effectively implement countermeasures to mitigate damage caused by slope failures, it is necessary to identify locations where the risk of slope failure is high. The geologic and topographic features of slope failure in the Aso Caldera wall induced by the 2016 Kumamoto earthquake were examined as a case study. The geology was roughly divided into three categories: pyroclastic flow deposits, andesite, and talus accumulation. The elevation, slope, and curvature were calculated using geographic information system (GIS) software and a digital elevation model (DEM) obtained before the earthquake; these parameters were then used as topographic indices. The analysis results showed that slope failures occurred most densely in the pyroclastic flow deposits. Within this geology, slope failure frequency increased proportionally with slope, and more slope failures occurred at sites with a positive curvature (i.e., convex slopes). There was no relationship between elevation and slope failure. We conclude that sites with these geologic and topographic features are prone to slope failure induced by large-scale earthquakes.

Key words: 2016 Kumamoto earthquake, geology, GIS, slope failure, topography

1. INTORODUCTION

A series of earthquakes with epicenters mainly in Kumamoto Prefecture, Kyushu Region, Japan, occurred in April 2016. The main shock of the 2016 Kumamoto earthquake on April 16 had a maximum seismic intensity of 7 on the Japan Meteorological Agency (JMA) 7-stage seismic scale and a JMA magnitude of 7.3. The Aso Caldera is a large caldera in Kumamoto Prefecture that was formed by catastrophic eruptions 270,000–90,000 years ago, and which measures about 17 km in the east–west direction and about 25 km from north to south. A JMA seismic intensity of 6 lower occurred in the Aso Caldera wall, which resulted in numerous slope failures and extensive damage (**Fig. 1**).

Several studies have been conducted of the geologic and topographic features of sites that

Fig.1 Photographs of slope failures in the Aso Caldera wall (taken by the authors, December 19–20, 2017)

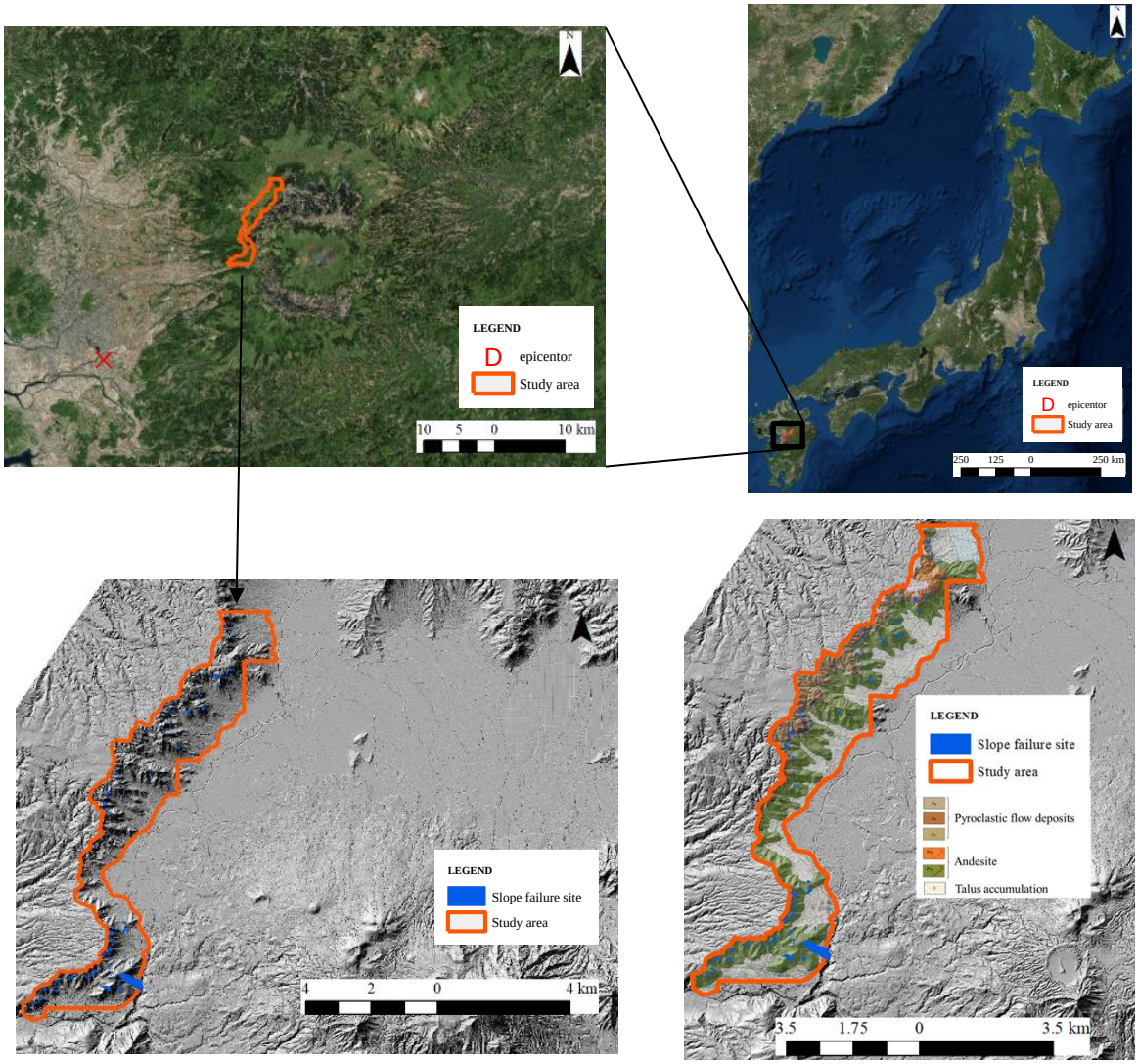

Fig.2 Study area (drawn based on the map provided by the Geospatial Information Authority of Japan)

including the 1995 Southern Hyogo Prefecture Earthquake [*Kawabe et al.*, 1997], the 1997 northwestern Kagoshima earthquake [*Jitousono et al.*, 1998], and the Kamishiro fault earthquake in Nagano Prefecture [*Katsura et al.*, 2016]. However, cases of slope failure due to earthquake remain greatly outnumbered by slope failure due to rainfall. To effectively implement countermeasures to mitigate damage caused by earthquake-induced slope failures, it is necessary to identify locations where the risk of slope failure is high. The purpose of this study was to clarify the geologic and topographic features of sites in the Aso Caldera wall where slope failure was caused by the 2016 Kumamoto earthquake.

2. EARTHQUAKE SUMMARY

According to the JMA, the main shock of the 2016 Kumamoto earthquake had a magnitude of 7.3 (seismic center: 32°45.3'N, 130°45.8'E; 12 km depth) on April 16 at 01:25, 2016. This right strike-slip fault earthquake had a tensile axis in the north–south direction [*Japan Meteorological Agency*, 2016]. The earthquake caused numerous landslides and 190 sediment-related disasters in Kyushu Region [*Ministry of Land, Infrastructure, Transports and Tourism*, 2018], killing 10 people and causing the complete destruction of 22 houses and severe damage to a further 13 houses.

3. METHOD

3.1 SUTUDY AREA

The study area was the northwestern part of the Aso Caldera wall, Kumamoto Prefecture, Japan (20.7 km^2; **Fig. 2**). The geology of the Aso Caldera wall consists of pyroclastic flow deposits, including welted tuff formed by catastrophic eruptions about 270,000–90,000 years ago (Aso-1 to 4), andesite older than Aso-1 to 4, and talus accumulations (formed by rock debris accumulation), roughly from the top to the bottom. The area and average slope of each geologic feature are shown in **Table 1**.

3.2 DATA COLLECTION

3.2.1 SLOPE FAILURE SITES

In the study area, light detection and ranging (LiDAR) data were obtained for 2012 (before the earthquake) and 2016 (after the earthquake). A digital elevation model (DEM) created from the LiDAR data before and after the earthquake was converted to create raster data. Using geographic information system (GIS) software, we outlined an area where the elevation showed a negative change from before to after the earthquake, and defined this area as the slope failure site. We confirmed the locations of slope failure by comparison with aerial photographs taken by the Geospatial Information Authority of Japan (GSI) immediately after the earthquake (April 16–20, 2016). As a result of this analysis, we identified 184 slope failure sites.

3.2.2 GEOLOGY AND TOPOGRAPHY

We used the geology and elevation, slope, and curvature of the sites as topographic indices because these factors are frequently cited as influential factors in studies of earthquake-induced slope failure.

Slope and the curvature were calculated from the DEM before the earthquake using GIS. Curvature is an index representing the unevenness of the terrain; positive and negative values indicate convex and concave shapes, respectively. Both slope and curvature are calculated using the elevation of the target cell and that of the surrounding eight cells. For example, for a DEM with a 10-m cell size, these topographic indices represent a slope shape in the range of 30 m × 30 m (i.e., 900 m^2). To determine the appropriate cell size for the DEM, we investigated the area of each slope failure site (histogram, **Fig. 3**). We classified these areas into cell sizes of 5 (i.e., 225 m^2), 10 (900 m^2), and 15 m (2,025 m^2); 60% of the slope failure sites had an area between 225 and 2,025 m^2, and we determined that a 10-m DEM cell size was appropriate for this study.

The geology of the slope failure sites was identified based on a geological map of the Aso volcano [*Ono and Watanabe*, 1985]. As described above, we roughly classified the geology into three categories: Aso-1 to 4 pyroclastic flow deposits (including welted tuff), andesite older than Aso-1 to 4, and talus accumulation.

3.3 ANALYSIS OF SLOPE FAILURE SITE FEATURES

Table 1 Area, average slope, the number of slope failure, and the slope failure density for each geology

Geology	Area (km^2)	Average slope (^{o})	Number of slope failure	Slope failure density ($/km^2$)
Pyroclastic flow deposits	3.2	31.4	59	18.4
Andesite	10.1	31.3	121	12.0
Talus accumulation	7.4	14.5	4	0.5
Total/Average	20.7 (total)	24.4 (average)	184 (total)	8.9 (average)

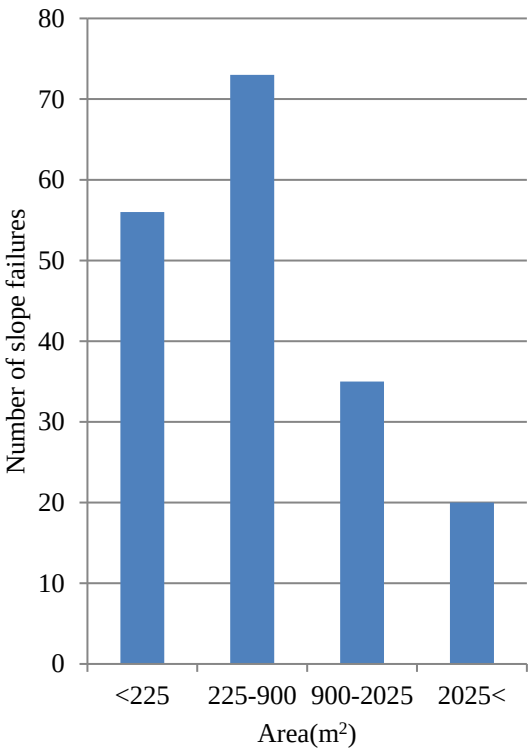

Fig.3 Area of slope failure sites

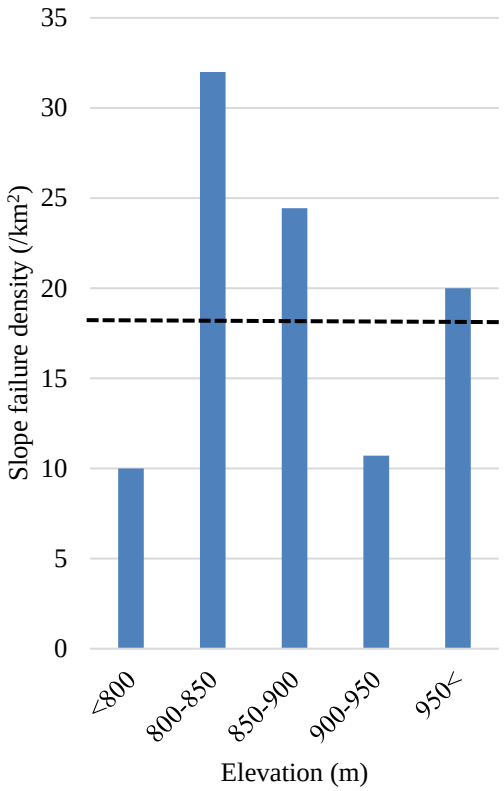

Fig.4 Slope failure density for each elevation class within the pyroclastic flow deposits

Topographic indices for each slope failure site were calculated by averaging the values of all cells overlapping all or part of the polygon representing the slope failure site. The geology of each site was determined by superposing its polygon on the geological map using GIS. When a polygon overlapped more than one geology class, we adopted the geology class that covered the highest elevation within the site. Slope failure density (the number of slope failures per unit area) was used to evaluate the risk, rather than the number, of slope failures, because the area of each class within each factor was different.

4. RESULTS AND DISCUSSION

4.1 GEOLOGY

The slope failure density for each geology class is shown in **Table 1**. The slope failure density of pyroclastic flow deposits (18.4/km^2) and andesite (12.0/km^2) exceeded the average slope failure density for the whole study area (8.9/km^2), suggesting that pyroclastic flow deposits and andesite are more prone to slope failure than talus accumulation, likely because the average slope among the pyroclastic flow deposit and andesite classes was larger than that of the talus accumulation class (**Table 1**); moreover, as will be described later, slope failure tends to occur at locations with larger slopes. The slope failure density of the pyroclastic flow deposits was larger than that for andesite, probably because the pyroclastic flow deposits were formed more recently and the degree of consolidation was small.

Therefore, we focused on pyroclastic flow deposits in the following sections.

4.2 ELEVATION

The slope failure density for each elevation class is shown in **Fig. 4**. The average slope failure density in the pyroclastic flow deposits (18.4/km^2) is indicated by a broken line. In the 800–900 m and > 950 m classes, slope failure density was larger than 18.4/km^2, indicating that slope failure occurred more frequently at these elevation ranges. Although some previous studies [e.g., *Jitousono et al.*, 1998] have suggested that slope failure density increases with increasing elevation, probably due to the amplification of seismic waves at high

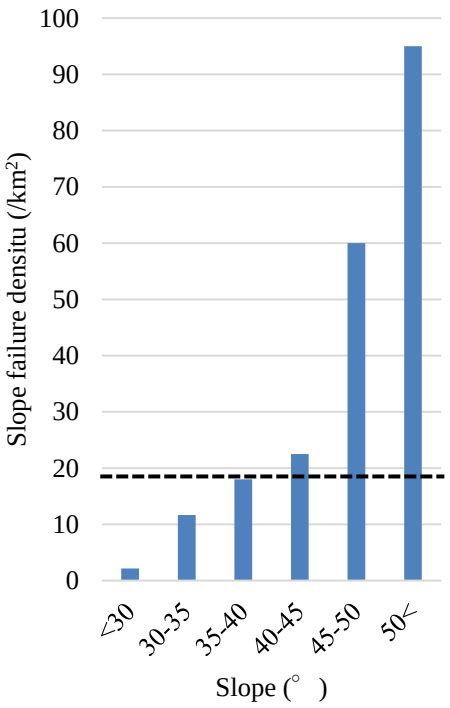

Fig.5 Slope failure density for each slope class within the pyroclastic flow deposits

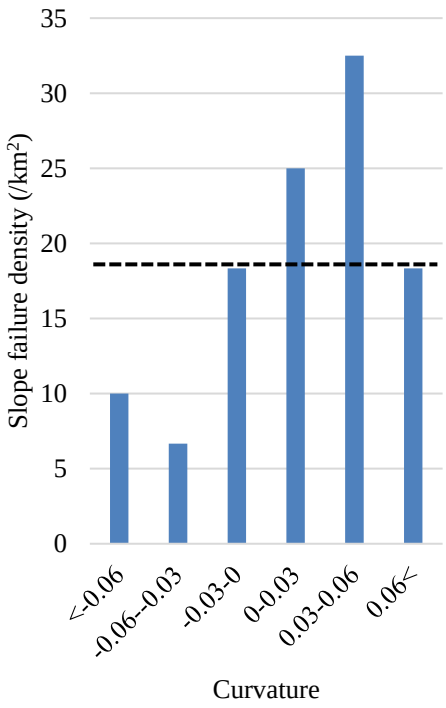

Fig.6 Slope failure density for each curvature class within the pyroclastic flow deposits

elevation [*Yamaguchi and Kawabe*, 1982], the current study detected no such tendency. We concluded that there was no relationship between elevation and slope failure.

4.3 SLOPE

The slope failure density for each slope class is shown in **Fig. 5**. Slope failure density clearly increased with increasing slope, and the average slope failure density (18.4/km^2) was exceeded in slope classes > 40°. Therefore, slope was found to influence slope failure, with steeper slopes being more prone to failure, probably because downward force on an inclined soil mass increases as slope increases, as has been reported in many previous studies [e.g., *Okimura et al.*, 1997].

4.4 CURVATURE

The slope failure density for each curvature class is shown in **Fig. 6**, which demonstrates that the average slope failure density was exceeded for curvatures between 0 and 0.06. This finding suggests that a convex slope is more prone to slope failure, likely because seismic waves are amplified at convex slopes [*Yasuda et al.*, 2006; *Nishida et al.*, 1997].

5. SUMMARY

In this study, we analyzed the geologic and topographic features of the Aso Caldera wall at sites that had experienced slope failure caused by the main shock of the 2016 Kumamoto earthquake, which occurred on April 16, 2016. Our findings are summarized as follows.

1) Pyroclastic flow deposits are more prone to slope failure than andesite and talus accumulation, probably due to their steeper slopes and recent age of formation.

2) There was no relationship between elevation and slope failure.

3) Slope failure was more likely to occur with increasing slope, especially at slopes > 40°.

4) Convex slopes were more prone to slope failure than concave slopes, probably due to the amplification of seismic waves.

In this study, we clarified the geologic and topographic features of the slope failure sites caused by the 2016 Kumamoto earthquake in the Aso Caldera wall. In future work, we recommend

the further development of these methods of evaluating slope failure risk induced by a large-scale earthquake, to include risk assessment for individual slopes.

ACKNOWLEDGMENTS: This research was conducted under the subject “Occurrence and flow of mountain slope failure with driftwood in volcanic regions” and “Mechanisms of and countermeasures against chain and complex sediment-related disasters caused by large earthquakes and accompanying ground deterioration” by the river and sabo technology open research and development system of the Ministry of Land, Infrastructure Transport and Tourism (MLIT). The LiDAR data used in this study were provided by the Kyushu Regional Development Bureau, MLIT.

REFERENCES

Japan Meteorological Agency (2016): The 2016 Kumamoto Earthquake, http://www.data.jma.go.jp/svd/eqev/data/2016_04_14_kumamoto/index.html#kumamoto_data. Reference date: November 30, 2017 (in Japanese).

Jitousono, T., Shimokawa, E., Matsumoto, M. and Teramoto, Y. (1998): Distribution and topographical characteristics of slope failures caused by earthquake in Northwestern part of Kagoshima in 1997, Journal of the Japan Society of Erosion Control Engineering, Vol. 51, No. 1, pp. 38–45 (in Japanese with English abstract).

Katsura, S., Kimura, T., Maruyama, K. and Ishida, K. (2016): Characteristics of landslides induced by the Kamishiro Fault Earthquake in Nagano Prefecture on November 22, 2014, Journal of the Japan Landslide Society, Vol. 53, No. 3, pp. 11–20 (in Japanese).

Kawabe, H., Tsujimoto, F. and Hayashi, S. (1997): The distribution of slope collapses in the Rokko Mountains caused by the 1995 Hyogo-ken Nanbu Earthquake, Journal of the Japan Society of Erosion Control Engineering, Vol. 49, No. 5, pp. 12–19 (in Japanese with English abstract).

Ministry of Land, Infrastructure, Transports and Tourism (2018): Occurrence of sediment-related disasters in 2016,http://www.mlit.go.jp/river/sabo/jirei/h28dosha/H28dosyasaigai.pdf. Reference date: May 7, 2018 (in Japanese).

Nishida, K., Kobayashi, S. and Mizuyama, T. (1997): DTM based topographical analysis of landslide caused by an earthquake, Journal of the Japan Society of Erosion Control Engineering, Vol. 49, No. 6, pp. 9–16 (in Japanese with English abstract).

Okimura, T., Yoshida, N., Okunishi, K. and Torii, N. (1997): A consideration of the mechanism of slope failure in the Rokko mountain range caused by the 1995 Southern Hyogo Prefecture Earthquake, Disaster Prevention Research Institute Annuals, Kyoto University, No. 40B-1, pp. 115–125 (in Japanese; the title is a tentative translation by the authors from the original).

Ono, K. and Watanabe, K. (1985): Geological map of Aso Volcano (1:50,000) (in Japanese).

Yamaguchi, I. and Kawabe, H. (1982): Study of characteristics of disaster at mountainous district due to earthquake, Shin-Sabo, Vol. 35, No. 2, pp. 3–15 (in Japanese with English abstract).

Yasuda, Y., Tsuchiya, S., Mizuyama, T., Matsumura, K., Ochiai, H., Takahashi, M. and Tang, W. (2006): Topographic effects of the seismic slope displacement and ground acceleration by earthquake using a dynamic response analysis, Journal of the Japan Society of Erosion Control Engineering, Vol. 59, No. 4, pp. 3–11 (in Japanese with English abstract).

Topic 2: Large scale sediment disasters: Phenomena and countermeasures

Characteristics of a Landslide Occurred in May 2015 in Mt. Hakusan and its Influence on Downstream System

Seiji YANAI

Department of Environmental Sciences, Ishikawa Prefectural University (Suematsu, Nonoichi, Ishikawa 9218836, Japan)
*Corresponding author. E-mail: yanai@ishikawa-pu.ac.jp

In May 2015, a large landslide occurred in the headwaters of the Tedori River at the foot of Mt. Hakusan. Airborne LiDAR data and a series of aerial photographs taken over 60 years were used to analyze the topographical features and geomorphological factors that triggered the landslide. The landslide was 800 m long and 300 m wide, with a total sediment volume of 1.3 million m^3. Most of this accumulated at the bottom of the slope and buried the stream channel. However, half of the sediments washed into the river and generated very turbid water for 6 months after the landslide. This influenced the downstream area when the very turbid water entered rice paddies, fresh water, and coastal fisheries, and led to groundwater depletion. Countermeasures were extremely difficult to institute because there was no road access to the landslide, which occurred in a strictly protected national park. Although the Forestry Agency currently uses a helicopter to scatter anti-erosion material, fundamental measures should be taken to ensure the early recovery of native vegetation species, eliminate the source of turbid water, and enhance sedimentation by using sediment ponds.

Key words: Mt. Hakusan, Tedori River Basin, landslide, turbid water, countermeasure

1. INTRODUCTION

In May 2015, a large landslide occurred on Mt. Hakusan (2,702 m asl), Ishikawa Prefecture, Japan, in the headwaters of the Tedori River (**Fig. 1**). The very turbid water generated by this landslide flowed downstream, where it affected the water supply system, freshwater fisheries, farmland, paddies, and the coastal marine ecosystem from late May until June. This landslide became a major concern not only within Ishikawa Prefecture but also at a national level, involving discussions in the prefectural assembly and a petition for countermeasures to diet members.

The volcanic body of Mt. Hakusan formed hundreds of thousands of years ago (*Nagaoka et al*. 1985), and the collapse of mountain bodies is an ongoing geomorphological process. However, erosion can create large alluvial fans downstream. Erosion has many benefits, producing rough terrain, large plains, and beautiful sandy beaches. Because collapse is an inevitable phenomenon, we must be prepared for such occurrences.

This paper analyzed the geomorphological process involved in the 2015 landslide, documented the effects of turbidity on the downstream ecosystems, and discussed future countermeasures.

2. STUDY SITE

The Tedori River is the largest river in Ishikawa Prefecture. It originates from the major Hakusan peaks and is joined by dozens of tributaries, including the Ushikubi, Ozo, and Dainichi Rivers. The Tedori River flows northward and turns west at the town of Tsurugi (**Fig. 2**), ultimately reaching the Sea of

Fig. 1 Whole view of the landslide occurred in May 2015 taken on June 2, 2015 by Ishikawa Forest Management Office.

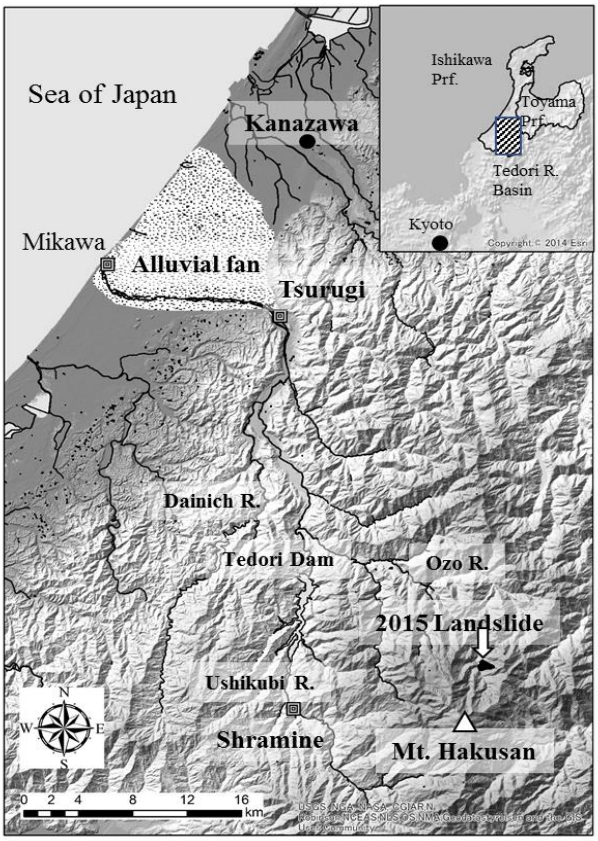

Fig. 2 Location of Mt. Hakusan, the 2015 landslide and Tedori River basin.

Japan. The catchment area is 809 km^2, the main trunk channel is 72 km long, and the average gradient from the source to the mouth of the estuary is 1/27. A typical alluvial fan is formed downstream from Tsurugi. The fan has an area of about 17,000 ha, the elevation of the apex is about 80 m above sea level, and the average gradient of its ground surface is about 1/150 (*Maruyama et al*. 2012). This alluvial fan is mainly used for rice paddies and is the largest area of rice production in the prefecture.

Mt. Hakusan is located in the headwaters of the Tedori River basin (**Fig. 2**). The upstream part of the basin has many steep slopes, and large landslides are common. The geology of the basin ranges from underlying Hida metamorphic rock formed in the Paleozoic to Quaternary volcanic deposits (**Fig. 3**). The metamorphic rocks include gneiss to the east of the Tedori River Dam and in the Ozo River sub-basin. The Tedori group, which is mainly composed of sedimentary rock from the Jurassic to Cretaceous, is distributed upstream in the Tedori River. The eastern part of the Ozo River basin is Nohi Rhyolitic rock from the Cretaceous to the early Paleogene period. Miocene marine volcanic deposits of green tuff are distributed in the middle reach of the Tedori basin. New and old Mt. Hakusan volcanic deposits, from eruptions that occurred from the late Pleistocene to the early Holocene, cover the main peak of Mt. Hakusan and associated ridges. The erosion of the volcano has created barren landforms, such as landslides and slope failures, and generated a large amount of sediment. Most of the old landslide topography formed during the last glacial period until the early Holocene (*Kojima et al*. 2015).

The currently active landslide area involves the southern part of Mt. Hakusan, including the Jinnosuke (*Wang et al*. 2007) and Yunotani Valleys. These landslides occur mainly in an area with a dip flow structure in the Tedori Group. A large landslide area has been also recognized in an altered zone of the Nohi Rhyolitic zone, which is caused by sulfidic alternation (*Koide* 1973). The National Research

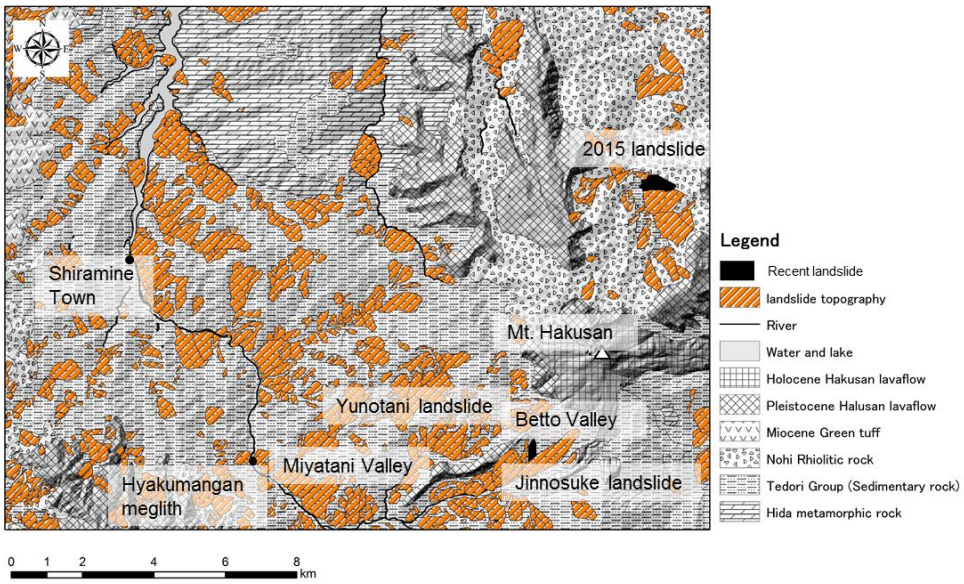

Fig. 3 Geology and landslide topography surrounding the 2015 landslide in Hakusan Mountain Range. Geological data and landslide data were provided by AIST Geological Survey and Integration Center (2016) and Disaster prevention science and technology research institute (2016), respectively.

Institute for Earth Science and Disaster Prevention (2016) identified a landslide more than 1 km long and covering tens of hectares involving the northern part of the Hakusan Volcano.

The biggest natural disaster in the history of Ishikawa Prefecture involved a deep-seated slope failure that occurred in 1934 in the southern part of Mt. Hakusan (*Shimazu* 1996). This collapse occurred in the Betto Valley, was 900 m long and 150–200 m wide, and followed torrential rain in July 1934, which involved a total rainfall of 466 mm with a maximum daily rainfall of 352 mm. The discharged sediments reached the other side of the river, and the debris flow seriously damaged the village of Shiramine located downstream (*Shimazu*, 1996). The estimated collapse area was 16.9 ha and the volume of collapsed sediment was 164,100 m^3 (*Nishikawa* 1988). Another debris flow in the Miyatani Valley transported a megalith measuring more than 16 m high and 52 m in circumference. This rock was called the "one-million-kan rock" (more than 4,800 tons) and was designated as a prefectural natural monument to remember the tragic disaster.

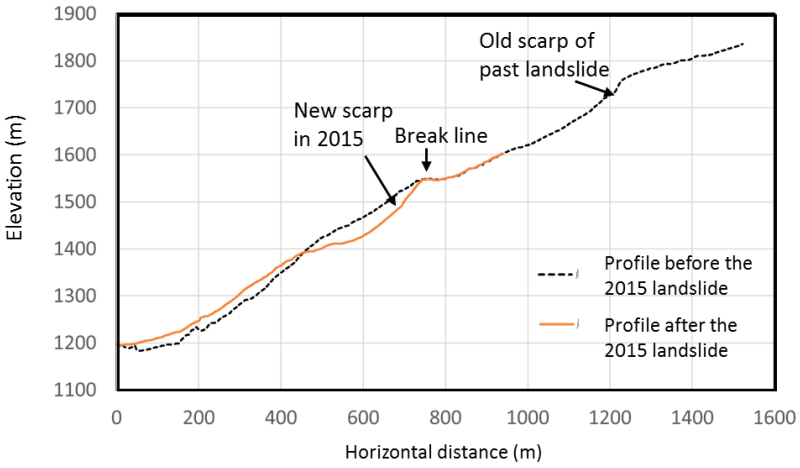

Fig. 4 Longitudinal profile before and after the 2015 landslide.

.

3. STUDY METHOD

Geomorphological analysis was carried out using airborne Light Detection and Ranging (LiDAR) data for the ground surface to calculate the sediment volume and sediment budget. The LiDAR data were collected before (August 2014) and after (June and October 2015) the landslide by the Kanazawa River National Highway Office. A series of aerial photographs was used to analyze the process leading to the 2015 landslide. The oldest aerial photographs were taken in 1955 by the US Air Force and were georeferenced using ArcGIS 10.3.1. More recent aerial photographs taken in 1977, 2009 were imported into ArcMap from the Geographical Survey Institute web (2016) using the ESRI import tool. The recent photographs taken before and after the 2015 landslide were provided by the Kanazawa River National Highway Office.

The hydrological analysis was performed using AMeDAS precipitation data collected in Shiramine, Hakusan, which is located 10 km south of the 2015 landslide. Discharge and turbidity data were collected using an automated measurement system installed in Tsurugi by the Ministry of Land, Infrastructure and Transport. These data were used to analyze the relationship between turbidity and hydrological conditions.

4. RESUT AND DISCUSSION

4.1 The topographical change before and after the landslide in 2015

Fig. 1 shows an overall view of the landslide, which was 800 m long and 300 m wide. The scarp was 400 m long and 300 m wide; the collapse depth was up to 45 m; and the elevation difference was about 400 m. The cross-sectional profiles generated from digital elevation models before and after the landslide are also shown in **Fig. 4**. A large scarp at

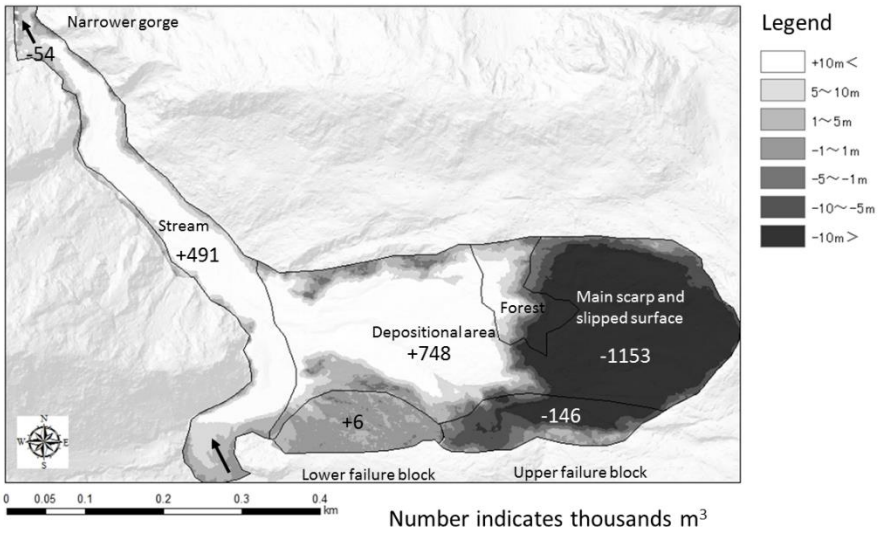

Fig. 5 Elevational change between Oct 2014 and June 2015. The numbers indicate degraded and aggraded sediment volume (thousands m^3).

around 1,700 m in elevation, which was formed by previous movement, already existed and a break line was recognized in the middle slope at 1,500 m. The new scarp formed by the 2015 landslide was located below the break line at 1,390–1,550 m; the collapsed area was 6.4 ha. Before the landslide, an old-growth forest composed of birch (*Betula ermanii*) and beech (*Fagus crenata*) covered an area of 5 ha. However, this forest was destroyed completely by the landslide and buried in the streambed. Some forest slipped down from the upper slope and was retained on the middle slope, which looks as though it has not moved. Nevertheless, many of the tree trunks in this area now tilt in various directions, and most trees were seriously damaged and withered.

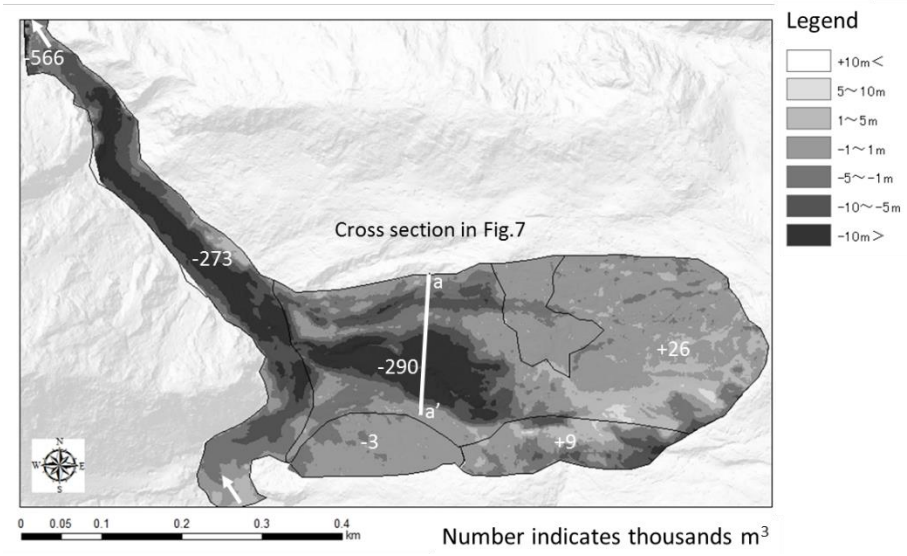

Fig. 6 Elevational change between June and October 2015. The numbers indicate degraded and aggraded sediment volume (thousands m^3).

4.2 Sediment volume produced by the landslide

The generated sediment volume was 1.154 million m^3. The minor scarp on the southern flank also collapsed. The fallen slope was divided into two blocks; the upper failure block covered 5 ha, had a depth of 8.5 m, and a sediment volume of 146,000 m^3. Totally, 1.3 million m^3 of sediment was produced by this landslide.

The collapsed sediment covered the original slope up to 500 m from the downstream portion of the slide, which had a maximum thickness of 35 m (mean 11 m) (**Fig. 5**). The deposited sediment volume was 748,000 m^3. There was a narrow gorge 500 m downstream from the bottom of the collapsed slope, and most of the transported sediments were stored there. These sediments created a sand bar about 100 m in width, and the riverbed was raised about 10 m above its original level. The sediment accumulated in the 500-m section from the landslide slope to the gorge had an estimated volume of 491,000 m^3. The volume stored on the lower slope and in the stream section was 1.25 million m^3, sediment transported farther downstream was 50,000 m^3.

4.3 Generated sediment volume after the landslide

After the landslide, the collapsed deposits (about 750,000 m^3) that accumulated on the slope eroded into the stream. **Fig. 6** shows the eroded sediment volume from June 20 to October 2015 determined from the LiDAR data; the denuded volume was also calculated. On the slipped surface in the upper part of slope, the topographical change was slight, and sediment (26,000 m^3) supplied from the upper rim of the scarp was retained within the slipped slope. Two gullies, which were buried by the landslide debris, have since been carved out with a large amount of landslide deposits. The estimated amounts of degraded deposits were 290,000 m^3 from the slope and 273,000 m^3 from the channel; in total 563,000 m^3 of sediment flowed downstream.

In August 2015, the forest management office sprayed mortar on the slide to prevent surface erosion. This material remained on most of the upper slope and on the left and right sides of the lower slope, but none remained in the center of the lower slope, where a deep gully formed. **Fig. 7** shows a

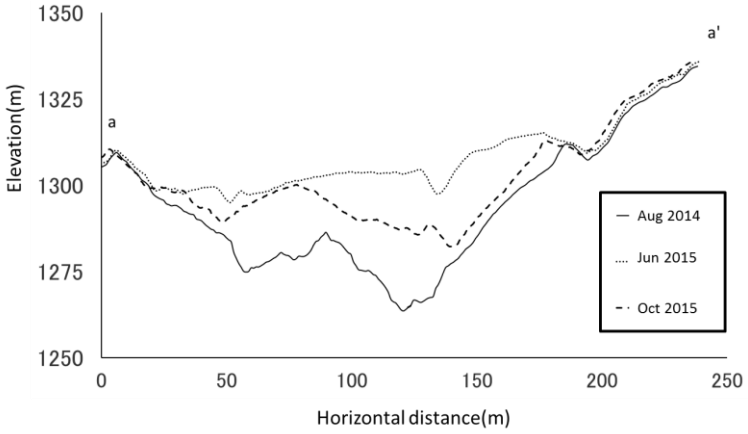

Fig. 7 Cross sections before, just after and a half year later of the 2015 landslide at the bottom of landslide.

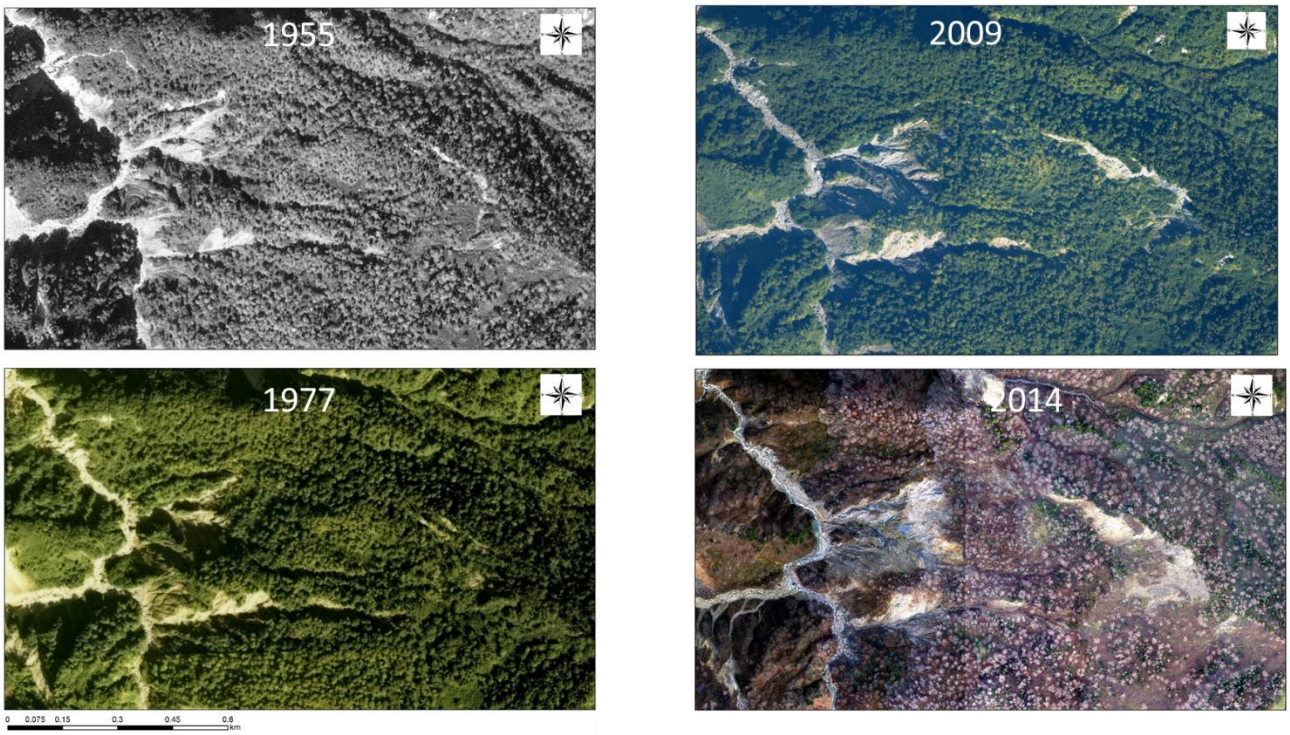

Fig. 8 A series of aerial photos since 1955. Upper left: taken by US Airforce in 1955, Lower left: Color photo taken by Geographical Survey in 1977, Upper right: photo taken by Geographical Survey in 2009 and Lower right: taken by Kanazawa River and National Highway Road Office in 2014.

cross-section of the lower slope, where the accumulated deposits were deeply incised. In the spring of 2015, just after the landslide, the slope was deeply covered with landslide deposits over a horizontal distance of 200 m. However, this surface changed drastically: within 6 months, a 20-m-deep V-shaped valley had formed in the middle section, and the deposits flowed downstream.

4.4 Precursor phenomenon for the 2015 landslide

Several phenomena were regarded as precursors of the landslide. The scarp of the older landslide block is clearly recognized in the oldest photo taken by the US Airforce in 1955 (**Fig. 8**), although it was not quite as wide as at present. A large bare slope also existed on the bottom of the lower part of the 2015 landslide. A color aerial photograph taken by the Geographical Survey Institute in 1977 shows no initial change compared with aerial photographs taken in 1955. In 2009, this changed dramatically. The crack in the scarp reopened and the area of bare slope along the channel became larger, indicating that the landslide movement had been accelerating since 1977.

A small portion of the lower edge of the middle slope collapsed in October 2014. This had an area of 2 ha and a collapse volume of 50,000 m^3. Subsequently, the movement of the landslide became

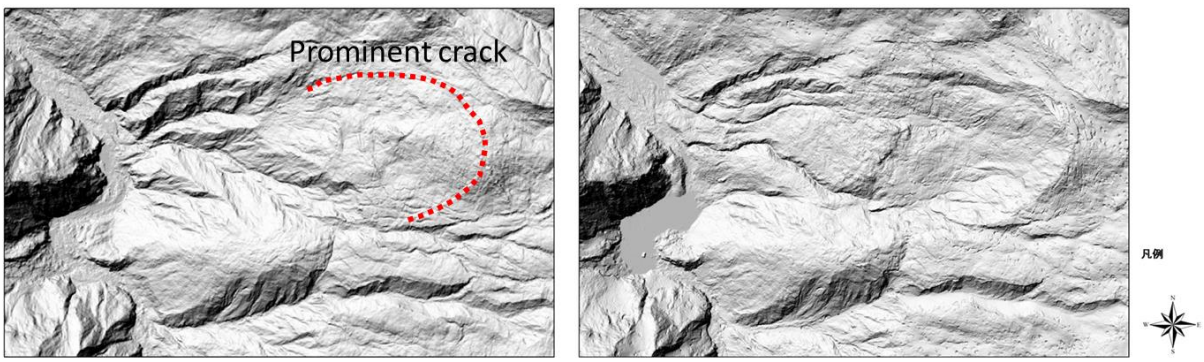

Fig. 9 Micro-topography comparison before (left, November 2014) and after (right, June 2015) the 2015 landslide. Break line indicates boundary of landslide block analyzed by LiDAR data.

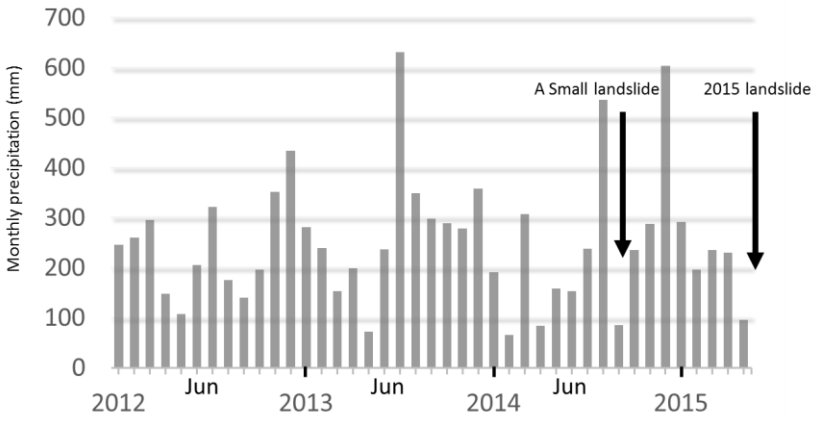

Fig. 10 Monthly precipitation from 2012 to 2015 before the landslide at Shiramine weather observation point.

prominent, and numerous cracks became visible in the center of the landslide. **Fig. 9** compares the topography before and after the landslide. Before the 2015 landslide, the lower part of the slope had been denuded and bedrock was exposed, while the upper part of the slope had been torn by many arc-shaped cracks. The crack shown by the dashed line was prominent, and this coincided precisely with the scarp of the 2015 landslide. This implies that the landslide had already begun moving before 2015. Therefore, it should be possible to predict where a landslide will occur by searching for such microtopography.

4.5 Meteorological factors that caused landslides

The metrological factors affecting the 2015 landslide were analyzed using AMeDAS data. **Fig. 10** shows the monthly maximum rainfall over the past 4 years in Shiramine, Hakusan. High rainfall occurred in the period from 2013 to 2014 and the monthly precipitation in July 2013 was 630 mm. This intense rainfall caused serious flooding damage downstream in the Tedori River. In 2014, torrential rain also occurred, with monthly rainfall of 535.5 mm and hourly rainfall of 29 mm. After this rainfall event, a small slope failure that presaged the 2015 landslide occurred at the lower end of the landslide area. The amount of snowfall in the winter of 2014 was high and the monthly precipitation in December reached 603 mm. The 2015 landslide was very likely caused by melting of the snowfall that accumulated on the slope in December 2014.

4.6 Generation of turbid water

The aerial photographs taken in June 2015 showed that turbid water was generated from two gullies that formed in the collapsed area, and this water was clearly different from the stream water flowing from the upper part of the landslide. The muddy water flowed down from this point to the Ozo River, and there was a distinct difference in water color at the confluence of the Ozo River and the main

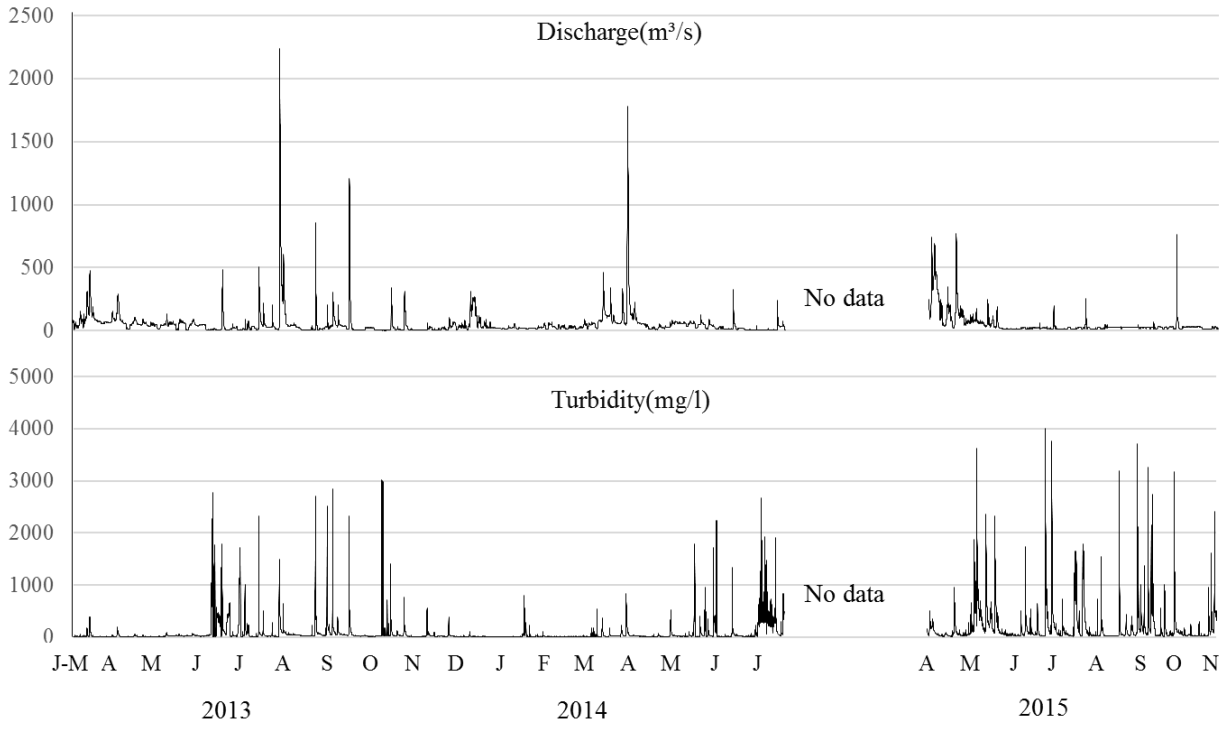

Fig. 11 Discharge and turbidity from 2013 to 2015 at Tsurugi gaging station.

channel of the Tedori River. **Fig. 11** shows the turbidity and discharge over the 3 years from 2013 to 2015 measured at Tsurugi gaging station. Turbidity exceeding 2,000 mg/l was observed once in 2013, but not in 2014. In comparison, turbid discharge exceeding 2,000 mg/l occurred frequently after May 2015, and a peak turbidity exceeding 4,000 mg/l was recorded in June when the discharge was the lowest. During the summer, turbidity tends to increase when the rainfall exceeds 40 mm, and the peak turbidity in June was recorded when rainfall exceeded 80 mm.

4.7 Influence of turbid water on downstream system

Sediment generated by turbid water flowed to the vicinity of the water intake of the Shichikayosui Irrigation Network, which supplies the paddy fields of five cities and one town in the Tedori River alluvial fan. Although there was concern about a decline in crop growth, the effect was limited, and the rice yield in some places exceeded the annual average. In sedimentation ponds installed near the water intake, the deposition was more than 10 times higher than normal. In addition, the inner water surface and coastal fishery were directly influenced by the turbid water. In the river, plans to release juvenile ayu (*Plecoglossus altivelis*) for leisure fishing in May were suspended because of the turbid water. Ice gobies (*Leucopsarion petersii*; shirauo in Japanese), which spawn over gravel in the estuary, could not be captured because of the fine sediment accumulation. Furthermore, the turbid water that diffused in the coastal area caused mud to adhere to fishing nets (**Fig. 12**), which resulted in net breakage. As coastal area in Kaga region has been suffering from serious erosion (*Hayakawa et al*. 2010), these sediments may contribute to prevent coastal erosion. Further study is needed to clarify the coastal topographical change before and after the landslide.

In the alluvial fan, a marked decline in groundwater was observed from just after the landslide until mid-November 2015. This decline was the largest in the last 20 years in terms of both the rate of decline and the minimum water level (*Yanai et al.* 2016). A significant decline of percolation on paddy fields after the landslide was observed and groundwater recharge from paddy fields was reduced by 36 % (*Tanaka et al.* 2017). Fine sediment accumulation on paddy field from turbid water was apparently responsible for this marked decline of groundwater.

Freshwater species of stickleback (P*ungitius* sp.) dwell in brooks originating from spring water, and are designated as both rare wild species in Ishikawa Prefecture and Ishikawa Prefecture endangered species type I. The lowering of the groundwater level caused the riverbed to dry up for the longest period in 20 years and the extent of the dry area was the largest in the lower part of the Tedori River. As a result, submerged aquatic vegetation disappeared and the sticklebacks that dwell among it were unable to survive. The decline in the infiltration rate from river to underground had a devastating impact on their populations (*Yanai et al*. 2016).

Fig. 12 Fine sediment adhered with Squid fishing net.

4.8 Future measures

Countermeasures against this landslide were very difficult to institute for several reasons. First, as there is no access road, it is impossible to implement any erosion control works. Second, because the area is a special protection area in a national park, we need to consider biological diversity, including the protection of native species and prevention of the invasion of exotic species. The Forestry Agency planned to spray a mixture of an organic material with cement to fix the denuded soil from a helicopter. Standard greening techniques that use a mixture with exotic grass seeds could not be used there to conserve native plant species.

To achieve early vegetation colonization, it is essential to stabilize the ground surface because serious surface erosion results from the high elevation, fragile geology, and freeze–thaw action. After stabilizing the soil surface, it is necessary to perform a variety of bioengineering tasks, which include collecting seeds from the surrounding trees to scatter widely. As willow (*Salix sachalinensis*), poplar (*Populus maximowiczii*), and alder (*Alnus maximowiczii*) are typical pioneer species in the area surrounding the affect slope, the planting of willow cuttings is one effective measure to promote vegetation establishment. Furthermore, as mentioned above, sediment ponds are very efficient for capturing sediment. Therefore, this type of facility

should be included within drainage areas to minimize high turbidity water in the event of the future occurrence of a landslide.

ACKNOWLEDGMENT: The LiDAR and turbidity data were provided by the Kanazawa River National Highway Office of the Ministry of Transport and Infrastructure. The aerial photos were provided by the Kanazawa Forest Management Office. The author sincerely thanks the staff of these public offices.

REFERENCES

AIST Geological Survey and Integration Center (2016): Seamless geological map. (https://gbank.gsj.jp/seamless/seamless2015/2d/ [confirmed February 20, 2016)]).

Disaster prevention science and technology research institute (2016): Landslide topography GIS data "Kanazawa" (http://dil-opac.bosai.go.jp/publication/nied_tech_note/landslidemap/gis.html [Confirmed February 20, 2016]).

Forestry Agency Kinki Chugoku Forestry Administration Bureau (2015): On the immediate collapse site in the large-scale national forest upstream of the Tedori River (http://www.rinya.maff.go.jp/kinki/kikaku/pdf/270615_houkaititaisaku.pdf [Confirmed on 15th December 2015]).

Geographical Survey Institute (2016): Geographical Survey Institute web (http://maps.gsi.go.jp/#14/36.531571/136.672754 [Confirmed February 20, 2016]).

Hayakawa K., Yui P., Ishida K. (2010): Basic research on beach topography change on the Senri Beach coast of Ishikawa prefecture. Japan Sea Area Study 40: 37-49 (in Japanese with English abstract).

Japan Meteorological Agency (2015): Hakusan Shiramine AMeDAS Data. (Http://www.data.jma.go.jp/obd/stats/etrn/index.php?prec_no=56&block_no=0973&year=&month=&day=&view= [2015 12 Monday 15th confirmation]).

Koide H. (1973): Japan's land (lower) Nature and development. Tokyo Daigo kai, Tokyo, pp. 556 (in Japanese).

Kojima S., Kaneda H., Nagata H., Niwa R., Iwamoto N., Kayamoto H. and Ohtani T. (2015): Development History of Landslide-Related Sagging Geomorphology in Orogenic Belts: Examples in Central Japan. In: Lollino G. et al. (eds) Engineering Geology for Society and Territory 2. Springer, Cham: 553-558.

Maruyama T., Hayase Y., Takimoto Y., Noto F. and Yoshida F. (2012): Healthy water circulation centered on agricultural water - Case of the Tedori River Basin on the premise of global warming - Ishikawa Prefectural University Press Conference, Nonoichi, pp. 266(in Japanese).

Nagaoka M., Shimizu S., Yamasaki M. (1985): Geology and formation history of Hakusan volcano. Research report on Hakusan nature conservation center, Ishikawa prefecture 12: 9-24 (in Japanese with English abstract).

Nishikawa I. (1988): The great collapse of Toya Valley. Sabo Engineering Journal 40 (6): 33-35(in Japanese).

Shimazu H. (1996): Topographic characteristics and sediment transport in the upper part of the Tedori River. Kanazawa University Faculty of Letters. History Dept. 16: A45 - A59(in Japanese).

Tanaka K., Segawa M., Fujihara Y., Takase K., Maruyama T. and Chono S. (2017): High-turbidity water from landslides affects groundwater recharge of paddy fields in the Tedori River Alluvial fan. J. Japan. Soc. Hydrol. and Water Resour. 30(3): 173-180. (in Japanese with English abstract).

Wang F., Okuno T. and Matsumoto T. (2007): Deformation characteristics and influential factors for the giant Jinnosuke-dani landslide in the Haku-san Mountain area, Japan. Landslide 4: 19-31.

Yanai S., Okazaki M., Takimoto Y., Ichion E. and Takase K (2016): Influence of high turbid water generated from a huge landslide occurred in the headwater area of Mt. Hakusan on the Tedori River Basin environment. Annual Bulletin of Ishikawa Prefectural University 27: 8-27 (in Japanese with English abstract).

Small Flume Experiment on Deep-seated Landslide Collapsed Material Movement

Hefryan S. KHARISMALATRI[1*], Yoshiharu ISHIKAWA[2], Takashi GOMI[3] and Katsushige SHIRAKI[4]

[1] Department of Symbiotic Science of Environment and Natural Resources, Tokyo University of Agriculture and Technology, Japan
[2] Toa Grout Kogyo Co. Ltd.
[3] Department of International Environmental and Agricultural Science, Tokyo University of Agriculture and Technology, Japan
[4] Institute of Agriculture, Tokyo University of Agriculture and Technology, Japan
*Corresponding author. E-mail: kharismalatri@gmail.com

Previous researches revealed that inflow angle and stream gradient are two major factors that distinguish the formation of landslide dam and debris flow from collapsed material of deep-seated landslide. Yet their significance mobilization of landslide material has yet to be clarified. This research aimed to clarify the influence of inflow angle and stream gradient on rapid deep-seated landslide collapsed material movement and the possibility of landslide dam formation by using small flume apparatus. The small flume consisted of inflow segment and main channel where the junction angle between them were modified into 0°, 30°, 60°, and 90°, while the gradient of the inflow segment and main channel was fixed on 45° and 10° respectively. Experiment was conducted on 6 classes of water content, namely from 0% to 100% with 20% increment. Soil samples from Nigoridani, Nara Prefecture where deep-seated landslide occurred in 2011 due to Typhoon Talas, with D_{50} of 7 mm and saturated water content of 21% was used in the experiment. The result revealed that on its saturated water content, collapsed material formed deposition at junction area of 11%, 14%, 32%, and 49% on inflow angle of 0°, 30°, 60°, and 90° respectively. The deposition on inflow angle of 60° and 90° was relatively significant and possibly forming landslide dam. In contrast, the material was mainly transported to the lowest part of the flume as debris flow on inflow angle of 0° and 30°. The experiment result confirmed that collapsed material of DSL that encountered large inflow angle will experience large collision with the opposite slope which cost a large amount of energy and thus the material deposited at or near the junction area. Water content also has an important role in determining the mobilization of landslide material.

Key words: small flume, landslide dam, inflow angle, saturated water content

1. INTRODUCTION

Collapsed material of rapid deep-seated landslides (hereafter noted as DSL) mainly mobilizes in two main types: debris flow and landslide dam. Debris flow is known as the most powerful mechanism for transporting landslide sediment far downslope [*Bathurst et al.*, 1997] and holds serious impact on human life and infrastructures since it moves rapidly, large in volume, destroys object without warning, and often occurs without warning [e.g., *Nishiguchi et al.*, 2012; *Highland et al.*, 1997]. While landslide dam defined as natural blockage of river channel caused by landslide, having significant height and potentially causing inundation of water behind it [*Canuti et al.*, 1998; *MLIT*, 2006]. Landslide dam holds further threats than debris flow; upon the dam creation, back-flooding threaten upstream area; and when the dam breaks, which commonly due to overflowing of inundated water, large surges and debris flow threaten downstream area [e.g., *Ermini and Casagli*, 2003; *Inoue et al.*, 2012].

Severe rainfall brought by Typhoon Talas in 2011 catastrophically damaged Kii Peninsula including Mie, Nara, and Wakayama Prefectures. The heavy rainfall induced many sediment disasters including 33 DSL, 30 rock falls, and 21 stream blockages, with total sediment amount of approximately 1×10^8 m^3 [*MLIT*, 2011; *MLIT*, 2013]. From 33 DSL found

in Kii Peninsula, 30% of them mobilized downstream as debris flow and deposited far from the failure area, while the 64% of them formed landslide dam in the adjacent stream of the failure area [*Kharismalatri et al.*, 2017]. Based on investigation of these DSL, stream gradient and inflow angle are the major factors which established a boundary between landslide dam and debris flow formation. The collapsed material of DSL which mobilized as debris flow were occurred in stream with gradient of >10° and inflow angle of <60°. While on stream gradient of <10° and inflow angle of >60°, the collapsed material of rapid DSL were likely to form landslide dam.

Yet, very few researches discussed the interaction between landslide, junction/merging/inflow angle, and the gradient of receiving stream. *Benda and Cundy* [1990] developed an empirical model of channel slope (<3.5°) and tributary junction angle (>70°) and found out that deposition of material started at gradient less than 3.5°. While *Takahashi* [2007], focusing on the travel distance of debris flow, constructed an experiment apparatus of 500-m-long slope and 200-m-long river channel (with two types of channel spanning angle: 100° and 140°) where the merging angle between them was 45° and 90°. The experiment revealed that the behaviors of material flow intricately vary depending on the combinations of merging angle, channel gradient, and the opening angle of cross-section.

However, to date, the significance of these topographic characteristics (i.e. stream gradient and inflow angle) to collapsed material movement has yet to be clarified and the possibility of landslide dam formation need to be analyzed further. Additionally, the boundary of whether collapsed material of DSL will mobilize as landslide dam or debris flow has yet to be determined. In this research, small flume experiment was conducted to analyze the mobilization and separate the phenomena of soil deposition by using collapsed material from DSL as soil sample. A small flume of 10 cm wide and 15 cm high was developed to represent the slope where the landslide occurs and the stream where the collapsed material mobilize into. Small flume is easy to develop and the amount of material needed for the experiment also smaller, yet it can give general description of the collapsed material movement and considered more efficient rather than large flume of several meters size. Since inflow angle and stream gradient are the major factors on landslide dam formation, variation of inflow angle and stream gradient were applied on the small flume apparatus. The aim of this experiment is to clarify the significance of inflow angle to the movement and deposition of DSL material and to examine the possibility of landslide dam formation.

2. METHODOLOGY

A small flume consisted of a main channel and an inflow segment was developed for the experiment (**Fig. 1**). Both segments were 10 cm wide and 15 cm high by 1-cm thick acrylic material. The gradient of the inflow segment was 45°. The length of the main channel was 130 cm and a bucket was placed at the end of it to capture transported soil sample. Since inflow angle and stream gradient were the major factors for material movement, experiment was applied on four different inflow angles (90°, 60°, 30°, and 0°) and stream gradient of 10°. The authors used 6 classes of water content (0%, 20%, 40%, 60%, 80%, and 100%) because water content of collapsed material also alter the mobility of soil.

Soil mixture was placed in 10 cm upstream from the junction area, and then the lid was opened manually to let the soil mixture flows. After the experimental flushing, percentages of material deposition were measured in 5 sections (**Fig. 2**). Each experiment was conducted 3 times. This flume experiment was not a scale down from an actual landslide event and was not intended as a model of the DSL in Nigoridani, but to describe the general tendency and features of material movement under several conditions. By flume experiment, the principle of material movement which is important to understand the mobilization and deposition of material can be obtained.

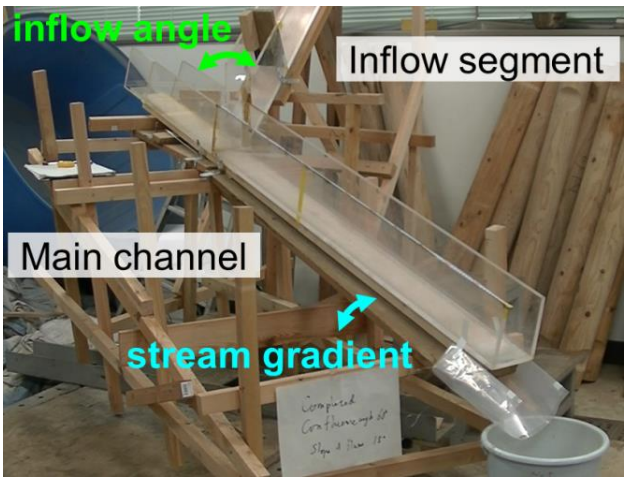

Fig. 1 Small flume apparatus

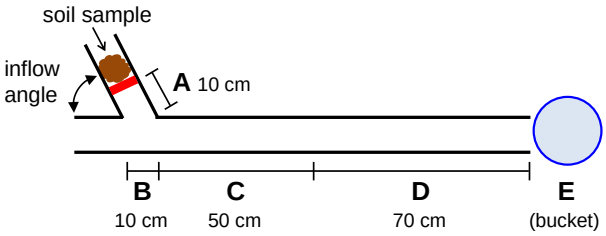

Fig. 2 Sections division of the small flume

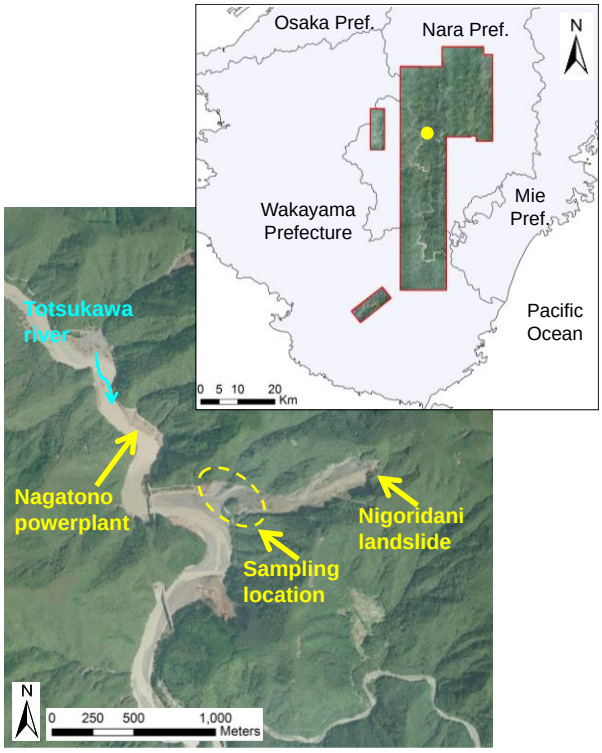

Fig. 3 Location of soil sampling

3. SOIL SAMPLES

Soil samples were taken from Nigoridani, Totsukawa Village, Nara Prefecture, where rapid DSL occurred due to Typhoon Talas in September 2011 (**Fig. 3**). A short-term landslide dam was formed at stream gradient of 0.8° and inflow angle of 121° [*Kharismalatri et al.*, 2017]. The main collapsed area was about 30 m depth [*Chigira et al.*, 2012] and located at the upper part of the slope for about 950 m above the sea level. The amount of collapsed material was increased as it flows to the Totsukawa River for about 650 m below. According to *IEA Hydropower Implementation Agreement* [2016], the total amount of material was estimated for about 4 million ton which rushed at about 200 km/h, creating a mountain tsunami upstream and downstream. Nagatono hydropower plant, located about a kilometer upstream from the failure area, was completely destroyed as the impact of the >10 m mountain tsunami wave [*IEA Hydropower Implementation Agreement*, 2016]. The main failure area consists of well-fractured muddy alternation of sand and shale of Cretaceous Miyama Formation, with a large dense block of felsic tuff intercalated beneath the lower part of the slope, thus groundwater is easily backed up in the mass at the upper part of the slope [*Mitamura et al.*, 2014].

Soil samples were taken at the lower part of the slope due to difficulties to reach the main failure zone at the top of the slope. Soil properties tests were conducted to the disturbed samples, i.e. soil density, particle size analysis, and Atterberg limits tests. From the tests, the author obtained water content at saturated condition of 21%, plastic limit of 14%, and liquid limit of 19%. The plastic limit test was conducted based on Test Method for Liquid Limit and Plastic Limit of Soils (JIS A 1205:2009), while the liquid limit test was conducted based on Test Method for Liquid Limit of Soils by the Fall Cone (JGS 0142-2009). Based on the particle size analysis, the D_{50} of the soil sample was 7 mm.

4. RESULT AND DISCUSSION

4.1 Influence of inflow angle to material deposition

The result of flume experiment is summarized in **Table 1**. Material deposition at section A was increased with larger inflow angle, but the increasing became less significant as the water content increased. The largest material deposition was on 90° inflow angle with 0% water content, and in contrast, very few material were deposited at section A on water content of more than 40% in all inflow angle cases. At section B, the largest material deposition by trend was 64% which was generated on 90° inflow angle with 0% water content. Whereas the smallest material deposition of 0.3% was generated on 0° inflow angle with 80% and 100% water content.

Section C was the deposition zone for 0% water content and the transportation zone for other water contents. A clear correlation between deposition percentage, inflow angle, and water content was not found at this section. Further, material deposition at section D was zero for 0% water content since the fluidization was stopped at section C. Material deposition at section D tended to be small on inflow angle of 60° and 90° rather than on inflow angle of 0° and 30°. Lastly, the largest material deposition at section E was found on inflow angle of 0°, followed by 30°, 60° and 90° for all water contents. Since the movement of material with 0% water content was stopped at section C, thus the deposition at section E was zero.

Table 1 Summary of soil deposition percentage on each section

Flume section	Water content	Inflow angle			
		0°	30°	60°	90°
A	0%	4%	21%	12%	34%
	20%	1%	11%	3%	20%
	40%	1%	3%	1%	2%
	60%	0.4%	1%	1%	2%
	80%	0.3%	1%	0.3%	1%
	100%	0.4%	1%	0.3%	1%
B	0%	56%	41%	71%	64%
	20%	19%	27%	37%	50%
	40%	2%	5%	16%	39%
	60%	0.4%	2%	6%	30%
	80%	0.3%	1%	7%	31%
	100%	0.3%	1%	4%	22%
C	0%	40%	38%	17%	2%
	20%	67%	57%	57%	30%
	40%	43%	60%	57%	45%
	60%	10%	60%	46%	44%
	80%	5%	54%	47%	33%
	100%	1%	19%	26%	38%
D	0%	0%	0%	0%	0%
	20%	12%	1%	1%	0.2%
	40%	41%	19%	14%	6%
	60%	56%	17%	25%	11%
	80%	56%	15%	19%	14%
	100%	29%	27%	24%	11%
E	0%	0%	0%	0%	0%
	20%	1%	3%	2%	0.1%
	40%	13%	13%	13%	9%
	60%	32%	20%	22%	12%
	80%	38%	29%	27%	21%
	100%	69%	52%	45%	29%

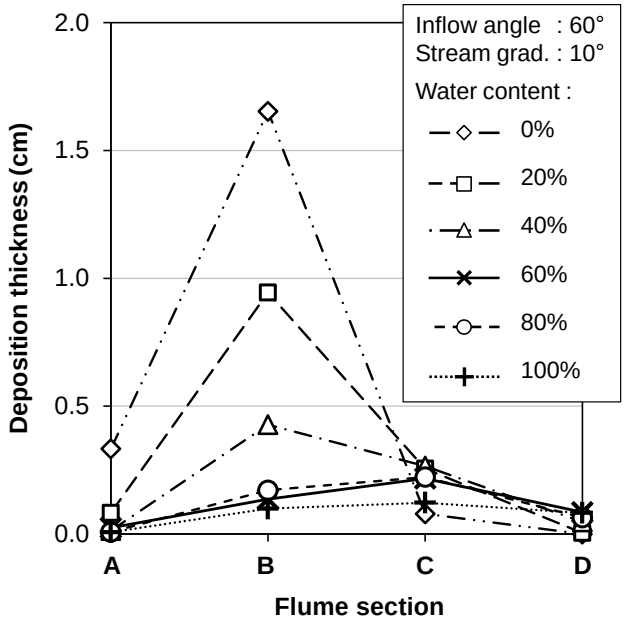

Fig. 4 Average material deposition thickness on 60° inflow angle

4.2 Possibility of landslide dam formation

Among 5 flume sections, the thickest material deposition was generally found at section B (**Fig. 4**) particularly on low water content. Average material deposition thickness was obtained by dividing volume of material deposited on each section with the section area. The inflow angle of 90°, 30°, and 0° has the similar pattern of deposition thickness with 60° inflow angle. Among 4 inflow angles, the thickest deposition at section B was found on 90° inflow angle in all water content classes. At the same water content, inflow angle of 60° and 90° generally generated material deposition of about 0.4 cm thicker than those on 0° and 30° inflow angle. The thickest deposition at section B was generated on 60° and 90° inflow angle on 0% water content which was 1.6 and 1.5 cm respectively. Water content of ≤40% and inflow angle of 60° and 90° generated a thick material deposition at section B. Deposition thickness at section E was not included in **Fig. 4** because the length was unknown and the soil deposited at section E was actually still have potential to mobilize further to downstream if the flume being extended.

By the material deposition thickness, it can be assumed that landslide dam possibly formed at section B, since it generally has the thickest material deposition among other sections and thus has the possibility of blocking the river flow. In addition, section B is the junction area between the contributing slope and receiving channel where the collision between the collapsed material and the opposite slope occurs, possibly knocked down trees and scrapped the soil on the opposite slope, and loss some energy.

Fig. 5 describes the material deposition formed at section B in accordance with inflow angle modification. By trend, 90° inflow angle generated the largest material deposition in all water content classes, while the smallest material deposition was generated by 0° inflow angle. *Yamamoto et al.* [1999] stated that heavy rainfall-induced DSL are commonly occurred on soil's saturated water content condition. The bold dash line on **Fig. 5** represents the saturated water content of Nigoridani soil sample (21%). Following *Yamamoto et al.* [1999] if DSL occurred on Nigoridani soil samples at their saturated water content, inflow angle of 90° and 60° formed material deposition at section B of 49% and 32% respectively. While only 14% on 30° inflow angle and 11% on 0° inflow angle. In accordance with *Kharismalatri et al.* [2017] that landslide dam possibly formed on inflow angle of more than 60°,

the material deposition on 90° and 60° inflow angle in this flume experiment possibly formed landslide dam. Yet the boundary of how much material deposition at the junction area can be considered as landslide dam is uncertain.

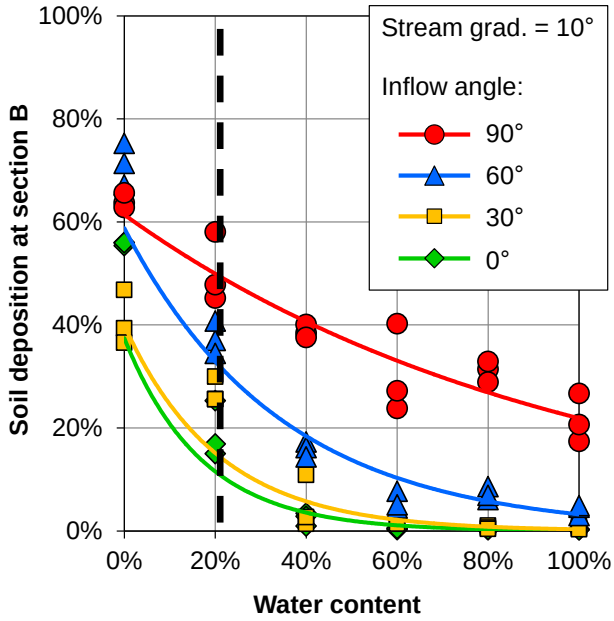

Fig. 5 Material deposition at section B

4.3 Discussion

Inflow angle defined as the upstream junction/merging angle between contributing slope with the stream channel which strongly influenced the mobilization of rapid DSL collapsed material on the stream (e.g. *Benda and Cundy*, 1990; *Ishikawa*, 1999; *Kimura et al.*, 2016; *Takahashi*, 2007). The inflow angle contributed to material deposition at flume sections and possibility of landslide dam formation. *Benda and Cundy* [1990] remarked that material movement with junction angle of less than 70° predicted to be mobilize downstream as debris flow. In accordance, most of the collapsed material movements change into debris flows when the inflow angle of earthquake-triggered DSL is less than 70° [*Ishikawa*, 1999]. From 13 rainfall-triggered DSL, the inflow angle which induced debris flow ranges from 10° to 62° with the stream gradient ranges from 6° to 25° [*Yamada et al.*, 2000]. While from 77 DSL induced by snowmelt, *Kimura et al.* [2016] found that steep valley of more than 9° and sharp inflow angle of less than 70° induced long-travelling landslides which traveled longer than their slope lengths.

Collapsed material of DSL tends to travel in long distance as debris flow when the DSL occurs on slope with pre-existing landslide, sharp inflow angle, and coupling with steep valley topography [*Kimura et al.*, 2016; *Yamada et al.*, 2000]. In contrast, collapsed material of DSL that encountered large inflow angle will experience large collision with the opposite slope which cost a large amount of energy and thus the material deposited on or near the collision/junction area [*Ishikawa*, 1999]. Additionally, *Kharismalatri et al.* [2017] remarked that the threshold between landslide and debris flow is 60° inflow angle and 10° stream gradient. Experiment on this research revealed that inflow angle of 90° and 60° formed large material deposition at the junction area which possibly forming landslide dam. This research agreeing with previous researches that landslides with <60° inflow angle are likely to mobilize to lower stream/channel, while those with >60° inflow angle are likely to be deposited at junction area and has high possibility of forming landslide dam.

DSL' collapsed material movement and landslide dam formation is not solely depends on the topographic characteristics. The natural conditions (e.g. the stream bed and slope soil layer, stream flow, slope and stream soil layers, fallen trees, stream flows, and the condition of the opposite slope) are the factors that also influence the mobilization of collapsed material. On the actual DSL event, these factors will affect the mobilization of DSL' collapsed material. As the collapsed material sliding downwards along the slope, the motion involves not only the material from the initial failure zone but also the soil added along the path of the travel [*Sassa and Wang*, 2005]. Therefore the volume of the material will increase and might form larger deposition at the junction area with the receiving stream.

Fallen trees as well as large boulders also have influence on the formation of larger deposition at the junction area. After colliding with the opposite slope, collapsed material mixed with fallen trees or large boulders drifted by the material motion will stop and formed large deposition at the junction area. Due to resistance to erosion of large boulders and reduction of water pressure due to seepage through the void created by the boulders and logs [*Yin et al.*, 2009], deposition of material mixed with fallen trees and large boulders will be harder to be eroded by the stream flow and thus easier to form landslide dam. Meanwhile, stream flow on the receiving channel/stream has two roles on the collapsed material movement; (1) on the event of the DSL disaster, its high flood runoff discharge helped collapsed material movement to flow downstream as debris flow [*Takahashi*, 2014] and the formed landslide dam will be at the risk of breaching due to raid rise in water level [*Chigira*,

2011]; and (2) after the formation of landslide dam, the impounded stream flow behind the dam will affect the dam stability (e.g. *Dong et al.*, 2011; *Li et al.*, 2011).

Those natural conditions are influencing the mobility of landslide material and the possibility of landslide dam formation. However, they are not being considered in this experiment as it is a simplified landslide material movement so that the experiment become more feasible and focused more on the topographic factors. In future researches, it is suggested to consider those natural factors in the experiment in association with the topographic characteristics. Deposition formed at the junction area possibly larger than the result obtained in this experiment and the formation of landslide dam will be more apparent if the natural factors are being considered, yet the experiment process will be much more complex.

5. CONCLUSION

Previous researches agree that topographic characteristics (i.e. stream gradient and inflow angle) are major factors that distinguish the formation of landslide dam and debris flow from DSL collapsed material. Small flume experiment was conducted to examine these major factors for understanding the general description of the collapsed material movement under given experimental conditions. DSL material on inflow angle of 30° and 0° was mainly transported to the lowest section of the flume as debris flow. Particularly when the material contained a lot of water (over its saturated condition), it mainly transported to lower sections and less likely to form landslide dam at the junction area.

In contrast, material with low water content (lower or equal to its saturated condition) is more likely to form landslide dam. Particularly on inflow angle of 60° and 90°. On its saturated condition, material deposition at junction area was estimated to be 32% and 49% on inflow angle of 60° and 90° respectively, which has high possibility of forming landslide dam. This experiment clarified that collapsed material movement on inflow angle of 60° and 90° has high possibility to form landslide dam at the junction area, while on inflow angle of 0° and 30° the material was likely to travel in long distance as debris flow. In addition to topographic characteristics, water content also has an important role in determining the mobilization of DSL collapsed material.

Other than topographic characteristics, natural conditions such as fallen trees, stream and slope soil layer, and stream flow also affecting the formation of landslide dam. Stream and slope soil layer and fallen trees increase the possibility of landslide dam formation while stream flow helps the collapsed material to transport downstream. In future researches, it is suggested to consider these natural factors in the experiment in association with the topographic characteristics. Clarifying the threshold between landslide dam and debris flow will be very useful for estimation of future disaster and determination of hazard area. Thus land use management, spatial planning, and appropriate countermeasures can be performed effectively.

REFERENCES

Bathurst, J. C., Burton, A., and Ward, T. J. (1997): Debris flow run-out and landslide sediment delivery model tests. Journal of Hydraulic Engineering, Vol. 123, No. 5, pp. 410-419.

Benda, L.E. and Cundy, T.W. (1990): Predicting deposition of debris flows in mountain channels. Canadian Geotech Journal, vol. 27, pp. 409–417.

Canuti, P., Casagli, N., and Ermini, L. (1998): Inventory of landslide dams in the northern Apennine as a model for induced flood hazard forecasting, in: Andah, K. (Ed.). Managing hydro-geological disasters in a vulnerable environment. CNR-GNDCI Publication No. 1900, pp. 189-202.

Chigira, M. (2011): Geological and geomorphological characteristics of deep-seated landsldies induced by rain and earthquakes. Journal of Chinese Soil and Water Conservation, vol. 42(4), pp. 265–278.

Chigira, M., Matsushi, Y., Tsou, C. Y., Hiraishi, N., Matsuzawa, M., and Matsuura, S. (2012): Deep-seated catastrophic landslides induced by Typhoon 1112 Talas. Annuals of Disaster Prevention Research Institure, Kyoto Univ, vol 55A, pp. 193–211.

Dong, J. J., Tung, Y. H., Chen, C. C, Liao, J. J., and Pan, Y. W. (2011): Logistic regression model for predicting the failure probability of a landslide dam. Engineering Geology, vol. 117, pp. 52–61. doi:10.1016/j.enggeo.2010.10.004.

Ermini, L. and Casagli, N. (2003): Prediction of the behaviour of landslide dams using a geomorphological dimensionless index. Earth Surface Processes and Landforms, vol. 28, pp. 31-47, doi:10.1002/esp.424.

Highland, L. M., Ellen, S. D., Christian, S. B., and Brown III, W. M. (1997): Debris-flow hazards in the United States. US Geological Survey Fact Sheet, pp. 176-197.

IEA Hydropower Implementation Agreement (2016): Annex-11 Update and enhancement of hydroelectric power plant, vol 2: case histories report, Jp.40: Nagatono power plant. Retrieved from: http://www.nef.or.jp/ieahydro/actresult_a11_report.html.

Inoue, K., Mori, T. and Mizuyama, T. (2012): Three large historical landslide dams and outburst disasters in the North Fossa Magna Area, Central Japan. International Journal of Erosion Control Engineering, vol. 5, no. 2, pp. 145–154.

Ishikawa Y., (1999): Morphological and geological features of

debris flows caused by earthquakes. Journal of the Erosion Control Engineering Society, vol. 51, no. 5, pp. 35-42 (in Japanese with English abstract).

Kharismalatri, H.S., Ishikawa, Y., Gomi, T., Shiraki, K., Wakahara, T. (2017): Collapsed material movement of deep-seated landslides caused by Typhoon Talas 2011 on the Kii Peninsula, Japan. International Journal of Erosion Control Engineering, vol. 10, no. 3, pp. 108-119.

Kimura, t., Katsura, S., Maruyama, K., Ishida, K. (2016): Topographic features of source and transfer-deposition areas of long-travelling landslides induced by snowmelt. Landslides - Journal of the Japan Landslide Society, vol. 53, no. 2, pp. 31-42 (in Japanese with English abstract).

Li, M. H., Sung, R. T., Dong, J. J., Lee, C. T., and Chen, C. C. (2011): The formation and breaching of a short-lived landslide dam at Hsiaolin Village, Taiwan — Part II: Simulation of debris flow with landslide dam breach. Engineering Geology, vol. 123, pp. 60–71. doi:10.1016/j.enggeo.2011.05.002.

Mitamura, M., Tochimoto, Y., Uto, H., Asahina, T., Thoda, J., Murahashi, Y., Okajima, S., Yamashita, D., and Kato, T. (2014): Geologic and geomorphologic features on groundwater situation of large scale landslides induced by Typhoon 1112 (Talas) in Nara Prefecture, Japan. International Symposium on Geoinformatics for Spatial Infrastructure Development in Earth and Allied Sciences (GIS-IDEAS) 2014. December 6-9, Danang, Vietnam.

MLIT (Ministry of Land, Infrastructure, Transport and Tourism) (2006): Explanatory of committee on crisis management of large-scale river blockage (natural dam), available at http://www.mlit.go.jp/common/001024697.pdf (last access: 11 Dec 2015, in Japanese).

MLIT (Ministry of Land, Infrastructure, Transport and Tourism) (2011): Report of sediment-related disasters caused by Typhoon No. 12 in 2011, available at http://www.mlit.go.jp/stream/sabo/dosyahou_review/02/111031_shiryo2.pdf (last access: 11 Dec 2015, in Japanese).

MLIT (Ministry of Land, Infrastructure, Transport and Tourism) (2013): Sabo in the Kii Mountain District, Kii Mountain District Sabo Office, Kinki Regional Development Bureau, Nara.

Nishiguchi, Y., Uchida, T., Takezawa, N., Ishizuka, T. and Mizuyama, T. (2012): Runout characteristics and grain size distribution of large-scale debris flows triggered by deep catastrophic landslides, International Journal of Japan Erosion Control Engineering, Vol. 5, No. 1, pp. 16–26.

Sassa, K., and Wang, G. H. (2005): Mechanism of landslide-triggered debris flows: Liquefaction phenomena due to the undrained loading of torrent deposits. in: Jakob, M. and Hungr, O. (Eds) Debris-flow hazards and related phenomena. Springer, Berlin, pp. 81–101.

Takahashi, T. (2007): Debris flow: mechanics, prediction and countermeasures. Taylor & Francis Group, London.

Takahashi, T. (2014): Debris flow: mechanics, prediction and countermeasures. 2nd edition. Taylor & Francis Group, London.

Yamamoto, S., Ishikawa, Y., Miyoshi, I., and Mizuhara, K. (1999): Soil characteristics and fluidity of debris flows at the Gamahara River, at the Harihara River and at the Hachimantai Area. Journal of the Japan Society of Erosion Control Engineering, vol. 51, no. 5, pp. 28–34.

Yamada, T., Minami, N., Kikuchi, H., and Miura, I. (2000): Multiple discriminant analysis on the topographic factors of the deep-seated slope failure-induced debris flow occurrence. Journal of the Erosion Control Engineering Society, vol. 53, no. 4, pp. 23-29 (in Japanese with English abstract).

Yin, Y., Wang, F., Sun, P (2009): Landslide hazards triggered by the 2008 Wenchuan earthquake, Sichuan, China. Landslides, vol. 6, pp. 139–151. DOI:10.1007/s10346-009-0148-5.

A Method for Predicting and Taking Measures Against Soil Slips Generating Debris Flows in a Case Study of the 2014 Hiroshima Sediment Disasters

Yoshiharu ISHIKAWA[1], Hiroyuki UMEZAWA[1], Risa TANABE[1],
Aya TAMEIKE[1*] and Quoc Dung DANG[2]

[1] Toa Grout Kogyo Co., Ltd,(2-10-3 Yotsuya Shinjuku-ku TOKYO 160-0004 Japan)
[2] Dept. of Environmental Technology, Ton Duc Thang University,
(19 Nguyen Huu Tho Street, Tan Phong Ward, District 7, Ho Chi Minh City, Vietnam)
*Corresponding author. E-mail: aya.tameike@toa-g.co.jp

The previous studies indicated that most of debris flows were generated by the soil slips in zero-order channels. If the places of soil slips were predicted accurately before occurrence of them, we could conduct more effective countermeasures against soil slips than usual countermeasures such as check dams for capture the large amount of debris for preventing disasters. The purpose of this study is to propose a method of predicting the places of soil slips and propose the way for preventing occurrence of soil slips or trapping the small amount of debris in the upper reaches of streams. The places of soil slips were examined in case study of the 2014 Hiroshima sediment disasters. The results indicated that about half of soil slips occurred in the zero-order channels and most of soil slips generated debris flows. We proposed that effective measures against the soil slips in zero-order channels to prevent debris flow disasters.

Key words: soil slip, debris flow, zero-order channel, slope stability work, flexible debris flow barrier

1. INTRODUCTION

According to research by *Tsukamoto et al.* [1973], soil slips that cause debris flows are highly likely to occur in zero-order channels. They called all depressions seen on mountainside slopes that have not grown into first-order channels as zero-order channels (under-first-order channels). The zero-order channels are generally defined as terrain whose depth is less than the frontages of depressed contour line groups by using 1/25,000 topographical maps or large-scale topographical maps [*National Institute for Land and Infrastructure Management, Ministry of Land, Infrastructure, Transport and Tourism*, 2016]. *Tsukamoto et al.* [1973] made it clear that soil slips in zero-order channels are widely distributed. However, if one is to predict the causes of debris flows and consider measures to be taken against them, the area of causes of debris flows must be limited because the scope of prediction of points of soil slips is widely distributed, and cost superiority cannot be maintained.

Against such a background, in this paper we have classified the points of soil slips which generate debris flows by geographic feature in consideration of the August 2014 sediment disasters due to heavy rainfall in Hiroshima Prefecture (Fig.1) with the aim of predicting the generation of debris flows with high probability, and we have calculated the ratio of such occurrences. Then, based on the results thereof, we conducted basic research on a method for predicting

Fig. 1 Study area

and taking measures against generation of debris flows, which we report here. We chose the 2014

Hiroshima disaster as a study area because we could collect a lot of data concerning soil slips and debris flows in a small region and obtain a 1/5,000 contour diagram by using aerial photographs.

Our research covered two geographic areas, namely Mt. Abu (about 585 meters above sea level) and Mt. Takamatsu (about 340 meters above sea level), where debris flows have frequently occurred.

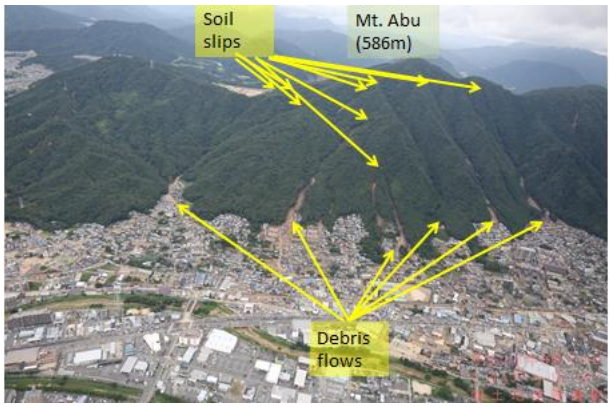

Photo 1 East side of Mt. Abu where many debris flows occurred
(Photo taken by the Geographical Survey Institute, Japan)

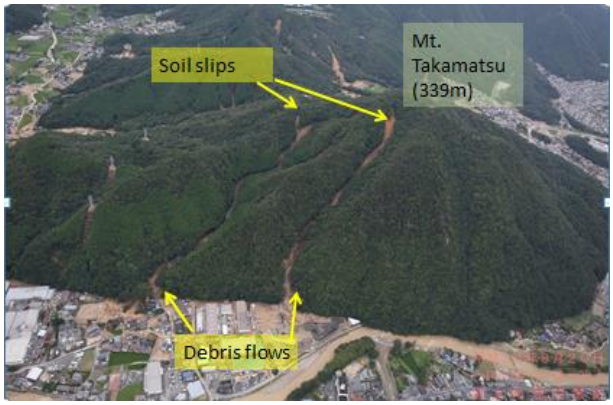

Photo 2 West side of Mt. Takamatsu where many debris flows occurred
(Photo taken by the Geographical Survey Institute, Japan)

2. OUTLINE OF THE SEDIMENT DISASTER IN HIROSHIMA

From 3:00 to 4:00 AM on Aug. 20th, maximum hourly rainfall of 101mm (AMeDAS Miiri Observatory) occurred in the northern part of Hiroshima City, almost at the same time, many soil slips occurred in the headwater of streams around Mt. Abu and Mt. Takamatsu, triggering debris flows (Photo 1,2). The debris flows containing boulders flowed down streams and generated great quantities of sediment and woody debris by eroding the stream bank and stream bed in the middle and upper reaches [*Kaibori et al.*, 2014]. The debris flows flooded on the alluvial fans and caused great injury with 74 fatalities, and great damage, with 133 totally destroyed houses and 297 houses half and partially destroyed. The areas are geologically made up of weathered granite and sedimentary rock.

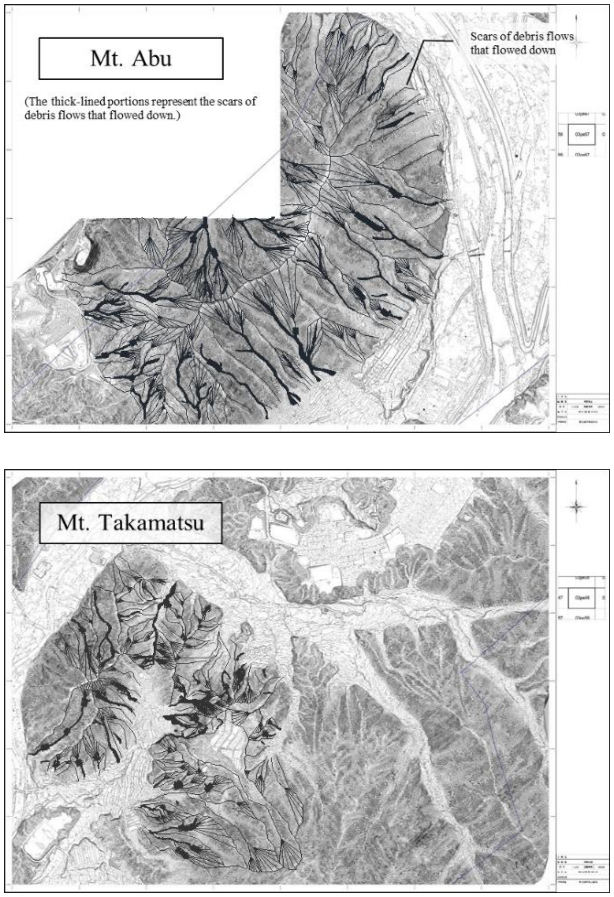

Fig. 2 Reading Conditions of Mt. Abu (top) and Mt. Takamatsu (bottom)
(Provided by Aero Asahi Crop.)

3. METHOD

The scars of the debris flows are shown in a 1/5,000 contour diagram by using aerial photographs taken (by Aero Asahi Crop.) after the occurrence of disasters in the areas covered by our research (Fig 2). In conformity to the set definitions, we classified the points of occurrence of soil slips and calculated the ratios thereof.

Moreover, we classified the soil slips in zero-order channels into three categories to narrow down the areas to predict and then calculated the ratios thereof.

4. DEFINITIONS OF CATEGORIES IN THE OCCURRENCE AREAS

The areas where soil slips were caused in surveyed areas are classified as follows: Category Ⅰ refers to soil slips in zero-order channels, Category Ⅱ to bank collapses, and Category Ⅲ to other soil slips (Fig 3). These definitions are elaborated below.

4.1 Zero-order channels (Category Ⅰ)

Here, only the upper part of a basin that has grown into a first-order channels is classified as a zero-order channels, which is defined as the areas surrounded by the line of the basin divide and straight lines which each open by 30 degrees toward the right and left bank sides from an extension line that extends from the top end of the first-order channels. The points of soil slips in the areas of a zero-order channels are each divided by 10 degrees from the 0-degree line toward the right and left banks into three equal parts, and they are classified as follows: Category (a) refers to less than 10 degrees, Category (b) to at least 10 but less than 20 degrees, and Category (c) to at least 20 but less than 30 degrees (Fig 4). The areas of soil slips are identified by using aerial photographs and a 1/5,000 contour diagram, then the sizes of areas inside each Category (a), (b), (c) are measured. The Category in which the largest size of area occupies is recognized as the Category for the soil slips.

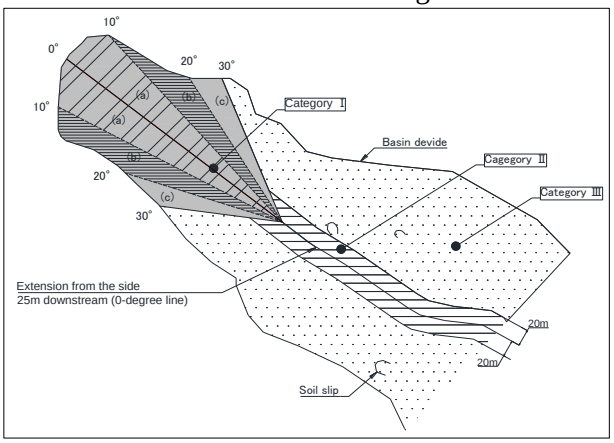

Fig. 3 Soil slip point categories

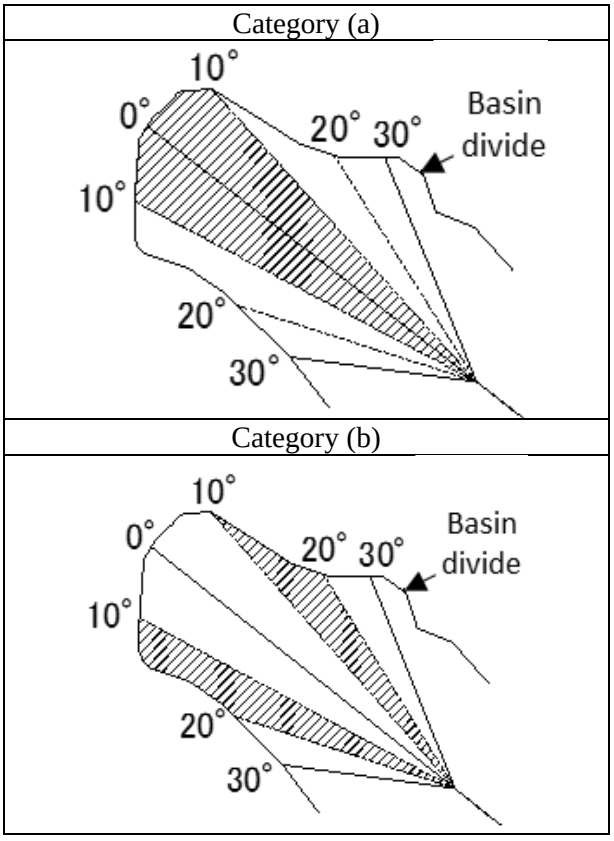

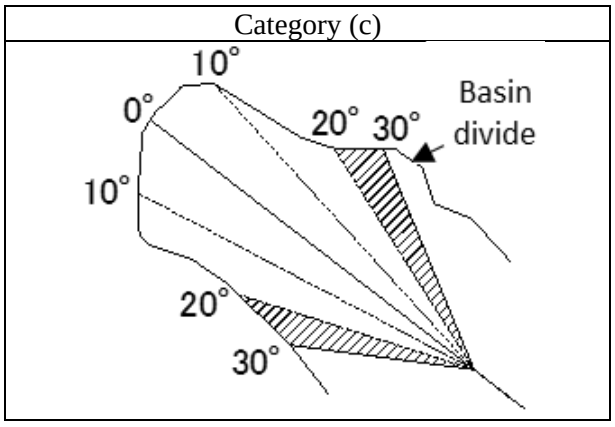

Fig. 4 Zero- order channel categories

4.2. Banks (Category Ⅱ)

Within the areas of a basin divide, the areas surrounded by right and left riverbanks from the trough line within a horizontal distance of 20 meters are classified as banks.

4.3 Others (Category Ⅲ)

Areas that do not fall under either Category Ⅰ or Ⅱ are classified as Category Ⅲ. These areas are further classified into rising terrain (ridge) or depressed terrain (hollow) based on the terrain of the points of soil slips.

4.4 Debris flows

We define the movements of collapsed materials over 100 meters travel distance as debris flows. Because fluidization of collapsed materials causes long distance travel. Such a movement distance refers to the distance from the source of soil slips to the point where the debris stop; it does not include areas where debris spread out. Also, in the case in which debris flows two or more sources of soil slips join together and flow down, in the same manner, we measure the horizontal distance from each point of

soil slips to the point where the debris stop.

5. RESULTS

5.1 Assessment of points of soil slips

The number of points of soil slips surveyed was 181. According to the classification results, Category Ⅰ had 96 points and the highest rate of occurrence, about 53%. Category Ⅱ had 18 points and a rate of occurrence of about 10%, while Category Ⅲ had 67 points and a rate of occurrence of about 37%. Of the Category Ⅲ collapses, 64 points and about 35% occurred in depressed terrain (hollow), showing the second highest rate of occurrence after Category Ⅰ (Table 1 and Fig.5). Then, we further sub-classified the Category Ⅰ collapses. Of the 96 points, Category (a) had 43 points and the highest rate of occurrence, about 45%. Category (b) had 25 points and a rate of occurrence of about 26%, while Category (c) had 28 points and a rate of occurrence of about 29%(Table 2).

Moreover, the number of existing zero-order channels we read in the overall area was 155, and there were 73 points of zero-order channels that had soil slips. Thus, this value accounted for about 47% of all zero-order channels (Table 3).

As to why the rate of occurrence of soil slips increases in depressed terrain in Category Ⅰ or Ⅲ, we think that because surface water concentrates in such terrain during times of rainfall, the subsurface water that has concentrated in the surface soil induces soil slips. Therefore, we considered at which point where rainwater from the upper part of the slope concentrates was most likely to soil slips. So, we think that reading such points can contribute to reducing the areas of prediction of points of soil slips.

Table 1 Point of soil slips categories

	Collapsed point categories			
	Ⅰ. In zero-order channels	Ⅱ. Banks	Ⅲ.Others	
			Rising terrain.	Depressed terrain.
Mt.Abu	50	4	2	27
Mt.Takamatsu	46	14	1	37
(1) No of collapsed points	96	18	3	64
			67	
(2) Total No. of collapsed points	181			
(3) Rate of occurrence ((1) / (2)×100)%	53.0	9.9	1.7	35.4
			37.0	

Table 2 Zero-order channels categories

	Ⅰ.zero-order channels		
	a	b	c
(4) No. of points of soil slips.	43	25	28
(5) Total No.of points of soil slips.	96		
(6) Rate of occurrence ((4) / (5)×100)%	44.8	26.0	29.2

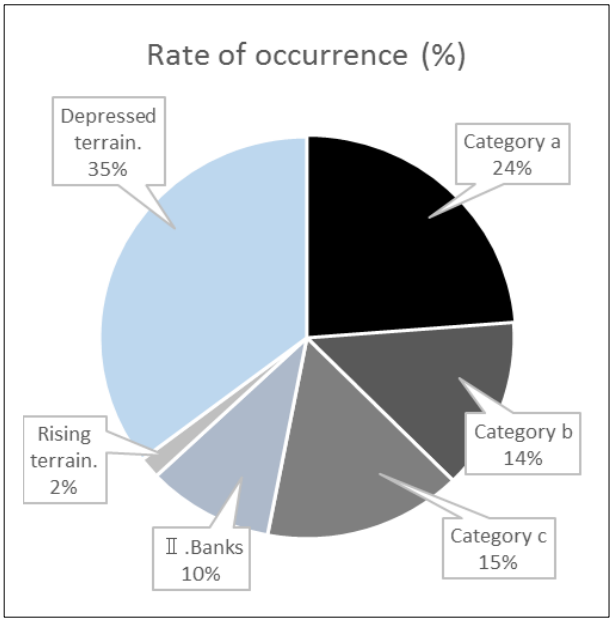

Fig. 5 Rate of occurrence of soil slips

Table 3 Total No. of zero-order channels and rate of occurrence

	No. of soil slips in zero-order channels.			No soil slips.
	1 point.	2 points.	3 points.	
(4) No. of zero-order basins with soil slips.	54	15	4	82
	73			
(5) Total No.of zero-order basins among areas interpreted.	155			
(6) Rate of occurrence ((4) / (5)×100)%	74.0	20.5	5.5	52.9
	47.1			

Table 4 Debris flows that moved by category

	Flowed down	stopped
(7) No. of points of soil slips.	156	25
(8) Total No. of points of soil slips.	181	
(9) Flow-down rate ((7) / (8)×100)%	86.2	13.8

Table 5 Debris flows that stopped by category

	Ⅰ	Ⅱ	Ⅲ
(10) No. of debris flow.	90	14	52
(11) Total No. of points of soil slips.	96	18	67
(12) Rate of occurrence(%) ((10) / (11)×100)	93.8	77.8	77.6

5.2 Assessment of the flow-down distance of debris flows

We measured the movement distance of debris flows at all 181 points of soil slips. The result indicate that soil slips at 156 points caused debris flows, while at 25 points the soil slips stopped along the way. Thus, we found that about 86% of soil slips that occurred developed into debris flows (Table 4). Nevertheless, regarding the categories of the soil slips that occurred at 25 points where the debris movements stopped along the way, Category Ⅰ had 6, Category Ⅱ had 4, and Category Ⅲ had 15. Thus, we found that the Category Ⅱ stop along the way is very low (Table 5).

As to why Category Ⅰ and Category Ⅱ soil slips developed into debris flows at a high rate, one can point out that there the environment is such that debris can move over a relatively longer distance because of the presence of an area that has grown into a first-order channel, which leads debris directly below or within a horizontal distance of 20 meters. However, regarding the Category Ⅰ or Category Ⅱ soil slips that did not develop into debris flows, there are two conceivable patterns, namely soil slips that did not reach first-order channels and soil slips that stopped within first-order channels. Nevertheless, we think it necessary to further consider these by making use of inclination classification drawings and other materials. For reference, in Category Ⅲ, collapses at 52 points developed into debris flows, and among these, soil slips at 2 points did not flow into first-order channels.

6. PROPOSAL OF MEASURES AGAINST DEBRIS FLOWS

The most debris flows in Hiroshima were generated by soil slips triggered by the heavy rainfall. As for measures preventing occurrence of debris flows, we propose that measures against the soil slips in zero-order channels, namely at the headwater of streams are effective. In the areas surveyed in this research, soil slips occurred in about half of all zero-order channels in the surveyed areas, and most such soil slips developed into debris flows. So, we consider that about half of such debris flows could have been prevented by taking measures against soil slips in zero-order channels. When the debris generated by several soil slips flow together in the middle reaches and the debris flows cause damage in houses or loss of lives in the lower reaches, the measures against soil slips can decrease the volume of harmful debris, even if the generation of debris flows are not completely prevented. As for which points to take such measures at, we think that the places classified as Category (a) under Category Ⅰ are important.

When the areas of Category (a) in the areas of zero-order channels with high probability of soil slips are small, slope stability works are suitable for the measures to prevent soil slips which generate debris flows. Since the areas of Category (a) locate in the

Photo 3 An example of slope stability works used by high tensile strength steel net

Photo 4 An example of capture of debris by the flexible debris flow barriers

Photo 5 An example of capture of debris by the flexible debris flow barriers

headwater of the streams, the construction of measures should be possible by human power and the materials for the measures should be light. Under this construction conditions, the slope stability works used by high tensile strength steel net as shown in Photo 3 are suitable for preventing soil slips and debris flows. The high tensile strength net is manufactured by braiding high tensile strength steel wires in a lattice shape and is fixed on the surface of slope using earth anchors or rock bolts.

Whereas, if the areas of Category (a) are large, flexible debris flow barrier as shown in Photo 4 and 5 which catch the debris generated in the areas of zero-order channels located in the headwater of the streams is suitable for the measures, because when the slope stability works are used, the large scale of structures is necessary. However, in the construction of the flexible debris flow barrier in the headwater of the streams, the transportation materials is small and construction should be conducted in a simple way. The ring net used for the flexible debris flow barrier is manufactured by braiding high tensile steel wires in a ring shape.

Both of the slope stability works and the flexible debris flow barrier used by the high tensile strength steel net have many their record of construction in Japan. Concerning the flexible debris flow barrier, examples of capture of debris are reported as shown in Photo 4 and 5. However, as both the number and area of all zero-order channels are enormous, we think it necessary to determine levels of importance by narrowing down the areas to be surveyed based on which mountain streams have the possibility of causing debris flows as well as the presence or absence of measures for mountain streams and their lower reaches that may stop the debris flows.

Both of the high tensile strength net and the flexible debris flow barriers have their limits of application in size and strength. For example, the strength of anchors which support the wire ropes and posts have their limits, no matter the tensile strength of steel tension members is very high. Then the flexible debris flow barrier is limited in size and in capture volume. It is not suitable for large size structure.

7. CHALLENGES TO ADDRESS IN THE FUTURE

According to the previous researches on debris flows by *Tsukamoto et al.* [1973] and our researches on the Hiroshima disaster in 2014, most of debris flows were triggered by soil slips in zero-order channels and we proposed the slope stability works used by high tensile strength steel net to prevent occurrence of soil slips and the flexible debris flow barrier to capture the collapsed material and prevent the debris flow from flowing down. However, the geographical features differ place to place and the amount of data which is the basis of our proposal is not sufficient for using it as a general method. We will provide high reliable prediction method for occurrence of soil slips by obtaining many objective data and analyzing those data sorted by every geological feature in various locations in the future.

REFERENCES

Kaibori, M. et al. (2014): Sediment – related disasters induced by heavy rainfall in Hiroshima City on 20th August, 2014, Journal of the Japan Society of Erosion Control Engineering, Vol.67 ,No.4, pp. 49 – 59.

National Institute for Land and Infrastructure Management, Ministry of Land, Infrastructure, Transport and Tourism, Japan (2016): Manual of Technical Standards for establishing Sabo master plan for debris flow and driftwood ,Technical Note of National Institute for Land and Infrastructure Management, No.904, pp.17

Tsukamoto, Y. et al. (1973): Study on the growth of stream channel (Ⅲ) ― Relationship between 0 (zero) order channels and landslides. Journal of the Erosion – Control Engineering Society, Vol.26 ,No.2, pp.14 – 20.

Safety Verification of Sabo Dams Against Large Scale Debris Flow

Nobutaka ISHIKAWA[1*], Joji SHIMA[2], Ryo MATSUZAWA[3]
and Takahisa MIZUYAMA[4]

[1]Research Association for Steel Sabo Structures (2-7-4 Hirakawa-cho, Chiyoda-ku, Tokyo102-0093,Japan)
[2] Sabo & Landslide Technical Center (4-8-21 Kudan-Minami, Chiyoda-ku, Tokyo102-0074, Japan)
[3] ITOCHU Techno-Solutions Corporation (3-2-5 Kasumigaseki, Chiyoda-ku,Tokyo100-6080, Japan)
[4]National Graduate Institute for Policy Studies (7-22-1 Roppongi,Minato-ku, Tokyo106-8677, Japan)
*Corresponding author. E-mail: cgishikawa@m4.dion.ne.jp

Recently concrete and steel open-type Sabo dams (hereafter, steel open dam) have been damaged by large scale debris flow load (hereafter, load level 2). This was caused due to large rocks carried in the debris flow resulted from torrential rainfall of abnormal weather. This paper presents safety verification methods of concrete and steel open dams against load level 2. First, the estimation methods of load level 2 are explained. The fluid force and rock impact of load level 2 are assumed by performing the extreme stability analysis and by the field survey of the past debris flow disaster. Second, the safety verification methods for concrete and steel open dams are proposed against the load level 2 from the viewpoint of performance-based design. Finally, numerical examples of concrete and steel open dams are illustrated against load level 2 by performing the FEM impact analysis using the software of ANSYS AUTODYN.

Key words: Safety verification, Sabo dam, load level 2, performance-based design, FEM impact analysis

1. INTRODUCTION

In Japan, many concrete and steel open-type Sabo dams (hereafter, steel open dam) have been constructed as defensive measures in order to prevent and mitigate the debris flow hazards and sediment-related disasters.

However, concrete and steel open dams were recently collapsed by the large scale debris flow (hereafter, load level 2), as shown in **Figs. 1** and **2**. These disasters may have resulted from torrential downpour as a result of abnormal weather conditions. The site survey after disaster was conducted in order to examine the cause of collapse at Nagiso, Nagano Prefecture, Japan in July 2014 [Chubu Regional Burea,2014]. Taking the opportunity, it has been needed to investigate the structural safety of concrete and steel open dams against load level 2.

This paper proposes a safety verification method of Sabo dams from a view point of performance-based design [JSCE, 2017].

First, the performance-based design for Sabo dams is proposed about the relationship between load level and limit state. Second, a Sabo dam is designed so that the external stability conditions (overturn, sliding and ground bearing capacity) may be satisfied against both normal design load (load level 1) and extremely large scale load (load level 2). Third, the internal structural safety methods for concrete and steel open dams are proposed by setting the load

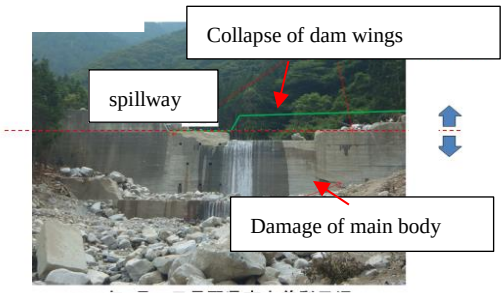

Fig.1 Collapse of concrete dam body and wing

Fig. 2 Damage of steel open dam by large rocks

level 2. Finally, the numerical examples of safety verification for concrete and steel open dams against load level 2 are demonstrated by performing the FEM impact analysis using the software of ANSYS AUTODYN.

2. PERFORMANCE-BASED DESIGN OF SABO DAM

2.1 Objective of Sabo dam

A Sabo dam is constructed to control sediment and to capture the debris flow and woody debris.
Especially, woody debris can be easily captured by a steel open dam.

2.2 Requirement performance

As for the requirement performance for a Sabo dam, capturing function and safety performance are required as follows.

(1) Capturing function is defined that a Sabo dam can capture large rocks and woody debris and sediment in the debris flow [Ishikawa,N. et al., 2014].
(2) Safety performance is defined that a Sabo dam have to keep external stability (overturn, slide, bearing capacity) and internal structural safety (evaluation of strength and deformation).

In this paper, only safety performance is dealt with.

2.3 Load acts on dams

The loads on a Sabo dam are considered as self-weight load, hydrostatic pressure, deposited sediment pressure, debris flow fluid force, earthquake load, rock impact load, woody debris load, uplift pressure.

Herein, the loads onto the dams are classified as load levels 1 and 2 as follows.

(1) Load level 1 means the current design load considering the return period of 100-years of rainfall.
(2) Load level 2 means the large scale debris flow load considering the return period of 200-years of rainfall. The aim of load level 2 is to design and construct the resilient dams .

2.4 Necessity of load level 2

If the one of the following conditions is expected to be happend, then the load level 2 should be considered from the viewpoint of the safety performance of a Sabo dam.

(1) The possibility of large scale sediment movement (large volume, flow rate, flow velocity and large rocks with the diameter of more than 3m).
(2) The dangerous possibility of deep-seated landslide.
(3) The important protective structures are existed in the downstream, e.g., school, hospital and nuclear power plant facilities, etc..

2.5 Determination methods of load level 2

(1) By examining the possibility of the deep-seated landslide.
(2) By investigating the relationship between annual exceedance probability of rainfall and large scale sediment movement (volume, flow rate, flow velocity, huge boulder diameter).
(3) By examining the field survey report of the past large scale debris flow disasters i.e., fluid force, impact force, direction and acting position, etc..
(4) By developing the load estimate methods such as DEM [Horiguchi, et al., 2016] or DEM-MPS [Beppu, et al., 2016] simulations.
(5) By using the extreme stability analysis or an elastic-plastic analysis for the exsisting Sabo dams expediently.

2.6 Limit states of Sabo dam

(1) Serviceability limit state (SLS)
Serviceable limit state (SLS) corresponds to the limit of damage not affecting the capturing function of a Sabo dam. The local and global deformations must be kept less than the allowable ones, respectively. SLS doesn't tend to put people's lives at risk nor do they risk property damage.

(2) Repairable Limit State (RLS)
Repairable limit state (RLS) corresponds to moderate damage. RLS is defined as the maximum damage level which allows planned maintenance and repair methods to be used.

(3) Ultimate limit state (ULS)
Ultimate limit state (ULS) corresponds to very severe damage, for instance, collapse or excessive deformation of the component or the structure under debris flow hazards.

2.7 Safety verification of Sabo dam

The current safety verification should be satisfied against the load level 1. However, the new safety verification is proposed against load level 2 as shown in **Table 1**.

2.7.1 External stability against load level 2

(1) Over turn condition
The safety ratio between resistant moment and overturn moment should be larger than 1.0.

(2) Sliding condition
The safety ratio between the shearing force capacity and the acting shearing force at the dam base should be larger than 1.0.

(3) Bearing capacity condition
The base bearing reaction should be less than the base bearing capacity.

(4) Internal stress condition:
The internal stress of concrete should be less than the extreme internal stress of base concrete.

Table 1 External stability condition

Stability condition	Load level 1	Load level 2
Sliding	$F_S \geqq 1.2$	$F_S \geqq 1.0$
Over turn	$e \leqq B/6$ $e \leqq B_S/6$	$F_r \geqq 1.0$
Bearing capacity	$Q_1, Q_2 \leqq Q_a$	$Q_1, Q_2 \leqq Q_{a'}$
Internal stress of concrete	$\sigma_1, \sigma_2 \leqq \sigma_{ca}$	$\sigma_1 \leqq \sigma_{ca}'$ $\sigma_2 \geqq \sigma_{ta}'$

where, F_S : safety factor for sliding, e : eccentric distance, F_r : safety factor for over turn, B : base width of concrete dam, B_S : base width of steel open dam, Q_1 : bearing reaction at lower stream, Q_2 : bearing reaction at upper stream, Q_a : allowable bearing capacity, $Q_{a'}$: extreme bearing capacity, σ_1 : internal stress at lower stream, σ_2 : internal stress at upper stream, σ_{ca} : allowable compressive stress, σ_{ca}' : extreme compressive stress, σ_{ta}' : extreme tensile stress.

2.7.2 Internal structural safety

(1) Damage level

The damage level is defined as an index of performance criteria by combining with the limit states, as shown in **Fig.3**.

Damage level 1: This level is less than the SLS and as it is.

Damage level 2: This level is from SLS to RLS and needs the small repair.

Damage level 3: This level is from RLS to ULS and needs the large repair .

Damage level 4: This level is larger than ULS and needs the exchange.

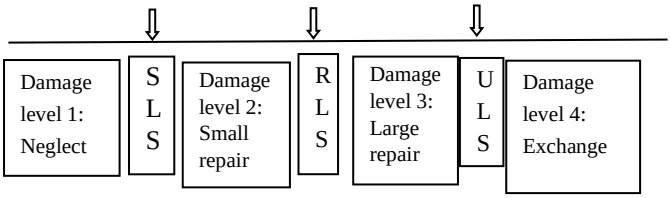

Fig.3 Relationship between damage level and limit state

(2) Local failure

Local failure of a concrete dam is expressed as **Fig.4.**

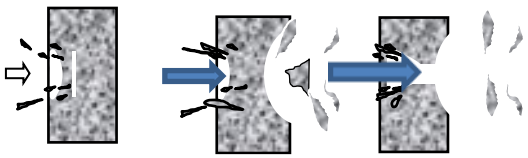

(a)SLS(penetration/spalling) (b) RLS(scabbing) (c) ULS(perforation)

Fig.4 Local failure of concrete dam

Local deformation of a steel open dam is classified and the limit state of local deformation is assumed as shown in **Table 2** referring to **Fig.5** 〔JSCE,2017〕.

Table 2 Local deformation of steel open dam

Limit state	**SLS**	**RLS**	**ULS**
Local deformation / Steel pipe diameter (δ/D)	0.1	0.4	0.7

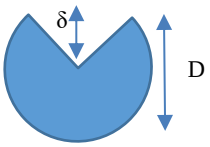

Fig. 5 Local deformation of steel pipe

(3) Global failure

Global failures of concrete and steel open dams are illustrated as shown in **Figs.6,7** and assumed as shown in **Table 3**, respectively〔JSCE,2017〕.

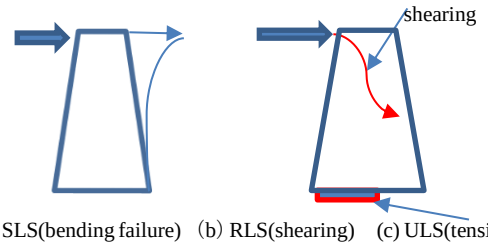

(a) SLS(bending failure) (b) RLS(shearing) (c) ULS(tensile failure)

Fig.6 Global failure of concrete dam

Table 3 Global deformation of steel open dam

Limit state	**SLS**	**RLS**	**ULS**
Horizontal displacement /dam height (⊿/H)	0.02	0.05	0.1

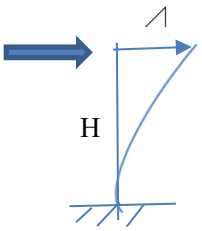

Fig.7 Horizontal displacement of steel open dam

2.8 Performance matrix

Therefore, the performance matrix for a Sabo dam against load levels 1 and 2 is expressed as two step design method as shown in **Table 4**.

Table 4 Performance matrix against debris flow

Scale of debris flow	SLS	RLS	ULS
Load level 1	◆	○	△
Load level 2		◆	○

The symbol in **Table 4** means the following Sabo dams.

△ is an emergency Sabo dam,

○ is a current usual Sabo dam,

◆ is an important Sabo dam constructed at the upper stream of an important protective facility.

Accordingly, the contents of **Table 4** can be explained as follows.

(a) In case of an emergency Sabo dam, the design aims at the Ultimate Limit State (ULS) against load level 1.
(b) In case of an existing usual Sabo dam, the design aims at the Repairable Limit State (RLS) against load level 1, and Ultimate Limit State (ULS) against load level 2.
(c) In case of an important Sabo dam, the design aims at the Serviceable Limit State (SLS) against load level 1 and Repairable Limit State (RLS) against load level 2.

2.9 Safty verification of Sabo dams against load level 2

The safety verification of a Sabo dam should be conducted against load level 2 as follows:

(1) Rock impact :

A Sabo dam against rock impact should be verified by internal safety based on an impact analysis.

(2) Debris flow fluid force:

A Sabo dam should be checked by both external stability and internal safety against debris flow fluid force.

(3) After damage:

A remaining dam after debris flow disaster should be confirmed by the external stability. Because, the dam may be damaged and may be required to be safe against deposited sediment pressure.

Therefore, the safety verification of a Sabo dam should be conducted as shown in **Table 5.**

Table 5 Safety verification of Sabo dam

Scale of debris flow	External stability	Internal safety
Load level 1 (return period of 100 years)	Stability check against fluid force Stability check against filled soil	Stress check against rock impact Stress check against fluid force Stress check against filled soil
Load level 2 (return period of 200 years)	Stability check against fluid force Stability check against filled soil after damage	Strain and deformation check against rock impact Strain check against fluid force Strain check against filled soil after damage

3. NUMERICAL EXAMPLE

First, the concrete and steel open dam shapes are determined by satisfying the stability conditions (i.e., overturn, sliding and bearing capacity) against the design debris flow load (load level 1). Second, the load level 2 is determined by either or combination of the methods mentioned in **2.5 (3),(5)**.

Finally, the safety verifications of concrete and steel open dams are confirmed by performing the impact FEM analysis against load level 2.

3.1 Dam and debris flow models

The dam and debris flow load models are assumed as shown in **Fig.8(a),(b**) and **Table 6,** respectively. The concrete dam has the height of H_c=10m, the slope of downstream of n=0.2, the thickness of spillway of B_w=3m, as shown in **Fig.8(a)**. The steel open dam has the height of H_s=8m, the width of B=5.2m, the footing concrete thickness of H_{sc}=2m, as shown in **Fig.8(b) [**Shima, J., et al.2017]**.**

3.2 Properties of Concrete

The properties of concrete are assumed as shown in **Table 7**.

Table 6 Properties of debris flow

Drainrange area	A=0.32 km^2
Bed slope	I=1/6
Peak discharge of debris flow	Q_{sp}=73.50 m^3/s
Width of stream	B_{da}=15.0 m
Water depth	D_d=1.12 m
Flow velocity	U = 4.37 m/s
Table 7 Properties of concrete	
Allowable bearing capacity (level 1)	Q_a = 1200 kN/m^2
Ultimate bearing capacity (level 2)	Q_a' = 3600 kN/m^2
Shearing strength	τ_c =600 kN/m^2
Design concrete strength	σ_{ck}= 18000 kN/m^2
Allowable concrete compressive strength	σ_{ca}= 4500 kN/m^2
Ultimate concrete compressive strength	σ_{ca}= 6750 kN/m^2
Allowable concrete tensile strength	σ_{ta}= -337.5 kN/m^2
Friction coefficient of dam base	f = 0.7

3.4 Computational results of stability analysis

(1) Results against load level 1

The computational results of stabilty analysis against load level 1 are shown in **Tables 8 and 9**. The shape of concrete dam was determined as the slope of upstream of m=0.3 and the width of base of B=8.00m. The shape of footing of steel open dam was determined as the width of B_s=8.40m.

(2) Results against load level 2

Computational results of load level 2 were found by increasing the flow volume until the extreme limit stability condions were satisfied as shown in **Tables 8 and 9.**

The maximum fluid forces were found as F=723.0kN/m in case of the concrete dam, as F=583.5kN/m in case of steel open dam.

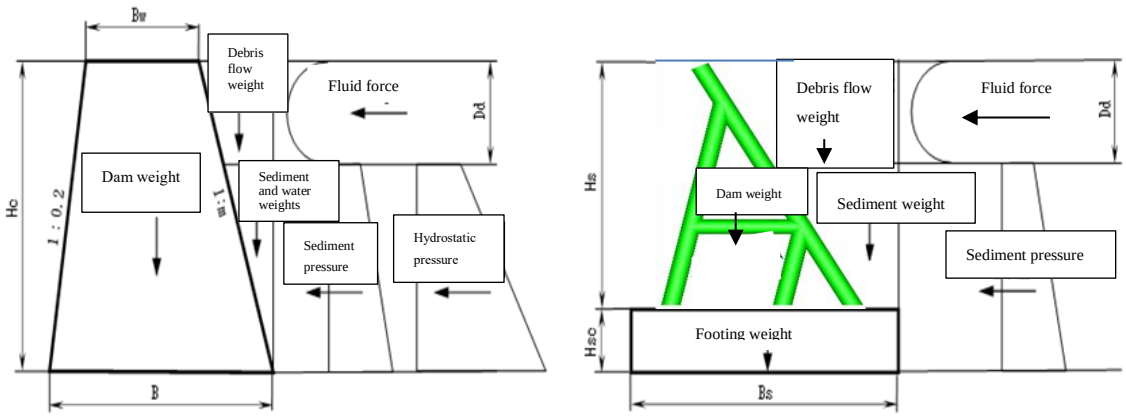

(a) Concrete dam model (b) Steel open dam model

Fig.8 Dam and debris flow models

Table 8 Results of stability analysis for concrete dam

	Load level 1	Load level 2
Sliding	8.09> 4.0	4.97>1.0
Over turn eccentric distance e (m)	$\|e\|$ =1.28< 1.33	F_r=1.07 ≥1.0
Ground bearing capacity (kN/m^2)	Q_1=374.24 < 1200 Q_2=7.64< 1200	Q_1=707.78 < 3600 ----------
Internal stress (kN/m^2)	σ_1= 374.24 <4500 σ_2= 7.64< 4500	σ_1= 707.78 <6750 σ_2= -335.02 > -337.5

Table 9 Results of stability analysis for steel open dam

	Load level 1	Load level 2
Sliding	21.52> 4.0	7.47>1.0
Over turn eccentric distance e (m)	$\|e\|$ =0.09 < 1.40	F_r=1.0 ≥1.0
Ground bearing capacity (kN/m^2)	Q_1=112.2 < 1200 Q_2=98.67 < 1200	Q_1=425.1 < 3600 ----------
Internal stress (kN/m^2)	σ_1= 112.2 <4500 σ_2= 98.67 < 4500	σ_1= 425.1 <6750 σ_2= -211.8 > -337.5

Table 10 Results of Load level 2 by stability analysis and Nagiso disaster

	Load level 1	Load level 2 for concrete dam	Load level 2 for steel open dam	Load level 2 by Nagiso disaster
Peak discharge of debris flow Q_{sp} (m^3/s)	73.50	754.0	638.0	730
Water depth D_d(m)	1.12	5.68	5.04	2.27
Flow velocity U (m/s)	4.37	8.86	8.45	8.28
Unit volume weight of debris flow γ_d (kN/m^3)	15.90	15.90	15.90	16.42
Fluid force F(kN/m)	34.7	723.0	583.5	260.8
Rock diameter D_{max}(m)	1.1		----------	3.0

(3) Determination of load level 2

In this study, F=583.50kN/m in case of steel open dam was assumed as the fluid force of load level 2, since this value was smaller than the one in case of concrete dam. Futhermore, the maximum rock diameter D_{max} =3.0m was found by the field suvey of Nagiso disaster,2014. Therefore, the fluid force F=583.5 kN/m, the flow velocity U=8.45m/s, and the rock diameter D_{max}=3.0 m were adopted as the load level 2.

3.5 Safety verification of concrete dam against load level 2

Fig.9(a) and (b) shows the fluid force and rock impact of load level 2 acting on the concrete dam with height of 10m, respecyively. The concrete dam base is assumed to be fixed in the ground.

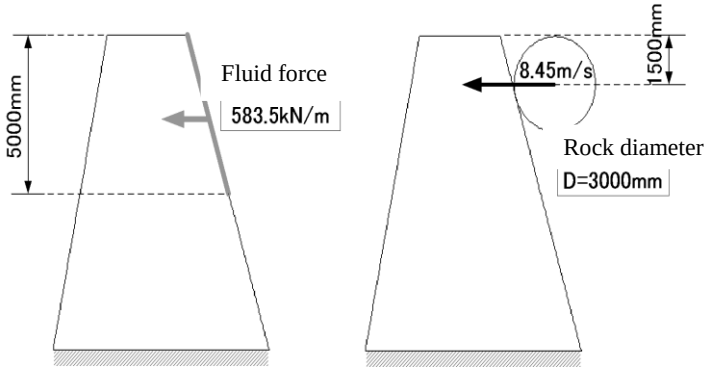

(a) Fluid force (b) Rock impact

Fig. 9 Concrete dam model and load level 2

Fig.10 illustrates the tensile failure at the base of concrete dam against fluid force of load level 2 which means the turnover of the dam. On the otherhand, **Fig.11** shows the shearing failure + tensile failure of concrete dam against rock impact which means the complete collapse of the concrete dam [Matsuzawa, et al.2017].

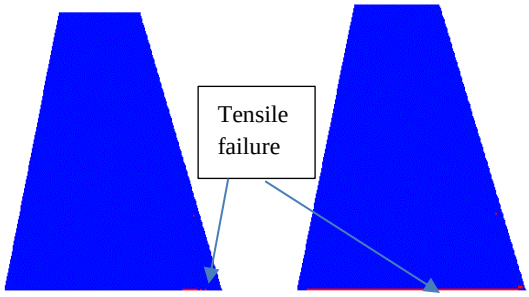

(a) Initiation of crack (b) Final failure

Fig. 10 Failure mode by fluid force of load level 2 acting on concrete dam

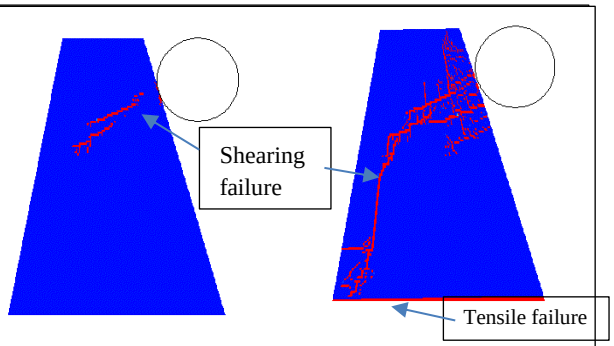

(a) Initiation of crack (b) Final failure

Fig. 11 Failure mode by rock impact of load level 2 acting on concrete dam

3.6 Safety verification of steel open dam against load level 2

3.6.1 Analytical model

Fig. 12 shows the bird's-eye view of the steel open dam which is composed of pipe components with diameters of 508mm and 318mm. **Fig.13** (a) and (b) illustrate the front and side of the steel open dam with the

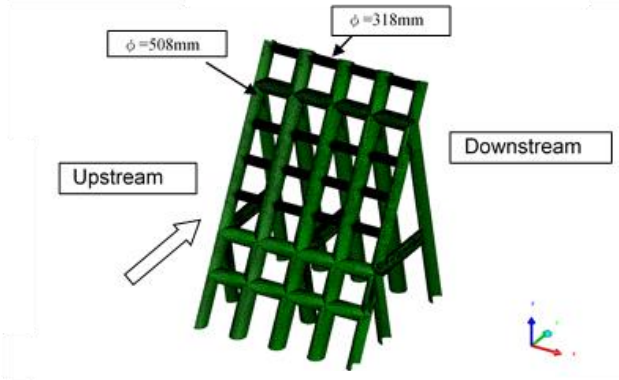

Fig. 12 Bird's-eye view of steel open dam

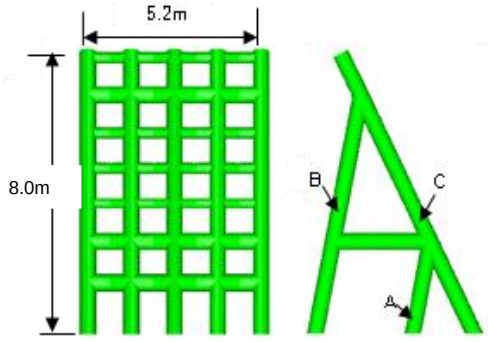

(a) front (b) side

Fig.13 Steel open dam analytical model

hieght of 8m and the width of 5.2m. The steel open dam is fixed into the base foundation and is verified by an impact FEM analysis against load level 2 (fluid force of F=583.5kN/m, flow velocity of U=8.45m/s and rock diameter of D_{max} =3.0m).

3.6.2 Load level 2 acting on steel open dam

Fig. 14 shows the steel open dam subjected to the fluid force (F=583.5 kN/m) of load level 2, which acts on the range from the top to the depth of 5.04m.

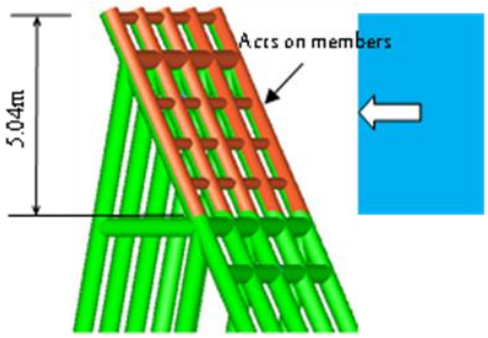

Fig.14 Fluid force for FEM analysis (3-D)

Fig. 15 illustrates the steel open dam subjected to the rock imapct with the diameter of D_{max} =3.0m and the velocity of U=8.45m/s which acts on the position of 1.5m from the top.

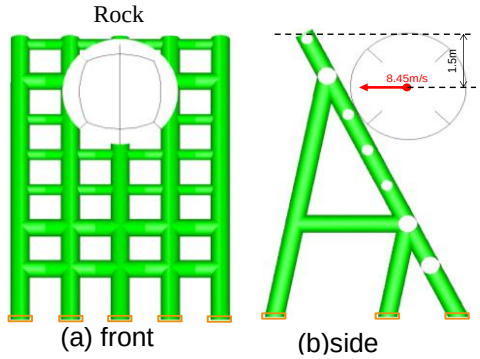

(a) Front (b) side

Fig.15 Rock impact for FEM analysis (3-D)

3.6.3 Computational results

(1) Horizontal dispalacement – time relations

Fig.16 shows the horizontal displacement at crown of dam – time relation against the fluid force. The maximum resuidual displacement was 55mm. This value was larger than the one of 20mm at the crown of dam and smaller than the one of 85mm at the imapct point by the rock impact as shown in **Fig. 17.**

(2) Impact load- time relation

Fig.18 shows the impact load – time relation, and the maximum average impact load was 5.2MN. It is found that the real impact load is vibrating during the contact period between rock and steel open dam. This vibration will dissipate the kinetic energy due to rock impact.

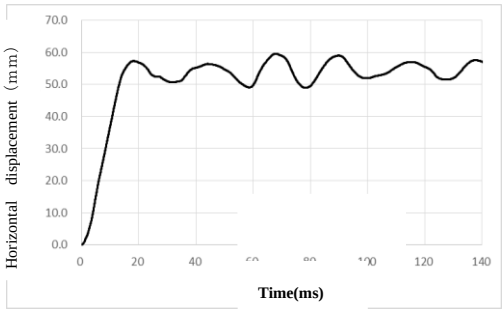

Fig.16 Horizontal displacement – time relation against fluid force

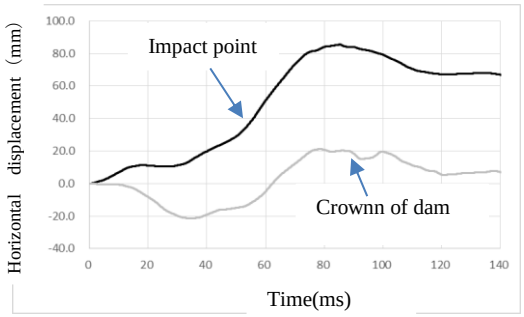

Fig. 17 Horizontal displacement – time relation against rock impact

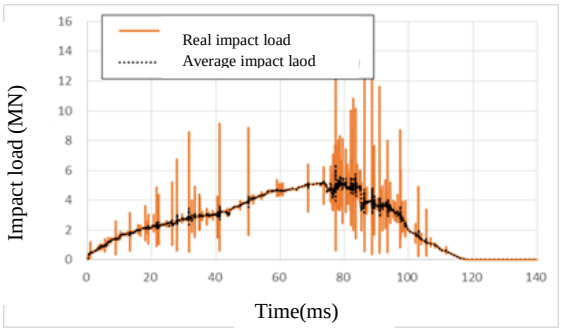

Fig.18 Impact load-time relation against rock impact

(3)Local deformation profile

Fig.19 illustrates the local deformation profile of pipe component at the impact point, and the residual local deformation / pipe diameter (δ/D) was found as 0.75 as shown in **Fig.20.** This value exceeds 0.7 of ULS in **Table 2**.

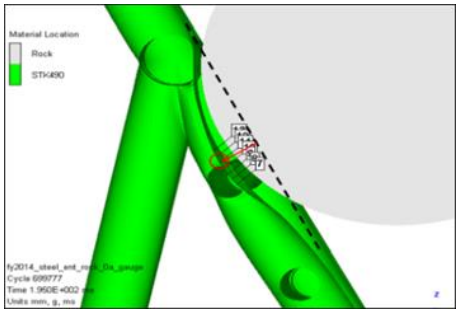

Fig. 19 Local deformation profile at imapct point against rock impact

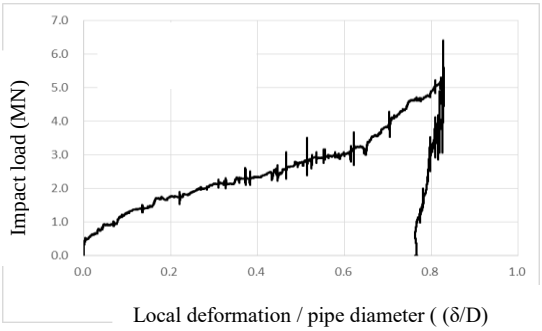

Fig.20 Impact load – local defromation/pipe diamter relation against rock impact

(4) Absorbed Energy

Fig.20 shows the impact load-(local deformation /pipe diameter) relation obtained and the area surrounded by the curves means the local absorbed energy.

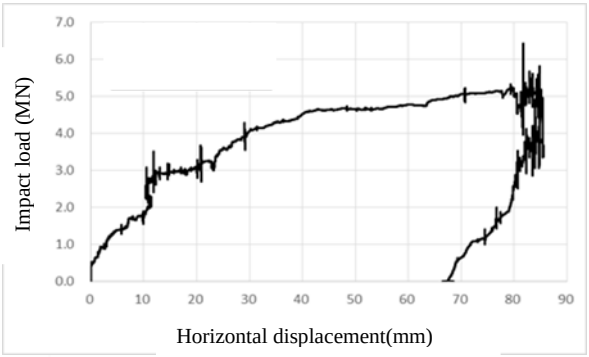

Fig.21 Impact load - horizontal displacement relation against rock impact

Fig.21 demonstrates the imapct load – horizontal dispacement relation at impact point, and the area surrounded by curves is defined as the global absorbed energy.

3.6.4 Safety verification of steel open dam

(1) Safety verification of global deformation

(a) Against fluid force**;**

$\Delta_{max}/H=55/8000=0.007<0.02$

It is less than serviceability limit, then it can be neglected.

(b) Against rock impact;

$\Delta_{max}/H=70/6500=0.01<0.02$

It is less than serviceability limit, then it can be neglected.

(2) Safety verification of local deformation

Against rock impact; $\delta_{max}/D=0.75>0.7$

It is larger than ultimate limit, then, the pipe component at impact point should be exchanged.

(3)Energy verification

(a) External energy

$$E_R=\frac{1}{2}mv^2=36.7tx(8.45m/sec)^2/2=1310kJ$$

(b)Internal energy

The local and global absorbed enegies are obtained by computing the areas surrounded by curves in **Figs.20** and **21,** respectively, as follows.

U_L= 1016kJ, U_G= 285kJ

Therefore, the total internal energy is 1301 kJ which corresponds to 99.3% of the external energy E=1310 kJ. The difference of 0.7% may be dissipated by the vibration during impact period. It was also found that about 78% of rock impact energy was absorbed by the local deformation of pipe component.

4. CONCLUSIONS

(1) The safety verification of dams against load level 2 was proposed from the viewpoint of performance-based design.

(2) The load level 2 was decided by the the extreme limit stability analysis and the past large scaled debris flow disaster.

(3) The concrete dam against load level 2 was over turned by the fluid force and completely collapsed by rock impact.

(4) The steel open dam against load level 2 was not so damaged by the debris flow fluid force. However, the pipe component at impact point was severely damaged by rock impact load, and it should be exchanged.

REFERENCES

Beppu,M., Matsuzawa,R., Shima,J., Ishikawa,N. and Mizuyama (2016): A Study on the Debris Flow Load Evaluation and Load Carrying Capacity of Sabo Dam by DEM-MPS Method, The 2016 Conference Proc. of Erosion Control Engineering, R5-24, B222-2023.

Chubu Regional Bureau, Ministry of Land, Infrastructure and Transport (2014) : Survey Report of Nashizawa Debris Flow, Nagiso, Nagano Prefecture, Japan, July (2014).

Horiguchi,T., Tsuji, Y., Katsuki, S., Shima,J., Ishikawa,N. and Mizuyama,T. (2016): A Study on the Estimation of Debris Flow Loads acting on Steel Open Dam, The 2016 Conference Proc. of Erosion Control Engineering, R5-14, B202-203.

Ishikawa,N., Shima,J.,Matsubara,T., Tatesawa,H., Horiguchi,T. and Mizuyama,T.(2014): Trapping Mechanism of Debris Flow by Steel Open Dams, INTERPRAEVENT2014, Natural Disaster Mitigation to Establish Society with the Resilience, Nara, Japan.

Japan Society of Civil Engineers (2017): Safety Evaluation for Civil Engineering Structures under Impact and Blast loadings -Preparing for Rare Events- Structural Engineering Series 27 (Edited by K. Fujikake).

Matsuzawa,R., Shima, J., Takeda, I., Ishikawa,N. and Mizuyama,T. (2017): Current Design Problems and Impact Analysis of Concrete Sabo Dam against Rock Impact, Journal of the Japan Society of Erosion Control Engineering, Vol.69,No.5, pp.59-65.

Shima,J.,Matsuzawa.R.,Takeda,I.,Yamaguchi,M.,Ishikawa,N., and Mizuyama,Y.(2017): Current design problems and impact analysis of steel open type Sabo dam under rock impact, Journal of the Japan Society of Erosion Control Engineering, Vol.70,No.1, pp.54-59.

Emergency Responses to Debris Flow Disaster at Serizawa District, Nikko City Triggered by the 2015 Torrential Rains in the Kanto and Tohoku Region

Kenji MIWA[1] and Kenji TAKETOSHI[1]

[1]Member, Nikko Sabo Office, Kanto Regional Development Bureau, Ministry of Land, Infrastructure, Transport and Tourism (2390 Hangakimen, Nikko City, Tochigi 3211414, Japan)
*Corresponding author. E-mail: taketoshi-k92en@mlit.go.jp

In September 2015, torrential rain hit the Kanto and Tohoku regions causing debris flow in seven mountain streams in the Serizawa District of Nikko City, Tochigi Prefecture, where the greatest rainfall was observed in recorded history. As a result seven houses were completely or partially destroyed and the municipal road was cut off by sediment runoff from the mountain streams. River bed aggradation and swelling of the main Serizawa River eroded river banks and partly washed away the municipal road. As a result, 25 inhabitants from 14 households were temporarily isolated in an upstream village. The Nikko Sabo Office of the Ministry of Land, Infrastructure, Transport and Tourism, immediately began to investigate the damage caused in the Serizawa District. Based on the results of the investigation we first made emergency repairs to the road followed by construction of temporary water channels to divert the water flow from the mountain streams. As the next step, we set up monitoring equipment and created a system to alert vehicles and people traveling on the road of the impending dangers. With these efforts we were able to ensure immediate safety until more permanent measures were constructed.

Key words: torrential rains, debris flow, emergency reactions, effects of erosion control facilities

1. INTRODUCTION

In September 2015, torrential rains hit the Kanto and Tohoku regions (hereinafter “the torrential rains”). After Typhoons No. 17 and 18, the resultant atmospheric depression brought record rainfall to the Kanto and Tohoku regions.

In the Kinugawa Basin, which connects with the Tone River, flood damage spread extensively throughout Ibaraki Prefecture, located downstream. Worse, floods and landslides killed and injured people and damaged numerous houses in an upstream area of Tochigi Prefecture resulting in a major disaster.

The following reports the debris flow disaster in the Serizawa District, Nikko City, Tochigi, and the emergency actions taken to counteract it.

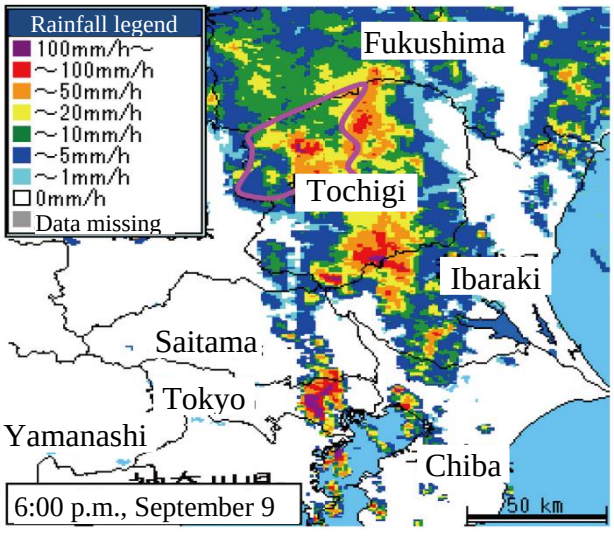

*The Nikko City area is highlighted with the pink line.

Fig. 1 Changes in radar rainfall (6:00 p.m., September 9)

2. OUTLINE OF THE DISASTER

2.1 Weather

From the 9th to the 11th in September 2015, southerly winds flowed into the atmospheric depression, which resulted from Typhoon No. 18. In addition, moist air persistently flowed in from the southeast winds around Typhoon No. 17. This led to numerous and continued occurrences of north-south linear rainfall zones from the Kanto to the Tohoku regions (**Fig. 1**), resulting in record rainfall.

Located upstream in the Kinugawa River Basin, Nikko City, Tochigi, suffered more from the torrential rains than most other parts of the country, with the total rainfall ranging between 500 and 600 millimeters or more. Three AMeDAS observation points in Nikko City confirmed the greatest daily rainfall in recorded history (**Fig. 2**) [*Japan*

Meteorological Agency, 2015].

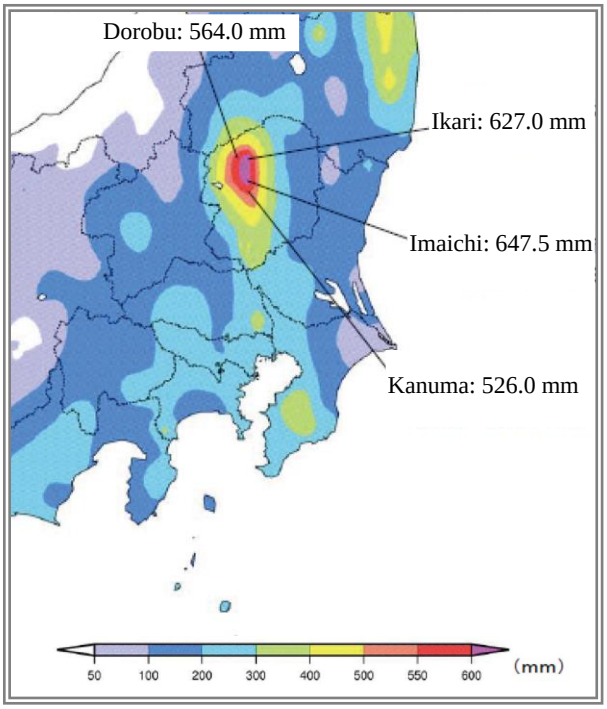

Fig. 2 Overall rainfall distribution (September 7 to 11, 2015) [*Japan Meteorological Agency*, 2015]

2.2 Damage

Tochigi Prefecture, located upstream from the basin, saw more than 500 cases of sediment-related damage mainly in Nikko City and Kanuma City, because these cities had an especially large rainfall. One person was killed and one person was injured in Kanuma City and two people were injured in Nikko City. Some inhabited houses were damaged. The network of roads, railroads and other means of transport were cut off. Some inhabitants were temporarily isolated. Many parts of Tochigi Prefecture were damaged by flooding and other events. The torrential rains caused an enormous amount of damage: three deaths, six injured persons, approximately one thousand houses completely or partially destroyed and approximately five thousand houses flooded in the entire prefecture [Cabinet Office, 2016; Secretariat Office of Tochigi Disaster Control Headquarters, 2015; Secretariat Office of Tochigi Disaster Control Headquarters, 2016].

3. DEBRIS FLOW DISASTER IN THE SERIZAWA DISTRICT, NIKKO CITY

3.1 Information about the Serizawa District

A debris flow disaster occurred in Serizawa District, an area located in Nikko City, which has villages and shares the northern border with

Fig. 3 Location of Serizawa District, the affected district

*This map is based on the 1:1,000,000 INTERNATIONAL MAP published by Geospatial Information Authority of Japan

Fukushima Prefecture (**Fig. 3**).

Seventy-one people from 33 households live in Serizawa District [*Uenaka*, 2016], including some younger people. However, aging and depopulation is progressing in this area.

3.2 Topography and geology of the Serizawa District

3.2.1 Topography

Serizawa District has a mountainous river with an average bed slope of 1/17 that flows down to its confluence where it joins the Ojika River, a main branch of the Kinugawa River. The river flows from its source, with a river basin area of 22.8 square kilometers and a channel length of 11.8 kilometers, sitting at an altitude higher than 1,500 meters, down to a midstream area of the Ojika River nearly 600 meters above sea level. Villages in the Serizawa District are distributed in a downstream valley.

The torrential rains brought debris disasters to seven mountain streams that flow into Serizawa District from behind the villages located along the downstream left bank. Six of these mountain streams are designated as the sediment disaster hazard area. The slopes of the beds in these mountain streams are steep, ranging between 1/6 and 1/3. Most of the mountain streams are small, with a watershed area smaller than 1 square kilometer.

3.2.2 Geology

In terms of geology, Paleogene granites are mainly distributed in the Serizawa District Basin. Slope failures and sediment runoff resultant from

weathering and other phenomena are recognizable and volcanic rocks such as Neogene rhyolite can be found in some areas.

3.3 Weather in Serizawa District

Fig. 4 shows the rainfall before and after the disaster, recorded at the MLIT Nakamiyori Precipitation Station located nearly one kilometer from the Serizawa District. The total amount of rainfall is 603 millimeters (4:00 p.m., September 6 to 10:00 p.m., September 10) with the maximum rainfall per hour of 57 millimeters (2:00 – 3:00 a.m., September 10), both were the highest in recorded history.

Heavy rainfall of over 50 millimeters continued for more than ten hours from the afternoon of September 9 until the early hours of September 10. The cumulative rainfall also rose sharply.

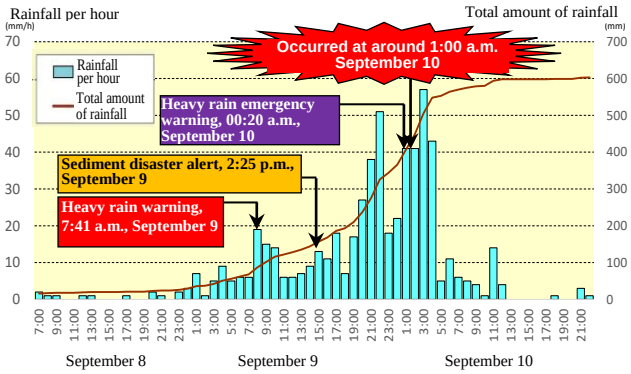

Fig. 4 Rainfall recorded at the MLIT Nakamiyori Precipitation Station (September 8 - 10, 2015)

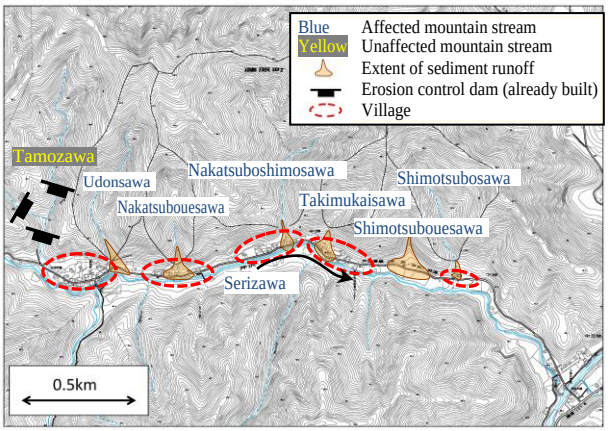

Fig. 5 Planimetric map of Serizawa District

3.4 Damage in the Serizawa District

Before dawn on September 10, debris flows from the seven mountain streams in Serizawa District affected the villages and the damage extended over six of the mountain streams: among the seven, only Tamozawa was unaffected (**Fig. 5**). In Shimotsubosawa, Takimukaisawa and Nakatsuboshimosawa, seven houses were completely or partially destroyed, or washed away (**Fig. 6**).

In Takimukaisawa, two people were injured and their houses were washed away. Debris flows completely or partially destroyed many houses. Luckily there were no deaths. Later we interviewed the inhabitants. “The house tilted after being hit by a debris flow. I was shocked and jumped out of the house.” “A fallen beam fell onto the bed board where it stopped, which created a space and saved me.” “I was covered in mud up to my waist. Somehow I managed to crawl out by following the directions of my neighbors. This is how I survived.” These are some of the stories from the inhabitants whose houses were completely destroyed. Considering these stories, it was clearly miraculous that there were no deaths.

(a)

(b)

Fig. 6 Damage in Takimukaisawa, Serizawa District
(a) Sediment and driftwood run off
(b) A damaged house (two people injured and three houses completely destroyed)

Sediment runoff from the mountain streams cut off traffic on the municipal road. River bed aggradation and swelling of the main river of Serizawa eroded river banks and partly washed away the municipal road (**Fig. 7**). Lifeline utilities installed along the municipal road, such as electric, telephone (land line and mobile), water and communication lines were also severed and 25 inhabitants in 14 households were temporarily isolated in an upstream village [*Uenaka*, 2016; *Nikko City, Tochigi prefecture*, 2016].

3.5 Sediment runoff

3.5.1 Sediment movement in the mountain streams

Traces of sediment production phenomena such as slope failures, longitudinal erosions, gully erosions and bank collapses were recognizable in the mountain streams. These phenomena occurred from torrential rains and the resultant swelling of the water. The swollen water may have combined with the sediment before turning into a debris flow (**Fig. 8**).

Fig. 7 Municipal road washed

Headwaters in Shimotsubouesawa

Fig. 8 Sediment production

Each of the seven mountain streams from which the debris flow occurred lacked gigantic stones and the accumulation of many substances such as fine grains and breccia with particle sizes ranging between 10 and 40 centimeters were identified. A large quantity of driftwood washed away and accumulated in all of the affected areas excluding Shimotsubosawa. Because there was no evidence of deep erosion like exposed bedrock, with the exception of the upper part, we inferred that sediment movement mainly took the form of sediment flow (**Fig. 9**) [*Sakurai*, 2015; *Kanto subgroup of the Japan Society of Civil Engineers/Japanese Geotechnical Society collaborative group for investigation of the 2015 Kanto and Tohoku torrential rain disaster*, 2016; *Sabo Department, National Institute for Land and Infrastructure Management and Erosion and Sediment Control Research Group, Public Works Research Institute*, 2015].

According to interviews with the inhabitants, the sediment runoff occurred in Takimukaisawa around 4:00 a.m. on September 10, in Nakatsuboshimosawa

Shimotsubosawa

Fig. 9 Sediment runoff

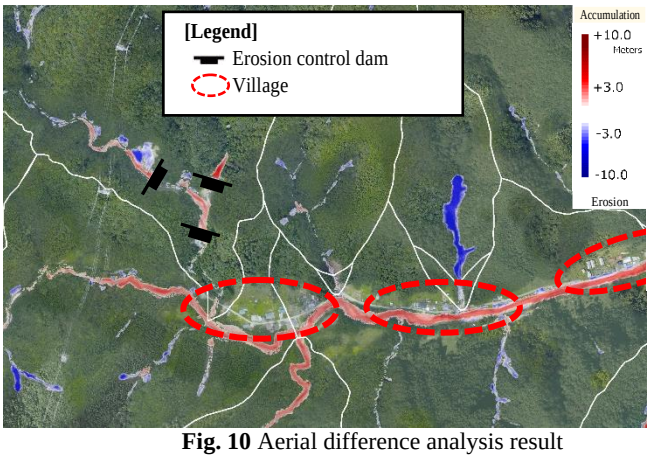

Fig. 10 Aerial difference analysis result

(a)

(b)

Fig. 11 Effect of an erosion control facility (Tamozawa Erosion Control Dam 1)
(a) Before catching the debris flow (August 18, 2015)
(b) After catching the debris flow (September 26, 2015)

around 5:20 a.m. and three times in Udonsawa, at 00:47 a.m., 2:17 a.m. and 3:20 a.m.

3.5.2 Extensive sediment movement

Fig. 10 shows the result of an analysis of the difference between the aerial laser survey measurements obtained in the Serizawa District Basin in 2012 and those obtained right after last year's disaster. The degree of damage is classified according to shades of colors, with accumulations indicated in red and erosions in blue. Upstream areas of the mountain streams, characterized by their steep slopes, underwent sediment runoff due to slope failures and bank erosions, while sediment accumulation is obvious in the downstream areas of the mountain streams, characterized by mild slopes, as well as the main river of Serizawa and the erosion control facilities. Sediment accumulation was remarkable in the main river of Serizawa, where the river bed rose locally three to four meters at its maximum.

Concerning the sediment balance, erosions and accumulations amounted to nearly 876 thousand cubic meters and 689 thousand cubic meters, respectively in the Serizawa District Basin overall (the sediment amount controlled by the eight existing erosion control dams was approximately 140 thousand cubic meters). We inferred that nearly 187 thousand cubic meters of sediment might have entered the Ojika River. Considering that the last survey measurements before the disaster were obtained in 2012, the amount of sediment movement described above may or may not be attributable to the torrential rains. But it may serve as reference data for understanding the tendency of sediment runoff because no significant flood had occurred during the period between 2012 and when the torrential rains came.

3.6 Effects of erosion control facilities

Debris flows also occurred in Tamozawa. Three erosion control dams are in operation (one impermeable dam under the control of Tochigi Prefecture and two steel-permeable dams under the control of the Ministry of Land, Infrastructure, Transport and Tourism). These dams caught and controlled sediment and driftwood and prevented the damage from extending to the village located below. The sediment caught by the steel-permeable erosion control dams was relatively small in size, but was blocked by things such as driftwood, rootstock and small particle gravel (**Fig. 11**).

3.7 Evacuation warning

3.7.1 Issuances of weather warnings, etc.

As shown in **Fig. 4**, Utsunomiya Local Meteorological Office issued a heavy rain warning (sediment disaster) for Nikko City at 7:41 a.m., on September 9. It issued a sediment disaster alert at 2:25 p.m. on the same day with Tochigi Prefecture. A heavy rain emergency warning was issued at 00:20 a.m., on September 10, throughout the entire Tochigi Prefecture.

3.7.2 Issuances of evacuation advisories, etc. in Serizawa District

Concerning the torrential rains, sediment disaster alert was issued for Nikko City at 2:25 p.m., on September 9. According to the real-time landslide risk map, the grid corresponding to Serizawa District showed no excessive risk above the standard for sediment disaster alert. For this reason, the local government of Nikko City (Disaster Control Department) did not issue an evacuation advisory or similar for Serizawa District.

When a heavy rain emergency warning was issued at 00:20 a.m., on September 10, a wide area of Nikko City was hit by torrential rain after midnight. Worse, Serizawa District was far from any shelter, which posed difficulty in securing the evacuees' safety. For these reasons, no evacuation advisory or similar was issued for Serizawa District.

After all, no evacuation advisory or similar had been issued for Serizawa District during the torrential rains. However, an evacuation order was issued at 9:00 a.m., on September 13, when a secondary disaster was feared to occur in the next rain.

Fig. 12 On-site survey

Fig. 13 Aerial view of Serizawa District

4. EMERGENCY REACTIONS TO THE DISASTER

4.1 Survey on damage

4.1.1 Learning the status of damage

Around 8:00 a.m., on September 10, soon after the disaster, a contractor that was then-involved in construction work in Serizawa District reported the occurrence of disaster there. Nikko Sabo Office immediately entered into emergency readiness mode and started gathering information about the status of damage in its jurisdiction including Serizawa District.

Staff was divided into teams and sent via many different routes. However, they found it very difficult to arrive to the affected site because the transportation network had been cut off at many places in Nikko City. One of the staff members took a detour via Nasushiobara City and entered Serizawa District in the evening of September 10, and successfully gathered information about the status of damage on the day of the disaster.

4.1.2 On-site survey

Four construction consultants were urgently mobilized in accordance with the Staff and Disaster Agreement. In the early morning of September 11, they entered the Serizawa District and started a detailed on-site survey of the mountain streams in an effort to stay updated on the status of sediment runoff and damage (**Fig. 12**).

4.1.3 Using a helicopter for the survey

From September 11 to 13, Aozora, a disaster-control helicopter from the MLIT Kanto Regional Development Bureau, was used to extensively survey the damage from above the jurisdiction including Serizawa District, focusing on the upstream areas of the mountain streams where ground-based surveys would be difficult to carry out (**Fig. 13**).

(a)

(b)

(c)

Fig. 14 Removing obstacles from the road
(a) Removing sediment and driftwood
(b) Damaged areas are temporarily repaired with large sandbags
(c) Road temporarily restored

(a)

(b)

Fig. 15 Emergency construction
(a) Right after the disaster
(b) A temporary diversion channel is constructed with large sandbags

4.1.4 Aerial survey

On September 12 and after, four aerial survey companies received an urgent request for aerial photography and aerial laser surveys, in an effort to keep updated on the post-disaster topography and to analyze the differences from the results obtained in previous years. The aerial photographs and the results of the differential analysis helped extensively to quickly learn the status of damage in a way that would have been impossible with ground-based surveys or short-time aerial surveys with a helicopter. Laser survey measurements were very helpful in these emergencies during which swift actions would be required, since they quickly provided the necessary topographical data for such purposes as the construction of facilities.

4.2 Removing obstacles from the road

As the construction of an erosion control dam was underway in the Udonsawa stream of Serizawa District, efforts to remove debris from the municipal road and to temporarily restore the area that had been washed by the flooding started on September 11, with the purpose of solving the isolation problem and securing evacuation routes. The road was opened before September 20 (**Fig. 14**).

4.3 Emergency construction

Unstable sediment continued to accumulate and the collapses kept expanding in the affected mountain streams. This led to the concern that another disaster would result from even a regular amount of rainfall unless construction of the anti-disaster facilities was completed. For the purpose of ensuring a minimum level of safety required in the inhabited houses around the mountain streams and the temporarily-restored municipal road, four constructors were urgently mobilized in accordance with the anti-disaster agreement and the construction of a temporary diversion channel using large sandbags commenced on September 14. The construction was largely completed by September 24 (**Fig. 15**).

4.4 Monitoring equipment

As a means for monitoring the affected site, small devices for the transmission of satellite images (Ku-SAT II; under the control of the Ministry of Land, Infrastructure, Transport and Tourism) were installed in Takimukaisawa and Nakatsuboshimosawa, where inhabited houses had been damaged. On September 26, the devices started transmitting video footage to related organizations such as the municipal office of Nikko City and the Prefectural Office of Tochigi.

For the purpose of helping Serizawa District to establish an effective evacuation warning system, debris flow sensors and alarms were placed in the six affected mountain streams by October 7. In addition, webcams were installed in the three mountain streams neighboring inhabited houses, in order to facilitate the monitoring of the mountain streams and to stay updated on the flow of the main river of Serizawa. The webcams proved to be extremely effective as they could transmit footage using the mobile telephone network and cloud service, thereby eliminating the need for the construction of communication cables or similar. Furthermore, webcams can be quickly installed at a reasonable cost and make it possible to view the images from anywhere in real-time.

(a)

(b)

Fig. 16 Activities of sediment disaster specialists and the Technical Emergency Control Force
(a) Technical guidance at the site
(b) Urgent inspection of a hazardous area

4.5 Activities of sediment disaster specialists and Technical Emergency Control Force

For technical guidance and advice on anti-disaster actions, the Ministry of Land, Infrastructure, Transport and Tourism sent three “sediment disaster specialists” from the National Institute for Land and Infrastructure Management and the Public Works Research Institute to the affected area on September 15.

On September 14, twenty staff members from the MLIT Kanto Regional Development Bureau were sent to Serizawa District as the Technical Emergency Control Force (TEC-FORCE), with the aim to urgently perform an inspection of sediment disaster hazards, including the mountain streams that could be affected by debris flow and steep slopes with the potential to collapse (**Fig. 16**).

Fig. 17 Mayor of Nikko City receives a report and advice

On September 17, the sediment disaster specialists gave the mayor of Nikko City a report on the status of the damage and advice on the readiness for an evacuation warning. The Head of the Technical Emergency Control Force also reported their inspection results (**Fig. 17**) [*Sabo Department, Water and Disaster Management Bureau, Ministry of Land, Infrastructure, Transport and Tourism*, 2015].

5. FUTURE ACTIONS

5.1 Construction of permanent anti-disaster facilities

Preventing the recurrence of the disasters urgently required permanent anti-disaster facilities to be constructed. Immediately after the torrential rain disaster, efforts were started to file an application for the permission for an urgent erosion control project. On October 26, a project for constructing erosion control dams for the four mountain streams (Shimotsubosawa, Takimukaisawa, Nakatsuboshimosawa and Nakatsubouesawa) was adopted.

It was decided that the construction of erosion control dams for Shimotsubouesawa and the groundsills for the damaged parts of the municipal road along the main river of Serizawa would be included in the regular erosion control project for fiscal 2016. In addition to the abovementioned four mountain streams, facilities were designed and sites underwent construction during the short period of time between late fall and winter. Construction successively commenced in and after March 2016 when the snow began to melt.

Construction was underway for Udonsawa, but was temporarily stopped, because, after the damage, the sediment treatment plan needed to be reviewed. The design of the erosion control dam was quickly corrected and construction resumed in March 2016.

5.2 Reviewing the evacuation warning system

Completing the construction of permanent anti-disaster facilities for preventing the recurrence of disasters takes at least one year, even if urgent construction works like those described above are undertaken. Until the completion of the construction of the facilities, the risk of sediment disaster remains higher than before the disaster. Because of this, the municipal government of Nikko City temporarily lowered the standard for the issuance of evacuation information for Serizawa District based on the advice from sediment disaster specialists.

Furthermore, Nikko City provided rules for local people's evacuation activities and reviewed the system of an evacuation warning with the aim of encouraging quick evacuations (**Fig. 18**) [*Uenaka*, 2016; *Sabo Department, National Institute for Land and Infrastructure Management and Erosion and Sediment Control Research Group, Public Works Research Institute*, 2015].

To support the effort, the Utsunomiya Local Meteorological Office is providing restoration personnel and affected people with daily weather forecasts for the Serizawa District and if heavy rain beyond a certain level is expected, rainfall estimates for the affected areas will be sent to those concerned by e-mail.

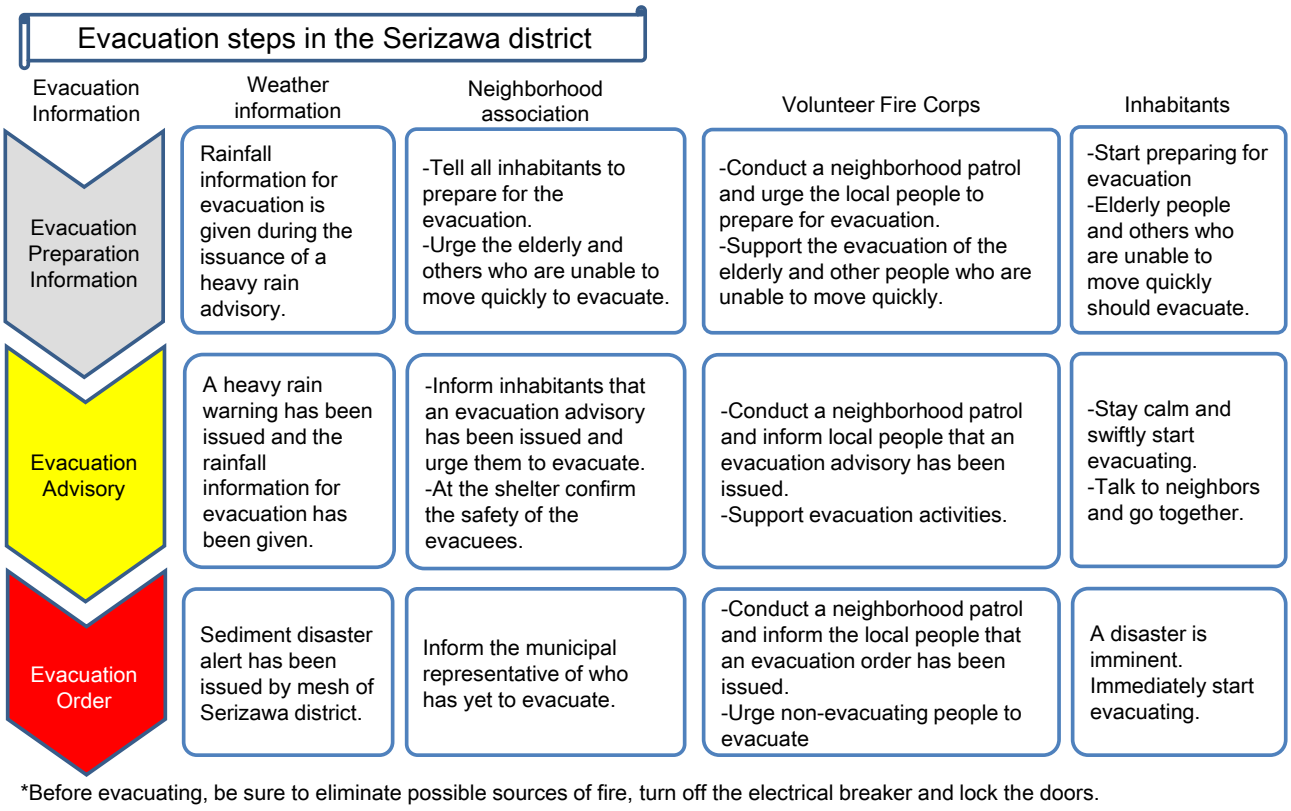

Fig. 18 Post-disaster evacuation warning system in the Serizawa district [Uenaka, 2016]

ACKNOWLEDGMENT: The urgent actions in the Serizawa District had a great deal of effort from constructors, construction consultants and survey companies as well as generous support and cooperation from other related organizations. I would like to take this opportunity to express my heartfelt gratitude to all of these organizations and people.

REFERENCES

Cabinet Office (2016): Status of damage from the September 2015 Kanto and Tohoku torrential rains, as of 12:00 p.m., February 19, 2016, reference: July 5, 2016.

Ibaraki Disaster Control Headquarters (2015): Damage in the prefecture from the September 2015 Kanto and Tohoku torrential rains and countermeasures, as of 4:00 p.m., October 30, 2015, reference: July 5, 2016.

Japan Meteorological Agency (2015): Weather report on the September 2015 Kanto and Tohoku torrential rains and heavy rains resulting from Typhoon No. 18 in 2015, reference: July 5, 2016.

Kanto subgroup of the Japan Society of Civil Engineers/ Japanese Geotechnical Society collaborative group for investigation of the 2015 Kanto and Tohoku torrential rain disaster (2016): Report of investigation of damage to Kanto region from the September 2015 Kanto and Tohoku torrential rains, p.158-161, reference: July 5, 2016.

Nikko City, Tochigi prefecture (2016): Report of damage from the September 2015 Kanto and Tohoku torrential rains, as of 15:00, March 31, 2016, reference: July 5, 2016.

Sabo Department, National Institute for Land and Infrastructure Management and Erosion and Sediment Control Research Group, Public Works Research Institute (2015): Report of investigation of disaster in the Serizawa District of Nikko City, Tochigi prefecture, reference: October 13, 2015.

Sabo Department, Water and Disaster Management Bureau, Ministry of Land, Infrastructure, Transport and Tourism (2015): Document on the status of damage from and reactions to simultaneous debris flow disasters in Serizawa District, Nikko City, Tochigi (as of October 7, 2015), reference: February 17, 2016.

Sakurai, M (2015): Slope disasters from the September 2015 Kanto and Tohoku torrential rains (preliminary report), preliminary report session of the Kanto subgroup of the Japan Society of Civil Engineers/Japanese Geotechnical Society collaborative group for investigation of the 2015 Kanto and Tohoku torrential rain disaster, reference: January 5, 2016.

Secretariat Office of Tochigi Disaster Control Headquarters (2015): Damage from the September 2015 Kanto and Tohoku torrential rains (25th report), as of 13:00, November 19, 2015, reference: March 28, 2016.

Secretariat Office of Tochigi Disaster Control Headquarters (2016): Damage from the September 2015 Kanto and Tohoku torrential rains, as of March 24, 2016, reference: July 5, 2016.

Uenaka, T (2016): Efforts to facilitate evacuation on warning in the Serizawa District of Nikko City, Sabo-to-chisui, Vol. 49 No. 1, p. 23-27.

Grain Size Distribution of the 1926 Volcanic Mudflow at Mt. Tokachi, Japan

Tomoyuki NANRI[1*], Takashi YAMADA[2], Mio KASAI[2], Tomomi MARUTANI[2], Shigenori TAKASHIMA[1] and Takayuki YAMAHIRO[1]

[1] Department of Construction, Hokkaido Prefecture Government
(Kita 3 jo Nishi 6 chome, Chuo-ku, Sapporo, Hokkaido 0608588, Japan)
[2] Research Faculty of Agriculture, Hokkaido University
(Kita 9 jo Nishi 9 chome, Kita-ku, Sapporo, Hokkaido 0608589, Japan)
*Corresponding author. E-mail: nanri.tomoyuki@pref.hokkaido.lg.jp

In May 1926, a volcanic mudflow triggered by the eruption of Mt. Tokachi, referred to as "the 1926 mudflow," ran through the Furano and Biei rivers in Hokkaido, Japan, killing 144 residents. This study analyzed the grain size distribution of this mudflow to determine the reason why it sustained such a large force across a gentle plain. The mudflow deposits were sampled and analyzed along the Furano River. To compare the results with those of previous studies, the grain size distribution of deposits were identified in eight different sections. Then the distribution was categorized into three groups: very fine (<0.1 mm in diameter), fine (0.1–2 mm in diameter), and coarse (≥2 mm in diameter). In each section, the proportion of grains in each group were multiplied by the net volume of the mudflow deposition provided by *Nanri et al*. [2009] to estimate the volume of each grain group. At the downstream end of the source and scouring zones, the very fine group comprised 54% of the transported sediment. This increased to 61% at the end of the transport zone, and reached 85% at the downstream end of the deposition zone. Hence, the 1926 mudflow contained a large amount of very fine materials and the resulting high gap density of the fluid in the mudflow enabled it to extend for more than 20 km from its point of origin across a gentle plain. The large fluid dynamic force resulted in extensive damage to buildings on the plain.

Key words: the 1926 mudflow, mudflow contents, mudflow volume, deposition sampling, mudflow behavior

1. INTRODUCTION

Following the eruption of Mt. Tokachi on May 24, 1926, a volcanic mudflow occurred. Referred to as "the 1926 mudflow," the event is considered the worst volcanic disaster in Japan in the 20th century. It ran through the Furano and Biei rivers in Hokkaido, Japan (**Fig. 1**), killing 144 residents [*Tokachidake Explosion Afflicted Relief Committee*, 1929; *Ishikawa et al*., 1971]. Immediately after the event, the details of the eruption, inundation area, injuries and fatalities among residents, and damage caused to buildings were documented by various researchers and organizations [*Tada and Tuya*, 1927; *Tanakadate*, 1926; *Tokachidake Explosion Afflicted Relief Committee*, 1929]. *Tada and Tuya* [1927] reported that deep snow layers melted by a hot debris avalanche from the crater contributed to the massive volume of the mudflow, which was estimated to be approximately 2.0 million m^3. The mudflow that ran through the Furano River was estimated to have a volume of 0.45 million m^3 (**Table 1**) [*Nanri et al*., 2009]. Later *Ikari* [1940] reexamined the event and revised the inundation area, depth of sediment deposit, and material sizes along the course of the mudflow. More recently, *Nanri et al*. [2016] estimated that the fluid dynamic force of the mudflow reached more than 10^2 KN/m, even on a gentle plain where the gradient was just 1:100, leading to the complete destruction of buildings in the path of the mudflow. The strong force was attributed to the fine grain sizes that comprised the extremely heavy flow, the density of which was estimated to be 1.6 to 1.7×10^3 kg/m^3 [*Nanri et al*., 2004]. Such a heavy and destructive mudflow is not unusual for an event initiated by a volcanic eruption. For example, the mudflow produced by the eruption and subsequent debris avalanche at Mount St. Helens, USA, in 1981 was equivalent to the 1926 mudflow, with a density of 1.7×10^3 kg/m^3 [*Takahashi*, 1981]. The flow was

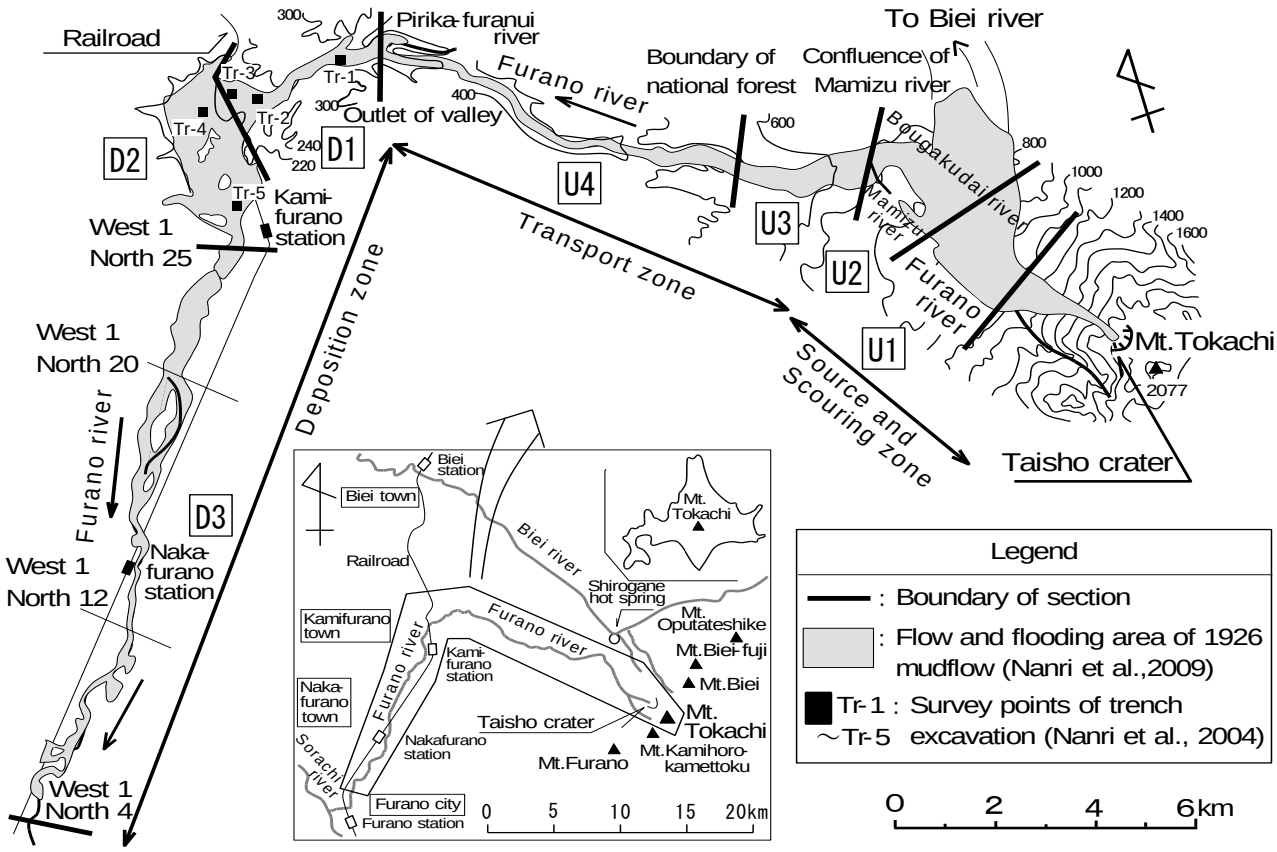

Fig. 1 Location of the study areas and the area affected by the 1926 mudflow

reported to resemble a cement paste in the Toutle River, 64 km from its point of origin, and also caused major damage to properties in the area. Previous studies have indicated that the materials within mudflows become finer with distance. To examine spatial changes in grain size distribution of the mudflow downstream, we sampled and analyzed the mudflow deposits that still remain along the Furano River.

2. METHODS

2.1 Study area

The 1926 mudflow was initiated from the Taisho Crater on Mt. Tokachi when it erupted (**Fig. 1**). It traveled down to the confluence of the Mamizu River, scoring the adjacent ground (source and scouring zone: U1 and U2 sections in **Fig. 1**). The average channel slope of each section was greater than 1:12. *Nanri et al*. [2009] estimated that in these zones, 3.35 million m^3 of sediment was produced and 0.45 million m^3 was deposited in total (**Table 1**). Then the flow ran along a gorge to the junction of the Furano and Pirika-furanui rivers at the outlet of the valley (transport zone: U3 and U4 sections in **Fig. 1**), where it eroded a volume of 0.65 million m^3 and deposited 0.5 million m^3 of sediment [*Nanri et al*., 2009]. The channel bed gradients in this section ranged from 1:20 to 1:50. After passing through the gorge, the flow deposited approximately 1.55 million m^3 of sediment (deposition zone: D1, D2, and D3 sections in **Fig. 1**), while a volume of 1.5 million m^3 traveled further downstream [*Nanri et al*., 2009]. The channel slope was 1:50–1:120 for D1, 1:130–1:460 for D2, and 1:300–1:500 for D3. The mudflow spread across a plain in D2 and then converged in the downstream part of the section (**Fig. 1**), where it partially destroyed the Kamifurano Bridge [*Nanri et al*., 1995]. The volume of erosion and deposition per distance of each section is presented in **Fig. 2**. In this study, the components of the mudflow passing the downstream end of U4 (outlet of the valley) were assumed to be similar to the eroded materials in the U1 to U4 sections.

Nanri et al. [2004] examined the stratigraphy of the 1926 mudflow deposits in the D1 and D2 sections. They found that the deposition presented only a single layer in D1, while two layers were identified in D2. The upper layer was distinctly finer than the lower layer. An equilibrium experiment on

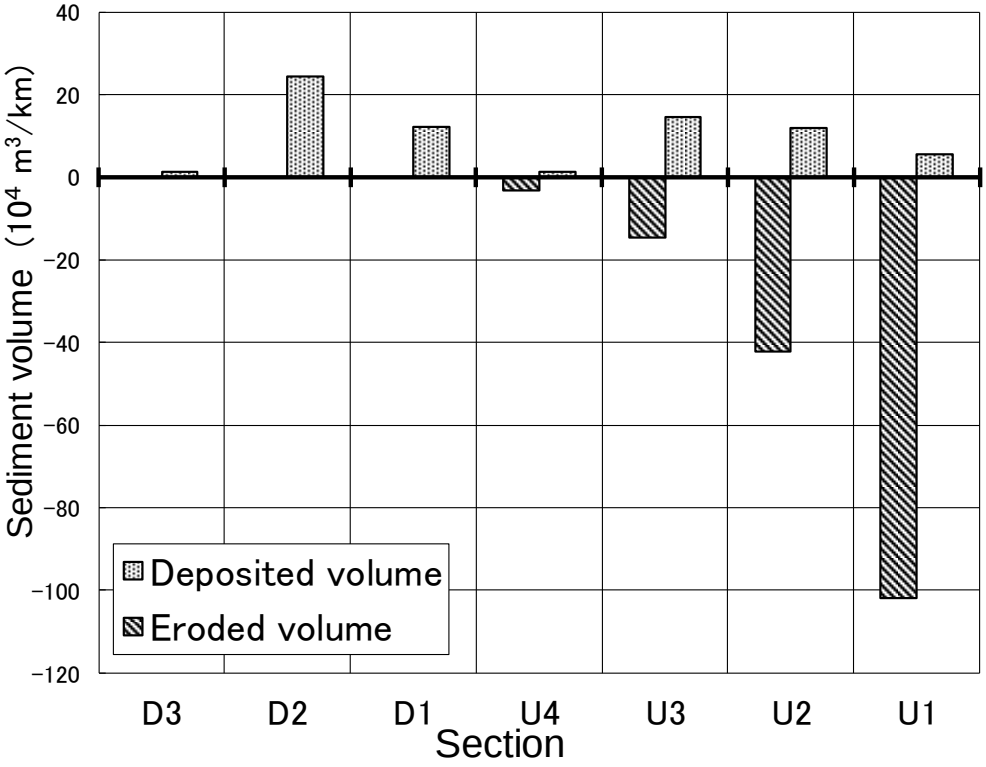

Fig. 2 Longitudinal changes in deposited and eroded sediment volume per unit stream length following the 1926 mudflow
※The data used in this diagram were obtained from *Nanri et al*. [2009].

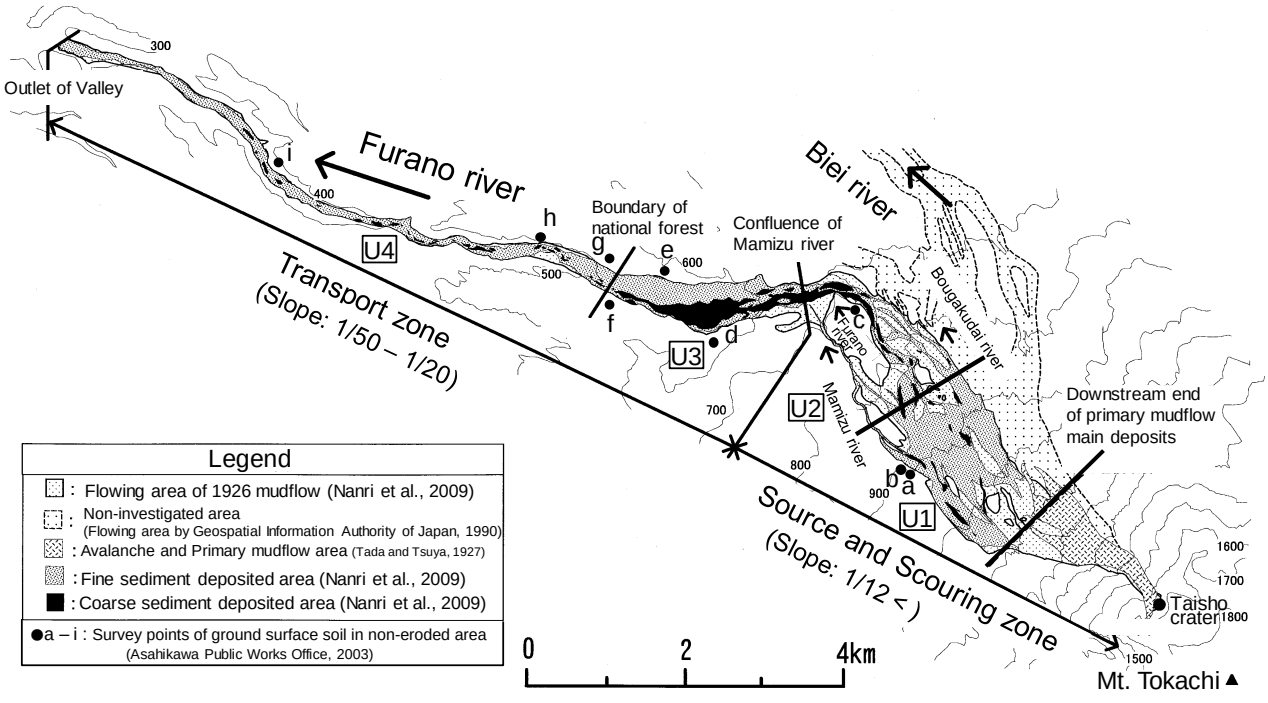

Fig. 3 Distribution of sediment remnants and survey points of ground surface soil in the non-eroded area
※This figure was revised from *Nanri et al*. [2009].

the separation of the fluid and solid phase was conducted by *Nanri et al*. [2009]. From these results, two possible interpretations for the phenomena were proposed: successive flow was finer than the first flow that arrived in the section, or the mudflow itself had two layers.

2.2 Methods

The materials of the 1926 mudflow deposits were collected from the U1, U2, U3, and U4 sections by

Table 1 Volume of each grain size group of sediment deposited, eroded, and transported by the 1926 mudflow

($10^4 m^3$)

Zone	Location / Section	※1 Deposited volume	Grain size			※1 Eroded volume	Grain size			※1 Transported volume	Grain size		
			Very fine	Fine	Coarse		Very fine	Fine	Coarse		Very fine	Fine	Coarse
Source and Scouring zone	Crater					※2 45	21	11	13				
	EL 1,100m									45	21	11	13
	U1	9	2	3	4	163	81	39	43				
	Prefectural road									199	100	47	52
	U2	36	6	7	23	127	63	30	34				
Transport zone	Confluence of Mamizu river									290	157	70	63
	U3	38	1	1	36	38	19	9	10				
	Boundary of national forest									290	175	78	37
	U4	12	3	3	6	27	13	6	8				
Deposition zone	Outlet of valley									**305**	185	81	39
	D1	37	7	9	21								
	Railroad									268	178	72	18
	D2	100	46	36	18								
	North 25 road									168	132	36	0
	D3	18	4	14	0								
	North 4 road									150	128	22	0
Downstream of Deposition zone	Outflow volume from Deposition zone	150	128	22	0								
Total volume		400	197	95	108	400	197	95	108				

※1 : Nanri et al. (2009)
※2 : The volume of debris avalanche around 1926 crator (Taisho crator)

the *Hokkaido Asahikawa Public Works Office* [2002, 2003], from the D1 and D2 sections by *Nanri et al*. [2004], and from the D3 section by *Ikari* [1940]. Samples were obtained by *Hokkaido Asahikawa Public Works Office* [2002, 2003] from five sites in U1, five in U2, three in U3, and six in U4. A grid line method was applied to sample surface materials, while subsurface materials were sieved. For other sections, the sampled materials were sieved and sedimentation analyses were applied to collect fine materials. *Nanri et al*. [2004] excavated five trenches, Tr1–Tr5 (**Fig. 1**), with depths of approximately 2 m. The samples in D2 (Tr4 and Tr5) were obtained from each layer. In addition, surface soil was collected from the ground at all nine sites at locations close to the mudflow course (non-eroded area) (**Fig. 3**). These samples were used to determine any differences between the original soils and mudflow deposits. They were subjected to the same analyses as those conducted by *Nanri et al*. [2004].

The material composition obtained from the sampling sites was averaged for each section. The sampled components were classified into three groups: coarse (≥2 mm in diameter), fine (from 0.1 to 2 mm in diameter), and very fine (<0.1 mm in diameter). After the proportion of each group at each site was obtained, it was multiplied by the deposition and erosion volumes of the mudflow following *Nanri et al*. [2009] (**Table 1**).

3. GRAIN SIZE DISTRIBUTION

The grain size distribution is presented in **Fig. 4**. Coarse materials accounted for 95% of the deposits, with the D_{60} and D_{95} being 200 and 1,000 mm, respectively, in U3. *Nanri et al*. [2009] reported that deposits of similar components were widely spread out over this section (**Fig. 3**). On the other hand, deposits in U1, U2, and U4 were much finer, with 35–60% of them being in the fine and very fine groups.

In the deposition zone, D1 consisted of mainly coarse deposits (55%) (**Fig. 4**). On the other hand, less than 20% of the sampled materials in D2 and D3 were in the coarse group, while materials from the very fine group accounted for 45% and 20% of the materials in D2 and D3, respectively. It was estimated that 85% of the mudflow consisted of very fine materials when it traveled downstream of D3 (**Fig. 4**).

The results shown in **Table 1** indicate that deposited sediment was distributed mainly throughout the deposition zone and downstream of the deposition zone. All eroded sediment was supplied from the transport zone and the source and scouring zone. It was estimated that at the outlet of the valley the volume of the mudflow reached 3.05 million m^3, with 61% of all materials being from the very fine group (**Table 1**). The material composition of the original ground soil was compared to the

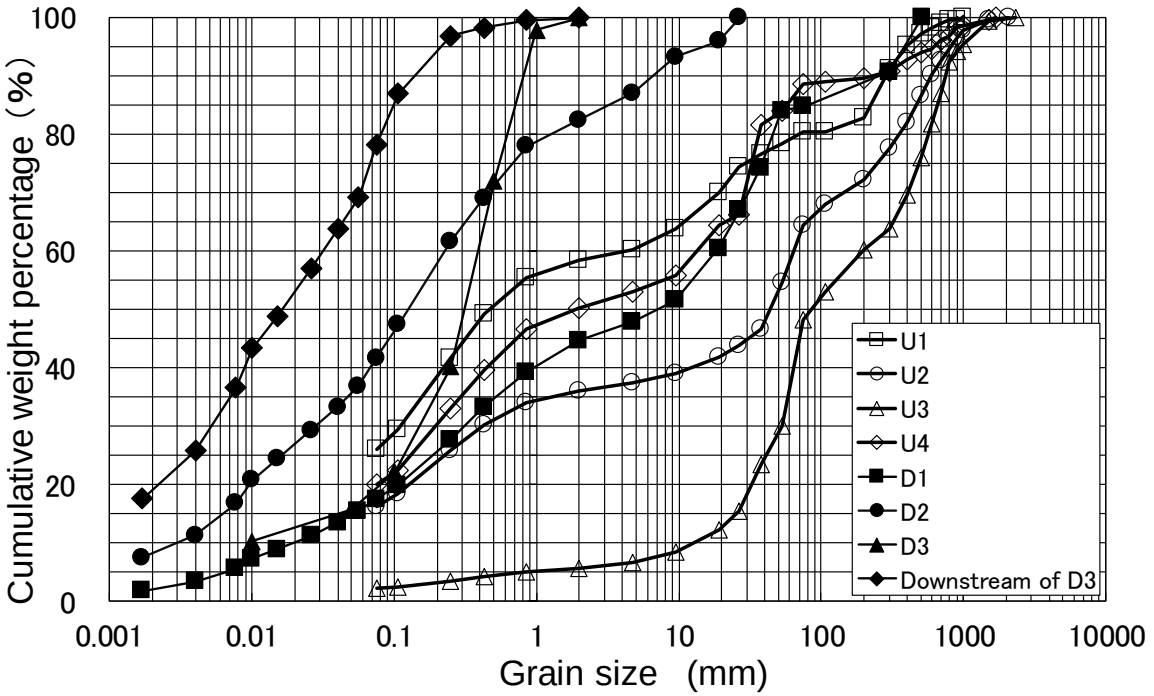

Fig. 4 Grain size distribution of 1926 mudflow deposits
※The data for the U1, U2, U3, and U4 sections, and the D1, D2, and D3 sections, and downstream of D3 sections were obtained from the *Hokkaido Asahikawa Public Works Office* [2002, 2003], *Nanri et al*. [2004], and *Ikari* [1940].

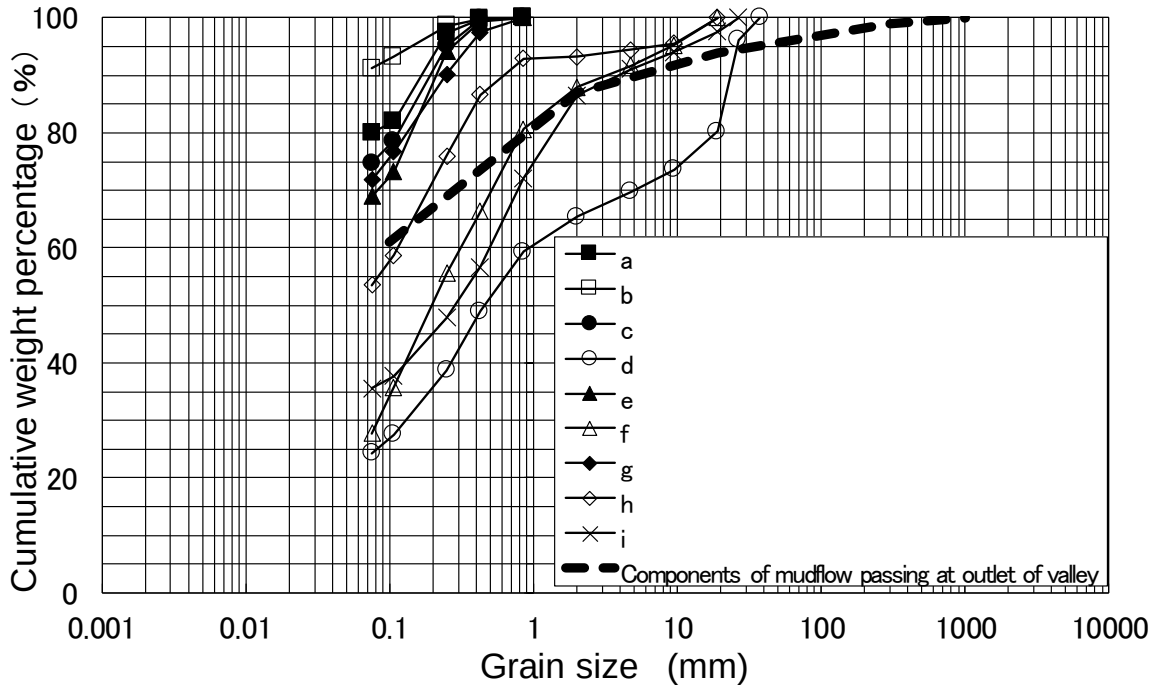

Fig. 5 Comparison of the grain size distribution in sediments from the 1926 mudflow at the outlet of the valley and ground surface soil in a non-eroded upstream area
※The data for a–i were obtained from *the Hokkaido Asahikawa Public Works Office* [2003].

deposited sediment (**Fig. 5**). The 'f' and 'i' samples in the transport zone were similar to the coarse group materials.

As shown in **Fig. 6**, at the downstream end of the source and scouring zone, very fine materials accounted for 54% of the transported sediment. This increased to 61% at the end of the transport zone and reached 85% at the downstream end of the deposition

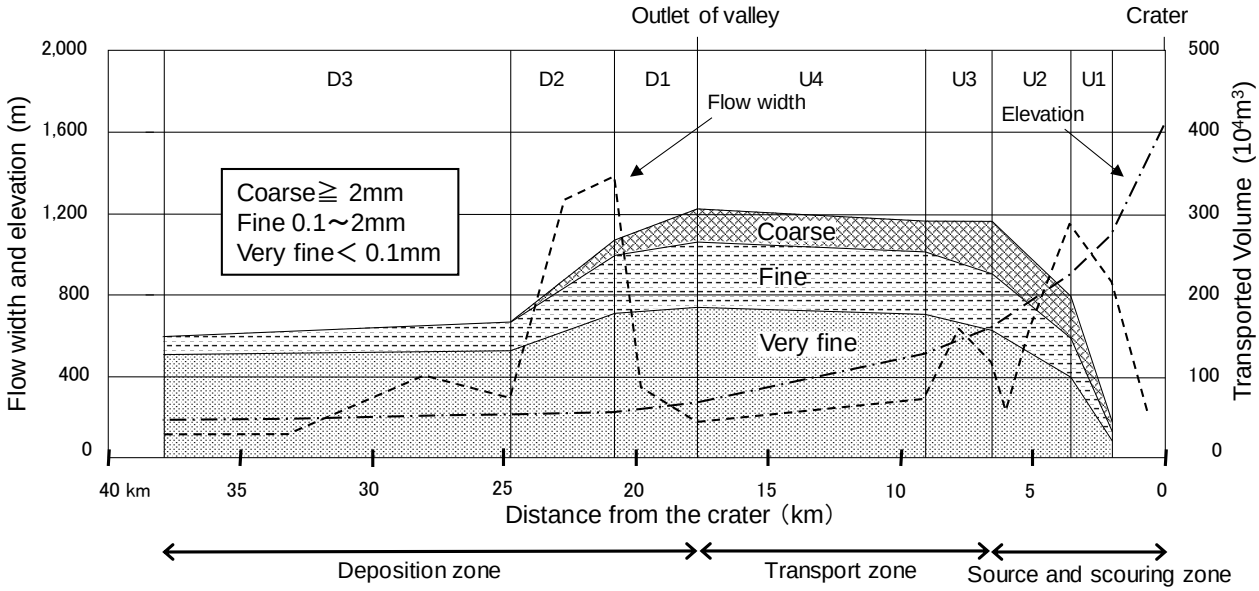

Fig. 6 Spatial changes in grain size components of sediment transported by the 1926 mudflow

zone.

4. CONCLUSIONS

We analyzed the grain size distribution of the 1926 mudflow and found that the grains rapidly became finer throughout the D2 section. This would have produced a dense fluid that could have yielded a large dynamic force of more than 10^2 KN/m, accounting for the extensive damage to houses across the gentle plain more than 20 km from the 1926 crater. The material composition at the downstream end of the U4 section (outlet of the valley) was similar to the original ground soil. Hence, it is possible that the materials present in the channel course could be used to estimate the fluid dynamic force in the flood plain, which would help create a hazard map in preparation for possible future disasters.

ACKNOWLEDGMENT: We wish to thank Dr. T. Araya for his helpful suggestion throughout the study.

REFERENCES

Geospatial Information Authority of Japan (1990): 1:50,000 The land condition map of volcano, Mt. Tokachi (in Japanese).

Hokkaido Asahikawa Public Works Office (2002): Furano River erosion control No. 3 dam: Full report on the Taisho mudflow (in Japanese).

Hokkaido Asahikawa Public Works Office (2003): Furano River erosion control No. 3 dam: Full report on the Taisho mudflow (in Japanese).

Ikari. G. (1940): Survey report on mudflow due to the eruption of Mt. Tokachi, Bulletin of Hokkaido Agricultural Experiment 39, 136 pp. (in Japanese).

Ishikawa. T., Yokoyama. I., Katsui. Y., Kasahara. M. (1971): The Mt. Tokachi volcano: Volcanic geological features, history of eruption, present activity, disaster prevention, Hokkaido Disaster Prevention Conference, 136 pp. (in Japanese).

Nanri. T., Kaneko. Y., Fujiwara. A. (1995): State of Volcanic Mudflow Descent in 1926 into the Furano River at Mt. Tokachi: According to Witnesses of the Mudflow, J. Jpn. Soc. Erosion Control Eng., Vol. 47, No. 5, pp. 30–35 (in Japanese with English abstract).

Nanri. T., Kurebayashi. M., Yamahiro. T., Natori. T., Kaneko. Y., Hasegawa. K., and Araya. T. (2004): The characteristics of 1926 volcanic mudflow at Mount Tokachi, the evidences of eyewitnesses and examination of the deposited materials, J. Jpn. Soc. Erosion Control Eng., Vol. 56, No. 5, p. 33–44 (in Japanese with English abstract).

Nanri. T., Fukuma. H., Harada. N., Ando. H., Ito. H., Hashinoki. T., and Yamada. T. (2009): Flow and sedimentation process of 1926 volcanic mudflow based on the field investigation data analysis at Mt. Tokachi, J. Jpn. Soc. Erosion Control Eng., Vol. 61, No. 5, pp. 21–30 (in Japanese with English abstract).

Nanri. T., Yamada. T., Kasai. M., and Marutani T. (2016): Disaster map of the Taisho volcanic mudflow informing the arrival time and the level of damage after the eruption of Mt. Tokachi in 1926, J. Jpn. Soc. Erosion Control Eng., Vol. 69, No. 1, pp. 12–19 (in Japanese with English abstract).

Tada. F., Tsuya. H. (1927): The Eruption of the Tokachidake Volcano, Hokkaido, on May 24th, 1926, Bulletin of the Earthquake Research Institute, University of Tokyo 2, pp. 49–84 (in Japanese with English abstract).

Takahashi. T. (1981): Volcanic hazard phenomena due to the eruption of Mt. Saint Helens, J. Jpn. Soc. Erosion Control Eng., Vol. 33, No. 3, pp. 24–34 (in Japanese).

Tanakadate. S. (1926): The cause and present condition of the

Mt. Tokachi eruption, Journal of Geography 38, pp. 518–527 (in Japanese).

Tokachidake Explosion Afflicted Relief Committee (1929): Hazard report of the Tokachidake explosion, 521 pp. (in Japanese).

Extreme Torrential Flooding at Simbach on June 1st, 2016 - Key Findings of a Detailed Event Analysis -

Andreas RIMBÖCK[1*], Johannes HÜBL[2] and Rainer HÖHNE[1]

[1] Bavarian Environment Agency (Bürgermeister-Ulrich-Straße 160, 86179 Augsburg, Germany)
[2] University of Natural Resources and Life Sciences (Peter Jordan Straße 82, 1190 Vienna, Austria)
*Corresponding author. E-mail: andreas.rimboeck@lfu.bayern.de

In 2016 an extreme flood event occurred in Simbach, Germany, which caused enormous damages and also 5 fatalities. Some characteristics of the event were unexpected such as a very quick rise of the water level to an extreme height. Additionally a street dam upstream of the city and a dyke in the settlement area got overflown and both broke.
To better understand the event and its processes a detailed event documentation and analysis were initiated. In addition to the collection of lots of photos and videos the event was reproduced in a hydrologic model. Further a hydraulic model was built up to simulate the flow patterns. Finally the peak discharge could be reconstructed by all these calculations and analyses of the photos. It was far more than the design flood, a 100years flood. Additionally the main questions about the processes could be answered by this analysis.
Thereby we learned a lot about such extreme events and could draw first conclusions. So this highlights the necessity of a sound event documentation and analysis. But also many of the questions need further analyses of more events. Nevertheless also further discussion and societal consensus about the strategies how to handle remaining risks is necessary.

Key words: Simbach, event analysis, dam failure, hydrologic modeling, hydraulic modeling

1. OVERVIEW SIMBACH CATCHMENT

In the town of Simbach the torrent Simbach flows into the Inn river. The catchment comprises around 33 square kilometers. Already during the 1950s torrent control measures with state of the art techniques were installed in the Simbach. After the flood events in 1991 and 1999 the flood protection of the town Simbach was further improved. The Simbach is primarily fed through the Antersdorfer Bach (catchment of 13 square kilometers) and the Kirchberger Bach (15 square kilometers), which merge into the Simbach north of the town. The Simbach is crossed by the Schulstraße and subsequent by the heavy frequented federal road B12. At both road embankments the river passes the road via a culvert. The culverts are designed for a 100 years flood event (assessed at time of construction). Between the both junctions a sawmill is situated right near the channel of the Simbach.

Subsequently the torrent flows for around 500 meters along a stretch without control measures before passing through a funnel-shaped inlet structure into a rectangular channel just above Passauer Straße. The gauge Simbach is situated in this developed stretch. In the lower reach flood protection dykes run along the Simbach up to the mouth into the Inn. The channel of the Simbach in the town was designed for a discharge of 60 cubic meters per second plus freeboard.

In the south the town is differentiated from the Inn through levees (= flood protection dyke Inn). As a result the polders Simbach (in the west) and Erlach (in the east) are formed which are drained through pumping stations.

2. EVENT ON JUNE 1st, 2016

On June 1st, 2016 heavy rainfall caused a sudden and extreme flood event in the torrent Simbach. The culvert in the street dam Schulstraße was not able to drain the huge discharge. Therefore the dam was overflown and eroded. The channel of the Simbach in the town could not keep the mass of

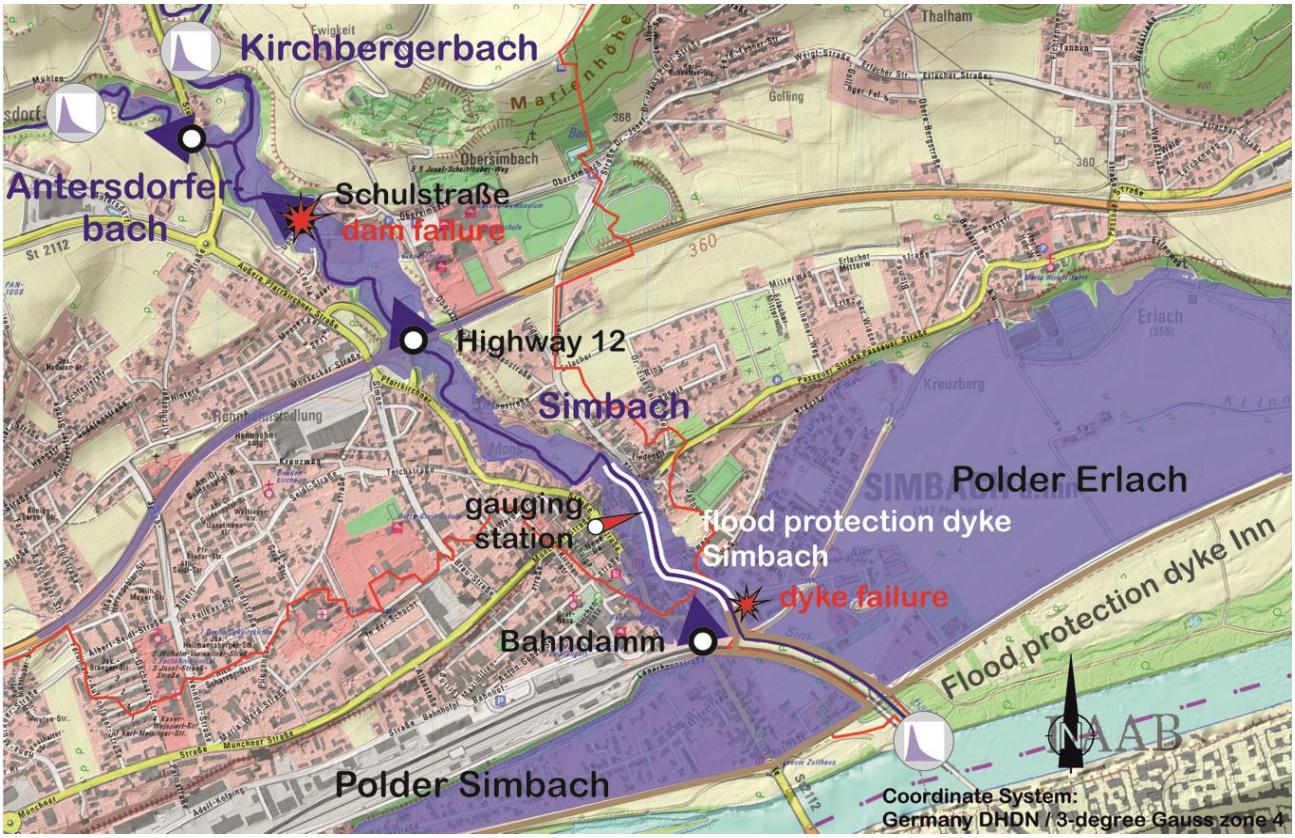

Fig. 1 General map of the town of Simbach (BOKU Vienna)

water. As a result large quantities of water were flowing through the center of Simbach. The dykes along the torrent were overflown and the left one to the Polder Erlach (at Wilhelm-Dieß-Straße) eventually breached. More than two million cubic meters water accumulated in both polders together (**Fig. 1**). Due to the levees along the Inn the water could not drain into the receiving stream, which at that time was not prone to flooding. The pumping stations were overburdened by the extreme amounts of water. To relief the polder Erlach a levee was opened temporarily (**Fig. 2**). In addition mobile pumps were used.

At the gauge in Simbach the channel depth is around three meters. The maximum water level during the event was more than five meters – determination of discharge through the rating curve was not possible.

The event caused very high damages. Besides the high damage to property five casualties were to be mourned. A lot of people had to be evacuated or rescued from acute danger to life. Several citizens could not return to their homes due to danger of collapse. Fresh water supply and waste water disposal was limited and partly broken down. Important traffic routes were interrupted causing major traffic problems (**Fig. 3**).

Fig. 2 Artificial levee breach (Source: VERBUND Innkraftwerke GmbH)

Fig. 3 Flooded federal road B12 (Source: Polizei Niederbayern)

3. MOTIVATION FOR DETAILLED EVENT DOCUMENTATION AND ANALYSIS

Such an extreme event should always be a reason to critically evaluate currently used protection strategies. It also helps to deepen the knowledge about natural processes and also to scrutinize established models. An important prerequisite is a prompt event documentation and therefore collection of valuable data. For that reason the Bavarian Environment Agency (LFU) commissioned the University of Natural Resources and Life Sciences, Vienna (BOKU) for a detailed event analysis.

The discharge pattern in Simbach was complex. Important elements were the backwater at intersecting structures, the failure of the street dam at Schulstraße, the dyke failure at Wilhelm-Dieß-Straße and numerous log jams. For experts as well as persons concerned the course of events raised numerous questions.

According to the EU Floods Directive areas prone to flooding were calculated in three scenarios (frequent, medium and extreme flood) before 2016. These calculations showed correct tendencies for the cases of overload. But the event in 2016 was even more extreme (**Fig. 4**).

After the event the search for someone/something to blame immediately started in the media. It was especially focused on the overloaded culvert at Schulstraße – together with the failure of the street dam – and was seen as the central cause for the catastrophe.

Other headlines such as “Maize and the century flood” targeted agriculture as main cause for the flooding. One aspect certainly is the increased surface runoff on compacted cropland, which is only slightly covered at the start of the vegetation period. In addition soil erosion is playing an important role during heavy rain. During the event on 1st of June 2016 large quantities of fine sediment were transported. After the retreat of the flood these sediments covered wide areas of the town.

The large quantity of press releases with various theories regarding this exceptional event in Simbach shows that many aspects need to be taken into account.

Through an elaborated event analysis the University of Natural Resources and Life Sciences tried to reconstruct discharge patterns on the basis of Data, measured values, photos, videos and interviews.

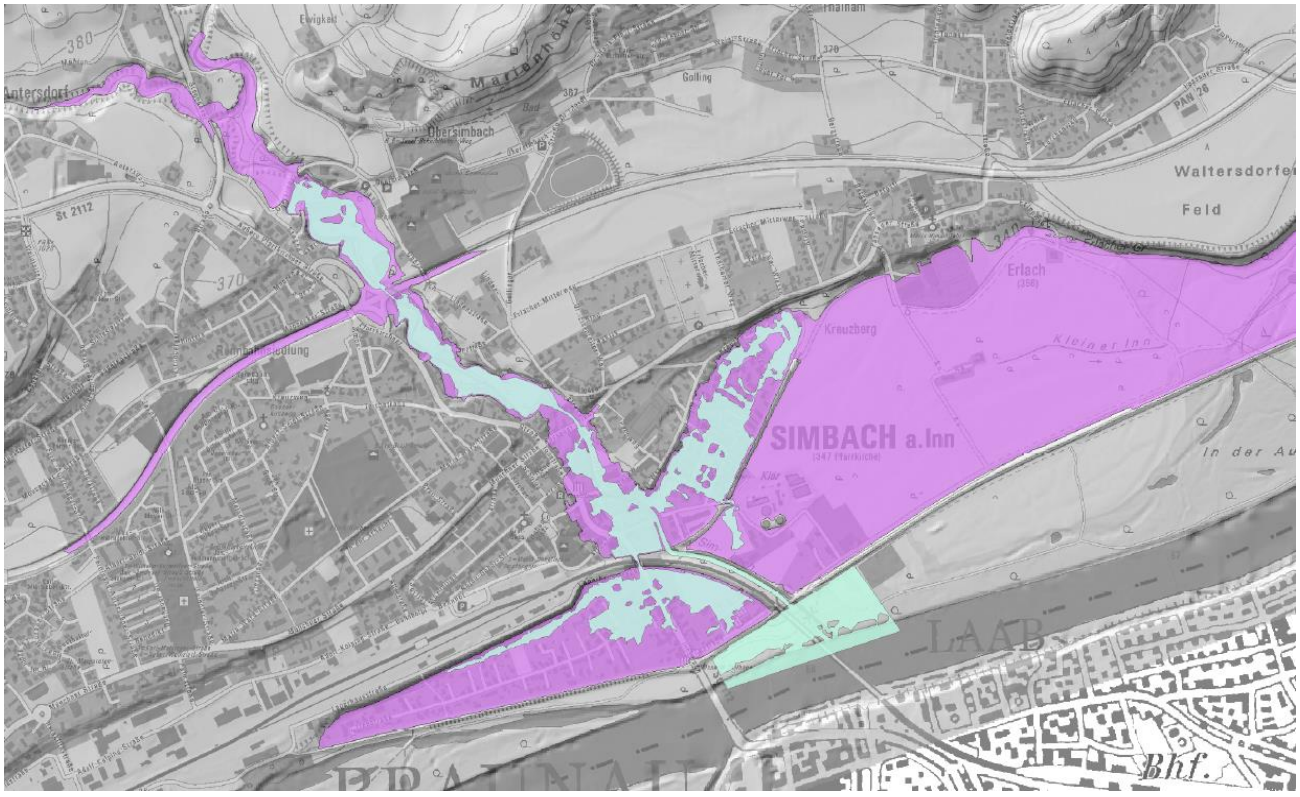

Fig. 4 Comparison of the flooded area on June 1st (purple) and the hydraulic simulation for an extreme event (cyan)

4. INVESTIGATIONS AND RESULTS

The investigations should help to answer the following questions:

- What would have happened, if no failures of structural measures would have occurred?
- How much did the dam failure influence the hydrograph and the flooded area?
- What would have happened, if the dyke would not have failed?

The first questions aim for the definition of a "natural" hydrograph, which is subsequently adapted to the failure situations. This means to combine a hydrological model with a hydraulic model, because downstream of the junction of the two tributaries two road embankments are situated, each crossed by a corrugated steel pipe arch, which caused remarkable retention effects. In addition, the hydraulic model should facilitate the simulation of the inundation areas to compare the flooding areas according to the research questions.

The first objective of the detailed analysis was to reconstruct the triggering rainfall and the maximum discharge during the event. Therefore, data of recorded rainfall at the observation stations in Bavaria and Austria were used to calibrate the weather radar data from the Germany's National Meteorological Service (**Fig. 5**). The water height was monitored by a gauging station within the town. The recorded water level was far above a proven rating curve, therefore the rating curve had to be expanded from 2.6 to more than 5 meters. With this upgraded rating curve and using 1D and 2D hydraulic simulations of the area around the gauging station, the hydrograph of the flood event was derived. However, this hydrograph represents the "natural" event, including the retention effects of the dams, the breach surge, and, after the depletion of the retention areas, the natural runoff of the catchment. To get more insights into the flood

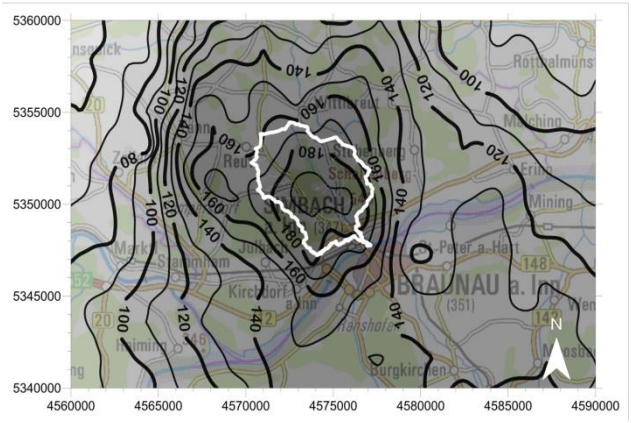

Fig. 5 Areal precipitation for the period from May 31st 07:00 to June, 2nd 00:00. The black lines indicate the calculated isohyetes, the white line the boundary of the Simbach catchment.

dynamics at different sites and to detect the time of dam failures, nearly thousand photos and more than 60 videos were analyzed and the time record of the pictures determined by individual inquiry (**Fig. 6**). Additional water marks were surveyed in the flooded areas to ascertain the flow height at different locations and to later compare these values with the results of the hydraulic simulation.

The second objective was to set up a conceptual hydrological model and to calculate the natural runoff at the junction of the two tributaries. Spatial distributed data of soil types and their hydraulic properties, vegetation and land use were applied as input data as well as the derived time and space distributed rainfall. The model was than calibrated with several minor flood events of the last decades. The resulting hydrograph was used as input for the 2D hydraulic simulation. The hydraulic model has to cover all the flooded areas. The topographical model was based on a one meter grid and the channel geometry on a detailed survey. The culverts and bridges were implemented as boundary condition. Because of the clogging of some of these structures, different scenarios were calculated.

Fig. 6 Discharge at the upper end of the channel through the town about 120 meters upstream of the gauging station. Natural runoff (left) just before the arrival of the breaching surge (right) (Source: Köck)

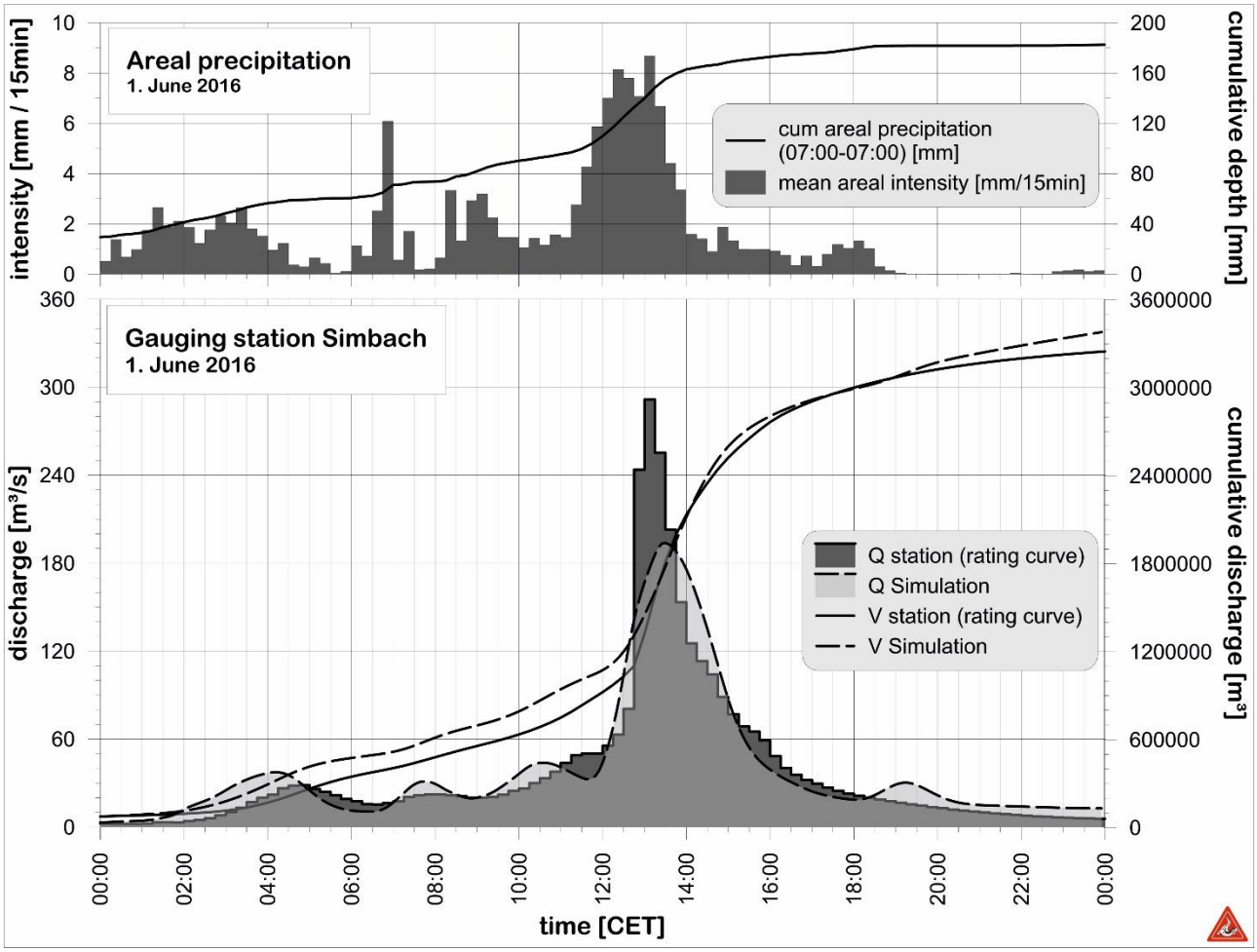

Fig. 7 Areal daily precipitation for the Simbach catchment and observed discharge at the gauging station compared with the hydrological simulation results for the „natural“ runoff.

Roughness coefficients were assessed according to the land use. Buildings were identified as no-flow areas. With these input data the flooding area of the “natural” flood was simulated.

The third objective was to identify the effect of the dam failure in the upstream area and the dyke failure within the town of Simbach. Therefore, the failures of the street dam and the dyke were implemented into the hydraulic model. Different scenarios were defined, varying the model parameters like breaching time and opening width development. The flooding areas were then calculated and a resulting hydrograph at the gauging site compared with the recorded one. Additionally the flow heights at the locations with water marks were compared with the simulation results.

The analysis estimated the maximum discharge of about 280 cubic meters per second at the gauging station during the event. This value resulted from the superposition of the natural runoff with the breaching discharge (**Fig. 7**). The natural peak discharge was estimated with 180 cubic meters per second, meaning a specific discharge of 6.6 $m^3/s \cdot km^2$. This very high runoff resulted from:

- the high amount of rainfall, corresponding to an aerial daily precipitation depth of more than 180 mm. The return period of this daily rate exceeds 100 years.
- the cell of the shower moved downstream from the headwater.
- the shape of the hyetograph. Considering the period from May, 31st 07:00 to June, 1st 19:00 the hyetograph shows, that 50 percent of the precipitation fell within 20, or 40 percent in about 10 percent of this period, more or less concentrated at the end of the rainfall period.
- the development of a dense system of rills and small gullies on agricultural areas and the use of paths, tracks and roads as flow paths that led to a short time to peak.

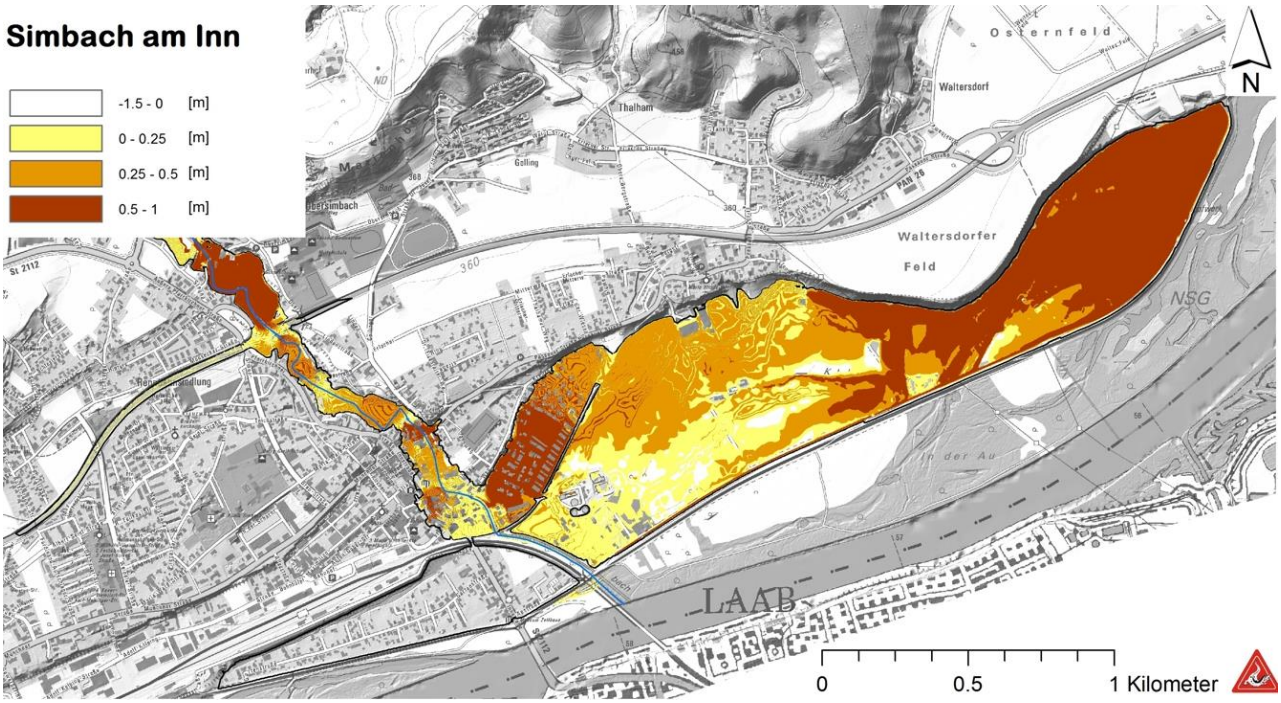

Fig. 8 Difference of flow heights in the flooded area of Simbach by comparing the results of the flood under "natural" conditions versus the results of the flood including the effects of the failures of the structures.

The calibration of the hydrological model was quite difficult, because the already recorded peak discharges were quite smaller. Utilizing long time series of rainfall and runoff a peak discharge of only 95 cubic meters per second could be calculated. Therefore, the model parameter (esp. retention parameter for surface runoff and interflow) were adjusted to get more plausible simulation results. A comparison with the peak rate factor, which is implemented in the HEC-HMS model, yields to a doubling of the suggested value of 484 [-].

The dam breaching resulted in an increase of the discharge of more than 120 cubic meters per second downstream of the dam (~350 cubic meters per second) and diminished along the channel down to the gauging site. Comparing the flooded area of the natural runoff and the scenario including the dam and dyke failure, it can be stated that the flooded area was not considerable enlarged by the breaching hydrograph, but the flow height increased about 0.5 meters in the town (**Fig. 8**).

The scenario without the dam and dyke failure lead to a peak discharge of about 180 cubic meters per second at the gauging stations, the polder Simbach is filled up with 0.6 million cubic meters, whereas the polder Erlach is charged with approximately 0.15 million cubic meters. Assuming the discharge with dam and dyke failure, the polder Simbach gets a surplus of 0.35 million cubic meters and the polder Erlach 0.75 million cubic meters. This means, that the structural failures changed the charging behavior of the polders by the flood.

5. INSIGHTS FROM SIMBACH

The event on 1st of June 2016 in Simbach and the following event analysis provides valuable and important findings with regard to dealing with extreme events in the future. It also showed possible conflicts in the course of flood risk management.

5.1 Technical recommendations

The calibration of a hydrological model with time series without flood events of medium to low probability may lead to an underestimation of a calculated peak discharge for an extreme flood. The Simbach example shows, that a rainfall with a return period of about 300 years lead to a peak discharge that is more than twice of a one hundred years flood. Therefore, hydrological critical spatio-temporal rainfall conditions have to be considered.

Extreme events do not behave in a regular way. Hydraulic critical conditions usually lead to failures of structural measures, drastically modifying the hydrograph and the extent of flooded areas.

5.2 Strategic consequences for the management of extreme events

5.2.1 Preparation for extreme events

After a flood event the question arises, how to prepare for events in the future at the best. The risk management cycle, which is also positioned in the

Bavarian flood protection program „AP2020plus“, provides several aspects in this context. In the following two examples are explained:

1.) Take necessary time for in-depth planning: Immediately after an event the reconstruction starts. The authorities in charge have to repair damaged infrastructure facilities and protection works as fast as possible. A balanced mixture of urgent measures and an in-depth planning is essential in practice. On the one hand legal obligations have to be fulfilled. Otherwise an economic and in every respect optimized solution should be strived.

Structural protection measures are usually expensive. Therefore an in-depth and detailed planning should be taken as basis for every measure. Even if wide-ranging researches take up a lot of time and occasion additional costs, the gained information help to save expenses in the execution of construction work.

2.) Prepare for phase of reconstruction: In many villages the settlement area moved steadily closer to the streams within the years. Riverine zones, which would provide enough space for structural protection measures or sufficient discharge sections, are rare. After a flood event the authorities in charge should try to acquire land along the waterbodies. People concerned recently are more likely to allocate a part of their property for protection measures or even resettle in a more secure area.

But the timeframe for this bargain is only short. Even serious events vanish into oblivion surprisingly fast.

In this context it is necessary to be prepared for (extreme) flood events and at least consider possible cases of overload. So in-depth considerations before the event can lead to a reasonable reaction (“build back better”). It is also a necessary prerequisite to reach a real improvement and to better cope with such events.

5.2.2 Necessary discussion: how society wants to deal with extreme events

For a lot of questions regarding extreme events there are currently not yet clear answers respectively not yet a societal consensus on how to deal with them.

For example, events such as the one in Simbach raise questions up to which level technical flood protection for a recently affected municipality should be designed. Affected persons frequently demand that „such an event may never happen again“ (implying a desire for a higher protection level). A (fair) statewide consistent approach requires fair and comparable calculation of design events.

In both cases a residual risk will remain. Central questions are: How do we want to deal with this residual risk? Accept it? Reduce it by (cost-effective) measures such as alert strategies and emergency plans? Or transfer the risk to others such as insurances?

Flood risk management is a collective task where many parties are to be involved – from state to municipality as well as individuals. The role of the state is established up to the design event. To what extent the state is in duty to care for protection above the design event? Can the responsibility for personal provision be expected by the citizen or is this expectation too much for the individual? Does the state in the field of residual risk need to take action additionally to increasing hazard awareness in municipalities and the society through continuous and targeted risk communication?

The relatively young approach of integral flood risk management has to be filled with life in the future. Through this the impacts of natural events on livelihoods, environment, cultural heritage and economy can be further reduced. On this occasion aspects of extreme events need to be incorporated.

6. CONCLUSION

Extreme events like the one in Simbach show that these are no theoretic scenarios but can become real quite quickly. Society has to deal with these risks. In addition to it discussions are needed which risks can be accepted and how to deal with residual risks. Risk dialogue in an integrated risk management offers an ideal platform. Though many existing measures for risk reduction have to be adapted for extreme events or further developed.

REFERENCES

Bayerisches Landesamt für Umwelt (2017): Sturzfluten- und Hochwasserereignisse Mai/Juni 2016 – wasserwirtschaftlicher Bericht, Augsburg

Hübl, J., Heiser, M., Braito, S., Tscharner, S., Kuntner, K., Schraml, K., Falkensteiner, M. and Rabanser, E. (2017): Ereignisdokumentation und Ereignisanalyse 2016 Rottal-Inn, IAN Report 180, Band 1: Ereignisdokumentation; Institut für Alpine Naturgefahren, Universität für Bodenkultur, Wien

Hübl, J., Heiser, M., Braito, S., Tscharner, S., Kuntner, K., Prenner, D., Falkensteiner, M. and Rabanser, E. (2017): Ereignisdokumentation und Ereignisanalyse 2016 Rottal-Inn, IAN Report 180, Band 2: Ereignisanalyse Simbach; Institut für Alpine Naturgefahren, Universität für Bodenkultur, Wien

Experimental Study of the Use of Stakes to Prevent Driftwood and Natural Debris from Blocking Bridges

Norio HARADA[1*], Kana NAKATANI[2], Yoshifumi SATOFUKA[3] and Takahisa MIZUYAMA[4]

[1] Mitsui Consultants Co., Ltd. (Benten, Minatoku, Osaka 5520007, Japan)
[2] Kyoto University (Kitashirakawa, Sakyo-ku, Kyoto 6068502, Japan)
[3] Ritsumeikan University (1-1-1 Noji higashi, Kusatu city, Shiga 525-8577, Japan)
[4] National Graduate Institute for Policy Studies (7-22-1, Roppongi, Minatoku, Tokyo 106-8677, Japan)
*Corresponding author. E-mail: harada@mccnet.co.jp

Historically, Japanese bridges have been protected from blockage by stakes that control the passage of driftwood. It is important to clarify the function of these stakes; for example, stakes can be used to prevent debris accumulation near a pier. However, no design codes have been established for the optimal placement of stakes to prevent blockage. Furthermore, no studies have been conducted to compare the blockage prevention performance of stakes at different distances, or how their gradient with respect to the riverbed affects debris accumulation. We performed a laboratory-based experiment to observe the effects of stakes on the flow of driftwood within rivers. We found that driftwood passed between piers after rotating around the stakes. We conclude that bridges would be better protected by vertical stakes, which take advantage of this mechanism.

Key words: bridge, driftwood, experiment, natural debris, stake

1. INTRODUCTION

Many areas experience damage by debris flow and driftwood every year in Japan. This damage is the result of debris from mountain forests and landslides due to local downpours, caused in part by global warming [*Fujita*, 2012]. Recent disaster reports have indicated that blockage by driftwood contributed to damage and flooding around bridges [*e.g.*, *Ishino et al*., 2006; *Izu-Oshima Disaster Research Committee*, 2014]. There have been a number of studies concerning bridge damage and countermeasures to prevent the accumulation of driftwood [*Nakagawa et al.*, 1992; *Goto et al.*, 2001; *Shimizu et al*., 2007; *Shibuya et al*., 2011]. In some studies [*e.g.*, *Adachi and Daido*, 1957; *Ishikawa et al*., 1989], mechanisms were proposed to explain the formation of driftwood blockage at bridges and in narrow channels. *Adachi and Daido* [1957] found that the variables determining whether a bridge is blocked by driftwood were the density of flowing driftwood, surface flow velocity, and the relationship between bridge pier interval and driftwood length. *Ishikawa et al*. [1989] proposed a model to predict driftwood blockage rates based on the Froude number, channel width, and driftwood length and diameter; numerical predictions of driftwood behavior have been conducted in several studies [*Nakagawa et al.*, 1992; *Goto et al*., 2001; *Shimizu et al.*, 2007; *Shibuya et al*., 2011]. *Ishikawa et al*. [2007] proposed the installation of steel within bridge beams as a countermeasure to prevent bridges from being blocked.

Historically, stakes installed before bridges that control the direction of driftwood flow have been used to protect bridges from blockages, for example, at Togetsu Bridge in Arashi-yama and Uji Bridge in the Ise Shrine (**Fig. 1**). Stakes also prevent other types of natural debris from blocking the bridges; Takebayashi [2014] described how stakes functioned during a 2013 flood (**Fig. 2**). Many bridges have narrow intervals between piers; these require protection from blockage by driftwood and other natural debris. Traditional stakes are considered effective countermeasures against blockage by debris. However, design codes for the stakes have not been established; thus, the arrangement of stakes differs between bridges.

At Togetsu Bridge (**Fig. 1**), one stake is installed at every other pier. At other bridges, such as Uji Bridge

Fig. 1 Traditional Japanese technique to prevent damage to historical bridges using stakes, Upper: Togetsu Bridge, Arashi-yama, Kyoto; lower: Uji Bridge, at the Ise shrine, Mie

Fig. 2 Stakes at Togetsu Bridge during a 2013 flood [*Takebayashi*, 2014]

(**Fig. 1**), stakes are installed at every pier.

Furthermore, no study has been conducted to compare the effectiveness of different arrangements of stakes in preventing blockages, or how their gradients with respect to the riverbed affect debris accumulation. We thus conducted laboratory flume experiments to observe the effects of stakes on the behavior of driftwood flowing in rivers. Based on our

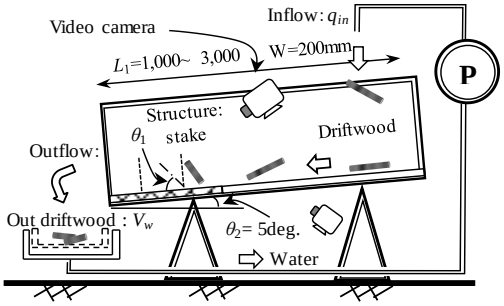

Fig. 3 Schematic diagram of the experimental flume

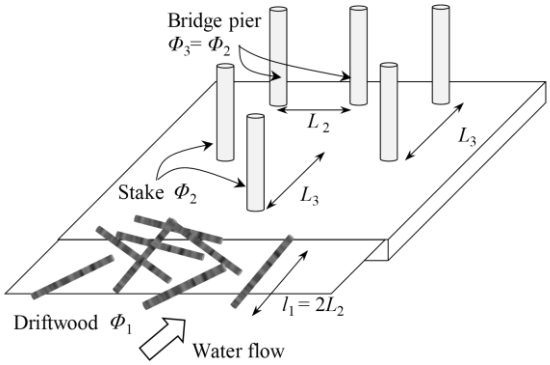

Fig. 4 Schematic diagram of the experimental set-up

experimental results, we propose an effective plan for the use of stakes in preventing blockages.

2. DRIFTWOOD CONTROL EXPERIMENT

We supplied water and driftwood to the upper part of a flume and observed the mechanisms of driftwood control by the stakes (**Fig. 3**).

2.1 Outline

Fig. 4 shows the experimental set-up; the experimental waterway of fixed bed, which was within the flume, was 20 cm high, 20 cm wide, and 300 cm long. We counted the small pieces of driftwood blocked by the stakes or piers, which were installed at the downstream edge of the flume (**Fig. 4**). The driftwood and water were supplied to the upper point at a rate of q_{in}. The driftwood was Φ_1 in diameter, 10 cm in length, and had a dry density of 0.75. The flume was inclined at an angle of 5° [*Ishikawa et al.*, 1989]. The riverbed was covered in stones, such that the flow was stable, as in a real river. The stakes and piers were cylindrical, with a diameter

Table 1 Combinations of parameters used in the experiments

CASE	Φ_1 (mm)	L_1 (mm)	V_w	Direction of flow	Type	θ_1 (°)	L_3	q_{in} (ℓ/s)
1-1	3	1,000	1/s *50s	Horizontal	Without stake			1.0
1-2								2.3
1-3		2,000						
1-4				Vertical				
2-1		1,000		Horizontal	B	90	1.0*l_1	1.0
2-2								
2-3							1.5*l_1	
2-4								
2-5							1.0*l_1	
2-6		2,000					0.5*l_1	
2-7					Without stake			
2-8					A	90	1.0*l_1	
2-9							1.5*l_1	
3-1					No structure			2.3
3-2			50		B	90	1.5*l_1	
3-3								
3-4		3,000			Without stake			
3-5			1/s *50s		B	45	1.5*l_1	
3-6						135		
4-1	1	2,000			Without stake			

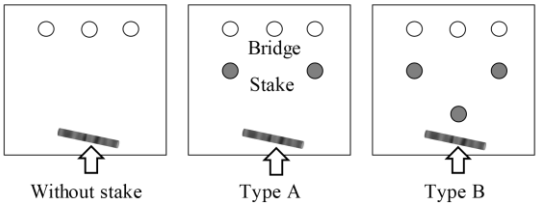

Fig. 5 Stake configurations tested in this study

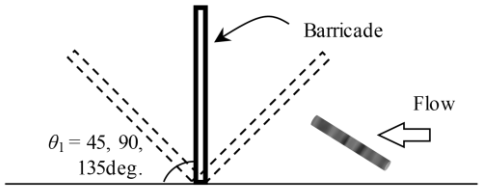

Fig. 6 Angle between the stakes and the riverbed

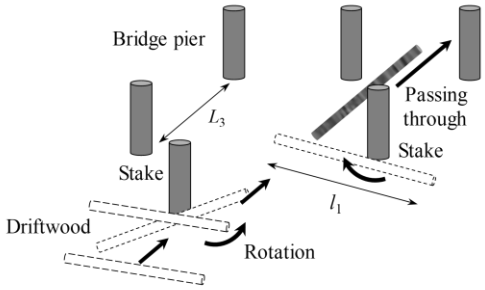

Fig. 7 Driftwood build-up prevention mechanisms

of 1 cm (**Fig. 4**). The experiment was easier to control using cylindrical stakes instead of prism-shaped stakes because flow around prism-shaped stakes is disordered. We used a pier interval, L_2, of 5 cm, which was half the length of the driftwood, l_1, 10 cm. *Ishikawa et al*. [1989] reported that driftwood can easily block the spaces between stakes when the driftwood is longer than the distance between stakes.

Table 1 shows the parameters that we controlled during the experiments. We observed the effect of stakes on driftwood flow as we varied the driftwood diameter, Φ_1, the distance between the stakes, and the supply point, L_1, the driftwood supply rate, V_w, the direction of driftwood flow, and the arrangement of the stakes (**Fig. 5**), the incline of the stakes against the riverbed, θ_1 (**Fig. 6**), the distance between the piers and stakes, L_3, the driftwood length, l_1 (**Fig. 4**), and the upstream water supply rate, q_{in}.

As shown in **Fig. 5**, we proposed a new, houndstooth-shaped stake arrangement, which we called Type B. In the Type A arrangement, we placed stakes at alternating piers, after the arrangement at Togetsu Bridge (**Figs. 1** and **2**). The maximum driftwood volume concentration ratio was approximately 0.3. When the supply water discharge rate was 1.0 l/s, the water height was 1.1 cm and the Froude number was 1.3. When the supply water

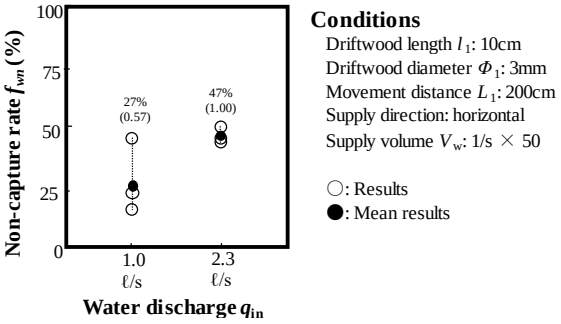

Fig. 8 Effect of water discharge on the non-capture rate, f_{wn}

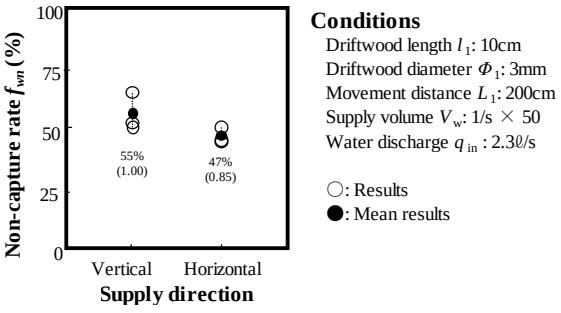

Fig. 9 Effect of the direction of driftwood supply on f_{wn}

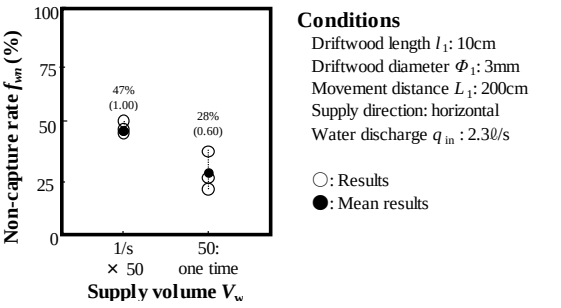

Fig. 10 Effect of driftwood supply volume/speed on f_{wn}

discharge rate was 2.3 l/s, the water height was 1.9 cm and the Froude number was 1.4.

Fig. 7 shows the mechanisms by which the stakes might control the flow of driftwood under the bridge. We believe that driftwood rotates around the stakes, enabling it to flow between the piers. The experiment was repeated three times under each condition and was recorded using video cameras **(Fig. 3**).

2.2 Effect of stake arrangement on driftwood control performance

The non-capture rate, f_{wn}, which is the rate at which driftwood pieces passed between the bridge

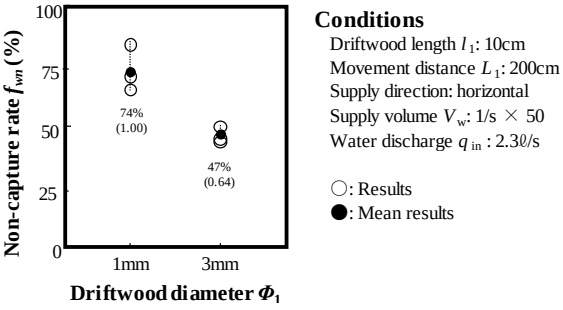

Fig. 11 Effect of driftwood diameter on f_{wn}

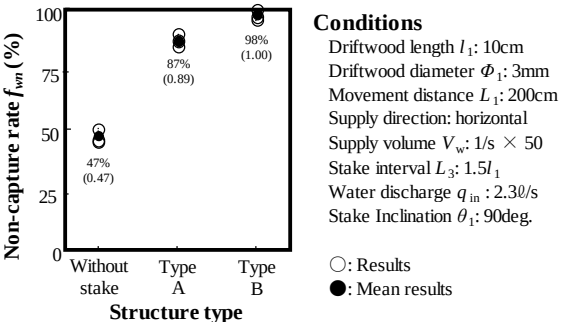

Fig. 12 Effect of stake arrangement on f_{wn}

piers, is given by:

$$f_{wn} = {}^{V_{wout}}/_{V_{out}} \quad (1)$$

where V_{wout} is the number of driftwood pieces that passed under the bridge and V_{out} is the number of driftwood pieces supplied.

Fig. 8 shows the relationship between the supplied water discharge rate from upstream q_{in} (**Fig. 3**) and f_{wn}. f_{wn} increased with q_{in} and water flow speed (**Fig. 8**). In fast-flowing areas, we observed that driftwood passes between bridge piers by rotating smoothly around the stakes, whereas driftwood pieces did not rotate around the stakes in slow-flowing areas, and so were captured by the stakes or piers. Some results for slow-flowing areas agreed with those from fast-flowing areas, which suggests that the capture of driftwood is a probabilistic process.

Fig. 9 shows the relationship between the driftwood supply direction and f_{wn}. In particular, we studied driftwood orientated perpendicular and parallel to the direction of flow. The driftwood orientation did not have a significant effect on f_{wn} (**Fig. 9**). We observed that the driftwood rotated irregularly, such that some driftwood pieces started

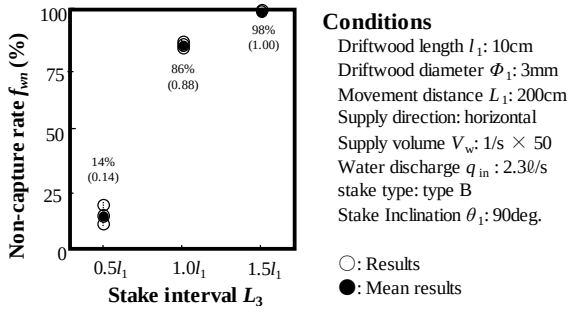

Fig. 13 Effect of the distance between the stakes L_3 on f_{wn}

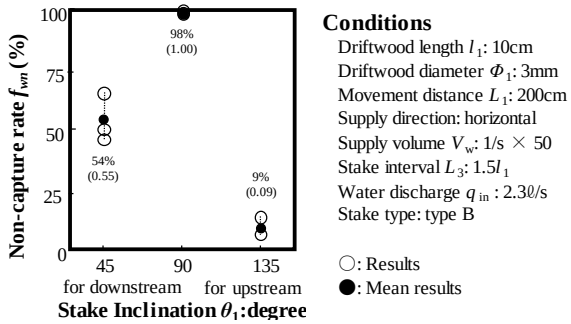

Fig. 14. Effect of the incline of stakes to the riverbed θ_1 on f_{wn}

to be orientated in the direction of water flow.

Fig. 10 shows the relationship between driftwood supply volume/speed and f_{wn}. We introduced one piece of driftwood per second for 50 seconds, and 50 pieces of driftwood simultaneously. When all driftwood was released at once, it was captured easily. f_{wn} was affected by differences in driftwood density, as was shown in a previous study [*Adachi and Daido*, 1957]. However, the results of experiments in which all driftwood was released at once were very similar to those in which driftwood was released slowly (**Fig. 10**).

Fig. 11 shows the relationship between driftwood diameter Φ_1 and f_{wn}. f_{wn} decreased with Φ_1 (**Fig. 11**). [*Ishikawa et al*., 1989] suggested that there is a relationship between the driftwood capture rate in a narrow flume, the Froude number, and driftwood diameter and length. We observed experimentally that fast-flowing water, as seen when the Froude number is larger, enabled driftwood captured by stakes or bridge piers to be released by rotation around the stakes. Additional research is required to confirm this release mechanism.

Fig. 12 shows the relationship between stake arrangement and f_{wn}. We tested no-stake, Type A, and Type B (**Fig. 5**). The stakes enabled driftwood to pass easily through the bridge piers by rotating around them (**Fig. 7**). The presence of stakes approximately doubled the driftwood capture rate. Furthermore, the Type B arrangement was more effective than that of Type A (**Fig. 12**). We observed that some driftwood that had passed through stakes without contact in the Type A arrangement was captured by bridge piers.

Fig. 13 shows the relationship between L_3 (**Fig. 4**), and f_{wn}. A wide stake interval enabled driftwood to rotate around the stakes easily [Fig. 13]. We concluded that driftwood could not rotate around the stakes if the distance between them was insufficient, that is, when the stakes were separated by more than 1.5 times the driftwood length.

Fig. 14 shows the relationship between θ_1 [Fig. 6] and f_{wn}. The driftwood rotated more easily around the stakes when it was perpendicular to the riverbed. We observed that driftwood was not able to rotate easily around the stakes when the stakes pointed upstream or in the direction of the water flow.

We propose that, to control driftwood accumulation at bridges, stakes should be installed vertically in a houndstooth formation (Type B), with a separation distance L_3 of 1.5 times the driftwood length, l_1.

3. CONCLUSION

To understand the traditional technique of using stakes to prevent driftwood from blocking bridges, we varied the stake arrangement and performed experiments to evaluate their effect on driftwood accumulation. We then proposed an effective stake design based on our experimental results.

We observed that driftwood rotates around the stakes, and then passes between the bridge piers. Driftwood accumulation prevention performance was affected by water flow speed, driftwood density, inclination of the stakes with respect to the riverbed, and stake installation interval. We proposed a new houndstooth-shaped stake configuration, which should act as an effective countermeasure against blockages by driftwood and other floating debris. In the future, additional experiment that is changed the length of driftwood is needed.

REFERENCES

Adachi S. Daido A. (1957): Experimental study on washed timbers. Disaster Prevention Research Institute Annuals, Vol. 1, pp. 41-49.

Fujita M. (2012): Influence of climate change on sediment disasters. Journal of the Japan Society of Erosion Control Engineering, Vol. 65-1, pp. 14-20.

Gotoh H., Sakai T., and Hayashi M. (2001): Lagrangian particle method for analysis of dam-up process by drift timbers. Annual journal of hydraulic engineering, JSCE, Vol. 45, pp. 919-924.

Ishikawa Y., Mizuyama T., and Fukuzawa M. (1989): Generation and flow mechanisms of floating logs associated with debris flow. Journal of the Japan Society of Erosion Control Engineering, Vol. 42-3, pp. 4-10.

Ishino K., Hashimaru D., and Tamai N. (2006): Research the Fukui flooding hazardous in 2004, JSCE Annual Meeting, Vol. 2, pp. 9-10.

Ishino K., Watanabe R., and Anzai M. (2007): Proposed counter measure against the driftwood on the bridges. JSCE Annual Meeting, Vol. 2, pp. 117-118.

Nakagawa H., Takahashi T., and Ikeguchi M. (1992): Numerical simulation of drift wood behavior. Disaster Prevention Research Institute Annuals, Vol. 35 B-2, pp. 249-266.

National Research and Development Agency. (2015): Report on investigations into disaster in Izu Oshima island caused by Typhoon Wipha in 2013. Technical note of public works research institute, Vol. 4302.

Shibuya H., Horiguchi T., Katsuki S., Ohsumi H., and Ishikawa N. (2011): Trap simulation of woody debris by using cylindrical assembled element with roots in distinct element method. Journal of Applied Mechanics, JSCE, Vol. 14, pp. 323-334.

Shimizu Y., and Osada K. (2007): Numerical experiments on accumulation process of driftwoods around piers by using a dem-flow coupling model. Annual journal of hydraulic engineering, JSCE, Vol. 51, pp. 829-834.

Takebayashi H. (2014): Research Kyoto and Shiga flooding hazardous in 2013. Journal of Natural Disaster Science, Vol. 33-1, pp. 5-16.

Study on Risk Analysis of Large-scale Landslide

Teng-Chieh HSU[1], Yuan-Jung TSAI[2*], Chjeng-Lun SHIEH[3] and Jen-Yuen CHENG[4]

[1] Graduate student, Department of Hydraulic and Ocean Engineering, National Cheng Kung University, Taiwan
[2] Researcher, Disaster Prevention Research Center, National Cheng Kung University, Taiwan
[3] Director, Disaster Prevention Research Center, National Cheng Kung University, Taiwan
[4] Engineer, Southern Region Water Resources Office, WRA, MOEA, Taiwan
*Corresponding author. E-mail: rongtsai@dprc.ncku.edu.tw

With the implement of mitigation work of large-scale landslide, hundreds of potential large-scale landslide areas were identified in Taiwan since 2010. The topographical features, geological conditions and situation of property and residents were used to evaluate the risk for each potential large-scale landslide in the first stage. Therefore, a lot of countermeasures and monitoring systems were setup to reduce the risk of potential large-scale landslide. However, the approach of risk assessment in the first stage did not consider risk distribution in a regional area, so that the effect of mitigation work and land-use management cannot be estimated. In this study, we present a risk assessment approach to evaluate the risk of large-scale landslide and the effect of the mitigation work.
The risk is the probability of potential loss. In this study, we define the risk is the function of hazard, exposure and vulnerability. Hazard is considering the deposition depth and movement velocity. Exposure is considering the land use (building, road, agricultural land, forest), which is exposed in the hazard area. Vulnerability is considering the relationship between land use, hazard, and loss curve. Furthermore, this approach considers the effect of mitigation work such as land-use management and sabo work. The result shows that, the potential loss can be well quantify with the approach. Furthermore, the effect of the mitigation work, such as land use managements and sabo works, can be also well described in this approach.

Key words: large-scale landslide; risk analysis; landslide disaster

1. INTRODUCTION

Large-scale landslide disasters have caused severe damages in Taiwan in the past years. As a result, it is an urgent task for the government and the research communities to start series mitigation work to reduce the loss of the disaster. With the implement of mitigation work of large-scale landslide, hundreds of potential large-scale landslide areas were identified in Taiwan since 2010. The topographical features, geological conditions and situation of property and residents were used to evaluate the risk for each potential large-scale landslide in the first stage.

Therefore, lots countermeasures and monitoring systems were setup to reduce the risk of potential large-scale landslide. However, the approach of risk assessment in the first stage was setup to identify the risk from hundreds of potential large-scale landslide areas with topography, geology and number of buildings. The current method could only prioritize the sequence of countermeasure based on the risk of each potential large-scale landslide, the post effectiveness assessment of countermeasures, is dismissed.

The main propose of this research, in terms of the response action in the disaster management, is to study the risk of large-scale landslide, and to provide the foundation for mitigation work. In this study, we present a new risk assessment approach, which can evaluate the risk for each potential large-scale landslide and can identify risk map in a regional area. Moreover, the presented approach considers the effect of mitigation work.

2. METHODS

2.1 Risk assessment

In this study, risk is defined as the probability of potential loss. The risk index approach, which can help to understand the contribution of hazard, vulnerability and exposure to overall risk is used to analyze the risk of large-scale landslide. The risk is the function of hazard, exposure and vulnerability. Risk is expressed as:

$$R = f(H, E, V) \quad (1)$$

R is risk of large-scale landslide, ***H*** is hazard, ***E*** is exposure, ***V*** is vulnerability. **Fig.1** show the concept of the risk mapping in this study. Consequently, the risk mapping is processed by GIS tools. First drawing the 2m x 2m square grid meshes on the case study areas. In this size of mesh, the damage of buildings could be well evaluated in spatial distribution.

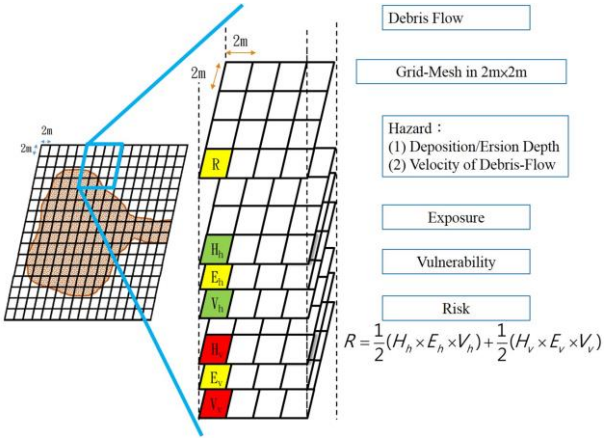

Fig1. Concept of risk mapping

The hazards are evaluated with the velocity of landslide movement and depth of landslide deposition, which are evaluated by numerical. Because of high water content of landslide mass, the landslide movement is considered as a continuous solid-liquid phase flow. This research simulated the process of landslide by the numerical model, which was developed by Egashira et al. (1997) and was modified by Miyamoto (2002).

The exposures are evaluated with four kinds of land use, such as building, road, agricultural land and forest.

The vulnerability was evaluated with the loss curve of four kinds of land use and the population composition, which is considering the distribution of population age. Consequently, the risk mapping is processed by GIS tools.

Therefore, we can evaluation the hazards, exposures, vulnerability of each grid mesh with Eq. (1) to evaluate the large-scale landslide risk of all each grid mesh. Finally, we can map the risk distribution in a regional area.

2.2 Hazard assessment

We considered the landslide movement as a continuous solid–liquid phase flow. This model assumes that (1) the movement of landslide mass can be considered as the movement of solid–liquid mixture at constant solid concentration on a fixed bed and (2) the quasi-static inter-granular friction stress dominates the flow characteristics. This model uses kinematic energy balance in shear flow to simulate the rheology of the solid–liquid mixture of the landslide. During the movement of landslide mass, the concentration of solid particles is assumed unchanged, and the quasi-static inter-granular friction stress is not balanced with the external shear stress at the bed. Based on the evaluation of the static inter-granular friction stress, the dynamics of the landslide mass can be determined.

In the model, the friction angle is constant in the model, which the friction is changing with the velocity of the landslide mass. The governing equations include continuity equation and momentum equation:

Continuity equation

$$\frac{\partial h}{\partial t}+\nabla g\boldsymbol{M}=0 \tag{2}$$

Momentum equation

$$\frac{\partial \boldsymbol{M}}{\partial t}+\beta(Mu^t)\nabla=-gh\nabla H-\frac{T}{\rho_m} \tag{3}$$

where h is landslide thickness, **M** is the flux vector, β is the coefficient of momentum, and u is depth-averaged velocity. Superscript t of **u** means transverse of the corresponding vector or matrix, that is, $\mathbf{u}^t$ is the transverse vector of u, g is gravity acceleration, H is the surface level of the landslide, and the lateral earth pressure within the debris mass is assumed to be unity. ***T*** is the shear stress acting on the slip surface, and ρ_m is the mass density of a hyper-concentrated sediment–water mixture. The density is determined as

$$\rho_m=c\sigma+(1-c)\rho \tag{4}$$

where σ is the mass density of solid phase, ρ is the mass density of liquid phase, and c is the volumetric concentration of solid phase, and ∇ is defined as $\nabla=\partial/\partial x_i+\partial/\partial y_j$, in which i and j are base vectors of Cartesian coordinates. In Eq.(2), deposition and erosion are assumed not to occur during the landslide movement so the right side of the equation is set to zero. Egashira et al. (1997) established the shear stress **T** based on energy consideration, $\Phi=(\partial u/\partial x_j)$ **T**. In this equation, the shear stress **T** is obtained from the energy dissipation of particle and stream flow Φ. The shear stress is then introduced into the momentum equation. We assumed that shear stress **T** acts on the slip surface and can be expressed as:

$$\mathbf{T}=\mathbf{T_s}+\mathbf{T_d}+\mathbf{T_f} \tag{5}$$

where T_S is the shear stress due to static inter-granular contacts, T_d is the shear stress due to particle-to-particle collisions, and T_f is the shear stress due interstitial liquid phase turbulent and those can be expressed as:

$$\mathbf{T}_s = \alpha C(\sigma - \eta\rho)ghcos\theta tan\phi_s \frac{\mathbf{u}}{|\mathbf{u}|}, \quad (6)$$

$$\alpha = (\frac{C}{C_*})^{1/5} \quad (7)$$

$$\mathbf{T}_d = \frac{25}{4} k_g \sigma(1-e^2) C^{1/3} (\frac{d}{h})\mathbf{u}|\mathbf{u}| \quad (8)$$

$$\mathbf{T}_f = \frac{25}{4} k_f \sigma(1-c)^{5/3} C^{2/3} (\frac{d}{h})\mathbf{u}|\mathbf{u}| \quad (9)$$

where ϕ_s is the friction angle, e is the restitution coefficient, c_* obtained from the field investigation are the concentrations of the solid phase in volume in the flow and at a packed state, d is the diameter of particles of the solid phase, k_g and k_f are constants (k_g=0.0828 and k_f=0.16 to 0.25), θ is the gradient of the slip surface, and η=0.808 is the coefficient of the effect of buoyancy and takes a value from 0 to 1. In this study, η is suggested by Miyamoto (2002). $\mathbf{T}_S$ and $\mathbf{T}_d$ will change according to the speed of the sediment movement. When the sediment is moving slow, $\mathbf{T}_S$ has larger impact than $\mathbf{T}_d$. Otherwise, it will be the other way around. The internal friction angle is constant. The static inter-granular contact $\mathbf{T}_S$ is updated automatically with the movement.

The dynamics of landslide mass is determined using the revised momentum equation. The revised momentum equation can be written as:

$$\mathbf{M}^{n+1} = \mathbf{M}^n - \left[\beta(\mathbf{M}^n \mathrm{u}^{tn})\nabla + (\mathbf{T}_s^n + \mathbf{T}_d^n + \mathbf{T}_f^n)/\rho_m + gh^n \nabla H^n\right]\Delta t \quad (9)$$

where n denotes the present time step and n+1 denotes the next time step. As shown in the equation, the dynamics is determined not by the friction but the value of **M**. When **M**>0, the mass is in motion. On the other hand, the mass is not in motion when **M**<0. For more details, please refer to Miyamoto (2002).

There are two limitations for the proposed model. First, the erosion of the slide surface due to the movement of landslide mass is not considered in the model. Second, the water content of landslide material is constant. In this case, the soil mass is saturated during the landslide event.

The hazards of velocity of landslide movement and depth of landslide deposition, which are evaluated by numerical model could be set with **Table 1**.

Table1 Hazard values base on numerical result

velocity of landslide (m/s)	H_v	depth of landslide deposition(m)	H_h
0.5~1	0.2	1.5~2.5	0.2
1~2	0.4	2.5~6	0.4
2~3	0.6	6~8	0.6
3~5	0.8	8~12	0.8
>5	1	>12	1

2.3 Exposure assessment

In this study, we quantified exposure based on the depth of landslide deposits and landslide velocity, which were represented as E_h and E_v, respectively.

These two exposure factors were assessed as follows. Each grid cell was assigned a deposition depth value that reflected the final deposition condition in the earth covered by that cell. If deposition becomes hazardous once its depth exceeds 0.5 m, then E_h equals 1 if the depth of landslide deposits is greater than 0.5 m; otherwise E_h equals 0, as shown in **Table 2**.

Grid cells were assigned landslide velocity values that matched the maximum velocity of landslide material passing through them. If landslide velocity becomes hazardous once it exceeds 1.5 m/s, then E_v equals 1 if landslide velocity is greater than 1.5 m/s; otherwise E_v equals 0, as shown in **Table 3**.

Table 2 Exposure values based on depth of landslide deposits

Depth-based exposure	Value
depth of deposits>0.5m	1
depth of deposits<0.5m	0

Table 3 Exposure values based on landslide velocity

Velocity-based exposure	Value
landslide velocity >1.5 m/s	1
landslide velocity <1.5 m/s	0

2.4 Vulnerability assessment

In this study, we quantified vulnerability according to the depth of landslide deposits, landslide velocity, and the village dependency ratio. These factors were represented as V_h, V_v, and I_{DR}, respectively.

V_h and V_v were determined for a variety of land-cover types (buildings, roads, agriculture, and forests). Specifically, V_{hh}, V_{hr}, V_{ha}, and V_{hf} respectively quantify how depth of landslide deposits affect the vulnerability of building, road, agriculture, and forest land-cover types. V_{vh}, V_{vr}, V_{va}, and V_{vf} respectively quantify how landslide velocity affects the vulnerability of building, road, agriculture, and forest land-cover types. Note that the first letter of the subscripts denotes the hazard

type (depth of landslide deposits or landslide velocity), and the second letter of the subscript denotes the land-cover type (building, road, agriculture, or forest). In other words:

$V_{\alpha\beta}$: represents the vulnerability of land-cover type β exposed to hazard α, *where* α: depth of landslide deposits (h) or landslide velocity (v); β: building (h), road (r), agriculture (a), or forest (f).

The formulas used to combine the various $V_{\alpha\beta}$ values were as follows (Eqs. 10 and 11):

$$V_h=(0.4V_{hh}+0.3V_{hr}+0.2V_{ha}+0.1V_{hf})\cdot I_{DR} \quad (10)$$

$$V_v=(0.4V_{vh}+0.3V_{vr}+0.2V_{va}+0.1V_{vf})\cdot I_{DR} \quad (11)$$

The partial vulnerability score assigned to each land-cover type was weighted differently, according to the monetary value associated with each land-cover type. In other words, land-cover types with greater monetary value were weighted more highly in the calculation of vulnerability scores.

Below, we explain the analytical methods used to determine (1) vulnerability to depth of landscape deposits and (2) vulnerability to landslide velocity in detail:

Vulnerability of the building land-cover type to depth of landslide deposits, V_{hh}: We referred to the building loss ratio curve used by Lo et al. (2012) to assess the vulnerability of structures located in mountainous areas of Taiwan (**Fig.2**). By substituting the upper limit of values which quantify the depth of landslide deposits in each interval into Eq. (12), we can derive the vulnerability of land used for buildings (**Table 3**).

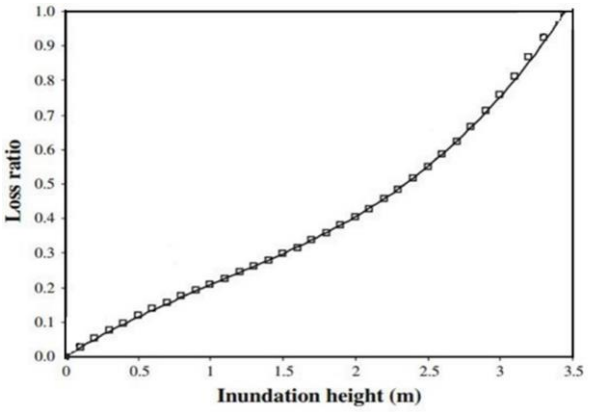

Fig 2. Loss ratio curve at different inundation depths (Lo et al. 2012)

$$V_{build}(h)= 0.0266h^3-0.2663h \quad if\ 0 \leqq h<3$$
$$1 \quad if\ h \geqq 3 \quad (12)$$

Vulnerability of the road land-cover type to depth of landslide deposits, V_{hr}: We posit that the primary expenses related to road damage following a landslide are those incurred clearing and removing landslide deposits. Therefore, these expenses are proportional to deposit volume. All grids cells in this study measured 2m × 2m. Therefore, the vulnerability of the road land-cover type is proportional to the depth of landslide deposits. When the depth of landslide deposits is greater than 5 m, then V_{hr}=1; when it is less than 0.5 m, then V_{hr}=0. **Table 3** presents the relationship between vulnerability to financial loss and depth of landslide deposits.

Vulnerability of the agriculture land-cover type to depth of landslide deposits, V_{ha}: Agricultural crops can be easily damaged from landslides. Crops completely lose economic value when buried under landslide debris, so we assumed that V_{ha} =1 if the depth of landslide deposits was greater than 0.5 m.

Vulnerability of the forest land-cover type to depth of landslide deposits, V_{hf}: Broad-leaved trees are the primary type of commercially valuable wood in forests. According to Design and Technique Specifications for Greenery of Site, large broad-leaved trees are defined as trees whose height exceeds 10 m at maturity. For trees on forest land that are 10 m in height; losses are incurred when the depth of landslide deposits reaches 1/4 of tree height, and destruction occurs when landslide deposition depth reaches 1/2 of tree height (**Table 3**).

Vulnerability of the building land-cover type to landslide velocity, V_{vh}: We assumed that damage to buildings begins to occur when landslide velocity reaches 2.5 m/s. At this speed, financial losses are minor (approximately 10% of total possible loss). In contrast, a landslide velocity greater than 12 m/s results in 100% losses. Percent loss values that occur at landslide velocities between 2.5 m/s and 12 m/s were derived using linear interpolation. The relationship between vulnerability to financial loss and landslide velocity is presented in **Table 4**.

Vulnerability of the road land-cover type to landslide velocity, V_{vr}: We assumed that the vulnerability of the road land-cover type to landslide velocity is equal to that of the building land-cover type (**Table 4**).

Vulnerability of the agriculture land-cover type to landslide velocity, V_{va}: We assumed that landslide velocities between 1.5 m/s and 2.5 m/s result in the loss of 50% of crops and that velocities greater than 2.5 m/s cause 100% of crops to be lost (**Table 4**.)

Vulnerability of the forest land-cover type to landslide velocity, V_{vf} : We assumed that landslide velocities between 1.5 m/s and 2.5 m/s result in 25% of forest land being lost and that velocities between

8 m/s and 12 m/s result in 100% of forest land being lost. Losses that occur at velocities between 2.5 m/s and 12 m/s were derived using linear interpolation. This relationship is presented in **Table 4**.

This index I_{DR} describes the ability of a village to respond to large-scale landslide disasters according to the age structure of the population. Children and the elderly tend to have poorer mobility than do individuals in other age groups. These individuals are therefore less able to flee from disasters. Therefore, the dependency ratio of a village can be defined as the ratio of children and elderly individuals to the total population, as shown in Eq. 13. A higher I_{DR} indicates that age structure makes the village more vulnerable in the face of a disaster.

$$I_{DR} = \textit{(Number of children and elderly) / (Total population)} \quad (13)$$

Table 3 vulnerability corresponding to depth of landslide deposits

Z(m)	V_{hh}	V_{hr}	V_{ha}	V_{hf}
0~0.5	0	0	0	0
0.5~1	0.21	0.15	1	0
1~2	0.41	0.3	1	0
2~3	0.75	0.5	1	0.33
3~5	1	0.8	1	0.66
>5	1	1	1	1

Table 4 vulnerability corresponding to landslide velocity

V_s (m/s)	V_{vh}	V_{vr}	V_{va}	V_{vf}
0~1.5	0	0	0	0
1.5~2.5	0	0	0.5	0.25
2.5~6	0.1	0.1	1	0.5
6~8	0.4	0.4	1	0.75
8~12	0.7	0.7	1	1
>12	1	1	1	1

3. STUDY AREA

Typhoon Morakot, a medium-strength typhoon, invaded Taiwan from August 5 to 10, 2009, and brought with extremely high intensity and accumulative rainfall. The abnormal heave rainfall influenced southern and eastern Taiwan. In this research, the risk map of Xinkai landslides, which was triggered by Typhoon Morakot, was evaluated with the presented risk assessment approach.

The Xinkai landslide took place in Xinfa Village, located in the Liouguei District of Kaohsiung City (**Fig.3**). According to the major landslide disaster report provided by the Soil and Water Conservation Bureau, this large-scale landslide occurred on the upstream slopes of a wild stream, behind Xinkai Village, forming a debris flow that caused 38 deaths and damaged 38 buildings.

The Xinkai landslide was located upstream of the potential debris flow torrent known as Kaohsiung DF078. The area of this watershed is approximately 52 ha, and the elevation range 400m to 1100m. In 2009, Xinkai village had a population of 1,711 people, and its dependency ratio was 0.3007.

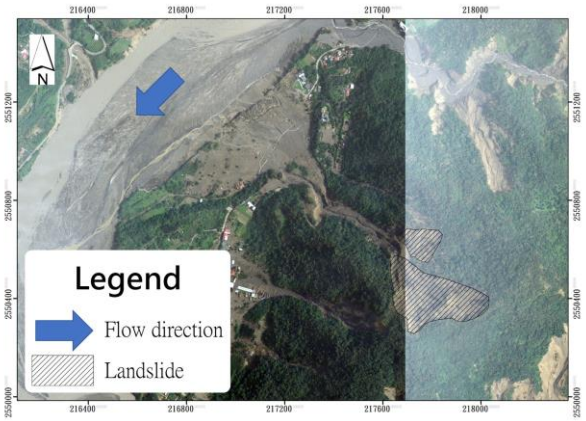

Fig 3. The aerial photo after typhoon Morakot

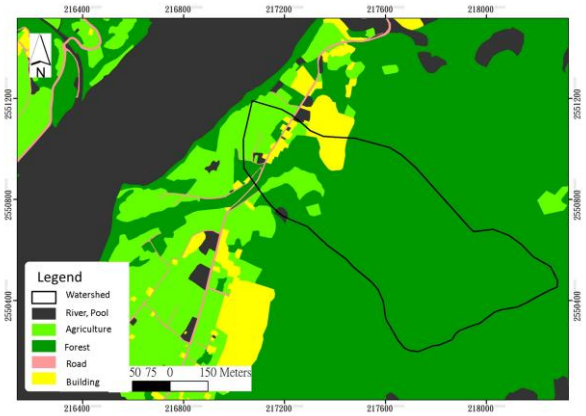

Fig 4. Land cover in Xinkai in 2009

4. RESULT AND DISCUSSION

4.1 Result of Xinkai Village

(a) Result of Hazard assessment

Fig.5 and **Fig.6** present hazard area of the Xinkai landslide. The primary hazard was depth of landslide deposits depth. In this study, grid cells were assigned values that corresponding to the maximum velocity that was reached during the Xinkai landslide. Therefore, the vulnerability score assigned to most of these grid cells was 1. Only a

few cells at the edge of the deposition zone received a vulnerability score of less than 1 for landslide velocity. Conversely, the depth of landslide deposits gradually decreased from the apex of the alluvial fans to the outer edges. As shown in **Fig. 5**, the vulnerability score for depth of landslide deposits for most of the buildings in Xinkai Village ranged from 0.8 to 1.

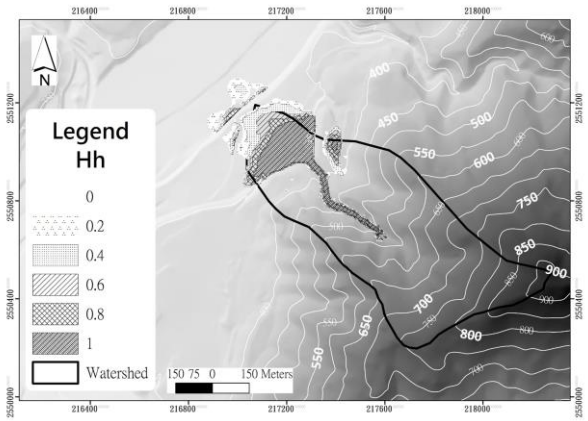

Fig 5. Hazard from landslide deposition depth

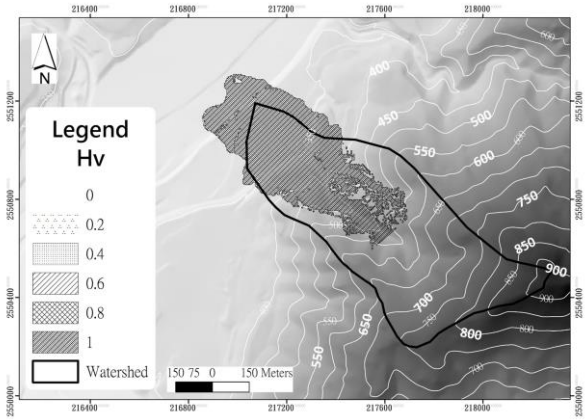

Fig 6. Hazard from landslide velocity

(b) Result of Exposure assessment

The exposure assessment of the Xinkai landslide were shown in **Fig.7** and **Fig.8**. The extent of exposure due to landslide velocity was greater than the extent of exposure due to depth of landslide deposits. This is because, in Eq. 12, we adopted values which corresponded to the maximum velocity that was reached during the landslide. The depth of landslide deposits merely reflects the outcome of the landslide. While the sliding debris of the landslide passed through many grid cells, it was not necessarily deposited there. In other words, the extent of exposure due to landslide velocity equals the extent of the transportation zone plus the extent of the deposition zone, whereas the deposition zone accounts for most of the extent of exposure that results from the depth of landslide deposits.

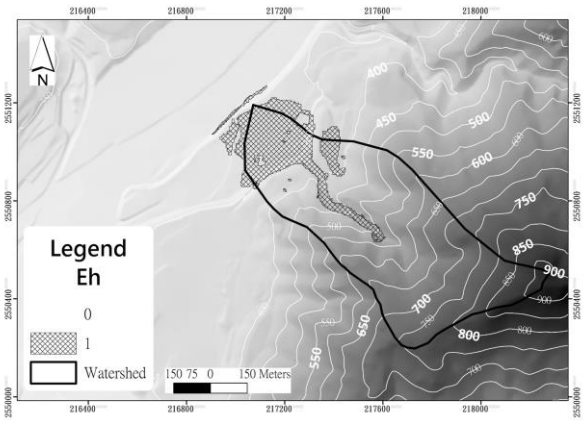

Fig 7. Exposure from landslide deposition depth

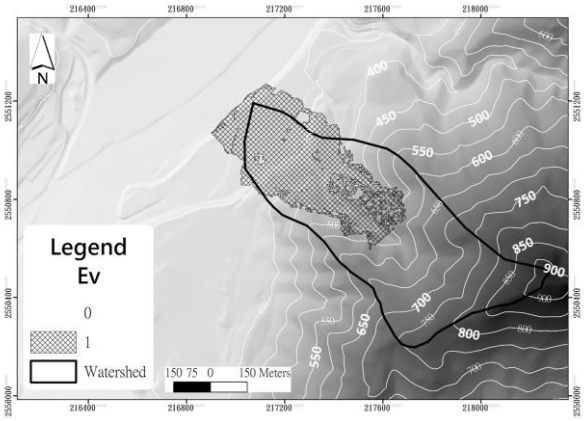

Fig 8. Exposure from landslide velocity

(c) Result of Vulnerability assessment

The vulnerability assessment of Xinkai landslide was shown in **Fig.9** and **Fig.10**. To effectively differentiate the degree of vulnerability of each land-cover type, the weights were set as 0.4, 0.3, 0.2, and 0.1 for buildings, roads, agriculture, and forest, respectively (i.e. buildings have the highest monetary value and forested land has the lowest monetary value). The grid mesh in this study was segmented into 2m×2m square cells. If the land in each grid can only contain a single cover type, the maximum vulnerability value in this study was $V=0.4I_{DR}$, and the minimum vulnerability value was $V=0$.

The building was most vulnerable to landslides. Landslide deposits became shallower further away from the mouth of the valley, whereas landslide velocity did not show much variation. Thus, according to the vulnerability analysis that was performed for depth of landslide deposits, roads on the outer edges of the alluvial fan have moderate vulnerability, while the vulnerability analysis for landslide velocity indicates that roads have high vulnerability.

In **Fig.10** show that the landslide velocity of the

area is very high so that the vulnerability form landslide velocity; on the other hand, some area of oval in **Fig.9** is no color means that the landslide debris passed this area but was not deposited there.

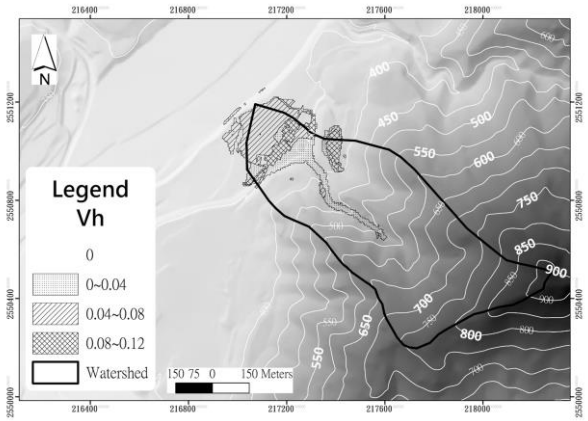

Fig 9. Vulnerability from landslide deposition depth

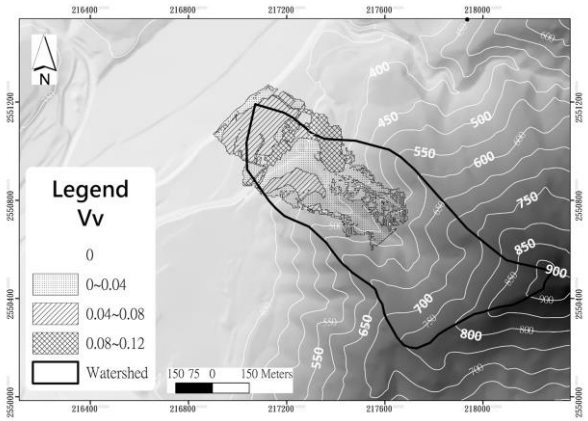

Fig 10. Vulnerability from landslide velocity

(d) Result of Risk assessment

The map of large-scale risk for the Xinkai landslide (**Fig.11**) reveals that most of the high-risk areas occur on the building land-cover type, This is due to greater hazard, exposure, and vulnerability scores that characterize this land-cover type.

The risk was lower in the transportation zone for two reasons. (1) There were no important protected targets in the transportation zone as most of it was forest land. (2) There were no landslide deposits in grid cells which corresponded to the transportation zone; therefore, the hazard from depth of landslide deposits was 0, which lowered the overall risk. The risk was also lower on the outer edges of the alluvial fan due to shallower landslide deposits, lower landslide velocity, and the fact that most of these areas were forested. Therefore, even with the same degree of exposure, areas with lower hazard and vulnerability scores are at lower risk.

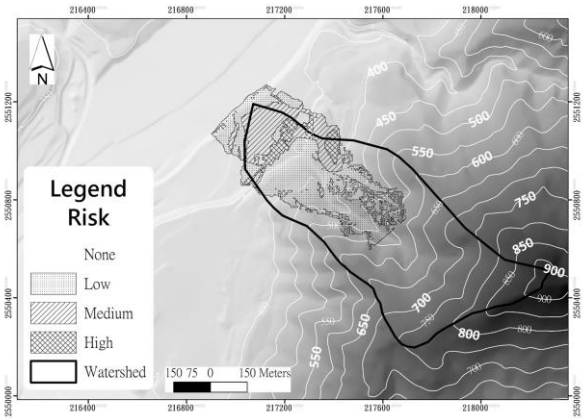

Fig 11. Risk map of Xinkai

4.2 Effect of land use management

Fig.4 shows the land-use adjacent to Xinkai Village before typhoon Morakot. The result of risk mapping before typhoon Morakot (**Fig.11**) is verified by disaster during the event (**Fig.3**), leaving 38 dead and destroying 38 building, which located at high risk level area of assessment result. In addition, this research also discusses the relationship between land-use management and risk map (**Fig.12**, **Fig.13**).

Comparing **Fig.11** with **Fig. 13**, we find there are some differences. For instance, the high and medium risk level were reduced to no risk due to most residents moved out after sediment disaster in 2009, thus the land-use was change from building and farm to barren land. The effect of sabo works is considering in the presented approach as well (**Fig.14**, **Fig.15**). According to **Fig.15** the sabo works can reduce the hazard and exposure of the large-scale landslide as well as the risk.

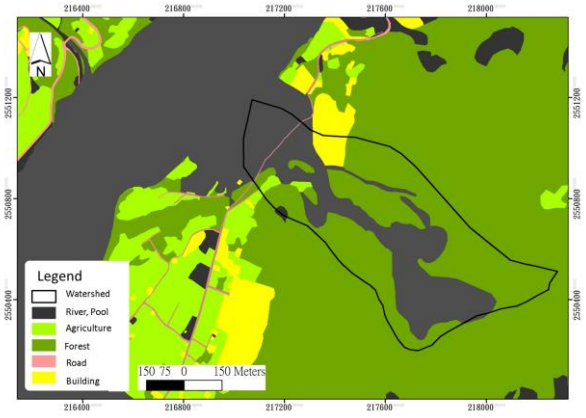

Fig 12. Risk map of Xinkai land use in 2011

4.3 Effect of sabo works

One of the objectives of this study was to propose an approach that can be used to (1) assess the risk of large-scale landslides, (2) effectively compare the risk of large-scale landslides before and after the construction of soil and water conservation

facilities, and (3) provide relevant government agencies with a reference that can benefit soil and water conservation projects. an assessment of risks related to large-scale landslides is applied after soil and water conservation facilities (**Fig.14**) that had been constructed in response to a large-scale landslide that took place in Xinkai.

Four sabo dams were constructed in a stream located in Xinkai Village. The heights of dams (from upstream to downstream) were 35 m, 30 m, 30 m, and 25 m, respectively, and the locations of these dams are shown in **Fig.14**. According to our results (**Fig.14**), the range of landslide deposits after building the sabo dams should be smaller than that in **Fig. 11**, as should deposition depth and landslide velocity. The forest land in the transportation zone is still considered to be at low risk, and the primary land used for buildings at the valley mouth is considered to be at moderate or low risk rather than high risk. The agricultural land near the edge of the alluvial fan is not within the scope of influence and not at risk.

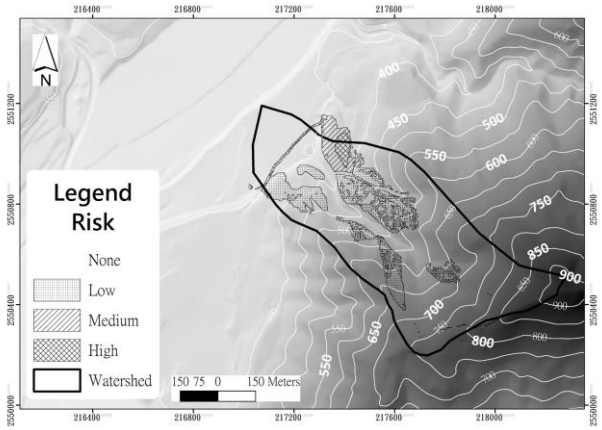

Fig 13. Risk map of Xinkai in 2011

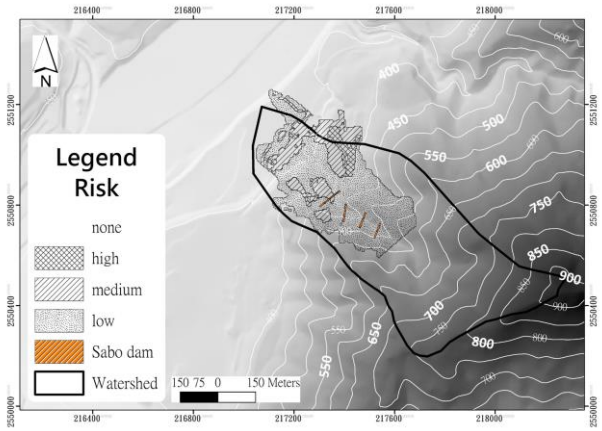

Fig 14. Location of sabo dams in upstream and risk map after completion of sabo works

5. CONCLUSION

The proposal of this study is presenting an approach can evaluate the risk of Large-scale landslide. The presented approach can not only rank the risk for each potential large-scale landslide but also can identify risk distribution in a regional area. In this research we apply the risk index approach, which can help to understand the contribution of hazard, vulnerability and exposure to overall risk is used to evaluate the risk of Large-scale landslide.

Furthermore, this approach considers the effect of mitigation work such as land-use management and sabo work. The result shows that, the potential loss can be well quantify with the approach. Furthermore, the effect of the mitigation work, such as land use managements and sabo works, can be also well described in this approach.

ACKNOWLEDGMENT: We thank the Soil and Water Conservation Bureau of the Council of Agriculture under the Executive Yuan for providing information regarding the Development and Application of Disaster Prevention and Mitigation Technologies for Large-scale Landslides project.

REFERENCES

Australian geomechanics society (AGS), Landslide Risk Management Concept and Guidelines, Australian Geo.

B.Yin Liu, Y.L Siu, Gordon Mitchell, Wei Xu (2016) The danger of mapping risk from multiple natural hazards. Natural Hazards, 82(1)

Egashira S, Miyamoto K, Itoh T (1997) Constitutive equations of debris flow and their applicability, Debris-flow hazards Mitigation. Water Resources Eng Div/ASCE, pp 340‑349

Miyamoto K (2002) Two-dimensional numerical simulation of landslide mass movement. J Jpn Soc Eros Control Eng 55(2):5‑13 (in Japanese)

W.C Lo, T.C. Tsao, C.H. Hsu (2012) Building vulnerability to debris flows in Taiwan: a preliminary study, Natural Hazards, Volume 64, Issue 3, pp 2107–2128.

Yu-Shu Kuo, Yuan-Jung Tsai, Yu-Shiu Chen, Chjeng-Lun Shieh, Kuniaki Miyamoto, Takahiro Itoh (2013) Movement of deep-seated rainfall-induced landslide at Hsiaolin Village during Typhoon Morakot, Landslides 10, 191‑202 DOI 10.1007/s10346-012-0315-y

Topic 3: Structural countermeasures: New technology and strategy

Ten Years' Experience in Flexible Debris Flow Barriers

Corinna WENDELER[1*], Nobuhito NISHIMRUA[2]
and Matthias DENK[3]

[1] Geobrugg AG (Romanshorn, Switzerland)
[2] Geobrugg Japan K. K., Japan
[3] EMDES Environmental Engineering, Switzerland
*Corresponding author e-mail: corinna.wendeler@geobrugg.com

More than 20 flexible ring net barriers for debris flow protection were installed in the last 20 years, in over 25 countries and have been protecting infrastructure, roads and railway tracks from great damage. These flexible ring net debris flow barriers have been in the meantime established as a certified European product, obtaining the CE marking. This contribution relates the evolution of the first real scale testing barriers, leading to standardized barriers up to fully working debris flow barrier projects. Case studies will highlight advantages and challenges of this technology in regards to construction technics, economical aspects and its environmental friendly characteristics.

Key words: debris flow, flexible protection, ring net, CE-marking

1. INTRODUCTION

Since 2005, over 250 flexible debris flow barriers have been installed, in more than 25 countries. Between 2005 and 2008, full scale experiments at the test site Illgraben, in Switzerland, proved the feasibility of retaining debris flows.

The efficiency of some of the first reference projects, mostly installed in Switzerland, was analysed and a load design was then established together with the Forest, Snow and Landscape Federal Institute (WSL). Standard systems were then developed with the simulation software FARO. Data from real-scale testing were used to verify and calibrate the software outputs.

Following this development, the flexible ring nets became increasingly an alternative to classical debris flow barriers in Europe, USA and South America. In large scale projects, where flexible nets were installed in a row in the same channel, the efficiency of retaining large volumes and the feasibility of this type of installation in a row were proven as well.

Flexible nets are appreciated, by designers and engineers, as a practical and economical addition or alternative to existing classical debris flow protections.

Ten years of experience with flexible ring net barriers signify that their advantages have been recognised and their efficiency in the field have been established. The increasing knowledge of single barriers, barriers in a row and large scale barriers have allowed to understand the advantages but also the limits of such a flexible debris flow barrier. This acquired knowledge is presented in the following paper, accompanied by case studies.

2. REAL-SCALE TESTING IN ILLGRABEN, DEVELOPMENT OF STANDARDIZED FLEXIBLE DEBRIS FLOW BARRIERS AND CE MARKING

2.1 Real-scale testing in Illgraben

Between 2005 and 2008, real-scale testing was conducted in the Illgraben debris flow channel, in Wallis, in Switzerland (Wendeler, 2008). Prior testing it was observed that rockfall protection nets were retaining some slides but the dimensioning concept was missing to prove that flexible ring nets could retain larger debris flows in a channel without sustaining damage. In Illgraben, a middle to large debris flow is occurring at least once a year naturally and therefore a flexible ring net could be tested yearly (see **Figure 1**).

Two key characteristics were defined and analysed with testing. On one hand, a single barrier could, depending on the channel geometry, retain

over 1000 m^3. On the other hand, it was observed that over 10'000 m^3 were flowing over the barrier without damage. This led to planning and constructing a debris flow retention system with several flexible nets in a row in order to retain successfully most of the

Figure 1: Testing of debris flow retention system with ring net in the Illgraben channel, 2006. Retention volume approx. 1000 m^3

material.

On the dimensioning side, the weight acting on a debris flow barrier during an event were better understood, thanks to an extensive measuring concept on and around the system (Wendeler, 2006), which lead to the final dimensioning concept (Wendeler, 2008).

2.2 Development of standardized barriers

The dimensioning concept as well as the distribution of the loading on the flexible net were integrated in the finite element software FARO (Volkwein, 2004) and first projects, mostly in Switzerland, were dimensioned with it.

Following the first projects, flexible standardized debris flow barriers were designed with a given load capacity in kN/m^2. VX-barriers are conceived for channels up to 15m in width und barrier height of up to 6m, taking loads up to 160 kN/m^2. UX-barriers find their application in larger channels, are installed with additional posts, a barrier height up to 6m and taking up loads of 180 kN/m^2 (Geobrugg, 2016) (see **Figure 2**).

The dimensioning concept for debris flows is now state of the art and freely accessible through the software DEBFLOW on Geobrugg's website[1]. After registration on the website, everybody can use this software and produce a first estimate for the dimensioning of a barrier.

Figure 2: UX debris flow barrier, with posts for wider stream channels application. Example of the Trachtbach in Switzerland. Additional scour protection, rip-rap and lean concrete were placed along the stream bed.

2.3 CE marking

The real scale testing was also basis for certifying all flexible standardized debris flow barriers. Certification was achieved in 2017 (EAD document Nr. 340020-00-106[2]). The CE marking is based on a "European Assessment Document" which defines precisely the suitability, the type classification and yearly quality controls necessary to correspond to a certain standard. This states that the products with CE marking fulfil the European guidelines for product quality and field appropriateness and allows an unrestricted trade within the European Union (ETA 17/0268-17/0276 and ETA 17/0439).

3. DIMENSIONING

An easy predetermination of the dimensioning of a flexible standardized debris flow barrier up to 6 m in height can easily be performed with DEBFLOW. A more complicated scenario can still be dimensioned by Geobrugg or WSL with FARO simulation software. A few special cases in regards to construction are described in the section 6.

3.1 Special load case scenario such as snowslides and rockfall

In certain cases, mostly very steep slopes (>35°) and at high altitude, snow slides, small avalanches or rockfall will be encountered, which could or will impact the debris flow barriers.

An example of this situation is the multiple barrier setup in Hasliberg in Switzerland. Some of the barriers are situated above 2000m in elevation. Since flexible net barriers are also used as a protection against avalanches and rockfall, a certain degree of combined loading can be guaranteed. The combined loading can be calculated and a barrier dimensioned for every special case with the use of FARO

simulation software (Volkwein, 2004). Specific components of the debris flow barrier can be individually reinforced depending on the simulation results (Wendeler, 2014).

Figure 3 illustrates the simulated load case for barrier number 2 in Hasliberg in a situation of a lateral avalanche impact, with an angle of 10° and a load of 120 kN/m^2. In this special case, the upslope guy wires are loaded up to 70% of their capacity. **Figure 4** shows snow load on the barrier in winter.

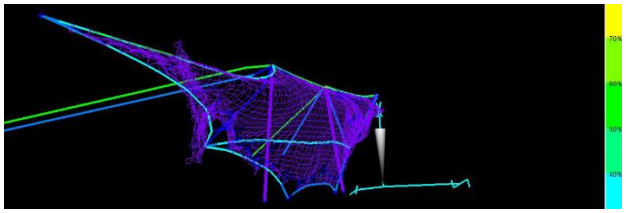

Figure 3: FARO simulation software output when barrier number 2 is impacted by an avalanche in Hasliberg, Switzerland.

Figure 4: Same net than in figure 3, partially snowed in during winter. The snow load has to be taken into account when designing the barrier.

4. CONSTRUCTION ASPECTS

4.1 Subsurface and anchoring

While the netting itself is easy to model and to dimension, safe anchoring is more complicated.

Ideally, a detailed geological profile of the section to be protected is available as well as the geotechnical parameters of the subsurface. Having the possibility to perform pulling tests on the soil nails to assess the friction between the subsurface and the grout is another advantage.

Debris flow deposits are heterogeneous in nature and deposited along the sides of the channel affecting the subsurface quality for anchoring. The dimensioning of anchor forces need to be determined by experts in those cases. It is as well recommended to use self-drilling anchors with a flexible anchor head. The barrier when loaded is largely deformed and the forces of the ropes on the anchors can change up to 30° in angle. This eccentricity without flexible anchor head is often not bearable for a normal threaded anchor since the pushing resistance is much smaller than the pulling component.

4.2 Reuse of the anchoring after a debris flow event

Without additional flank stabilisation, a certain degree of washing out can be observed along these stream banks, especially in loose soil (see **figure 5**).

When exchanging the net, the anchoring can technically be reused when the top of the anchor is cut off, a loading test is performed and a new flexible anchor head is mounted. Assuming that the anchor length was drilled the first time with a safety factor and possesses a certain length in reserve. In the case of frequent filling of the net it is recommend to design the anchors with sufficient length or to prevent the washing out of the banks with structural countermeasures.

Figure 5: Washed out anchoring of the debris flow barrier number 25 in the Illgraben channel. Anchoring partially in loose material and partially in disused concrete debris flow barrier.

4.3 Structural countermeasures: protection of the banks in stream bends

Especially in bends along the stream, the washing out of the outer bank and its erosion are prevalent when a debris flow occurs. The amount of erosion is dictated by the volume and the velocity of the flow. Depending on the project a reinforcement of the outer bank should be considered (rock blocks, wall, gabions or additional flank stabilization by netting with or without erosion control mats (see **Figure 6**)).

It is important to consider that the shearing forces of a debris flow are much higher than of water and this has to be incorporated in the design calculation for the protection measures.

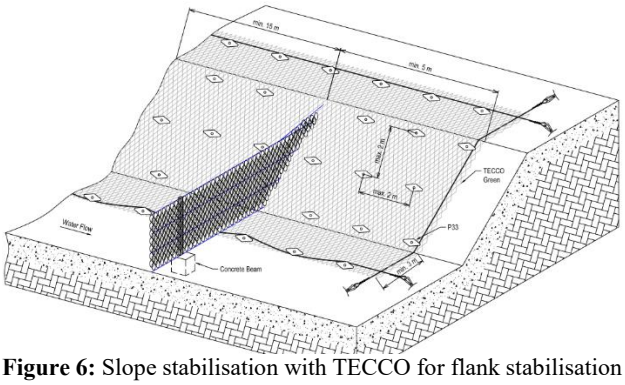

Figure 6: Slope stabilisation with TECCO for flank stabilisation when installing a debris flow barrier in loose material.

4.4 Scour protection

Scouring occurs around construction base or posts due to sediment erosion and leads to scour holes which directly affects the construction stabilisation. When barriers are filled or partially filled, the stream flow passes at its lowest level. Optimally the lowest level is at the cross-section centre of the flexible net system and the flow path stays within the original stream bed. Since the optimal case does not always exist, stream flow path passes lateral at the flank side and erodes material around the construction base or posts. This is especially important for barriers retaining a debris flow in an open field rather than in the stream bed itself. To avoid scouring, flank stabilisation with a rock wall became established and anchored rock blocks as well as rip-rap and lean concrete along the stream bed (**Figure 2**). Further, it has to be considered whether a field needs an artificial channel back to the original stream underneath the flexible net system, in case of lateral stream flow paths.. When choosing rock walls as solution flexible net system dimensioning further downstream should take into account the possibility of these rock blocks getting torn away. The additional load being potentially fatal to the barrier.

5. PLANNING ASPECTS

Often debris flow barriers are installed close to the source zone of the debris flows while greater structural measures such as a retaining basin or deviation measures are constructed further down.

Flexible net barriers and large steel and concrete construction can therefore be perfectly combined. The advantages of both methods can be specifically used together. An example of this combination are the streams Trachtbach in Brienz and Milibach in Hasliberg, both located in Switzerland. In both projects, the combination of the nets upstream and the larger construction measures downstream allowed to increase the retained mass upstream and diminish erosion in the stream bed.

Therefore the capacity of the concrete protection measures could be lowered and constructed at smaller scale and existing protection structures were easily and cost effectively renovated and added to the protection measures series.

5.1 Flexible net barriers as an immediate solution

Flexible net barriers installed in the source zones of debris flows, slow these down, which allows for longer warning and evacuation time in the endangered areas. This is especially of importance in small catchment zones where debris flows are rapid and travel along short distances only.

The easily installed flexible net barriers are therefore practical for an immediate protection solution. They increase the safety of the infrastructure downstream and even allow for the protection of the construction crew building a retaining basin for example. These protection nets can be equipped as well with a warning system (more details are given in section 7).

5.2 Visual and landscape protection aspects

Debris flow barriers instead of concrete dams are more and more an alternative in regards to landscape protection and visual aesthetics. The filigree design is almost invisible from far away and a primary argument for protection measure construction in landscape protection zones.

An example is the Unesco World Cultural Heritage along the Rhine close to Koblenz (**Figure 7**). At the back of the village debris flow barriers are installed and even with one barrier partially filled in 2017, the nets are still barely visible but fulfilling their purpose (**Figure 8**).

Figure 7: Almost invisible debris flow barrier close to Koblenz along the Rhine above an Unesco World Culture Heritage protected village.

Additionally, environment friendly building and sustainability is more and more an important

argument for construction. For example, a debris flow barrier (ten by 4 meters) is 30 times lighter than a concrete barrier of the same dimensions, making it the 'greener solution'. On top of that with less weight, less carbon dioxide is emitted during transport to site (Wendeler, 2008).

Figure 8: Partially filled debris flow barrier above the German Railway close to Koblenz.

5.3 Passage for small animals and greening

The relatively large openings of the ring nets allow for passage of small animals, when the barrier is not filled, even fishes when the barrier is immersed in water, in contrast to a concrete structure (Wendeler, 2008). There are examples where this was an expressed wish of the developer. Ring nets are as well appropriate for greening and blend perfectly into the landscape.

6. DIFFERENT TYPES OF DEBRIS FLOW BARRIERS

6.1 Single barriers

Figure 9: Debris flow barrier in Isenflue above a settlement. The outer bank of the stream was reinforced with a rock wall.

Most barriers installed are single barriers along roads and railway tracks or above settlements (see **Figure 9**).

6.2 Barriers in a row (multi-level barriers)

Debris flow nets can be installed in a row, to increase the retained volume. The first mutli-level barriers were installed in Merdenson in Switzerland for observational purposes by the WSL (Denk et al., 2008).

Subsequent laboratory tests to analyse the overflow behaviour, and more specifically the overflow velocity evolution during a flow, confirmed the developed load design for multi-level barriers (Wendeler et al., 2010).

Examples for this setup are the multi-level barriers in Hasliberg (Wendeler et al., 2014) in Switzerland but also in Portainé in Spain (Luis et al., 2010) as well as Ana Chosica in Peru.

Most of the multi-level barriers have already been successfully filled during events (see **Figure 10**). Chosica is the most recent example in 2017, protecting efficiently several cities built downstream (see **Figure 11**).

Figure 10: 11 debris flow protection barriers, successfully filled in Hasliberg in 2011.

Figure 11: Filled debris flow barrier in 2017 in Peru, protecting successfully a large city downstream.

6.3 Large debris flow retention with single barrier (special construction)

In special cases an adapted design higher than 10m and larger than 40m can be constructed. A typical example is the debris flow barrier in Hüpach, next to Oberwil in the canton Berne in Switzerland (Berger et al., 2016).

This barrier has a retaining capacity of more than 12'000 m^3. Such a construction necessitates strong abutments of steel reinforced concrete, long anchors and needs special ropes used for cable cars which need precise adjustment (see **Figure 12**). Special calculations for the netting and the ropes, adjustment to the anchoring and special foundation engineering in exposed terrain was necessary to complete the project. The decision to install a large retaining structure with netting was based on the topography, the difficulty of access and lack of alternatives to protect the village below. The debris flow barrier has not been filled yet.

Another special construction is situated in Sitäbach along the stream Lenk, in Switzerland. The construction is based on concrete slices and netting in between (see **Figure 13**).

Figure 12: Special construction of a debris flow barrier in Hüpach, in Switzerland, with a width of 40m and a netting height of 10m.

Figure 13: Another special construction acting as a debris flow barrier in Sitäbach consisting of concrete slices piled up and netting mounted in between.

7. SURVEILLANCE

Flexible debris flow barriers can be monitored with sensors (Sentinel System). In larger systems, some components can be monitored such as the ring brakes and when a loading threshold is reached, an alarm is triggered.

An example is the debris flow barrier, installed as an immediate protection solution, in Magnacun in Switzerland. The railway tracks of the Rhaetian Railway are perfectly protected since 2009, with the surveillance system working faultlessly, according to the developer.

8. MAINTENANCE AND CLEANING OF BARRIERS

As any protection structure, debris flow barriers require maintenance from time to time. It is recommended to undertake regular, for example yearly, checks of the protection system if no event (debris flow, slides, …) occurred during that time span. Working with a checklist and a maintenance scheme, such as for any other protection structures, should facilitate regular controls.

After an event, the barrier needs emptying and replacement of certain components. A filled barrier can for example be cleaned from behind with an excavator. It is essential, when planning for the system, to consider what happens to the material of the debris flow and to organise a deposit area. Budget wise, it has to be considered that after a fully filled barrier, parts have to be replaced, whereas the anchoring can often be reused, as explained earlier.

A net can be emptied from the front when certain conditions are fulfilled. The material of the debris flow has to be dry and stable and the netting has to be stabilized upslope and safety aspects for the working crew have to be respected.

9. ADVANTAGES AND LIMITS OF FLEXIBLE NETTING FOR DEBRIS FLOW PROTECTION

The main advantages of these systems is their relative low weight and rapid installation. Especially in steep and in terrain difficult of access. The material can be transported with helicopters wherever construction machines cannot reach the site or where it would not be economical.

Ring nets can be used for immediate protection in endangered zones to safeguard the construction of a permanent structure below. These practices are common for example in Japan. Ring nets can therefore be incorporated in an overall protection

concept for an entire catchment area.

At the same time it has been proven over time that ring net barriers are fully equivalent to large concrete structures when properly planned, with an erosion control concept and an established maintenance plan.

Obviously in easy access areas with high frequency of debris flows, permanent concrete structures are to be favoured as they are more economical in such a particular case.

10. CONCLUSIONS

Since the publication of the load design of flexible debris flow barriers and their appropriateness tests in the Illgraben in Switzerland, many projects have been successfully installed in the last 10 years.

Several construction details have been revised and improved. When taking into account the hydrological processes affecting the stability of the stream banks and planning for reinforcement, the flexible ring net systems can be considered as equivalent to classical large concrete protection structures. To prevent steel corrosion the used flexible net system has a zinc- aluminum coating. For more restrictive corrosion conditions, other solutions such as stainless steel or a thicker coating layers are options for longer lifetime guarantee. Therefore no material disadvantage is evident compared to concrete barriers. Further, the lighter conception of the barriers make it an unavoidable solution when easy handling, environmental requirements and landscape protection are key issues of a project.

The dimensioning concept developed at the WSL, in use worldwide, has been verified by several filling and successfully retaining events. A further adaptation and refining of the dimensioning concept could be achieved with more testing, but is hampered by lack of funding.

REFERENCES

Berger C., C. Wendeler, L. Stieglitz and G. Lauber (2016): Examples of debris retention basins combining concrete and net structures, Interpraevent Luzern, Switzerland.

Denk M., A. Roth, C. Wendeler und A. Volkwein (2008): 1:1 Feldversuche für flexible Schutznetze gegen Murgang – Versuche, Bemessung, Anwendung, Publikation für die Technische Akademie Esslingen, Deutschland.

Geobrugg (2016): Ringnetzbarrieren aus hochfestem Stahldraht: Die ökonomische Lösung gegen Murgänge, Schweiz.

Luis-Fonseca R.., C. Raimat, J. Albalate and J. Fernandez (2010): Protecion contra Corrientes de derrubios en areas del Pirineo. Obras Urbanas, Julio/Agosto 2010 numero 22, Spain.

Speerli J., R. Hersperger, A. Roth and C. Wendeler (2010): Physical modeling of debris flow over flexible ring net barriers, Conference on Physical Modelings in Geotechnics ETHZ, Switzerland.

Volkwein A. (2004): Numerische Simulation von flexiblen Steinschlagschutzsystemen, Dissertation ETHZ, Schweiz.

Wendeler C., B.W. McArdell, D. Rickenmann, A. Volkwein, A. Roth and M. Denk (2006): Testing and numerical modeling of flexible debrs flow barriers. In Zhang, M. and H. Wang (eds.): Proc. Of the sixth International Conference on Physical Modeling in Geotechnics, pp. 1573-1578. Balkema.

Wendeler C. (2008): Murgangrückhalt in Wildbächen – Grundlagen zu Planung und Berechnung von flexiblen Barrieren, Dissertation ETHZ, Schweiz.

Wendeler C., J. Glover (2014): Multiple load case on flexible shallow landslide barriers – mudslide and rockfall, IAEG Conference Turin, Italy.

Wendeler C., A. Volkwein, A. Roth and N. Nishimura (2014): Successful hazard prevention using flexible multi-level barriers, Interpraevent in Nara, Japan.

[1]:https://www.geobrugg.com/en/Welcome-to-myGeobrugg-79860.htmlintegriert)

[2]:http://eur-lex.europa.eu/legal-content/DE/TXT/PDF/?uri=CELEX:52017XC1013(01)

Assessing Torrential Endangered Areas in Bavaria - Consideration of Log Jams at Culverts and Bridges -

Peter DRESSEL[1], Peter WAGNER[2] and Andreas RIMBOECK[2*]

[1] Engineering consultants aquasoli (Haunertinger Str. 1a, 83313 Siegsdorf, Germany)
[2] Bavarian Environment Agency (Buergermeister-Ulrich-Str. 160, 86179 Augsburg, Germany)
*Corresponding author. E-mail: Andreas.rimboeck@lfu.bayern.de

According to the Bavarian Water Act there is an obligation for the water management authorities to determine torrential endangered areas. In a legal sense these areas are primarily potential flood areas however under consideration of typical torrential characteristics. Especially the involvement of solids has to be regarded. In order to enable a systematic and transparent determination of the design event, a standardized modular approach to assess torrential hazards was developed at the Bavarian Environment Agency. In the approach bedload and woody debris are being considered as two separate components. Bedload is considered as a surcharge added to the design hydrograph (100-year discharge). Problems resulting from woody debris in relevant zones (areas of spatial planning) are individually evaluated during hazard assessment. A method which quantifies the potentially accumulating woody debris in the torrent catchment area was developed for this purpose. On this basis, the dangers for log jams at the particular structures are categorized. Subsequently hydraulic calculation is done with a 2D hydraulic model.

Key words: woody debris, log jam, risk assessment, 2D hydraulic modeling

1. TORRENTIAL ENDANGERED AREAS

Subject to Article 46 of the Bavarian Water Act, water management authorities are obliged to determine torrential endangered areas. They further have to be legally set as regulation by the district office. Torrential endangered areas are floodplains inundated by a 100-year-flood taking into consideration the characteristics of torrents (design event).

In the determination of torrential endangered areas solid materials like bedload and woody debris play a decisive role in the modular system applied. The Bavarian Environment Agency identified resp. developed standardized state-of-the-art methods to deal with these issues.

This paper focuses on the role of woody debris in the procedure of determining torrential endangered areas. Consistent with the practice in flood-endangered areas and floodplains the areas affected by torrential events of high as well as low occurrence probability are displayed in the form of susceptibility maps. Apart from temporarily high discharge, particularly the involvement of solids in the process is regarded as distinctive for torrents.

2. WOODY DEBRIS IN HAZARD ANALYSIS

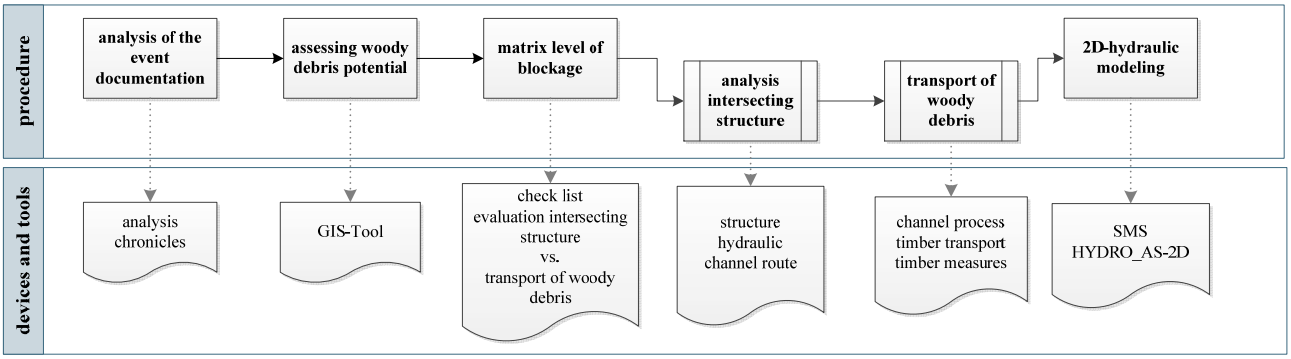

Fig. 1 Overview of the work steps to assess woody debris in torrent endangered areas

Possible hazards due to woody debris are evaluated in line with the hazard analysis of torrential catchments. The term “woody debris” covers all wood being transported in the water during a flood event. At both natural and artificial constrictions this can lead to log jams causing tremendous damage in housing as well as industrial areas. Hereafter the standardized procedure for considering woody debris in hazard analysis is outlined in **Fig. 1**. Following the steps are described in detail.

2.1 ANALSYING THE EVENT DOCUMENTATION

Initially an evaluation whether woody debris played a role in past events and whether it lead to problems has to be carried out. Further it has to be examined if the problem is still relevant or if any further hazards have to be considered. Only if the preliminary works show indications for an endangerment by woody debris, it has to be considered in the following.

2.2 ASSESSING WOODY DEBRIS POTENTIAL

2.2.1 Status quo

So far the quantity of woody debris was either calculated using empirical formulas or estimated by experts in the course of a field survey of the catchment. Whereas the first holds major uncertainties, the latter is time consuming. Other methods such as the “Aerial photograph-based procedure for the estimation of woody debris potential in torrential catchments” developed by [Rimböck 2001] have to be adapted due to technical innovations.

Now, an extensive data base is available which can be used to quantify woody debris potential. Among the data are hazard susceptibility maps, maps on potential geological hazards, forest data and slope inclinations. They are all digitally available and can be displayed in a GIS.

A new approach is represented by a GIS-tool invented by the Bavarian Agency Administration using the data stock systemically to provide a first estimation. This should be verified or falsified in the following (obligatory) field survey.

2.2.2 Quantification of woody debris potential

Initially the quantification of woody debris potential is achieved using a specifically programmed GIS-tool and finishing with an Excel-spreadsheet. The approach developed for this purpose is depicted in **Fig. 2**. The required workflow consists of the following steps which are commented on below [Meyer & Rimböck 2014].

(a) Collection of input data
(b) Automated GIS-based data processing using the woody-debris-tool
(c) Calculation of woody debris potential using the Excel-spreadsheet

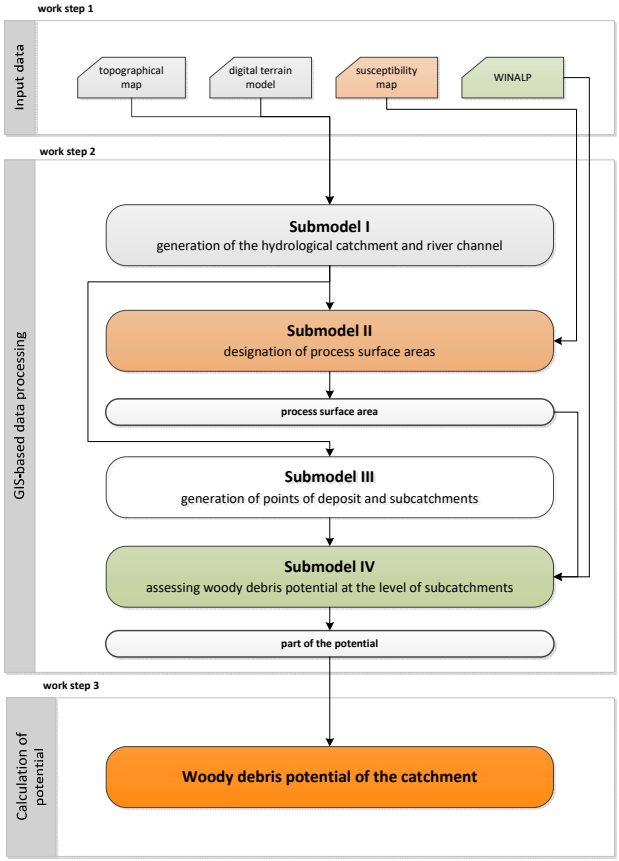

Fig. 2 Basic concept of GIS-based estimation of the amount of woody debris: Delineation of input data, model parts and intermediate and final results

2.2.3 Input data

The first step is the compilation of input data. The following data is used in the GIS-analysis:

- Topographic map (scale 1:25’000): Definition of a coarse frame of the catchment boundaries and the basin drainage point
- Digital elevation model (DEM) with a resolution of 5 x 5 m
- “Susceptibility map geological risks” of the Bavarian Alps (scale = 1:25’000): provides information on areas endangered by landslides
- WINALP-map [Reger and Ewald 2011], (scale = 1:25’000): provides information on forest types within the torrential catchments; growing stocks of wood are assigned to the different forest types based on physical inventory data

2.2.4 GIS-based data processing

The GIS-tool automatically identifies the woody debris potential for each partial catchment (in general for each 1000 m of channel length) based on the design event. The automatic data processing is carried out in the following 4 steps resp. submodels:

Submodel I – identification of the hydrological catchment and river channel

Based on topographic maps the relevant area is roughly located and the basin drainage point is defined. The basin drainage point is the position where discharge from the catchment is fed into the 2D hydraulic model. The 2D hydraulic model usually covers building areas or land that is potentially suitable for housing and/or economic activities.

In the second step, the hydrological catchment is automatically identified on the basis of the digital elevation model (DEM), the rough catchment boundaries and the basin drainage point.

Further the stretch of river relevant for woody debris transport is identified. For this purpose only those stretches are considered where woody debris transport is possible. **Fig. 3** shows the result of the analysis by *Submodel I.*

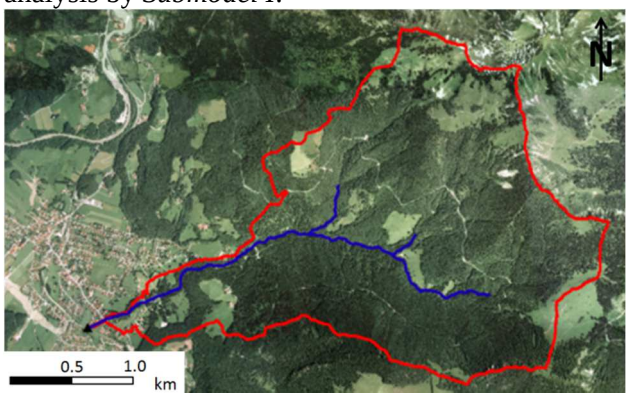

Fig. 3 Hydrological catchment (red) and river stretches relevant for woody-debris-transport (blue). The black triangle marks the previously defined basin drainage point

Submodel II – determination of process areas

The areas from which woody debris can be brought into the channel in case of an event are identified as process surface areas. In *Submodel II* these areas are disclosed by blending and analysing extensive geospatial data covering all topics relevant for woody debris transport.

Therefore the following important processes according to [Rickli and Bucher 2006] are considered, which have been implemented into the woody debris GIS-tool. Each can optionally be deactivated if not appropriate for a particular location.

a) Erosion of forest covered riverbanks
b) Bank erosion
c) Landslide
d) Windthrow

Erosion of forest covered riverbanks: This process is restricted to a narrow zone accompanying the riverbanks. The corresponding process areas are generated using a buffer representing the channel width at flood discharge. The flood channel width is set to 10 m as default. It can be adjusted manually if further information is available from hydraulic simulations.

Bank erosion: Areas where bank erosion is possible are normally part of the default flood channel width of 10 m (see above). Bank erosion zones beyond this extent have to be added manually (cp. **Fig. 5**). In these cases the model doubles the buffer width and a 20 m width is regarded.

Landslide and debris flow: The areas affected by landslides and debris flows mapped in the susceptibility maps of the Bavarian Alps constitute the basis for the identification of landslide-related process-areas. The woody debris GIS-tool selects those landslide and debris flow deposits reaching the channel sections as relevant for woody debris transport.

Windthrow: Storm events can cause the input of woody debris into the channel from the adjoining slopes up to a distance of one tree-length [Handschin and Duss 1997]. At steep slopes logs from a distance of up to two tree-lengths can reach the channel. The identification of the affected areas is achieved automatically by generating slope angle classes based on the DEM.

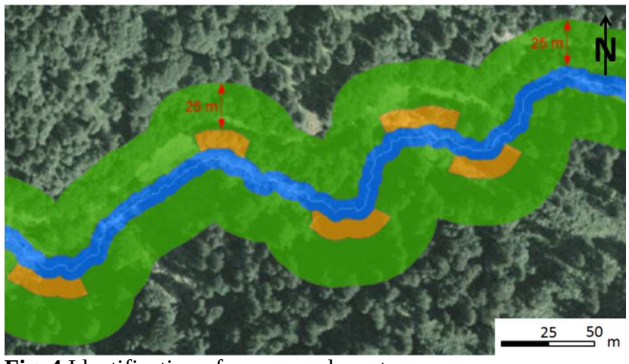

Fig. 4 Identification of process-relevant areas: Windthrow-affected areas with a distance of one tree-length from the channel are depicted in green. The areas related to erosion of forest covered riverbanks are shown in blue. Bank erosion related-areas are plotted in orange. In this example, no landslide reaches the channel

Submodel III – generation of potential woody debris deposits and subcatchments

In order to model transport and deposition of woody debris, *Submodel III* automatically creates deposition points at intervals of 1.000 m along the channel section relevant for woody debris transport (cp. **Fig. 5**). It is additionally possible to choose

known constrictions or deposition zones manually. These points are subsequently used for the identification of subcatchments.

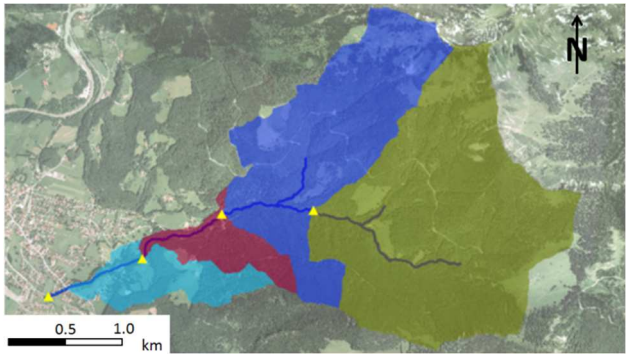

Fig. 5 Generating the subcatchments based on the deposition points (yellow point symbols)

Submodel IV – assessing woody debris potential for the subcatchments

Submodel IV (cp. **Fig. 6**) assigns the process-related areas from *Submodel II* to each subcatchment derived in *Submodel III*. Eventually the relevant areas are multiplied with the corresponding stock-of-wood data from the WINALP-dataset. As a final result the GIS-woody-debris-tool provides a dbf-file for each subcatchment. The file contains the woody debris potentials of each input process and can be directly calculation.

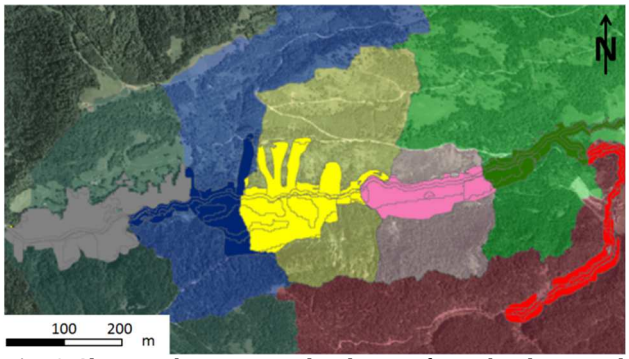

Fig. 6 Clipping the process-related areas from the designated subcatchments

2.2.5 Excel-spreadsheet for estimating the woody debris potential

The scoring sheet templates contain the woody debris potentials of each subcatchment. These potentials calculated using the GIS-tool are multiplied in the Excel-spreadsheet with process- and region-specific reduction factors. In order not to overestimate the quantity of wood being mobilized and transported, all processes involved are weighted by an appropriate factor.

Among the crucial factors for a reduction is that not the whole woody debris potential gets mobilized and delivered into the channel during one event. The reduction factor considers the geological, geomorphologic, topographic and silvicultural conditions within the catchment. Further not every process-related area (e.g. landslides or bank erosion) will be activated during a single event. Due to remaining uncertainties in choosing the reduction factors it is recommended to examine three different scenarios of frequent, average and rare occurrence.

In the last step the probability for transport resp. deposition is considered: Only a certain percentage of the woody debris is transported from one subcatchment to the next one downstream (default setting: 80 %). The rest is either deposited within the subcatchment or disintegrated into smaller pieces so it no longer represents a hazard.

The weighting factors hold enormous degrees of uncertainty leading to the result only being an indication. Only woody debris of natural origin finds its way into the model described. Man-made sources of woody debris like timber yards or forest residues disposed of into the channel have to be added manually into the model.

2.3 EVALUATION OF EVENT DOCUMENTATION

The documentation of events gives hints whether the regarded bridge is prone to log jams or not. If log jams have been observed previously and neither the bridge's construction has been changed nor any wood retention measures have been built since, blockage has to be considered at the regarded location. The level of blockage is to be determined using the matrix described in *chapter 2.4*. A minimum level of blockage of 25 % is to be applied in these cases.

If the event documentation can be considered as complete and comprises at least 2 events in the range of a design event and no log jams have been recorded, the risk of the bridge being blocked by woody debris can be considered as negligible.

In cases when no log jams are recorded at a certain bridge or culvert, but it is uncertain how far the event documentation can be trusted, the matrix described in *chapter 2.4* is to be applied without limitations.

2.4 MATRIX LEVEL OF BLOCKAGE

The specific woody debris load determined by the GIS-tool does not allow drawing conclusions on the probability of a log jam on its own. Thus both aspects – woody debris transport and the characteristics of the intersecting structures – have to be rated.

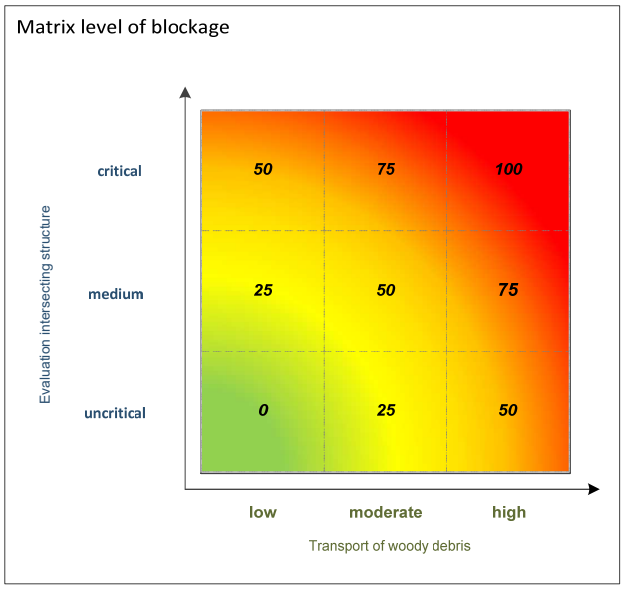

Fig. 8 Matrix level of blockage for 2D hydraulic modeling: Combination between evaluation intersecting structures (y-axis) and transport of woody debris (x-axis)

Assessing the interaction of these aspects by means of a matrix designed for this purpose allows determining the grade of closure needed for subsequent 2D hydraulic simulation. The grade of closure characterizes the decrease of the bridge's cross section.

2.4.1 ANALYSING INTERSECTING STRUCTURES

- intersecting structure
- hydraulics
- channel route

2.4.1.1 Intersecting structure

In most cases, the first bridge within the hydraulic model poses the highest risk for being jammed by woody debris compared to bridges further downstream [Gschnitzer et al. 2014]. Corners, rims, sharp bends and structural elements protruding into the stream channel increase the risk of log jams at constructions. The same applies to pipes protruding into the channel section on the upstream-facing side of the bridge.

2.4.1.2 hydraulics

A first hydraulic simulation is done with the design hydrograph (100-year discharge) including bedload surcharge. This calculation provides important data for evaluation of the risk of log jams. Apart from the degree of freeboard, relative flow depth and the Froude number have to be categorized as well (cp. **Fig. 9**). Knowledge of the freeboard during a 100-year event can be considered as a key element in hazard evaluation. A freeboard of less than 0.5 m is to be considered as critical. Furthermore relative flow depth and Froude number obtained in the 2D hydraulic simulation provide valuable information and have to be classified into one of the three classes uncritical, moderate or critical.

structure	Disposition at modeling sector	bridge with greater/similar log jam risk above		first bridge in the model space
	inner width B	$B > b_W$	$B = b_W$	$B < b_W$
	typ of bridge	bridge with plate		arch bridge, girder bridge, framework bridge
	bridge pier	no pillar		one/more pillar(s)
	supply line(s)	none		below design level
hydraulic	freeboard Fb	≥ 1.0 m	1.0 – 0.5 m	≤ 0.5 m
	relative depth of flow h/H	< 0.5	0.5 ≤ 0.75	0.75 ≤ 1
	froude-number Fr	< 1		≥ 1
channel-route	free surface-width b_W upstream$_O$	$b_{WO} < B$	$b_{WO} = B$	$b_{WO} > B$
	free surface-width b_W downstream$_U$	$b_{WU} = B$	$b_{WU} > B$	$b_{WU} < B$
	channel bottom structure upstream	slick, fastened		raw, unsurfaced
	channel bottom structure downstream	slick, fastened		raw, unsurfaced
evaluation - structure		**UNCRITICAL**	**MEDIUM**	**CRITICAL**

Fig. 9 Evaluation intersecting structure

In the course of hazard assessment, the intersecting structure has to be classified concerning the risk for a potential log jam. The following three aspects have to be considered (cp. **Fig. 9**):

2.4.1.3 Channel route

A continuous stream channel near the culvert reduces the probability of woody debris getting

stuck and thus causing a log jam. On the contrary expansion or narrowing of the channel section as well as drops in the channel increase the probability of log jams due to the varying flow conditions and hydraulic framework conditions.

2.4.2 TRANSPORT OF WOODY DEBRIS

In order to assess woody debris transport a representative stretch of about 1 km upstream of the intersecting structure can be taken as reference for estimating timber sizes. For hazard analysis a log length (L) corresponding to the minimum channel width along the representative stretch (b_{wo}) can be chosen as reference value [Stetter 2015]:

$$L \cong b_{wo} \qquad (1a)$$

Furthermore the following aspects have to be evaluated (cp. **Fig. 10**):

- channel (flow) process
- wood transport
- wood dimensions

2.4.2.1 Channel process

The category channel process evaluates process type, disposition and the relevant framework conditions for woody debris transport. For this purpose, the supposed flow process in the torrent is essential. Discharges featuring strong turbulences lead to frequent collisions of woody debris with the channel bed and the channel banks. This increases the probable occurrence of log jams. The classification of process type is hierarchically arranged as follows: Flood and fluvial sediment transport, hyperconcentrated flow and debris flow.

Another factor covers the classification of the intersecting structure. It is to be classified according to the channel's gradient. Further the bank vegetation has to be assigned to a certain category. The method takes the effects of different habitats into account. Stem-forming bank vegetation tends to trap woody debris, thus holding it back and preventing further transport. Shrub vegetation fulfills this function as well but to a much lesser degree.

2.4.2.2 Wood transport

The parameter wood transport is significantly controlled by the amount of wood being transported, channel routing, channel roughness and course of the longitudinal section. For this purpose, the flow conditions are to be evaluated concerning their homogeneity. Due to frequently changing hydraulic conditions, highly braided channels tend to transport logs with a less critical length compared to stretched channels with nearly constant flow velocities.

2.4.2.3 Wood dimensions

Finally woody debris size (length and diameter) as well as local and hydraulic framework conditions affect the risk of jamming. The maximum length of the logs can approximately be estimated taking the minimum channel width upstream of the bridge as a reference. A minimum flow depth (h) of half the logs' diameter (d) is required for woody debris transport to begin [Imhof 2008; Lange & Bezzola 2006].

$$h = \frac{d}{2} \qquad (1b)$$

2.5 2D HYDRAULIC MODELING

The determination of the torrential endangered area is achieved by a 2D hydraulic simulation of a 100-year event using the program Hydro_AS-2D. By default a simulation of the basic scenario without

channel process	typ of process	flood – fluvial sediment transport	debris flood/hyperconcentrated flow	debris flow
	equivalent friction angle	≤ 10 %	10 – 30 %	≥ 30 %
	stream bank vegetation	stem forming growth	shrub vegetation	hardly growth
timber transport	woody debris potential (GIS-Tool)	≤ 20 m³/m²	20 – 40 m³/m²	≥ 40 m³/m²
	alignment	highly curved	slightly curved	streched
	channel roughness	rough		slippy
	long profile	drop structures	stepped	uniform
timber-measures	tree length L	$L \geq b_{WO}$		$L < b_{WO}$
	stem diameter d	$d/2 \geq h$		$d < h/2$
	root plate diameter d_W	$d_W \geq h$		$d_W < h$
evaluation - transport of woody debris		**LOW**	**MODERATE**	**HIGH**

Fig. 10 Classification of woody debris transport

any log jams or sediment accumulation is carried out. A maximum of two further scenarios considering log jams, sediment accumulations or both can be taken into account and simulated. Additional scenarios only should be considered if they most likely occur during a design event.

The level of blockage defined in the previous steps has to be considered appropriately. Depending on the channel course two configurations are to be distinguished. In curved channel courses, the log jam is incorporated into the model by moving the bridge's outer abutment into the channel bed. In stretched channel courses, the lowest line of structure is lowered by the amount needed to reproduce the level of blockage. The reduced channel section makes it possible to show effects of the log jam on the extent of the flooded area.

The method of determining the level of blockage and the subsequent implementation into the hydraulic model is illustrated in the following case study.

2.5.1 Case study Weisslofer, Reit im Winkl

The bridge at Entfelderstrasse is the third bridge in the local area of Reit im Winkl (Upper Bavaria) crossing the Weisslofer river (see overview in **Fig. 11**). It is thus not regarded as the most critical one in the hazard assessment. Nonetheless, it is still capable of posing problems since there is no woody debris retention and the bridges further upstream did not show a high probability of jamming and thus holding back incoming woody debris. Between the last bridge further upstream and the bridge at Entfelderstrasse the Weisslofer's outer bank runs along a wooded hillside toe for about 700 m. If bank erosion occurs along this stretch, woody debris is expected to accumulate at the bridge at Entfelderstrasse.

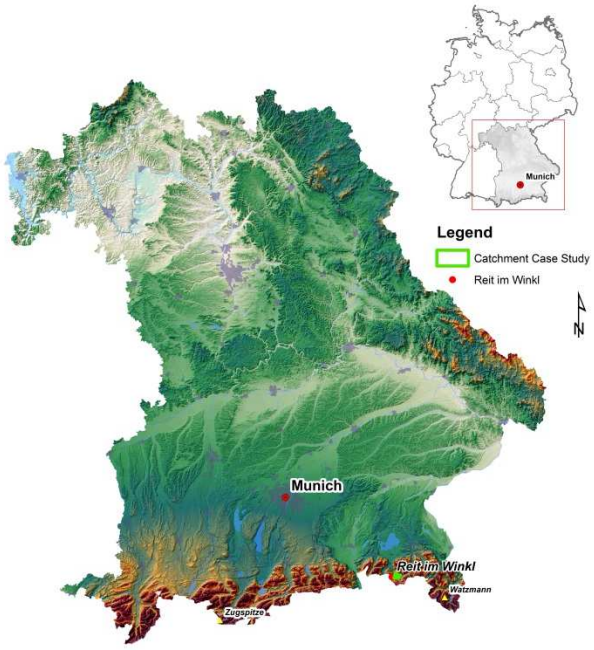

Fig. 11 Relief map of Bavaria and general map of Germany. The case study catchment of the Weisslofer near Reit im Winkl, Upper Bavaria, is highlighted by a green frame.

Due to the bridge's dimensions and constructive design it is regarded as a critical structure, especially as the flow depth exceeds the clearance height. Further aspects are: rough and unsurfaced channel bottom, structures upstream and downstream of the bridge. Furthermore the free surface width of the channel is wider than the bridge's inner width (see **Fig. 12**).

Fig. 12 Bridge at Entfelderstrasse

The longitudinal section of the channel is stepped, the channel route can be classified as slightly curved. The log diameters are less than the flow depth and the maximum tree length is smaller than the upstream channel width. This classifies the woody debris transport at the bridge's location as moderate.

The evaluation of the structure and the assessment of a moderate wood transport plotted into the matrix results in a blockage level of 75 %.

2.5.2 Results

The first hydraulic simulation run considers the basic scenario without log jams or other scenarios (**Fig. 13**). The results show minor flooding near the bridge at Entfelderstrasse mostly affecting lawns and agricultural land. At the adjacent bridge where the Weisslofer is crossed by the Alpenstrasse, the simulation results show an overtopping of the banks resulting in major inundations along the Alpenstrasse. The overflowing affects settled land to a large extent even in the scenario with an unblocked bridge at Alpenstrasse.

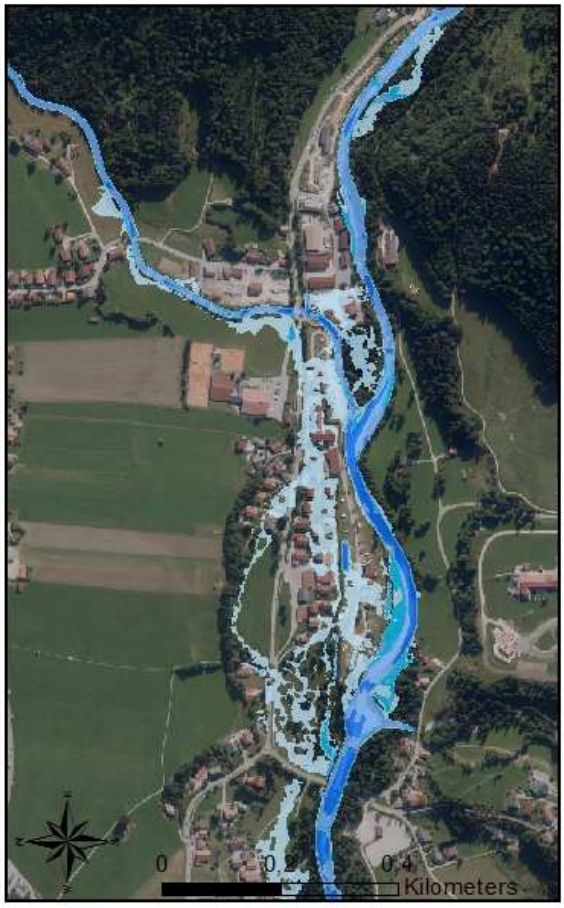

Fig. 13 Simulation result for the default scenario without any log jams or sediment accumulations. The Entfelderstrasse bridge's position is marked with a *green* dot. The bridge at Alpenstrasse is marked with a *red* dot

The second scenario (see **Fig. 14**) takes into account the log jam at the bridge at Entfelderstrasse. Compared to the default scenario, the river overtops near the Entfelderstrasse bridge. This results in an additional inundation of major settled areas east of the Entfelderstrasse. However, the log jam at the bridge at Entfelderstrasse does not affect the extent of the inundated areas along the Alpenstrasse.

Fig. 14 Simulation result for the scenario considering a log jam at the bridge at Entfelderstrasse. The Entfelderstrasse bridge's position is marked with a *green* dot. The bridge at Alpenstrasse is marked with a *red* dot

3. CONCLUSION

The torrential endangered area determined by 2D hydraulic simulation displays the range of most probable scenarios of the design event. This systematic approach enables a reproducible determination and consideration of possible log jams and a comparability of obtained results is achieved.

First assessments of the proposed procedure show that the approach to calculate the level of blockage at intersecting structures is feasible to document the susceptibility for blockages through woody debris at bridges or culverts.

REFERENCES

Gschnitzer, T., Gems, B., and Aufleger, M. (2014): Laborversuche zu Schwemmholztransport und einhergehenden Brückenverklausungen und Erstellung eines Leitfadens zur Berücksichtigung dieser Phänomene in der Gefahrenzonenplanung. Innsbruck.

Handschin, W. and Duss, H. (1997): Holzprobleme an Wildbächen, 1. Phase. Literaturstudium und Prozessanalyse, Altdorf, den 13. Oktober 1997.

Imhof, M. (2008): Verklausung von Schwemmholz an Brücken.

Einfluss der Abflussverhältnisse. Zürich: ETH.

Lange, D., and Bezzola, G. (2006): Schwemmholz: Probleme und Lösungsansätze. Zürich: Mitteilung der Versuchsanstalt für Wasserbau, Hydrologie und Glaziologie. Zürich.

Meyer, J. and Rimböck, A. (2014): GIS-basierter Ansatz zur Abschätzung des Schwemmholzpotenzials in Wildbächen; Internationales Symposium „Wasser- und Flussbau im Alpenraum“, 25.-27.06.2014 in Zürich; Tagungspublikation S. 443 ff; Mitteilungen der Versuchsanstalt für Wasserbau, Hydrologie und Glaziologie der Eidgenössischen Technischen Hochschule Zürich Nr. 228; Zürich; Eigenverlag DOI: 10.13140/2.1.1460.5768. Richards, L.A. (1931): Capillary conduction of liquids through porous mediums, Physics, Vol. 1, pp. 318-333.

Reger, B. and Ewald, J. (2011): Waldtypenkarte Bayerische Alpen. In AFZ – Der Wald (2011), 24, 14-26.

Rimböck, A (2001): Luftbildbasierte Abschätzung des Schwemmholzpotentials (LASP) in Wildbächen. In: Festschrift 75 Jahre Oskar von Miller-Institut, 1926-2001: Berichte des Lehrstuhls und der Versuchsanstalt für Wasserbau und Wasserwirtschaft der technischen Universität München (2001), 91. 202-221.

Stetter, F. (2014): Verkleinerungsprozesse von Schwemmholz in Gebirgsflüssen und Wildbächen. Projektarbeit. WSL, Versuchsanstalt für Wasserwirtschaft (VAW)

Literature-based Expedient Criterion for Assessing the Impact Strength of Switzerland's Rockfall Protection Embankment Inventory

Stéphane LAMBERT[1*], Bernd KISTER[2] and Bernard LOUP[3]

[1] Irstea, (Saint Martin d'Hères, France)
[2] Lucerne University of Applied Sciences and Arts, (Lucerne, Switzerland)
[3] Federal Office for the Environment (FOEN) (Bern, Switzerland)
*Corresponding author. E-mail: stephane.lambert@irstea.fr

This article proposes an expedient criterion for assessing the ability of any type of rockfall protection embankment in resisting the impact by the rock block. The approach consists in comparing the design kinetic energy of the block to the embankment dimensions. The embankment is deemed impact resistant if the block kinetic energy is such that the downhill face displacement remains below a threshold value. A differentiation is made between reinforced and non-reinforced embankment. This criterion was developed considering the available literature concerning real-scale impact experiments conducted on embankments. It was then applied to 54 well described embankments built in Switzerland. Even if the Swiss inventory appears globally well designed with respect to impact strength, this criterion draws the attention on 6 potentially highly critical embankments.

Key words: rockfall, embankment, impact, assessment, criterion

1. INTRODUCTION

Rockfall protection embankments (RPE) are massive civil engineering structures built in elevation with respect to the soil in the aim of arresting or deviating rockfall with kinetic energies up to 150 MJ (**Fig. 1**). RPEs are generally built from soil or other granular materials, sometimes compacted, sometimes including reinforcements. The uphill face may be made of different materials: soil, rockery, gabions or recycled-tires, for example.

The design of RPEs normally addresses both their ability in controlling the rock block trajectory and their mechanical stability. As for this latter facet, the challenging issue is the response of the structure to the impact by a block of given mass and velocity. This complex question has motivated various research works since the 90's, based on real-scale experiments, small-scale experiments or numerical modeling (for references and synthesis, see [*Lambert and Bourrier, 2013*] or [*Lambert and Kister, 2017a*]). These works progressively contributed to the development of design rules with respect to embankment impact strength, as proposed only recently (e.g. [*ONR, 2013*]).

In some countries of the Alpine arch (France, Switzerland, Italy in particular) large structure inventories exists, mainly with public ownership. Such structure inventories are heterogeneous in terms of construction date, structure technology, constitutive materials, dimensions, and designed capacity. In fact, most of existing RPEs had been designed with minimum or no consideration for the impact load resulting from the block interception.

In such a context, questions concerning the efficiency of existing RPEs may rise, in particular when dealing with risk management revising natural risk prevention plans. In such cases, it is not affordable to use complex methods to assess the efficiency of embankments. This article introduces an expedient criterion for assessing the impact strength of RPEs. The criterion is based on data from real-scale experiments available in the literature and conducted by different research teams. It aims at helping public authorities in assessing their inventory. It is here applied to Swiss RPEs.

Fig. 1 Example of a 7m-tall reinforced embankment protecting a road (S. Lambert)

This work is part of the research project entitled "Analysis of Existing Rockfall Embankment of Switzerland" (AERES) commissioned and funded by the Federal Office for the Environment (FOEN). This project includes a detailed state-of-the-art ([*Lambert and Kister, 2017a*]), the analysis of the inventory ([*Lambert and Kister, 2017b*]), small scale experiments on rockery facing embankments ([*Kister and Lambert, 2017*]) and an analysis of post-construction events. This article gives a condensed version of these documents for what concerns the expedient criterion and its application to the embankments built in Switzerland.

2. THE SWISS EMBANKMENT INVENTORY

A recently conducted survey showed that the number of RPEs in the different cantons of Switzerland by far exceeds 250 units [*Lambert and Kister, 2017b*]. This inventory mainly consists of compacted earth/soil structures, with a rockery facing. A minority consists of earth-reinforced structures. Even if the very first ones were built in the beginning of the 80's, most of them were built less than 10 years ago. During this survey, the available technical documentation appeared very poor in some cases. At the end, only 54 embankments were sufficiently well described to be considered in this study. These constructions were less than 20 years old.

The 54 structures were designed by different companies, using different approaches and design tools for both defining the design event (rock block trajectory, velocity and mass) and designing the embankment. As for this latter facet, only 10 embankments were designed in an attempt to account for the dynamic loading among which 4 considered the recommendations given by [*ONR, 2013*], and 4 based on the recommendations established by [*FEDRO, 2008*] for computing the impact force acting on sheds.

The dimensions of these 54 RPEs range between 15 and 700 m in length and 1.5 and 13 m in height. Approximately 64% of the embankments have a height of 4 m or less, but only approximately 6% have a height larger than 7 m. The average values are 155 m in length and 4.3 m in height respectively.

These 54 RPEs were designed considering reference blocks with a weight and a kinetic energy in very wide ranges: 15 to 1600 kN and 160 kJ to 50 MJ, respectively. About 40% and 64% of the embankments have been designed for stopping blocks with a kinetic energy less than or equal to 2000 and 4000 kJ respectively. 18% of the embankments were designed for kinetic energies higher than 10 MJ.

Fig. 2 cross-compares the embankments by providing the project block kinetic energy, considered for the design, and the structure mid-height width, for structures ordered according to their height. It can be seen that for similar structure dimensions (width and height) embankments were designed for intercepting blocks with kinetic energy over wide ranges (see examples in the red rectangles). This suggests that either some structures are undersized or others are oversized.

Of course, this comparison is conducted without any reference to the location where the embankment is built, neither to the design companies concerned. The aim here is rather to globally evaluate the relevance of the embankment design in general, and considering that there are lacks in the design recommendations.

3. EXPEDIENT CRITERION FOR IMPACT STRENGHT ASSESSMENT

The criterion was developed with the aim of finding a simple relation between the embankments characteristics and its ability in resisting the impact by the block. The parameters describing the embankment were voluntarily kept simple so that this criterion could be applied for a very large panel of embankment types. It was also motivated by the fact that available data concerning some existing structures are very limited.

This criterion was developed based on the current state of knowledge concerning the impact strength of embankments.

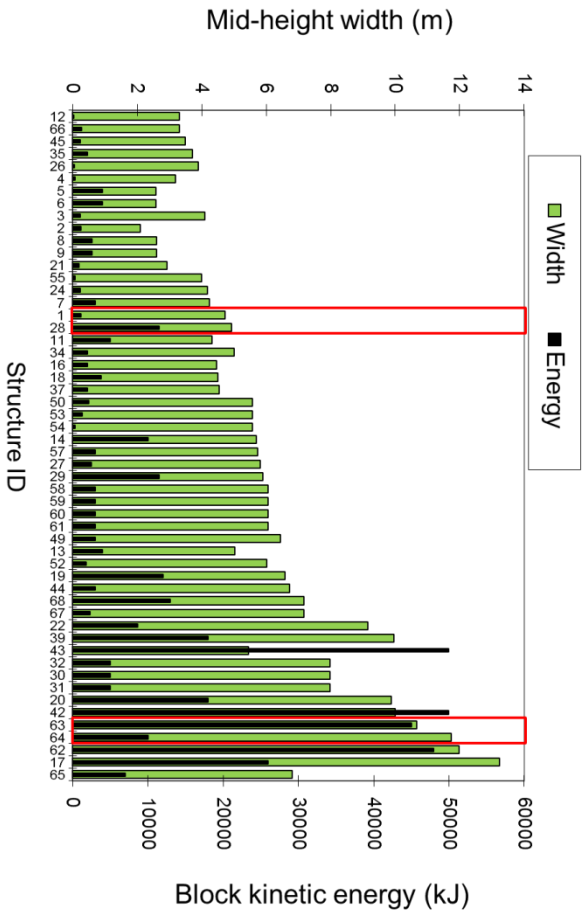

Fig. 2 Cross-comparison of the embankments considered in this study. Mid-height width and design block kinetic energies for embankments ordered according to their height. Red rectangles: see text for explanation.

3.1 State of knowledge

Different studies have addressed the response of embankments to impact, involving real-scale experiments, small scale experiments or numerical modeling (review in [*Lambert and Bourrier, 2013*]). The proposed criterion was developed emphasizing data from real-scale experiments, as providing concrete evidences concerning real structures.

The literature provides detailed data related to 5 studies involving real-scale experiments with block kinetic energies beyond 1000 kJ. Studies with lower kinetic energies were not considered as leading to limited structure deformation, far from structure collapse. **Fig. 3** shows the 5 reinforced structures concerned by the studies involving real-scale experiments. Their cross sections were either rectangular or trapezoidal, with height ranging between 3 and 4.2 m. At mid-height, the embankment width ranged from 3 to 4.3 m. It must be noted that for some of these studies, there were some differences between the tested structures, but of minor importance compared to the differences between the different studies.

Among the impact experiments conducted on these RPEs, only those carried out in similar impact conditions had been considered. These conditions were defined as a single block of kinetic energy higher than 1000 kJ impacting the embankment close to its mid-height. The block incident trajectory was also considered. In most of the cases, the trajectory was oriented downward with a 30° inclination approximately. **Table 1** gives the structure dimensions, test conditions and measurements related to the 20 tests considered. The maximum block kinetic energy involved was 4350 kJ. The residual deformation on the uphill and downhill faces (i.e. exposed to impact and opposite to impact, respectively), when available, are the only data describing the embankment response to impact.

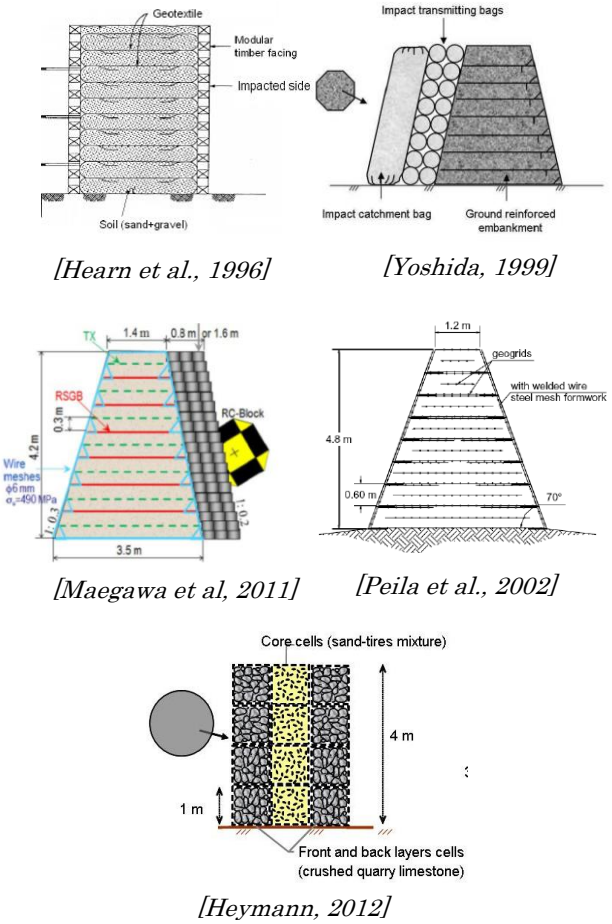

Fig. 3 Embankments subjected to real-scale impact experiments by different authors

Table 1 Data related to real-scale experiments considered in this study

Source	Structure Height (m)	Structure Thickness (crest/base) (m)	Impact energy (kJ)	Deformation Uphill -face (m)	Deformation Downhill -face (m)
Hearn et al., 1995	3.05	1.82/1.82	1010	0.6	0.21
	3.05	1.82/1.82	1400	0.9	0.7
	3.05	1.82/1.82	1410	-	0.76
	3.7	2.4/2.4	1410	-	0.34
	3.7	2.4/2.4	1300	-	0.25
	3.7	2.4/2.4	1410	-	0.34
Peila et al., 2002	4.2	0.9/5	2500	0.6	0.23
	4.2	0.9/5	4350	1	0.9
Yoshida, 1999	4	3.3/5.3	970	0.22	0
	4	3.3/5.3	2000	-	0.09
	4	3.3/5.3	2700	-	0.5
Maegawa et al., 1991	4.2	2.2/4.3	1060	1.13	0.09
	4.2	2.2/4.3	1240	1.57	0.27
	4.2	2.2/4.3	1760	1.73	0.24
	4.2	3/5.1	1050	1.44	0.09
	4.2	3/5.1	1650	0.76	0.1
	4.2	3/5.1	1670	1.8	0.13
	4.2	3/5.1	2270	1.9	0.44
Lambert	4	3/3	2200	1.4	0.55
	4	3/3	2200	0.9	0.4

3.2 Impact response of embankments

Behind the differences in structure types and test conditions, these experiments globally provide a trustworthy source of results for understanding the embankment impact response ([*Lambert and Bourrier, 2013*] or [*Lambert and Kister, 2017a*]). The analysis of the embankment response reveals that, among other mechanisms, the impact by the block first induces compaction and crushing of coarse materials close to the impacted area. Then, it progressively induces displacement of part of the embankment, with friction along shear planes. Basically, the higher the kinetic energy, the larger is the RPE deformation and consequently the downhill face displacement (**Fig. 4**). And finally, if the block kinetic energy is in excess with respect to the RPE nominal capacity, collapse is reached as a result of a large downhill face displacement. In the end, the downhill face displacement appears to be a good indicator of the impact response of the embankment: the higher this displacement and the closer to collapse, whatever the amplitude of the various mechanisms involved in this structure deformation.

In order to account for the differences in dimensions of the tested embankments, it is proposed to normalize the downhill face displacement by the structure mid-height width, which is representative of the embankment width opposed to the block penetration.

The block kinetic energy is also normalized by the area of the structure cross-section, which is considered here representative of the mass of the embankment associated to the impact. This approach is consistent with the fact that the larger the structure, the higher the required block kinetic energy for reaching a same embankment deformation [*Hearn et al.* 1996].

Fig. 5 presents the normalised results received from the real-scale experiments on the structures presented in **Fig. 3**. It shows a rather linear relationship between the relative downhill face displacement and the normalised kinetic energy.

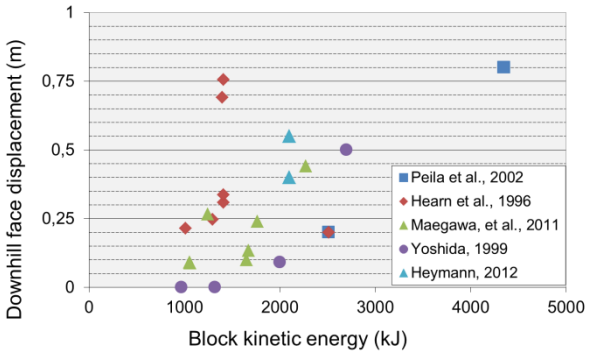

Fig. 4 Results from the real-scale experiments presented in **Fig. 3** and **Table 1**.

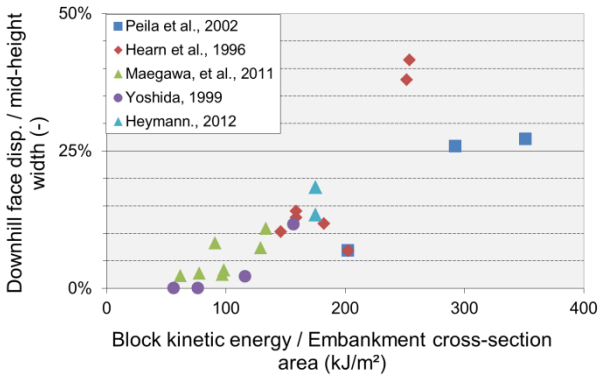

Fig. 5 Normalised results of **Fig. 4**

3.3 Criterion

The results presented in **Fig. 5** show that below a normalised kinetic energy of 250 kJ/m², the downhill displacement remains on a level less than 25% of the structure width. The 25% threshold for the downhill face displacement is considered as a relevant limit beyond which the structure may not be stable anymore. It is in line with previously proposed threshold values proposed in the literature in relation with analytical methods [e.g. *Ronco et al.*, 2009].

This practically implies that the downhill face displacement of an impacted embankment is acceptable if:

$$\frac{KE}{A} < 250$$

where KE is the block kinetic energy (kJ) and A is the structure cross-section area along the vertical axis calculated from the ditch elevation (m²).

Based on this finding, it is proposed to consider that an embankment is impact resistant if $E'_{25}<1$, with:

$$E'_{25} = \frac{KE}{250 * A}$$

E'_{25} is a normalized block kinetic energy, where the subscript 25 refers to the ratio of accepted downhill face displacement with respect to the structure width (here 25%).

The validity domain of this criterion is conditional on the experimental conditions. With respect to the embankment, the criterion is valid for reinforced structures, with height in the 3-4.2 m range and a mid-height width in the 3-4.3 m range. With respect to the loading, the criterion is valid for a block diameter typically half the embankment height, with an incident downward trajectory inclined by 30° approx. with respect to the horizontal axis, having a kinetic energy in the 1-5 MJ range and leading to an impact point close to the embankment mid-height, and thus at a sufficient distance from the crest. Out of this domain, the criterion validity may be altered.

4. APPLICATION TO THE SWISS EMBANKMENT INVENTORY

4.1 Inventory evaluation

The proposed expedient criterion was applied to the 54 previously mentioned embankments (**Fig. 6**). In this figure, the embankments are ordered according to their height, with result bars in violet for non-reinforced structures and yellow bars for reinforced structures (4 out of 54).

As for the reinforced embankments, E'_{25} slightly exceed the value of 1 in 2 cases. Exceeding a value of 1 is not detrimental for a reinforced structure: it indicates that a large downhill face displacement takes place, not necessarily implying an impending collapse. Indeed, the experiments conducted by Peila et al. (2002) showed that a reinforced embankment was able to survive two successive impacts with a E'_{25} exceeding 1. The 2 other reinforced embankments meet the requirement.

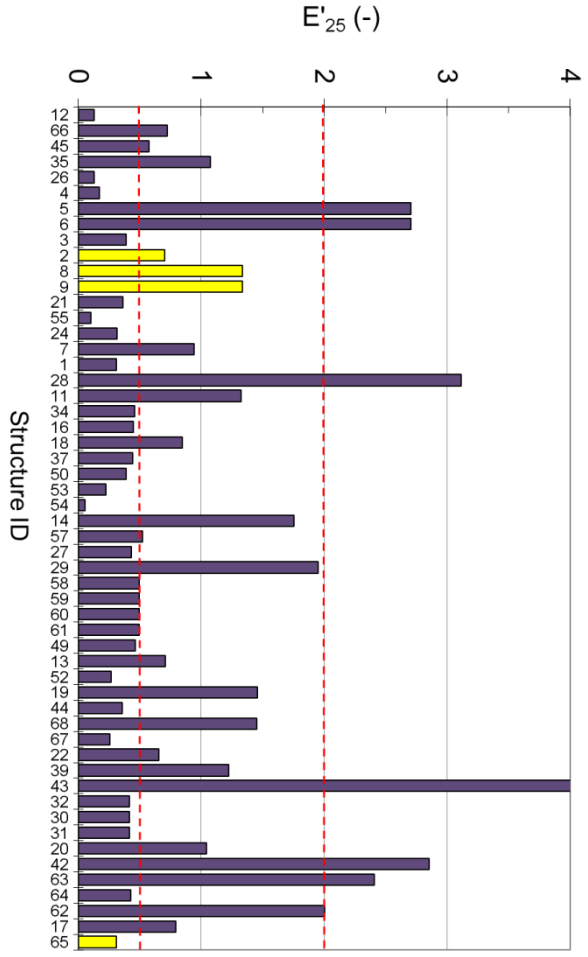

Fig. 6 Embankment inventory evaluation (violet and yellow for non reinforced and reinforced embankments resp. (see the text for explanations about dotted lines)

As for non-reinforced structures, the validity of the criterion is questionable. Indeed, for such embankments, the downhill face displacement is

much higher than for a reinforced embankment impacted by a block of same kinetic energy. Considering the results from the literature [*Peila et al.*, 2002][*Brandl and Blovsky*, 2004] it is proposed to account for this lower impact strength by dividing the acceptable downhill face displacement by 2, such that the criterion becomes $E'_{25}<0.5$. 27 non-reinforced embankments meet this specific requirement out of 50. On the opposite, in 6 cases E'_{25} exceeds the value of 2, which is considered highly critical for unreinforced RPEs. In 2 out of these 6 cases, the criterion is applied within its validity domain in terms of embankment height, mid-height width and block kinetic energy. In the 4 remaining cases, at least one condition is not fulfilled with respect to the validity domain.

On total, for 17 non-reinforced embankments out of 50 E'_{25} is within the 0.5-2 range, which is critical but to a lesser extent.

At the end, applying the criterion on this inventory draws the attention on about 10% of highly critical cases (6 non reinforced embankments). To a lesser extent, about 35% of the embankments exceed the criterion (17 non reinforced embankments and 2 reinforced ones). Finally, around 60% of the inventory meets the criterion.

4.2 Discussion

On the whole, it is a noticeable good point that more than 50% of the embankments meet the criterion while less than 20% were designed with consideration for the dynamic loading by the rock block. Analysing more specifically the E'_{25} value for embankments for which the impact was considered in the design process, it appears that using [*ONR, 2013*] led to slightly more efficient structures in resisting the impact than [*FEDRO, 2008*]. Nevertheless, only 1 out of the 8 structures concerned by these designs meets the E'_{25}-based criterion.

For embankments for which the criterion is not met, complementary analysis could be conducted to assess their impact strength based on deeper investigations and calculations. Nevertheless, some practical limitations rose applying this criterion. These limitations relate to the available information with respect to each case and its quality. First, the definition of the embankment height is not unique. Depending on the case, this value may be measured along the vertical axis or along the embankment face, as a difference between the crest elevation and either the ditch elevation or the natural ground elevation. Second, the definition of the impact height is also not unique: in some cases, the block lower point is considered while in other it is the gravity centre. More generally, questions in relation with parameters related to the rock block trajectory raise. Indeed, the impact height and the block trajectory inclination are not always provided by the documentation while these two parameters clearly influence the response of the embankment. For instance, the embankment deformation resulting from an impact close to its toe will be limited. On the contrary, an impact close to the crest, or by a block with a sub-horizontal incident trajectory will be more detrimental to the embankment safety. In the absence of these data, the criterion was applied considering that these unknown parameters met the validity domain requirements. For this reason, it is recommended that, prior to any further assessment of apparently critical structure, the relevance of using the E'_{25}-based criterion should be checked depending on the impact case vs. the experimental conditions.

5. CONCLUSIONS

In order to assess the efficiency of large structure inventories an expedient criterion for the impact strength of rockfall protection embankments has been developed based on data from real-scale experiments available in the literature. This expedient criterion basically relates the displacement of the downhill face of the embankment, which results from the impact by the rock block, to the impact energy. This criterion is voluntarily kept simple to be applied to a wide variety of existing structures.

This criterion was applied to a sample of 54 well documented embankments built in Switzerland during the last 20 years. In spite of the fact that their design seldom accounts for the dynamic loading, about 60 % of the embankments appear to be impact resistant. On the opposite, the attention of owners is drawn on 10% of the structures for which impact strength is highly questionable.

Even if easy and convenient to use, it is not recommended to use this criterion for design of new structures.

REFERENCES

Brandl, H. and Blovsky, S. (2004): Protective barriers against rockfall. Proceedings of the 3rd European geosynthetics conference-Eurogéo III, Munich, Germany, 95-100.

FEDRO (2008). Directive 12006/ Actions des chutes de pierres sur les galeries de protection. OFROU, Bern, Switzerland, 22 pp.

Hearn, G.. Barrett, R.K.. Henson, H.H. (1996): Testing and modeling of tow rockfall barriers. Transportation research records vol. 1504. National Research Council, Washington DC, 11 pp.

Heymann, A. (2012). Approche expérimentale du comportement mécanique des géo-ouvrages à technologie cellulaire. Application aux ouvrages pare-blocs. Doctoral thesis, U. Joseph Fourier, Grenoble (in French).

Kister, B. and Lambert, S. (2017): Analysis of Existing Rockfall Embankments of Switzerland (AERES); Part C: Small-scale experiments. Federal Office for the Environment. Bern. 90 p.

Lambert, S. and Bourrier, F. (2013): Design of rockfall protection embankments: a review. Engineering geology 154 (28), 77-88.

Lambert, S. and Kister, B. (2017a): Analysis of Existing Rockfall Embankments of Switzerland (AERES); Part A: State of Knowledge. Federal Office for the Environment. Bern. 55 p.

Lambert, S. and Kister, B. (2017b): Analysis of Existing Rockfall Embankments of Switzerland (AERES); Part B: Analysis of the collected data and comparison with up-to-date knowledge. Federal Office for the Environment. Bern. 21 p.

Maegawa, K. Tajima, T. Yokota, T. Tohda, M. (2011): Slope-rockfall tests on wall embankments reinforced with geosynthetics. Proceedings of the 6th international structural engineering and construction conference. Zürich. Switzerland. 641-646.

ONR, (2013): ONR 24810: Technischer Steinschlagschutz – Begriffe, Einwirkungen, Bemessung und konstruktive Durchbildung, Überwachung und Instandhaltung, ASI Austrian Standards Institute (Österreichisches Normungsinstitut), Ausgabe 15.01.2013.

Peila, D. Oggeri, C. Castiglia, C. Recalcati, P. Rimoldi, P. (2002): Testing and modelling geogrid reinforced soil embankments to high energy rock impacts. Proceedings of the 7th International conference on geosynthetics. Nice. France. 133-136.

Ronco, C., Oggeri, C., Peila, D., 2009. Design of reinforced ground embankments used for rockfall protection. Natural hazards and earth system sciences 9. 1189-1199.

Yoshida, H. (1999): Recent experimental studies on rockfall control in Japan. Proceedings of the Joint Japan-Swiss Scientific Seminar on Impact load by rock fall and design of protection structures. Kanazawa. Japan. 69-78.

Experimental Study on Sediment Deposition Using Bandal Like Structure with Different Ratio of Permeable and Impermeable Part

Yuji HASEGAWA[1*], Shuichi TAI[2], SHAMPA[2], Kenji KAWAIKE[1] and Hajime NAKAGAWA[1]

[1] Graduate School of Integrated Arts and Sciences, Hiroshima University, Japan
(1-7-1 Kagamiyama, Higashi-Hiroshima, Hiroshima, 7398521, Japan)
[2] Dept. of Civil and Earth Resources Engineering, Kyoto University, Japan (Gokasyo, Uji, Kyoto 6110011, Japan)
*Corresponding author. E-mail: y-hasegawa@hiroshima-u.ac.jp

Spur dikes of the impermeable type have been found to demonstrate a significant effect in controlling sediment deposition when compared to those of the permeable type. However, instances of local erosion have been observed in impermeable spur dikes leading to numerous problems. On the other hand, a number of spur dikes comprising Bandal like structures have been successfully employed and observed to have performed effectively. The Bandal comprises two parts; the upper part is of the impermeable type while the lower part is permeable. When a high-velocity fluid stream impinges on the upper (impermeable) part, the water-splash effect guides the flow towards the mainstream direction. The low-velocity stream around a riverbed with high concentration suspended load flows through the lower (permeable) part, thereby causing deposition. Owing to significantly different flow characteristics existing in the permeable and impermeable parts under the same landform or hydraulic conditions, the ratio of sizes of the permeable and impermeable parts tends to influence the controlling function. However, such effects are solely qualitative and influence of the above size ratio on sediment deposition has not been considered in previous studies. In this study, channel experiments were performed to examine changes in the deposition function of the Bandal at different size ratios of the permeable and impermeable parts under similar hydraulic conditions. Results demonstrate that the suspended load volume passing through the permeable part and that moving from the main stream towards the Bandal installation section affects the total sediment-deposition volume. The most upstream Bandal was found to control the moving sediment volume. At different size ratios of the upper and lower parts, the suspended flow discharge changed. Discharge through the permeable part demonstrated change owing to low flow velocity downstream of the structure while that from the main-stream direction towards the Bandal demonstrated change owing to the splash effect.

Key words: riverbed deformation, suspended load, channel experiment, Bandal like structure, deposition function

1. INTRODUCTION

Recently occurrences of heavy rainfall have been on the rise owing to extreme climatic changes. Consequently, instances of flood damage—caused by overflowing rivers—and riverbank erosion have become frequent worldwide. To exercise better control over river flows and prevent flood damage, attention must be focused on riverbed variations sediment deposition and erosion because such phenomena greatly influence river-flow behaviors.

To prevent erosion on the outer banks of curved or meandering rivers, deployment of various types of spur dikes have been proposed and implemented (Fukuoka et al., 1992; Ghodsian and Vaghefi, 2009; Dehghani et al., 2013). Typically, in comparison to the permeable type, impermeable spur dikes play a significant role in controlling sediment deposition. However, impermeable spur dikes are prone to erosion, which in turn leads to several problems. Interestingly, many spur dikes comprising Bandal like structures (hereafter, described as Bandal) have been employed in Bangladesh and have been observed to perform effectively (Rahman et al., 2003; Alauddin et al., 2011; Nakagawa et al., 2011).

A Bandal typically comprises two parts; the upper part is made of the impermeable type while lower part remains permeable. When flow surface with high velocity hit the Bandal impermeable part, water splash effect lead the flow to main-stream direction. Flow around riverbed with high concentration of

suspended flow pass the Bandal permeable part and deposition occur due to the slow velocity at Bandal downstream. Because the flow characteristics are different in permeable part and impermeable part even with in same landform or hydraulic condition, the ratio of permeable and impermeable part seems to influence on the controlling function. However, Bandal effects are considered only qualitatively and how deposition effect change due to different ratio of permeable and impermeable part is even not considered (Nakagawa et al., 2013; Nishio et al., 2016).

In this study, we conducted channel experiment to examine the deposition function of Bandal with different ratio of permeable and impermeable part on same hydraulic condition.

2. EXPERIMENT CONDITIONS

Experiments were performed using a rectangular channel measuring 2,000 cm in length, 30 cm in height, and 100 cm in width. The slope was set as 1/1,000 with a fixed bed condition. Water, at a flow rate of 31.6 l/s, was supplied under steady state (Froude number 0.55). A 0.6-cm dam-up was employed at the downstream end, and steady-state flow conditions were confirmed.

In the strict sense, fixed-bed conditions are significantly different from actual river conditions, wherein local scouring and complicated flow behaviors usually occur. Different flow characteristics were observed in the permeable and impermeable parts of the Bandal under similar hydraulic condition, and the ratio of the sizes of the two parts was found to significantly influence the sediment controlling function. Recent studies on Bandals were performed considering a fixed value of the permeable/impermeable size ratio. Thus, in this study, we performed fixed-bed experiments employing different Bandal size ratios to reveal the velocity and spatial distributions of the suspended load around the Bandal to obtain clarity regarding the deposition function.

Uniform sediments measuring 0.093 mm in diameter and density with 2.65 g/cm^3 were employed. The diameter 0.093 mm seems to be rather small, but in this experiment, we confirmed that exchanging with riverbed especially deposition have occurred. During experiments, the ratio u_*/w_0 (u_*: friction velocity, w_0: settling velocity) was set as 4.1 to represent the suspended load condition. Sediments were supplied at the rate of 1.92 cm^3/s under steady state using a sand feeder. Ripples were generated in this condition; however, it was ensured that sediment deposition didn't exceed the number of ripples appeared in results without setting dikes from preliminary experiment.

A non-overflow type Bandal model measuring 15 cm in height was used. The permeable part comprised 0.7 cm diameter brass columns placed 1.2 cm apart. The upper impermeable part of the model comprised a stainless steel plate. Height of the permeable part could be adjusted to 1.5, 3.5, or 5.5 cm. The length of Bandals and spur dikes were set to 15.2 cm with reference to the previous studies (Akikusa et al., 1960). Four Bandal models were placed at 30 cm intervals between 1,000-1,090 cm downstream of the left bank. An outline of experimental channel and relevant conditions are depicted in **Fig.1** and **Fig.2**. **Table 1** shows the experimental cases hydraulic and Bandal model conditions.

The flow depth was measured using an ultrasonic sensor in time series, and the deposition and surface flow velocity were measured approximately 4.5 hours after attainment of the equilibrium condition.

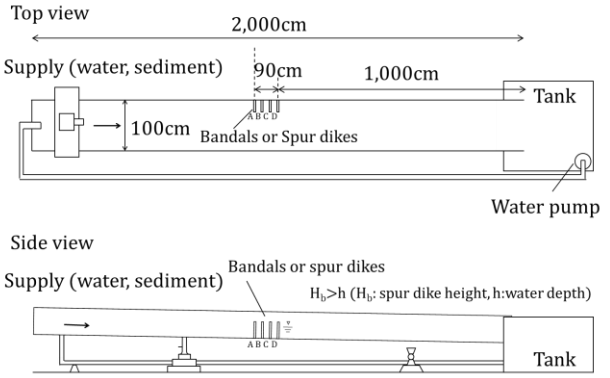

Fig. 1 Outline of experiment channel and Bandal conditions

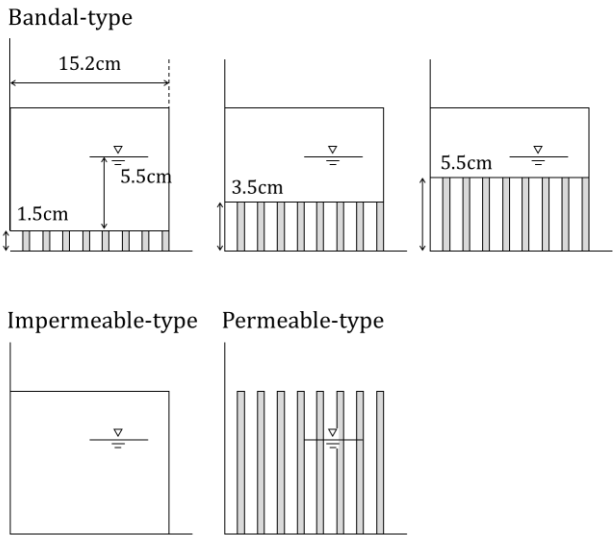

Fig. 2 Outline of Bandal models

Table 1 Experimental cases

Case	Discharge (l/s)	Channel width(cm)	Slope	Sediment diameter(mm)	Permeable height /Water depth
1	31.6	100	1/1,000	0.093	0.22
2					0.51
3					0.80
4					1.00
5					- (Impermeable type)

When measuring the surface flow velocity using PIV software, we used PCV powder (average diameter 0.113 mm, density 0.59 g/cm^3). A laser-displacement sensor was used to measure sediment thickness before and after the experiment.

3. RESULTS AND DISCUSSION

3.1 Results obtained using bed-level contour

Experimental results obtained using the bed-level contour are depicted in **Fig.3**. Ripple formation was observed in all cases considered during experiments. When setting spur dikes, stripe-shaped ripples were observed across the channel proceeding from the left bank towards the right remarkably formed in Case 2. This was attributed to the water-splash due to spur dikes. In Cases 1 and 5, the size of the impermeable part of the structure was rather large. Consequently, separated flow was observed due to water splashing. This separated flow demonstrated an effect on the main flow section by causing an increase in flow velocity. **Fig.4** depicts results of the surface flow velocity distribution along the longitudinal direction. A major difference between the types of spur dikes was observed—closed- and Bandal-type spur dikes led to formation of horizontal vortices; this, however, was not true in the case of open-type dikes. In the absence of spur dikes, the ripples had an average height 0.35 cm. When using spur dikes, sediment deposition was observed to be higher compared to the ripples at locations upstream of spur dike A. This was attributed to the dam-up effect caused during spur-dike setting. **Fig.5** depicts results of the water-surface profile. The broken line indicates steady-flow depth. In Case 5, the flow depth demonstrated a change upstream as well as downstream of spur dike A. In Cases 1-3, identical Bandal setting conditions and flow depth were maintained on the frontal side of spur dike A. However, the flow depth on the back side was altered in proportion to the height of the permeable part. In Case 4, the flow depth on the frontal side of the spur dike was observed to be slightly larger compared to its steady-state value; however, its value on the back side remained unaltered. When setting spur dikes, left-bank side between coordinates x = 1,100-1,150 cm, y = 0-10 cm demonstrated deposition; describing from larger cases, Case 5 with 0.8 cm, Case 1 with 0.78 cm, Case 3 with 0.56 cm, Case 2 with 0.55 cm and Case 4 with 0.31 cm. Similarly, the right-bank side bounded by coordinates x = 1,100-1,150 cm, y = 90-100 cm demonstrated a deposition height of approximately around 0.3-0.4 cm, which was comparable to that observed along the left bank. The deposition height was observed to almost identical to that observed in cases void of spur dikes.

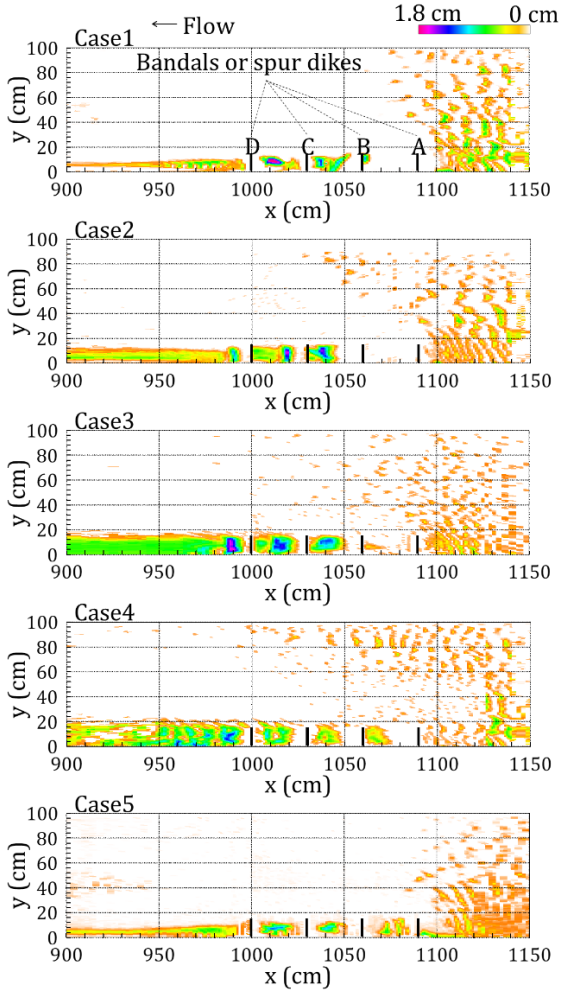

Fig.3 Bed-level contour

Furthermore, downstream right bank side from spur dikes installation, ripples didn't form. This was attributed to the increase in main-flow velocity due to the water-splash effect and changes in hydraulic conditions. The former trend was found to be significant in the impermeable part in Case 5. In other cases (Case 1-3), the effect was observed to be rather small and proportional to the height of the permeable part.

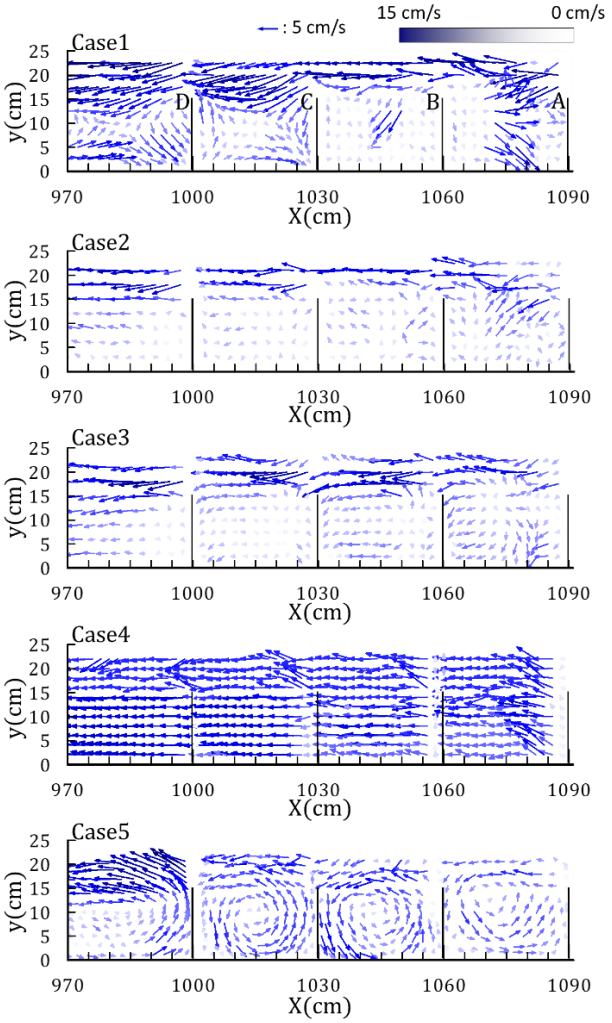

Fig.4 Water surface flow velocity distribution

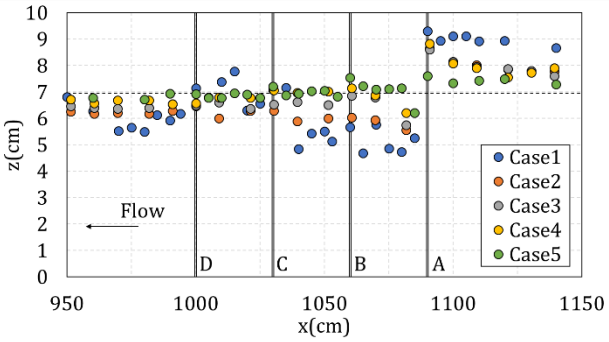

Fig.5 Water-surface profile（y=8 cm）

3.2 Comparison of sediment-deposition volume

Experimental results based on the sediment-deposition volume are summarized in **Table 2**. Here, the volume of sediments deposited between spur dikes were considered, because downstream of spur dike D showed different deposition process to that observed in sections between spur dikes. Furthermore, to compare the deposition process downstream of the spur dikes, attributes of the affected area of spur-dike installation were required to be understand. As observed in **Table 2**, the highest sediment deposition was observed between dikes C and D except for Case 1. Spur dikes set downstream seemed demonstrated smaller flow velocities compared to those set upstream, therefore prospected deposition enhanced on the downstream side. Comparing the volume of deposition between spur dikes A–D, the highest deposition was observed in Case 3 followed by Cases 2, 4, 5, and 1. Recent studies have reported that the Bandal-type structure demonstrates a larger deposition function compared to a purely impermeable type spur dike. However, Case 1 corresponding to the smallest permeable/impermeable size ratio of 0.27 demonstrated least deposition function. On the other hand, at an upstream section between spur dikes A and B, the largest deposition was observed in Case 4 followed by cases 5, 3, 2, and 1. The results demonstrate that the deposition function of the Bandal type was smaller compared to both impermeable and permeable type spur dikes.

3.3 Velocity distribution at sharp end of spur dike along x-y direction

From the experiments, it was observed that the most upstream spur dike A had the greatest influence on flow characteristics in all cases. This was especially true for impermeable type and Bandal type case, water splash occurred at spur dike frontal part and enlarge the main flow velocity due to the flow toward the right bank side. Downstream spur dikes (B, C, and D) didn't demonstrate the water-splash effect, thereby causing flow pulling into the section between successive spur dikes.

Tabel 2 Sediment-deposition volume

	Dikes A-B	Dikes B-C	Dikes C-D	Total
Case1	12.39	85.90	81.10	179.39
Case2	1.98	127.57	146.02	275.57
Case3	14.15	143.79	205.68	363.61
Case4	54.04	64.61	118.72	237.37
Case5	50.37	55.41	90.52	196.29

Unit: cm^3

In Case 5, the section between spur dikes A and B demonstrated presence of a vertical vortex due to shearing of fast flows separated from the frontal part of spur dike A (around y = 15 cm). This could lead to scouring and cause structural damage. Observing the flow direction between spur dikes, horizontal vortices occurred and seemed to expect deposition due to sediment settling. However, sediments must exist at spur dike intervals for deposition. Therefore, sediment inflow is expected. In cases corresponding to impermeable-type spur dikes, sediment inflow doesn't occur through the spur dike. Therefore, sediment inflow must be provided from the main flow section. **Fig.6** depicts velocity distribution at the upstream spur dike (y=15 cm) along the x–y direction at several sections.

Upstream of spur dikes A and B, no vertical sections demonstrated fluid flow into the spur-dike interval owing to the water splash effect at spur dike A. Downstream of spur dikes A and B, low-velocity flow was observed and due to shearing of the main flow section, the flow direction was altered towards the left bank of the channel. Subsequently, the flow collapsed in the frontal part of spur dike B and moved into the interval section between spur dikes A and B. Although flow velocities were observed to be different, all cases demonstrated the same trend along the vertical direction. Downstream of the interval between spur dikes B and C and that between C and D, the flow direction showed toward right bank side at the back of spur dike B and C. Then at downstream of the dike, flow toward left bank side occurred and sediment flow into the spur dikes interval. It happened remarkably at downstream C-D interval which appeared at the deposition volume results.

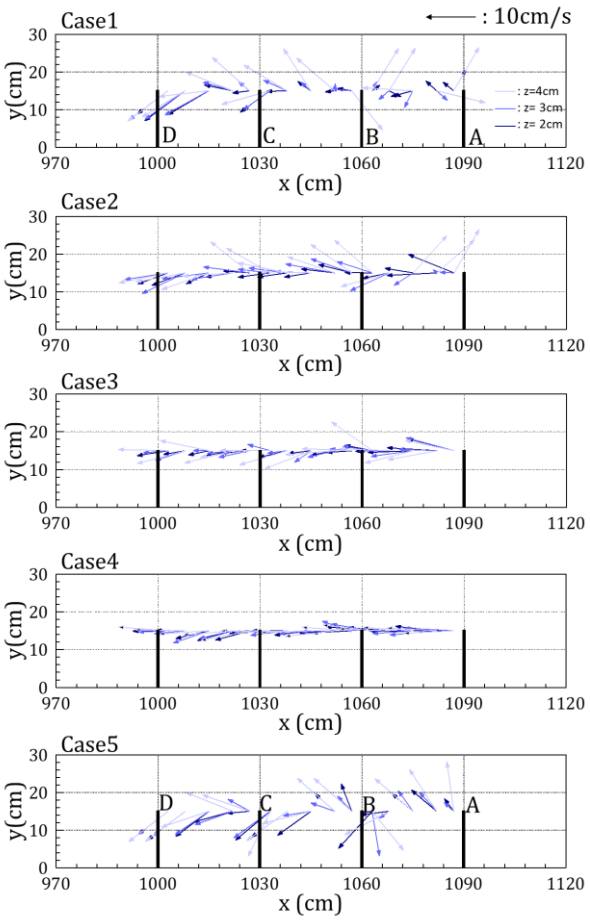

Fig.6 Velocity distribution (y = 15 cm) along the x–y direction

In Case 1, flow towards the right bank of the channel occurred due to water-splash effect of spur dike A similar to that in Case 5. However, flow toward preamble part around river bed caused flow toward upstream side at back of the spur dike A. Therefore, it became difficult to cause the fluid to flow into the interval between spur dikes A and B. In the interval between spur dikes B and C, flow velocity around the river bed was observed to be small, and the flow coming into the interval didn't appear so much, and in the interval between spur dikes C and D, the flow entered the interval in a manner similar to that observed in Case 5. In Cases 2 and 3, effect of flow toward the permeable part of Bandal became large, and flow separation caused by the splash effect was negligible in comparison to that observed in Cases 1 and 5. In Case 4, the former trend was observed more significantly. Flow moving into the spur-dike interval was hardly noticeable. In view of these results, it may be inferred that the flow entering the spur-dike intervals served to transport suspended sediments and promoted their deposition.

3.4 Velocity distribution along x–z direction around spur dikes

Fig.7 depicts results of the velocity distribution along the x–z direction around spur dikes. The center point of the four spur dikes was determined at y = 8 cm. For the impermeable-type spur dikes in Case 5, the flow velocity was found to have reduced because the flow was inhibited even without passing through the spur dikes. Therefore, flow velocity had reduced, and upward flow was found to predominate. The Bandal-type cases (Cases 1–3) demonstrated different water levels around spur dike A as a boundary, and the flow velocity through the transmission section was observed to be large, thereby indicating downward flow. All three cases demonstrated similar flow characteristics, such as flow rising at downstream of spur dike A. However, the cause of this phenomenon was different in Case 1 from that in Cases 2 and 3. In Case 1, the phenomenon was caused by shearing with rapid

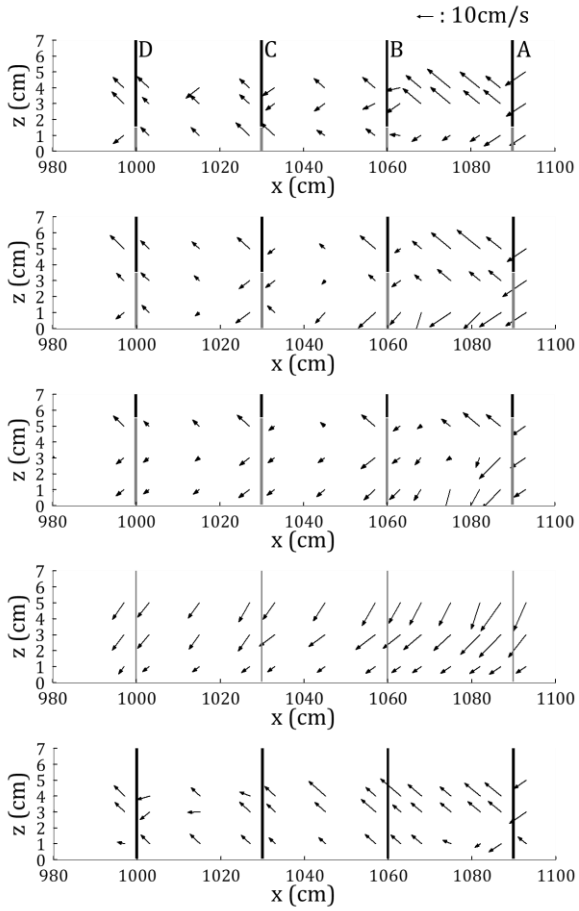

Fig.7 Velocity distribution along the x–z direction

separated flow. In Case 4 with transmission type, the flow becomes downward, and there wasn't mixing flow with upward and downward flow.

4. Consideration of sediment-deposition function around spur dikes

Fig.8 depicts shapes of sediment deposition corresponding each type of spur dikes. Corresponding to the impermeable type spur dike, the deposited sediments were settled from a horizontal vortex. Permeable-type spur dikes offered resistance to the flow passing through the permeable part; therefore, part of the sediment deposition demonstrated a convex form. Deposition shape for Bandal type spur dikes could best be described as a combination of sediments settled from the horizontal vortex generated in the impermeable part and those deposited owing to inhibited fluid flow against the permeable part. The proposed study reveals the sediment-deposition effect of Bandal type spur dikes. The maximum size ratio of the permeable/impermeable parts was 0.2 during experiments, and the results were observed to be

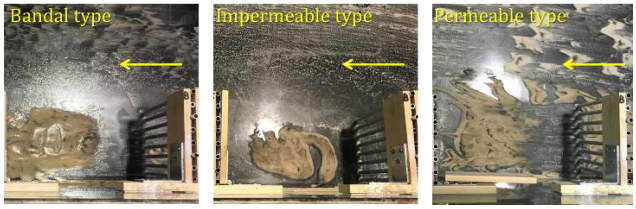

Fig.8 Shapes of sediment deposition corresponding each type of spur dikes

strongly influenced by the presence of the impermeable part serving to promote sediment deposition. Therefore, reducing the size of impermeable part would make it difficult to cause sediment deposition owing to changes in flow characteristics.

5. CONCLUSIONS

In this study, we conducted channel experiments to examine the suspended-load-deposition function of Bandal-type spur dikes with different size ratios of permeable and impermeable parts. Results of the study demonstrate two characteristics of the Bandal deposition function. It was observed that the suspended load volume passing through the permeable part strongly affects the deposition function. This may be attributed to low flow velocity downstream of the Bandal. Secondly, the suspended load volume moving from the main stream towards the Bandal-installation section also affects the deposition function. This effect is caused by the water-splash effect resulting from flow impingement on the impermeable part of the Bandal, thereby causing three-dimensional flow. Furthermore, it was observed that the most upstream Bandal—with the greatest splashing effect—controls the moving sediment volume. Because the deposition volume was the largest at the section between the first and second Bandal installations, the sediment volume flowing into the section affect. When the size ratio of permeable/impermeable parts is large, a large sediment volume tends to flow into the Bandal; however, attainment of three-dimensional flow becomes difficult. The study demonstrates that by setting a Bandal comprising a large permeable part leads to greater flow impingement on the impermeable part, thereby promoting sediment deposition.

In future studies, we intend to conduct experiments under movable-bed conditions to consider the effects of local scouring and planning to demonstrate effective deployment of Bandals along actual rivers as countermeasures against river-bank erosion.

ACKNOWLEDGMENT: The research is supported by JST/JICA SATREPS program on disaster prevention/ mitigation measures against floods and storm surges in Bangladesh (PI: Prof. Hajime Nakagawa) and future development funding program Kyoto university research coordination alliance.

REFERENCES

Akikusa, I., Kikkawa, H., Sakagami, Y., Asida, K. and Tsutiya, A. (1960): Study on spur dikes, Research report of Public Works Research Institute, Vol. 107, pp. 61-153. (in Japanese with English abstract).

Alauddin M., Tashiro T, and Tsujimoto T. (2011): Design of groynes modified with both alignment and permeability for lowland river problems. Journal of Applied Mechanics, JSCE, 2(67), pp. 645-652.

Dehghani, A.A., Azamathulla, Md. H., Hashemi Najafi, S.A. and Ayyoubzadeh, S.A. (2013): Local scouring around L-head groynes, Journal of Hydrology, Vol. 504, pp. 125-131.

Fukuoka, S., Watanabe, A. and Nishimura T. (1992): On the groin arrangement in meandering rivers, Journal of Hydraulic, Coastal and Environmental Engineering, JSCE443/II-18, pp.27-36. (in Japanese with English abstract).

Ghodsian, M. and Vaghefi, M. (2009): Experimental study on scour and flow field in a scour hole around a T-shape spur dike in a 90° bend, Internationaxl Journal of Sediment Research, Vol. 24, Issue 2, pp. 145-158.

Nakagawa, H., Teraguchi, H., Kawaike, K., Baba, Y. and Zhang, H. (2011): Analysis of Bed Variation around Bandal-like Structures, Annuals of Disaster Prevention Research Institute, Kyoto University, No.54B, pp. 497-510.

Nakagawa, H., Zhang, H., Baba, Y., Kawaike, K. and H. Teraguchi (2013): Hydraulic characteristics of typical bank pro-tection works along the Brahmaputra/Jamuna River, Bangladesh, Journal of Flood Risk Management, Wiley, Vol.6, No.4, pp. 345-359.

Nishio, K., Nakagawa, H., Kawaike, K. and Zhang, H. (2016): Experimental study on flow field around Bandal-like structures under suspended load transport condition, Annual Journal of Hydraulic Engineering, JSCE, Vol.60, pp. I_841-I_846. (in Japanese with English abstract).

Rahman, M.M., Nakagawa, H., Ishigaki, T. and Khaleduzzaman, A. (2003): Channel stabilization using Bandalling, An-nuals of Disaster Prevention Research Institute, Kyoto University, No.46B, pp. 613-618.

New Strategy for Landslide Mitigation Considering Cost Sustainability

Giulia BOSSI[1] and Gianluca MARCATO[1*]

[1]CNR-IRPI – National Research Council of Italy, Research Institute for Geo-Hydrological Protection, Italy
*Corresponding author. E-mail: gianluca.marcato@irpi.cnr.it

In most developed countries the budget devoted to structural risk mitigation of natural hazards such as floods and landslide is reducing. On top of that, mitigation structures constructed decades ago require some maintenance that it is seldom guaranteed since they are widespread in all the territory and inspections are infrequent. In some cases, the cost correlated with the engineering activities could be compensated through the association of works that provide economic return on the long term.
The case study consists of a slope instability phenomenon crossed by a National Road that connects the Veneto and Friuli Venezia Giulia regions. Due to the risk conditions the phenomenon has been investigated and monitored for more than 15 years. The landslide is crossed by a torrent and near the crown of the instability phenomenon some springs are present. The opportunity to use the water removed from the slope to produce energy through a small hydropower plant could help sustain economically the remediation project.

Key words: SABO, slope stability, countermeasure works, micro hydro, economic sustainability

1. INTRODUCTION

While population in mountain areas increase do to anthropic pressure, question arise about how to cope with the risk related to landslide in a cost effective manner [*Blaikie et al.,* 1994*; Eisbacher,* 1982].

Some authors approach the issue using a large scale of analysis, calculating the cost of damage associated with landslides at national scale [*Hilker et al.,* 2009; *Klose et al.,* 2016]. These estimates are of great use for insurance companies or nations that centralize the budget devoted to landslide protection measures. However, other nation de-centralize the jurisdiction for risk mitigation to local authorities such as regions or even municipalities.

In Italy rarely National or Regional authorities undertake the costs associated with countermeasure works for slope stability. For these reason most of the times the financial burden for structural mitigation works must been sustained by municipalities and local communities [*Scolobig et al.*, 2014*; Prenger-Berninghoff et al.*, 2014). However small municipalities rely on small budget and if the landslide does not threaten lives directly, the construction investments are often sub-prioritized. Besides local communities are often against large stabilization intervention with significant impacts on landscapes or that would lead to the expropriation of some of their land [*Scolobig et al.*, 2016]. In this framework the definition of slope stability works that would financially self-sustain themselves could be the only option for reducing risk with local support.

In some cases, it could be feasible to install micro hydro power plants to convoy and collect the water that induces slope instability and use the water drop to generate electric power. These plants on the medium run will then pay themselves and provide some resources for maintenance works of already present structural countermeasure works such as check dams and culverts.

In this work, we present the case study of a medium-size landslide located in the Eastern Italian Alps that has been monitored for more than a decade. The landslide intercepts a National Road but despite that, the mitigation work that have been implemented do not protect the entire exposed road segment due to the lack of resources of the municipality and disputes between the national and local authorities. The countermeasure works design consists in extracting and convoying the water that flows above and within the slope in order to reduce the landslide displacements, then using the available

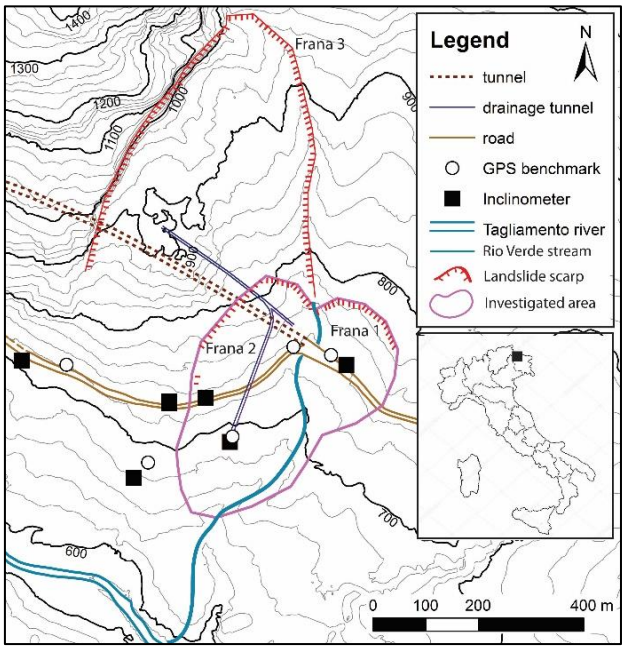

Fig. 1 Study area of Passo della Morte, the bigger scarp on the top of the figure belongs to the blockslide (Frana 3)

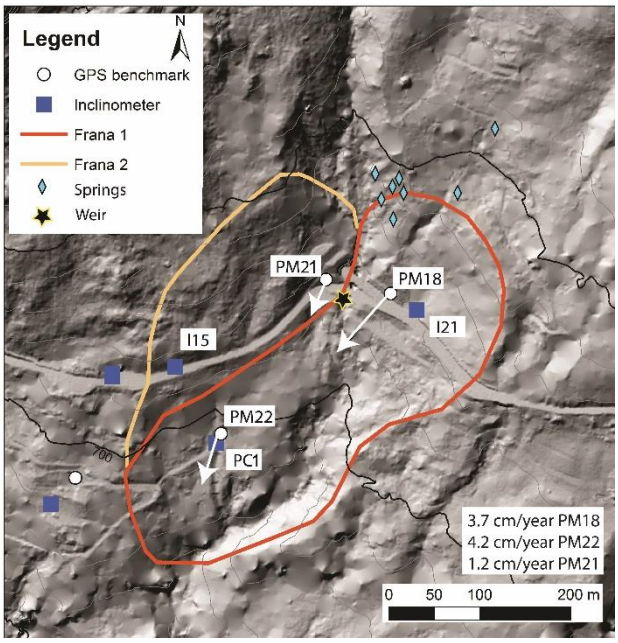

Fig. 2 Monitoring network for Frana 1 and Frana 2 and location of the springs. The white arrows represent the displacement directions of the GPS benchmarks

130 m drop to produce hydroelectric power. In this way the plant would provide economic return on the long term that would pay the costs of the stabilization and provide funds for maintenances.

2. THE STUDY AREA

Passo della Morte is a narrow gorge of the Tagliamento river in the municipality of Forni di Sotto (UD); the former National Road, that was the only route along the valley, was subject to rockfalls and snow -avalanches in the area. For these reason a new road tunnel was designed and then constructed since 1994 and opened in 2008. The eastern tunnel portal was located just after the crossing of a small stream called Rio Verde.

In 1996 the road tunnel was disrupted at during a major rainfall events. In fact a large block slide (called "Frana 3") is present and the increase of displacements due to the meteoric events caused the collapse of the structure at about 300 m from the eastern entrance [*Bossi et al.*, 2017]. During the same event a se condary slope instability (called "Frana 2") affected the tunnel portal. Concurrently also 200 m of national road before the entrance has been displaced and subsided of some centimeters due to the activity of a landslide called ("Frana 1"). The peculiarity of Frana 1 and Frana 2 is that while they have distinct scarps they converge at the toe forming a heart shaped slope instability that needs to be investigated as a whole (**Fig. 1**). The two scarps are divided by the Rio Verde torrent, a small stream that flows just before the eastern tunnel entrance. The tunnel and the old national road cross the Rio Verde above two concrete box culverts.

In the following years a new project for the tunnel restoration was designed; the construction, that started in 2004 and was finished in 2008, was coupled with a drainage tunnel located underneath the road tunnel in order to drain the water from the slope and mitigate the displacements of Frana 3 and Frana 2.

2.1 Societal background

Managing the damage induced by the landslides of the study area and associated risk for the road tunnel is responsibility of the Italian National Road Authority (ANAS) that is the formal owner of the infrastructure.

On the other hand, there is no direct responsible for the 200 meters of road before the eastern entrance as there are several institutions that may and may not have interest in the slope stabilization. In this framework, CNR–IRPI was involved to monitor and modelling the landslides of the area and provide reliable risk scenarios. This would help also in assessing the public body that will be responsible for the Frana 1-Frana 2 issue. The municipality of Forni di Sotto is particularly interested in solving the problem since, if the road suffers disruptions, the traffic would be diverted in another valley with local commuters facing more than one hour of additional travel-time. However small municipalities in Italy are subject to several budget constrains so a

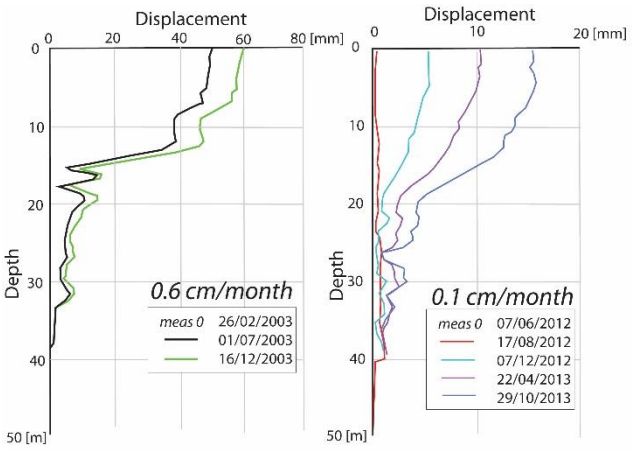

Fig. 3 Displacements and velocities measured in inclinometer I15 series (Frana 2). On the left before the construction of the drainage tunnel; on the right after the drainage tunnel was finished and operative.

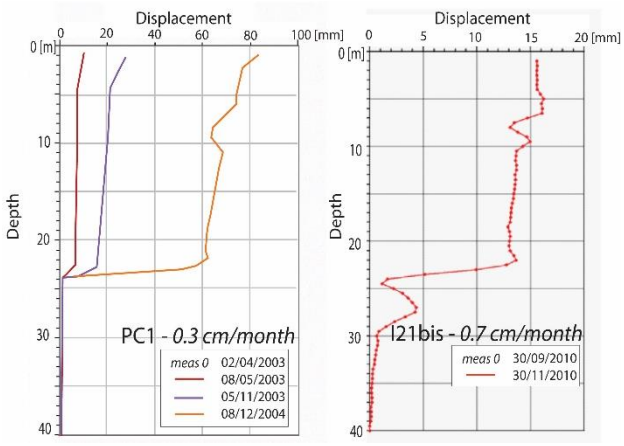

Fig. 4 Displacements and velocities measured in inclinometers PCbis and I21bis (Frana 1).

cost-effective mitigation strategy that would also provide some economic return for the local community is the only win-win strategy that would guarantee the remediation of the Frana 1-Frana 2 problem.

3. INVESTIGATION

3.1 Monitoring

The landslides of Passo della Morte have been monitored for more than a decade with piezometers, inclinometers (periodic and in place) and GNSS surveys. Some instruments were deployed by ANAS while others were installed by the National Research Council of Italy (CNR-IRPI) since 2002.

The monitoring instruments were deployed to control the movements of the landslides and to understand the slope kinematics; moreover, to see if the mitigation works were effective and to provide data on which design new countermeasure if the already implemented ones were not sufficient (**Fig. 2**).

Periodical Global Navigation Satellite System (GNSS) survey provided information about superficial displacements.

Several inclinometric tubes have been installed within the years. That helped define with good accuracy the tri-dimentional shape of the slip surface. The protocol adopted by CNR-IRPI called for the deployment of in-place inclinometers once the location of the slip surface was defined through periodic inclinometric surveys. Moreover, when a borehole broke another one was drilled nearby to follow the evolution of the landslides for several years in order to gain a large dataset. At the moment there are still active three inclinometers in the heart-shaped landslide. Each inclinometer hole is also coupled with a piezometer equipped with a sensor to acquire data in real-time. The monitoring system was integrated in 2012 with a sharp crested thin plate weir that was installed in the Rio Verde to assess the water discharge of the torrent. The regular shape of the culverts made easier the installation of the weir and of the piezometer that measures the water height.

4. RESULTS

Analyzing data from the inclinometers installed on Frana 2 it is possible to see that the construction of the drainage tunnel changed the displacement pattern of the landslide (**Fig. 3**). In the measures of 2003 there is a distinct slip surface and the velocity of the movement is of 6 mm per month. In contrast, in 2012 the drainage tunnel was operative since 5 years and the rate of movement reduced to 1 mm/month (**Fig. 3**). Moreover, while before the drainage tunnel a distinct slip surface was detectable, in the 2012-2013 inclinometer the displacements are distributed along the whole landslide body as the slope moves under creep.

On the other hand, inclinometers PC1 and I21 shows a very distinct slip surface (**Fig. 4**). This evidence allowed to define the range of each of the two landslides as it is indicated in **Fig. 2**. This hypothesis is also supported by the different degree of activity measured by the GNSS benchmarks. PM18 moves with an average velocity of 3.7 cm/year, PM22 of 4.2 cm/year while PM21 of 1.2 cm/year. The velocities obtained from I21bis are above the annual average because the autumn of 2010 was particularly rainy.

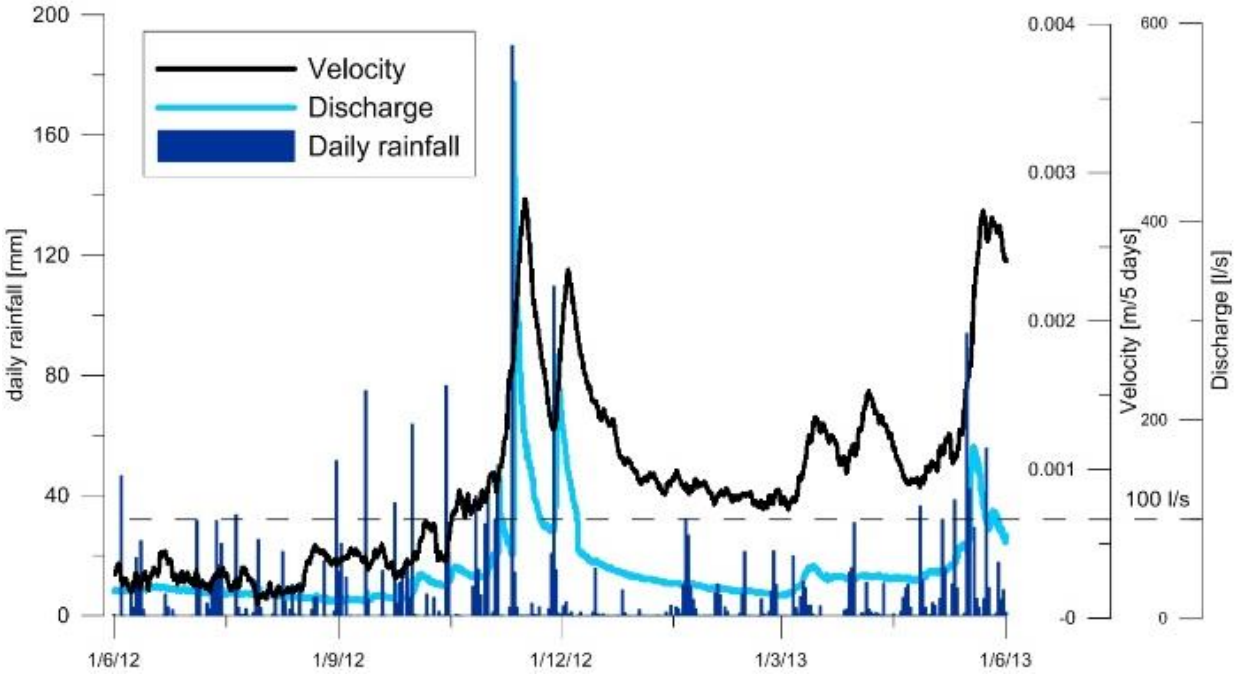

Fig. 5 Velocity of the landslide along the slip surface in I21bis in comparison with the daily rainfall and the discharge in the Rio Verde – the dashed line represents the proposed plant's maximum discharge

Piezometers show that the water table does not reach the slip surface of Frana 1. This evidence it is particularly interesting since it excludes one of the main causes of landslide activity such the variation of the phreatic level inside the landslide body.

What appears from data from the in-place inclinometers is that after the construction of the drainage tunnel the lower part of Frana 2 is an epiphenomenon of Frana 1. In fact Frana 1 dynamic is characterize by sudden accelerations that are then followed by a smaller increase of activity in Frana 2. The movement of Frana 1 disturbs the creeping dynamic Frana 2 than sacks down of few millimeters.

The displacement pattern of the in-place inclinometer in PC and I21 was analyzed and confronted with rainfall data and the discharge measured in the thin plate weir along Rio Verde.

Data support the hypothesis that the displacement pattern of the landslide is influenced by the water discharge of the Rio Verde rather than rainfall. A Pearson test results with a correlation of 0.85 for water discharge. Lesser correlation values have been observed confronting directly displacements with precipitation or cumulated precipitation in the 1, 2, 3, 6, 10 days intervals.

This could be explained by toe erosion and internal erosion near the toe of Frana 1-2 during high discharge events. The well graded soil forming the landslide body has been in fact analyzed with geotechnical tests and has been proven to be extremely sensitive to water content. Besides the groundwater circulation near the slip surface in the lower part of Frana 1 transports the finer particles of the landslide body away inducing displacements and sagging.

In **Fig. 5** more than a year of monitoring data is represented: usually during autumn and spring snowmelt the aquifer that feeds the stream recharges and higher discharges are observed. The discharge of Rio Verde originates from the springs located at the crown of Frana 1 and only on rare major rainfall events has a contribute from the upper basin. This is due to the complex hydrogeology of the area where highly fractured limestones collect and convoy rainfall disregarding superficial topography.

5. MITIGATION

In Italy micro hydro plants (5 kW to 100 kW) are subsidized on a National basis, giving 0.22 €/kWh. Mountain municipalities are therefore incentivized to exploit every drop available to generate electric power to sell to the national network.

For the Forni di Sotto municipality using the discharge of the Rio Verde torrent could be a win-win strategy. The power plant would pay for itself in few years and concurrently the measure would stabilize the heart-shaped landslide "Frana 1-2" of Passo della Morte.

5.1 Hydrology and hydraulics

The Rio Verde Basin covers an area of about 2 km^2 with a drop between 2122 m a.l.s. of Mt. Tinisa to 580 at the outlet in the Tagliamento river.

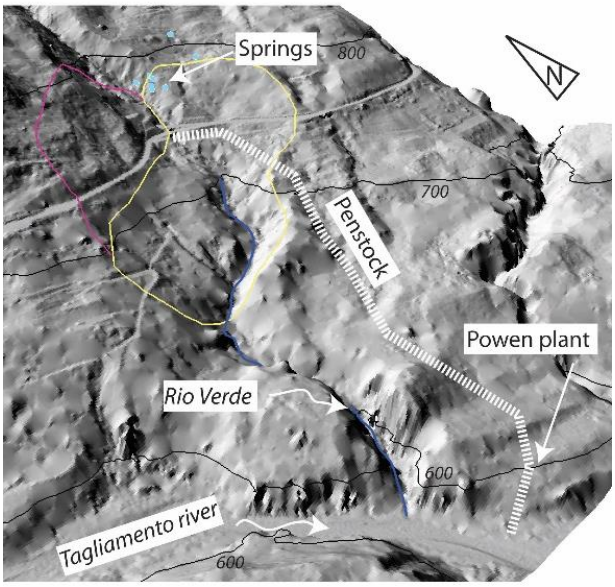

Fig. 6 Intervention areas, capitation of water from the springs and buried penstock layout

Water discharge in the Rio Verde however is more sustained by the flow exiting from the springs on the left hand side of Rio Verde (**Fig. 2**) rather than from superficial runout from the upper basin. For most of the year in fact the river bed upstream of the springs is dry and does not carry any water.

The risk regarding excessive sediment transport that may compromise the plant operation is negligible. The stream is characterize by low sediment transport, the main channel has a well developed natural armour since for most of its track it is directly in contact with limestone. The springs do not carry much sediment, just a little amount of sand that could be easily segregated in a transversal deposition tank that would treat the water before entering into the penstock. The tank could be easily placed in the box culvets below the roads.

Not considering the contribution of the peaks induced by extreme rainfall events runoff the average discharge of the stream has been quantified in 45 l/s. The minimum discharge measured in three years was 12 l/s after an extremely dry year.

The project propose to intercept a maximum of 100 l/s and leave to flow in the Rio Verde the exceeding discharge that may occur during intense rainstorm. The value of 100 l/s represent a balance between economic long-term sustainability and expected effect since based on our measures when the water discharge is sufficiently low the movements of the landslide stop (**Fig. 5**).

The intake catch box will be placed below the bridge that leads to the road tunnel at 735 m a.s.l. A HDPE (High Density Polyethylene) penstocks would carry the water in pressure to the powerhouse

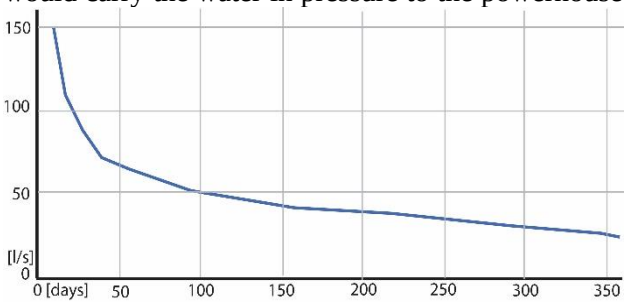

Fig. 7 Flow duration curve of the extractable discharge from the springs and Rio Verde torrent

located at 603 m a.s.l..

The restitution of water to the natural network will occur at 575 m a.s.l. through a natural channel that will need to be protected with local stones from erosion.

5.2 Economic evaluation

A flow duration curve has been derived from the seven year dataset (**Fig. 7**). The available data does not cover a long time-span, however the climate regime of the observation period was sufficiently various to allow a statistical analysis. Moreover, the springs regime is seldom as variable as the superficial discharge.

For the plant the minimum intake is 14 l/s, the maximum intake is 90 l/s. Since the average intake is 45 l/s it is possible to calculate the average nominal power at 58.27 kW with a drop of 132 m. Therefore the yearly average production will be of 378000 kWh. If we consider an average price of 219 €/MWh the annual gross income generated by the plant will be of 65745 €.

The cost of construction for the plant will be around 300.000 €. The turbine will be installed in an old isolated building property of the municipality to reduce the impact of landscape and reduce costs. The excavation of the soil to bury the penstock will be very easy since it may be performed by light trencher digging in the soft colluvium located on right hand side of the Rio Verde. All these elements allow to reduce the costs and the impact on landscape of the micro hydro plant.

6. CONCLUSIONS

A mitigation strategy of the landslide that affects the only route that serves the Upper Tagliamento valley has been defined by investigation of its cinematic through long-term monitoring. Evidence gathered in the ten year observation period show that the displacements of Frana 1-2 are strongly influenced by the water discharge in the Rio Verde. Collecting the water from the stream and use it to generate hydro power could be a win-win intervention for an economically self-sustained slope stabilization measure. Moreover, the countermeasure would produce lesser environmental impact than extensive engineering stabilization works but it may be coupled in a second phase with lesser impacting SABO works collecting all the water directly from the springs.

Since anthropic pressure in mountain environment is increasing so it is the request for protection from natural hazard of new allotments and infrastructures. At the same time the SABO works serving the most dangerous areas, which in general have been constructed more than fifty years ago, start to require maintenances or downright reconstruction. The conjunction between the need for maintenances of fundamental mitigation works and the increasing request of safety by mountain population represents a great challenge in times of budget constraints for local and national governments. In this framework the possibility to provide design solution for countermeasure works that would economically self-sustain themselves and eventually produce revenues, like micro hydro plants, should always be considered.

ACKNOWLEDGMENT: We thank Protezione Civile Friuli Venezia Giulia and in particular Gianni Burba and Gabriele Peressi for the support.

REFERENCES

Blaikie P, Cannon T, Davis I, and Wisner, B (1994): At risk: natural hazards, people's vulnerability and disasters. Routledge, 2014.

Bossi G, Schenato L, Marcato G (2017): Structural Health Monitoring of a Road Tunnel Intersecting a Large and Active Landslide. Applied Sciences, Vol. 7:1271.

Eisbacher RH (1982): Slope stability and land use in mountain valleys. Geoscience Canada Vol. 9, pp. 14-27.

Hilker N, Badoux A, Hegg C (2009): The Swiss flood and landslide damage database 1972–2007. Natural Hazards and Earth System Sciences, Vol. 9, pp. 913–925.

Klose M, Maurischat P, Damm B (2016): Landslide impacts in Germany: A historical and socioeconomic perspective. Landslides, Vol. 13, pp.183–199.

Prenger-Berninghoff K, Cortes VJ, V. J., Sprague, T., Aye, Z. C., Greiving, S., Głowacki, W. and Sterlacchini, S. (2014): The connection between long-term and short-term risk management strategies for flood and landslide hazards: examples from land-use planning and emergency management in four European case studies. Natural Hazards and Earth System Sciences, Vol.14, pp. 3261–3278.

Scolobig A, Linnerooth-Bayer J, Pelling M (2014): Drivers of transformative change in the Italian landslide risk policy. Internationa Journal of disaster risk Reduction, vol. 9, pag124–136.

Scolobig A, Thompson M, Linnerooth-Bayer J (2016): Compromise not consensus: designing a participatory process for landslide risk mitigation. Natural Hazards, Vol. 81, pp. 45–68.

Load Evaluation of Debris Flow Against Steel Open Sabo Dam Using DEM

Toshiyuki HORIGUCHI[1*], Yoshiharu KOMATSU[1], Satoshi KATSUKI[1] and Nobutaka ISHIKAWA[2]

[1] Dept. of Civil Eng., National Defense Academy, (1-10-20 Hashirimizu, Yokosuka, Kanagawa, 239-0811, Japan)
[2] Professor Emeritus of National Defense Academy, (1-10-20 Hashirimizu, Yokosuka, Kanagawa, 239-0811, Japan)
*Corresponding author. E-mail: htoshi@nda.ac.jp

Although latest statistics indicate a decrease in the number of victims of natural disasters in Japan, numbers of sediment disasters have actually increased. For instance, a torrential downpour hit the mountain areas of northern Kyusyu in July 2017, and this caused loss of live and damage to property. Development of sediment control structures is necessary for countering sediment and debris flow disasters. One of such counter measures is steel open type check dam (hereafter, steel open Sabo dam). By utilizing segregation mechanism of boulders in a debris flow, the steel open dam is expected to capture them. When the debris flow attacks the steel open Sabo dam, huge impact load occurs between boulders and steel pipes. Therefore, it is very significant to evaluate the debris flow load of steel open Sabo dam from the design point of view. This paper presents experimental and computational approaches to impact load of debris flow including boulders hitting the steel open Sabo dam. First, debris flow experiments are carried out by using 1/40 scale channel slope, and the impact load is measured by using a load cell. Second, the distinct element method is used for a simulation analysis of the model test. Herein, the computational results show good reproducibility of experiments. This debris flow load analysis will be very useful for the safety assessment of steel open dam against rock impact in the debris flow.

Key words: Steel open Sabo dam, impact load, DEM, simulation, debris flow

1. INTRODUCTION

Although latest statistics indicate a decrease in the number of victims by natural disasters in Japan, there has been an increase in the number of sediment disasters. In addition, the latest worldwide statistics of a natural disaster such as typhoons, tsunamis, floods, avalanches, landslides, debris flows and earthquakes indicate that the number of victims is increasing. Among those problems, debris flow hazards have increased removal costs of debris flows from dam reservoir or general damage to dam sites. One of such countermeasures is the steel open type check dam (hereafter, steel open Sabo dam) as shown in **Photo 1**, which is composed of steel pipes. They are designed to allow sand and gravels to pass downstream through open spaces. But, when the debris flow occurs, the steel open Sabo dams are expected to capture huge rocks and/or boulders which are concentrated in a front part of debris flow, and the following gravels and sand [*Sabo & Landslide Technical Center*, 2016]. During the process to capture the boulders, the steel pipes are directly hit by huge boulders, then large impact loads occur between boulders and steel pipes. Then the impact load sometimes breaks the pipes. Therefore, the impact load evaluation of steel open Sabo dam is very significant from the design point of view.

Photo 1 Steel open Sabo dam

There are research works discussing debris flow load evaluation including boulder impact. Ikeya[3] et. al., classified the type of debris flow model by means of fluid theory and also solid state theory, which disposes of the system of the impact load [*Ikeya*;1987]. Mizuyama investigated the method of impact load estimation on concrete dam using two

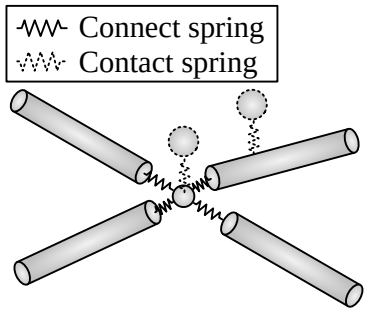

Fig. 1 Structural model

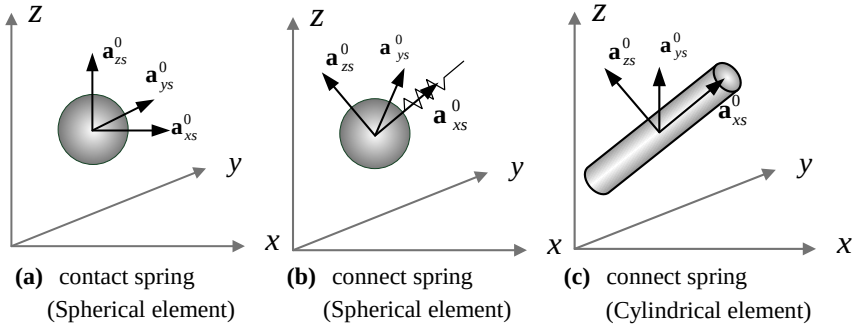

Fig. 2 Initial posture of element and spring

characteristic debris flow, which utilizes fluid theory [*Mizuyama*; 1987]. Among them, focusing on the load due to the collision of the boulder, local failure energy in a collision is estimated. This technique is adopted in the design manual [*Sabo & Landslide Technical Center*, 2016].

Miyoshi et al., carried out the Sabo dam experiment on impact load evaluation in the unsteady jet [*Miyoshi*; 1990]. Consequently, the mechanism of impact which occurs debris flow against Sabo dam was clarified. Daido et al., evaluated the pressure of mud-debris flow acting on a flat face of the dam [*Daido*; 1994]. The debris flow was regarded as a non-compressible fluid or as a tiny-compressible fluid. Yamamoto et al., discussed impact load caused by debris flow on a Sabo dam by DEM analysis [*Yamamoto*; 1998]. The impact load experiment was performed for the wall type dam. And those are analysed by the modified DEM analysis which takes into account the rolling resistant moment buoyancy and drag force of water. Ishikawa et al., investigated the impulsive load of debris flow by using pumice stones in the channel flume and simulated it by using smoothed particle hydrodynamics [*Ishikawa*; 2009]. However, the study on the debris flow load acting on a steel open dam has not been carried out sufficiently.

This paper presents experimental and computational approaches to impact load of debris flow including boulders against the open type check dam. First, the debris flow experiments are carried out by using 1/40 scale channel, and the impact loads are measured by using a load cell. Second, DEM is used for a simulation analysis of the model test.

2. DEM SIMULATION AND LOAD EVALUATION

2.1 Outline of distinct element method

The DEM normally uses spherical model. Contact judgement between the elements are done each time. If one element contacts with another element, a spring action is generated between the elements and that equation of motion is solved based on the contact force.

2.2 Contact spring and connect spring

Fig. 1 shows an image of the contact spring and the connect spring. The functions of the connect spring and the contact spring have a little difference. If a spherical element touches the cylindrical element, then the contact spring between two elements is set. On the other hand, the connect spring is set between two cylindrical elements at the beginning. In addition, the spring is always kept between those elements. Moreover, the position and direction of the contact spring at the action point was updated based on the combination and position of those elements, and removed by contact judgement. On the other hand, the connect spring is fixed at the connected elements. Updating manner of those spring deformation and force is described later.

2.3 Displacement and posture matrix of element

A spherical element with contact spring function in the global coordinate system and the local coordinate system is shown in **Fig. 2 (a)**. The direction of the connected spring is assumed to be the local *x*-coordinate of the local coordinate system, and the posture matrix that has *y* direction vector of the *xy* plane of the global coordinate system is used as shown in **Fig. 2 (b)**. In this study, the following relation has been applied to denote the posture matrix at each point in time:

$$\mathbf{A}_s = \begin{bmatrix} \mathbf{a}_{xs}^{\mathrm{T}} \\ \mathbf{a}_{ys}^{\mathrm{T}} \\ \mathbf{a}_{zs}^{\mathrm{T}} \end{bmatrix} = \mathbf{T}_s \mathbf{A} \tag{1}$$

where $\mathbf{A}_s$: posture matrix corresponding to connect spring of spherical element, $\mathbf{T}_s$: coordinate conversion matrix for converting posture matrix $\mathbf{A}$ to $\mathbf{A}_s$ that denotes the spherical element, and $\mathbf{a}_{xs}$, $\mathbf{a}_{ys}$, $\mathbf{a}_{zs}$: *x*, *y*, *z* of posture matrix corresponding to connect spring of spherical element $\mathbf{A}_s$.

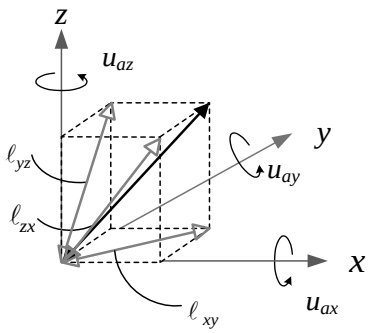

Fig. 3 Renewal of posture matrix

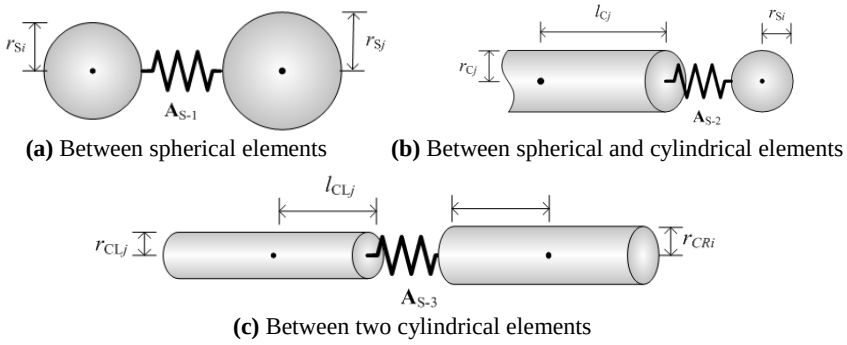

(a) Between spherical elements **(b)** Between spherical and cylindrical elements

(c) Between two cylindrical elements

Fig. 4 Each of connect spring

In addition, the *x* coordinate in the local coordinate system is specified as the central axis of the cylindrical element as shown in **Fig. 2 (c)**. Initial posture matrix coordinates are parallel to the specified global coordinate system. The following procedure is conducted for updating the posture matrix. The posture matrix is a matrix composed of the direction cosine vector and with unit vector length.

Here, the posture matrix of connect spring is assumed to be updated by the following approximate solutions with reference to **Fig. 3**:

$$x_{ax}(t+\Delta t)=\ell_{xy}\cdot\cos\left\{\tan^{-1}\left(\frac{y_{ax}}{x_{ax}}\right)+\Delta u_{az}\right\}+\ell_{zx}\cdot\sin\left\{\tan^{-1}\left(\frac{x_{ax}}{z_{ax}}\right)+\Delta u_{ay}\right\}+x_{ax}(t) \quad (2a)$$

$$y_{ax}(t+\Delta t)=\ell_{yz}\cdot\cos\left\{\tan^{-1}\left(\frac{z_{ax}}{y_{ax}}\right)+\Delta u_{ax}\right\}+\ell_{xy}\cdot\sin\left\{\tan^{-1}\left(\frac{y_{ax}}{x_{ax}}\right)+\Delta u_{az}\right\}+y_{ax}(t) \quad (2b)$$

$$z_{ax}(t+\Delta t)=\ell_{zx}\cdot\cos\left\{\tan^{-1}\left(\frac{x_{ax}}{z_{ax}}\right)+\Delta u_{ay}\right\}+\ell_{yz}\cdot\sin\left\{\tan^{-1}\left(\frac{z_{ax}}{y_{ax}}\right)+\Delta u_{ax}\right\}+z_{ax}(t) \quad (2c)$$

where ℓ_{xy}, ℓ_{yz} and ℓ_{zx} : length of the vector $\mathbf{a}_x$ at time *t* projected to *xy*, *yz*, *zx* plane as indicated in **Fig. 3**: x_{ax}, y_{ax}, z_{ax} : *x*, *y*, *z* direction elements of $\mathbf{a}_x$ at time *t*: Δu_{ax}, Δu_{ay}, Δu_{az} : incremental quantity of rotation angle vector $\mathbf{u}_a$ along *x*, *y*, *z* directions in the incremental time Δt, respectively.

Therefore, $\mathbf{a}_x$, $\mathbf{a}_y$, $\mathbf{a}_z$ are obtained as follows.

$$\mathbf{a}_x(t+\Delta t)=\frac{1}{\sqrt{(x_{ax}(t+\Delta t))^2+(y_{ax}(t+\Delta t))^2+(z_{ax}(t+\Delta t))^2}}\begin{bmatrix}x_{ax}(t+\Delta t)\\ y_{ax}(t+\Delta t)\\ z_{ax}(t+\Delta t)\end{bmatrix} \quad (3a)$$

$$\mathbf{a}_y(t+\Delta t)=\frac{1}{\sqrt{(x_{ay}(t+\Delta t))^2+(y_{ay}(t+\Delta t))^2+(z_{ay}(t+\Delta t))^2}}\begin{bmatrix}x_{ay}(t+\Delta t)\\ y_{ay}(t+\Delta t)\\ z_{ay}(t+\Delta t)\end{bmatrix} \quad (3b)$$

$$\mathbf{a}_z(t+\Delta t)=\mathbf{a}_x(t+\Delta t)\times\mathbf{a}_y(t+\Delta t) \quad (3c)$$

2.4 Equation of motion

The equation of motion considering the damping effect in the DEM is usually expressed as follows.

$$\mathbf{M}\ddot{\boldsymbol{u}}_t+\mathbf{D}\dot{\boldsymbol{u}}_t+\boldsymbol{f}_K\boldsymbol{u}_t=\boldsymbol{f}_t \quad (4)$$

where $\mathbf{M}$: mass matrix, $\mathbf{D}$: damping matrix, $\mathbf{f}_K$: internal force vector caused by contact spring force or connect spring force, $\mathbf{f}$: external force vector, $\mathbf{u}$: displacement vector, and $\dot{(\cdot)}$, $\ddot{(\cdot)}$: each of the first or second derivatives of time, respectively.

2.5 Equilibrium condition

Equilibrium in the connect spring between the spherical and cylindrical elements is illustrated by the structural model in Fig.1. Herein, the direction of the compression force is considered as the *x*-axis. The connect spring between two spherical elements is illustrated in **Fig. 4 (a)**. The connect spring between the spherical and cylindrical elements is illustrated in **Fig. 4 (b)**. The connect spring between two cylindrical elements is illustrated in **Fig. 4 (c)**.

Then, the equilibrium of forces is converted into the spring force in the global coordinate by considering connect spring of element in local coordinate as follows:

$$\widetilde{\mathbf{S}}_n=\mathbf{T}_{ns}\mathbf{S}_c \quad (5)$$

where $\widetilde{\mathbf{S}}_n$: force vector in the spring local coordinate, $\mathbf{S}_c$: force vector in connected spring, $\mathbf{T}_{ns}$: a geometric transformation matrix.

By using posture matrix $\mathbf{A}_n$ of the element and posture matrix $\mathbf{A}_s$ of connected spring, $\mathbf{T}_{ns}$ is given by the following equation:

$$\mathbf{T}_{ns}=\mathbf{A}_n\mathbf{A}_s^{\mathrm{T}}=\begin{bmatrix}\mathbf{a}_{xn}^{\mathrm{T}}\\ \mathbf{a}_{yn}^{\mathrm{T}}\\ \mathbf{a}_{zn}^{\mathrm{T}}\end{bmatrix}\begin{bmatrix}\mathbf{a}_{xs}^{\mathrm{T}}\\ \mathbf{a}_{ys}^{\mathrm{T}}\\ \mathbf{a}_{zs}^{\mathrm{T}}\end{bmatrix}^{\mathrm{T}}=\begin{bmatrix}\mathbf{a}_{xn}^{\mathrm{T}}\mathbf{a}_{xs} & \mathbf{a}_{xn}^{\mathrm{T}}\mathbf{a}_{ys} & \mathbf{a}_{xn}^{\mathrm{T}}\mathbf{a}_{zs}\\ \mathbf{a}_{yn}^{\mathrm{T}}\mathbf{a}_{xs} & \mathbf{a}_{yn}^{\mathrm{T}}\mathbf{a}_{ys} & \mathbf{a}_{yn}^{\mathrm{T}}\mathbf{a}_{zs}\\ \mathbf{a}_{zn}^{\mathrm{T}}\mathbf{a}_{xs} & \mathbf{a}_{zn}^{\mathrm{T}}\mathbf{a}_{ys} & \mathbf{a}_{zn}^{\mathrm{T}}\mathbf{a}_{zs}\end{bmatrix} \quad (6)$$

where $\mathbf{a}_{xn}$, $\mathbf{a}_{yn}$, $\mathbf{a}_{zn}$: vector of each unit coordinate axis that comprises posture matrix of element assuming $n = L$ (Left side) or $n = R$ (Right side).

The equilibrium condition is expressed as follows:

$$\widetilde{\mathbf{f}}_{\mathrm{L}}=\widetilde{\mathbf{C}}_{\mathrm{L}}^{\mathrm{T}}\widetilde{\mathbf{S}}_{\mathrm{L}} \quad (7a)$$

$$\widetilde{\mathbf{f}}_{\mathrm{R}}=\widetilde{\mathbf{C}}_{\mathrm{R}}^{\mathrm{T}}\widetilde{\mathbf{S}}_{\mathrm{R}} \quad (7b)$$

where $\widetilde{\mathbf{f}}_{\mathrm{L}},\widetilde{\mathbf{f}}_{\mathrm{R}}$: each external force vector of the element of posture matrix in the coordinate system, $\widetilde{\mathbf{S}}_{\mathrm{L}},\widetilde{\mathbf{S}}_{\mathrm{R}}$: spring force vector at the point of action according to the posture matrix $\mathbf{A}_n$, $\widetilde{\mathbf{C}}_{\mathrm{L}}^{\mathrm{T}},\widetilde{\mathbf{C}}_{\mathrm{R}}^{\mathrm{T}}$:

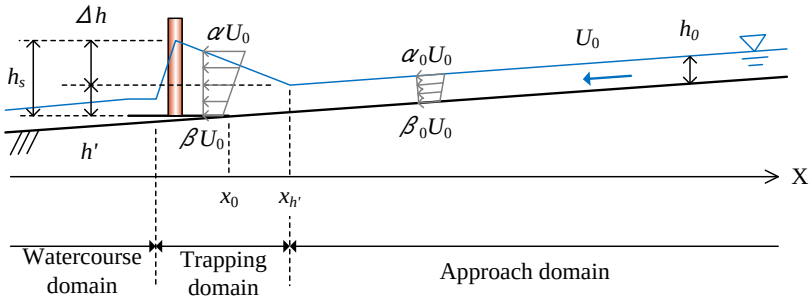

Fig. 5 Water flow domain model

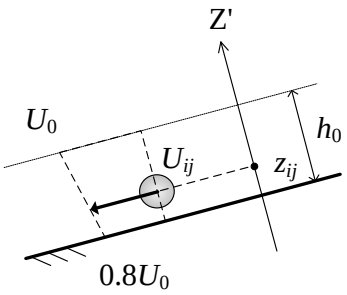

Fig. 6 Velocity distribution in approach domain

equilibrium matrix of the local coordinate system.

In addition, the local coordinate force is converted into the global coordinate system by the following equation:

$$\mathbf{f}_{\mathrm{K}n} = \mathbf{T}_{\mathrm{G}n}\tilde{\mathbf{f}}_n \tag{8}$$

where $\mathbf{f}_{\mathrm{K}n}$: force vector of gravity of the element n in the global coordinate system, $\tilde{\mathbf{f}}_n$: point gravity force vector according to posture matrix $\mathbf{A}_n$, $\mathbf{T}_{\mathrm{G}n}$: $n = L$ *or* $n = R$ is a coordinate transformation matrix converted from local coordinate system to global coordinate system. The transformation matrix is expressed as follows:

$$\mathbf{T}_{\mathrm{G}n} = \begin{bmatrix} \mathbf{x}_{\mathrm{G}}^{\mathrm{T}}\mathbf{a}_{xn} & \mathbf{x}_{\mathrm{G}}^{\mathrm{T}}\mathbf{a}_{yn} & \mathbf{x}_{\mathrm{G}}^{\mathrm{T}}\mathbf{a}_{zn} \\ \mathbf{y}_{\mathrm{G}}^{\mathrm{T}}\mathbf{a}_{xn} & \mathbf{y}_{\mathrm{G}}^{\mathrm{T}}\mathbf{a}_{yn} & \mathbf{y}_{\mathrm{G}}^{\mathrm{T}}\mathbf{a}_{zn} \\ \mathbf{z}_{\mathrm{G}}^{\mathrm{T}}\mathbf{a}_{xn} & \mathbf{z}_{\mathrm{G}}^{\mathrm{T}}\mathbf{a}_{yn} & \mathbf{z}_{\mathrm{G}}^{\mathrm{T}}\mathbf{a}_{zn} \end{bmatrix} \tag{9}$$

where $\mathbf{x}_{\mathrm{G}}, \mathbf{y}_{\mathrm{G}}, \mathbf{z}_{\mathrm{G}}$: Vector of the whole coordinate system of unit coordinate axes.

Derived from eq. (5) to eq. (9), the following formula is obtained:

$$\mathbf{f}_{\mathrm{K}n} = \mathbf{T}_{\mathrm{G}n}\tilde{\mathbf{C}}_n^{\mathrm{T}}\mathbf{T}_{ns}\mathbf{S}_{\mathrm{c}} \tag{10}$$

2.6 Water flow model

The debris flow is composed of boulders, cobbles, and water flow. Therefore, it is necessary to assume the water flow model which affects as driving force of the debris. The water flow velocity around debris flow changes owing to the interactive action of debris motion. However, this interaction is ignored in this study to reduce the computational load. Accordingly, the water flow model is adapted to two different domains in this study, as shown in **Fig. 5**.

2.6.1 Approach domain

In the approach domain, as shown in Fig.6, water flows parallel to the bottom surface of the channel. And the velocity changes proportionally in depth as follows:

$$\mathbf{U}_d = U\left(1 - 0.2\frac{d}{h_0}\right) \quad (0 \le d \le h_0) \tag{11}$$

where U: water velocity at the surface, $\mathbf{U}_{\mathrm{d}}$: water velocity vector at depth d, d: depth of related drift wood element, and h_0: depth of water in approach domain.

The water depth is obtained from experimental observations. The surface velocity is determined such that the integration of these velocities for a section area of the water flow should be equivalent to the experimental discharge.

2.6.2 Trapping domain

The water depth in the trapping domain increase proportionally closing to the steel open dam as shown in **Fig. 6**. The depth of debris flow at the steel open dam is given by the ratio of the projection area of the captured drift woods and the cross-sectional area of the water flow, as shown in **Fig. 7** as follows:

$$\begin{cases} h' = h_0 & \left(\sum A_{di}/A_0 \le 0.2\right) \\ h' = \dfrac{H - h_0}{1.3}\left(\dfrac{\sum A_{di}}{A_0} - 0.2\right) + h_0 & \left(0.2 \le \sum A_{di}/A_0 \le 1.5\right) \\ h' = H & \left(1.5 \le \sum A_{di}/A_0\right) \end{cases} \tag{12}$$

where H: height of the anti-drift-wood structure, $\mathbf{A}_{\mathrm{di}}$: the sum of the captured drift woods projection area, and A_0: cross-sectional area of the water flow.

The cross-sectional average velocity $\overline{U}$ is given by the depth h' based on the law of conservation of discharge as follows.

$$\overline{U} = \frac{h_0}{h'}U \tag{13}$$

The increment of the damping-up depth Δh is given as follows:

$$\Delta h = k_m \sin\theta_m\left(\frac{D}{W}\right)\frac{U_h}{2g} \tag{14}$$

where k_{m}: section modules, θ_{m}: angle of capturing columns to bottom, D: diameter capturing columns, W: a gap of capturing columns, and U_{h}: upstream water velocity.

Furthermore, considering the turbulence and waves of the water surface, the damping-up depth h_s is given by a random number according to the normal distribution, as shown in **Fig. 8.** Then, the maximum h_s is $h'+\Delta h$, the average of h_s is $h'+\Delta h/2$, and the

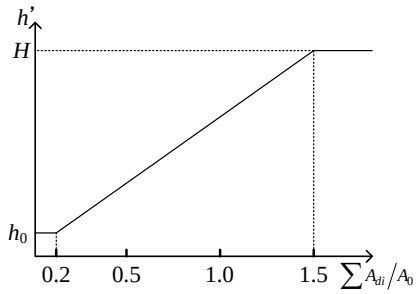

Fig. 7 Depth and relative area

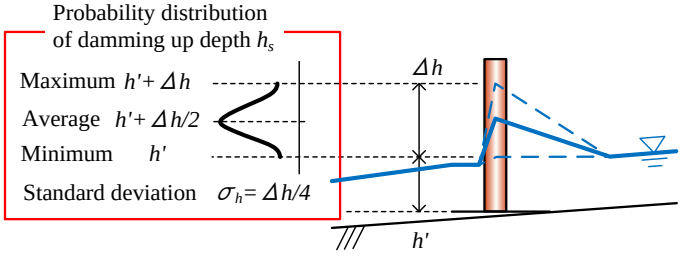

Fig. 8 Probability distribution of damming up depth h_s

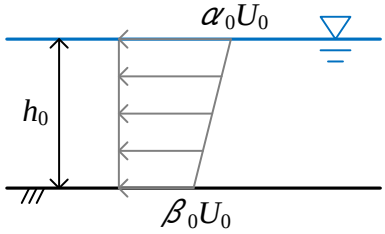

Fig. 9 Velocity distribution in trapping domain

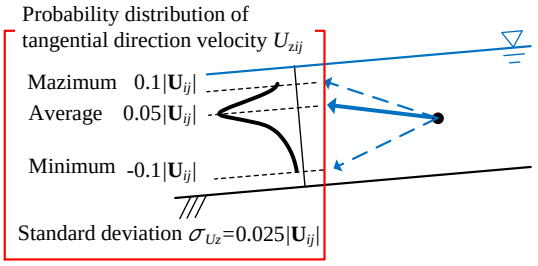

Fig. 10 Probability distribution of tangential direction velocity

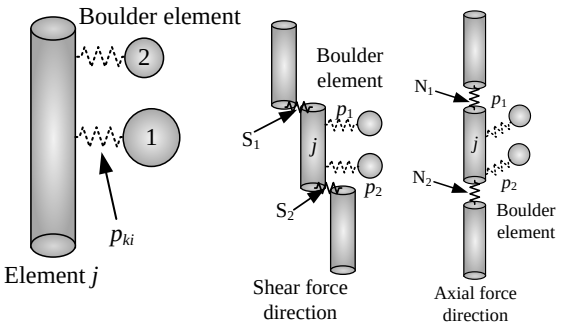

(a) Contact of element **(b)** Contact of member

Fig. 11 Load evaluation (member)

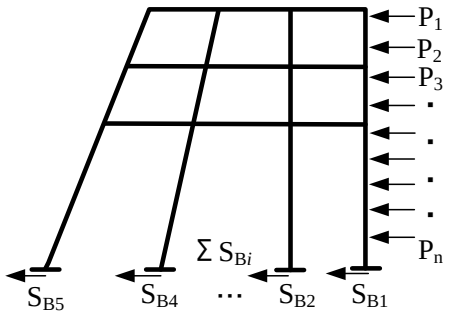

Fig. 12 Load evaluation (structure)

standard deviation of h_s is defined as $\Delta h/4$.

The velocity distribution in the trapping domain changes as shown in **Fig. 9**. To keep a constant discharge, the decrement coefficients α and β are given by coefficient γ based on the law of conservation of flow, respectively, as follows.

$$\alpha = \alpha_0 + \gamma \tag{15}$$

$$\beta = \beta_0 - 2\gamma \tag{16}$$

$$\gamma = \frac{1}{3}\left(1 - \frac{h_0}{h'}\right)(\alpha_0 + \beta) \tag{17}$$

Therefore, the velocity in the trapping domain is given as follows.

$$U_d = \frac{d}{h'}(\alpha - \beta)\overline{U} + \beta\overline{U} \tag{18}$$

Finally, by considering the turbulence of water flow, the tangential direction velocity turbulent component U_z can be given by a random number according to the normal distribution as shown in **Fig. 10**. Then, the maximum of U_z is defined as $0.3U_d$, the minimum of U_z is $-0.3U_d$, the average of U_z is $-0.15U_d$, and the standard deviation of U_z is $0.3U_d/4$.

This velocity U_z is considered only in a supercritical flow, and it is defined as follows:

$$\Delta h \le h_c = \sqrt[3]{\frac{(h_0 U)^2}{g}} \tag{19}$$

where h_c: critical depth.

2.7 Evaluation of debris flow load on a steel open dam

DEM with proposed flow model can calculate the debris flow load by assembling contact forces between boulder elements and cylindrical elements as shown in **Fig. 11 (a)**. In case of contact with a number of boulder elements, as shown in **Fig. 11 (b)**, the debris flow load acting on j cylindrical element is calculated as follows:

$$P_j = \sum_{i=1}^{n} p_{ki} \tag{20}$$

where P_j : the debris flows load acting on cylindrical element j, p_{ki} : the spring force between boulder element k and cylindrical element j.

The force of tangential direction is generated in the cylindrical elements. Then, the shear spring force

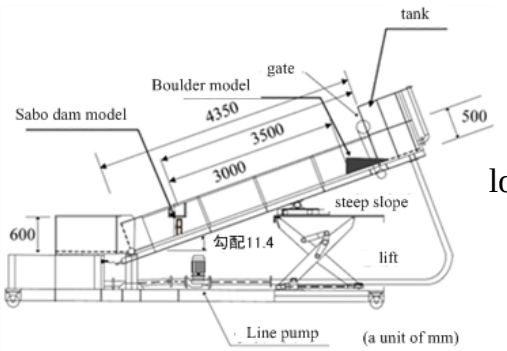

(a) Experimental flume

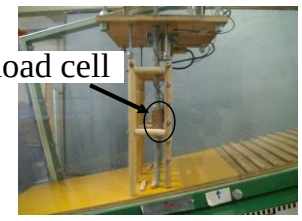

(b) Dam model

Fig. 13 Outline of experimental setup

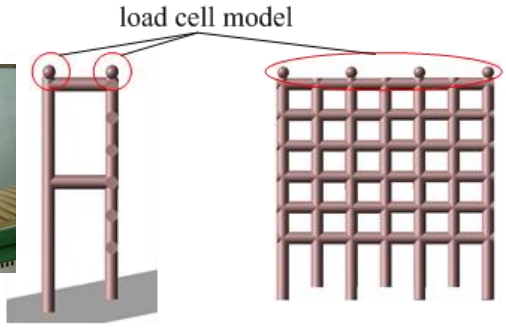

Fig. 14 Analytical dam model

Table 1 Parameters of analysis

item		value
Flux	Initial velocity U_0 (m/s)	2.0
	Initial depth h_0 (cm)	10
	Drag force C_D	0.49
Dam model	Cylindrical element	119
	Spherical element	8
Channel	Plane element	3
	Cylindrical element	26
	Slope θ	11.4°
Boulder model	Spherical element	1000
Interparticle	Normal spring constant K_n (N/m)	1.0×10^6
	Tangential spring constant K_s (N/m)	3.5×10^5
	Damping constant h	0.8
	Viscosity C	0
	Friction coefficient $\tan\varphi$	0.466
Time increment Δt		1.0×10^{-6}

of the tip of cylindrical element j can be obtained as shown in **Fig. 11 (b)** as follows:

$$P_{Sj} = S_{1j} - S_{2j} \tag{21}$$

where P_{sj} : the shearing force acting on the orthogonal directions of cylindrical element j, the S_{1j}, S_{2j} : shearing force acting on the tip of j cylindrical element.

The difference between axial forces acting on j cylindrical element is found as follows.

$$P_{Nj} = N_{1j} - N_{2j} \tag{22}$$

where P_{Nj} : the difference between two axial forces acting on both of tips of j cylindrical element in axial force direction, N_{1j} : the axial force of tip of j cylindrical element.

Finally, the whole debris flow load P_T is obtained by integrating the front contact force i and the shearing force of base element i as shown in **Fig.12**:

$$P_T = \sum_{i=1}^{n} P_i = \sum_{i=1}^{n} S_{Bi} \tag{23}$$

where P_T : the horizontal load acting overall structure, P_i : the contact force of boulder element i acting on each point to structure, S_{Bi} : the shearing force acting on the base element i of the dam, which corresponds to the value of load cell as shown in **Fig. 13**, because the load was measured by load cell upside-down against the dam.

In order to examine the validity of this analytical approach, the model experiment is carried out to measure the impact load which is compared with computational results.

3. EXPERIMENTS OF OPEN DAM MODEL

Fig. 13 (a) shows the experimental set-up using channel flume, length of 4.35 m, width of 0.3 m and height of 0.5 m. Water flow is made by using a line pump and a cistern. The inclination of experimental flume was fixed at θ = 11.4 °. The initial position of water is 3.5 m far from the dam model. The potentiometer is set at the top of open Sabo dam model to measure the impact load of debris flow.

The diameters of grains are from 30 to 40 mm (2.6 in the specific gravity) and the debris flow model is made by rushing water and gravels.

The dam model with height of 260 mm, width of 270 mm and depth of 90 mm is made as shown in **Fig. 13 (b)**. This is 1/40 scale of a real steel open dam in which is made by a wooden column with a diameter

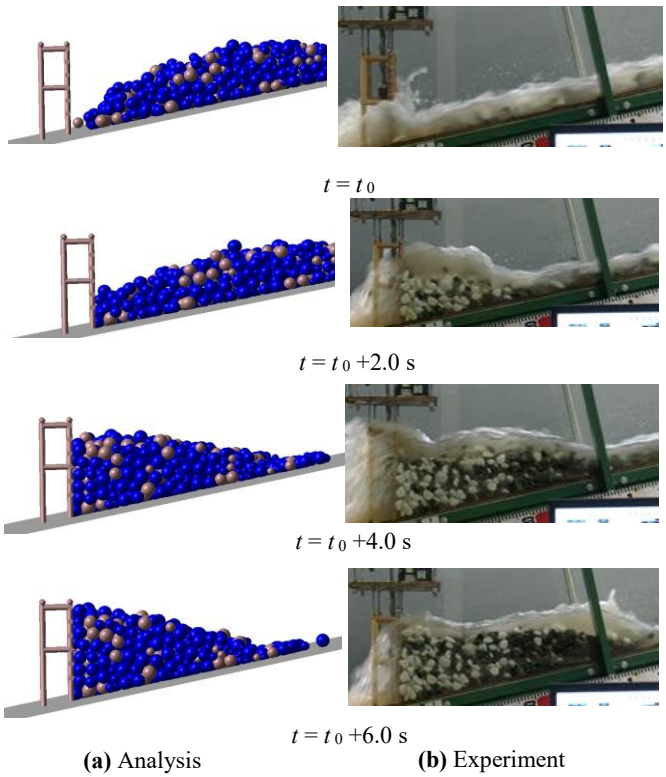

Fig. 15 Comparison of debris flow behavior

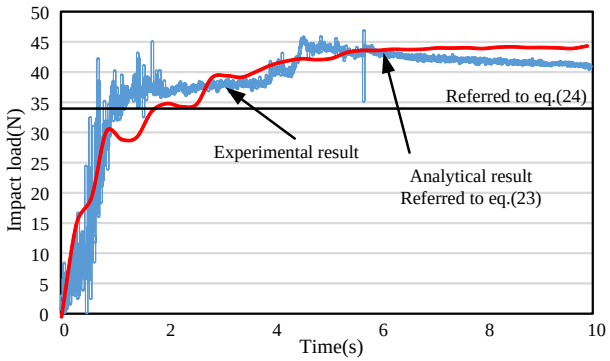

Fig. 16 Time history of debris flow load

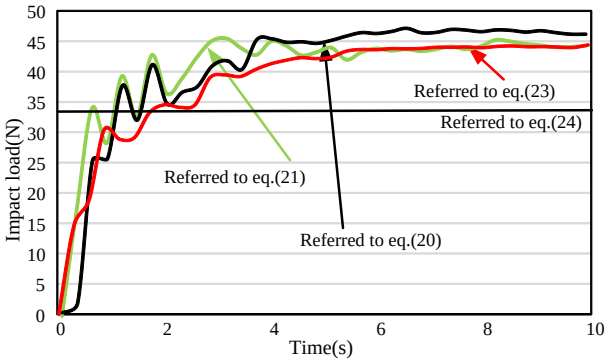

Fig. 17 Comparison of debris flow load

of 15 mm. Moreover, the steel open dam model is hung from the measurement trestle to measure the debris flow load by using the load cell.

4. ANALYSIS OF OPEN DAM MODEL

4.1 Analytical dam model

The analytical dam model is composed of cylindrical elements which are connected with springs between those elements as shown in **Fig. 14**. The load cell model is also connected with springs between spherical and cylindrical model at top of the structure, and the spring force is evaluated as impact load acting on the whole structure [*Katsuki*, 2012; *Shibuya*, 2012].

4.2 DEM parameter

The parameters used in the analysis are shown in **Table 1**. First, the depth and the flow velocity were identical to the experimental ones. The channel model is formed by using plane elements. The drag force C_d = 0.49 is adjusted to spherical and cylindrical shape. A spring constant (K_n=1.0×10^{6}N/m) is determined from boulder rigidity. The damping constant (h=0.8), and the friction coefficient (φ=25°) are also fit to experiment [*Katsuki*, 2012; *Shibuya*, 2012].

4.3 Computational and experimental results

Fig. 15 (a) shows the computational results of debris flow behavior, in which the gravels are hitting to the dam model from the start time ($t = t_0$) to fill up the front space of the dam ($t = t_0$ +6.0 s). In comparison, **Fig. 15 (b)** shows the experimental results of debris flow behavior at each time. Those behaviors show good agreement with each other at the same time.

Fig. 16 illustrates the time history of the debris flow load which is measured at back face of the dam in the experiment, and computational result by Eq. (24) in the analysis. The debris flow loads through the test and the analysis quickly increase more than 20 N at the time of 1.0 s, at which the front of debris flow hit the dam. Then, the loads gradually increase to 45 N until the time of 4.0 s, at which the front height of debris flow almost reaches the height of the dam, at the time (t=t_0+6.0 s) as shown in **Fig. 15**. After the time of 4.0 s, the loads keep the value of about 45 N.

Fig. 17 shows a comparison of loads obtained by Eqs. (20), (21), (23). Debris flow loads evaluated by using Eqs. (20), (21) are larger than one of Eq.(23). It is also found that the local forces integrated by Eqs. (20), (21) are much similar to the experimental one as shown in **Fig. 16**.

4.4 Comparison with design guideline

The design debris flow load is shown in **Fig. 18**. This formula is specified by the design guideline of Japan as follows [*Sabo & Landslide Technical*

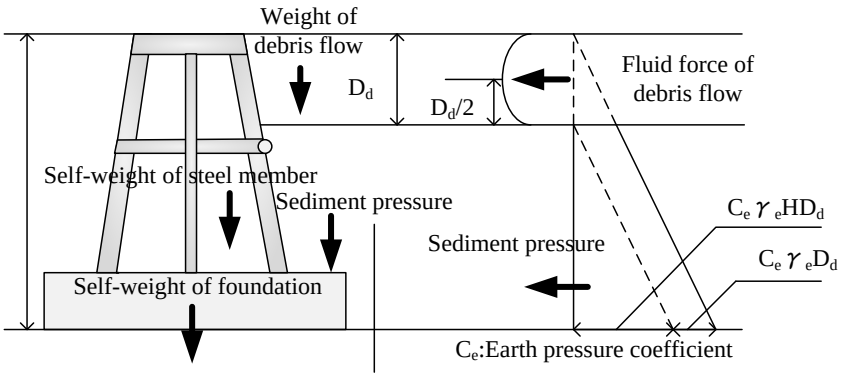

Fig. 18 design debris flow load [*Osanai*; 2010].

Center, 2016; *Kiyomiya*, 2003]. The design load is static sediment pressure and fluid force of debris flow. Here, the fluid force of debris flow is shown only below:

$$P_g = \frac{1}{2} C_e \gamma_e h^2 B \qquad (24)$$

where, P_g : sediment sand pressure, C_e : coefficient of earth pressure ($\varphi_e = 35$ °), γ_e : unit weight of debris flow (15.9 kN/m^3), h : height from sediment sand, B : channel width.

The load P_g is obtained as 34 N by using experimental parameters and this value is indicated as shown in **Fig. 15** by a brown line. Therefore, it was recognized that loads of experiment and simulation are 1.3 times as large as one of Eq. (24).

5. CONCLUSION

This paper presents experimental and computational approaches to impact load of debris flow including boulders against the steel open dam. After the front part of debris flow hit the structure, the load quickly increases to the maximum value, and keeps this value over the whole experiment time. DEM can simulate gravels' behaviors around the structure and time history of the impact load very well.

Therefore, the proposed DEM can simulate the relationship debris flow load and time and productivity of the debris flow behavior sufficiently. The maximum debris flow load (45N) by the test and the analysis was larger than the design load (34N).

This method may be applied to estimate the debris flow load acting on the actual steel open dam in the future.

REFERENCES

Daido, A., Yoshizumi, M., and Nakazima, K. (1994): Impact force of mud-debris flows acting on structure, Journal of hydraulic engineering, Vol.38, pp.557-562 (in Japanese with English abstract).

Ikeya, H. (1987): Classification of an avalanche of earth and rocks, Journal of Civil Engineers, pp.150-155, (in Japanese with English abstract).

Ishikawa, N., Inoue, R., Beppu, M., Hasegawa, Y. and Mizuyama, T. (2009): Impulsive loading test of debris flow model, Proc. of the 8th International Conference on Shock and Impact Loads on Structures, Adelaide, Australia, pp.53-62.

Katsuki, S., Shibuya, H., Ohsumi, H. and Ishikawa, N. (2012): Trap performance analysis of steel open Sabo dam subjected to woody debris by using 3-D DEM, Journal of Japan Society of Civil Engineers, A2 (Applied Mechanics), Vol.69, pp.16-29, (in Japanese with English abstract).

Kiyomiya, O. (2003): Structure Design Overview, Gihodo Publisher, (in Japanese with English abstract).

Miyoshi, I. and Suzuki, M. (1990), Experimental study on impact load on a dam due to debris flow, Journal of the Japan Society of Erosion Control Engineering, Vol.43, No.2(169), pp.11-19, (in Japanese with English abstract).

Mizuyama, T. (1979): Estimation of debris flow impact load against check dam and Its problems, Journal of the Japan Society of Erosion Control Engineering, Vol.32, No.1, pp.40-43, (in Japanese).

Osanai, N., Mizuno, H. and Mizuyama, T. (2010): Design Standard of Control Structures Against Debris Flow in Japan, Journal of Disaster Research, Vol.5, No.3, pp.307-314.

Sabo & Landslide Technical Center (2016): Actual conditions of a landslide disaster in 2016, pp.1-42, (in Japanese).

Shibuya, H., Katsuki, S., Kokuryo, H., Ohsumi, H. and Ishikawa, N. (2012): Experimental study of load for steel open Sabo dam caused by debris flow with woody debris, Journal of the Japan Society of Erosion Control Engineering, Vol.65, No.1, pp.54-61, (in Japanese with English abstract).

Yamamoto, A., Yamamoto, S., Torihira, M. and Hirama, K. (1998): Impact load on Sabo dam due to debris flow, Journal of the Japan Society of Erosion Control Engineering, Vol.51, No.2, pp.22-30, (in Japanese with English abstract).

Debris Capture Example by Flexible Barrier and Its Performance Verification

Hiroyuki UMEZAWA[1], Risa TANABE[1*] and Peihong ZHU[1]

[1] Toa Grout Kogyo Co., Ltd., Japan (2-10-3 Yotsuya Shinjuku-ku TOKYO 160-0004 Japan)
[*]Corresponding author. E-mail:risa.tanabe@toa-g.co.jp

In recent years, sediment-related disasters occur frequently in various places. Although voluntary evacuation is being emphasized, countermeasures by structures are still important. We have developed a new type of protective barrier, which is compact and flexible, as one of the slope failure control sediment capture works. This flexible protective barrier has been installed in various locations since its first installation in 2011 and has captured debris at some of the installation sites. In this report, we will introduce examples of these debris capture cases and pick one of the examples as a sample into detailed analysis. In the detailed analysis, the validity of the existing design method was verified with reference to the slope condition after debris capture situation. The items to be verified were (1) amount of sediment captured and (2) acting force on the components. As a result, we confirmed that the existing designing method was a reasonable and safe design method.

Key words: debris capture, performance verification, existing designing method

1. INTRODUCTION

Flexibly structured slope failure control sediment capture works (hereinafter "impact barrier") is a type of works designed to control steep slope failure composed mainly of posts, wire ropes, nets, energy absorbers (hereinafter "brake ring") and underground reaction bodies (**Fig. 1**). This barrier was so far installed at 118 locations in Japan, and three of them have captured collapsed sediment successfully.

Forces in wire ropes and axial force to the post are calculated by using the static equilibrium of force based on the acting force in the net when the fence undergoes maximum deformation.

A force transmission process under impact force is shown as follows (**Fig. 2**).

(a) Impact force acts on the net.
(b) Tension is generated in the net.
(c) The tension generated in the net is transmitted to the wire ropes and posts.
(d) Forces transmitted to the wire ropes and posts are transmitted to the anchors or underground reaction bodies.

Size of cross section surfaces for each component is designed by using the allowable stress intensity method based on these forces (hereinafter the "existing design method"). The barrier is verified in a full-size experiment by validating the viability of its constituent factors including the safety factor of each component and the force equilibrium.

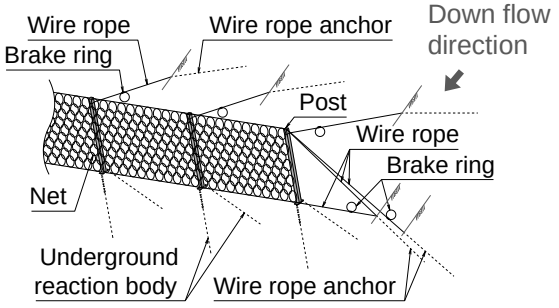

Fig. 1 Schematic diagram of structure

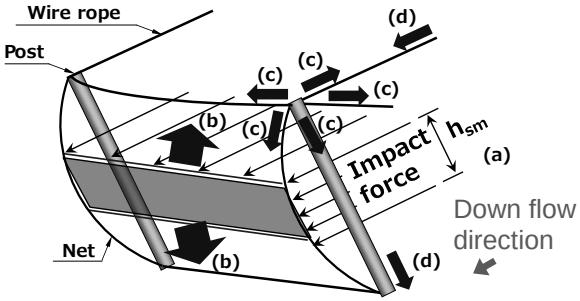

Fig. 2 Design model (under impact force)

Fig. 3 Deformation of ring net - (left) unloaded, (right) loaded

Fig. 4 Deformation of brake ring - (left) unloaded, (right) loaded

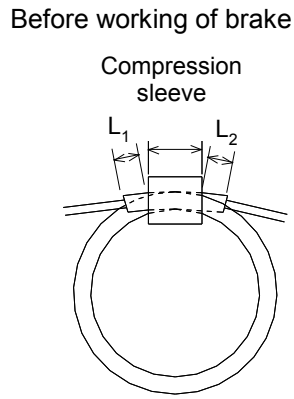

Fig. 5 Conceptual diagram of brake ring travel (before working)

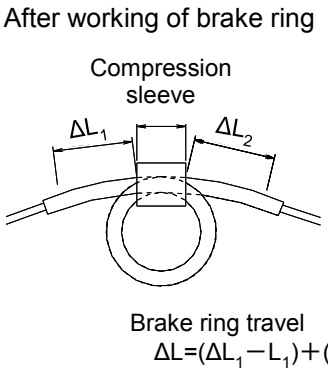

Fig. 6 Conceptual diagram of brake ring travel (after working)

This paper reports the verification result of the validity of the design with (1) amount of sediment captured and (2) acting force on the components used as focal points while using actual sediment capture data.

Table 1 Outline of collapsed sediment capture cases

Case		(a)	(b)	(c)	(d)
Construction site		Miyazaki		Hyogo	Shizuoka
Construction completed year		2011		2013	2014
Sediment captured year		2011	2012	2014	Around 2016
Fence height		5.0 m		4.0 m	5.5 m
Fence length		20 m		120 m	24 m
Impact force of the failed sediment	Design conditions 1)	135.9 kN/m^2		135.7 kN/m^2	108.9 kN/m^2
	Estimation 2)	87.7 kN/m^2	120.7 kN/m^2	41.5 kN/m^2	-
	3) = 2) / 1)	0.65	0.89	0.31	-
Estimator of sediment capture		40 m^3	360 m^3	450 m^3	55 m^3
Effective fence height (deposit height)	Design conditions	4.5 m		3.45 m	5.0 m
	Estimation	(2.0 m)	(4.5 m)	(2.5 m)	(1.7 m)

2. Main energy absorbing components of Impact barrier

The main energy absorbing components of impact barrier are ring net and brake ring.

The net is knitted with rings, which are consist of high-tensile steel wire and bundled into a circular shape with a diameter of 30 cm. Each ring is connected to another ring at 4 points. When a load acts on the net, a ring is extended and deformed from a circle to quadrangle and absorbs the energy (**Fig. 3**). Because of its flexible character, it is utilized for capturing various objects such as falling rocks, debris flow, driftwood and high-speed flying objects besides collapsed sediment.

The brake ring, an energy absorber consists of steel tube, which is bent into a loop and a wire rope is guided through this steel tube. The end of steel tube is held by compression sleeve. When a tension above a certain level acts on the wire rope, the steel tube is deformed to narrow down and defuses the working load, reduce the acting force on the wire rope (**Fig. 4, 5,** and **6**). It is a major feature, even if the brake ring is transformed, the wire rope is not damaged by friction.

In addition, in order to capture the collapsed sediments safely by impact barrier, replacement criteria are set up for components that allow

Fig. 7 Capture case of collapsed sediment (a)

Fig. 8 Capture case of collapsed sediment (b)

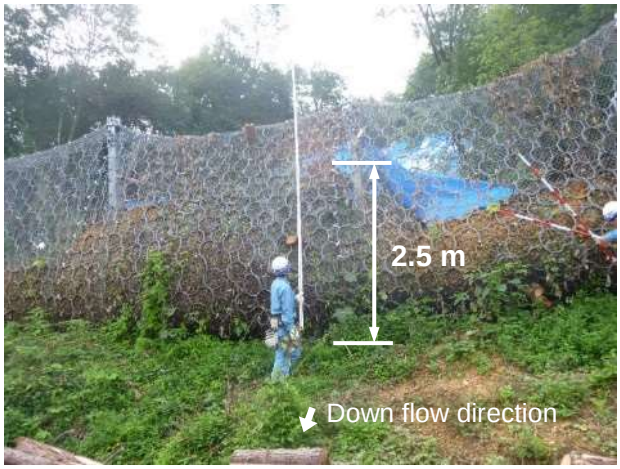

Fig. 9 Capture case of collapsed sediment (c)

Fig. 10 Capture case of collapsed sediment (d)

deformation. For example, in the case of ring net, replacement is performed, when the wire of ring is greatly plastically deformed or fractured. In the case of brake ring, replacement is performed, when the travel of brake ring exceeds 40cm (**Fig. 5** and **6**).

3. Outline of collapsed sediment capture cases

So far impact barriers have collected a record of capturing collapsed sediment in three locations. One of the impact barriers has captured collapsed sediment twice. An outline of collapsed sediment capture cases is shown in **Table 1**. Case (a) and Case (b) were captured by the same impact barrier. The capture situation of collapsed sediment in each case is shown in **Fig. 7, 8, 9** and **10**.

3.1 Capture case of collapsed sediment (a)

The impact barrier of case (a) was installed for road damage restoration work conducted in Miyazaki prefecture in 2011. This impact barrier has a 20 m long and 5 m high fence. In 2011, small slope failure occurred and the barrier captured about 40 m^3 of collapsed sediment (**Fig. 7**). The impact force acting on the barrier estimated from the slope collapse situation was 87.7 kN/m^2, which was about 65% of the design condition of 135.9 kN/m^2.

Since deformation and damage of the components were not observed, the barrier remained to be used after the removal of the sediment without any replace of the components.

3.2 Capture case of collapsed sediment (b)

Case (b) is a case of capturing collapsed sediment again the year after case (a). When the upper part of the slope, at the foot of which this barrier was constructed, failed as a result of heavy rainfall in July 2012, the barrier captured about 360 m^3 sediment that collapsed from the slope (**Fig. 8**). The estimated impact force acting on the barrier was 120.7 kN/m^2, which was about 89% of the design condition of 135.9 kN/m^2. Since deformation exceeding the replacement criteria was seen in ring nets and brake rings on the retaining ropes, replaces of components were carried out to restore the performance after the removal of the sediment.

3.3 Capture case of collapsed sediment (c)

The impact barrier of case (c) was applied to the steep slope failure prevention project in Hyogo prefecture in 2013.The installation length was long (about 240m). The design external force and the sediment capture capacity of the barrier of each slope were different. Considering these conditions and the ease of land use, the barrier was divided into 3 fences. The fence that captured the collapsed sediment is 120m long and 4m high.

In 2014, the impact barrier captured about 450 m^3 of collapsed sediment caused by Typhoon No.11 (**Fig. 9**). The estimated impact force acting on the barrier was 41.5 kN/m^2, which was about 31% of the design condition of 135.7 kN/m^2.

Although deformation of the ring net around the post head in the sediment capturing part was observed, it was not such an extent of deformation or damage of components as to hinder the performance. After removing the sediment, since deflection was observed in the support rope, which is a net suspension rope, it was re-tensioned. And the wire mesh, which is installed on the mountain side of ring net and prevents the passage of small sized soil, was damaged in the sediment capturing part, so it was replaced to restore the initial performance at the time of installation.

3.4 Capture case of collapsed sediment (d)

Impact barrier in case (d) was installed also for road damage restoration work in Shizuoka prefecture in 2014. The timing of the occurrence of collapse sediment was not clear, while impact barrier had captured about 55 m^3 of the collapsed sediment was confirmed during the field survey conducted in 2016 (**Fig. 10**). In this site, since the slope situation after collapse was considered to be dangerous, we had not confirmed the slope collapse situation.

Since deformation and damage of the components were not observed, the barrier remains being used after the removal of the sediment without any replace of the components.

3.5 Capture case for performance verification

For impact barrier, replacement criteria are set for each component, and when the amount of deformation of the component exceeds the standard, it has to be replaced. Therefore, we choose case (b), where the estimated impact force was closest to the design condition and the components deformation exceeding the replacement criteria were observed, to be the performance verification study case.

Fig. 11 Works completed

Fig. 12 Sediment deposit height

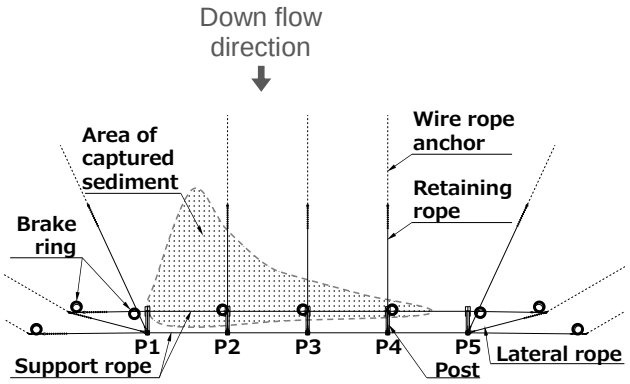

Fig. 13 Capture of sediment (plan view)

4. Details of collapsed sediment capture situation of case (b) subject to performance verification

The barrier when completed is shown in **Fig. 11** and the barrier when it captured the sediment is shown in **Fig. 8, 12, 13**. The design conditions and the field slope failure conditions confirmed by the follow-up survey are shown in **Table 2** and schematic sectional diagrams of the fence in its design condition

Table 2 Design conditions and the estimation based on actual capture of sediment

Item	Sign	Design conditions	Estimation based on actual capture of sediment	Ratio to the design conditions
		1)	2)	(3) = 2) / 1)
Impact force of the failed sediment	F_{sm}	135.9 kN/m^2	120.7 kN/m^2	0.89
Deposited earth pressure of the failed sediment	F_{sa}	19.8 kN/m^2	24.1 kN/m^2	1.22
Amount of sediment captured	V	312 m^3	360 m^3	1.15

Table 3 Design and slope failure site conditions

Item	Sign	Design conditions	Actual phenome-non
Slope height	H	92.69 m	106.9 m
Maximum failure depth	D	2.0 m	1.5 m
Height of sediment movement	h_{sm}	1.0 m	0.75 m
Slope gradient	θ	35°	37°
Internal friction angle	φ	35°	30°
Effective fence height (deposit height)	h	4.5 m	(4.5 m)

and in the condition when it captured the sediment is shown in **Fig. 14, 15**. The maximum failure depth estimated from the ground surface line before and after the slope failure is about 1.5 m (**Fig. 16**).

5. Comparison Between Follow-up Survey Results and Calculated Value of the Existing Design Method

5.1 Comparison of acting forces on the impact barrier

The design conditions and the impact force that worked on the impact barrier upon capture of the sediment and the deposited earth pressure are shown in **Table 3**. For the force that worked on the impact barrier when the sediment was captured, the slope failure conditions were considered (**Fig. 12, 13 14, 15, 16**), and the impact force and deposited earth

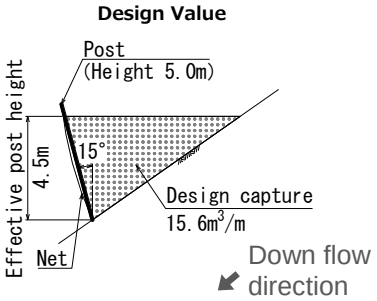

Fig. 14 Schematic sectional diagrams of the fence in the design condition

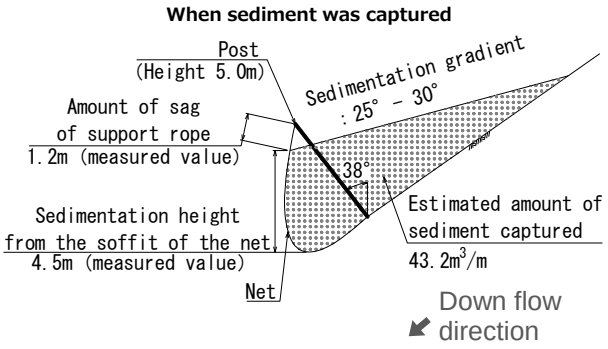

Fig. 15 Schematic sectional diagrams of the fence in the sediment capture condition

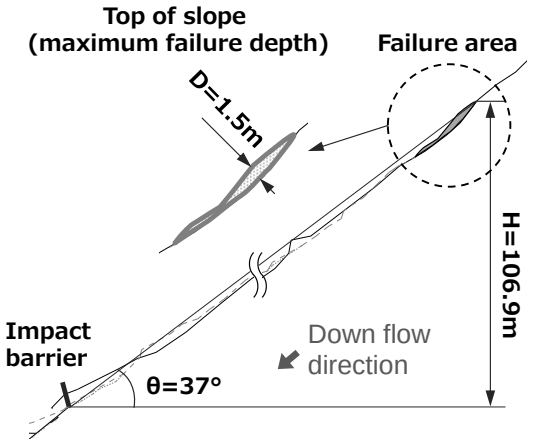

Fig. 16 Condition of collapse at the slope failure site

pressure were calculated using the calculation equation specified by MLIT Notification No. 332 (March 28, 2001). The calculation results indicate an impact force smaller by about 10% than the design value and a deposited earth pressure, calculated from the sediment deposition height at the site that was larger by about 22% than the design value. This is due to the difference in internal friction angle. Although the internal friction angle was set to 35 ° under design conditions, in the actual phenomenon, it was set to 30 ° with reference to the sediment gradient of the sediment deposited inside the impact barrier.

One of the factors that made the impact force at the time of sediment capture come out smaller than

Fig. 17 Measuring the reading of the brake ring travel

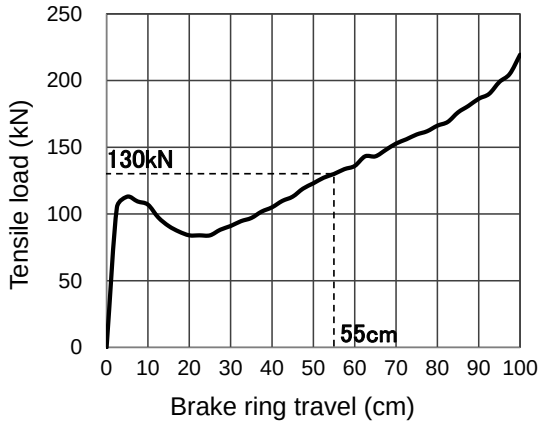

Fig. 18 Relationship between the loading and travel of the brake ring

the one determined by the design conditions is that the actual maximum failure depth (D) was smaller than the one determined by the design conditions.

5.2 Comparison of the amount of sediment captured

The impact barrier is a structure that tolerates large deformations under the impact of the failed sediment. When the effective fence height is determined according to the existing design method, the deformation of the net and slanting of the posts are considered based on the full-size experiment so that the predetermined amount of sediment can be captured even after the fence is deformed by capturing the failed sediment. The amount of sediment captured by the subject impact barrier is 360.9 m^3 according to the calculation using the reference data of the survey longitudinal profile and plan view after the slope failure. When compared with the design capture (312 m^3), the actual capture was about 15% greater.

The maximum amount of capture by the unit width is 43.2 m^3/m according to the calculation based on the survey longitudinal profile, which is about 180% larger than the design value (15.6 m^3/m). The actual values turned out to be considerably larger than the design values because the design conditions allow for no sedimentation gradient, the actual sedimentation gradient at the failure site was 25˚ to 30˚, and sediment was intensively deposited because of the valley topography.

Table 4 Estimate of force acting on the retaining rope and the margin of the existing design method

Estimate based on the brake ring travel	Acting force based on the existing design method	Margin of the existing design method
4)	5)	6) = 5) / 4)
260.0 kN	280.8 kN	1.08

6. Comparison of force acting on wire ropes

For the force acting on components, 1) the estimate made from the brake ring travel based on the survey result was compared with 2) the force acting on the rope calculated from the existing design method based on the slope conditions at the subject site, with respect to the retaining ropes, which are the mountainside stay ropes on the post.

6.1 Estimation of the acting force on the wire rope based on the measurement of the brake ring travel

The force acting on the wire rope based on the survey result was estimated from the travel of the brake ring connected to the wire rope (**Fig. 5, 6, 17**) and the load and travel relational curve in the static material tensile test (**Fig. 18**).

At the subject failure site, sediment deposited mainly among the left-end posts, or from P1 to P3 (**Fig. 13**). Considering this, the retaining rope on the P2 post is used for comparison. The measured travel of the brake ring is 55 cm. Considering this and based on **Fig. 18**, a load of about 130 kN is considered to have worked. Since two retaining ropes were connected to the P2 post, the force acting on the ropes is estimated to be 260 kN (130 kN × 2).

6.2 Estimation of the force acting on the wire rope based on the existing design method

The maximum force acting on the retaining rope based on the existing design method is 280.8 kN, with the slope failure condition at the failure site (**Fig. 12, 13 14, 15, 16**) taken into consideration. The retaining rope acting force based on the existing design method turned out to be about 8% larger than the acting force estimated from the brake ring travel. The estimate of force acting on the retaining rope and the margin of the existing design method are shown in **Table 4**.

7. COMPONENT DEFORMATION

The deformation of the net, post head and post base after capturing sediment are shown in **Fig. 19, 20,** and **21**. Deformation that may affect sediment capture performance was not confirmed at any component.

8. CONCLUSIONS

The amount of sediment captured and the force acting on the wire rope were verified base on the condition of the slope after failure and the condition of the captured sediment. The impact barrier chosen as the subject of verification is a structure that satisfies the three conditions required of a sediment capture works for steep slope failure control. To be specific, this structure is (1) a structure that satisfies the conditions specified by MLIT Notification No. 332, (2) a structure that resists the predetermined deposited earth pressure, and (3) a structure that can maintain the predetermined amount of sediment to be captured. In addition, the existing design method is confirmed a reasonable and safe design method.

We have identified some tasks to solve in the future. To be specific, we will need to conduct a dynamic material tensile test for the brake ring and understand the relationship with the load and travel in order to ensure a precise evaluation of acting force under the impact of a collapsed sediment. We will also need to conduct more follow-up surveys and enhance the reliability for validity of the design method by the verification method used herein.

Fig. 19 Deformation of the ring net

Fig. 20 Deformation of the post head

Fig. 21 Deformation of the base plate

REFERENCES

Chiba, M., Sakaguchi, T., Shimojo, K., Imura, T. and Buginion, L. (2011): Effect of flexible protection barriers on slope failure, Journal of the Japan Society of Erosion Control Engineering, Vol. 64, No. 1, pp. 25-29

MLIT Notification No. 332 (2001): Notification on the methods specified by the Minister of Land, Infrastructure, Transport and Tourism as per the provision of Item 2, Article 2, Enforcement Order for the Law related to Promotion of Measures for Sediment-related Disaster Area etc. due to Sediment-related Disaster (March 28, 2001)

Musashi, Y., Kimura, Y., Umezawa, H. and Mizuyama, T. (2014): Distinct Element Simulation on the Process of Impact Force Absorption of the Flexibly Structured Sediment Capture Works, FY2014 JSECE Research Presentation Compendium, pp. B-248-B-249

Sabo & Landslide Technical Center (2011): Construction Technology Examination Certificate (Sabo Technology) Report "Impact Barrier Method"

Effect of Emergency Measures to Minimize Debris Flow Disaster after the Pyroclastic Material Deposition in Gendol River due to the 2010 Eruption of Mt. Merapi, Indonesia

Naryo Widodo, ST., MT[1], Suyanto, ST., M.Tech[2], Ir. Tri Bayu Adji, MA[2] and Masaharu MIZOGUCHI[3*]

[1] Mt. Merapi Lahar Control Office, Ministry of Public Works and Housing
(Jl. Magelang Km.4, Yogyakarta 55244, Indonesia)
[2] Serayu Opak Rivers Basin Agency, Ministry of Public Works and Housing
(Jl. Solo Km.6, Yogyakarta 55281, Indonesia)
[3] Yachiyo Engineering Co., Ltd.
(CS Tower, 5-20-8 Asakusabashi, Taito-ku, Tokyo 1118648, Japan)
*Corresponding author. E-mail: ms-mizoguchi@intl.yachiyo-eng.co.jp

In 2010, the largest eruption in record occurred at Mt. Merapi in Indonesia. The largest pyroclastic flow which occurred on November 5, 2010 completely buried the valley of the middle reach of the Gendol River. Due to the river blockage, the risk of debris flow inundation in rainy season was increased. In order to guide debris flow to downstream, Mt. Merapi Lahar Control Office carried out emergency measures consisting mainly of temporary guide channel work of 23~30 m width and embankment work during the rainy season between 2010 and 2011. Although the inside of the pyroclastic flow deposit was high-temperature, the construction work had to be implemented using general heavy equipment. As a result, the construction work with excavation volume of 1.3 million m^3 was achieved and effectively prevented the debris flow disaster. This paper describes the outline and effectiveness of the emergency measures so that it can be applied in other volcanoes in the future.

Key words: Merapi Volcano, the 2010 eruption, debris flow, emergency measures, sediment control

1. INTRODUCTION

In 2010, the largest eruption in record occurred at Mt. Merapi in Indonesia. The largest pyroclastic flow in the eruption which occurred on November 5, 2010 flowed down the Gendol River and reached the 15 km point from the crater. Due to the deposition of the pyroclastic flow material on the riverbed, the valley in the middle reach of the Gendol River was completely buried. In this situation, it was obvious that the debris flow which would occur in the following rainy season overflows extensively and causes great damage to the surrounding area. In order to try to minimize the debris flow disaster, the Government of Indonesia carried out emergency measures consisting mainly of temporary guide channel work and embankment work, which are categorized in “river normalization work” in Indonesia.

According to the temperature measurement result of the pyroclastic flow deposit from January to March, 2011, the temperature at the depth of 30 cm from the surface of the deposit was maintained at a high temperature of 90 degrees centigrade or more [*Shimizu et al.*, 2014]. There has been no report of any earth work on such hot pyroclastic flow deposit. Therefore, this paper presents the outline of the emergency measures and introduces the effects and the findings obtained in the measures.

2. MT. MERAPI AND SABO WORKS

Mt. Merapi in Central Java, Indonesia is one of the most active volcanoes in the world erupting once every 3 to 5 years. The surrounding area of Mt. Merapi has been suffered from pyroclastic flow and debris flow disasters caused by volcanic eruption. Since there are densely populated areas including

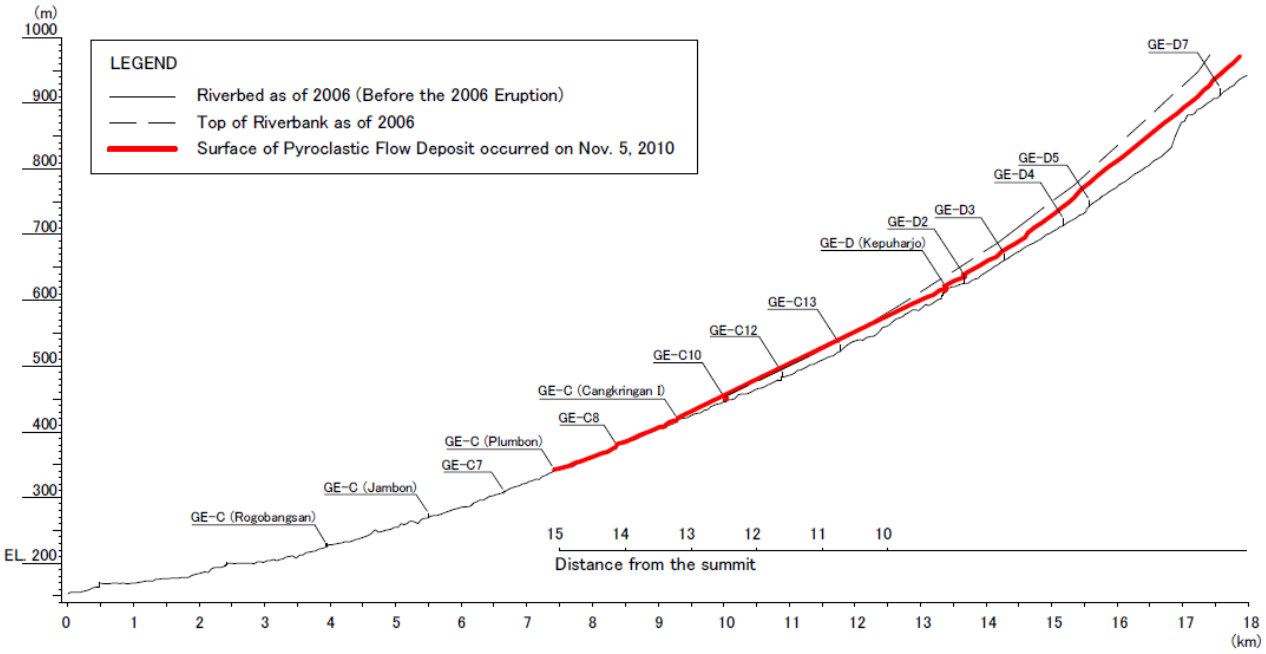

Fig. 1 Longitudinal pyroclastic flow deposit and major sabo dams in the Gendol River

Yogyakarta City at the southern foot of Mt. Merapi, the Government of Indonesia started the national disaster control program consisting of structural and non-structural measures from the 1970s. In order to promote those measures systematically, a master plan for the mitigation of volcanic disasters was formulated under the technical cooperation of Japan International Cooperation Agency (JICA) in 1980. In response to the flowing direction of pyroclastic flows changing from west to south, the master plan was reviewed in 2001. According to the reviewed master plan (hereinafter referred to as "Review Master Plan (2001)"), structural measures are aimed at controlling sediment discharge amount arising from accumulative largest 30 days daily rainfall with 10-year return period after the major eruption occurring once in 10 years, which supplies approximately 5 million m^3 of pyroclastic material. To date approximately 250 check dams and consolidation dams (hereinafter call generically "sabo dam") to control debris flow and to stabilize the riverbed have been constructed in the Mt. Merapi area.

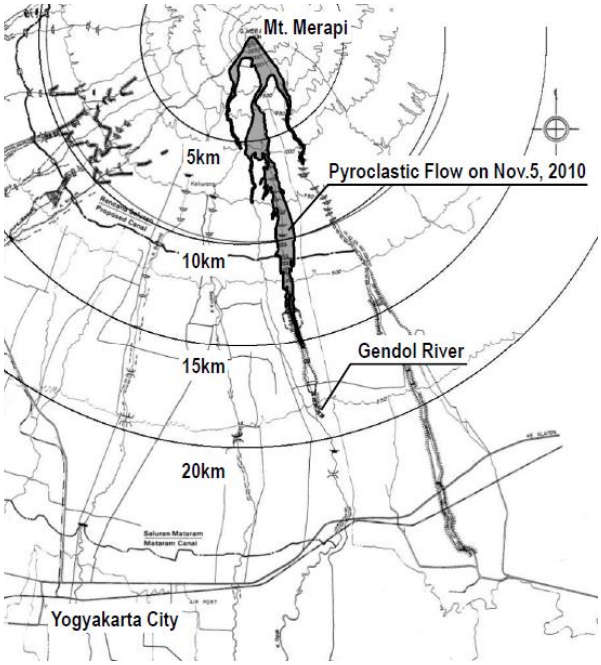

Fig. 2 Pyroclastic flow occurred on Nov. 5, 2010

3. THE 2010 ERUPTION

A series of eruptions which started on October 26, 2010 was not "Merapi-type" characterized by the growth and collapse of lava dome, but was explosive eruptions with a smoke column. Total amount of pyroclastic material ejected during the 2010 eruption reached 140 million m^3 [*Posko Aju BNPB*, 2010]. As the crater of Mt. Merapi has been opened in the direction of the Gendol River since the eruption of 2006, pyroclastic flows mainly ran into the Gendol River several times during the series of eruptions. According to the analysis of radar images, the eruption occurred on October 26, 2010 removed ~6 million m^3 of mainly non-juvenile material from the summit [*Surono et al.*, 2012]. Most of the removed material was flowed down to the Gendol River. Furthermore, on November 5, 2010, the largest pyroclastic flow occurred and

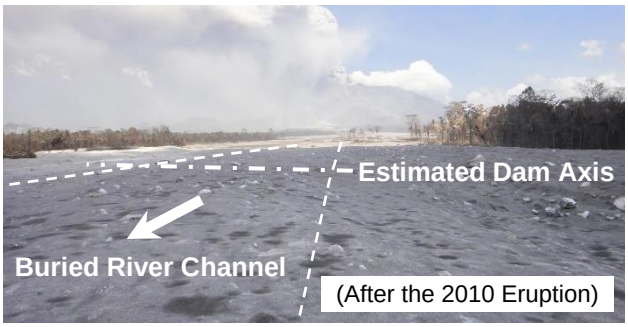

Fig. 3 Riverbed aggradation due to the pyroclastic flow deposition at sabo dam GE-C13, 11 km from the summit

Table 1 Implementation of emergency measures

Year	2010		2011									
Month	11	12	1	2	3	4	5	6	7	8	9	10
Rainy Season	◄	———	———	———	———	———	———	►				
Event												
Pyroclastic Flow	★ Nov. 5, 2010											
Debris Flow Ocurrence Days	10	11	3	3	4	1	2	0	0	0	0	0
Emergency Measures												
Guide Channel & Embankment Work		———	———	———	———	———	———					
Gabion Work							———	———	———	———	———	———

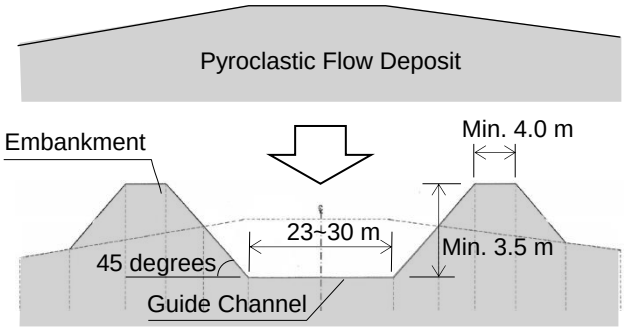

Fig. 4 General cross sectional shape of guide channel and embankment

flowed down to the point 15 km from the summit through the Gendol River. Longitudinal topographic change of the Gendol River and range of the pyroclastic flow are summarized in **Fig. 1** and **Fig. 2** based on topographic survey results and satellite images. Volume of lava dome and non-juvenile material which collapsed due to the eruption on November 5, 2010 was estimated to be ~5 million m^3 and 10 million m^3 respectively [*Surono et al.*, 2012]. According to the above, total 20 million m^3 of materials were flowed down to the Gendol River from October 26 to November 5, 2010. This amount is equivalent to four times the design pyroclastic flow amount assumed in Review Master Plan (2001). The pyroclastic flow raised the riverbed by up to 50 m as shown in **Fig. 1**. Especially in the river section between 10 km and 13 km from the summit, the river channel was completely buried, and surface of the pyroclastic flow deposits became higher than the surrounding riverbank (see **Fig.1, 3**). Because of that, the flooding risk of debris flow, which frequently occurs in the rainy season after the volcanic eruption, was increased.

4. EMERGENCY MEASURES

4.1 Outline

In order to try to minimize the damage from debris flow, Mt. Merapi Lahar Control Office (*PPK Pengendalian Lahar Gunung Merapi*), the execution agency of sediment control works for the Mt. Merapi area, carried out emergency measures after the 2010 eruption in coordination with National Disaster Management Authority (*Badan Nasional Penanggulangan Bencana*) and other organizations concerned. Due to the pyroclastic flow occurred on November 5, 2010, reservoir of the sabo dams upstream from GE-C (Plumbon) were already filled with the pyroclastic flow material, while remaining downstream sand pocket consisting of several sabo dams were still empty (see **Fig. 1**). In order to guide the debris flow to the empty downstream sand pocket, construction of temporary guide channels and embankments was implemented during the rainy season from November 2010 to May 2011. For the embankments located at important places from the viewpoint of disaster prevention, an additional gabion work to protect the surface of the embankments was implemented in the dry season from the end of May 2011 (see **Table 1**).

4.2 Guide channel and embankment

The guide channel is an unlined channel formed by excavating the pyroclastic flow deposits. The excavated materials were dumped on the both bank of the channel as the temporary embankment. Since main objective of the temporary guide channel work and embankment work was to form a series of flow paths on the completely buried river channel in a short period, cross sectional dimensions of those were determined based on the capability and quantity of heavy equipment which can be mobilized in the rainy season, and minimum required discharge capacity of the channel. As a

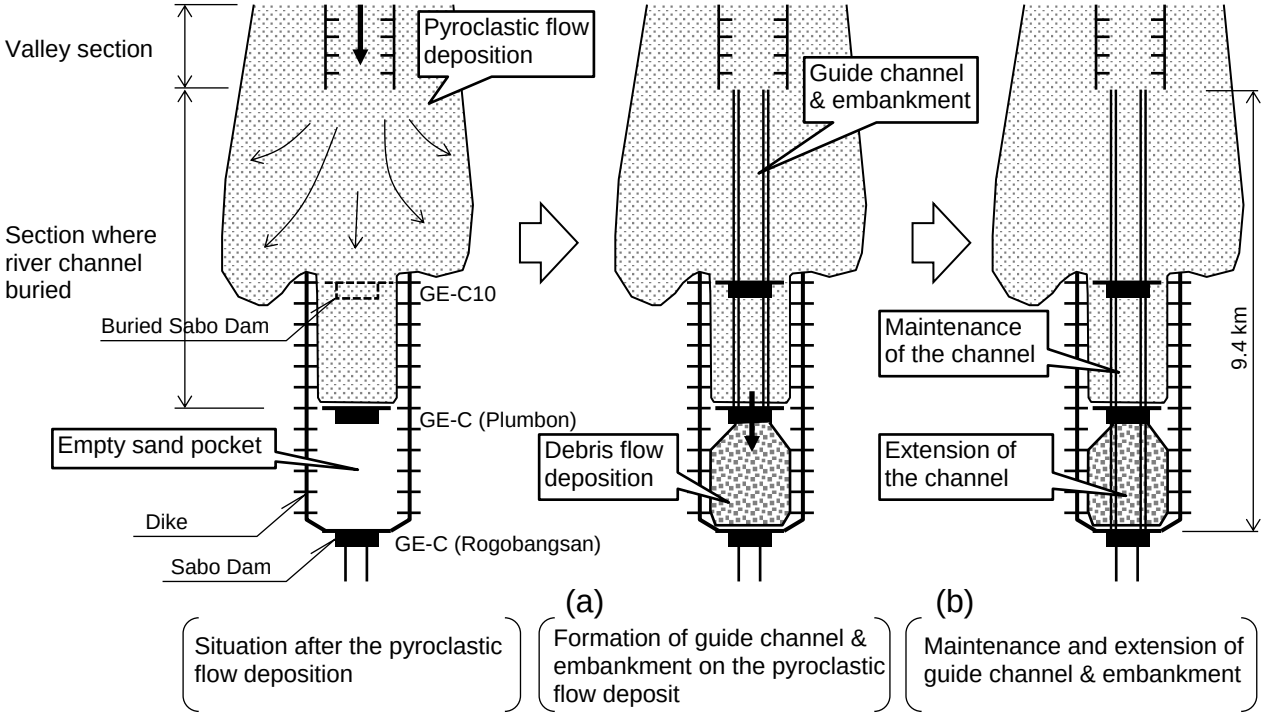

Fig. 5 Schematic plane diagram of the construction areas and process

Fig. 6 Situation of the construction work

result, general width and minimum depth of the channel were set at 23~30 m and 3.5 m respectively. The minimum top width of the embankment was set at 4 m so that heavy equipment can be placed on it to proceed the construction work (see **Fig. 4**). The riverbed slope where the guide channel was constructed was 5 % (1/20) to 2.57 % (1/39) which is generally classified into debris flow deposition zone. The above-mentioned guide channel was confirmed to have the capability to discharge the debris flow of 222 m^3/s caused by daily rainfall with 2-year return period.

4.3 Construction work

The process of the construction of the temporary guide channel and embankment can be divided into the follows:

(a) Formation of the channel on the pyroclastic flow deposit from the upstream valley section to the downstream empty sand pocket, and digging out the buried sabo dam GE-C10 (see **Fig. 5**),

(b) Maintenance and extension of the channel after the deposition of debris flow materials.

The heavy equipment used for this construction work was a backhoe and a bulldozer for general construction work (see **Fig. 6**). Although the construction period was in the rainy season, the construction work could be proceeded during a sunny time because of a simple construction work. Since the construction work had to be interrupted when heavy rain came or debris flow occurred, it was carried out not only on weekdays but also on Saturdays and Sundays. Because debris flow often occurred during the construction period, deposited debris flow material also needed to be removed as mentioned in (b) above. As a result, total 1.3 million m^3 of pyroclastic flow and debris flow deposits could be excavated during the construction period of

6.3 months from November 22, 2010 to May 30, 2011. The average daily excavation amount was 6,900 m^3/day. Average number of heavy equipment for the construction work was about 30 units/day.

4.4 Safety measures

Fig. 7 Debris flow flowing in the guide channel under construction (December 30, 2010)

In order to ensure the safety of construction workers in the river, safety measures not only against general construction accidents but also accidents caused by debris flow or secondary hydro-eruption of the pyroclastic flow deposits had to be taken. The occurrence of debris flow in the Gendol River was monitored by the community organized mainly by local governments. According to the radio communication record of the community, the number of debris flow occurrence days in the Gendol River in the first rainy season after the 2010 eruption was total 34 days (see **Table 1**). Even if debris flow occurred consecutively several times in a day, it seemed that it was recorded as one debris flow. Therefore, we adopted the number of debris flow occurrence days as an index of the frequency of debris flow occurrence.

The safety measures consist of communication system and evacuation system as shown below:

(a) Communication system: When the above-mentioned community observed the occurrence of water flow or debris flow in the Gendol River, where no water flow is in normal times, that information was shared with the Contractor wirelessly from the community.

(b) Evacuation system: The Contractor set up escape routes and evacuation places so that construction workers and heavy equipment can evacuate from the river to a safe high place. Evacuation activities were conducted based on the information from the community.

5. RESULTS

As a result, this simple guide channel was effective enough to prevent flooding of debris flow by guiding it to downstream. **Fig. 7** shows that the debris flow flowing in the guide channel under construction. Despite the high frequency of debris flow occurrence, flooding of debris flow did not occur in the section where the guide channel was constructed. After the occurrence of debris flow, debris flow sediment accumulated on the channel and raised the riverbed maximum 2 m. On the other hand, debris flow often caused maximum 2 meter wide lateral erosion on the foot of the embankment. Maintenance work to remove the accumulated sediment and to fix the partially eroded embankment were required after the occurrence of major debris flow.

Fig. 8 Difference in color of pyroclastic flow deposit by temperature

We also tried to investigate the rainfall that caused the debris flow. However, there was no available rainfall data because all rain gauge stations in the upstream area did not work properly during the rainy season after the 2010 eruption due to accumulation of volcanic ash fall.

6. DIFFICULTY

Because it rained frequently, the surface of the pyroclastic flow deposit was wet and relatively low temperature, while the interior of the deposit, 30 cm deep or more from the surface, were dry at high temperature of 90 degrees centigrade or more. However, we had no choice but to use a general heavy equipment. High temperature pyroclastic flow deposit immediately after the excavation (light gray soil in **Fig. 8**) often caused the hydraulic pressure hoses of heavy equipment to damage and the shoe

sole of construction workers to melt. These damage affected the progress of the construction work. Since the heavy equipment had to be operated manned, there was the possibility of encountering unexpected disasters.

7. CONCLUSION

The findings obtained by this emergency measures were the following two points:

(a) For the river buried with pyroclastic flow deposit, the construction of the simple unlined channel was effective for guiding the debris flow to downstream as long as proper maintenance work is carried out.

(b) It was able to excavate high-temperature pyroclastic flow deposits using general heavy equipment to build and maintain the guide channel.

In order to improve the efficiency and safety of construction, it is ideal to introduce heat-resistant heavy equipment and unmanned construction system. However, it is not always possible to introduce the ideal system for emergency measures in all volcanoes. Further research is necessary for temperature change of pyroclastic flow deposits, but the measures introduced here may be applicable to similar cases in other volcanoes.

ACKNOWLEDGMENT: We are grateful to Muhammad Fahruroyi, ST for arranging construction documents and materials.

REFERENCES

Posko Aju BNPB: (2010) Laporan Harian Tanggap Darurat Gunung Merapi, Tanggal 16 November 2010 pukul 12.00 WIB, p.2

Shimizu, T., Fukushima, J., Ishizuka, T., Morita, K. and Yamakoshi, T. (2014): Fixed point observation of pyroclastic flow deposit resulting from Merapi volcano eruption in October 2010, Abstracts of Japan Society of Erosion Control Engineering study meeting in 2014, pp.B-398-399 (in Japanese)

Surono, Philippe J., John P., Marie B., M. Fabrizia B., Agus B., Fidel C., Supriyati A., Fred P., David S., Lieven C., Hanik H., Sri S., Christian B., Julie G., Simon C., Clive O., Franck L. (2012): The 2010 explosive eruption of Java's Merapi volcano – a '100-year' event, Journal of Volcanology and Geothermal Research, Vol. 241-242, pp. 121-135.

Yachiyo Engineering Co., Ltd. and Associates (2001): Main Report for Review Master Plan Study, Consulting Services for Mt. Merapi and Mt. Semeru Volcanic Disaster Countermeasures Project (Phase II), Directorate General of Water Resources, Ministry of Settlement and Regional Infrastructure, Indonesia.

A Novel Approach to Assess the Ability of a Protection Barrier to Mitigate Rockfall Hazard

David TOE[1*], Alessio MENTANI[3], Stéphane LAMBERT[2], Laura, GOVONI[3], Guido GOTTARDI[3] and Franck BOURRIER[1]

[1] Universitée Grenoble Alpes, Irstea, UR EMGR (2 rue de la Papeterie-BP 76, F-38402 Saint-Martin-d'Hères, France)
[2] Universitée Grenoble Alpes, Irstea, UR ETGR (2 rue de la Papeterie-BP 76, F-38402 Saint-Martin-d'Hères, France)
[3] Università di Bologna (Via Zamboni, 33 - 40126 Bologna)
*Corresponding author. E-mail: david.toe@irstea.fr

The paper presents a novel approach to assess the ability of a protection barrier to mitigate rockfall hazard. Using a meta-modeling approach, a simplified model of a widely used type of rockfall protection barrier was developed to predict the barrier capability to stop the block. A meta-model was created based on FE simulation results considering six input parameters relevant for the wide variety of impact conditions observed on natural sites. The meta-model was then used in combination with a rockfall trajectory simulation tool to evaluate the efficiency of the barrier to mitigate rockfall hazard for two real cases. The results of the study reveal that the meta-model is effective to accurately predict the response of the barrier for different impact conditions. In addition, the coupling of the meta-model with a rockfall trajectory simulation tool provides a better assessment of the barrier efficiency compared to classical design guidelines as it accounts for the distribution of the various parameters describing the block incident trajectory. This approach appears promising to improve rockfall quantitative hazard assessment and optimize rockfall mitigation strategies.

Key words: rockfall mitigation, barrier, meta-model, rockfall simulation

1. INTRODUCTION

Various types of rockfall countermeasures can be used to intercept falling blocks such as barriers, nets and embankments. There is a growing demand in considering the real effect of these protection structures on rockfall trajectories, both for protective structure design and risk assessment. There is thus a strong need for developing tools and methods that can integrate the protective effect of these structures in rockfall trajectory simulation tools.

The most versatile and widely used protection structures are rockfall protection barriers. In practice, the design of a barrier for a given site is done by comparing the barrier reference capacity to the the block kinematic energy at the barrier location as obtained from rockfall simulations. The barrier reference capacity may be determined based on the European guidelines ETAG 027 [*Eota*, 2013]. However this design approach does not account for the wide variety of loading cases resulting from the block kinematics (translational velocity, rotational velocity, impact angle, impact position). In the end, a simple ETAG 27-based design may lead to inefficient barriers.

Quantifying the response of the barrier for different loading conditions requires complex and time consuming modeling approaches (Finite Element Method (FEM) or Discrete Element Method (DEM)) [*Nicot et al.*, 2001; *Volkwein*, 2005; *de Miranda et al*., 2010; *Bertrand et al*., 2012; *Gentilini et al*., 2012; *Gentilini et al*., 2013; *Escallon et al*., 2014; *de Miranda et al*., 2015; *Bourrier et al*., 2015b; *Mentani et al*., 2015; *Coulibaly et al*., 2017]. These models can hardly be directly coupled with classical rockfall trajectory analysis models due to their high computational cost. To overcome this problem, meta-models which can mimic the behavior of complex models with reduced computational time can be created [*Sudret*, 2008; *Blatman and Sudret*, 2010; *Mollon et al*., 2011]. In the context of rockfall protection structures, the meta-model is dedicated to model the barrier response to varying impact conditions. This approach is already widely used in civil engineering [*Jin et al*., 2001; *Farhang-mehr and Azarm*, 2005;

Gonzalez-Perez and Henderson-Sellers, 2008; *Toe et al*., 2017]. Applications in the field of rockfall protection structures were addressed by *Bourrier et al*., 2015b, *Mentani et al*., 2016 and *Toe et al*., 2018.

This study is dedicated to the development and evaluation of a new approach to integrate variable and realistic impact loading conditions into the assessment of the barrier efficacy. It considers a low-energy barrier for which a FEM model is available. First, a meta-model is created based on the FEM model simulation results, considering input parameters relevant to realistic impact conditions. Then, the meta-model is used to evaluate the effectiveness of the barrier in stopping blocks for two real rockfall scenarios. Finally, the advantages and limitations of this approach are discussed and compared to current practice in protection structure design.

2. MATERIALS AND METHODS

2.1 Barrier model and simulations

2.1.1 Finite Element model

The cable-net barrier was model using the Finite Element (FE) modeling approach and the commercial code Abaqus [*Abaqus*, 2013]. For this barrier type, the interception structure is made of longitudinal cables, connected to steel posts fully restrained at their base. The structure type is provided with a secondary hexagonal meshwork fastened to the longitudinal cables.

The study considers a three spans, 5 m spaced, cable-net barrier of 3.2 m reference height (**Fig. 1a**). Longitudinal cables, 12 mm in diameter, pass through the internal posts (IPE 200) and are knotted to the external posts (IPE 300), connected to the ground by side cables of 18 mm diameter. A secondary meshwork, made of a double twisted hexagonal mesh is connected to the top and bottom longitudinal cables with steel wires. The FE model of the barrier is three-dimensional and made of one-dimensional elements, whose behavior is governed by elasto-plastic constitutive laws. The mechanical response of the barrier elements was described based on available results of laboratory tests in *de Miranda et al*., 2015. Particular attention was devoted to model the behavior of the wires within the hexagonal mesh, following data of experiments carried out on mesh portions [*Thoeni et al*., 2013; *Mentani et al*., 2015]. The posts behave following an elastic-perfectly-plastic law up to a failure limit, cables harden in the plastic phase and may undergo indefinite deformations once a second yielding threshold is attained. Mesh wires are prescribed to soften prior to failure.

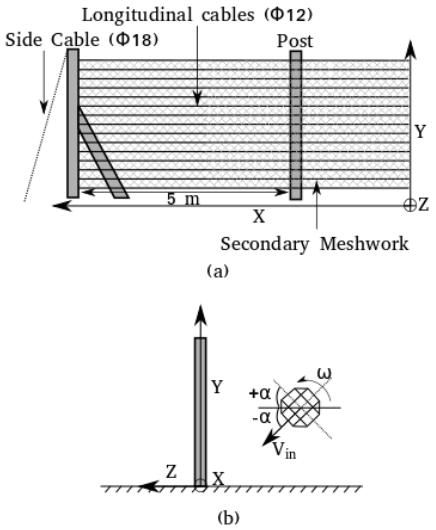

Fig. 1 Geometry and impact conditions for the cable-net protection barrier: a) back view and b) side view.

2.1.2 FE simulations

The reference capacity of the barrier was defined in accordance to the procedure described in Annex A of ETAG 027 [*Eota*, 2013]. Simulations of a centered impact with a block translational velocity of 25 m/s and no rotational velocity were considered. The maximum block mass for which all the Guideline requirement were fulfilled was found equal to 640 kg yielding to a reference capacity of 200 kJ for the cable net barrier.

Six input parameters were considered for creating the meta-model: the block volume *V*; the block impact position on the barrier *X* and *Y*; the incident angle of the impact α; the translational velocity *v*; and the rotational velocity ω (**Fig. 1**). The parameters were sampled in ranges adapted to the reference barrier capacity (**Table 1**). A free-board was considered to avoid direct impact of blocks on the top cable. Latin Hypercube (LH) sampling method [*Sacks et al*., 1989; *Fang et al*., 2005] was used to minimize the number of simulation runs needed to build the meta-model and to keep an optimized sample along the range of each input parameter. This sampling resulted in 280 simulations carried out.

Table 1 Input parameters for loading condition

Input parameter	Unit	Range Min-max
Translational velocity, v	m/s	5 – 22.5
Rotational velocity, ω	rad/s	0 - 35
Volume of the block, V	m^3	0.03 – 2.5
Incident angle, α	deg	-60 - 60
Impact position, X	m	0 - 7.5
Impact position, Y	m	1 – 2.5

2.2 The meta-modelling approach

The developed meta-model can be assimilated to a mathematical operator describing the response of the cable-net barrier while accounting for multiple input variables. Due to its mathematical structure and negligible computational cost, the meta-model can be easily coupled with a probabilistic rockfall trajectory simulation tool.

The meta-models were developed using the results of the FE simulations carried out on the cable-net barrier with the input parameters ranges defined in **Table 1**. Within the context of this study, the meta-model is developed to predict two possible events: success or failure of the barrier to stop a block. These events are grouped in two classes: class B_{Succ} for arrested blocks and class B_{Fail} for blocks passing the barrier. As dealing with two classes, a Support Vector Machine (SVM), was used for creating the meta-model [*Brereton and Lloyd*, 2010; *Kausar et al*., 2011].

2.2.1 Support Vector Machine

The Support Vector Machine (SVM) approach is based on statistical learning theory [*Vapnik*, 1995], and can be used to build a meta-model which can predict the class of an output data (success/failure of the barrier in this study).

The basic SVM approach (M_{SVM}) consists of defining, in a space of input parameters, the optimal hyper-plane separating the regions associated with the considered classes. For that purpose, among all points of the space only those that are closest to the hyperplane, called support vector, are considered. The optimal hyperplane is defined as the hyperplane whose margin, i.e. distance from these closest points is maximal. It is thus calculated by maximizing the distance from the hyperplane to the closest points on each side.

The optimal definition of the hyperplane can require non-linear transformation of the data to another space of potentially higher dimension using kernel functions [*Baudat and Anouar*, 2001].

In this study, the space of the input parameters corresponds to the different parameters associated with the impact conditions. Linear and radial kernels have been used to build accurate meta-models (function *svm* in R (V 3.2.3) package *e1071*).

2.2.2 Error quantification

The developed meta-model accuracy was estimated by comparison with the data obtained from the FE simulations described Section 2.1. The meta-model prediction error was estimated using the leave-one-out cross validation method [*Allen*, 1971].

The global accuracy of the meta-model ($Q(M_{SVM})$) is evaluated using n results $M(x_i)$ from the FE model simulations. For each parameters combination x_i, a meta-model is created using all FEM simulation results except $M(x_i)$. The meta-model prediction for x_i ($M^i_{SVM}(x_i)$) is compared to the remaining result $M(x_i)$ observed from the FEM simulations. This comparison is repeated for all xi ranging between x_1 and x_n.

$$Q(M_{SVM}) = 1 - \frac{1}{n}\sum_{i=n}^{n} M(x_i) - M^{i}{}_{SVM}(x_i) \quad (1)$$

The quality of the meta-model is also estimated regarding the misclassification rate defined as follows. With reference to the FE observations, the SVM based meta-model can provide bad (false, *F*) or good prediction (true, *T*). As described in **Table 2**, a good prediction is either positive (*TP*) when barrier success (B_{Succ}) is both estimated and observed or negative (*TN*) when barrier failure (B_{Fail}) is both estimated and observed. Similarly, a false prediction is either positive (*FP*) when barrier success is estimated while failure was observed or negative (*FN*) when barrier failure is estimated while success was observed. Based on these definitions, two indicators were used to discuss the performance of the meta-model: the false negative rate ($FN_r = FN / (FN+TP)$) and the false positive rate ($FP_r = FP / (FP+TN)$). In the context of this study, the false positive rate is the most relevant to deal with as it focuses on the most critical situation. Indeed, a high FP_r value is associated to an overestimation of the barrier capacity by the meta-model.

2.3 Practical evaluation of the barrier efficiency using the meta-model

The objectives of this section are to evaluate the accuracy of barrier design for two rockfall scenarios following current practice and using the meta-modeling approach. First, two rockfall scenarios were selected to test the influence of the loading conditions on the barrier efficacy. The scenarios were chosen so that the blocks reach the barrier with a maximum translational kinetic energy

around the reference capacity of the barrier as previously determined. Then, the ability of the barrier to stop blocks in the two scenarios is evaluated using rockfall trajectory simulations coupled with the meta-model presented in section 2.2.

Table 2 Definition of cases for assessing the meta-model performance

	SVM prediction	
FE observation	B_{Fail}	B_{Succ}
B_{Fail}	*TN*	*FP*
B_{Succ}	*FN*	*TP*

The considered real-case site is located in the 'Forêt communal de Vaujany' in the French Alps. The scenarios focus on protecting a forest road located on the slope (38°) from cubic blocks (volume: 0.1 to 1 m^3). On this site, rockfalls are reactivated from small topographical outgrowths as indicated in *Bourrier et al*., 2015a. In the first scenario (SCR1) the release area of the block is located at mid slope (130 m from the road) in a snow avalanche corridor (**Fig. 2**). The barrier position is projected 60 m below the release area. In the second scenario (SCR2) the release area of the block is located 100 m above the road and the barrier is located just above the road.

Rockfall simulations were conducted using the 3D rockfall model RockyFor3D (RF3D) [*Dorren*, 2015]. RF3D is a model that simulates block trajectories on forested or non-forested slopes. The model simulates the propagation of spherical blocks along a slope modeled as a Digital Terrain Model (DTM) in raster format. The block propagation is modeled by a succession of free flights, impacts on the slope surface and impacts on trees. The rolling motion of the block is considered as a succession of rebounds and the sliding of the block over the slope surface is not taken into account. The parameters governing the block rebound had been defined according to field measurement campaigns done in previous study [*Dorren et al*., 2006; *Bourrier et al*., 2009; *Bourrier et al*., 2015a].

10 000 blocks were released for each scenario. The initial falling height of the block was set at 0.5 m. In the numerical model, two lines of measure were defined at the location of the rockfall barriers in order to register the blocks kinematic parameters (6 parameters presented in **Table 1**). The 6 blocks kinematic parameters presented in **Table 1** were recorded along measuring lines along the barrier location. The barrier meta-model was then used considering these records to evaluate the barrier efficacy.

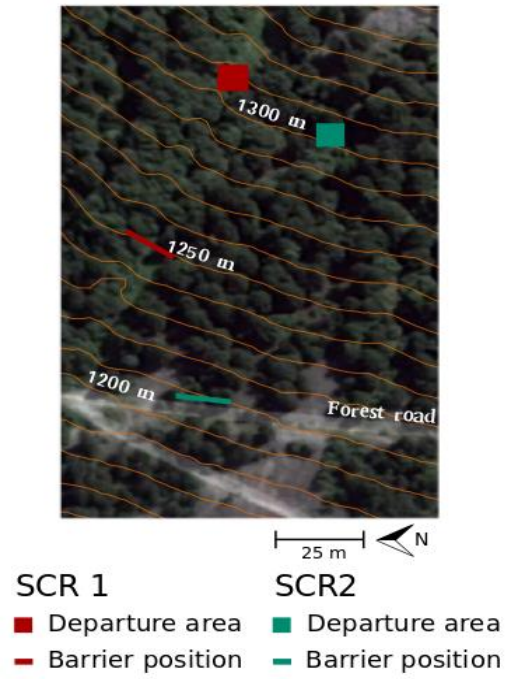

Fig. 2 Presentation of the two rockfall scenarios.

3. RESULTS

3.1 FE simulations results

In **Fig. 3**, the results of the FEM model simulations are grouped on the block translational velocity-block volume plane. Four types of block-barrier interactions were observed depending on the loading condition:

- The block is arrested by the barrier.
- The block passed the barrier by rolling over it.
- The block passed the barrier as a result of the perforation of the secondary hexagonal meshwork.
- The block passed the barrier as a result of the failure of the whole structure.

Over the 280 simulations, the barrier succeeded in stopping the blocks in 61 cases. The barrier inefficiency observed in the 219 other cases resulted from block rolling over (78 cases); mesh perforation (66 cases) and barrier global failure (75 cases).

On the whole, the prevailing parameters in the barrier response are the block velocity and mass, the influence of other impact parameters being limited (**Fig. 4**). Nevertheless, some trends are worth being highlighted. For negative values of incident angle (upward trajectory), the rolling over mechanism is prevailing. Arrested blocks tend to concentrate for low translational/rotational velocities. A higher number of global failure cases are observed close to the post (*X*-axis position). A slight decrease in block

arrest is observed increasing the impact point position (*Y*-axis) for impact velocities above 10m/s. These trends illustrate the complexity of the barrier response when varying the impact conditions.

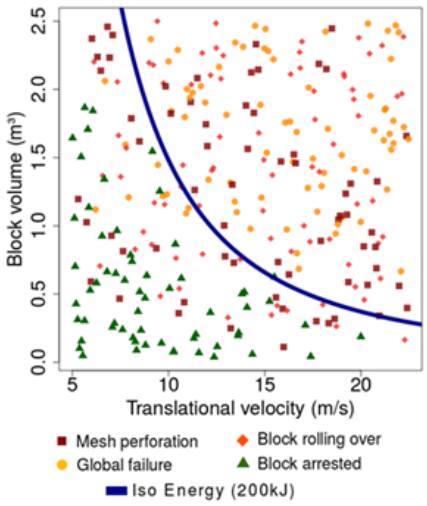

Fig. 3 Influence of block volume and translational velocity on the block-barrier response.

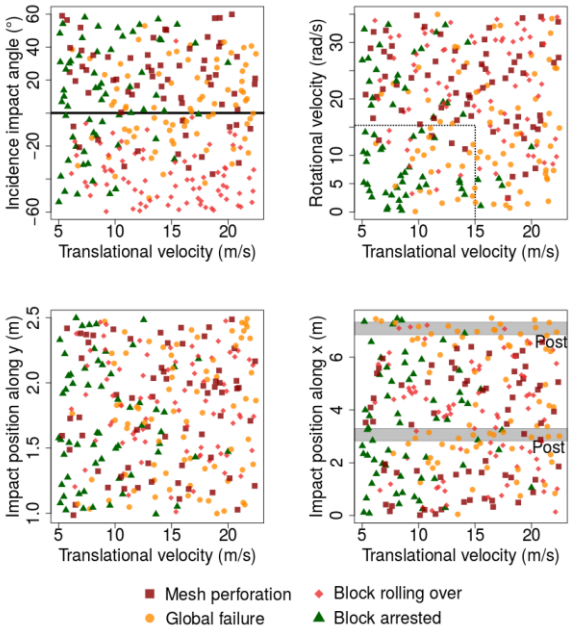

Fig. 4 Block-barrier interaction mechanisms: a) block rolling over; b) mesh perforation and c) global failure.

3.2 Meta-models quality evaluation

The meta-model was created using the plan of experiments consisting of 280 combinations of the 6 input parameters (**Table 1**). Its validation was pursued by comparison with the results from the FE simulations.

Table 3 Quality evaluation for the meta-model created

	Prediction		
Observation	B_{Fail}	B_{Succ}	
B_{Fail}	213	6	FR_r = 3%
B_{Succ}	16	45	FN_r = 27%

The accuracy of the model was evaluated according to eq. 1 and resulted in M_{SVM} equal to 92%. The meta-model failed to predict 16 barrier success over 61 (FN_r = 27%) and failed to predict 6 barrier failures over 219 (FP_r = 3%) (**Table 3**). Over these 6 misclassified cases, 5 are related to mesh perforation and 1 is related to global failure (**Fig. 5**). This indicates that the meta-model overestimates the barrier capacities as 3% of the failure cases are not predicted.

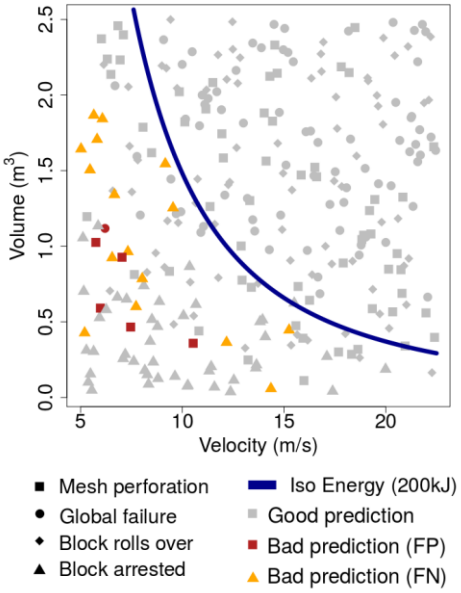

Fig. 5 Prediction of the B_{Succ} and B_{Fail} for the narrow range scenario. Good and bad predictions are indicated by grey and red symbols receptively. The shape of the symbols indicates the mode of failure.

3.3 Estimation of the barrier efficiency

Over the 10,000 rockfall simulations only 2,677 blocks reach the barrier location for SCR1 and 4,712 blocks reach the barrier location for SCR2. For the two scenarios, 95% of the blocks reaching the line of measure had energy below 200 kJ which confirms the choice of this low energy barrier.

The distributions of the block kinetic parameters registered at the two barriers locations are presented (**Fig. 6**). These distributions show significant differences in the block kinematic parameters depending on the scenario. The block impact heights are smaller in SCR2 (0 to 1m) compared to SCR1 (0

to 2.5m). The incidence impact angle ranges between 20 to 40° for SCR2 and between 40 to 80° for SCR1. In SCR2 rotational velocities are slightly larger (10 to 30 rad/s) compared to SCR1 (5 to 20 rad/s). The block volume distribution are more spread for SCR2 with volume ranging between 0.3 to 1 m^3 compared to ranges between 0.55 to 1 m^3 for SCR1.

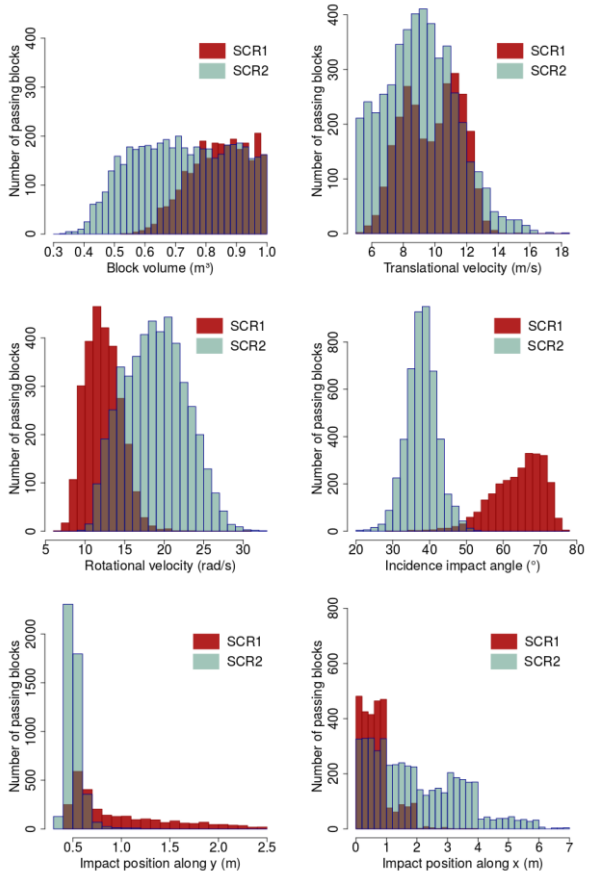

Fig. 6 Distribution of parameters measured at the barriers location from rockfall simulations.

The impact position along the *X*-axis is more spread for SCR2 with block impact distributed from the center to the edge of the barrier compared to block impact positions located around the center of the barrier for SCR1. Finally, only small differences are observed between the two distributions of block translational velocity.

Fig. 7 presents the meta-model predictions for the two rockfall scenarios. For SCR1 the meta-model predicted that 131 blocks (5.3%) lead to barrier failure. Among these, 84 blocks (3%) are below the 200 kJ limit. On the opposite, 37 blocks (1.3%) lead to barrier success above the 200 kJ limit. For SCR2, the meta-model predicted that 2248 blocks (47.5%) lead to barrier failure, with 42% of the blocks below the 200 kJ limit. 5% of the blocks lead to barrier failure above the 200 kJ limit.

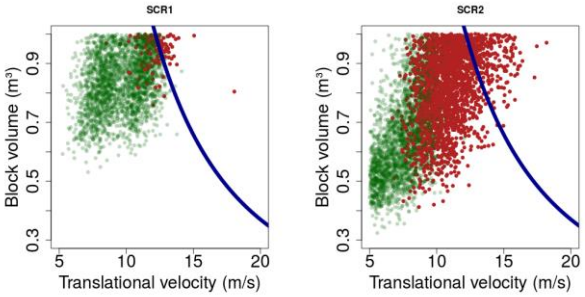

Fig. 7 Prediction of the B_{Succ} (green) and B_{Fail} (red) for the two rockfall scenarios in the translational velocity - block volume plane. The blue line represents the Iso-Energy limit of 200 kJ

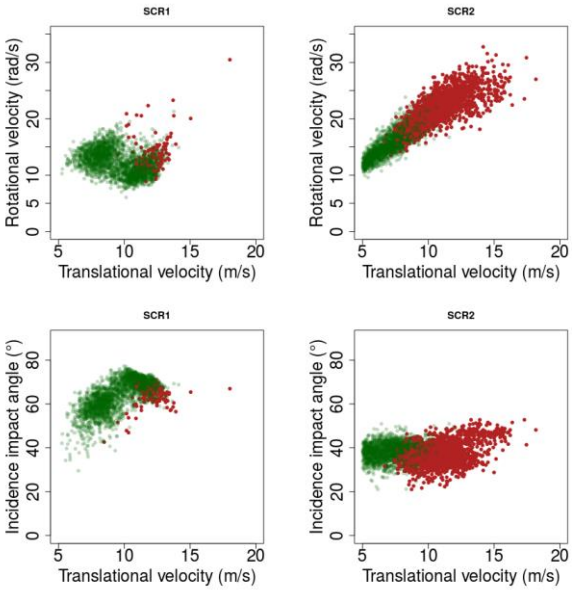

Fig. 8 Prediction of the B_{Succ} (green) and B_{Fail} (red) for the two rockfall scenarios in the translational velocity - rotational velocity plane and in the translational velocity - incident impact angle plane.

Fig. 8 and **9** show the influence of the rotational velocity, incidence impact angle, and impact position along the *X*-axis and *Y*-axis as function of the translational velocity for the two rockfall scenarios. For SCR1, the impact position along the *Y*-axis has a significant influence on the prediction. A higher number of barrier failures are associated to impact heights greater than 2 m. For SCR2 the impact position along the *X*-axis and the rotational velocity of the block show a significant influence on the prediction. The number of barrier failure increases for increasing impacts position along the *Y*-axis and for increasing rotational velocities.

On the whole, it appears that the real efficacy of a barrier in stopping the blocks strongly depends on the impact conditions related to the studied case and

that the only translational kinetic energy may not be sufficient for estimating the ratio of stopped blocks.

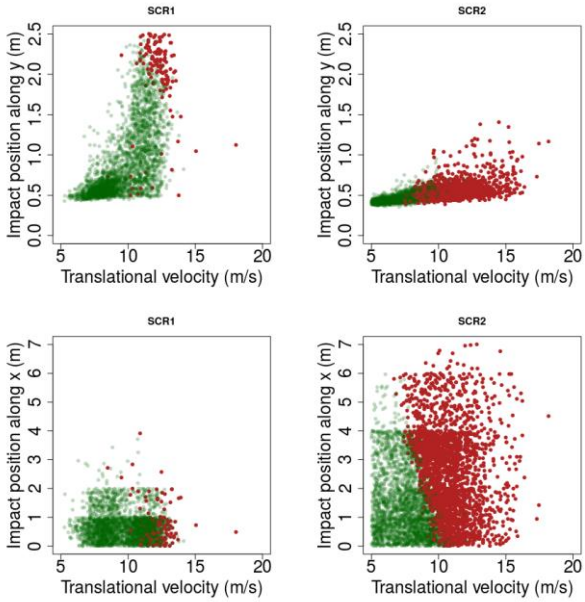

Fig. 9 Prediction of the B_{Succ} (green) and B_{Fail} (red) for the two rockfall scenarios in the translational velocity - impact position along *X* plane and in the translational velocity - impact position along *Y* plane.

4. DISCUSSION

4.1 Benefits of the meta-models

The current design practices are mainly based on the barrier reference capacity. In this study, the reference capacity of the barrier was considered as the reference value obtained from impacts following the recommendations of the European guideline ETAG 027 [*Eota*, 2013]. A straightforward design for this specific barrier would consider that all the block having a kinetic energy less than 200 kJ are stopped.

However, it was shown from FEM simulations that barrier failures occur below the 200 kJ limit. These behaviors appear to be dependent on the impact conditions. Analysis of the data also showed that, although some trends could be observed, there is no a simple correlation between input parameters and block-barrier interaction mechanisms. These results bring to light the shortcomings of deterministic barrier design approaches based on a single impact assessment test. This limitation can be accommodated by using probabilistic approaches to predict the barrier response as a function of the impact conditions.

A detailed analysis of the results presented in **Fig. 5** shows that the prediction of the meta-models below the the iso-kinetic energy line results in 4.8% of False Positive cases (critical cases associated to an overestimation of the barrier capacity) while considering the barrier reference capacity as a criterion led to a value of 52% (see **Fig. 3**). Restricting the comparison to a block size of 1 m (1/3 of the height of the barrier), leads to values of 4.5% for the meta-model compared to 40% for the barrier reference capacity based approach.

This means that the reference capacity of the barrier is far too optimistic with respect to the barrier ability in stopping the blocks. This demonstrates the benefit in using the meta-model for design or hazard assessment purpose.

4.2 Application to real sites

The assessment of the effectiveness of the barrier for two rockfall scenarios has brought to light the importance of the loading conditions on the barrier response. In scenario SCR1, impacts were rather centered on the barrier with high impact heights and impact angle ranging between 40 to 80° directed downward. In scenario SCR2, impacts were more spread to the edge of the barrier with low impact height and impact angle ranging between 20 to 50°.

Comparing the barrier reference capacity to the translational kinetic energy, the barrier may be considered efficient in stopping the block for the two rockfall scenario. This is confirmed by the meta-model results for SCR1, where only a limited number of block impacts (3% of the blocks) lead to barrier failure under the barrier reference capacity. On the contrary, the use of the meta-model to assess the barrier efficiency for SRC2 shows a substantial number of block impacts leading to barrier failure under the barrier reference capacity (42%). This high number of failure indicates the existence of critical loading conditions for this specific barrier type.

This last result shows the practical benefit in using the meta-model to evaluate the efficiency of the barrier by comparison with an approach based on the direct use of the barrier reference capacity.

5. CONCLUSION AND PERSPECTIVES

This article has proposed a method to assess the effectiveness of a cable net barrier through the development and the application of a meta-model.

The results of 280 FE simulations showed that the barrier efficiency to arrest the block depends not only on the block volume and its translational velocity but it is also controlled by other parameters related to the block trajectory. As a consequence, quantifying the barrier efficiency without

accounting for their influence may lead to un-conservative estimates. For instance, 40% of the impact cases below the reference barrier capacity, as deduced from a normal-to-the-fence and centered impact, in fact leads to barrier failure in arresting the block.

A meta-model has been developed, based on the results of the 280 FE simulations concerning the ability of the barrier to arrest the block. The parameters ranges were defined considering the barrier reference capacity. The meta-models have been shown to provide an accurate prediction of the barrier response. In particular, the meta-model unconservative error associated to the ability of the barrier in arresting the block is less than 5%, compared to 40% following a straightforward design approach.

The meta-model was then coupled to a rockfall trajectory simulations tool to estimate the barrier effectiveness for two rockfall scenarios. This coupling approach allows accounting for the real distributions of the various parameters describing the possible block trajectories. It was shown that, depending on the scenarios studied the barrier effectiveness can be highly overestimated by using only the reference capacity of the barrier instead using the meta-model. The meta-model appears to be an important tool to assist practitioners and will represent a significant improvement in quantitative rockfall hazard assessment in presence of a protective barrier [*Corominas et al*., 2005].

It is worth highlighting that the considered impact conditions did not consider biased trajectories or rotational velocities around all block axes. This simplification is thought not to call into question the conclusions drawn and is assumed to be of negligible influence on the developed meta-models accuracy.

Finally, one perspective would be to use the meta-model developed to help in the optimization of the design of rockfall barriers, allowing for the identification of detrimental mechanisms leading to structure failure. In this case parameters related to the design of the structures may be considered, such as the position and initial tension of the cables, post spacing, position of energy dissipating device, if present. This does represent an inspiring perspective for manufacturers, designers and researchers.

REFERENCES

Abaqus (2013): Abaqus Analysis User's Manual. Version 6.11.

Allen, D. M. (1971): The Prediction Sum of Squares as a Criterion for Selecting Predictor Variables. University of Kentucky.

Baudat, G. and Anouar, F. (2001): Kernel-based methods and function approximation. volume 2, pages 1244--1249.

Bertrand, D., Trad, A., Limam, A., and Silvani, C. (2012): Full-Scale Dynamic Analysis of an Innovative Rockfall Fence Under Impact Using the Discrete Element Method: from the Local Scale to the Structure Scale. Rock Mechanics and Rock Engineering, 45(5):885--900.

Blatman, G. and Sudret, B. (2010): Efficient computation of global sensitivity indices using sparse polynomial chaos expansions. Reliability Engineering & System Safety, 95(11):1216--1229.

Bourrier, F., Baroth, J., and Lambert, S. (2015a): Accounting for the variability of rock detachment conditions indesigning rockfall protection structures. Natural Hazards, 81(1):365--385.

Bourrier, F., Dorren, L., Nicot, F., Berger, F., and Darve, F. (2009): Toward objective rockfall trajectory simulation using a stochastic impact model. Geomorphology, 110(3-4):68--79.

Bourrier, F., Lambert, S., and Baroth, J. (2015b): A Reliability-Based Approach for the Design of Rockfall Protection Fences. Rock Mechanics and Rock Engineering, 48(1):247--259.

Brereton, R. G. and Lloyd, G. R. (2010): Support Vector Machines for classification and regression. Analyst, 135(2):230--267.

Corominas, J., Copons, R., Moya, J., Vilaplana, J. M., Altimir, J., and Amig, J. (2005): Quantitative assessment of the residual risk in a rockfall protected area. Landslides, 2(4):343--357.

Coulibaly, J. B., Chanut, M., Lambert, S., and Nicot, F. (2017): Nonlinear Discrete Mechanical Model of Steel Rings. Journal of Engineering Mechanics, 143(9).

de Miranda, S., Gentilini, C., Gottardi, G., Govoni, L., Mentani, A., and Ubertini, F. (2015): Virtual testing of existing semi-rigid rockfall protection barriers. Engineering Structures, 85:83--94.

de Miranda, S., Gentilini, C., Gottardi, G., Govoni, L., and Ubertini, F. (2010): A simple model to simulate the fullscale behaviour of falling rock protection barriers. In Proceedings of the 7th International Conference on Physical Modelling in Geotechnics-ICPMG, volume 2, pages 103--108, Tokyo, Japan.

Dorren, L. (2015): Rockyfor3d (v5.2) revealed. Transparent description of the complete 3d rockfall model. Technical report, ecorisQ.

Dorren, L., Berger, F., and Putters, U. S. (2006): Real-size experiments and 3-D simulation of rockfall on forested and non-forested slopes. Natural Hazards and Earth System Science, 6(1):145--153.

Eota (2013): ETAG 027: Guideline for European Technical Approval of Falling Rock Protection Kits.

Escallon, J. P., Wendeler, C., Chatzi, E., and Bartelt, P. (2014): Parameter identification of rockfall protection barrier components through an inverse formulation. Engineering Structures, 77:1--16.

Fang, K.-T., Li, R., and Sudjianto, A. (2005): Design and Modeling for Computer Experiments. Chapman and

Hall/CRC, Boca Raton, FL.

Farhang-mehr, A. and Azarm, S. (2005): Bayesian meta-modeling of engineering design simulations: a sequential approach with adaptation to irregularities. International Journal for Numerical Methods in Engineering.

Gentilini, C., Gottardi, G., Govoni, L., Mentani, A., and Ubertini, F. (2013): Design of falling rock protection barriers using numerical models. Engineering Structures, 50:96--106.

Gentilini, C., Govoni, L., de Miranda, S. d., Gottardi, G., and Ubertini, F. (2012): Three-dimensional numerical modelling of falling rock protection barriers. Computers and Geotechnics Complete (44):58--72.

Gonzalez-Perez, C. and Henderson-Sellers, B. (2008): Meta modelling for Software Engineering. Wiley Publishing.

Jin, R., Chen, W., and Simpson, T. W. (2001): Comparative studies of meta-modelling techniques under multiple modelling criteria. Structural and Multidisciplinary Optimization, 23(1):1--13.

Kausar, N., Samir, B. B., Abdullah, A., Ahmad, I., and Hussain, M. (2011): A Review of Classification Approaches Using Support Vector Machine in Intrusion Detection. In Informatics Engineering and Information Science, pages 24--34. Springer, Berlin, Heidelberg.

Mentani, A., Giacomini, A., Buzzi, O., Govoni, L., Gottardi, G., and Fityus, S. (2015): Numerical Modelling of a Low Energy Rockfall Barrier: New Insight into the Bullet Effect. Rock Mechanics and Rock Engineering, 49(4):1247--1262.

Mentani, A., Govoni, L., Gottardi, G., Lambert, S., Bourrier, F., and Toe, D. (2016): A New Approach to Evaluate the Effectiveness of Rockfall Barriers. Procedia Engineering, 158:398--403.

Mollon, G., Dias, D., and Soubra, A. (2011): Probabilistic Analysis of Pressurized Tunnels against Face Stability Using Collocation-Based Stochastic Response Surface Method. Journal of Geotechnical and Geoenvironmental Engineering, 137(4):385--397.

Nicot, F., Cambou, B., and Mazzoleni, G. (2001): From a constitutive modelling of metallic rings to the design of rockfall restraining nets. International Journal for Numerical and Analytical Methods in Geomechanics, 25(1):49--70.

Sacks, J., Welch, W. J., Mitchell, T. J., and Wynn, H. P. (1989): Design and Analysis of Computer Experiments. Statistical Science, 4(4):409--423.

Sudret, B. (2008): Global sensitivity analysis using polynomial chaos expansions. Reliability Engineering & System Safety, 93(7):964--979.

Thoeni, K., Lambert, C., Giacomini, A., and Sloan, S. W. (2013): Discrete modelling of hexagonal wire meshes with a stochastically distorted contact model. Computers and Geotechnics, 49:158--169.

Toe, D., Bourrier, F., Olmedo, I., Monnet, J.-M., and Berger, F. (2017): Analysis of the eect of trees on block propagation using a DEM model: implications for rockfall modelling. Landslides, pages 1--12.

Toe, D., Mentani, A., Govoni, L., Bourrier, F., Gottardi, G., Lambert, S. (2018): Introducing Meta-models for a More Efficient Hazard Mitigation Strategy with Rockfall Protection Barriers Rock Mechanics and Rock Engineering, 51(4):1097--1109.

Vapnik, V. (1995): The Nature of Statistical Learning Theory. Springer.

Volkwein, A. (2005): Numerical Simulation of Flexible Rockfall Protection Systems. Computing in Civil Engineering

Sabo Works in Wakayama Prefecture - Evolution Through Learning a Lesson from 2011 Disasters -

Keio CHITO[1], Yasuyoshi MIKI[2], Shigenori IMADA[3], Satoru MORIKAWA[3*], Takehiro SAKAGUCHI[4] and Tsuneshi NISHIOKA[4]

[1] Wakayama sewage public corporation (Wakayama, Wakayama 6496245, Japan)
[2] Wakayama Shimotsu Port office, Wakayama Prefectural Government (Wakayama, Wakayama 6408287, Japan)
[3] Erosion and sediment control division, Wakayama Prefectural Government (Wakayama, Wakayama 6408585, Japan)
[4] Wakayama Sabo Research and Education Institute (Nachikatsu-ura, Wakayama 6495302, Japan)
*Corresponding author. E-mail: morikawa_s0003@pref.wakayama.lg.jp

Wakayama prefecture has high potential risk of sediment disasters due to geomorphological and geological factor and climate condition. The Wakayama prefectural government has been implementing various structural and non-structural measures in order to achieve zero death tolls by sediment disasters. However, many human losses were caused by typhoon TALAS in 2011 and large-scale sediment disasters occurred in the southern part of the prefecture. Taking this opportunity of the event, the central government began directly Sabo works and the Wakayama prefectural government established the Wakayama Sabo Research and Education Institute (IWSRE), as the base institution for researching sediment disasters and for succeeding disaster remembrance, in the Nachikatsu-ura town where was severely damaged by debris flow disaster events in 2011. The IWSRE implements various programs to mitigate sediment disaster impacts in cooperation with concerned organizations. This study introduces new programs that the prefectural government has been implementing after typhoon in 2011.

Key words: 2011 disasters, Sabo works by the central government, Wakayama Sabo Research and Education Institute

1. INTRODUCTION

Recently, severe sediment disasters such as the Hiroshima disaster in 2014 occur every year in Japan due to increase of intensive heavy rainfall that may be caused by global-scale climate change. The circumstances that local residents suffer from sediment disasters have been keeping because the specification of affected areas and the prediction of disaster events are very difficult.

About 80% of the Wakayama prefectural area is covered by mountains and hills which have steep and fragile slopes. And the mountainous area in the southern part of the prefecture is nationally renowned for having heavy rainfall and being vulnerable to typhoon threats. Therefore, the Wakayama prefecture has high potential risk of sediment disasters.

Aiming to achieve zero death tolls, the Wakayama prefectural government has been implementing various non-structural measures such as public notification of restricted area due to sediment-related disaster and issue of sediment-related disaster warning information, i.e. in order to support warning and evacuation activities. However, many human losses were caused by the typhoon TALAS in 2011[1)].

This study shows 1) the outline of 2011 sediment disasters and lessons from typhoon TALAS, 2) Sabo works by the central government, 3) various new programs the prefectural government has been implementing after 2011 disaster event.

2. 2011 DISASTERS CAUSED BY TYPHOON TALAS

The typhoon TALAS has recorded a remarkable amount of rainfall that dreadfully focused on the mountainous areas of the Kii-peninsula. Widespread of continuous rainfall of more than 1,000mm through the period from 29th of August to 4th of September was observed and the Osugi rain gauging station eventually estimated a record-breaking rainfall figure of 1,998mm. This typhoon caused

flood and stimulated the occurrence of landslides and debris flows in the southern part of the prefecture[2]. The damage of the disaster event brought total 61 casualties as well as 40 villages isolated by 180 cut off the road. The world heritages were also damaged by this event.

The rainfall contour map of the typhoon TALAS, the contour map of major sediment disasters and the statistics of the damages are respectively indicated in **Fig.1**, **Fig.2**, **Table 1.**

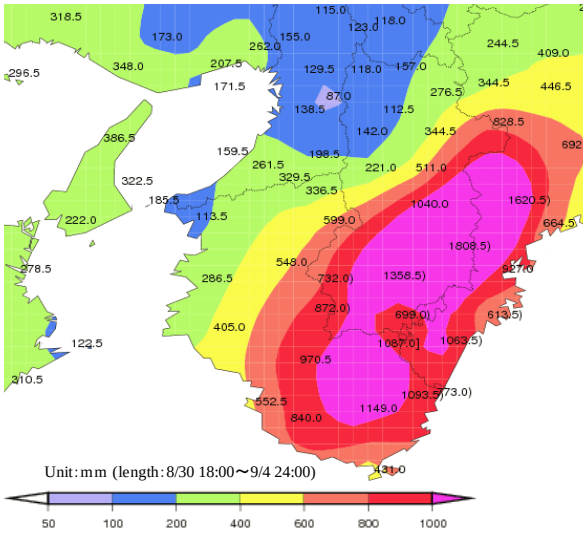

Fig. 1 Rainfall contour map of the typhoon TALAS

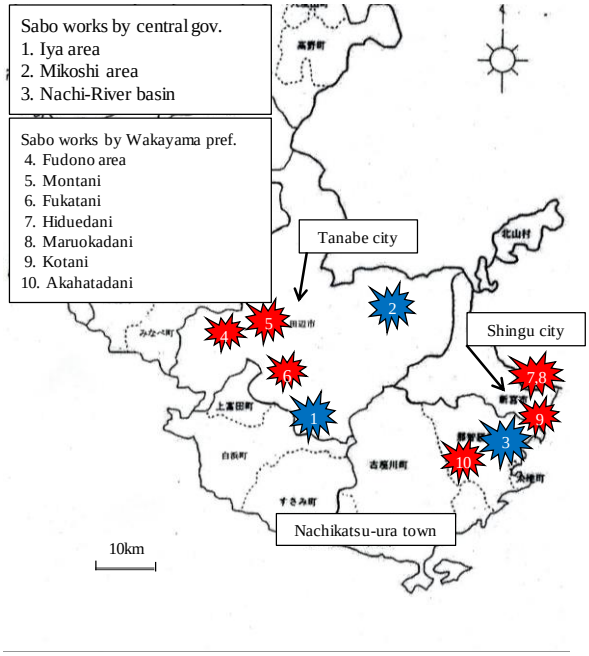

Fig. 2 Distribution map of major sediment disasters

Table 1 Damages by the typhoon TALAS

people			house destroyed	
dead	missing	injured	completely	partly
56	5	8	240	1,838

In particular, in the Iya area (Tanabe city), a landslide dam was formed by a large-scale deep-seated landslide. The potential damage that may be caused by the collapse of the landslide dam was under apprehensiveness and stimulated urgent circumstances. As for the Nachikatsu-ura town, debris flows occurred at many branch torrents in the Nachi-River basin and debris flow sediments deposited in its river area. As the result, the river area was affected by widespread flood damages. Emergency Sabo works were required in order to avoid the occurrence of secondary sediment disasters. The damage situation of the Iya area and the Nachikatsu-ura town is shown in **Fig. 3** and **Fig. 4.**

Fig. 3 Damage situation of the Iya area

Fig. 4 Damage situation of the Nachikatsu-ura town

This catastrophe revealed problems about preparedness for warning and evacuation and crisis management against large-scale sediment disaster etc. The prefectural government learned lessons as below.

- It is important to establish warning and evacuation system through confirmation of information on area affected by disasters, places and routes for evacuation, etc. in normal period.
- It is necessary to provide suitable information timely and to support municipalities in emergency period.
- It is necessary to establish crisis management system in order to take measures against large-scale sediment disasters.
- It is important to succeed disaster remembrance and to learn lessons from past disaster events.

3. SABO WORKS CONTRLED BY THE CENTRAL GOVERNMENT

High developed technology was required in order to implement Sabo works in the Iya area, the Mikoshi area and the Nachi-River basin among areas where the large-scale sediment disasters had occurred. The prefectural government requested the Ministry of Land, Infrastructure, Transportation and Tourism (MLIT) emergency Sabo works directly controlled by the central government and research about the mechanism of large-scale sediment disasters. The MLIT established the Kii Mountain Area Sabo Office in 2012 and the Sediment Disaster Prevention Technology Center (SDPTC) in 2014. The outline of the events and Sabo works by the central government are explained as below

3.1 Iya area

A landslide dam with a reservoir was formed due to the occurrence of a large-scale deep-seated landslide. The size of the landslide recorded approximately 450m in width and 650m in length. The volume of sediment caused by the landslide was estimated approximately 410,000m^3.

Drainage works, backfilling of the reservoir and temporary channel works were carried out as emergency works. Sabo dam, stream preservation works and surface drainage works, etc. are carried out as restoration measures. Disaster prevention works are shown in **Fig. 5**.

Fig. 5 Disaster prevention works of the Iya area

3.2 Mikoshi area

A large-scale deep-seated landslide blocked the Mikoshi-River temporarily and a new river channel was formed in the center of a residential area located in left bank of the river.

Temporary revetment works and backfilling of reservoir were carried out as emergency works. Groundsels and revetment works are carried out as restoration measures. Disaster prevention works are shown in **Fig. 6.**

Fig. 6 Disaster prevention works of the Mikoshi area

3.3 Nachi-River basin

The Nachi-River area was affected by debris flows and drift woods, which were caused by surface failures at many branch torrents in the Nachi-River basin, and widespread flood damages that are accompanied by the debris flow sediments.

As the restoration works, Sabo dams are constructed at branch torrents where debris flow occurred and Sabo works are also constructed at main steam of the Nachi-River in order to entrap debris flows and drift woods. Disaster prevention works are shown in **Fig. 7**.

Fig. 7 Disaster prevention works of the Nachi-River basin

Sabo works, as mention above, raised safety level of affected areas. However, sediment discharge has been keeping from devastated river basin. Therefore, the MLIT established a permanent Sabo office in the Kinki Regional Bureau and began new Sabo works by the central government on Apr 2017.

4. WAKAYAMA SABO RESEARCH AND EDUCATION INSTITUTE (IWSRE)

In order to mitigate sediment disaster impact like 2011 disaster event, the Wakayama prefectural government established IWSRE in the Nachikatsu-ura town where severe sediment disasters had occurred. The duties of the IWSRE are to do research on the Sabo technology, to share information on the results of the research and to hand down disaster remembrance to posterity. The institute is shown in **Fig. 8**.

Fig. 8 Wakayama Sabo Research and Education Institute

In the IWSRE, the SDPTC implements research and development activities about advanced Sabo technology in cooperation with the Sediment Disaster Prevention Research Organization (SDPRO) that was organized by central and local governments, universities, institutes in 2014. The organization chart is shown in **Fig. 9**.

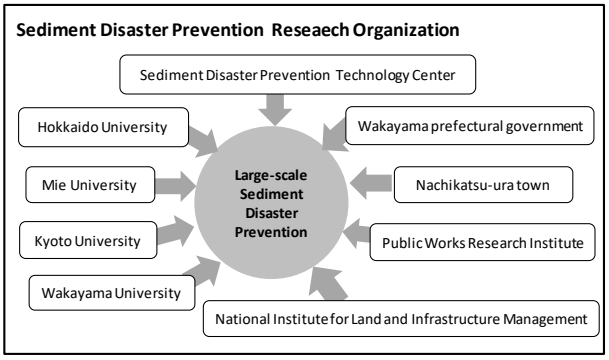

Fig. 9 Organization chart of SDPRO

In the respect that persons from academician to local government officer can participate research and development activities, the SDPRO is a unique organization in Japan.

The IWSRE implements two activities as below.

4.1 Research and development activities

The SDPTC, in cooperation with the SDPRO, does research on task as below in the IWSRE[3)].

- Extraction and evaluation of dangerous spots for large-scale sediment disasters
- Countermeasures for crisis management in mountain area
- Strengthening national land observation and national land management
- Development and introduction of next generation technology for disaster prevention

In addition to the tasks, the SDPRO has roles as below.

- Support of promoting trainings for sediment disaster prevention
- Support of enriching and strengthening community-based disaster prevention
- Public information for disseminating knowledge on disaster prevention
- Sharing disaster prevention technology to foreign countries

Staffs of the IWSRE make an effort for improvement of their skill through assistance of research, which the SDPTC carries out, and give presentations at academic conference. It is expected that the results of the research will be utilized on the site.

4.2 Awareness-raising activity

The erosion and sediment control division in the Wakayama prefectural government gives local residents trainings and lectures as awareness-raising activities. The IWSRE gave 123 groups such as

self-governing bodies, self-organizations for disaster prevention, fire fighters, etc. lectures till Mar 2017 after the IWSRE opened on Apr 2016. Many groups which live in other prefectures also visited the institute. A detail of groups which took lectures are indicated in **Fig. 10**.

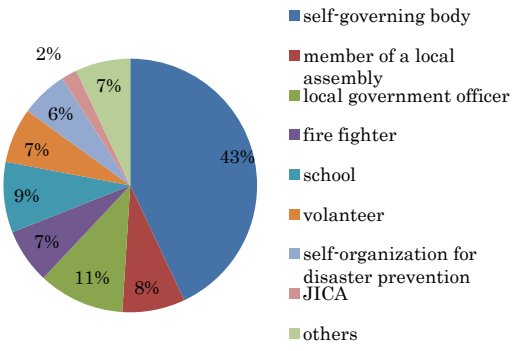

Fig. 10 A detail of groups

The IWSRE implements hearing about trainee's request at the time of reservation and makes materials that the trainee can understand easily. For example, information on sediment disaster at the trainee' home is utilized as the materials.

The IWSRE accepted Japan International Cooperation Agency (JICA) study tours from Latin America and Turkey. The IWSRE explained Sabo works in Wakayama prefecture and 2011 disaster to participants of the tours. Accepting the study tour from foreign countries is a significant way because information on the organization, facility and activities of the IWSRE can be widely given and information on disaster events and countermeasures in foreign countries can be exchanged. It is necessary to promote acceptance of the study tour in the future. Scenes of the study tour and discussion are shown in **Fig. 11** and **Fig. 12** respectively.

Fig. 11 Scenes of the study tour

Fig. 12 Scenes of discussion

Moreover, the IWSRE gave primary and secondary school students a lecture as a general study. Using a model channel, an experiment showing a debris flow runs and function of Sabo dam, etc. was carried out in the class. And a victim who had suffered from 2011 disaster talked her experience to the students using a picture story show. The students could understand a basic knowledge about sediment disaster. The lecture that uses a general study at primary and secondary schools are effective way that students can learn basic knowledge about sediment disasters and save their being by themselves. This way has another effect that their parents can have an interest on sediment disaster through conversation in their family. The **Fig. 13** is the picture of the class.

Fig. 13 Class

Their awareness-raising activities are shown on HP as below.
http://www.pref.wakayama.lg.jp/prefg/080604/top.html

As above mentioned, the IWSRE implements various awareness-raining activities. However, there is a problem about sustainability because of their passive activities.

Therefore, the IWSRE plans to hold a roving

seminar for local residents. The IWSRE divides the prefecture into 7 blocks and holds a seminar at each block for 4 years. The seminar consists of a special lecture by a man of learning and experience, introduction of the SDPTC and the IWSRE and Sabo works in the local area. The first seminar was held in the Nachikatsu-ura town and about 150 residents participated in the seminar. The seminar is shown in **Fig. 14**.

Fig. 14 Roving Seminar

Besides, the IWSRE will send a message through making an English version HP in order to introduce its activities to the world. The IWSRE will plan various sustainable activities such as building database on sediment disasters, systematizing disaster mitigation education, etc. in the future.

5. CONCLUSION

Taking the opportunity of 2011 catastrophe, establishment of the IWSRE and start of the Sabo works directly controlled by the central government are epoch making for the Sabo history of the Wakayama prefectural government.

The activity-base for research and enlightenment has been established through setting up the IWSRE. In order to mitigate sediment disaster impact, the prefectural government in cooperation with related organizations will make an effort in the future.

ACKNOWLEDGMENT: Authors wish to express sincere appreciation for support provided by persons concerned with restoration from 2011 disaster and establishment of the IWSRE.

REFERENCES

1) Keio CHITO, et al. (2014): Sabo works in Wakayama Prefecture –Historical disasters and Sabo-. INTERPRAEVENT 2014, proceedings, vol.1,pp. 703-708
2) Sediment Disaster Prevention Research Organization (2015): Annual report. (in Japanese total pages 67)
3) Wakayama prefectural government (2013): 2011 disaster record. (in Japanese total pages 304)

Small Fish-pond Design for Debris Flow Disaster Measure with Kanako-2D

Masato KOBIYAMA[1*], Rossano D.L. MICHEL[1], Maurício A. PAIXÃO[1] and Gean P. MICHEL[1]

[1] Hydraulic Research Institute, Federal University of Rio Grande do Sul (Av. Bento Gonçalves, 9500, Caixa Postal 15029, Porto Alegre/RS, 91507-970, Brazil)
[*] Corresponding author. E-mail: masato.kobiyama@ufrgs.br

Natural disasters related to debris flows have been increasing in Brazil. This phenomenon occurs mainly in rural and mountainous regions where farmers live without much support from public authorities. Therefore, it is necessary to seek structural preventive measures appropriate to the current situation of rural communities. An alternative is the construction of small fish-ponds along the river channel that support to mitigate the debris flow propagation. Therefore, the present study used the Kanako-2D model to analyze how different geometries and positioning of fish pond can influence on the debris flow propagation and deposition. The case study was carried out with the Böni creek catchment (2.27 km^2) which is located in the southern Brazil. The results of 5 different scenarios showed that the fish-pond location was more relevant than its geometry. If a pond is constructed at a less appropriate location, a much larger volume of the pond is required to break the downstream and to stop the debris flow. The fish-pond construction for debris flow disaster reduction can be considered a kind of socio-engineering and should be popularized more widespread in Brazil.

Key words: Kanako-2D, debris flow, fish-pond design, southern Brazil, socio-engineering

1. INTRODUCTION

Without adequate planning, expansion of agriculture, forestry, ecotourism, urbanization, water resources exploration, and hydroelectric power plant construction have been accelerated in mountainous regions in Brazil. Then, it results in the significant increase of debris flow disasters in this country (*Kobiyama et al.*, 2016).

Many European countries, Japan, USA and so on tend to construct check dams and/or barriers against these disasters (*Jakob and Hungr*, 2005). Mountainous and rural regions in Brazil have farmers´ villages which do not usually receive much support from municipal, state and national governments. Under such economic circumstances, these farmers have not been able to construct check dams, which requires simple and low-cost measures for Brazilian mountainous and rural communities.

Therefore, the objective of the present study was to investigate the simple fish-pond design for debris flow disasters reduction by using the Kanako-2D model proposed by *Nakatani et al.* (2008). As these ponds are small, simple and popular among farmers, their construction can be one of the solutions for debris flow disaster measures in Brazil.

The fish production by using the small pond will certainly increase farmers' income and also improve their food circumstances (*Guimarães*, 2012; *ACEB*, 2014). Furthermore, such ponds can be used as parts of irrigation facilities which also increase their income. That is why the pond construction has been promoted at the state and national levels in Brazil, for example, *Meschkat* (1975), *FAO-DNOCS* (1988) and *Assembleia Legislativa do RS* (2013). Therefore, the fish-pond construction should be even more widespread and popularized in order to ensure social and economic security.

There is a tendency where natural sciences intentionally deal with social systems as well as natural phenomena in order to advance themselves more. In this case, such natural sciences analyze interactions between natural phenomena that the sciences have investigated since their beginnings and social processes. For example, socio-hydrology (*Sivakumar*, 2012; *Pande and Sivapalan*, 2017), socio-hydraulics (*Kobiyama et al.*, 2018) and socio-geomorphology (*Ashmore*, 2015; *Mould et al.*, 2017). The socio-hydrology studies the interactions between social processes and hydrological processes while the socio-geomorphology between social processes and geomorphic processes. According to *Pande and Sivapalan* (2017), the socio-hydrology

tries to understand the dynamics of coupled human-water systems. Therefore, it can be said that the aim of the socio-geomorphology is to the dynamics of coupled human-earth surface systems. It implies that these kinds of natural sciences cannot be established anymore without consideration on social factors.

This fact can be valid for the technology and engineering for natural disaster reduction. Analogically thinking, it is natural to desire that the socio-technology and socio-engineering concepts spread over the society more. As *Sharples et al.* (2002) emphasized, the design of human-centered technology is strongly required in Brazil. Thus, the present study would support a kind of socio-engineering.

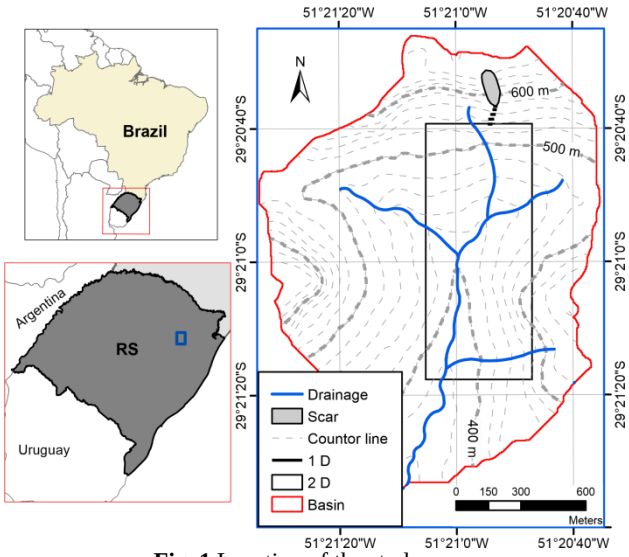

Fig. 1 Location of the study area

2. MATERIALS AND METHODS

The study area is the Böni creek catchment (2.27 km^2) located at the border between São Vendelino and Alto Feliz municipalities, southern Brazil (**Fig. 1**). This area is located in the Serra Geral formation which characterizes a kind of Brazilian mountainous landscape, whose most areas are underlain by basalt (*Viero and Silva*, 2010). The predominant soils of this region are Entisols and Ultisols (*Flores et al.*, 2007). In December 2000, a rainfall-triggered debris flow occurred in this catchment, causing various damages with the death of 4 persons (*Godoy et al.*, 2015).

In July 2016, field survey with GPS navigator was carried out in order to delimit the scars of this debris flow, to identify its three zones: source, transport (1D channel) and deposition (2D area), to estimate the total sediment volume flowing into the channel, and also to establish the common input parameters for all the computational simulations.

The Kanako 2D is a physically-based computational model developed by *Nakatani et al.* (2008). Its version used in the present study, i.e., KANAKO-2D v2.0.0, has a graphical interface defined friendly by the developers themselves. The model simulates the flow from its entrance in the channel with 1D equations and the propagation and deposition in the alluvial plain is simulated with 2D scheme. The more detailed explanation of this model is encountered in *Nakatani* (2008).

The terrain information files generated from the digital elevation model (DEM) with an element size of 2.5 m x 2.5 m were used for the Kanako-2D simulations. The values of the common input parameters for all the simulations are shown in **Table 1**.

Parameter	Value	Parameter	Value
Simulation time	1800 s	Angle of internal friction	37^o
Simulation time step	0.01 s	Concentration of movable bed	0.65 m^3/m^3
Diameter of material	0.45 m	Manning´s coefficient	0.03 s/m$^{1/3}$
Mass density of bed material	2650 kg/m^3	Interval of 1D calculation points	23 m
Mass density of fluid phase	1000 kg/m^3	1D calculation points	5
Coefficient of erosion rate	0.0007	1D calculation width	15 m
Coefficient of deposition rate	0.05	Mesh size of 2D calculation	2.5 m x 2.5 m
Sediment concentration	50%	2D calculation points	472 x 196

Table 1 Input data for Kanako-2D simulation

In order to verify the adequate locality and size of fish-pond along the channel in the catchment, the present study carried out simulation with 5 scenarios characterized with different conditions of fish-pond.

The insertion of the ponds was performed directly in the DEM before each simulation. For this purpose, a raster of the same resolution as the DEM was manually constructed, which allowed containing the

desired configuration of the ponds. To insert the pond into the DEM, this raster was used for a mathematical operation between the rasters by using a geoprocessing software.

The Case 0 without fish pond represents the former situation before the debris flow disaster occurrence. Just after the debris flow occurrence in 2000, the inhabitants (local farmers) of the destroyed house constructed one fish pond which exists till now. This is the current situation represented by the Case 1 with the pond P1 (6850 m^3 = 3425 m^2 x 2 m). The Cases 2, 3 and 4 show planned ponds P2, P3 and P4, respectively. Though the volumes of P1, P2 and P3 are approximately equal, the depth of P2 and P3 is twice as large as that of P1. The difference between P2 and P3 is their orientation. In the Case 4, the volume of the planned P4 is very large (30,000 m^3 = 100 m x 60 m x 5 m) (**Table 2**). The locality of P2 and P3 is about 100 m upstream from P1, meanwhile, P4 about 400 m upstream from P1.

Based on field data, *Michel* (2015) found that the soil mean depth on the slopes in the study region is 2 m. Therefore, with the consideration of the landslide areas (10,000 m^2), the total sediment volume into the transport channel for the event occurred in 2000 was calculated 20,000 m^3. This value was used for all the simulation.

Case	Pond	Dimensions	Volume
0	No pond	-	-
1	P1	3425 m² x 2 m	6850 m³
2	P2	35 m x 45 m x 4 m	6300 m³
3	P3	50 m x 35 m x 4 m	7000 m³
4	P4	100 m x 60 m x 5 m	30000 m³

Table 2 Ponds´ characteristics.

The input hydrograph in the 1D component of the model was constructed based on the triangular hydrograph theory of *Whipple* (1992), with a rise time of 1/3 of the total time (99 s), i.e., the calculated rise time is 33 s. By using the formula proposed by *Rickenmann* (1999) and the total sediment volume of 20,000 m^3, the hydrograph peak flow rate was calculated 382 m³/s. These values are just estimated without field monitoring confirmation.

3. RESULTS AND DISCUSSION

Fig. 2 demonstrates that the Kanako 2D has a good performance to simulate the debris flow which occurred in 2000 and also permits to analyze the pond effect on debris flow deposition in the Böni creek catchment.

In **Fig. 2**, the deposition thickness (Dt) can be positive and negative. Its positive and negative values mean the deposition and erosion, respectively. The Case 0 satisfactorily reconstructed the deposition areas occurred in the 2000´s debris flow disaster (**Fig. 2a**).

As mentioned above, just after this disaster, local farmers constructed one simple fish-pond (P1). Then the Case 1 verified P1´s performance against the same debris flow occurrence, demonstrating that P1 could totally stop the sediment flow. However, it is observed that a part of the sediment reached an existing house (**Fig. 2b**), which suggests that the pond should be constructed at more upstream area.

Fig. 2c demonstrates that the P2 could stop all the sediments and its volume is less than that of P1. The P3 whose volume is slightly larger than those of P1 and P2 also stopped all the sediment (**Fig. 2d**). It is noted that the pond´s orientation is different between P2 and P3, where P2 is elongated perpendicular to the stream direction and P3 parallel to the stream. In the present calculation condition, P2 is more effective than P3. However, if the topography (gradient) around pond installed in the neighborhood of the protection target is steeper, or when the reaching volume of debris flow is larger, this tendency cannot be always true. Therefore, it would be necessary to verify the influence of various conditions in the future.

Though its volume is very large, P4 could not effectively store the sediment because of the high flow velocity at the P4 locality. A part of the sediment that was not deposited in P4 reached very close to the place of the houses (**Fig. 2e**). Thus it can be said that the pond locality is very important to have a good effectiveness of sediments capture and storage.

The results from 5 scenarios permit to say that the P2 is the best design for debris flow disaster reduction in the case of the Böni creek catchment.

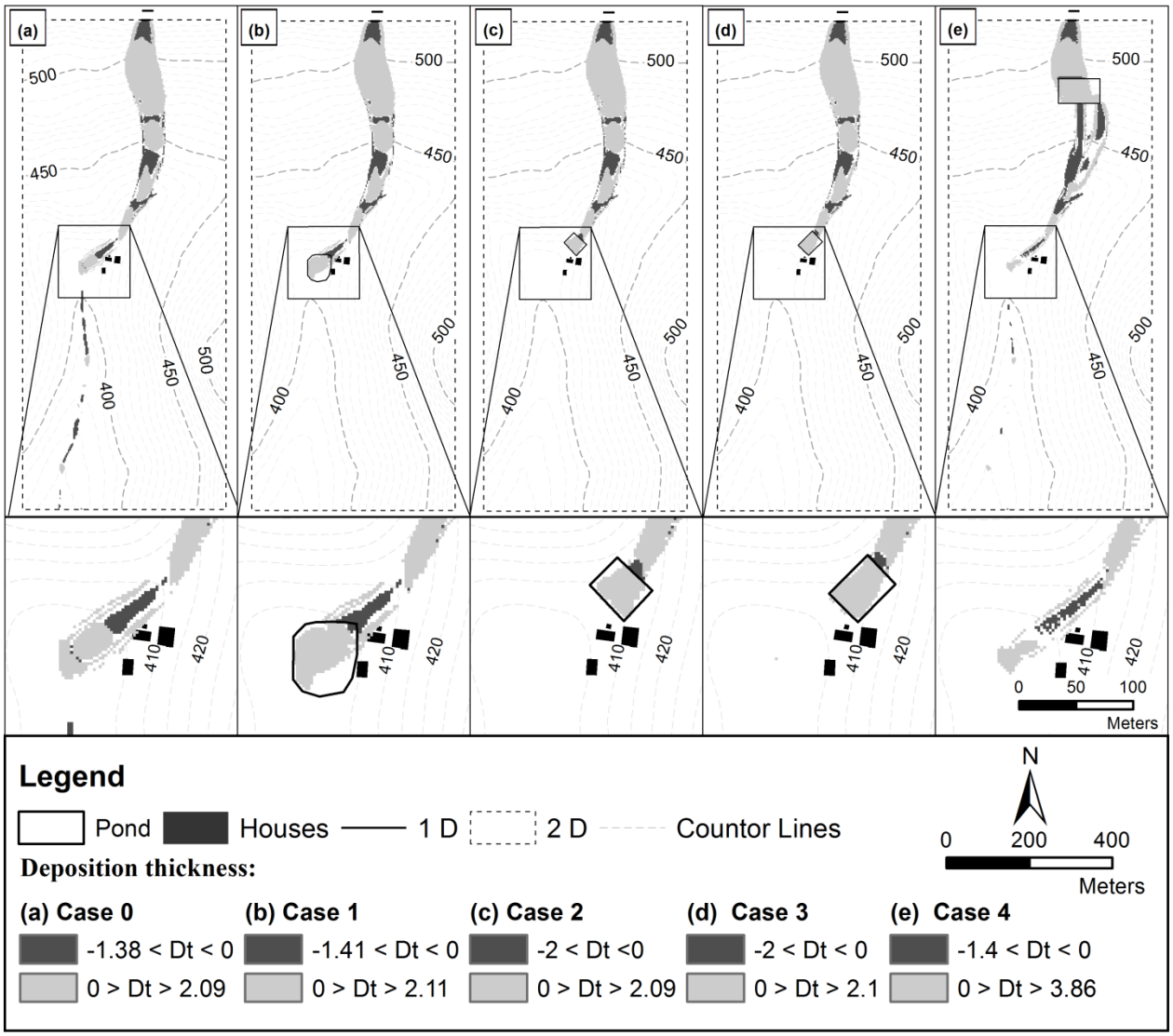

Fig. 2 Deposition areas of debris flow in Böni creek catchment with 5 different cases: (a) Case 0; (b) Case 1; c) Case 2; (d) Case 3; and (e) Case 4.

To understand the deposition feature inside a pond, **Fig. 3** demonstrates the transversal section and longitudinal profile in four different ponds. Note that the longitudinal profile shows the topographic feature along the thalweg and the transversal section passes the pond´s center, being perpendicular to the thalweg. It is observed that the deposition surface presents its lineament transversally, which creates the lens shape with the largest deposition thickness normally near the thalweg point.

When the debris flow is moving down, it digs the stream-bed at the upper part of the pond. This phenomenon occurred very slightly in the Case 4 with P4. In the Case 1 to 3, the sediment concentration of the debris flow reaching to the pond was small. Then, at the upper part of the pond the erosion strongly occurred by removing materials because of the steep step gradient. On the other hand, in the Case 4, erosion did not occur notably due to the high sediment concentration in the vicinity of the upper pond area.

4. CONCLUSIONS

The debris flow triggered by a heavy rainfall in the Böni creek catchment (southern Brazil) in 2000 was investigated with the Kanako-2D. The model showed the good performance to simulate the deposition area reconstructed with field survey conducted in 2016.

Because of current social and economical situations in Brazilian rural and mountainous regions, simple fish-ponds construction can be thought one of adequate measures to reduce debris flow disasters.

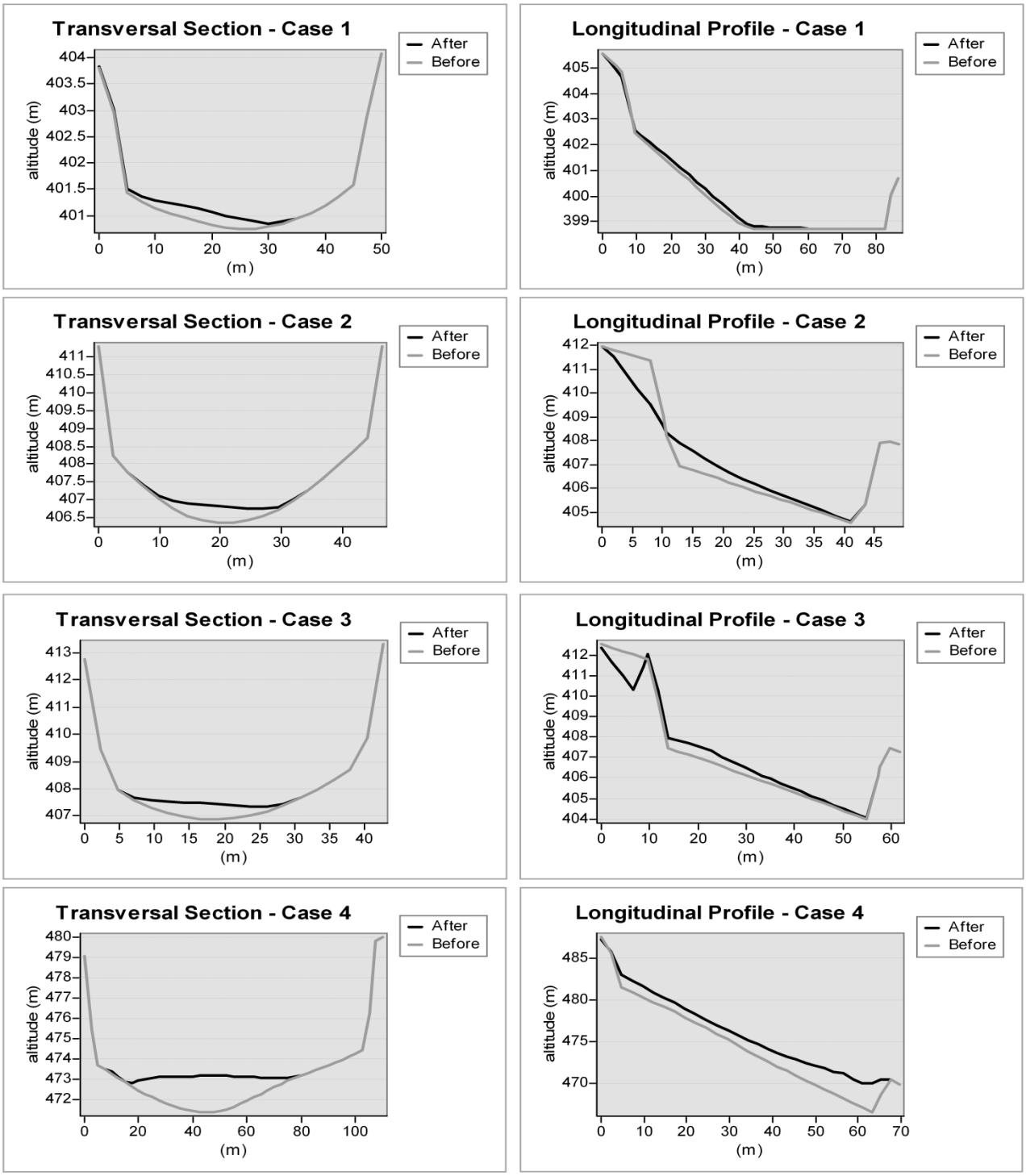

Fig. 3 Transversal section and longitudinal profiles in cases with reservoir before and after the simulations.

Though the present study showed that the pond locality has strong influences on the debris flow storage and deposition, a quantitative formula to establish pond design was not obtained. In order to obtain more adequate design of fish-ponds and more quantitative procedure, computational modeling with detailed and intensive field survey should be carried out in the future.

The present study mentions that the objectives of small fish-pond construction are to increase income for farmers, to improve their food circumstances, and to reduce the debris flow damage. Hence, the fish-pond construction can be called one of fruits of socio-technology and/or socio-engineering.

ACKNOWLEDGEMENTS: The authors are strongly appreciative to the members of Research

Group of Natural Disasters (GPDEN) of Federal University of Rio Grande do Sul (UFRGS) for their daily discussion on debris flow. Special thanks are also due to two anonymous reviewers who provided constructive comments.

REFERENCES

ACEB (2014): 1º Anuário brasileiro de pesca e aquicultura. Ministério de Pesca e Aquicultura, 133p.

Ashmore, P. (2015): Towards a sociogeomorphology of rivers. Geomorphology, Vol. 251, pp.149–56.

Assembleia Legislativa do RS (2013): Lei No. 14.244 de 27 de maio de 2013. Estado do Rio Grande do Sul, 4p.

FAO-DNOCS (1988): Manual sobre manejo de reservatórios para a produção de peixes. (Documento de Campo 9. Programa Cooperativo Governamental. FAO – Itália)

Flores, C.A., Pötter, R.O., Fasolo, P.J., Hasenack, H. and Weber, E. (2007): Levantamento semidetalhado de solos: Região da Serra Gaúcha - Rio Grande do Sul. Porto Alegre: UFRGS/Embrapa Clima Temperado.

Godoy, J.V.Z., Baumbach, M.F., Michel, G.P., Zambrano, F.C., Barragan, M.L.M. and Kobiyama, M. (2015): Análise estatística de chuva na região da bacia do arroio Forromeco, RS, Brasil. In: Proceedings of XXI Brazilian Symposium of Water Resources, Brasília, 2015. 8p.

Guimarães, A.F. (2012): Criação de peixe. CEPLAC, 28p.

Jakob, M. and Hungr, O. (eds.) (2005): Debris-flow hazards and related phenomena. Springer-Verlag, 739p.

Kobiyama, M., Michel, G.P. and Goerl, R.F. (2016): Historical views and current perspective of debris flow disaster management in Brazil. In: Aversa, S., Cascini, L., Picarelli, L. and Scavia, C. (eds.) Landslides and Engineered Slopes. Experience, Theory and Practice, CRCPress/ Balkema, pp.1189-1194.

Kobiyama, M., Goerl, R.F. and Monteiro, L.R. (2018): Integração das ciências e das tecnologias para redução de desastres naturais: Sócio-hidrologia e sócio-tecnologia. Revista Gestão & Sustentabilidade Ambiental, (in press).

Meschkat, A. (1975): Aquacultura e pesca em águas interiores no Brasil. Rio de Janeiro, PNUD/FAO, 47p.

Michel, G.P. (2015): Estimativa da profundidade do solo e seu efeito na modelagem de escorregamentos. UFRGS-IPH (PhD dissertation) 164p.

Mould, S.A., Fryirs, K. and Howitt, R. (2017): Practicing sociogeomorphology: Relationships and dialog in river research and management. Society & Natural Resources, 16p. doi: 10.1080/08941920.2017.1382627

Nakatani, K. (2008): GUI Equipped user friendly debris flow simulator "Kanako 2D (Ver.2.02)" handy manual. Laboratory of Erosion Control/ Kyoto University, 44p.

Nakatani, K., Wada, T., Satofuka, Y. and Mizuyama, T. (2008): Development of "Kanako 2D (Ver.2.00)," a user-friendly one- and two-dimensional debris flow simulator equipped with a graphical user interface. International Journal of Erosion Control Engineering, Vol. 1, No. 2, pp.62-72.

Pande, S. and Sivapalan, M. (2017): Progress in socio-hydrology: a meta-analysis of challenges and opportunities. WIREs Water, Vol. 4, 18p. doi: 10.1002/wat2.1193

Rickenmann, D. (1999): Empirical Relationships for Debris Flows. Natural Hazards, Vol. 19, No. 1, pp.47-77.

Sharples, M., Jeffery, N., du Boulay, J.B.H., Teather, D., Teather, B. and du Boulay, G.H. (2002): Socio-cognitive engineering: a methodology for the design of human-centred technology. European Journal of Operational Research, Vol. 136, No. 2, pp.310-323.

Sivakumar, B. (2012): Socio-hydrology: not a new science, but a recycled and re-worded hydrosociology. Hydrological Processes, Vol. 26, pp.3788–3790.

Viero, A.C. and Silva, D.R.A. (orgs.) (2010): Geodiversidade do estado do Rio Grande do Sul. CPRM, 256p.

Whipple, K.X. (1992): Predicting debris-flow runout and deposition on fans: the importance of the flow hydrograph. IAHS Publication, Vol. 209, pp.337-345.

The Effects of Hydraulic Structures on Streams Prone to Bank Erosion in an Intense Flood Event: A Case Study from Eastern Hokkaido

Daisuke AOKI,[1*] Mio KASAI[1] and Mari IGURA[2]

[1] Hokkaido University, Japan
[2] Sabo & Landslide Technical Center, Japan
*Corresponding author. E-mail: daisuke-aoki@eis.hokudai.ac.jp

Bank erosion can induce huge financial damage by eroding lands and destroying properties and infrastructures along the river. Understanding the process is first necessary so that hydraulic structures could be placed efficiently to prevent disasters. This study examined the process during an intense storm in August 2016 in Pekerebetsu and Kobayashi Rivers, the eastern Hokkaido Island in Japan, which caused disastrous damage in the area. The analyses of airborne LiDAR data, satellite imagery, and field survey revealed that debris flows produced from weathered granites in the headwaters triggered drastic channel widening by eroding banks consisted of incoherent periglacial colluviums in the upstream reaches. Sediment produced there deposited in the next gentler downstream reach (< 2 degrees), naturally in Kobayashi River, and by a dam in Perekebetsu River. For the former reduction in the amount of sediment transported limited bank erosion in the further downstream. In contrast, for the latter flow travelled encouraged vertical and then lateral erosion at the outlet of a reach containing a gorge and groundsills. Sediment produced from there aggraded beds in the further downstream to cause more bank erosion in turn. The results suggested that change in hydraulic condition created by valley configuration or hydraulic structures should be first understood for efficient and effective disaster prevention planning not only at a reach scale but also a catchment scale.

Key words: bank erosion, debris flow, periglacial colluvial deposits, hydraulic structure

1. INTRODUCTION

Bank erosion is globally recognized as a major sediment source for a basin [*Janes et al.*, 2018]. It can cause huge financial damage to the area by eroding lands and destroying properties and infrastructures along the river. It occurs when the lateral force of the flow dominates vertical one, so that either sediment deposition or channel incision can induce the phenomena [*Simon and Rinaldi*, 2006]. For example, bed aggradation across the valley, or bar formation with excessive amount of sediment supplied to a channel reach will offer flow more opportunities to contact banks and undercut their feet. In contrast, prominent channel incision, which is likely to happen with flow containing small amount of sediment, can result in the exposure of bedrocks on the bed, to redirect erosion force laterally. Once a bank is eroded, the phenomena could propagate downstream with materials yielded from there, which may aggrade beds in its downstream reaches in turn. Since the installation of hydraulic structures is a common practice for disaster prevention and the effect can

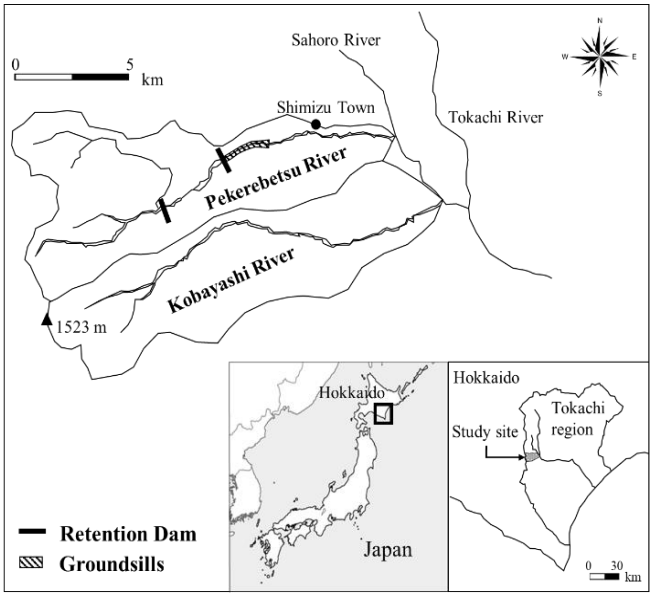

Fig. 1 Study site

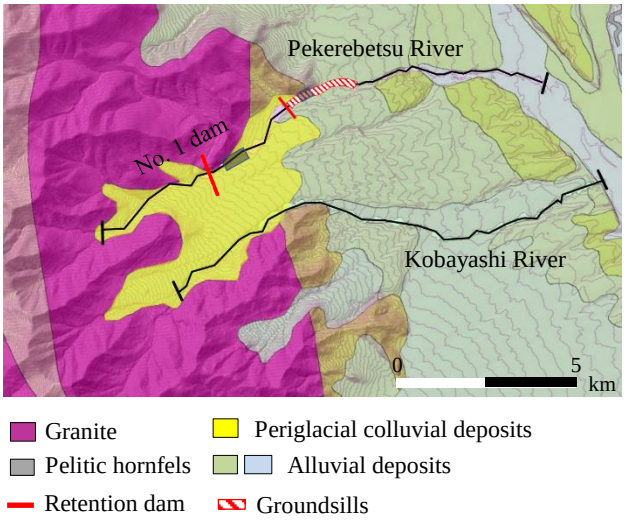

Fig. 2 Geological map of the study area (Based on Seamless Digital Geological Map of Japan, AIST, JAPAN). The study reaches were also shown with solid black lines.

Table 1 Study reaches

River	Catchment area at the downstream end (km^2)	Study reach length (km)
Kobayashi	41.9	14.3
Pekerebetsu	46.6	14.1

propagate through the channel course, a good understanding of bank erosion process is first required in planning for efficient and effective erosion control at a catchment scale. In this study, the process during an intense storm was examined for two neighboring rivers of the Tokachi River Basin, Pekerebetsu and Kobayashi Rivers, in the eastern Hokkaido Island, Japan (**Fig. 1**). Their channel feature had changed drastically through the courses to damage the area by the Typhoon Lionrock in August 2016. Totally more than 500 mm of rainfall was recorded for three days at most of the meteorological stations in the basin. The catchments are geomorphologically and geologically resembled, while two dams and groundsills were equipped in Pekerebetsu River (**Fig. 1**, **Fig. 2** and **Table 1**). Comparison of the channel responses of these rivers to the event will help understand not only the propagation process of the phenomena but also appraise the roles of the structures in the event. The outcome will also present a clue for catchment management planning considering and utilizing natural channel processes.

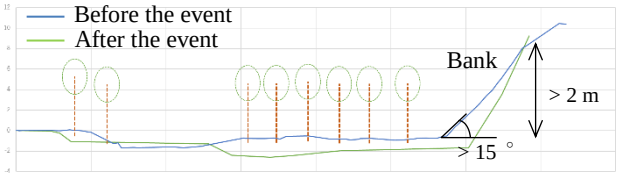

Fig. 3 Schematic image of cross section

2. STUDY SITE

Pekerebetsu River and Kobayashi River run from the East flank of Hidaka Mountain Range. The region is usually dry in summer months. The rivers appeared to be stable with channel width from 10 to 20 m prior to the event, while even-aged riparian forests along the rivers suggest that the floods of the same magnitude as in 2016 occasionally occurred in the past. Weathered granites intruded in the headwaters (**Fig. 2**), from which a sequence of debris flow produced during the 2016 event. At the feet of granites, periglacial colluvial deposits are widely distributed. Further downstream, a floodplain was spread between the terraces formed in the last glacial period. In Pekerebetsu River, peritic hornfels form two gorges. The channel reach installed a series of groundsills contains one of them. The channel beds for both the rivers were composed of materials mainly from sand to boulders.

3. METHODS

This study examined bank erosion process in association with the spatial pattern of net aggradation and degradation. Based on field observation, a bank was defined as a morphologic feature that the cliff by the river floor is steeper than 15 degrees and the height is over 2 m in this study (**Fig. 3**). The degree of bank erosion was appraised with the help of change in channel width measured for the pre- and post-event every 100 m along the rivers on aerial photographs and high-resolution satellite imagery from Worldview-2 and 3. The resolution of the imagery is 0.46 m and 0.31 m, respectively. Since the expansion of channel width is caused by not only bank erosion but also overbank deposition, the distinction was made with airborne LiDAR survey data taken after the event or field evidence, depending on the data availability.

The magnitude of channel aggradation and degradation was estimated based on cross section which was set every about 500 m along the rivers. The elevation for the lines were obtained from either airborne LiDAR data, otherwise field survey. The area laterally eroded was also given from these cross sections.

To highlight change in bank erosion process through the courses, this study divided the channel courses into three reaches based on channel slope. Channel slope was measured along the stream centerline at about 200 m intervals with LiDAR data, otherwise by field survey with a laser rangefinder. Smoothing channel slope by moving average for every 600 m, the reach above 2 degrees was termed as 'Upper Reach', for it is the slope that debris flows generally stop the motion. In field, these reaches are confided by either valley walls, terraces, or periglacial colluviums. On the other hand, 'Lower Reach' runs through an alluvial plain and channel slope was almost stable to be around 1 degrees. The reach situated between them is 'Middle Reach', along which channel slope fluctuates between 1 and 2 degrees.

4. RESULTS

Spatial changes in cross-sectional area and width caused by the event are presented in **Figs. 4** and **5.** Field photographs and selected cross sections representative of those changes are also shown in **Figs. 6** and **7**. Bank erosion processes characteristic of each reach are summarized below.

4.1 Upper Reach

4.1.1 Kobayashi River (4.7 – 9.4 km)

Debris flows induced bank erosion in the reach, as mainly incising the beds, down to 7 km (**Fig. 4** and **Fig. 6-A**). After the event the width of the section was mostly below 50 m but expanded to be above 70 m locally (**Fig. 5**). From 7 to 9 km, debris flow deposition triggered intensive lateral erosion into periglacial colluviums, forming the beds measured about 100 m (**Fig. 4, Fig. 6-B,** and xs1k in **Fig. 7**). The river starts flowing in a flood plain at 9 km. From there overbank deposition was observed down to 9.4 km.

4.1.2 Pekerebetsu River (3.8 – 8.0 km)

It was typical in this reach that debris flow deposition redirected channel courses to undercut the feet of incoherent periglacial colluvium and induce bank erosion (**Fig. 6-C** and xs1p in **Fig. 7**). As a result, channel width expanded up to 100 m, similarly to the upper reach of Kobayashi River (**Fig. 5**). No. 1 dam at 6.9 km then trapped coarse materials, although it was destroyed during the event. Boulders carried with debris flow stopped at the inlet of gorge (7.5 km, **Fig. 4**). Little morphological change occurred through the gorge.

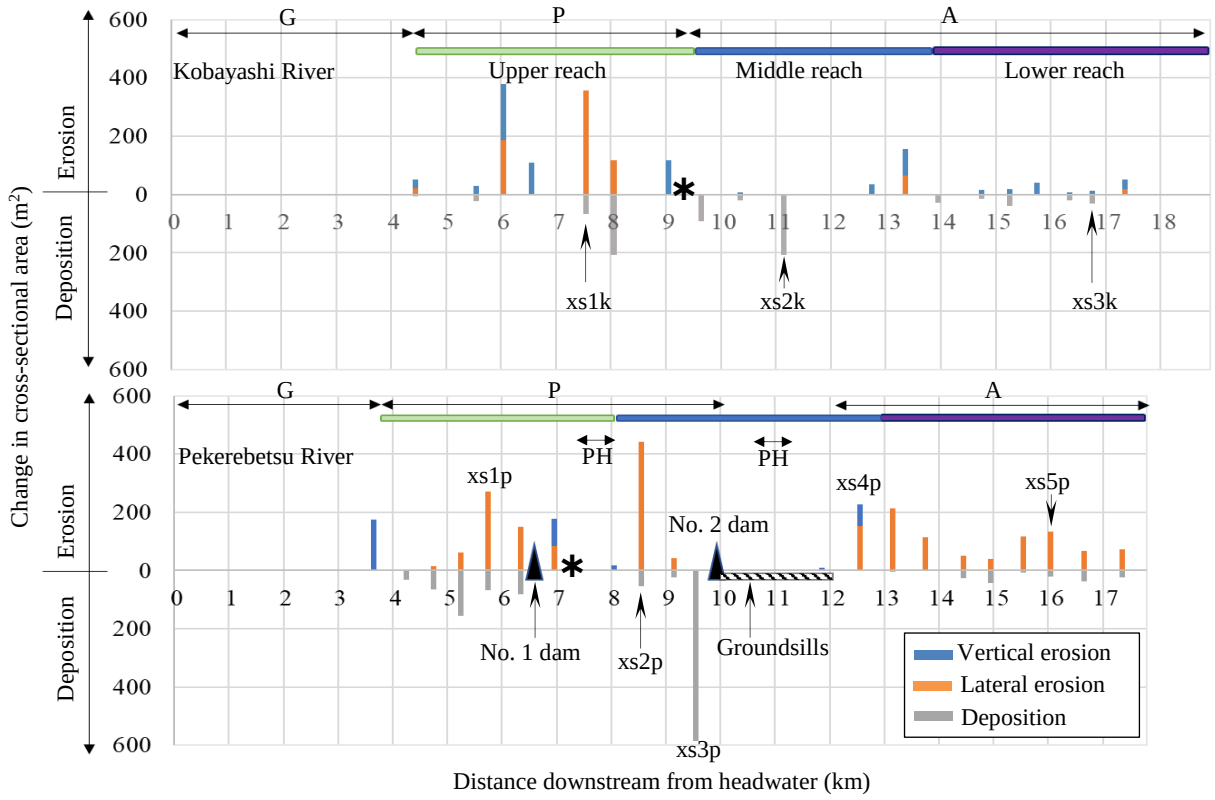

Fig. 4 Sediment deposition and channel erosion by the typhoon Lionrock. G: granite, P: periglacial colluvial deposits, A: alluvial deposits, and PH: pelitic hornfels forming gorges. ✱: The most downstream point that debris flow deposition was found.

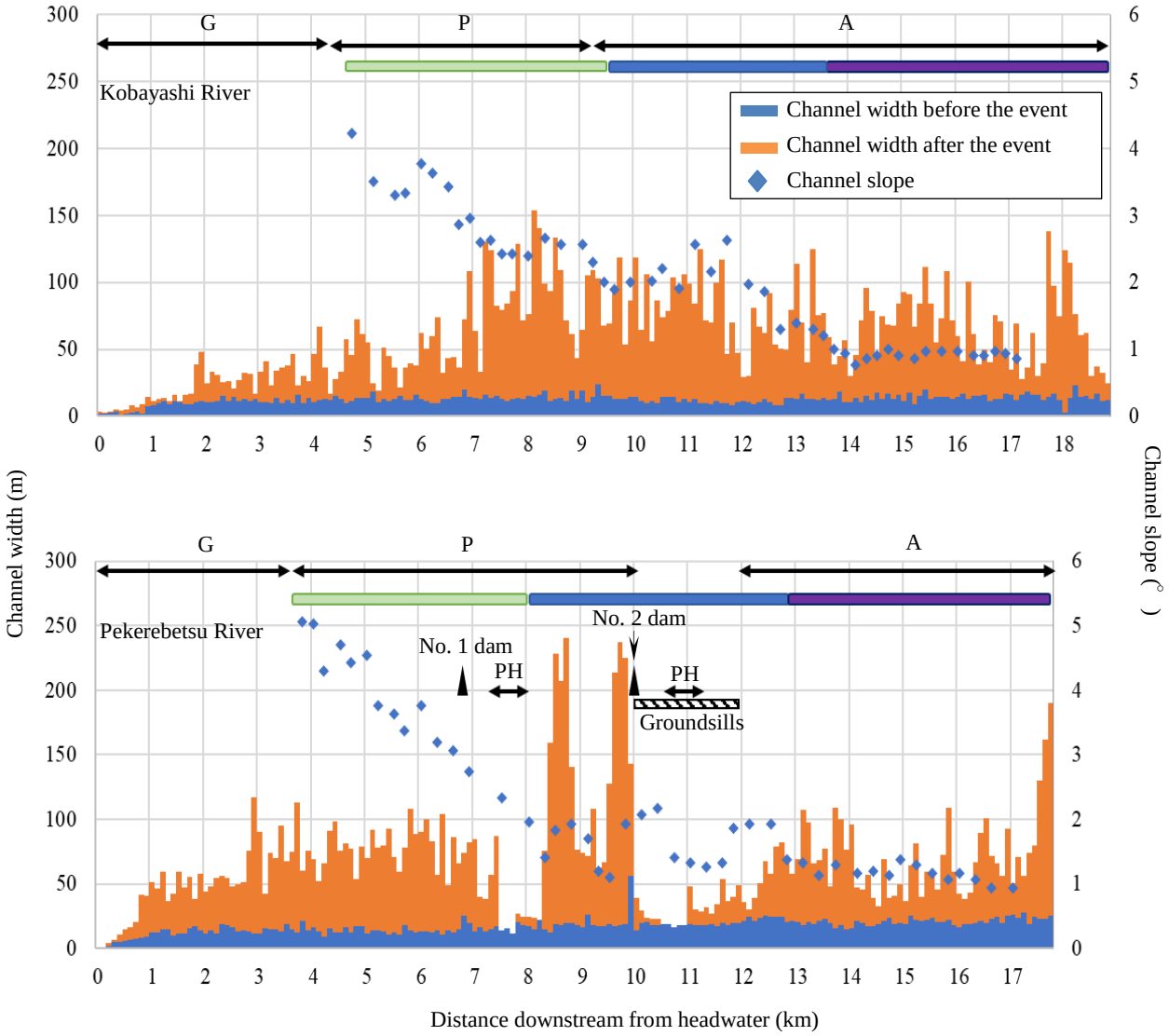

Fig. 5 Channel slope and change in channel width before and after the typhoon Lionrock in 2016

4.2 Middle Reach

4.2.1 Kobayashi River (9.4 - 13.7 km)

Overbank sediment deposition was dominant and bank erosion was not evident in the reach (**Fig.4**, **Fig. 6-D** and xs2k in **Fig. 7**), most probably resulting in decrease in the amount of coarse sediment travelled further. Channel width including the deposition area was mostly between 50 and 100 m along the course (**Fig. 5**).

4.2.2 Pekerebetsu River (8.0 – 12.8 km)

The most intensive bank erosion occurred in the reach starting from the outlet of the gorge (8.0 km, **Fig. 4**, and **Fig. 6-E**), which was caused by channel aggradation (e.g. the right bank of xs2p in **Fig. 7**). Eroding the bank composed of periglacial colluvial deposits, the channel width increased up to over 200 m for 300 m in distance from 8.5 km to 8.7 km (**Fig. 5**). Sediment deposition by No. 2 dam at 9.8 km also brought about the beds wider than 200 m over 300 m upstream of the dam (**Fig. 5**). This expansion, however, was caused by mere bed aggradation (xs3p in **Fig. 7**), and not accompanied with bank erosion. In the reach stretching over 2 km downstream of No. 2 dam, a series of groundsills prevented either vertical and lateral erosion or sediment deposition, similarly to the gorge in the upper reach (**Fig. 4**). At the down end of the sequence channel bed was incised, to have exposed bedrocks and then caused excessive bank erosion from 12.0 to 12.8 km **(Fig.4, Fig. 6-F** and xs4p in **Fig. 7**).

4.3 Lower Reach

4.3.1 Kobayashi River (13.7 - 18.8 km)

The magnitude of change in cross sectional areas were much smaller than Pekerebetsu River (**Fig. 4**), and aggradation and degradation cyclically appeared along the course (**Fig. 4**). Newly transported sediment mantled thinly over the old channel bed, on which riparian forests grew (**Fig. 6-G** and xs3k in **Fig. 7**). The bank was rarely eroded. Average channel width after the event was 65.3 m in this reach.

4.3.2 Pekerebetsu River (12.8 - 17.7 km)

A large amount of sediment supply from the down end of the middle reach triggered to widen the beds

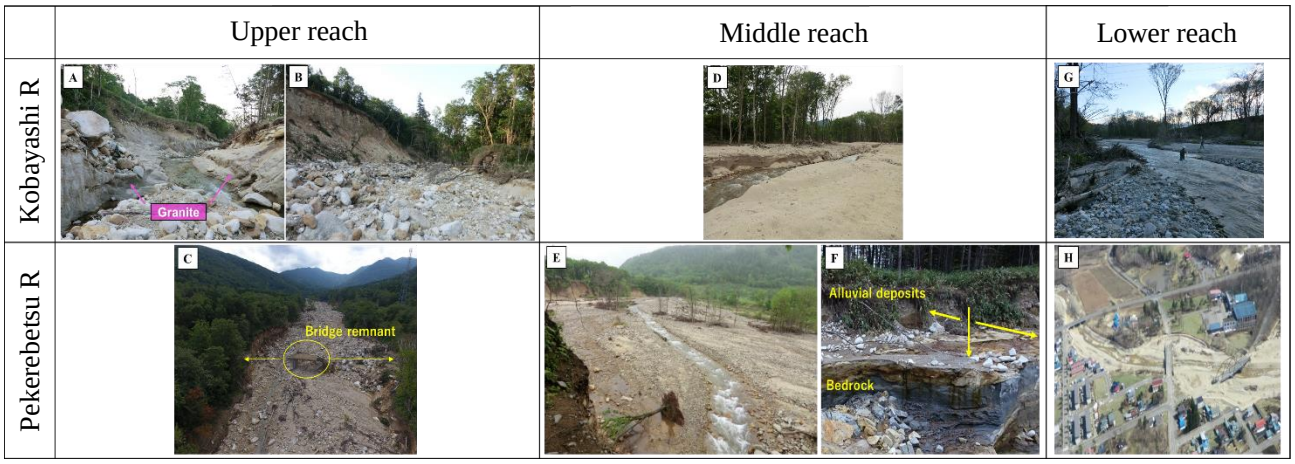

Fig. 6 Field photographs taken after the event. Upper reach: A; Debris flows stripped sediment off as they ran down the stream, B and C; Debris flow deposition triggered lateral erosion into periglacial colluvial deposits. Middle reach: D; Fresh sediment deposition covered old beds, E; Sediment deposition at the outlet of a pelitic hornfels gorge triggered expansive lateral erosion, F; Bedrock denudation on the channel floor by intense flow subsequently induced extensive bank erosion. Lower reach: G; Deposition of coarse materials, H; Shimizu Town damaged by sediment overflow and floodplain erosion.

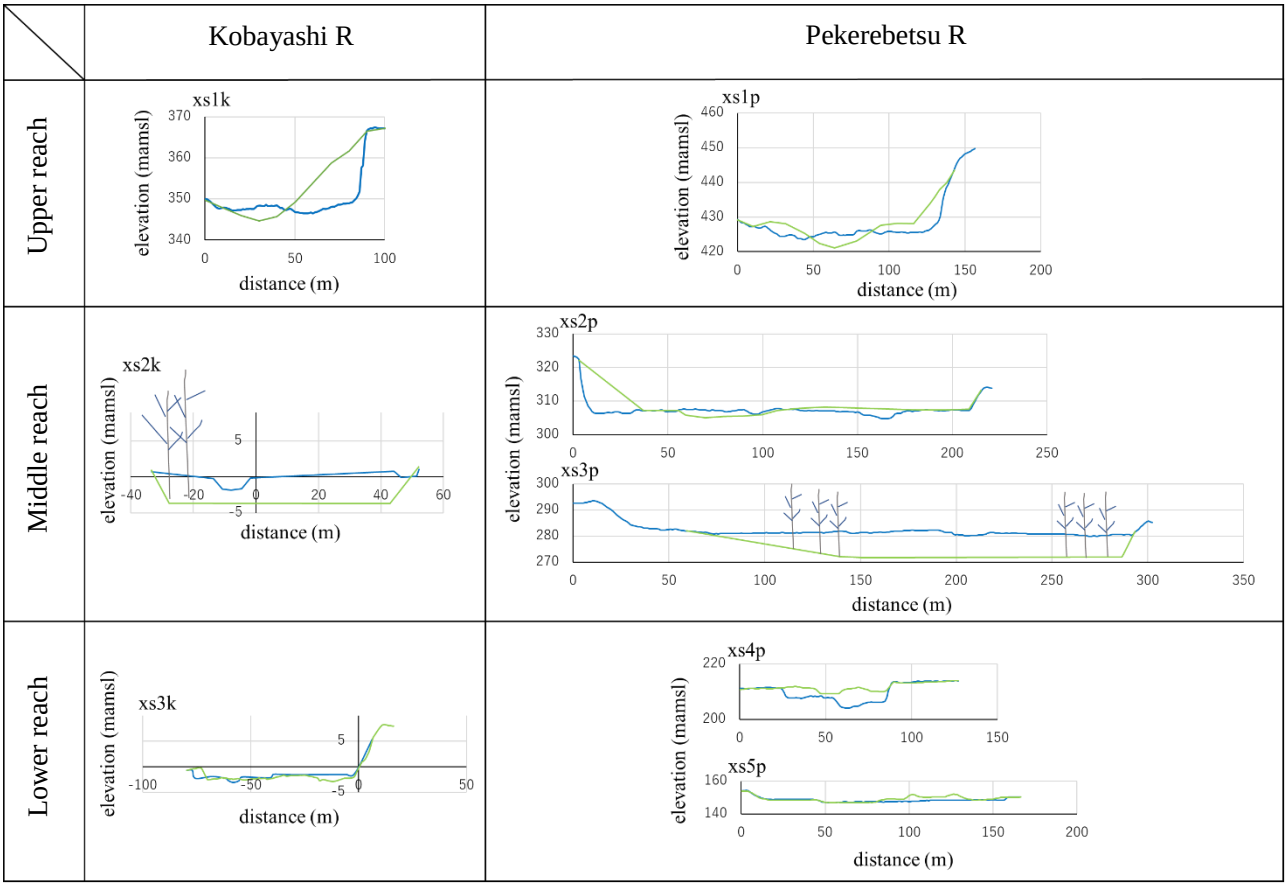

Fig. 7 Representative cases of cross-sectional changes. The locations are indicated in Fig. 4

of the reach as well (**Fig. 4**), consequently damaging bridges, houses, and roads along the course in Shimizu Town (**Fig. 6-H**). Bank erosion process in the reach was driven by sediment deposition that leveled the bed across the lines and offer water course to contact the existing banks (**Fig. 4** and xs5p in **Fig. 7**). Average active channel width in the lower reach was 71.4 m, similarly to Kobayashi river.

5.DISCUSSION

In both the upper reaches, debris flows played a major role on bank erosion. Since periglacial slope deposits nearby the channel courses were incoherent and erodible, channel width could drastically expand and the banks became a significant sediment source for both the rivers. Sediment transported into the middle reach then deposited there whether there was a dam or not. This deposition did not necessarily induce bank erosion except for the section at the outlet of the gorge in Pekerebetsu River. Reduction of a large amount of materials transported probably induced by this deposition in the middle reach could be responsible for limiting change in channel forms and bank erosion in the lower reach in Kobayashi River. Although the active channel width during the flood was similar to Pekerebetsu River, the exchange of sediment between flow and the river bed, including the past deposits, was a major process for the width expansion. In comparison, volumetric sediment contribution from the lower reach estimated from cross sectional changes was much larger in Pekerebetsu River. This is due to intense bank erosion, or the creation of sediment source at the end of the section with groundsills, although it is uncertain whether the phenomena attributed to the structures or the gorge itself. At least the case indicates that the interruption of sediment flux in the upstream was not a solution to control bank erosion for the downstream course in Pekerebetsu River. Rather, the outlet of a gorge is a key site to control change in channel morphology not only at a reach scale but also a catchment scale. There sudden increase in the amount of sediment deposition due to the reduction of transport capacity, caused by channel widening and lowering the depth of flow, can induce extreme lateral erosion if the bank consists of erodible materials. The results highlighted the importance of the recognition of intrinsic roles that each reach owns regarding sediment delivery, in planning hydraulic structures to control bank erosion at a catchment scale.

6. CONCLUSION

This study compared bank erosion process in an extreme flood between two similar sized rivers from the Tokachi river basin. In both the upper reaches, debris flows played a major role on bank erosion. In Kobayashi River, the nature of the middle reach to deposit sediment could work on buffering the event impact for the downstream channel forms. On the other hand, lithological and artificial control in the middle reach could have enhanced bank erosion in the lower reach, in Pekerebestu River. The results suggested that change in hydraulic condition created by valley confinement and underlying geology should be understood first for efficient and effective structure planning to prevent from unwanted bank erosion and related disasters.

ACKNOWLEDGMENT: We are greatly thankful for the support from Obihiro Development and Construction Department of Hokkaido Development Bureau, Ministry of Land, Infrastructure, Transport and Tourism, Japan.

REFERENCES

Janes, V., Holman, I., Birkinshaw, S., O'Donnell, G. and Kilsby, C. (2018): Improving bank erosion modelling at catchment scale by incorporating temporal and spatial variability, Earth Surface Process and Landforms, Vol. 43, pp. 124-133.

Simon, A. and Rinaldi, M. (2006): Disturbance, stream incision, and channel evolution: The roles of excess transport capacity and boundary materials in controlling channel response, Geomorphology, Vol. 79, pp. 361-383.

Topic 4: Integrated basin-scale sediment management for sustainable development

Maintenance and Utilization of a Sabo Facility Designated as an Important Cultural Property - The Shiraiwa Sabo Dam -

Takeshi OSAKA[1]* and Hisashi WATANABE[2]

[1] Tateyama Mountain Area Sabo Office (61 Buna-zaka Ashikuraji Tateyama-cho, Naka-niikawa-gun, Toyama Prefecture 9301405, Japan)
[2] Sabo Frontier Foundation (Hirakawacho, Chiyoda-ku, Tokyo 1020093, Japan)
*Corresponding author. E-mail: ohsaka-t847x@mlit.go.jp

This report introduces the effort of maintenance and utilization of Tateyama Mountain Area Sabo office against maintenance and management issues surrounding modern sabo works. The maintenance of the Shiraiwa Sabo Dam is described, particularly in the context of maintaining its disaster prevention function and conserving its value as a cultural property. It is hoped that this report on the Shiraiwa Sabo Dam will help guide the maintenance and management of other Sabo facilities designated as Important Cultural Properties.

Key words: Historic sabo facilities, Important Cultural Property, maintenance of sabo facilities, disaster-prevention, cultural value

1. Introduction

Sabo work in Tateyama started in 1906. The initial sabo works were undertaken by Toyama Prefecture. At that time, construction of structures such as sabo dams was very difficult and expensive.

Consequently, direct control of sabo works was handed to the Ministry of Home Affairs (now the Ministry of Land, Infrastructure, Transport and Tourism, MLIT) in 1926.

Over the next 90 years, many advances were made to sabo design and construction. The Shiraiwa Sabo Dam was the first sabo facility built by the Ministry at the Tateyama Caldera; it is an important sabo facility that prevents sediment discharge from the Tateyama Caldera.

The Shiraiwa Sabo Dam continues to be an important disaster-prevention measure. In addition, the historical and cultural value of the Shiraiwa Sabo Dam was recognized by the Agency for Cultural Affairs in June 2009, when it became the first sabo dam in Japan to be designated as an Important Cultural Property.

This paper reports on the maintenance and management of the Shiraiwa Sabo Dam, and examines the goal to preserve both the dam's original disaster-prevention function and its value as a cultural property.

2. Overview of the Sabo works in Tateyama

2.1 Overview of the Joganji River

Toyama Prefecture is located in the central part of Japan. The prefecture area is about 4,300 km^2, occupying approximately 1% of the total area of Japan, and the prefecture population is about 1.1 million, approximately 1% of Japan's total population. Toyama Prefecture is surrounded by high mountains to the east, south, and west. About 72% of the prefecture is occupied by mountains and hills with an altitude of 100 m or more. There is abundant rain fall in the winter, and precipitation in the mountains exceeds 5,000 mm per year.

The Joganji River is one of steepest rivers in Japan, flowing 56 km from the 3,000 m-high mountainous area in the east of Toyama Prefecture to Toyama bay. The average slope of the riverbed is about 1/30 (**Fig. 1**). In the upstream area of the Joganji River lies the Tateyama Caldera, which extends 6.5 km east-west and 4.5 km north-south, and has a fragile geology composed of Tateyama Volcano ejecta. In addition, the Atotsugawa fault, which is prone to collapse, lies in the vicinity.

During the 1858 Hietsu earthquake (magnitude 7.1), a gigantic landslide, named the Tonbi landslide, occurred at the Tateyama Caldera, and about 400 million m^3 of sediment accumulated, of which 200 million m^3 flowed out of the caldera.

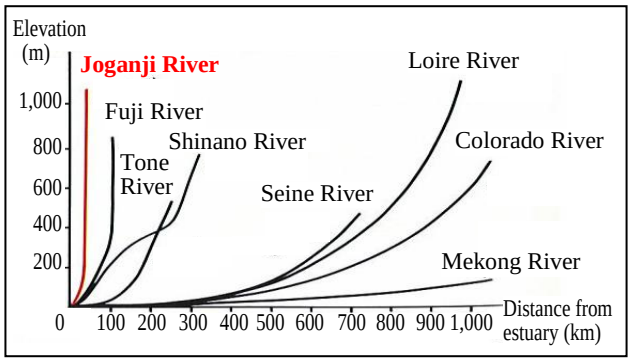

Fig. 1 Slope of the Joganji riverbed relative to other of other rivers

As a result, 140 people died, and 8,945 people were injured. After this disaster, the Joganji River became more prone to additional sediment-related disasters.

2.2 Outline of the sabo works in the Tateyama Mountain Area

In the Tateyama Caldera, there is still about 200 million m^3 of accumulated sediment, some of which flows to the downstream area of the Joganji River every time heavy rainfall occurs.

To protect the Joganji River Basin from sediment-related disasters, modification of the Joganji River began in the Meiji era, but disasters still occurred repeatedly. In 1906, sabo works started in the upstream area of the Joganji River.

However, several major sabo facilities were destroyed by a large flood in 1919, and there were difficulties associated with the cost and construction of the sabo works. At the request of Toyama Prefecture, direct control of the Sabo works was handed to the Ministry of Home Affairs (now the Ministry of Land, Infrastructure, Transport and Tourism, MLIT) in 1926.

3. Historical sabo facilities

3.1 Historical sabo facilities in the Tateyama Mountain Area

Within the management area of the Tateyama Mountain Area Sabo Office, there are many (about 30%) sabo dams that were completed over 50 years ago or more, such as the Shiraiwa Sabo Dam, Yukawa Sabo Dam, Matsuo Sabo Dam, Onigajo Sabo Dam, and Sabudani Sabo Dam.

Since their completion, these sabo facilities have protected, and continue to protect, the Joganji River Basin from sediment-related disasters.

3.2 Shiraiwa Sabo Dam

The Shiraiwa Sabo Dam is an important sabo facility constructed between October 1929 and December 1939. The dam was constructed based on a plan designed by Masao Akagi, an engineer for the Japan Department of Interior, to stabilize the hillside of the Joganji River upstream area, including the Tateyama Caldera, and to prevent erosion of the river bed.

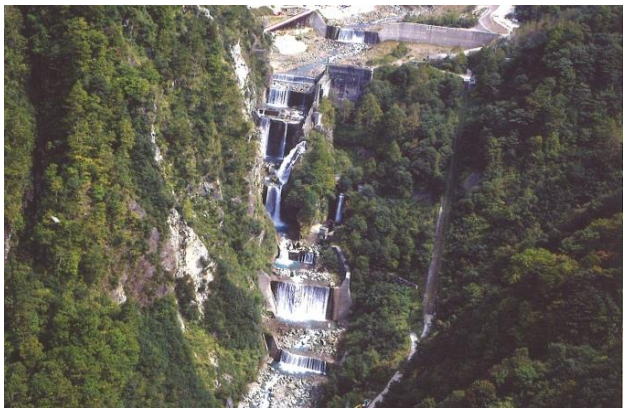

Fig. 2 Shiraiwa Sabo Dam

The Shiraiwa Sabo Dam was constructed at the outlet of the Tateyama Caldera in the upstream area of the Joganji River (41.8 km from the river's estuary). This location was chosen for the dam construction site due to the suitable rock foundation, and the ability to secure a large sedimentary area at a narrow part of the river. The Shiraiwa Sabo Dam is a complex sabo facility including a main dam with a non-overflowing section height of 63 m (Japan's largest), seven counter dams, and a retention frame. In addition, this was the first sabo dam in Japan for which a seismic design method was used.

In Japan, sabo facilities that still exist more than 50 years after completion, and are deemed to have historical and cultural value, are defined as Historical Sabo Facilities. Sabo dams with particularly high value are recognized as Cultural Properties by the Agency for Cultural Affairs, Government of Japan.

The Shiraiwa Sabo Dam was built using the seismic design method, with large machines that were considered state-of-the-art technology at the time. It is a complex sabo facility, composed of multiple large-scale structures. The Shiraiwa Sabo Dam has been deemed "particularly technically superior," "highly historical," and "a great technical achievement among modern sabo facilities". In June 2009, it was the first sabo facility in Japan to be designated an Important Cultural Property.

The Shiraiwa Sabo Dam is composed of many facilities, including the main dam, the retention frame, and a number of counter dams. The extent of the Important Cultural Property designation is shown in **Fig. 3**.

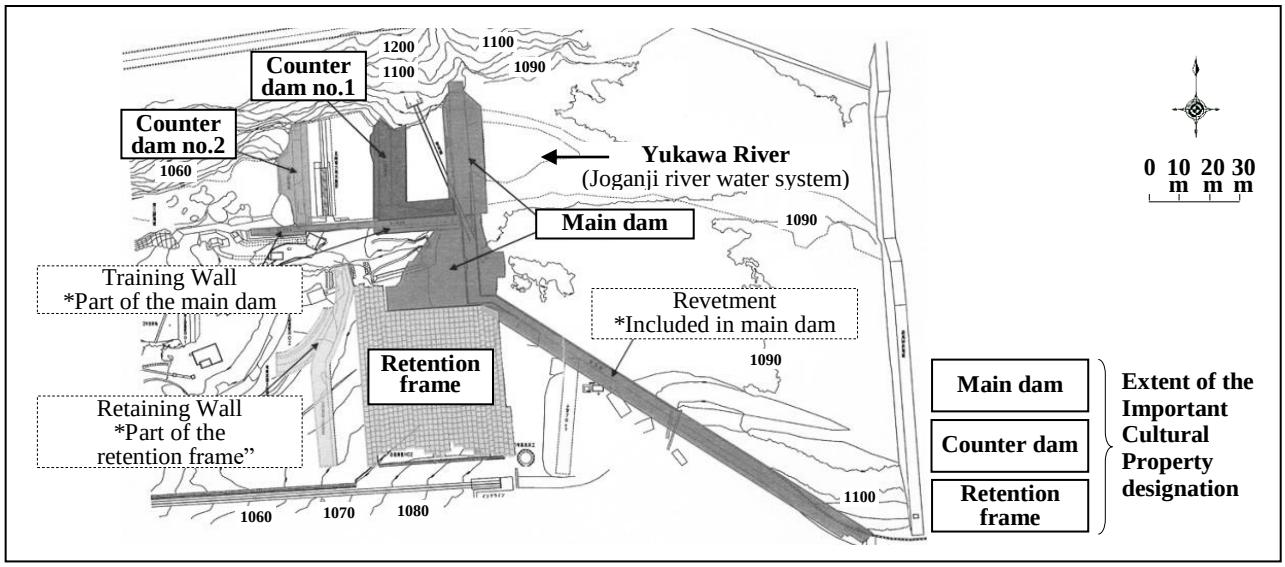

Fig. 3 Extent of the Important Cultural Property designation of the Shiraiwa Sabo Dam

3.3 Hongu Sabo Dam

The Hongu Sabo Dam is a main check dam that was constructed between 1935 and 1937 in the midstream area of the Joganji River (26.8 km from the estuary), for the prevention and control of sediment discharge.

The dam height is 22.0 m and the crest length is 107.4 m; a total of 23,500 m^3 of concrete was used in the construction of the dam body. There are five counter dams, and the sediment trap capacity is the largest in Japan, at 5 million m^3.

At the time of construction of the Hongu Sabo Dam, large-scale state-of-the-art equipment and methods, such as tower cranes, were introduced. Therefore, despite its large scale, the dam was completed in less than 2 years (**Fig. 4**).

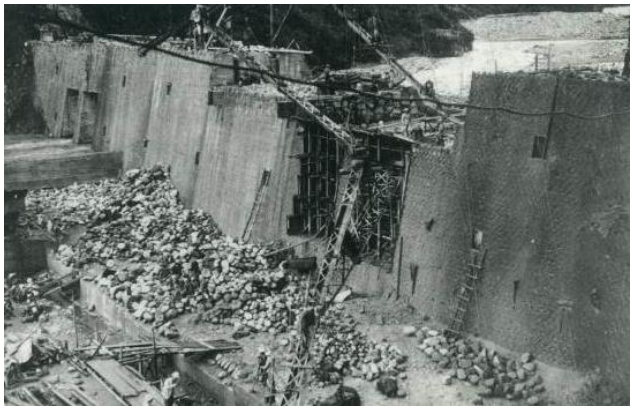

Fig. 4 Hongu Sabo Dam (under construction)

The Hongu Sabo Dam has been highly praised for demonstrating "the technical level of sabo facility design in the early Showa period". The dam has been deemed a "valuable example of mechanized construction techniques". In November 2017, the Hongu Sabo Dam was designated an Important Cultural Property (**Fig. 5**).

Fig. 5 Hongu Sabo dam (present day)

3.4 Dorodani Sabo Dams

The Dorodani Sabo Dams were constructed just under the Tonbi landslide area to prevent devastation of the Dorodani valley (**Fig. 6**). The Dorodani Sabo Dams are a series of stepped dams consisting of 20 check dams, 3 groundsills, and hillside works.

Initially, Toyama Prefecture constructed sabo facilities in Dorodani, but these were damaged during the heavy rains of 1929. The Ministry of Japan started re-construction of the Dorodani Sabo Dams in 1930 (**Fig. 7**).

The Dorodani Sabo Dams have also received praise for showing "the technical level of sabo facility design in the early Showa period" and for the value of its "hillside works to prevent slope failure". In November 2017, the Dorodani Sabo Dams were designated an Important Cultural Property.

Fig. 6 Dorodani Sabo Dams (under construction)

Fig. 7 Dorodani Sabo Dams (present day)

4. Problems and solutions for sabo facilities in Japan

4.1 Deterioration of infrastructure

A large proportion of Japan's infrastructure, such as roads, bridges, and river management facilities, was constructed during the high growth period after World War Ⅱ. Thus, 10 years from now, many of these facilities will have been in place for about 50 years. Twenty years from now, 60% of all sabo facilities will be at least 50 years old. Therefore, there is concern about the deterioration of this infrastructure.

4.2 Plan to prolong the lifespan of Japan's infrastructure

In December 2012, the ceiling board of a tunnel fell onto the Chuo Expressway, one of the major expressways of Japan. This event prompted the MLIT to create a plan to prolong the lifespan of Japan's infrastructure (hereafter referred to as the Action Plan), in September 2013. Based on this plan, the MLIT began taking appropriate action to maintain and prolong the lifespan of Japan's infrastructure.

4.3 Approach of the Erosion and Sediment Control Department of the MLIT

Sabo facilities prevent sediment-related disasters, and their functions (**Table 1**) must be sustained.

Table 1 Major functions of sabo facilities

Debris flow control
Landslide control
Prevention of steep slope failure

To maintain sediment-related disaster protection, the Erosion and Sediment Control Department of the MLIT ordered all sabo offices in Japan to develop a plan to prolong the lifespan of sabo facilities, based on MLIT's Action Plan.

In addition, the Erosion and Sediment Control Department of the MLIT issued manuals to sabo offices, which were designed to help facility managers investigate the soundness of existing facilities and plan lifespan-prolonging maintenance activities (**Fig. 8**).

4.4 Action at the Tateyama Mountain Area Sabo Office

The Tateyama Mountain Area Sabo Office is currently implementing a plan to maintain and prolong the lifespan of Sabo facilities in accordance with the manuals issued by the MLIT.

The main tenets of the Tateyama Mountain Area Sabo Office plan are shown below.

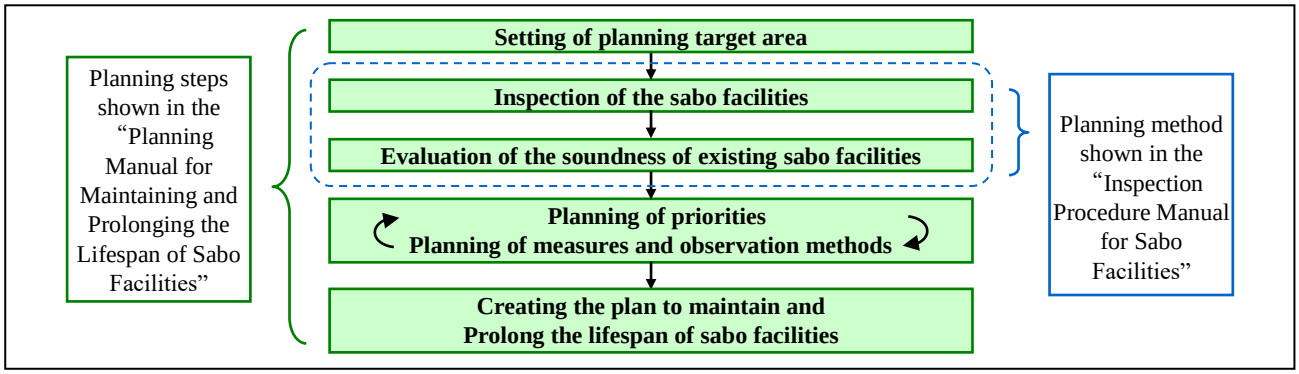

Fig. 8 Contents of the "Planning Manual for Maintaining and Prolonging the Lifespan of Sabo Facilities" and the "Inspection Procedure Manual for Sabo Facilities"

(1) Inspect and evaluate the soundness of sabo facilities.

We will conduct periodic, detailed inspections to evaluate any deterioration of facility functions or performance, based on structural and material characteristics. Using the results of the inspections, we will comprehensively evaluate the soundness of the facilities (**Fig. 9**).

The characteristics of materials and structures that are not currently used, such as stone and concrete rubble, will be considered.

In addition, facilities that have been deemed Important Cultural Properties will be carefully inspected and scrutinized via detailed inspection, boring surveys, elastic wave surveys, etc., to maintain their status as Important Cultural Properties (**Table 2**, **Fig. 10**).

(2) Planning of priorities for corrective measures.

At the Tateyama Mountain Area Sabo Office, the priority for implementing corrective measures was determined using multiple evaluation indicators, as shown in **Table 3**.

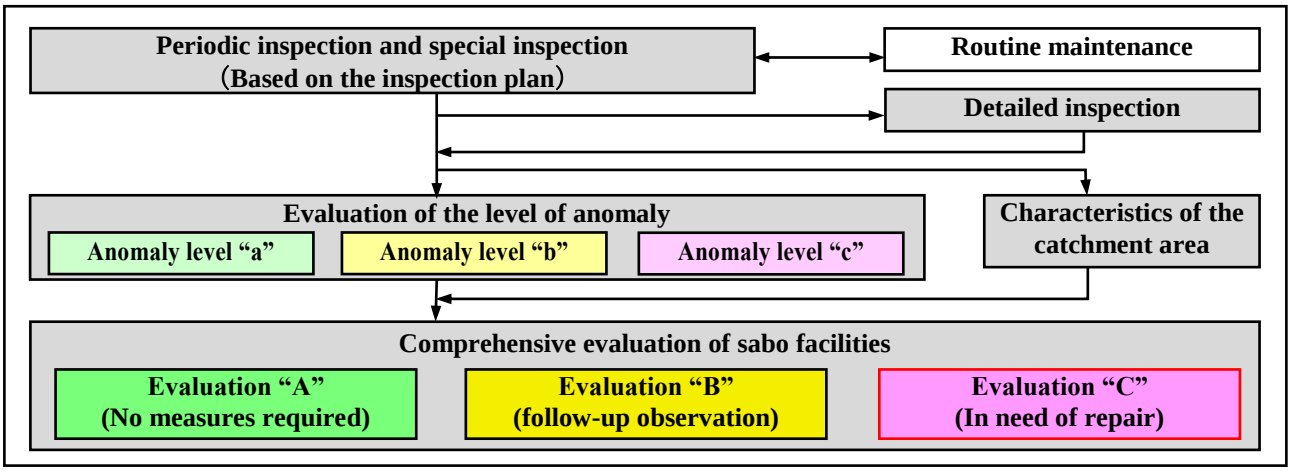

Fig. 9 Comprehensive evaluation of sabo facilities

Table 2 Examples of detailed inspection items for historical Sabo facilities

Investigation method	Investigation aims	Description
Boring investigation	To determine the physical properties of the internal material of the dam and sedimentation area	In-situ test and laboratory tests
Detailed visual inspection	To determine characteristics (material, color, shape, arrangement) and damage or deterioration of the outer stone material	Carried out by researchers with expertise using appropriate technology
Elastic wave exploration	To determine the density of the internal material	Non-destructive inspection

Fig. 10 Example images of detailed visual inspections of sabo facilities

Table 3 Indicators for determining the priority of corrective measures

Indicator	Contents	Evaluation A	Evaluation B	Evaluation C
Soundness of the facilities	Results of the soundness evaluation of the facilities	No need to repair sabo facilities	Follow-up observation of sabo facilities	In-need-of-repair sabo facilities
Core facility determination	Core facility of the basin	Not a Core facility of the basin	—	Core facility of the basin
Stability of the facility	Results of the stability check	Stable	Metastable	Unstable
Flow capacity	Flow capacity of the overflow section of the facility	Water flow	Water barely flows	Water does not flow
Importance of the facility	Type of torrent	Not applicable; debris flow torrent	—	Applicable; debris flow torrent
	Sediment trap capacity	≤ 100,000 m^3	100,000–430,000 m^3	≥ 430,000 m^3
Distance to conservation target	Distance from sabo facilities to the conservation target (houses, public facilities, power stations, etc.)	≥ 1.0 km	0.1–1.0km	≤ 0.1 km
Support in the event of a disaster	Facilities covering areas in which people who need disaster support reside.	Not in the torrent	—	Within the torrent
Characteristics of the basin	Sediment movement potential in basin	Low	Medium	High
	Deep-seated landslide zone	Not applicable	—	Applicable

(3) Creating a maintenance and life-prolonging plan for the sabo facilities.

The measures were determined based on the extent of damage and local situation. Measures that have already been implemented were selected (**Table 4)**.

5. Preservation of cultural properties in Japan

5.1 Schematic diagram of cultural properties

To protect precious historical cultural properties, the Law for the Protection of Cultural Properties was enacted in Japan.

Cultural properties include structures such as shrines and private houses; artifacts such as Buddhist statues, paintings, and calligraphy; manners and customs; traditional events and festivals; and landscapes, historic villages, and townscapes (**Fig. 11**).

5.2 Movements to protect the cultural value of Sabo facilities

In Japan, sabo facilities have been constructed for over 100 years, to recover devastated mountains and prevent sediment-related disasters. Sabo facilities were built using the technology available at the time of construction, and though some of these construction methods are now outdated, the facilities themselves still continue to function as disaster prevention systems.

Japan's Agency of Cultural Affairs feared that various historical structures that contributed to the modernization of Japan were being destroyed, without being evaluated. In 1996, the Agency of Cultural Affairs revised the laws regarding protection of cultural properties, established a "Registered Cultural Property System," and began protecting historical structures, including sabo facilities, as cultural properties.

To register a sabo facility as a Tangible Cultural Property, it is necessary to evaluate, preserve and use it as a cultural property based on its characteristics. For this reason, the MLIT and the Agency of Cultural Affairs held a committee meeting on the preservation and utilization of historical sabo facilities in December 2002, and established guidelines for the preservation and utilization of historical sabo facilities in May 2003.

In September 2003, the MLIT notified the Sabo facility administrators about these guidelines, which were used as a basis for preservation and utilization as cultural properties.

In May 1997, the Katsunuma Sabo Dam became the first Sabo facility to be registered as a Tangible Cultural Property. Since then, over 160 Sabo facilities have been registered as Tangible Cultural Properties.

In June 2009, the Shiraiwa Sabo Dam was the first sabo facility to be designated an Important Cultural Property in Japan. In July 2012, the Ushibuse River French-style channel works system was also designated as an Important Cultural Property. In addition, in November 2017, the Hongu Sabo Dam and Dorodani Sabo Dams, which are under the jurisdiction of the Tateyama Mountain Area Sabo Office, were designated as Important Cultural Properties.

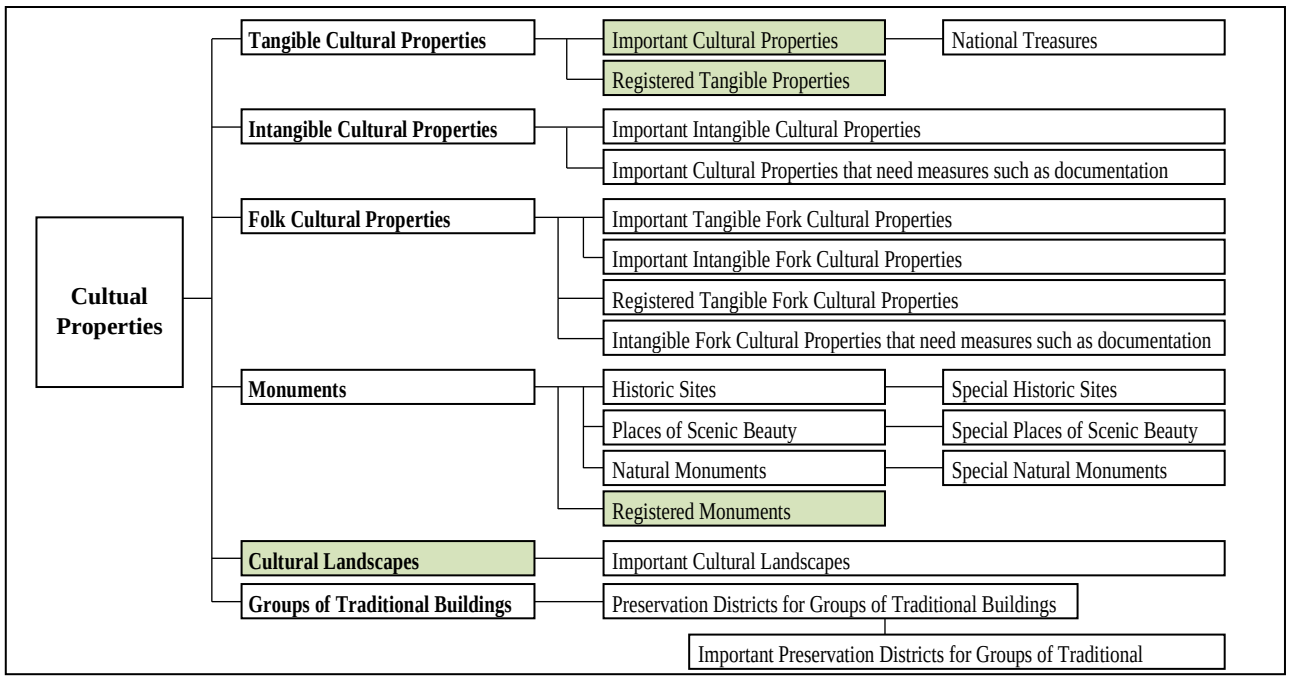

Fig. 11 Schematic diagram of cultural properties

6. Preservation of the historical cultural value of sabo facilities

The purpose of historical sabo facility management efforts by the Tateyama Mountain Area Sabo Office is to maintain the disaster prevention functions of the facilities and preserve their value as cultural properties. In particular, management of the Shiraiwa Sabo Dam, designated as an Important Cultural Property, was discussed with the Agency for Cultural Affairs. In accordance with the "Guidelines for the Preservation and Utilization of Important Cultural Properties" established by the Agency for Cultural Affairs, a preservation plan for the Shiraiwa Sabo Dam was established and is currently in operation.

Some of the key details of this plan are described below.

(1) Fundamental policies

The fundamental policies for conservation and management of the Shiraiwa Sabo Dam are:

a) Maintain disaster prevention functions
b) Avoid modifications where possible
c) Classify the structures and materials
d) Accelerate and simplify response measures

(2) Policy for conservation.

The Agency of Cultural Affairs' "Guidelines for the Preservation and Utilization of Important Cultural Properties" requires the establishment of "parts" and "positions" for the target facilities, and the formation of conservation policies.

The Shiraiwa Sabo Dam is a complex structure including the main dam, seven counter dams, a retention frame, and a retaining wall.

The Important Cultural Property designation includes the main dam, counter dams nos. 1 and 2, and the retention frame.

In the Shiraiwa Sabo Dam conservation and management plan, the main structures were classified as "parts" (**Tables 5** and **6**).

Each individual "position" is categorized according to the construction materials used. To preserve the value of Important Cultural Properties, the Tateyama Mountain Area Sabo Office has established four standards for the preservation of material characteristics such as shape, finish, and color, and has applied these standards to each "position" (**Fig. 12, Table 7**).

Table 5 Parts and component of the Shiraiwa Sabo Dam

Part	Component
Main dam	Overflow section of the main dam
	Non-overflow section of the main dam
	Revetment nos. 1–4
	Training walls nos. 1 and 2

Table 6 Parts and component of the Shiraiwa Sabo Dam

Part	Component
Counter dam no.1	Counter dam no.1
	Training levee no.3
Counter dam no.2	Counter dam no.2
Retention frame	Retention frame
	Retaining wall

Table 7 Policy for the conservation of each "position" of the Shiraiwa Sabo Dam

	Policy for conservation of each position		Example of the corresponding position
	If the facility is damaged or deteriorated, repairs must be made using materials that are the same or almost the same as the original materials. Repairs must be carried out in a manner that does not degrade the cultural value of the facility.		
Part to be conserved Part composed of "positions" corresponding to standards 1–2	**Standard 1**	**Positions that must be repaired using materials having the same shape, finish, and color as the originals.** The repair is made using the original material. If this is not possible, the repair is made using a material with the same shape, finish, and color.	Stone materials Retention frame (reinforced concrete bar)
	Standard 2	**Positions that must be repaired using materials having the same shape and color as the originals.** The repair is made using the original material. If this is not possible, the repair is made using a material with a similar shape and color.	Rubble concrete
	Standard 3	**Positions that must be repaired with due consideration for of compatibility with the surrounding design.** Repairs should be made with consideration to the surrounding design, when changes are required to maintain or reinforce the facilities.	Raised position of the dam
Other parts	**Standard 4**	Except for countermeasures for the repair and prevention of damage during a disaster, will be left in its current state.	Side wall of diversion channel no. 2 Masonry retaining wall of diversion channel no. 2

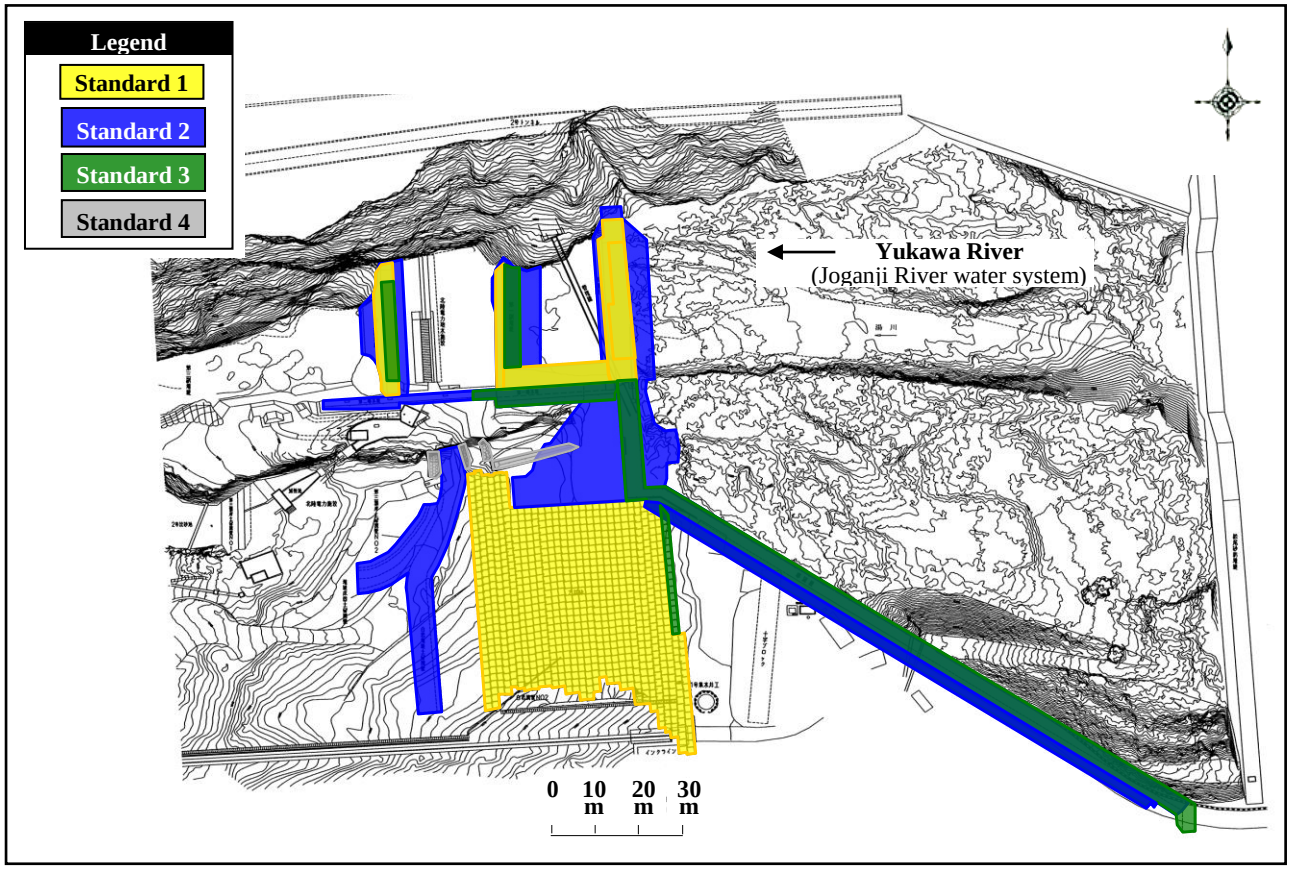

Fig. 12 Extent of the Important Cultural Property designation and standards for the conservation of each "position" of the Shiraiwa Sabo Dam

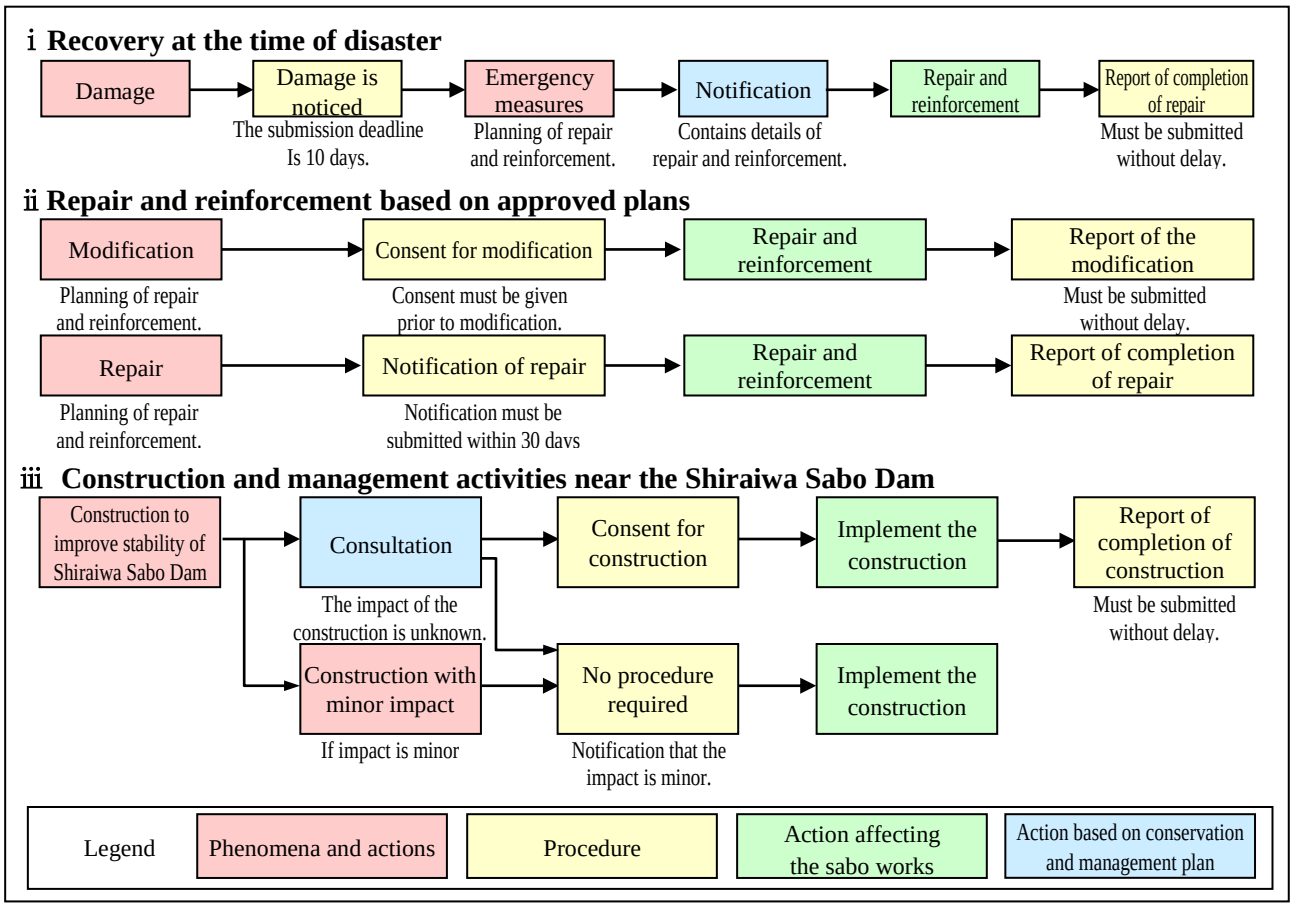

Fig. 13 Basic process flow diagram

(3) Preservation of the value of Important Cultural Properties and maintenance of disaster prevention functions

In general, when an important cultural property is damaged and subsequently repaired or reinforced, it is necessary to confer with the Agency of Cultural Affairs, and the repair often takes a significant amount of time.

However, the Shiraiwa Sabo Dam is a disaster prevention facility, so repairs and reinforcement must be carried out quickly to protect the Joganji River basin from sediment-related disasters.

Therefore, the Tateyama Mountain Area Sabo Office has already convened with the Agency for Cultural affairs regarding how to make repairs to the Shiraiwa Sabo Dam, and how best to cooperate with related organizations (**Fig. 13**).

7. Examples of utilization of sabo facilities at the Tateyama Mountain Area Sabo Office

7.1 Education

The Tateyama Mountain Area Sabo Office utilizes the sabo facility and its surrounding area to provide education about the sabo works, and to improve regional disaster prevention abilities.

Since sabo facility construction/operation is still ongoing in the Tateyama Caldera, entrance to the general public is restricted. However, the Sabo works are used as an “experiential learning” facility, operated by the administrative inspection team and the Toyama Prefectural Caldera Sabo Museum (see **Fig. 14** and **15**).

The Tateyama Mountain Area Sabo Office also dispatches lecturers to provide extracurricular lessons about the sabo works.

Fig. 14 Experiential learning at the observation deck above the Rokkyu-Dani valley

Fig. 15 Experiential learning at the ruins of the Tateyama Hot Springs

Table 8 Number of participants in dam activities by year.

Year	Government inspection	Experience & study tours	Extracurricular lessons
2013	625	716	0
2014	751	1,043	0
2015	761	914	41
2016	538	904	83
2017	539	640	378

7.2 Utilization of the facility as a regional revitalization resource

Historical sabo facilities are valuable assets that contribute to regional revitalization. It is important to appropriately evaluate and preserve these facilities, and to make appropriate use of the facilities and surrounding areas.

The Tateyama Mountain Area Sabo Office preserves the historical cultural values of Sabo facilities. The area around the Hongu sabo Dam is being developed by the Joganji River Waterfront School project (**Fig. 16**), and there is also a Joganji River Waterfront School Liaison Council.

Through these initiatives, the local community is considering measures to revitalize the region.

Fig. 16 Hongu Sabo dam maintenance bridge

8. Conclusion

Sabo facilities were constructed using the materials, designs, and construction methods available at the time. These ingenious facilities were designed to protect people from sediment-related disasters in an era where modern materials and mechanized equipment did not exist. These facilities are valuable treasures that must be preserved.

It is hoped that this report on the Shiraiwa Sabo Dam will help guide the maintenance and management of other Sabo facilities designated as Important Cultural Properties.

REFERENCES

Ministry of Land, Infrastructure, Transport and Tourism Water Management and National Land Conservation Bureau, Erosion and Sediment Control Department (2014): Planning Manual for Maintaining and Prolonging the Lifespan of SABO Facilities, pp. Ⅰ-1–Ⅱ-24.

Ministry of Land, Infrastructure, Transport and Tourism Water Management and National Land Conservation Bureau, Erosion and Sediment Control Department (2014): Inspection Procedure Manual for SABO Facilities, pp. 1-56.

Ministry of Land, Infrastructure, Transport and Tourism Hokuriku Regional Development Bureau, Tateyama Mountain Area Sabo Office (2015): Plan of the maintaining and prolonging lifespan of Sabo facilities in Tateyama Mountain Area Sabo Office.

Agency for Cultural Affairs (1999): Guidelines for the Preservation and Utilization of Important Cultural Properties (structures), pp. 1-24.

Ministry of Land, Infrastructure, Transport and Tourism Hokuriku Regional Development Bureau, Tateyama Mountain Area Sabo Office(2013): Preservation plan of Important Cultural Property Shiraiwa Sabo Dam, pp. 5-68.

Watanabe, H. and Toshio, M. (2016): Actions for the Maintenance and Lifespan Prolongation of SABO Facilities, INTERPRAEVENT 2016, pp. 862-870.

Watanabe, H. et al. (2016): Maintenance of Historical Sabo Facilities in Tateyama Sabo Mountain Area Sabo Office, Japan Society of Erosion Control Engineering Publication No.78, http://www.jsece.or.jp/event/conf/abstruct/2016/pdf/T1-01.pdf

Engineering Assessment of Aging Degradation for Small Sediment Control Structures

Sangjun IM,[1,*] Won CHOI[2] and Song EU[1]

[1] Department of Forest Sciences, Seoul National University, Korea
[2] Department of Landscape Architecture & Rural System Engineering, Seoul National University, Korea
*Corresponding author. E-mail: junie@snu.ac.kr

Landslides and associated debris flow are major natural disasters in Korea. Sediment-related disaster prevention structures, such as erosion control dam (ECD) and check dam, have been practically implemented on forested watersheds to control landslide hazards. After construction, engineering strength of ECDs could be lost partly or completely due to aging degradation. Thus, long-term scale, weaker force than design strength can induce loss of designed function or failure of structure exceptionally. In this study, a numerical approach was applied for performance evaluation to aging concrete ECDs. With finite element technique considering static and dynamic loads, simplified ECD and debris flow as dynamic load were simulated. Age degradation curve of concrete strength was derived from previous studies. Because this research is in progress, numerical analysis will be conducted with results of this paper, and the effect of earthquake will be also considered in future works. This study provides with engineering techniques for an accurate structural performance assessment of landslide disaster mitigation/prevention structures.

Key words: aging degradation, erosion control dam, performance capacity, reliability analysis, finite element method

1. INTRODUCTION

Landslides and associated debris flow are major drivers of natural disasters in Korea, and these disasters seem to occur more frequently due to climate changes [*Kim et al*., 2014; *Jeong et al*., 2015]. To prevent damages from those hazardous events, sediment retention structures, such as erosion control dam and check dam, have been implemented for steep torrents on forested watersheds [*Suda et al*., 2009; *Scheidl et al*., 2013].

In Korea, more than 10,000 erosion control dams (ECDs) have installed to date since ECD project has first employed in 1985 [*Song*, 2013]. There ECDs are structurally small, with typically 5~7 m height and 30~50 m width, and are usually receiving sediment mixture from small forest watersheds (< 300 ha). Although these structures could be varied in construction material and structure type, majority of ECD in Korea is a concrete closed-type dam [*Song*, 2013].

As other field structures, time dependent deterioration of ECDs is random and irreversible phenomenon in nature. Although ECD materials are inherently durable, engineering strength of dam could be lost partly or completely due to aging degradation [*Ellingwood and Tekie*, 2001]. Aging degradation can slowly and progressively change the engineering characteristics of materials over a period [*Mori and Ellingwood*, 1993; *Burman et al*., 2009]. In cases of submerged concrete structures like ECD, water induced aging processes, which include freezing and thawing, leaching, cracking due to temperature variation, corrosion of concrete structures, and cement debonding, are the main sources of aging deterioration [*Kuhl et al*., 2004; *Burman et al*., 2009].

Age-related degradation can lead to changes in structural performance and resistance capacity of ECDs [*Kuhl et al*., 2004; *Burman et al*., 2009]. These degraded structures are more vulnerable to unexpected extreme events, such as earthquake or debris flow. Thus, when structural stability of ECD is examined in landslide or earthquake hazard zone, age degradation on structure strength should be considered.

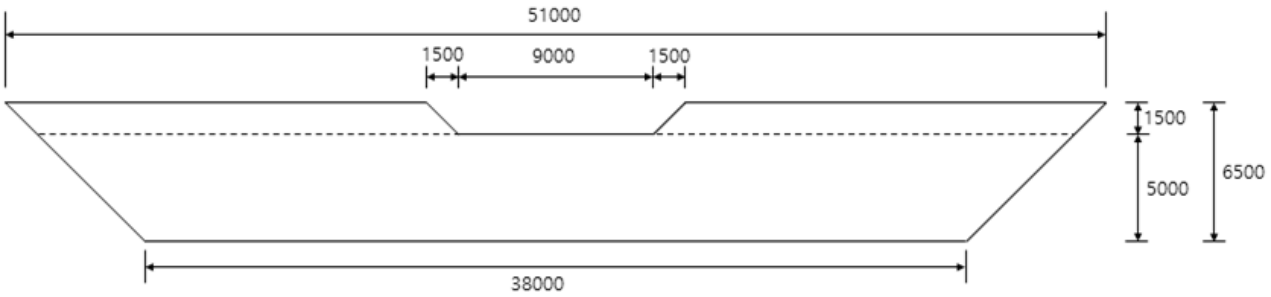

Fig. 1 Dimension of modeled erosion control dam from front-view (unit: millimeter).

In this study, a numerical approach is applied for performance evaluation to aging concrete ECDs. To assess the resistance with static and dynamic loads, such as debris flow impact force and earthquake, numerical analysis of aged ECDs has been done using the finite element method coupling with aging degradation function.

2. METHODOLOGY

2.1 Dam structure modeling

We chose a test dam that constructed at 2012 in the Hyungchon watershed in Seoul, Korea. This young ECD was installed as part of restoration project of debris flow disaster in 2011. [*Jeong et al*., 2015]. **Fig. 1, 2** are the schematic design of front-view and side-view of modeled ECD, respectively, and the dimension of the dam is summarized in **Table 1**. When the structure dimension was drawn from ECD in the Hyungchon watershed, we simplified the dam structure by omitting some components, such as drainage hole and fishway, for convenience of numerical analysis of desired structure.

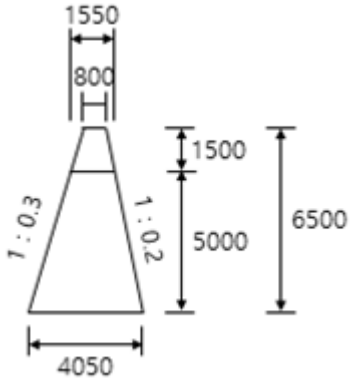

Fig. 2 Dimension of modeled erosion control dam from side -view (unit: millimeter).

Table 1 Summary of dimension of front and side-view of modeled ECD.

View of section	Elements	Size [m]
Front-view	Length at top of dam	51
	Length at base of dam	38
	Height to crest	5
	Total height	6.5
	Spillway width	9
Side-view	Base width	4.05
	Width at the crest	1.55
	Top width	0.8
	Slope of upstream face	1:0.2
	Slope of downstream face	1:0.3

2.2 Debris flow impact force modeling

When an ECD is constructed, strength of structure against destruction and resistance against momentum is evaluated by several engineering methods. However, in many cases of ECD in Korea, only static pressure induced by water and deposited sediment have been considered to calculate the structural stability, regardless unexpected dynamic force, i.e. seismic wave or debris flow. The design process of the modeled dam was also considered only static pressure although it aimed to endure debris flow hazard. Therefore, to analyze behavior of structure under dynamic force condition, we simulated debris flow impact force derived from debris flow events on the Hyungchon watershed in 2011.

2.2.1 Debris flow simulation

To simulate debris flow behavior, we employed debris flow simulator "Kanako 2D" [*Nakatani et al*., 2008]. Kanako 2D is a GUI-equipped simulator that has the combined model of 1D-channel flow and 2D-deposition in alluvial fan. To simulate debris flow event, several conditions should be assumed as follows. First, stream channel has no branch, and is a rectangular-shape open channel. Second, soil particles in debris flow have uniform in size, and evenly distributed in any part of flow. These

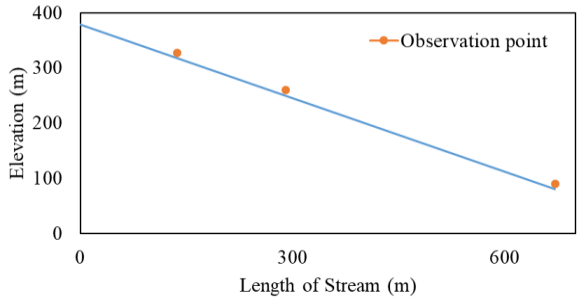

Fig. 3 Schematic design of stream channel input data for Kanako 2D.

assumptions does not exactly correspond to debris flow event in 2011. Despite this disagreement, we chose Kanako 2D and operated it due to convenience of handling input data.

We designed stream channel as shown in **Fig. 3**. According to *Jeong et al*., [2015], mean slope of the watershed was 24° and length of stream channel from top of stream to ECD was 671.32 m. In case of hydrograph for input data, simplified hydrograph (**Fig. 4**) was applied referring to rainfall data when debris flow at 2011 occurred [*Jeong et al*., 2015].

Other initial condition for Kanako 2D simulation, such as material properties, was derived from field examination of debris flow, which includes geological data, soil test, and survey of channel morphology [*Jeong et al*., 2015]. However, some parameters required for Kanako 2D was not directly obtained from field data, i.e. Manning's coefficient. In those cases, we applied commonly used value. Initial input data for Kanako 2D, including time scale of simulation and material properties, was summarized in **Table 2**.

2.2.2 Impact force modeling

Unfortunately, few debris flow simulators calculate impact force of debris flow directly. Thus, it is necessary to estimate impact force from the flow behavior of debris flow. Many researchers have been suggested various estimation methods with flume experiences or real time measurements [*Hungr et al*., 1984; *Hübl et al*., 2009; *Suda et al*., 2009; *Scheidl et al*., 2013]. Although some equations have been suggested based on hydrostatic model or hydrodynamic model [*Armanini*, 1997; *Scheidl et al*., 2013; *Koo et al*., 2017], *Proske et al*. [2011] pointed out that those models show reliable estimation under only limited Froude number. On the other hand, hybrid model suggested by *Hübl et al*. [2009] and *Suda et al*. [2009] estimated impact force regardless of range of Froude number. Thus, we estimated debris flow impact force using a hybrid model as shown as Eq (1).

$$p_{max} = 4.5\rho v^{0.8}(gh)^{0.6} \qquad (1)$$

Table 2 Summary of values used in simulations.

Parameter/variables [unit]	Value
Stream channel length [m]	671.32
Mean slope of channel [degree]	24
Simulation continuance time [sec]	600
Time interval of calculation [sec]	0.01
Diameter of material [m]	0.005
Mass density of bed material [kg m^{-3}]	2665
Mass density of fluid phase [kg m^{-3}]	1000
Internal friction angle [°]	29.3
Concentration of movable bed	0.606
Coefficient of erosion rate	0.0007
Coefficient of accumulation rate	0.05
Manning's roughness coefficient	0.03
Interval of calculation point in 1D [m]	15.26

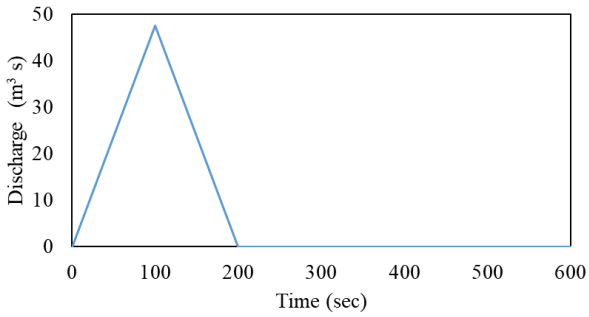

Fig. 4 Simplified hydrograph for initial input data of Kanako 2D

where p_{max} is maximum impact force per unit area [N m^{-2}], ρ is density of debris flow [kg m^{-3}], v is flow velocity [m s^{-1}], g is gravitational acceleration [9.807 m s^{-2}], and h is flow depth [m]. Impact force calculated by Eq (1) is maximum value acting on the base part of ECD near by channel bed. To analyze behavior of structure against impact force accurately, force distribution on dam surface should be considered. *Suda et al*. [2009] considered the distribution of impact force based on results of HüBl and *Holzinger* [2003]. According to *Suda et al*. [2009], distribution of impact force is different whether type of debris flow is granular flow or mudflow. In case of debris flow in the Hyungchon watershed in 2011, it seems to be similar to mudflow type from *Suda et al*. [2009]. Therefore, we used mudflow-type impact force distribution (**Fig. 5**) on numerical analysis.

2.3 Age degradation modeling

Age-related degradation of structural materials is a complicated process. Various approaches have been conducted to quantitatively examine the

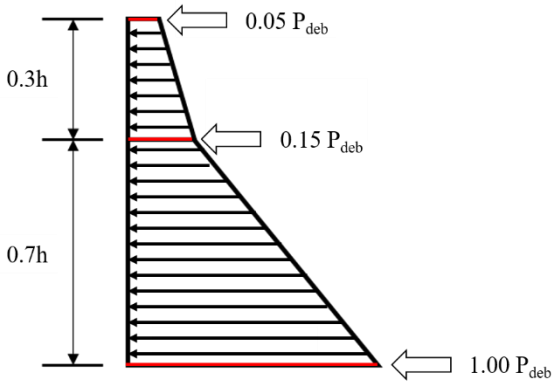

Fig. 5 Debris flow impact force distribution (mudflow type). h means height of dam surface and p_{max} is maximum impact force per unit calculated from hybrid model from *Suda et al.* [2009].

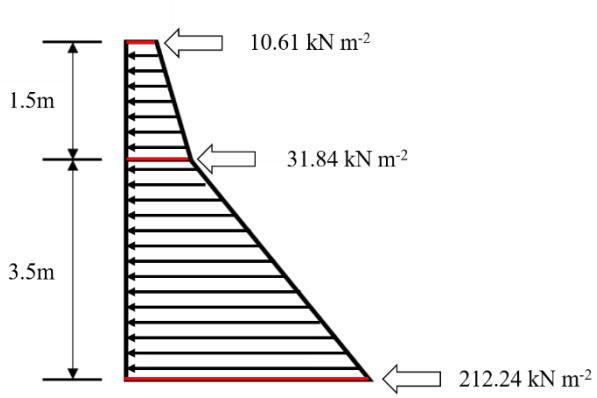

Fig. 6 Simulated impact force distribution on modeled dam surface suggested by *Suda et al.* [2009].

Table 3 Summary of debris flow simulation.

Variables [unit]	Value
Time at maximum velocity and depth [sec]	126
Maximum flow velocity [m s^{-1}]	14.50
Maximum flow depth [m]	0.60

engineering performance for aging concrete structures to avoid catastrophic consequences due to failure of engineering structures [*Mori and Ellingwood*, 1993; *Shinozuka et al*., 2000; *Tekie and Ellingwood*, 2003; *Gogoi and Maity*, 2007; *Burman et al*., 2009]. Time-based reliability analysis was traditionally utilized to evaluate resistance decrease over time [*Mori and Ellingwood*, 1993]. Symptom-based reliability was also employed to predict the safety and performance for existing structural components in future condition [*Gogoi and Maity*, 2007; *Burman et al*., 2009]. Other studies have quantified the degradation effects on stability with fragility curve (or conditional probability of failure) [*Shinozuka et al*., 2000; *Tekie and Ellingwood*, 2003]. Since some parameters in models suggested by those techniques cannot be calculated using visual inspection or non-destructive tests, these methods are hard to apply on field structures that is still functioning.

In this study, time-dependent compressive strength degradation model for concrete material was derived from previous studies [*Koo et al*., 1994; *Kim et al*., 2000; *Song et al*., 2010; *Park et al*., 2013]. It is obvious that the age-related degradation pattern of ECDs is considerably different with general concrete structure/building. ECDs are exposed in natural condition, and many cases of ECDs have reservoir in there upstream side inducing aging process under submerged condition. As *Park et al*. [2013] is the only research that measured compressive strength of ECD in situ until now, there are not enough strength data of ECD for developing time-dependent degradation model. Considering this limitation, we used both general structure [*Koo et al*., 1994; *Kim et al*., 2000; *Song et al*., 2010] and ECD data [*Park et al*., 2013] to produce in this study the age degradation model. Curve fitting analysis was conducted using curve fitting tool package in MATLAB R2017b.

3. RESULTS AND FURTURE WORKS

3.1 Debris flow impact force estimation

Table 3 is summary of debris flow simulation with Kanako 2D. Maximum value of flow velocity and flow depth was 14.50 m s^{-1} and 0.60 m, respectively, and it was occurred at same time. Maximum impact force per unit area was estimated as 212.24 kN m^{-2} from Eq (1). Based on estimated impact force, distribution of impact force for numerical analysis was derived from *Suda et al*. [2009] suggestion (**Fig. 6**).

3.2 Age-dependent strength degradation model

Using least square error method, we made the aging deterioration of concrete strength model (**Fig. 7**). As mentioned above, we made this model using previous results including cases of general structures due to lack of ECD data, but there are different environmental background between them. ECDs studied by *Park et al*. [2013] are constructed in forest watersheds. Most of them have dry reservoir with sediments deposition. Meanwhile, general structures [*Koo et al*., 1994; *Kim et al*., 2000; *Song et al*., 2010] including various type of structures, such as building or bridge, are usually installed in urban area.

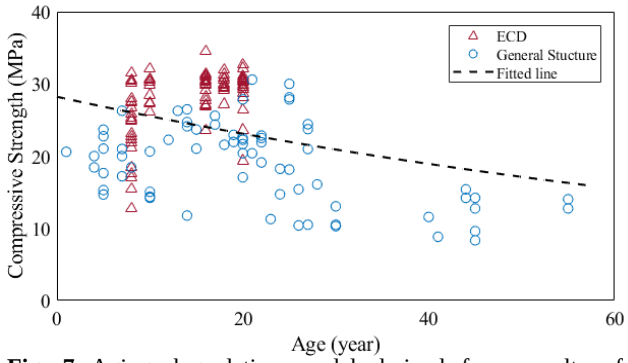

Fig. 7 Aging degradation model derived from results of previous studies [*Koo et al.*, 1994; *Kim et al.*, 2000; *Song et al.*, 2010; *Park et al.*, 2013]. Red triangle means data from ECD measurements [*Park et al.*, 2013]; blue square means general structure researches [*Koo et al.*, 1994; *Kim et al.*, 2000; *Song et al.*, 2010].

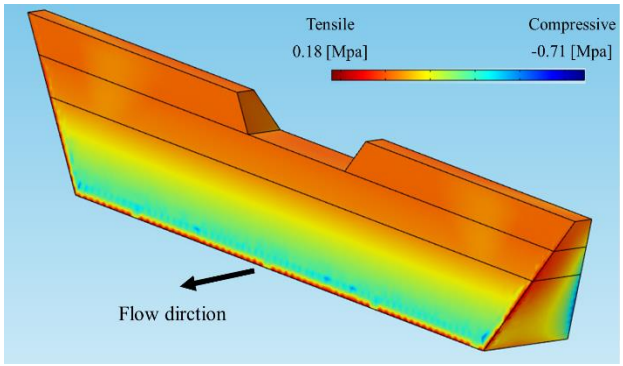

Fig. 8 The result of numerical analysis of ECD under debris flow impact force. Blue color means compressive stress, and red color represents tensile stress.

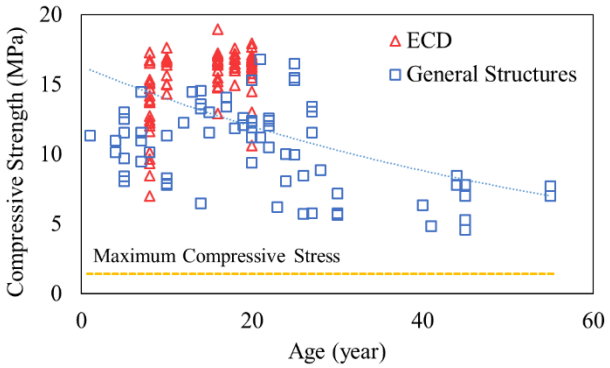

Fig. 9 The result of comparison between compressive strength regarding strength reduction factor (0.55) and maximum compressive stress multiplied by safety factor (2.0). In addition to same symbol to **Fig. 7**, yellow dash line means maximum compressive stress.

As shown in **Fig. 7**, compressive strength of ECD, represented as red triangle, seems to be higher than that of general structures, and ECD strength changed little as becoming older. However, this tendency cannot be explain clearly because of several reasons. First, all of cited previous researches [*Koo et al.*, 1994; *Kim et al.*, 2000; *Song et al.*, 2010; *Park et al.*, 2013] did not mentioned specific location or long-time environmental condition of concrete structures. Thus, it is hard to compare those structures on same conditions. Second, due to sampling methods of *Park et al.* [2013], it is hard to conclude that strength pattern of ECDs can be generalized. According to *Park et al.* [2013], ECD samples were selected by their appearance regardless random sampling. However, as mentioned by *Park et al.* [2013], some ECDs that were regarded as poor condition had enough strength despite their surface damage.

Considering those limitations, we cannot derive different aging degradation model from each groups, Thus, in this study, we made aging degradation model regardless the difference of strength tendency between ECDs and general structures. This model composed of an exponential equation, as shown as Eq (2),

$$Fc = 28.22e^{-0.01t} \qquad (2)$$

where Fc is compressive strength of concrete [MPa], and t means age of ECD [year]. As Statistical parameters, SSE, R^2, and RMSE of this model were 5,924, 0.1426, and 6.202, respectively.

3.3 Numerical analysis of ECD under debris flow impact force

With distribution of impact force and modeled ECD, numerical analysis of ECD was conducted. We conducted Finite Element Analysis (FEA) using COMSOL Multiphysics. Before numerical analysis, we applied several factors based on structure design guideline of Korea. As results, we multiplied safety factor, set up as 2.0, by debris flow impact force. As strength reduction factor, which is regarded as uncertainty of the structure stability, we applied 0.55 that standard factor for structure under compressive strength.

As a result, **Fig. 8** represents the response of ECD structure under designed impact force condition. Blue colored area with negative pressure value shows structural elements under compressive stress, while red colored elements with positive value are under tensile stress. Maximum compressive stress due to impact force was calculated as 0.71 MPa. Considering the safety factor (2.0), we used 1.42 MPa as maximum compressive stress, and we compared this stress to time dependent strength model. However, we cannot estimate the effect of age degradation directly. Due

to lack of data of aging effects on dynamic parameters of concrete, such as elastic modulus, we assumed that those parameters are constant during aging process. This means that maximum stress by impact force is constant during its life cycle. Thus, to consider the effect of aging of ECD, we need to compare maximum stress to compressive stress considering safety factor and strength reduction factor in structure design guideline.

Fig. 9 shows the results of comparison between compressive strength and stress regarding structure guideline. When we consider only debris flow impact force as force, modeled ECD in this study can bear impact force regardless aging deterioration. Thus, ECD constructed in the Hyungchong watershed is considered to be able to endure debris flow event without the loss of its function during its whole life. However, this result was obtained under the condition when debris flow impact force is only applied force. Especially, in upstream side of ECD, dead loads, such as water pressure and earth pressure due to sediment deposition, is continuously changed during its life cycle. Thus, in respect of managements, resistant capacity of ECD should be evaluated regarding not only age-dependent deterioration, but also continuous water and sediment change during life cycle of ECD.

3.4 Future works

In this study, we selected and simplified an ECD as object of analysis, and a simple model of concrete strength change over time was developed. Considering the strength reduction following to the aging process using our model, the response of ECD under debris flow disaster simulated using Kanako 2D was analyzed with Finite Element Method (FEM) conducted by COMSOL Multiphysics.

In terms of force applied in numerical analysis, both static and dynamic forces will be input. Although static pressure was already considered in design step of original dam, stability analysis at the time of design cannot ensure long-term stability regarding strength decrease on time. Thus, we will analyze the effect of static pressure under the condition that strength of dam degraded. Moreover, considering recently increased earthquake risk, seismic response of aged ECD will be also analyzed. Some researchers examined the effect of earthquake to structure using computer programs, such as SHAKE91 [*Tekie and Ellingwood*, 2003] or QUAKE/W [*Castro et al*., 1992].

4. SUMMARY

Aging is a natural phenomenon that leads to change in engineering strength with life cycle. This deterioration can reduce the resistance capacity of structure materials and give rise to serious problem of ECDs.

In this study, to examine aging degradation effects of concrete structures using finite element method, we targeted an ECD as the subject of study. Debris flow impact force was calculated and then input as dynamic load on modeled structure. Strength degradation over time was quantified according to previous study. As ongoing research, finite element analysis about the modeled ECD, which has decreased strength along time, will be conducted considering static load and dynamic load, such as debris flow impact force and seismic wave.

Engineering performance monitoring and structural maintenance (such as inspection and repair) are essential to reduce the risk of structural failure, and enhance structural functionality over operational period. This study provides with engineering techniques to assess the structural performance of landslide disaster mitigation/ prevention structures accurately.

4. SUMMARY

Aging is a natural phenomenon that leads to change in engineering strength with life cycle. This deterioration can reduce the resistance capacity of structure materials and give rise to serious problem of ECDs.

ACKNOWLEDGMENT:
This study was carried out with the support of ´R&D Program for Forest Science Technology (Project No. 2017061B10-1819-AB01)´ provided by Korea Forest Service(Korea Forestry Promotion Institute).

REFERENCES

Armanini, A. (1997): On the dynamic impact of debris flows, Recent Developments on Debris Flows (eds A. Armanini and M. Michiue). Springer Berlin Heidelberg, pp. 208-226.

Burman, A., Maity, D., Sreedeep, S., and Gogoi, I. (2009): The behavior of aged concrete gravity dam under the effect of isotropic degradation caused by hygro-chemo-mechanical actions, Int. J. Eng. Stud., Vol. 2, pp. 105-122.

Castro, G., Seed, R. B., Keller, T. O., and Seed, H. B. (1992): Steady-state strength analysis of lower San Fernando Dam slide, Journal of Geotechnical Engineering, Vol. 118, No. 3, pp. 406-427.

Ellingwood, B., and Tekie, P. B. (2001): Fragility analysis of concrete gravity dams, Journal of infrastructure systems, Vol. 7, No. 2, pp. 41-48.

Gogoi, I., and Maity, D. (2007): Influence of sediment layers on dynamic behavior of aged concrete dams, Journal of

engineering mechanics, Vol. 133, No. 4, pp. 400-413.

HüBl, J., and Holzinger, G. (2003): Development of design basis for crest open structures for debris flow management in torrents: miniaturized tests for the efficiency estimation of debris flow breakers. WLS Report, Vol. 50. (in German)

Hübl, J., Suda, J., Proske, D., Kaitna, R., and Scheidl, C. (2009): Debris flow impact estimation, The proceedings of the 11th International Symposium on Water Management and Hydraulic Engineering, pp. 137-148.

Hungr, O., Morgan, G., and Kellerhals, R. (1984): Quantitative analysis of debris torrent hazards for design of remedial measures, Canadian Geotechnical Journal, Vol. 21, No. 4, pp. 663-677.

Jeong, S., Kim, Y., Lee, J. K., and Kim, J. (2015): The 27 July 2011 debris flows at Umyeonsan, Seoul, Korea, Landslides, Vol. 12, No. 4, pp. 799-813.

Koo, R., Kwan, J. S., Ng, C. W. W., Lam, C., Choi, C., Song, D., and Pun, W. (2017): Velocity attenuation of debris flows and a new momentum-based load model for rigid barriers, Landslides, Vol. 14, No. 2, pp. 617-629.

Kuhl, D., Bangert, F., and Meschke, G. (2004): Coupled chemo-mechanical deterioration of cementitious materials Part I: Modeling, International Journal of Solids and Structures, Vol. 41, No. 1, pp. 15-40.

Mori, Y., and Ellingwood, B. R. (1993): Reliability-based service-life assessment of aging concrete structures, Journal of Structural Engineering, Vol. 119m No. 5, pp. 1600-1621.

Nakatani, K., Wada, T., Satofuka, Y., and Mizuyama, T. (2008): Development of “Kanako 2D (Ver. 2.00),” a user-friendly one-and two-dimensional debris flow simulator equipped with a graphical user interface, International Journal of Erosion Control Engineering, Vol. 1, No. 2, pp. 62-72.

Proske, D., Suda, J., and Hübl, J. (2011): Debris flow impact estimation for breakers, Georisk, Vol. 5, No. 2, pp. 143-155.

Scheidl, C., Chiari, M., Kaitna, R., Mullegger, M., Krawtschuk, A., Zimmermann, T., and Proske, D. (2013): Analysing Debris-Flow Impact Models, Based on a Small Scale Modelling Approach, Surveys in Geophysics, Vol. 34, No. 1, pp. 121-140.

Shinozuka, M., Feng, M. Q., Lee, J., and Naganuma, T. (2000): Statistical analysis of fragility curves, Journal of engineering mechanics, Vol. 26, No. 12, pp. 1224-1231.

Song, B. (2013): Domestic current situation for Forest disaster prevention program, Geoenvironmental engineering, Vol. 14, No. 1, pp. 27-34.

Suda, J., Strauss, A., Rudolf-Miklau, F., and Hübl, J. (2009): Safety assessment of barrier structures, Structure and Infrastructure Engineering, Vol. 5, No. 4, pp. 311-324.

Tekie, P. B., and Ellingwood, B. R. (2003): Seismic fragility assessment of concrete gravity dams, Earthquake engineering and structural dynamics, Vol. 32, No. 14, pp. 2221-2240.

Koo, B. K., Oh, B. H., Kim, Y. E., Kim, T. B., and Han, S. H. (1994): Estimation of Compressive Strength for Existing Concrete Structures by Non-Destructive Tests, Magazine of the Korea Concrete Institute, Vol. 6, No. 6, pp. 159-172. (in Korean)

Kim, M.-h., Song, B.-C., Ko, J.-S., Jung, S.-C., Kwon, Y.-J., Kim, G.-Y., and Kang, S.-P. (2000): A Study on the Evaluation of Deterioration Degree for Reinforced Concrete Apartments in Korea, Journal of the architectural institute of Korea: Structure and construction, Vol. 16, No. 6, pp. 89-95. (in Korean)

Park, K.-H., Kim, M.-S., Joh, S.-H., Lee, C.-W., Youn, H.-j., and Kim, K.-h. (2013): Study on the Stability Evaluation of Concrete Erosion Control Dam by using Non-destructive Test for Compressive Strength, Journal of Korean Forest Society, Vol. 102, No. 1, pp. 90-96. (in Korean)

Song, J.-U., Park, H., and Kim, S.-K. (2010): A Study on the Physical Property and Damage Index of Decrepit Concrete Materials, Explosives and blasting, Vol. 28, No. 2, pp. 59-68. (in Korean)

Effects of Landslide and Forest Fire on Rainfall Threshold to Induce Bedload Discharge in Watershed in Republic of Korea

Junpyo SEO[1,2], Kihwan LEE [2], Changwoo LEE[1*], Dongyeob KIM[1], Choongshik WOO[1], Heonho LEE[2], Taro UCHIDA[3] and Wataru SAKURAI[3]

[1] Division of Forest Disaster Management, National Institute of Forest Science
(57 Hoegi-ro, Dongdaemun-gu, Seoul 02455, Republid of Korea)
[2] Department of Forest Resources, Yeungnam University
(280 Daehak-Ro, Gyeongsan, Gyeongbuk 38541, Republic of Korea)
[3] Sabo Department, National Institute for Land and Infrastructure Management
(Asahi 1, Tsukuba, Ibaraki 305-0804, Japan)
*Corresponding author. E-mail: leecwfr@korea.kr

In Korea, there are six sites that are using hydrophone (Japanese pipe microphone) developed in Japan. In this study, the rainfall threshold for the occurrence of bedload events was analyzed in forest disaster sites and control site. As a result, the total rainfall amount and the peak rainfall intensity among the rainfall characteristics were analyzed to be the best representations of bedload events. The difference between the bedload events and the rainfall threshold was clear in control site (normal forest), landslide site and forest fire site. In the control site, the rainfall threshold of bedload events was high, while the rainfall threshold of bedload events was low in the landslide and the forest fire site. In the forest fire site, the rainfall threshold of the bedload events was found to be higher after three years of forest fire damage. Therefore, an urgent soil erosion control work seems to be required to prevent the second damages in damaged forests.

Key words: bedload event, bedload monitoring system, forest disaster, hydrophone, rainfall threshold

1. INTRODUCTION

Recently, disaster management is important because natural disasters frequently occur due to global climate change, and disaster types have increased [*O'Brien et al.*, 2006]. Korea has four distinct seasons as it is located in the mid-latitude of the Northern Hemisphere and has cool-temperate climate. Also, it's dry and strong wind blows in spring and fall while most of rainfalls in summer because of the East Asian monsoon and continental climate. Though annual average rainfall is 1,200 mm or more, more than 60% falls in from June to September.

Such unique pattern causes two major forest disasters in Korea; landslide and forest fire. Forest fires do significant damage in spring. Over the past five years, on annual average, 486 forest fire cases occurred, damaging 593 hectare of forests on annual average. In 2017, there reported 692 cases, damaging 1,479 hectare of forests. The high temperature of forest fire changes the physical and chemical properties of the soil, and the plant was lost.

Therefore, soil erosion easily occurs due to the exposure of the hillslope, and the probability of occurrence of landslide and debris flow increased [*Lee et al.*, 2004; *Shin et al.*, 2013]. Also, the annual average of landslide-damaged areas keeps growing: it was 231 hectares in the 1980s, 349 hectares in the 90s, and 713 hectares in the 2000s [*KFS*, 2013].

In the case of Korea, various erosion control works have been carried out to rehabilitate forest disasters such as landslide and forest fire. Cases in point are constructing structures (like sabo dam), and planting vegetation. Related monitoring data such as the bedload discharge mechanism of the planning area are important for effective soil erosion work design and construction. Despite the fact that study on the bedload transport has continued for more than 100 years, there are still limitations in steep slopes such as mountain streams [*Tsutsumi and Laronne*, 2017]. Therefore, it is necessary to continue the study related to the bedload such as

bedload transport, bedload discharge, bedload event, etc.

There are two types of methods to monitoring bedload transport; direct and indirect. Direct measurments for bedload transport is relatively accurate, though it requires human resources, time and cost, whereas the indirect method uses some hydrological data for calculation of the amount of sediment, which is less accurate, but more efficient in terms of human resources, time and cost. Besides, there are various monitoring methods related to the discharge of bedload from the watershed [*Itakura et al.*, 2005; *Arattano and Marchi*, 2008]. In the past, direct methods were used such as bedload and suspended load samplers.

Then, in Japan and Europe, we developed a device that can calculate the bedload discharge amounts using pulse and sound pressure when the soil collision [*Mizuyama et al.*, 2010; *Rickenmann et al.*, 2017]. Japan has developed hydrophone (Japanese pipe microphone) using acoustic sensors. Since hydrophone continuously monitoring changes in bedload events in watershed, it has the advantage of accurately analyzing the time of the occurrence of the debris flow in flood [*Uchida et al.*, 2018]. In addition, it can be important data to understand not only the bedload discharge amount but also the changes in the runoff in watershed characteristics and the mechanism of bedload transport due to rainfall characteristics.

Hydrophone developed in Japan was first installed in Korea in 2013. Since it is not possible to install hydrophone monitoring devices throughout the country, it was necessary to select representative monitoring sites. There are two objectives of monitoring. The first object is the test of effects of forest disasters on bedload discharge. So, we installed the system at watershed damaged by forest fire and landslide, and watersheds covered by undamaged forest. Second objective is the test of role of bedrock geology on bedload discharge. So, the systems were installed at three typical rock type areas in Korea, including igneous, metamorphic and sedimentary rocks.

There are many factors that affect the bedload transport, but the most direct cause of bedload event in Korea is rainfall. Therefore, this study analyzed rainfall characteristics of bedload events in landslide site, forest fire site and control site as beginning level of bedload monitoring study using hydrophone. In addition, this study was carried out to investigate the effect of forest damage on the rainfall threshold of bedload events. The results of this study are expected to be used as basic data to prevent secondary damage such as forest disasters management in Korea.

Fig. 1 Site photos of the bedload monitoring sites (A: Control site, B: Landslide site, C: Forest fire site)

2. MATERIAL AND METHOD

2.1 Device for bedload monitoring

In Korea, a bedload monitoring system using acoustic sensors developed in Japan was introduced in 2013 [*Seo et al.*, 2017]. This equipment is called Japanese pipe geophone, Japanese acoustic pipe, Japanese pipe microphone, etc. However, recent study has called hydrophone or Japanese pipe microphone [*Uchida et al.*, 2018]. In addition to hydrophone, there are slot sampler, water - level gauges, current meters, rain gauges, turbidity meters and CCTV in the bedload monitoring systems (**Fig. 1**).

2.2 Method of bedload monitoring

The hydrophone was installed in the spillway of the sabo dam and was expressed by the colliding number and the sound pressure that occur when the particles hit the steel pipe.

The slot sampler can be weight using the load cell sensors. It is also used for hydrophone calibration. The operation's principle of the hydrophone device installed in Korea was considered to be general because there are many precedent studies such as *Mizuyama et al.* [2010; 2011].

2.3 Study sites

The purpose of this study is to investigate the characteristics of bedload events in Korea's representative forest disaster sites through bedload monitoring. We selected one site for each of the typical forest disaster like landslide and forest fire sites in Korea. And for comparison, one site of the

no disasters forest was selected as a control site (**Fig. 2**). **Table 1** shows the basic characteristics such as the watershed area of the study sites.

The bedload monitoring system was installed in the spillway of the sabo dam in downstream of each watershed.

2.4 Selection of effective data

In this study, the monitoring data for three sites were used for three years from 2014 to 2016, and data of missing such as machine defect were excluded from the analysis. Rainfall data were obtained from the tipping - bucket rain gauge at the downstream of each watershed (**Figs. 1**C and **2**). We thought rainfall measurements were appropriate because the watershed area was small and open terrain. In addition, rainfall more than 1 mm per hour was selected as effective data for the analysis of bedload events and rainfall characteristics, and the same rainfall event was considered when rainfall persisted.

We analyzed the characteristics of rainfall when bedload transport started. The starting point of bedload transport was regarded as the time when the change of the load-cell or hydrophone pulse (ch. 1024) started. This study applied the most sensitive channel because it is a study of rainfall thresholds at which bedload transport starts.

Table 1 A general situation of study sites

	Control site	Landslide site	Forest fire site
Monitoring started year	2014	2014	2014
Watershed area	142 ha	283 ha	25 ha
Country rock	Igneous rock	Igneous rock	Igneous rock
Forest physiognomy	Mixed Forest	Mixed Forest	Mixed Forest
Age class	6	5	4
Occurrence date	-	2012	Mar. 2013
Affected area	-	> 0.1 ha [a]	10 ha
Remarks	Non-damage	Small slope failure every year	Reforestation in Apr. 2014

[a] Recovery area at the time. So, it was estimated to be at least that much.

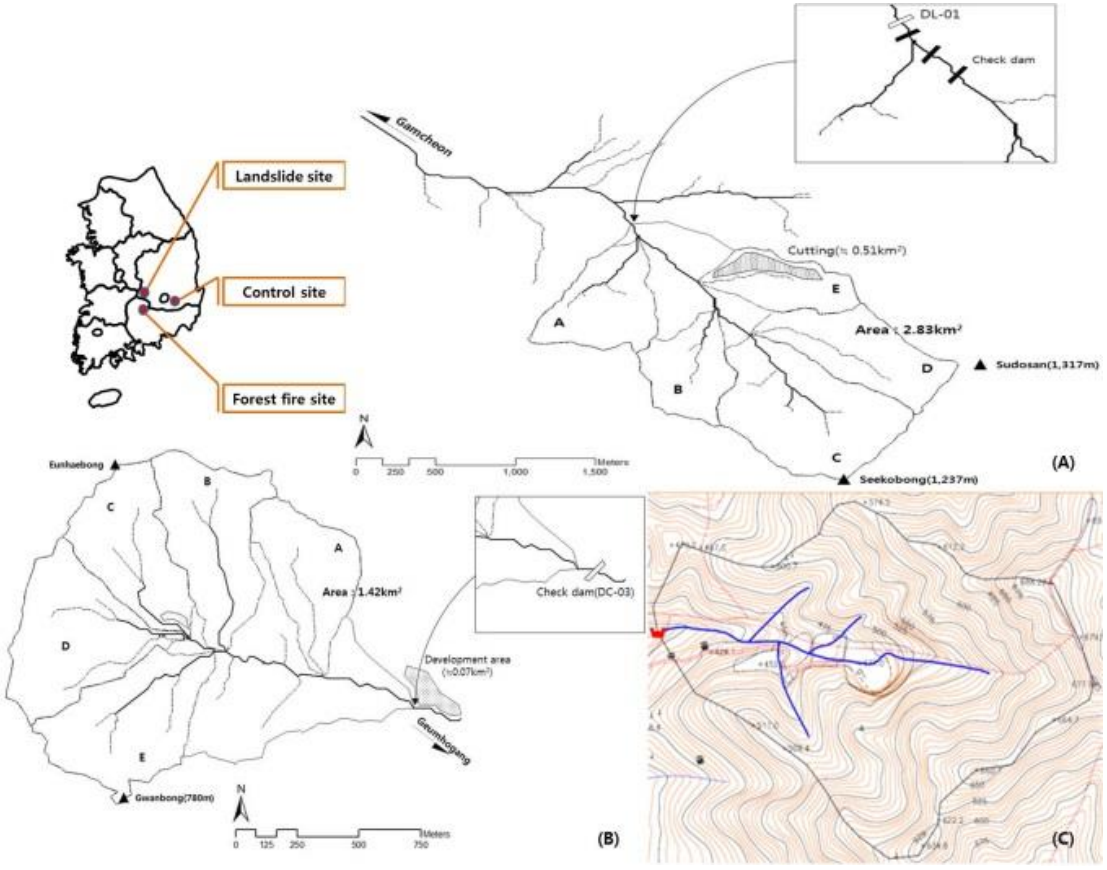

Fig. 2 Location of the study sites (A: landslide site, B: control site, C: forest fire site, Blue triangle: location of bedload monitoring system)

For the analysis, data from control site (Non-bedload events - 69, Bedload events - 19), landslide site (Non-bedload events - 41, Bedload events - 15), and forest fire site (Non-bedload events - 24, Bedload events - 31) were used.

Badoux et al. [2012] showed the rainfall threshold of bedload events (large, small) using rainfall intensity and rainfall duration. Similarly, in this study, the analysis showed that total rainfall amount and peak rainfall intensity were used to characterize rainfall condition to induced bedload discharge. So, for bedload events, we clarified the total rainfall amount and peak rainfall intensity until the start of bedload discharge. While, for non-bedload events, we used the total rainfall amount and peak rainfall intensity of given rainfall event.

3. RESULT AND DISCUSSION

3.1 Relation between bedload events and rainfall threshold

The total rainfall amount and peak rainfall intensity were plotted for bedload events and non-bedload events at the all sites. **Fig. 3** shows the relationship between total rainfall amount and peak rainfall intensity for the bedload events and non-bedload events in each study site. The difference rainfall threshold to induce bedload discharge between control site (no disaster forest), landslide site and forest fire site were clear. In all sites, when the rainfall condition was smaller than that of red line, most of events did not produce bedload events. In contrast, once rainfall magnitude exceeded red lines, most of events induced bedload discharge.

The rainfall threshold (red line) in the forest disaster sites (landslide, forest fire) was smaller than that of the control site. So, the rainfall threshold (red line) for control site in X and Y axes are 28 mm and 16 mm/hr, respectively. While, those in landslide site and forest fire site were 18 mm – 5 mm/hr and 5 mm – 4 mm/hr, respectively. The rainfall threshold in forest fire site was smaller than that of landslide site.

Although rainfall condition was the same, but the occurrence of sediment discharge was differed. For example, in **Fig. 3**, the orange line was also drawn under the same rainfall conditions at all three sites to clarify difference of occurrence of sediment discharge. In the control and landslide sites, even if the orange line was exceeded, there were both the bedload events and the non-bedload events. While, in the forest fire site, except for one rainfall condition, it was observed that the bedload events occurs when the orange line was exceeded.

These results indicate that the bedload started even in small rainfall condition in the forest disaster sites, suggesting that landslide and forest fire gave an impact on the rainfall threshold on bedload discharge. Moreover, the difference between landslide site and forest fire site indicates that effects of forest damage on rainfall threshold differed according to the types of damage and the affected area. Therefore, similar to previous studies by Johansen et al. [2001], Lee et al. [2004] and Seo et al. [2016], it can be thought that it is important that not only the prevention of direct damage caused by landslide and forest fire, but also the prevention of secondary damage such as soil erosion.

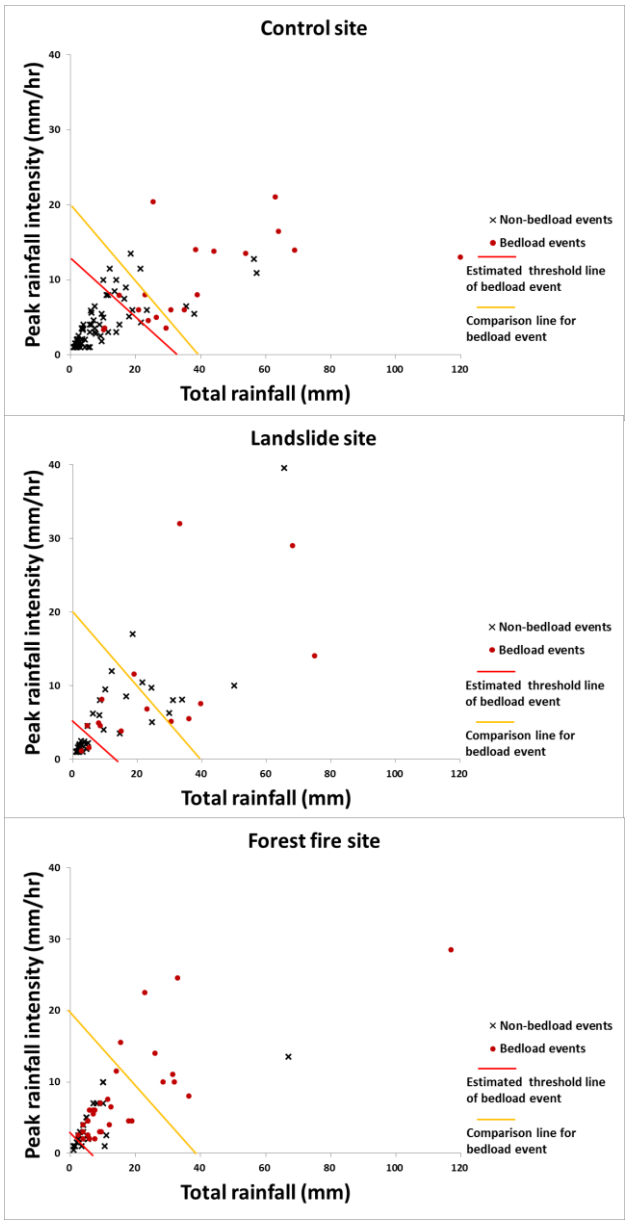

Fig. 3 Relation between the bedload events and rainfall condition in study sites

3.2 Annual changes of bedload events and rainfall threshold

In this chapter, bedload events and non-bedload events were marked by year to find out how long effects of landslide and forest fire disaster continue. In addition, the point of this study is the rainfall threshold to induce bedload discharge. So, we focused on this and lowered the graph scale (Total rainfall amount ≤ 40 mm, Peak rainfall intensity ≤ 15 mm/h). Because there were cases where data such as mechanical defects of the field monitoring system were missed, it was difficult to make a clear comparison of time series analysis such as annual change and seasonal change. However, the results of marking the annual change with available data were showed in **Fig. 4**.

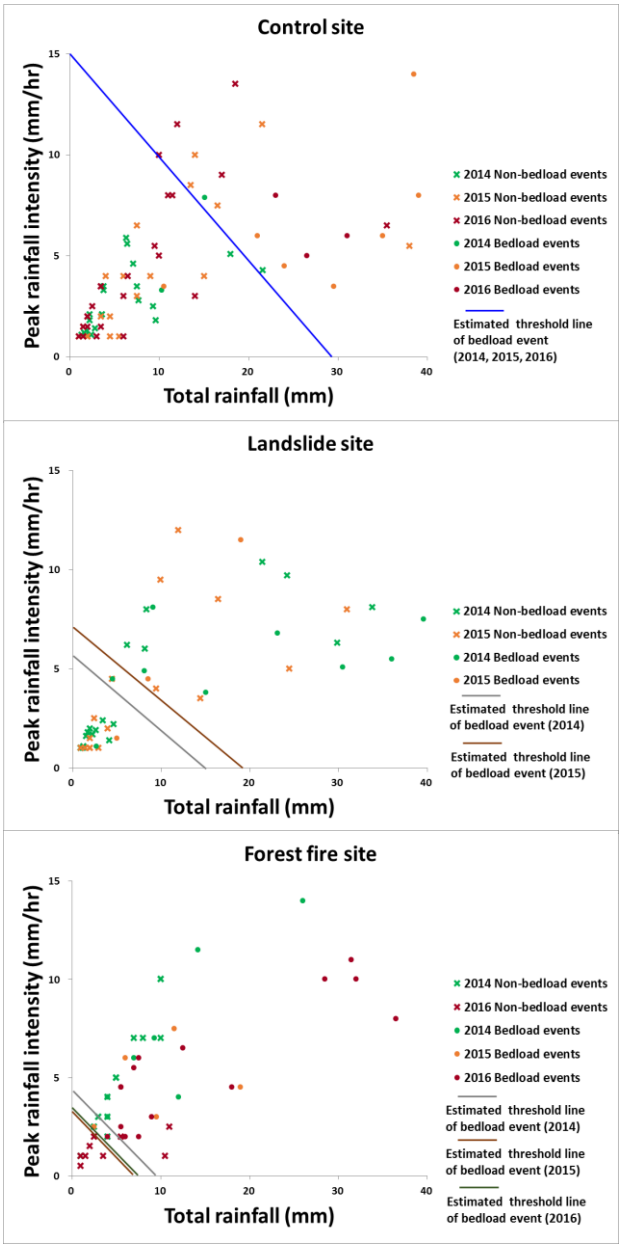

Fig. 4 Annual change of bedload events and rainfall threshold in study sites

Since the control site was a healthy forest without any forest disaster, there were no temporal change in rainfall threshold from 2014 to 2016 in control site.

The forest disaster sites were similar to the control site, the annual change in rainfall threshold in forest disaster sites. From this result, we considered that the effects of landslide and forest fire prolonged several years and effects of disaster on rainfall threshold did not change at least few years after the disasters.

3.3 Seasonal changes of bedload events and rainfall threshold

There are four seasons in Korea: spring, summer,

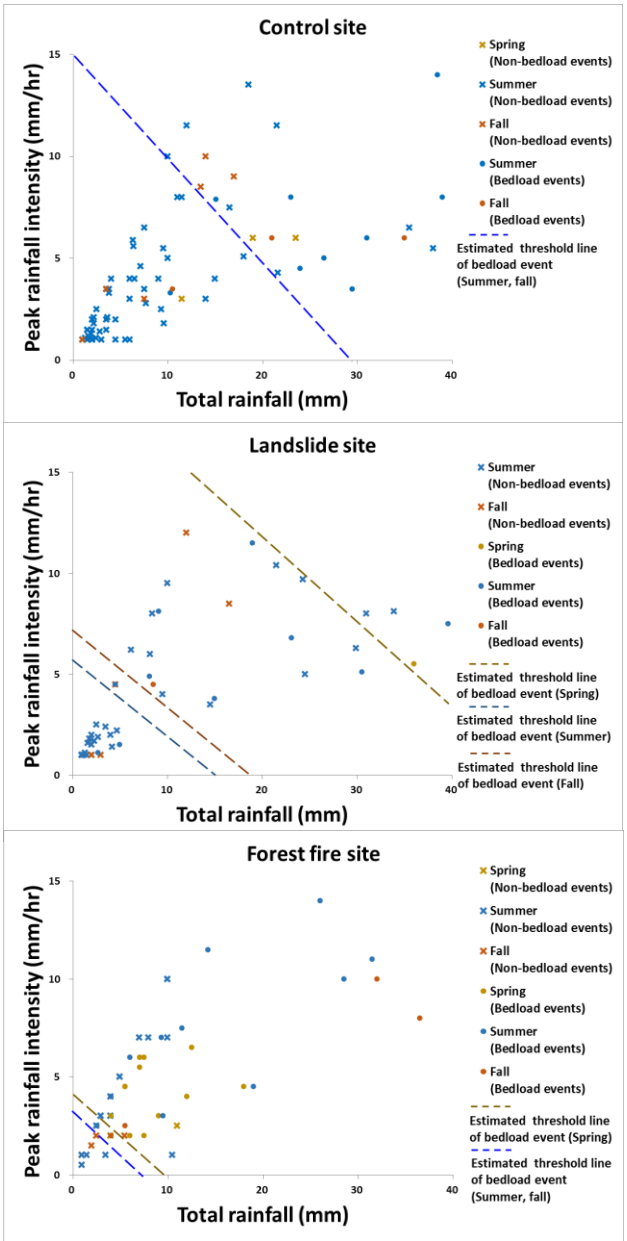

Fig. 5 Seasonal change of bedload event and rainfall threshold in study sites

fall and winter. In spring (Mar. to May) and fall (Oct. to Nov.), dry climatic conditions cause many forest fires. During the rainy season (Jun. to Sept.), which is often affected by heavy rainfall and typhoons in the summer, a landslide and debris flow occurs most of the time. Therefore, seasonal effects need to be considered to understand the threshold of bedload events and rainfall condition in Korea. For example, it can be thought that during the summer, since a lot of sediment yielded on damaged hillslope due to heavy rainfall, so, sediment deposition in riverbed might be increased. If so, rainfall threshold should become small. While, in summer periods, sediment discharge might be larger than sediment input from hillslope. In this case, the sediment availability should decrease, thus, rainfall threshold becomes large.

In **Fig. 5**, the bedload events and non-bedload events were marked according to each season. There is no clear difference in rainfall threshold in terms of seasons, regardless of forest disasters. This suggests that there is no seasonal change in sediment availability. Although there are several possible explanations about this result, it can be thought that the sediment transport capacity due to flood is no so large, thus, still a lot of unstable sediment caused by landslide and forest fire deposited in riverbed in forest damaged watershed. This well agrees with the prolonged effect of forest damage on sediment discharge argued in the previous section.

4. CONCLUSION

In Korea, there are six sites that are using a hydrophone (Japanese pipe microphone) developed in Japan. There are two objectives of monitoring. The first object is the monitoring of effects of forest disasters on bedload discharge. So, we installed the bedload monitoring system at watersheds damaged by landslide and forest fires, and watersheds covered by undamaged forest.

In this study, the rainfall threshold for the occurrence of bedload events was analyzed in forest disaster sites and control site. As a result, the total rainfall amount and the peak rainfall intensity among the rainfall characteristics were analyzed to be the best representations of bedload events. The difference between the bedload events and the rainfall threshold were clear in control site (no disaster forest), landslide site and forest fire site.

In the control site, the rainfall threshold of bedload events was high, while the rainfall threshold of bedload events was low in the landslide and forest fire sites. Compared with the control site, the forest disaster sites showed bedload events even in the low rainfall conditions of about 10 - 23 mm in the total rainfall amount and 11 - 12 mm/hr in the peak rainfall intensity. Therefore, it was thought that landslide and forest fire gave an impact on the rainfall threshold on bedload event. Especially, in the forest fire site, bedload events occurred even in the lowest rainfall conditions. In addition, it was found that most bedload events occurred when the rainfall condition exceeded the orange line.

In analysis of seasonal effects, rainfall events and bedload events were the most frequent in the

summer, the rainy season of all sites. Also, the most bedload events occurred in the summer. Because many sediments yielded on damaged hillslope by heavy rainfall, and rainfall threshold was decreased due to increased sediment deposition in the riverbed.

Therefore, an urgent soil erosion control work seems to be required to prevent the second damages in forest disasters. It is expected that a larger database will increase the reliability of this result, and will help better understanding of the soil erosion control works and the bedload transportation mechanism.

REFERENCES

Arattano, M. and Marchi, L. (2008): System and sensors for debris-flow monitoring and warning, Sensors, Vol. 8, No. 4, pp. 2436-2452.

Badoux, A., Turowski, J. M., Mao, L., Mathys, N. and Rickenmann, D. (2012): Rainfall intensity–duration thresholds for bedload transport initiation in small Alpine watersheds. Natural Hazards and Earth System Sciences, 12, pp. 3091-3108.

Itakura, Y., Inaba, H. and Sawada, T. (2005): A debris-flow monitoring devices and methods biliography, Natural Hazards and Earth System Sciences, Vol. 5, No. 6, pp. 971-977.

Johansen, M.P., Hakonson, T.E. and Breshears, D.D. (2001): Post-fire runoff and erosion from rainfall simulation: contrasting forests with shrublands and grasslands, Hydrological Processes, No. 15, pp. 2953-2965.

KFS (Korea Forest Service) (2013): 2013 Main business plan detail (in Korean).

Lee, C.W., Lee, C.Y., Kim, J.H., Youn, H.J. and Chol, K. (2004): Characteristics of soil erosion in forest fire area at Kosung, Kangwondo, Journal of Korean Forest Society, Vol. 93, No. 3, pp. 198-204 (in Korean with English abstract).

Mizuyama, T., Hirasawa R., Kosugi, K., Tsutsumi, D. and Nonaka, M. (2011): Sediment monitoring with a hydrophone in mountain, International Journal of Erosion Control Engineering, Vol. 4, No. 2, pp. 43-47.

Mizuyama, T., Laronne, J.B., Nonaka, M., Sawada, T., Satofuka Y., Matsuoka, M., Yamashita, S., Sako, Y., Tamaki, S., Watari, M., Yamaguchi, S. and Tsuruta, K. (2010): Calibration of a Passive Acoustic Bedload Monitoring System in Japanese Mountain Rivers, U.S. Geological Survey Scientific Investigations Report 2010-5091, pp. 296-318.

O'Brien, G., O'Keefe, P., Rose, J. and Wisner, B. (2006): Climate change and disaster management, Disasters, Vol. 30, No. 1, pp. 64-80.

Rickenmann, D., Antoniazza, G., Wyss, C.R., Fritschi, B. and Boss, S. (2017): Bedload transport monitoring with acoustic sensors in the Swiss Albula mountain river, Proceedings of the International Association of Hydrological Sciences, No. 375, pp. 5-10.

Seo, J.P., Jung, Y.G., Lee, K.H., Lee, C.W., Kim, D.Y., Uchida, T. and Iuchi, T. (2017): Current condition and future challenges of sediment transport monitoring system in Korea, Japan Society of Erosion Control Engineering, Vol. 69, No. 5, pp. 71-74 (in Japanese with English abstract).

Seo, J.P., Lee, C.W., Kim, D.Y. and Woo, C.S. (2016): Estimating of annual sediment yield at mountain stream in fire/landslide damaged forest by using terrestrial LiDAR spatial analysis, Journal of Korean Society Hazard Mitigation, Vol. 16, No. 6, pp. 219-227 (in Korean with English abstract).

Shin, S.S., Park, S.D. and Lee, K.S. (2013): Sediment and hydrological response to vegetation recovery following wildfire on hillslopes and the hollow of a small watershed, Journal of Hydrology, 499, pp. 154-166.

Tsutsumi, D. and Laronne, J.B. (2017): Gravel-bed rivers (Processed and disasters), Wiley Blackwell, pp. 798.

Uchida, T., Sakurai, W., Iuchi, T., Izumiyama, H., Borgatti, L., Marcato, G. and Pasuto, A. (2018): Effects of episodic sediment supply on bedload transport rate in mountain rivers. Detecting debris flow activity using continuous monitoring, Geomorphology, doi: 10.1016/j.geomorph.2017.12.040.

Maintenance of Historical Sabo Facilities by the Tateyama Mountain Area Sabo Office - An Evaluation of the Soundness and Utility of Sabo Facilities -

Hisashi WATANABE[1*]

[1] Sabo Frontier Foundation (Hirakawacho, Chiyoda-ku, Tokyo 1020093, Japan)
*Corresponding author. E-mail: kenkyu2@sff.or.jp

In the middle reach of the Joganji River, the Hongu Sabo Dam, which is as important as the Shiraiwa Sabo dam installed in Tateyama Caldera, is installed. More than 80 years, Hongu Sabo Dam has been proteced the Joganji River basin from a sediment-related disaster. And it was designated as an important cultural property in 2017. In this paper, I introduce the inspection and soundness evaluation of Hongu Sabo Dam carried out based on the "Planning Manual for Maintaining and Prolonging the Lifespan of Sabo Facilities" issued by Ministry of Japan in 2014. And also I introduce the utilization of the Hongu Sabo Dam in recent years.

Key words: Historical and cultural value; Maintenance; Rubble concrete; Soundness evaluation; Utilization of sabo dams

1. Introduction

Sabo work in Tateyama started in 1906. The initial sabo works were undertaken by Toyama Prefecture, and were continued by the Japanese Government as of 1926. Over the past 90 years, the techniques used in sabo works have advanced considerably; some of the sabo dams in Tateyama are made of materials, structures, and construction methods that are now obsolete. Several sabo dams have been certified as cultural properties by the Agency for Cultural Affairs, based on their historical or cultural value.

This paper examines recent efforts by the Tateyama Mountain Area Sabo Office to maintain the Hongu Sabo Dam, a large sabo dam located in the middle reach of the Joganji River that has been designated a cultural property

2. Outline of the basin and its two main sabo facilities

2.1 The Joganji River

The Joganji River, controlled by the Tateyama Mountain Area Sabo Office, is one of the steepest rivers in Japan. It flows 56 km from the mountainous area 3,000 m in eastern Toyama Prefecture to Toyama Bay. Its average bed slope is about 1/30.

During the 1858 Hietsu earthquake (7.1 magnitude), the massive Tonbi landslide occurred, originating at the Tateyama Caldera (**Fig. 1**). About 400 million m^3 of sediment were accumulated, of which 200 million m^3 flowed down the mountainside. As a result, 140 people died and 8,945 people were injured.

After this disaster, the Joganji River became prone to sediment-related disasters. In the Tateyama Caldera, 200 million m^3 of sediment remains. During heavy rainfalls, accumulated sediment flows into the downstream reaches of the Joganji River.

Fig. 1 Tateyama Caldera

2.2 Two main sabo facilities of the Tateyama Mountain Area Sabo Office

Modification of the Joganji River began during the Meiji era to protect the Joganji River Basin from sediment-related disasters. However, disasters continued to occur despite these efforts. Therefore, in 1906, Toyama prefecture started sabo works in the upstream area of the Joganji River.

Direct control over the sabo works was given to the Ministry of Home Affairs (now the Ministry of Land, Infrastructure, Transport and Tourism, MLIT) in 1926. Two of the main sabo facilities on the Joganji River were constructed to protect the basin from sediment disasters. One is the Shiraiwa Sabo Dam (**Fig. 2**), which is located at the exit of the Tateyama Caldera in the upstream portion of the Joganji River. The other is the Hongu Sabo Dam (**Fig. 3**), which was constructed in the middle of the Joganji River.

Shiraiwa Sabo Dam was built to stabilize the hillside of the Joganji River upstream area (Tateyama Caldera) and to prevent erosion of the river bed. From October 1929 to December 1939, the main dam and counter dams 1 and 2 were constructed. Counter dams 3–7 were constructed after 1951 to prevent riverbed degradation, completing the dam in its current form. Hongu Sabo Dam was built for the prevention and adjustment of sediment discharge in the midstream area of the Joganji River, 26.8 km from the estuary. From April 1935 to December 1937, the main dam and counter dams 1 and 2 were constructed. Counter dam 2 was modified and counter dams 3–5 were created after 1947, producing the current dam structure.

Thus, the Shiraiwa Sabo Dam and Hongu Sabo Dam have protected the Joganji River Basin from sediment disasters for a long period of time. These dams, designated as "particularly technically superior" and "highly historical", are important cultural sabo facilities in Japan.

Fig. 2 Shiraiwa Sabo Dam

3. Hongu Sabo Dam

3.1 Hongu Sabo Dam specifications

Hongu Sabo Dam is a main check dam that was constructed from 1935 to 1937 in the midstream area of the Joganji River (26.8 km from the estuary), for the prevention and adjustment of sediment discharge.

Its height is 22.0 m, and its crest length is 107.4 m, a total of 23,500 m^3 of concrete was used in the construction of the dam body, with a sediment trap capacity of 5 million m^3 (Japan's largest). It has five counter dams.

Hongu Sabo Dam was built before the existence of the materials and machine tools now used for dam construction. To save cement, which was then prohibitively expensive, stone material was used for the outside of the dam (front and crest) and rubble concrete was used for interior construction.

Fig. 3 Hongu Sabo Dam

3.2 Hongu Sabo Dam construction

Since 1926, when construction began on Shiraiwa Sabo Dam, sabo works in Tateyama have been controlled by the Ministry of Home Affairs (now the MLIT). The construction of Shiraiwa Sabo Dam took many years. During this time there was a collapse of the Onigajo rock wall downstream of the dam. As such, Shiraiwa Sabo Dam cannot solely prevent all sediment-related disasters in the Joganji River Basin.

Similarly, heavy rainfall of 400 mm per day occurred in the upper part of the Joganji River in 1934, and a large disaster occurred in the Joganji River Basin destroying 1,080 m of the revetment in ten places. Following the disaster, a river improvement project was initiated, and Hongu Sabo Dam was constructed.

3.3 Dam construction features

During the construction of the Hongu Sabo Dam

(**Figs. 4** and **5**), large tower cranes, chutes, and rubble concrete were introduced. These were state-of-the-art equipment, materials, and methods for the period. Despite its size, the dam was completed in less than 2 years.

Hongu Sabo Dam demonstrates the technical level of sabo facilities during the early Showa period and is a valuable example of early construction methods. In November 2017, the dam was designated an important cultural property among Japanese sabo facilities.

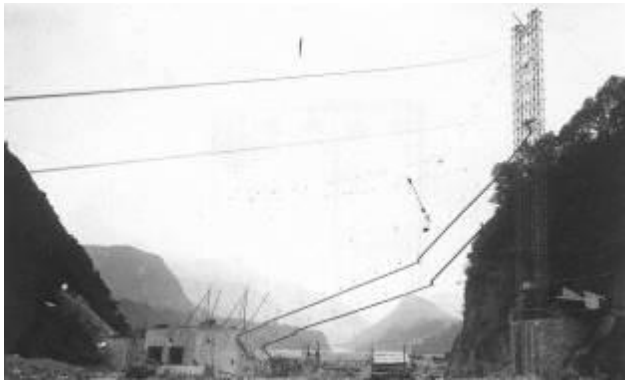

Fig. 4 Large tower cranes and chutes (1935)

Fig. 5 Hongu Sabo Dam construction (1936)

4. Maintaining and prolonging the lifespan of sabo facilities

4.1 Deterioration of physical infrastructure

In Japan, a large amount of physical infrastructure such as roads, bridges, river management facilities, and quay walls was constructed during the high growth period following World War II. These facilities will approach 50 years of age within the next decade. Within 20 years, 60% of Japan's sabo facilities will exceed 50 years of age. Therefore, there is concern that these sabo facilities will deteriorate.

4.2 Approach of the MLIT Erosion and Sediment Control Department

In this context, an accident occurred in which a tunnel ceiling board fell on the Chuo Expressway, a major Japan highway, in December 2012. The MLIT created a maintenance action plan to prolong the lifespan of physical infrastructure in September 2013. To prevent sediment-related disasters, the Ministry ordered all sabo offices in Japan to create their own plans to prolong the lifespan of sabo facilities, based on the Ministry's action plan.

The MLIT Erosion and Sediment Control Department issued a manual to help sabo office facility managers investigate the soundness of existing facilities and to create plans to maintain the function and performance of the facilities in good working order over a long period (**Fig. 6**).

4.3 Actions taken at the Tateyama Mountain Area Sabo Office

The Tateyama Mountain Area Sabo Office has implemented a plan to maintain and prolong the lifespan of sabo facilities in accordance with manuals issued by the Ministry.

The plan defines countermeasures according to the soundness of the sabo facility. Therefore, it is extremely important to accurately evaluate the soundness of the target sabo facilities during planning.

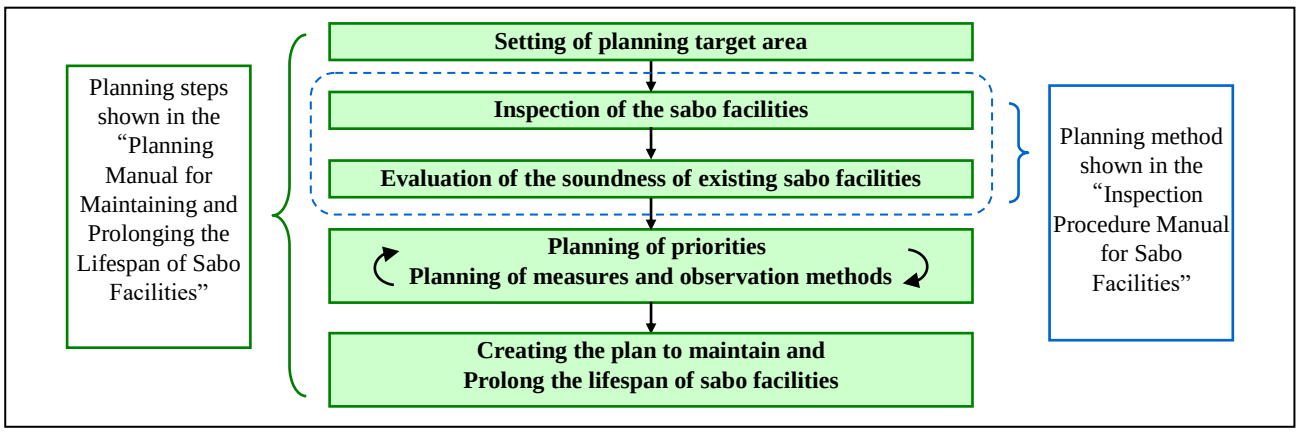

Fig. 6 Manual contents

5. Characteristics of sabo facilities and soundness evaluation

5.1 Rubble concrete check dams

Hongu Sabo Dam is a check dam with a rubble concrete structure (**Fig. 7**). The rubble concrete within such a dam may be of poorer quality and therefore weaker than modern ready-mixed concrete. However, if the outer material (e.g., stone) is undamaged, the dam will not fail catastrophically. In other words, the soundness of rubble concrete dams depends largely on the state of the outer materials

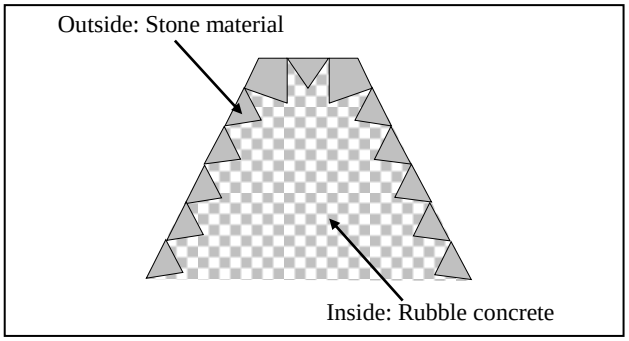

Fig. 7 Check dam with rubble concrete structure

Hongu Sabo Dam is a large-scale check dam constructed in the middle reach of the Joganji River. Recent inspections have found that some stone was missing or abraded at the crest of the dam, exposing the material in the interior (**Fig. 8**).

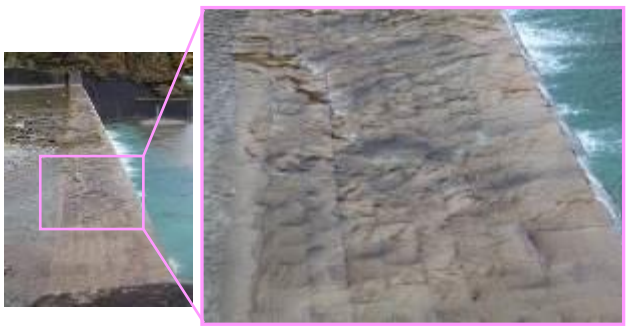

Fig. 8 Deterioration at the crest of the dam

The sediment trap capacity of Hongu Sabo Dam is 5 million m^3 (Japan's largest), such that the loss of facility functions can have an enormous influence downstream. Hongu Sabo Dam has also been designated an important cultural property; thus, the cultural value of the facility must be preserved when repairs are undertaken. In general, when an important cultural property is repaired and/or reinforced, it is necessary to consult with the Agency of Cultural Affairs to preserve the value of the property. Therefore, immediate inspection of the Hongu Sabo Dam was necessary, to evaluate its soundness and to judge whether the repairs were necessary.

5.2 Information necessary for evaluating the soundness of a facility

When the soundness of a sabo facility is evaluated, basic information about the planning and design of the facility is collected through a literature survey. Next, an inspection of the sabo facility is conducted to evaluate the extent of the deterioration.

Water flows continuously over the Hongu Sabo Dam; thus, damage to the outer stones at the crest or front of the dam cannot be examined during a normal inspection. In addition, it is difficult to implement large-scale river diversion for inspections, in terms of both time and budget.

Further, documents containing information about the design of the Hongu Sabo Dam were burned during the Toyama air raid during World War II. Thus, we could not obtain information about the materials used to construct the interior of the dam.

5.3 Inspection based on the importance of the facilities

To maintain the disaster-prevention function of the dam, preserve its value as a cultural property, and determine the soundness of the sabo facilities within a short time and at low cost, a survey was conducted (**Table 1**).

Table 1 Detailed inspection items for historical sabo facilities

Item No.	Investigation method	Investigation aims	Supplemental information
i	Boring investigation (includes laboratory investigations)	Physical properties of the internal material of the dam and sedimentation area	Six representative locations
ii	Detailed visual inspection	Damage or deterioration of the outer stone material	Divert the flow Rappel down the dam
iii	Elastic wave exploration	Density of the internal material	Eight representative sections

i. Boring investigation

Boring investigations were conducted at four locations (**Fig. 8** and **9)** at the crest of the dam where the interior rubble concrete was exposed. Water leakage and internal cracks were investigated within the borehole using a borehole video camera. Rubble concrete collected from four locations on the body of the dam permitted an evaluation of its physical properties in a laboratory investigation. The sedimentary area was also investigated at two locations, including observations of the sediment condition and water level.

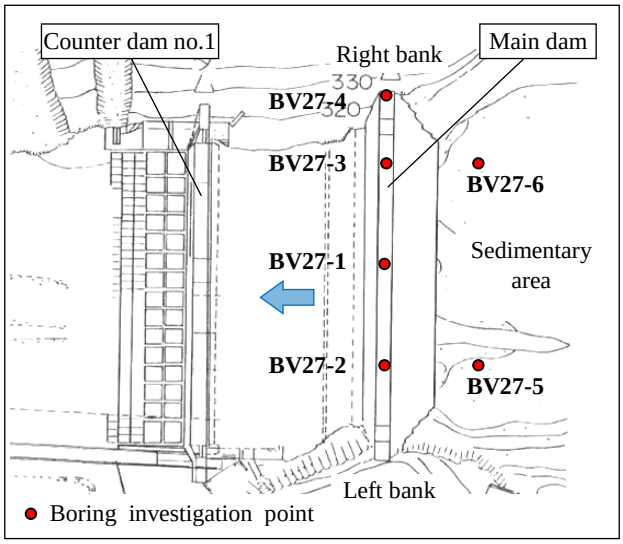

Fig. 9 Boring investigation point

ii. Detailed visual inspection

To confirm the material, color, shape, arrangement, and condition of the stones used at the crest and downstream of the Hongu Sabo Dam, a detailed visual investigation was conducted (**Fig. 10**).

Hongu Sabo Dam is a check dam with historical and cultural value and has been designated a culturally important sabo facility. Maintaining the original appearance of the facility as much as possible is a priority during maintenance and repair.

Therefore, a detailed visual inspection was conducted, and all stone materials used in the crest and downstream of the Hongu Sabo Dam were investigated.

During this inspection, a small-scale diversion of the river was carried out, exposing the stone materials for assessment. To conduct the inspection safely and in detail, and to accurately record the results of the inspection, engineers with climbing skills were added to the inspection team.

Fig. 10 Detailed visual inspection

iii. Elastic wave exploration

The boring survey was carried out at only four locations on the Hongu Sabo Dam; these measurements may not have been representative of the internal conditions of the dam. Therefore, to supplement the results of the boring investigation, an elastic wave exploration was performed, which permitted easy, non-destructive evaluation of the dam body.

The elastic wave exploration was conducted along eight lines (eight sections) as shown in **Fig. 11**.

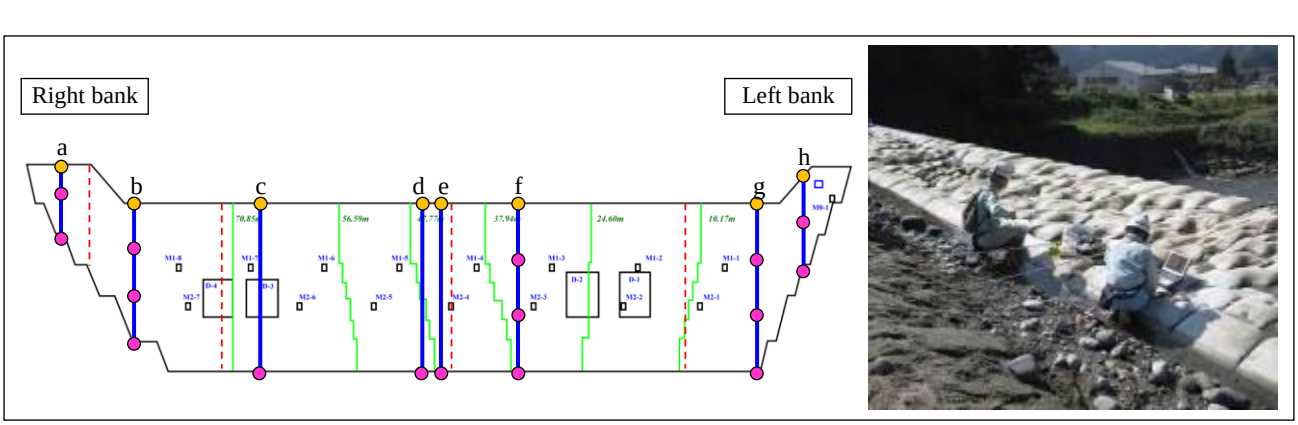

Fig. 11 Elastic wave exploration

6. Results and evaluation

6.1 Inspection results

i. Result of the boring investigation

Rubble concrete within the Hongu Sabo Dam consists mainly of 3- to 4-cm gravel and stones (rubble) with diameters ranging from 10 to 30 cm. The boring core did not exhibit many cracks, and almost no cracks were found by the borehole video camera (**Fig. 12** and **13**). The aggregate and cement in the rubble concrete were firmly adhered, unweathered, and hard. Therefore, the condition of the rubble concrete within Hongu Sabo Dam was determined to be in good condition (**Table 2**).

Fig. 12 Example of a boring core picture (BV27-1 0.0–10.0 m)

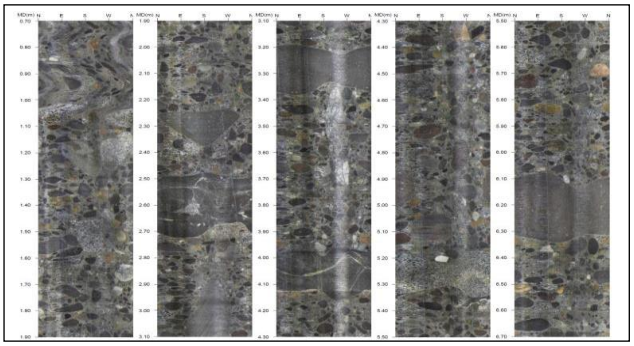

Fig. 13 Example of borehole camera images (BV27-1 0.7–6.5 m)

Table 2 Example of laboratory investigation results for concrete (BV27-1 4.2–5.0 m)

Classification	Symbol	Unit	Concrete
Wet density	ρt	g/cm^3	2.324
P wave velocity	V_P	km/s	4.50
S wave velocity	V_S	km/s	2.40
Dynamic Poisson ratio	V_d	–	0.301
Dynamic shear modulus	G_d	MN/m^2	13386
Dynamic elastic modulus	E_d	MN/m^2	34830
Uniaxial compressive strength	Qu	MN/m^2	24.6
Modulus of deformation	E_{50}	MN/m^2	10250
Tensile strength	σ_t	MN/m^2	3.55

ii. Results of detailed visual inspection

As a result of detailed investigation, the material, color, shape, and arrangement of the stones used in the crest and downstream of Hongu Sabo Dam were confirmed. The following signs of deterioration were also detected (**Table 3**, **Fig. 14**–**16**). The stone at the crest of the dam and the mortar in the joints were abraded. No damage to the stone on the upstream or downstream sides of the crest of the dam was detected. Seven central rows of stone and mortar at the crest of the dam were missing, over a maximum area of 2 m × 2.5 m and a depth of 0.4 m.

In the past, abrasion countermeasures were implemented downstream of the Hongu Sabo Dam; abrasion was found to have occurred again in a downstream part of the dam.

Table 3 Major deterioration detected in Hongu Sabo Dam

Position	Major deterioration
Crest of dam	Abrasion of stone material Missing stone material
Downstream of dam	Missing stone material Missing mortar Re-abrasion of repaired concrete Re-scoring at repaired concrete Leak

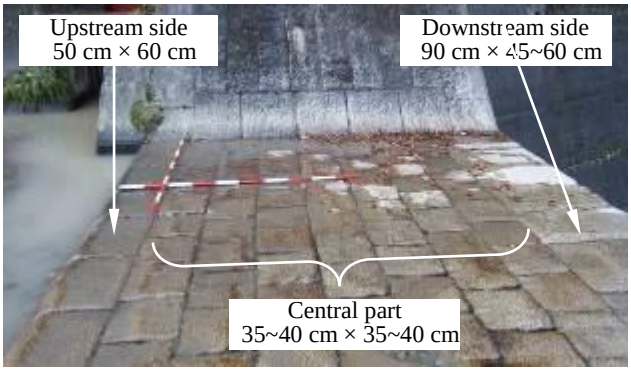

Fig. 14 Stone material on the crest of Hongu Sabo Dam

Fig. 15 Stone material downstream of Hongu Sabo Dam

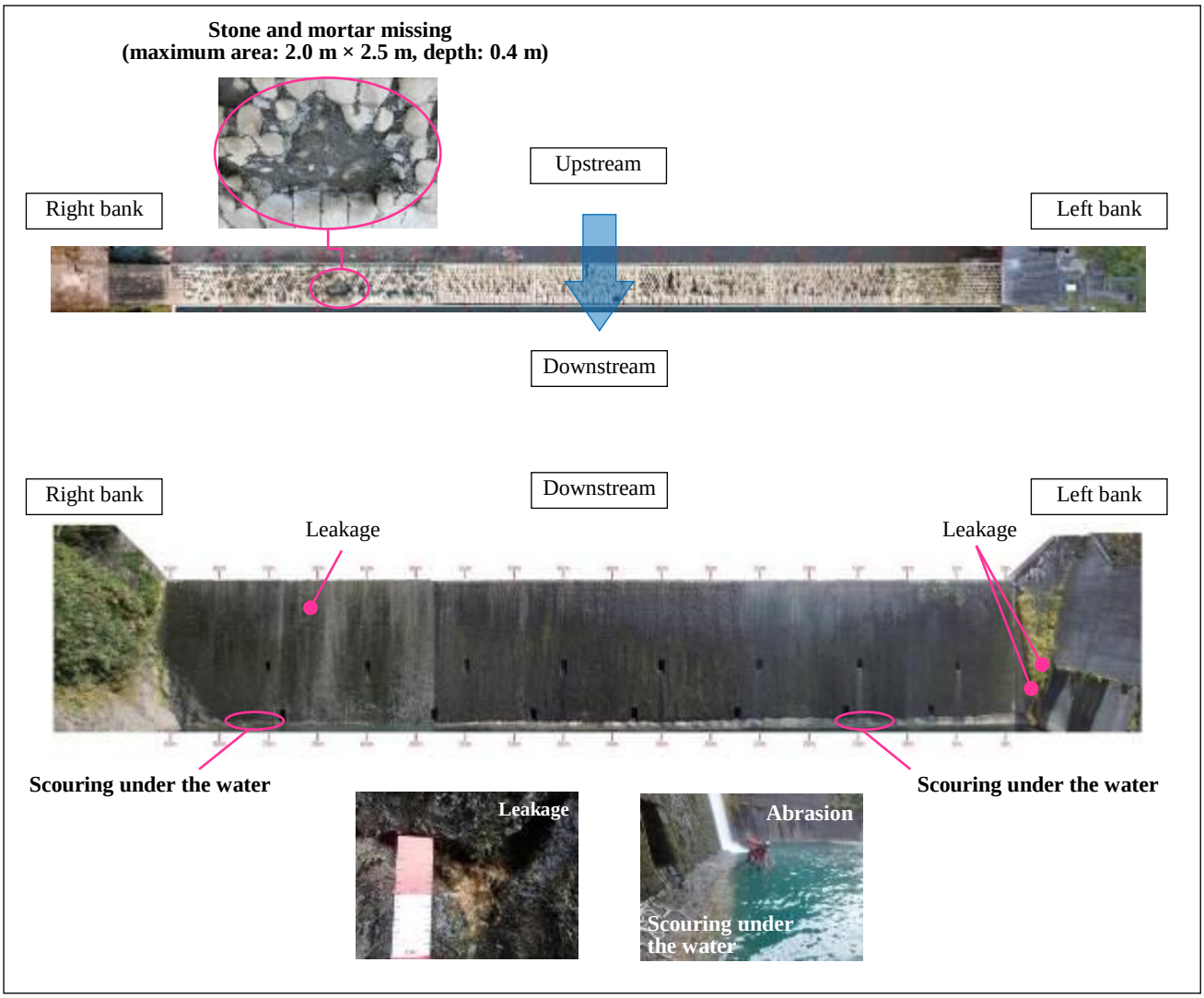

Fig. 16 Main deterioration on the crest and downstream of Hongu Sabo Dam

iii. Results of elastic wave exploration

The threshold value for elastic wave velocity indicating soundness in modern ready-mixed concrete is 3.5–4.5 km/s.

Hongu Sabo Dam, as an 80-year-old rubble concrete structure, was expected to have a low elastic wave velocity. However, contrary to expectation, the elastic wave velocities exceeded 4.4 km/s in all sections. From these results and those of the aggregate and cement that form the rubble concrete of the dam interior, the dam materials remain firmly adhered to each other and are considered to be hard.

6.2 Soundness evaluation of Hongu Sabo Dam

As a result of the boring investigation, visual inspection, and elastic wave exploration, two types of damage were identified: missing stone material and mortar at the crest of the dam, and re-abrasion of repaired concrete downstream of the dam, which has the potential to cause loss of function in terms of sediment-related disaster prevention. However, the results of the boring investigation and elastic wave exploration indicated that the fine rubble concrete within the dam was of good quality, like that of modern ready-mixed concrete.

Dam scouring does not reach the foundation of the dam. Therefore, the probability of loss of sediment-related disaster prevention function at Hongu Sabo Dam was estimated to be low.

The performance (stability) of the Hongu Sabo Dam cannot be verified precisely because the ground-bearing capacity of the dam site and the stability at the time of design remain unknown. However, we estimate that the dam is at low risk of suddenly losing sediment-disaster prevention function, due to the results of a recent stability check of the facility and because stability was not lost during a major flood in 1969.

6.3 Timing and method of measurements

Damage or deterioration in Hongu Sabo Dam

detected during the inspection described in this report will continue to be monitored. Rubble concrete within Hongu Sabo Dam was determined to be in good condition. As such, the dam did not require immediate repair. In the future, extensive damage or large missing stone sections upstream or downstream of the dam crest will initiate repair actions beginning at the dam ends (**Fig. 17**).

Downstream of Hongu Sabo Dam, abrasion and scouring have not progressed to the dam foundation and thus do not require immediate repair.

Hongu Sabo Dam is a facility with historical and cultural value and was designated an important cultural property in November 2017. Therefore, it is necessary to maintain both the disaster-prevention function and cultural property value of Hongu Sabo Dam throughout repairs.

The Tateyama Mountain Area Sabo office plans to establish a conservation and management plan for Hongu Sabo Dam.

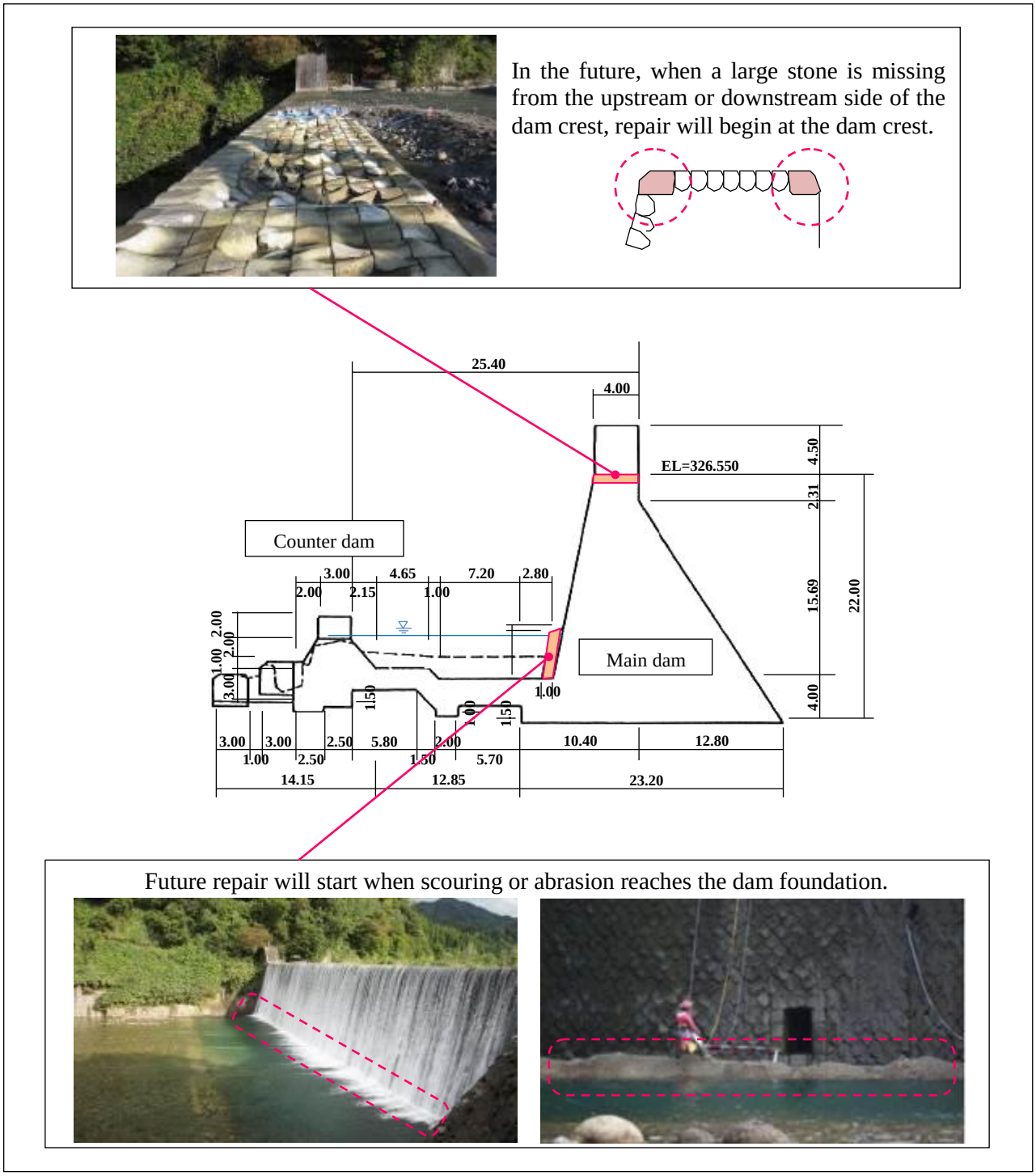

Fig. 17 Timing of repair measures

7. Utilization of Hongu Sabo dam

7.1 Effect of sabo works

In Japan, many sabo facilities were constructed more than a century ago to recover devastated mountains and prevent sediment-related disasters. These sabo facilities were created using contemporary technologies for the time and remain in use to the present day as disaster-prevention facilities.

The MLIT and Agency of Cultural Affairs created a Committee on the Preservation and Utilization of Historical Sabo Facilities in December 2002 to preserve and utilize sabo facilities of historical value. In May 2003, these organizations established guidelines for the preservation and utilization of historical sabo facilities. According to these guidelines, it is important to consider metrics of visitor experience, as described by the words "see", "learn", and "know" when establishing practices for sabo facilities (**Fig. 18**).

The Tateyama Mountain Area Sabo Office, in cooperation with the Tateyama Caldera Sabo Museum, has been conducting an experiential learning tour to teach the history of past disasters and the function and effects of sabo facilities. Hongu Sabo Dam is a major site for experiential learning tours, because it is a large-scale check dam with Japan's largest sediment trap capacity (5 million m^3). Its placement in the middle reach of the Joganji River, one of the steepest rivers in Japan, provides relatively easy access

Fig. 18 Experiential learning

7.2 Improvement around the Hongu Sabo Dam

The area around the Hongu Sabo dam is designed such that elementary school students can engage in outdoor activities and be in direct contact with the water (**Fig. 19**).

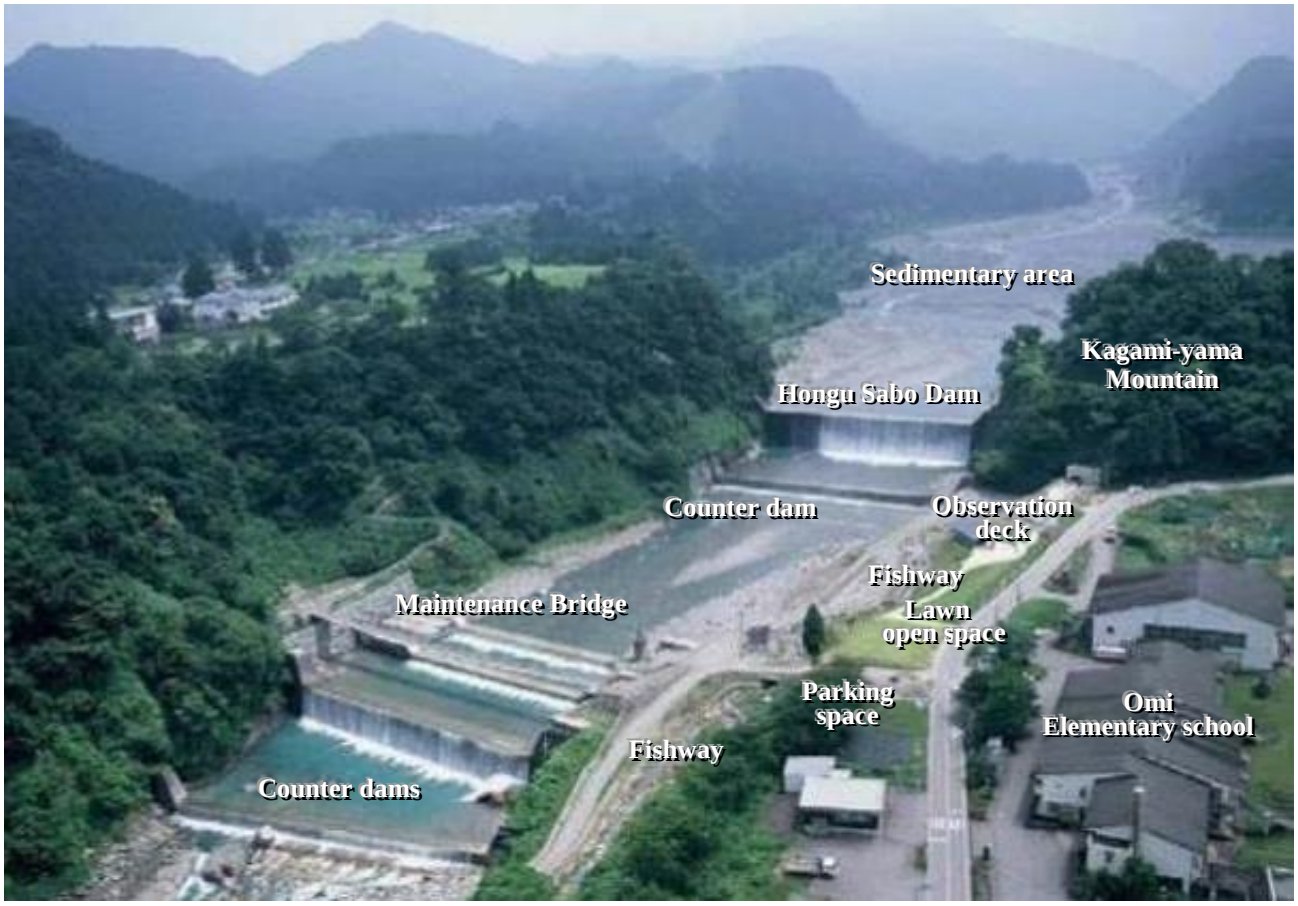

Fig. 19 Environmental improvement around Hongu Sabo Dam

Improvement is based on the subsidy system for improving the hydrophilicity of rivers, and facilities have been developed, including an observation deck, maintenance bridge, lawn, and fishway.

The Tateyama Mountain Area Sabo Office and Tateyama Caldera Museum also dispatch instructors upon the request of users who wish to engage in outdoor activities and learn about sabo works around Hongu Sabo Dam.

The Tateyama Mountain Area Sabo Office, in cooperation with regional residents and construction workers, conduct safety inspections and cleanup activities several times per year in the area surrounding Hongu Sabo Dam. In addition, the Tateyama Mountain Area Sabo Office sometimes holds public discussions with local residents on the subject of future dam maintenance and management and better ways to revitalize regional communities..

7.3 Utilization of the facility as a regional resource

The historical sabo facility has academic value with respect to its technology and design philosophy, landscape/environmental value for its contribution to the abundant natural ecosystem in the middle mountains, and public relations value due to its contribution to the conservation and modernization of parts of these lands. It is important to disseminate these values widely.

The Tateyama Mountain Area Sabo office has held an informal meeting to educate local residents about the value of Hongu Sabo Dam, so that they can utilize Hongu Sabo Dam as a regional resource (**Fig. 20**).

Fig. 20 Informal meeting with local residents

8. Conclusion

In recent years, the environments surrounding sabo works have changed greatly. The maintenance costs of sabo facilities are expected to increase.

To maintain and improve the safety of these regions in the future, new and existing sabo facilities must be utilized effectively, especially the historical sabo facilities, to convey the risk of sediment-related disasters, inform the public of the valuable role of sabo works in disaster prevention, and determine how best to use sabo facilities as regional resources. All of these aims require the cooperation of regional communities.

It is our hope that this report will contribute to the achievement of these goals

REFERENCES

Ministry of Land, Infrastructure, Transport and Tourism Water Management and National Land Conservation Bureau, Erosion and Sediment Control Department (2014): Planning Manual for Maintaining and Prolonging the Lifespan of SABO Facilities, pp. Ⅰ-1–Ⅱ-24.

Ministry of Land, Infrastructure, Transport and Tourism Water Management and National Land Conservation Bureau, Erosion and Sediment Control Department (2014): Inspection Procedure Manual for SABO Facilities, pp. 1-56.

Ministry of Land, Infrastructure, Transport and Tourism Hokuriku Regional Development Bureau, Tateyama Mountain Area Sabo Office (2015): Plan of the maintaining and prolonging lifespan of Sabo facilities in Tateyama Mountain Area Sabo Office.

Ministry of Land, Infrastructure, Transport and Tourism Hokuriku Regional Development Bureau, Tateyama Mountain Area Sabo Office (2013): Preservation plan of Important Cultural Property Shiraiwa Sabo Dam, pp. 5-68.

Ministry of Land, Infrastructure, Transport and Tourism River Bureau erosion control department Maintenance Section and Agency of Cultural Affairs (2003): Guidelines for the preservation and utilization of historical sabo facilities, pp. 5-11.

Watanabe, H. and Toshio, M. (2016): Actions for the Maintenance and Lifespan Prolongation of SABO Facilities, INTERPRAEVENT 2016, pp. 862-870.

Watanabe, H. et al. (2016): Maintenance of Historical Sabo Facilities in Tateyama Sabo Mountain Area Sabo Office, Japan Society of Erosion Control Engineering Publication No.78, http://www.jsece.or.jp/event/conf/abstruct/2016/pdf/T1-01.pdf

The History of Sediment Disasters and Sabo Projects in the Yomase River Basin, Nagano Prefecture, Japan

Makoto KITAHARA[1*], Masashi TASHITA[1], Masaru NISHIZAWA[1], Masaaki KINOSHITA[2], Takao YAMAZAKI[2], Kunihiro HASEGAWA[2], Junichi KANBARA[3], Kimio INOUE[4], Kouji OYA[4] and Kazuhiko NAKANE[4]

[1] Sabo Section, Nagano Prefectural Government, Japan (692-2 Habashita, Minaminagano, Nagano, Nagano 3808570, Japan)
[2] Hokushin Construction Office, Nagano P.G. , Japan (955 Hekida, Nakano, Nagano 3838515, Japan)
[3] Sabo Department, Ministry of Land, Infrastructure, Transport and Tourism, Japan (2-1-3 Kasumigaseki, Chiyoda-ku, Tokyo 1008918, Japan)
[4] Sabo Frontier Foundation, Japan (2-7-4 Hirakawacho, Chiyoda-ku, Tokyo 1020093, Japan)
*Corresponding author. E-mail: kitahara-makoto@pref.nagano.lg.jp

The Yomase River originates from the Shiga Highlands, which is an ancient volcano, and runs for a total length of 26 km with a catchment area of 117 km^2. A vast alluvial fan of 6 km in length and 25 km^2 in area is formed at the downstream area of the river. There are hot springs located along the Yomase River, including the Yudanaka/Shibu Hot Spring in the midstream reach of the river, and they have often suffered devastating sediment and flood disasters. The prefectural government of Nagano started sediment control projects in 1906, but the sabo facilities constructed by the prefecture were destroyed by heavy rainfall between 1909 and 1910, and the hot spring resorts also suffered serious damage. The authors studied the topography and geology of the Yomase River, the history of sediment disasters, and the relationship between the disasters and the sabo projects, and learned that the location maps of the sabo facilities constructed from 1906 to 1910 are stored at the Nagano Prefectural Museum of History. Then, we performed a detailed review of those documents. Analysis of the relationship between the catchment area and the bed slope provided knowledge useful in our review of the limit conditions related to the past construction of dry masonry dams and to the future preservation of those old dams.

Key words: Historical sediment disaster, Sabo projects history, Historical sabo facilities, Dry masonry dams

1. INTRODUCTION

The Yomase River is a torrential wild river that discharges a large amount of sediment from the Shiga Highlands, an area that used to be a volcano, and joins the Chikuma River at Yanagisawa, Nakano City. It has a total length of 26 km and a catchment area of 117 km^2. The Yokoyu River and Kakuma River, both of which originate from the Shiga Highlands with an elevation of about 2,000 m, join near the Yudanaka/Shibu Hot Spring in Yamanouchi Town. Hot spring towns, such as Yudanaka and Shibu, develop over dried riverbeds or fluvial terraces of the Yokoyu, Kakuma, and Yomase Rivers, and have often suffered devastating damage by sediment and flood disasters. The downstream reach of the Yomase River also forms a vast alluvial fan of 6 km in length and 25 km^2 in area, indicating very active discharge of sediments.

The prefectural government of Nagano started sediment control projects in 1906, but the majority of the sabo facilities constructed by the prefecture were seriously destroyed by heavy rainfall between 1909 to 1910, and the hot spring resorts located along the midstream channels also suffered serious damage. Therefore, the authors studied the topography and geology of the Yomase River, the history of the sediment disasters, and the relationship between the disasters and the sabo projects (sediment control projects). The results are reported in this paper.

Fig. 1 Location map

2. METHOD

We gathered and organized relevant materials and documents from the Sabo Section of the Construction Department, the Nagano prefectural government, Hokushin Construction Office, Nagano Prefectural Museum of History, Nakano Municipal Library, Wagokai, and Sabo Library. In particular, the Nagano Prefectural Museum of History maintains large survey maps prepared by actual measurement carried out from 1909 to 1910 and documents related to the Yokoyu River sabo works (sediment control works). We perused these historical documents and photographed them with the permission of the Museum.

We also prepared slope gradation maps using 1mDEM, prepared by the Forestry Affairs Department of Nagano Prefecture, to clarify the topographic conditions of the area.**Fig. 2** is a colored slope gradation map of the upstream area of the Yomase River. The detailed microscopic topography of the area upstream of the confluence of the Yokoyu River and Kakuma River is described. When conducting the field survey, we had with us aerial photos as well as enlarged slope gradation maps so that we could understand the topographic and geologic conditions, the status of existing sabo dams, and the condition of sedimentation. The map shows the lava flow topography flowing down from Mt. Shiga, the former lake area judged to be dammed by this lava flow (shown by a dotted line), the Ochiai Landslide that stretched from west to east at the center of the former lake, a narrow part of the Yokoyu River near Yaen-Koen Park, and the dried riverbed and fluvial terrace at the confluence of the Yokoyu River and Kakuma River.

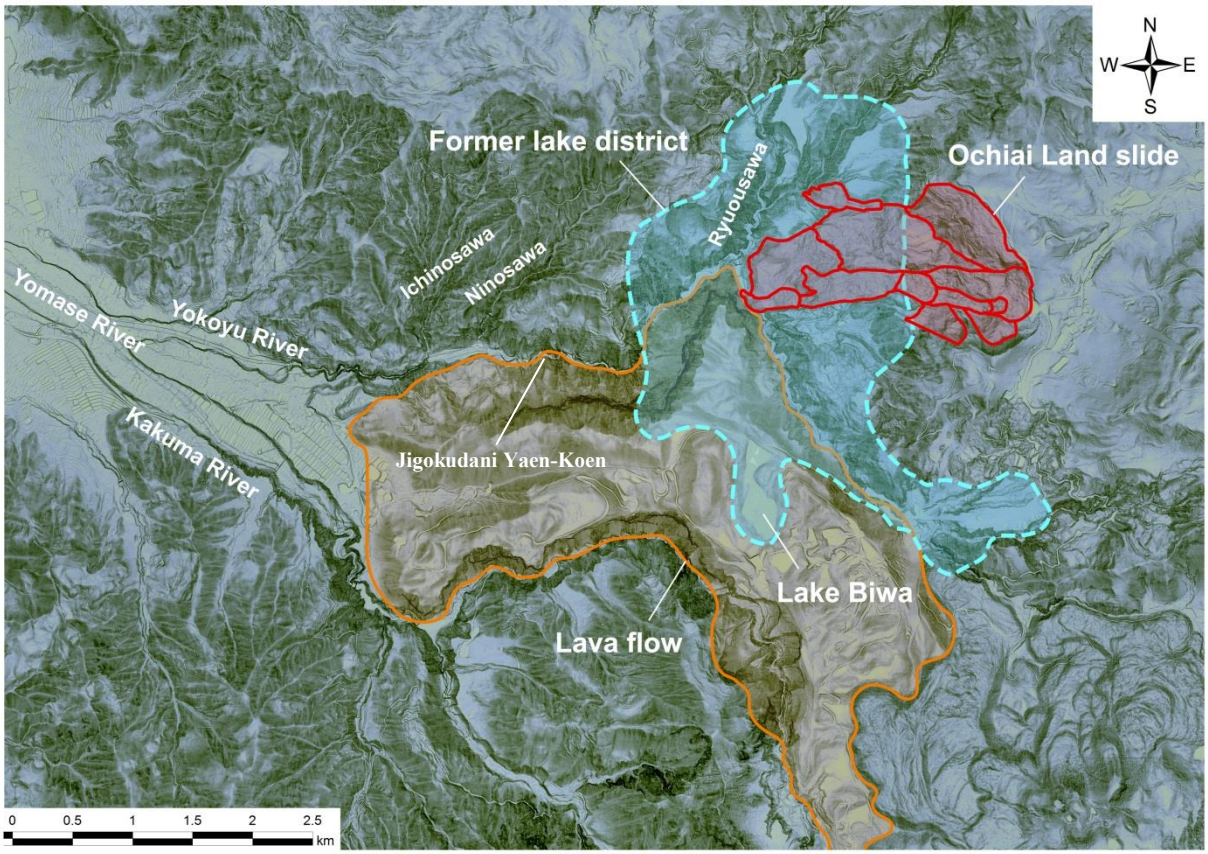

Fig. 2 Colored slope gradation map of the upstream reach of the Yomase River

3. TOPOGRAPHY AND GEOLOGY OF THE CATCHMENT AREA OF THE YOMASE RIVER

Fig. 3 shows the geology of the catchment area of the Yomase River and a distribution map of the landslide topography. The current landslide sites and landslide configurations are concentrated on the right bank of the Yokoyu River and the left bank of the Kakuma River. The geology is characterized by the wide distribution of intrusive rocks such as diorite porphyry and quartz diorite porphyry that constitute the bedrock and the andesitic lava and andesitic pyroclastic rocks erupted from Shiga volcanic mountains. Diorite porphyry and quartz diorite porphyry are exposed on the right bank of the Yokoyu River and the left bank of the Kakuma River, and lacustrine deposits and debris flow deposits are distributed at the Ochiai area.

Lava flows erupted from the Shiga volcanoes from the Middle Pleistocene to the Late Pleistocene stopped river flows to create a lake area in the landslide area of Ochiai, and highly fragile lacustrine sediments were developed in

the lake area. The Yokoyu River and Kakuma River currently run along the boundary between the lava flow from the Shiga Volcano and the bedrock.

4. PAST SEDIMENT DISASTERS IN THE YOMASE RIVER BASIN

The midstream reach of the Yomase River has been used as a hot spring resort since the Kamakura Period. It is believed that even back then, the hot spring resort was popular with many bathers. Records including the Nakano City History of Chikuma River Flood Control (1994) also indicate that the midstream reach had suffered many sediment disasters. Table 1 compiles the past sediment disasters that occurred in the basin of the Yomase River.

The Entoku Tanbo (Entoku Paddy Field), which covers the area between Nakano City and Obuse Town, used to be a lake called Lake Endo. It is recorded that the shogun Minamoto Yoritomo enjoyed viewing cherry blossoms from a boat on Lake Endo in 1197. It is believed that the Yomase River wildly ran in the alluvial fan and drained into Lake Endo until around the 15th century. The river flooded repeatedly during the Edo Period, causing damage to hot spring towns and surrounding villages (**Fig. 4**). In one of the recent flood events, the Kakuma River flooded in 1950, destroying the dike, and damaging the Honami Hot Spring.

Table 1 Past sediment disasters in the Yomase River basin

No.	Year	Description
1	1406	A major flood changed the course of the Yomase River, which originally ran toward Entoku Paddy Field, to what it is today.
2	1614	Major landslides occurred in Mt. Kosha due to heavy rainfall. Two landslides ran down toward the Yomase River and crushed villages on the way. Flooding occurred in the river, and the damage to Entoku Paddy Field was particularly serious.
3	1742	An enormous flood (called Inu-no-Mansui) occurred in the Chikuma River and inundated the paddy and upland fields in the alluvial fan of the Yomase River.
4	1757	Heavy rainfall caused a flood, making the Yokoyu River overflow and washing away the Kawara-yu hot spring building. A major landslide occurred on the mountain behind Shibu Oyu hot spring.
5	1847	A major earthquake, the Zenkoji Earthquake, occurred, and there were major landslides from Mt. Iwakura, which dammed the Sai River. The vast landslide dam was breached and resulted in a big flood in Entoku Paddy Field.
6	1910	A major flood occurred in the Yomase River basin, washing away the sabo facilities that had been constructed previously.
7	1950	Heavy rainfall caused a major flood in the Yomase River. The overflowing water of the Kakuma River breached the levees and almost totally destroyed Honami Hot Spring.

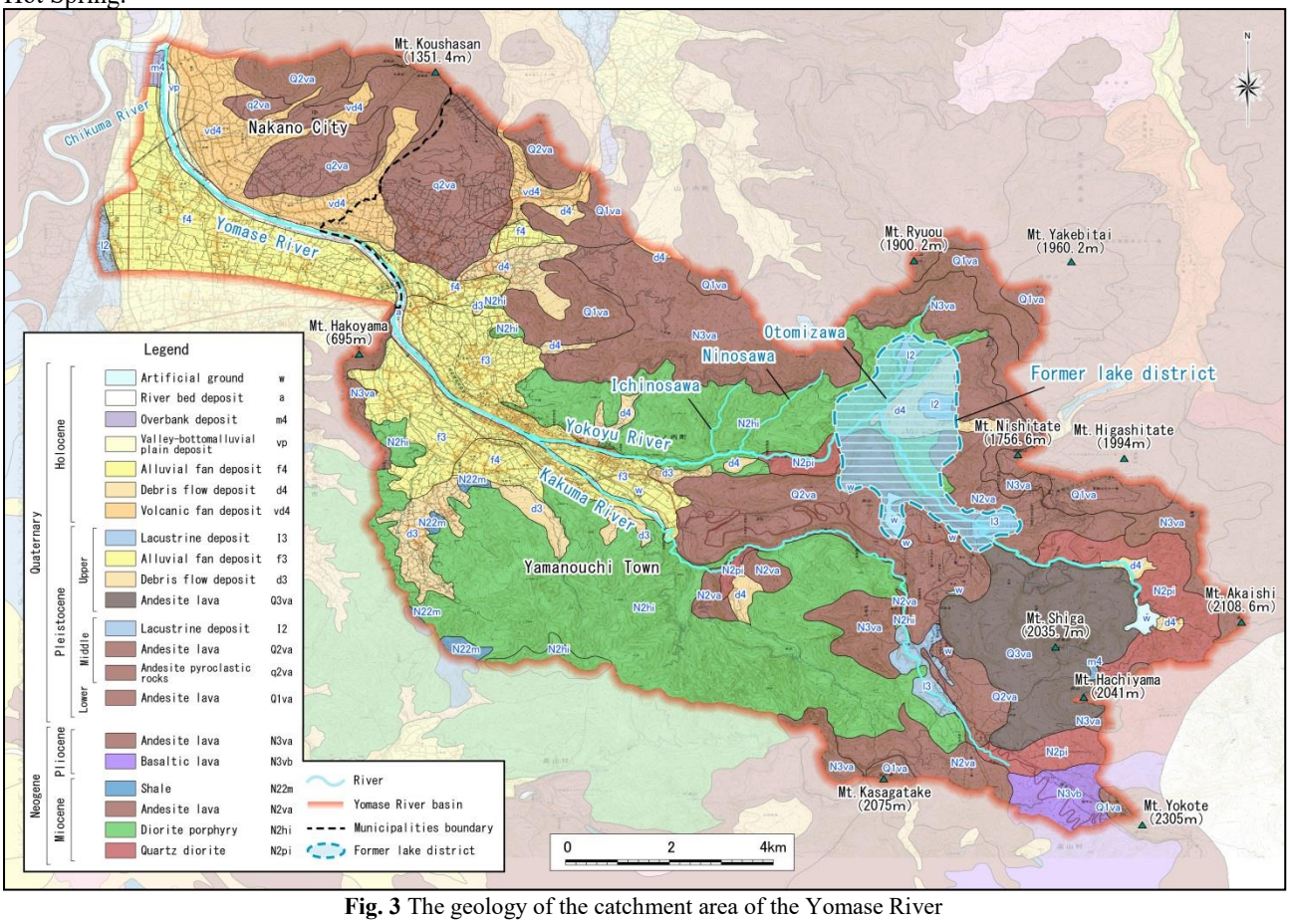

Fig. 3 The geology of the catchment area of the Yomase River

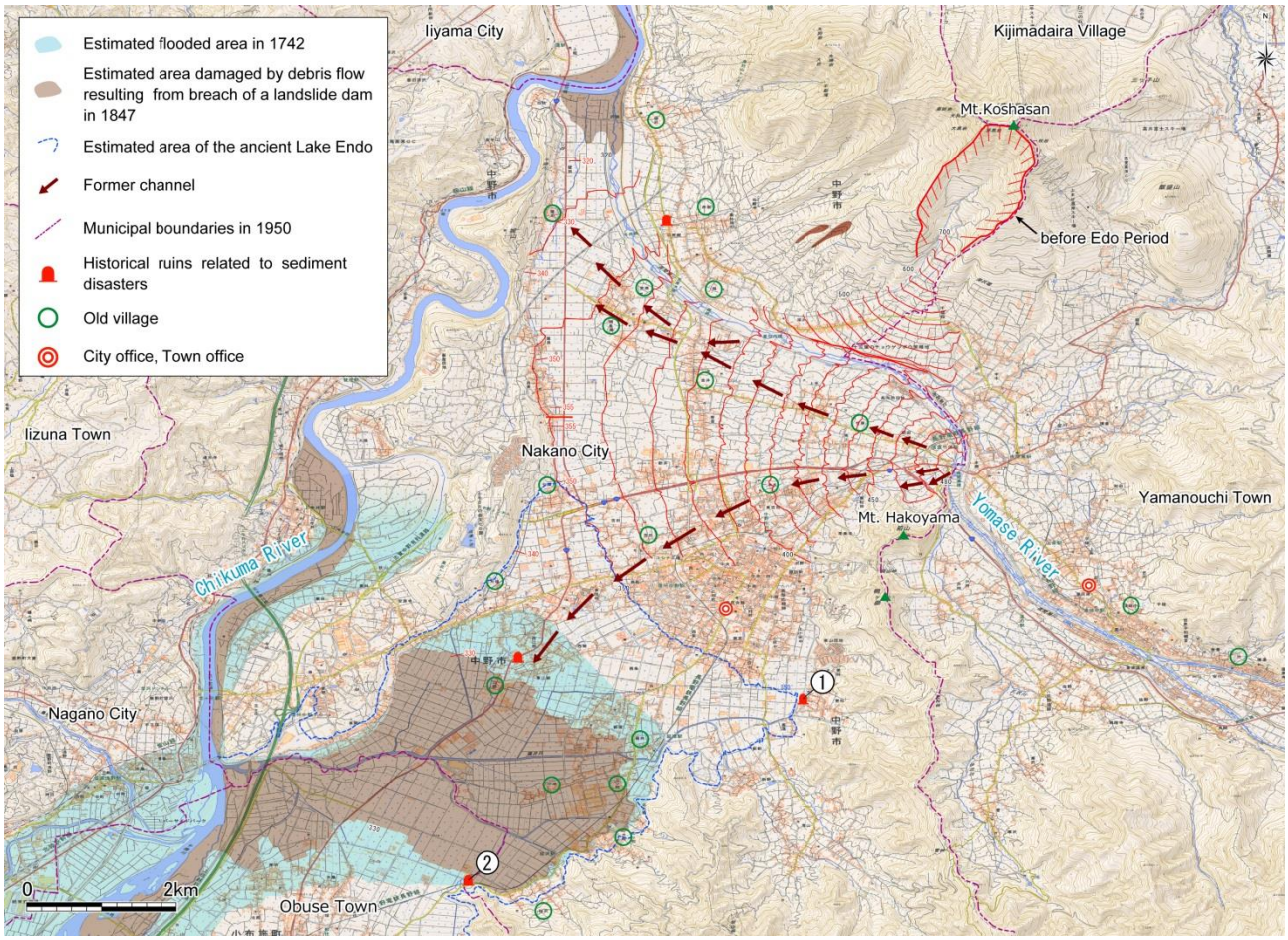

Fig. 4 Damage map of the alluvial fan of the Yomase River

Fig. 5 Boat-mooring stones in the compound of Takaifunatsuki Shrine (Fig. 4, Historical ruins related to sediment disasters ①)

Fig. 6 Remnants of a boat-mooring stone of Sakurasawa (Fig. 4, Historical ruins related to sediment disasters ②)

Fig. 7 Part of the Shinshu Earthquake Illustration (illustration of the Zenkoji Earthquake in 1847) (stored at the Sanada Treasures Museum)

5. HISTORY OF SEDIMENT DISASTERS AND THE SABO PROJECTS

The Nagano prefectural government started sabo work for the Asa River, Ushibuse River, and Hoshina River when the Sabo Act was promulgated in 1897, and started a sabo project in the upstream reach of the Yokoyu River, a right tributary of the Yomase River, in 1906. **Fig. 8** is a 1908 map of the sabo facility construction locations in the Yokoyu River stored in the Nagano Prefectural Museum of History. It was found that many sabo works were planned and constructed near the bottom of the Ochiai Landslide area (the Birikuso area) near the confluence of Ryuozawa on the right bank of the Yokoyu River. In those days, major works included dry masonry dams, diversion canal works, and sodding works. However, a serious sediment disaster occurred in August 1910, and the majority of the sabo facilities constructed were destroyed and washed away. Almost none survived until today. While some facilities under planning can be seen in **Fig. 8**, this diagram is very valuable as a layout map of sabo facilities constructed from 1906 to 1910.

In the 5th Book of the History of Nagano Prefecture (1915), it is recorded that sabo facilities constructed between 1906 and 1910 were seriously destroyed by a flood disaster in 1910, and since the damage was so serious that it was judged impossible to reconstruct them, it was decided that those facilities be put to disuse. Hence, the sabo project was aborted in October 1910.

However, partially due to the strong petition from affected local residents, the Home Ministry started a sabo project, as a national project, in the upstream reach of the Shinano River in 1918, and the Yokoyu River was included in the project area. The facilities were constructed directly by the Hirao Sabo Factory of the Niigata Civil Engineering Branch Office until 1933, and 65 sabo facilities were constructed for the Yokoyu River. Many of them still remain extant. The field survey discovered some of those facilities including wet masonry dams.

In 1932, a public works project for rural promotion was planned. The authority of this project was transferred from the Home Ministry to Nagano Prefecture, and the sabo works project was then started as prefectural public works.

In 1964, the Jigokudani Yaen-Koen Monkey Park opened. International fame followed, and many tourists came to visit the valley of the Yokoyu River.

After a disaster in 1990, the Ochiai area was designated as a landslide prevention area, and full-scale landslide control works started.

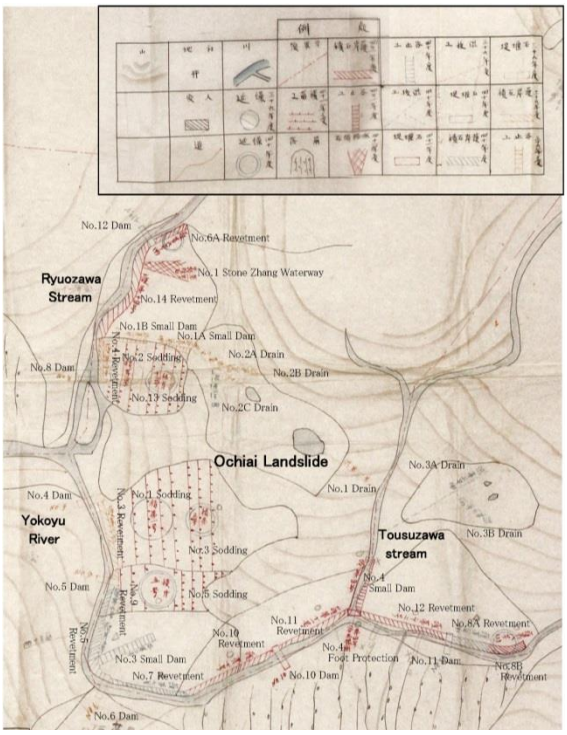

Fig. 8 A sketch of the sabo facility locations in the Yokoyu River in 1908
(stored in the Nagano Prefectural Museum of History)

6. DEVELOPMENT OF THE HONAMI HOT SPRING TOWN AND THE DISASTER IN 1950

According to the Publication Society of Yamanouchi Town History (1973), the Honami area located on the opposite side of Yudanaka Hot Spring was devastated and denuded by a flood in 1898 and had remained barren land for a long time. In 1925, a hot spring was found by drilling at Honami, and channel works were developed for the Yomase River, which led to Honami's establishment and prosperity as a hot spring community.

A torrential rainfall in August 1950 caused a flash flood and burst the dike on the left bank of the Kakuma River. Debris entered into the Honami Hot Spring, killing six people and destroying many buildings and cultivated land (**Fig. 9** to **13**).

In response to this damage, many channel works were constructed centering on the area near the confluence of the Yokoyu River and Kakuma River, and Honami Hot Spring Town was restored.

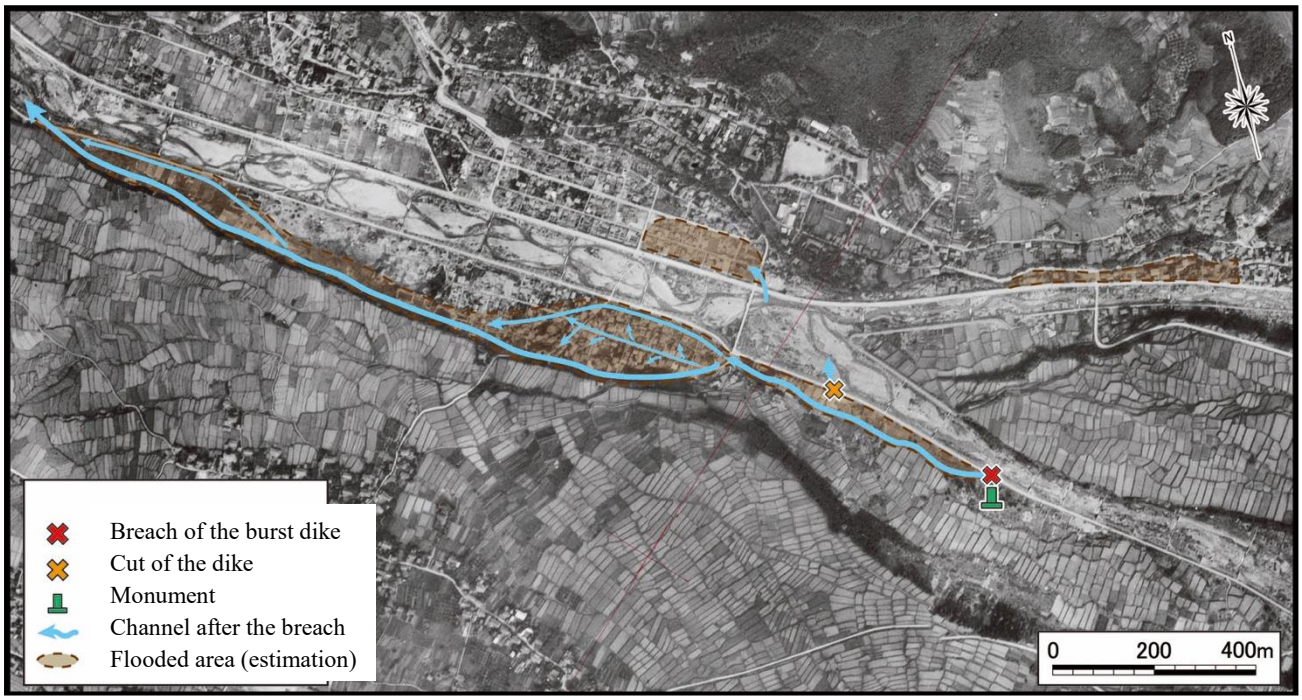

Fig. 9 Status of damage in 1950 (aerial photo taken by the US Forces in 1947)

Fig. 10 Status of disaster

Fig. 11 Status of disaster

Fig. 12 Dike breach

Fig. 13 Monument at the former site of the Honami Hot Spring flood damage

7. DISCUSSION

It is understood that the first use of concrete in the construction of sabo dams was the Ashiyasu Sabo Dam in the Midai River in Yamanashi Prefecture. This dam was started construction in 1916. It is reasonable to believe that when concrete came to be used as a construction material, it had a major effect on the sediment control works for the Yomase River, where sabo facilities had been often washed away by floods. One of major causes of sabo dam destruction is the scouring of the foundation. Considering the fact that scouring is more likely to be caused by flooding in a river with wide catchment area and a greater bed slope, the locations of well-known historical sabo facilities (excluding stepped dams), including those of the Yomase River, are analyzed with the catchment area and bed slope as indicators (**Fig. 14**).

The No. 34 and No. 28 Sabo Dams, constructed as a direct project of the national government, were constructed as wet masonry dams at locations where dry masonry sabo dams had been constructed in the Meiji Period. These two dams still remain today (**Fig. 15** and **16**).

The analysis revealed that more dry masonry sabo dams are located in zones where the river catchment area is smaller and the bed slope is softer compared with wet masonry sabo dams. Sabo dams, which were originally built as dry masonry dams but replaced by wet masonry dams, are located between dry masonry zones and wet masonry zones.

This research includes reorganization of data from these viewpoints, for example, and it is expected to provide information useful in our review of the limit conditions related to the construction conditions of dry masonry dams used from when they were constructed and our discussion on future preservation planning.

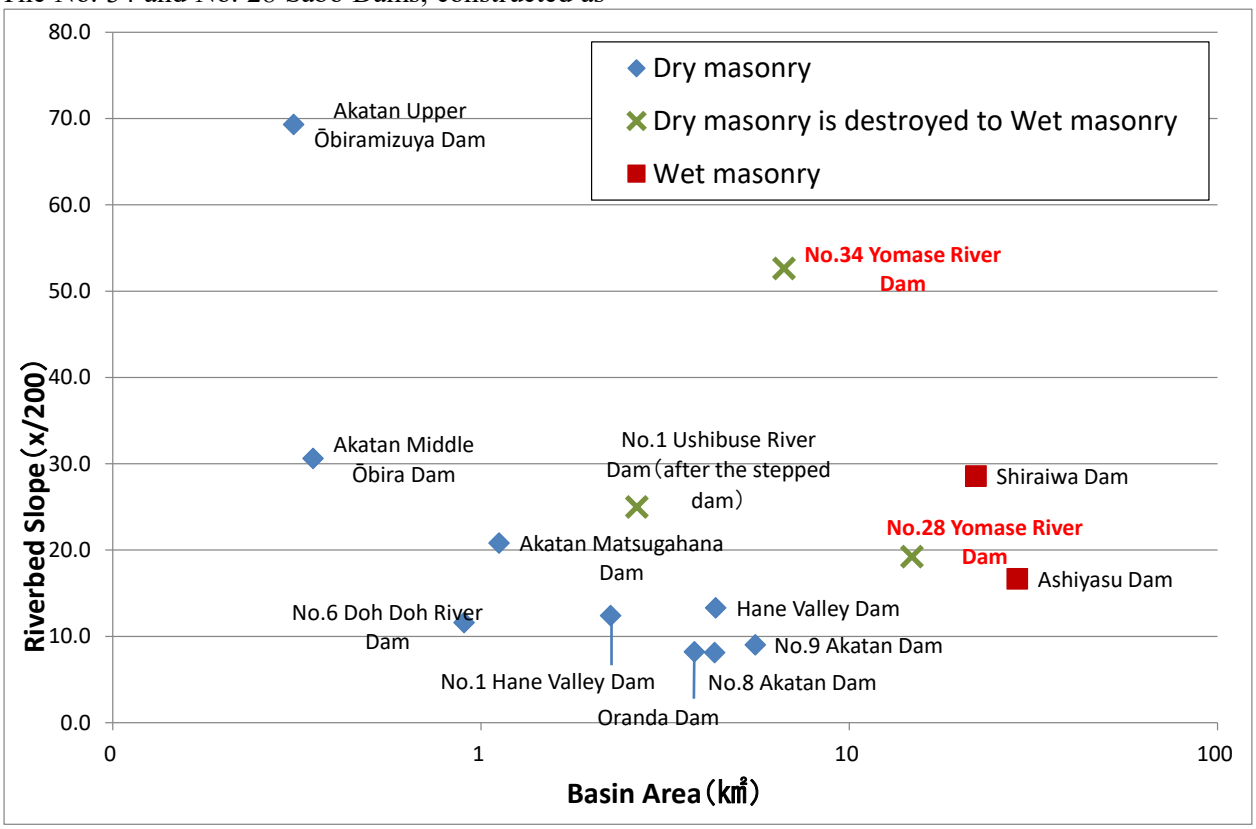

Fig. 14 The relationship among historical sabo dams, basin areas, and riverbed slopes

Fig. 15 No. 28 Sabo Dam of the Yomase River (constructed in 1924)

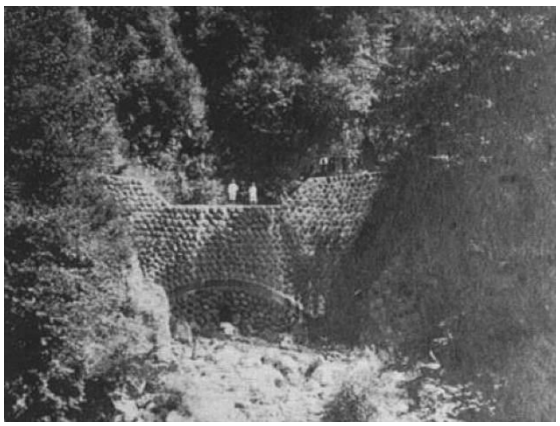

Fig. 16 No. 34 Sabo Dam of the Yomase River (constructed in 1923)

8. CONCLUSIONS

Our research provided valuable data that helps us to understand the development of sediment control and landslide control measures for the Yomase River. **Fig. 8** contains very valuable information on the layout of sabo facilities constructed at the end of the Meiji Period. It also provided us with the knowledge useful in reviewing the limit conditions about the then construction conditions of dry masonry dams and future preservation.

Many sabo dams were constructed in the Yokoyu River and Kakuma River basins even after the end of World War II. In addition, many channel works have also been constructed in the Yokoyu, Kakuma, and Yomase Rivers, which ensures greater safety for hot spring resorts.

Full-scale research and control work started in the Ochiai landslide prevention area in 1978. Many collection wells and drainage tunnels were constructed up until 2016, and it is understood that these facilities control landslide anomalies.

However, some measuring devices have indicated changes in the snow-melting period of 2017. In response, we intend to conduct a field survey again to check landslide anomaly points and reconsider the landslide occurrence mechanism in conjunction with the topographic and geologic conditions of the area.

The year 2018 will mark the 100th anniversary of the start of sediment control works for the sabo project for the Yomase River, as a direct project of the central government.

The authors intend to construct new sabo dams, improve existing sabo dams (including raising of the height of the dams), and repair existing sabo dams to prevent the degradation or deterioration of their functions or performance and further ensure the safety of the downstream reaches, including reinforcement of measures against woody debris. Since it is feared that awareness of disaster management has diminished because a few decades have passed without a major sediment disaster, the authors intend to put in order the records of past sediment disasters and sabo and landslide prevention projects conducted in the catchment area of the Yomase River and think up effective measures to encourage local residents to reacquaint themselves with the danger of sediment disasters and improve their sense of disaster preparedness.

REFERENCES

Editing Committee of the History of Honami Hot Spring Area and Editing Office of the History of Honami Hot Spring Area (1991): History of Honami Hot Spring Area, p. 459.

Inoue, Kimio, et al. (2017): History of Sediment Disasters and Sabo and Landslide Prevention Projects for the Yomase River, the Japan Landslide Society, Collection of Papers from the 56th Annual Meeting of the Japan Landslide Society, 1-5.

Inoue, Makoto (2009): Study How to Utilize the DEM for Geological Information, No. 1 Slope Gradation Map, Geographical Data Processing, Vol. 20, No. 2, pp. 114-115.

Japan Sabo Association (1981): History of Japanese Sabo, p. 1368.

Kanbara, Junichi, et al. (2017): History of Topographical Formation and Sediment Disaster and Sabo Projects for the Yomase River, Collection of the Papers from the 2017 Annual Meeting of the Japan Society of Erosion Control Engineering, Pb-98.

Nakano City History Editing Committee (1981): History of Nakano City - Nature, p. 559.

Nakano City History of Chikuma River Flood Control History Editing Committee (1994): Flood Control History of the Chikuma River of Nakano City, p. 350.

Publication Society of Yamanouchi Town History (1973): History of Yamanouchi Town, p. 1416.

Sediment Control Section, Civil Engineering Department, Nagano Prefecture, and Nagano Prefectural Flood Control and Sabo Association (1992): History of Nagano Prefecture's Sabo, 1992 - 50th Anniversary of Establishment of the Sabo Section, p. 365.

Shinano River Upstream Direct Sabo Work 100 Year History Editing Committee (1979): History of Matsumoto Sabo - Shinano River Upstream Direct Sabo 100 Year History, p. 893.

Wakita, Koji, and Inoue, Makoto (2011): Japanese Geosites Presented in Terms of Geology and Topography - World Developed by Slope Gradation Map, p. 168.

Yomase River General Irrigation Association (1939): History of the Hakkago Union, p. 153.

Topic 5: Non-structural countermeasures: Early warning and hazard mapping

A Pilot Construction of a Real-Time Monitoring System for Slow-Moving Landslide, Republic of Korea

Dongyeob KIM[1*], Changwoo LEE[1], Choongshik WOO[1], Junpyo SEO[1], Minjeng KANG[1], Kidae KIM[1], Man-Il KIM[2] and Jaehyun PARK[3]

[1] Department of Forest Disaster Management, National Institute of Forest Science
(57, Hoegi-ro, Dongdaemun-gu, Seoul 02455, Republic of Korea)
[2] Forest Engineering Research Institute, National Forestry Cooperative Federation
(1800, Dongseo-daero, Daedeok-gu, Daejeon 34417, Republic of Korea)
[3] Department of Forest Resources, Gyeongnam National University of Science and Technology
(33, Dongjin-ro, Jinju-si, Gyeongsangnam-do 52725, Republic of Korea)
*Corresponding author. E-mail: Dongyeob.kim1@gmail.com

The objective of this paper was to introduce a recent case of slowing-moving landslide in Republic of Korea, and discuss utility of a monitoring system for the landslide as a preventive measure. The study site was a 2.6 ha slow-moving landslide area situated in the Southern part of Korean Peninsula. Preliminarily, eight-month-temporary monitoring with fixed stakes was conducted, and its result indicated the moderate probability of landslide movement despite of measurement error. Moreover, following detailed site investigation support the landslide progress with the results of underground tests. Considering results of the preliminary monitoring and investigation with an expense of restoration work, a real-time and sensor-based monitoring system using the ubiquitous sensor network technique was finally introduced to the study site. The system was designed to provide emergency measures by real-time monitoring for the slow-moving landslide. The results of its three-month operations showed that the landslide appeared to enter a stable phase, but the system had high missing rate of sensors more or less. Consequently, the monitoring system could be cost-effective measure compared to restoration work, but it still requires improved hardware performance such as lower data missing rate.

Key words: slow-moving landslide, real-time monitoring system, non-structural measure, sensor threshold

1. INTRODUCTION

In Republic of Korea, 10-year average of damaged area by sediment-related disaster has been increased by threefold from 231 ha in 1980's to 713 ha in 2000's [*Korea Forest Service*, 2013]. However, it has shown signs of decrease to 256 ha in 2010's (2010-2017). Accordingly, budget for structural measure such as debris barrier dam has been reduced gradually since middle of 2010's. A reduction in the budget for the structural measure causes various changes in the policy of sediment-related disaster. Against this backdrop, the Korea Forest Service (KFS) is committed to fully utilizing cost-effective non-structural measure such as operation of shallow landslide forecast system, establishment of early warning and evacuation system, and designation of vulnerable area.

Sediment-related disaster occurring in Republic of Korea has some characteristics: it occurs mostly in the rainy season, and the dominant types are rapid, shallow landslides and its transformed debris flow. Meanwhile, although a slow-moving landslide has been rare in Republic of Korea so far, recent years has witnessed an increase in the number of such landslide with official reports of the slow-moving landslide including 28 cases in 2013 and 35 cases in 2017. Because compared to its very slow progressing pace of 0.01-10mm per day [*Woo et al.*, 1996], it happens in huge area relatively deep underground and occurs around urbanized areas such as construction area in mountainous residential area or road slope, slow-moving landslide has drawn social interest.

In other countries, various types of study on slow-moving landslides have been conducted since mid 1900's along with long term monitoring. *Handwerger et al.* [2013] analyzed the deformation characteristics of ten slow-moving landslides ranged from 16 to 310 ha in North California, U.S. by InSAR technology. In addition, *Miao et al.* [2014] conducted ring shear

tests on soil samples taken from 21 slow-moving landslide sites to identify mechanism of the landslides in Jurassic red-strata in the Three Gorges Reservoir, China. In this study, the sizes of the slow-moving landslides were 2 to 50 ha and they were monitored using by GPS system. Meanwhile, *Van Asch et al.* [2007] discussed problems in predicting the mobility of slow-moving landslides based on monitoring result of the La Valette landslide, the 7.2 ha-landslide areas located in the French Alps. However, while the events of slow-moving landslides in abroad are mass-scale but occurred in non-urban areas, Korean events have characteristics of occurring mostly in urban areas. Against this backdrop, the Korean government has to come up with much active and systematic policy to deal with this situation.

The present paper is to introduce a recent case of slowing-moving landslide monitoring and the establishment and operation of the real-time and sensor-based monitoring system in Republic of Korea. Furthermore, advantages and shortcomings of establishment and operation of the monitoring system as for countermeasure against a newly emerging 'slow-moving landslide' are discussed.

2. STUDY SITE

The study site is a slow-moving landslide area situated in the Hadong city, Gyeongsangnam province of Korean Peninsula (**Fig. 1**). With an estimated damaged-area of 2.6 ha, the site of slow-moving landslide is located in the quite low hill whose highest elevation is 300 m a. s. l. Its ground comprises of anorthosite of metamorphic rock and is predominantly occupied by 40-years-old oak species and bamboo species. At the upper part of the landslide area, forest road was constructed for forest management. And the reservoir for drinking water is close to lower part of the area. If sediment inflows to the reservoir when slow-moving landslide happens, reservoir overflow could cause secondary damages to neighboring residential areas. Although slow-moving landslide was reported by local governmental officials in Korea for the first time in April 2015, it is assumed from local residents' statements that such phenomenon has already been progressed since early 2000's.

At this area, indicators following slow-moving landslides, including tensile crack and trees growing bended and twisted, are easily found. *Western Regional Office of KFS* [2016] reported that tensile

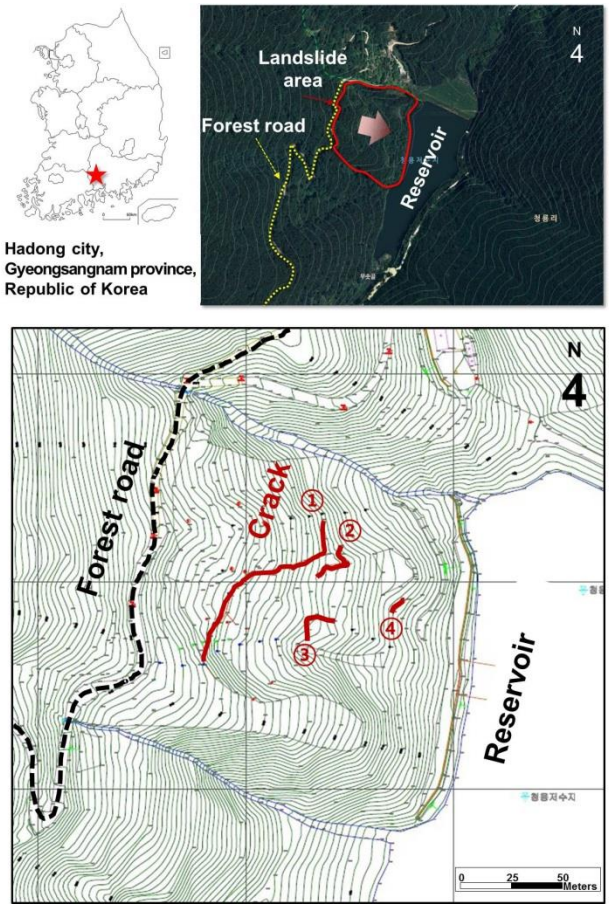

Fig. 1 Location of the study site and the distribution of tensile cracks

Fig. 2 Site photos taken from the tensile crack of the study site (upper: crack ①, lower: crack ②)

cracks were found in 4 areas (**Fig. 1** and **2**) and assumed that tensile cracks developed as slow-moving landslide progressed toward south-east. The width of each tensile crack ranged from between 0.2 to 0.5 m with its level difference from 0.25 to 0.45 m. A total length of 4 areas of tensile cracks is 170 m, and among which, the longest crack of more than 100 m is situated in the upper slope.

Kim et al. [2016] conducted temporary monitoring on displacement of tensile fracture by using fixed stakes from August 2015 to March 2016. They installed 5 fixed stakes at 5 meters apart to manually measure lengths between each 5 fixed stakes every month on the longest tensile crack.

The results found that the final length increased by 10.4 cm compared to the initial length measured eight months ago. Based on the results of the temporary monitoring, the need to conduct detailed site investigation had been steadily raised.

3. DETAILED SITE INVESTIGATION

Western Regional Office of KFS assigned detailed site study for slow-moving landslide to the National Forestry Cooperative Federation to conduct surface survey, underground survey with borehole test, in-situ geotechnical test and electrical resistivity test in July of 2016.

At the detailed site investigation for the slow-moving landslide area, a total of 8 borehole investigations were conducted to identify geological, geotechnical and hydrological characteristics of the area. The results showed that while the maximum thickness for colluvium for this area was 12.8 m and weathered soil layer was between 3.0 m to 19.4 m, the thickness for weathered rock layer was distributed thinly within 1.5 m. In addition, when looking up the slow-moving landslide slope with backdrop of the reservoir, soil layer of the left side was thicker than one of the right side from the same altitude above sea level. Therefore, it was concluded that the thick soil layer of the left side reflected the slope of rock layer.

Along with this, the electrical resistivity survey on crack ① in **Fig. 1** proved that distribution of weathered layer gradually became thicker from right to left of the layer, corresponding well with those of borehole investigations. In addition, the borehole image log interpretation on the center of the landslide slope found cavity at the depth of between 8.3-8.8 m under surface, and direction of the joint set of bedrock was similar with those of slow-moving landslide slope as 37 ° /157 ° (dip angle/dip direction).

Overall, it was assumed that colluvium and weathered anorthosite layers distributed thickly as well as loosely had the site move downwards slowly. Moreover, on the evidence of a possibility of having cut the lower part of the area when constructing the reservoir and the potential changes of groundwater level cause by the reservoir water level, ‘constructing reservoir’ was judged as one of the critical factors that accelerated the slow-moving landslide.

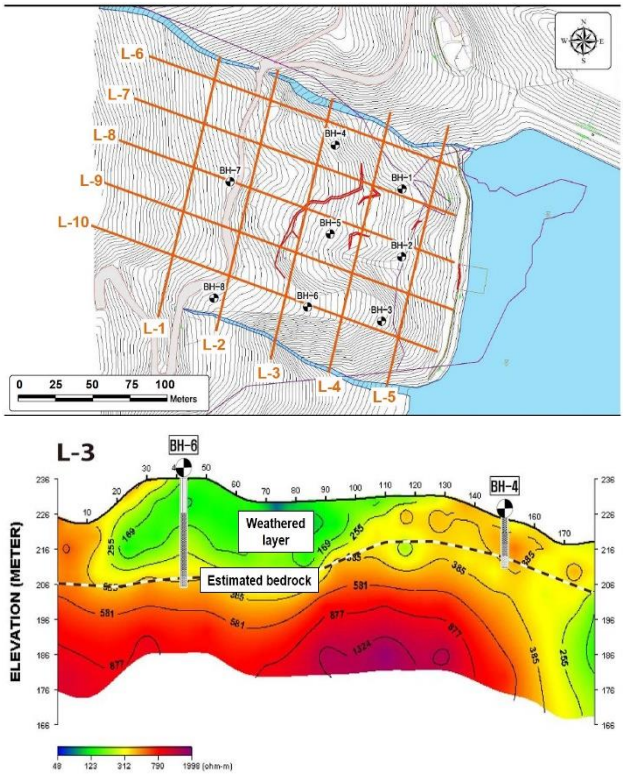

Fig. 3 Result of the electrical resistivity survey (L-3 cross section) on the study site

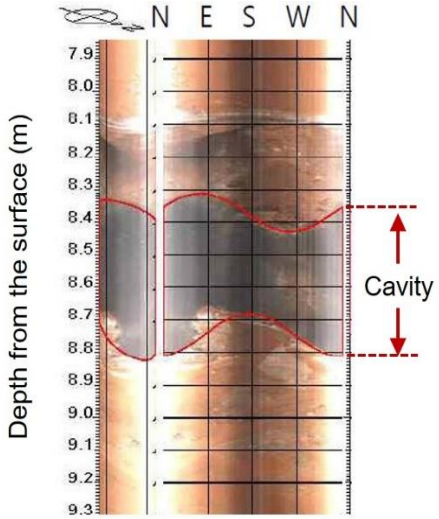

Fig. 4 The borehole image capturing cavity at the depth of 8.3-8.8 m from the ground surface

4. REAL-TIME AND SENSOR-BASED MONITORING SYSTEM

4.1 Overview

Generally, landslide restoration works including pile and water collector well have been carried out as preventive measure after detailed filed investigation in Republic of Korea. However, monitoring system using measuring sensors were finally chosen at the site of slow-moving landslide in Hadong after considering issues of securing expenses of restoration work and slow pace of the slow-moving landslide.

Monitoring system was designed to provide emergency measures such as evacuation measure for local residents if necessary by monitoring slow-moving landslide real-time. Monitoring system consists of three main parts, of i) sensor part, ii) communication part, and iii) data collection server and analysis system (**Fig. 5**). Sensor part refers to all sorts of sensors installed at the site to notice slow-moving landslide directly or indirectly. In December of 2016, 6 wire extensometers, 2 borehole inclinometers, 2 groundwater level meters and 1 rainfall gauge were placed. 6 wire extensometers were installed centering on the 2 tensile cracks situated on the up-slope of the site. A borehole inclinometer and a groundwater level meter were set up respectively at the upper and lower part of the slope. As for the rainfall gauge, it was set up closer to the forest road with its top exposed to prevent interference of trees(**Figs. 6** and **7**).

Communication part where ubiquitous sensor network (USN) is applied is in charge of transmitting data measured from the sensor to data collection server indoor. Every single data measured from each sensor is collected to the gateway through the sensor node. And then, such collected data from the gateway is transmitted to data collection server in the analysis center of the National Institute of Forest Science in Seoul, Republic of Korea. There is a total of 4 sensor nodes and 1 gateway installed at the competent area of slow-moving landslide (**Fig. 7**).

Data collection server and analysis system is responsible for continuously storing raw data measured from the gateway, conducting close analysis on the hazard information and sending them to persons in charge of. If the measured data reaches beyond the threshold which had been set by sensors before, analysis system forwards hazard information through SMS to the designated persons. This system also allows users to search for and display the existing data stored before.

Monitoring system for the slow-moving landslide in Hadong completed its installation in December 2016. After undergoing setting time for smooth operation of the instrument, monitoring system has been in full operation since May first, 2017. Currently, it is run on solar battery with its measurement interval of every hour. Threshold of hazard messaging for sensor is only applied to the wire extensometers. When the measured displacement of each wire extensometer exceeds 10 mm, it is supposed to be sent to persons in charge of from the National Institute of Forest Science and Korea Forest Service.

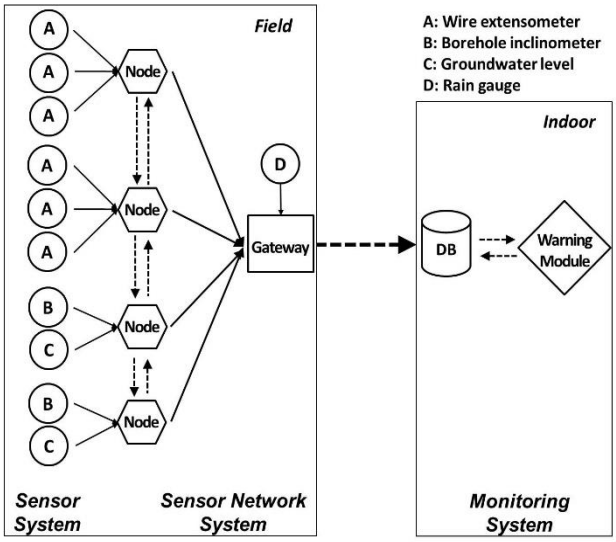

Fig. 5 Schematic diagram of the slow-moving landslide monitoring system at study site

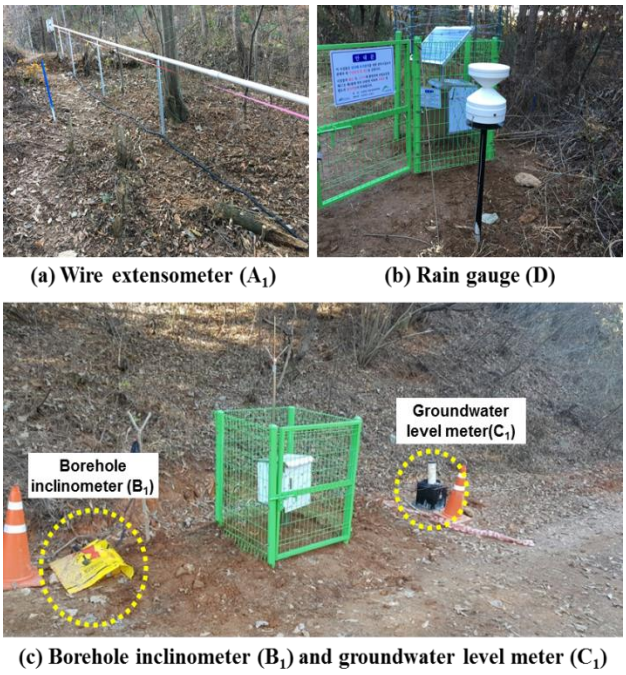

(a) Wire extensometer (A_1) (b) Rain gauge (D)

(c) Borehole inclinometer (B_1) and groundwater level meter (C_1)

Fig. 6 Sensors installed at the site

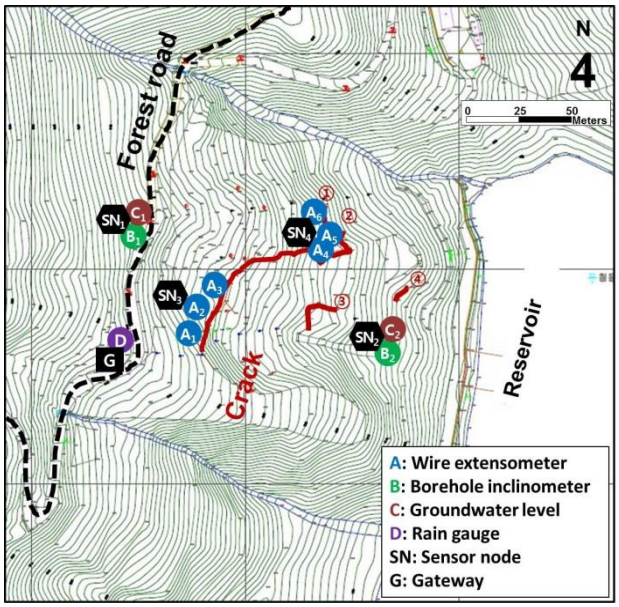

Fig. 7 Sensor arrangement of the monitoring system at the field

Table 1 Result of ratio of missing values by sensor nodes

Month	Sensor node			
	#1	#2	#3	#4
May	0.3%	0.7%	0.3%	9.9%
June	1.7%	4.4%	2.2%	12.5%
July	0.3%	7.0%	0.4%	10.9%
August	0.8%	3.2%	0.8%	8.3%
September	2.1%	2.9%	0.6%	1.9%
October	1.3%	1.9%	0.3%	0.5%
November	0.4%	0.4%	0.4%	0.4%
December	5.5%	8.9%	5.6%	5.9%
Average	**1.5%**	**3.7%**	**1.3%**	**6.3%**

4.2 Result of monitoring

Since May 1st in 2017, monitoring has been conducted until now and this paper includes data analyzed for 8 months from May to December, 2017. The monitoring results showed that the landslide was not accelerated during the period. The monthly rainfall ranged from 0 mm (November) to 270 mm (August), and the groundwater table varied depending on rainfall but finally get lowered to 14.0 m underground at the upper slope (C1) and 12.5 m underground at the lower slope(C2), respectively (**Fig. 8**). Meanwhile, there were no significant displacements exceeding measuring errors of sensors for 6 wire extensometers and 2 borehole inclinometers, respectively.

Table 1 presents results of missing rate of measurement data by monthly and each sensor node. During the period, the total missing rate stood at 3.2% and monthly missing rate of sensor node #4 was 6.3% of the highest. When considering the fact that all the missing values occurred simultaneously from the sensors connected to the same sensor nodes, cause of the missing was boiled down to 'communication part', that is to say, the matter of sensor nodes. It is reasonable to conclude that weather conditions, i.e. daily highest and lowest temperature, were the main cause of communication part error when assuming from the relationship of temperature and missing rate in daily. However, to pinpoint the clear cause of the missing data, close analysis is required on the results conducted during relevant monitoring period.

5. DISCUSSION AND CONCLUDING REMARKS

Monitoring system has been in operation now since the detailed filed study was completed at the competent area of slow-moving landslide. According to the results of monitoring conducted so far, slow-moving landslide is considered to enter a stable phase. However, it is highly possible that progressing speed will be faster again if groundwater level changes caused by localized heavy rain or reservoir level fluctuation. If current slow-moving landslide continues to reaches the point where accumulated surface displacement exceeds 10 mm by wire extensometers, it is expected that related agencies such as Western Regional Office of KFS could take prompt and expeditious actions by sending hazard information to a person in charge of real time.

Although a slow-moving landslide monitoring system is not the fundamental measure to eliminate dangers, it could be an effective way in terms of installment / operation expenses of monitoring system compared to expense for restoration work. While the minimum expense of restoration works for this area was estimated at 1 million dollars, it took (only) 150,000 dollars to establish the monitoring system. However, relatively high missing rate indicates that monitoring system shall be improved for its better function. And the current sensor threshold used to send hazard information is deduced after applying the Japanese standard shown in **Table 2** [*Public Work Research Institute, Japan*, 2007], not the Korean standard. Therefore, it calls for efforts aiming at drawing the threshold which reflects characteristics of slow-moving landslides occurring in Republic of Korea. The hardware performance and effectiveness of the monitoring system require improvement by carrying out long-term monitoring and flume experiment for various types of slow-moving landslide.

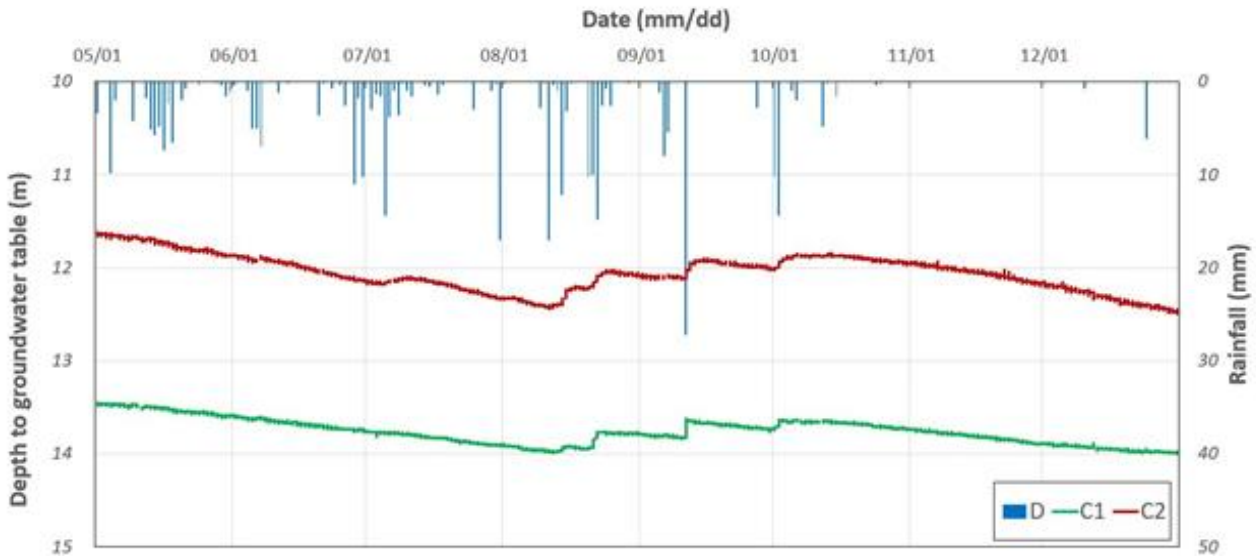

Fig. 8 Temporal variation of groundwater tables of the site with rainfall (D = rainfall, C1 and C2 = groundwater table in **Fig. 7**)

Table 2 The warning thresholds according to wire extensometer measurements

Level	Watch	Alert	Evacuation	No entry
Threshold	1 mm/d	10 mm/d	2 mm/h × 2 or 4 mm/h	10 mm/h

REFERENCES

Handwerger, A.L., Roering, J.J. and Schmidt, D.A. (2013): Controls on the seasonal deformation of slow-moving landslides, Earth and Planetary Science Letters, Vol. 377-378, pp. 239-247.

Kim, K., Kang, M. and Park, J. (2016): Experimental research for collapse of tension crack in land creeping area - The case of land creeping area in Okjong, Hadong, Journal of Agriculture and Life Science, Vol. 50, No. 6, pp. 11-17. (in Korean with English abstract)

Korea Forest Service (2013): 2013 Detailed Strategy for Primary Policy, http://ibook.forest.go.kr/Viewer/R-GSDN3 GDGDFX (accessed: Dec. 12, 2017).

Miao, H., Wang, G., Yin, K., Kamai, T. and Li, Y. (2014): Mechanism of the slow-moving landslides in Jurassic red-strata in the Three Gorges Reservoir, China, Engineering Geology, Vol. 171, pp. 59-69.

Public Work Research Institute (PWRI), Japan. (2007): Guidelines for Preventing Landslides and Commentary (Proposal), PWRI Report No. 4077. 163pp. (in Japanese)

Van Asch, Th.W.J., Van Beek, L.P.H. and Bogaard, T.A. (2007): Problems in predicting the mobility of slow-moving landslides, Engineering Geology, Vol. 91, pp. 46-55.

Western Regional Office of KFS (2016): Report on Investigation of Cause of Hadong Slow-Moving Landslide Area and Its Restoration Work, 196pp. (in Korean)

Woo, B.M., Park, J.H., Choi, H.T., Jeon, G.S. and Kim, K.H. (1996): A study on the characteristics of the landslide in Hyuseok-dong (I) - Topographical characteristics and surface displacement -, Journal of Korean Forest Society, Vol. 85, No. 4, pp. 565-570. (in Korean with English abstract)

Advanced Hazard Information and Methods for Appropriate Evacuation during Sediment Disasters

Kana NAKATANI[1*], Kazuki YAMANOI[2], Yuji HASEGAWA[3], Seiya HAYASHI[1], Shusuke MIYATA[4] and Masaharu FUJITA[4]

[1] Dep. of Erosion Control, Graduate School of Agriculture, Kyoto University, Japan
(Kitashirakawa, Sakyo-ku, Kyoto, Kyoto 6068502, Japan)
[2] Computational Disaster Mitigation and Reduction Research Unit, Advanced Institute for Computational Science, Inst. of Physical and Chemical Research (RIKEN)
(Minatojima-minamimachi, Chuo-ku, Kobe, Hyogo 6500047, Japan)
[3]Graduate School of Integrated Arts and Sciences, Hiroshima University, Japan
(Kagamiyama, Higashi-Hiroshima City Hiroshima, 7398521, Japan)
[4] Disaster Prevention Research Institute, Kyoto University, Japan
(Yoko-ojishimomisu Higashinokuchi, Fushimi-ku, Kyoto, Kyoto 6128235, Japan)
*Corresponding author. E-mail: kana2151@kais.kyoto-u.ac.jp

In Japan, recent sediment disasters have resulted in substantial damage. For appropriate evacuation to minimize damage, it is necessary to provide residents with suitable hazard information on a routine basis and to develop high awareness of disaster risks. Although numerical simulations are useful tools for obtaining advanced information, the associated systems are generally developed by experts with specialized knowledge and techniques. Consequently, non-expert residents experience difficulty understanding the input conditions and output results. Furthermore, the information that local governments and communities require to develop evacuation methods might be different from that received from researchers using simulations. To avoid this conundrum, we therefore presented our simulation systems to local government engineers and discussed examples of input and output data. The important factor was the simulation accuracy and reliability for applying to evacuation. Moreover, for providing information to local residents, we confirmed that the information for both the input and output data needs to be compared with the recorded or experienced rainfall or disaster events for intuitive understanding. To utilize numerical simulations as effective information, we applied the proposed simulation system to a village in Miyazu City, Kyoto Prefecture with three scenarios considering past disaster rainfall records. For secure high accuracy and reliability to the target site, we conducted field survey and observation, and estimated some suitable parameters, then run simulations. And we presented the results of our simulations on GIS, which better helps residents to be cognizant of the disaster risks.

Key words: sediment disasters, advanced hazard information, providing methods, evacuation, numerical simulations

1. INTRODUCTION

In Japan, recent sediment disasters have caused substantial damage. In August 2014, Tamba City, Hyogo Prefecture and Hiroshima City, Hiroshima Prefecture were affected by sediment disasters caused by heavy rainfall. Although the difference in the estimated volume of sediment displaced in the two disaster was not significant, the respective number of fatalities in Tamba was one. In Tamba, local governments and communities had been working together toward disaster prevention. Consequently, residents were highly aware of sediment disaster risks; during the rainfall, appropriate evacuation advice, namely, vertical evacuation instead of moving to a shelter at the time of the flood in the night, was effective and minimized the damage.

Therefore, for appropriate evacuation, it is necessary to provide residents with useful hazard information on a routine basis and to develop high

awareness of disaster risks. In this study, aiming for appropriate evacuation against sediment disasters, we considered advanced hazard information and also useful means of providing such information.

2. STUDY OUTLINE

Since 2015, we have been conducting studies on sediment disaster risks and hazard information on several mountainside villages in Kyoto Prefecture, Japan. Not only have we been conducting field research and applying simulations, we have also been cooperating with local government engineers to discuss and search for effective information required for evacuation.

2.1 Simulation systems for advanced hazard information

Currently, most of the hazard information for sediment disasters, such as time and place, can be forecast using numerical simulations.

2.1.1 Outline of our recently proposed systems

We recently proposed a multi-hazard simulator (SiMHiS) based on the landslide prediction model and water and sediment runoff model in the watershed scale [*Yamanoi and Fujita*, 2017]. The system can spatially and temporally simulate the risk level of three multi-hazard categories: rainfall, landslide, and flood (see **Fig.1,** left). This system can provide a rough estimate of the time and magnitude of sediment disasters based on the rainfall condition; however, it cannot provide details of the flooding/deposition area and distribution.

We have also developed and applied a GIS-related debris flow simulation system called Hyper KANAKO [*Nakatani et al*., 2016]. Using this system and by setting specific debris flow scenarios, we can predict the details of the flooding/deposition area and the distribution and indicate which residential area is at risk (see **Fig.1**, right). However, users are required to set the specific input debris flow data, such as volume and time, due to the heavy rainfall.

2.1.2 Solving the problems affecting recent systems

We connected the two simulation systems in order to obtain advanced hazard information. When the initial rainfall data information is set, the system not only provides the occurrence time of sediment disasters but also indicates the flooding/deposition area and the distribution.

However, runoff process from rainfall to small basin such as 0.01-10 km^2 which faces debris flow risks in Japan is still not clear. Especially for large runoff event such as landslides and debris flows occur, the detail process is not clear but presumed that water and sediment seemed to move in large volume comparing to normal conditions. Applying runoff analysis such as SERMOW or other CommonMP tools, it can describe normal and small rainfall event and runoff, but usually underestimate large events. In basins with 5-10 km^2, empirically it is difficult to obtain runoff simulation results with peak discharge results larger than 10 m^3/s; though observed data show larger peak discharge. Therefore, for calculating rainfall, landslides, and runoff process in SiMHiS, parameters and input conditions must be estimated properly for the large rainfall event. To set suitable parameters, we need to acquire the target site information, such as recorded disaster data or with field survey and observations.

2.2 Providing effective information

In general, numerical simulation systems are developed by researchers and experts with specialized knowledge and techniques. Consequently, non-expert residents experience difficulty intuitively understanding the input conditions and output results. Furthermore, the information that local governments and communities require to develop evacuation methods might be different from that presented by researchers using simulations.

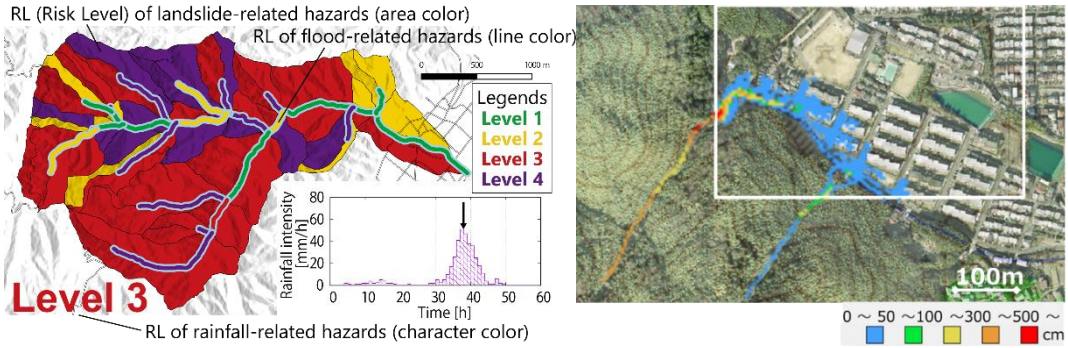

Fig. 1 Simulation results of Kyoto Prefecture (left: using SiMHiS, which considers multi-hazard; right: using Hyper KANAKO, which considers debris flow deposition)

Therefore, we presented our simulation systems to local government engineers in Kyoto Prefecture and in Miyazu City, and discussed examples of input and output data.

We obtained comments from the engineers. The important factor was the simulation accuracy and reliability for applying to evacuation. Moreover, for providing information to local residents, we confirmed that the information for both the input and output data needs to be compared with the recorded or experienced rainfall or disaster events for intuitive understanding (see **Table 1**).

To apply numerical simulations as effective information, researchers must consider the request, set input conditions, and improve the input and output to such an extent that it is sufficiently understandable for residents to realize the risk intuitively. Moreover, we have to consider the target recipients, such as local people, voluntary disaster prevention groups, and local government engineers, and provide information suitable for each standpoint and select the necessary information with appropriate style.

And for securing high accuracy and reliability to the target site, we need to acquire the target site information, such as rainfall, flow depth and discharge at the torrent and downstream site, sediment details such as size and thickness, flooding and deposition area and distribution. The preferable information is the recorded disaster or large rainfall event data, but those can't always be acquired except for the rainfall data. Especially, recorded discharge data in mountains torrent is few. But for accuracy verification, we must know those data somehow for considering the sediment disaster risk designated sites; in Miyazu City approx.600 and in Kyoto Prefecture approx.16,700 (on 2018 March). Therefore, when we don't have enough data for verifying, we can obtain data from field survey and observations. Although large-scale surveys and observations can get detail data but requires high cost, we tried to conduct with small-scale and get minimum requirement effectively in low cost. The minimum requirement seemed to be as following: rainfall data, discharge at basin or torrent downstream, sediment details.

3. STUDY TARGET: HATA RIVER

We conducted advanced simulation considering an effective provision method on Hata river, a local river administrated by Miyazu City, Kyoto Prefecture, Japan (see **Fig. 2**).

Table 1 Discussion results for providing effective information to residents

Data (input/output)	Comments
Rainfall (input)	Residents find it difficult to understand probable rainfall. The disaster scale can be understood using the records of past maximum rainfall or of rainfall during other disasters.
Flooding/deposition area or distribution (output)	Residents will realize the risks when the flooding/deposition area or distribution results of the recent disaster are compared with the past disasters results. Images or animation results on the GIS map will help residents realize the risks, but they might believe that the other scenarios may not occur.

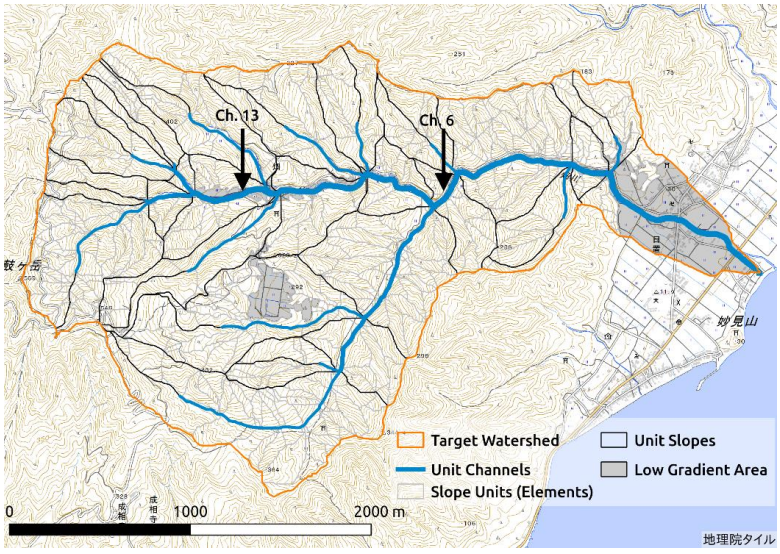

Fig. 2 Map of the simulation target watershed

3.1 Outline of Hata river

The Hata river watershed is 5.4 km^2. A residential area is located in the center of the watershed and is fully covered by the sediment disaster prone areas set by Kyoto Prefecture. Therefore, evacuation to the outside area of the watershed is important for the people when large-scale rainfall events that trigger flooding occur. There is only one road leading to the outside from the watershed, and it is quite close to the river, which has a high potential risk of overflowing its banks. Here, there weren't recorded discharge data at the downstream of torrent and basin at large rainfall, disaster event, or in small rainfall event.

In this study, we considered three sediment disaster scenarios due to heavy rainfall. Taking into account the provision of effective information for evacuation from simulations, we considered actual large rainfall events that recently occurred in Kyoto and other places.

3.2 Observations and field survey for setting simulation parameters

Runoff characteristics, such as depth of the soil layer and hydraulic conductivity, are very important for quantitatively estimating the rainfall runoff process. However, verification is difficult in small watersheds without discharge data, especially in a river managed by a local government. Therefore, we conducted a simple and low-cost observation utilizing a time-lapse camera (Brinno, TLC200) and identified the runoff parameters using the observed and field survey results.

The installation of the time-lapse camera is shown as Ch. 6 in **Fig.2**. The camera took one picture every 10 minutes, except at nights and in low-light conditions. **Fig.3** shows the pictures taken during a target flood event that occurred September 17–18, 2017. The water level during the event was estimated via visual observation of representative pictures. The large boulder, with a height of approximately 1.2 m, at the center of the picture was utilized as an indicator for the water level estimation. However, because the peak of the flood occurred during the night, no pictures were obtained for that even. Therefore, we estimated the peak water level value from the trace mark of the flood. From the sediments distributed on the large boulders by the flow, we estimated the maximum water depth as approximately 1.2 m.

Following estimation of the water level, we estimated the water discharge using Manning's formula (eq. 1), where n is the Manning's roughness coefficient, A is the cross-sectional area of the flow, S is the wet perimeter, and I is the slope of the hydraulic grade line-which seemed to be assumed being equal

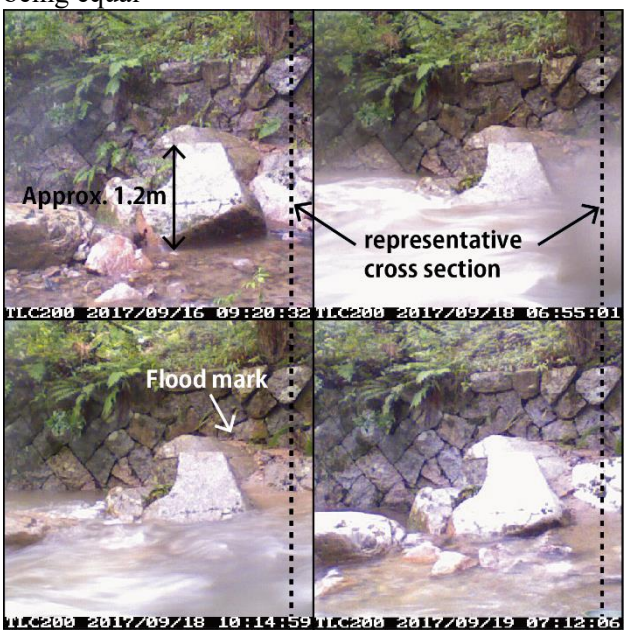

Fig. 3 Observed photo of the flood event that occurred on September 17–18, 2017, taken by Brinno TLC200 (A: One day before the event, B: During the event, C: Recession period of the event, D: One day after the event.)

to the channel bed slope.

$$Q = \frac{1}{n} A^{\frac{5}{3}} S^{-1} I^{\frac{1}{2}} \qquad (1)$$

The relationship between the observed water level (h) and A or S was estimated from the geometry of the representative cross-section shown in **Fig.4**. The location of representative cross-section is shown in **Figs. 3** and **5**. Furthermore, n was set as 0.04, and I was assumed to be 0.07 based on the longitudinal profile survey shown in **Fig. 5**. From **Fig.4** and field surveys and observed photos, normal river width seemed to be 2-3 m, and for the maximum flow depth time, the flow width was estimated approx. 10 m.

Applying this method, water discharge during the 2017/9/17-21 rainfall event was obtained as point plots in **Fig.6** and maximum water discharge was estimated at approximately 30 m^3/s.

4. CASE STUDY SIMULATIONS ON HATA RIVER

4.1 Calculation model and identification of runoff parameters on rainfall runoff model

As outlined in Section 2, *Yamanoi and Fujita* (2016) developed a SiMHiS (Storm induced Multi Hazard information System) that simulates a rainfall

runoff, sediment production due to landslide, and sediment transport in a watershed.

The model comprises a landslide prediction model

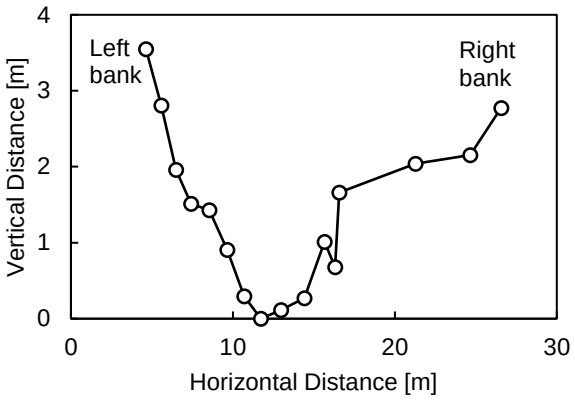

Fig. 4 Profile of the representative cross-section.

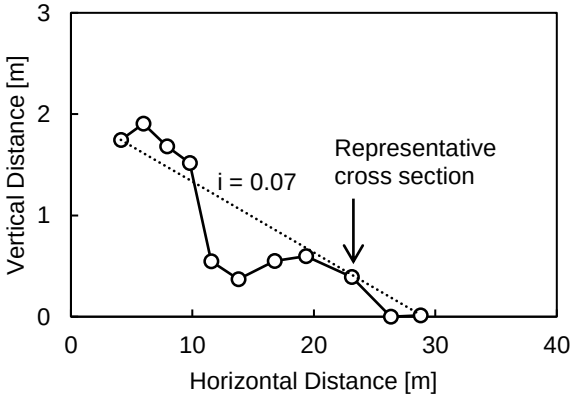

Fig. 5 Longitudinal profile around the observed channel.

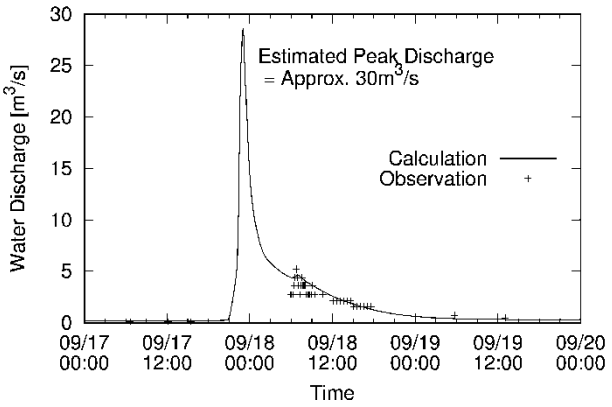

Fig. 6 Comparison between calculated and observed water discharge in the 2017/9/17–9/20 runoff event

based on a water content indicator [*Chen and Fujita*, 2014], a sediment supply model that considers the deposition volume outside the river, and a rainfall and sediment runoff model [*Egashira and Matsuki*, 2000]. The landslide prediction model is a simplified model of the integrated landslide prediction model of rainfall-infiltration adopting Richard's equation, slope stability analysis depends on a simplified Janbu method, and a dynamic programming method to determine the critical slip surface [*Tsutsumi, et al.*, 2007]. The model calculates not only the time of landslide occurrence, but also the scale of the landslide mass volume. When a landslide occurs, the sediment supply model accumulates the produced sediment in unit slopes. The excess sediment is supplied to the channel when the cumulative volume exceeds the specific deposition volume of the unit slopes calculated from the topographical data. The rainfall runoff model employs a kinematic wave model considering a two-layer infiltration flow (layer A, surface erodible layer and layer B which is difficult to permeate water) and surface flow. Further, the sediment runoff model simulates the sediment transport as bed load and suspended load depending on the sediment transport equation considering heterogeneous bed material.

Firstly, we derived a parameter for the rainfall runoff model from the observed water discharge data of the September 17–18, 2017 flood event. We tried some calculation cases employing multiple parameters for the event. The parameters selected for this watershed are shown in **Table 2**.

Applying these parameters, the water discharge at Channel 6 was calculated as shown in **Fig.6**, which corresponds with the observed value from the time-lapse camera.

4.2 Evaluation of debris flow hydrographs caused from probable rainfall event

To set realistic scenarios of possible sediment disaster, it is important to know the scale of phenomena due to possible extreme rainfall events. Therefore, carried out calculations applying the three probable rainfall datasets shown in **Fig. 7**.

Case 1 is the actual rainfall data observed during Typhoon #23 in 2004 at Kamiseya station, which is located approximately 3 km north of the target area. This typhoon caused disasters such as flood, inundation, and sediment deposit due to debris flow to Miyazu City. According to the report from Miyazu City, the road to the Hata area was closed owing to river bank erosion along the main stream of the Hata river. Case 2 is the virtual rainfall data for a 400-year return period at the Maizuru weather station, Japan Meteorological Agency, which is located approximately 20 km south-east of the target area.

Table 2 Identified Parameters

Parameters	Values
Layer A depth, surface erodible layer [m]	0.1
Layer B depth, difficult to permeate water [m]	0.3
Initial Water Depth [m]	0.2
Hydraulic Conductivity of Layer A[m/s]	6.0×10^{-3}
Hydraulic Conductivity of Layer B [m/s]	1.0×10^{-4}
Manning's Roughness Coefficient of Slopes $[m^{-1/3}s]$	0.7
Manning's Roughness Coefficient of Channels $[m^{-1/3}s]$	0.3

Case 3 is the actual rainfall data obtained at the Susa weather station, which brought huge sediment and water-related disaster to Yamaguchi and Shimane Prefectures in 2013. This station is located far from the target area; however, the surrounding area has a Japan-Sea side climate pattern, which is similar to the target area.

The condition of the grain size distribution is shown in **Fig. 8**. The grain size distribution of the produced sediment was set from the sampling and sieving test in the target basin.

However, because measuring the ratio of the coarser materials such as cobbles and boulders via the sieving test is difficult, we assumed that the riverbed material in the exchange layer contains 50% boulders and cobbles. We also assumed that the entire deposition layer at riverbed consists of materials from field survey conditions with boulders and cobbles.

The calculated flow discharge in Ch. 13, the exit of the debris flow prone valley, is shown in **Fig. 9**. The calculated sediment discharge for the three cases are also shown in **Fig. 9**. The peak discharge of Case 3 is the largest among the three cases. And the sediment runoff volume was the smallest in Case 3 because the total rainfall was the smallest. Runoff of water and sediment seemed to correspond with input rainfall data. And in all 3 cases, peak discharge was larger than 10 m^3/s at torrent downstream describing relatively large runoff.

4.3 Debris flow simulations

As outlined in Section 2, we have developed and applied a GIS-related debris flow simulation system called Hyper KANAKO [*Nakatani et al.*, 2016]. The simulation method is based on the Takahashi model *[Takahashi*, 1991 and *Takahashi*, 2007] considering erosion/deposition due to equilibrium concentrations.

4.3.1 Simulation conditions

We set the debris flow simulation target area as shown in **Fig.10** and applied the digital elevation model (DEM) landform data provided from Geospatial Information Authority of Japan (GSI).

The interval of the 1D simulation points was set as 5 m, with 181 simulation points, and the river width in the 1D area was set as 10 m. As shown in Section 3.2, normal river width seemed to be 2-3 m in Hata River. However, when debris flow occur, the flow width become larger due to erosion and high flow depth. And from the observation, the flow width

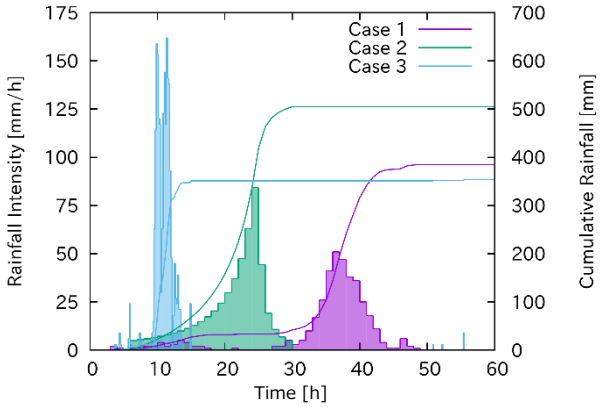

Fig. 7 Target rainfall events. Case 1 is the rainfall event during Typhoon #23 in 2004, observed at Kamiseya station, Kyoto Pref. Case 2 is the virtual rainfall data, which has a 400 years return period. Case 3 is the rainfall event observed in the Yamaguchi-Shimane sediment disaster in 2013 at Susa station, Yamaguchi Pref.

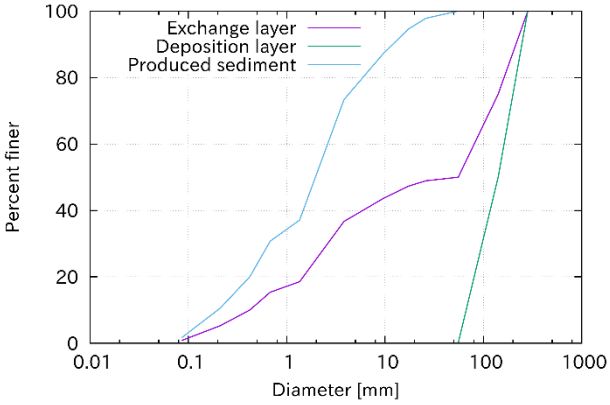

Fig. 8 Condition of the grainsize distribution of the material in the exchange layer, deposition layer, and produced sediment.

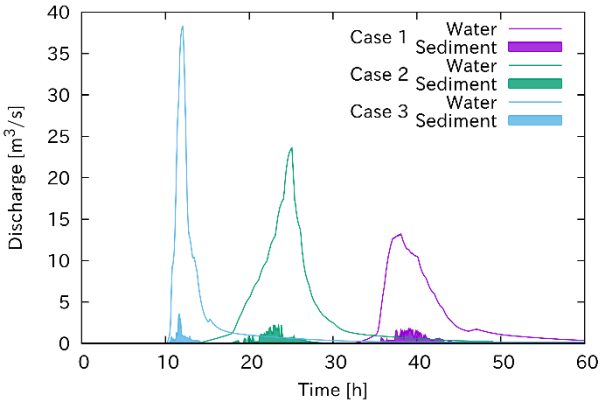

Fig. 9 Calculated water and sediment discharge in Ch. 13.

was estimated approx. 10 m at time of the maximum flow depth, we set 10 m width for initial condition. For the 2D area, we set a 10-m mesh, the same resolution as the input DEM data. Further, the 2D area range (flow direction × transverse direction) was set as (1240 m × 820 m).

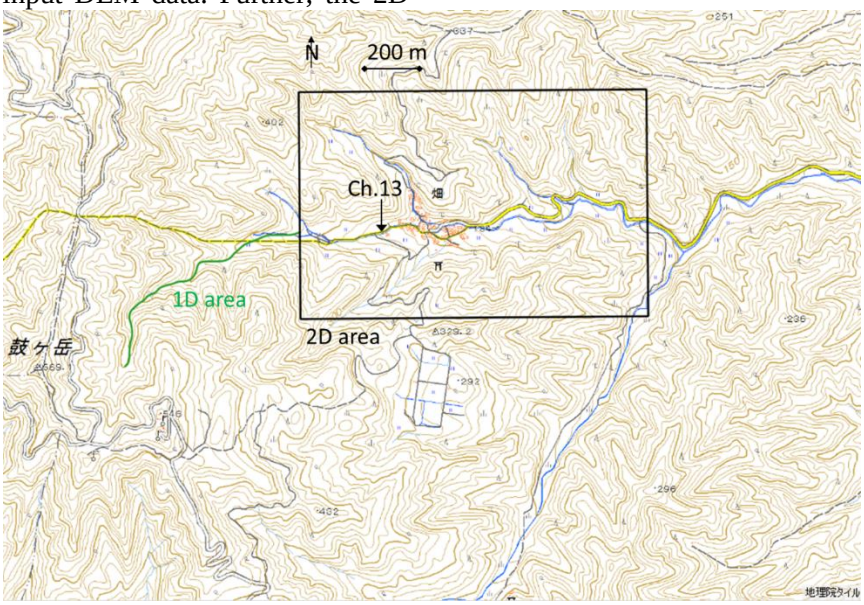

Fig. 10 Debris flow simulation target in Hata river

We did not set unstable soil in the 1D or 2D area for all cases.

To set the debris flow conditions, we applied the three scenarios, Cases 1-3, assumed from the large rainfall and actual disaster in Section 4.2. In the strict sense, discharges at the 1D upstream of the simulation target should be smaller from Ch. 13. However, in this study, we applied the calculated water and sediment discharge at Ch. 13, shown in **Fig. 9**, considering that the total amount of water and sediment supply should become as large when arriving at Ch. 13 during the debris flow event. This approach of using downstream discharge as the supplied condition in the upstream considering the total basin, is widely applied for debris flow studies and planning in Japan.

In the Hyper KANAKO system, debris flow simulation is applied using uniform grain size. In SiMHiS, focusing on sediment, it consider sediment product containing rather fine sediment from the slope and individual motion in river such as bed load rather large as set in **Fig.8** deposition layer. Hyper KANAKO is focusing on debris flow and fine particle such as produced sediment doesn't effect to the behavior if the ratio is small. In this target area, we checked the produced sediment and riverbed deposition layer, but we the mixed ratio is not clear and also hard to obtain. Therefore, we set a representative diameter as 0.2 m, the maximum diameter at the riverbed deposition layer from field survey and also representing stony debris flows occurred in Japan.

The other simulation parameters are shown in **Table 3**. The erosion and deposition coefficients were set as 0.007 and 0.05, typical values for debris flow simulations in Japan (*Takahashi*, 2007). For the simulation time, we set different time durations owing to the **Fig. 9** results.

Table 3 Parameters applied for debris flow simulation

Parameters	Values
Time steps [s]	0.01
Diameter of material [m]	0.2
Mass density of sediment [kg/m^3]	2650
Mass density of fluid phase[kg/m^3]	1000
Concentration of movable bed	0.65
Internal friction angle[deg]	35
Coefficient of erosion rate	0.0007
Coefficient of deposition rate	0.05
Manning's Roughness Coefficient[m$^{-1/3}$s]	0.03

4.3.2 Simulation results

The simulation results for the debris flow trace, including data for the maximum flow depth and deposition thickness, are shown in **Fig. 11**. From the results, large flow depth and deposition thickness values such as 50-100 cm and 100-300 cm are found outside of the main channel. Flooding and deposition appear to arise when these debris flow scenarios occur. The areas in which flooding and deposition occur appear to be similar in all cases, with some areas showing large values that are different in each case. This occurs because not only

is water discharge condition different but so are the condition of sediment discharge and the time series. Considering all cases, from upstream to section A, Case1-2 showed larger maximum flow depth. From section A to downstream, Case3 showed larger maximum flow depth and area showing large depth was wide.

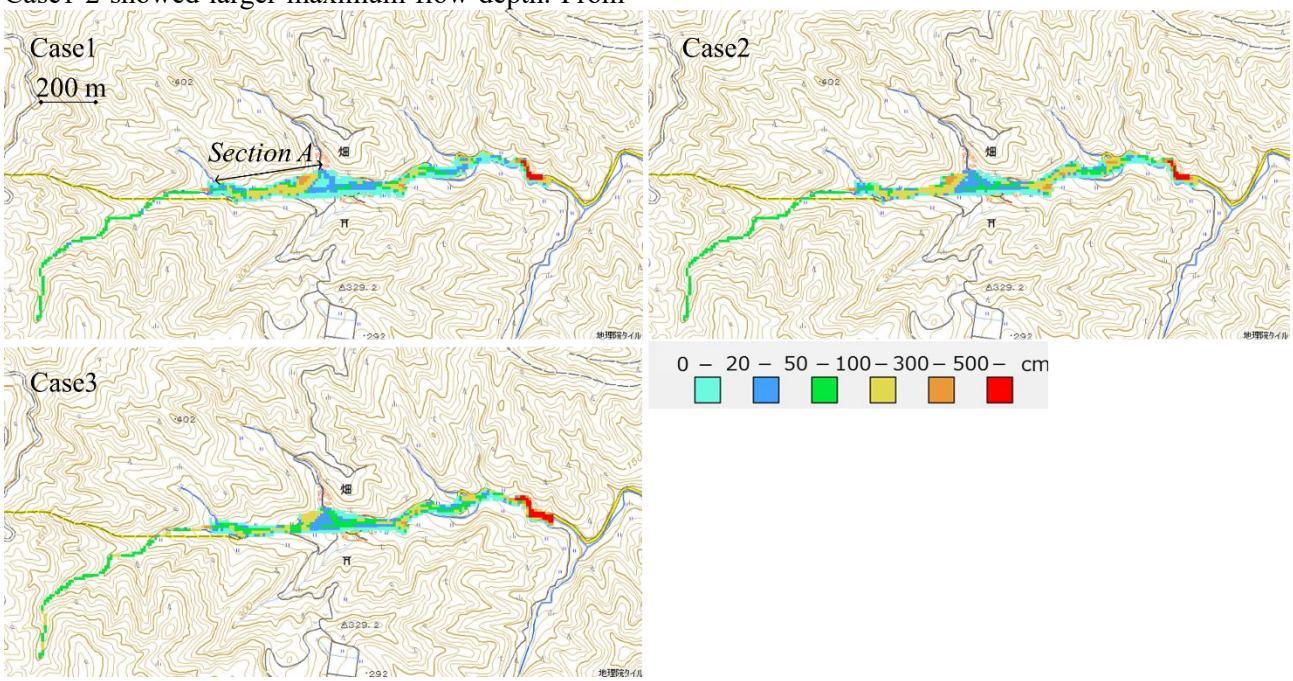

Fig. 11 Debris flow simulation results in Hata river; maximum flow depth and deposition thickness during simulation

For the Hata river target, we did not have information on past disaster results. As a result, we could not show the information together or compare them for effective information provision.

However, we indicated the results on the map in order to help residents become cognizant of the risks. Further, to avoid bias to one set of simulation results as the actual scenario, we utilized three realistic scenarios and showed the results for all three. The results will help residents to understand that even when the influence area due to debris flow is virtually the same, the area at risk of significant damage from flooding and deposition various according to the scenario.

On the other hand, using recent studies and method might show similar results to our proposed method. But our method have advantage on setting realistic continuous scenario from rainfall, sediment supplying, and debris flow verifying with field observed data.

5. CONCLUSIONS

In this study, with the objective of facilitating appropriate evacuation in the event of sediment disasters, we considered advanced hazard information and useful means of providing information to residents. In particular, in order to provide understandable and useful information to residents and local government engineers, we engaged in discussions and developed a set of scenarios based on recent disaster rainfall. Further, we combined two simulation systems to obtain advanced hazard information. By setting the initial rainfall data in the resulting system, we were provided with not only the occurrence time of sediment disasters but also indications of the flooding/deposition area and distribution. We conducted simulations on Hata river, Miyazu City, Kyoto Prefecture, Japan and considered three scenarios involving different levels of rainfall and also considered the target site conditions from field survey results. After running the simulations, we indicated the results on a map of the area to help residents become cognizant of the risks. Further, showing multiple scenario results helps residents to understand that even when the influence area due to debris flow is virtually the same the area at risk at significant damage from flooding and deposition varies for different scenarios.

The important factor was the simulation accuracy and reliability for applying to evacuation. Moreover, for providing information to local residents, we confirmed that the information for both the input and output data needs to be compared with the recorded or experienced rainfall or disaster events for intuitive understanding. For securing high accuracy and reliability to the target site, we found that conducting field survey and observation, and

estimating some suitable parameters, then running simulations will be required.

ACKNOWLEDGMENT: This study was the Collaborative Research (28P-02) funded by the Disaster Prevention Research Institute, Kyoto University. The authors are grateful to Sabo Division, Construction Transportation Department, Kyoto Prefecture, for supporting the topic discussed in this paper. We applied rainfall data from RADAR-AMeDAS COMPOSITE PRECIPITATION, JMA. We applied landform data from the Geospatial Information Authority of Japan. This study was partially supported by Grant-in-Aid for Research Activity Start-up Grant Number JSPS 17H06769 and by the River Fund of The River Foundation, Japan.

REFERENCES

Chen, CY., and Fujita, M (2014) A Method for Predicting Landslides on a Basin Scale Using Water Content Indicator, Journal of JSCE, Ser. B1 (Hydraulic Engineering), Vol.70, No.4, pp. I_14-I_18

Egahsira, S., and Matsuki, K. (2000) A Method for Predicting Sediment Runoff Caused by Erosion of Stream Channel Bed, Annual Journal of Hydraulic Engineering, JSCE, Vol. 44, pp. 735-740 (in Japanese with English abstract).

Nakatani, K., Hayami, S., Satofuka, Y., Mizuyama, T. (2016): Case study of debris flow disaster scenario caused by torrential rain on Kiyomizu-dera, Kyoto, Japan; using Hyper KANAKO system, Journal of Mountain Science, 13(2), pp.193-202

Takahashi T. (1991): Debris Flow. Balkema, Rotterdam, 165pp.

Takahashi T (2007): Debris flow: Mechanics, Prediction and Countermeasures. Taylor & Francis, Leiden, CRC Press, London, UK.

Tsutsumi, D., Fujita, M., Hayashi, Y. (2007) Numerical Simulation on a Landslide Due to Typhoon 0514 in Taketa City, Oita Prefecture, Annual Journal of Hydraulic Engineering, JSCE, Vol. 51, pp. 931-936 (in Japanese with English abstract).

Yamanoi, K. and Fujita, M. (2016) Risk Estimation of Multiple Hazards Related to Sediment and Water Disasters Occuring in Heavy Rainfall, The Journal of JSCE, Ser. B1 (Hydraulic Engineering), Vol.72, No.4, pp. I_1291-I_1296 (in Japanese with English abstract).

Towards an Auto-nowcasting System for Landslide Hazards

Cheng-Chien LIU[1, 2*], Hsiao-Yuan YIN[3], Hsiao-Wei CHUNG[2], Wei LUO[4] and Ke-Wei YAN[3]

[1] Dept. of Earth Sciences, National Cheng Kung University (Tainan, 70101 Taiwan)
[2] Global Earth Observation and Data Analysis Center, National Cheng Kung University (Tainan, 70101 Taiwan)
[3] Debris Flow Disaster Prevention Center, Soil and Water Conservation Bureau (Nantou, 54044 Taiwan)
[4] Dept. of Geography, Northern Illinois University (DeKalb, IL, USA)
*Corresponding author. E-mail: ccliu88@mail.ncku.edu.tw

This paper reports the efforts we made in the past four years to develop an auto-nowcasting system of landslide hazards, as well as the accuracy assessment of the I-Lan case in 2012 and 2013. This system uses a nondeterministic geometric mean model of landslide susceptibility index (*LSI*) to integrate three grid-based preparatory factors: slope, aspect, lithology, as well as one region-based factor: total flux. The weight of each preparatory factor is calculated by excluding the union of all shaded areas in the time series of satellite observations. The coefficients of the nondeterministic geometric mean model are determined by maximizing the positive right and negative right regions, and minimizing the missing and false alarm regions. By assuming that landslide hazard index (*LHI*) is related to *LSI* and accumulated precipitation (*AP*), the event-based inventory and *AP* for Typhoon Saola (11 July 2012) and Typhoon Soulik (12 July 2013) are used to develop and validate the *LHI* of I-Lan. Results show that the overall accuracy is as high as 85%. This *LHI* model has been implemented through SWCB Sediment-related Disaster Geospatial Information System (SDGIS) to provide an auto-nowcasting service with a map of five-level warning updated every hour.

Key words: preparatory factor, triggering factor, landslide susceptibility model, landslide hazard model, landslide inventory, nowcasting

1. INTRODUCTION

Landslide is one of the most common and dangerous natural hazards in mountainous regions, which alone caused a total death toll of at least 32,322 in 2,626 events between 2004 and 2010 [*Petley* 2012]. To minimize human and material losses, landslide-related maps are widely recognized to be crucial in implementing disaster prevention and mitigation strategies [*Hervas, et al.* 2003]. With the map of landslide susceptibility, for example, various measures can be implemented to build engineering structures and plan evacuation routes. Despite of the fact that different levels of assumptions and uncertainties are associated with different methods, the bottom line is to get a few hours of warning at least, in order to secure enough time of evacuation. This requires the nowcasting technique that provides a reliable prediction of the very near future from a large quantity of data series. This paper reports the efforts we made in the past four years to develop an auto-nowcasting system of landslide hazards, as well as the accuracy assessment of the I-Lan case.

2. METHOD

2.1 Shadow inventory and its influences on landslide susceptibility models

Landslide susceptibility describes the relative spatial likelihood for the occurrence of landslides, based on the landslide inventory prepared from space-borne or air-borne optical imagery. Most of the landslides are occurred in mountainous areas, where the imagery are acquired with some incline angles and the sun is not always in the nadir direction. Therefore, shadow is inevitable on these optical imageries. **Fig. 1** gives one example of mapping landslides triggered by the extreme rainfall of Typhoon Morakot in August of 2009. Most of the aftermath images available were acquired in the winter of 2009 or in the spring of 2010, because of the urgent needs to map the landslides and evaluate the damage. During that period of time, however, the sun elevation is low in the sub-tropical zone and the shadows could occupy as high as 30% of the entire image over the mountainous area, such as the example shown in **Fig. 1(b)**.

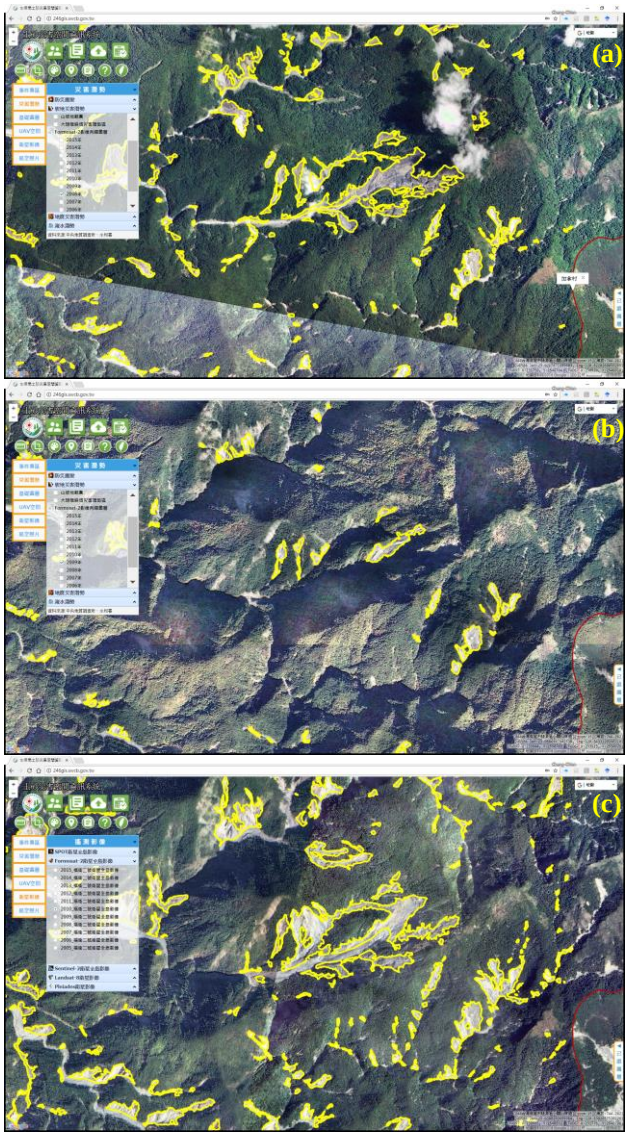

Fig. 1 Example of mapping landslides (yellow polygons) triggered by the extreme rainfall of Typhoon Morakot in August of 2009, using the Formosat-2 imagery acquired in (a) 2008, (b) 2009, and (c) 2010. A misleading conclusion of less landslide areas after Typhoon Morakot would be drawn, if the shadow inventory is not taken into account with special care.

The landslide areas delineated from the 2008 imagery (yellow polygons in **Fig. 1a**) are even larger than the landslide areas delineated from the 2009 imagery (yellow polygons in **Fig. 1b**). As a result, a misleading conclusion of less landslide areas after Typhoon Morakot would be drawn, if the shadow inventory is not taken into account with special care. The landslide areas delineated from the 2010 imagery (yellow polygons in **Fig. 1c**) clearly illustrates the destruction level of Typhoon Morakot: the landslide areas of 2010 are still much larger than the one of 2008, even after one year of recovery.

Two simple approaches were proposed and validated to compensate the error caused by shadows [*Lin, et al.* 2013], which requires a detailed shadow inventory prepared from the Expert Landslide and Shaded Area Delineation System [*Liu* 2015]. Our recent study evaluates the possible errors affecting landslide susceptibility models (LSMs) by neglecting the shadow inventory. We concluded that the weight of each preparatory factor *pf* should be calculated by excluding the union of all shaded areas in the time series of satellite observations.

2.2 A new region-based preparatory factor for landslide susceptibility models: the total flux

Current LSMs are mostly based on conditions represented by the data contained within each gridded cell, namely grid-based preparatory factor. Although drainage distance has been used to account for landslides occurring on slopes adjacent to main streams, *Liu et al.* [2016] demonstrated that drainage distance is not the best region-based preparatory factor, because the cells in the same drainage distance buffer zone may experience different total water flux as tributaries join the main stream when water flows downstream. Taking into account of the topography and hydrology conditions upstream of each gridded data cell, a new region-based preparatory factor total flux (TF) was proposed to represent the total flux of water in the stream. TF is proved to be strongly associated with the occurrence of landslides and is a good region-based preparatory factor for LSM [*Liu, et al.* 2016].

As suggested by *Liu et al.* [2004] that the preparatory factors should be obtainable and applicable anywhere, and reviewed by Süzen *et al.* [2011] that slope, aspect and lithology are the most influential natural factors, we build up a standard LSM that covers the entire country. Note that two cell-based factors, slope (**Fig. 2a**) and aspect (**Fig. 2b**), and the region-based factor, TF (**Fig. 2c**) are all derived from a digital elevation model (DEM) made available by the Ministry of Interior Affairs of Taiwan. The lithology map is provided by the Central Geological Survey of Taiwan at the scale of 1/250,000 (**Fig. 2d**). Detailed description of these preparatory factors can be referred to the project report [*GEODAC* 2014].

Note that only the mountainous regions of Taiwan are taken into consideration, which is about two-third of Taiwan. There are still some rooms of improvement of these preparatory factors. For example, the 5-m resolution DEM was produced before Typhoon Morakot in 2009, which might not be able to represent the current situation of surface elevation in some area. The lithology map provided at the scale of 1/250,000 is also too coarse comparing to the other data.

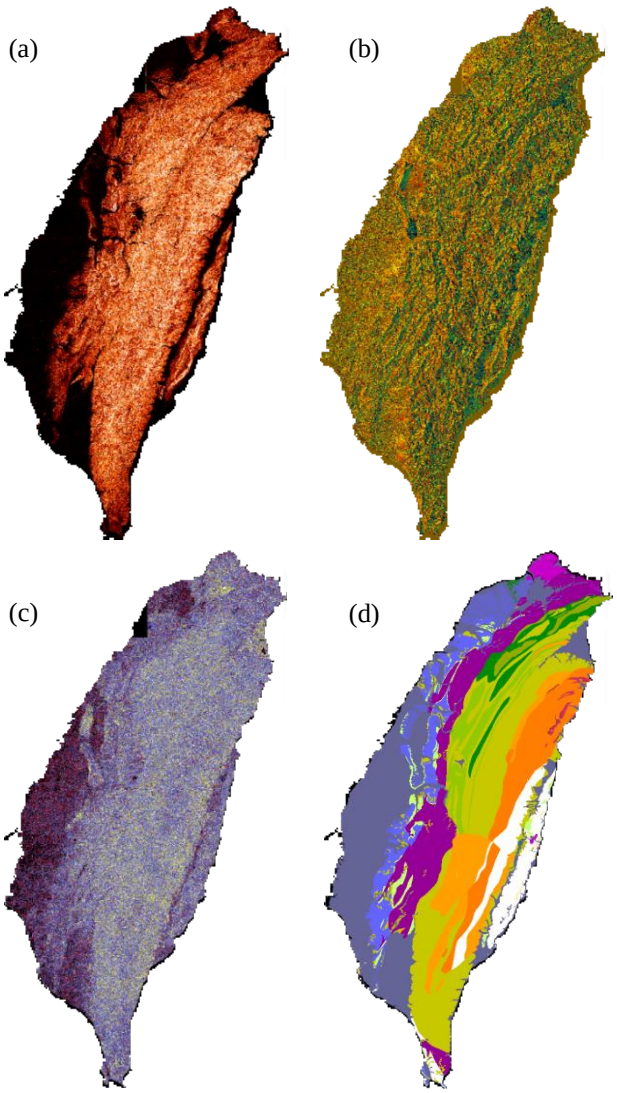

Fig. 2 Preparatory factor for landslide susceptibility models (a) slope, (b) aspect, (c) total flux, and (d) lithology.

2.3 Landslide susceptibility model based on geometric mean with indeterminate coefficients

LSM computes landslide susceptibility index (*LSI*) at each cell *j* of gridded raster data that indicates the susceptibility based on preparatory factors weighted according to importance. After excluding the union of all shaded areas in the time series of satellite observations and weighting each preparatory factor by the landslide inventory, two types of LSMs are usually employed, i.e., the arithmetic mean model [*Lee and Talib* 2005, *Yilmaz* 2009]

$$LSI(j) = \frac{1}{m}\sum_{k=1}^{m} W_{pf_k(i_k)} \qquad (1)$$

and the geometric mean model [*Fourniadis, et al.* 2007, *Nguyen and Liu* 2014]

$$LSI(j) = \left(\prod_{k=1}^{m} W_{pf_k(i_k)}\right)^{\frac{1}{m}} \qquad (2)$$

where *m* is the number of *pf* considered in *LSI*, *W* is the weight of *pf* at interval *i* defined as the frequency ratio [*Liu, et al.* 2016]. For one particular pf_k, i_k is the corresponding interval of pf_k at that cell *j*. *Liu et al.* [2004] discussed and recommended the geometric mean model (Eq. 2), which implies that the contribution of each *pf* is the same. This restriction can be removed by introducing a set of nondeterministic coefficients and searching an optimized value for each coefficient, namely the nondeterministic geometric mean model

$$LSI(j) = \prod_{k=1}^{m} W_{pf_k(i_k)}^{C_k} \qquad (3)$$

Note that Eq. (3) requires a well-defined criteria of optimization, which motivates us to revisit the evaluation indicators of landslide susceptibility model as described as follows.

2.4 Revisit the evaluation indicators of landslide susceptibility model

The percentage of landslide occurrence (POLO) and its cumulative (CPOLO) are commonly used as indicators to measure the performance of landslide susceptibility model. To evaluate the performance of landslide prediction or issue a warning, however, requires a fixed value of threshold that cannot be determined directly and solely from the CPOLO curve. Following the practice in weather forecast, two CPOLO curves are plotted within (yellow line) and outside (green line) the landslide areas, respectively, resulting in four regions of prediction: positive right, negative right, missing and false alarm (**Fig. 3**). Maximizing the first two (76.93%, 75.17%) and minimize the last two regions (23.07%, 24.83%) enables us to explicitly determine a new indicator that is especially suitable for determining the threshold: a value of 0.0125 for the case of I-Lan and the nondeterministic geometric mean model is

$$LSI = W_{\text{slope}}^{0.2746} \times W_{\text{aspect}}^{0.2712} \times W_{\text{TF}}^{0.2562} \times W_{\text{lithology}}^{0.2384} \qquad (4)$$

A detailed explanation of this new indicator, as well as Eq. (4) can be referred to the project report.

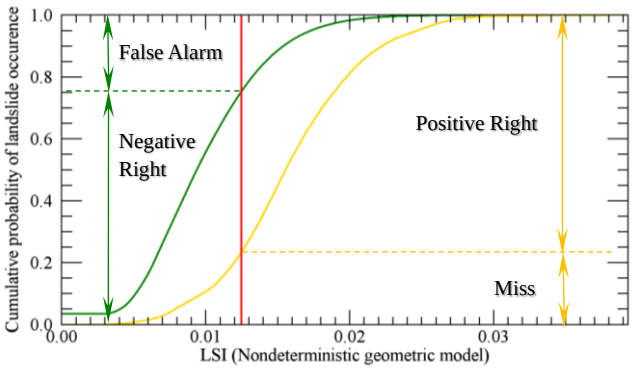

Fig. 3 Landslide susceptibility index of I-Lan calculated by using the nondeterministic geometric mean model (Eq. 3).

3. RESULTS

To attain the goal of nowcasting landslide hazards, the contribution of precipitation needs to be quantified first. Since the events of Typhoon and landslide are frequently reported in I-Lan, we prepare the event-based inventory and calculate the accumulated precipitation (*AP*) for Typhoon Saola (11 July 2012) and Typhoon Soulik (12 July 2013), respectively, as shown in **Fig. 4**.

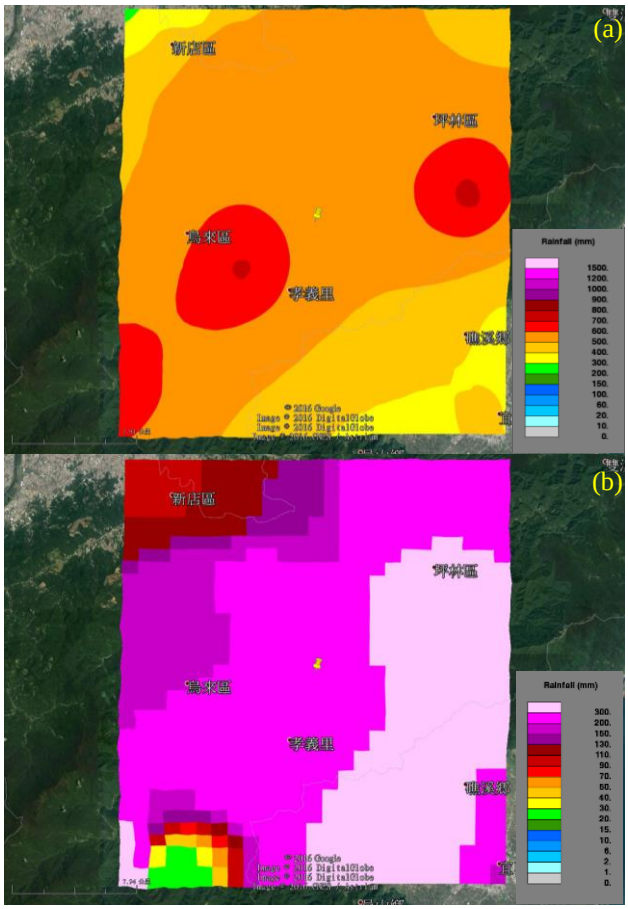

Fig. 4 Accumulated precipitation (*AP*) for (a) Typhoon Saola (11 July 2012), and (b) Typhoon Soulik (12 July 2013).

By assuming that landslide hazard index *LHI* is related to *LSI* and *AP* by

$$LHI = LSI \times AP^{C_{AP}} \qquad (5)$$

and employing the same technique of optimization using the event-based inventory of I-Lan of Typhoon Saola, a value of 0.0674 is obtained for C_{AP} (**Fig. 5a**). This *LHI* model is then validated by using the *AP* and event-based inventory of Typhoon Soulik (**Fig. 5b**). **Table 1** lists the accuracy in four regions of prediction: positive right, negative right, missing and false alarm. The overall accuracy is as high as 85%. By implementing this *LHI* model through SWCB Sediment-related Disaster Geospatial Information System (SDGIS) (http://246gis.swcb.gov.tw/) (**Fig. 6a**), we provide an auto-nowcasting service with a map of five-level warning updated every hour (**Fig. 6b**). Note this *LHI* model is only valid for I-Lan, since C_{AP} is a regional parameter that needs to be determined from the actual event.

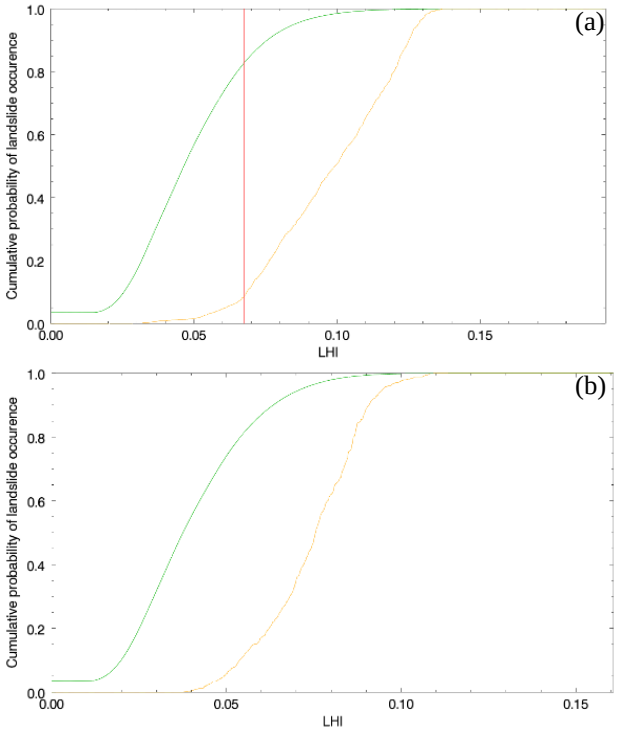

Fig. 5 (a) Development of *LHI* model using *AP* and the event-based inventory of I-Lan of Typhoon Saola (11 July 2012), and (b) Validation of *LHI* model using *AP* and the event-based inventory of I-Lan of Typhoon Soulik (12 July 2013).

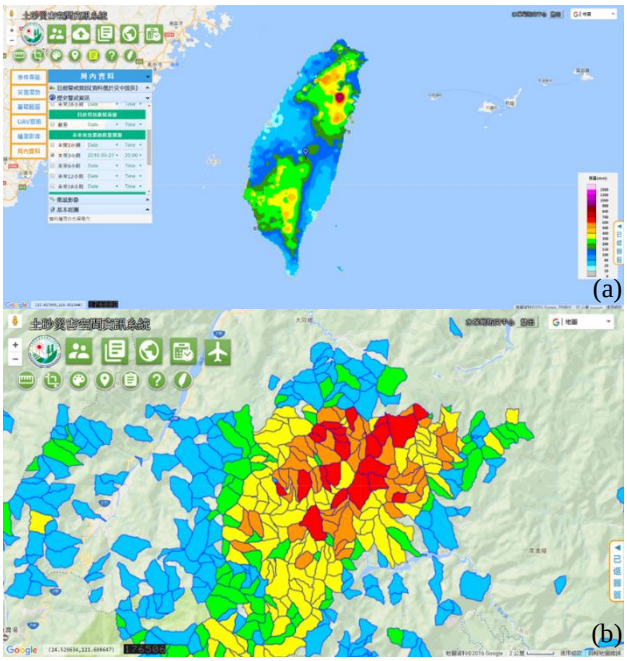

Fig. 6 (a) SWCB Sediment-related Disaster Geospatial Information System (SDGIS), and (b) an auto-nowcasting service with a map of five-level warning updated every hour.

Table 1 Accuracy report in four regions of prediction: positive right, negative right, missing and false alarm. (a) Development of *LHI* model using *AP* and the event-based inventory of I-Lan of Typhoon Saola (11 July 2012), and (b) Validation of *LHI* model using *AP* and the event-based inventory of I-Lan of Typhoon Soulik (12 July 2013).

	Development	Validation
LHI threshold	0.06744	0.0588
Positive Right (%)	91.62	84.73
Negative Right (%)	82.71	85.81
Miss (%)	8.38	15.27
False Alarm (%)	17.29	14.19

4. CONCLUDING REMARKS

An auto-nowcasting system of landslide hazards has been developed for Taiwan, which uses a nondeterministic geometric mean model of *LSI* to integrate three grid-based preparatory factors: slope, aspect, lithology, as well as one region-based factor: total flux. The weight of each preparatory factor is calculated by excluding the union of all shaded areas in the time series of satellite observations. The coefficients of the nondeterministic geometric mean model are determined by maximizing the positive right and negative right regions, and minimizing the missing and false alarm regions. By assuming that *LHI* is related to *LSI* and *AP*, the event-based inventory and *AP* for Typhoon Saola (11 July 2012) and Typhoon Soulik (12 July 2013) are used to develop and validate the *LHI* of I-Lan. Results show that the overall accuracy is as high as 85%. This *LHI* model has been implemented through SWCB Sediment-related Disaster Geospatial Information System (SDGIS) (http://246gis.swcb.gov.tw/) to provide an auto-nowcasting service with a map of five-level warning updated every hour.

ACKNOWLEDGMENT: This research is funded by Soil and Water Conservation Bureau, Council of Agriculture, Taiwan ROC, under Contract Nos. 106AS-7.3.1-SB-S2, as well as Ministry of Science and Technology of Taiwan ROC, under Contract Nos. MoST 106-2628-M-006-002.

REFERENCES

Fourniadis, I. G., J. G. Liu, and P. J. Mason (2007): Regional Assessment of Landslide Impact in the Three Gorges Area, China, Using Aster Data: Wushan-Zigui, Landslides, 4, pp. 267-278.

Global Earth Observation and Data Analysis Center (2014): 2014 Multi-Scale Remote Sensing Information System Data Establishment, Expansion and Maintenance, pp. 364. (in Chinese with English abstract)

Hervas, J., J. I. Barredo, P. L. Rosin, A. Pasuto, F. Mantovani, and S. Silvano (2003): Monitoring Landslides from Optical Remotely Sensed Imagery: The Case History of Tessina Landslide, Italy, Geomorphology, 54, pp. 63-75.

Lee, S., and J. Talib (2005): Probabilistic Landslide Susceptibility and Factor Effect Analysis, Environmental Geology, 47, pp. 982-990.

Lin, E.-J., C.-C. Liu, C.-H. Chang, I.-F. Cheng, and M.-H. Ko (2013): Using the Formosat-2 High Spatial and Temporal Resolution Multispectral Image for Analysis and Interpretation Landslide Disasters in Taiwan, Journal of Photogrammetry and Remote Sensing, 17, pp. 31-51.

Liu, C.-C. (2015): Preparing a Landslide and Shadow Inventory Map from High-Spatial-Resolution Imagery Facilitated by an Expert System, Journal of Applied Remote Sensing, 9, pp. 096080-096080.

Liu, C.-C., W. Luo, M.-C. Chen, Y.-T. Lin, and H.-L. Wen (2016): A New Region-Based Preparatory Factor for Landslide Susceptibility Models: The Total Flux, Landslides, 13, pp. 1049-1056.

Liu, J. G., P. J. Mason, N. Clerici, S. Chen, A. Davis, F. Miao, H. Deng, and L. Liang (2004): Landslide Hazard Assessment in the Three Gorges Area of the Yangtze River Using Aster Imagery: Zigui–Badong, Geomorphology, 61, pp. 171-187.

Nguyen, T.-T.-N., and C.-C. Liu (2014): Combining Bivariate and Multivariate Statistical Analyses to Assess Landslide Susceptibility in the Chen-Yu-Lan Watershed, Nantou, Taiwan, Sustainable Environment Research, 24, pp. 257-271.

Petley, D. (2012): Global Patterns of Loss of Life from Landslides, Geology, 40, pp. 927-930.

Süzen, M. L., and B. Ş. Kaya (2011): Evaluation of Environmental Parameters in Logistic Regression Models for Landslide Susceptibility Mapping, International Journal of Digital Earth, 5, pp. 338-355.

Yilmaz, I. (2009): Landslide Susceptibility Mapping Using Frequency Ratio, Logistic Regression, Artificial Neural Networks and Their Comparison: A Case Study from Kat Landslides (Tokat—Turkey), Computers & Geosciences, 35, pp. 1125-1138.

The Educational Methods Immediately after the Sediment -Related Disasters on a Basis of Local Historical Experience - The Case Study of Environmental Educational Programs in Kumamoto Earthquake 2016 -

Reiko MACHIDA[1*], Mito ICHIKAWA[2], Miu KITAZATO[3], Junya MACHIDA[4]
Hijiri SHIMOJIMA[1], Teruaki IRIE[1], Tadakazu KANEKO[3] and Naomasa HONDA[1]

[1] Department of Regional Regeneration Science, Tokyo University of Agriculture, Japan
[2] Kumamoto City
[3] Department of Landscape Architecture Science, Tokyo University of Agriculture, Japan
[4] Environment Design Institute, Japan
*Corresponding author. E-mail: r3machid@nodai.ac.jp

This study suggested a mentally considerate approach for educational methods of disaster prevention immediately after the earthquake disasters, incorporating the learnings of local historical experience. The education programs, based on the disaster situation, were planned in cooperation with the locals and the elementary and junior high school teachers. The education programs were carried out in two Minami-Aso Elementary School, and a Minami-Aso Junior High School by scientist, locals and NPO, teachers. After the education programs, it carried out the free description to 36 the elementary students (9-12 years old), 7 junior high school students (15years old). This educational program was accepted by both local children and teachers even half a year after the earthquake, and demonstrated successful educational effects in Knowledge and understanding of social event and local identity.

Key words: Kumamoto Earthquake 2016, Aso, Education method, Local historical experience

1. INTRODUCTION

The Disaster Risk Education plays important roles to take over the memory of the disaster and to provide the preparation for future disasters. The education methods for sediment-related disaster utilizes the scientist simulation model, the hydraulic apparatus and field seminar [Yamada, 2006]. Besides, importance of the local wisdoms of elderly generations is re-realized through the experience of Great East Japan Earthquake in 2011.

As a response to the 2011 Great East Japan Earthquake, the Ministry of Education, Culture, Sports, Science and Technology (MEXT) set up an expert committee for reviewing disaster prevention education and management. Additionally, at a 2012 Cabinet meeting, the Promote Plan for School Safety was approved, which also stated the country's need to secure educational time in schools for security.

MEXT published a revised material in 2013 titled Zest for Living, which includes not only the evacuation procedures during disasters, but also educational programs from the viewpoint of local life and customs.

However, in the disaster areas of the Great East Japan Earthquake, only 30 percent of schools practiced disaster risk education in consideration of local characteristics and disaster histories. On the other hand, the Education Psychology studies reported that the children who experienced a disaster have effect of serious psychology stress in the daily life [Fujimori, 2011]. There are several examples of disaster prevention educational programs that encourage children's participation in the recovery, while paying considerable attention to children's mental care immediately after the disaster [Matsuno 2013, Yamazaki 2016]. Mitsuhashi points out that the understanding of local culture serves as the basis of disaster risk education, in reference to the education theory of Katsue Misawa [Mitsuhashi, 2013].

Therefore, the disaster risk education programs need to provide not only the technique and knowledge of the disaster prevention, but also the correct understanding of local life style and environment for children who continue to live in the disaster area after the disasters. These disaster risk education programs are expected to help foster a sense of local patriotism. Moreover, these programs

are also expected to increase the children's motivation to participate in the recovery of the region.

The Kumamoto Earthquake struck the Aso Area of Kumamoto Prefecture on April, 14 and April 16 in 2016, killing at least 20 people. The vast grasslands of Aso Area, historically managed by local agricultural activities such as controlled burning, mowing and pasturage for centuries, has suffered from the sediment-related disasters caused by torrential rainfalls in Northern Kyushu in 2012. The local residents overcame shortly after the disaster by the cooperation in local community, which have evolved historical land use management.

However, there is only one elementary school providing disaster prevention education in the Aso area in 2017. Promotion of disaster prevention education is required based on traditional life style and knowledge that have helped local people to coexist with the volcano and overcome disasters such as eruptions and landslides. Especially at the immediate aftermath of the sediment-related disasters, the traditional lifestyle, knowledge and feelings of local patriotism are considered to have helped the children psychologically.

This study aims to propose the method of mentally considerate education immediately after the sediment-related disasters on a basis of local historical experience based on Kumamoto Earthquake 2016 cases. The study set the evaluation criteria based on "Zest for Living", the ministry's curriculum guideline. Then, based on students' oral comments and written, open-ended survey answers it evaluated the effectiveness of the educational programs.

The following articles from the Education Ministry guidelines are incorporated into the elementary school curriculum: "to help pupils become aware of the close relationship between the national land, people's lives and livelihoods" - from the objectives of Social Studies; "to help pupils develop interest in the relationships between themselves, the people around them, the various local places, public facilities; to enable them to appreciate their locality and to develop a feeling of attachment to it; at the same time, to enable them to think about their roles and actions as members of their groups or society and to act safely and appropriately" - from the objectives of Life Environment Studies.

For the programs conducted in junior high schools, the following article was included in the curriculum: "learning activities should be conducted according to the conditions of each school: for example, learning activities about interdisciplinary topics, including environment, welfare, health; learning activities about tasks based on students' interests; learning activities about tasks depending on the characteristics of the local community and the school; and learning activities concerning employment and their own futures" from the objectives of Integrated Studies.

Existing literature on the development of educational programs for disaster prevention [Ishihara, 2014] served as a reference to the perspective of evaluation. Articles such as "interest, motivation and attitude in relation to social events", "consideration and judgement from a social viewpoint" and "knowledge and understanding of social events" were included in the evaluation criteria. Additionally, this program's concept of local identity "disaster area considered as an irreplaceable place" [Funami, 2016] was also included in the evaluation.

2. THE LOCAL HISTORICAL EXPERIENCE IN THE ASO

The topographic characteristic of Aso is that it is a huge caldera which was created by four volcanic eruptions with pyroclastic flows. The central cone of the caldera hosts Mt. Taka (1,592m), Mt. Naka (1,506m), Mt. Eboshi (1,337m), Mt. Kijima (1,270m), Mt. Oujyo (1,235m), and is therefore called "Aso Go Gaku" or the Aso Five Mountains. Mt. Naka is an active volcano. Inside the outer rim of the somma caldera is home to a vast grassland lying at 700 to 800 meters above sea level.

The annual rainfall reaches approximately 3,200 mm in Aso which makes it the second highest rainfall in Japan. The wind from the Ariake Sea southwest of Kumamoto at 1,000m altitude meets with the wind from the Pacific Ocean to cause heavy rainfall in the Aso area during the summer. Also, the influence of the hot and humid air flow from the East China Sea increases the possibility of torrential rains in the rainy season [Tanaka, 2010]. The volcanic soil and the weather conditions are not suitable for cultivation, so the Aso area was developed using drainage engineering techniques and the local people have been using the grassland for livestock for centuries. The grasslands in Aso have been managed by local agricultural activities such as controlled burning (**Fig. 1**), mowing and pasturage for centuries. The grasslands of Aso are managed as commons in the region. There is a local custom in Aso placing wild flowers on ancestor's graves (**Fig. 2** and **3**).

Fig. 1 Controlled burning

Fig. 2
Polemonium kiushianum

Fig. 3
Echinops setifer Iljin

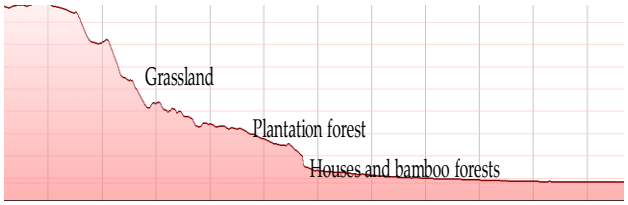

Fig. 4 The historical land use in Aso

Fig. 5 The grassland in top of the Caldera

This custom is called “bonbana”. People gather wild flowers from the grasslands to celebrate their ancestors’ spirits. It is a symbolic custom of Aso uniting local people and the grasslands. The historical land use in Aso has been a balanced combination of rice fields, bamboo forests, orangeries, tea plantations, timber forests, fuel forests and pasture (**Fig. 4** and **5**). The local people traditionally avoided forestation at the higher slopes, because those areas were more difficult to access, more difficult to maintain and because such activities could also cause landslides.

From the 1950’s some neglected grasslands were converted into timber forests, but the historical land use area did not suffer landslides at the time of the Kumamoto Earthquake. The grasslands of Aso were certified as Globally Important Agricultural Heritage Systems (GIAHS) in 2013, and they were also certified as Geopark in 2014. The international reputation of the grasslands of Aso has increased. On the other hand, the decline of the livestock industry and the increasingly aging population, the landscape management of grasslands has become increasingly difficult. To address the shortage of manpower, the volunteer activity in Aso attracted a lot of motivated people outside of Aso since 1990’s.

3. METHODS

3.1 Investigation of the damage situation of sediment-related disaster in Kumamoto Earthquake

A wide variety of research materials were used, including academic journals of sediment-related disaster and the survey result of sediment-related disaster by Ministry of Land, Infrastructure, Transport and Tourism and the local newspapers (KUMANICHI). Also, directly after the earthquake, surveys using telephone and SNS were conducted with 11 local residents to check the conditions of disaster areas. Subsequently, on-site interview surveys were conducted with 11 local residents on an ongoing basis in June, September and October of 2016 and February and March of 2017.

3.2 The development of the method of mentally-considerate education immediately after the sediment-related disasters based on local historical experience

The education programs, based on the disaster situation, were planned in cooperation with the locals and the elementary and junior high school teachers. The education programs were carried out in two Minami-Aso Elementary School, and a Minami-Aso Junior High School by scientist, locals and NPO, teachers (**Table 1**). After the education programs, it carried out the free description to 36 the elementary students (9-12 years old), 7 junior high school students (15years old).

The study looked at the effects of the program based on the selected keywords from children's comments adopting the text-mining approach [Nakamura, 2016]. The questionnaire survey about this educational program was carried out by 3 class teachers. After the program, the comments from the children were collected and the effectiveness of the program was evaluated.

4. RESULTS

4.1 The damage situation for sediment-related disaster in Kumamoto Earthquake

As a result, the first research clarified the characteristics of the Sediment disaster caused by Kumamoto Earthquake. The particular multiplex sediment disaster occurred in Aso area such as the large-scale slope failures (e.g. Tateno area), the landslides and slope failures in the low-pitched slope (e.g. Ko-you area), and the debris flow occurrences (e.g. Cho-yo area). The earthquake (7.3 M) caused by the multiplex sediment disaster in the mountain slope. Together with the torrential rainfalls (19-25, June 2016) expanded the sediment disaster damages in Mt. Yomine, Tateno and Nagano area, Minami-Aso Village [Kurokawa, 2017]. The following figure is a GIS overlay map of the distribution of secondary grasslands and plantation forests, and the distribution of landslides and cracks in Aso's grasslands recorded by the Kyushu District Office of the Ministry of Environment (**Fig. 6**).

According to interviews with 11 local peoples in Minami Aso Village, when the disaster happened, local communities of grassland management worked together to support the evacuated locals. Three days after the earthquake, farmers also offered food to the evacuated people to help them recover and get back to their daily activities more quickly (19th April 2016). The traditional life style, utilizing the local fresh water supply also helped people during the recovery (16th April 2016 - 8th May 2016). In this way, the local residents recovered after the disaster thanks to the cooperation of local community, which has recovered quickly evolved historical land use management. On the other hand, the several natural disasters in the Aso area, it has suffered from landsides caused by torrential rainfalls in Northern Kyushu in 2012. In addition, Mt. Aso became the subject of volcanic activity from 2014.

Table 1 The responsibility matrix chart of program

Process of the program	After Disaster	University	School	NPO
Start of discuss the program	2 weeks	○	○	○
Plan to the program	2 – 4 Months	◎	○	○
Implementation of the program	5 Months	◎	○	○
Feedback of the program	6 Months	○	◎	○

◎ The chief of practitioner
○ The coauthor of the program

4.2 The mentally considerate approach for educational program immediately after the sediment-related disasters based on local historical experience

4.2.1 The plan of educational program

The conclusion of the advance meeting with local teachers was that the educational program aimed at helping children deal with the damage and trauma of the earthquake was too early. Therefore, the educational program leveraged the local historical experiences, such as the grassland management techniques (controlled burning, fire belt or seven plants in season). The culture of "bonbana" was rejected as being premature in the program.

Meanwhile, the program also included the introduction of charitable fundraising conducted in Tokyo for the recovery from the Kumamoto Earthquake. Furthermore, the educational program used the National Park and GIHAS for the promotion of the local historical experience. Moreover, the educational program was a prime example of people becoming aware of the importance of the conservation of the grasslands and where voluntary

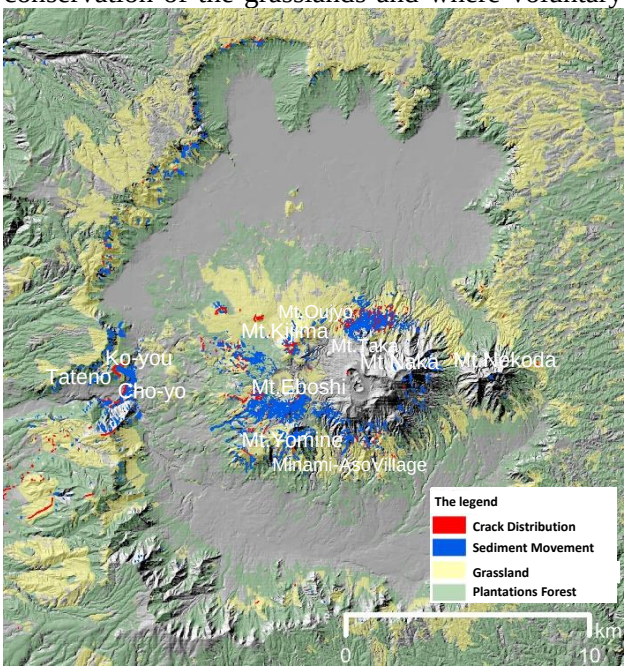

Fig. 6 The crack distribution and sediment movement by Kumamoto Earthquake

activities were organized bringing together various members of the local rural communities and the urban residents. The junior high school students planned self-directed programs in which agricultural and regional resources were included. This education program proposes the five learning objectives.

This study aims to propose the method of mentally considerate education immediately after the sediment-related disasters on a basis on local historical experience based on Kumamoto Earthquake 2016 cases.

a) Instead of facing the reality of the recovery from the disaster of Kumamoto Earthquake, it aims to turn children's attention to the values of local community and local historical experience such as the grassland management.
b) It used the National Park and GIHAS, Geo-Park for realization of the local historical experience.
c) It introduced the voluntary activities of the local rural communities and the urban residents.
d) It promotes the friendship of elementary students and junior high school students through the recreational program.
e) It provides junior high school students with the problem to debate on the restoration of grasslands by locals and NPOs after the torrential rainfalls in Northern Kyushu in 2012, and the visions of local community in the future.

The Introduction of this program featured fun quizzes and games. In the latter half of the program, children discussed their impressions and their most memorable experiences (**Fig. 7**).

4.2.2 The educational program based on the local historical experience

The children enjoyed the program with very little sign of anxiety from the prior earthquake. During the discussion session the elementary school students made the following comments about the local historical experiences (**Table 2**). The elementary school students commented about the local historical experience, saying "I did not know about controlled burning and fire belt mowing" or "I realized that so many hands are needed for grassland management" and so on. The rest of the comments included their first realization that Aso is a national park and their expression of emotional attachment to the community, saying "I am happy to be living in Minami-Aso".

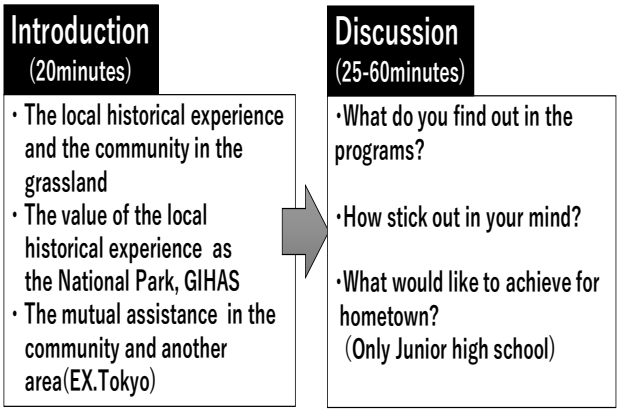

Fig. 7 The Education Program

Judging from the free comments about their impressions, the words "national park" appear frequently and the role of controlled burning seemed to have been a particularly memorable part of the program teaching about local historical experiences (**Table 3**).

From the children's feedback we can say that the result of the educational program was that children were able to raise their knowledge and understanding of social events. Through the learnings of the local historical experience in the national park and geo-park, children came to realize the strength of local patriotism and the importance of the local community.

The junior high school students made various comments about the conservation of grasslands such as "We have no one but each other to conserve the plants and flowers in Aso". The experience of seeing the elderly engaged in grassland management seemed to develop their interest in succeeding the local historical experience. Also, some students expressed their intention to share information online about grasslands and plants.

The expressions "scarce species of grasslands" appeared frequently in their comments. Also, they wrote that the educational program about the local historical experience gave them the opportunity to learn about grassland management for the first time. Additionally, some of them expressed their will to continue the agriculture and grassland management activities even after the Kumamoto Earthquake, in order to further contribute to the recovery from the disaster (**Table 4**). The results showed the presence of educational effects on "the understanding and knowledge of social events". Therefore, the program about the local historical experience widened their attention from the conservation of the local environment to regional revitalization.

4.2.3 The questionnaire to class teachers about the educational program

The question items were as follows: children's behavior during the program, the timing of implementation, the educational effect of the program and requests regarding the content and venue of the next program. Concerning the results, all

the class teachers answered that the children enjoyed the program and timing of the program based on the local historical experience was not premature even though it was held shortly after the earthquake. Regarding the educational effect of the program, through the learning of local historical experiences the children were able to rediscover the value of the local community following the earthquake, which can be easily forgotten in daily life. Requests relating to the contents of the next program were to learn more about historical precedents where the people of Aso had to overcome natural disasters and to include further activities to strengthen the bond within local communities.

5. CONCLUSIONS

This study suggested a mentally considerate approach for educational methods of disaster prevention immediately after the earthquake disasters, incorporating the learnings of local historical experience. This educational program was accepted by both local children and teachers even half a year after the earthquake, and demonstrated successful educational effects in nurturing local patriotism and pride. Regarding to the effect of the program for the elementary school students, the learning of the program led to the realization of the state of Aso as National Park and the nurture of place attachment to the community. Regarding to the effect of the program for the junior high school students, their experience led to the understanding of the importance of succeeding the local historical experience, with positive opinions on the recovery from Kumamoto Earthquake.

The program also achieved to encourage local teachers' inclinations to further develop the programs by incorporating the learning points of the disaster struck region and by learning more about the disaster specific characteristics of the region.

The future challenge is to establish educational methods of disaster prevention in order to promote the practical understanding of the type of disaster damages, through the learning of local history and culture to successfully coexist with disasters.

Table 3 Extracted words by elementary school students (multiple answers allowed, N = 36)

Extracted key words	Numbers
National park	11
Yellowstone national park	11
The numbers of national park in Japan	4
The designation of national park	9
The numbers of volunteers for the controlled burning	1
The season of the controlled burning	3
The reason of the controlled burning	1
Geo-park	1

Table 4 Extracted words by junior high school students (multiple answers allowed, N = 7)

Extracted key words	Numbers
The conservation of scarce species of the grasslands	7
The conservation of the grasslands	4
The regional activation	2
Geo-park	1
The Yellowstone national park	1
The Kumamoto earthquake	1
The reconstruction	1
The agriculture in Aso	1
The tourism resources for reconstruction	1

ACKNOWLEDGMET: This work was supported by JSPS KAKENHI Grant Number JP17K02130 and the strategic research project of Tokyo University of Agriculture. I received the support from Mr. Sumio Sei and the Takamori Higashi Junior High School, the Takamori Higashi elementary school and the Ryohei elementary school and Mr. Masaki Shimomura of Tokyo University of Agriculture. Finally, we are grateful to the anonymous referees and editorial table members for their useful comments.

REFERENCES

Fijimori, T. (2011): The care for the children who experience with a disaster (in Japanese, the title is tentatively translated by the author), Fukumra Syuupan.

Funami, T. (2016): A study on place attachments as fostered by geopark–activities: toward the creation of sustainable local communities: Study of Graduate School of Social Design Studies in Rikkyo University, No.15, pp. 149-161. (in Japanese with English abstract)

Hiroshi Mitsuhashi, H. (2013): Trends of disaster educational research in social studies education: after the great east Japan earthquake, The Journal of Social Studies, No.119, pp. 100-110. (in Japanese with English abstract)

Ishihara, R. and Matsumura, N. (2014): The Development and Evaluation of Teaching Material for Disaster Reduction in Daily Life, The Journal of Japan Society of Civil Engineers (H) (Education), Vol.70 No.1 pp. 1-12. (in Japanese with English abstract)

Kurokawa, U. (2017): The damage of the Kumamoto Earthquake and the progress of reconstruction, the materials of the symposium in the Japanese society of revegetation of technology. (in Japanese, the title is tentatively translated by the author)

Na, J., Okada, N. and Fang, L. (2009): A collaborative action development approach to improving community disaster reduction using the Yonmenkaigi system, Journal of Natural Disaster Science, Vol. 30, No. 2. pp. 57-69.

Nakamura, K. (2016): Bring light to a focus on the evaluation which cannot quantify in Environment Education (the title is tentatively translated by the author), The children of the

Earth11.12, JEEF.
Sakurai, A. (2013): A preliminary study on disaster education in Japan, from a perspective of disaster risk management, Journal of international cooperation studies, Vol. 20, No. 2.3, pp. 147-169.
Tanaka, N. (2010): Mt. Aso and the water (in Japanese, the title is tentatively translated by the Author) the history books of town of Ichinomiya (8).
Yamada, T. (2006): Education method for sediment-related disaster prevention based on the combination of field seminar and teaching hydraulic apparatus use for school children, Japan Society of Erosion Control Engineering, Vol. 59, No. 3, pp. 13-22. (in Japanese with English abstract)
Yamazaki, K. (2016): Disaster learning holds the key to the creation of resilience, The Journal of Social Studies, No.127, pp. 147-169. (in Japanese with English abstract)
Yamori, K. (2009): Research on disaster reduction education: building a “community of practice” through a gaming approach, Journal of Natural Disaster Science, Vol. 30, No. 2, pp. 83-96.

Table 2 The Objective of educational program and the evaluation effect

(Educational goal: the understanding of local life style and environment on a basis of local historical experience for children who continue to live in the disaster area after the disasters)

School curriculum		The objective of education program	The comments from elementary school students	The comments from junior high school students	The evaluation criteria			
					Interest, motivation and attitude	Knowledge and understanding	Consideration and judgement	Local identity
Elementary school and junior high school curriculum [Social Studies] To help pupils become aware of the close relationship between the national land, people's lives and livelihoods [Life environment studies] To help pupils developed interest in the relationships between themselves, the people around them, the various local places, public facilities To enable them to appreciate their locality and to develop a feeling of attachment to it To enable them to think about their roles and actions as members of their groups or society and to act safely and appropriately	a)	Instead of facing the reality of the recovery from the disaster of Kumamoto Earthquake, it aims to turn children's attention to the values of local community and local historical experience such as the grassland management	・I did not know about the controlled burning and fire belt mowing ・I learned the necessity of manpower for grassland management ・I learned the topography of caldera in Aso ・I am happy to live in Minami-Aso ・It was great that we are involved in the culture of Aso such as grassland management	・I have seen a lot of conservation for the grasslands from a young age ・We have no one but each other to conserve the plants and flowers in Aso	○	○		○
	b)	It used the National Park and GIHAS, Geo-park for realization of the local historical experience	・I did not know about the national park ・I did not know that the Aso was designated a national park ・I was surprised at the national park in foreign countries ・I was surprised at the numbers of national park in foreign countries	・It will expand opportunities to transmit the agriculture in Aso		○	○	○
	c)	It introduced the voluntary activities of the local rural communities and the urban residents	・I realized that so many hands are needed for grassland management	・I was surprised at the amount of the volunteers		○		○
	d)	It promotes the friendship of elementary and junior high school students through the recreational program	-	-				
Junior high school curriculum [Integrated studies] Learning activities about interdisciplinary topics, including environment, welfare, health Learning activities about tasks based on students' interests Learning activities about tasks depending on the characteristics of the local community and the school Learning activities concerning employment and their own futures	e)	It provides junior high school students with the problem to debate on the restoration of grasslands by locals and NPOs after the torrential rainfalls in Northern Kyushu in 2013, and the visions of local community in the future	-	・I wish to provide the information about the grassland in Aso ・I try to consider the direction for the conservation and the transmission of Aso ・The adults don't know the appealing of flowers in Aso ・It is necessary to confirm the values of plants in Aso ・I hope to publish the digital books about the grasslands	○	○	○	○

Comparison of Debris Flow Hazard Mapping between Empirical Function and Numerical Simulation - a Case Study in Taiwan

Ting-Chi TSAO[1*], Chuan-Yi HUANG[1], Jung-Hsing CHIEN[1], Hsiao-Yuan YIN[2] and Chen-Yu CHEN[2]

[1] Disaster Prevention Technology Research Center, Sinotech Engineering Consultants, INC.
(280 Xinhu 2nd Rd., Neihu Dist., Taipei 11494, Taiwan)
[2] Soil and Water Conservation Bureau, Council of Agriculture
(6, Guanghua Rd., Nantou City, Nantou County 54044, Taiwan)
*Corresponding author. E-mail: tctsao@sinotech.org.tw

In this study we performed field investigation of a debris flow hazard event in eastern Taiwan, and conducted debris flow hazard mapping with empirical (SWCB guideline) and numerical methods (RAMMS::DebrisFlow). Finally we compared the mapping results with the damage of the housings and infrastructures, and discussed the applicability of these two methods. The preliminary inundation area following the empirical method is the greatest (13 Ha), after modification with local topography it reduces to 4.6 Ha. The numerical simulation result is the closest to the actual scenario. By applying the hazard degree classification based on velocity and inundation height, a hazard map is provided. The high hazard degree in the map matched with the damage status on the field, indicating that the hazard map could be used for land-use planning and local protection engineering purposes.

Key words: debris flow, hazard mapping, numerical simulation, RAMMS

1. INTRODUCTION

Debris flow has been one of the most devastating sediment disasters around the world. The direct and indirect damages caused by debris flow had cost tremendous economic losses and great casualties [*Jakob and Hungr*, 2005]. In Taiwan, the steep terrain, frequent occurrence of earthquake and heavy rainfall has made debris flow a major natural hazard in mountainous region [*Lo et al.*, 2012].

Debris flow is a hazard with high repeat potential, thus mitigation based on the mapping of possible inundation area for debris flow hazard could effectively reduce the casualty and economic losses.

The technique of debris flow hazard mapping has been greatly improved in the past decade [*Yu et al.*, 2006; *Takanashi et al.*, 2007; *Uchida et al.*, 2009;], and both empirical and numerical methods had been proposed to estimate the run-out distance and inundation area of debris flow [*Scheidl and Rickenmann*, 2010; *Cui, et al.*, 2011; *Rickenmann*, 2016]. However, there might be different degree of impact, which would result to different degree of damage and losses within the inundation area, thus introducing a classification method is worth to study.

2. METHOD

In this chapter we will introduce the empirical method currently applied by the Soil and Water Conservation Bureau, Taiwan, and the numerical simulation model and hazard classification introduced from Switzerland studies.

2.1 Empirical method

To better practice the task of debris flow hazard mapping, the Soil and Water Conservation Bureau (SWCB), the agency in charge of debris flow hazard management and mitigation in Taiwan, published the Manual for Potential Debris Flow Torrent Mapping in 2013. The manual is a guideline based on empirical method derived from Japanese studies and modified with local experiences. With estimated debris volume based on watershed size, run-out distance based on topography inputs, together with some criteria of terrain in deposition area, one could follow the steps and complete the hazard mapping.

The empirical equations for designated volume and run-out distance follow the previous studies in Japan [*Ikeya*, 1981] and Taiwan [*Hsieh and Tsai*, 1997], are written as Eq.(1*a*) and Eq.(1*b*).

$$V = 70{,}992 \times A^{0.61} \qquad (1a)$$

$$\log(L) = 0.42 \times \log(V \times \tan\theta) + 0.935 \qquad (1b)$$

In which A=catchment area (km^2), V=estimated debris volume (m^3), L=run-out distance (m), θ=slope of torrent (transportation zone, in degree).

Usually the start point of the run-out distance is the apex of the deposition zone, with the run-out distance as the radius, a 105-degree fan would be drawn. The shape of the fan is then modified according to on-site investigation and local topography, the most important is delineating areas exceeded 10 to 12 m height from the riverbed, considering the height as none-influence area under normal condition [*Hsu et al.*, 2010; *SWCB*, 2013].

Following the concept of the manual, the inundation areas of 1,719 torrents with debris flow hazard potential were mapped out in Taiwan, and corresponding mitigation strategies were then conducted.

2.2 Numerical simulation

In this study we adopted the RAMMS (Rapid Mass Movement Simulation) software system developed by WSL (Swiss Federal Institute for Forest, Snow and Landscape Research) for debris flow numerical simulation. The RAMMS system contains avalanche, rockfall, and debris flow modules [*Bartelt et al.*, 2012; *Hussin et al.*, 2012; *Leine et al.*, 2013] and were applied in several case studies in Taiwan [*Chung et al.*, 2017; *Lee et al.*, 2016a, 2016b].

The debris flow module of RAMMS is designed for flow phenomena containing fast move particulate debris. The model is based on 2-D depth-averaged shallow-water equations for granular flows in three dimensions given by the coordinates of the topographic surface of the digital elevation model in a (x,y,z) coordinate system and at time (t) [*WSL*, 2017; *Frank et al.*, 2017]. With the input of DEM (digital elevation model) the model could chose either hydrograph (when only the rainfall hydrograph is available) or block release (when the specific volume of the event is known) to input the release volume, and with the setting of parameters the maximum flow velocity and inundation height as the output. The input process is shown in **Fig. 1** (for more detail of the RAMMS::DebrisFlow module, please see [*WSL*, 2017] or [*Frank et al.*, 2017]).

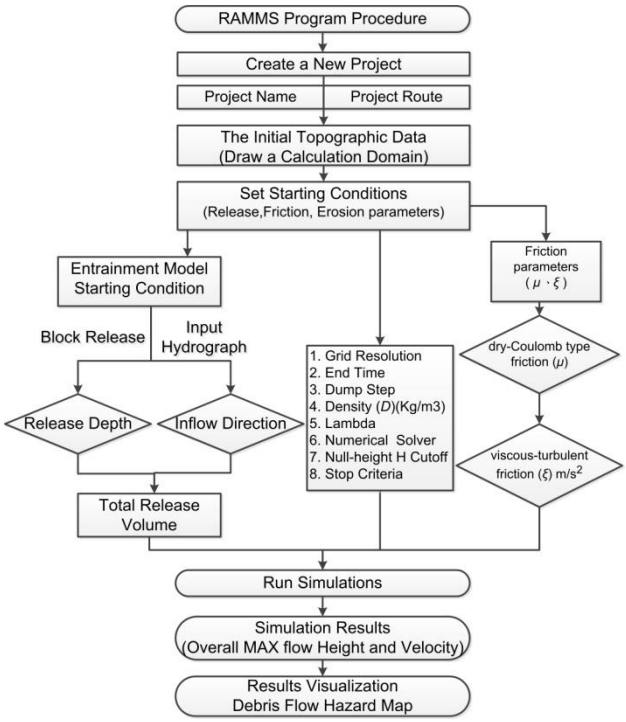

Fig. 1 RAMMS::DebrisFlow input procedure

2.3 Hazard mapping and hazard classification

In Switzerland the hazard mapping of natural hazards (floods, snow avalanches, and mass movements) had been developed for decades, with the preparation of natural hazard maps the spatial distribution of possible hazard hot spots become a vital information in land-use planning, infrastructure planning, and hazard mitigation. The Swiss hazard maps could be applied in the following purpose: spatial planning, risk reduction measures, instruments used in emergency planning, and raising the awareness among the population [*SDC*, 2005].

However the inundation area alone does not specify the intensity or the possible risks within the zones, thus it is difficult to classify and implant proper treatments. For example different intensity of velocity or inundation height may lead to different degree of loss, thus using velocity or inundation height, or both in combination, become a common method to classify the different degrees.

The hazard degrees were usually classified into high, medium, low and none-hazard, often shown on the map with respectively colors to indicate the differences. *BUWAL* [1997] and *Rickenmann* [2005] suggested the classification of debris flow hazards with different intensity combination of h (inundation height) and v (velocity), an update of the 2005 classification proposed by *Rickenmann* [personal communication, 2015] was adopted in this study, with more details in "medium" class, as shown in

Fig. 2.

The classification, definition and color of debris flow hazard degrees based on intensity are shown in **Table 1**.

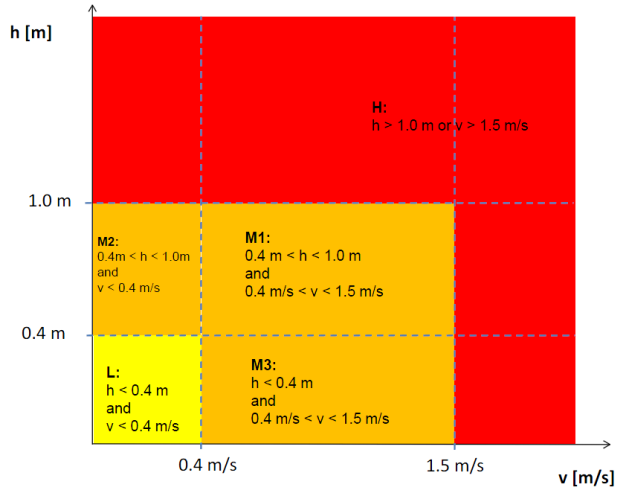

Fig. 2 Debris flow intensity classification [Rickenmann, personal communication, 2015]

Table 1 Debris flow hazard degree classification and definition

	Intensity classification	Hazard degree	Definition
Intensity	h>1.0 m or v>1.5 m/s	High	Persons are in danger both inside and outside their houses. Buildings are in danger of being destroyed.
	0.4m<h<1.0 m and 0.4 m/s<v<1.5 m/s	Medium	Persons are in danger outside their houses. Buildings may suffer damage and possible destruction depending in construction characteristics.
	0.4m<h<1.0m and v<0.4m/s		
	h<0.4m and 0.4m/s<v<1.5m/s		
	h<0.4 m and v<0.4 m/s	Low	Danger to persons is low or non-existent. Buildings may suffer little damage, but flooding or sedimentation may affect house interiors.

3. CASE STUDY

The Hualien DF168 potential debris flow torrent is located at the 8th settlement of Mayuan Village, Hualien County, which is at eastern Taiwan. There are approximately 40 households, 120 residents in the settlement, most of them indigenous people. The area of the catchment is about 18 hectare, the 1,226 m long torrent is east-west direction, and descending from 455 m (west) to 115 m (east), and the average slope of the torrent is 16 degree.

The upper part of the catchment consists of Tananao schist, which is rich of schist, limestone, and gneiss. The lower part consisted of tableland deposit, which mainly contained unconsolidated gravel deposits and were easily eroded and washed away by surface runoff. Also the region has some mining history with several abandoned mines around, with some mineral waste on the hillslope.

3.1 Hazard event

The record shows that the region had 2 debris flow hazard events, at the 1989 and 2001 typhoon events the accumulated rainfall were 447mm and 489.5 mm respectively. During July 2014 when Typhoon Matmo hit Taiwan, the rainfall and surface runoff eroded the banks of the torrent, resulted in torrent banks collapsed and formed a debris flow. The debris flow overflew at a box culvert and buried, damaged 3 residential houses of the 8th settlement. Fortunately the residents were evacuated in the previous afternoon so no one was injured.

From the rainfall hydrograph of nearby rainfall station, it is estimated that when the debris flow occurred (mid-night of July 23, 2014) the rainfall intensity and accumulated rainfall were 74.5 mm/hr and 328.5 mm respectively, the total accumulated rainfall of the event was 544 mm, which exceeded the debris flow red alert value (500 mm) set by the Soil and Water Conservation Bureau.

The field investigation of the disaster was conducted right after the event (Jul. 24, 2014, **Fig. 3**). The debris had blocked the drainage system and overflew. Three residential houses (Nos.157, 157-1, 157-2) at the left bank with their farmhouse, warehouse and farming machineries were buried by 1 to 1.5 m deep debris (boulders diameter ranging from 8 to 30 cm). Three other residential houses and a grocery store located at the right bank were close to the torrent and considered hazardous. The apex of the deposition zone was 80 m upstream of the drainage box culvert, the total deposition length is approximately 275 m with the terminate slope at approximately 2 degrees and the apex around 6 degrees. The inundation area was 4,782 m^2 and debris volume around 5,000 m^3.

The riverbed was full of collapsed boulders and the cross section was U-shape due to the eroded and transportation of the debris. Only some small size bank collapses were discovered at the transportation zone, totally less than 400 m^2. No large area of landslides could be found in the initiation zone, however a deep incision which resulted to bank erosion and collapse could be observed. The size of the boulders were mostly greater than 30 cm, some of them exceeded 2 m. It was estimated that the

incision and erosion of the torrent bed and banks were the main source of the debris in this event.

UAV photo (provided by NCDR)

(Google Map)

(this study)

(Google Map)

(Chinatimes.com)

Before the event | After the event

Fig. 3 Hualien DF168 torrent before and after the disaster

3.2 Empirical run-out distance and numerical simulation results

From Eq.(1*a*) and Eq.(1*b*) the calculated run-out distance of Hualien DF168 is 400 m, as indicated by the yellow fan shape in **Fig. 4**. The modified inundation area based on local topography is shown as the red region in **Fig. 4**.

The input of RAMMS::DebrisFlow of this study is shown in **Table 2**, the simulation results (maximum inundation height and velocity) and hazard map are shown in **Fig. 5**.

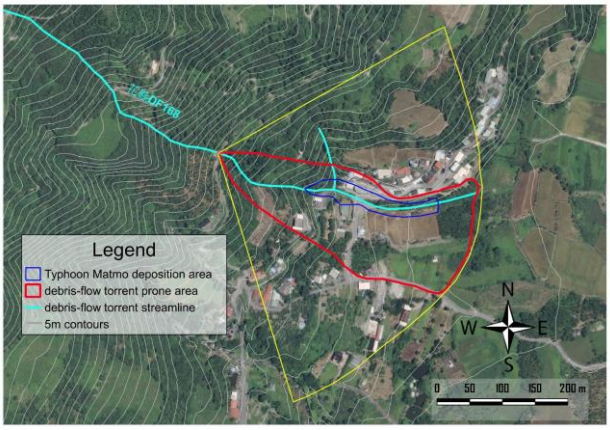

Fig. 4 Empirical run-out distance (yellow fan shape) and inundation area

The further downstream the hazard degree decreases, which is in consistent with the in situ gradient changes. The heavily damaged houses and culvert shown in **Fig. 3** located close to the apex appoint, which matched the red (high hazard) region shown in the hazard map (**Fig. 5**) and indicated that the debris would deposit at when the gradient has a sudden reduce.

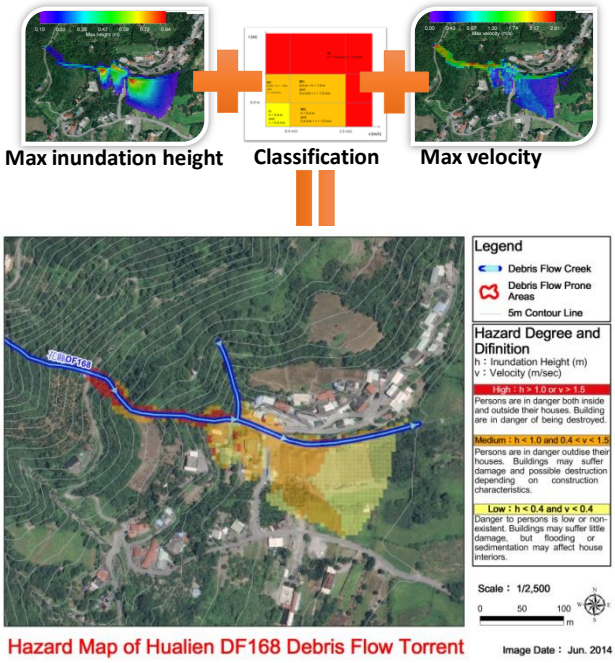

Fig. 5 RAMMS::DebrisFlow simulation result and hazard map

Table 2 RAMMS::DebrisFlow input data of Hualien DF168

	Input data
Terrain (DEM)	5 m*5 m
Dry-Coulomb type friction (μ)	0.225
Viscous-turbulent friction (ξ)	150 m/sec^2
Density (D)	2.65 kg/m^3
Stop criteria	12 hr or momentum < 5%
Block release	5,000 m^3
Hydrograph	2014/7/22 AM10:00 to 2014/7/23 PM21:00 rainfall data from C1Z030 station

4. COMPARISON AND DISCUSSION

By overlaying the areas we could compare the differences of the outputs (**Fig. 6**), the inundation area of the real event is 0.48 Ha (blue region in **Fig. 6**), the preliminary area following the empirical method of SWCB guideline is the largest (13 Ha, yellow region in **Fig. 6**), after modification and adjustment based on local topography this reduced to 4.6 Ha (red region in **Fig. 6)**, and the numerical simulation result (shown with 3 hazard degree color shades) is the closest to the actual hazard event.

After the delimitation of preliminary result, the inundation area reduced by 65% (from yellow to red region), however compared to the numerical result it is still 60 to 70% larger.

For evacuation purposes the empirical method would provide enough information alone, however for land-use planning, local protection engineering or insurance purposes the numerical method could provide more useful information.

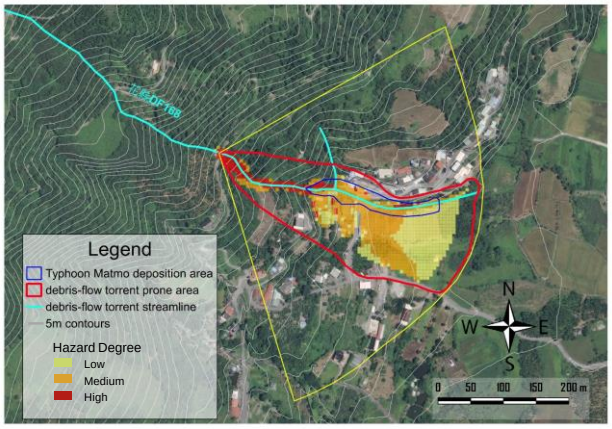

Fig. 6 Comparison the inundation area of empirical (yellow fan shape) and numerical (3 color shades) methods

5. CONCLUSIONS

Debris flow hazard mapping is an important task in the preparedness stage of natural hazard management, applying the empirical method could produce a hazard map more quickly, but the expert judgment and adjustment at the field would play a vital role. Also it would be difficult to further classify the hazard degrees within the inundation area. The numerical simulation could provide intensity information for hazard degree classification, but it requires more data and resources for calibration, choosing different parameter and inputs may lead to different results, which also requires expert and professional knowledge for interpretation [*Wu and Chen*, 2016].

In the future the hazard mapping of debris flow would still play an important role in land-use planning and hazard mitigation, a long-term data collection and observation of debris flow events together with post-event documentary could benefit both empirical and numerical approaches [*Tang et al.*, 2012].

ACKNOWLEDGMENT: The authors give their greatest thanks to the Soil and Water Conservation Bureau of Taiwan, which provided part of the research funding. The authors also thank the kindly help from Dr. Rickenmann of WSL for the discussion of hazard classification.

REFERENCES

Bartelt, P., Bühler, Y., Buser, O., Christen M. and Meier, L. (2012): Modeling mass-dependent flow regime transitions to predict the stopping and depositional behavior of snow avalanches, Journal of Geophysical Research, Vol. 117, No. F1, 2012.

BUWAL (1997): Berücksichtigung der Hochwassergefahren bei raumwirksamen Tätigkeiten. Empfehlungen, Bundesamt fur Umwelt Wald und Landschaft, Berne, Switzerland.

Chung, M.C., Chen, C.H., Tan, C.H., Lee, C.F. and Huang, W.K. (2017): Investigation and Assessment Plan at the Xinzhuang Potential Large-Scale Landslide in Southern Taiwan. In: Mikos, M., Tiwari, B., Yin, Y., Sassa, K. (eds) Advancing Culture of Living with Landslides. WLF 2017. Springer, Cham.

Cui, P., Hu, K., Zhuang, J., Yang, Y. and Zhang, J. (2011): Prediction of debris-flow danger area by combining hydrological and inundation simulation methods, J. Mt. Sci., 8, pp.1-9.

Frank, F., McArdell, B. W., Oggier, N., Baer, P., Christen, M. and Vieli, A. (2017): Debris-flow modeling at Meretschibach and Bondasca catchments, Switzerland: sensitivity testing of field-data-based entrainment model, Nat. Hazards Earth Syst. Sci., 17, pp.801-815.

Hsu, S. M., Chiou, L. B., Lin, G. F., Chao, C. H., Wen, H. Y. and Ku, C. Y. (2010): Applications of simulation technique on debris-flow hazard zone delineation: a case study in Hualien County, Taiwan, Nat. Hazards Earth Syst. Sci., 10, pp.535-545.

Hussin, H. Y., Quan Luna, B., van Westen, C. J., Christen M., Malet J. P. and van Asch, Th. W. J. (2012): Parameterization of a numerical 2-D debris flow model with entrainment: a case study of the Faucon catchment, Southern French Alps, Nat. Hazards Earth Syst. Sci., Vol. 12, No. 10, pp. 3075-3090.

Ikeya, H. (1981): A method for designation for areas in danger of debris flows. Erosion and Sediment Transport in the Pacific Rim Steeplands. IAHS Special Pub. 132, pp.576-588.

Jakob, M. and Hungr, O. (2005): Ch.1 Introduction, In: Jakob, M. and Hungr, O. (eds), Debris-flow Hazards and Related Phenomena, Springer Berlin Heidelberg, pp.1-7.

Lee, C.F., Chou, H.T., Tsao, T.C., Hsu, C.H., Huang, C.H. and Liao, W.S. (2016a): Heliu debris flow induced by Typhoon Soudelor: failure mechanism and numerical simulation, Journal of Chinese Soil and Water Conservation, 47(4), pp.171-184 (in Chinese).

Lee, C.F., Tsao, T.C., Wei, L.W. and Huang, W.K. (2016b): The case study of Badouzih rockfall in northern Taiwan: mechanism, numerical simulation and hazard assessment, In: Koboltschnig, G. (ed.): Internationales Symposion Interpraevent – Lucerne (30 May – 02 June). Klagenfurt: Internationale Forschungsgesellschaft Interpraevent. pp. 698-707.

Leine, R. I., Schweizer, A., Christen, M., Glover, J., Bartelt P. and Gerber, W. (2013): Simulation of rockfall trajectories with consideration of rock shape, Multibody System Dynamics, Vol. 32, No 2, pp.241-271.

Lo, W.C., Tsao, T.C. and Hsu, C.H. (2012): Building vulnerability to debris flows in Taiwan - a preliminary study, Natural Hazards, 64(3), pp.2107-2128.

Rickenmann, D. (2005): Hangmuren und Gefahrenbeurteilung. Kurzbericht fur das Bundesamt für Wasser und Geologie, Unpublished report, Universitat fur Bodenkultur, Wien, und Eidg. Forschungsanstalt WSL, Birmensdorf.

Rickenmann, D. (2016): Debris-flow hazard assessment and methods applied in engineering practice, International Journal of Erosion Control Engineering, 9(3), pp.80-90.

Scheidl, C. and Rickenmann, D. (2010): Empirical prediction of debris-flow mobility and deposition on fans, Earth Surface Processes and Landforms, 35(2), pp.151-173.

Shieh, C. L. and Tsai, Y. F. (1997): Experimental study on the configuration of debris-flow fan. In: International Conference on Debris-Flow Hazards Mitigation: Mechanics, Prediction, and Assessment, Proceedings, ASCE, pp.133-142.

Soil and Water Conservation Bureau [SWCB] (2013): Potential debris flow hazard torrents mapping guideline, Soil and Water Conservation Bureau, Council of Agriculture, Nantou, Taiwan (in Chinese).

Swiss Agency for Development and Cooperation [SDC] (2005): Vademecum: hazard maps and related instruments: the Swiss system and its application abroad - capitalisation of experience, Swiss Agency for Development and Cooperation, Bern, Switzerland.

Takanashi, K., Mizuyama, T., and Nakano, Y. (2007): A method for delineating restricted hazard areas due to debris flow. 4th International Workshop Debris Flow Hazard Mitigation, Chengdu, China.

Tang, C., Zhu, J., Chang, M., Ding, J. and Qi, X. (2012): An empiricalestatistical model for predicting debris-flow runout zones in the Wenchuan earthquake area, Quaternary International, 250, pp.63-73.

Uchida, T., Nishimoto, H., Osanai, N. and Shimizu, T. (2009): Countermeasures for sediment-related disasters in Japan using hazard maps, International Journal of Erosion Control Engineering, 2(2), pp.46-53.

WSL (2017): RAMMS::DEBRISFLOW User Manual v1.7.0, Switzerland.

Wu, T. and Chen, S.C. (2016): Debris flow non-rectilinear motion case study to reflect hazard zone delimitation, Journal of Chinese Soil and Water Conservation, 47(1), pp.24-35 (in Chinese).

Yu, F., Chen, C.Y., Chen, T.C., Hung, F.Y. and Lin, S.C. (2006): A GIS process for delimitating areas potentially endangered by debris flow, Natural Hazards, 37(1-2), pp.169-189.

Debris Flow Detection Using LVP Sensors in Japan

Hitoshi KATO[1], Nobuyuki NODA[2], Kazuhiko HASHI[3], Satoshi TAGATA[4], Takahiro ITOH[5*] and Takahisa MIZUYAMA[6]

[1] Nara Prefectural Office (Nara City, Nara 630-8213, Japan: Former in Osumi Office of River and Highway, MLIT)
[2] Yamakuni River Office in Kyushu Regional Bureau, MLIT
(Nakatsu, Oita 871-0026, Japan: Former in Osumi Office of River and Highway, MLIT)
[3] Osumi Office of River and Highway, Kyushu Regional Bureau, MLIT
(1013-1 Kimutsuki-cho, Kimotsuki, Kagoshima 893-1207, Japan)
[4] Nippon Koei Co., Ltd. (1-14-6 Kudankita, Chiyoda-ku, Tokyo 102-0083, Japan)
[5] Research and Development Center, Nippon Koei Co., Ltd. (2304 Inarihara, Tsukuba, Ibaraki 300-1259, Japan)
[6] National Graduate Institute for Policy Studies (GRIPS) (22-1, Roppongi 7 chome, Minato-ku, Tokyo 106-0032, Japan.)
*Corresponding author. E-mail: a6556@n-koei.co.jp

Sakura-jima Island is an active volcano in the southwest region of Kyushu in Japan. The area surrounding the volcano is impacted by significant debris flows when rainfall follows an eruption. Various studies have investigated the use of sensors including wire sensors and accelerometers to detect such events. Wire sensors typically incorporate three horizontal wires set at heights of 60, 120, and 180 cm from the river bed and can be used to quantify the magnitude of the debris flow. We have developed an LVP (load, vibration, pressure) sensor [*Itoh et al.*, 2017] and installed it at two test sites to establish its suitability for continuous detection of debris flows. The sensor consists of a load cell, an accelerometer, and a pressure meter. The sensor is mainly used for debris flow detection but also measures the load of the surge. In this paper, we present the results of an analysis of LVP and wire sensor data that were recorded at the test sites to verify the accuracy of the LVP data, and propose threshold values for debris flow occurrences which were observed using the LVP sensors.

Key words: debris flow detection, bed pressure, vibration, LVP sensor

1. INTRODUCTION

The rivers around the Sakura-jima volcano are highly susceptible to debris flows caused by the large volumes of volcanic ash that are frequently deposited across the region. The debris flows are triggered by rainfall after an eruption and contain huge volumes of sediment. The early detection of such events is therefore very important and the use of various sensors including wire sensors, accelerometers [*Osumi Construction Office*, 1988] and geophones [e.g., *Arattano et al.*, 2008] has been proposed for this purpose. Wire sensors have been used in Japan because they are cheap and easy to maintain. In addition, we have identified occurrences of debris flow on Sakura-jima Island using CCTV images and by monitoring the disconnection of the wires. This enabled for the flow to be quantified from knowledge of the separation of the wire from the river bed such as debris flow height of 60, 120 and 180 cm [*Osumi Office of River and Highway*, 2013].

LVP (load, vibration, pressure) sensors consist of a load cell, accelerometer, and pressure meter. A proposal for continuous monitoring of debris flow using a combination of wire and LVP sensors was first proposed by Itoh et al. [2017]. However, wire sensors are unable to detect further debris flow events after disconnection and wires are sometimes disconnected by random objects in the river and animal activities. In this study, we present the further development of an LVP sensor, its installation on Sakura-jima Island and the results from the field study.

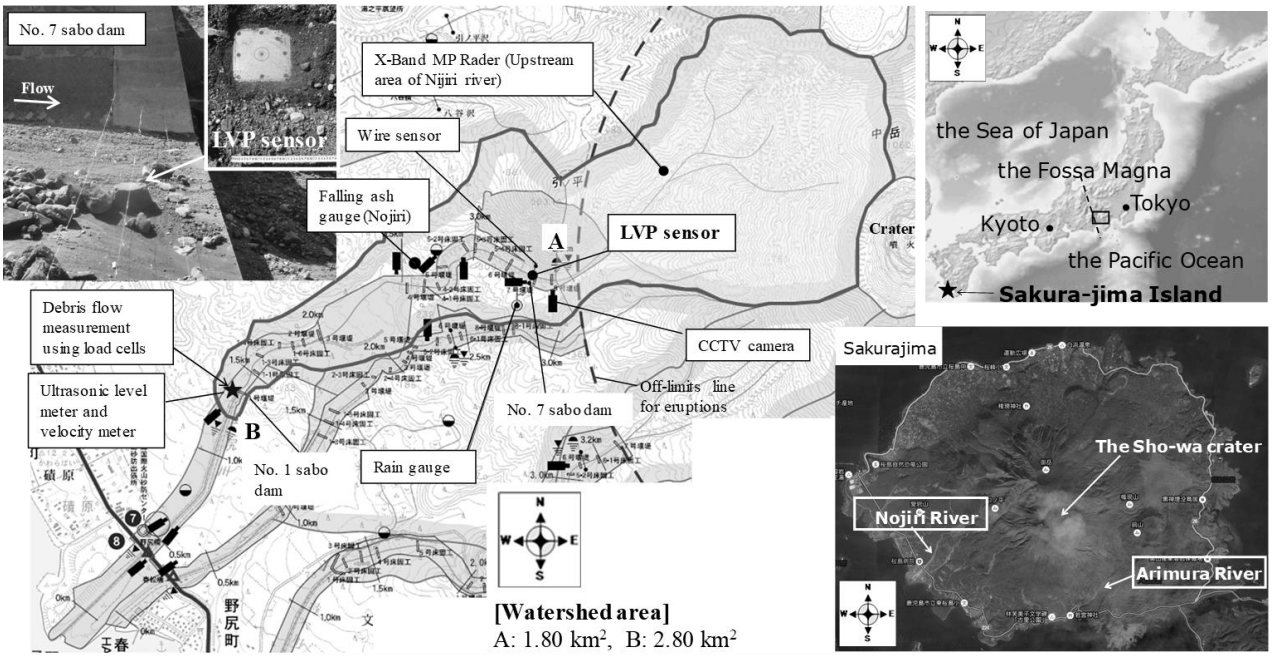

Fig. 1 Several kinds of sensors for debris flow monitoring in Sakura-jima Island

2. EXISTING DEBRIS FLOW DETECTION SENSORS

Various sensors have been used to detect debris flow including wire sensors, optical beams and accelerometers [e.g., *Okuda et al.*, 1980; *Hirano et al.*, 1999; *Suwa et al.*, 2011]. Wire sensors have been widely used after the applicability was confirmed by field surveys at Kami-Kami-Hori Creek in Japan [*Okuda et al.*, 1980]. Surface velocity sensors and spatial filter velocimetry were also used at the study site [*Itakura et al.*, 1985; *Itakura and Suwa*, 1989]. However, the sensor was not used at other sites. Other studies have looked at various sensors for debris flow monitoring [e.g., *Arattano et al.*, 1999 & 2008; *Scott et al.*, 2011]. Wire sensors identify the occurrence of debris flow by monitoring the disconnection of the wires and the magnitude of the flow is estimated using knowledge the height of wire from the riverbed, which is usually 60 cm, 120 cm, and 180 cm from the bed surface. However, they require intervention to reconnect the wires after each event. CCTV cameras are also used but cannot observe night-time surges. Therefore, there is a need for a new type of sensor that will mitigate against the drawbacks of the existing technology.

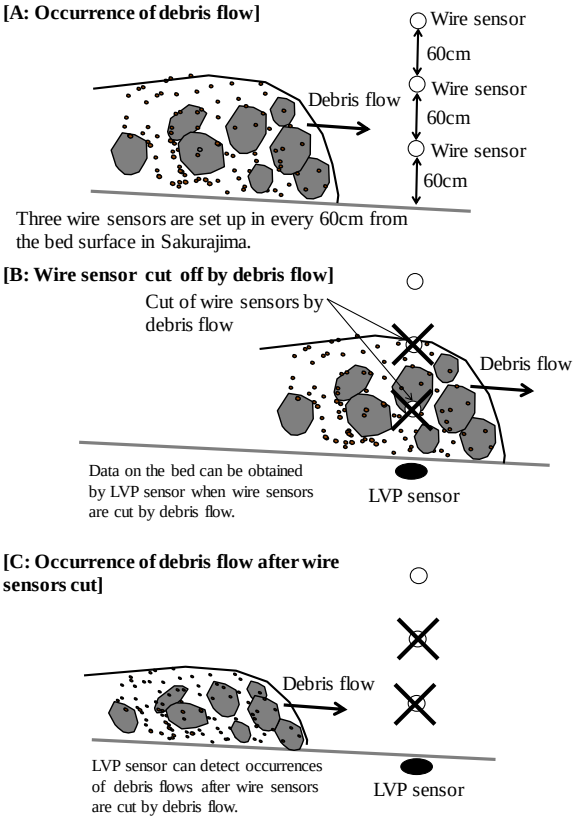

Fig. 2 Schematics of debris flow detections by combination of a wire and a LVP sensors

3. DEVELOPMENT OF THE LVP SENSOR

3.1 Monitoring sites

Fig. 1 shows the location of the study site on the Nojiri River on Sakura-jima Island. Several types of sensors in addition to the LVP sensor were installed, including rainfall gauges, falling ash gauges, CCTV cameras, wire sensors, ultrasonic level sensors, and velocity meters. Continuous direct debris flow measurement using loadcell and pressure meters (DFLP) [*Osaka et al.*, 2014] was

Table 1 Debris flow detection by wires and the LVP sensor that has a round small force plate of 60 mm in diameter

No.	Date	Disconnected wires			Detection by a LVP sensor		
		1st (60cm above from the bed)	2nd (120cm)	3rd (180cm)	Flow depth	Vibration	Weight
1	March 19th, 2015	○	○	○	○	○	○
2	April 6th, 2015	○	—	—	○	○	○
3	April 19th, 2015	○	—	—	(○) *1	(○) *1	(○) *1
4	May 3rd, 2015	○	○	—	○	○	○
5	May 12th, 2015	○	○	—	○	○	○
6	June 3rd, 2015	○	—	—	○	○	○
7	June 8th, 2015	○	○	—	○	○	○
8	June 14th, 2015	○	—	—	○	○	○
9	Augus 16th, 2015	○	○	—	○	○	○
10	August 30th, 2015	(○) *2	—	—	○	○	○
11	September 6th, 2015	○	—	—	○	○	○
12	October 1st, 2015	○	—	—	○	○	○
13	December 10th, 2015	○	○	—	○	○	○
14	April 21st, 2016	○	○	—	○	○	○
15	May 9th, 2016	○	—	—	○	○	○
16	June 13th, 2016	○	—	—	○	○	○
17	June 16th, 2016	○	—	—	○	○	○
18	June 19th, 2016	○	○	—	○	○	○
19	June 27th, 2016	○	—	—	○	○	○
20	June 27th, 2016	○	○	—	○	○	○
21	July 11th, 2016	○	—	—	○	○	○
22	July 2oth, 2016	○	—	—	○	○	○
23	September 17th, 2016	○	○	—	○	○	○
24	September 20th, 2016	○	○	○	○	○	○

also performed to evaluate mass density and sediment concentration.

3.2 Development LVP sensor and detections of debris flows

The LVP sensor consists of a load cell [e.g., *McArdell et al.*, 2007; *Osaka et al.*, 2014], accelerometer, and pressure meter. The sensor was modified by trial and error at the study site [*Itoh et al.*, 2017] and installed on the river bed to directly measure debris flow.

Fig. 2 shows the arrangement of the wire and LVP sensors used for the detection of debris flow. **Fig. 3** shows the longitudinal bed profile of the Nojiri River. The bed slope at the Nojiri No. 7 sabo dam test site is 1/7.6 (7.50 degrees) and the supposed equilibrium sediment concentration for the bed slope is 0.147 for a specific weight of 2.65 and an interparticle friction angle of the sediment particles of 34 degrees.

The No. 2 sensor, which was installed on the bed on February 6th, 2015, was modified to minimize the risk of direct impact from large boulders by fitting a smaller 6 cm diameter force plate [*Itoh at al.*, 2017]. The advantage of the smaller plate is that the risk of damage due to a direct impact from a boulder is reduced. However, the accuracy of the load reading is also reduced as a result [e.g., *Scott et al.*, 2011]. The data sampling rate was 10 Hz.

The No. 2 sensor detected 23 of 24 occurrences

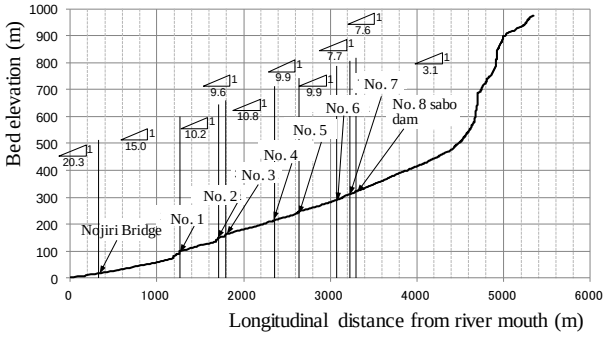

Fig. 3 Longitudinal bed profiles and sabo dam layout the Nojiri River in Sakura-jima Island

of debris flow events as shown in **Table 1**. In the table, "O" denotes a successful debris flow detection, and "*1" and "*2" denote an estimation of debris flow occurrences. These estimated events occurred on April 15th and August 30th, 2015. The 24 events detected between February 6th, 2015 and March 31st, 2016 were observed by both the wires and CCTV camera. A wire also detected only 23 occurrences of debris flows, because the disconnected wire could not be maintained due to active eruption during the middle to the end of August in 2015, while the LVP sensor detected debris flows around 60 cm in depth, and because the LVP sensor could not detect debris flow surges due to transverse flow shifting on April 19th, 2015.

Data typical of a debris flow event were observed using the LVP sensor on June 8th, April

6th, and April 19th, 2015 and on June 27th, June 19th, and September 20th, 2016. The events were observed by the wire and LVP sensors at approximately the same time and the LVP sensor also detected several surges after the wires had been disconnected. However, at the Arimura No. 3 sabo dam test site on the Arimura River, the sensors and cables were destroyed by debris flow surges on April 16th, 2017, so data could not be recorded at that site.

Fig. 4a and **4b** show typical data from the LVP sensor. The load was calculated from the differences in the force plate area between 10,000 cm^2 and 28.3 cm^2 (ϕ= 6cm in diameter). As shown in **Fig. 4**, there are several patterns of data. For example, the LVP sensor detected several surges

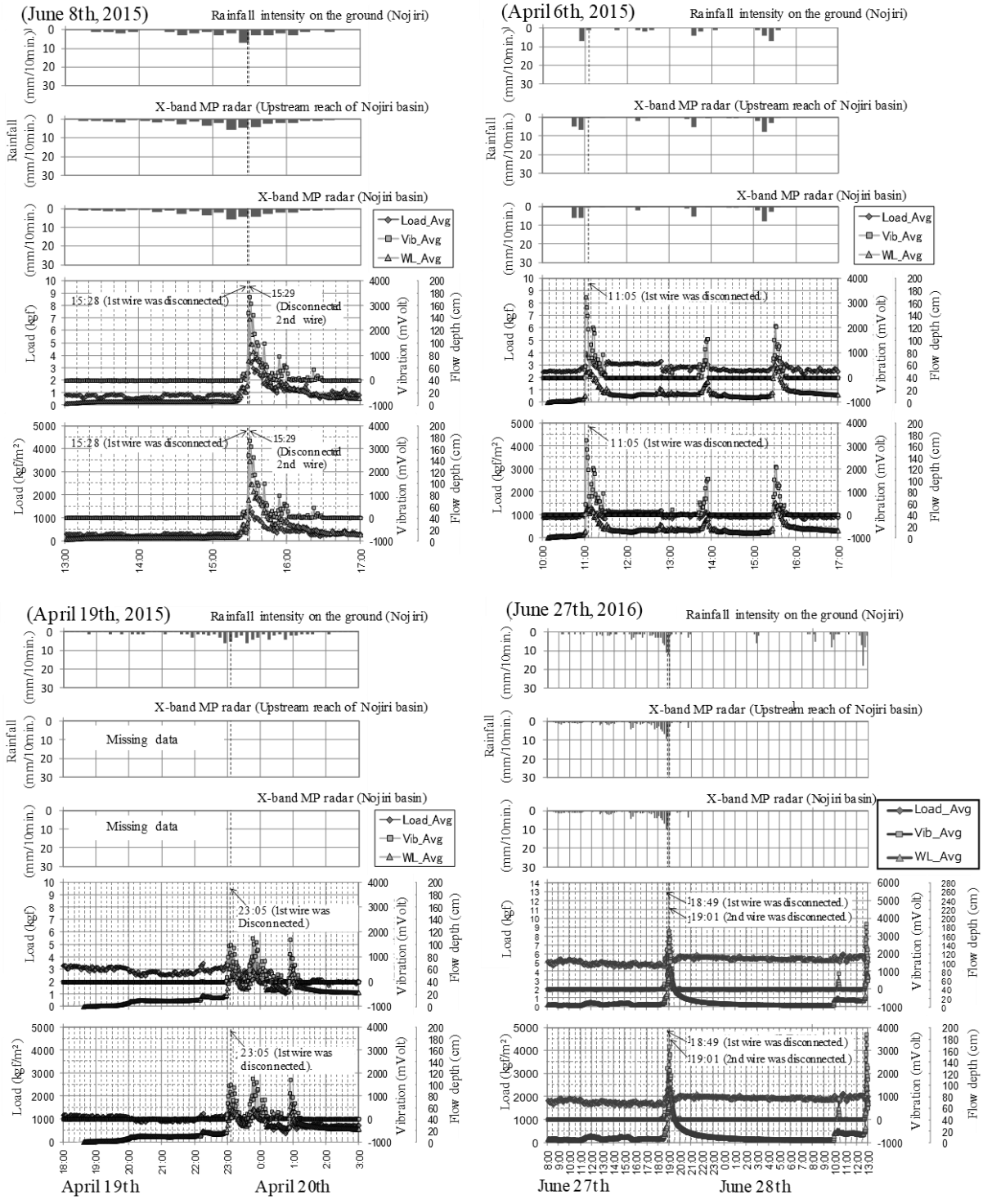

Fig. 4a Typical debris flows detected by LVP sensor on June 8th, April 6th and April 19th in 2015 and on June 27th in 2016

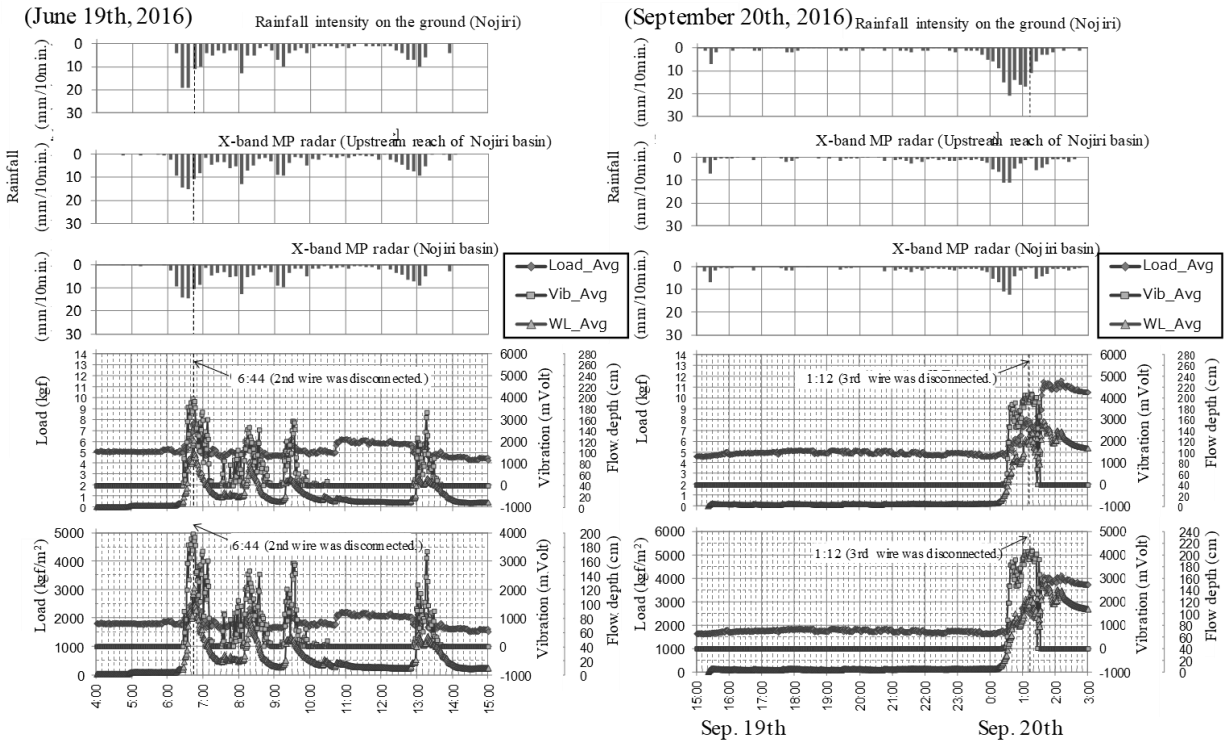

Fig. 4b Typical debris flows detected by LVP sensor on June 19th and September 20th in 2016

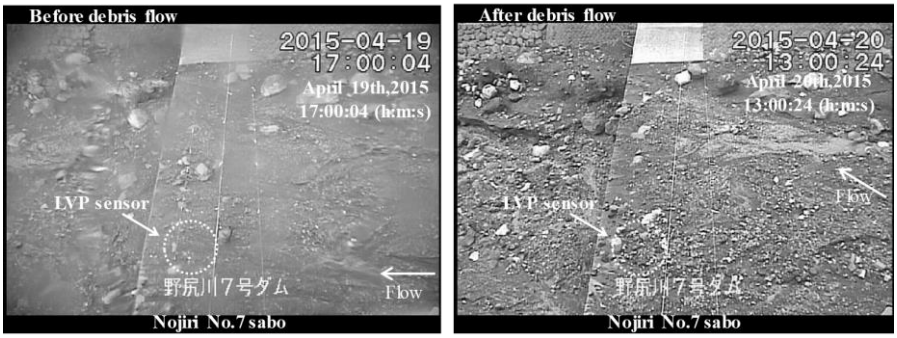

Fig. 5 Debris flow events with transvers flow shifting on April 19th in 2015

after wires were disconnected. Debris flows on September 20th, 2016 cut the 1st to 3rd wires, and were of a relatively large magnitude. Debris flows detected by both the wire and the LVP sensors after wires were disconnected were observed on April 6th, 2015 and June 19th, 2016. However, the LVP sensor did not detect the debris flows on April 19th, 2015 because of transverse flow shifting.

Fig. 5 and **6** show data from debris flow events that occurred on April 19th, 2015, and transverse installation of the LVP sensor could minimize the effects of transverse flow shifting of debris flows, but further investigation of this proposal is required.

4. EMPIRICAL EVALUATION OF DEBRIS FLOW OCCURRENCES

The relationships between flow depth and load and between flow depth and vibration at the time of wire disconnect were evaluated using the measured data.

Fig. 7 shows examples of attempts to identify threshold values of debris flow load using data from the LVP sensor and **Fig. 8** shows the threshold values for acceleration due to vibration. The threshold values are estimated to be 400 kgf/m^2 and 200 mV although it is suggested that further data are required to verify the accuracy of this information. **Fig. 9** shows a comparison of observed data and expected load measurements using the LVP sensor. Calculations for load for specific mass densities of 1.50 (c= 0.3), 1.83 (c= 0.5), and 2.65 are shown,

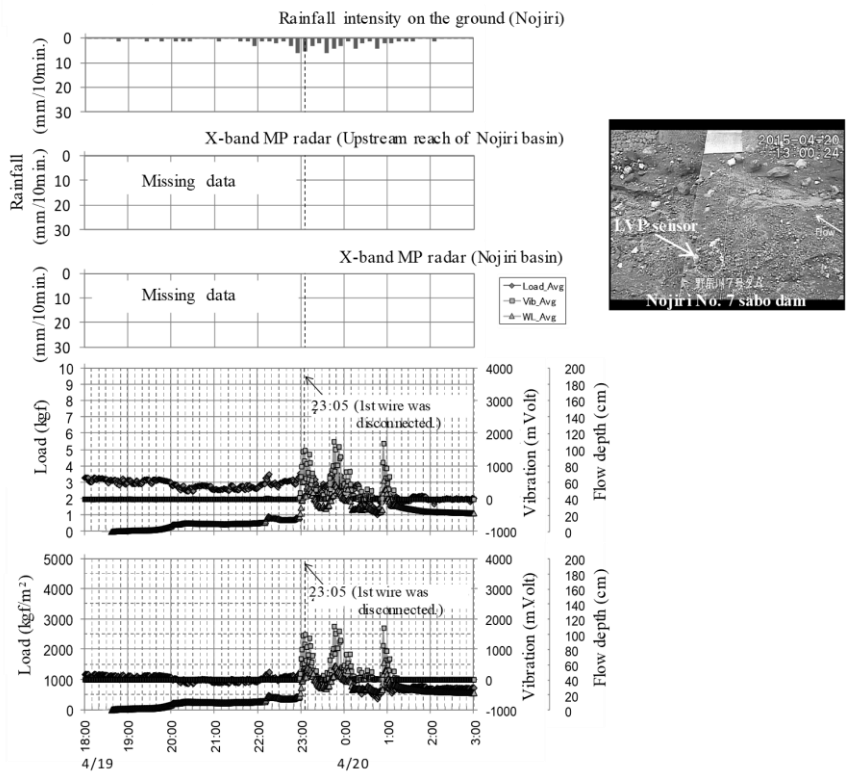

Fig. 6 Measured data obtained by the LVP sensor for debris flow events with transverse flow shifting (April 19th in 2015)

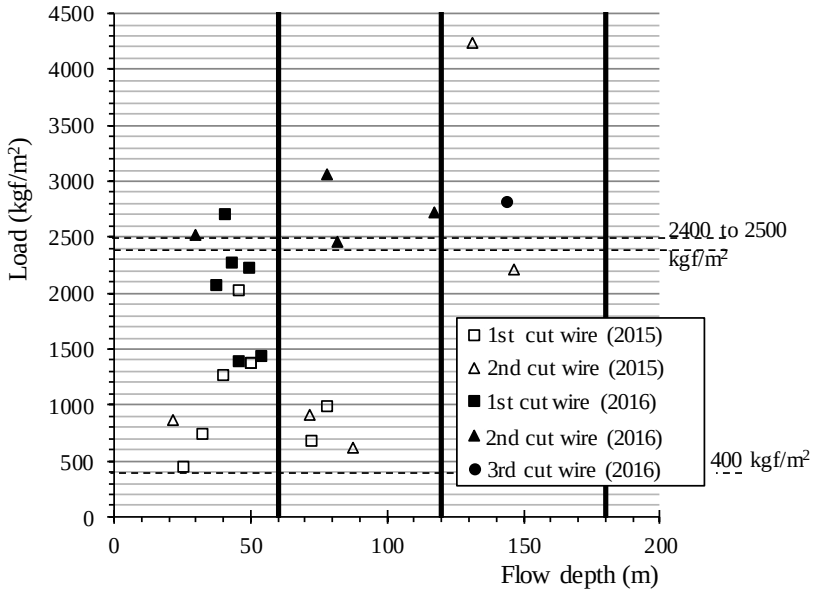

Fig. 7 Threshold values for debris flow occurrences by the relationship between flow depth and load

where *c* is the volumetric sediment concentration of debris flow and the specific weight of the solid particles is 2.65.

The measured load does not exhibit a linear relationship with flow depth because the force plate of the LVP sensor is too small to obtain absolute values. However, the purpose of the LVP sensor is to detect debris flows and evaluate threshold values. As seen in **Fig. 7** and **8**, the values are 2400 to 2500 kgf/m^2 and 2800 to 3000 mV at the second wire level (120 cm from the bed), while the threshold values for debris flow occurrences are 400 kgf/m^2 and 200 mV. The results show the possibility of estimating the magnitude of debris flow surges.

5. CONCLUSIONS

This study investigated the use of both LVP and wire sensors for debris flow detection and identified threshold values for occurrences of debris flow. The

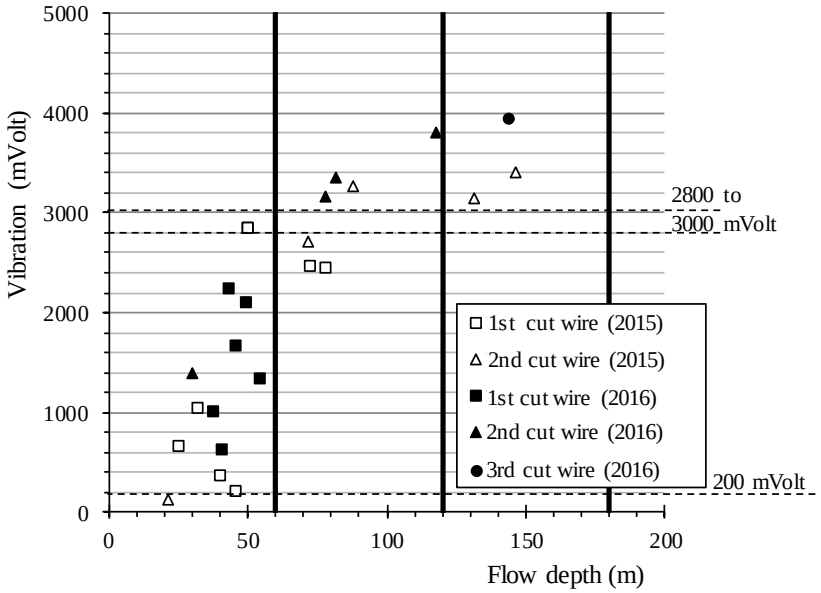

Fig. 8 Threshold values for debris flow occurrences by the relationship between flow depth and vibration

results indicate that the threshold load and vibration values for debris flow occurrences are 400 kgf/m^2 and 200 mV, respectively. Additionally, the values are 2400 to 2500 kgf/m^2 and 2800 to 3000 mV at the second wire level. Continuous data collection will be performed for several years to identify more accurate threshold values.

In addition, an optimal installation method needs to be identified to ensure reliable readings are obtained. In addition, the number of LVP sensors installed at each site needs to be considered if the effects of transverse flow shifting are to be minimized.

ACKNOWLEDGMENT: The authors are grateful to the Osumi Office of River and National Highway, Kyushu Regional Development Bureau and the Ministry of Land in Japan (MLIT) for their advice and to Dr. Koji YOKOYAMA for his advice on the development of the sensor. Additionally, the authors are grateful for research grant (KAKENHI: Scientific Research C, No. 15K07502) from the Japan Society for the Promotion of Science (JSPS) which was used to fund aspects of the present study.

REFERENCES

Arattano, M., Marchi, L., Genevois, R., Berti, M., Simoni, A., Tecca, P.R. and Bonte, M. (1999): Field monitoring and real time management of debris flows, European Project "Debris Flow Risk" (N. ENV4960253), Final Report, 30 p.

Arattano, M., and Marchi, L. (2008): Systems and sensors for debris-flow monitoring and warning. Sensors, 8, pp. 2436-2452.

Hirano, M., Hashimoto, H., Park, K., Kouno, M. and Onda, K. (1999): Field measurements of debris flows in the Mizunashi and Nakao Rivers on Mt Unzen-Hugen Dake. Journal of JSCE, No. 635, II-49, pp. 49-65 (in Japanese with English Abstract).

Itakura, Y., Ogawa, K., Suwa, H. and Mizuhara, K. (1985): Trends and fluctuation of the surface-velocity of debris flow measured by a non-contact speed sensor with a spatial filter, In Harada M. (ed.), Fluid control and measurement, Pergamon Press, Tokyo, pp. 1079-1084.

Itakura, Y. and Suwa, H. (1989): Measurement of surface velocity of debris flows by spatial filtering velocimetry, Proceedings of the Japan-China Symposium on Landslides and Debris Flows, Niigata, Tokyo, 1989, pp. 199-203.

Itoh, T., Mizuyama, T. and Tagata, S. (2017): Direct debris flow monitoring using load cell systems in Sakurajima Island, Proceedings of the 37th IAHR World Congress, 13-18 August 2017 in Kuala Lumpur, Malaysia: pp. 1142-1150, 2017.

McArdell, B. W., Perry, B., and Julia, K. (2007): Field observations of basal forces and fluid pore pressure in a debris flow, Geophysical Research Letters. 34, L07406, pp. 1-4.

Osaka T., Utsunomiya R., Tagata S., Itoh T., and Mizuyama T. (2014): Debris Flow Monitoring using Load Cells in Sakurajima Island. Proceedings of the Interpraevent 2014 Pacific Rim (edited by Fujita, M. et al.), November 25-28, Nara, Japan, 2014, O-14.pdf in DVD.

Okuda, S., Suwa, H., Okunishi, K., Yokoyama, K. and Nakano, M. (1980): Observation of the motion of debris flow and its geomorphological effects. Zeitschrift fur Geomorphology, Suppl.-Bd.35, pp.142–163.

Osumi Construction Office in the Ministry of Construction (1988): Debris flow in Sakura-jima Island, SABO Publicity Center, 65 p. (in Japanese).

Osumi Office of River and Highway in the Ministry of Land (2013): Technical report of Sabo research related to volcanic activity in Sakura-jima Island (2), SABO Publicity Center, 160 p. (in Japanese).

Scott, W. M., Coe, J. A., Kean, J. W., Turker, G. E., Staley, D. M. and Wasklewicz, T. A. (2011): Observations of debris flows at Chalk Criffs, Colorado, USA: Part1, Italian Journal of Engineering Geology and Environment, 1, pp.65-75.

Suwa, H., Okano, K. and Kanno, T (2011): Forty years of debris-flow monitoring at Kamikamihorizawa Creek, Mount Yakedake, Japan. Debris-Flow Hazards Mitigation ed. By Genevois, Hamilton & Prestinzi©2011, Casa Editrice, Università La Sapienza, pp. 605-613.

Monitoring System of a Large Rockslide in Heisei-Shinzan Lava Dome, Mt. Unzen, Japan

Yasuyuki HIRAKAWA[1*], Nobuhiro USUKI[1], Kouji FUJITA[1], Toshiaki TANAKA[1], Masafumi KANEKO[1], Toshiyasu UENO[2], Hidenori EGUCHI[2] and Kazuhiro SHIMOKUBO[2]

[1] Asia Air Survey Co., Ltd. (Shinyuri 21 Building, 1-2-2 Manpukuji, Asao-ku, Kawasaki City, 215-0004, Japan)
[2] Ministry of Land, Infrastructure, Transport and Tourism (2-1-3 Kasumigaseki, Chiyoda-ku, Tokyo, Japan)
*Corresponding author. E-mail: ys.hirakawa@ajiko.co.jp

It is concerned that a large rockslide is possible to occur at lobe 11 in Heisei-Shinzan lava dome, Mt. Unzen. Predicted collapse block of 10^7 m^3 was delimited based on geological structure and distribution of groundwater and superficial fractures. 6 types of in-situ and long-distance monitoring instruments have been installed. Surface of lobe 11 has moved to SE-ESE at rate of 2.45-5.77 cm/year in last decade, similar to other European rockslides or a little smaller. Results of the monitoring and other investigations indicate that creep deformation of subsurface pyorclastic-flow deposits induces slide and settlement of lobe 11, leading to toppling movement at the back-crack. For emergency managements, thresholds and evaluation procedure were established based on measurement. Threshold consists of three categories (i.e. "immediate", "short-term" and "long-term") according to length of lead time before the final collapse. A new index-value ISSV was adopted for threshold of seismometer. In the evaluation procedure, a flowchart using each instrument's status was prepared to mitigate either overestimation or underestimation.

Key words: Rockslide, Monitoring System, Monitoring Instrument, Threshold, Seismometer

1. INTRODUCTION

Landslides are one of the most frequent natural disasters. Especially, large rockslides such as Mayuyama in Japan, 1792 [*Inoue*, 1999] and Vajont in Italy, 1963 [*Kiersch*, 1965] have caused large human or economic loss.

In Mt. Unzen, southern Japan, a lava dome called "Heisei-Shinzan" was formed by eruptions during 1990-1995 [*Nakada et al.,* 1999]. An unstable rock mass named lobe 11 exists on east-side steep slope of the lava dome. It is concerned that a huge collapse and consequent debris avalanche are possible to occur, because lobe 11 has moved about 1.2-m downslope during last 20 years according to an observation by total station (hereafter TS) started in 1997 [*Hirakawa et al.*, 2017]. A result of numerical calculation showed debris avalanche would cause a severe damage to residential area, farmland and Route 57 and 521, located at 4-6 km downstream from lobe 11 in Shimabara city and Minami-Shimabara city [*Kondo et al.*, 2014]. Thus, as measures against the possible lava dome collapse, the Unzen Restoration Work Office of the Ministry of Land, Infrastructure, Transport and Tourism (hereafter MLIT) has been providing the non-structural measurements such as construction of monitoring system to minimize human loss, as well as the structural measurements to minimize damage in influenced area.

Several reports of monitoring large rockslides, including in-situ observations, have been presented in a few decades, mostly in Europe - e.g., Séchiliene in France [*Helmstetter and Grambois*, 2010], Runion in Italy [*Crosta and Agliardi*, 2002], La Saxe in Italy [*Manconi and Giordan*, 2014; *Manconi and Giordan*, 2015], Mannen in Norway [*Kristensen and Blikra*, 2013; *Blikra and Kristensen*, 2016] and Åknes in Norway [*Oppikofer et al.*, 2009]. However, their objects are not a lava dome like Mt. Unzen. On the other hand, in Japan, report of continuous measurement of large rockslide is rare, while mounts of slow-moving landslides on gentle slopes have been instrumented.

In this report, the authors introduce the integrated monitoring system constructed by MLIT, and then discuss the results of measurement and establishment of thresholds for huge collapse of lobe 11, Heisei-Shinzan lava dome.

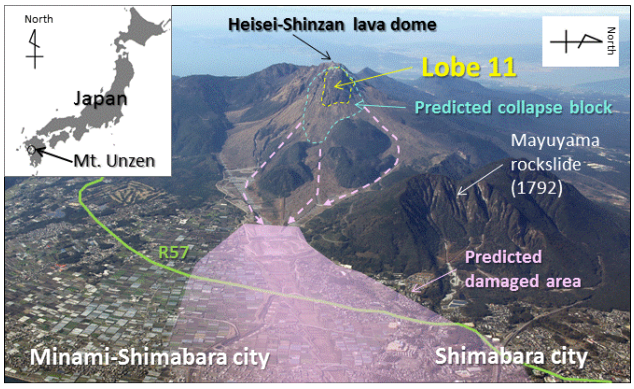

Fig. 1 Location and aerial view Mt. Unzen

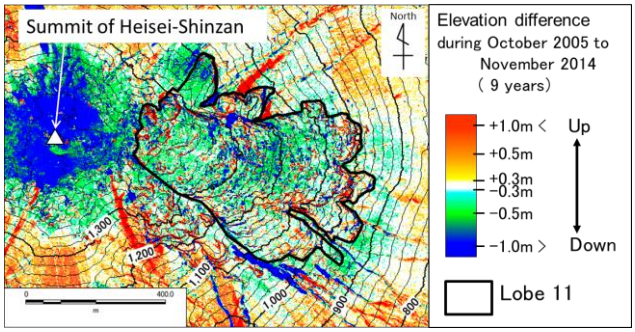

Fig. 2 Elevation difference calculated using LiDAR DTM

2. SITE DESCRIPTION

2.1 Forming process of lobe 11

Mt. Unzen is a volcano with 25km wide north-south which occupies most part of the Shimabara Peninsula, western Kyusyu region, southern Japan (shown in **Fig. 1**). The volcano consists of dozens of summits including Mt. Fugen.

A small eruption started at the summit of Mt. Fugen in November 1990, which was followed by thousands of pyroclastic-flow eruptions [*Nakada et al.,* 1999; *UI et al.*, 1999]. Since the eruption, lava lobes repeated growth and collapse. Lava blocks changed to pyroclastic flows as falling downslope and made large fan with pyroclastic-flow deposits. In total 13 lobes were appeared during May 1991 to March 1995, before Shimabara Earthquake and Volcano Observatory of Kyushu University (hereafter SEVO) stated the eruptive activity came to an end. Lobe 11 is located on east-side slope of the lava dome as an unstable, large rock mass with approximately 500m in width, 600m in length and 35-40 degrees in incline.

Data set obtained by TS measurement from 1997 revealed that surface of lobe 11 had moved downslope approximately 100 cm in 14 years [*Tamura and Maeda*, 2012]. Result of calculation using DTM from LiDAR showed that whole lobe 11 had been lowered around several dozen centimeters in 9 years (shown in **Fig. 2**). Field survey started at 2008 revealed that several rockfalls occurred every year at cliffs edge of lobe 11. These results inferred that slide and settlement are coinciding on whole lobe 11, which possibly lead to large rockslide in the future. Thus MLIT started construction of integrated monitoring system since 2011.

2.2 Delimitation of predicted collapse block

Preparing arrangement plan of monitoring instruments, delimitation of predicted collapse block is important. Although predicted breaking line on a longitudinal cross section was showed [*Kondo et al.*, 2014], the definite position of scarp or limit in transverse direction were not specific. Therefore we determined them based on results of investigation shown below.

DTMs, superficial geological maps and geological profiles on cross sections at 8 periods during 1991-2009 were provided by topographical and geological analysis using multi-temporal aerial photographs and sketch drawings during eruptions [*Watanabe et al.*, 2010]. They showed subsurface geological structure beneath the lava dome which consists of 3 lava lobes and pyroclastic-flow deposits (possibly including failure deposits) accumulated alternatingly above old ground surface that existed before 1990-1995 eruptions (hereafter "pre-eruption surface"), and planar and vertical distributions of the lobes. Coinciding of slide and settlement of lobe11 is considered to be caused by creep deformation of the pyroclastic-flow deposits, which have only past 26 years from their deposition and easy to be compressed and fractured by heavy rock mass of lava lobe.

On the other hand, we suggested a possibility that groundwater or high-moisture layer exists between pre-eruption surface and pyroclastic-flow deposits from studies of debris-flow causes on downslope of lobe 11 [*Hirakawa et al.*, 2015a; *Hirakawa et al.*, 2016]. It coincides with the results of airborne and field electromagnetic surveys [*Mantoku et al.*, 2013; *Ueno et al.*, 2017]. Furthermore, we presented detailed maps showing topographical features and ground cover (shown in **Fig. 3**) by interpreting DTM from LiDAR and hundreds of aerial photographs taken at close range in October 2014 [*Hirakawa et al.*, 2015b]. The maps disclosed cracks, gullies and fumarole areas which are possible to make boundary of collapse.

We predicted collapse block based on the results of investigation above, considering as follow [*Ueno et al.*, 2016]. Creep or slide would occur in vulnerable pyroclastic-flow deposits or at the

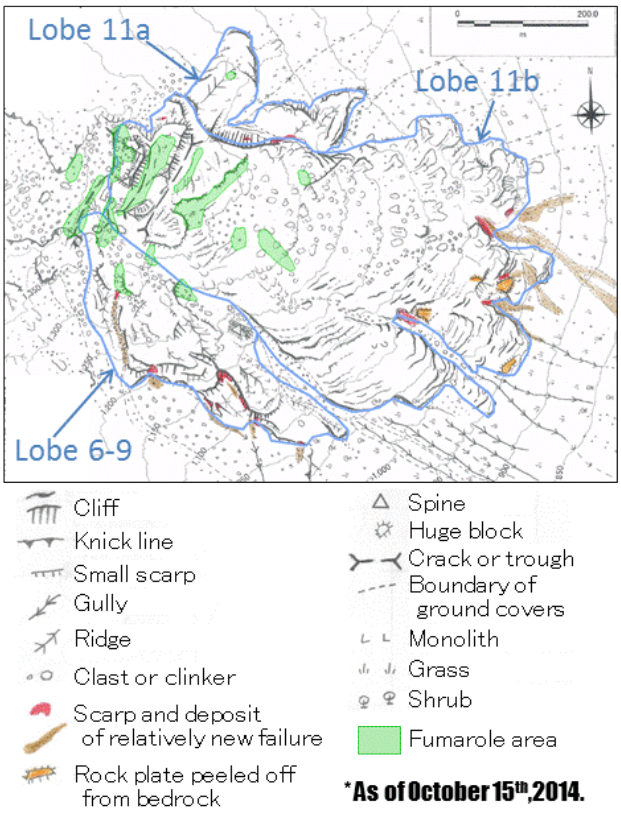

Fig. 3 Detailed map showing topographic features and groundcover of lobe 11

boundaries of them. Pyroclastic-flow deposits layer directly above the pre-eruption surface is particularly easy to be vulnerable because of pore water pressure or piping with existence of rich groundwater. Just under the right and left limit of lava lobes, shear fracture of pyroclastic-flow deposits would be caused by drastic change of upper load in transverse direction. Fumaroles and distinct cracks would make collapse boundary because clefts are likely continued to deep zone. Based on these ideas, we draw breaking lines of collapse on 3 longitudinal cross sections and 19 transverse ones (shown in **Fig. 4 and 5**), and then reflected them to planar map (shown in **Fig. 6**). As a result, four scenarios of collapse were predicted. Area and volume of the largest collapse was estimated as 70 ha and in order of 10^7 m^3, respectively.

3. MONITORING INSTRUMENTS AND METHODS

6 types of in-situ and long-distance monitoring instruments have been set on and around lobe11 as of September 2017 as shown in **Fig. 6, Fig. 7** and **Fig. 8**. Rain gauges and cameras are also installed by MLIT but not shown in the figures.

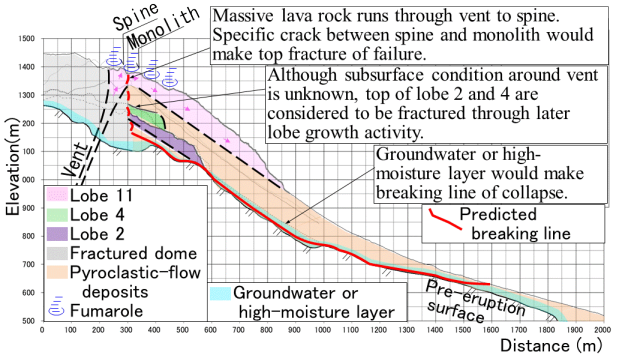

Fig. 4 Cross section corresponding to Line A

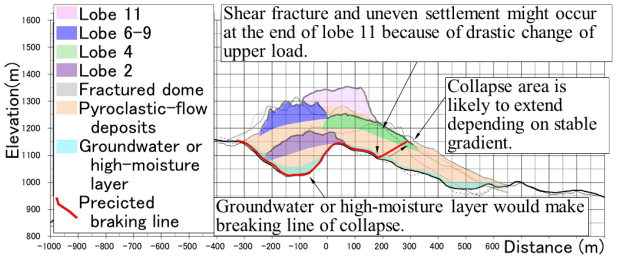

Fig. 5 Cross section corresponding to Line B

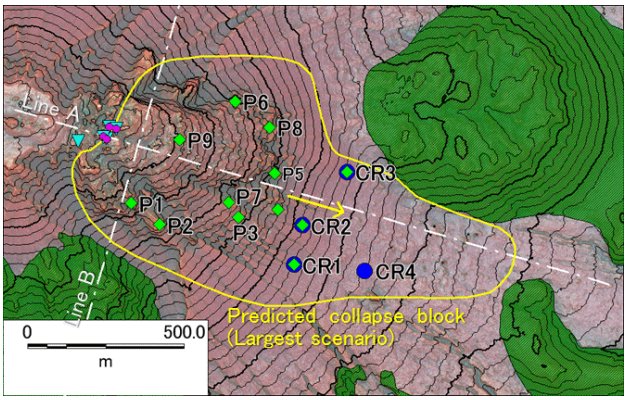

Fig. 6 Predicted collapse block and lines of cross sections. Instrumentation sites are also shown for the same legend as Fig. 7. Green shade shows pre-eruption surface

3.1 Total stations (TS)

Measuring distance between 2 TSs and 10 prisms on lobe 11 was started in March 1997 [*Tamura and Maeda*, 2012]. Because surface of lobe 11 is covered by spines and unstable blocks, transporting and setting prisms by hand was too risky and helicopter was used to transport 1-ton concrete blocks as the foundation of the prisms [*Nakazato et al.*, 2006]. While 10 prisms had been set at first, they got out of use except P7 and P8 because of volcanic gas, and were supplemented with new P1-6 prisms in May, 2006 [*Sawada et al.*, 2007]. After predicting collapse block, new 3 prisms (CR1-3) were added on downslope in July, 2016, and 1 prism (P9) on upper slope in the predicted collapse block in November, 2016. As of September 2017, 12 prisms are arranged in total. Distance between TSs

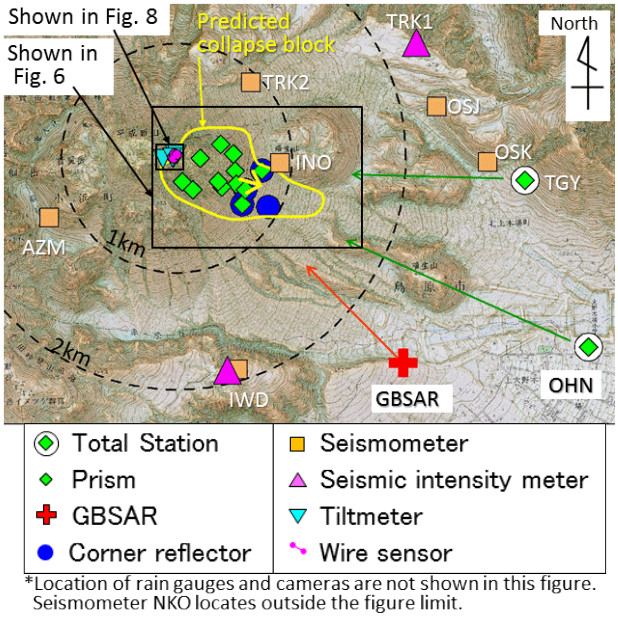

Fig. 7 Arrangement of monitoring instruments

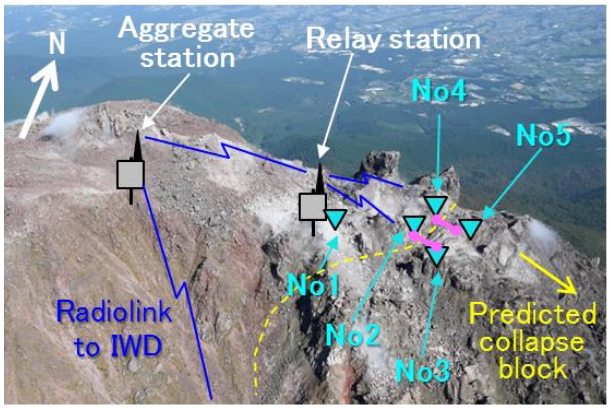

Fig. 8 Photograph of top of lobe 11. Location of tiltmeters and wire sensors are shown for the same legend as Fig. 7

and prisms are approximately 2-4 km. TSs were at first located approximately 1km away from OHN and TGY, but relocated in 2006.

Periodical and manual measurement was performed at first, but continuous automatic measurement with 1-hour time intervals was started in September, 2007 [*Tamura and Maeda*, 2012]. Data set of distance obtained every hour varies so widely that average value for 24 hours is usually used, but every hourly data is used to compare with "immediate" threshold which will be described later.

3.2 Ground-based SAR (GBSAR)

TS has disadvantage that it can measure distance only to the prisms (in other words point-based), and only in good weather conditions with no clouds and no fogs. To cover this disadvantage, Ground-Based Synthetic Aperture Rader (hereafter GBSAR) started measurement in October 2011 [*Tamura and Maeda*, 2012]. However, reflected radar intensity from downslope of lobe 11 was poor due to dense growth of bushes and grasses. Thus 4 corner reflectors were set in July 2016, although it is point-based measurement same as TS.

Displacement is analyzed using two data sets measured at different times. While data is acquired every 7 minutes, analyzing interval was set to two days to distinguish actual displacement from atmospheric effects [*Satou et al.*, 2014]. However, displacement of every 7 minutes is analyzed for comparison with "immediate" threshold which will be described later.

3.3 Seismometers and seismic intensity meters

Though several seismometers are installed on and around the lava dome, in this paper, we only refer to those installed by MLIT.

Seismometers were installed to detect pyroclastic flows or debris flows at first, but they started being treated as useful instruments to detect rockfalls through the discussion about monitoring system for large rockslide. The oldest of them were installed at IWD which contains 2 types of seismometer (described later), and started measurement in April 1994 [*Miki et al.*, 1998]. Although 2 more seismometers were set at the same time at other sites, they were moved to OSJ and OSK in 2005. Other seismometers were installed at NKO in 2005, INO and TRK2 in 2007, AZM in 2016. As of September 2017, 8 seismometers are arranged on 7 sites in total.

Short-period vertical sensor corresponding to frequencies of 1-20 Hz was installed at each site, and in addition also broadband 3-component sensor responding to 0.008-50 Hz was installed at IWD. All of them are velocity sensors and have sampling rate of 100 Hz. Acquired data is sent to MLIT by wire except particular sections using radio-link from INO and TRK2 to wired antennas.

Two seismic intensity meters started measurement in May 2017 to detect the outbreak of the earthquake that may become the inducement of the large collapse.

3.4 Tiltmeters and wire sensors

Five tiltmeters and 2 wire sensors were set on and around the top of the predicted collapse block in December, 2016 (shown in **Fig. 8**). It was a very hard mission to set the instruments because of severe weather conditions, inaccessible rock cliffs, and farness from electric power supply and telecommunications infrastructure. However, since grasping the behavior of the upper area of the block is essential for the monitoring of whole rockslide,

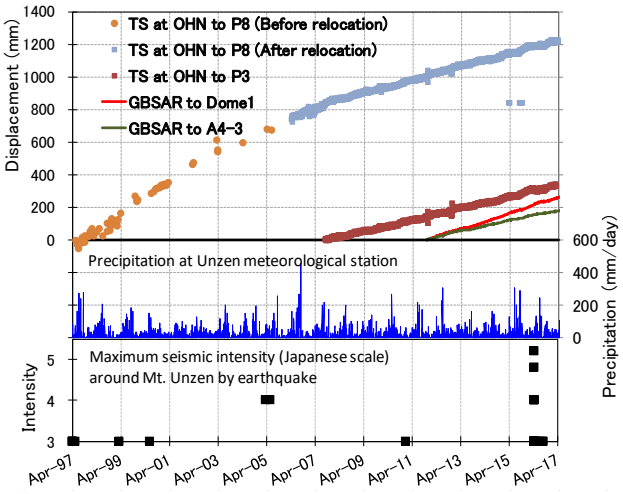

Fig. 9 Surface displacement measured by TS and GBSAR. Precipitation and seismic intensity of earthquake by Japan Meteorological Agency are also shown

we overcame the hardness and completed the setting of instruments. The mission was made possible by making system configuration which includes state-of-the-art power-saved tiltmeters, solar batteries and wireless installations, and taking 3 flights of helicopter for 700 kg material handling and 8 times field work.

Tiltmeter consists of three-axis acceleration sensors so that tilt fluctuation of each axis is calculated. Data is sent to IWD using radio-link. Though measuring time interval of tiltmeter is set to 24 hours to save power, it can be changed shorter by remote control in emergencies.

4. RESULTS OF OBSERVATION

4.1 Surface displacement

Sample of the observation result of the surface displacement is shown in **Fig. 9**. Displacement of P8 seems to decelerate around 2005, which probably indicate transition from the first creep phase to the second creep phase, though conclusion is not easy because the TS was relocated at the same period. Total displacement of P8 is 1.26 m in 20 years since May 1997, corresponding to 6.2 cm/year. After automatic observation of P1-P8 began in September 2007, their displacement rates are 2.45-5.77 cm/year, which differ depending on sites of TSs and prisms. Moving directions of P1-P8 are analyzed to SE-ESE from two displacement rates of different TS sites [*Satou et al.*, 2014].

Spatial distribution of total displacement by GBSAR in a year is shown in **Fig. 10**. Terrain sheds and low-reflection zones are shown in gray color. The largest displacement is exhibited in "Dome1" area located at knick line, while larger and smaller

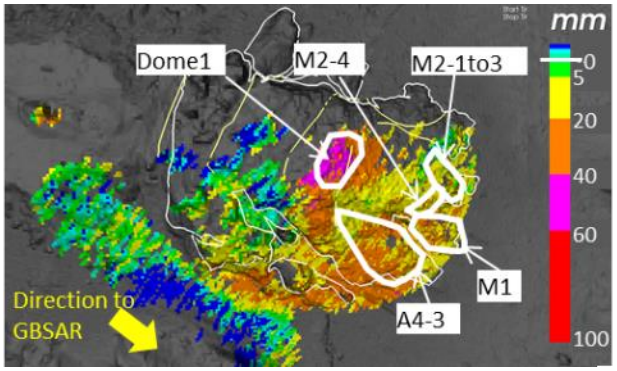

Fig. 10 Spatial distribution of total displacement measured by GBSAR from March 1st, 2016 to February 28, 2017

displacement zones are distributed complexly in other area. Although the distribution likely reflects subsurface geological structures, interpretation is difficult, because tendency of distribution is more complicated than mention in past documents [*Tamura and Maeda*, 2012; *Satou et al.*, 2014]. Five areas shown in **Fig. 10** (e. g. "Dome1" and "M2-4" and so on) are monitoring subjects for comparison with thresholds.

Displacement rates by GBSAR at "Dome1" and "A4-3" area are substantially constant, 4.8cm/year and 3.3cm/year respectively, during October 2011 and February 2017 (shown in **Fig. 9**). TS's measurement of P3 prism located within "A4-3" area indicate 3.6 cm/year displacement rate, which is consistent with GBSAR's measurement.

As for new sites P9 and CR1-4, observation periods are too short to estimate long term trend, but displacement rate P9 is faster and CR1-4 are slower than the other prisms.

4.2 Seismic signals and seismic intensity

From 2004 to 2016, every seismogram was automatically stored only when one or more sensor detected amplitude larger than 3.5 millikine (kine means cm/s) with duration longer than 10 seconds. Number of the records is 80 - 538 per a year. It is thought that the amplitude relatively larger among them is caused by rockfalls, failures, debris flows, earthquakes and noises. Representative of them is shown in **Fig. 11**.

In case of rockfalls and failures, duration tends to be several seconds or several tens of seconds including rapid increase and decrease of amplitude. However, failures of relatively larger magnitude can exhibit seismograms similar to debris flow with duration of several minutes. In case of debris flow, the seismogram exhibits long duration of several minutes to few hours with fusiform envelope featured by gentle increase and decrease. Some seismograms of debris flows include impulsive

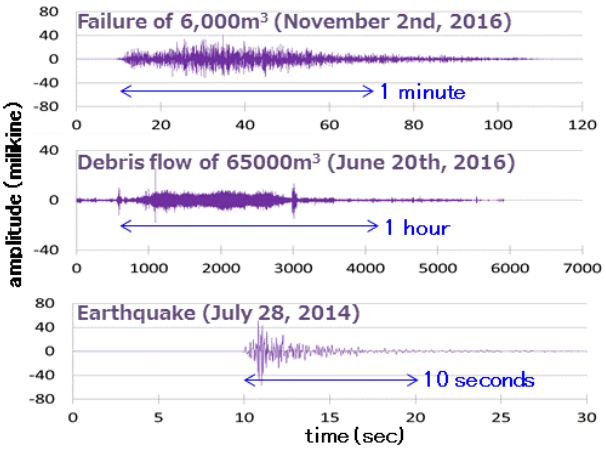

Fig. 11 Different types of seismograms measured at INO

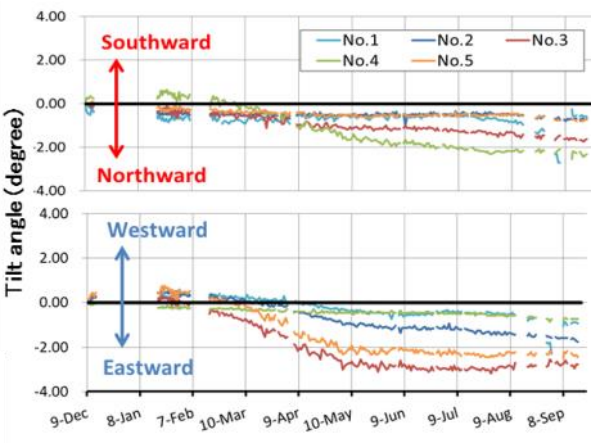

Fig. 12 Tilt fluctuation at the top of lobe 11 from tiltmeter in 9 months from the end of 2016

signals, which are probably caused by bank failures in debris flow. In case of earthquake, all sensors provide similar seismograms at almost the same time, which are featured by rapid increase followed by gradual attenuation.

Results of seismic intensity measurement are consistent with announcement of Japan Meteorological Agency and results of seismometer measurements.

4.3 Tilt fluctuation at the top of lobe 11

Time series of measurement by tiltmeters are shown in **Fig. 12**. Although the data before middle of February 2017 lack by system error, after that, data has been stored successfully. Generally all sensors exhibit northward and eastward fluctuation. Especially No.3 and No.5 exhibit the largest fluctuations eastward among all sensors during March and May, and No.2 follows. Comparing this fact with the location of each sensor (see **Fig. 8**), it is indicated that toppling deformation is evolving at the top of the predicted collapse block. However,

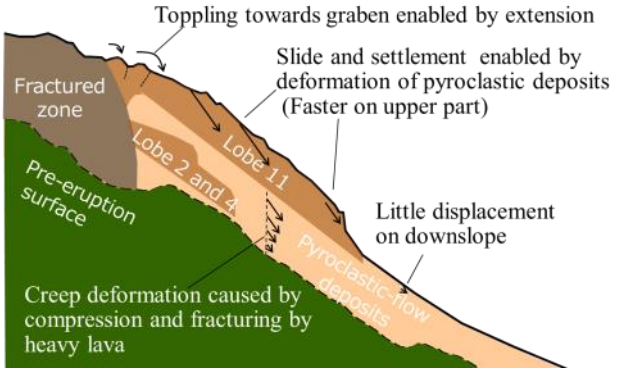

Fig. 13 Schematic profile across lobe 11 rockslide

there is a possibility that it is only seasonal fluctuation influenced by external factors such as temperature. At least a year measurement will be needed for initial calibration.

4.4 Interpretation and instability mechanisms

Based on results of investigations and observations above, instability mechanisms are considered as below (shown in **Fig. 13**). Primary factor of instability is considered to be creep deformation of pyroclastic-flow deposits caused by compression and fracturing by upper load of heavy rock mass of lava lobe. It induces slide and settlement of lobe 11 as measured by TSs, GBSAR and LiDAR. The reason why displacement is faster on upper part is possibly related to subsurface geological structure. Toppling deformation on the top of lobe 11 is possible to infer opening of back-crack depending on slide movement.

5. ESTABLISHING THRESHOLDS

5.1 Approach

Debris avalanche following large collapse of lobe 11 is estimated to reach Route 57 and residential area in approximately 5 minutes. Therefore the information about occurrence of large collapse or precursory phenomena is needed to be provided to decision makers for emergency managements.

Useful methods for this purpose are, for instance, comparing measured data with thresholds established previously, or forecasting time of failure. *Crosta and Agliardi* [2002] proposed a method to define different values of threshold velocities corresponding to time before failure, by developing an equation between velocity and acceleration under power-law creep movement [*Voight*, 1988]. *Manconi and Giordan* [2014, 2015] presented straightforward statistical method to forecast time of failure in near-real-time, using time

Table 1 Summary of thresholds. "TW" means reference time-window

Instru-ment	Cate-gory	Index-value and threshold
Seismic intensity meter	Imme-diate	**Intensity >= 4** (on the Japanese scale) Measured at TRK1 or IWD
Seismo-meter	Imme-diate	**1) ISSV >= 10^5 milikine^2 *s or** **2) [Duration with amplitude >= 40milikine] >= 30s** Measured at more than 1 site among INO, TRK2, IWD and AZM
TS	Imme-diate	**Velocity >= 20mm/h** (TW= 1h) Measured at more than 1 combination of arbitrary 1 prism and both of 2 TS's
	Short-term	**Difference from regression line >= 4cm or successive twice 2cm** (Regression line of TW= 100days)
	Long-term	**Velocity >= 0.3mm/day** (TW= 100days)
GBSAR	Imme-diate	**Velocity >= 4mm/h twice consecutively** (TW= 1h)
	Short-tem	**Velocity >= 1.45mm/day** (TW= 2 days)
	Long-term	**Velocity >= 5cm/year** (TW= 1 year)
Wire sensor	Imme-diate	Cut of both of 2 sensors

series of inverse-velocity. However, these methods are useful in tertiary creep stage when displacement exhibits acceleration. Lobe 11 at Mt. Unzen is considered to be in second creep stage when displacement rate is constant (shown in **Fig. 9**), which not allow to apply these methods. Hence we established thresholds for each instrument corresponding to the maximum level of deviation of index-value calculated from past observation. It is a rather traditional but available method as of now.

5.2 Categories of thresholds

We established three categories of thresholds (i.e. "immediate", "short-term" and "long-term") according to length of lead time before the final collapse. "Immediate" thresholds were set to detect inducement, premonitory phenomena (e.g. rapid increase of rockfalls or acceleration) or final large-scale collapse. "Short-term" and "long-term" thresholds were set to find change of coefficient of creep curve. Among the thresholds, the "immediate" is most important because it might be applied to evacuation order for residence, and because "short-term" and "long-term" are not useful in case of sudden collapse by a heavy external force (e.g. earthquake) with no tertiary creep curve previous. Thresholds we established are summarized in **Table 1**. Among them, the thresholds for TS, GBSAR and seismometer are taken up below.

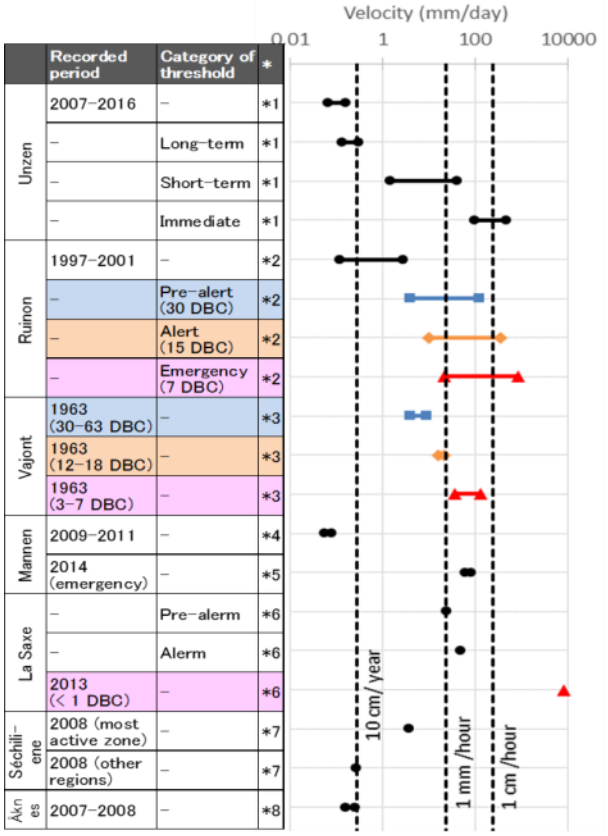

*References
*1: This paper
*2: *Crosta and Agliardi* [2002]
*3: Read from a graph shown in *Voight* [1988]
*4: *Kristensen and Blikra* [2013]
*5: *Blikra and Kristensen* [2016]
*6: *Manconi and Giordan* [2014]
*7: *Helmstetter and Garambois* [2010]
*8: *Oppikofer et al.* [2009]

Fig. 14 Velocities recorded or set as thresholds. "DBC" means "Days before Collapse"

5.3 TS and GBSAR

"Long-term" thresholds are aimed at detecting gentle acceleration of long-term displacement rate (velocity), which possibly indicates start of tertiary creep phase. Index-values of TS and GBSAR were set to velocities in reference time-windows of 100 days and 1 year respectively, because seasonal deviation is large in short time-windows. "Short-term" and "immediate" thresholds are aimed at detecting relatively swift and significantly rapid acceleration, respectively. Index-values are velocities in time-windows shorter than "long-term".

Velocities recorded in the past or set as thresholds in 7 rockslides are shown in **Fig. 14**. Red, orange and blue colors indicate days before collapse of less than 10 days, 10-20 days and 30-70 days, respectively. The monitoring subjects are in the order of 10^6 - 10^8 m^3, though actually collapsed or active blocks are a portion of them except Vajont.

As shown in **Fig. 14**, the recent velocity and "long-term" threshold of Mt. Unzen is on the same level as other rockslides in normal state or a little smaller. When increase of the "long-term" threshold will be needed because of frequent excess of measured data in the future, **Fig. 14** will be useful as reference.

On the other hand, “immediate” threshold is not smaller than alert (orange color) and emergency (red color) level in other rockslides. Note that it is larger than the velocity at 3 days before huge collapse of 200 million m^3 at Vajont. The “immediate” threshold velocity is so large because reference time-window was set to short time aiming at detecting rapid acceleration in near-real-time, and because velocity in short time-window exhibit wide-range deviation. In case real velocity including no measurement error exceeds the threshold, circumstances might be very risky.

5.4 Seismometer

Seismometers as well as wire sensors take important places as real-time measuring instrument. Two index-values were set for thresholds of seismometer. One is "Integrated value of Square of Seismic Velocity (hereafter ISSV)", a new index-value we propose, which indicates the increase of rockfalls, failures or fracture openings leading to final collapse. Another is combination of amplitude and duration.

5.4.1 ISSV

It is known that rockfalls or partial failures occur as precursory phenomena of rockslides. Observing the records of past rockslides, both frequency and volume of rockfall seem to increase with time. In that cases, it is considered that counting number of collapse blocks or estimating volume of each block is very difficult because seismic signals caused by some rockfalls and subsequent avalanches would overlap within durations. But detecting increase of seismic energy generated by hitting of rock blocks is possible. According to literatures, collapse volume of lava dome was proportional to the tremor energy calculated from linear envelope manually drawn on seismogram of pyroclastic flow during 1991 eruption at Mt. Unzen [*Takarada et al.*, 1993]. Volume of debris flow was strongly correlated with time-integrated amplitude of seismic acceleration [*Suwa et al.,* 1999].

We defined ISSV at time of t_0 which indicates seismic energy by Eq. (1):

$$ISSV = \int_0^{T_w} v_{t_0-t}{}^2 dt \qquad (1)$$

where v_t is the seismic velocity at time of t and

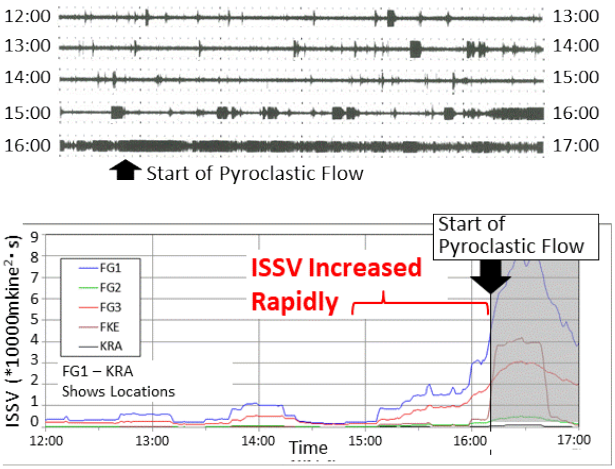

Fig. 15 Seismograms (upper) and time series of ISSVs (lower) before a pyroclastic flow at June 3rd, 1991

T_w is reference time-window. Time series of ISSVs with different T_w were calculated using seismic signals measured by SEVO at two pyroclastic flows in the order of 10^5-10^6 m^3 on June 3rd and 8th, 1991. The results showed ISSVs increased rapidly just before occurrence of pyroclastic flow in case T_w is around 30-120 minutes (case of 30 minutes is shown in **Fig. 15**). Compared to seismogram, it is understood that increase of ISSV is associated with increase of intermittent large waveforms since about 15:00 followed by sequential wave since about 15:50. These seismic waves are possibly induced by rockfalls, partial failures or micro-earthquakes caused by fracture openings, considering that 99% of pyroclastic flows during 1990-1995 eruptions were triggered by partial collapse of lava dome [*Nakada et al.,* 1999] and that rockfalls are frequently observed before rockslides. Moreover, larger amplitude than sensor's range seems to have occurred from the waveform in the seismogram. If it had been recorded, ISSV value would exhibit more rapid increase. Hence we adopted ISSV for an index-value which can detect precursory phenomena, for “immediate” threshold. Because we set the ISSV values using current seismometers location, the defined threshold (10^5 millikine^2 *s) is different from **Fig. 15**.

5.4.2 Amplitude and duration

We adopted combination of amplitude and duration of seismic wave for the index-value to detect final large-scale collapse. Based on past measurement, relatively larger amplitude is considered to be caused by rockfalls, failures, debris flows or earthquakes except noises. Because large-scale collapse would induce much larger amplitude than rockfalls, failures and debris flows past recorded, amplitude threshold (40 millikine)

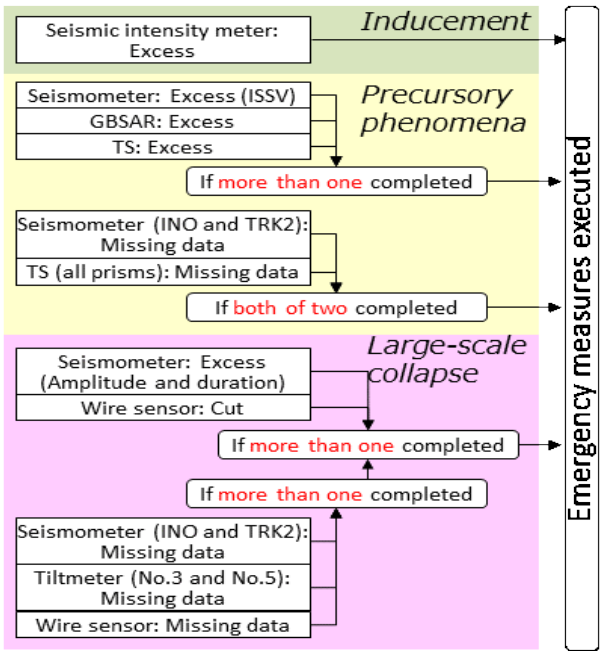

Fig. 16 Evaluation flowchart for "immediate" thresholds

was set to larger level than maximum value of them. On the other hand, seismic wave of earthquakes frequently exceed 40 millikine, but most of them end quickly so that duration threshold was set to 30s. Exceeding the threshold at more than one site is required to avoid overestimation. In two years since setting threshold, that condition occurred 19 times during the 2016 Kumamoto Earthquakes (Mw 7.0), but only 2 times at other earthquakes.

6. EVALUATION PROSEDURE

We set two steps of evaluation because of wide variety of monitoring instruments. In the first step, measurement by each instrument is compared with the thresholds. And in the second step, condition is evaluated based on combination of the excesses. As for "long-term" and "short-term" thresholds, corresponding actions will be executed simply when data set of one type of instrument exceed the threshold. In contrast, evaluation for "immediate" thresholds must be performed carefully because it might be applied to evacuation order for residence. Hence a flowchart was prepared to judge whether emergency measures should be executed (shown in **Fig. 16**).

In the flowchart, we paid attention to mitigate either overestimation or underestimation. To avoid overestimation, necessary condition was set to cases in which measurement records exceed the thresholds for more than one type of monitoring instruments. To avoid underestimation, we regarded missing data of multiple instruments as indicator of occurrence of precursory phenomena or final large-scale collapse, because instruments and prisms on or near lobe 11 are easy to get useless by destruction, disappearance, or loss of radio directivity in case of large displacement or frequent rockfalls.

Condition corresponding to emergency measures has never occurred in six months, since April 2017, after the new warning system incorporating the thresholds and the flowchart was installed.

7. CONCLUSIONS

MLIT has been providing structural and non-structural measurements against large rockslide in Heisei-Shinzan lava dome, Mt. Unzen. This report shows delimitation of predicted collapse block, methods and results of monitoring, establishment of the thresholds and evaluation procedure based on combination of the thresholds. Recent displacement rate of lobe 11 was on the same level to other European rockslides or a little smaller. A new index-value ISSV calculated from seismic signals was proposed for detecting precursory phenomena. Future issues will be maintenance of instruments, initial calibration of newly installed instruments, to verify the thresholds based on accumulated data and to discuss definite action when thresholds will be exceeded.

ACKNOWLEDGMENT: We wish to appreciate Dr. E. Shimokawa, Dr. H. Shimizu, Dr. Y. Jiang and Dr. T. Yamada for helpful constructive suggestions and discussions. We also thank Dr. K. Umakoshi and H. Takeishi for analyzing seismic data, and K. Yoshikawa and T. Shibata for making available GBSAR and TS data. Instrumentation at top of the lobe 11 could not been possible without the help from many engineers including K. Tada and T. Toyoshima. Finally, we thank Dr. H. Bateer, Dr. W. Yagi and an anonymous reviewer who helped improve the manuscript and the English.

REFERENCES

Blikra, L. H. and Kristensen, L. (2016): Monitoring a rockslide in development, INTERPRAEVENT 2016, extended abstracts, pp.158-159.

Crosta, G. and Agliardi, F. (2002): How to obtain alert thresholds for large rockslides, *Physics and Chemistry of the Earth*, Vol. 27, pp.1557-1565.

Helmstetter, A. and Garambois, S. (2010): Seismic monitoring of Séchilenne rockslide (French Alps): Analysis of seismic signals and their correlation with rainfalls, *JGR*, Vol. 115, F03016.

Hirakawa, Y., Okano, K., Tanaka, M., Takeishi, H., Sato, Y., Metoko, J. and Okamoto, T. (2015a): Relationship between

sediment movement and topographical and geological factor at Mizunashi river, Mt. Unzen, Proc. 64th Annual Congress of JSECE, B, pp.54-55 (in Japanese).

Hirakawa, Y., Fujita, K., Tanaka, M., Usuki, N., Chiba, T., Satoh, Y., Metoko, J. and Okamoto, T. (2015b): Detailed interpretation of topography and ground cover at lobe 11, Mt.Unzen, Proc. 64th Annual Congress of JSECE, B, pp. 432-433 (in Japanese).

Hirakawa, Y., Okano, K., Takeishi, H., Ueno, T. and Mitsutake H. (2016): Occurence condition of debrisflow at Mizunashi river, Mt. Unzen, Proc. 65th Annual Congress of JSECE, JSECE Publication No.78, B, pp. 252-253 (in Japanese).

Hirakawa, Y., Usuki, N., Fujita, K., Tanaka, T., Kaneko, M., Ueno, T., Eguchi, H. and Shimokubo, K. (2017): Monitoring system for a large collapse of Heisei-Shinzan, Mt. Unzen, Proc. 66th Annual Congress of JSECE, JSECE Publication No. 81, pp.598-599 (in Japanese).

Inoue, K. (1999): Shimabara-Shigatusaku earthquake and topographic changes by Shimabara catastrophe in 1792, *J. of JSECE*, Vol. 52, No. 4, pp. 45-54 (in Japanese with English abstract).

Kiersch, G. A. (1965): The Vaiont Reservoir Disaster, Mineral Information Service, Vol.18, No. 7, pp. 129–138.

Kondo, R., Anyoji, N., Fujisawa, Y. and Sato, Y. (2014): Evaluation of potential hazards from lava dome collapse on Mt. Unzen-Fugen-Dake, INTERPRAEVENT 2014, Vol. 1, pp. 84-91.

Kristensen, L. and Blikra, L. H. (2013): Monitoring displacement on the Mannen rockslide in western Norway, C. Margottini et al. (eds.), Landslide Science and Practice, Vol. 2, pp.251-256.

Manconi, A. and Giordan, D. (2014): Landslide failure forecast in near-real-time, *Geomatics, Natural Hazards and Risk*, Vol. 7, pp.639-648.

Manconi, A. and Giordan, D. (2015): Landslide early warning based on failure forecast models: the example of the Mt. de la Saxe rockslide, northern Italy, *NHESS*, Vol. 15, pp. 1639-1644.

Mantoku, M., Sugiyama, M., Todaka, T., Yuuki, Y., Kuroki, M., Ohuchi, H., Sakurai, K. and Kawahara, Y. (2013): Analysis of subsurface structure of Mt. Unzen based on airborne electromagnetic survey, Proc. 62th Annual Congress of JSECE, A, pp. 118-119 (in Japanese).

Miki, Y., Igarashi, S., Itoh, H. and Ozeki, N. (1998): Analysis of seismic waveform by debris flow in Mt. Fugen, Unzen, Proc. 47th Annual Congress of JSECE, pp.322-323 (in Japanese).

Nakada, S., Shimizu, H. and Ohta,K. (1999): Overview of the 1990–1995 eruption at Unzen Volcano, *JVGR*, Vol. 89, pp. 1-22.

Nakazato, K., Matsui, M., Yamaguchi, K., Hata, K. and Ohbayashi, K. (2006): Development of emergency observation system for a large-scale slope, Proc. 55th Annual Congress of JSECE, pp. 138-139 (in Japanese).

Oppikofer, T., Jaboyedoff, M., Blikra, L., Derron, M.-H. and Metzer, R. (2009): Characterization and monitoring of the Åknes rockslide using terrestrial laser scanning, *NHESS*, Vol. 9, pp. 1003-1019.

Satou, Y., Ishizuka, T., Kuraoka, S., Nakashima, Y. and Kmijo, T. (2014): Deformation characteristics of Unzen lava dome based on long range displacement monitoring, INTERPRAEVENT 2014, Vol. 1, pp.92-100.

Sawada, E., Matsui, M., Yamaguchi, K., Hata, K., Ishitsubo, S. and Mizuta, T. (2007): Study of lava dome's behavior using target prism at Mt. Fugen, Unzen volcano, Proc. 56th Annual Congress of JSECE, pp. 234-235 (in Japanese).

Suwa, H., Yamakoshi, T. and Sato, K. (1999): Estimation of debris-flow discharge by monitoring ground tremor, *J. of JSECE*, Vol. 52, No. 2, pp. 5-13 (in Japanese with English abstract).

Takarada, S., Kazahaya, K., Kawanabe, Y., Sakaguchi, K., Sudo, S., Yamamoto, T., Soya, T. and Unzendake Weaher Station, JMA (1993): Volume estimation of 1991-92 eruption of Unzen Volcano, and initiation mechanisms of pyroclastic flows on June 3 and June 8, 1991, *Bull. Geol. Surv. Japan*, Vol. 44, No. 1, pp.11-24 (in Japanese with English abstract).

Tamura, K. and Maeda, A. (2012): Monitoring of lava dome of Unzen volcano by EDM and ground based synthetic aperture radar, *J. of JSECE*, Vol. 65, No. 1, pp. 69-72 (in Japanese).

Ueno, T., Mitsutake, H., Fujita, K., Usuki, N. and Hirakawa, Y. (2016): Dilimiting predicted collapse blocks based on topographical development process of lava dome, Mt. Unzen, Proc. 65th Annual Congress of JSECE, JSECE Publication No. 78, B, pp.400-401 (in Japanese).

Ueno, T., Mitsutake, H., Shimokubo, K., Miki, Y., Ohuchi, H., Kitahara, T., Uehara, Y., Sakurai, K. and Todokoro, H. (2017): Estimating subsurface structure and mechanisms of large collapse based on airborne and field electromagnetic survey at Heisei-Shinzan lava dome, Mt. Fugen, Proc. 66th Annual Congress of JSECE, JSECE Publication No.81, pp. 66-67 (in Japanese).

Ui, T., Matsuwo, N., Sumita, M. and Fujinawa, A. (1999): Generation of block-and-ash flows during the 1990–1995 eruption of Unzen Volcano, Japan, *JVGR*, Vol. 89, pp. 123–137.

Voight, B. (1988): A method for prediction of volcanic eruptions, *Nature*, Vol. 332, pp. 125-130.

Watanabe, F., Maeda A., Takaba, E., Matsuo, Y., Sakka, S., Hasegawa, R., Nakamura, T. and Yamaguchi, S. (2010): Estimating subsurface structure of a lava dome at Mt. Fugen, Unzen volcano, Proc. 59th Annual Congress of JSECE, pp. 338-339 (in Japanese).

Subsurface Investigation and Landslide Monitoring as a Basis for Planning Protection Measures - Case Study Doren Landslide -

Thomas FRANDL[1] and Margarete WÖHRER-ALGE[1]

[1]Forest Technical Service for Torrent and Avalanche Control, Regional Office Vorarlberg, Austria
*Corresponding author. E-mail: thomas.frandl@die-wildbach.at

Large or widespread slope movements are often characterised by a very complex interplay of various mass movement processes which are in turn caused by saturated water conductivity regimes in the underground that are difficult to assess or model. The planning of protection measures is therefore often met with great challenges. The importance of monitoring measures for determining protection measures is to be demonstrated using the example of the Doren landslide in Austria. The oral tradition about this landslide, situated on the orographic right hand side of the Weißach river, dates back to the year 1847. The first geological investigations, stabilization measures and monitoring measures were carried out after a mass movement in 1935. Due to unfavourable rock properties and a complex water regime, stabiliziation measures which were successfully implemented in other landslides in Austria failed in the Doren landslide. In the summer and autumn of 2014 two different systems to stabilize the head scarp of the Doren landslide were tested.

Key words: mass movement, monitoring, Doren landslide, head scarp, erosion control

1. GENERAL INFORMATION

Fig. 1 Landslide area of Doren after the event of 1988. At the left side of the upper image border the center of the village Doren is visible.

The oral tradition about a landslide area on the orographic righthand side of the Weißach river in close vicinity to the town center of Doren/Austria reach back to the year 1847. Mass movements in 1927, 1935, 1988 (see **Fig. 1**) and 2007 in each case involved the movement of 2 – 3 million m³ of material. In 1935 and 2007 the Weißach was completely dammed up by this material, causing a lake of approximately 500 m in length behind the landslide deposit. Following the mass movement of 1935, the first geological investigations were carried out and drainage tunnels of circa 700 m length were mechanically bored and filled with coarse boulders for stability. The aim of the study is to find out the advantages and disadvantages of each system.

2. CLIMATIC CONDITIONS

Doren is situated on the fringes of the Northern Alps. Distinct oceanic influence is shown by the high rainfall, the moderately warm summers and the moderately cold winters. The average annual rainfall totals 1875 mm.

The maximum precipitation recorded within a period of 24 hours totalled 143 mm on May 30th 1940.

3. GEOLOGY

The geological subsurface in the landslide area consists of rocks of the so-called Weißach layers of the Lower Freshwater Molasse. The landslide area is divided into various sections (see **Fig. 2**):

Section A: Terrace covered with quaternary sedimentsthat lead to subordinate secondary slides in the upper sections of the head scarp.

Section B: A scarp face of up to 70 m height with slope parallel marlstone and sandstone layers of the Lower Freshwater Molasse. The marl layers contain up to 45% swellable clay minerals and produce solid rock slips along the steeply inclined bedding planes that dip towards the valley bottom. These bedding planes consist alternatingly of formerly competent layers and incompetent layers.

Section C: Rotational slide bodies at the foot of the scarp face that consist of loose rock masses, bedrock components that have slid downslope as well as moraine deposits that formerly overlay those bedrock components.

Section D: Further downslope an approximately 600 m long earth and rock waste stream of loose rock masses that are predominantly saturated to the tributary Weißach. [*Van Husen et al.*, 2008]

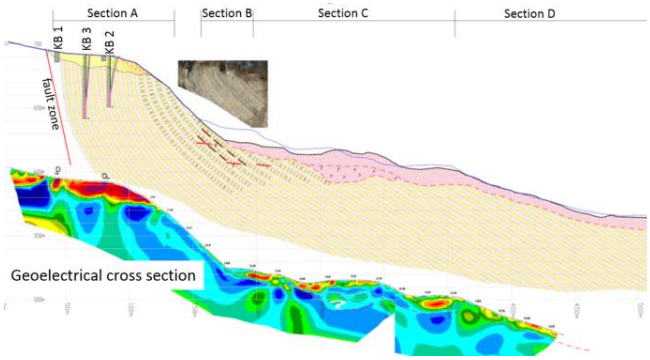

Fig. 2 Schematical geotechnical cross section of the landslide with the different sections A, B, C and D.

The layers of marl weather very rapidly into their components. Spring outlets at the interface between the Weißach layers and moraine deposits continuously supply water so that weathering products are soon eroded.Weathering along with the three landslide processes (bedrock slipage in the scarp, rotational slides at the foot of the scarp face, as well as the immediately adjoining earth and rock waste stream) which interact with one another lead to a retrogressive erosion of the scarp face on the order of 1 m per annum.

4. SLIDING PHENOMENON

Primarily the slide affected the bedrock (interbedded strata of clay/marl/calcareous marl/sandstone), as well as the quaternary sediment cover. Today the landslide scar has the form of a conch and rotational slides are prevailing. The material in the accumulation area is creeping and flowing towards the axis of the river (earth/debris flow). The quaternary sediment cover atop of the Weißach strata provides supply of material to the earth/debris flow. The earth/debris flow is periodically mobilised by seeping water in the quaternary sediment cover and surface runoff. **Fig. 3** shows the change in altitude between 2006 and 2007.

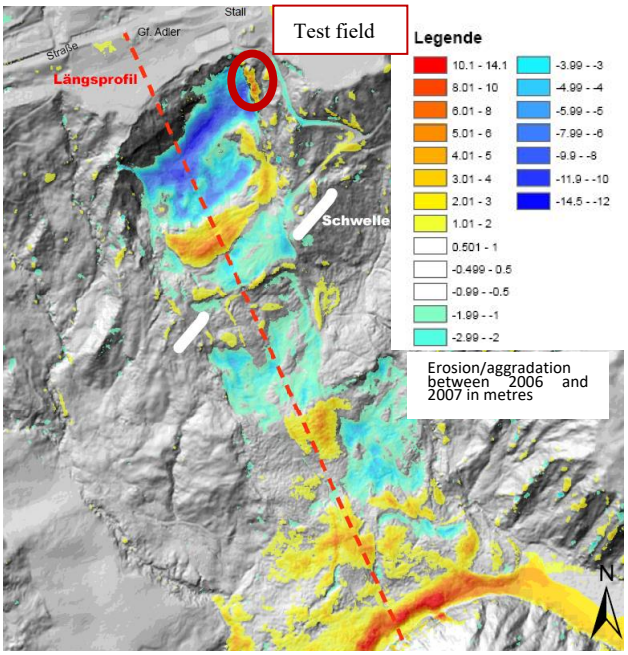

Fig. 3 Differences in the ground height between 2006 and 2007

5. SLOPE WATER SITUATION

The marls of the Weissach strata are nearly impermeable because of the high content of fine grained material. Coarse clastics within the heterogenously composed quaternary sediment body act as groundwater and slope water bearing horizons. 4 different groundwater conductors (aquifers) can be distinguished:

- Water bearing horizons within the redeposits
- Water bearing horizons at the border between redeposits and glacial deposits
- Water bearing horizons within the glacial deposits
- Water bearing horizons at the border between glacial deposits and bedrock [Weißach strata]

The existing water bearing horizons are dependent to small tubular and lenticular ground water conductors, a compact slope water conductor is not evolved.

6. SUBSURFACE MODEL

To survey the depth and the extent of the impermeable rocks and the depth of the earth/debris flow geoelectrical measures with multielectrode configuration were carried out.

All profiles on the terrace showed a clear double segmentation in the distribution of resistivity (see **Fig. 4**). A horizont which shows a remarkable low resistivity [< 40 ohm.m] is coated with a horizont of higher resistivity [80 – 200 ohm.m].

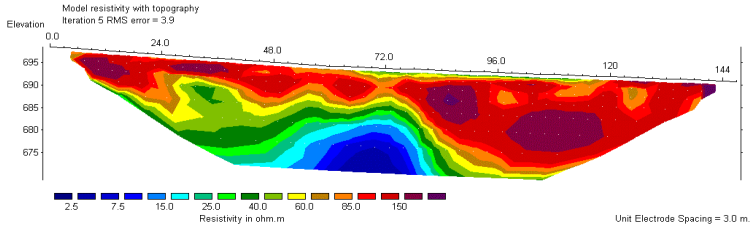

Fig. 4 The cross section on the terrace shows a clear double segmentation in resistiviy

The depth of the cover which shows high resistiviy (glacial deposits) ranges between 1,09 m and > 22 m.

According to the results of the geoelectrical measurement, the depth of the actually moving earth/debris flow at the base of the scar is 10 -15 m. Noticeable is the steep slope of the earth/debris flow in an altitude of 600 m (see **Fig. 7** geoelectric). This escarpment is visible in all aerial photographs since 1950. A rock escarpment seems to exist.

- The reason for the "global slide" is a failure of the base of the steep rock layers in the scar
- The failure occurs by an overload of the competent parts (sandstone) of the layer.
- The increase of stress up to the failure is caused by the water pressure, which is efficacious along joints and faults. The incompetent layers (marl) are impermeable to water.
- After the failure of the base the sliding mass becomes part of the earth/debris flow. Due to the characteristics of the materials (marl/sandstone = ductile/prattle) and the influx of water the mass is extremely plastified and flows downwards to the river.

7. MITIGATION EFFORTS

The first mitigation efforts were carried out for the Doren landslide starting in 1938, following the mass movement event of 1935. The Viennese geologist Josef Stiny (Vienna University of Technology) carried out the first geological surveys of the site and planned mitigation measures on the basis of these investigations. In order to drain the landslide's catchment area, a 700 m long drainage tunnel was mined at approximately 10 m depth to the north-east of the scarp head, and filled with coarse rock material. This drainage system drained between 150 and 520 m³ of water per day between 1938 and 1940. Today, 80 years later, this drainage system is still continually discharging a few liters per second and therefore a sum of water in the same order of magnitude as in those first years.
Following the mass movement event of 1988 an additional subsurface drainage system was installed north of the scarp head.

Geophysical investigations carried out in 2002 and 2007 revealed that the drainage tunnels were not situated in bedrock only, for which reason, they were presumably underflowed in part; slope seepage water situated below the system can also not be collected and discharged through it.
Further mitigation efforts aimed primarily to drain the earth and rock waste stream situated at the foot of the scarp. The ultimate aim of such measures are to secure the foot of the scarp against further erosion, which would destabilize the entire upslope area. However, also these measures were not successful and did not bring about the wished for stabilization, which became very apparent in 2007 when, following a long period without precipitation, mass movements occured once again.

8. ESTABLISHING A MONITORING SYS TEM IN THE DOREN LANDSLIDE

The first monitoring efforts at the Doren landslide site encompass the discharge

measurements from the drainage tunnels between 1938 and 1940.

Following the massive reactivation of the landslide in the spring of 1988, the installation of the monitoring system currently in use was begun. A probe drill hole as well as two drill holes fitted with inclinometer tubes were constructed in order to better understand the underground and the processes taking place in it. The monitoring system was expanded step by step in the years thereafter, although the drill holes from 1988 have since become unmeasurable. Measurements are made in yearly increments. In conjunction with the inclinometer data, the position and elevation of the inclinometer head was also determined, so that the posibility of a sliding plane beneath the foot of the inclinometer could be excluded. The monitoring system at present includes the following measurement instruments:

8.1. Terrace above the scarp

- GPS survey point, manual
- 5 inclinometers (2002, 2007), manual
- 6 piezometers in 3 drill holes (2007), manual
- 5 piezometers in 1 drill hole (2009), automatic
- 2 level gauges (2001, 2013), automatic
- 1 level gauge (2013), manual
- 1 gauge of the water volume discharged from the vacuum well, automatic using a water meter.
- 1 gauge of the subsurface drainage system discharge, automatic using a measuring weir and gauge

8.2. Foot of the scarp face, rotational slide bodies and earth- and rock waste stream

The survey points used to assess movement of the landslide had to be newly set numerous times following the high rates of movement in the years 2005 and 2007. Following the large surge of movement during Easter 2007, an automatic movement monitoring system was installed in May of the same year (see **Fig. 5**). In February 2010 it was decided to revert back to periodic manual measurements (of movement). This was due to financial reasons. At the first hints of a reactivation of the landslide, an automatic measurement can be reimplimented immediately, however.

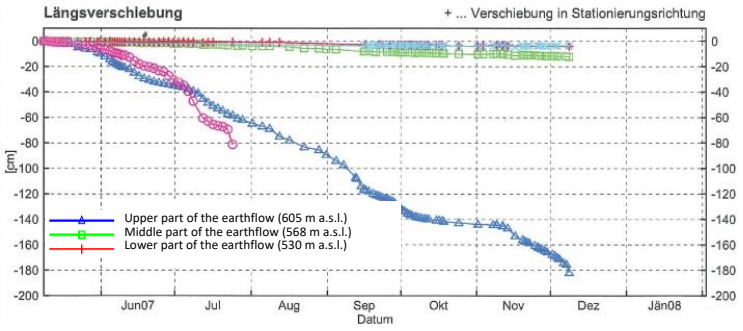

Fig. 5 Longitudinal displacement of monitoring points in the Western part of the landslide Doren 2007.

Many of the measurement instruments were destroyed during larger mass movement events in 2016:

- 2 well gauges, manual (2012)
- 1 automatic level gauge (2012)
- 5 electric contact gauges (2012)
- Manual measurent of water discharge from 6 horizontel drill holes (2012, 2013)
- Water discharge from 2 vertical bore holes (2012)

8.3. Orthophotos and Laserscans

The comparison of orthophotos taken since 1950 in conjuntion with numerous laserscans since 2003 has provided information about the landslide's mass balance, whose head scarp has over the past 65 years moved an average of 1 m in the direction of the town center, and it has furthermore shown the importance of securing the scarp face.

9. PROBLEMS

Due to the surges of movement, which can hardly be predicted, measurement instruments installed in the earth- and rock waste stream downslope of the scarp face are soon destroyed. For this reason, manual measurements are preferred in this lower section of the landslide, or, as an alternative, low cost mobile measurement instruments (for example, mobile gauge level loggers). The inclinometers installed directly below scarp head likewise have very limited lifespan.

The possible extent of a rise in groundwater was also underestimated so that the level gauge installed in the conglomerate zone was unable to measure the peak value that occured on 02.06.2013 (see **Fig. 3**).

10. RESULTS

A number of mitigation measures have been employed in the Doren landslide since 1935. The objective of these measures have been, on the one hand, to safely drain subsurface water out of the upper scarp face (drainage tunnels 1938, depth drainage measures 1988 and 2002-3) and from the lower section of the scarp (surface drainage, horizontal drill holes at the foot of the scarp face), and on the other hand, to protect the scarp face from weathering (afforestation in the 1950s, securing the scarp face with erosion protection systems since 2014). All of these mitigation measures raised hopes of a stabilization in the short run, however, in the long run were unable to prevent further surges of mass movements.

Little is known about the origin of groundwater streams. In the meantime it is known, that the groundwater has different conductivities. One problem is the water at the foot of the scarp face. For construction of better mitigation measures it is necessary to learn more about the origin of groundwater streams.

In order to adapt the mitigation measures accordingly, it is important to have more information about the subsurface hydrological balance, water conductivity and how these relate to mass movement surges in this landslide. An important function of the monitoring system is to evaluate the efficacy of the mitigation measures employed (for example by measuring the discharge of the subsurface drainage system).

10.1 Subsurface hydrological balance and water conductivity

The water level in the probe drill hole (2010-13) was measured in part automatically with a gauge and in part manually with an electric contact gauge. Well discharges in the earth- and rock waste stream, discharges from horizontal drill holes at the foot of the scarp face as well as overflow of the vertical drill holes were all measured manually. All of the data does gathered provided important information about the ground water level within the landslide. During the heavy precipitation event from the 31st of May to the 1st of June 2013 the groundwater level in the drill hole situated in the conglomerates rose, with a temporal delay of only a few hours to the precipitation, approximately 12 m over the course of two and a half days (see **Fig. 6**).

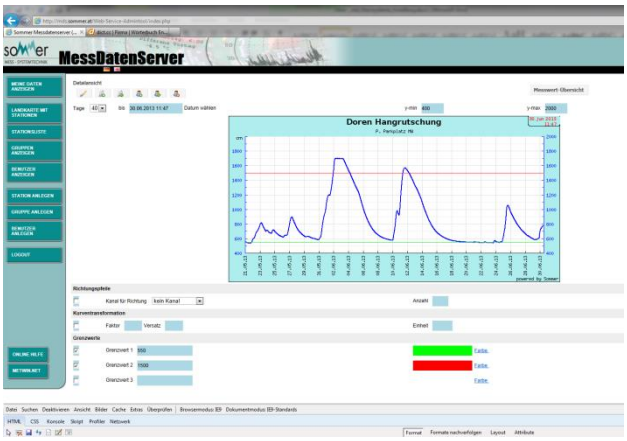

Fig. 6 Chart of a groundwater gauge situated slightly above the Doren landslide during the floods in June 2013.

Robust gauge data loggers have proven to be very useful for speedy and mobile deployment. For example, they were used to establish the interrelation between the ground water level of two bore holes spaced 125 m apart, while boring was taking place at the site (see **Fig. 4**).

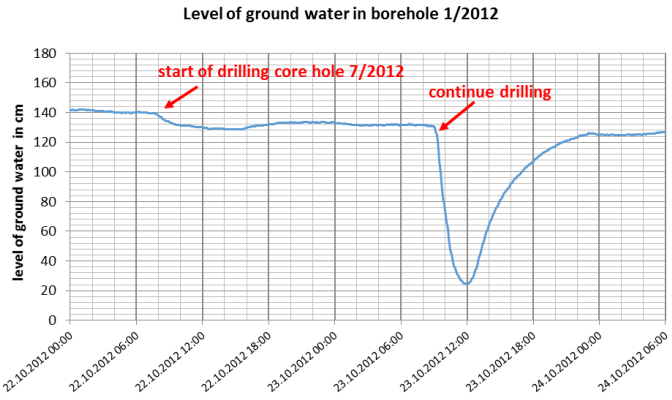

Fig.7 Response of the groundwater in the Doren landslide to drilling operations at a distance of 125 m.

10.2 Evaluating the mitigation measures used

Measurements of the discharge from the subsurface drainage system allow inferences to be made about the size of the catchment area as well as the efficacy of the mitigations measures employed.

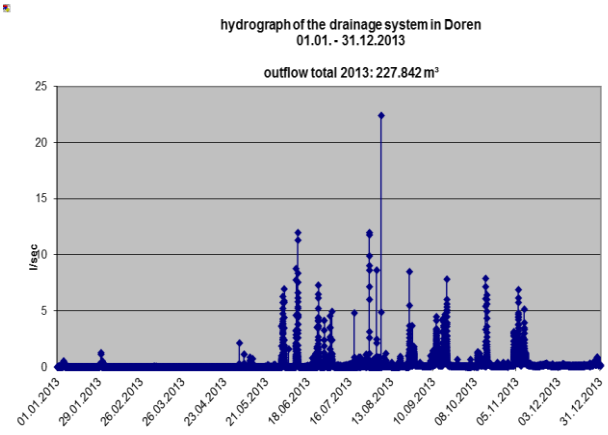

Fig.8 Hydrograph of the drainage in the landslide Doren 2013.

11. TEST SITE FOR SLOPE STABILIZATION

A characteristic feature of the Doren landslide is the speed at which weathering of the marl layers is occuring. The composition of this material causes it to swell upon wetting, following which it is eroded by concentrated ingress of water, by frost or other forms of loading. The marl layers were overlain with moraine deposits of numerous meters thickness during glacial periods. Due to their high permeability, these moraine deposits allow precipitated water to penetrate to the marl subsurface. During heavy precipitation events this water is discharged in the boundary layer between marl and moraine layers, thus eroding the weathering layer situated there. On average, the regression of the upper edge of the marl layer constitutes 1 m per annum over the last 50 years. To prevent further regression, the surface of the landslide must be protected from weathering.

Further difficulties are caused by the subsurface drainage of the landslide area. The entire area of the landslide as well as the adjacent area above it contains wellsprings, subsurface flows, infiltrations, etc., the exact position and drainage of which is unclear. This water causes an upslope hydraulic pressure, which contributes to the erosion of the rock face and the regression of the upslope terrain. The combination of weathering and upslope hydraulic pressure provides a precarious challange, since the slope must on the one hand be protected from weathering, whilst the water must on the other hand be able to be discharged from these upper sections of the landslide. The slope can therefore not be secured in the classical sense, since securing the slope with a net will not solve the weathering problem, whilst using shotcrete would prevent water from being discharged through the surface.

11.1 Products used in the test site of the Doren landslide

In an attempt to secure and stabilize the landslide of Doren with nets or meshes, two systems have been tested to date: the "Krismer-3D"® system, which is a three-dimensional mesh, and the "Tecco"® system, a high strength square wire mesh produced by Geobrugg. Both of these products were tested in the Doren landslide area, by installing the respective meshes on test sites demarkated within the larger landslide area, in order to evaluate the long-term performance of these two products. The criteria chosen for evaluating the functioning of these systems were structural safety as well as weathering protection, in addition to which the installation of each system was also considered.

DYWI® Drill hollow bar anchors were used to anchor the respective mesh systems in the Doren landslide test sites. These are self-drilling hollow bolts that are installed either during the drilling process itself or thereafter by means of grout injection. This system is typically employed when dealing with unstable boreholes. The hollow bolts of this system can be assembled modularly, like building blocks, in order to meet the requirements of the mesh system and the particular site in question. Using sleeves, the hollow bolts can be extended as much as is required, while the drill bit is chosen in accordance with the material conditions of the underground that needs to be drilled.

These anchors (DYWI self-drilling hollow bolts) were used to secure both products tested. Drilling into the slope was carried out on a raster of 1.5 m x 1.5 m, which has the advantage that should one of the systems fail or fail to provide adequate weathering protection, another mesh net could be installed over it or even completely replace the inadequate product.

11.2. The Krismer-3D system

The Krismer-3D system is a three-dimensional steel wire mesh mat that forms a wire frame directly on top of the slope that needs to be secured. This wire frame is filled with angular particles of sizes 35-60 mm, over which a 1-2 mm thick humus layer is then applied and vegetated (see **Fig. 9** and **10**). This layered construction should provide a fast growing and well rooted biological protection measure against weathering. The criteria of geotechnical measurements are also met by this system. However, geologists in the provincial service have expressed misgivings that the system might in practice not be strong enough to withstand the resulting loads. Another disadvantage of the Krismer system concerns its installation: the steel wire mesh mats are delivered as separate parts, each 6

m² in size. These panels must be individually installed after all the nails or anchors have been set in the slope, following which, they must as a second step be filled. On slopes that are not too steep this presents no problem, however, on steeper slopes like that found in individual sectors of the Doren landslide (with over 80°), bringing the elements into place can be problematic and involves a significant effort. Moreover, on such steep slopes the filling material crumbles out of the wire frame holding it, thus losing its protective function against weathering processes.

All in all, the Krismer-3D system constitutes an appropriate solution to the problem in question here, as it forms a protective layer on the slope to be stabilized yet is water permeable, allowing water to be discharged from the slope through it.

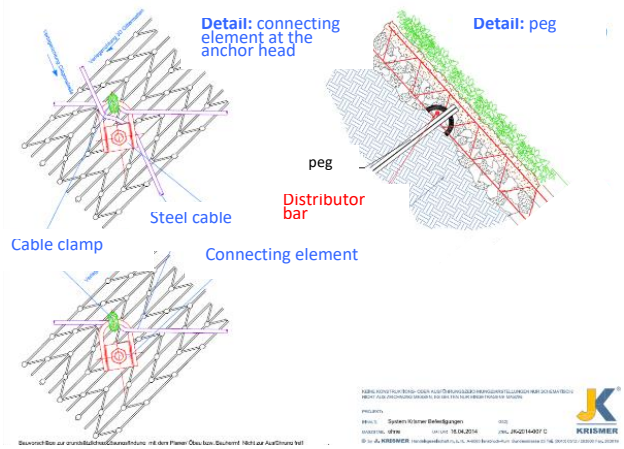

Fig. 9: Detail diagram of the Krismer-3D system

Fig. 10 Krismer-3D system

11.3 The TECCO system

The TECCO system is a high strength square wire mesh that in principle is a classical slope net system. Nevertheless, certain sections of the Doren landslide was fitted with this system for testing purposes. The fear is that due to its large mesh size (65 mm), the products of weathering could readily fall through this net and also that a vegetation layer would only develop with difficulty on this mesh, if at all.

For this reason, Teccmat, a structured mat made of randomly arranged polypropylene filaments, produced by Geobrugg, was laid beneath parts of the square wire mesh covering. The lifespan of these filaments is roughly two years. This three dimensional mat was intended to provide additional erosion protection immediately following the installation, as well as support for the vegetation process. However, this additional part of the trial was soon aborted, as the mat was dislodged by a heavy precipitation event prior to its having been completely anchored, falling toward the foot of the scarp.

REFERENCES

Van Husen, D., Breymann, H. and Jaritz, W. (2008): Rutschung Doren, Geologisch-geotechnischer Abschlussbericht-, Forsttechnischer Dienst für Wildbach- und Lawinenverbauung.

Relationship Between the Process of Large-scale Sediment Movement and Ground Vibration

Hiroshi ASAHARA[1*], Atsuhiko KINOSHITA[2], Yasutaka TANAKA[3], Hiroaki SUGAWARA[3], Gengo YOSHIMURA[3], Wataru SAKURAI[2], Teruyoshi TAKAHARA[2] and Soichi KAIHARA[4]

[1] KANAME Technological Development Co., Ltd. (2-7-4 Torigoe, Taito-ku, Tokyo 1110054, Japan)

[2] National Institute for Land and Infrastructure Management, MLIT (1 Asahi, Tsukuba, Ibaraki 3050804, Japan)

[3] Sediment Disaster Prevention Technology Center, Kinki Regional Development Bureau, MLIT (3027-6 Ichinoro, Nachikatsu-ura Town, Higashimuro-gun, Wakayama 6495302, Japan)

[4] Eight-Japan Engineering Consultants Inc. (3-1-21 Tsushimakyoumachi, Kita-ku, Okayama, Okayama 7008617, Japan)

*Corresponding author. E-mail: asahara@kaname-tec.co.jp

Vibration sensors are expected to be used as an effective means of detecting a large-scale sediment movement triggered by rainfall. However, there is as yet no clear understanding of the relationship between ground vibration and the process of large-scale sediment movement. So we analyzed the relationship, comparing ground vibration of high frequency range (higher than 1 Hz) to vibration of low frequency range (lower than 0.1 Hz) for the Akadani large-scale landslide in Japan in 2011, and comparing video images with seismic data for its re-collapse in 2014. We can explain observation facts consistently, assuming that high frequency vibration is generated by the impact when crushed soil collides with the riverbed or the opposite bank, and that low frequency vibration occurs only when the rock mass slides down without being crushed. High frequency vibration can be used for collapse detection, and the direction of the collapse can be easily estimated using low frequency vibration close to the collapse if it is observed, although low frequency vibration is often not observable due to the collapse process. Furthermore, the detailed process of Akadani landslide was verified from the time difference of vibration observed for each frequency band.

Key words: Large-scale landslide, Sediment movement process, Seismic wave, Video image

1. INTRODUCTION

When a large-scale deep-seated landslide occurs and it forms a landslide dam, submergence damage by flooding can occur in the upstream area and large flood damage can be caused by natural dam breakdown in the downstream area. In a large-scale rain disaster in which deep-seated landslide occurs in multiple places, it usually takes much time to find landslide dams due to bad weather or blocking of the transportation network.

It is known that a high sensitivity seismic network with some 20 km interval stations can detect small ground vibration caused by a deep-seated landslide [e.g., *Moriwaki*, 1999; *Ohsumi et al*., 2005, 2006; *Yamada et al*., 2012]. As such, vibration sensors are expected to be used as an effective means of detecting a large-scale sediment movement triggered by rainfall. MLIT (Ministry of Land, Infrastructure, Transport and Tourism), Japan is now developing an automatic deep-seated landslide detection system using real-time seismic data. MLIT has constructed about 200 seismograph observation stations around areas with high deep-seated landslide probability, and uses Hi-net (High sensitivity seismic observation network) data whose network consists of about 800 stations by NIED (National Research Institute for Earth Science and Disaster Resilience). MLIT plans to use this information for providing to local governments and finally leading to provision of disaster information to citizens. However, there is as yet no clear understanding of the relationship between ground vibration and the sediment movement process.

In this study, we compared ground vibration in the range of 1 – 7 Hz and low frequency ground vibration in the range of 0.01 – 0.1 Hz, which were caused by the Akadani large-scale landslide in Gojo City, Nara Prefecture, Japan on September 4, 2011 to establish the sediment movement process and the

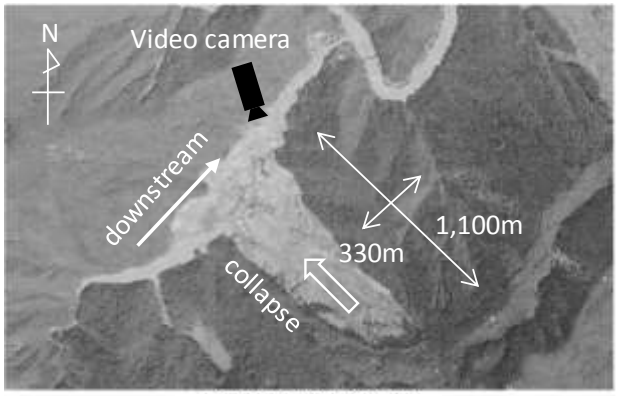

Fig. 1 Top view of the Akadani landslide. It also shows the position and shooting direction of the video camera installed for collapse monitoring (Fig. 7).

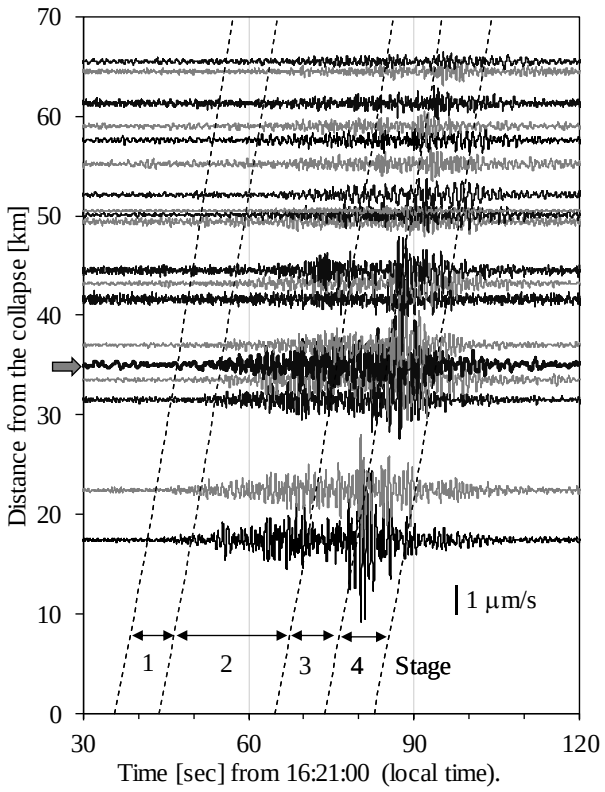

Fig. 2 1 − 7Hz filtered velocity waveforms of vertical component of the Akadani landslide in 2011. The waveforms are arranged by distance from the collapse. Adjacent records are shown alternatingly in black and gray for clarify. The oblique dashed lines correspond to each stage shown in Fig. 3. The arrowed waveform at 35.1 km is F-net Nokami station, whose data is analyzed in Fig. 3 and Fig. 4.

mechanism causing ground vibration. Video images recorded at the re-collapse on August 10, 2014 were also examined comparing with seismic data.

2. GROUND VIBRATION CAUSED BY AKADANI LANDSLIDE IN 2011

On September 3 – 4, 2011, over 30 large-scale sediment movements occurred across a wide region

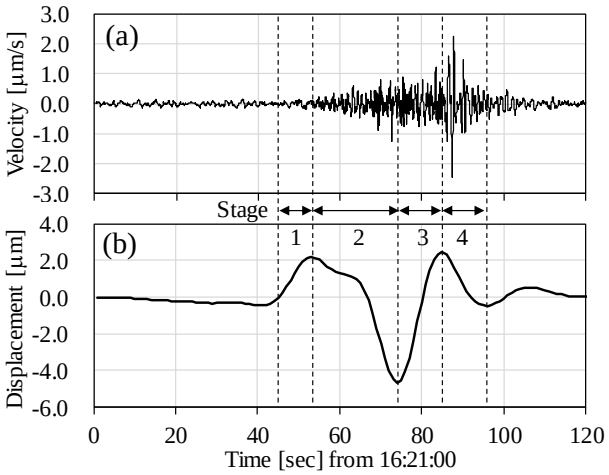

Fig. 3 Vertical components of (a) 1 − 7 Hz velocity and (b) 0.01 − 0.1 Hz displacement waveforms observed at F-net Nokami station.

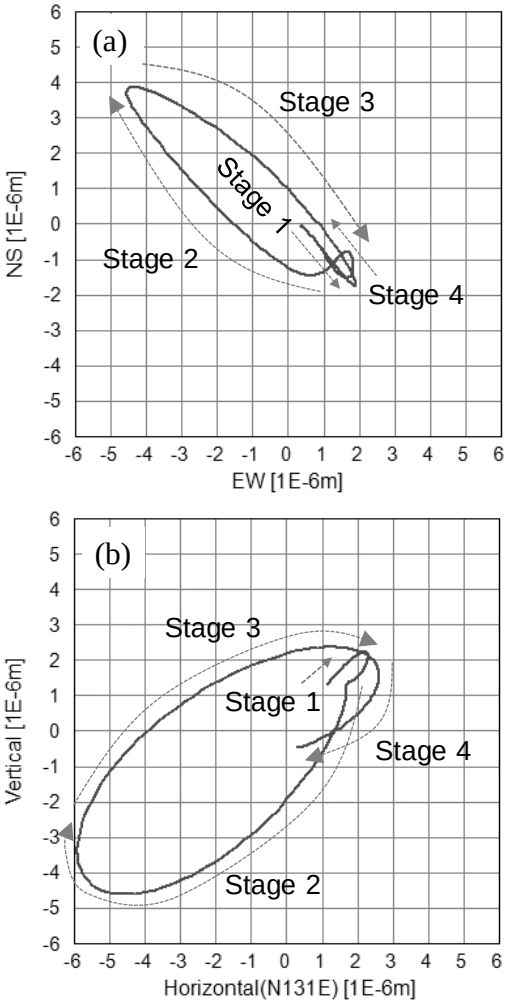

Fig. 4 0.01 − 0.1 Hz particle motion of F-net Nokami station (a) in a horizontal plane and (b) in a vertical plane along slope direction (N131°E).

of the Kii Peninsula, as Typhoon Talas (2011) produced heavy rainfalls across western Japan, and 17 river channels were blocked by landslide dams.

The Akadani landslide, one of the largest events, occurred at 16:21 on September 4, 2011 (local time) in Nara Prefecture, Japan (34.127°N, 135.725°E). **Fig. 1** shows the collapse area. The collapse occurred from a ridge at an altitude of 1,050 m. The area was about 330 m width in average, 1,100 m length along the slope and the collapsed volume was 9.3 million m^3. The direction of collapse was northwest (parallel to the slope; N131°E), and the slope angle was 33°.

Fig. 2 shows seismic records (applying a band-pass filter of 1 – 7 Hz to velocity vertical components) of the Akadani landslide by Hi-net and the broadband seismic network F-net. These seismic networks are both operated by NIED. Here we have studied with the filter of 1 – 7 Hz band, since the dominant frequency of vibration accompanying the deep-seated landslides is analyzed to be about 1 – 3 Hz [*Moriwaki*, 1999; *Ohsumi et al*., 2005, 2016]. The waveforms are arranged by distance from the collapse (This graph is called a record section). Vibration due to the collapse was observed at even 70 km ahead. The oblique dashed lines correspond to each stage shown in **Fig. 3**. The slopes of these lines show that these seismic wave propagations are explained by S wave velocity. The times when the dashed lines cross 0 km represents the moment when each phenomenon occurred at Akadani area. The collapse start time is assumed to be 16:21:35.

Fig. 3 shows the vertical components of 1 – 7 Hz velocity and 0.01 – 0.1 Hz displacement waveforms, observed at F-net Nokami station, 35.1 km away from Akadani area, which is the nearest broadband seismograph station from the collapse. Stages in the figure are explained in **Table 1**. The displacement waveforms were obtained by performing Fourier transformation on the velocity waveform, integrating once in the frequency domain and performing inverse Fourier transformation to the time domain. **Fig. 4** shows the 0.01 – 0.1 Hz particle motions of Nokami station in a horizontal plane and in a vertical plane along the slope from Stage 1 to 4. The orbit which the particle motion draws almost coincided with the slope direction (**Fig. 1**).

In order to explain the sediment movement process using ground vibration data, it was assumed that the dominant frequency of vibration represents the size of rocks which generate vibrations. We assumed that larger rock masses may produce vibration of lower frequencies. In particular, (1) the low frequency (0.01 – 0.1 Hz) displacement waveform corresponds to a large force exerted on the ground in one direction when a large rock mass collides against the opposite bank without being crushed, and (2) the high frequency (1 – 7 Hz) velocity waveform represents the collision of fractured sediments against the riverbed or the opposite bank.

Table 1 shows the relationship between low

Table 1 Relationship between low frequency or 1 – 7 Hz vibration data and sediment movement.

Stage	Horizontal displacement	Vertical displacement	Time duration	1 – 7 Hz velocity	Interpretation of sediment movement
1	Towards↘ southeast	Upward	8 sec.	No vibration	Start of movement of the rock mass and reaching the riverbed
2	Towards↖ northwest	Downward	21 sec.	Start of vibration	Collision of the rock mass with the opposite bank
3	Towards↘ southeast	Upward	9 sec.	In the midst of increasing	Reaction to displacement (continued flowing down of fractured sediment)
4	Slight change	Downward	9 sec.	Peak	Settlement (flowing down of fractured sediment)

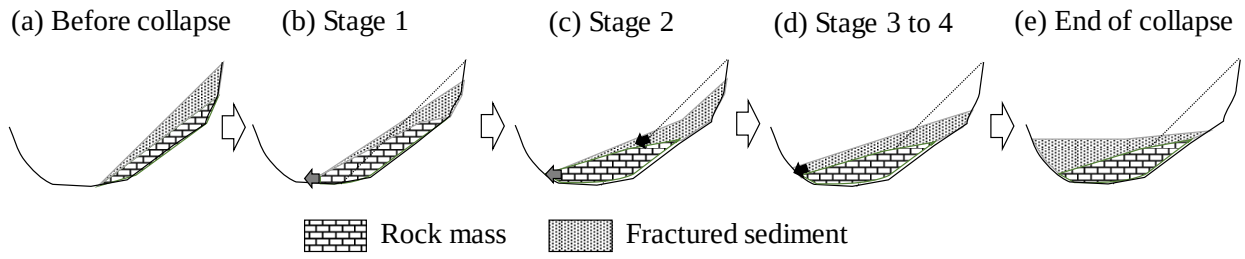

Fig. 5 Sedmient movement process estimated from ground vibration data. (a) Before collapse: fractured soil is accumulated on the rock mass. (b) Stage 1: Start of movement of the rock mass. The rock mass has not reached the opposite bank yet. (c) Stage2: Collision of the rock mass with the opposite bank. The fractured sediment flows on the rock mass. (d) Stage 3 to 4: The fractured sediment continued flowing down after the settlement of the sliding rock mass. (e) End of collapse.

frequency and high frequency vibration data at each stage, and **Fig. 5** shows our sediment movement process model of this landslide considering the above two hypotheses. Before collapse, fractured sediment is accumulated on the rock mass. In Stage 1, the rock mass starts to move but has not reached the opposite bank yet. The fractured sediment still moves almost together with the rock mass. At this period, the upward force is inferred to be caused by the friction force of the descending rock mass and no vibration was observed for high frequency. In the following Stage 2, the rock mass collides with the opposite bank, so the force changed to the downward. The high frequency vibration starts increasing, as the fractured sediment starts to flow down on the rock mass, then collides with the riverbed and the opposite bank. As there was no factor causing upward force after the collision in Stage 2, Stage 3 and 4 are inferred to be a reaction to the former stage. Particle motion of low frequency almost moves on the slope surface through 4 stages. On the contrary, the high frequency vibration increases around Stage 3, and peaked in Stage 4. The fractured sediment is still flowing down even after the settlement of the sliding rock mass, so the high frequency vibration is in the midst of increasing and peak time for high frequency delayed by some ten seconds. The inferred sediment movement process is the collision of transported rocks with the riverbed and the opposite bank at first, followed by the deposition of fractured sediment. The relationship between high frequency vibration and the movement of fractured sediment was confirmed by video image in Chapter 3 later.

This model can explain the following two observed facts without contradiction.

Fact 1: The geological structure of the landslide dam in Akadani area shows a little fractured sliding rock mass layer at the bottom and fractured collapsed sediment above this layer [*Sakurai et al*., 2015].

Fact 2: The low frequency vibration is observed several ten seconds earlier than high frequency vibration.

3. GROUND VIBRATION CAUSED BY AKADANI LANDSLIDE IN 2014 AND VIDEO IMAGES

A re-collapse occurred at Akadani area at 07:27 on August 10, 2014 by Typhoon Fengshen (2014). The collapsed volume was estimated to be 0.76 million m^3. This collapse was filmed in a video camera by MLIT for collapse monitoring. The

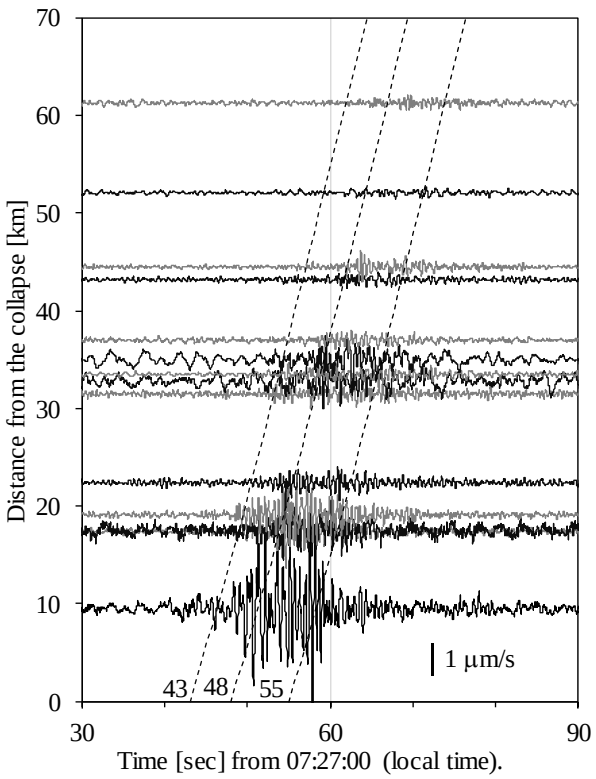

Fig. 6 1 – 7Hz filtered velocity waveforms of vertical component of the Akadani re-collapse in 2014. The waveforms are arranged by distance from the collapse. Adjacent records are shown alternatingly in black and gray for clarify. The oblique dashed lines correspond to the video image times in Fig. 7.

position and shooting direction of the video camera is shown in **Fig. 1**. MLIT had also started to operate seismic stations about 9.5 km away from Akadani area and succeeded in measuring the vibration of this event. **Fig. 6** shows seismic records (applying a band pass filter of 1 – 7 Hz to velocity vertical components) by Hi-net, F-net and MLIT seismic observation network. The waveforms are arranged by distance from the collapse. **Fig. 7** is video images at the moment (a) when the collapsed front reached the riverbed, (b) when the collapsed front collided against the opposite bank and (c) when the collapsed front was presumed to reach the highest altitude of the opposite bank, splash by the collision reached the highest. The oblique dashed lines in **Fig. 6** show propagation of S waves departing at the video image times of **Fig. 7**.

We compared the video images and vibration data at 9.5 km away from the collapse, considering the travelling time of seismic wave. Almost no ground vibration was observed during collapsed sediment flowing down the slope (prior to 07:27:43). Although it was difficult to identify the start time of collapse since the video images were unclear due to raindrops and dust, it was confirmed

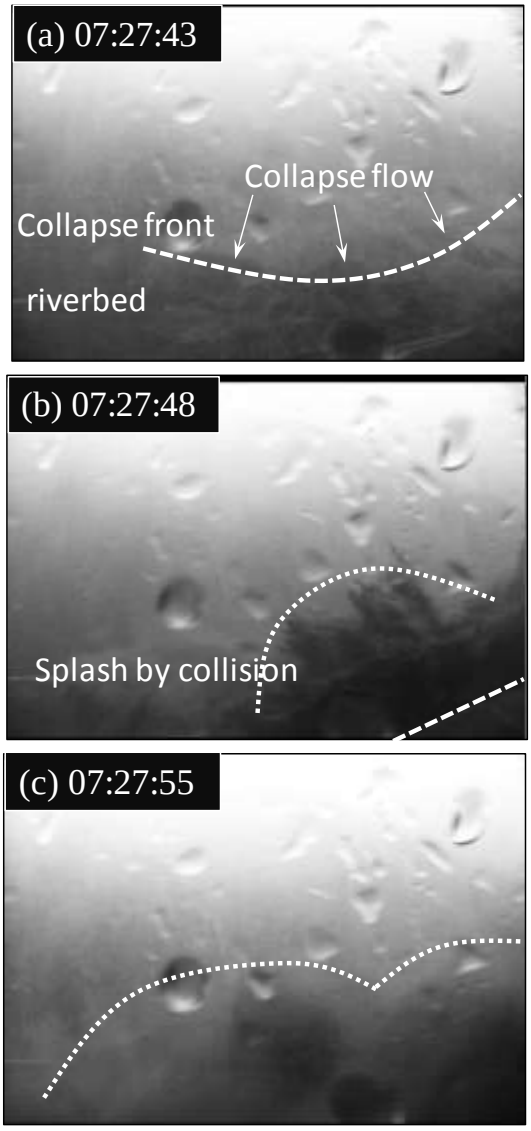

Fig. 7 Video images at the secondary collapse in 2014 from the opposite bank. White dashed lines show the collapse front of fractured sediments and dotted lines show the splash of soils accompanying with the collision with the opposite bank.
(a) 07:27:43; The collapsed front reached the riverbed. (b) 07:27:48; The collapsed front collided against the opposite bank. (c) 07:27:55; The collapsed front was presumed to reach the highest altitude of the opposite bank.

that the sediment was flowing down the slope at 07:27:35 at the latest even from the unclear video images. It was found that high frequency vibrations were hardly observed when the soils were flowing down the slope.

The vibration started when the collapsed sediment reached the riverbed (07:27:43), and the amplitude reached the first peak at the moment when the fractured sediment collided with the opposite bank (07:27:48). The second peak 07:27:55 is the moment when the collapsed front reached the highest altitude of the opposite slope. It is thought that the soils reached the maximum elevation was not the cause of the vibration peak, but that the collision of soils flowing down from the subsequent high elevation to the riverbed or the opposite bank was the cause. After the collapse front reached the highest altitude of the opposite slope (07:27:55), the vibration settled down. The collapsed soil is inferred to be a state where crushing has advanced since the sediment flowing down seems to have high fluidity from the video images. These results make it clear that the collision of fractured sediment to the riverbed and to the opposite bank causes the 1 – 7 Hz vibration.

Although 1 – 7 Hz vibration was observed, 0.01 – 0.1 Hz vibration was not observed at any broadband seismic stations including at the MLIT observation station closest to 9.5 km to the collapse (Broadband seismographs are used for MLIT stations).

4. DISCUSSION

4.1 Relationship between the landslide process and ground vibration

The relationship between ground vibration and sediment transport process can be arranged as follows from the low frequency and high frequency vibration data of 2011 Akadani landslide and the vibration data and video images of 2014 re-collapse.

High frequency vibration is generated by the impact when crushed soil collides with the riverbed or the opposite bank. Therefore, the small-scale landslide detection by vibration sensors is difficult as large ground vibration does not occur in a small-scale collapse such that the soils stop on the slope sliding. On the other hand, in a collapse that causes river blockage, large amount of soil collides against the riverbed and the opposite bank, so there is a high possibility that it can be detected with vibration sensors.

Low frequency vibration occurs only when the rock mass slides without being crushed, conversely it does not occur when it falls apart at the moment of landslide occurrence.

From the time difference between low frequency vibration and high frequency vibration, it is considered that the rock mass first slide without being crushed, then the upper fractured sediment flowed down.

4.2 Low frequency vibration

Fig. 8 shows deep-seated landslide cases whether low frequency vibration was observable or not for each distance from the collapse. In general, the larger the size of the collapses are, the more cases are observable. However, there are some cases

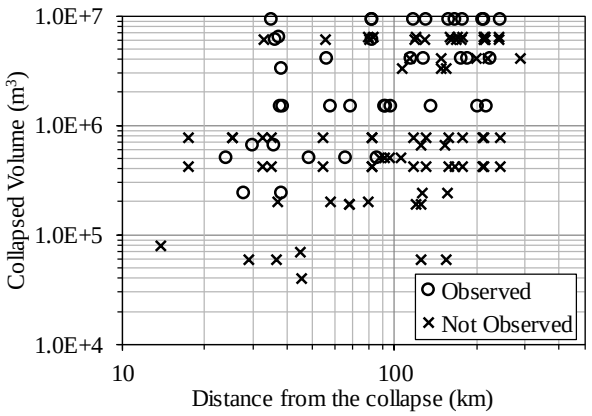

Fig. 8 Deep-seated landslide cases whether low frequency vibration was observable or not for each distance from the collapse.

that low frequency vibrations are not observed for exceeding 5 million m^3 volume, despite in other cases low frequency vibrations are observed for smaller than 1 million m^3. Considering that low frequency vibration occurs only when the rock mass slides without being crushed, whether it is observable or not is influenced by the process of collapse. The low frequency vibration was also observable at the stations 200 km away in 2011 Akadani landslide, but it was not observed at the station nearest 9.5 km in the re-collapse of 2014. The re-collapse is considered that low frequency vibration did not occur because the sediment flowing down has high fluidity, judging from the camera images in addition to being small volume. Large scale landslides are always observable by high frequency vibration, but low frequency vibration is not necessarily observed even if the scale is large. Therefore, it is more effective to use high frequency vibration than low frequency vibration to detect the occurrence of collapse. Moreover, the earthquake including the teleseismic earthquake influence greatly in the low frequency band. In the case of Magnitude 6 class or larger teleseismic earthquake, a few minutes of vibration is observed in the high frequency band, whereas in the low frequency band it may last for more than two hours. This also makes it difficult to use the low frequency band for landslide detection.

Inversion analysis is generally required to obtain the force acting on the surface (source time function) from the low frequency waveforms observed at multiple points [*Kanamori and Given*, 1982; *Yamada et al*., 2013]. However, a displacement waveform obtained at the point where is sufficiently nearer than one wavelength from the collapse shows almost the same shape as the force acting on the surface, as the influence of reflection or scattering due to underground discontinuities and inhomogeneities is small. This property is useful from the viewpoint of engineering. Assuming that S wave velocity is 3 km/s, the wavelength of 50 seconds period vibration is 150 km. When the observation point is far from the collapse, the particle motion deviates from the collapse direction and draws a complicated shape. **Fig. 4** shows that we can know the direction of the collapse from particle motion even at 35 km away from the collapse. Therefore, it was found that the force acting on the surface can be roughly and easily known from the displacement waveform even at the distance of about 1/4 wavelength which is sufficiently shorter than one wavelength, without complicated inversion analysis. Although low frequency vibration is not necessarily observed, if the vibration is observed at a nearby point and the position estimation by high frequency vibration is accurate, there is a possibility that it can be used for judging the presence or absence of river channel blockage.

5. CONCLUSION

The relationship between the deep-seated landslide process and the ground vibration was analyzed from the vibration data of two frequency bands and video images. As a result, it is not contradictory to the observation facts, assuming that high frequency (higher than 1 Hz) vibration is generated by the impact when crushed soil collides with the riverbed or the opposite bank, and that low frequency (lower than 0.1 Hz) vibration occurs only when the rock mass slides without being crushed. High frequency vibration can be used for the detection of collapse compared more effectively than low frequency band, because high frequency vibration is observed at any time as the scale of collapse is large, and less affected by teleseismic earthquakes than low frequency band. Furthermore, if the low frequency vibration is observed at the station within about 35 km from the collapse site, the direction of the collapse can be easily estimated by particle motion, but low frequency vibration is often not observable due to the collapse process. If the low frequency vibration is observed at a nearby point and the position estimation by high frequency vibration is accurate, there is a possibility that it can be used for judging the presence or absence of river channel blockage.

In this study, we examined the landslide process for Akadani area. However, different interpretations might be possible for the collapse that occurs under different conditions. It is necessary to conduct the

same examination for other cases for verifying the validity of interpretation of this study.

ACKNOWLEDGMENT: We acknowledge the National Research Institute for Earth Science and Disaster Resilience (NIED) for the use of the seismic data (Hi-net and F-net).

REFERENCES

Kanamori, H. and Given, J. (1982): Analysis of long-period seismic waves excited by the May 18, 1980, eruption of Mount St. Helens – a terrestrial monopole, Journal of Geophysical Research, Vol. 87, No. B7, pp. 5422 – 5432.

Moriwaki, H. (1999): Characteristics of a ground seismogram due to a debris flow originating from a landslide -a Gamaharasawa debris flow-, Journal of Japan Landslide Society, Vol. 36, No. 3, pp. 99 – 107 (in Japanese with English abstract).

Ohsumi, T., Asahara, H. and Shimokawa, E. (2005): Analysis of ground-vibration induced by the 10 August 2004 Ohtou landslide in Nara Prefecture, Japan using the data of high sensitivity seismograph network: Application to landslide detecting, Journal of Natural Disaster Science, Vol. 24, No. 3, pp. 267 – 277 (in Japanese with English abstract).

Ohsumi, T., Asahara, H. and Shimokawa, E. (2006): Hypocenter detecting analysis using the data of high sensitivity seismograph network applied for the mass movement on Mt. Shirouma, Nagano in 2005, Journal of the Japan Landslide Society, Vol. 43, No. 1, pp. 27 – 32 (in Japanese with English abstract).

Ohsumi, T., Kaihara, S., Sakai, R. and Sakurai, W. (2016): Verifications of the noise reduction by down hole sentinel vibration sensors for “Deep-seated landslide detection” and “Detectable landslide volume” in the Kii peninsula, Journal of the Japan Society of Erosion Control Engineering, Vol. 68, No. 5, pp. 32 – 37 (in Japanese with English abstract).

Sakurai, W., Sakai, R., Okuyama, Y., Ogawauchi, Y., Fukuda, M., Sato, M., Kaihara, S., Tadakuma, N. and Fujiwara, Y. (2015): Differences in hydrological and erosion conditions caused by the internal structure of a landslide dam, Journal of the Japan Society of Erosion Control Engineering, Vol. 68, No. 3, pp. 21 – 30 (in Japanese with English abstract).

Yamada, M., Matsushi, Y., Chigira, M. and Mori, J. (2012): Seismic recordings of landslides caused by Typhoon Talas (2001), Japan, Geophysical Research Letters, Vol. 39, L13301, doi:10.1029/2012GL052174.

Yamada, M., Kumagai, H., Matsushi, Y. and Matsuzawa, T. (2013): Dynamic landslide process revealed by broadband seismic records, Geophysical Research Letters, Vol. 40, No. 12, pp. 2998 – 3002.

A Study on Criteria of Warning and Evacuation for Large-scale Sediment Disasters Considering the Relationships with Sediment Movement and Damage

Yuna SUZUKI[1], Shin-ichiro HAYASHI[2*], Shin'ya KATSURA[2], Mio KASAI[2], Nobutomo OSANAI[2] and Tomomi MARUTANI[2]

[1] Saitama City Office, (Tokiwa 6, Urawa-ku, Saitama, Saitama 3309588 Japan)
[2] Research Faculty of Agriculture, Hokkaido University, (Kita 9, Nishi 9, Kita-ku, Sapporo, Hokkaido 0608589, Japan)
*Corresponding author. E-mail: shayashi@cen.agr.hokudai.ac.jp

In Japan, Sediment Disaster Warning Information pertaining to a debris flow and slope failures due to rainfall is provided to residents based on the criteria of rainfall between the occurrence and non-occurrence of such sediment disasters. Early warning information system for large-scale sediment disasters has not yet been established, and the criteria that must be met to trigger warning have not yet been established. In this study, to estimate suitable criteria of warning and evacuation for large-scale sediment disasters in Japan, we examined and clarified the relationships among sediment movement, damage, and return period of rainfall causing large-scale sediment disasters by conducting a statistical analysis of 22 previous large-scale sediment disasters. We found that 1) large-scale sediment disasters may occur during rainfall events with a 30 to 50 year return period, and 2) longer rainfall return periods, as recorded in long-term rainfall indices (more than 24 hours), may indicate imminent large-scale sediment movement and demand attention as indicators of large-scale sediment disasters.

Key words: criteria, early warning information, large-scale sediment disaster, rainfall

1. INTRODUCTION

In Japan, Sediment Disaster Warning Information (SDWI) predicting a debris flow and slope failures due to rainfall is disseminated by both by prefectural governments and the Japan Meteorological Agency (JMA) [*Japan Meteorological Agency*, 2017a; *Osanai et al.*, 2010]. However, SDWI does not predict the scale of sediment disasters [*Japan Meteorological Agency*, 2017b]. Several previous studies on early warning information have focused on rainfall conditions predicting the occurrence or non-occurrence of landslides (i.e. *Keefer et al.*, [1987], *Baum and Gobt* [2010], *Osanai et al.*, [2010]). In contrast, few studies have been conducted on the relationships among sediment movement, damage (which are related to the scale of sediment movement, location of houses, population density and facilities to prevent sediment disaster), and rainfall. Warning and evacuation criteria for large-scale sediment disasters, e.g., multiple and/or simultaneous deep-rapid landslides [*Hayashi et al.*, 2013] and debris flows [*Nishi et al.*, 2014], which can result in large numbers of causalities and/or significant property damage, have not been fully established.

Regarding the receptivity to, and recognition of, early warning information by residents, such information currently does not effectively promote evacuation [*National Institute of land and infrastructure management and Tsukuba University* 2012; *Ministry of Land, Infrastructure Transport and Tourism*, 2013]. Ministry of Land, Infrastructure Transport and Tourism (MLIT) has therefore proposed a graded warning information linked with the actions that should be taken by residents to ensure their safety [*Ministry of Land, Infrastructure Transport and Tourism*, 2013]. Moreover, *Ushiyama* [2014] indicated that graded warning information is easier for residents to understand than public early warning statements. Although the JMA extensively disseminates Emergency Warnings regarding extreme weather conditions to individual prefectures [*Japan Meteorological Agency*, 2017c], to date no early warning information system for large-scale sediment disasters has been established.

In this study, we analyze the relationships among

sediment movement, damage, and the return period of rainfall events causing sediment disasters to estimate suitable criteria of warning and evacuation for large-scale sediment disasters.

2. METHODS

Fig. 1 illustrates our research methods. We first evaluate the scale of sediment disasters regarding 22 previous rainfall-triggered sediment disasters, which are selected by literature search (i.e. *Japan Sabo Association* [2015]), in Japan based on the Sediment Disaster Scale [*Hayashi et al.*, 2015]. For the 22 disasters, we specify triggering rainfall which may contribute to cause sediment disaster and evaluate its return period respectively. Then we statistically analyze the relationship between the scale of sediment disaster and the return period of triggering rainfall. Finally, based on the results of this analysis, we estimate suitable criteria of warning and evacuation for large-scale sediment disasters.

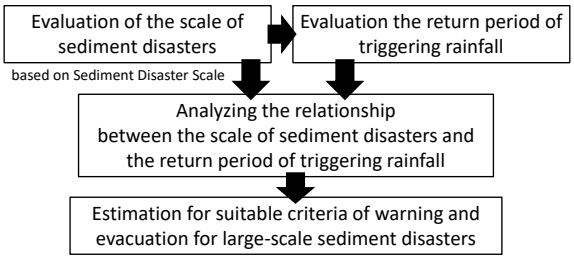

Fig. 1 Research methods

2.1 Evaluation of the scale of sediment disasters based on Sediment Disaster Scale

Of the 22 disasters, 17 were evaluated the scale of sediment disasters by *Hayashi et al.*, [2015] and *Hayashi et al.*, [2016]; we evaluate additional 5 disasters based on the Sediment Disaster Scale (SDS; *Hayashi et al.*, [2015], **Table 1**, SDS ≥ 3, from 1961 to 2014). SDS classifies sediment disasters into five categories using two indices - one that pertaining to sediment movement, "Sediment Movement Magnitude" (SMM; *Uchida et al.*, [2005]), and one that related to damage, "Damage Level" (DL; *Kojima et al.*, [2009]). SMM is calculated using Eq. (1):

$$SMM = log_{10} \sum_{i=1}^{n} (V_i H_i) \quad (1)$$

where V is the volume of sediment movement (m^3), and H is the relative height (m). DL is calculated using Eq. (2):

$$DL = 0.69\, log_{10}\, x_1 + 0.16\, log_{10} \left(x_2 + x_3 + \frac{x_4}{3} \right) + 1.07 \quad (2)$$

where x_1 is the number of persons killed or missing, x_2 is the number of persons injured, x_3 is the number of houses totally collapsed, x_4 is the number of houses partially collapsed. SDS categories are defined as follows (excluding overlapping portions within the upper category):

SDS 1: SMM < 4.0 and DL < 1.0
SDS 2: 4.0 ≤ SMM < 6.0 or 1.0 ≤ DL < 1.5
SDS 3: 6.0 ≤ SMM < 8.0 or 1.5 ≤ DL < 2.0
SDS 4: 8.0 ≤ SMM < 10.0 or 2.0 ≤ DL < 2.5
SDS 5: 10.0 ≤ SMM or 2.5 ≤ DL

According to *Hayashi* [2017], multiple and/or simultaneous deep-rapid landslides and debris flows, which are typical disasters of large-scale sediment disaster, were are classified as SDS ≥ 3. Based on historical disaster records, most of sediment disasters included in SDS 1 and 2 were single debris flow and slope failure, which can be caused by daily rainfall exceeding 10 yr return period [*Ministry of Land, Infrastructure Transport and Tourism*, 1999 and 2012]. Therefore, we define large-scale sediment disasters as SDS ≥ 3.

2.2 Evaluation the return period of triggering rainfall

For the 22 sediment disasters, we evaluate the return period of "Triggering Rainfall" (hereafter "TR") that caused the disaster (**Table 1**) using AMeDAS (Automated Meteorological Data Acquisition System, operated by JMA) return period calculation program (hereafter "ARPCP") [*Public Works Research Institute*, 2003]. We defined TR as the rainfall index that had the longest return period of nine different rainfall indices (maximum 1 h, 2 h, 3 h, 6 h, 12 h, 24 h, 48 h, 72 h and total rainfall). Precipitation records for each sediment disaster are obtained from literatures of sediment disasters. The ARPCP can evaluate return period in 748 AMeDAS stations within nationwide AMeDAS stations (1302 stations, as of November 30, 2016), where can obtained yearly maximum value. For the sake of simplicity, we evaluate the return period of TR using the nearest AMeDAS station that can be evaluated by the ARPCP (hereafter "$AMeDAS_e$") from the rainfall observation station which written in the literature (hereafter "ROS_l"). The distance between $AMeDAS_e$ and ROS_l is always less than 30km; this may have led to the positive correlation between rainfall records of different rainfall observation stations (i.e. *Irasawa and Taguchi* [1996]).

Table 1 List of sediment disasters evaluated SMM, DL, SDS and RPTR

Year	Name of disaster	Prefecture	SMM	DL	SDS category	Literature regarding SMM and DL	ROS_l	Literature regarding ROS_l	$AMeDAS_e$	The rainfall indices of TR	The amount of TR (mm)	RPTR
1961	Onishiyama	Nagano	9.05	2.45	4	*Hayashi et al.*, [2016] based on *Public Works Research Institute* [2010]	Iida	*Japan Meteorological Agency* [2017d]	Iida	24	354.4	410
1966	Ashiwada	Yamanashi	8.45	2.74	5	*Hayashi et al.*, [2016] based on *Oka and Katsurajima [1971], Sabo division of Yamanashi Prefecture* [1994]	Kawaguchiko	*Sabo division of Yamanashi Prefecture* [1994]	Kawaguchiko	1	68.2	45
1982	Nagasaki	Nagasaki	7.14	3.13	5	*Hayashi et al.*, [2016] based on *Egashira* [1983], *Mizuyama et al.*, [1985], *Nakano* [1982]	Nagasaki	*Public works department of Nagasaki Prefecture* [1983]	Nagasaki	6	432	110
1988	Kake	Hiroshima	6.18	2.23	4	*Hayashi et al.*, [2016] based on *Himegi* [1999], *Tochigi and Kaibori* [1989], *Tochigi et al.*, [1989]	Kake public works office	*Mizuyama et al.*, [1988]	Kake	6	238	140
1997	Hariharagawa	Kagoshima	7.18	2.22	4	*Hayashi et al.*, [2015] based on *Moriwaki et al.*, [1997]	Izumi	*Moriwaki et al.*, [1997]	Izumi	48	544	63
1999	Hiroshima and Kure	Hiroshima	6.63	2.34	4	*Hayashi et al.*, [2016] based on *Miura et al.*, [1999], *The committee for countermeasure against sediment disasters in Hiroshima Prefecture* [1999]	Uokiri-dam	*Sabo & Landslide Technical Center* [2000]	Kake	6	207.5	77
2003	Minamata	Kumamoto	7.48	2.09	4	*Hayashi et al.*, [2015] based on *National Institute for Land and Infrastructure Management and Public Works Research Institute* [2003]	Fukagawa	*National Institute for Land and Infrastructure Management and Public Works Research Institute* [2003]	Minamata	6	313	240
2003	Dazaifu	Fukuoka	6.68	1.27	3	*This study based on National Institute for Land and Infrastructure Management and Public Works Research Institute* [2003]	Futaba nursery home	This study based on *National Institute for Land and Infrastructure Management and Public Works Research Institute* [2003]	Dazaifu	6	258	170
2004	Izumozaki	Niigata	7.69	1.20	3	*Hayashi et al* ., [2015] based on *Noro et al.*, [2004]	Nagaoka	*Noro et al.*, [2004]	Nagaoka	24	231	51
2004	Miyama	Fukui	8.45	1.91	4	This study based on *Yao et al.*, [2005]	Miyama	This study based on *Yao et al.*, [2005]	Miyama	6	254	17,000
2004	Oyochi	Tokushima	8.78	1.28	4	*Hayashi et al* ., [2015] based on *Hiura and Sasahara* [2005]	Sawadani	*Noro et al.*, [2004]	Fukuharaasahi	48	1518	1,500
2004	Niihama	Ehime	7.67	1.60	3	*Hayashi et al* ., [2015] based on *Sabo & Landslide Technical Center* [2005]	Niihama	*Ministry of Land, Infrastructure Transport and Tourism* [2005]	Niihama	2	107	26
2004	Miyagawa	Mie	7.37	1.80	3	*Hayashi et al* ., [2015] based on *Hayashi et al.*, [2004]	Miyagawa	*Hayashi et al.*, [2004]	Miyagawa	1	110	67
2005	Mimikawa -shimado	Miyazaki	8.92	0.55	4	*Hayashi et al* ., [2016] based on *Public Works Research Institute* [2010]	Morotsuka	*Chigira* [2006]	Kuraoka	48	943	500
2006	Okaya	Nagano	6.46	1.93	3	*Hayashi et al.* , [2015] based on *Hiramatsu et al.*, [2006]	Tatsuno	*Hiramatsu et al.*, [2006]	Suwa	72	403	380
2009	Hofu	Yamaguchi	8.48	2.14	4	*Hayashi et al.*, [2015] *based on Hayashi et al.*, [2010]	Manao	*Ministry of Land, Infrastructure Transport and Tourism* [2009]	Hofu	6	229	310
2012	Kii peninsula	Nara, Wakayama, Mie	10.46	2.64	5	*Hayashi et al.*, [2015]	Kazaya	*Kinki regional development bureau of Ministry of Land, Infrastructure Transport and Tourism* [2013]	Kazaya	72	1302.5	2,200
2013	Tazawako	Akita	6.20	1.75	3	*This study based on Touhoku regional development bureau of Ministry of Land, Infrastructure Transport and Tourism* [2013]	Yoroibata	*This study based on Touhoku regional development bureau of Ministry of Land, Infrastructure Transport and Tourism* [2013]	Tazawako	6	231.5	960
2013	Izu-oshima	Tokyo	8.16	2.51	5	*This study based on The committee for countermeasure against sediment disasters in Izu-oshima island* [2014]	Oshima	*This study based on The committee for countermeasure against sediment disasters in Izu-oshima island* [2014]	Inatori	12	694.5	51,000
2014	Nagiso	Nagano	8.19	1.25	4	*This study based on Chubu regional development bureau of Ministry of Land, Infrastructure Transport and Tourism* [2014]	Nagiso	*This study based on Hiramatsu et al.*, [2014]	Nagiso	2	88	48
2014	Hiroshima	Hiroshima	8.01	2.75	5	*Hayashi et al.*, [2016] *based on Ministry of Land, Infrastructure Transport and Tourism* [2014]	Takase	*Ministry of Land, Infrastructure Transport and Tourism* [2014]	Higashihiroshima	2	166	750
2014	Tanba	Hyogo	7.85	1.31	3	*Hayashi et al* ., [2016] based on *Ministry of Land, Infrastructure Transport and Tourism* [2014]	Kitaokamoto	*Sakamoto and Uezono* [2014]	Kaibara	12	345	910

3. RESULTS & DISCUSSION

Fig. 2 and **Table 2** show the relationship between the SDS category and the return period of TR (RPTR). For the upper value of RPTR (approx. from 960 to 51,000 yr), higher values of SDS category coincided with higher RPTR, average value and median value. However, for the lower value of RPTR (approx. from 30 to 50 yr), higher SDS category (e.g. 4 and 5) was not associated with higher RPTR.

We divided the rainfall indices of TR into two groups, short-term (ST, 1 to 12 h) and long-term (LT,

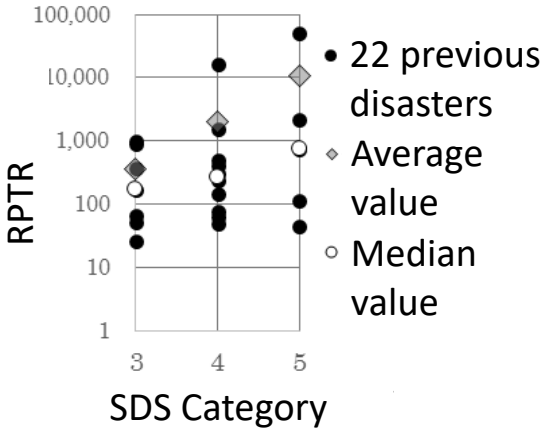

Fig. 2 The relationship between SDS category and RPTR, arithmetic average value and median value

Table 2 The upper, arithmetic average, median and lower value of RPTR and sample standard deviation for SDS categories (2 significant figures)

	3	4	5
Upper value of RPTR (yr.)	960	17,000	51,000
Average value (yr.)	360	2,000	11,000
Median value (yr.)	170	270	750
Lower value of RPTR (yr.)	26	48	45
Standard deviation (yr.)	410	5,100	23,000

more than 24 h) and then analyzed the relationships among SMM, DL and RPTR for each group separately using Spearman's rank correlation coefficient (SRCC) computed in R software (**Fig. 3** and **4**). As shown in **Fig. 3**, SMM and RPTR were not correlated in the ST group (SRCC = 0.11, P = 0.70); however, they were strongly positively correlated in the LT group (SRCC = 0.71, P = 0.09). As shown in **Fig. 4**, DL and RPTR had no correlation in the ST (SRCC = 0.08, P = 0.77) or LT group (SRCC = 0.29, P = 0.56). Because TR tends to cause large-scale sediment movement in LT cases (SMM ≥ 8.5, **Fig. 3b)**), it may modulate the relationships among SDS category and the upper, average and median values of RPTR (**Fig. 2**). In addition, Damage of any severity level may occur irrespective of RPTR, and thus may also affect the relationship between SDS category and the lower value of RPTR (**Fig. 2**).

Based on our analysis of the relationships among sediment movement, damage, and return period of rainfall events causing large-scale sediment disasters, we suggest for estimation of suitable criteria of warning and evacuation for large-scale sediment disasters as follows. 1) Large-scale sediment disasters may occur with approximately 30 yr and 50 yr of return period rainfalls in ST and LT, respectively (**Fig. 4**). Therefore 30 yr and 50 yr of return period rainfall can be criteria of warning and evacuation for large-scale sediment disasters in ST and LT, respectively. 2) In LT, longer return period of rainfall may cause large-scale sediment movement (**Fig. 3b)**). Therefore, if exceeding 50 yr of return period rainfall coincides with a prediction of intense rainfall, attention should be paid to it for the occurrence of large-scale sediment disasters.

Our suggestions is supported by the findings of several previous studies. Suggestion 1) corresponds to that JMA operates Emergency Warning based on exceeding 50 yr return period of Soil water index [*Okada et al.*, 2001], 3hr and 48hr rainfall [*Japan Meteorological Agency*, 2017e], which were mainly determined based on flood damage. *Saito et al.*, [2014] also found that large landslide events (>10^6 m^3) in Japan occurring from 2001 to 2011 were associated with greater-than 40 yr return period of rainfall events. Suggestion 2) correspond to findings of *Uchida and Okamoto* [2012], indicating that past multiple deep-rapid landslides in Japan, which are the major cause of large-scale sediment disasters, occurred when cumulative rainfall exceeded 600 mm within 48 hr and 72 hr. Based on these findings, and our own results detailed herein, we clarify approximate criteria of warning and evacuation for large-scale sediment disasters to establish graded early warning information.

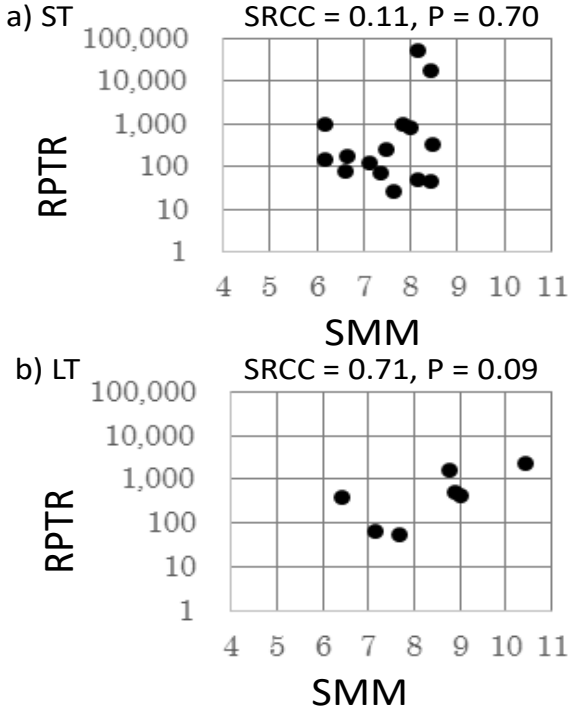

Fig. 3 The relationship between SMM and RPTR (a) in ST, b) in LT)

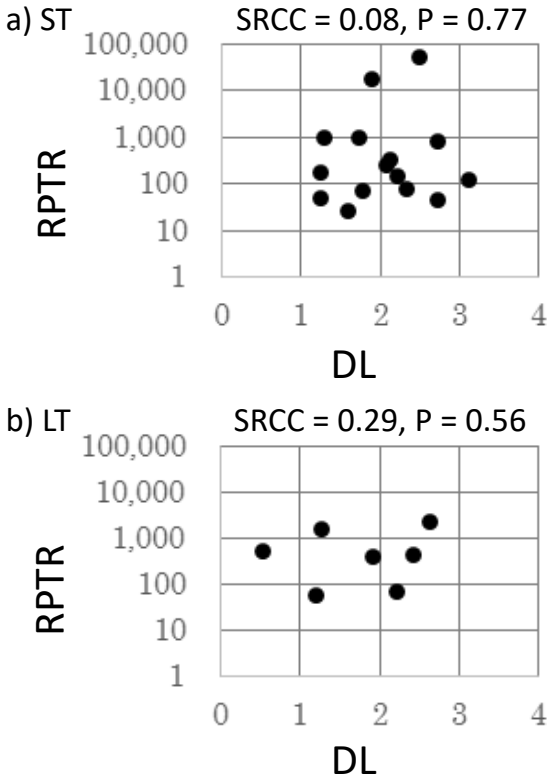

Fig. 4 The relationship between DL and RPTR in LT (a) in ST, b) in LT)

4. CONCLUSIONS

In this study, to estimate suitable criteria of warning and evacuation for large-scale sediment disasters, we analyzed and clarified the relationships among sediment movement, damage, and return period of rainfall causing large-scale sediment disasters (SDS ≥ 3), We found that 1) large-scale sediment disasters may occur with 30 to 50 yr of return period rainfalls and 2) longer return period of rainfall in LT may cause large-scale sediment movement (SMM ≥ 8.5); thus attention should be paid to it for the occurrence of large-scale sediment disasters.

Further examination is necessary to improve our study. Regarding evaluation for RPTR, the minimization of distances between where disaster occurred, rainfall observation station nearest where disaster occurred and evaluated rainfall observation station for RPTR improve the accuracy of RPTR evaluations. By increasing the number of reports on previous large-scale sediment disasters, future studies could help improve the general applicability of our method.

ACKNOWLEDGMENT: This study was supported by the R & D support program of the Sabo & Landslide Technical Center, Japan.

REFERENCES

Baum, R.L., and Godt, J.W. (2010): Early warning of rainfall-induced shallow landslides and debris flows in the USA, Landslides, vol. 7, pp. 259-272.

Chigira, M. (2006): Landslide hazards induced by the 2004 Typhoon 14 in Kyushu, Disaster Prevention Research Institute Annuals, Kyoto University, Vol. 49A, pp. 23-34 (in Japanese with English abstract).

Chubu regional development bureau of Ministry of Land, Infrastructure Transport and Tourism (2014): Nashizawa debris flow in Nagiso Town, Nagano Prefecture, http://www.cbr.mlit.go.jp/saigai/NEWS/MAIN/140709taifuu8/01kisya/141017nashizawa.pdf (in Japanese).

Egashira, S. (1983): Disaster due to slope failure and debris flow caused by heavy rain of July 1982, Disaster Prevention Research Institute Annuals, Kyoto University, Vol. 26A, pp. 1-17 (in Japanese with English abstract).

Hayashi, S. (2017): A study for prompt survey techniques against large-scale sediment disaster, doctoral thesis, Hokkaido Univ., 135pp. (in Japanese).

Hayashi, S., Osanai, N. and Uchida, T. (2016): A study for characteristics of magnitude of sediment disaster evaluated by unified method, Proceedings of the 65th Research Meeting of the Japan Society of Erosion Control Engineering, pp. B-352-353 (in Japanese).

Hayashi, S., Tsuchiya, S. Kondo, K. Shibano, H., Numamoto, S. Kosugi, K., Yamakoshi, T. and Ikeda, A. (2004): Sediment related disasters caused by typhoon Meani (T 0421) in Miyagawa village, Mie prefecture on September 29, 2004 (prompt report), Journal of the Japan Society of Erosion Control Engineering, Vol. 57, No. 4, pp. 48-55 (in Japanese with English abstract).

Hayashi, S., Uchida, T., Okamoto, A., Ishizuka, T., Yamakoshi, T. and Morita, K. (2013): Countermeasures against landslide dams caused by typhoon Talas 2011, Asia-Pacific Tech Monitor, Vol.30, No.1, pp. 20-26.

Hayashi, S., Uchida, T., Okamoto, A., Osanai N., Lee, C. and Woo, C. (2015)：Estimation of the socio-Economic impacts of sediment disasters by using evaluation indexes of the magnitude of sediment movement and level of damage to society, International Journal of Erosion Control Engineering Vol. 8, No. 1, pp. 1-10.

Himegi, K. (1999): Debris flow disaster in northwest part of Hiroshima Prefecture in Showa 63, Journal of the Japan Society of Erosion Control Engineering, Vol. 52, No. 2, pp. 54-58 (in Japanese).

Hiramatsu, S., Fukuyama, T., Yamada, T., Ohsaka, O., Nakatani, K., Matsumoto, N., Fujimura, N., Kato, M., Shimada, T., Kubo, T. Matsuo, S., Nishio, Y. and Yoshino, K. (2014): Disaster report on the debris flow occurred on 9 July 2014 in Nagiso, Nagano prefecture, Journal of the Japan Society of Erosion Control Engineering, Vol. 67, No. 4, pp. 38-48 (in Japanese with English abstract).

Hiramatsu, S., Mizuno, H., Ikeda, A. and Kato, N. (2006): Sediment disaster caused by heavy rain in July, 2006 – disaster due to debris flows in Okaya, Nagano, Vol. 59, No. 3, pp. 51-56.

Hiura, H. and Sasahara, K. (2005): Sediment disasters in Shikoku, Proceedings of Symposium of the Japan Society of Erosion Control Engineering, pp. 25-40 (in Japanese).

Irasawa, M. and Taguchi, T. (1996): Layouts of telemeters based on characteristics of rainfall, Journal of the Japan Society of Erosion Control Engineering, Vol. 49, No. 4, pp. 22-27 (in Japanese with English abstract).

Japan Meteorological Agency (2017a): Real-time Landslide Risk Map, https://www.jma.go.jp/en/doshamesh/

Japan Meteorological Agency (2017b): Sediment disaster warning information and real-time landslide risk map, http://www.jma.go.jp/jma/kishou/know/bosai/doshakeikai.html (in Japanese).

Japan Meteorological Agency (2017c): Emergency Warning System, http://www.jma.go.jp/jma/en/Emergency_Warning/ew_index.html

Japan Meteorological Agency (2017d): Heavy rain caused by baiu rain front in Showa 36, http://www.data.jma.go.jp/obd/stats/data/bosai/report/1961/19610624/19610624.html (in Japanese).

Japan Meteorological Agency (2017e): The indices related to weather for Emergency Warning System, http://www.jma.go.jp/jma/kishou/know/tokubetsu-keiho/sanko/shihyou.pdf (in Japanese).

Japan Sabo Association (2015): Sabo Binran, 708pp. (in Japanese).

Keefer DK, Wilson RC, Mark RK, Brabb EE, Brown WM-III, Ellen SD, Harp EL, Wieczorek GF, Alger CS, Zatkin RS (1987): Real-time landslide warning during heavy rainfall, Science, Vol. 238, pp.921-925.

Kinki regional development bureau of Ministry of Land, Infrastructure Transport and Tourism (2013): The Great Flood in the Kii peninsula, http://www.kkr.mlit.go.jp/bousai/kiroku/qgl8vl0000008lkt-att/kiihantou-kirokushi.pdf (in Japanese).

Kojima, S., Osanai, N., Nishimoto, H., Ogawa, K. and Matsuda, M. (2009): Study of damage indices based on questionnaire surveys of the damage image of sediment disasters, Journal of the Japan Society of Erosion Control Engineering, Vol. 62, No. 3, pp. 47-54 (in Japanese with English abstract).

Ministry of Land, Infrastructure Transport and Tourism (1999): The manual of cost-benefit analysis for countermeasure against slope failure (proposed), 30pp. (in Japanese).

Ministry of Land, Infrastructure Transport and Tourism (2005): Assessment of disaster damages in 2004, http://www.mlit.go.jp/river/pamphlet_jirei/bousai/saigai/2005/ (in Japanese).

Ministry of Land, Infrastructure Transport and Tourism (2009): Sediment disasters caused by heavy rain in Yamaguchi Prefecture, July 21, Heisei 21, http://www.mlit.go.jp/river/sabo/tokushu_dosha/tokushu_dosha1_sanko1.pdf (in Japanese).

Ministry of Land, Infrastructure Transport and Tourism (2012): The manual of cost-benefit analysis for countermeasure against debris flow (proposed), 41pp. (in Japanese).

Ministry of Land, Infrastructure Transport and Tourism (2013): The final report of the review meeting for dissemination of warning against sediment disaster, http://www.mlit.go.jp/river/sabo/yobikake/houkokusyo/01houkokusyo.pdf (in Japanese).

Ministry of Land, Infrastructure Transport and Tourism (2014): Occurrence of sediment-related disasters in 2014, http://www.mlit.go.jp/river/sabo/jirei/h26dosha/150331_H26saigai.pdf (in Japanese).

Miura, K., Anan, S, Fujimoto, M., Niimi, T., Ueda, T. and Okamura, M. (1999): Journal of the Japan Society of Engineering Geology, Vol. 40, No. 5, pp. 316-321 (in Japanese with English abstract).

Mizuyama, T., Ishikawa, Y. and Kurihara, J. (1988): 1988 Debris-flow disaster in Hiroshima Prefecture, Journal of the Japan Society of Erosion Control Engineering, Vol. 41, No. 3, pp. 48-49 (in Japanese).

Mizuyama, T., Ohba, A. and Manzen, H. (1985): Production and transport of woody trash and logs associate with debris flow occurrence, Journal of the Japan Society of Erosion Control Engineering, Vol. 38, No. 1, pp. 1-6 (in Japanese).

Moriwaki, H., Sato, T. and Chiba, M. (1997): Report on the Hariharagawa debris flow disaster on July 10, 1997 in Kagoshima prefecture, Japan, Natural Disaster Research Report, No.35, 69 pp. (in Japanese).

Nakano, K. (1982): The prompt report of 57.7.23 Nagasaki sediment disaster caused by heavy rain, Journal of the Japan Society of Erosion Control Engineering, Vol. 35, No. 1, pp. A1-A2 (in Japanese).

National Institute for Land and Infrastructure Management and Public Works Research Institute (2003): Sediment disasters caused by torrential rainfall of Baiu front from July 18 to 20, Heisei 15 (Prompt report), http://www.nilim.go.jp/lab/bbg/saigai/h15dosha/minamata_dazaifu.pdf (in Japanese).

National Institute for land and infrastructure management and Tsukuba University (2012): The data analysis regarding warning and evacuation information against sediment-related disaster, Technical note of NILIM, No. 682, 75pp. (in Japanese)

Nishi, M., Watanabe, F., Kanbara, J., Uchida, T., Hayashi, S., Okuyama, Y., Ekawa, M., Hata, M. and Niwa, S. (2014): Debris flow disasters caused by Typhoon Wipha (T1326) on Izu-Oshima Island and Technical Support of NILIM TEC-FORCE, 2014 Annual Report of NILIM, p.177-178

Noro, T., Mizuno, H., Uchida, T., Yamakoshi, T., Nishimoto, H., Fujisawa, K., Tanaka, H., Akiyama, K. and Kojima, S. (2004): Sediment related disasters caused by heavy rainfalls in Niigata, Fukui and Tokushima in July and August 2004 (prompt report), Journal of the Japan Society of Erosion Control Engineering, Vol. 57, No. 3, pp. 47-52 (in Japanese with English abstract).

Oka, S. and Katsurajima, S. (1971): Topographic investigation for debris flows occurred by the heavy rain in Ashiwada-mura district, Monthly report of Geological Survey of Japan, Vol. 22, No.4, p.179-220 (in Japanese with English abstract).

Okada, K., Makihara, Y., Shimpo, A., Nagata, K., Kunitsugu, M. and Saito, K. (2001): Soil Water Index. Tenki, Vol. 48, pp. 349-356 (in Japanese).

Osanai, N., Shimizu, T., Kuramoto, K., Kojima, S. and Noro, T. (2010): Japanese early-warning for debris flows and slope failures using rainfall indices with Radial Basis Function Network, Landslides, Vol. 7, p. 325–338.

Public works department of Nagasaki Prefecture (1983): History of the great floods in Nagasaki, June 23, 331pp. (in Japanese).

Public Works Research Institute (2003): Research report on probabilistic rainfall calculation at nationwide AMeDAS observation stations, Technical Note of PWRI, No. 3900, 177pp. (in Japanese).

Public Works Research Institute (2010): Historical large-scale landslides, Technical Note of PWRI, No. 4169, 218pp. (in Japanese).

Sabo division of Yamanashi Prefecture (1994): After Ashiwada sediment disaster, Journal of the Japan Society of Erosion Control Engineering, Vol. 46, No. 6, pp. 40-45 (in Japanese).

Sabo & Landslide Technical Center (2000): Sediment disasters, Heisei 11, 60pp. (in Japanese).

Sabo & Landslide Technical Center (2005): Sediment disasters, Heisei 16, 56 pp. (in Japanese).

Saito, H., Korup, O., Uchida, T., Hayashi, S. and Oguchi, T. (2014) Rainfall conditions, typhoon frequency, and contemporary landslide erosion in Japan. Geology, Vol. 42, pp. 999-1002.

Sakamoto, M. and Uezono, T. (2014): The prompt report for sediment disasters caused by heavy rain in Tanba City, Hyogo Prefecture, August, Heisei 26, http://www.gensai.nagoya-u.ac.jp/wp-content/uploads/2014/09/20140826_tanba.pdf (in Japanese).

The committee for countermeasure against sediment disasters in Hiroshima Prefecture (1999): Third meeting discussion material, (in Japanese).

The committee for countermeasure against sediment disasters in Izu-oshima island (2014): The final report of the committee for countermeasure against sediment disasters in Izu-oshima Island, http://www.kensetsu.metro.tokyo.jp/content/000006697.pdf, (in Japanese).

Tochigi, S. and Kaibori, M. (1989): Investgation and research regarding debris flow disaster in northwest part of Hiroshima Prefecture in July, Showa 63 (part 1), Proceedings of the 38th Research Meeting of the Japan Society of Erosion Control Engineering, pp. 1-4 (in Japanese).

Tochigi, S., Kaibori, M. and Suzuki, S. (1989): Investgation and research regarding debris flow disaster in northwest part of Hiroshima Prefecture in July, Showa 63 (part 2), Proceedings of the 38th Research Meeting of the Japan Society of Erosion Control Engineering, pp. 5-8 (in Japanese).

Touhoku regional development bureau of Ministry of Land, Infrastructure Transport and Tourism (2013): The summary report of sediment disaster at Tazawako-tazawa, Senboku, Akita in August 9, Heisei 25, http://www.thr.mlit.go.jp/yuzawa/17_sabou/tazawako/pdf/H260205_gaiyou.pdf (in Japanese).

Uchida, T., Kunitomo, M., Terada, H., Ogawa, K. and Matsuda, M. (2005): Study of methods of representing the scale of sediment disasters, Journal of the Japan Society of Erosion Control Engineering, Vol. 57, No. 6, pp. 51-55 (in Japanese with English abstract).

Uchida, T. and Okamoto, A. (2012): Characteristics of rainfall induced deep catastrophic landslides in Japan, Civil engineering journal, Vol. 54, No.11, pp. 32-35 (in Japanese).

Ushiyama, M., (2014): An analysis of understanding of users for graded weather warning information, Journal of Japan Society of Civil Engineers, Ser. B1 (Hydraulic Engineering), Vol. 70, No. 4, pp. I_1513-I_1518 (in Japanese with English abstract).

Yao, Y. Kurahashi, M. and Fukuyama, T. (2005): The result of investigation and countermeasures for sediment disasters in Fukui, July, Heisei 16, Journal of Civil Engineering, Vol. 46, No. 6, pp. 16-22, (in Japanese).

New Prediction of Sediment-related Disaster Critical Rainfall Using Meteorological Model WRF

Toshihide SUGIMOTO[1], Toshiyuki SAKAI[2] and Hiroshi MAKINO[1*]

[1] NEWJEC Inc. (2-3-20 Honjo-Higashi, Kita-ku, Osaka 5310074, Japan)
[2] Japan Weather Association (2-3-2 Minamisenba, Chuo-ku, Osaka 5420081, Japan)
*Corresponding author. E-mail: sugimotots@newjec.co.jp

A large number of sediment-related disasters have recently occurred in Japan due to record heavy rains exceeding 1,000 mm in cumulative rainfall and concentrated heavy rains equivalent to an hourly rainfall of 100 mm. These heavy rainfall events are likely to increase in frequency because of the impact of an increase in water vapor content caused by rising temperatures associated with global warming. Today, sediment disaster alert information is made public to ready people for sediment disasters. However, since calculation is based on the actually measured rainfall, announcement is generally made just before a sediment disaster occurs. There is no sufficient time left before people can leave their homes for shelter. This is one of the major problems related to the current system of sediment disaster alert information announcement. In this research, we conducted rainfall prediction based on rainfall simulation that uses numerical calculation meteorological model Weather Research and Forecasting (WRF) as a new evaluation technique that predicts a rainfall event likely to cause a sediment disaster at an early stage or two to three days in advance and made a comparative review of the simulation results with recent rainfall events that actually caused sediment disasters. Consequently the research results revealed that the technique is precise enough to clarify areas where orographic rainfall likely to cause sediment disasters will occur and suggests it may be able to provide the data qualified as sediment disaster alert information at an early stage before actual rainfall.

Key words: meteorological model, WRF, orographic rainfall, rainfall prediction, sediment-related disaster

1. Background and Purpose

A large-scale deep-seated landslide in the Kii Peninsula in 2011, a debris flow disaster in Nashizawa mountain stream, Nagiso town, in 2014, and a debris flow disaster in Serizawa area, Nikko city, in 2015, are only some of a large number of sediment-related disasters that have recently occurred in Japan due to record heavy rains exceeding 1,000 mm in cumulative rainfall or concentrated heavy rains equivalent to an hourly rainfall of 100 mm attributable to long-staying fronts that or highly powerful typhoons. Heavy rain events that trigger those sediment disasters tend to increase in frequency because of the impact of an increase in water vapor content caused by rising temperatures associated with global warming [Fujibe, 2 011].

Currently, sediment disaster alert information is announced by the corresponding municipality to make citizens ready for frequent occurrence of sediment disasters. However, the present system of sediment disaster alert information has a few problems. For example, when it is announced, the guideline announcement timing is the point in time when the snake curve based on the rainfall and soil water index exceeds the critical line. Since calculation is done based on the measured rainfall, announcement is generally made just before occurrence of the actual sediment disaster. Therefore, there is no sufficient time left before people can evacuate. In recent years, precision of forecasting a few hours ahead is improving as a result of development of XRAIN and polarimetric radar. These advances, however, are not good enough to drastically improve the prediction precision of sediment disasters based on the snake curve.

Therefore, it is considered effective to evaluate and organize sediment disaster occurrence risk in relation to rainfall factors and meteorological conditions by the

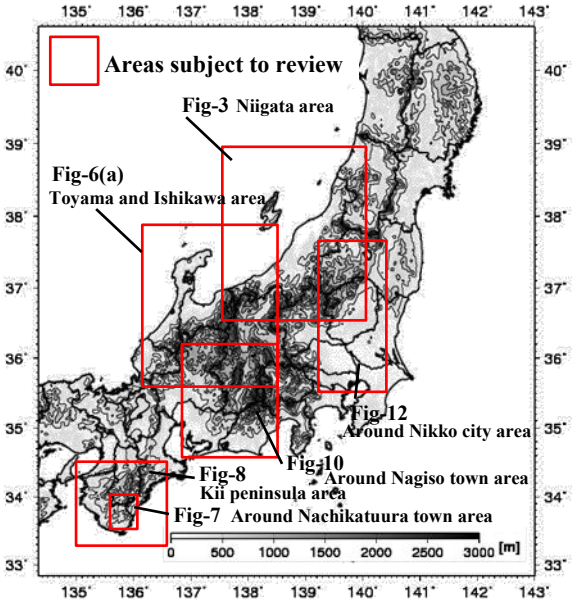

Fig.1 Areas for meteorological model calculation

topography and area in advance and judge the condition in combination with existing sediment disaster alert information [Sugimoto, 2017].

As Japan has many mountainous areas, there has been much research conducted from the meteorological and hydrological viewpoints about the relationship between rainfall and topography. It was eventually clarified that the topography has a big impact on rainfall, with a relatively long time scale in terms of daily or total rainfall or orographic rainfall phenomena where heavy rainfall stays for a long time on a windward slope or a high altitude area [Ninomiya,1977] or [Oki,1990] or [Kurihara,2009].

In this research, we conducted rainfall simulation using numerical calculation meteorological model Weather Research and Forecasting (WRF) to clarify areas where orographic rainfall will occur with respect to wind direction and velocity, compared the simulation results with the actual rainfall events that caused sediment disasters in recent years and the areas where rainfall growth occurred and verified the validity of WRF simulation for the purpose of developing a new evaluation technique that predicts rainfall likely to cause sediment disasters at an early stage, or two to three days in advance. The authors also discussed an early prediction technique of orographic rainfall that may cause sediment disasters based on the simulation results.

2. About Idealized Simulation

Idealized simulation with wind direction and velocity kept constant was conducted using WRF to study the relationship between wind direction and velocity and an increase in rainfall precipitation by the region. The calculation areas are set to longitude of 134°30′ to 143° east and latitude of 33° to 40°30′ north as shown in **Fig. 1**, and the calculation setting conditions shown in **Table 1** are used. For the initial conditions, the values obtained by Wajima Aerological Observation Station immediately before the occurrence of the heavy Niigata/Fukushima heavy rainfall in July 2011 are uniformly set to the horizontal grids in the calculation area as a vertical profile (**Fig. 2**).The interval of horizontal grids is set to 2 km so that the training that brings heavy rainfall and orographic rainfall can be represented.

Calculations were made using the assumed wind direction and velocity conditions as follows: 16 directions and 15 km/s in the rainy season and 30 m/s in the typhoon season. Since westerly and southerly winds prevail during the rainy season and typhoon season, respectively, the wind velocity measured by the Wajima and Shionomisaki Aerological Observation Station, respectively, is assumed.

3. Verification of Calculation Results

3.1 Comparison of rainfall distribution

The results of idealized simulation were compared with the rainfall condition of the Meteorological Agency's analyzed rainfall (hourly integrated values obtained by correcting the synthesized data of MLIT and MA radar

Table 1 Calculation setting conditions

Calculation conditions	Settings
Interval of horizontal grids	2km
No. of horizontal grids	East-west 375 x north-south 425
No. of vertical layers	50 layers
Calculation integration time	4 hours
Calculation time step	10 sec
Lateral border condition	Periodic boundary
Distribution of temperature and humidity	Temperature/humidity at the Wajima Aerological Observation Station (Observation data at 9:00 am, July 28, 2012)
Soil water content	0.30 (m3/m3) uniform
Soil temperature	290 K: uniform
Wind direction	16 cases (= 16 directions)
Wind velocity	2 cases (1)15 m/s (stationary front assumed) (2)30 m/s (typhoon rainfall assumed)

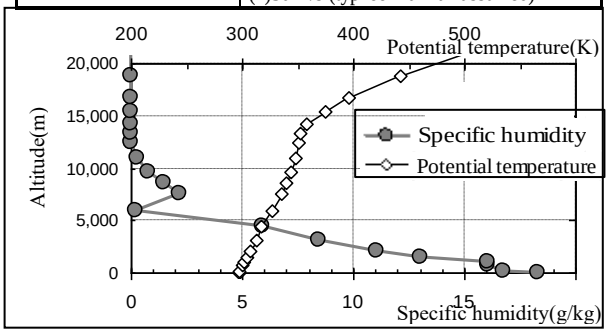

Fig. 2 Vertical profile of initial conditions of temperatures and specific humidity

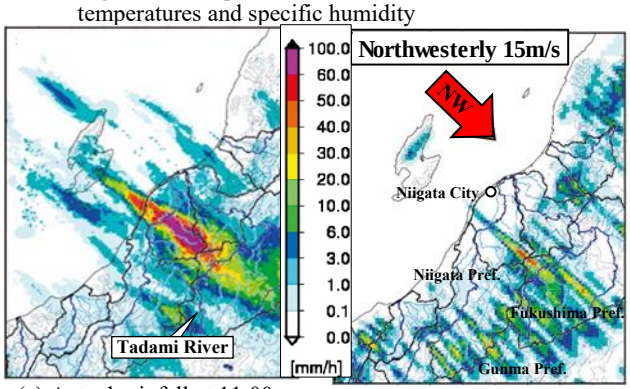

(a) Actual rainfall at 11:00, July 29, 2011

(b) Simulation results

Fig. 3 Comparison of simulation results

data with the surface rainfall) to verify the precision of the simulation. The rainfall distribution of the Niigata and Fukushima heavy rainfall (11:00, July 29, 2011) that caused many sediment disasters because of the training is shown in **Fig. 3(a)**, while the rainfall distribution of the idealized simulation for the same area (under the condition of northwesterly wind of 15 m/s) is shown in **Fig. 3(b)**.The condition of rain area development is similar to the radar rainfall observation results. It is shown that developed rainy clouds existed near the prefectural border between Niigata and Fukushima or with Gunma particular, rain clouds stretching from around Niigata city to the Tadami

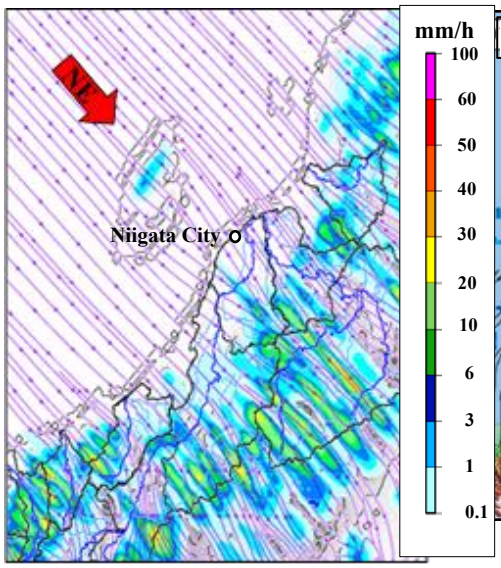

Fig. 4 Flow line graphs of surface wind
(wind direction: northwesterly; wind velocity: 15 m/s)

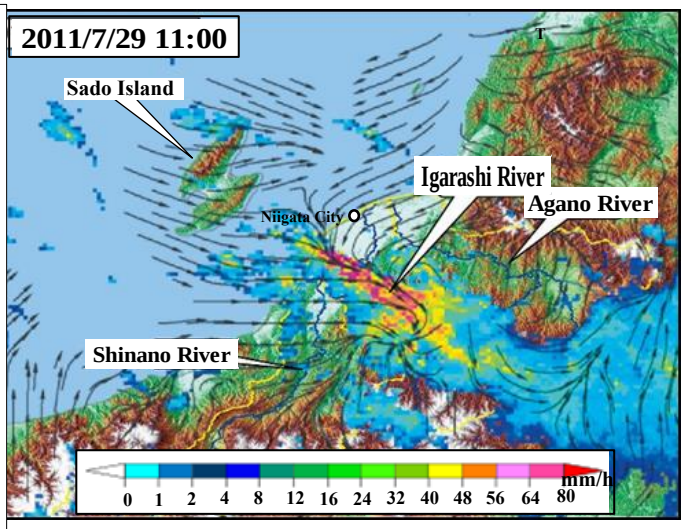

Fig. 5 Status of wind settling on the ground
(11:00, July 29, 2011)

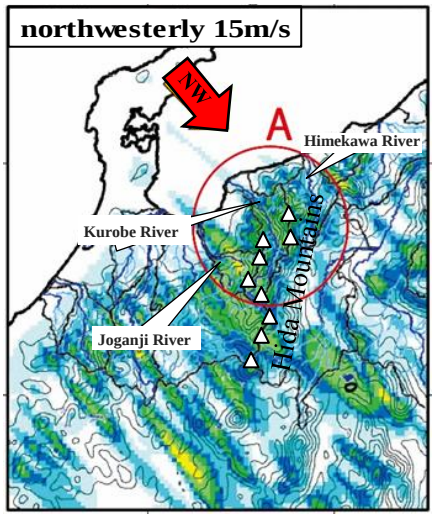

(a) Toyama and Ishikawa area: 15 m/s in wind velocity

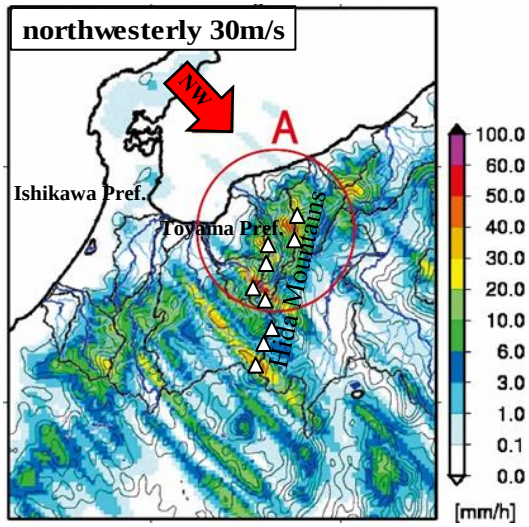

(b) Toyama and Ishikawa area: 30 m/s in wind velocity

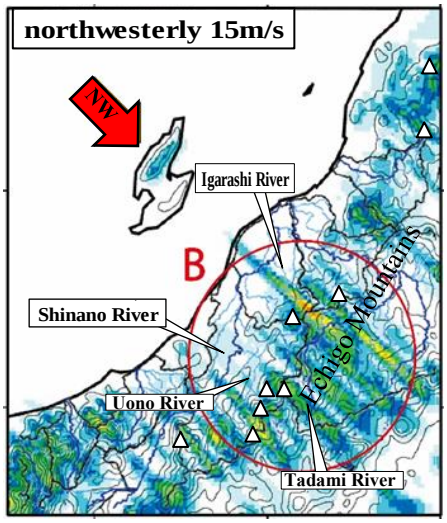

(c) Niigata area: 15 m/s in wind velocity

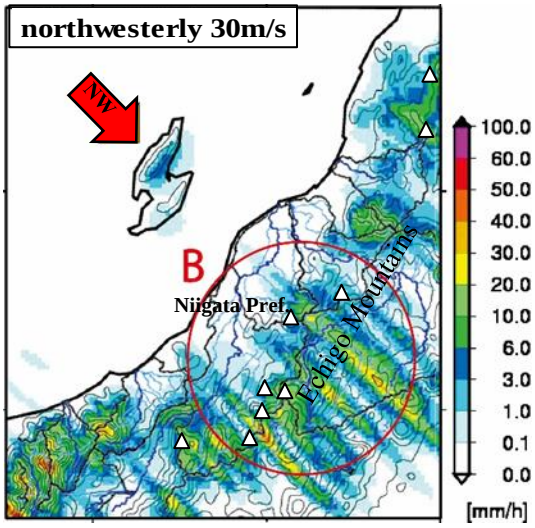

(d) Niigata area: 30 m/s in wind velocity

Fig. 6 Comparison of rainfall area between wind velocity of 15 m/s and 30 m/s

River basin in Fukushima prefecture grew bigger and a localized strong rainy area came about near the mountainous area.

3.2 Horizontal convergence of wind by topography

Flow line graphs were prepared from the simulation results to review the condition of wind convergence by topography to study the relationship with topography. The flow line graphs of surface wind are shown in **Fig 4,** and the wind direction vectors on the ground analyzed from AMeDAS data at the peak time of the Niigata and Fukushima heavy rainfall in July 2011 (11:00, 29th) overlapped with the MA radar image are shown in **Fig. 5.** The warm and wet air currents in the horizontal direction converged from the coastal area, leeward of the Sado Island, to the flat area and flowed in along the valley of the Igarashi River. The wind then converged along the mountain slopes as it went upstream, and ascending air currents were intensified along the way to finally cause torrential rainfall. This is the estimated mechanism of heavy rainfall. The figures clearly show converging winds at the peak time of the torrential rainfall.

This actual wind convergence that occurred during the torrential rain was confirmed over the plains behind the Sado Island and along the valley of the Igarashi River as in the case of the simulation results. As explained earlier, the simulation is based on a condition where the vertical distribution of potential temperature and specific humidity is evenly set in the horizontal direction as the initial conditions as shown in **Fig. 2**. It is therefore difficult to make the simulation match the actual phenomena where temperature and humidity complicatedly change in a three-dimensional manner. The simulation, however, is still similar to the actual rainfall event when it comes to the condition of rainfall area growth from plains to mountains. The idealized simulation results are considered to be sufficiently precise in clarifying areas of orographic rainfall growth by the wind direction.

3.3 Augmentation effect of rainfall in mountains

The influence of the rainfall amplification effect of topographic conditions such as wind velocity conditions or altitude in mountains was discussed using the idealized simulation results.

Fig. 6(a)(b) show the rainfall distribution based on the idealized simulation in the Hida Mountain Range with high peaks of over 3,000 m in height under the condition of northwesterly wind of 15 m/s and 30 m/s in wind velocity, respectively. **Fig. 6(c)(d)** show the rainfall distribution in the Echigo Mountain Range with 1,500 to 2,000 m high mountains under the same conditions. For the Kurobe River, Joganji River and Hime River characterized by rapid torrents originated from 3,000 m high class mountains as shown in **A of Fig. 6(a)(b)**, when the wind velocity rises from 15 m/s to 30 m/s, the hourly rainfall in the river basin increases from 6 mm/h to 13 mm/h for the Kurobe River and 3 mm/h to 9 mm/h for the Hime River. It suggests the orographic rainfall more than doubled in precipitation because of the influence of steep mountains, and heavy rainfall is conspicuous at high altitudes. For the basins of the midstream reaches of the Shinano River, Uono River, and Tadami River shown in **B of Fig. 6(c)(d)**, orographic rainfall is developed because of the influence of the Echigo Mountain Range (1,500 to 2,000 m high mountains) under the condition of 15 m/s in wind velocity. In particular, a training is grown in the plain areas to the mountainous areas along the Ikarashi River in the lower reaches of the Shinano River. On the other hand, rain clouds move over the mountains to cause a lot of rainfall in the Tone River and Tadami River basins under the condition of 30 m/s in wind velocity. For 3,000 m class mountains, when the wind velocity increases, wet currents slide up the slope to strengthen the ascending air current and cause heavy rainfall. For 2,000 m high class mountains, the air current rode over the mountains and moved downwind. These observations indicate the height of mountains affects the location of rainfall or amplification of rainfall.

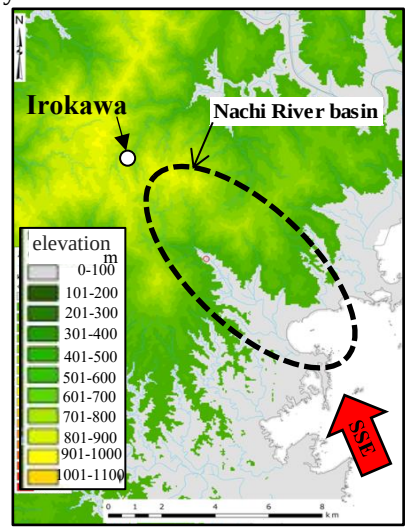

Fig. 7 Topographic map of the Nachi River basin

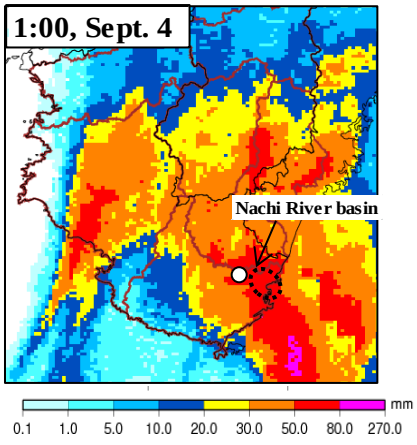

Fig. 8 Analyzed rainfall distribution map MSM

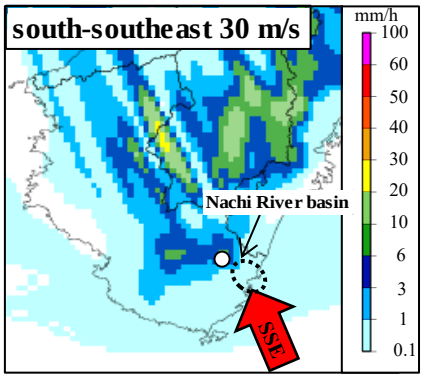

Fig. 9 WRF (south-southeasterly and 30 m/s)

4. Comparison between Calculation Results and Actual Rainfall Event That Caused Sediment-related Disasters

Three heavy rainfall disasters were selected: (1) heavy rainfall by Typhoon No. 12 that moved slow and caused large-scale deep-seated landslide in the Kii Peninsula in September 2011, (2) concentrated heavy rainfall due to a rainy season front activated by the approaching Typhoon No. 8 that caused a sediment disaster in Nashizawa stream, Nagiso town, Nagano prefecture, in July 2014, and (3) heavy rainfall by the training formed by the influence of Typhoon No. 18 and others that caused a sediment disaster in Serizawa area, Nikko city, Tochigi prefecture, in September 2015, the simulation results were compared with the aerological observation data and analyzed hyetographs of actual rainfall, and the validity of the orographic rainfall simulation was reviewed.

4.1 Sediment disaster in Nachikatsuura town, Wakayama prefecture, in September 2011

Typhoon No. 12 moved at a slow speed of about 10 km/h, landed the eastern part of Kochi prefecture, and became an extratropical cyclone in the Japan Sea in September 2011. Rain clouds surrounding this typhoon or inflow of wet air brought heavy rain with a total precipitation of 1,180.5 mm from 1:00 on Aug. 31 to 2:00 on Sep. 5 at the Irokawa Observation Station in the southern part of Wakayama prefecture. Very heavy rainfall with an hourly precipitation of 50 mm was observed at 1:00 on the 4th. A debris flow occurred in the basin of the Nachi River from around 2:00 to 3:00 on the 4th. The damage done to Nachikatsuura town included 28 dead and many destroyed houses.

At 0:00, September 4, which is about the peak of the rainfall when the debris flow occurred, the initial value of the meso numerical prediction model MSM (grid interval of 5 km) gives 500 hPa, south-southwesterly wind, 20.4 m/s in wind velocity, 850 hPa, south-southeasterly wind, and 26.5 m/s. **Fig. 8** is the analyzed rainfall distribution map at the peak time of the heavy rainfall at the Irokawa Observation Station (1:00, Sept. 4) by Typhoon No. 12, while **Fig. 9** is the result of idealized simulation under the condition of southeasterly wind of 30 m/s in velocity. It shows a strong rain area in the basin of the Nachi River in the southern part of Wakayama prefecture.

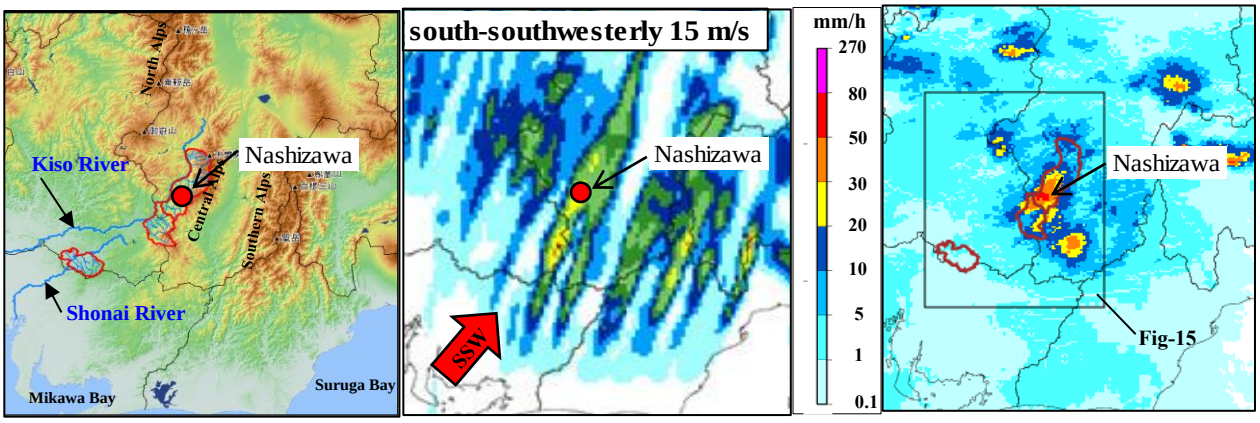

Fig. 10 WRF simulation (south-southwesterly wind of 15 m/s in velocity) and topographic map

Fig. 11 Analyzed rainfall distribution map MSM (18:00, July 9)

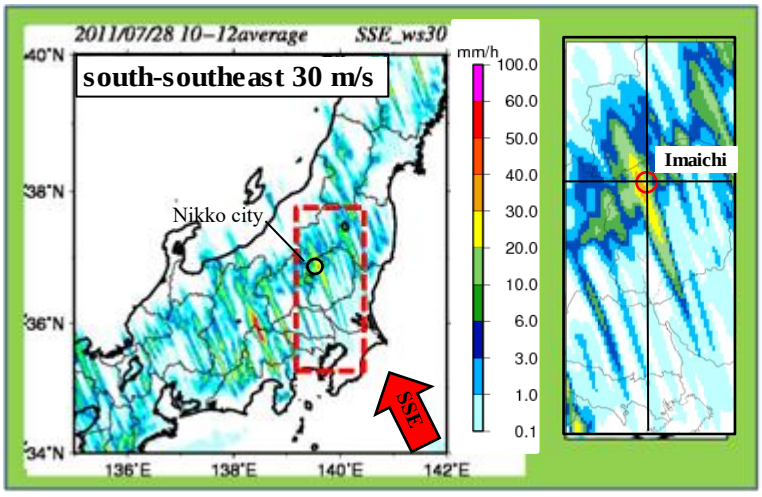

Fig. 12 WRF simulation result and enlarged map of the area around Nikko city

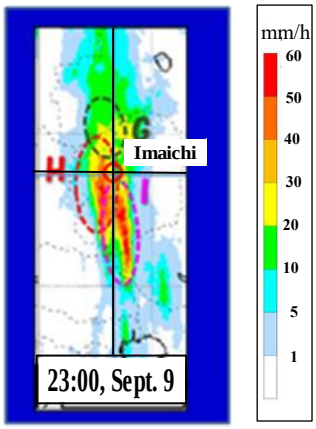

Fig. 13 Heavy rainfall in Kanto and Tohoku in September 2015
Analyzed rainfall distribution map
(23:00, September 9, 2015)

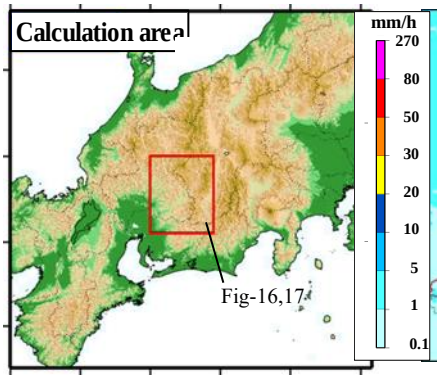

Fig. 14 Calculation area diagram

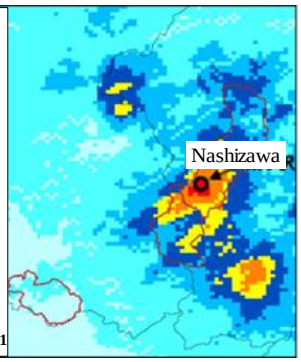

Fig. 15 Analyzed rainfall distribution map

Fig. 16 MSM prediction (6 hours in advance)

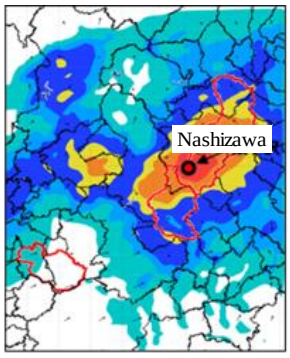

Fig. 17 WRF prediction diagram (6 hours in advance)

4.2 Debris flow disaster in Nashizawa stream, Nagiso town, Nagano prefecture, in July 2014

Warm and wet air associated with Typhoon No. 8 flowed into the rainy season front on July 9, 2014, and an hourly maximum rainfall of 55 mm (18:00, 9th) and cumulative rainfall of 119 mm (18:00, 8th, to 21:00, 9th) were recorded at the Nagiso Observation Station. A debris flow occurred in Nashizawa stream, Nagiso town, at 17:40 on the 9th, and the debris flow overflowing from the channel works damaged many houses, the JR Chuo Line railroad track, and national highway Route 19 and caused death of one person (south-southeasterly wind and 30 m/s of wind velocity).

A rainfall observation station near Nashizawa stream, where the debris flow occurred, measured a peak rainfall of about 50 to 80 mm at around 17:00 to 18:00 on the 9th. At Shionomisaki, where one of the nearest aerological observation stations is located, wet and warm air with a relative humidity of 91% and a temperature of 18.2˚C started to enter in the lower layers (850 hPa and at an altitude of about 1,500 m) at a speed of 11 to 12 m/s from the southwest to south-southwest at around 9:00, July 9, while a cold current (-6.7˚C) at around 9:00, July 9, to become strong southwesterly wind at a velocity of 9 to 23 m/s in the upper layers (500 hPa at an altitude of about 5,700 m).

Fig. 10 shows the result of south-southwesterly wind simulation with a velocity of 15 m/s, while **Fig. 11** shows an analyzed rainfall distribution map (18:00, July 9).

As a result of the simulation, orographic rainfall developed because of south-southwesterly wind, and localized strong rain area occurred in Nagiso town, the same area where rain actually fell (18:00, July 9).

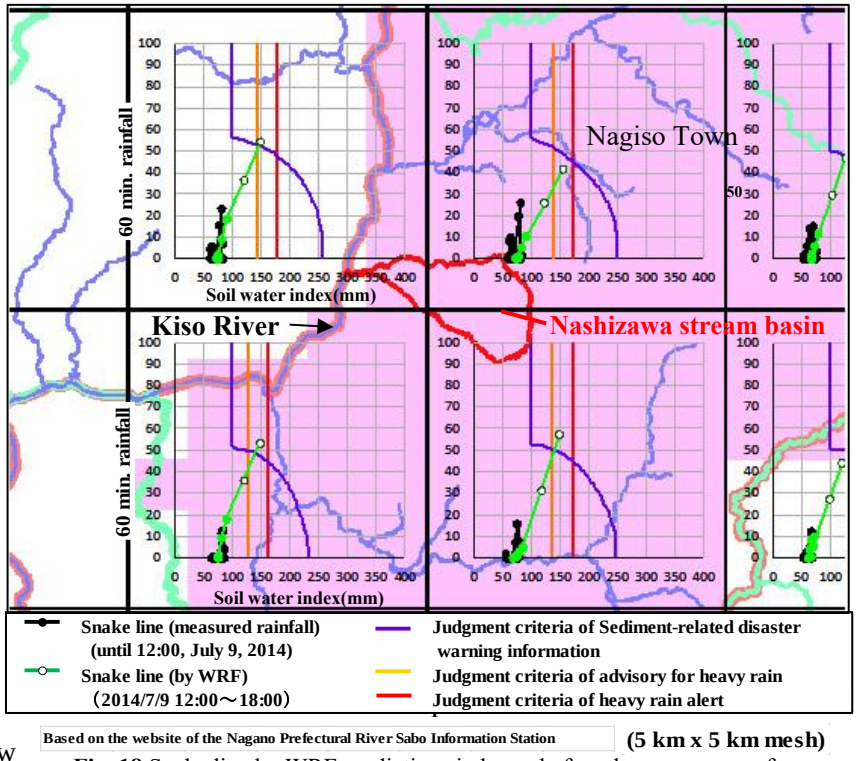

Fig. 18 Snake line by WRF prediction six hours before the occurrence of Nagiso disaster

4.3 Debris flow disaster at Serizawa area, Nikko city,Tochigi Prefecture,in September 2015

In comparison with the Kanto/Tohoku heavy rainfall that caused a debris flow disaster in Serizawa area, Nikko city, a training occurred at exactly the same location as suggested by WRF simulation result (Fig. 12) in the case of 30 m/s south-southeasterly wind. Good agreement with the actual rainfall condition is achieved.

5. Advance Forecast of Heavy Rainfall in Meteorological Model WRF Simulation

For the early stage prediction technique of orographic rainfall that triggers sediment disasters, a heavy rainfall event that caused a debris low disaster in Nashizawa stream, Nagiso town, is taken as a subject of review. To be specific, WRF-based prediction

simulation using MA's meso model MSM for certain hours before the peak rainfall time of Typhoon 8/rainy season front heavy rainfall in July 2015 was conducted. Then the advance rainfall prediction results were compared with the sediment disaster alert information using the rainfall short-time forecast.

The advance heavy rainfall prediction calculation using WRF is based on a one-way nesting with a 5 km grid for the area outside the calculated area map shown in **Fig. 14** and a 1 km grid for the internal area. Assuming 18:00, July 9, which is the peak rainfall time is the target time of calculation, calculations were made in four ways for 34 hours, 24 hours, 12 hours and 6 hours before the said peak time. The results indicate that the prediction with 6 hours before the disaster occurrence as the initial time gave a rainfall area very similar to an actual strong rainfall event that exceeded 50 mm in the Nashizawa stream basin. **Fig. 15** is the analyzed rainfall distribution map at 18:00, July 9, **Fig. 16** the MSM-based prediction for 6 hours in advance, and **Fig. 17** the WRF-based prediction 6 hours in advance. **Fig. 18** shows the judgment result of sediment disaster alert information based on the WRF six-hour advance prediction. According to the rainfall short-time forecast 2 hours in advance, all the prediction snake lines face downward, which means the predicted rainfall is too small to realize advance prediction of rainfall that exceeds the judgment criteria. However, WRF-based 6-hour ahead prediction successfully predicted the result exceeding the judgment criteria of sediment disaster alert information.

6. Discussion and Results

Factors that bring heavy rainfall include typhoon, rainy front, and combined actions of both of them. Topographic characteristics are deeply related to how strong rainfall is likely to occur in which area depending on the factor. This research used three heavy rainfall disasters: the Kii Peninsula debris flow disaster in 2011, the Nashizawa debris flow disaster in 2014, and the Nikko Serizawa area debris flow disaster in 2015 to verify the prediction technique proposed in this paper. The condition of rain area growth suggested by the rainfall simulation results using numerical calculation meteorological model WRF by the wind direction and velocity turned out to be similar to the actual rainfall condition. The technique is therefore indicated to be precise enough to clarify areas where orographic rainfall that is likely to cause sediment disaster grows. In addition, when WRF-based rainfall prediction value for the Nashizawa debris flow disaster, Nagiso town, is applied to the snake curve, it is found that it is possible to make advance analysis of rainfall likely to cause a sediment disaster.

As discussed above, when real-time orographic rainfall prediction using meteorological prediction data such as WRF-based global spectral model (GSM: 20 km mesh, 264 hours ahead prediction) and meso spectral model (MSM: 5 km mesh and 39 hours ahead prediction) is conducted and its prediction value is applied to the measured rainfall that caused large-scale sediment disasters such as river blockage or to snake curves, it may help early warning of the type of rainfall that may cause a sediment disaster.

REFERENCES

Fujibe,F.(2011): Long term fluctuation of climate in Japan and urbanization, Weather,Vol58.1,pp5-14

Sugimoto,T.,Makino,H.,Kageyama,Y.,Fujita,A.,Sakai,T., Michihiro,Y.,Fujita,H.,Tsunakawa,H.,Arisawa,T.,(2017):About Factors of Sediment Disaster Critical Rainfall in the Tajimi Sabo Jurisdiction, JSECE Publication, 2017

Ninomiya,K(1977):Geographical distribution of precipitation intensity poles from the time scale of heavy rain, Weather,Vol24.1,pp63-70

Oki,D.,Musiakira,K.,Koike,T.(1990): Estimation of rainfall distribution during heavy rain due to topography and wind direction, Japan Society of Civil Engineers Papers,No.417/ II -13,pp190-207

Kurihara,K.,Kanamori,T.,Seko,H.,(2009): Linear rainfall that occurred in Hiroshima Prefecture on July 18, 2003 ,Weather,Vol56.8,pp613-626

A Method for Estimating Maximum Damage Caused by Sediment Disaster by Surveying with Artificial Satellite SAR Imagery

Shin-ichiro HAYASHI[1*], Shin'ya KATSURA[1], Mio KASAI[1], Nobutomo OSANAI[1], Takashi YAMADA[1], Tomomi MARUTANI[1], Tomoyuki NORO[2] and Joko KAMIYAMA[2]

[1] Research Faculty of Agriculture, Hokkaido University, (Kita 9, Nishi 9, Kita-ku, Sapporo, Hokkaido 0608589, Japan)
[2] National Institute for Land and Infrastructure Management, (Asahi 1, Tsukuba, Ibaraki 3050804, Japan)
*Corresponding author. E-mail: shayashi@cen.agr.hokudai.ac.jp

Estimating the maximum damage caused by sediment disasters is necessary for reducing the time required for determining critical risk management resources. In this study, we proposed a method for estimating maximum damage using the Sediment Disaster Scale (SDS); our method calculates the Sediment Movement Magnitude (SMM) , an index pertaining to sediment movement that is based on survey implementing synthetic aperture radar (SAR) imagery, that can be obtained even during bad weather and at night, and is extensively used within disaster surveys. We then evaluated and confirmed the applicability of our proposed method by comparing the maximum damage estimated from SAR imagery to the actual damage incurred. Our method reduces the time necessary for surveying compared with conventional disaster survey techniques.

Key words: damage estimation, prompt survey, SAR, Sediment Movement Magnitude, Sediment Disaster Scale

1. INTRODUCTION

Artificial satellite synthetic aperture radar (SAR) imagery (that can be obtained during bad weather and night conditions), has been used extensively for detecting large-scale landslides and landslide dams during several recent sediment disasters, including those caused by Typhoon Talas in the Kii Peninsula (in Japan, 2011) [*Hayashi et al.*, 2013a]; and Anbon Island (Indonesia, 2012) [*Mizuno et al.*, 2014]; as well as the Kumamoto earthquake (Japan, 2016) [*National Institute for Land and Infrastructure Management and Public Works Research Institute*, 2017].

Sediment disasters, including large-scale landslides and landslide dams, can cause large numbers of causalities and/or property damage (e.g. *Ishizuka et al.*, [2015]; *Tabata et al.*, [2002]). Estimating the maximum damage caused by a sediment disaster (hereafter called 'maximum damage') is an efficient means of assessing and managing risk. However, few previous studies have assessed methods for estimating the maximum damage. Using SAR imagery to estimate directly the maximum damage could help reduce the time required to determine essential resources for risk management and disaster mitigation.

Here we propose a method for estimating maximum damage using an index pertaining to sediment movement that is derived from SAR imagery. We evaluated the applicability of our method by comparing the estimated maximum damage with the actual damage, in addition to the time necessary for our method versus conventional disaster survey techniques.

2. METHOD USED TO ESTIMATE MAXIMUM DAMAGE

Our proposed method for estimating the maximum damage is shown in **Fig. 1**. Surveys utilizing SAR imagery were used to determine the area and location of landslides. We calculated the volume of sediment movement using the Guzzetti equation [*Guzzetti et al.*, 2009], based on the area of landslide:

$$V = 0.074A^{0.175} \quad (1)$$

where V is the volume of sediment movement (m^3), A is the area of landslide (m^2).

The relative height of sediment movement can be measured on a map using the location of landslide. The sediment movement magnitude (SMM) [*Uchida et al.*, 2005] can be calculated from volume and relative height, as follows:

$$SMM = log_{10} \sum_{i=1}^{n} (V_i H_i) \quad (2)$$

where V is the volume of sediment movement (m^3), and H is the relative height (m). The maximum damage is estimated using the Sediment Disaster Scale (SDS, **Fig. 2**) [*Hayashi et al.*, 2015]. SDS classifies sediment disasters into five categories using two indices - one that pertains to sediment movement (as SMM), and one that relates to the damage (as DL, [*Kojima et al.*, 2009]), which is based on the relationship between SMM and DL of past sediment disasters. DL is calculated using Eq. (3):

$$DL = 0.69\, log_{10}\, x_1 + 0.16\, log_{10} \left(x_2 + x_3 + \frac{x_4}{3}\right) + 1.07 \quad (3)$$

where x_1 is the number of persons killed or missing, x_2 is the number of persons injured, x_3 is the number of houses totally collapsed, and x_4 is the number of houses partially collapsed. SDS categories are defined as follows (excluding overlapping portions within the upper category):

Category I: SMM < 4.0 and DL < 1.0
Category II: 4.0 ≤ SMM < 6.0 or 1.0 ≤ DL < 1.5
Category III: 6.0 ≤ SMM < 8.0 or 1.5 ≤ DL < 2.0
Category IV: 8.0 ≤ SMM < 10.0 or 2.0 ≤ DL < 2.5
Category V: 10.0 ≤ SMM or 2.5 ≤ DL

According to *Hayashi* [2017], each SDS categories included typical sediment disasters as follows:

Category I: single slope failure
Category II: single slope failure or debris flow
Category III: multiple and/or simultaneous slope failure and/or debris flow
Category IV: single deep-rapid landslide and landslide dam
Category V: multiple and/or simultaneous deep-rapid landslides and landslide dams

3. SURVEY METHOD USING SAR IMAGERY

We included several examples of using SAR imagery surveys to detect large-scale landslides and landslide dams. **Fig. 3** shows the site locations and photos for each of the survey areas. We estimated the maximum damage by applying correlation coefficient difference analysis (CCDA, **Fig. 4**) [*Cao, et al.*, 2008] and normalized difference polarization index (NDPI) difference analysis (**Fig. 6**) [*Yamazaki et al.*, 2011] to areas affected by the 2008 Iwate-Miyagi inland earthquake (**Fig. 3a)**), the 2009 disaster in Hofu City caused by heavy rain (**Fig. 3b)**), [*Hayashi, et al.*, 2012] and by interpreting high-resolution SAR imagery to detect landslide dams in the Kii Peninsula that were affected by Typhoon Talas in 2011 (the Kii Peninsula Great Flood, **Fig. 3c)**) [*Hayashi et al.*, 2013b].

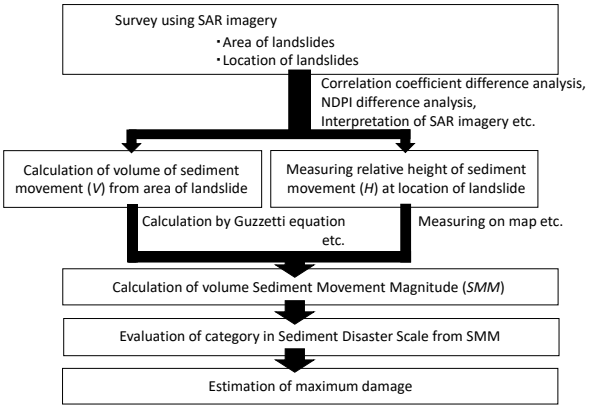

Fig. 1 Proposed method for estimating the maximum damage from synthetic aperture radar (SAR) imagery

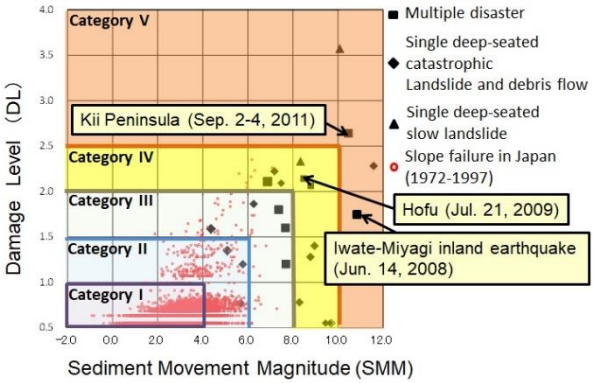

Fig. 2 Method of evaluating the Sediment Disaster Scale (SDS), based on *Hayashi et al.* [2015]

3.1 SAR imagery survey technique

Methods for detecting landslides that use SAR imagery taken before and after a disaster to calculate the difference and statistical value, or that are based on interpretation of SAR imagery, may reduce the time necessary for conducting these vital, time-sensitive surveys. Thus, we briefly review survey techniques that use SAR imagery to detect large-scale landslides and landslide dams.

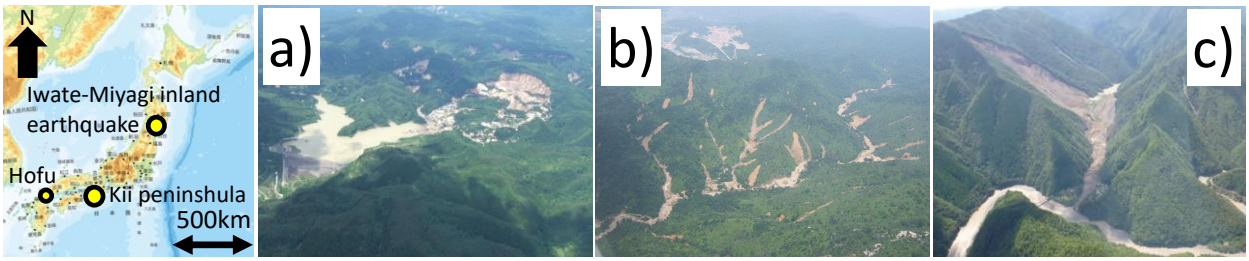

Fig. 3 Location map and photos of representative landslides within the survey areas: a) Iwate-Miyagi inland earthquake (Aratosawa landslide) [*Public Works Research Institute*, 2008], b) Hofu (Upper stream of Tsurugi River) and c) the Kii Peninsula Great Flood (Akadani landslide dam)

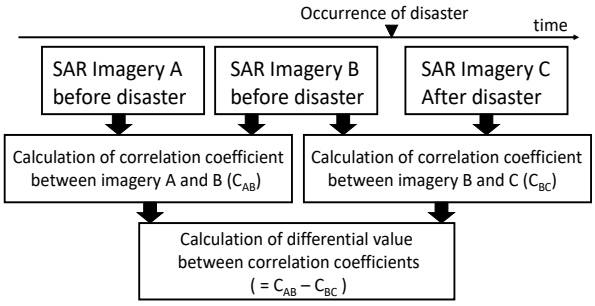

Fig. 4 Correlation coefficient difference analysis procedure

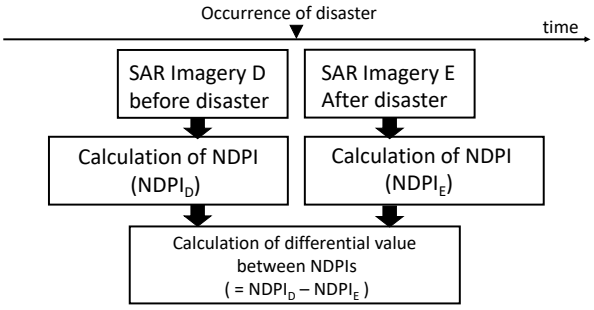

Fig. 6 NDPI defference analysis procedure

Table 1 List of SAR images for CCDA in *Hayashi et al.* [2012]

Name of disaster (Date of disaster occurrence)	Artificial satellite, Band, Polarization mode	Date of acquisition
Iwate-Miyagi inland earthquake (2008/6/14)	ALOS, L band, HH	2007/8/29 2008/5/31 2008/7/16
Hofu (2009/7/21)		2007/10/9 2009/7/14 2009/8/12

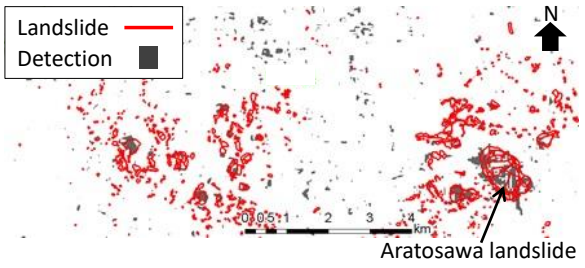

Fig. 5 The example of the result of CCDA against Iwate-Miyagi inland earthquake after *Hayashi et al.* [2012] (Red line indicates landslide interpreted by aerial photograph, Gray dot indicates detection result of CCDA)

Table 2 List of SAR images for NDPI difference analysis in *Hayashi et al.* [2012]

Name of disaster (Date of disaster occurrence)	Artificial satellite, Band, Polarization mode	Date of acquisition
Iwate-Miyagi inland earthquake (2008/6/14)	ALOS, L band, HH+HV	2007/6/21 2008/9/23
Hofu (2009/7/21)		2009/7/14 2009/8/12

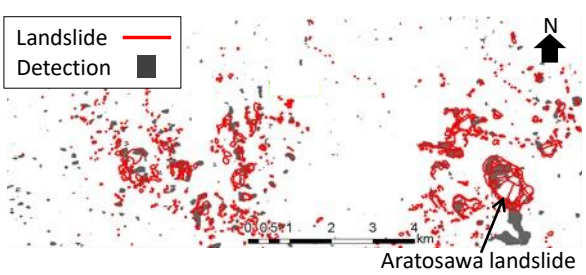

Fig. 7 The example of the result of NDPI difference analysis against Iwate-Miyagi inland earthquake after *Hayashi et al.* [2012] (Red line indicates landslide interpreted by aerial photograph, Gray dot indicates detection result of NDPI difference analysis)

3.2 CCDA

CCDA [*Cao, et al.*, 2008] is used to detect landslides using single-polarization SAR imagery (as shown in **Fig. 4**). CCDA uses three SAR images: two that are taken prior to the disaster (SAR images A and B) and one taken after the disaster (SAR image C). Correlation coefficients are calculated between SAR images A and B (C_{AB}), and SAR images B and C (C_{BC}). The difference value between C_{AB} and C_{BC} indicates potential landslide areas; the larger the value the more likely a landslide is to occur. According to *Hayashi et al.* [2012], the landslide area must be larger than 40,000 m^2 to be able to detect a landslide with 100% accuracy using CCDA. **Table 1** shows list of SAR images for

CCDA and **Fig. 5** shows the example of the result of CCDA in *Hayashi et al.* [2012].

3.3 NDPI difference analysis

NDPI difference analysis [*Yamazaki et al.*, 2011] is one of the methods used for detecting landslides using dual-polarization SAR imagery. NDPI difference analysis procedure is shown in **Fig. 6**. NDPI difference analysis uses two SAR images, one before and one after a disaster (SAR images D and E, respectively). For each SAR image, the NDPI is calculated as $NDPI_D$ and $NDPI_E$. The NDPI is defined as

$$NDPI = \frac{(HH-HV)}{(HH+HV)} \quad (4)$$

where *HH* is the horizontal transmit and the horizontal receive, *HV* is the horizontal transmit and the vertical receive. $NDPI_D$ and $NDPI_E$ values are then used to calculate the difference value; a large difference value indicates likely landslide candidates. According to *Hayashi et al.* [2012], the area of the landslide resulting from the Iwate-Miyagi inland earthquake was larger than 62,500 m^2, and 40,000 m^2 in Hofu, which is sufficiently large for NDPI difference analysis with 100% accuracy. **Table 2** shows list of SAR images for NDPI difference analysis and **Fig. 7** shows the example of the result of NDPI difference analysis in *Hayashi et al.* [2012].

3.4 Interpretation of high-resolution SAR imagery

To detect landslide dams, authors examined a high-resolution SAR imagery obtained using TerraSAR-X (X band, 2011/9/5), mainly from the southern part of the Nara Prefecture, for sediment disasters associated with the Kii Peninsula Great Flood (Date of disaster occurrence: 2011/8/31 to 9/4) [*Hayashi et al.*, 2013b]. Typical landslide dam shapes within a SAR images were identified, including lakes formed by landslide dams, landslide scarps and stream blockages. **Fig. 8** shows the example of interpretation of high-resolution SAR imagery in *Hayashi et al.* [2013b].

4. RESULTS AND DISCUSSION

We compared the maximum damage estimated by our method with the actual evaluated damages based on disaster records (**Fig. 2**). We also compared the time necessary using our proposed method with the time needed for conventional disaster survey techniques for sediment disasters caused by the Great East Japan Earthquake and the Great Flood in the Kii Peninsula [*Hayashi, et al.*, 2017].

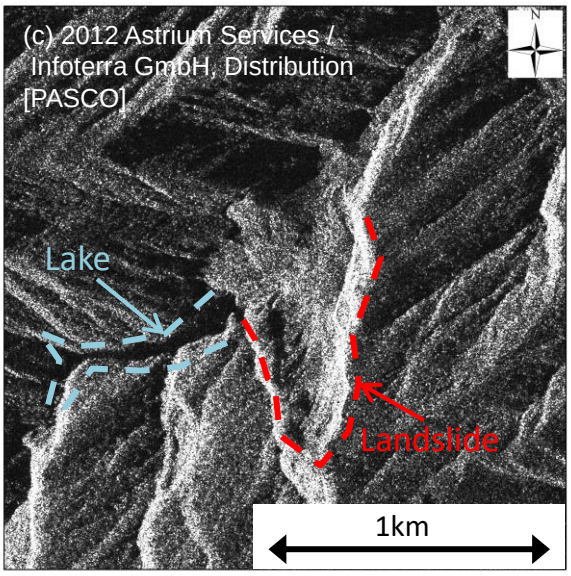

Fig. 8 The example of interpretation of high-resolution SAR imagery against the Kii Peninsula Great Flood after *Hayashi et al.* [2013b] (Akadani landslide dam)

4.1 Calculation of SMM and DL and SDS evaluation against actual damage

SMM and DL values from the actual damage were calculated for the Iwate-Miyagi inland earthquake based on disaster records [*Miyagi Prefecture*, 2008; *The Japanese Geotechnical Society*, 2010]. Values of SMM and DL were calculated both for Hofu, *Hayashi et al.* [2010], and the Great Flood in the Kii Peninsula, *Hayashi et al.* [2015]. The Iwate-Miyagi inland earthquake and the Kii Peninsula Great Flood were evaluated as category V, and Hofu evaluated as category IV (according to SDS category), as shown in **Fig. 2**.

4.2 Calculation of SMM and DL from SAR imagery

SMM can be calculated by our proposed method from SAR imagery. **Table 3** shows SMM values calculated by CCDA and NDPI difference analysis results from the Iwate-Miyagi inland earthquake and the Hofu disaster. Here, the area and number of landslides accurately detected by CCDA and NDPI difference analysis were identified; the relative height was 100 m with reference to the height difference between the altitude of the surrounding mountains and the riverbed. **Table 4** shows SMM values calculated by interpretation of SAR imagery from the Kii Peninsula Great Flood. *Hayashi et al.* [2013b] presented the location and area of large-scale landslides that caused landslide dams, where the relative heights were measured by *GSI Maps* [2017].

Table 3 SMM calculated by CCDA and NDPI (SMM: sediment movement magnitude; CCDA: correlation coefficient difference analysis; NDPI: NDPI difference analysis)

Name of disasters	Analysys method	Area of landslide per one landslide (m^2)	Volume of landslide per one landslide (m^3)	Provisional relative height (m)	Number of detedted landslide	SMM
Iwate-miyagi inland earthquale	CCDA	40,000	348,513	100	13	8.66
	NDPI	62,500	665,668	100	9	8.78
Hofu	CCDA	40,000	348,513	100	26	8.96
	NDPI	40,000	348,513	100	24	8.92

Table 4 SMM calculated by interpretation of SAR imagery

Name of landslide	Area (ha)	Volume of sediment movement (m^3)	Relative height (m)	SMM
Tsubonouchi-1	2.0	127,563	180	7.36
Tsubonouchi-2	11.8	1,672,864	180	8.48
Tsubonouchi-3	5.2	509,843	200	8.01
Ui	8.7	1,075,312	230	8.39
Nagatono	19.5	3,465,628	440	9.18
Akadani	28.2	5,916,882	570	9.53
Kuridaira	33.7	7,661,170	330	9.40
Mikoshi	6.3	673,404	180	8.08
All				9.91

Table 5 Comparison between SMM and SDS derived from actual damage and results of our estimation

Name of disaster	Analysys method	Result of estimation		Actual damage	
		SMM	Category	SMM	Category
Iwate-miyagi inland earthquale	CCDA	8.66	Ⅳ	10.37	Ⅴ
	NDPI	8.78	Ⅳ		
Hofu	CCDA	8.96	Ⅳ	8.48	Ⅳ
	NDPI	8.92	Ⅳ		
The Great Flood in the Kii Peninsula	Interpretation	9.91	Ⅳ	10.46	Ⅴ

4.3 Comparing actual damage to estimated maximum damage based on SDS

Table 5 shows results from comparing the maximum damage estimated by our proposed method (**4.2**) to the actual damage (**4.1**). Our method underestimated values for the Iwate-Miyagi inland earthquake compared with values of the actual damage. This was because the Aratosawa landslide (which was approximately 70 million m^3) increased the actual damage; this landslide was undetected by CCDA and NDPI difference analysis, as the precise landslide area could not be estimated. In Hofu, the estimated and actual damage were very close for SMM values, with the same SDS categories. For the Great Flood in the Kii Peninsula, values of SMM were close, despite the presence of the Iya deep-rapid landslide (which was approximately 4.1 million m^3) and the town of Nachi-katsuura (where simultaneous debris flows occurred) were outside of the SAR imagery interpretation area [*Hayashi et al.*, 2013b]. Because values of SMM straddle SDS category delineations, the SDS category that results from our estimation is one category lower than that derived from the actual damage. Thus, we confirmed the applicability of our proposed method as the maximum estimated damage is nearly the same as the actual damage. However, our proposed method may underestimate the maximum damage if a huge landslide (such as the Aratosawa landslide during the Iwate-Miyagi

earthquake) occurs within the SAR imagery area, due to the accuracy of the analysis method necessary to detect such landslides.

4.4 Comparing the survey time

Surveys for CCDA and NDPI difference analysis required 11.5 hours per ~300 km^2 [*Hayashi, et al.*, 2012], which equates to approximately 630 km^2/day. Interpretation of SAR imagery can survey 1,200 km^2/day [*Hayashi, et al.*, 2017]. If the location and area of landslides are determined by surveys using SAR imagery, SMM and SDS can be calculated promptly. Emergency inspections (EI) for high-risk areas to prevent secondary damage are conducted in Japan by special teams from the Ministry of Land, Infrastructure, Transport and Tourism (MLIT) and prefectural governments (PG) (i.e. *Minami and Osanai, et al.*, [2014]). EI can survey ~630 km^2/day [*Hayashi, et al.*, 2017], and offers the most immediate method of surveying large-scale sediment disasters. While our proposed method could be conducted even during bad weather and at night, EI is typically not conducted during such conditions. As a result, the proposed method can be conducted over a wider range of conditions, creating more opportunities to conduct surveys than EI.

5. CONCLUSIONS

In this study, we proposed a method to estimate maximum damage based on SDS using SAR imagery. This study evaluated and confirmed the applicability of this method, demonstrating that it could reduce the time necessary for surveying after a disaster. Our proposed method was validated using SMM values, in which the SDS category estimated by our proposed method was nearly that of actual damage from several past disasters. However, our method underestimated the maximum damage when a huge landslide (such as the Aratosawa landslide from the Iwate-Miyagi inland earthquake) was located in the SAR imagery. Significantly, our method can reduce the time necessary for surveying compared with conventional disaster survey techniques.

We did not compare our method to other analysis methods that use SAR imagery to detect landslides, and consider the time affected by cycle, return time, and satellite location to obtain SAR imagery. Therefore, further examination is necessary to improve our proposed method, specifically towards refining imagery detection accuracy (for determining the size and location of landslides), and improving the time necessary to obtain SAR imagery critical for estimating the maximum damage.

REFERENCES

Cao, Y., Yan, L., and Zheng, Z. (2008): Extraction of information on geology hazard from multi-polarization SAR images, XXIst International Society for Photogrammetry and Remote Sensing Congress, XXXVII-B4, pp. 1529-1532.

GSI Maps (2017): https://maps.gsi.go.jp/

Guzzetti, F., Ardizzone, F., Cardinali, M., Rossi M. and Valigi, D. (2009): Landslide volumes and landslide mobilization rates in Umbria, central Italy, Earth and Planetary Science Letters, Vol. 279, pp. 222-229.

Hayashi, S. (2017): A study for prompt survey techniques against large-scale sediment disaster, doctoral thesis, Hokkaido Univ., 135pp. (in Japanese).

Hayashi, S., Mizuno, M., Osanai, N., Nishi, M., Shimizu, Y. Nakagawa, K. and Matsumoto, S. (2012): Applicability of methods for detecting landslides by using synthetic aperture radar of ALOS (Daichi), Journal of the Japan Society of Erosion Control Engineering, Vol.65, No.4, pp.3-14 (in Japanese with English abstract).

Hayashi, S., Mizuno, M. Sato, T., Kamiyama, J., Okamoto, A., Yoshikawa, T., Udono, T., Yokota, H., Noda, A. and Yoshikawa, K. (2013b): Establishing a landslide dam detection methodology by interpreting artificial satellite high‐resolution SAR（synthetic aperture radar）images based on a case study of sediment-related disasters caused by Typhoon Talas in the Kii Peninsula, Journal of the Japan Society of Erosion Control Engineering, Vol.66, No.3, pp.32-39 (in Japanese with English abstract).

Hayashi, S., Osanai, N., Shimizu, Y., Nakata, M. Matsuda, M. and Ogawa, K. (2010): Study on the scale of sediment disasters caused in Hofu, Yamaguchi, Proceedings of the 59th Research Meeting of the Japan Society of Erosion Control Engineering, pp. 266-267 (in Japanese).

Hayashi, S., Uchida, T., Katsura, S., Kasai, M., Osanai, N. and Marutani, T. (2017): A quantitative analysis of emergency survey techniques for large-scale sediment disasters, Journal of the Japan Landslide Society, Vol.54, No.2, pp.18-25 (in Japanese).

Hayashi, S., Uchida, T., Okamoto, A., Ishizuka, T., Yamakoshi, T. and Morita, K. (2013a): Countermeasures against landslide dams caused by typhoon Talas 2011, Asia-Pacific Tech Monitor, Vol. 30, No. 1, pp. 20-26.

Hayashi, S., Uchida, T., Okamoto, A., Osanai N., Lee, C. and Woo, C. (2015)：Estimation of the socio-Economic impacts of sediment disasters by using evaluation indexes of the magnitude of sediment movement and level of damage to society, International Journal of Erosion Control Engineering Vol. 8, No. 1, pp. 1-10.

Ishizuka, T., Tokunaga, Y. and Sawano, H. (2015): Activities toward a landslide dam outburst flood in Ambon Island, Indonesia, Journal of Japan Society of Civil Engineers, Division F, Vol. 71, No. 2, pp. 24-32 (in Japanese with English abstract).

Kojima, S., Osanai, N., Nishimoto, H., Ogawa, K. and Matsuda, M. (2009): Study of damage indices based on questionnaire surveys of the damage image of sediment disasters, Journal of the Japan Society of Erosion Control Engineering, Vol. 62, No. 3, pp. 47-54 (in Japanese with English abstract).

Minami, N. and Osanai, N. (2014): Introduction to modern SABO studies, Kokon Shoin, 184pp. (in Japanese).

Miyagi Prefecture (2008): The final report of the technical committee for sediment-related disasters caused by the Iwate-Miyagi inland earthquake, 101pp. (in Japanese).

Mizuno, M., Kamiyama, J., Ekawa, M., Kanbara, J., Hayashi, S., Morita, K., Horiuchi, S., Udono, T. and Yoshikawa, K. (2014): Application of high-Resolution SAR satellite images to landslide disasters -Report on landslide-dam formation and collapse events in the Kii Peninsula, Japan and Ambon, Indonesia- , Proceedings of the INTERPAEVENT 2014 in the Pacific Rim, pp. 362-371.

National Institute for Land and Infrastructure Management and Public Works Research Institute (2017): Report on damage to infrastructures by the 2016 Kumamoto earthquake, Technical note of National Institute for Land and Infrastructure Management No. 967, Technical note of Public Works Research Institute No. 4359, 356pp. (in Japanese).

Public Works Research Institute (2008): Landslides and slope collapses triggered by Iwate-Miyagi Nairiku earthquake, https://www.pwri.go.jp/team/landslide/english%20pages/topics/topics_iwatemiyagi_e.htm

The Japanese Geotechnical Society (2010): The disaster report of the Iwate-Miyagi inland earthquake, 2008, 159pp. (in Japanese).

Tabata, S., Mizuyama, T. and Inoue, K. (2002): Landslide Dams and Disasters, Kokon Shoin, 205pp. (in Japanese).

Uchida, T., Kunitomo, M., Terada, H., Ogawa, K. and Matsuda, M. (2005): Study of methods of representing the scale of sediment disasters, Journal of the Japan Society of Erosion Control Engineering, Vol. 57, No. 6, pp. 51-55 (in Japanese with English abstract).

Yamazaki, F., Liu, W. and Inoue, H. (2011): Characteristics of SAR backscattered intensity and its application to earthquake damage detection, Computational Stochastic Mechanics, pp. 602-606.

Sediment Disaster Notification System Established for the Reservoirs in Southern Taiwan

Tsai-Tsung TSAI[1,2*], Kuang-Jung TSAI[3], Chjeng-Lun SHIEH[1,2] and Yie-Ruey CHEN[3]

[1] Disaster Prevention Education Center, National Cheng Kung University
(No.1, University Road, Tainan City 701, Taiwan R.O.C.)
[2] Department of Hydraulic and Ocean Engineering, National Cheng Kung University
(No.1, University Road, Tainan City 701, Taiwan R.O.C.)
[3] Department of Land Management and Development, Chang Jung Christian University
(No.1, Changda Road, Gueiren District, Tainan City 71101, Taiwan R.O.C.)
*Corresponding author. E-mail: victor@dprc.ncku.edu.tw

Typhoon Morakot struck Taiwan in 8th August 2009. It brought astonishing rainfall and caused extreme sediment disasters. This event awakens the public awareness of sediment disasters. Over the past few years, this study has devoted much resources constructing the Sediment Disaster Database of the reservoirs in southern Taiwan. The SDDB is currently available to assist the reservoirs managers quickly invoke the archiving environment data. To further assist the reservoir management issues, this study is now focusing on the establishment of Sediment Disaster Notification System to assist reservoir managers improving the grasp of the situation of sediment disasters in reservoir catchment.

Key words: Sediment Disaster Notification System, Standardization Specification for Data, HTML5

1. ORIGIN

In 8th August 2009, typhoon Morakot struck southern Taiwan and brought more than 2,900 mm accumulated rainfall within 4 days. Some extreme serious sediment disasters such as landslide and debris flows were induced by this event, for example, Nantou Branch, SWCB (2010) mentioned there were more than 10,904 sites of landslide with total sliding area of 18,113 ha occurred in Zengwen reservoir watershed after typhoon Morakot. This event awakens the public awareness of sediment disasters. Sediment disasters have negative effects on the operating functions of reservoirs. Base on the formats and characteristics of sediment disasters, here are some issues must be conquered:

(a) The trigger mechanism of large scale compound sediment disaster under extreme rainfall condition.
(b) The establishment of disaster prevention database and the revise of disaster prevention strategy.
(c) The predominance of sediment disasters information and status.
(d) The strategy and measure for disaster prevention, reducing and mitigation.

After these issues were conquered, the disaster resistance of reservoir catchment will be enhanced, the land conservation will be ensured, the reservoir development will be sustained, and most important is the water supply in southern Taiwan will be stable. To decrease the risk of these disasters within reservoir watershed, the establishment of a powerful tool for hazard mitigation / disaster prevention is necessary. In previous phase basic environment data was collected for establishing the Sediment Disaster Database (SDDB). In following phase, the establishment of Sediment Disaster Notification System (SDNS) to assist reservoir managers improving the grasp of the situation of sediment disasters in reservoir catchment will become the most important issue.

2. THE ESTABLISHMENT OF SEDIMENT DISASTER NOTIFICATION SYSTEM

In the premise of user friendly, the SDNS is developed based on the SDDB, and applied with the new generation technical protocols. Here is some information about this system.

2.1 Request analysis

Request analysis is the most important work before system construction. **Fig. 1** is the result. There were two main issue shown, "immediate disaster notification" and "decision support"

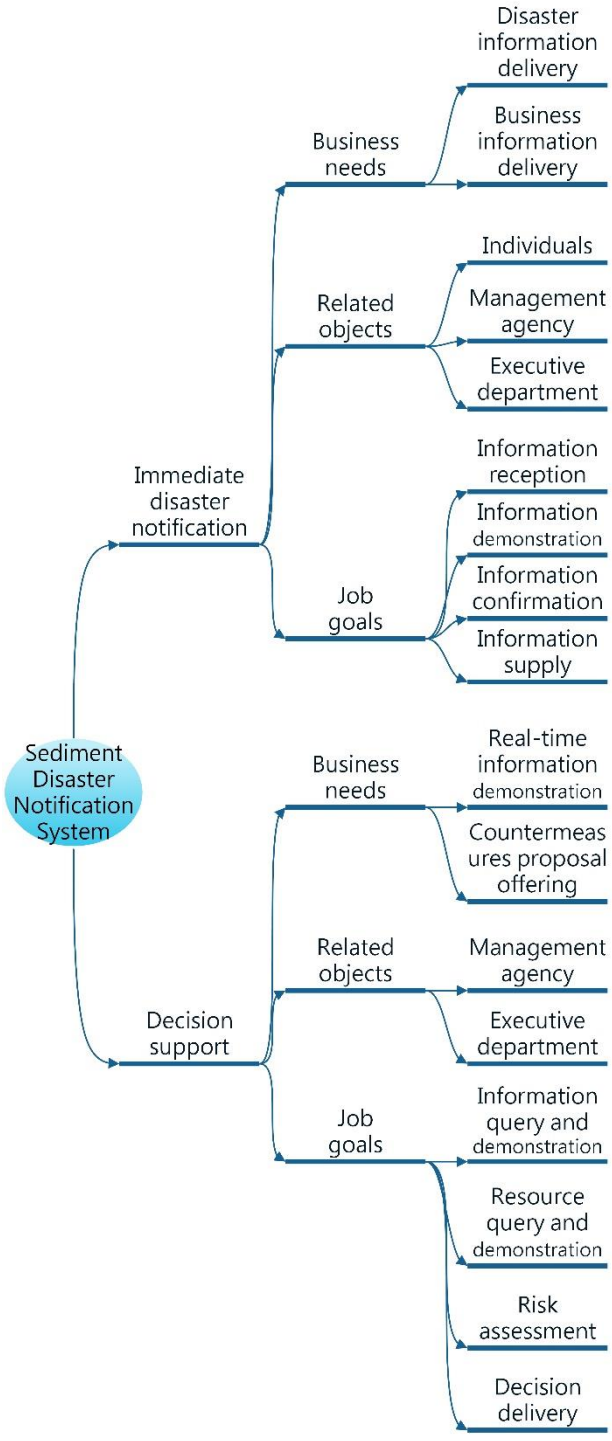

Fig. 1 Request analysis result

2.1.1 Immediate disaster notification

Disaster information delivery and business information delivery are the needs of this issue, individuals, management agency and executive department are related objects, reception, demonstration, confirmation, and supply of information are the goals of jobs. As **Fig. 2** shown, follow the concept of immediate disaster notification, there are many information streams should be delivered between individuals, management agency and executive department, to make every kind of information have been well known.

2.1.2 Decision support

Real-time information demonstration and countermeasures proposal offering are the needs of this issue, management agency and executive department are related objects, information/resource query and demonstration, risk assessment, and decision delivery are the goals of jobs. As **Fig. 3** shown, follow the concept of decision support, those primarily connection of information was between management agency and executive departments. Only partially controlled public information will be provided to individuals.

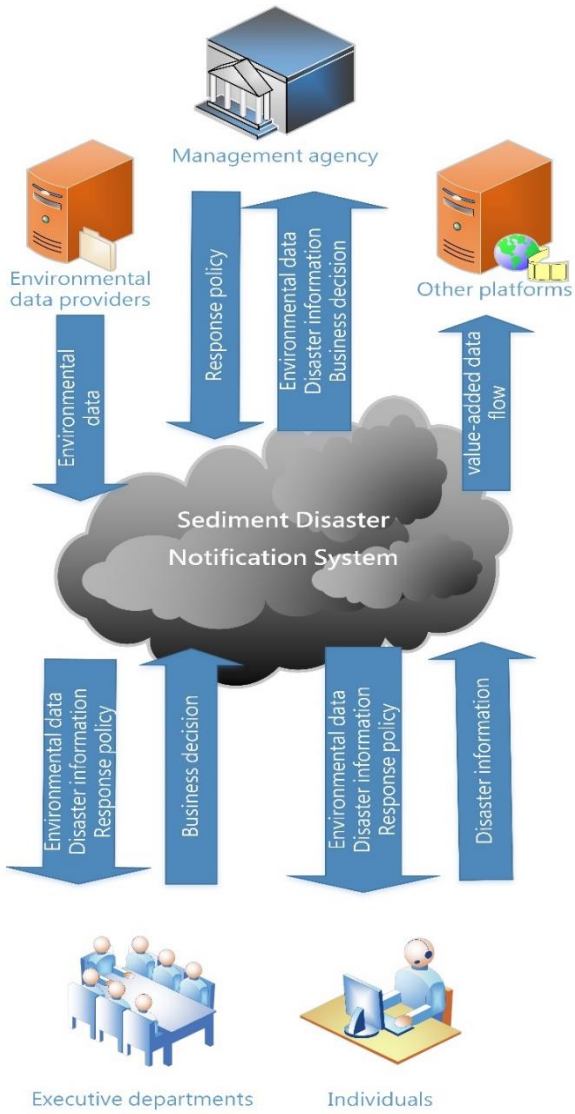

Fig. 2 concept of immediate disaster notification

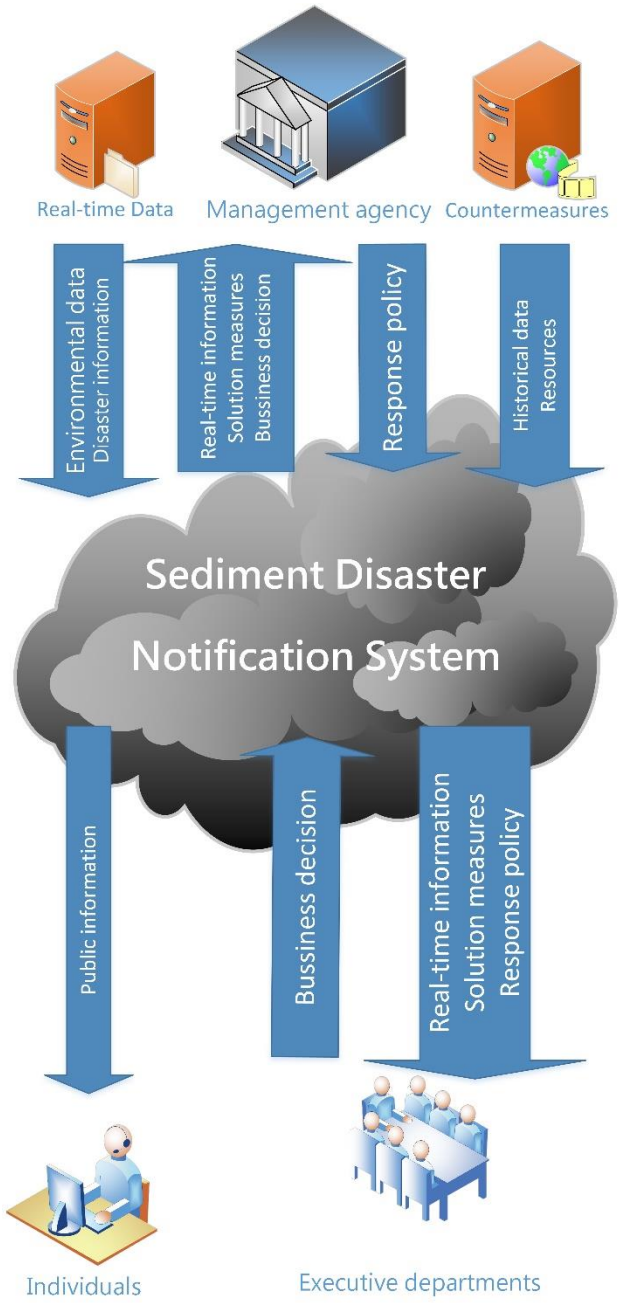

Fig. 3 concept of decision support

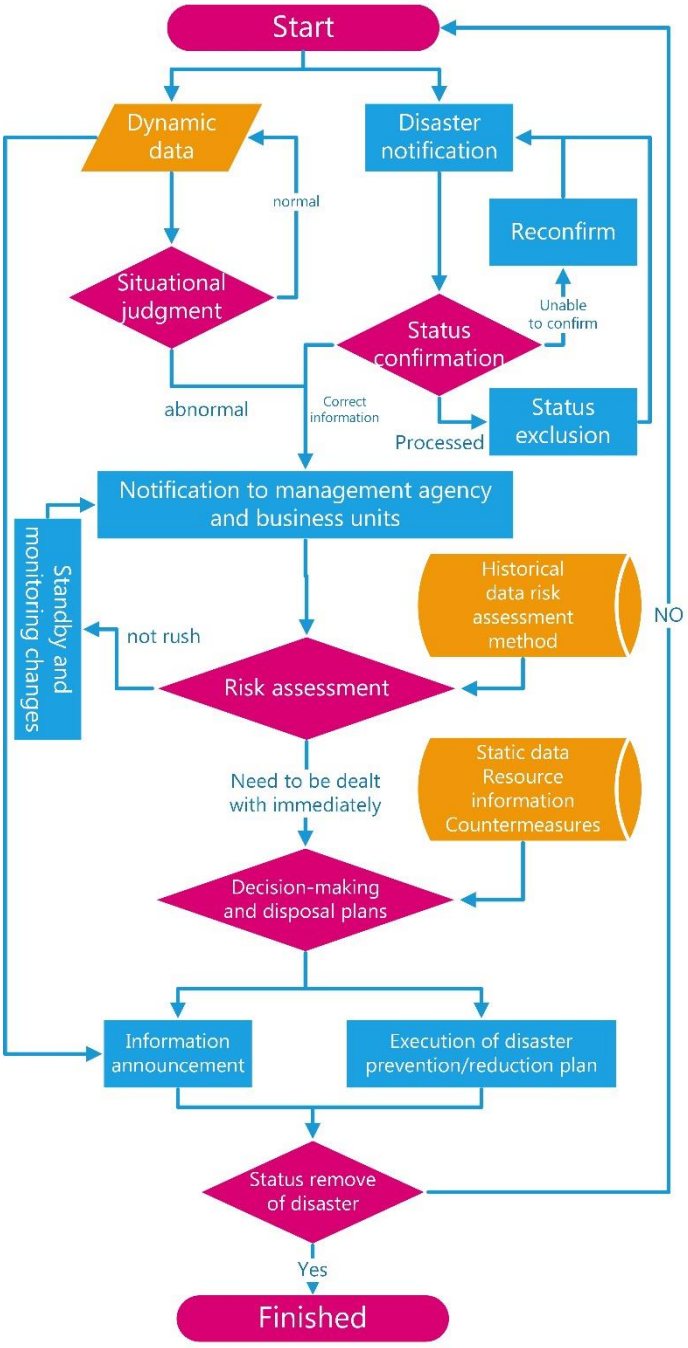

Fig. 4 Workflow of the SDNS

2.2 System analysis

After the request analysis, the requirements for SDNS could be grasped, system analysis is needed to be executed before system design.

As **Fig. 4** Shown, at the beginning of the assignment, the near-real-time environment data will be imported automatically form the data source, the situational analysis will be conducted at the same time to confirm the status of target area is normal or abnormal. These processes will be continued for normal situation cases. If the result of the judgment is abnormal, next procedure will be preceded, the management agency and the business units will be notified.

Meanwhile, the system also started receiving the notifications of disasters. All disaster information should be confirmed. That disaster information cannot be confirmed would not be imported but will be returned to the notification mechanism for confirmation; If the confirmed disaster information is the first report or is an update, the details will be moved to the next step, to notify the management agency and the business unit. However, if the disaster information received has been notified and there is no state change, it will be excluded from entering the notification procedure.

When the management agency and the business unit receive the notification, the risk assessment process will be started. Meanwhile, in addition to the existing dynamic data and disaster information, it is also necessary to retrieve historical disaster data with similar situation from the database for risk assessment. If the result of the assessment is not necessary for immediate processing, the record shall be placed on standby to pay attention to changes in its status and continue to pay attention to whether there is a new disaster. If the assessment requires immediate processing, proceed to the next stage for countermeasure development.

After entering the strategy development stage, the static data should be retrieved from the database to grasp the environmental conditions of the disaster site. In addition, the relief resources should be queried to confirm the available manpower, equipment, equipment, and material distribution. The disposal methods of similar situations in the past, the rules and regulations of the relevant laws, and the response strategies for similar situations were also should be queried at the same time. To synthesize the above information, management agency and business unit can formulate decision-making and disposal plans. And based on the results, some relevant information will be announced, and some necessary disaster prevention/reduction plan will be executed. When a single disaster is disposed of, it will come back to the initial step, Import dynamic data and disaster information until the end of the event.

2.3 Technical requirements analysis

To build this system platform with the required functions mentioned, some information technology was required.

2.3.1 Data analysis technology

How to handle Big Data is the key to affect the value of data. To meet the huge amount of disaster prevention data, R language will be adopted for data analysis, statistics, and statistics charts. In the SQL Server 2016, R has been added as the latest built-in analysis tool. Calculation of large number of disaster-resilient data through the R-linked database should make advanced analysis more accessible, the efficiency of all analysis would be increased.

2.3.2 Emergency alert message

With big data, under the concept of Open Data, to make data more profitable, a standard for information collaboration is needed. The Disaster Warning Public Information Platform (https://alerts.ncdr.nat.gov.tw/) shows very good example. The Common Alerting Protocol (CAP) of the "Common Alerting Agreement" was adopted. It is an international common standard agreement for data conversion technology consistency (current version is 1.2) used between different network platforms for exchanging communication data in emergency disaster situation. The purpose is to adopt an open, non-proprietary digital message format, and does not restrict any specific application or communication method to provide all types of alerts, warning notices. Therefore, the use of CAP can reduce the system design cost and complexity of operation. It can be used to customize various disaster warning messages in various media.

2.3.3 Platform service interface

The current information and communication technologies are on the fast track, and the media that can be used are also more diversified. Considering the conditions that will be faced, the actual usage of the platform, different devices such as desktop computers, notebook computers, tablet computers, smart mobile phones, etc. would be used, also consider the balancing of convenience, efficiency, user's convenience and efficiency. Under these limitation, for providing the best experience, while reducing the impact from software or operating environment. Therefore, those tools that have met the mainstream information protocols were chosen for the development of the SDNS service interface. After evaluating the user's operation fluency, reducing network traffic, and high browser support, HTML5, Angular.js, and jQuery will be used as the core tools for development.

2.3.4 Map service interface

This system aims to reduce the threshold for user operation and provide the best operating experience. After the evaluation, Google Map is used as the basic map platform, and the Google Map API and JavaScript suite D3.js are used to display the environment and resources. The format of kml, kmz, etc. were used as the main data format in this system, to facilitate the display of various types of data such as disaster prevention resources, rivers, rainfall stations, disaster spots, etc., and improve the convenience of query, operation and immediate efficiency.

2.4 System architecture

According to the requirements mentioned above, the architecture of the system is as **Fig. 5**.

2.4.1 Dynamic database

The dynamic database is mainly used to process and store real-time data of disaster incidents. To import and process external data, data import module and value-added module were needed to be established.

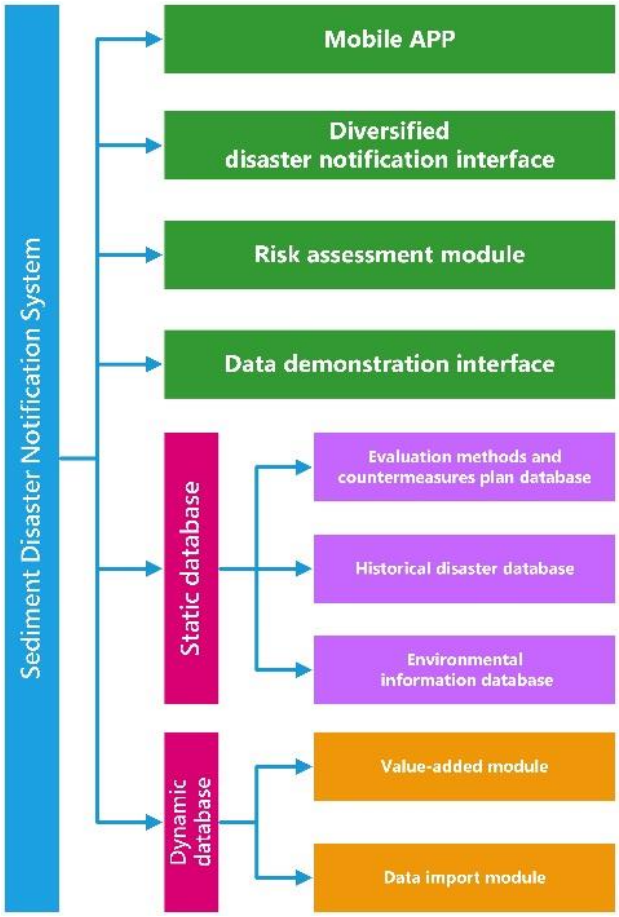

Fig. 5 System architecture of the SDNS

2.4.2 Static database

The static data base is mainly used to store all types of basic information needed for the operation of the pure platform. It can be divided into environmental information database, historical disaster database, evaluation methods and countermeasures plan database.

(a) Environmental information database:
The contents of the environmental information database mainly include information on administrative areas, traffic network, water systems, historical disaster sites, potential disaster areas, and so on.

(b) Historical disaster database:
Historical disaster database content is information related to past disaster events. It mainly includes information such as the event overview, location, time, type of disaster, scale of disaster, loss status, and disposal methods.

(c) Evaluation methods and countermeasures plan database:
The contents of the evaluation methods and countermeasures plan database mainly including various disaster risk assessment methods, possible scenarios, response strategies, and other information built on the platform for reference.

2.4.3 Data demonstration interface

The data demonstration interface is mainly used to demonstrate various dynamic information, the distribution of disasters, and the information that the management agency and the business unit released to the public.

2.4.4 Risk assessment module

The risk assessment module is a tool that compares the situations built in the platform database with dynamic data or user-defined conditions, to provide tools and countermeasures for the management agency and the business unit.

2.4.5 Diversified disaster notification interface

The diversified disaster notification interface enables the users to provide disaster information interfaces in various ways, including voice, SMS, fax, and mobile APP..., which is the main channel for the platform to exchange disaster information.

2.4.6 Mobile APP

The Mobile App is an action tool that is based on the needs of the platform to obtain disaster information and is designed to reduce the complexity of the operation of the public. It is also an important channel for the platform to directly push important information from the management agency and the business unit to the public.

2.5 System functions and goals

The SDNS is not traditional Management Information System (MIS) or Geographic Information System (GIS), is a system based on user friendly concept and considerate about the business needs of reservoir managers, the scalability of system structure, and the safety of information exchange, the main system functions and goals are:

2.5.1 To deliver the disaster information to managers.

Grasping the correct real-time situation is the most important issue for managers. Especially during the disaster process, the decision-making of manpower dispatching, resource dispatching, and personnel placement all relied on the correct disaster information. The functions of information delivering, receiving, and confirming should be built in SDNS.

2.5.2 To collect complete environment information of disaster regions.

To build a comprehensive system, each kind information about the study area should be digitized and imported into system database. Although some data has been built in the SDDB, the works of data collecting should be continued. Meanwhile, SDDB data format standard should be followed, all archive documents should be kept in two forms, one is the

original file format made by professional software, the other one is the pre-defined portable document format.

2.5.3 To establish convenient interface for query and management.

For efficiency usages for both data query and study area management user-friendly interfaces are necessary to be established. These interfaces should be provided in the easiest way for users to get information they want and feedback useful information to system. In this study there are 4 types of interfaces should be established, included system management interface, real-time data demonstration interface, disaster information exchange interface, and mobile device application interface.

2.5.4 To enhance the security of data access.

In the trend of "Big Data" and "Open Data", the achievements of database will be utilized cross-sectorally, even will be opened to public. For the balancing between "Open Data" and "information security", the "three–tier" structure was used. Data will not be contacted directly by users; all requests will be delivered through interfaces and be authorized by the interface. All system responses will also be delivered through the same interfaces.

2.5.5 To improve the efficiency of catchment management.

In the premise of user friendly and management efficiency, the mobilized needs were also considered. To provide more flexible interface, HTML5 standard was followed, meanwhile, Responsive Web Design (RWD) was used with. This means users could easily get the same use experience using this system in any kind of device and would not have to install any special plugins.

2.6 Standardization specification for data

Base on the experience from establishing SDDB, four basic data types were pre-defined, for reducing the complexity of data process and for enhancing the efficiency of data exchange.

2.6.1 General documents

- Definition:
  General software output, data file contains text, pictures, figures, or tables.
- Demonstration format:
  Portable Document Format (PDF), *.pdf.
- Archive format:
  *.pdf.
- Original formats:
  Common file types include plain text files (*.txt), Word files (*.doc, *.docx), Excel files (*.xls, *.xlsx), presentation files (*.ppt, *.pptx) Portable Document (*.pdf) ... and so on.

2.6.2 Graphics file

- Definition:
  A data file presented in a Raster format.
- Demonstration format:
  Joint Photographic Experts Group (Joint Photographic Experts Group, JPEG) format, *. jpg.
- Archive format:
  *. jpg.
- Original formats:
  Common file types include image files (*.jpg, *.png, *.bmp, *.tiff, *.img), AutoCAD files (*.dwg).

2.6.3 Geographic information file

- Definition:
  A data file presented in a Vector format.
- Demonstration format:
  Joint Photographic Experts Group (JPEG) format, *. jpg.
- Archive format:
  Keyhole Markup Language (KML) format, *. kml.
- Original formats:
  Common file types include Shapefile (*.shp), track file (*.kml).

2.6.4 Multimedia file

- Definition:
  A data file made up of audio, video, or audio and video.
- Demonstration format:
  Moving Picture Experts Group-4 Part 10 Advanced Video Coding (MPEG-4 AVC) format, *.mp4.
- Archive format:
  *.mp4.
- Original formats:
  Common file types include audio and video files (*.avi, *.mpg, *.Mp4), QuickTime ring file (*.mov), three-dimensional nested engineering environment project (*. sxd).

The flexibility of system architecture and standardization specification was reserved, the new data types and formats will be easily declared the definition by system administrator when there were some new data categories or formats will be used in this system in the future.

3. STAGE RESULTS

The SDNS is still under construction, core database come from SDDB was already re-processed to meet the needs of SDNS. Basic data request and feedback functions were done. In this stage, dynamic database and data demonstration

interface are ready, **Fig. 6** and **Fig. 7** show real-time data demonstrated on the system interface.

The notification functions such as voice message, SMS (**Fig. 8**), MMS, and FAX (**Fig. 9**) are ready now.

The mobile APP in under construction, partial functions have been completed (**Fig. 10~ Fig. 11**), the corresponding control interface of the system is still under development.

The follow-up will be the user interface optimization and testing phase.

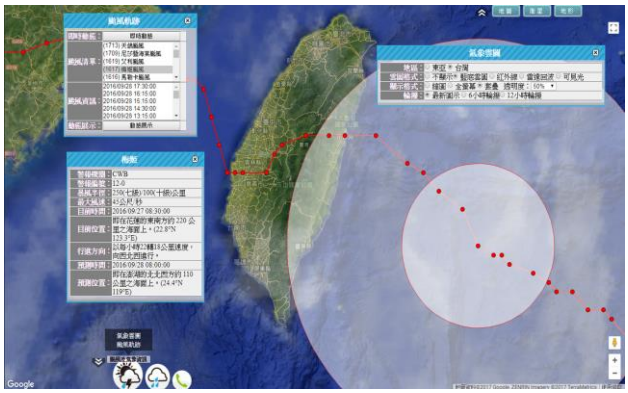

Fig. 6 Real-time typhoon data demonstrate on SDNS

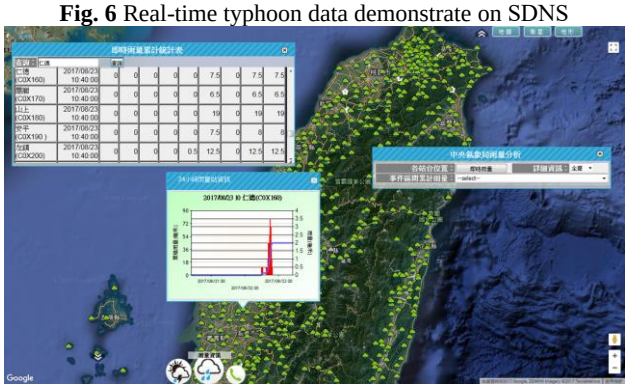

Fig. 7 Real-time rainfall data demonstrate on SDNS

Fig. 8 SMS interface on SDNS

Fig. 9 Fax interface on SDNS

Fig. 10 Data collection interface of mobile APP

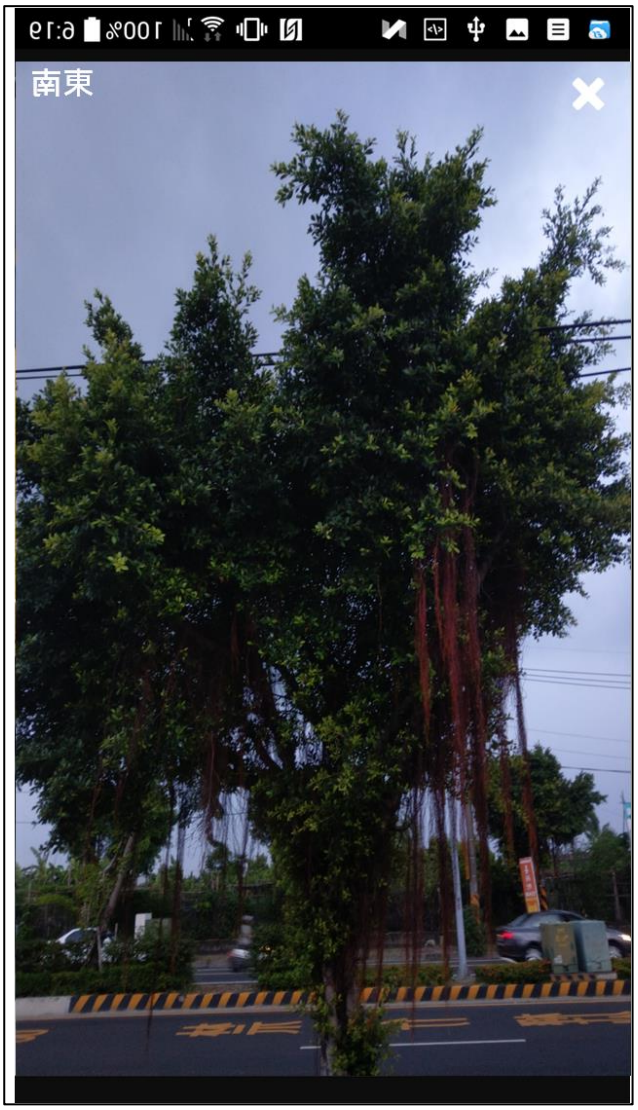

Fig. 11 Photo editing interface of mobile APP

4. CONCLUSIONS

To assist reservoir managers improving the grasp of the situation of sediment disasters in reservoir catchment, the development of SDNS was started. In the "Origin" part of this article mentioned there were four important issues must to be conquered, SNDS was based on the SDDB which built-in information for issue (b) and was designed with quick information exchange functions for issues (c) and (d). Although the establishment of SDNS is ongoing, users already can easily request archive data or documents now. Those achievement have been pre-processed with the "standardization specification for data", it means users need to do nothing but access the achievements directly. The notification feature will provide users with a more convenient way to publish or get disaster information. This will bring benefits on manpower saving and improve the performance on the management of sediment disasters in reservoir catchment.

ACKNOWLEDGMENT: Thank you for the financial funding supported by the Ministry of Science and Technology of the Executive Yuan.

REFERENCES

Nantou Branch, Soil and Water Conservation Bureau, Council of Agriculture, Executive Yuan (2010): The overall rehabilitation plan for the Morakot disaster in the upper catchment of Zengwen River, Report of the Soil and Water Conservation Bureau of the Agricultural Committee of the Executive Yuan.

Kuang-Jung Tsai et al. (2010): Development and application of the governance and engineering management information system for the Zengwen reservoir catchment, Journal of Sinotech Engineering, Vol.106, pp. 73-78.

Kuang-Jung Tsai et al. (2014): Investigation and analysis of the variability of hydrological and geochemical environment in the Gaoping River watershed under extreme climate change, Journal of Mining & Metallurgy, Vol.58, No. 1, pp.45-61.

Chjeng-Lun Shieh et al. (2010): Landslide interpretation of Typhoon Morakot using the Formosat-II imagery, Journal of the Taiwan Disaster Prevention Society, Vol. 2, No. 1, pp.35-42.

Charlton R. el al. (2006) Assessing the impact of climate change on water supply and flood hazard in Ireland using statistical downscaling and hydrological modeling techniques, Climate Change, Vol. 74, pp. 475-491.

Yie-Ruey Chen, Po-Ning NI, Kuang-Jung Tsai (2013) Construction of a sediment disaster risk assessment model, Environ Earth Sci (2013)70,pp.115-129. (SCI, IF:1.425)

Jones R. N.(2001) An Environmental Risk Assessment/Management Framework for Climate Change Impact Assessments, Natural Hazards, Vol.23, pp.197-230.

Kuang-Jung Tsai, Yie-Ruey Chen, Shun-Chieh Hsieh, Chia-Chun Shu, Ying-Hui Chen(2014) An Establishment of Rainfall-induced Soil Erosion Index for the Slope Land in Watershed, European Geosciences Union General Assembly 2014, Apr. 2014, Vienna, Austria.

Detection of Landslide Candidate Interference Fringes in DInSAR Imagery Using Deep Learning

Joko KAMIYAMA[1]*, Tomoyuki NORO[1], Masayuki SAKAGAMI[1], Yamato SUZUKI[1]
Kazuo YOSHIKAWA[2], Shuhei HIKOSAKA[2] and Ikushi HIRATA[2]

1 National Institute for Land and Infrastructure Management, MLIT, Japan
2 PASCO Corporation, Japan
*Corresponding author. E-mail: kamiyama-j253@mlit.go.jp

Interferometric synthetic aperture radar (InSAR) is an effective technique for monitoring the risk of large-scale sediment movements because it can broadly and routinely observe the extent of landslides. To detect interference fringes with the possibility of landslide movements from differential interferograms, it is common for experts to interpret these fringes considering the effects of water vapor as well as the topography and other factors. Increasing the accuracy of detecting landslides is an important issue in the usage of InSAR. Convolutional Neural Networks (CNNs) that enable image recognition with sufficient accuracy have recently been developed. To efficiently detect landslide candidate interference fringes, this study evaluated the effectiveness of introducing a CNN model to detect the interference fringes representing landslide movements using similar processes as experts techniques. As a result, the CNN model was able to detect landslide candidate interference fringes that had been detected by experts with a recall of approximately 90%.

Key words: Landslide detection, DInSAR, Deep Learning, Convolutional Neural Networks

1. INTRODUCTION

In Japan, serious damage is often caused by large-scale erosion and sedimentation processes, such as the heavy rain caused by the 2011 Typhoon No. 12 (Talas) and the deep-seated landslides and landslide dams caused by the 2008 Iwate-Miyagi Inland Earthquake. In the prevention/mitigation of sediment disasters, the monitoring of potential landslide slopes based on their detection is essential.

An interference analysis using synthetic aperture radar mounted on a satellite, i.e., interferometric synthetic aperture radar (InSAR), is a monitoring technique that can broadly and routinely observe minor landslide movements. Differential Interferometric SAR (DInSAR), which provides a measurement accuracy of several centimeters, is an effective technique for detecting landslides. Because Japan's mountainous areas are widely covered with forests, analyses of ground surface movements with a few SAR images can be performed to meet requirements such as the number of persistent scatterers or the need for multiple analytic pairs with good coherence.

In recent years, multiple artificial satellites equipped with SAR with resolutions of several meters have been in operation worldwide. Increases in the observation frequency due to the operation of multiple satellites and the expansion of the observation width will enable more frequent landslide monitoring in the same location and DInSAR for landslide monitoring will be used more than ever before.

Changes in the interference fringes in differential interferograms obtained from DInSAR may appear due to factors other than ground surface movements. There are various factors that produce interference fringes, such as satellite orbit differences or the delay of radio waves due to water vapor [*Shimada*, 1999]. However, it is difficult to thoroughly remove local effects that appear in slopes from global effects on a large spatial scale. Therefore, the detection of interference fringes that may indicate landslide movements depends on expert interpretations. However, it would require enormous amounts of time and effort for experts to interpret all the differential interferograms created from observational data obtained over wide areas at high frequency. In addition, variations in the judgment criteria are likely to occur among experts. To

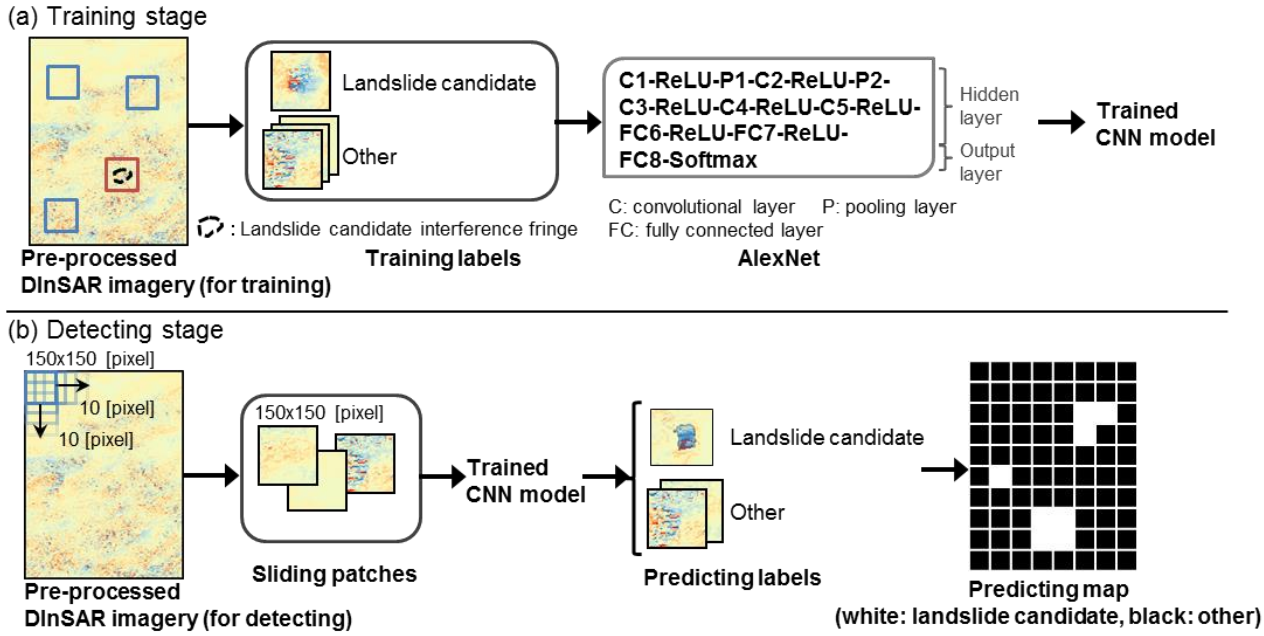

Fig. 1 Architecture of the CNN model and image of (a) the training stage and (b) the detection stage

increase the accuracy of landslide detection is an important issue in the usage of DInSAR.

In recent years, to deal with the large amount of image data, several models have been developed [e.g., *Krizhevsky et al.*, 2012] that recognize images with high accuracy using Convolutional Neural Networks (CNNs), one of the deep learning approaches. Case studies on CNNs for remote sensing images have been increasing. Deep learning using SAR data include studies on automatic target recognition from reflection intensity images [e.g., *Wilmanski et al.*, 2016] and on land cover classification using polarimetric SAR data [e.g., *Zhou et al.*, 2016]. However, there are no cases where the locations of ground surface movements are detected from differential interferograms.

Therefore, with the aim of efficiently detecting interference fringes that may represent landslides from differential interferograms, this study attempted to evaluate the effectiveness of introducing a CNN model to detect interference fringes representing landslide movements, using similar processes to those of experts.

2. METHOD

2.1 Learning model

We used CNNs for learning. CNNs are a type of forward-propagation neural network having two-dimensional convolution layers, and as a specific feature, high-level characteristics can be obtained by synthesizing low-level characteristics. [*LeCun et al.*, 2015].

Various architectures have been proposed for CNNs [*Okatani*, 2016]. In this study, we adopted AlexNet [*Krizhevsky et al.*, 2012] because the amount of training data is small, the learning takes less time than the deep architecture, and there are many research results (**Fig. 1**). In the AlexNet architecture, the hidden layer consists of five convolutional layers, two pooling layers, and two fully connected layers and ReLU was adopted as an activation function. The output layer consists of one

Table 1 The learning conditions for the CNN model

Parameter	Meaning	Setting value
Optimization method	Optimization calculation method for searching for optimal weight parameter in learning of neural network	SGD* (Stochastic gradient descent)
Initial learning rate	Parameter of SGD. The initial value of the coefficient that determines the size of update amount to the parameters (weight, bias) learned in the CNN.	0.01
Learning rate schedule method	Parameter of SGD. A method of changing the learning rate from the initial value as the learning time passes.	1/10 each time 5,000 times of iteration
Weight decay	Parameter of SGD. For the coefficient of reducing the weight of learning to be set for preventing overfitting to the learning data of the neural network.	0.0005
Momentum	Parameter of SGD. The techniques to enhance the convergence of learning.	0.9
Mini-batch size	Number of learning data units for calculating error with one iteration of learning.	50
Number of iterations	Number of times to learning iterations	30,000

*[*David et al.*, 1986]

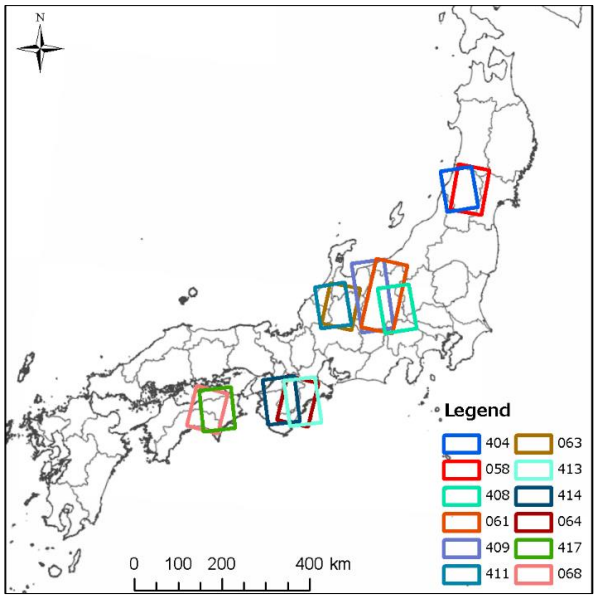

Fig. 2 Map of observed area of differential interferogram used for training data

fully connected layer, and Softmax was adopted as an activation function.

The CNN model conducted learning with back propagation using mini-batch stochastic gradient descent. For the learning conditions, the same conditions as that of AlexNet were adopted (**Table 1**), except for the parameters shown below. The parameters that depend on the number of training data (the learning rate schedule method, the mini-batch size, and the number of iterations) were determined considering the number of used training data after confirming that the learning converged.

2.2 Differential interferograms used for learning

For learning, we used the differential interferograms of ALOS/PALSAR from 2006 to 2011. We used images of Mt. Gassan in Yamagata Prefecture, the northern part of Nagano Prefecture, Mt. Hakusan in Ishikawa Prefecture, the Nara and Wakayama prefectures (the Kii Peninsula), and the eastern part of Kochi Prefecture, including locations previously detected as having the possibility of landslides [*Kamiyama et al.*, 2016, 2017]. **Fig. 2** shows the observed area and **Table 2** shows a list of the observed differential interferogram data used for the training data. The data are observed in high-resolution mode and the image processing level is L1.0.

Fig. 3 shows the processing flow of DInSAR. Interference fringes caused by changes in the vapor distribution in the atmospheric air between each observation often appear in DInSAR. When interference fringes resulting from atmospheric air are found in differential interferograms, it may be

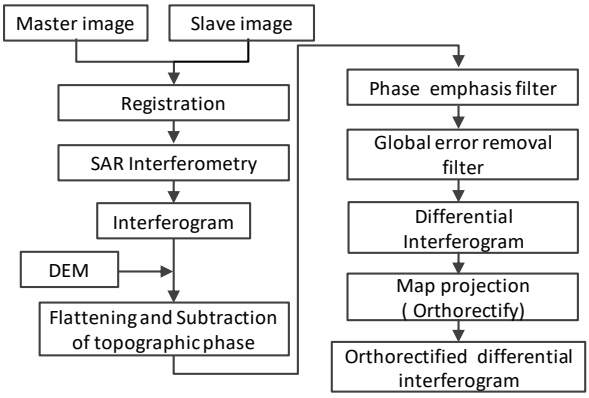

Fig. 3 Processing flow of DInSAR

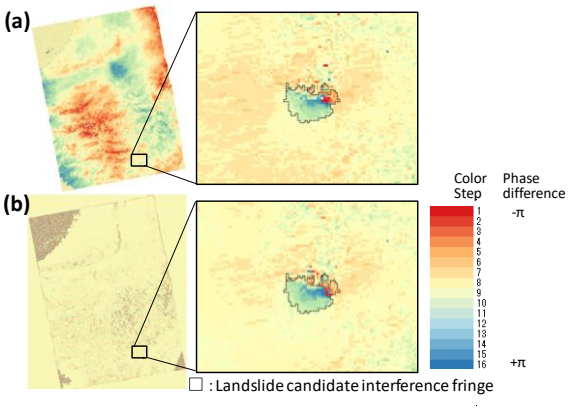

Fig. 4 Examples of differential interferograms (a) without global error removal filters and (b) with global error removal filters

unable to learn the interference fringes caused by landslides properly and may misdetect them. Therefore, we used the global error removal filter proposed by *Kusano et al.* [2015] to remove interference fringes resulting from atmospheric air, which have a larger spatial scale than landslides and appear at scales of several hundreds of meters or kilometers. The sizes of the filters we tried were 500 m, 1000 m, 2000 m, and 3000 m. We chose a filter size of 2000 m because it can detect the area of the interference fringes with the possibility of landslides, as in the case of no filters, and can remove interference fringes caused by atmospheric air. **Fig. 4** shows examples of differential interferograms for a case where the global error removal filters are applied and a case where they are not applied. In **Fig. 4**(b), the global interference fringes have been removed from the image in **Fig. 4**(a). There is nearly no change in the color gradation of the interference fringes with the possibility of landslides, as seen in the enlarged views of **Fig. 4**.

In addition, we used differential interferograms for learning by classifying the phase differences from $-\pi$ to $+\pi$ into 16 color gradation steps (**Fig. 4**).

Table 2 List of observation data for the differential interferograms used for training data

Area	Observed area		Observation date	
	Orbit number	Center frame number	Master	Slave
Mt. Gassan	404	760	25/10/2007	17/06/2010
	58	2840	12/09/2006	17/09/2008
			05/05/2009	05/08/2009
			05/05/2009	05/11/2009
			23/03/2010	08/05/2010
Northern Nagano	408	710	01/07/2007	16/08/2007
			01/07/2007	01/10/2007
			01/07/2007	03/07/2008
			01/07/2007	06/10/2009
			03/07/2008	21/08/2009
			03/07/2008	06/10/2009
			18/08/2008	06/07/2009
			03/10/2008	06/07/2009
			24/05/2010	24/08/2010
			24/05/2010	09/10/2010
			09/07/2010	24/08/2010
			09/07/2010	09/10/2010
	61	2880	05/11/2007	21/12/2007
			21/12/2007	22/03/2008
			07/08/2008	22/09/2008
	61	2890	05/11/2007	07/05/2008
			21/12/2007	22/03/2008
	409	710	20/07/2008	07/09/2009
	409	720	18/07/2007	20/07/2008
			18/07/2007	18/10/2007
			02/09/2007	18/10/2007
			20/07/2008	07/09/2009
			20/07/2008	23/10/2009
			20/10/2008	07/03/2009
			23/07/2009	07/09/2009
			07/09/2009	23/10/2009
			25/04/2010	10/09/2010
			10/06/2010	26/07/2010
			10/06/2010	10/09/2010
			10/09/2010	26/10/2010
Mt. Hakusan	411	710	06/07/2007	21/08/2007
			21/08/2007	06/10/2007
			26/08/2009	11/10/2009
			26/08/2009	26/11/2009
			29/05/2010	14/07/2010
			14/07/2010	29/08/2010
			29/08/2010	14/10/2010
			14/10/2010	29/11/2010
			06/07/2007	11/10/2009
			21/08/2007	11/10/2009
			23/05/2008	29/08/2010
			23/05/2008	14/10/2010
	63	2890	08/06/2007	24/07/2007
			08/06/2007	24/10/2007
			08/06/2007	29/10/2009
			24/07/2007	13/06/2009
			24/07/2007	29/10/2009
			24/10/2007	10/06/2008
			24/10/2007	29/10/2009
			13/06/2009	29/10/2009

Area	Observed area		Observation date	
	Orbit number	Center frame number	Master	Slave
Kii Peninsula	413	660	24/06/2007	09/08/2007
			24/06/2007	26/06/2008
			09/11/2007	11/05/2008
			26/03/2008	17/08/2010
			26/09/2008	11/02/2009
			29/09/2009	14/11/2009
	414	660	08/10/2006	13/07/2008
			08/01/2007	13/10/2008
			11/10/2007	03/03/2010
			11/10/2007	18/04/2010
			11/01/2008	18/04/2010
			11/01/2008	03/06/2010
			13/07/2008	16/07/2009
			16/07/2009	16/10/2009
			03/03/2010	19/07/2010
			18/04/2010	19/10/2010
			03/06/2010	03/09/2010
			03/06/2010	19/10/2010
			19/07/2010	19/10/2010
	414	670	08/10/2006	08/01/2007
			08/10/2006	13/07/2008
			11/07/2007	26/08/2007
			11/07/2007	11/10/2007
			11/07/2007	11/01/2008
			11/07/2007	01/12/2009
			26/08/2007	11/01/2008
			26/08/2007	16/01/2010
			26/08/2007	03/03/2010
			11/10/2007	11/01/2008
			11/10/2007	26/02/2008
			11/10/2007	03/03/2010
			11/10/2007	18/04/2010
			11/10/2007	03/06/2010
			11/01/2008	03/03/2010
			11/01/2008	18/04/2010
			11/01/2008	03/06/2010
			13/07/2008	28/02/2009
			13/07/2008	16/07/2009
			13/07/2008	16/10/2009
			28/08/2008	13/10/2008
			16/10/2009	18/04/2010
			16/10/2009	03/06/2010
			01/12/2009	18/04/2010
			01/12/2009	03/06/2010
			16/01/2010	03/06/2010
			03/03/2010	03/09/2010
			18/04/2010	03/09/2010
			18/04/2010	19/10/2010
			03/06/2010	19/10/2010
			19/07/2010	19/10/2010
	64	660	23/12/2006	30/09/2009
			26/12/2007	18/08/2010
	64	2940	23/12/2006	30/09/2009
			10/08/2007	30/09/2009
			26/12/2007	18/05/2010
			26/12/2007	18/08/2010
Eastern Kochi	417	660	28/08/2006	31/08/2007
			13/10/2006	18/07/2008
			13/01/2007	03/12/2008
			16/10/2007	08/03/2010
			16/10/2007	23/04/2010
			16/10/2007	08/06/2010
			01/12/2007	08/03/2010
			01/12/2007	23/04/2010
			01/12/2007	08/06/2010
			16/01/2008	23/04/2010
			16/01/2008	24/07/2010
	68	2940	14/01/2007	17/01/2008
			09/06/2010	25/07/2010
			09/06/2010	09/09/2010
			25/07/2010	09/09/2010
			25/07/2010	25/10/2010

2.3 Classes of training data

For the CNN model, we used two classes of training data, i.e., "landslide candidates", meaning interference fringes where landslides are likely to occur, and "others", areas detected in a random manner from areas other than the landslide candidates in the differential interferograms. Out of the 127 differential interferograms, we used 54 samples as landslide candidates (included in 51 differential interferograms). These samples were detected as possible candidates for locations where landslides could occur based on interference fringes detected on the slopes at multiple different times and on the existence of microtopography formed by landslides, as in the expert technique. Interference fringes representing landslide candidates are characterized by successive changes in color gradation as well as step-wise differences in the color gradation around the interference fringe [*Geospatial Information Authority of Japan*, 2011].

For others we sampled several locations at random from areas other than the landslide candidates from the 127 differential interferograms. Differential interferograms are expected to include interference fringes caused by various factors on ground surfaces with different gradients. Therefore, it is necessary to evenly prepare the model learning the features of the interference fringes of the slopes and flatlands. When the slopes and flatlands are defined to have an average gradient of 15 degrees or more or less than 15 degrees, respectively, slopes accounted for 37% and flatland accounted for 63% of the differential interferograms classified as others. The division between slope and flatland was set to 15 degrees (on a 1 km mesh) considering the lower limit value of the average relief energy of 1 km^2 in the mountainous area is 300 m [*Suzuki*, 2000a] and the value of the sedimentary topography due to debris flow e.g. the maximum inclination of sedimentary terrains such as alluvial fans belonging to flatlands is 15 degrees [*Suzuki*, 2000b]. We confirmed that the ratios of the slopes and the flatlands sampled at random in the others class were equivalent. Note that the elevation/gradient data of the 1-km mesh of the National Land Numerical Information archived by the *National Spatial Planning and Regional Policy Bureau, MLIT* [2011] was used for the average gradient.

For these training data, images were cut into small areas (150 × 150 pixels = 17.64 km^2 each) to be used for learning. The size of the small areas was set so that the landslide candidate interference fringes used for learning included those areas as well as the margins to include the information near the fringes.

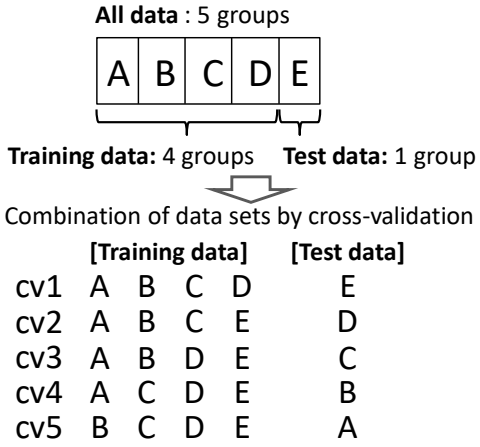

Fig. 5 The datasets used for cross-validation

2.4 Learning method and dataset

To evaluate the classification performance of the trained CNN model, it is necessary to divide the data for training and testing. However, the number of data in the landslide candidate class is small and the data for testing are limited; therefore, there was a concern that the validity of the validation result would be low. Accordingly, we used a k-fold cross-validation to maximize the use of the limited data and evaluate the generalization of the model. In this method, part of the data, which are divided into k pieces, is analyzed and the analysis result is verified using the remaining data. Then, the validity of the analysis is verified by averaging the k validation results. In this study, dividing the all data into five groups, four of which are used for training while the remaining group is used for testing, we conducted the training and validation five times in total by changing the combination of groups each time (cv1–cv5), as shown in **Fig. 5**. The number of divisions of data was determined taking into consideration the time required for validation.

In addition, to evaluate the performance of the model according to the difference in the number of training data, the 127 differential interferograms were divided into two groups, Dataset A and Dataset B. Dataset A consists of 107 differential interferograms and 42 landslide candidate samples. Dataset B consists of 127 differential interferograms (Dataset A plus 20) and 52 landslide candidate samples (Dataset A plus 12). Based on this, we prepared the training data (**Table 3**) and test data (**Table 4**) to perform the intersection validation five times. The number of landslide candidate data in the one-time training is 33 or 34 samples for Dataset A and 42–44 samples for Dataset B. Because there were few landslide candidate interference fringes for use as training data, there was a concern about the possibility of overlearning in the CNN model for the

Table 3 Number of samples for each class used for training

Class		cv1		cv2		cv3		cv4		cv5	
		Before padded	After padded	Before padded	After padded	Before padded	After padded	Before padded	After padded	Before padded	After padded
Dataset A	Landslide candidate	33	40,000	33	40,000	33	40,000	34	40,000	34	40,000
	Others	40,000	40,000	40,000	40,000	40,000	40,000	40,000	40,000	40,000	40,000
Dataset B	Landslide candidate	43	45,000	43	45,000	42	45,000	43	45,000	44	45,000
	Others	45,000	45,000	45,000	45,000	45,000	45,000	45,000	45,000	45,000	45,000

limited training data. It is generally desirable for the training data to represent the actual data space of the learning object. However, in this study, the number of landslide candidate interference fringes is small and the directions and positions in which the interference fringes appear are limited. Accordingly, we padded the numbers of training data, via rotation, reversal, and parallel movements, to 40,000 for Dataset A and to 5,000 for Dataset B so that the interference fringes in the interferograms have different directions and positions (**Table 3**). For rotation padding, the interferograms were rotated at random based on the rotation angle θ ($0° \leq \theta < 180°$). For reversal padding, they were vertically, horizontally, and vertically and horizontally reversed. For parallel movement padding, they were selected randomly within the scope of −10 to +10 pixels in the X-axial and Y-axial directions of images. The same numbers of other data and landslide candidate data were sampled.

In addition, test data were prepared from image data other than training data (Datasets A' and B' in **Table 4**).

We created CNN models that trained Dataset A (CNN-A) and another CNN model that trained Dataset B (CNN-B).

2.5 Evaluation index of the classification performance

The classification performance of the trained CNN models were evaluated using the following method. First, we evaluated the performance demonstrated when the sample data for testing (**Table 4**) was classified into each class using the trained CNN models. Next, from the differential interferograms including the samples of each class shown in **Table 4**, we cut out small area images of 150 × 150 pixels at intervals of 10 × 10 pixels and evaluated the results interpreted by the CNN models (**Fig. 1**(b)). When the classification result by the CNN models for the class of test data is correct, it is indicated as true positive (TP) and true negative (TN), and in case of error it is indicated as false positive (FP) and false negative (FN) (**Table 5**).

Table 4 Number of samples for each class used for testing

Class		cv1	cv2	cv3	cv4	cv5
Dataset A'	Landslide candidate	9	9	8	8	8
	Other	1,000	1,000	1,000	1,000	1,000
Dataset B'	Landslide candidate	11	11	11	11	11
	Other	1,500	1,500	1,500	1,500	1,500

Table 5 Evaluation index of the classification performance

		Class of test data	
		Landslide candidate	Other
Classification result	Landslide candidate	True Positive (TP)	False Positive (FP)
	Other	False Negative (FN))	True Negative (TN)

$$\text{Recall} = TP/(TP+FN) \quad (1)$$

$$\text{Precision} = TP/(TP+FP) \quad (2)$$

As indices for evaluating the classification performance, we used the recall, precision, and break even point (BEP). The recall value represents the ratio of the data classified by the CNN models as landside candidates to the data that are actually landside candidates (**Table 5**, Eq. (1)). The precision value represents the ratio of the data that are actually landside candidates to the data classified by the CNN models as landside candidates (**Table 5**, Eq. (2)). The recall and precision values are generally in a trade-off relationship; therefore, we used BEP to evaluate the classification performance when they are balanced. BEP is the value at which the recall equals the precision when the threshold to the probability value of the landside candidates class is raised or lowered. In this study, the recall and precision are calculated when the threshold value is varied in increments of 0.01 and the average value of the precision between the two points where the magnitude relationship between the recall and the precision is reversed is taken to be the BEP.

3. RESULT

3.1 Classification result of the test data

Table 6 shows the result of the classification of

Table 6 Evaluation result of classification performance of CNN models

Case	Model	Validation data	Evaluation Index	cv1	cv2	cv3	cv4	cv5	Average
1	CNN-A	Dataset A'	TP	448.4	504.5	504.0	441.0	504.0	–
			FN	56.1	0.0	0.0	63.0	0.0	–
			FP	2.0	1.5	1.0	0.0	1.5	–
			Recall	88.9	100	100	87.5	100	95.3
			Precision	99.6	99.7	99.8	100	99.7	99.8
			BEP	99.6	100	99.9	99.7	100	99.8
2	CNN-A	Dataset B'	TP	618.1	686.8	618.1	549.5	679.5	–
			FN	137.4	68.7	137.4	206.0	75.5	–
			FP	2.0	3.0	1.5	0.5	2.5	–
			Recall	81.8	90.9	81.8	72.7	90.0	83.5
			Precision	99.7	99.6	99.8	99.9	99.6	99.7
			BEP	95.8	98.5	91.9	99.3	96.8	96.3
3	CNN-B	Dataset B'	TP	618.1	755.5	618.1	686.8	755.0	–
			FN	137.4	0.0	137.4	68.7	0.0	–
			FP	3.5	6.0	2.5	2.0	5.0	–
			Recall	81.8	100	81.8	90.9	100	90.9
			Precision	99.4	99.2	99.6	99.7	99.3	99.5
			BEP	99.0	99.5	99.0	99.7	99.9	99.4

the test data in **Table 4** from models created using cv1–cv5 as training data in Datasets A and B in **Table 3**. Note that, because the numbers of test data between the classes are balanced in general classification evaluation, we conducted normalization (total number of test data/number of classes) for the evaluation result of the classification of the test data. Here, the validation was conducted for three cases with different combinations of the model and classification data. It is conceivable that the model CNN-B including the same training data as the model CNN-A learns features in a similar way. Validation against Dataset A' for the classification using model CNN-B was not performed because it is similar to Case 1 in **Table 6**.

The recall values of cv1–cv5 for each model range from 72.7% to 100%, the precision values range from 99.2% to 100%, the BEP values range from 91.9% to 100%, and the performance of cv1–cv5 varies. Because it is difficult to evaluate the detection method in this study in the validations of cv1–cv5, we believe that it is appropriate to take an average value of the five validation results for each model.

The average value of the five validations for each model and the classification was 95.3% for recall, 99.8% for precision, and 99.8% for BEP in Case 1 of **Table 6**. In Case 2, the recall value was 83.5%, the precision value was 99.7%, and the BEP value was 96.2%. In Case 3, the recall value was 90.9%, the precision value was 99.5%, and the BEP value was 99.4%; each of which was lower than the comparable values in Case 1.

Table 7 Evaluation result of detection performance of CNN model

(a) Size filtering not applied

Case	Model	Validation data	Evaluation Index	cv1	cv2	cv3	cv4	cv5	Average
1	CNN-A	Dataset A'	TP	9	9	8	8	10	–
			FN	0	0	0	0	0	–
			FP	319	291	284	288	222	–
			Recall	100	100	100	100	100	100
			Precision	2.7	3.0	2.7	2.7	4.3	3.1
2	CNN-A	Dataset B'	TP	10	10	9	10	11	–
			FN	1	1	2	1	1	–
			FP	344	357	375	495	308	–
			Recall	90.9	90.9	81.8	90.9	91.7	89.2
			Precision	2.8	2.7	2.3	2.0	3.4	2.7
3	CNN-B	Dataset B'	TP	9	9	8	7	10	–
			FN	0	0	0	1	0	–
			FP	700	658	677	320	573	–
			Recall	100	100	90.9	81.8	100	94.5
			Precision	1.4	1.4	1.3	1.7	1.6	1.5

(b) Size filtering applied

Case	Model	Validation data	Evaluation Index	cv1	cv2	cv3	cv4	cv5	Average
1	CNN-A	Dataset A'	TP	9	9	8	8	10	–
			FN	0	0	0	0	0	–
			FP	236	197	207	199	158	–
			Recall	100	100	100	100	100	100
			Precision	3.7	4.4	3.7	3.9	6.0	4.3
2	CNN-A	Dataset B'	TP	10	10	9	10	11	–
			FN	1	1	2	1	1	–
			FP	251	242	282	328	231	–
			Recall	90.9	90.9	81.8	90.9	91.7	89.2
			Precision	3.8	4.0	3.1	3.0	4.5	3.7
3	CNN-B	Dataset B'	TP	9	9	8	7	10	–
			FN	0	0	0	1	0	–
			FP	489	428	457	221	386	–
			Recall	100	100	90.9	81.8	100	94.5
			Precision	2.0	2.1	1.9	2.5	2.3	2.1

3.2 Result of the interpretation of the differential interferograms

Table 7 shows the result of the classification when the differential interferograms were interpreted using the trained CNN models. In Case 1 of **Table 7**(a), the recall value was 100% and the precision value was 3.1%, both of which were the highest values compared to the other cases. In Case 3, the recall value was 94.5%, higher than in Case 2, and the precision value was 1.5%, the lowest value of the precision seen.

Fig. 6 shows an example of an interpretation result. We created an interpretation result map considering that the center of each small area image with an area of 10 × 10 pixels corresponds to the interpretation result of the small area images. Many of the fringes detected as landslide candidates from the interpretation result (**Fig. 6** (b)), as detected by the CNN models, had an area smaller than landslide candidates used for the training data. For interference fringes with small areas, it is difficult even for experts to distinguish them as landslide candidates or as others.

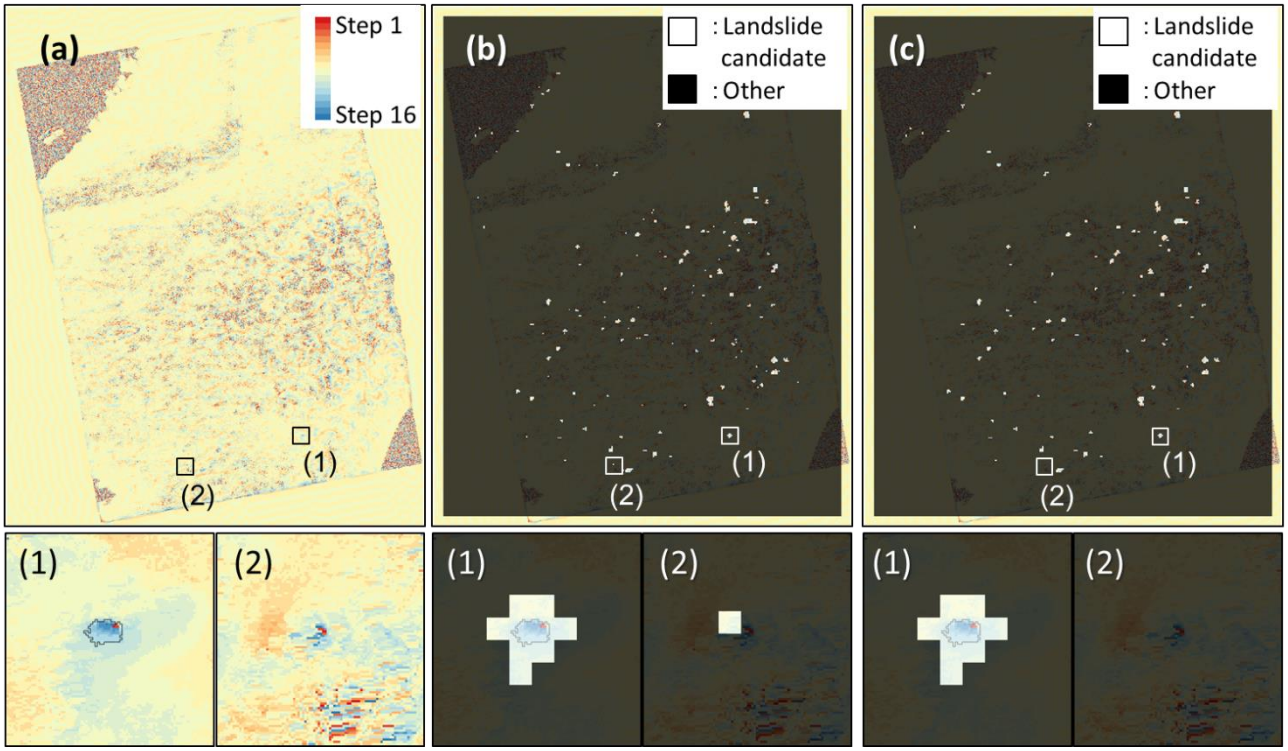

Fig. 6 An example of predicting map
(a) DInSAR imagery, (b) Predicting map (Not applied size filtering), (c) Predicting map (Applied size filtering)

Therefore, we provided size filtering to remove the landslide candidates of less than 10 × 10 pixels (approx. 0.078 km^2), which is less than the minimum area (0.16 km^2) of landslide candidates in the training data, from the interpretation result of the CNN model. The index value and predicting map in this case is shown in **Table 7**(b) and **Fig. 6** (c), respectively. As a result, in comparison with the case where no size filtering is applied (**Table 7(a)**), the recall value was the same but the precision value slightly improved for all cases. Because the filter size is smaller than the minimum area of the landslide candidates used for the training data, the number of true positives in Eq. (2) (**Table 5**) does not change. Meanwhile, interference fringes with a small area included in others were rejected by the filter and the number of false positives was reduced, so the precision improved.

4. DISCUSSION

4.1 Comparison of the validation result for each case

As a result of the classification of the test data in **Table 6**, others and landslide candidates were classified accurately in each case.

On the other hand, the interpretation result of **Table 7** is a high recall but low precision. Comparing the results of each case in **Table 7**; the value of the recall is lower in Case 2 than in Cases 1 and 3. **Fig. 7** shows samples of landslide candidates included in the dataset used for training the CNN models. Panels (a) and (b) in **Fig. 7** are included in Datasets A and B but panels (c) and (d) are included only in Dataset B. In Case 2, Dataset B' includes samples of landslide candidates having characteristics different from the training data (Dataset A) used for modeling (**Figs.7** (c) and (d)). Therefore, these samples could not be detected. In Case 3, the value of the precision was the lowest. Samples of landslide candidates in Dataset B include some patterns of interference fringes that are difficult to distinguish from those in others (**Figs.7** (c) and (d)). This likely caused misdetections of interference fringes in the others class. Even though in Case 3 a model with more training data than in

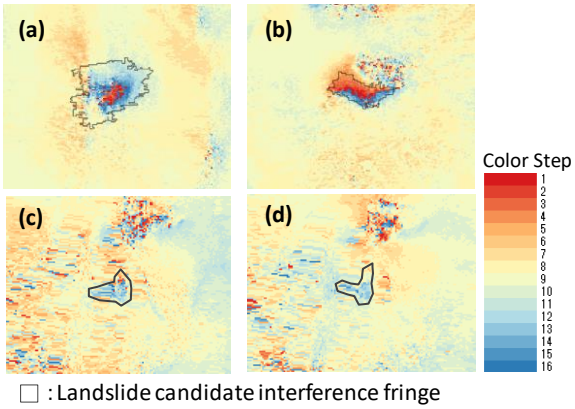

Fig. 7 Sample of Landslide candidate: (a) and (b) Dataset A, (c) and (d) Dataset B

Case 1 was created, the characteristics of the added landslide candidate interference fringes, rather than the increased amount of training data, might have affected the image classification performance.

4.2 Detection trends of models

Landslide candidate samples in the test data of Case 3 in **Table 7** have one or two candidate sites in a single differential interferogram. Conversely, in the interpretation result of Case 3, landslide candidate interference fringes detected by the CNN-B model averaged 46 sites in a single differential interferogram. In these areas, the ratios of the slopes, which were defined as 15 degrees or more in gradient, and the flatlands, which were defined as less than 15 degrees were 43% (approximately 20 sites) and 56% (approximately 26 sites), respectively. Because the ratios of the slopes and flatlands in the test data were 33% and 67%, respectively, the detection ratios of the interference fringes per unit area are higher on slopes.

For the sites misdetected on the flatlands and slopes, it is difficult to visually detect clear differences in the patterns of their respective interference fringes. However, compared to the flatlands, differences are more likely to appear on slopes where continuous interference fringes recognized as landslide candidates are characterized by step differences from neighboring areas. In addition, another cause could be the misdetection of noise as landslide candidate interference fringes; noise occurs because the coherence is lower on the slopes than on the flatlands.

5. CONCLUSIONS

In this study, we verified the possibility of detecting landslides from differential interferograms using CNN models. As a result, it was found that CNN models can detect interference fringes having the possibility of landslides with high reproducibility with recall values of approximately 90% in the validation case. However, landslide candidate interference fringes were detected in numbers larger than that of the training data, which shows that the precision is low. The image classification performance of this CNN model might be affected by the patterns of the landslide candidate interference fringes in the training data. In addition, interference fringes detected in the interpretation by the CNN model are more likely to be detected on slopes than on flatlands.

Therefore, CNN models with high recall values may be effective as a means of detecting interference fringes with the possibility of landslides from differential interferograms regularly observed over a wide area. However, the misdetection of noise is likely to occur on slopes because many landslide candidates are detected on slopes, which have lower coherences than flatlands. Therefore, it is necessary to further narrow down the interference fringes that are likely to be landslide movements from the landslide candidates detected by the CNN models based on features of the topography and geology related to landslides. Then, this model will be able to contribute to the efficient risk management of sediment disasters by prioritizing sites where on-site surveys and observations should be conducted.

However, because this study did not have sufficient training data for landslide candidates, it is difficult to say that a CNN models with high generalization have been established. Therefore, to improve the model performance, training data on interference fringes with various characteristics need to be increased. However, it is not easy to prepare a large amount of interference fringes with the possibility of landslides as training data. In this study, only differential interferograms were used as training data. However, it is sometimes difficult to detect interference fringes with the possibility of landslides only from differential interferograms. In reality, when experts detect interference fringes with the possibility of landslides, they also consider the topography and other characteristics of the site. Therefore, the use of other data such as topography for learning in addition to differential interferograms may enable more accurate detections of sites with the possibility of landslides.

Our challenge for the future is to study combinations of training data and learning methods appropriate for the detection of sites with the possibility of landslides and therefore improve the accuracy of the CNN models.

ACKNOWLEDGMENT: The authors appreciate JAXA (Japan Aerospace Exploration Agency) for provision of ALOS/PALSAR data. ALOS/PALSAR data belong to JAXA and METI (Ministry of Economy, Trade and Industry).

REFERENCES

David E. Rumelhart, Geoffrey E. Hinton and Ronald J. Williams (1986): Learning representations by back-propagating errors, Nature, No.323, pp.533-536

Geospatial Information Authority of Japan (2011): Manual for Interpretation of SAR Interference Images for Landslide Monitoring, http://www.gsi.go.jp/chirijoho/chirijoho40089.html (accessed November 15 2017)

Ishii, T., Nakamura, R., Nakada, H., Mochizuki., Y. and Ishikawa, H. (2015): Surface object recognition with CNN and SVM in Landsat 8 images, MVA2015 IAPR International Conference on Machine Vision Applications, pp.341-344.

Japan Aerospace Exploration Agenc HP: http://www.satnavi.jaxa.jp/project/alos4/ (accessed November 15 2017)

Kamiyama, J., Kunitomo, M., Sakagami, M., Nagai, Y., Hirata, I., Niahikawa, D., Yoshikawa, K. and Sango, D. (2016): A Study of Risk Assessment Method for Landslides etc. with InSAR Analysis, Proceedings of Research Meeting of Japan Society of Erosion Control Engineering, pp.B-484-485 (in Japanese)

Kamiyama, J., Noro, T., Sakagami, M., Mantoku, M., Hirata, I., Yoshikawa, K. and Sango, D. (2017): Verification of Applicability of the Large-scale Sediment Movement Risk Assessment Method by InSAR Analysis, Proceedings of Research Meeting of Japan Society of Erosion Control Engineering, pp.198-199 (in Japanese)

Krizhevsky, A., Sutskerver, I. and Hinton, G.E. (2012): ImageNet Classification with Deep Convolutional Neural Networks, Advances in Neural Information Processing Systems 25, pp.1106-1114.

Kusano, S., Sango, D., Yamanoguchi, T. and Shimada, M. (2015): A spatial filter adaptive to slope size applied to differential SAR interferograms for landslide detection, Japan Geoscience Union Meeting 2015, STT54-P-04 (in Japanese)

LeCun, Y., Bengio, Y. and Hinton, G. (2015): Deep learning, Nature, Vol.521, pp.436-444

National Spatial Planning and Regional Policy Bureau, MLIT of Japan (2011): elevation / gradient third mesh data of the National Land Numerical Information, http://nlftp.mlit.go.jp/ksj/gml/datalist/KsjTmplt-G04-a.html (accessed November 15 2017)

Okatani, T. (2016): Recent Research Trends on Deep Learning and Application Thereof to Image Recognition, http://acsi.hpcc.jp/2016/download/ACSI2016-tutorial2.pdf (accessed November 15 2017)

Shimada, M. (1999): Correction of the Satellite's State Vector and the Atmospheric Excess Path Delay in the SAR Interferometry - An Application to Surface Deformation Detection, Journal of the Geodetic Society of Japan, Vol.45 , No.4 , pp.327-346. (in Japanese with English abstract).

Suzuki, R. (2000 a) Chapter 12 General characteristics of hills and mountains, “Introduction to topographic map interpretation for construction engineers” volume 3 Terraces/ Hills/ Mountains, p.651-684, Kokonshoin

Suzuki, R. (2000 b) Chapter 15 15.6 Debris flow topography, “Introduction to topographic map interpretation for construction engineers” volume 3 Terraces/ Hills/ Mountains, p.849-860, Kokonshoin

Wilmanski, M., Krucher, C. and Lauer, J. (2016): Modern Approaches in Deep Learning for SAR ATR, SPIE 9843, Algorithms for Synthetic Aperture Radar Imagery XXIII, 98430N

Y. Zhou, H. Wang, F. Xu, and Y. Q. Jin (2016): Polarimetric SAR image classification using deep convolutional neural networks, IEEE Geoscience and Remote Sensing Letters, Vol.13, No.12, pp.1935-1939

Topic 6: Management for sustainable land use

A Quantitative Approach for Classifying Governance Unit of Watershed Management and Flood Mitigation Based on a Long-term Landslide Inventory

Cheng-Chien LIU[1, 2*], Ming-Hsun KO[2], Huei-Lin Wen[2], Kuei-Lin FU[3] and Shu-Ting CHANG[3]

[1] Dept. of Earth Sciences, National Cheng Kung University (Tainan, 70101 Taiwan)
[2] Global Earth Observation and Data Analysis Center, National Cheng Kung University (Tainan, 70101 Taiwan)
[3] Watershed Conservation and Management Division, Soil and Water Conservation Bureau (Nantou, 54044 Taiwan)
*Corresponding author. E-mail: ccliu88@mail.ncku.edu.tw

Extreme weather makes it difficult to estimate the intensity of typhoon rainfalls, which results in aggravating landslide potential and hazards in forested watersheds. To increase the efficiency of operations and management, it is needed to monitor landslide evolvement continuously, assess quantitatively the classification of landslides, as well as, establish landslide management plans. Take the Qingquan watershed in Wufeng Township, Hsinchu County for example, large-scale landslides occurred in four potential debris flow torrents when Typhoon Aere hit Taiwan in 2004. The Qingquan watershed is classified as 22 optimum watersheds after being processed by hydrologic analysis. The result from overlaying landslide data sheet of these 22 optimum watersheds from 2005 to 2016 shows major landslides occurred mostly during typhoon Aere. After typhoon Aere, vegetation recovery in the landslide zones was getting better, despite landslides occurred sporadically. Only in 2008, landslides occurred near Tuchang bulao caused severe damage. Two large-scale landslide zones, where the average rate of landslide occurrence is higher than 10%, are Debris-flow source areas. Several large-scale landslides occurred by two sides of Shangping Creek flowing through Tuchang bulao, Qingquan bulao, and Minduyou bulao, which are defined as low stability zone and severe landslide. Unstable levels determined by the long-term landslide data sheet of each watershed can serve as a tool to quantify the classification measures of mountain management and flood control of management units. Chinese version of this paper can be referred to [*Liu, et al.* 2017].

Key words: forest watershed, landslide susceptibility, landslide inventory, watershed management and flood mitigation, unstable index

1. INTRODUCTION

Extreme weather events caused by global warming intensify rainfalls. Together with high mountains, broken terrains, and frequent earthquakes, Taiwan has one of the highest erosion rates in the world [*Dadson, et al.* 2003] and is one of the places on Earth that is most vulnerable to landslides [*Dilley, et al.* 2005]. Taiwan's government, therefore, has been endeavoring to manage watersheds and mitigate the issue of flooding by developing various measures. This paper proposes a quantitative approach for classifying governance unit of watershed management and flood mitigation based on a long-term landslide inventory, with the intention to evaluate their effects and facilitate the planning.

Large-scale landslides occurred in four potential debris flow torrents in the Qingquan watershed in Hsinchu County when Typhoon Aere hit Taiwan in 2004. This watershed is classified as 22 optimum watersheds after being processed by hydrologic analysis. The result from overlaying landslide data sheet of these 22 optimum watersheds from 2005 to 2016 shows major landslides occurred mostly during Typhoon Aere. After Typhoon Aere, vegetation recovery in landslide areas was getting better, despite landslides occurred sporadically. Only in 2008, landslides occurred near Tuchang Tribe causing severe damage. Two large-scale landslide areas, where the average rate of landslide occurrence is higher than 10%, are debris-flow source areas. Several large-scale landslides occurred by two sides of Shangping Creek flowing through

Tuchang Tribe, Qingquan Tribe, and Minduyou Tribe, which are defined as low stability zone and severe landslide zone. Unstable levels determined by the long-term landslide data sheet of each watershed can serve as a tool to quantify the classification measures of mountain management and flood control of management units.

2. LANDSLIDE INVENTORY

To establish landslide database and assist Taiwan government in improving mountain management, disaster prevention, disaster reduction, and the restoration of degraded areas, the Forest Bureau had commissioned a 7-year project, Application of satellite optical imagery to islandwide landslide interpretation and disaster analysis, since 2011. By using the Formosat-2 owned and operated by Taiwan, images with a lower ratio of cloud coverage from 2005 to 2016 were selected based on the features of mobility as well as high spatiotemporal resolution. After having the selected images processed by the Formosat-2 automatic image processing system [*Liu* 2006] and the expert landslide and shaded area delineation system [*Liu* 2015] to interpret landslide disasters, this project establishes a 12-year regional landslide inventory.

Traditional fieldwork is time- and manpower-consuming and is unable to provide comprehensive information instantly. Manual delineation is the most accurate method to interpret landslide disasters [*Kumar, et al.* 2006, *Singhroy* 1995, *Singhroy, et al.* 1998] however, it inevitably generates inaccuracy and consumes time as well as manpower. Although automatic classification methods such as supervised classification [*Nichol and Wong* 2005, *Nichol and Wong* 2005], unsupervised classification [*Dymond, et al.* 2006], and ratio image [*Cheng, et al.* 2004] can save manpower and time, the accuracy is limited and the landslide inventory is therefore unreliable.

Through the normalized difference vegetation index (NDVI), the greenness index, and the intensity of panchromatic band, the expert landslide and shaded area delineation system [*Liu* 2015] can automatically and accurately delineate the non-vegetation area and the shaded area, as shown in **Fig. 1** Then, based on the concept of region growing, the unconnected data in the layer of non-vegetation area and shaded area can be separated into independent units by the system to generate geographic information. Then, in light of standard interpretation, experts' experiences, previous aerial images, 3D false-color image of Taiwan, and ASO Taiwan Image supplier and service System, interpreters select and cut potential landslide units to determine landslide location. Shadow as well as vector layer of landslide areas can be quickly selected and outputted. Not only can this method be used to reduce the time of manual delineation, but it also ensures the accuracy of manual interpretation. Through comparing with 25cm aerial photography manually interpreted in the same area by the Aerial Survey Office, the average accuracy is 98%.

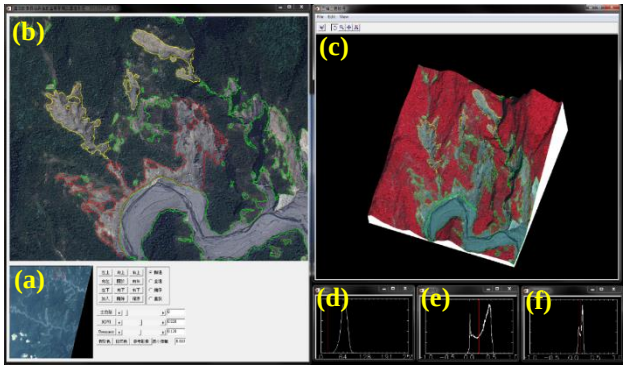

Fig. 1 Introduction to Expert Landslide and Shaded Area Delineation System and user interface. (a)True-color FORMOSAT-2 image; (b) In red frame, proposed image enhancement algorithms, maintaining same resolution as (a); (c) Standard false color composite processing of a digital terrain model could be transposed, rotated and scaled; (d) Histogram of the panchromatic image; (e) Histogram of NDVI; (f) Greenness histograms. The red line is defined by a local threshold determined by the system. The green line (non-vegetation area) and white line (shaded area) also are defined in the same method. Image interpreters would hit the red line, and export the blue line (shaded area) and the yellow line (landslide area) based on some data, such as the interpretation policy, expert experience, early stage images, 3D false color image of Taiwan, images from Taiwan Image Service and Supplier System [*Liu* 2015].

The aerial images shot by Formosat-2 from 2005 to 2016 and the landslide inventory are available to use after approval made by the Forest Bureau. The multi-temporal landslide inventory has been

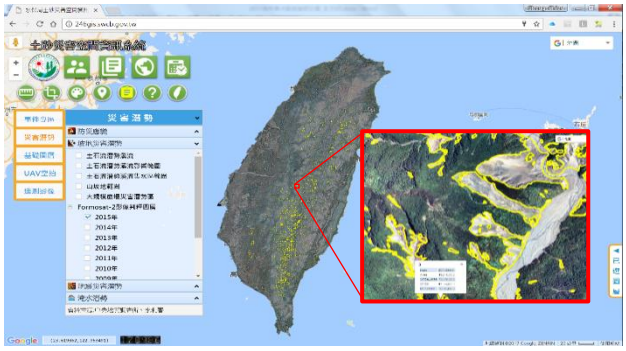

Fig. 2 Applied of satellite images shoot by FORMOSAT-2 from 2005 to 2016, and landslide data sheets of years. Vector tiles approved by Forestry Bureau are shared to the system built by SWCB.

published in the form of vector map on the Soil and Sand Disaster Spatial Information System (http://246gis.swcb.gov.tw) established by the Soil and Water Conservation Bureau (SWCB), as seen in **Fig. 2**.

3. APPROACH

3.1 Governance unit of watershed management and flood mitigation

The Soil and Water Conservation Bureau is responsible for soil conservation and flood mitigation in the upstream slopeland. To make the best use of budget, the government divides watersheds into governance units based on the classification of soil conservation and flood mitigation, and furthermore uses protected targets, potential debris flow torrent, and landslide ratio as standards to make a budget. The ratio standard and implementation strategy are shown in **Table 1**. Among all the standards of interpretation, some critical principles are associated with the condition of stability:

Table 1 Quantified the classification measure of mountain management and flood control of management units.

Class	Principle	Strategy
Maintenance area (level A): previous management has effectiveness; low disaster risk area	Initiation zone: landslides have been stabilized Transportation zone: the necking zone has been dredged Accumulation zone: the riverbed changes has been stabilized	The inspection and maintenance of structures The monitoring of watershed condition The program of disaster prevention and evacuation
Staging management area (level B): previous management has not completed, but the assessment shows the management is effective in reducing disaster risk	Initiation zone: the landslide rehabilitation has not been completed Transportation zone: partial necking zone is dredged Accumulation zone: the sediment deposition potential remains high	Yearly management project and rolling-wave planning The program of disaster prevention and evacuation
Fundamental protection area (level C): previous management has no obvious effectiveness; high disaster risk area	Initiation zone: Large landslides are difficult to rehabilitate so that engineering works cannot be carried out Transportation zone: large sediment production; the reoccurrence of necking zone Accumulation zone: the riverbed accumulation is serious	Adopting low intensity construction method before relocation Adopting temporary mitigation and prevention of disaster and fundamental disaster control Enhancing disaster prevention and evacuation

whether the landslide area has been rehabilitated and reaches stability; whether the necking zone has been dredged; whether the riverbed changes in the accumulation zone has been stabilized, or is the problem of accumulation still serious and the sediment deposition potential remains high? Since these critical principles are associated with stability, a method quantifying conditions of stability should be proposed.

Watersheds and gradients are used to divide areas while discussing landslides; however, the areas would be variant if discussed from different perspectives. From the perspective of debris flow, it can be divided into the initiation zone, the transportation zone, and the accumulation zone. From the perspective of geological condition, the classification standard includes the property of rock formation, the geological structure, and the cause of landslide. To avoid divergent policies made by distinct decision makers, there should be a general classification method for classifying governance units regarding geomorphologic characteristics of watershed.

3.2 Optimum Watershed

Concerning the work of mountain management and flood mitigation, classifying governance units of watershed is the principal task to have temporal and spatial variation under control, and quantifies whether governance units reach stability. With the condition fulfilled, the government is able to make a budget based on priority. The original aerial images used to produce landslide inventory may vary in different shooting periods depending on varied degree of cloud coverage, which will cause the aerial image variant at different times. A landslide area may be divided into two or more portions on account of the influence of cloud coverage. The variation of landslide cannot be interpreted correctly if we only analyze a certain landslide area. From the perspective of management, however, the government should classify all landslides with similar geomorphologic characteristics for regional governance. Since the areas that have not collapsed in landslide regions are crucial areas to determine whether the collapse will expand or occur in the future, it is necessary to make a plan, monitor, and manage. The task of classifying governance units of watershed means to establish a classification method.

This study proposes the method of classifying landslides based on the concept of optimum

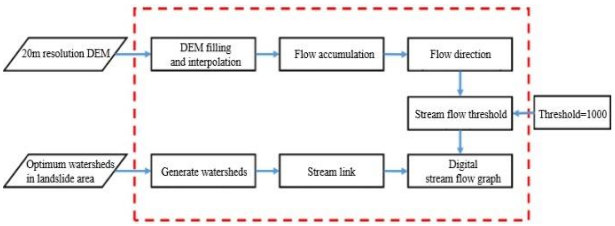

Fig. 3 The procedure of classifying watershed management units based on the optimum watershed size.

watershed. Initially, use Digital Elevation Model (DEM) to analyze accumulated flow, and then find suitable thresholds to determine the classification of watersheds. Once the amount of watershed

composed of severe landslide (10 hectares) reaches maximum value, the watershed classified based on the threshold of flow is the optimum watershed. The detailed procedure for classifying watershed management units is shown in **Fig. 3**.

The idea of classifying landslide area by optimum watershed is derived from the concept of hydrology. The DEM used in Taiwan has high accuracy and high resolution, making the data of hydrology as well as geomorphology more accessible to get. The numerical result reveals that even in distinct areas the outcome of result has its consistency and reproducibility. The concept of optimum watershed is firstly proposed to investigate the variation of landslides and correct the influence of shadow on landslide area in the project of "Application of satellite optical imagery to islandwide landslide interpretation and disaster analysis" delegated by the Forest Bureau. The range of optimum watershed is consistent with the "compartment boundary" set by the Forest Bureau.

3.3 Instability index

In terms of the size of observation area, we can use optimum watersheds to define and calculate the instability index as the standard deviation of annual landslide area. In terms of the time period of observation, we should use as much data obtained from 2005 to 2016 as we could to discuss the instability index. After processing the information of landslide variation, we can be certain that whether the quantification of slopelands qualify the condition of stability. One thing should be noted is that the area of each optimum watershed is distinct. Considering the influence of shadow in different periods varies dissimilarly, correcting the shadow is indispensable. The total area of landslide, however, cannot be compared directly. With the 12-year landslide inventory, we can determine the standard deviation of annual landslide area to get the result of landslide variation. If the value of standard deviation is low, it implies that the variation of the very landslide area is slight and relatively stable; in contrast, if the value of standard deviation is high, it implies that the variation of the very landslide area is huge and relatively unstable.

To represent varying degree of the stability, this study proposes to use the instability index with five levels shown as **Table 2** to deal with the statistics of standard deviation regarding the landslide area of optimum watersheds. Then, uses Jenks natural breaks classification method to calculate the instability index and determine the degree of stability of optimum watersheds in the research region. One point need to be emphasized is that the threshold determined by

Table 2 Grading scale chart of unstable levels.

Unstable levels	Grading scale	Explanation
1	Stable zone	Landslides never occurred or only a few landslides occur in this area with good natural restoration, not easily been destroyed
2	Low active landslide zone	Some landslides occur, but the area of landslide is small or the restoration of landslide becomes obvious
3	Unstable landslide zone	Some landslides occur with massive area of landslide, or the restoration of landslide is less obvious
4	Severe landslide zone	Massive area of landslide or the area where landslides occur frequently
5	Large-scale landslide area	The area where large-scale landslides occur

Jenks natural breaks classification method is not an absolute value and is not necessarily suitable for other research regions. However, we can get an absolute value if we analyze all the data of slopelands in Taiwan. By using the threshold, we can quantify the degree of variation of each governance unit, assess the hot spots where collapse easily take place, and update the latest upriver situation to evaluate current management practices and future planning.

4. RESULT AND DISCUSSION

Take the sub-watershed of Qingquan in Wufeng Township as example; Typhoon Aere devastated this area in 2004, causing four potential debris flow torrents and large-scale landslide. The main protected targets include Tuchang Tribe, Qingquan

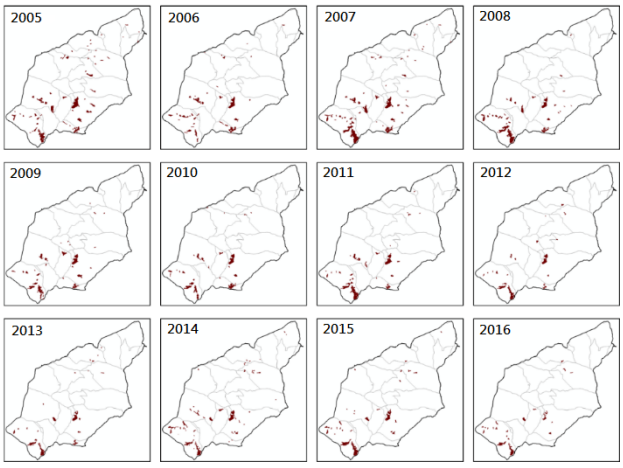

Fig. 4 Locations of landslides over years of 22 optimum watersheds of the Qingquan watershed in Wufeng Township, Hsinchu County.

Tribe and Minduyou Tribe. With the hydrological analysis and landslide layer interpreted from 2005 to 2016 as seen in **Fig. 4**, there was a severe landslide occurred during Typhoon Aere. In spite of fragmentary collapse, the landslide area gradually restored. The most serious natural disaster was the landslide near Tuchang Tribe in 2008.

We can get **Table 3** based on the result of instability index. There are two large-scale landslide areas in Qinquan watershed and the average landslide ratio is more than 10%. As for two sides of river embankment of the Shangping Creek, the average landslide ratio is between 2 to 5%. In light of the principle of classification, the Qinquan watershed is classified as region B+. Based on the classification method proposed in this study, the instability index of 22 optimum watersheds shows that a part of region is severe landslide zone whereas a part of region is stable zone. The result of analysis provides varied perspectives for current management and future planning.

Table 3 Landslide hazard areas of years and the unstable levels (UL) of 22 optimum watersheds of the Qingquan watershed in Wufeng Township, Hsinchu County.

No	Watershed Area (ha)	Landslide hazard areas of years (ha)												SD	UL
		2005	2006	2007	2008	2009	2010	2011	2012	2013	2014	2015	2016		
20894	11.23	0.37	0.00	0.26	0.00	0.00	0.00	0.00	0.00	0.00	0.00	0.00	0.00	0.01110	4
21735	324.94	9.36	5.81	9.98	6.36	3.81	4.11	4.75	1.46	2.56	4.05	2.71	1.80	0.00843	4
21897	372.25	18.69	11.93	14.92	11.09	11.71	11.19	10.75	7.65	7.41	10.33	9.08	3.93	0.01003	4
22062	108.72	1.13	1.11	1.52	1.04	2.51	1.14	0.95	0.00	0.00	1.30	0.54	0.70	0.00620	4
22253	298.04	16.24	10.24	29.37	29.58	15.86	15.17	21.38	14.67	12.43	16.27	19.87	13.98	0.02062	5
20610	150.57	0.53	0.42	0.28	0.00	0.00	0.00	0.00	0.00	0.00	0.27	0.16	0.00	0.00128	2
20759	11.29	0.18	0.00	0.29	0.33	0.00	0.00	0.21	0.00	0.14	0.00	0.00	0.00	0.01130	5
20928	163.21	0.47	0.10	0.00	0.00	0.19	0.00	0.00	0.70	0.71	0.36	0.36	0.38	0.00162	3
21045	89.31	0.32	0.01	0.00	0.00	0.00	0.00	0.00	0.00	0.00	0.26	0.00	0.00	0.00126	2
21084	106.23	0.11	0.00	0.00	0.00	0.00	0.00	0.00	0.00	0.00	0.00	0.00	0.00	0.00029	1
21100	155.90	1.84	1.10	1.42	0.00	0.00	0.39	0.00	0.10	0.20	0.00	0.00	0.00	0.00420	3
21191	270.83	1.16	0.23	0.50	0.00	0.51	0.18	0.70	0.47	0.29	1.27	1.09	0.83	0.00153	2
21414	145.41	2.46	0.00	1.47	0.54	0.00	0.27	0.00	0.00	0.10	0.42	0.70	0.00	0.00520	3
21704	277.64	0.83	0.00	0.32	0.36	0.21	0.00	0.00	0.20	0.00	0.11	0.00	0.00	0.00089	2
22057	76.77	4.40	5.41	5.81	4.12	3.36	5.82	2.34	1.40	2.07	0.23	0.00	0.00	0.02899	5
22061	7.39	0.12	0.12	0.17	0.00	0.00	0.00	0.00	0.00	0.00	0.00	0.00	0.00	0.00853	4
22191	117.37	0.06	0.21	0.39	0.00	0.31	0.00	0.00	0.00	0.00	0.00	0.00	0.00	0.00120	2
21628	73.18	0.00	0.16	0.00	0.00	0.39	0.00	0.00	0.77	0.00	0.00	0.00	0.00	0.00327	3
20713	175.81	0.00	0.00	0.45	0.00	0.00	0.00	0.00	0.00	0.00	0.00	0.00	0.00	0.00073	2
21512	58.93	0.00	0.00	0.17	0.00	0.00	0.00	0.12	0.00	0.00	0.00	0.00	0.00	0.00098	2
21793	10.98	0.00	0.00	0.00	0.00	0.00	0.01	0.00	0.00	0.00	0.00	0.00	0.00	0.00026	1
21320	207.05	0.00	0.00	0.00	0.00	0.00	0.00	0.00	0.00	0.00	0.20	0.22	0.00	0.00040	1

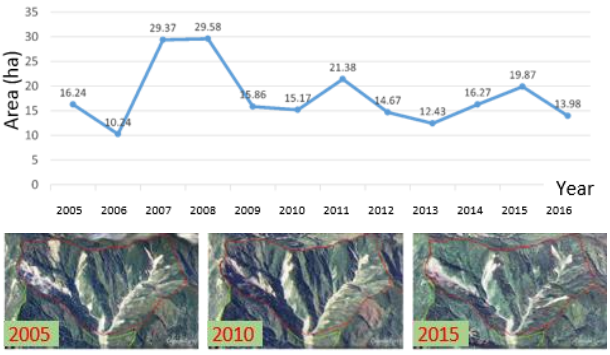

Fig. 5 Landslide hazard areas of years of optimum watershed, No.22253, of the Qingquan watershed in Wufeng Township, Hsinchu County, and its satellite images in 2005, 2010 and 2015. The unstable level is 5, and classified as large-scale landslide zone.

With historical images and topography, this study then nests the result of instability index in Google Earth to represent the large-scale landslide area. Take the optimum watershed of No. 22253 as an example (**Fig. 5**). Its original area is 298.01 hectares; after Typhoon Aere, the area of collapse is 16.24 hectares and the area keeps expanding to 29.58 hectares in 2007 to 2008, and the average landslide ratio is about 9.92%. The area of collapse remains 13.98 hectares until 2016. The instability index is five, which can be counted as large-scale landslide zone.

Take the optimum watershed of No. 21735 as an example (**Fig. 6**). Its original area is 324.94 hectares. The collapse is located in the tributary of Tuchang River and potential debris flow tureen of DF044. The historical curve chart reveals that the landslide area gradually stabilizes, from the area of 9.36 hectares in 2005 to the area of 3.81 hectares in 2009. The instability index is four, which can be

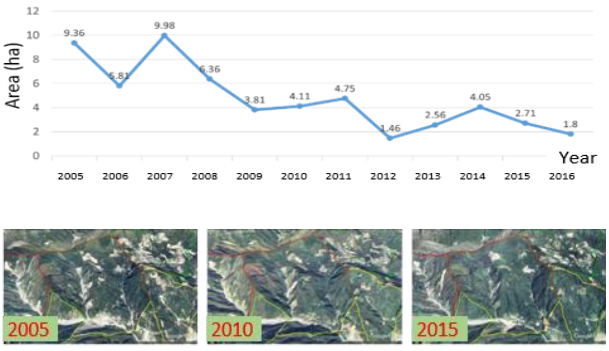

Fig. 6 Landslide hazard areas of years of optimum watershed, No. 21735, of the Qingquan watershed in Wufeng Township, Hsinchu County, and its satellite images in 2005, 2010 and 2015. The unstable level is 4, and classified as severe landslide zone.

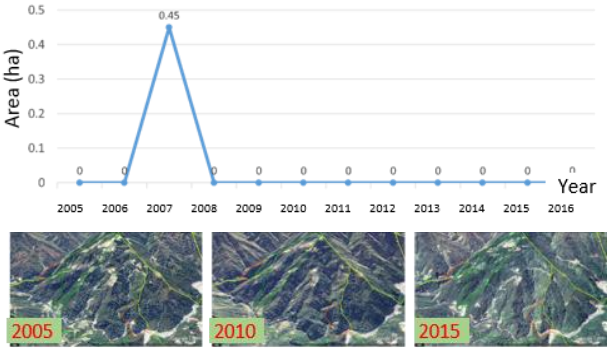

Fig. 7 Landslide hazard areas of years of optimum watershed, No. 20713, of the Qingquan watershed in Wufeng Township, Hsinchu County, and its satellite images in 2005, 2010 and 2015. The unstable level is 2, and classified as stable zone.

counted as severe landslide zone. Then, take the optimum watershed of No. 20713 as an example (**Fig. 7**). The area of watershed is 175.81 hectares. Maipalai Creek is seldom influenced by rainfall on account of the location of leeward. This area is stable, except the collapse (the area of 0.45) in 2007. The instability index is 2, which can be counted as stable zone.

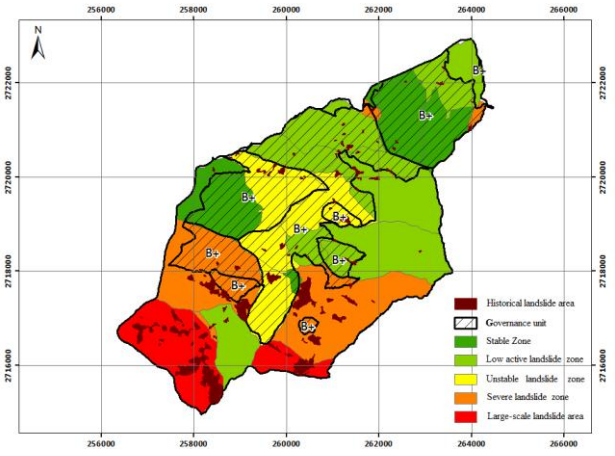

Fig. 8 The outcome of applying the classification qualified measures of mountain management and flood control of management units to watersheds of the Qingquan watershed in Wufeng Township, Hsinchu County.

Fig. 8 shows the quantified result of 22 optimum watersheds in Qinquan watershed by using the classification method proposed in this study. The multi-temporal landslide inventory of 2005-2016 reveals that numerous significant landslide events took place in Qinquan watershed; nonetheless, the distribution of collapse is not even, for it mainly takes place in optimum watersheds.

The slash and grid blocks represent the region B+. Most of the areas are relatively stable, whereas some collapse events take place in a few optimum watersheds. The instability index quantifies the trend of collapse in each district over time, which not only highlights the location of hot spot but also helps to find the regions where the collapse continues to deteriorate, to stabilize or to restore. This study demonstrates that quantifying the instability index based on multi-temporal landslide inventory provides the method of quantification and grading for mountain management and flood mitigation.

This study proposes a method of classification as well as grading based on multi-temporal landslide inventory by taking Qinquan watershed as an example to demonstrate that the instability index is able to quantify collapse in each district over time. However, the thresholds determined by the Jenks natural breaks classification method is not an absolute value, which is primarily used to assess the hot spots in regions where the collapse easily takes place. Therefore, the thresholds are not necessarily suitable for other research regions. In the future, an absolute threshold will be acquired after analyzing the data of the slopelands in Taiwan. With the thresholds, the geomorphology variation of each governance unit can be quantified and analyzed, and the main hot spots of collapse can be evaluated. Additionally, after the completion of engineering, the thresholds can be used to update the upriver situation for the purpose of evaluating current and future strategies in terms of management as well as planning.

The engineering mainly centers on the region where collapse easily takes place. The method of comparing the area of management with the area of landslide or the area of watershed is not an ideal way to highlight the effectiveness of management.

Suppose applying the method proposed in this study to divide the watershed into optimum watersheds and find out unstable or severe landslide area by using the instability of index. The variation of landslide area before and after engineering can be analyzed and the standard deviation can be calculated, which reveals that the instability index of optimum watersheds is apparently decreased, manifesting the effectiveness of management and the achievement of quantitative evaluation.

While applying the aerial images shoot by Formosat-2 from 2005 to 2016 and the multi-temporal landslide inventory, it should be aware that the result might vary because of varied degree of cloud coverage. To acquire the variation of landslide area, it is necessary to consider the influence of shadow and revise the area of landslide. Furthermore, the following conditions should be taken into consideration when referring to the task of mountain management and flood mitigation: controlling the landslide condition in initiation zone, getting through the bottleneck in transportation zone and analyzing the variation of river. Similarly, the river as well as the area of vegetation should be taken into account while calculating the instability index. Apart from the discussion of landslides caused by natural disasters, how to quantify the influence of human development and the importance of protected targets are goals worth striving for.

5. CONCLUDING REMARKS

This paper demonstrates that the unstable levels determined by the long-term landslide data sheet of each watershed can serve as a tool to quantify the classification measures of mountain management

and flood control of management units.

ACKNOWLEDGMENT: This research is funded by Soil and Water Conservation Bureau, Council of Agriculture, Taiwan ROC, under Contract Nos. 106AS-7.3.1-SB-S2, as well as Ministry of Science and Technology of Taiwan ROC, under Contract Nos. MoST 106-2628-M-006-002. Chinese version of this paper can be referred to [*Liu, et al.* 2017].

REFERENCES

Cheng, K. S., C. Wei, and S. C. Chang (2004): Locating Landslides Using Multi-Temporal Satellite Images, in Monitoring of Changes Related to Natural and Manmade Hazards Using Space Technology. Kidlington, Oxford, U.K.: Elsevier, pp. 296-301.

Dadson, S. J., N. Hovius, H. Chen, W. B. Dade, M.-L. Hsieh, S. D. Willett, J.-C. Hu, M.-J. Horng, M.-C. Chen, C. P. Stark, D. Lague, and J.-C. Lin (2003): Links between Erosion, Runoff Variability and Seismicity in the Taiwan Orogen, Nature, 426, pp. 648-651.

Dilley, M., R. S. Chen, U. Deichmann, A. L. Lerner-Lam, M. Arnold, J. Agwe, P. Buys, O. Kjekstad, B. Lyon, and G. Yetman (2005): Natural Disaster Hotspots: A Global Risk Analysis, pp. 29.

Dymond, J. R., A. G. Ausseil, J. D. Shepherd, and L. Buettner (2006): Validation of a Region-Wide Model of Landslide Susceptibility in the Manawatu-Wanganui Region of New Zealand, Geomorphology, 74, pp. 70-79.

Kumar, K. V., T. R. Martha, and P. S. Roy (2006): Mapping Damage in the Jammu and Kashmir Caused by 8 October 2005 M-W 7.3 Earthquake from the Cartosat-1 and Resourcesat-1 Imagery, International Journal of Remote Sensing, 27, pp. 4449-4459.

Liu, C.-C. (2006): Processing of Formosat-2 Daily Revisit Imagery for Site Surveillance, IEEE Transactions on Geoscience and Remote Sensing, 44, pp. 3206-3214.

Liu, C.-C. (2015): Preparing a Landslide and Shadow Inventory Map from High-Spatial-Resolution Imagery Facilitated by an Expert System, Journal of Applied Remote Sensing, 9, pp. 096080-096080.

Liu, C.-C., M.-H. Ko, H.-L. Wen, K.-L. Fu, and S.-T. Chang (2017): A Quantitative Approach for Classifying Governance Unit of Watershed Management and Flood Mitigation Based on a Long-Term Landslide Inventory, Taiwan Forestry Research Institute, Taipei: Taiwan Forestry Research Institute, pp. 75-92. (in Chinese with English abstract)

Nichol, J., and M. S. Wong (2005): Detection and Interpretation of Landslides Using Satellite Images, Land Degradation & Development, 16, pp. 243-255.

Nichol, J., and M. S. Wong (2005): Satellite Remote Sensing for Detailed Landslide Inventories Using Change Detection and Image Fusion, International Journal of Remote Sensing, 26, pp. 1913-1926.

Singhroy, V. (1995): Sar Integrated Techniques for Geohazard Assessment, in Natural Hazards: Monitoring and Assessment Using Remote Sensing Technique, ed. by R. P. Singh, and R. Furrer, pp. 67-78.

Singhroy, V., K. E. Mattar, and A. L. Gray (1998): Landslide Characterisation in Canada Using Interferometric Sar and Combined Sar and Tm Images, in Remote Sensing: Inversion Problems and Natural Hazards, ed. by J. Susskind, V. Singhroy, and S. Tanaka, pp. 465-476.

INTERPRAEVENT2018 in the Pacific Rim

-Large scale sediment disasters in orogenic zones and countermeasures-

Date: October 1-4,2018 in Toyama,Japan

Published and copyrighted by
The Organizing Committee of INTERPRAEVENT 2018

Edited by
The Editorial Board of INTERPRAEVENT 2018
Chairman: Dr.Takashi YAMADA